Yukikazu Iwasa

Case Studies in Superconducting Magnets

Design and Operational Issues

Second Edition

Springer

Case Studies in Superconducting Magnets

Design and Operational Issues

Second Edition

Cover Design The blue and red shades of the covers symbolize, respectively, low- and high-temperature superconducting (LTS/HTS) magnets. The drawings of two magnets, by Wooseok Kim (SNU), represent, left to right, a 1.1 GHz and a 1.3 GHz LTS/HTS NMR magnet, both to be sequentially completed in the 2010s at the M.I.T. Francis Bitter Magnet Laboratory under the sponsorship of the National Institutes of Health. The magnet drawings, in-scale and in proportion to each other, are based on designs of a 500 MHz and a 700 MHz LTS magnet (both in mauve) by Masatoshi Yoshikawa (JASTEC) and that of a 600 MHz HTS insert (in light pink) by Seungyong Hahn (FBML).

ISBN 978-0-387-09799-2

Yukikazu Iwasa

Case Studies in Superconducting Magnets

Design and Operational Issues

Second Edition

Springer

Yukikazu Iwasa
Francis Bitter Magnet Laboratory
Massachusetts Institute of Technology
Cambridge, MA
USA

ISBN: 978-0-387-09799-2 e-ISBN: 978-0-387-09800-5
DOI: 10.1007/b112047

Library of Congress Control Number: 2009922081

Printed on acid-free paper.

springer.com

Preface to the Second Edition

The Second Edition, as was the First Edition, is based on *Superconducting Magnets*, a graduate course in the Department of Mechanical Engineering at the Massachusetts Institute of Technology that I started teaching in 1989, after the discovery of high-temperature superconductors (HTS); in this book I'm classifying MgB_2, a superconductor with a critical temperature of 39 K, as an HTS. The book, intended for graduate students and professional engineers, covers the basic design and operational issues of superconducting magnet technology.

As prefaced in the 1st Edition, the student in the course was assigned many "tutorial" problems to review lecture materials, to discuss topics in more depth than covered in the lecture, or to teach subjects not presented in the lecture at all. Because the use of tutorial problems accompanied, a week later, by solutions has been successful in the course, this format, adopted in the 1st Edition, is maintained in the 2nd Edition. In the new edition, most problems in the 1st Edition have been retained, either as Problems or converted to *Discussions*, to which more topics in the form of Problems & *Discussions* have been added. Because the principal magnet projects at the Francis Bitter National Magnet Laboratory (FBNML), until 1995, and Francis Bitter Magnet Laboratory (FBML) thereafter, have chiefly been high-field *DC* solenoidal magnets, problems directly related to other applications, with a few exceptions, are not represented. However, important topics covered in this book, particularly on field distribution, magnets, force, thermal stability, dissipation, and protection, are sufficiently basic and generic in concept that solenoidal magnets are suitable examples.

The 2nd Edition is more than 200 pages longer than the 1st Edition for four reasons: 1) included now are topics that should have been covered but were omitted in the 1st Edition; 2) new materials, relevant and applicable chiefly to HTS magnets, are added; 3) some concepts are given fuller explanations; and 4) more homework and quiz problems, created since 1995, are incorporated. This time the presentation should be significantly improved and afflicted with far fewer (but alas, *not* free of) errors and typos than previously. Encountering the reader of the 1st Edition, I often had to warn him/her of many errors, stating, though, that these errors would in most part be obvious if the book was read with eyes wide open.

It took less than 18 months to complete the 1st Edition—the project began in May of 1993, and the textbook came out in October 1994; by contrast, it has taken more than 10 years to complete the 2nd Edition, starting in 1997 with the rewriting and expansion of *Chapter 3*. In preparing both editions, I relied heavily on the magnet projects with which I was personally involved, and am indebted to my colleagues, the members of the Magnet Technology Division, past (FBNML) and recent (FBML): the past members included John Williams, Mat Leupold, Emanuel Bobrov, David Johnson, Vlad Stejskal, Andy Szczepanowski, Mel Vestal, Robert Weggel, and Alex Zhukovsky; recent members include Juan Bascuñán, my friend and colleague the late Emanuel Bobrov (1936–2008), David Johnson, Haigun Lee (now at the Korea University, Seoul), Seungyong Hahn, and Weijun Yao.

During the more than 10 years writing this new edition, many people helped me to complete it. In our Division, I would particularly thank: Juan going through the entire book more than once, checking carefully axial force equations involving complete elliptic integrals, and providing many cryogenic data; Emanuel for his suggestion that axial force formulas be included in the new edition and that they are derivable from equations given in a paper by Milan Wayne Garrett; Haigun for thoroughly going through and finding many errors in early drafts; Weijun for key inputs in early chapters; and most of all Seungyong for his incisive critiques on many key issues and helpful suggestions for improvement. Many recent visitors and postdoctoral fellows made contributions to the new edition, particularly: Min Cheol Ahn for many graphs and help in preparing the Index; Wooseok Kim (now at Seoul National University) and Frederic Trillaud (now at Lawrence Berkeley National Laboratory) for graphs; and Ryuya Ando (Hitachi Ltd.) for cryogenic data. Also my former student Benjamin Haid (now at Lawrence Livermore National Laboratory) contributed to this new edition. Robert Weggel went through the entire text several times not only looking for typos and errors but also, more importantly, making critical comments and suggestions, and checking several versions of the Index. To them, my deepest gratitude.

From members of the Plasma Science and Fusion Center, across the street from the Magnet Lab, I received many valuable inputs: Joe Minervini (who taught the course while it was also a graduate course in the Department of Nuclear Engineering), Joel Schultz, Makoto Takayasu, Chen-Yu Gung, Brad Smith, and Alex Zhukovsky. I thank them for their contributions.

From my colleagues and friends outside M.I.T. I also received valuable contributions and I thank them: Dr. Luca Bottura of CERN for figures and data; Dr. Masaki Suenaga of Brookhaven National Laboratory and Prof. Kazuo Funaki of Kyushu University on AC losses; Drs. Hans Schneider-Muntau, Mark Bird, and John Miller (then) of the National High Magnetic Field Laboratory (NHMFL) on their water-cooled magnets and the 45-T hybrid magnet; Dr. Chris Rey of Oak Ridge National Laboratory on magnetic separation; Prof. Hiroyuki Fujishiro of Iwate University for electrical resistivity data for solder materials (*CHAPTER* 7); Prof. Atsushi Ishiyama of Waseda University, Dr. Robert Duckworth of Oak Ridge National Laboratory, and Dr. Xiaorong Wang of NHMFL for their experimental results on normal zone propagation in HTS test samples used in *CHAPTER* 8.

I also thank the following friends for reviewing selected chapter drafts and making valuable suggestions: Dr. Michael Gouge of Oak Ridge National Laboratory, Dr. François-Paul Juster of the Commissariat à l'Energie Atomique (CEA), Saclay, Prof. John Pfotenhauer of the University of Wisconsin, Dr. Soren Prestemon of Lawrence Berkeley National Laboratory, and Dr. Martin Wilson.

Since 1995, our projects have focused principally on HTS magnets, their specific design and operation issues, e.g., protection, and their applications to advanced NMR and MRI magnets. These magnet projects have been inspired by our Division's close association with Prof. Robert Griffin, Director of FBML and M.I.T. Department of Chemistry; Prof. Gerhard Wagner of Harvard Medical School; and Prof. David Cory of M.I.T. Department of Nuclear Science & Engineering.

The protection projects were supported initially by the Department of Energy, then until recently by the Air Force Office of Scientific Research. The NMR and MRI magnet projects have been supported by two branches of the National Institutes of Health, and recently the third branch as well. I am particularly indebted to Dr. Abraham Levy of the National Center for Research Resources (NCRR); Dr. Alan McLaughlin of the National Institute of Biomedical Imaging and Bioengineering (NIBIB); and Dr. Janna Wehrle of the National Institute of General Medical Sciences (NIGMS), all for their keen interest in and commitment to our magnet programs.

A large portion of the writing project, including lectures based on draft chapters, was done at the CEA Saclay, every year since 2001, in the Accelerator, Cryogenics and Magnetism Department (SACM). I thank not only the friendship of my colleagues in the SACM, particularly Drs. François Kircher, Antoine Daël, and Jean-Michel Rifflet, but also for this wonderful opportunity. In early 2000s I used draft chapters for lectures at the Applied Superconductivity Laboratory of the Institute of Electrical Engineering, Chinese Academy of Sciences, and I thank Profs. Luguang Yan, Liangzhen Lin, Liye Xiao, and Qiuliang Wang for the opportunity. Beginning 2005 I also used draft chapters for three lecture series in the Applied Superconductivity Laboratory of the Southwest Jiaotong University, Chengdu, and I thank Profs. Jiasu Wang, Suyu Wang, and their students.

In this new edition, in addition to quotations, I inserted several "Passages" and *Trivia*s to: 1) add another perspective to the subject matter under discussion; and 2) fill out the bottom space in the page to begin fresh on the next page a new subject or sub-subject. Two prominent sources are: 1) Francis Bitter, who published in 1959 a small book on magnets primarily for high school students; and 2) Isaac Asimov, arguably *the* most prolific writer of the 20$^{\text{th}}$ century on *every* subject. Several anecdotal quotations in *Trivia*s come from Asimov's writing.

Finally, I would express a word of appreciation to Kimiko, who has made it possible for me to continue working on this project at home with minimum household chore requests, enabling me to complete this new edition.

Yukikazu Iwasa
Weston, Massachusetts
January, 2009

"You know nothing till you prove it! FLY!" —Jonathan Livingston

To the Memory of My Parents,

Seizaburo and Shizuko Iwasa

and

To Future Generations, including

Erina, Alexa, Max,

Who Will Surely Benefit from More Things Superconducting

"Man plans, God laughs." —Old proverb

Contents

LIST OF PROBLEMS & DISCUSSIONS

SELECTED FIGURES & TABLES IN *CHAPTERS 1–9* OF GENERAL INTEREST

Tables of Complete Elliptic Integrals

TRIVIA (ANSWER) . . . . . .

Chapter 1

Superconducting Magnet Technology

1.1 Introductory Remarks

Superconducting magnet technology deals with the design, manufacture, and operation of superconducting magnets. A superconducting magnet is a highly stressed device: it requires the best that engineering has to offer to ensure that it operates successfully, is reliable, and at the same time is economically viable. A typical 10-tesla magnet is subjected to an equivalent magnetic pressure of 40 MPa (nearly 400 atm), whether it operates superconductively at 4.2 K (liquid helium) or 77 K (liquid nitrogen), or resistively at room temperature. Superconducting magnet technology is interdisciplinary in that it requires knowledge and training in many fields of engineering—mechanical, electrical, cryogenic, and materials.

Table 1.1 lists "first" events relevant to superconducting magnet technology. Particularly noteworthy events since the discovery of superconductivity in 1911 by Kamerlingh Onnes, who was also first to liquefy helium in 1908, are as follows:

1. Water-cooled 10-T electromagnets: Francis Bitter, the 1930s;
2. Large-scale helium liquefiers: Collins, the late 1940s;
3. Magnet-grade superconductors: Kunzler, et al., the early 1960s;
4. Cryostability of magnets: Stekly, the mid 1960s;
5. High-temperature superconductivity (HTS): Müller and Bednorz, 1986.

Although "Bitter" electromagnets, resistive and water-cooled, operate at room temperature, we may safely state that Bitter initiated modern magnet technology. Soon after the availability of Collins liquefiers, liquid helium—until then a highly prized research commodity available only in a few research centers—became widely available and helped to propel the rapidly growing field of low temperature physics. Many important superconductors were discovered in the 1950s, leading to the development in the 1960s of magnet-grade superconductors that continues today.

The formulation of design principles for cryostable magnets by Stekly and others by the mid 1960s was perhaps the single most important step in the early stage of superconducting magnet technology. It definitely helped transform superconductivity from a scientific curiosity to a realistic engineering option. Advances in superconducting magnet technology since then have succeeded in developing "high-performance" ("adiabatic," i.e., non-cryostable) magnets that now dominate most "marketplace" superconducting magnets.

The discovery of HTS lifted superconducting magnet technology from the depth of a liquid helium well. Together with advances in cryocooler technology, it has accelerated the development of "dry"(cryogen-free) superconducting magnets, HTS as well as low-temperature superconductor (LTS), refrigerated by cryocoolers—"cryocooled." In this early part of the 21st century, it is believed firmly by some and hoped fervently by many others that HTS will finally succeed in applications that LTS was once expected to but did not.

Y. Iwasa, *Case Studies in Superconducting Magnets: Design and Operational Issues*,
DOI: 10.1007/b112047_1,

Table 1.1: "First" Events Relevant To Superconducting Magnet Technology

Decade	*Event**
1930s	Meissner effect
	Type II low-temperature superconductors (LTS) identified
	Phenomenological theories of superconductivity
	Bitter electromagnets generating fields up to 10 tesla
1940s	Marketing of Collins helium liquefiers
1950s	Many more Type II LTS discovered
	GLAG and BCS theories of superconductivity
	Small superconducting magnets
1960s	Magnet-grade superconductors, e.g., NbTi, Nb_3Sn, developed
	National Magnet Laboratory established
	Bitter magnets generating fields up to 22 T (25 T with iron poles)
	Flux jumps in LTS
	LTS/normal metal composite superconductors
	Formulation of cryostability criteria
	Large cryostable LTS magnets (MHD and bubble chambers)
	Superconducting electric generators
	Magnets wound with internally-cooled LTS
	Multifilamentary NbTi/Cu superconductors
1970s	Multifilamentary Nb_3Sn/Cu superconductors
	Maglev test vehicles
	Superconducting dipoles and quadrupoles for accelerators
	Cable-in-conduit (CIC) conductors
	Hybrid magnets generating 30 T
	Commercial NMR systems using LTS magnets
1980s	Commercial MRI systems using LTS magnets
	Multinational experiments on fusion LTS magnets $\Longrightarrow$ITER (2001)
	Submicron superconductors for 60-Hz applications
	Superconducting accelerators
	Discovery of HTS
1990s	BSCCO-2223/Ag composite tape; magnets (1–7 T)
	"Cryocooled" "dry" magnets, LTS and HTS
	YBCO coated conductor
	45-T hybrid magnet
2000–	Discovery of MgB_2 "metalloid" superconductor ($T_c = 39$ K)
	HTS demonstration devices, e.g., cables; transformers; motors
	High-resolution 900 MHz–1 GHz all-LTS NMR magnets
	High-resolution LTS/HTS NMR magnets under development
	High-field MRI magnets for cerebral imaging
	Operation of Large Hadron Collider (LHC)

* Entries in each decade did not necessarily take place sequentially as listed. Acronyms are described in the Glossary (***Appendix VI***).

1.2 Superconductivity

The complete absence of electrical resistivity for the passage of direct current below a certain "critical" temperature (usually designated with the symbol T_c) is the basic premise of superconductivity. In addition to T_c, the critical field H_c and critical current density J_c are two other parameters that define a critical surface below which the superconducting phase can exist—see **1.2.4**. T_c and H_c are thermodynamic properties that for a given superconducting material are invariant to metallurgical processing; J_c is not. Indeed the key contribution of Kunzler and others in 1961 was to demonstrate that for certain superconductors it is possible to enhance J_c dramatically by means of metallurgy alone. No formal theories of superconductivity, phenomenological or microscopic, will be presented in this book to explain relationships among T_c, H_c, or J_c; however, the magnetic behavior of superconductivity, which plays a key role in superconducting magnets, will be briefly reviewed by means of simple theoretical models.

1.2.1 Meissner Effect

Discovered by Meissner and Ochsenfeld in 1934, the Meissner effect describes the absence of magnetic induction (B) within the bulk of a superconductor, i.e., $B=0$. This complete diamagnetism of a superconductor is in fact more fundamental than the complete absence of electrical resistivity (ρ), i.e., $\rho=0$, to the extent that a material's perfect diamagnetism *automatically* requires it to be a perfect electrical conductor. The Meissner effect, created by surface supercurrent, is observed in both Type I and Type II superconductors—see **1.2.3**. In Type I superconductors the Meissner effect is present up to the bulk thermodynamic critical magnetic field, H_c, while in Type II superconductors only up to the lower critical field, H_{c1}, beyond which the field penetrates into the bulk, until the field penetration is complete at the upper critical field, H_{c2}, at which point the Type II superconductor is completely in the normal state.

Figure 1.1a (top) illustrates a phase diagram of field, H, and temperature, T, for two spheres. The "critical temperature," T_c, divides two regions for both spheres: for $T<T_c$, one sphere, a superconductor (Sc), becomes superconducting ($B=0$), while the other, a perfect conductor (Pc), becomes perfectly conducting ($\rho=0$). The properties of both spheres are independent of H.

Figure 1.1b illustrates the magnetic field profiles of the Sc sphere as its H-T phase is changed A⇒B⇒C⇒D: the sphere satisfies its $B=0$ condition at C by inducing a surface current—its distribution is studied in ***CHAPTER 2***. With zero field in D this current also becomes zero. Figure 1.1c illustrates the field profiles of the Pc sphere for the same sequence of phase changes: the sphere maintains a constant field profile during the sequence B⇒C⇒D, implying $\partial B/\partial t = 0$, the condition consistent with $\rho=0$. Figure 1.1d illustrates another sequence for Sc or Pc. Here the initial field condition at A and D of $B=0$ or $\partial B/\partial t=0$ is preserved at C by a surface current of the same spatial distribution as that of the Sc sphere. Note that the field profiles of the Sc sphere actually do not depend on the sphere's initial condition or sequence of phase changes, while those of the Pc sphere do, as seen in those corresponding to C and D of Figs. 1.1c and 1.1d.

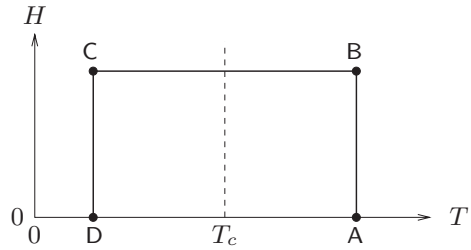

(a)

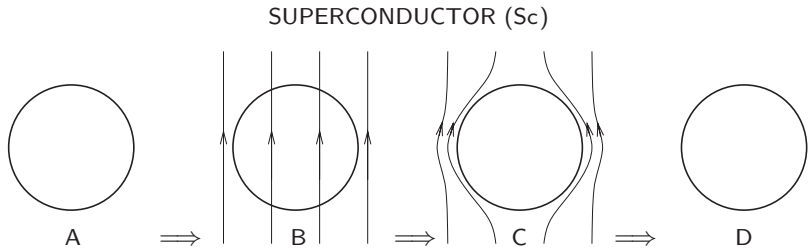

(b)

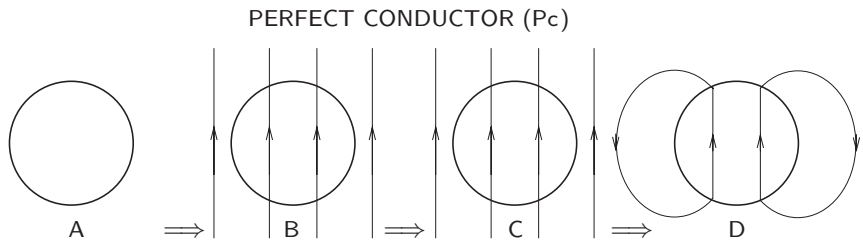

(c)

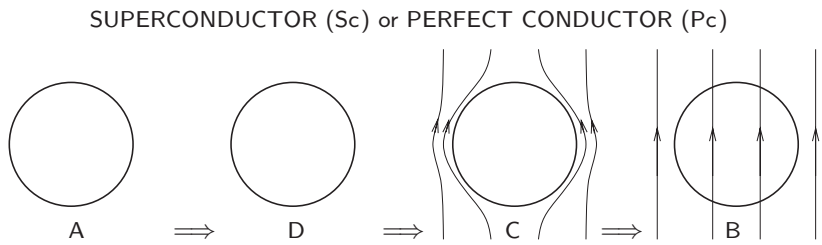

(d)

Fig. 1.1 (a): H-T phase diagram for two spheres, one a superconductor (Sc) and the other a perfect conductor (Pc), respectively, when $T < T_c$. (b): field profile of the Sc sphere for a sequence of H-T environments A⇒B⇒C⇒D. (c): field profiles of Pc for the same sequence of environments. (d): field profiles of Sc or Pc for sequence A⇒D⇒C⇒B. At points C (b) for the Sc sphere, D (c) for the Pc sphere, and C (d) for both the Sc and Pc spheres, a surface current is induced in the sphere to meet either the requirement of $B=0$ or $\partial B/\partial t=0$. The field profiles in (b)–(d) are schematic.

1.2.2 London's Theory of Superconductivity

Although a microscopic theory of superconductivity by Bardeen, Cooper, and Schrieffer—known as the BCS theory—was not completed until 1957, development of phenomenological theories of superconductivity began in the 1930s. Among these is the electromagnetic theory of London (1935), in which the concept of penetration depth was introduced to account for the Meissner effect. Simply stated, a bulk superconductor is shielded completely from an external magnetic field by a supercurrent that flows within the penetration depth (λ) at the surface. According to London's theory, λ is given by:

$$\lambda = \sqrt{\frac{m}{\mu_\circ e^2 n_{se}}} \tag{1.1}$$

where m and e are the electron mass (9.11×10^{-31} kg) and charge (1.60×10^{-19} C); $\mu_\circ$ is the permeability of free space ($4\pi\times10^{-7}$ H/m). Here, the density of superconducting electrons, n_{se}, is different from that of the free electrons, n_{fe}, being all fully superconducting at $T=0$ and zero at T_c. For a qualitative estimation in **PROBLEM 2.2** (***CHAPTER 2***) we may equate n_{se} to n_{fe} electrons, given by:

$$n_{se} \approx n_{fe} = \frac{\varrho N_A}{W_A} \tag{1.2}$$

where ϱ is the conductor's mass density [g/cm^3], N_A is Avogadro's number (6.023×10^{23} (particle/mole), and W_A is its atomic weight [g/mole]. The superconducting current density, J_s, is given by $en_{se}v \approx en_{fe}v$, where v is the drift velocity of superconducting electrons. Approximate values of λ and J_s for lead, a Type I superconductor (see below), are computed in In **PROBLEM 2.2**.

1.2.3 Type I and Type II Superconductors

Kamerlingh Onnes, in 1911, discovered superconductivity in pure mercury; subsequently other metals such as lead and indium were found to be superconductors. These materials, now called Type I superconductors, are unsuitable as magnet conductor materials because of their low H_c values: typically less than 10^5 A/m (or $\sim$0.1 T). Magnet-grade superconductors, described below (**1.3**), trace their origin to the first Type II superconductor discovered by de Haas and Voogd in 1930 in an alloy of lead and bismuth [1.1].

A Type II superconductor may be modeled as a finely divided mixture ("mixed state") of a Type I superconductor and normal conducting material. Indeed, in the early 1960s there were two physical models for this mixed state: lamina and island (vortex). In the lamina model, proposed by Goodman, a Type II superconductor consists of superconducting laminae separated by normal laminae. In the vortex model, proposed by Abrikosov [1.2], and later experimentally verified by Essmann and Träuble [1.3], the superconductor consists of many hexagonally-arranged normal-state "islets" in a superconducting sea. For the Type II superconductor to retain its bulk superconductivity well beyond 0.1 T, the radius of each normal-state islet must be smaller than λ. The islet's radius is the coherence length

(ξ), a spatial parameter, introduced by Pippard in 1953: it defines the distance over which the superconducting-normal transition takes place. According to the GLAG (after Ginsburg, Landau, Abrikosov, Gorkov) theory of superconductivity, formulated to account for the magnetic behavior of Type II superconductors, a superconductor is Type II if $\xi < \sqrt{2}\lambda$; it is Type I if $\xi > \sqrt{2}\lambda$. ξ decreases with alloying, which shortens the mean free path of the normal electrons and is inversely proportional to the material's normal-state electrical resistivity. The two magnet-grade superconductors—alloys of niobium titanium (NbTi) and an intermetallic compound of niobium and tin (Nb_3Sn)—have normal-state resistivities that are at least one order of magnitude greater than that of copper at room temperature. It has been noted that every HTS has ξ much smaller than λ.

DC and AC Responses

Figure 1.2 shows schematic drawings of three superconducting rods—Type I (Fig. 1.2a) and Type II (Figs. 1.2b, 1.2c)—each carrying a transport current that is less than its critical current. In the Type I rod (Fig. 1.2a), the current, DC or AC, flows only at the surface (within the London penetration depth) and generates no dissipation. In the Type II rod, DC current (Fig. 1.2b), though flowing over the entire rod, also generates no dissipation despite the presence of many normal-state (resistive) regions. We may picture "superconducting electrons" in the rod gliding through the material, dodging the normal-state regions. In terms of a circuit model, we may picture these resistive islets to be electrically short-circuited by the surrounding superconducting sea. With AC current through the Type II rod (Fig. 1.2c), however, there is dissipation (heat generation); i.e., the "mixed-state" rod is electrically resistive, though its effective resistivity is still orders of magnitude less than those of highly conductive normal metals. Each normal-state region contains flux bundles, the so-called fluxoids or vortices, and these flux bundles "flow" under time-varying conditions of magnetic field, current, or both. This dissipative flux flow is the major source of AC losses in Type II superconductors.

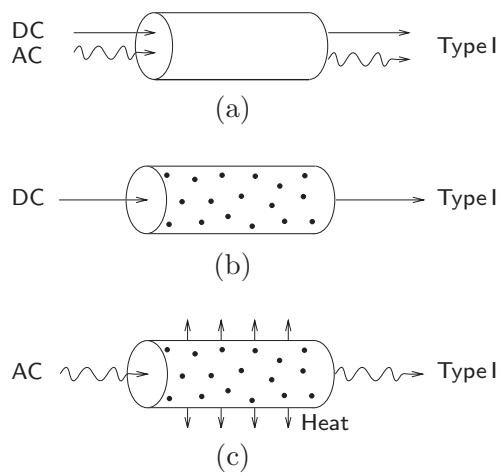

Fig. 1.2 Superconducting rods carrying a transport current. (a) Type I rod, DC or AC current—no Joule dissipation generated; (b) Type II rod, DC current—no dissipation; (c) Type II rod, AC current—Joule dissipation generated.

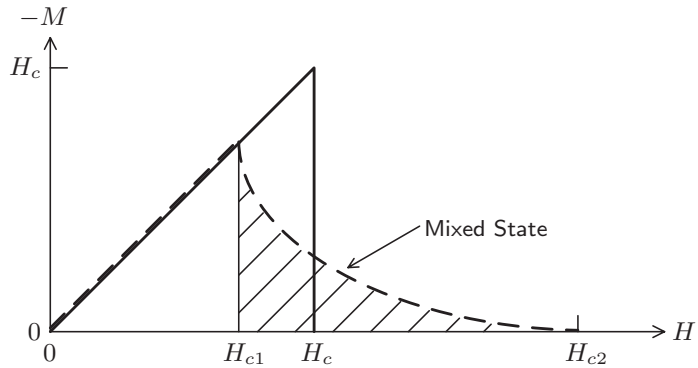

Fig. 1.3 *Schematic* $-M$ vs. H plots for Type I (solid) and Type II (dashed) superconductors. H_c is the critical field for Type I; H_{c1} and H_{c2} are, respectively, the lower and upper critical fields of Type II. The slant-lined area represents the mixed state.

Magnetic Behavior

Exposed to a magnetic field, a Type I superconductor is perfectly diamagnetic up to the bulk thermodynamic critical field, H_c; above H_c, it behaves as a normal nonmagnetic material. The magnetic behavior of a Type II superconductor is identical to that of Type I up to the lower critical field, H_{c1}; in the range between H_{c1} and H_{c2}, the upper critical field, the Type II is in the mixed state (p. 5). Figure 1.3 shows *schematic* (not in scale) plots of magnetization (M) vs. magnetic field (H) of Type I (solid curve) and Type II (dashed). (Because the superconductor is fundamentally diamagnetic, its magnetization is negative, and thus both curves are plotted as $-M$ vs. H.) The slant-lined region in Fig. 1.3 represents the mixed state of the Type II superconductor. Caveat: the magnetization curves of *all* Type II magnet-grade-superconductors, as studied in ***Chapter 5***, unlike that shown in Fig. 1.3, are irreversible, resulting in hysteretic magnetization curves. The hysteretic nature of magnetization is an important source of AC losses in Type II superconductors (***Chapter 7***).

Examples of Superconductors

Table 1.2 shows selected superconductors, Type I and Type II, with their critical temperatures in zero field, T_c, and critical magnetic inductions—$\mu_\circ H_c$ for Type I and $\mu_\circ H_{c2}$ for Type II. All Type I superconductors are metals, with low critical fields. It is no wonder that Kamerlingh Onnes' attempt, in 1913, to build the first superconducting coil, wound with lead wire, failed. Exposed to the field of its own coil (self field), lead could not remain superconducting. Even at that time 0.3 T was about the minimum field that an electromagnet needed to generate to be considered useful. Table 1.2 clearly shows that a superconducting magnet must employ Type II conductor. Unlike Type I, Type II comes in a variety of types: alloys; metalloids; metallic compounds; and even oxides. Note that all the oxides of Table 1.2 are HTS; MgB_2, a metalloid, is considered HTS. Figure 1.4 shows T_c vs. year data of selected LTS and HTS, together with boiling temperatures (horizontal lines) of important cryogens. The solid lines connect oxide superconductors, while the dashed line, beginning and ending, respectively, with Hg and MgB_2, connects "metallic" superconductors over a ∼90-year span.

Table 1.2: Critical Temperatures (T_c) and Fields ($\mu_\circ H_c$) of Selected Types I and II Superconductors

Type I	T_c [K]	$\mu_\circ H_c{}^*$ [T]	*Type II*	T_c [K]	$\mu_\circ H_{c_2}{}^*$ [T]
Ti (metals)	0.39	0.0100	Nb (metals)	9.5	0.2*
Zr	0.55	0.0047	NbTi (alloys)	9.8	10.5†
Zn	0.85	0.0054	NbN (metalloids)	16.8	15.3†
Al	1.18	0.0105	MgB_2	39.0	35–60‡
In	3.41	0.0281	Nb_3Sn (compounds)	18.2	24.5†
Sn	3.72	0.0305	Nb_3Al	18.7	31.0†
Hg	4.15	0.0411	Nb_3Ge	23.2	35.0†
V	5.38	0.1403	$YBa_2Cu_3O_{7-x}$ (oxides)	93	150*
Pb	7.19	0.0803	$Bi_2Sr_2Ca_{n-1}Cu_nO_{2n+4}$‡‡	85–110	>100*

* 0 K, estimated.

† 4.2 K, measured.

‡ 4.2 K, estimated (35 T, ∥ field, 60 T, ⊥ field).

‡‡ $n=2$, Bi2212; $n=3$, Bi2223.

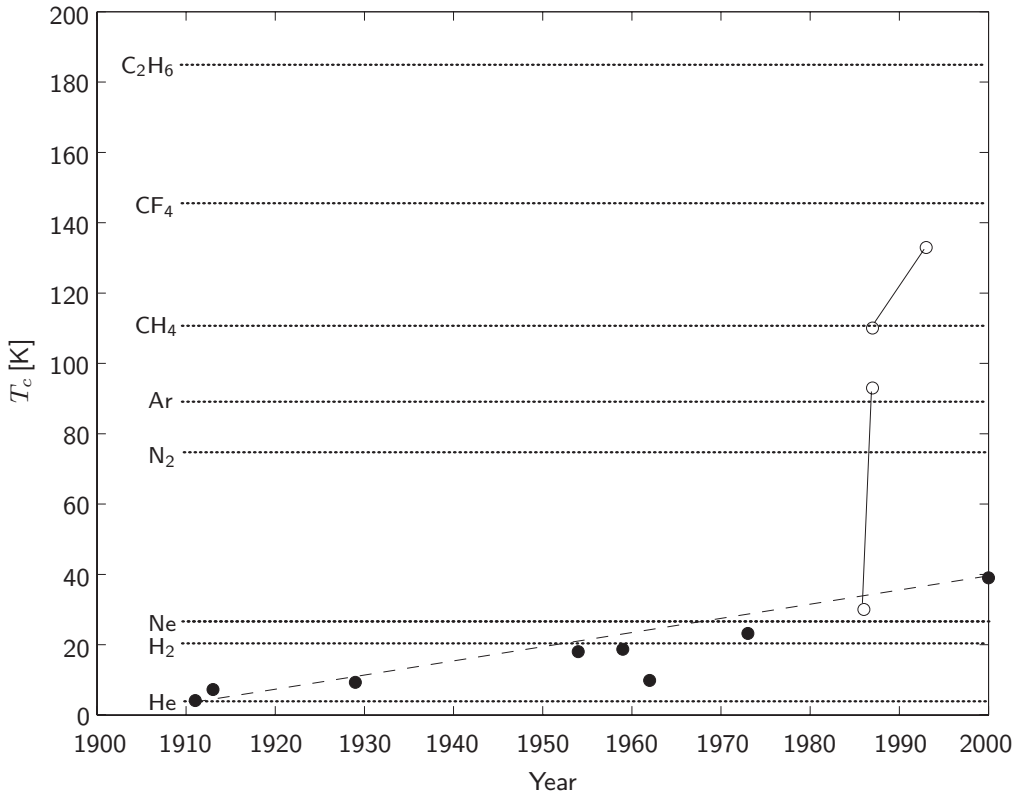

Fig. 1.4 T_c vs. Year data for selected superconductors, metallic (LTS) and oxide (HTS). Solid lines and open circles: HTS; Dashed line and solid circles: LTS, except MgB_2 ($T_c=$ 39 K; Year 2000), considered an HTS. Dotted horizontal lines: boiling temperatures of cryogens, from bottom to top: He (4.22 K); H_2 (20.39 K); Ne (27.09 K); N_2 (77.36 K); Ar (87.28 K); CH_4 (methane/111.6 K); CF_4 (Freon-14/145.4 K); C_2H_6 (ethane/184.6 K).

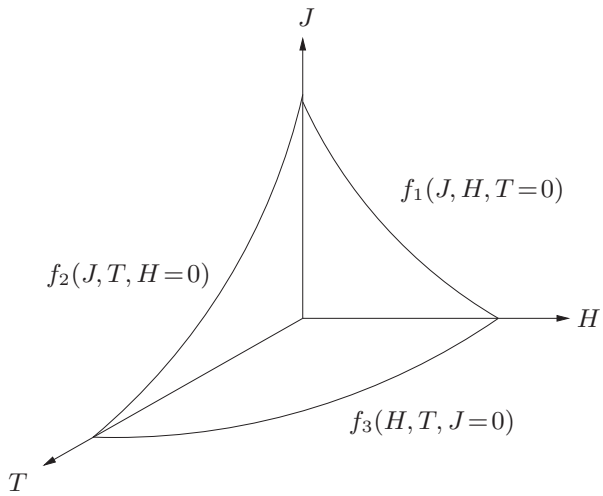

Fig. 1.5 Critical surface of a typical Type II superconductor.

1.2.4 Critical Surfaces of Type II Superconductor

Figure 1.5 shows the critical surface for a typical Type II superconductor usable for magnets, i.e., magnet-grade superconductor (**1.3**). Superconductivity exists within the phase volume bounded by the surfaces bordered by the functions, $f_1(J, H, T = 0)$; $f_2(J, T, H = 0)$; and $f_3(H, T, J = 0)$. During the early phase of the development of a superconductor, $f_2(J, T, H = 0)$ and $f_3(H, T, J = 0)$ are measured. For magnet engineers more useful is a general function $f(J, T, H)$.

Critical Current Density, J_c

In a Type II superconductor, J_c may be enhanced dramatically by means of metallurgical processing. This enhanced J_c performance is generally attributed to the creation of "pinning centers" that anchor the vortices against the $\vec{J}_c \times \vec{B}$ Lorentz force acting on them. These pinning centers are created in crystal structures by material impurities, metallurgical processes such as cold working to form dislocations, or heat treatment to create precipitates and grain boundaries. Kim and others obtained $J(H, T = \text{constant})$ given by [1.4]:

$$J_c \simeq \frac{\alpha_c}{H + H_\circ} \tag{1.3}$$

where α_c and $H_\circ$ are constants. Note that α_c implies an asymptotic force density that balances the Lorentz force density for $H \gg H_\circ$.

1.3 Magnet-Grade Superconductors

Magnet-grade superconductors are those conductors that meet rigorous magnet specifications as well as being *readily available commercially*. What follows is a brief comment on important differences between superconducting *materials* and *magnet-grade superconductors*. As has been the case with every successful magnet-grade superconductor so far developed, it is a long and laborious journey to transform a material discovered in the laboratory into a magnet-grade superconductor.

Table 1.3: Superconducting Materials vs. Conductors

Criterion	*Number*	*Criterion*	*Number*
1. Superconducting?	∼10,000	3. $J_c > 1\,\mathrm{GA/m^2}$?	∼10
2. $T_c > 4.2\,\mathrm{K}$; $\mu_\circ H_{c2} > 10\,\mathrm{T}$?	∼100	4. Magnet-grade?	< 10

1.3.1 Materials vs. Magnet-Grade Superconductors

Table 1.3 gives an estimate of the number of materials meeting certain superconductivity criteria: as the criteria move towards those required of a magnet-grade superconductor, the number decreases precipitously. Indeed, of nearly 10,000 superconductors discovered to date, only a few of them are usable for magnets. These include, LTS: NbTi and Nb_3Sn; and HTS: Bi2212, Bi2223, coated YBCO conductor, and MgB_2. A drop of over three orders of magnitude attests to the excruciatingly difficult task material scientists and metallurgists face in transforming a material into a magnet-grade superconductor.

1.3.2 Laboratory Superconductor to Magnet-Grade Superconductor

It is a long journey to transform a superconducting material, discovered in a laboratory, into a magnet-grade superconductor. The journey consists of six stages: 1) discovery; 2) improvement in J_c performance; 3) co-processing with matrix metal; 4) multifilament form; 5) $I_c > 100\,\mathrm{A}$ in length $> 1\,\mathrm{km}$; and 6) other requirements, e.g., strength and strain tolerance. Table 1.4 lists the six stages and their approximate beginning periods for Nb_3Sn and Bi2223. Note that Bi2223 was co-processed from the very beginning with normal matrix metal (silver). Note also that improvement in J_c (Stage 2) continues to this day, even for LTS and obviously for HTS. As for coated YBCO conductor, it is in the late phase of Stage 3 and about to enter Stage 4; small YBCO coils have been built and operated at 77 K. MgB_2, discovered in 2001, has already passed Stage 5, and "large" MgB_2 magnets have already been built and operated.

Despite more than a decade of intense R&D activities shortly after the development of Nb_3Sn conductors in 1961, Nb_3Sn conductors are *still* custom-designed for most magnet applications. Because of its brittleness and intolerance to strains above ∼0.3%, the material is inherently difficult to process and requires great care in handling. The situation is quite similar with BSCCO, which also is brittle.

Table 1.4: Material-to-Conductor Development Stages for Nb_3Sn and Bi2223

Stage	*Event*	*Nb_3Sn*	*Bi2223*
1	Discovery	Early 1950s	Late 1980s
2	Sufficient J_c in short samples	Early 1960s*	Early 1990s*
3	Co-processing with matrix metal	Late 1960s	Early 1990s†
4	Multifilament form	Early 1970s	Mid 1990s
5	$I_c \geq 100\,\mathrm{A}$; length $\geq 1\,\mathrm{km}$	Mid 1970s	Early 2000s*
6	Other magnet specifications	Late 1970s	Mid 2000s

* Improvement still continues.

† For Bi2223: Co-processed with silver from Stage 1.

1.4 Magnet Design

In this section, important magnet design issues are briefly discussed.

1.4.1 Requirements and Key Issues

A magnet, whether it is experimental or a system component, must satisfy the basic requirements of achieving the magnetic field, $\vec{H}(x, y, z, t)$, which include spatial distribution and temporal variation. Important parameters often given in the field specifications are: 1) $H_\circ$, the field at the magnet center ($x=0, y=0, z=0$); 2) $V_\circ$, the volume within which $\vec{H}(x, y, z)$ is specified; and 3) $H(t)$, the field time variation. ***CHAPTERS 2*** and ***3*** discuss $H_\circ$ and $\vec{H}(x, y, z)$ in some detail.

In addition to satisfying these basic field requirements, a magnet design must address the following key issues:

- Mechanical integrity: The magnet must be structurally strong to withstand large magnetic stresses, under both operating and fault conditions. ***CHAPTER 3*** also deals with magnetic forces and stresses.
- Operational reliability: The magnet must be stable in order to reach and stay at its operating point reliably. This reliability of a magnet is generally referred to as magnet stability; the process of a magnet losing superconductivity in operation is called a "quench." ***CHAPTERS 5***, ***6***, and ***7*** deal with this issue.
- Protection: In the event the magnet suffers an excursion into the normal (resistive) state, it must remain undamaged and be capable of being energized to its operating point repeatedly. ***CHAPTER 8*** is devoted to this subject.
- Conductor: For magnets produced in large numbers, the overall cost of a superconducting magnet system can be influenced to a large extent by the cost of the superconductor. That is, in such superconducting magnets, conductor cost may dominate the magnet cost. This book, however, rarely quantifies the issue of conductor cost, e.g., the economic choice between NbTi operated at 1.8 K and Nb_3Sn at 4.2 K or between NbTi at 4.2 K and MgB_2 at 15 K. Selected properties of superconductors are given in ***APPENDIX V***.
- Cryogenics: Because it requires power to create and maintain the cryogenic environment for the operation of superconducting magnets, cryogenics is an important issue for superconducting magnets. ***CHAPTER 4*** is devoted to this subject. Cryogenics is often overemphasized relative to its importance to the *overall system*. It is worthwhile noting that even in many applications where superconducting magnets are to play critical roles, the magnets are but one component among many in the overall system, and consequently the cryogenics is only a subcomponent. The power requirement for the cryogenic system is generally a modest fraction of the total power associated with the overall system, where in some instances ease and reliability of operation warrant the price in capital and/or operating costs.

For a superconducting magnet to succeed in the marketplace—the ultimate goal of most superconducting magnets—two more requirements should be added to the above list: 1) price; and 2) ease of operation.

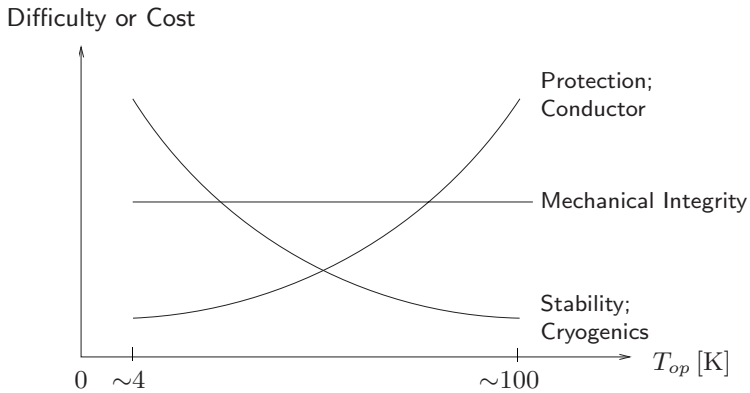

Fig. 1.6 Effects of temperature on five key magnet issues.

1.4.2 Effect of Operating Temperature

The baseline temperature for LTS magnets is generally 4.2 K. Operation at a temperature substantially higher than 4.2 K, which is possible only with HTS magnets, impacts five key magnet issues differently. These key issues are mechanical integrity, stability, protection, conductor, and cryogenics. Figure 1.6 shows *qualitative* trends of "difficulty or cost" vs. operating temperature, T_{op}, for the five key issues over the temperature span that covers both LTS and HTS magnets. For LTS, the span is generally in the range 1.8–10 K; for HTS generally 20–80 K, but in an LTS/HTS system that consists of LTS and HTS magnets, its T_{op} is dictated by the LTS magnet, i.e., ≤ 10 K. Although in Fig. 1.6 Protection and Conductor are represented by a single curve, as are Stability and Cryogenics, *actual* curves for each pair will not be identical.

Figure 1.6 indicates that difficulty in meeting mechanical integrity requirements is essentially independent of operating temperature. This statement is true for operating temperatures up to ∼100 K, over which differential thermal expansions among most magnet materials are negligible. For a magnet of given field requirements, the necessary number of ampere-turns is independent of operating temperature. Because critical current density decreases with increasing temperature universally among known superconductors, the conductor cost always increases with operating temperature; the expected benefit of a decrease in the cost of cryogenics with temperature must be compared with this expected increase in conductor cost. Operating temperature has profound impacts on stability (easier at higher temperatures) and protection (more difficult at higher temperatures), as discussed in ***CHAPTERS 6*** and ***8***. These chapters, through **PROBLEMS & *DISCUSSIONS***, illuminate the positive and negative impacts of increasing the operating temperature.

TRIVIA 1.1 It is said that the most intense magnetic field is in a neutron star. Of the large numbers below, which is closest to the ratio of its magnetic field to the earth's?

i) 10^{23}; ii) 10^{18}; iii) 10^{13}; iv) 10^{8}.

1.5 Numerical Solutions

As stated at the outset of this chapter, superconducting magnet technology is interdisciplinary in that it requires expertise in engineering areas chiefly of mechanical, electrical, cryogenic, and materials. It is thus impossible for a single individual to obtain a *trustworthy numerical* solution to every design and operational parameter for most *real-world* magnets. A team of specialists is required.

1.5.1 *Ballpark* Solutions

This does not mean that a cryogenic engineer, for example, should trust every magnetic field computation to the field specialist. The cryogenic engineer should be able to compute *ballpark* field figures even for a rather complex situation—an objective of this book is to enable every member of a design team to compute *ballpark* figures not only in each member's speciality area but also outside his/her areas of speciality. That is, the primary aim of this book is to enable the reader to condense every magnet system, complex or simple, into a set of simple models, each amenable to *ballpark* numerical solution. Indeed every new magnet system should begin with this exercise of each design team member computing a *ballpark* figure for every important design and operation parameter. Later, figures *much closer* to *true* values required for construction and successful operation of such a magnet system will diligently be computed by the design team specialists, each using a computer code.

1.5.2 Code Solutions

For actual construction and subsequent operation of a magnet system, every design and operation parameter must generally be computed with the aid of a code. Most design teams have access to codes such as ANSYS, Vector Fields, COMSOL, all of which are applicable for magnetic field, stress and strain, and thermal analyses.

Special codes, e.g., GANDALF and THEA, have been developed to tackle quench initiation and propagation phenomena in *cable-in-conduit* conductors (***Discussion 6.6***) used in "large" superconducting magnets, specifically for fusion magnets. The phenomena encompass thermal, hydraulic and electrical transients, where the changes of the cable and coolant temperatures are large and span a large range—one to two orders of magnitude—in the thermophysical and electrical properties. For this reason the analysis of a quench transient often, and sometimes solely, relies on numerical simulations that can deal with non-linear heat generation and thermal conduction in the cable coupled with heating-induced, compressible, viscous flow along the cooling channels. Each code is the product of over 25-year's work by many specialists [1.5–1.24].

GANDALF and THEA are both commercially available codes. GANDALF [1.19], was originally written to analyze thermo-hydraulic transients in the ITER (see ***Discussion 3.9***) conductors. The main feature of THEA (Thermo-Hydraulic and Electric Analysis) [1.20] is to extend the thermal and flow model to multiple parallel paths, e.g., several strands with different temperature, or parallel flow paths in the conductor, and to include nonuniform current distribution and transient redistribution in the cables.

1.6 The Format of the Book

As stated in the Preface, the format adopted for this book is the use of tutorial **PROBLEMS** accompanied by solutions. (In this 2nd Edition, principally to save space, some **PROBLEMS** in the 1st Edition have been converted into ***DISCUSSIONS***.) Each problem requires many steps in its solution, and through these steps the reader should gain deeper insight—some discussions also retain these steps. Because most of the problems are solvable analytically in closed form, they deal chiefly with ideal cases; nevertheless, solutions to these problems are quite useful for real-world problems with all the usual complexities. One needs the engineer's essential talent: the ability to approximate a complex problem by an ideal case without losing any essentials. Each problem (or discussion) is intended to develop the reader's ability to quickly grasp the zeroth or first order solution to a real-world situation of a similar nature, thus making it possible for the reader to retain the essence of the problem even after it moves into a numerical-analysis phase. In discussing design and operational issues, particularly field distribution, types of magnets, forces, thermal stability, dissipation, and protection, we focus primarily on solenoidal magnets. These issues are sufficiently basic and generic in concept that solenoidal magnets are suitable examples.

In this 2nd Edition, each chapter begins with an introductory section, followed by **PROBLEMS** & ***DISCUSSIONS***. Although emphasis, particularly in ***CHAPTERS 4–9***, is on HTS, important issues may still be studied with LTS magnets. ***CHAPTER 1*** has been expanded to include more materials on superconductivity; also, three problems have been added, each dealing with a subject not directly addressed in the remainder of this book but that the author hopes the reader is well prepared to tackle—classical thermodynamics; elementary circuit analysis; and MRI spectroscopy. ***CHAPTER 2*** has been expanded to include a more detailed discussion of the Legendre polynomials required in ***CHAPTER 3***. ***CHAPTER 3*** introduces several topics not covered in the 1st Edition. These, all based on analytical expressions and chiefly for solenoidal magnets, include: 1) field analysis at the magnet center; 2) axial forces; 3) inductances; 4) maximum field; 5) load lines; 6) minimum-volume; 7) superposition technique; and 8) magnet scaling. In ***CHAPTER 4*** new topics include "dry" (cryogen-free) magnets—cooled not by a liquid cryogen but conduction-cooled by a cryocooler—and vapor-cooled current leads incorporating HTS. Because magnetization and stability are not as pressing issues for HTS as for LTS, both ***CHAPTERS 5*** and ***6*** are down-sized. Similarly in ***CHAPTER 7***, the topic on mechanical disturbances is less emphasized in the new edition; instead more emphasis is placed on AC losses. Because protection is more pressing for HTS than for LTS, ***CHAPTER 8*** has been expanded. The new ***CHAPTER 9*** includes examples of solenoidal magnets, each accompanied by the study section, ***QUESTIONS/ANSWERS*** (***Q/A***) that covers topics studied in ***CHAPTERS 2–8***.

The main text includes physical and material property data relevant to particular **PROBLEMS** or ***DISCUSSIONS***. Other data useful to magnet engineers are in ***APPENDICES***. A glossary describes acronyms and terms that are of general interest in superconducting magnet technology and its areas of application but that are discussed only briefly or not at all in the main text.

PROBLEM 1.1: Thermodynamics of Type I superconductors

The specific heat per unit volume [J/m^3 K] of Type I superconductors may be approximated by [1.25]:

$$\textit{superconducting state} \quad C_s(T) = aT^3 \tag{1.4a}$$

$$\textit{normal state} \quad C_n(T) = bT^3 + \gamma T \tag{1.4b}$$

where a, b, and γ are constants.

a) Show that the transition temperature in zero field is given by:

$$T_c = \sqrt{\frac{3\gamma}{a-b}} \tag{1.5}$$

Use the following steps: 1) obtain expressions of entropy, $S_n(T)$ and $S_s(T)$ from $C(T) = T\,\partial S(T)/\partial T$; and note that 2) $S_n(T_c) - S_s(T_c) = 0$ at $H = 0$.

b) Show that $H_{c_\circ}$, the critical field at $T = 0$ K, $H_{c_\circ} \equiv H_c(0)$, is given by:

$$H_{c_\circ} = T_c\sqrt{\frac{\gamma}{2\mu_\circ}} \tag{1.6}$$

and that the critical magnetic field, $H_c(T)$, is a quadratic function of T:

$$H_c(T) = H_{c_\circ}\left[1 - \left(\frac{T}{T_c}\right)^2\right] \tag{1.7}$$

To derive Eq. 1.7, note that volumetric free energy at T in zero field in the normal state, $G_n(T)$, and superconducting state, $G_s(T)$, are related by:

$$G_n(T) - G_s(T) = \tfrac{1}{2}\mu_\circ H_c^2(T) \tag{1.8}$$

From Eq. 1.8 and $S(T) = -\partial G(T)/\partial T$, Eq. 1.6 may be derived.

c) The difference between the internal energy densities, $U_n - U_s$, in zero field is maximum at T_{ux}. By noting that $U(T) = \int C(T)\,dT$ in zero field, show:

$$T_{ux} = \frac{T_c}{\sqrt{3}} \tag{1.9}$$

d) Suppose that a magnetic field is applied very slowly and adiabatically to the superconductor initially at T_i, $0 < T_i < T_c$. The field is applied to a level just above the critical value; this transition to the normal state lowers the superconductor's temperature to T_f ($< T_i$). Derive an expression relating T_f and T_i. Also, show the process in a thermodynamic phase diagram.

e) To the same superconductor initially at T_i, $0 < T_i < T_c$, in *zero* field, a magnetic field H_e is applied *suddenly*. If H_e exceeds a critical level, H_{ec}, the metal will be *heated*. Show that H_{ec}, which depends on T_i, is given by:

$$H_{ec}(T_i) = H_c(T_i)\sqrt{\frac{1 + 3\left(\dfrac{T_i}{T_c}\right)^2}{1 - \left(\dfrac{T_i}{T_c}\right)^2}} \tag{1.10}$$

Solution to PROBLEM 1.1

a) Because $C(T)=TdS(T)/dT$ and $S(T=0)=0$, we have:

$$S(T) = \int_0^T \frac{C(T)}{T} dT \tag{S1.1}$$

Substituting Eqs. 1.4*a* and 1.4*b* into Eq. *S*1.1, we obtain:

$$S_s(T) = \int_0^T \frac{C_s(T)}{T} dT = \tfrac{1}{3} aT^3 \tag{S1.2a}$$

$$S_n(T) = \int_0^T \frac{C_n(T)}{T} dT = \tfrac{1}{3} bT^3 + \gamma T \tag{S1.2b}$$

and therefore:

$$S_n(T) - S_s(T) = \gamma T - \tfrac{1}{3}(a-b)T^3 \tag{S1.3}$$

Because, as noted above, $S_n(T_c)-S_s(T_c)=0$ at $H=0$, we have from Eq. *S*1.3:

$$\gamma = \tfrac{1}{3}(a-b)T_c^2 \tag{S1.4}$$

Solving Eq. *S*1.4 for T_c, we obtain:

$$T_c = \sqrt{\frac{3\gamma}{a-b}} \tag{1.5}$$

b) From Eq. 1.8 and $S(T)=-\partial G(T)/\partial T$, we have:

$$S_n(T) - S_s(T) = -\mu_\circ H_c(T) \frac{\partial H_c(T)}{\partial T} \tag{S1.5}$$

By combining Eqs. *S*1.3 and *S*1.4, rewritten as $(a-b)/3=\gamma/T_c^2$, we obtain:

$$S_n(T) - S_s(T) = \gamma T \left[1 - \left(\frac{T}{T_c} \right)^2 \right] \tag{S1.6}$$

Equating Eqs. *S*1.5 and *S*1.6, and integrating each side with respect to T, we have:

$$-\tfrac{1}{2}\mu_\circ H_c^2(T) = \tfrac{1}{2}\gamma T^2 - \tfrac{1}{4}\gamma T_c^2 \left(\frac{T}{T_c} \right)^4 + A \tag{S1.7}$$

where A is a constant. With $H_c(T=0)\equiv H_{c_\circ}$, we have: $A=-\mu_\circ H_{c_\circ}^2/2$.

At $T=T_c$, because $H_c(T_c)=0$, Eq. *S*1.7 becomes:

$$0 = \tfrac{1}{2}\gamma T_c^2 - \tfrac{1}{4}\gamma T_c^2 - \tfrac{1}{2}\mu_\circ H_{c_\circ}^2 \tag{S1.8}$$

TRIVIA 1.2 Of the following early students of magnetism (born c. 640 B.C.–1777 A.D.) below, who showed that garlic did not destroy magnetism?

i) Gilbert; ii) Oersted; iii) Peregrinus; iv) Thales.

Solution to PROBLEM 1.1 (continuation)

Solving Eq. $S1.8$ for $H_{c_\circ}$, we have:

$$H_{c_\circ} = T_c \sqrt{\frac{\gamma}{2\mu_\circ}} \tag{1.6}$$

From Eq. 1.6, we have:

$$\gamma = \frac{2\mu_\circ H_{c_\circ}^2}{T_c^2} \tag{S1.9}$$

Combining Eq. $S1.7$ (with $A = -\mu_\circ H_{c_\circ}^2/2$) and Eq. $S1.9$, we have:

$$-\tfrac{1}{2}\mu_\circ H_c^2(T) = \mu_\circ H_{c_\circ}^2 \left(\frac{T}{T_c}\right)^2 - \tfrac{1}{2}\mu_\circ H_{c_\circ}^2 \left(\frac{T}{T_c}\right)^4 - \tfrac{1}{2}\mu_\circ H_{c_\circ}^2 \tag{S1.10}$$

Equation $S1.10$ may be rewritten as:

$$H_c^2(T) = H_{c_\circ}^2 \left[1 - 2\left(\frac{T}{T_c}\right)^2 + \left(\frac{T}{T_c}\right)^4\right] = H_{c_\circ}^2 \left[1 - \left(\frac{T}{T_c}\right)^2\right]^2 \tag{S1.11}$$

From Eq. $S1.11$, we have:

$$H_c(T) = H_{c_\circ} \left[1 - \left(\frac{T}{T_c}\right)^2\right] \tag{1.7}$$

Values of $H_{c_\circ}$: Equation 1.6 and Experimental

Using Eq. 1.6, we may predict $H_{c_\circ}$ for a Type I superconductor from its measured values of γ and T_c. Table 1.5 gives values of $\mu_\circ H_{c_\circ}$, computed from Eq. 1.6 and experimental, for the Type I superconductors given in Table 1.2. The table also gives measured values of γ and T_c; density (ϱ) and atomic weight (M) are also given because γ usually is given in units of [J/g mole K^2] [1.26]. Table 1.5 shows that agreement between Eq. 1.6 and measured (Table 1.2) is good.

Table 1.5: $H_{c_\circ}$: Equation 1.6 and Experimental (Table 1.2)

Type I	ϱ*	M	γ	T_c	$\mu_\circ H_{c_\circ}$ [mT]	
	[g/cm^3]	[g/mole]	[J/m^3 K^2]	[K]	Eq. 1.6	Table 1.2
Ti	4.53	47.88	316.8	0.39	5.6	10.0
Zr	6.49	91.22	199.2	0.55	6.1	4.7
Zn	7.14	65.38	69.8	0.85	5.6	5.4
Al	2.70	26.98	135.1	1.18	10.9	10.5
In	7.31	114.8	107.6	3.41	28.0	28.1
Sn	7.31	118.7	109.6	3.72	30.9	30.5
Hg	13.55	200.6	120.9	4.15	36.2	41.1
V	6.11	50.94	1111	5.38	142.7	140.3
Pb	11.35	207.2	163.2	7.19	72.8	80.3

* At 18–25 °C.

Solution to PROBLEM 1.1 (continuation)

c) From $dU(T)=C(T)dT$ in zero field, where $U(T)$ is free energy, we have:

$$U(T) = \int_0^T C(T)\, dT \tag{S1.12}$$

Applying Eq. $S1.12$ to Eqs. 1.4a and 1.4b, we obtain:

$$U_n(T) = \int_0^T (bT^3 + \gamma T)dT = \tfrac{1}{4}bT^4 + \tfrac{1}{2}\gamma T^2 \tag{S1.13a}$$

$$U_s(T) = \tfrac{1}{4}aT^4 \tag{S1.13b}$$

The difference between the two free energies is given by:

$$\begin{aligned} U_n(T) - U_s(T) &= \tfrac{1}{4}(b-a)T^4 + \tfrac{1}{2}\gamma T^2 \\ &= \left(\frac{a-b}{4}\right)\left[\left(\frac{2\gamma}{a-b}\right)T^2 - T^4\right] \end{aligned} \tag{S1.14}$$

Differentiating Eq. $S1.14$ and equating it to zero at $T = T_{ux}$, we obtain:

$$\left.\frac{d(U_n - U_s)}{dT}\right|_{T_{ux}} = \left(\frac{a-b}{4}\right)\left[\left(\frac{4\gamma}{a-b}\right)T_{ux} - 4T_{ux}^3\right] = 0 \tag{S1.15}$$

Thus:

$$\left(\frac{4\gamma}{a-b}\right)T_{ux} - 4T_{ux}^3 = 0 \tag{S1.16}$$

Solving $S1.16$ for T_{ux} and using Eq. 1.5, we have:

$$T_{ux} = \sqrt{\frac{\gamma}{a-b}} = \frac{T_c}{\sqrt{3}} \tag{1.9}$$

d) Since the process is adiabatic and reversible, $S_n(T) = S_s(T)$ as the field is applied slowly. Thus, from Eq. $S1.2$, we have:

$$S_n(T_f) - S_s(T_i) = \tfrac{1}{3}bT_f^3 + \gamma T_f - \tfrac{1}{3}a\,T_i^3 \tag{S1.17}$$

With $S_n(T_f) - S_s(T_i) = 0$, we obtain an expression relating T_f and T_i:

$$\tfrac{1}{3}bT_f^3 + \gamma T_f = \tfrac{1}{3}aT_i^3 \tag{S1.18}$$

From Eq. 1.5, we have:

$$b = a - \frac{3\gamma}{T_c^2} \tag{S1.19}$$

Combining Eqs. $S1.18$ and $S1.19$, we obtain:

$$\tfrac{1}{3}a(T_f^3 - T_i^3) = -\gamma T_f\left[1 - \left(\frac{T_f}{T_c}\right)^2\right] \tag{S1.20}$$

Because $T_f < T_c$, the right-hand side of Eq. $S1.20$ is negative, and thus $T_f < T_i$. Figure 1.7 shows schematic T-S plots for the superconducting (solid) and normal (dashed) states. The $T_i \rightarrow T_f$ transition is indicated by the vertical solid line.

Solution to PROBLEM 1.1 (continuation)

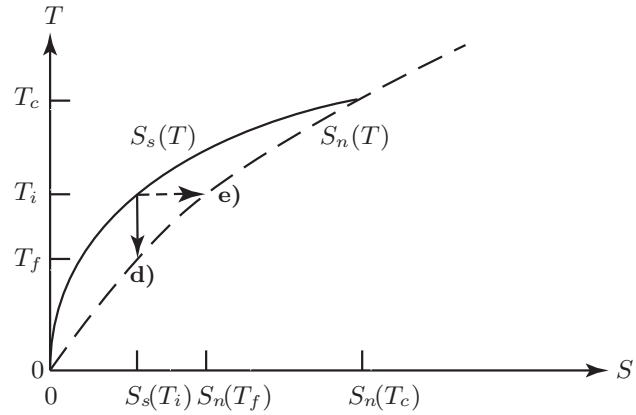

Fig. 1.7 Schematic T-S plots, superconducting (solid curve) and normal (dashed) states. The solid vertical line corresponds to **d)**; the dotted horizontal line to **e)**.

e) To be heated the superconductor must first be driven to the normal state; a magnetic energy of $\mu_\circ H_c^2(T_i)/2$ must be supplied by the external field. Because the transition absorbs heat, $T_i[S_n(T_i) - S_s(T_i)]$, H_{ec} must also supply this absorption energy. The transition is shown by the dotted horizontal line in Fig. 1.7. Thus:

$$\tfrac{1}{2}\mu_\circ H_{ec}^2(T_i) = \tfrac{1}{2}\mu_\circ H_c^2(T_i) + T_i[S_n(T_i) - S_s(T_i)] \qquad (S1.21)$$

Combining Eq. $S1.21$ with Eq. $S1.3$, we have:

$$\tfrac{1}{2}\mu_\circ H_{ec}^2(T_i) = \tfrac{1}{2}\mu_\circ H_c^2(T_i) + T_i\left[\tfrac{1}{3}(b-a)T_i^3 + \gamma T_i\right] \qquad (S1.22)$$

Inserting Eq. S1.9 into Eq. $S1.22$, and applying $S1.19$, we obtain:

$$\tfrac{1}{2}\mu_\circ H_{ec}^2(T_i) = \tfrac{1}{2}\mu_\circ H_c^2(T_i) + 2\mu_\circ H_{c_\circ}^2 \left(\frac{T_i}{T_c}\right)^2 \left[1 - \left(\frac{T_i}{T_c}\right)^2\right] \qquad (S1.23)$$

Combining Eqs. $S1.23$ and 1.7, we have:

$$H_{ec}^2(T_i) = H_c^2(T_i) + 4H_c^2(T_i)\frac{\left(\frac{T_i}{T_c}\right)^2}{1 - \left(\frac{T_i}{T_c}\right)^2} = H_c^2(T_i)\frac{1 + 3\left(\frac{T_i}{T_c}\right)^2}{1 - \left(\frac{T_i}{T_c}\right)^2} \qquad (S1.24)$$

Hence:

$$H_{ec}(T_i) = H_c(T_i)\sqrt{\frac{1 + 3\left(\frac{T_i}{T_c}\right)^2}{1 - \left(\frac{T_i}{T_c}\right)^2}} \qquad (1.10)$$

Note that $H_{ec}(T_i) \geq H_c(T_i)$ and that $H_{ec}(T_c) = 0$ because $H_c(T_c) = 0$.

PROBLEM 1.2: A superconducting loop

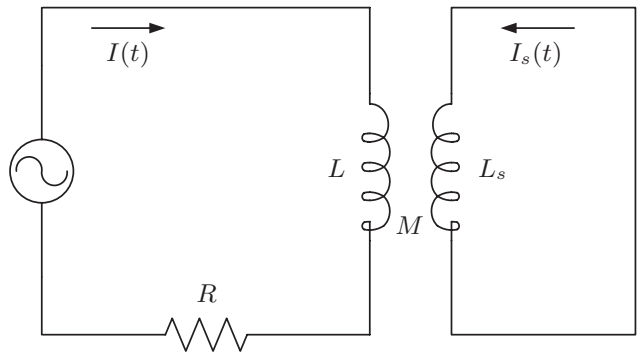

Fig. 1.8 Circuit of a superconducting coil inductively coupled to another loop that is connected to a current source.

This problem demonstrates that it is impossible to induce a "persistent" current in a *closed* superconducting loop, coil, or disk by means of an external current source. This may be obvious to some; it is proven here using a circuit model. Figure 1.8 shows a superconducting loop coupled inductively to another loop that is connected to a current source. The superconducting loop, with current $I_s(t)$, is represented by an inductor of self inductance L_s. The loop with the current source of $I(t)$ is represented by an inductor of self inductance L and a resistor of resistance R. The two circuits are coupled inductively through a mutual inductance M.

a) Write two circuit equations, relating voltage in each of the two circuits.

b) Solve the above voltage equations for $I_s(t)$ and show that it is not possible to establish a current in a *closed* superconducting circuit with a current source whose current $I(t)$ is zero at the beginning and at the end, i.e., $I(t=0) = I(t=\infty) = 0$. The closed superconducting circuit may be a magnet with its terminals joined by superconducting splices, a bulk disk or a stack of disks, or a disk with a hole in the middle or a stack of such disks.

Answer to TRIVIA 1.1 iii). Neutron star: $\sim 10^9$ T; earth: $\sim 10^{-4}$ T.

Solution to PROBLEM 1.2

a) Two voltage equations are:

$$L\frac{dI(t)}{dt} + M\frac{dI_s(t)}{dt} + RI = 0 \qquad (S2.1a)$$

$$M\frac{dI(t)}{dt} + L_s\frac{dI_s(t)}{dt} = 0 \qquad (S2.1b)$$

b) Solving for $I_s(t)$ from Eq. $S2.1b$, we obtain:

$$I_s(t) = -\frac{M}{L_s}I(t) + C \qquad (S2.2)$$

Because $I_s(t=0) = 0$, $C = 0$, and because $I(t=0) = I(t=\infty) = 0$, $I_s(t) \neq 0$ only when $I(t) \neq 0$. That is, a "virgin" closed superconducting circuit cannot remain energized alone, with an external current source shut off.

This impossibility of current induction in a *closed* superconducting circuit poses a practical problem in some applications, a few prominent examples of which are "persistent-mode" superconducting magnets, bulk disks, and annuli. A persistent-mode magnet must be energized by a current source through its terminals, as is a "driven-mode" magnet; after the magnet is energized, its terminals are shunted by the so-called "persistent current switch" (PCS), and the current source may be shut off. Design issues for persistent-mode magnets are studied in ***CHAPTER 7*** (***DISCUSSION 7.8***). A method to energize a magnet assembled from a stack of HTS annuli—each annulus a circular disk with a center hole—is discussed in ***CHAPTER 9*** (***EXAMPLE 9.2D).***

Answer to TRIVIA 1.2 i). The English physician and physicist William Gilbert (1540–1603), a pioneer of experimentation, refuted many superstitions by direct testing; his experiments on magnetism earned him the title "father of electricity." The Danish physicist Hans Christian Oersted (1777–1851) discovered in 1819 that a compass needle aligned at right angles to a current-carrying conductor, thus initiating the science of electromagnetism. The French crusader Petrus Peregrinus (c. 1240–?), discoverer of magnetic poles, showed it is impossible to separate the poles by breaking a magnet in two, and was first to describe in detail the pivoted compass. The Greek philosopher Thales (640 B.C.–546 B.C.), considered the first to study magnetism, is now known chiefly for having predicted an eclipse of the sun that occurred in Asia Minor on May 28, 585 B.C.

PROBLEM 1.3: Magnetic resonance imaging (MRI)

One of the most successful areas of commercial applications of superconducting magnets is in medical diagnostic instrumentation, specifically, magnetic resonance imaging (MRI). Here are a few basic questions for the magnet engineer.

a) In MRI why are nuclei of hydrogen-1, nitrogen-14, etc. detectable, while nuclei of carbon-12, oxygen-16, etc. are *not* detectable?

b) If the frequency resolution is 10 Hz, what must be the minimum field homogeneity over a specified volume at the magnet center of a 1-T whole-body MRI magnet? For a "whole-body" MRI magnet, with a room temperature bore diameter of 80 cm, this uniform field region occupies typically a 25-cm DSV (diameter spherical volume).

c) What role does the pulse gradient magnet in an MRI unit play?

d) For a 1-T unit, what is the typical dB/dz generated by the pulse magnet?

Solution to PROBLEM 1.3

a) Nuclei with **odd** numbers of protons or neutrons possess a *net* angular momentum. Exposed to a magnetic field, these nuclei will precess at a frequency (Larmor) proportional to the field intensity—the Larmor frequency of hydrogen, i.e., a proton, is 42.576 MHz in a field of 1 T. Table 1.6 lists selected elements and their atomic details, identifying detectable ones.

b) Since 10 Hz is 0.23×10^{-6} of 42.576×10^{6} Hz, the field must also be within 0.23×10^{-6} of 1 T, or about 0.002 gauss. Note that the earth field is ~0.7 gauss.

c) By purposely introducing a spatial distribution in a magnetic field, one can restrict resonance to selected subvolumes. This enables one to map (image) the concentration of nuclei of a selected species.

d) The gradient amplitude is directly related to the spatial resolution of the image. Higher gradient would allow proportionately finer resolution, but there are limits to what the magnet and the patient can tolerate. Medical MRI has to limit the gradient strength, or at least the gradient slew rate, to avoid nerve and muscle stimulation. Medical MRI has a maximum gradient of 3–4 gauss/cm, and a maximum slew rate around 12 (gauss/cm)/ms or 120 (T/m)/s.

Table 1.6: Atomic Details of Selected Elements

Atomic No.	*Element*	*Atomic W*	*Protons*	*Neutrons*	*Detectable?*
1	Hydrogen	1	***1****	0	yes
6	Carbon	12	6	6	no
		13	6	***7***	yes
7	Nitrogen	14	***7***	***7***	yes
8	Oxygen	16	8	8	no
11	Sodium	23	***11***	12	yes
15	Phosphorous	31	***15***	16	yes

* Bold slanted numbers indicate detectability.

REFERENCES

[1.1] J.K. Hulm and B.T. Matthias, "Overview of superconducting materials development," in *Superconductor Materials Science—Metallurgy, Fabrication, and Applications*, Eds., S. Foner and B.B. Schwartz (Plenum Press, New York, 1981).

[1.2] A.A. Abrikosov, "On the magnetic properties of superconductors of the second type (English translation)," *Zh. Eksp. Teor. Fiz. (Soviet Union)* **5**, 1174 (1957).

[1.3] U. Essmann and H. Träuble, "The direct observation of individual flux lines in Type II superconductors," *Phys. Lett.* **24A**, 526 (1967).

[1.4] Y.B. Kim, C.F. Hempstead, and A.R. Strnad, "Magnetization and critical supercurrents," *Phys. Rev.* **129**, 528 (1963).

[1.5] J.K. Hoffer, "The Initiation and propagation of normal zones in a force-cooled tubular superconductor," *IEEE Trans. Mag.* **15**, 331 (1979).

[1.6] C. Marinucci, M.A. Hilal, J. Zellweger, and G. Vecsey, "Quench studies of the Swiss LCT conductor," *Proc. 8th Symp. on Eng. Prob. Fus. Res.*, 1424 (1979).

[1.7] V.D. Arp, "Stability and thermal quenches in force-cooled superconducting cables," *Proc. of 1980 Superconducting MHD Magnet Design Conference, MIT*, 142 (1980).

[1.8] J. Benkowitsch and G. Kraft, "Numerical analysis of heat-induced transients in forced flow helium cooling systems," *Cryogenics* **20**, 209 (1980).

[1.9] E.A. Ibrahim, "Thermohydraulic Analysis of Internally Cooled Superconductors," *Adv. Cryo. Eng.* **27**, 235 (1982).

[1.10] C. Marinucci, "A numerical model for the analysis of stability and quench characteristics of forced-flow cooled superconductors," *Cryogenics* **23**, 579 (1983).

[1.11] M.C.M. Cornellissen and C.J. Hoogendoorn, "Propagation velocity for a force cooled superconductor," *Cryogenics* **25**, 185 (1985).

[1.12] A.F. Volkov, L.B. Dinaburg, and V.V. Kalinin, "Simulation of helium pressure rise in hollow conductor in case of superconductivity loss," *Proc. 12th Int. Cryo. Eng. Conf.* (Southampton, UK), 922 (1988).

[1.13] R.L. Wong, "Program CICC flow and heat transfer in cable-in-conduit conductors," *Proc. 13th Symp. Fus. Tech.* (Knoxville, TN), 1134 (1989).

[1.14] L. Bottura and O.C. Zienkiewicz, "Quench analysis of large superconducting magnets. Part I: model description," *Cryogenics* **32**, 659 (1992).

[1.15] C.A. Luongo, C.-L. Chang, and K.D. Partain, "A computational model applicable to the SMES/CICC," *IEEE Trans. Mag.* **30**, 2569 (1994).

[1.16] A. Shajii and J.P. Freidberg, "Quench in superconducting magnets. I. Model and implementation," *J. Appl. Phys.* **76**, 3149 (1994); "Quench in superconducting magnets. II. Analytic Solution," *J. Appl. Phys.* **76**, 3159 (1994).

[1.17] R. Zanino, S. De Palo, and L. Bottura, "A two-fluid code for the thermohydraulic transient analysis of CICC superconducting magnets," *J. Fus. Energy* **14**, 25 (1995).

[1.18] L. Bottura, "A numerical model for the simulation of quench in the ITER magnets," *J. Comp. Phys.* **125**, 26 (1996).

[1.19] L Bottura, C. Rosso, and M. Breschi, "A general model for thermal, hydraulic, and electric analysis of superconducting cables," *Cryogenics* **40**, 617 (2000).

[1.20] Q. Wang, P. Weng, and M. Hec, "Simulation of quench for the cable-in-conduit-conductor in HT-7U superconducting Tokamak magnets using porous medium model," *Cryogenics* **44**, 81 (2004).

[1.21] T. Inaguchi, M. Hasegawa, N. Koizumi, T. Isono, K. Hamada, M. Sugimoto, and Y. Takahashi, "Quench analysis of an ITER 13T-40kA Nb_3Sn coil (CS insert)," *Cryogenics* **44**, 121 (2004).

[1.22] L. Bottura, "Numerical aspects in the simulation of thermohydraulic transients in CICC's," *J. Fus. Energy* **14**, 13 (1995).

[1.23] L. Bottura and A. Shajii, "Numerical quenchback in thermofluid simulations of superconducting magnets," *Int. J. Num. Methods Eng.* **43**, 1275 (1998).

[1.24] L. Bottura, "Modelling stability in superconducting cables," *Physica C* 316 (1998).

[1.25] A.B. Pippard, *The Elements of Classical Thermodynamics* (Cambridge University Press, Cambridge, 1966).

[1.26] C. Kittel, *Introduction to Solid State Physics* 3rd Ed. (John Wiley & Sons, 1966).

Other Sources of Information

Textbooks

Here only a few textbooks familiar to the author are listed.

[1.27] Martin N. Wilson, *Superconducting Magnets* (Clarendon Press, 1983). An excellent treatise on superconducting magnets; predates discovery of HTS.

Peter J. Lee, *Editor*, *Engineering Superconductivity* (John Wiley & Sons, Inc., New York, 2001). Covers physics and applications of superconductivity.

Thomas S. Sheahen, *Introduction to High-Temperature Superconductivity* (Plenum, 1994). A good introductory book on HTS and applications.

Terry P. Orlando and Kevin A. Delin, *Foundations of Applied Superconductivity* (Addison -Wesley, 1991). Discussion of superconductivity basics for the engineer.

Conference Proceedings

Proceedings of the conferences listed below, not all-inclusive, contain the latest information on superconductors and applications.

Applied Superconductivity Conference (ASC): Held in the U.S. in even-numbered years. Three major topics: large-scale applications; materials; electronics.

Cryogenic Engineering Conference (CEC) and *International Cryogenic Materials Conference* (ICMC): Held jointly in a U.S. city in odd-numbered years.

European Conference on Applied Superconductivity (EUCAS): The European version of the ASC, in odd-numbered years.

International Conference on Magnet Technology (MT): In a U.S., European, or Asian city, in odd-numbered years.

International Symposium on Superconductivity (ISS): annually since 1988 in Japan. Its proceedings are good sources to track the development chiefly of HTS materials.

"Why sir, there is a very good chance that you will soon be able to tax it."

—Michael Faraday's reputed reply to William Gladstone, the Prime Minister, who, after being shown by Faraday a demonstration of the first dynamo, asked "*But, after all, what use is it?*"

Chapter 2
Electromagnetic Fields

2.1 Introduction

In this chapter we review electromagnetic theory by presenting Maxwell's equations. This review is intended to refresh the reader's understanding of electromagnetic theory so as to allow the main subject matter of this book—superconducting magnets—to be approached in a quantitative manner. After a presentation of Maxwell's equations and simple solutions that are not only tractable analytically but also useful in most magnet applications, specific cases familiar to most magnet engineers will be presented and studied.

2.2 Maxwell's Equations

There are four basic Maxwell's equations: 1) Gauss' law; 2) Ampere's law; 3) Faraday's law; and 4) the law of magnetic induction continuity. In addition to these, we will make frequent use of the equations of charge conservation and other constituent relationships. Each equation is briefly discussed below.

In this book SI units are used *almost* exclusively, particularly for electromagnetic quantities, summarized in Table 2.1. There is a widespread practice in the magnet community of interchanging magnetic field $\vec{H}$ and magnetic induction (or magnetic flux density) $\vec{B}$, expressing, for example, a magnetic field in the unit of tesla [T]. Although the practice is usually harmless and causes no confusion, care must be exercised, for example, when computing energy from an M vs. H plot.

The magnetic permeability of free space, $\mu_\circ$, is by definition $4\pi \times 10^{-7}$ H/m; the electric permittivity of free space, $\epsilon_\circ (= 1/\mu_\circ c^2$, where c is the speed of light), is approximately 8.85×10^{-12} F/m. ***Appendix IA*** presents other physical constants and selected conversion factors relating "common" non-SI units to SI units.

Current density is by far the dominant source of the $\vec{H}$ fields associated with superconducting magnets. Thus, the relatively small time-varying $\vec{D}$ field contribution to the $\vec{H}$ field is not included in our presentation of Maxwell's equations.

Table 2.1: Electromagnetic Quantities

Symbol	*Name*	*SI Unit*	
E	Electric field	volt/meter	[V/m]
H	Magnetic field	ampere/meter	[A/m]
B	Magnetic induction (or magnetic flux density)	tesla	[T]
J	Current density	ampere/meter^2	[A/m^2]
K	Surface current density	ampere/meter	[A/m]
ρ_c	Charge density	coulomb/meter^3	[C/m^3]
σ_c	Surface charge density	coulomb/meter^2	[C/m^2]
ρ_e	Electrical resistivity	ohm meter	[Ω m]

Y. Iwasa, *Case Studies in Superconducting Magnets: Design and Operational Issues*,
DOI: 10.1007/b112047_2,

2.2.1 Gauss' Law

In integral form, Gauss' law in free space is given by:

$$\oint_{\mathcal{S}} \epsilon_\circ \vec{E} \cdot d\vec{\mathcal{A}} = \int_{\mathcal{V}} \rho_c \, d\mathcal{V} \tag{2.1}$$

The surface integral of the $\epsilon_\circ \vec{E}$ field is equal to the total electric charge within the volume $\mathcal{V}$ enclosed by the surface $\mathcal{S}$. In Eq. 2.1, $d\vec{\mathcal{A}} = \vec{n} d\mathcal{S}$, where $\vec{n}$ is the unit vector normal (outward) to the surface element. In differential form, Eq. 2.1 is:

$$\epsilon_\circ \nabla \cdot \vec{E} = \rho_c \tag{2.2}$$

Boundary Condition: At a surface with charge density σ_c [C/m^2], the discontinuity in the normal component of the electric field, from Region 1 ($\vec{E}_1$) to Region 2 ($\vec{E}_2$), is given by $\sigma_c/\epsilon_\circ$:

$$\vec{n}_{12} \cdot (\vec{E}_2 - \vec{E}_1) = \frac{\sigma_c}{\epsilon_\circ} \tag{2.3}$$

Here, the unit vector $\vec{n}_{12}$ points from Region 1 to Region 2.

2.2.2 Ampere's Law

In integral form, Ampere's law is given by:

$$\oint_{\mathcal{C}} \vec{H} \cdot d\vec{s} = \int_{\mathcal{S}} \vec{J}_f \cdot d\vec{\mathcal{A}} \tag{2.4}$$

The equation states that the line integral of the $\vec{H}$ field is equal to the total "free" (subscript f) electric current, i.e., not including magnetization currents, within the surface $\mathcal{S}$ enclosed by contour $\mathcal{C}$. In differential form, Eq. 2.4 is:

$$\nabla \times \vec{H} = \vec{J}_f \tag{2.5}$$

Equations 2.4 and 2.5 omit $\partial \vec{E}/\partial t$ as a source of $\vec{H}$.

Boundary Condition: In the presence of a "free" surface current density $\vec{K}_f$ [A/m], there will be a discontinuity in the tangential component of the magnetic field in passing through the surface from Region 1 ($\vec{H}_1$) to Region 2 ($\vec{H}_2$), given by:

$$\vec{n}_{12} \times (\vec{H}_2 - \vec{H}_1) = \vec{K}_f \tag{2.6}$$

2.2.3 Faraday's Law

In integral form, Faraday's law is given by:

$$\oint_{\mathcal{C}} \vec{E} \cdot d\vec{s} = -\frac{d}{dt} \int_{\mathcal{S}} \vec{B} \cdot d\vec{\mathcal{A}} \tag{2.7}$$

The equation states that the line integral of the $\vec{E}$ field is equal to the negative of the time rate of change of the total magnetic flux through surface $\mathcal{S}$ enclosed by contour $\mathcal{C}$. In differential form, Eq. 2.7 is:

$$\nabla \times \vec{E} = -\frac{\partial \vec{B}}{\partial t} \tag{2.8}$$

Boundary Condition: The tangential component of the $\vec{E}$ field is always continuous in passing through a surface from Region 1 ($\vec{E}_1$) to Region 2 ($\vec{E}_2$). Namely:

$$\vec{n}_{12} \times (\vec{E}_2 - \vec{E}_1) = 0 \tag{2.9}$$

2.2.4 Magnetic Induction Continuity

In integral form, magnetic induction continuity is given by:

$$\oint_{\mathcal{S}} \vec{B} \cdot d\vec{\mathcal{A}} = 0 \tag{2.10}$$

Equation 2.10 states that the surface integral of the $\vec{B}$ field over the surface $\mathcal{S}$ is zero; i.e., there are no point sources of $\vec{B}$ field. In differential form, Eq. 2.10 is:

$$\nabla \cdot \vec{B} = 0 \tag{2.11}$$

Boundary Condition: The normal component of the $\vec{B}$ field is always continuous in passing through a surface from Region 1 ($\vec{B}_1$) to Region 2 ($\vec{B}_2$). Namely:

$$\vec{n}_{12} \cdot (\vec{B}_2 - \vec{B}_1) = 0 \tag{2.12}$$

As discussed below in **2.2.6**, in a magnetic medium $\vec{B}$ is the sum of the magnetic field $\vec{H}$ and magnetization $\vec{M}$. It means that continuity of the normal component of $\vec{B}$ through two different magnetic media is preserved despite any difference in magnetization from one medium to the other.

2.2.5 Charge Conservation

The "free" current density $\vec{J}_f$ is related to the time rate of change of "free" (non-dielectric) electric charge density, ρ_{c_f}. In integral form, the relation is given by:

$$\oint_{\mathcal{S}} \vec{J}_f \cdot d\vec{\mathcal{A}} = -\frac{d}{dt} \int_{\mathcal{V}} \rho_{c_f} \, d\mathcal{V} \tag{2.13}$$

In differential form, Eq. 2.13 is:

$$\nabla \cdot \vec{J}_f = -\frac{\partial \rho_{c_f}}{\partial t} \tag{2.14}$$

2.2.6 Magnetization and Constituent Relations

Magnetic induction $\vec{B}$, magnetic field $\vec{H}$, and magnetization $\vec{M}$ are related by:

$$\vec{B} = \mu_\circ(\vec{H} + \vec{M}) \tag{2.15}$$

In homogeneous, isotropic, linear media, which are generally assumed in this book, $\vec{B} = \mu\vec{H} = \mu_\circ(1+\chi)\vec{H}$, where permeability, μ, and susceptibility, χ, we generally assume to be field-independent. χ can be as high as 10^6 for ferromagnets such as "high-μ" *shielding* materials. For typical paramagnets, such as oxygen, χ is 10^{-6}. For diamagnets (monatomic gases such as helium, neon, and most liquids, e.g., water), χ is negative; for Type I superconductors, which are perfect diamagnets, $\chi = -1$; i.e., $\mu = 0$.

In conductive materials such as metals, the presence of an $\vec{E}$ field induces a current density $\vec{J}$ in the metal. The constituent relation between $\vec{J}$ and $\vec{E}$ is:

$$\vec{J} = \frac{\vec{E}}{\rho_e} \tag{2.16}$$

where ρ_e is the metal's electrical resistivity [Ω m].

2.3 Quasi-Static Case

The electric field $\vec{E}$ and magnetic induction $\vec{B}$ are coupled through Faraday's law. For free space, the following complete set of field equations must be solved:

$$\nabla \cdot \epsilon_\circ \vec{E} = \rho_c \tag{2.17a}$$

$$\nabla \times \vec{E} = -\frac{\partial \vec{B}}{\partial t} \tag{2.8}$$

$$\nabla \times \vec{H} = \vec{J}_f + \epsilon_\circ \frac{\partial \vec{E}}{\partial t} \tag{2.17b}$$

$$\nabla \cdot \vec{B} = 0 \tag{2.11}$$

$$\nabla \cdot \vec{J}_f = -\frac{\partial \rho_c}{\partial t} \tag{2.17c}$$

The problem of solving the above equations for $\vec{E}$ and $\vec{H}$ can be greatly simplified if $\vec{E}$ and $\vec{H}$ can be decoupled. Such a "quasi-static" analysis suffices for many important practical applications. Simplest of all are those cases in which Eqs. 2.8, 2.11, and 2.17*a*–2.17*c* may be solved through *static* equations. Thus, in the 0^{th}-order approximation, we have:

$$\nabla \cdot \epsilon_\circ \vec{E}_0 = \rho_{c0} \tag{2.18a}$$

$$\nabla \times \vec{E}_0 = 0 \tag{2.18b}$$

$$\nabla \times \vec{H}_0 = \vec{J}_{f0} \tag{2.18c}$$

$$\nabla \cdot \vec{B}_0 = 0 \tag{2.18d}$$

$$\nabla \cdot \vec{J}_{f0} = 0 \tag{2.18e}$$

Then the 0^{th}-order E-field, $\vec{E}_0$, for example, can be solved independently of the H-field. Next in order of complexity are cases in which the induced fields are negligible compared with the original time-varying fields. For the quasi-static, 1^{st} order approximation, we have:

$$\nabla \cdot \epsilon_\circ \vec{E}_1 = \rho_{c1} \tag{2.19a}$$

$$\nabla \times \vec{E}_1 = -\frac{\partial \vec{B}_0}{\partial t} \tag{2.19b}$$

$$\nabla \times \vec{H}_1 = \vec{J}_{f1} + \epsilon_\circ \frac{\partial \vec{E}_0}{\partial t} \tag{2.19c}$$

$$\nabla \cdot \vec{B}_1 = 0 \tag{2.19d}$$

$$\nabla \cdot \vec{J}_{f1} = -\frac{\partial \rho_{c0}}{\partial t} \tag{2.19e}$$

Note that $\vec{E}_1$ is still independent of $\vec{H}_1$. In general, $\vec{J}_f$ supplied by a source is given by $\vec{J}_{f0}$ only, and in a metal, $\vec{J}_{f1} = \vec{E}_1/\rho_e$.

The approximation process can continue indefinitely, but for the "low-frequency" cases of interest discussed in the **PROBLEMS & *DISCUSSIONS*** of this chapter, we need to solve for only the 0^{th}- and 1^{st}-order fields.

2.4 Poynting Vector

Poynting's theorem may be expressed as:

$$-\nabla \cdot \vec{S} = p + \frac{dw}{dt} \tag{2.20}$$

where $\vec{S}\,[\mathrm{W/m^2}]$ is the Poynting vector given by $\vec{S} = \vec{E} \times \vec{H}$, p is the power dissipation density, and w is the energy density stored magnetically and electrically.

Equation 2.20 states that the negative of the divergence of the S-vector is equal to the sum of p (the difference between dissipation and generation densities) and dw/dt, the rate of change of energy storage density. If $\nabla \cdot \vec{S} = 0$, then power is balanced within the system: no power in or out; if $\nabla \cdot \vec{S} < 0$, then power flows into the system to sustain dissipation or to store energy.

Sinusoidal Case

When dealing with a sinusoidally time-varying electric field $\vec{E}$ of complex amplitude $\vec{E}_\circ$, i.e., $\vec{E} = \vec{E}_\circ e^{jwt}$, and therefore $\vec{J} = (\vec{E}_\circ/\rho_e)e^{jwt}$, the time-averaged dissipation power density $<p>$ is expressed by:

$$<p> = \tfrac{1}{2}\vec{E} \cdot \vec{J}^* = \frac{1}{2\rho_e}|E|^2 = \frac{\rho_e}{2}|J|^2 \tag{2.21}$$

where $\vec{J}^*$ is the complex conjugate of $\vec{J}$.

In the sinusoidal case, the S-vector is given by:

$$\vec{S} = \tfrac{1}{2}\left(\vec{E} \times \vec{H}^*\right) \tag{2.22a}$$

$$-\oint_{\mathcal{S}} \vec{S} \cdot d\vec{\mathcal{A}} = <P> + j2\omega(<E_m> - <E_e>) \tag{2.22b}$$

where $< P >$ [W], $< E_m >$ [J], and $< E_e >$ [J] are, respectively, the total power dissipated, magnetic energy, and electric energy, each time-averaged and computed over the system volume, $\mathcal{V}$.

$$<P> = \frac{1}{2\rho_e}\int_{\mathcal{V}} |E|^2 \, d\mathcal{V} \tag{2.23a}$$

$$<E_m> = \frac{\mu_\circ}{4}\int_{\mathcal{V}} |H|^2 \, d\mathcal{V} \tag{2.23b}$$

$$<E_e> = \frac{\epsilon_\circ}{4}\int_{\mathcal{V}} |E|^2 \, d\mathcal{V} \tag{2.23c}$$

The complex Poynting vector, $\vec{S}$, expanded up to the 1st-order fields, is given by:

$$\vec{S} = \tfrac{1}{2}\left(\vec{E}_0 \times \vec{H}_0^* + \vec{E}_0 \times \vec{H}_1^* + \vec{E}_1 \times \vec{H}_0^*\right) \tag{2.24}$$

TRIVIA 2.1 Of the contemporary astronomers (born 1629–1656) below, who measured the speed of light to within 25% of the accepted modern value?

i) Flamsteed; ii) Halley; iii) Huygens; iv) Roemer.

2.5 Field Solutions from the Scalar Potentials

Any static electric field, because its curl is zero ($\nabla \times \vec{E} = 0$), is a conservative field and thus is the gradient of a scalar potential ϕ:

$$\vec{E} = -\text{grad}\,\phi = -\nabla\,\phi \tag{2.25}$$

Thus, $\nabla \cdot \vec{E}$ may be given by:

$$\nabla \cdot \vec{E} = -\nabla \cdot \nabla\phi = -\nabla^2\phi \tag{2.26}$$

In the absence of charge density ($\rho_c = 0$), Eq. 2.2 reduces to:

$$\nabla \cdot \vec{E} = 0 \tag{2.27}$$

Combining Eqs. 2.26 and 2.27, we obtain:

$$\nabla^2\phi = 0 \tag{2.28}$$

Equation 2.28, known as Laplace's equation, expresses scalar potentials from which physically realizable $\vec{E}$ fields can be derived.

Similarly, in the absence of free current and under the DC condition, any magnetic field $\vec{H}$, because $\nabla \times \vec{H} = 0$, is derivable from scalar potentials that satisfy the Laplace's equation; i.e., $\vec{H} = -\nabla\phi$. Besides electromagnetic fields, there are other well-known cases in engineering where Eq. 2.28 is applicable for time-independent variables: temperature (T) in a source-free, isotropic conductive medium; volume expansion; the sum of linear strains in the x-, y-, and z-axes in a force- and moment-free, isotropic elastic medium.

Selected solutions of Laplace's equation in two-dimensional cylindrical coordinates and three-dimensional spherical coordinates are presented below.

2.5.1 Two-Dimensional Cylindrical Coordinates

For a potential in two-dimensional cylindrical (r, θ) coordinates, $\nabla^2\phi$ is given by:

$$\nabla^2\phi = \frac{1}{r}\frac{\partial}{\partial r}\left(r\frac{\partial\phi}{\partial r}\right) + \frac{1}{r^2}\frac{\partial^2\phi}{\partial\theta^2} = 0 \tag{2.29}$$

The standard technique to solve Eq. 2.29 is to express ϕ as the product of two functions, each a function of only one of the two coordinates:

$$\phi = R(r)\,\Theta(\theta) \tag{2.30}$$

The solutions to Eq. 2.29 have the following general forms:

$$\text{for } n = 0 \qquad \phi_0 = (A_1 \ln r + A_2)\,(C_1\theta + C_2) \tag{2.31a}$$

$$\text{for } n > 0 \qquad \phi_n = (A_1 r^n + A_2 r^{-n})(C_1 \sin n\theta + C_2 \cos n\theta) \tag{2.31b}$$

where A_1, A_2, C_1, and C_2 are constants.

Special Cases

$n = 0$: The simplest form of field derivable from ϕ under this condition is one whose spatial dependence is $1/r$. Examples are the electric field due to a line charge ($\lambda = 2\pi\epsilon_\circ$) and the magnetic field associated with a current filament ($I = 2\pi$). Thus with a potential $[\phi_0]_E = \ln r$, we have: $\vec{E} = (1/r)\vec{\imath}_r$; with a potential $[\phi_0]_H = \theta$, we have: $\vec{H} = (1/r)\vec{\imath}_\theta$. Note that each field decays as $1/r$ from its source.

$n = 1$: Both $\phi_1 = \sin\theta/r$ and $\phi_{1'} = \cos\theta/r$ are potentials associated with two-dimensional electric or magnetic dipoles. Note that each form has a singularity at the origin ($r = 0$); they are usually associated with dipole fields that do not include the origin. The choice of $\sin\theta$ or $\cos\theta$ depends on field orientation in the coordinate system. In addition, the potentials $\phi_1' = r\sin\phi$ and $\phi_{1'}' = r\cos\phi$ are associated with uniform vector fields. Examples of 2-D dipole fields are studied in the **PROBLEMS** of ***CHAPTERS 2*** and ***3***.

$n = 2$: The potentials $\phi_2 = \cos 2\theta/r^2$ and $\phi_2' = r^2\cos 2\theta$ are associated with 2-D quadrupole fields. The potential $\phi_2 = \cos 2\theta/r^2$, because of the singularity at the origin, is valid only for space that excludes the origin; $\phi_2' = r^2\cos 2\theta$, for space that excludes infinity. An ideal quadrupole magnet is studied in ***CHAPTER 3***.

2.5.2 Spherical Coordinates

For a potential in spherical coordinates (r, θ, φ):

$$\text{div grad}\,\phi = \nabla^2\phi = \frac{1}{r^2}\frac{\partial}{\partial r}\left(r^2\frac{\partial\phi}{\partial r}\right) + \frac{1}{r^2\sin\theta}\frac{\partial}{\partial\theta}\left(\sin\theta\frac{\partial\phi}{\partial\theta}\right) + \frac{1}{r^2\sin^2\theta}\frac{\partial^2\phi}{\partial\varphi^2} \tag{2.32}$$

The solutions for $\nabla^2\phi$ also can be expressed as the product of functions, each involving only one of the three coordinates:

$$\phi = R(r)\,\Theta(\theta)\,\Phi(\varphi) \tag{2.33a}$$

Functions $R(r)$, $\Theta(\theta)$, and $\Phi(\varphi)$ have the following solutions:

$$R(r) = A_1 r^n + A_2 r^{-(n+1)} \tag{2.33b}$$

$$\Theta(\theta) = CP_n^m(\cos\theta) \qquad (m \le n) \tag{2.33c}$$

$$\Phi(\varphi) = D_1\sin m\varphi + D_2\cos m\varphi \tag{2.33d}$$

A_1, A_2, C, D_1, and D_2 are constants. $P_n^0(\cos\theta)$, or simply $P_n(\cos\theta)$, known as *Legendre Functions*, are useful for *designing* a spatially uniform solenoid magnet, which in the design phase may be assumed symmetric about the z-axis ($\theta = 0$). $P_n^m(\cos\theta)$, known as *Associated Legendre Functions*, are useful for minimizing "error" fields of a *real* solenoid. A magnetic field expression derived from Eq. 2.33 is discussed in more detail in ***CHAPTER 3***. Formulas for $P_n(\cos\theta)$ for $n = 0$–8 and $P_n^m(\cos\theta)$ for $n = 1$–4 ($0 < m \le n$) are given in Table 2.2. Table 2.3 presents $P_n^m(0)$ for combinations of selected values of n and m. Table 2.4 presents solutions of Eq. 2.33 in Cartesian coordinates; these expressions are of practical importance in the design and analysis of uniform-field electromagnetic and ferromagnetic devices.

Special Cases

$n = m = 0$: This case gives rise to the the simplest solution, $\phi_0 \propto 1/r$. A well-known solution is the electric field, $\vec{E} = 1/r^2\,\vec{\imath}_r$ valid for $r > 0$, that emanates from a point charge of magnitude $4\pi\epsilon_\circ$.

$n = 1$, $m = 0$: There are two solutions, $\phi_1 \propto \cos\theta/r^2$ and $\phi_1' \propto r\cos\theta$. ϕ_1 results in a dipole field outside of a sphere the surface of which is distributed with a source that generates this dipole field, while ϕ_1' results in a *uniform* field within the sphere. The dipole field of a magnetic moment is also derivable from ϕ_1.

2.5.3 Differential Operators in Orthogonal Coordinates

The four vector differential operators—grad (∇), div ($\nabla\cdot$), curl ($\nabla\times$), div grad (∇^2)—in three orthogonal sets of coordinates are given below.

Cartesian

The three orthogonal axes are: x, y, z.

$$\text{grad}\, U = \nabla U = \frac{\partial U}{\partial x}\vec{\imath}_x + \frac{\partial U}{\partial y}\vec{\imath}_y + \frac{\partial U}{\partial z}\vec{\imath}_z \tag{2.34a}$$

$$\text{div}\vec{A} = \nabla\cdot\vec{A} = \frac{\partial A_x}{\partial x} + \frac{\partial A_y}{\partial y} + \frac{\partial A_z}{\partial z} \tag{2.34b}$$

$$\begin{aligned}\text{curl}\,\vec{A} = \nabla\times\vec{A} = &\left(\frac{\partial A_z}{\partial y} - \frac{\partial A_y}{\partial z}\right)\vec{\imath}_x + \left(\frac{\partial A_x}{\partial z} - \frac{\partial A_z}{\partial x}\right)\vec{\imath}_y \\ &+ \left(\frac{\partial A_y}{\partial x} - \frac{\partial A_x}{\partial y}\right)\vec{\imath}_z\end{aligned} \tag{2.34c}$$

$$\text{div grad}\, U = \nabla^2 U = \frac{\partial^2 U}{\partial x^2} + \frac{\partial^2 U}{\partial y^2} + \frac{\partial^2 U}{\partial z^2} \tag{2.34d}$$

Cylindrical

The three orthogonal axes are: r, θ, z.

$$\text{grad}\, U = \nabla U = \frac{\partial U}{\partial r}\vec{\imath}_r + \frac{1}{r}\frac{\partial U}{\partial\theta}\vec{\imath}_\theta + \frac{\partial U}{\partial z}\vec{\imath}_z \tag{2.35a}$$

$$\text{div}\,\vec{A} = \nabla\cdot\vec{A} = \frac{1}{r}\frac{\partial(rA_r)}{\partial r} + \frac{1}{r}\frac{\partial A_\theta}{\partial\theta} + \frac{\partial A_z}{\partial z} \tag{2.35b}$$

$$\begin{aligned}\text{curl}\,\vec{A} = \nabla\times\vec{A} = &\left(\frac{1}{r}\frac{\partial A_z}{\partial\theta} - \frac{\partial A_\theta}{\partial z}\right)\vec{\imath}_r + \left(\frac{\partial A_r}{\partial z} - \frac{\partial A_z}{\partial r}\right)\vec{\imath}_\theta \\ &+ \left[\frac{1}{r}\frac{\partial(rA_\theta)}{\partial r} - \frac{1}{r}\frac{\partial A_r}{\partial\theta}\right]\vec{\imath}_z\end{aligned} \tag{2.35c}$$

$$\text{div grad}\, U = \nabla^2 U = \frac{1}{r}\frac{\partial}{\partial r}\left(r\frac{\partial U}{\partial r}\right) + \frac{1}{r^2}\frac{\partial^2 U}{\partial\theta^2} + \frac{\partial^2 U}{\partial z^2} \tag{2.29}$$

Spherical

The orthogonal axes are: r, θ, and φ.

$$\operatorname{grad} U = \nabla U = \frac{\partial U}{\partial r}\vec{\imath}_r + \frac{1}{r}\frac{\partial U}{\partial \theta}\vec{\imath}_\theta + \frac{1}{r\sin\theta}\frac{\partial U}{\partial \varphi}\vec{\imath}_\phi \tag{2.36a}$$

$$\operatorname{div} \vec{A} = \nabla \cdot \vec{A} = \frac{1}{r^2}\frac{\partial (r^2 A_r)}{\partial r} + \frac{1}{r\sin\theta}\frac{\partial (A_\theta \sin\theta)}{\partial \theta} + \frac{1}{r\sin\theta}\frac{\partial A_\varphi}{\partial \varphi} \tag{2.36b}$$

$$\begin{aligned}\operatorname{curl} \vec{A} = \nabla \times \vec{A} = &\left[\frac{1}{r\sin\theta}\frac{\partial (A_\varphi \sin\theta)}{\partial \theta} - \frac{1}{r\sin\theta}\frac{\partial A_\theta}{\partial \varphi}\right]\vec{\imath}_r \\ &+ \left[\frac{1}{r\sin\theta}\frac{\partial A_r}{\partial \varphi} - \frac{1}{r}\frac{\partial (r A_\varphi)}{\partial r}\right]\vec{\imath}_\theta \\ &+ \left[\frac{1}{r}\frac{\partial (r A_\theta)}{\partial r} - \frac{1}{r}\frac{\partial A_r}{\partial \theta}\right]\vec{\imath}_\phi\end{aligned} \tag{2.36c}$$

$$\begin{aligned}\operatorname{div}\operatorname{grad} U = \nabla^2 U = &\frac{1}{r^2}\frac{\partial}{\partial r}\left(r^2\frac{\partial U}{\partial r}\right) + \frac{1}{r^2\sin\theta}\frac{\partial}{\partial \theta}\left(\sin\theta\frac{\partial U}{\partial \theta}\right) \\ &+ \frac{1}{r^2\sin^2\theta}\frac{\partial^2 U}{\partial \varphi^2}\end{aligned} \tag{2.32}$$

Adrien Marie Legendre (1752–1833)

—Passage from Dirk J. Struik's *A Concise History of Mathematics**

In his history of mathematics of the Nineteenth Century Felix Klein has invited comparison between Gauss and the twenty-five year older French mathematician Adrien Marie Legendre. It is perhaps not entirely fair to compare Gauss with any mathematician except the very greatest; but this particular comparison shows how Gauss' ideas were "in the air," since Legendre in his own independent way worked on most subjects which occupied Gauss . . .

Like Gauss he did fundamental work on number theory where he gave a formulation of the law of quadratic reciprocity. He also did important work on geodesy and theoretical astronomy, was as assiduous a computer of tables as Gauss, formulated in 1806 the method of least squares, and studied the attraction of ellipsoids—even those which are not surfaces of revolution. He introduced the "Legendre" functions. He also shared Gauss' interest in elliptic and Eulerian integrals as well as in the foundations and methods of Euclidean geometry.

. . .His comprehensive textbooks were for a long time authoritative, especially his "Exercises du calcul intégral" (1811–19) and his "Traité des fonctions elliptiques et des intégrales eulériennes" (1827–32), still a standard work . . . In his "Elements de géométrie" (1794) he broke with the Platonic ideals of Euclid and presented a textbook of elementary geometry based on the requirements of modern education.

* Dover Publications, Inc., New York, 1948. For many years until his retirement in 1960, Dirk J. Struik (1894–2000) taught mathematics at M.I.T.

2.5.4 Legendre Functions

For $m=0$ the $P_n^m(\cos\theta)$ polynomials (Eq. 2.33c) are known as *Legendre Functions* of order n; i.e., $P_n^0(\cos\theta)\equiv P_n(\cos\theta)\equiv P_n(u)$, where $u=\cos\theta$. For $1\le m\le n$, the polynomials are known as *Associated Legendre Functions*. $P_n^m(\cos\theta)\equiv P_n^m(u)$ satisfies the following differential equation for v:

$$\frac{d}{du}\left[(1-u^2)\frac{dv}{du}\right]+\left[n(n+1)-\frac{m^2}{1-u^2}\right]v=0 \tag{2.37}$$

As stated earlier, $P_n(u)$, i.e., $m=0$, is of particular use in the solution of a magnetic field with *rotational symmetry* such as that in an *ideal* solenoid; $P_n^m(u)$ is useful for field analysis of a *real* solenoid that, because of imperfections, lacks rotational symmetry. $P_n(u)$ and $P_n^m(u)$ are given by:

$$P_n(u)=\left(\frac{1}{2^n n!}\right)\frac{d^n(u^2-1)^n}{du^n} \tag{2.38a}$$

$$P_n^m(u)=(1-u^2)^{m/2}\frac{d^m P_n(u)}{du^m} \tag{2.38b}$$

$$=\left[\frac{(1-u^2)^{m/2}}{2^n n!}\right]\frac{d^{m+n}(u^2-1)^n}{du^{m+n}} \tag{2.38c}$$

Some useful recurrence formulas for Legendre functions, $P_n(u)$, and Associated Legendre functions, $P_n^m(u)$, are:

$$(n+1)P_{n+1}(u)-(2n+1)uP_n(u)+nP_{n-1}(u)=0 \tag{2.39a}$$

$$(n+1-m)P_{n+1}^m(u)-(2n+1)uP_n^m(u)+(n+m)P_{n-1}^m(u)=0 \tag{2.39b}$$

$$P_n^{m+2}(u)-\frac{2(m+1)u}{\sqrt{(1-u^2)}}P_n^{m+1}(u)+(n-m)(n+m-1)P_n^m(u)=0 \tag{2.39c}$$

Table 2.2 lists Legendre functions, $P_n(u)$, for n up to 8; and Associated Legendre functions, $P_n^m(u)$, for m $(1\le m\le n)$ up to 4. Table 2.3 presents $P_n^m(0)$ for combinations of n of 2, 4, 6, 8, 10 and m of 0, 2, 4, 6, 8, and 10. Table 2.4 presents solutions of Eq. 2.32 in Cartesian coordinates.

Answer to TRIVIA 2.1 iv). The Danish astronomer Olaus Roemer (1644–1710) used two reference objects, Jupiter and earth, to clock light at 2.27×10^8 m/s, which is 76% of the modern accepted value: 2.99792458×10^8 m/s.

Table 2.2: Legendre and Associated Legendre Functions

Legendre Functions $(m=0)$ $[P_n(0)=0$ for n odd$]$		
n	$P_n(\cos\theta)\equiv P_n(u)$	*Multiple-Angle Form*
0	1	1
1	u	$\cos\theta$
2	$\frac{1}{2}(3u^2-1)$	$\frac{1}{4}(3\cos 2\theta+1)$
3	$\frac{1}{2}(5u^3-3u)$	$\frac{1}{8}(5\cos 3\theta+3\cos\theta)$
4	$\frac{1}{8}(35u^4-30u^2+3)$	$\frac{1}{64}(35\cos 4\theta+20\cos 2\theta+9)$
5	$\frac{1}{8}(63u^5-70u^3+15u)$	$\frac{1}{128}(63\cos 5\theta+35\cos 3\theta+30\cos\theta)$
6	$\frac{1}{16}(231u^6-315u^4+105u^2-5)$	$\frac{1}{512}(231\cos 6\theta+126\cos 4\theta+105\cos 2\theta+50)$
7	$\frac{1}{16}(429u^7-693u^5+315u^3-35u)$	$\frac{1}{1024}(429\cos 7\theta+231\cos 5\theta+189\cos 3\theta+175\cos\theta)$
8	$\frac{1}{128}(6435u^8-12012u^6+6930u^4-1260u^2+35)$	$\frac{1}{16384}(6435\cos 8\theta+3432\cos 6\theta+2772\cos 4\theta+2520\cos 2\theta+1225)$
Associated Legendre Functions $(1\le m\le n)$ $[P_n^m(1)=0]$		
$m,\ n$	$P_n^m(\cos\theta)\equiv P_n^m(u)$	*Multiple-Angle Form*
1, 1	$(1-u^2)^{1/2}$	$\sin\theta$
2	$3u(1-u^2)^{1/2}$	$\frac{3}{2}\sin 2\theta$
3	$\frac{3}{2}(1-u^2)^{1/2}(5u^2-1)$	$\frac{3}{8}(\sin\theta+5\sin 3\theta)$
4	$\frac{5}{2}(1-u^2)^{1/2}(7u^3-3u)$	$\frac{5}{16}(2\sin 2\theta+7\sin 4\theta)$
2, 2	$3(1-u^2)$	$\frac{3}{2}(1-\cos 2\theta)$
3	$15(1-u^2)u$	$\frac{15}{4}(\cos\theta-\cos 3\theta)$
4	$\frac{15}{2}(1-u^2)(7u^2-1)$	$\frac{15}{16}(3+4\cos 2\theta-7\cos 4\theta)$
3, 3	$15(1-u^2)^{3/2}$	$\frac{15}{4}(3\sin\theta-\sin 3\theta)$
4	$105(1-u^2)^{3/2}u$	$\frac{105}{8}(2\sin 2\theta-\sin 4\theta)$
4, 4	$105(1-u^2)^2$	$\frac{105}{8}(3-4\cos 2\theta+\cos 4\theta)$

Table 2.3: Values of $P_n^m(0)$ for m of 0, 2, 4, 6, 8, 10

m	$P_n^m(0)$
0	$P_2(0)=-\frac{1}{2};\quad P_4(0)=\frac{3}{8};\quad P_6(0)=-\frac{5}{16};\quad P_8(0)=\frac{35}{128};\quad P_{10}(0)=-\frac{63}{256}$
2	$P_2^2(0)=3;\quad P_4^2(0)=-\frac{15}{2};\quad P_6^2(0)=\frac{105}{8};\quad P_8^2(0)=-\frac{315}{16};\quad P_{10}^2(0)=\frac{3465}{128}$
4	$P_4^4(0)=3\cdot5\cdot7=105;\quad P_6^4(0)=-\frac{945}{2};\quad P_8^4(0)=\frac{10395}{8};\quad P_{10}^4(0)=-\frac{45045}{16}$
6	$P_6^6(0)=3\cdot5\cdot7\cdot9\cdot11=10395;\quad P_8^6(0)=-\frac{135135}{2};\quad P_{10}^6(0)=\frac{2027025}{8}$
8	$P_8^8(0)=3\cdot5\cdot7\cdot9\cdot11\cdot13\cdot15=2027025;\ P_{10}^8(0)=-\frac{3\cdot5\cdot7\cdot9\cdot11\cdot13\cdot15\cdot17}{2}=-\frac{34459425}{2}$
10	$P_{10}^{10}(0)=3\cdot5\cdot7\cdot9\cdot11\cdot13\cdot15\cdot17\cdot19=654729075$

TRIVIA 2.2 Identify the location for which each of the elements below is named.

i) Copper; i) Lutetium; ii) Magnesium; iv) Yttrium.

Table 2.4: Solutions of Equation 2.32 in Cartesian Coordinates

Legendre Functions ($m = 0$)		
n	$r^n P_n(u)$	
0	1	
1	z	
2	$z^2 - \frac{1}{2}(x^2+y^2)$	
3	$z^3 - \frac{3}{2}(x^2+y^2)z$	
4	$z^4 - 3(x^2+y^2)[z^2 - \frac{1}{8}(x^2+y^2)]$	
5	$z^5 - 5(x^2+y^2)[z^2 - \frac{3}{8}(x^2+y^2)]z$	
6	$z^6 - \frac{5}{2}(x^2+y^2)[3z^4 - \frac{9}{4}z^2(x^2+y^2) + \frac{1}{8}(x^2+y^2)^2]$	
7	$z^7 - \frac{7}{16}(x^2+y^2)[24z^4 - 30z^2(x^2+y^2) + 5(x^2+y^2)^2]z$	
8	$z^8 - \frac{7}{128}(x^2+y^2)[256z^6 - 480z^4(x^2+y^2) + 160z^2(x^2+y^2)^2 - 5(x^2+y^2)^3]$	
Associated Legendre Functions ($1 \le m \le n$)		
m, n	$r^n P_n^m(u)\cos(m\varphi)$	$r^n P_n^m(u)\sin(m\varphi)$
1, 1	x	y
2	$3zx$	$3zy$
3	$6x[z^2 - \frac{1}{4}(x^2+y^2)]$	$6y[z^2 - \frac{1}{4}(x^2+y^2)]$
4	$10zx[z^2 - \frac{3}{4}(x^2+y^2)]$	$10zy[z^2 - \frac{3}{4}(x^2+y^2)]$
2, 2	$3(x^2 - y^2)$	$3(2xy)$
3	$15z(x^2 - y^2)$	$15z(2xy)$
4	$45(x^2 - y^2)[z^2 - \frac{1}{6}(x^2+y^2)]$	$45(2xy)[z^2 - \frac{1}{6}(x^2+y^2)]$
3, 3	$15x(x^2 - 3y^2)$	$15y(3x^2 - y^2)$
4	$105zx(x^2 - 3y^2)$	$105zy(3x^2 - y^2)$
4, 4	$105(x^4 - 6x^2y^2 + y^4)$	$210(2xy)(x^2 - y^2)$

"It was absolutely marvelous working for Pauli. You could ask him anything. There was no worry that he would think a particular question was stupid, since he thought all *questions were stupid."* —Victor F. Weisskopf

PROBLEM 2.1: Magnetized sphere in a uniform field

This problem deals with a magnetic sphere exposed to a uniform external magnetic field. Note that there is no net force acting on the sphere (because the background field is uniform). The field expression inside the sphere may be used to estimate the force on a ferromagnetic object placed in the fringing field generated by a magnet nearby. This force on an iron object due to the fringing field of a magnet is the subject of ***DISCUSSION 3.12*** (p. 200) in ***CHAPTER 3***.

Figure 2.1 shows a magnetic sphere of radius R and permeability μ in a uniform external magnetic field given by:

$$\vec{H}_\infty = H_0(-\cos\theta\vec{\imath}_r + \sin\theta\vec{\imath}_\theta) \tag{2.40}$$

a) Show that expressions for the magnetic inductions outside ($\vec{B}_1$) and inside ($\vec{B}_2$) the sphere are given by:

$$\vec{B}_1 = \mu_\circ H_0(-\cos\theta\vec{\imath}_r + \sin\theta\vec{\imath}_\theta) + \mu_\circ\left(\frac{\mu_\circ - \mu}{2\mu_\circ + \mu}\right) H_0\left(\frac{R}{r}\right)^3 (2\cos\theta\vec{\imath}_r + \sin\theta\vec{\imath}_\theta) \tag{2.41a}$$

$$\vec{B}_2 = \frac{3\mu_\circ\mu H_0}{2\mu_\circ + \mu}(-\cos\theta\vec{\imath}_r + \sin\theta\vec{\imath}_\theta) \tag{2.41b}$$

Considering the following three limiting cases, $\mu/\mu_\circ = 0$, $\mu/\mu_\circ = 1$, and $\mu/\mu_\circ = \infty$, confirm that the resulting expressions for the field in the sphere are physically plausible.

b) Picture, in your mind, $\vec{B}$ distributions that would correspond to $\mu = 0.1\mu_\circ$ and $\mu = 100\mu_\circ$. These distributions are shown in Fig. 2.2.

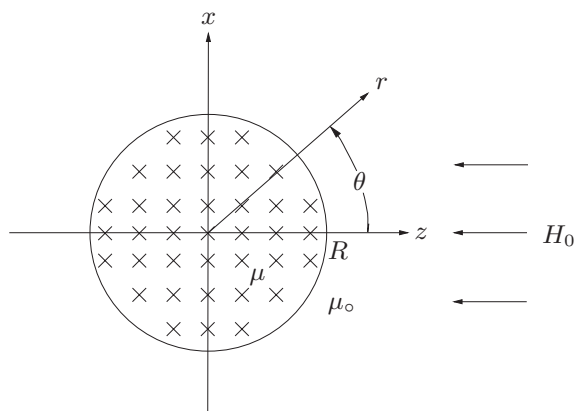

Fig. 2.1 Magnetized sphere in a uniform magnetic field.

Solution to PROBLEM 2.1

a) This problem is most easily solved using scalar potentials, as discussed in the introductory section of this chapter. Namely, the magnetic potential ϕ is a scalar field such that:

$$\vec{H} = -\nabla\phi \tag{S1.1}$$

In linear, isotropic media, magnetic field and magnetic induction are related by:

$$\vec{B} = \mu\vec{H} \tag{S1.2}$$

The problem is divided into two regions, Region 1 ($r \geq R$) and Region 2 ($r \leq R$). Based on solutions of Eq. 2.33 and because $H_\infty = H_0$ at $r = \infty$ and $H \neq \pm\infty$ at $r = 0$, the appropriate potential for each region is:

$$\phi_1 = H_0 r\cos\theta + \frac{A}{r^2}\cos\theta \qquad (r \geq R) \tag{S1.3a}$$

$$\phi_2 = Cr\cos\theta \qquad (r \leq R) \tag{S1.3b}$$

Note that $\phi_1 \to H_0 r\cos\theta$ for $r \to \infty$ (Eq. 2.40), and ϕ_2 remains finite at $r = 0$.

Using the ∇ operator in spherical coordinates (Eq. 2.36a), we have $\vec{H}_1$ and $\vec{H}_2$:

$$\begin{aligned}\vec{H}_1 &= -\frac{\partial}{\partial r}\left(H_0 r\cos\theta + \frac{A}{r^2}\cos\theta\right)\vec{\imath}_r - \frac{1}{r}\frac{\partial}{\partial\theta}\left(H_0 r\cos\theta + \frac{A}{r^2}\cos\theta\right)\vec{\imath}_\theta \\ &= H_0(-\cos\theta\vec{\imath}_r + \sin\theta\vec{\imath}_\theta) + \frac{A}{r^3}(2\cos\theta\vec{\imath}_r + \sin\theta\vec{\imath}_\theta)\end{aligned} \tag{S1.4a}$$

$$\begin{aligned}\vec{H}_2 &= -\frac{\partial}{\partial r}(Cr\cos\theta)\vec{\imath}_r - \frac{1}{r}\frac{\partial}{\partial\theta}(Cr\cos\theta)\vec{\imath}_\theta \\ &= C(-\cos\theta\vec{\imath}_r + \sin\theta\vec{\imath}_\theta)\end{aligned} \tag{S1.4b}$$

Boundary Conditions

1) At $r = R$, the tangential component ($\vec{\imath}_\theta$) of $\vec{H}$ is continuous, since there is no surface current. This is equivalent to equating the potentials at $r = R$ ($\phi_1 = \phi_2$):

$$H_0 + \frac{A}{R^3} = C \tag{S1.5}$$

2) At $r = R$, the normal component ($\vec{\imath}_r$) of $\vec{B}$ is continuous:

$$\mu_\circ\left(-H_0 + 2\frac{A}{R^3}\right) = -\mu C \tag{S1.6}$$

From Eqs. $S1.5$ and $S1.6$, we can solve for the constants C and A:

$$C = \frac{3H_0\mu_\circ}{2\mu_\circ + \mu} \tag{S1.7}$$

$$A = (C - H_0)R^3 = H_0\left(\frac{\mu_\circ - \mu}{2\mu_\circ + \mu}\right)R^3 \tag{S1.8}$$

Solution to PROBLEM 2.1 (continuation)

$\vec{B}_1$ and $\vec{B}_2$ are thus:

$$\vec{B}_1 = \mu_\circ H_0(-\cos\theta\vec{\imath}_r + \sin\theta\vec{\imath}_\theta) + \mu_\circ \left(\frac{\mu_\circ - \mu}{2\mu_\circ + \mu}\right) H_0 \left(\frac{R}{r}\right)^3 (2\cos\theta\vec{\imath}_r + \sin\theta\vec{\imath}_\theta) \qquad (2.41a)$$

$$\vec{B}_2 = \frac{3\mu_\circ \mu H_0}{2\mu_\circ + \mu}(-\cos\theta\vec{\imath}_r + \sin\theta\vec{\imath}_\theta) \qquad (2.41b)$$

Now, let us consider the three special cases of $\mu/\mu_\circ$.

Case 1: $\mu/\mu_\circ = 0$

With $\mu = 0$ inserted into Eqs. 2.41*a* and 2.41*b*, we obtain:

$$\vec{B}_1 = \mu_\circ H_0(-\cos\theta\vec{\imath}_r + \sin\theta\vec{\imath}_\theta) + \frac{\mu_\circ H_0}{2}\left(\frac{R}{r}\right)^3 (2\cos\theta\vec{\imath}_r + \sin\theta\vec{\imath}_\theta) \qquad (S1.9a)$$

$$\vec{B}_2 = 0 \qquad (S1.9b)$$

The sphere is like a Type I superconductor; no magnetic flux density is allowed inside the sphere—the Meissner effect. The profile is identical to the schematic profile corresponding to point C for superconductor (Sc) shown in Fig. 1.1b. As will be discussed in **PROBLEM 2.2**, a discontinuity in the θ component of the $\vec{H}$ fields at $r = R$ requires a surface current (confined within a thin layer). Because this current, once set up, must flow persistently, it implies that the sphere has zero resistivity to the flow of these currents. As discussed in ***CHAPTER 1***, a material that exhibits the Meissner effect must at the same time be a perfect conductor: such a material is automatically a superconductor.

Case 2: $\mu/\mu_\circ = 1$

The problem reduces to the trivial case, equivalent to the absence of the sphere. Note that with $\mu = \mu_\circ$ into Eqs. 2.41*a* and 2.41*b*, the equations become identical.

Case 3: $\mu/\mu_\circ = \infty$

This case is that of a perfectly ferromagnetic material; soft iron comes close. The magnetic field is *drawn* into the sphere. With $\mu = \infty$ in Eqs. 2.41*a* and 2.41*b*:

$$\vec{B}_1 = \mu_\circ H_0(-\cos\theta\vec{\imath}_r + \sin\theta\vec{\imath}_\theta) - \mu_\circ H_0 \left(\frac{R}{r}\right)^3 (2\cos\theta\vec{\imath}_r + \sin\theta\vec{\imath}_\theta) \qquad (S1.10a)$$

$$\vec{B}_2 = 3\mu_\circ H_0(-\cos\theta\vec{\imath}_r + \sin\theta\vec{\imath}_\theta) \qquad (S1.10b)$$

The important point to note is that the $\vec{B}$ field within the sphere of $\mu/\mu_\circ = \infty$ is three times the applied $\vec{B}$ field. Note that if the sphere's magnetization is saturated, μ no longer is ∞. The effects of field saturation, present in all magnetic materials, will be discussed in **PROBLEM 2.3**.

Solution to PROBLEM 2.1 (continuation)

b) Figure 2.2 shows field lines for two spheres of $\mu/\mu_\circ = 0.1$ and $\mu/\mu_\circ = 100$.

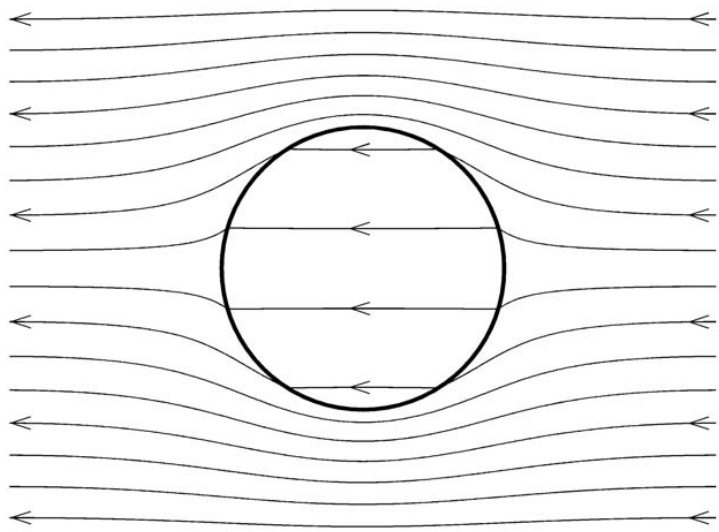

$\mu/\mu_\circ = 0.1$

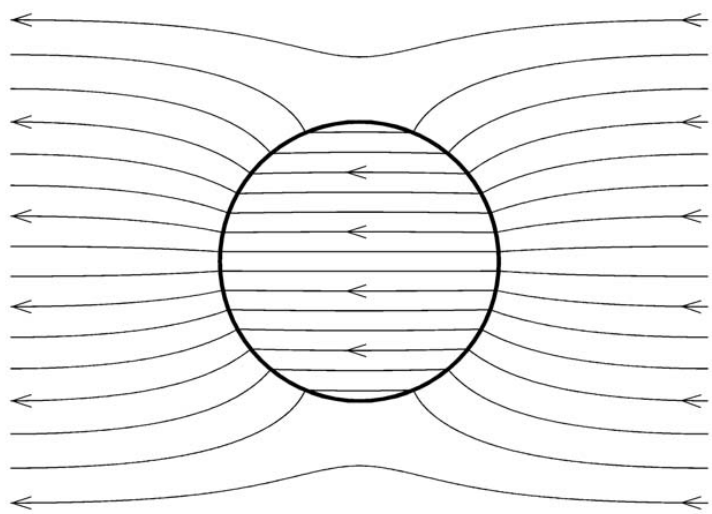

$\mu/\mu_\circ = 100$

Fig. 2.2 Field lines inside and near spheres of $\mu/\mu_\circ = 0.1$ (top) and $\mu/\mu_\circ = 100$ (bottom). For the top sphere, the line spacing at $r = \infty$ is $\sim 2.6 (= \sqrt{2.1/0.3})$ times denser than that inside the sphere, while for the bottom sphere, the inside line spacing is $\sim 1.7 (= \sqrt{300/101})$ times that at $r = \infty$. These ratios are valid in both the plane of the paper and that perpendicular to it. A *cylinder* of $\mu/\mu_\circ = 100$ would have a ratio of 200/101, but only in the plane of the paper. Note that the field lines entering and leaving the sphere are *nearly* perpendicular to the surface for $\mu/\mu_\circ = 100$—perpendicular for $\mu/\mu_\circ = \infty$.

PROBLEM 2.2: Type I superconducting rod in a uniform field

This problem deals with a Type I superconductor (Meissner effect). The field solution is interpreted in terms of the London theory of superconductivity.

Figure 2.3 shows an infinitely long lead (Pb) rod of circular cross section (radius R) subjected to a uniform external magnetic field perpendicular to its axis.

$$\vec{H}_\infty = H_0(-\cos\theta\vec{\imath}_r + \sin\theta\vec{\imath}_\theta) \tag{2.40}$$

where $\mu_\circ H_0 = 0.08\,\mathrm{T}$. Initially the rod is in the *normal* state. The field thus is everywhere the same, including inside the rod. The rod is then gradually cooled until it becomes superconducting.

a) Show that an expression for the field outside the superconducting rod, $\vec{H}_1$, after transient effects of the field change have subsided, is given by:

$$\vec{H}_1 = H_0(-\cos\theta\vec{\imath}_r + \sin\theta\vec{\imath}_\theta) + H_0\left(\frac{R}{r}\right)^2(\cos\theta\vec{\imath}_r + \sin\theta\vec{\imath}_\theta) \tag{2.42}$$

(Note that Eq. 2.41*a* corresponds to $\vec{B}_1$ for a magnetic *sphere*.)

b) Show that an expression for the surface current (free) density, $\vec{K}_f$ [A/m], flowing within a penetration depth $\lambda \ll R$, is given by:

$$\vec{K}_f = 2H_0\sin\theta\vec{\imath}_z \tag{2.43}$$

c) Convert the magnitude of the surface current density to that of current density, J_f [A/m^2], and confirm that its value is consistent with that for lead derivable from London's theory of superconductivity.

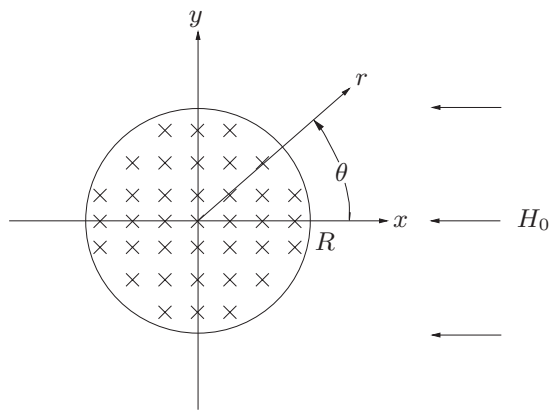

Fig. 2.3 Infinitely long, circular cross section superconducting rod in a uniform magnetic field.

Solution to PROBLEM 2.2

a) The problem is divided into two regions, Region 1 ($r \geq R$) and Region 2 ($r \leq R$). Because we are dealing with a Type I superconductor, $\vec{B}_2 = 0$ ($\phi_2 = 0$) when the rod is superconducting. The field in Region 1 is derivable from a potential:

$$\phi_1 = H_0 r \cos\theta + \frac{A}{r}\cos\theta \tag{S2.1}$$

Note that $\phi_1 \to H_0 r \cos\theta$ for $r \to \infty$, as required by Eq. 2.40.

Using the ∇ operator in cylindrical coordinates (Eq. 2.35a), we can derive $\vec{H}_1$:

$$\vec{H}_1 = -\frac{\partial}{\partial r}\left(H_0 r\cos\theta + \frac{A}{r}\cos\theta\right)\vec{\imath}_r - \frac{1}{r}\frac{\partial}{\partial\theta}\left(H_0 r\cos\theta + \frac{A}{r}\cos\theta\right)\vec{\imath}_\theta \tag{S2.2}$$

$$= -\left(H_0\cos\theta - \frac{A}{r^2}\cos\theta\right)\vec{\imath}_r - \left(-H_0\sin\theta - \frac{A}{r^2}\sin\theta\right)\vec{\imath}_\theta \tag{S2.3}$$

Rearranging Eq. $S2.3$, we have:

$$\vec{H}_1 = H_0(-\cos\theta\vec{\imath}_r + \sin\theta\vec{\imath}_\theta) + \frac{A}{r^2}(\cos\theta\vec{\imath}_r + \sin\theta\vec{\imath}_\theta) \tag{S2.4}$$

The continuity of the normal component of B requires that the coefficient of $\vec{\imath}_r$ in Eq. $S2.3$ be zero at $r = R$:

$$-H_0 + \frac{A}{R^2} = 0 \tag{S2.5}$$

Solving Eq. $S2.5$ for A, we obtain:

$$A = R^2 H_0 \tag{S2.6}$$

The field outside the superconducting rod (Region 1) is thus given by:

$$\vec{H}_1 = H_0(-\cos\theta\vec{\imath}_r + \sin\theta\vec{\imath}_\theta) + H_0\left(\frac{R}{r}\right)^2(\cos\theta\vec{\imath}_r + \sin\theta\vec{\imath}_\theta) \tag{2.42}$$

Note that at $r = R, \theta = 90°$, $|\vec{H}_1| = 2H_0$; the field amplitude is twice the far-field amplitude. Physically, the field originally inside when the rod is in the normal state is now pushed outside and compressed at and near $\theta = 90°$.

b) Because of the discontinuity at $r = R$ of $2H_0\sin\theta$ in the tangential ($\vec{\imath}_\theta$) component of $\vec{H}$, there must be a surface current density $\vec{K}_f$ flowing in the rod, as given by Eq. 2.6. We thus have:

$$\begin{aligned}\vec{K}_f &= \vec{\imath}_r \times 2H_0\sin\theta\vec{\imath}_\theta \\ &= 2H_0\sin\theta\vec{\imath}_z\end{aligned} \tag{2.43}$$

This "sine" (more commonly known as "cosine") current distribution is the basis for most of the dipole magnets in the so-called "atom smashers" used in high-energy physics facilities. An "ideal" dipole magnet is studied in **PROBLEM 3.8**.

Solution to PROBLEM 2.2 (continuation)

c) According to the London theory of superconductivity (**1.2.2** in ***CHAPTER 1***), the supercurrent density, J_s, of Type I superconductors is given by $J_s = en_{se}v$, where e is the electronic charge (1.6×10^{-19} C), n_{se} is the superconducting electron density, and v is the drift velocity of superconducting electrons. The superconducting electron density may be roughly equated to the density of free electrons, n_{fe} (Eq. 1.2):

$$n_{se} \approx n_{fe} = \frac{\varrho N_A}{W_A} \tag{1.2}$$

With values for lead of $\varrho = 11.4\,\mathrm{g/cm^3}$, $N_A = 6.023\times10^{23}$ particle/mole, and $W_A = 207.2\,\mathrm{g/mole}$, we have:

$$n_{se} \approx \frac{(11.4\,\mathrm{g/cm^3})(6.023\times10^{23}\,\mathrm{particle/mole})}{207.2\,\mathrm{g/mole}} \tag{S2.7}$$

$$\simeq 3.3\times10^{22}\,\mathrm{particle/cm^3} = 3.3\times10^{28}\,\mathrm{electron/m^3}$$

With $v \sim 200\,\mathrm{m/s}$ roughly equal to the drift velocity of superconducting electrons, we obtain an *order of magnitude* for J_s:

$$J_s = en_{se}v \sim (1.6\times10^{-19}\,\mathrm{C})(3.3\times10^{28}\,\mathrm{m^{-3}})(200\,\mathrm{m/s})$$

$$\sim 1\times10^{12}\,\mathrm{A/m^2}$$

The surface current density, $K_f = J_f\lambda$, required in this lead cylinder should be such that J_f is *roughly* equal to J_s, an order of magnitude of which is computed above. The London theory gives an expression (Eq. 1.1) for the penetration depth, λ, at the superconductor's surface within which superconducting current flows. Equation 1.1 is once again given below:

$$\lambda = \sqrt{\frac{m}{\mu_\circ e^2 n_{se}}} \tag{1.1}$$

With $m = 9.1\times10^{-31}\,\mathrm{kg}$ and n_{se} from Eq. $S2.7$, Eq. 1.1 becomes:

$$\lambda = \sqrt{\frac{(9.1\times10^{-31}\,\mathrm{kg})}{(4\pi\times10^{-7}\,\mathrm{H/m})(1.6\times10^{-19}\,\mathrm{C})^2(3.3\times10^{28}\,\mathrm{m^{-3}})}}$$

$$\simeq 3\times10^{-8}\,\mathrm{m}$$

Because $K_f = J_f\lambda$:

$$J_f = \frac{2H_0}{\lambda} = \frac{2(\mu_\circ H_0)}{\mu_\circ\lambda} = \frac{2(0.08\,\mathrm{T})}{(4\pi\times10^{-7}\,\mathrm{H/m})(3\times10^{-8}\,\mathrm{m})} \tag{S2.9}$$

$$\simeq 4\times10^{12}\,\mathrm{A/m^2}$$

That is, J_s and J_s are *roughly* equal.

DISCUSSION 2.1: Perfect-Conductor Sphere in a Uniform Field

Here we derive quantitative field expressions for a perfectly conducting ($\rho = 0$) sphere subjected to a field change, specifically the $C \Rightarrow D$ change illustrated in Fig. 1.1c (*CHAPTER 1*). At point C, the entire space, including that within the sphere, is in a uniform external field given by Eq. 2.40 of **PROBLEM 2.1**. The same spherical coordinates as those of Fig. 2.1 in **PROBLEM 2.1** apply.

When the uniform external field is reduced to zero (point D in Fig. 1.1c), because the magnetic induction cannot change within the sphere, its field, $\vec{H}_2$, must remain as the same:

$$\vec{H}_2 = H_0(-\cos\theta\vec{\imath}_r + \sin\theta\vec{\imath}_\theta) \qquad (r \le R) \tag{2.44a}$$

Far away from center, $r \to \infty$, the field outside the sphere, $\vec{H}_1$, is zero. Near the sphere, the field is derivable from a scalar potential, i.e., $\phi_1 = (A/r^2)\cos\theta$. The ∇ operation on ϕ_1 leads to a dipole field in spherical coordinates of the form:

$$\vec{H}_1 = \frac{A}{r^3}(2\cos\theta\vec{\imath}_r + \sin\theta\vec{\imath}_\theta) \qquad (r \ge R) \tag{2.44b}$$

At $r = R$, the normal component of B must be continuous. Because at $\theta = 0$ there is only a normal component of field both inside and outside of the sphere:

$$-H_0 = 2\frac{A}{R^3}$$

Therefore $A = -H_0R^3/2$, and thus:

$$\vec{H}_1 = -H_0\left(\frac{R}{r}\right)^3(\cos\theta\vec{\imath}_r + \tfrac{1}{2}\sin\theta\vec{\imath}_\theta) \tag{2.44c}$$

Equation 2.44*c* is a quantitative expression of the field distribution, except that in Fig. 1.1c the external field is from bottom to top, whereas in Fig. 2.1 the field points from right to left.

The discontinuity in the tangential component of magnetic field at $r = R$ is equal to a surface current density, $\vec{K}_f$, flowing in the sphere at $r = R$. Applying Eq. 2.6 and combining Eqs. 2.44*a* and 2.44*c*, we obtain:

$$\begin{aligned}\vec{K}_f &= \vec{\imath}_r \times [H_0\sin\theta\vec{\imath}_\theta - (-\tfrac{1}{2}H_0\sin\theta\vec{\imath}_\theta)] \\ &= \tfrac{3}{2}H_0\sin\theta\vec{\imath}_\varphi\end{aligned} \tag{2.45}$$

Note that the $\sin\theta$ distribution could be approximated with a "thin" coil wound on the surface of the sphere with a *uniform turn density in the the z-axis direction.*

Answer to TRIVIA 2.2 Cu: Latin *cuprum*, from Cyprus island; Lu: Lutetia, ancient name of Paris; Mg: Magnesia, district in Thessaly, Greece; Y: Ytterby, village in Sweden. Ytterby is also used for three other rare earth elements: erbium (Er); terbium (Tb); and ytterbium (Yb).

PROBLEM 2.3: Magnetic shielding with a spherical shell

This problem deals with passive magnetic shielding, an important subject for MRI, Maglev, and other high-field systems where people and field-sensitive equipment might be exposed to a fringing field. The U.S. Food and Drug Administration limits the maximum fringing field in MRI systems to 5 gauss (0.5 mT).

Within a spherical region of space, a uniform magnetic field, $\vec{H}_\infty$, is to be shielded:

$$\vec{H}_\infty = H_0(-\cos\theta\vec{\imath}_r + \sin\theta\vec{\imath}_\theta) \tag{2.40}$$

For shielding, a spherical shell of o.d. $2R$ and wall thickness $d/R \ll 1$ of highly permeable material ($\mu/\mu_\circ \gg 1$) may be used, as shown schematically in Fig. 2.4.

a) Treating the problem as one of a magnetic spherical shell in a uniform external field, show that an expression for H_{ss}/H_0, where H_{ss} is the magnitude of the magnetic field inside the spherical space ($r \le R-d$), is given by:

$$\frac{H_{ss}}{H_0} = \frac{9\mu\mu_\circ}{9\mu\mu_\circ + 2(\mu-\mu_\circ)^2\left[1-\left(1-\dfrac{d}{R}\right)^3\right]} \tag{2.46}$$

b) Show that in the limits of $\mu/\mu_\circ \gg 1$ and $d/R \ll 1$, the ratio H_{ss}/H_0 given by Eq. 2.46 reduces to:

$$\frac{H_{ss}}{H_0} \simeq \tfrac{3}{2}\left(\frac{\mu_\circ}{\mu}\right)\left(\frac{R}{d}\right) \tag{2.47}$$

c) Next, obtain Eq. 2.47 through a perturbation approach. First, solve the field in the shell ($R-d \le r \le R$) with $\mu=\infty$. Then, use a perturbation approach for the case $\mu/\mu_\circ \gg 1$ and obtain Eq. 2.47.

d) In reality the magnetic flux in the shielding material must be kept below the material's saturation flux, $\mu_\circ M_{sa}$. Show that an expression for d/R to keep the shell unsaturated is given by:

$$\frac{d}{R} \ge \frac{3H_0}{2M_{sa}} \tag{2.48}$$

e) Draw field lines for the case $\mu/\mu_\circ \gg 1$.

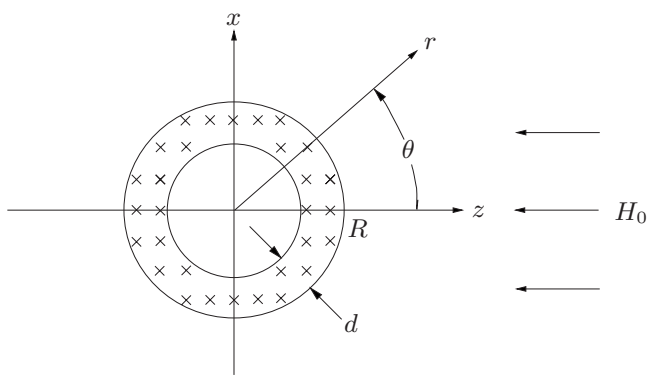

Fig. 2.4 Spherical magnetic shell in a uniform magnetic field.

Solution to PROBLEM 2.3

a) The problem is divided into three regions: Region 1 ($r \geq R$); Region 2 (the shell); and Region 3 ($r \leq R-d$). The appropriate potentials are given below:

$$\phi_1 = H_0 r\cos\theta + \frac{A}{r^2}\cos\theta \qquad (S3.1a)$$

$$\phi_2 = Cr\cos\theta + \frac{D}{r^2}\cos\theta \qquad (S3.1b)$$

$$\phi_3 = H_{ss} r\cos\theta \qquad (S3.1c)$$

Note that $\phi_1 \to H_0 r\cos\theta$ for $r\to\infty$ and that ϕ_3 remains finite as $r\to 0$.

Using the ∇ operator in spherical coordinates, we obtain:

$$\vec{H}_1 = H_0(-\cos\theta\vec{\imath}_r + \sin\theta\vec{\imath}_\theta) + \frac{A}{r^3}(2\cos\theta\vec{\imath}_r + \sin\theta\vec{\imath}_\theta) \qquad (S3.2a)$$

$$\vec{H}_2 = C(-\cos\theta\vec{\imath}_r + \sin\theta\vec{\imath}_\theta) + \frac{D}{r^3}(2\cos\theta\vec{\imath}_r + \sin\theta\vec{\imath}_\theta) \qquad (S3.2b)$$

$$\vec{H}_3 = H_{ss}(-\cos\theta\vec{\imath}_r + \sin\theta\vec{\imath}_\theta) \qquad (S3.2c)$$

Boundary Conditions

1) At $r=R$, the tangential ($\vec{\imath}_\theta$) component of $\vec{H}$ (H_θ) is continuous: $\phi_1 = \phi_2$.
2) Similarly, at $r=R-d$, H_θ is continuous: $\phi_2 = \phi_3$.
3) At $r=R$, the normal ($\vec{\imath}_r$) component of $\vec{B}$ (B_r) is continuous.
4) Similarly, at $r=R-d$, B_r is continuous.

The above boundary conditions give rise to the following four equations:

$$H_0 + \frac{A}{R^3} = C + \frac{D}{R^3} \qquad (S3.3a)$$

$$C + \frac{D}{(R-d)^3} = H_{ss} \qquad (S3.3b)$$

$$\mu_\circ\left(-H_0 + \frac{2A}{R^3}\right) = \mu\left(-C + \frac{2D}{R^3}\right) \qquad (S3.3c)$$

$$\mu\left[-C + \frac{2D}{(R-d)^3}\right] = -\mu_\circ H_{ss} \qquad (S3.3d)$$

Combining Eqs. $S3.3a$ and $S3.3b$ and eliminating C, we have:

$$\frac{A}{R^3} + D\left[\frac{1}{(R-d)^3} - \frac{1}{R^3}\right] - H_{ss} = -H_0 \qquad (S3.4)$$

Solution to PROBLEM 2.3 (continuation)

From Eqs. $S3.3b$ and $S3.3d$, we can obtain D in terms of H_{ss}:

$$D = \frac{\mu - \mu_\circ}{3\mu}(R-d)^3 H_{ss} \tag{S3.5}$$

Combining Eqs. $S3.4$ and $S3.5$, we have A/R^3 in terms of H_{ss}:

$$\frac{A}{R^3} = H_{ss}\left\{1 - \frac{\mu-\mu_\circ}{3\mu}\left[1-\left(1-\frac{d}{R}\right)^3\right]\right\} - H_0 \tag{S3.6}$$

From Eqs. $S3.3c$ and $S3.3d$, we obtain:

$$\frac{2A}{R^3} + 2\frac{\mu}{\mu_\circ}D\left[\frac{1}{(R-d)^3} - \frac{1}{R^3}\right] + H_{ss} = H_0 \tag{S3.7}$$

Combining Eqs. $S3.4$–$S3.7$ and expressing H_{ss} in terms of H_0, we obtain:

$$\frac{H_{ss}}{H_0} = \frac{9\mu\mu_\circ}{9\mu\mu_\circ + 2(\mu-\mu_\circ)^2\left[1-\left(1-\frac{d}{R}\right)^3\right]} \tag{2.46}$$

b) We may simplify Eq. 2.46 by dividing top and bottom by $\mu_\circ^2$ and applying the limits $\mu/\mu_\circ \gg 1$ and $d/R \ll 1$:

$$\frac{H_{ss}}{H_0} \simeq \frac{9\mu/\mu_\circ}{9\left(\frac{\mu}{\mu_\circ}\right) + 2\left(\frac{\mu}{\mu_\circ}\right)^2\left[1-\left(1-3\frac{d}{R}\right)\right]} \tag{S3.8}$$

$$\simeq \frac{3}{3 + 2\left(\frac{\mu}{\mu_\circ}\right)\left(\frac{d}{R}\right)} \tag{S3.9}$$

In the special case $\mu d/\mu_\circ R \gg 1$, Eq. $S3.9$ reduces to:

$$\frac{H_{ss}}{H_0} \simeq \tfrac{3}{2}\left(\frac{\mu_\circ}{\mu}\right)\left(\frac{R}{d}\right) \tag{2.47}$$

c) The same result given by Eq. 2.47 for H_{ss}/H_0 can be obtained directly by a perturbation approach for the case $\mu/\mu_\circ \gg 1$ and $d/R \ll 1$.

We proceed by assuming that μ of the shell material is infinite. This requires that the B lines be perpendicular to the shell at $r = R$. This is because $\vec{H}_1$ has only a radial ($\vec{\imath}_r$) component at $r = R$, because $\vec{H} = 0$ in the shell and H_θ must be continuous at $r = R$. (This can be seen quite readily by noting that when $\mu = \infty$, $C = D = 0$.) From Eq. $S3.3a$, $A = -R^3 H_0$, and thus at $r = R$:

$$\vec{H}_1 = -3H_0\cos\theta\vec{\imath}_r \tag{S3.10}$$

Solution to PROBLEM 2.3 (continuation)

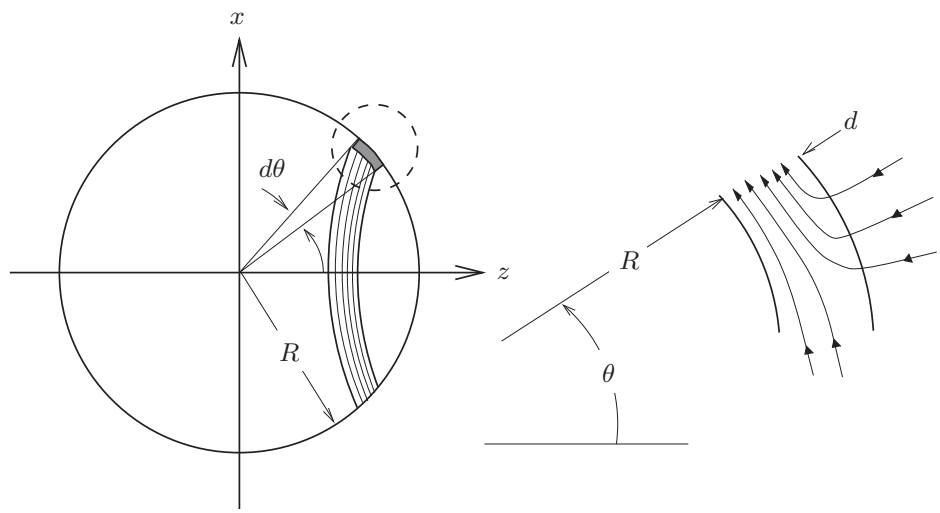

Fig. 2.5 Flux entering into the spherical shell over the surface bounded by $\pm\theta$.

The B lines stay inside the shell without "spilling" into Region 3; that is, B inside the shell has only an $\vec{\imath}_\theta$ component. Let us now apply magnetic flux continuity, i.e., $\nabla \cdot \vec{B} = 0$, and solve for $\vec{B}_2$ when $\mu = \infty$. Once $\vec{B}_2$ is solved for this case, an approximate expression for $\vec{H}_3$ can be deduced for $\mu \neq \infty$ but $\mu/\mu_\circ \gg 1$.

First, we calculate the total magnetic flux Φ entering into the shell over the surface area bounded by $\pm\theta$ (Fig. 2.5). This surface area, as indicated in the figure, is given by a differential area (a ring of radius $R\sin\theta$ times $Rd\theta$) integrated from 0 to θ. Thus, we have:

$$\Phi = \mu_\circ \int_0^\theta \vec{H}_1 \cdot d\vec{\mathcal{A}} = \mu_\circ \int_0^\theta 3H_0 \cos\theta \, 2\pi R^2 \sin\theta \, d\theta$$
$$= 3\pi\mu_\circ R^2 H_0 \sin^2\theta \qquad (S3.11)$$

This Φ must be equal to the total flux flowing in the θ-direction in the shell at θ. Because the shell's cross-sectional area, A_2, at θ is given, for $d \ll R$, by the shell thickness d times the circumference of a ring of radius $R\sin\theta$, we have:

$$A_2 \simeq d2\pi R\sin\theta \qquad (S3.12)$$

We thus have:

$$\Phi = 3\pi\mu_\circ R^2 H_0 \sin^2\theta$$
$$\simeq B_2 A_2 = B_2 d 2\pi R \sin\theta \qquad (S3.13)$$

Solution to PROBLEM 2.3 (continuation)

Solving for B_2 from Eq. $S3.13$, we obtain:

$$\vec{B}_2 \simeq \tfrac{3}{2}\mu_\circ \left(\frac{R}{d}\right) H_0 \sin\theta \vec{\imath}_\theta \qquad (S3.14)$$

Note that $\vec{B}_2$ is for $\mu = \infty$; we can now deduce an approximate solution for $\vec{H}_3$ because the $\vec{\imath}_\theta$-component of $\vec{H}$ must be continuous at $r = R - d$. Thus:

$$H_{\theta 3} \simeq \frac{B_{\theta 2}}{\mu} = \tfrac{3}{2}\left(\frac{\mu_\circ}{\mu}\right)\left(\frac{R}{d}\right) H_0 \sin\theta \qquad (S3.15)$$

Once $H_{\theta 3}$ is known, we have the complete expression for $\vec{H}_3$:

$$\vec{H}_3 \simeq \tfrac{3}{2}\left(\frac{\mu_\circ}{\mu}\right)\left(\frac{R}{d}\right) H_0(-\cos\theta \vec{\imath}_r + \sin\theta \vec{\imath}_\theta) \qquad (S3.16a)$$

$$\left|\frac{\vec{H}_3}{H_0}\right| \simeq \tfrac{3}{2}\left(\frac{\mu_\circ}{\mu}\right)\left(\frac{R}{d}\right) \qquad (S3.16b)$$

The ratio $|\vec{H}_3/H_0|$ given by Eq. $S3.16b$ agrees with H_{ss}/H_0 given by Eq. 2.47. Note that this perturbation approach requires the conditions $\mu = \infty$ and $d \ll R$, but not the condition $\mu d/\mu_\circ R \gg 1$ in the step from Eq. $S3.9$ to Eq. 2.47.

d) It is important to remember that d cannot be chosen arbitrarily small to satisfy the condition $d/R \ll 1$. The preceding analysis is valid, in fact, only when:

$$\frac{\mu_\circ}{\mu} \ll \frac{d}{R} \ll 1 \qquad (S3.17)$$

In reality μ cannot be infinite and the shielding material will eventually saturate as the external field increases. Hence, the maximum magnetic flux inside the shell, which occurs at $\theta = 90°$, must be less than the saturation flux $\mu_\circ M_{sa}$ of the shell material. Thus:

$$\tfrac{3}{2}\left(\frac{R}{d}\right)\mu_\circ H_0 \le \mu_\circ M_{sa} \qquad (S3.18)$$

Solving Eq. $S3.18$ for d/R, we obtain:

$$\frac{d}{R} \ge \frac{3H_0}{2M_{sa}} \qquad (2.48)$$

Table 2.5 presents approximate values of *differential* $\mu/\mu_\circ$, defined as $(\mu/\mu_\circ)_{dif} \equiv \Delta M/\Delta H_0|_{\mu_\circ H_0}$ and $\mu_\circ M(H_\circ)$ in the $\mu_\circ H_0$ range 1–1000 gauss (0.1–100 mT), as well as $\mu_\circ M_{sa}$ for annealed ingot iron, as-cast steel, and vanadium permendur (50%Co, 2%V). These materials are useful for magnetic shielding in external inductions up to ∼100 gauss. The materials have $\mu_\circ M_{sa}$ values, respectively, of roughly 2.1 T, 2.0 T, and 2.2 T.

TRIVIA 2.3 The permanent magnet is ubiquitous in daily life (***DISCUSSION 2.3***). From the figures below, choose the one that is closest to the number of permanent magnets in a modern passenger car.

i) 20; ii) 100; iii) 500; iv) 2,500.

Solution to PROBLEM 2.3 (continuation)

Table 2.5: Values of $(\mu/\mu_\circ)_{dif}$; $\mu_\circ M(H_\circ)$; and $\mu_\circ M_{sa}$ for Iron Alloys

$\mu_\circ H_0$	*Annealed Ingot Iron*		*As-Cast Steel*		*Vanadium Permendur*	
[gauss]	$(\mu/\mu_\circ)^*_{dif}$	$\mu_\circ M$ [T]	$(\mu/\mu_\circ)^*_{dif}$	$\mu_\circ M$ [T]	$(\mu/\mu_\circ)^*_{dif}$	$\mu_\circ M$ [T]
1	7710	0.375	n.a.	n.a.	n.a.	n.a.
3	3850	0.91	1660	0.25	4845	0.65
5	500	1.42	1155	0.51	1875	1.25
10	115	1.54	565	0.93	545	1.67
20	47	1.60	180	1.25	170	1.96
50	23.5	1.70	50	1.52	17	2.10
100	17.5	1.81	25	1.70	4.8	2.15
200	8.25	1.93	10	1.85	1.3	2.17
500	2.0	2.05	1.0	1.92	0.26	2.18
1000	0.4	2.11	0.45	2.01	0.07	2.19
$\mu_\circ M_{sa}$	2.13 T		2.03 T		2.20 T	

* Derived from $M(H)$ plots in *Permanent Magnet Manual* (General Electric Company, 1963).

e) Field lines for the case $\mu/\mu_\circ = 100$ are shown below in Fig. 2.6.

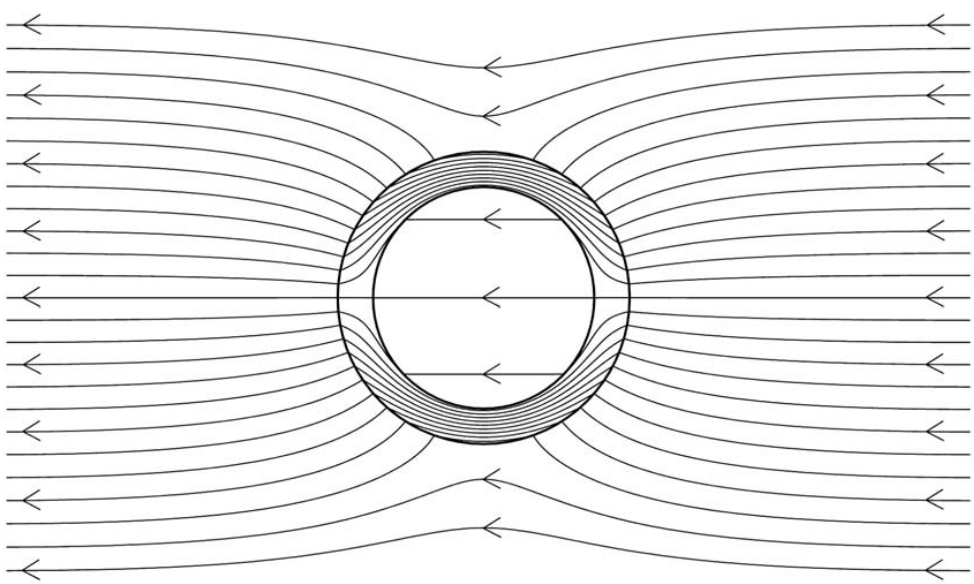

Fig. 2.6 Field distribution with a spherical shell of $\mu/\mu_\circ = 100$ in a uniform field. Note that the field lines entering and leaving the shell are *nearly* perpendicular to the shell.

*DISCUSSION 2.2: Shielding with a Cylindrical Shell**

We use a perturbation technique similar to that used in **PROBLEM 2.3** to derive an expression for H_{cs}/H_0, where H_{cs} is the magnitude of the magnetic field inside the cylindrical space ($r \leq R-d$) surrounded by a shell of o.d. $2R$ and wall thickness $d/R \ll 1$ of highly permeable material ($\mu/\mu_\circ \gg 1$) in a uniform external magnetic field, $\vec{H}_\infty$, of magnitude H_0. In 2-D cylindrical coordinates $\vec{H}_\infty$ is given by:

$$\vec{H}_\infty = H_0(-\cos\theta\vec{\imath}_r + \sin\theta\vec{\imath}_\theta) \tag{2.40}$$

θ is defined in Fig. 2.3.

We proceed by assuming that μ of the cylinder material is infinite. We then find that, as in **PROBLEM 2.3**, the B lines must be normal to the cylinder at $r = R$. Thus at $r = R$ we have:

$$\vec{H}_1 = -2H_0\cos\theta\vec{\imath}_r$$

B in the shell, however, is θ-directed. For $d/R \ll 1$, the flux continuity requirement for B may be expressed by:

$$B_2 d = \int_0^\theta 2\mu_\circ H_0 R\cos\theta\, d\theta = 2\mu_\circ R H_0 \sin\theta$$

Thus:

$$\vec{B}_2 = 2\mu_\circ\left(\frac{R}{d}\right)H_0\sin\theta\vec{\imath}_\theta$$

Once $\vec{B}_2$ is known for $\mu = \infty$, we know $\vec{H}_2$ for $\mu/\mu_\circ \gg 1$:

$$\vec{H}_2 = \frac{\vec{B}_2}{\mu} \simeq 2\left(\frac{\mu_\circ}{\mu}\right)\left(\frac{R}{d}\right)H_0\sin\theta\vec{\imath}_\theta$$

Because H_θ is continuous in the absence of surface current, the same H_θ must exist in Regions 2 and 3: $H_{\theta 2} = H_{\theta 3}$. Thus, at $r = R-d$:

$$H_{\theta 3} = H_{\theta 2} \simeq 2\left(\frac{\mu_\circ}{\mu}\right)\left(\frac{R}{d}\right)H_0\sin\theta$$

From the above expression, it follows that:

$$\vec{H}_3 \simeq 2\left(\frac{\mu_\circ}{\mu}\right)\left(\frac{R}{d}\right)H_0(-\cos\theta\vec{\imath}_r + \sin\theta\vec{\imath}_\theta)$$

$$\left|\frac{\vec{H}_3}{H_0}\right| \equiv \frac{H_{cs}}{H_0} \simeq 2\left(\frac{\mu_\circ}{\mu}\right)\left(\frac{R}{d}\right) \tag{2.49}$$

As in the spherical shell studied in **PROBLEM 2.3**, the cylindrical shell cannot be arbitrarily thin; it must be thick enough to keep it from saturating:

$$\mu H_{cs} = 2\mu_\circ H_0\frac{R}{d} \leq \mu_\circ M_{sa}$$

From the above, we obtain:

$$\frac{d}{R} \geq \frac{2H_0}{M_{sa}} \tag{2.50}$$

---

* **Problem 2.4** in the 1st Edition (Plenum, 1994).

PROBLEM 2.4: The field far from a cluster of four dipoles*

This problem considers the field far from a cluster of four *ideal* dipoles, 1–4, arranged as shown in Fig. 2.7, in which the direction of each dipole is indicated by the arrow within a circle. The center-to-center distance between two opposing dipoles is $2\delta_d$. The field of each jth dipole of zero winding thickness, diameter $2r_d$, and overall length ℓ_d in the y-direction, at a radial location (r_j) far from the dipole ($r_j \gg \ell_d$) may be modeled as a spherical dipole field, $\vec{B}_j$:

$$\vec{B}_j = \frac{r_d^2 \ell_d B_\circ}{2r_j^3}(\cos\vartheta_j \vec{\imath}_{r_j} + \tfrac{1}{2}\sin\vartheta_j \vec{\imath}_{\theta_j}) \tag{2.51}$$

where r_j is measured from the center of *each* dipole and ϑ_j in each dipole is defined such that the field inside the winding points in the r_j-direction when $\vartheta_j = 0°$. Figure 2.7 indicates the direction of the field inside each dipole. Also defined in Fig. 2.7 are r-θ coordinates and z-x coordinates common to all the dipoles. Note that for $r \gg \delta_d$, we have $\vartheta_1 = \theta + 180°$, $\vartheta_2 = \theta - 90°$, $\vartheta_3 = \theta$, and $\vartheta_4 = \theta + 90°$.

Show that an approximate expression for the far field ($\vec{B}$ for $r/\delta_d \gg 1$) of the combined system is given by:

$$\vec{B} \simeq \frac{3r_d^2 \ell_d B_\circ \delta_d}{r^4}(-\sin 2\theta \vec{\imath}_r + \tfrac{1}{2}\cos 2\theta \vec{\imath}_\theta) \tag{2.52}$$

Neglect end effects of each dipole, i.e., consider only the plane $y = 0$.

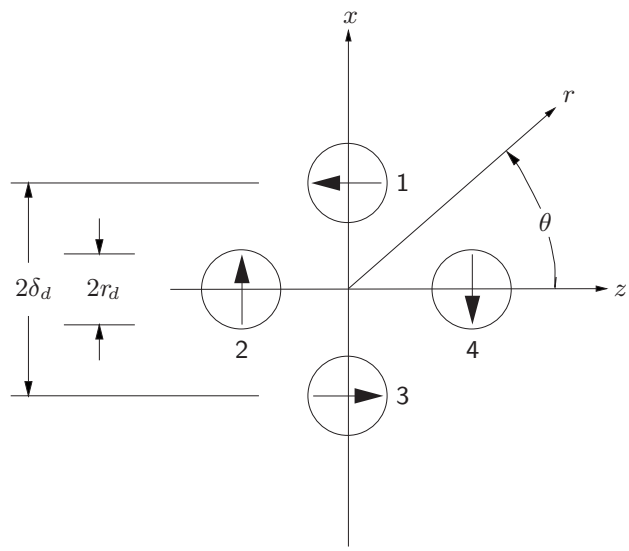

Fig. 2.7 Cross-sectional view of a four-dipole arrangement. The arrow in each dipole indicates the field direction inside the winding.

* **Problem 2.5** in the 1st Edition (Plenum, 1994).

Solution to PROBLEM 2.4

For $r \gg \delta_d$, r_j of each dipole may be given in terms of r and θ:

$$r_1 \simeq r - \delta_d \sin\theta \qquad (S4.1a)$$

$$r_2 \simeq r + \delta_d \cos\theta \qquad (S4.1b)$$

$$r_3 \simeq r + \delta_d \sin\theta \qquad (S4.1c)$$

$$r_4 \simeq r - \delta_d \cos\theta \qquad (S4.1d)$$

With Eq. $S4.1$ into Eq. 2.51 for each dipole and ϑ_j expressed in terms of θ:

$$\vec{B}_1 \simeq \frac{r_d^2 \ell_d B_\circ}{2(r - \delta_d \sin\theta)^3}(-\cos\theta\vec{\imath}_r - \tfrac{1}{2}\sin\theta\vec{\imath}_\theta) \qquad (S4.2a)$$

$$\vec{B}_2 \simeq \frac{r_d^2 \ell_d B_\circ}{2(r + \delta_d \cos\theta)^3}(\sin\theta\vec{\imath}_r - \tfrac{1}{2}\cos\theta\vec{\imath}_\theta) \qquad (S4.2b)$$

$$\vec{B}_3 \simeq \frac{r_d^2 \ell_d B_\circ}{2(r + \delta_d \sin\theta)^3}(\cos\theta\vec{\imath}_r + \tfrac{1}{2}\sin\theta\vec{\imath}_\theta) \qquad (S4.2c)$$

$$\vec{B}_4 \simeq \frac{r_d^2 \ell_d B_\circ}{2(r - \delta_d \cos\theta)^3}(-\sin\theta\vec{\imath}_r + \tfrac{1}{2}\cos\theta\vec{\imath}_\theta) \qquad (S4.2d)$$

For $r \gg \delta_d$ the denominator of each term may be expanded; to 1st order in δ_d/r Eq. $S4.2$ becomes:

$$\vec{B}_1 \simeq \frac{r_d^2 \ell_d B_\circ}{2r^3}\left[1 + 3\left(\frac{\delta_d}{r}\right)\sin\theta\right](-\cos\theta\vec{\imath}_r - \tfrac{1}{2}\sin\theta\vec{\imath}_\theta) \qquad (S4.3a)$$

$$\vec{B}_2 \simeq \frac{r_d^2 \ell_d B_\circ}{2r^3}\left[1 - 3\left(\frac{\delta_d}{r}\right)\cos\theta\right](\sin\theta\vec{\imath}_r - \tfrac{1}{2}\cos\theta\vec{\imath}_\theta) \qquad (S4.3b)$$

$$\vec{B}_3 \simeq \frac{r_d^2 \ell_d B_\circ}{2r^3}\left[1 - 3\left(\frac{\delta_d}{r}\right)\sin\theta\right](\cos\theta\vec{\imath}_r + \tfrac{1}{2}\sin\theta\vec{\imath}_\theta) \qquad (S4.3c)$$

$$\vec{B}_4 \simeq \frac{r_d^2 \ell_d B_\circ}{2r^3}\left[1 + 3\left(\frac{\delta_d}{r}\right)\cos\theta\right](-\sin\theta\vec{\imath}_r + \tfrac{1}{2}\cos\theta\vec{\imath}_\theta) \qquad (S4.3d)$$

Combining each field given by Eq. $S4.3$, we obtain:

$$\vec{B} = \vec{B}_1 + \vec{B}_2 + \vec{B}_3 + \vec{B}_4 \simeq \frac{3r_d^2 \ell_d B_\circ \delta_d}{r^4}(-\sin 2\theta\vec{\imath}_r + \tfrac{1}{2}\cos 2\theta\vec{\imath}_\theta) \qquad (2.52)$$

Note that $|\vec{B}|$ decreases $\propto 1/r^4$ rather than $\propto 1/r^3$, as would a single dipole.

Answer to TRIVIA 2.3 ii). A modern military aircraft, however, may contain up to ∼2,000 pieces of permanent magnet—J.D. Livingstone, *Driving Force: The Natural Magic of Magnets* (Harvard University Press, 1996).

PROBLEM 2.5: Iron electromagnet pole shape

Figure 2.8 shows the active section of an iron electromagnet, with two conically tapered cylindrical poles of ferromagnetic material—the shaded area of each pole indicates the material removed from the original cylindrical pole. When the windings (not shown in the figure) of the magnet are energized, a relatively uniform field is generated in the gap between the poles. The central field has no theoretical upper limit, because it increases $\propto \ln(R_2/R_1)$, where $2R_2$ and $2R_1$ are, respectively, the diameters of the base and tip of each cone. There is, however, a practical field limit of $\sim$7 T (in magnets at Bellevue, Paris and Uppsala University, Sweden) because as R_2 is increased, the magnet mass becomes prohibitively large. The tapering enhances the center field, because the field by each magnetic moment located in this section contributes a *negative* axial (z) field at the center.

Show that $\theta_{tp} = 54°44'$ is the optimal angle for this simple pole geometry if the iron is magnetized parallel to the axis of the system. Assume that the center field is the sum of the field generated by each magnetic moment distributed uniformly over the pole pieces. (As indicated in the figure, the four dotted lines, each projected from one of the four lines defining $\theta_{tp} = 54°44'$, meet at the center. Note that if the gap is large enough, tapering will not be beneficial.) Each moment, $\mathbf{m_A}$ [A m^2], magnetized in the z-direction, generates a dipole field, $\vec{H}_{\mathrm{m_A}}(r,\theta)$:

$$\vec{H}_{\mathrm{m_A}}(r,\theta) = \frac{\mathbf{m_A}}{r^3}\left(\cos\theta\vec{i}_r + \tfrac{1}{2}\sin\theta\vec{i}_\theta\right) \tag{2.53}$$

From symmetry $\vec{H}_{\mathrm{m_A}}(r,\theta)$ is axisymmetric with respect to the z-axis and it is derivable from a scalar potential $\cos\theta/r^2$. This derivation has been used in **PROBLEMS 2.1**, **2.3**, and **2.4**, and ***DISCUSSION 2.1***.

Hint Solve the z-axis *center* field due to a single magnetic dipole moment, $\mathbf{m_A}\uparrow$, located on the pole perimeter at the boundary between the tapered and untapered pole, as indicated by • in Fig. 2.8.

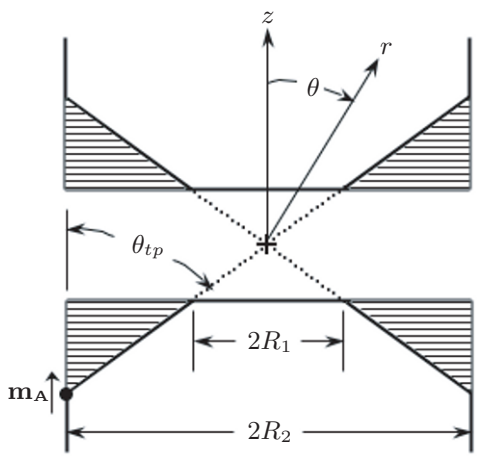

Fig. 2.8 Pair of pole pieces, each tapered at an angle of θ_{tp}.
• denotes the location of a magnetic dipole moment $\mathbf{m_A}\uparrow$.

Solution to PROBLEM 2.5

The z-component of the field at the center, $H_{\mathrm{m_A}z}$, due to moment $\mathbf{m_A}$ is given by:

$$H_{\mathrm{m_A}z} = \frac{m_{\mathbf{A}}}{r_A^3}(\cos^2\theta - \tfrac{1}{2}\sin^2\theta) \qquad (S5.1)$$

where r_A is the distance from $\mathbf{m_A}$ to the center. At $\theta = \theta_{tp}$, the right-hand side of Eq. $S5.1$ is zero. Thus:

$$\cos^2\theta_{tp} - \tfrac{1}{2}\sin^2\theta_{tp} = 0 \qquad (S5.2)$$

From Eq. $S5.2$, $\cos\theta_{tp} = 1/\sqrt{3}$ (or $\tan\theta_{tp} = \sqrt{2}$) and we find: $\theta_{tp} \simeq 54.736^\circ \simeq 54^\circ 44'$.

Note that moments located in the shaded area above the perimeter are at $\theta_{tp} > 54^\circ 44'$. Because $\cos\theta$ decreases with θ, while $\sin\theta$ increases, $H_{\mathrm{m_A}z}$ is negative for $\theta_{tp} > 54^\circ 44'$. Tapering the pole piece at this angle eliminates this negative contribution, thus maximizing the center field.

Remarkably, $54^\circ 44'$ is *identical* to the *magic angle* used in NMR spectroscopy. Often an NMR sample is oriented at this *magic angle* with respect to the principal axial field and spun to average out anisotropic interactions.

DISCUSSION 2.3: Permanent Magnets

The permanent magnet is a vital component in many devices used in daily life—cars (see ***Trivia 2.3***), TV's, computers, telephones, refrigerators, to name only a few. Indeed without permanent magnets modern life as we know it today would cease to function. They also compete with superconducting magnets for MRI in the low field range (<1 T). MRI magnets composed of permanent magnets are popular because they are not only free of cryogenics but also relatively inexpensive.

Table 2.6 shows developments of permanent magnets and superconductors over the past nine decades, from the 1910s to the 1990s, expressed in terms of maximum magnetic energy, $BH|_{mx}$, for permanent magnets and maximum critical temperature, $T_c|_{mx}$, for superconductors. The increase during this period by a factor of $\sim$30 in $BH|_{mx}$ is as remarkable as that by a factor of $\sim$20 in $T_c|_{mx}$.

If this pace of the development in permanent magnets continues, within the not-too-distant future MRI magnets based on permanent magnets should reach $\sim$1 T, the level above which superconducting counterparts dominate.

Table 2.6: Development of Permanent Magnets and Superconductors

Decade(s)	*Permanent Magnet*	$BH\|_{mx}$ [kJ/m^3]	*Superconductor*	$T_c\|_{mx}$ [K]
1910	Special steel	11	Pb	7.2
1920–1940	Alnico* 1–4	15	NbN	16
1950	Alnico 5	35	Nb_3Sn	18
1960	Alnico 8, 9	55	$Nb_{12}Al_3Ge$	19
1970	$SmCo_5$	140	Nb_3Ge	23
1980	Sm(CoCuFeZr)	240	$Bi_2Sr_2Ca_2Cu_3O_x$	118
1990	$Nd_2Fe_{14}B$	350	$(Hg,Pb)Sr_2Ca_2Cu_3O_x$	133

* Iron alloys principally of Al, Ni, and Co.

PROBLEM 2.6: Quasi-static field in a cylinder

A long thin cylinder of radius R is made of a sheet that is perfectly conducting ($\sigma = \infty$) but not superconducting and has a narrow slot of gap δ (Fig. 2.9). The cylinder is placed in a sinusoidally time-varying magnetic field, which is, to 0^{th}-order, uniform and z-directed (normal to the paper). Namely:

$$\vec{\mathcal{H}}_\infty(t) = \text{Re}[H_\circ e^{j\omega t}]\vec{i}_z \tag{2.54}$$

where $H_\circ$ is a complex amplitude. End effects may be neglected.

a) Neglecting terms of order δ/R, show that the 1^{st}-order complex voltage amplitude across the slot along the shortest path, $V_1|_0 \equiv V_1|_{\theta=0^\circ}$, is given by:

$$V_1|_0 \equiv V_1|_{\theta=0^\circ} = -j\omega\pi R^2 \mu_\circ H_\circ \tag{2.55}$$

b) Suppose now that a normal metal sheet of resistivity ρ [Ω m] is placed in the gap to connect the lips of the cylinder. Derive an expression for the 1^{st}-order complex current density (per unit axial length) amplitude, J_1 [A/m], through the sheet. Assume that the driving frequency ($\omega/2\pi$) is low enough that the magnetic field retains the quasi-static form given by Eq. 2.54 and that the current flows uniformly over the sheet cross section.

c) In the *absence* of the resistive sheet (or $\rho_s = \infty$), draw neatly six lines of the 1^{st}-order complex electric field ($\vec{E}_1$) vector within the space enclosed by the cylinder, clearly showing important features.

d) In the *absence* of the resistive sheet, derive an expression for the line integral of the 1^{st}-order voltage, $V_1|_{-\pi/2}^{+\pi/2}$, across the voltage taps attached, one at $\theta = +\pi/2$ and the other at $\theta = -\pi/2$.

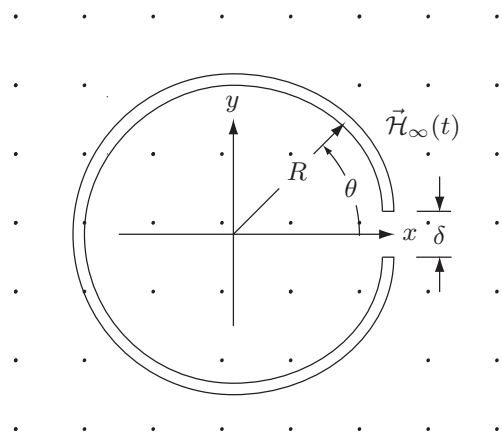

Fig. 2.9 Axial view of a long thin cylinder of radius R of perfect conductor with a narrow gap of δ at $\theta = 0$ exposed to a sinusoidally time-varying magnetic field in the z-direction.

Solution to PROBLEM 2.6

a) Using Faraday's integral law for the 1st-order electric field, $\vec{E}_1(t)$, we have:

$$\mathcal{V}_1(t) \equiv \int_C \vec{E}_1(t) \cdot d\,\vec{s} = -\pi R^2 \mu_\circ \frac{d\mathcal{H}_\circ(t)}{dt} \qquad (S6.1)$$

The line integral is taken around the cylinder, including the gap, in the counterclockwise direction. The right-hand side of Eq. $S6.1$ covers the entire area defined by the cylinder (πR^2). Because the cylinder is a perfect conductor, $\vec{\mathcal{E}}_1(t) = 0$ within the material. The only nonzero contribution to the line integral comes from the gap, which is equal to $\mathcal{V}_1(t)$. In terms of complex amplitudes, we have:

$$V_1|_0 = -j\omega\pi R^2 \mu_\circ H_\circ \qquad (2.55)$$

b) Using Ohm's law, we have for J_1 (per unit length):

$$J_1 = \frac{V_1|_0}{\rho_s} \qquad (S6.2)$$

c) Because the cylinder is a perfect conductor, the tangential component of $\vec{E}_1$ at the cylinder must be zero: $\vec{E}_1$ leaves or enters the cylinder at a right angle. As the line integral across the cylinder moves to the left of the gap, the integral area decreases, making $|E_1|$ smaller. Figure 2.10 shows six lines of $\vec{E}_1$.

d) This is a special case of **c)**, where from symmetry it is possible to compute the line integral exactly: the integral area is equal to $\pi R^2/2$. Thus:

$$V_1|_{-\pi/2}^{+\pi/2} = -\tfrac{1}{2} j\omega\pi R^2 \mu_\circ H_\circ \qquad (S6.3)$$

Equations 2.55 and $S6.3$ demonstrate that voltages across the cylinder at the same axial location depend on azimuthal locations of the voltage taps. This is an important point to be remembered when measuring voltage in the presence of a time-varying magnetic field, applied externally as in the present case or generated by a current flowing in the system. Electrical measurement of AC losses in a superconductor is a good example where one must be careful.

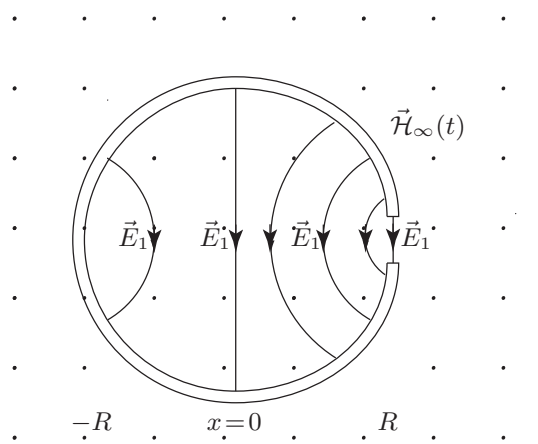

Fig. 2.10 Lines of $\vec{E}_1$ normal to the perfectly conducting cylinder. Note that the $|E_1|$ decreases as the line is moved from $x=R$ to $x=-R$.

PROBLEM 2.7: Induction heating of a cylindrical shell*

This problem deals with induction heating of a metallic (nonsuperconducting) cylindrical shell. It is a good example of a case involving sinusoidal electromagnetic fields, power flow (Poynting vector), and power dissipation. This and the next problem are the first examples of an AC loss, specifically an eddy-current loss, to be discussed further in ***CHAPTER 7***. Induction heating is widely used in electric furnaces to achieve high temperatures in conducting materials; it also is sometimes used as a research tool in the study of the thermal behavior of superconducting windings. In superconducting magnet technology research, induction heating is most often used in the form of pulsed fields to simulate transient disturbances that create small normal regions in otherwise superconducting windings.

Figure 2.11 shows a "long" metallic cylindrical shell of resistivity ρ_e, of o.d. $2R$, and of thickness $d \ll R$, in a sinusoidally time-varying magnetic field, which within 0^{th} order is uniform and z-directed (along the cylinder axis). Namely:

$$\vec{\mathcal{H}}_\infty(t) = \text{Re}(\vec{H}_0 e^{j\omega t}) = \text{Re}(H_0 e^{j\omega t})\vec{\imath}_z \tag{2.54}$$

where H_0 is a complex field amplitude.

We shall approach this problem first (Part 1) by solving for the appropriate fields by two methods and then (Part 2) solving for power dissipation in the cylinder by two methods.

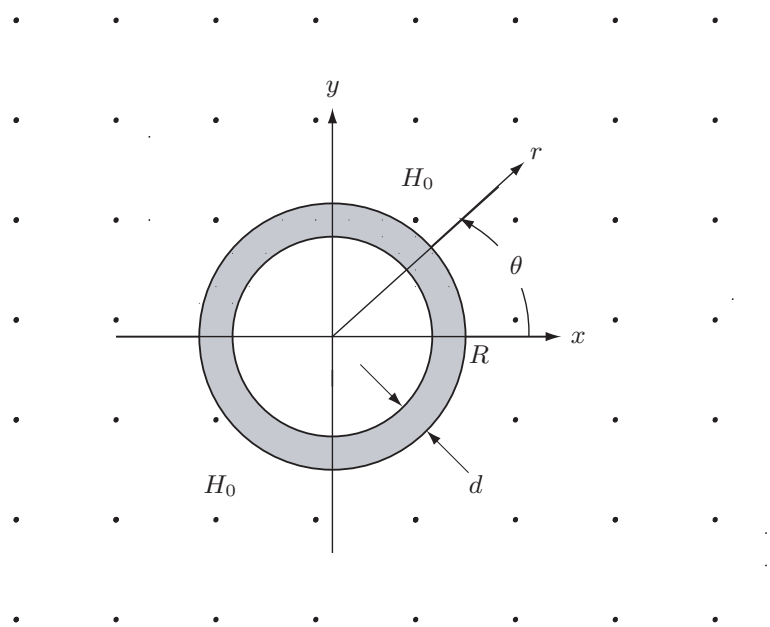

Fig. 2.11 Cylindrical metallic shell in a uniform sinusoidally time-varying magnetic field.

* **Problem 2.6** in the 1^{st} Edition (Plenum, 1994).

PROBLEM 2.7: Induction heating—Part 1 (Field)

First, we shall solve for appropriate fields using two methods, described below.

Method 1

a) Using the *integral* form of Maxwell's equations and neglecting end effects, show that expressions for the 1st-order electric field, $\vec{E}_1$, in the region $r \leq R$ and the 1st-order current density, $\vec{J}_1$, in the shell ($r \simeq R$) are given by:

$$\vec{E}_1 = -\frac{j\omega\mu_\circ r H_0}{2}\vec{\imath}_\theta \tag{2.56}$$

$$\vec{J}_1 \simeq -\frac{j\omega\mu_\circ R H_0}{2\rho_e}\vec{\imath}_\theta \tag{2.57}$$

b) Show that the resulting 1st-order magnetic field, $\vec{H}_1$, in the region $r \leq R - d$ can be expressed by:

$$\vec{H}_1 = -\frac{j\omega\mu_\circ R d H_0}{2\rho_e}\vec{\imath}_z \tag{2.58}$$

c) Equations 2.56–2.58, derived using the quasi-static approximation, are valid only in the "low" frequency limit, or frequencies much less than the "skin-depth" frequency, f_{sk}. Show that f_{sk} is given by:

$$f_{sk} = \frac{\rho_e}{\pi\mu_\circ R d} \tag{2.59}$$

Method 2

$\vec{E}_1$, $\vec{J}_1$, and $\vec{H}_1$, derived by Method 1, each increasing with ω, are valid only for frequencies well below f_{sk}. We now demonstrate a new technique that enables us to derive the total field, $\vec{H}_T = (\vec{H}_0 + \vec{H}_R)$, in the bore, valid for the *entire range* of frequencies. $\vec{H}_T$ is the total net field, $\vec{H}_0$ is the original field, and $\vec{H}_R$ is the reaction field of the system in the bore. In this approach, first find the reaction field $\vec{H}_R$ in the bore by treating $\vec{H}_T = (\vec{H}_0 + \vec{H}_R)$ as a 0th-order field and solve for $\vec{H}_R$ as the usual 1st-order magnetic field response.

d) Show that expressions for $\vec{H}_R$, $\vec{H}_T$, and $\vec{J}$ in the shell valid for $d \ll R$ are:

$$\vec{H}_R = -\frac{j\omega\mu_\circ R d H_0}{2\rho_e + j\omega\mu_\circ R d}\vec{\imath}_z \tag{2.60}$$

$$\vec{H}_T = \frac{2\rho_e H_0}{2\rho_e + j\omega\mu_\circ R d}\vec{\imath}_z \tag{2.61}$$

$$\vec{J} = -\frac{j\omega\mu_\circ R H_0}{2\rho_e + j\omega\mu_\circ R d}\vec{\imath}_\theta \tag{2.62}$$

TRIVIA 2.4: Which is responsible for the "humming" of a power transformer?

i) E field; ii) $J \times B$ force; iii) ρJ^2 heating; iv) H field.

Solution to PROBLEM 2.7—Part 1

a) From symmetry in the θ-direction, $\vec{E}_1$ and $\vec{J}_1$ are constant in the θ-direction; both are θ-directed and depend only on r. Thus the Faraday's induction law may be applied along contour $\mathcal{C}$ at r enclosing surface $\mathcal{S}$:

$$\oint_{\mathcal{C}} \vec{E}_1 \cdot d\vec{s} = -j\omega\mu_\circ \int_{\mathcal{S}} \vec{H}_0 \cdot d\vec{\mathcal{A}}$$

$$\int_0^{2\pi} rE_{1\theta}\, d\theta = -j\omega\mu_\circ \int_0^r 2\pi r H_0\, dr$$

$$E_{1\theta} \int_0^{2\pi} r\, d\theta = -j\omega\mu_\circ H_0 \int_0^r 2\pi r\, dr \qquad (S7.1)$$

For $r \leq R$,

$$E_{1\theta} 2\pi r = -j\omega\mu_\circ H_0 \pi r^2 \qquad (S7.2)$$

Dividing each side of Eq. $S7.2$ by $2\pi r$, we obtain:

$$E_{1\theta} = -\frac{j\omega\mu_\circ r H_0}{2} \qquad (S7.3)$$

Thus:

$$\vec{E}_1 = -\frac{j\omega\mu_\circ r H_0}{2}\vec{\imath}_\theta \qquad (2.56)$$

The 1st-order current flows only in the shell ($r \simeq R$):

$$\vec{J}_1 \simeq \frac{\vec{E}_1(r \simeq R)}{\rho_e} = -\frac{j\omega\mu_\circ R H_0}{2\rho_e}\vec{\imath}_\theta \qquad (2.57)$$

For $d \ll R$, we may treat the current as a 1st-order surface current, $\vec{K}_1$, by multiplying $\vec{J}_1$ by d:

$$\vec{K}_1 = -\frac{j\omega\mu_\circ R d H_0}{2\rho_e}\vec{\imath}_\theta \qquad (S7.4)$$

b) For $r > R$, $\vec{H}_1 = 0$; using Eq. 2.6, we can equate $\vec{K}_1$ to the discontinuity in $\vec{H}$ at $r = R$: $\vec{H}_0 + \vec{H}_1$ at the inner wall of the shell, and $\vec{H}_0$ outside. Thus:

$$\vec{K}_1 = \vec{\imath}_r \times [\vec{H}_0 - (\vec{H}_0 + \vec{H}_1)] = -\frac{j\omega\mu_\circ R d H_0}{2\rho_e}\vec{\imath}_\theta$$

$$= \vec{\imath}_r \times -\vec{H}_1 = -\frac{j\omega\mu_\circ R d H_0}{2\rho_e}\vec{\imath}_\theta \qquad (S7.5)$$

Solving Eq. $S7.5$ for $\vec{H}_1$ ($r \leq R - d$) with $d \ll R$, we have:

$$\vec{H}_1 = -\frac{j\omega\mu_\circ R d H_0}{2\rho_e}\vec{\imath}_z \qquad (2.58)$$

Solution to PROBLEM 2.7—Part 1 (continuation)

c) Equations 2.57, $S7.4$, and 2.58 predict that the magnitudes of $\vec{J}_1$, $\vec{K}_1$, and $\vec{H}_1$ all increase monotonically with frequency; this cannot be valid for the entire range of ω. These solutions are valid only in the "low" frequency limit, which is the applicable range of the quasi-static approximation. More specifically, $\vec{H}_1$ given by Eq. 2.58 is valid only when $|\vec{H}_1| \ll |\vec{H}_0|$:

$$|\vec{H}_1| = \frac{\omega \mu_\circ R d |H_0|}{2\rho_e} \ll |\vec{H}_0| \qquad (S7.6)$$

From Eq. $S7.6$, we can obtain the frequency limit, often called the skin-depth frequency, f_{sk}, below which the quasi-static approximation is valid:

$$f_{sk} = \frac{\rho_e}{\pi \mu_\circ R d} \qquad (2.59)$$

Note that f_{sk} depends not only on the metal's electrical resistivity but also on the size of the object in the sinusoidally time-varying applied magnetic field.

d) In the second approach for computing the shell's reaction field, we set $\vec{H}_1 \equiv \vec{H}_R$, and substitute $\vec{H}_0 + \vec{H}_R$ for $\vec{H}_0$ in the expression for $\vec{H}_1$ given in Eq. 2.58:

$$\vec{H}_R = -\frac{j\omega \mu_\circ R d (\vec{H}_0 + \vec{H}_R)}{2\rho_e} \qquad (S7.7)$$

Solving Eq. $S7.7$ for $\vec{H}_R$, we obtain:

$$\vec{H}_R = -\frac{j\omega \mu_\circ R d H_0}{2\rho_e + j\omega \mu_\circ R d} \vec{\imath}_z \qquad (2.60)$$

Combining Eq. 2.60 and $\vec{H}_T = \vec{H}_0 + \vec{H}_R$, we have:

$$\vec{H}_T = \vec{H}_0 + \vec{H}_R = H_0 \left(1 - \frac{j\omega \mu_\circ R d}{2\rho_e + j\omega \mu_\circ R d}\right) \vec{\imath}_z$$

$$= \frac{2\rho_e H_0}{2\rho_e + j\omega \mu_\circ R d} \vec{\imath}_z \qquad (2.61)$$

$\vec{J}$ and $\vec{H}_R$ are related by $\nabla \times \vec{H} = \vec{J}$, which, for $\vec{K} = \vec{J} d$, reduces to:

$$\vec{J} = \frac{1}{d} H_R \vec{\imath}_\theta \qquad (S7.8)$$

$$= -\frac{j\omega \mu_\circ R H_0}{2\rho_e + j\omega \mu_\circ R d} \vec{\imath}_\theta \qquad (2.62)$$

Note that in the low frequency limit, $\vec{H}_R$ given by Eq. 2.60 reduces, as expected, to $\vec{H}_1$ given by Eq. 2.58. In the high frequency limit, $\vec{H}_R$ reduces, also as expected, to $-\vec{H}_0$ and $\vec{H}_T$ becomes 0. Similar observations apply to $\vec{J}$.

PROBLEM 2.7: Induction heating—Part 2 (Power Dissipation)

Now, we can solve for power dissipation in the cylinder; two methods are used.

Method 1

e) We may calculate the resistive power dissipated in the cylindrical shell by directly computing $<p>=\vec{E}\cdot\vec{J}^*/2=\rho_e|J|^2/2$ (Eq. 2.21), where $\vec{J}$ is given by Eq. 2.62. Show that an expression for the time-averaged total dissipation power (per unit length) in the shell, $<P>$, for $d \ll R$ is given by:

$$\begin{aligned} <P> &= 2\pi R d <p> \\ &= \frac{\pi\rho_e\omega^2\mu_\circ^2 R^3 d}{4\rho_e^2+\omega^2\mu_\circ^2 R^2 d^2}|H_0|^2 \end{aligned} \tag{2.63}$$

Method 2

The same complex power supplied to the cylinder may also be viewed as a flow of Poynting power flux entering the cylinder at $r=R$ from a source located at $r > R$.

f) Show that the surface integral (per unit cylinder length) of the 1st-order complex Poynting vector $\vec{S}_1$ entering into the cylinder at $r=R$ is given by:

$$\begin{aligned} -\oint_{\mathcal{S}} \vec{S}_1\cdot d\mathcal{A} &= \tfrac{1}{2}(2\pi R)E_{1\theta}H_0^* \\ &= \frac{j\pi\rho_e\omega\mu_\circ R^2}{2\rho_e+j\omega\mu_\circ R d}|H_0|^2 \end{aligned} \tag{2.64}$$

Note that $E_{1\theta}=\rho_e J_\theta$, where J_θ is given by Eq. 2.62.

g) Take the real part of the right-hand side of Eq. 2.64 and show that it is identical to the expression for $<P>$ given by Eq. 2.63.

h) Plot $<P>$ as a function of ρ_e. Because both a perfect conductor ($\rho_e=0$) and a perfect insulator ($\rho_e=\infty$) obviously do not dissipate power, your $<P>$ vs. ρ_e plot should start with $<P>=0$ and return asymptotically to zero as $\rho_e\to\infty$. Note that $<P>$ given by Eq. 2.63 indeed indicates this behavior.

i) A consequence of this $<P>$ vs. ρ_e behavior is that there is a critical resistivity, ρ_{e_c}, at which $<P>$ is maximum. Show that ρ_{e_c} is given by:

$$\rho_{e_c}=\frac{\omega\mu_\circ R d}{2} \tag{2.65}$$

From Eq. 2.65, we note that for a given combination of resistivity (ρ_{e_c}) and sample size (R, d), there exists an optimal frequency that maximizes the heating: this is equal to the "skin depth" frequency, f_{sk}, given by Eq. 2.59.

j) Compute f_{sk} for a copper tube of 10-mm radius (R), 0.5-mm wall thickness (d), and $\rho_e = 2\times10^{-10}\,\Omega\,\mathrm{m}$ (roughly the electrical resistivity of copper at liquid helium temperatures).

Solution to PROBLEM 2.7—Part 2

e) In the sinusoidal case, the time-averaged dissipation power (per unit length), $< p >$, is given by $\vec{E}\cdot\vec{J}^*/2 = \rho_e|J|^2/2$, where $\vec{J}$ is the complex current density (Eq. 2.62). We thus have:

$$< p >= \frac{\rho_e}{2}|J_\theta|^2 = \frac{\rho_e}{2}\left(\frac{\omega^2\mu_\circ^2R^2}{4\rho_e^2+\omega^2\mu_\circ^2R^2d^2}\right)|H_0|^2 \qquad (S7.9)$$

The time-averaged *total* dissipation power (per unit length) in the shell, $< P >$, is obtained by multiplying $< p >$ by the cross sectional area of the shell:

$$\begin{aligned} < P > &= 2\pi Rd < p > \\ &= \frac{\pi\rho_e\omega^2\mu_\circ^2R^3d}{4\rho_e^2+\omega^2\mu_\circ^2R^2d^2}|H_0|^2 \end{aligned} \qquad (2.63)$$

We now examine two limits of ρ_e:

$$\rho_e \ll \omega\mu_\circ Rd\text{:} \quad < P > \simeq \frac{\pi\rho_eR}{d}|H_0|^2 \propto \rho_e \qquad \text{(excellent conductor)} \quad (S7.10a)$$

$$\rho_e \gg \omega\mu_\circ Rd\text{:} \quad < P > \simeq \frac{\pi\omega^2\mu_\circ^2R^3d}{4\rho_e}|H_0|^2 \propto \frac{1}{\rho_e} \quad \text{(poor conductor)} \qquad (S7.10b)$$

Note that in both limits, $< P > \to 0$, as expected.

f) The complex Poynting vector, $\vec{S}$, expanded to 1st-order, is:

$$\vec{S}_1 = \tfrac{1}{2}\left(\vec{E}_0\times\vec{H}_0^* + \vec{E}_0\times\vec{H}_1^* + \vec{E}_1\times\vec{H}_0^*\right) \qquad (S7.11)$$

Note that in computing the 1st-order Poynting vector, $\vec{S}_1$, the sum of the E-field subscript and H-field subscript must not exceed 1. In this particular case, we have $\vec{E}_0 = 0$; thus Eq. $S7.11$ simplifies to:

$$\vec{S}_1 = \tfrac{1}{2}\left(\vec{E}_1\times\vec{H}_0^*\right) \qquad (S7.12)$$

where from Eq. 2.62, $\vec{E}_1$ is given by:

$$\vec{E}_1 = \rho_e\vec{J} = -\frac{j\rho_e\omega\mu_\circ RH_0}{2\rho_e+j\omega\mu_\circ Rd}\vec{\imath}_\theta \qquad (S7.13)$$

We thus have:

$$\begin{aligned} -\oint_{\mathcal{S}}\vec{S}_1\cdot d\mathcal{A} &= \tfrac{1}{2}(2\pi R)E_{1\theta}H_0^* \\ &= \frac{j\pi\rho_e\omega\mu_\circ R^2}{2\rho_e+j\omega\mu_\circ Rd}|H_0|^2 \end{aligned} \qquad (2.64)$$

Solution to PROBLEM 2.7—Part 2 (continuation)

g) The real part of Eq. 2.64 is given by:

$$< P >= \frac{(\pi\rho_e\omega\mu_\circ R^2)(\omega\mu_\circ Rd)}{4\rho_e^2 + \omega^2\mu_\circ^2 R^2 d^2}|H_0|^2 = \frac{\pi\rho_e\omega^2\mu_\circ^2 R^3 d}{4\rho_e^2 + \omega^2\mu_\circ^2 R^2 d^2}|H_0|^2 \qquad (S7.14)$$

Note that Eq. $S7.14$ (Method 2) is identical to Eq. 2.63 (Method 1).

h) Figure 2.12 shows a plot of $< P >$ vs. ρ_e.

i) We differentiate $< P >$ with respect to ρ_e and equate it to 0 at ρ_{e_c}:

$$\left.\frac{d < P >}{d\rho_e}\right|_{\rho_{e_c}} = \left[\frac{\pi\omega^2\mu_\circ^2 R^3 d}{4\rho_{e_c}^2 + \omega^2\mu_\circ^2 R^2 d^2} - \frac{8\pi\rho_{e_c}^2\omega^2\mu_\circ^2 R^3 d}{(4\rho_{e_c}^2 + \omega^2\mu_\circ^2 R^2 d^2)^2}\right] = 0 \qquad (S7.15)$$

Solving Eq. $S7.15$ for ρ_{e_c}, we have:

$$\rho_{e_c} = \frac{\omega\mu_\circ Rd}{2} \qquad (2.65)$$

Equation 2.65 is important in induction heating, in which a uniform, sinusoidally time-varying magnetic field is applied to a conducting sample. The sample is heated by the eddy currents induced in the sample. At the skin-depth frequency, f_{sk}, given by Eq. 2.59, the induction heating is maximum.

j) For a copper cylinder of $R = 1\,\text{cm}$, $d = 0.5\,\text{mm}$, $\rho_e = 2\times10^{-10}\,\Omega\,\text{m}$ (corresponding to copper's resistivity at $\sim$4 K), we obtain, from Eq. 2.59:

$$f_{sk} = \frac{\rho_{e_c}}{\pi\mu_\circ Rd} \qquad (2.59)$$

$$= \frac{2\times10^{-10}\,\Omega\,\text{m}}{\pi(4\pi\times10^{-7}\,\text{H/m})(0.010\,\text{m})(0.0005\,\text{m})} \simeq 10\,\text{Hz}$$

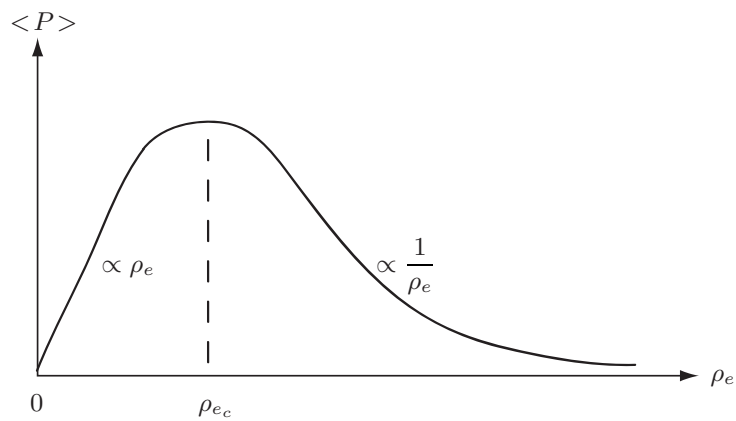

Fig. 2.12 Power dissipation vs. resistivity for induction-heated cylindrical shell.

Microwave Oven Cooking Cooking in a microwave oven involves induction heating, but it is different from the type studied here. In a microwave oven the frequency is set to the dominant vibration frequency of water molecules, enabling the water in the food to absorb the electromagnetic energy and be heated.

PROBLEM 2.8: Eddy-current loss in a metallic strip*

In this problem an expression for eddy-current loss in a metallic strip subjected to a time-varying magnetic field is derived. It is useful in computing eddy-current heating in copper-matrix superconductor strips. (When induced-current heating is beneficial, it is usually called induction heating; when it is detrimental, it is often called eddy-current loss.)

Figure 2.13 shows a "long" (in the x-direction) metallic strip of electrical resistivity ρ_e, width b (in the y-direction), and thickness a (in the z-direction) placed in a time-varying external magnetic induction, $dB_0/dt = \dot{B}_0$, which is, within zeroth order, uniform and z-directed.

a) Show that the 1st-order electric field, $\vec{E}_1$, can be expressed by:

$$E_{1x} = y\dot{B}_0 \tag{2.66}$$

b) Show that the *spatially-averaged* power dissipation density $\tilde{p}$ (over the unit strip volume) can be expressed by:

$$\tilde{p} = \frac{(b\dot{B}_0)^2}{12\rho_e} \tag{2.67}$$

c) When the external magnetic induction is sinusoidally varying in time with angular frequency ω, $B(t) = B_0 \sin \omega t$, show that an expression for the *time-averaged* $\tilde{p}$, $<\tilde{p}>$, is given by:

$$<\tilde{p}>= \frac{(b\,\omega\dot{B}_0)^2}{24\rho_e} \tag{2.68}$$

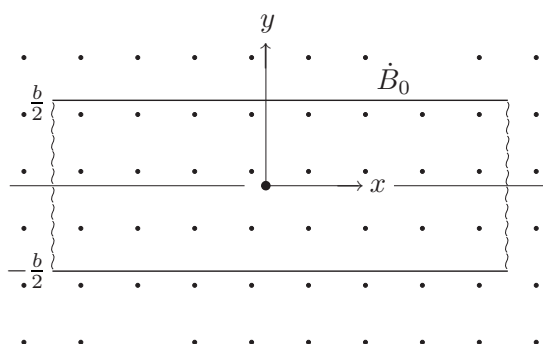

Fig. 2.13 Metallic strip of width b in a time-varying magnetic field, $\dot{B}_0$.

Answer to TRIVIA 2.4: iv). The "magnetostriction" effect of a magnetic field on iron causes cyclic changes in the iron sheet dimensions, creating hum of frequency twice that of the current. For 60-Hz current the hum is about an octave below middle C.

* **Problem 2.7** in the 1st Edition (Plenum, 1994).

Solution to PROBLEM 2.8

a) Because $\vec{B}_0$ is uniform and the system is independent of x, $\vec{E}_1$ points only in the x-direction and depends only on y. That is, $\nabla\times\vec{E}_1 = -\partial\vec{B}_0/\partial t$ reduces to:

$$-\frac{dE_{1x}}{dy} = -\frac{dB_0}{dt} = -\dot{B}_0 \qquad (S8.1)$$

From symmetry, $E_{1x}(y=0)=0$, and we have from Eq. $S8.1$:

$$E_{1x} = y\dot{B}_0 \qquad (2.66)$$

b) The *local* power density dissipated in the strip, $p(y)$, is given by $\vec{E}_1\cdot\vec{J}_1$. The total power dissipation (per unit strip length), P, is thus given by:

$$P = a\int_{-b/2}^{b/2} p(y)\,dy = \frac{2a(\dot{B}_0)^2}{\rho_e}\int_0^{b/2} y^2 dy = \frac{ab(b\dot{B}_0)^2}{12\rho_e} \qquad (S8.2)$$

Equation $S8.2$ is valid for "reasonably" slow variation of B_0 and "reasonably" resistive materials. That is, it is valid only when the induced (1^{st}-order) magnetic induction generated by $\vec{J}_1$ is small compared to B_0.

The *spatially-averaged* dissipation density, $\tilde{p}$, is P divided by the strip cross section:

$$\tilde{p} = \frac{P}{ab} = \frac{(b\dot{B}_0)^2}{12\rho_e} \qquad (2.67)$$

c) Under sinusoidal excitations the *time-averaged* total power dissipation density, $<p>$, is given by:

$$<p> = \tfrac{1}{2}E_{1x}J_{1x}^* \qquad (S8.3)$$

With $E_{1x} = j\omega y B_0$, $J_{1x} = E_{1x}/\rho_e$ and $<p>$ averaged over the strip volume is:

$$<\tilde{p}> = \frac{2a(\omega B_0)^2}{2\rho_e(ab)}\int_0^{b/2} y^2 dy = \frac{(b\,\omega B_0)^2}{24\rho_e} \qquad (2.68)$$

Note that $\tilde{p}$ and $<\tilde{p}>$ are proportional, respectively, to $(b\dot{B}_0)^2$ and $(b\,\omega B_0)^2$; i.e., both depend not only on the square of time rate of change of magnetic induction but also on the square of *conductor width*.

Discussion 2.4: Lamination to Reduce Eddy-Current Loss

Suppose the strip is cut into two strips, each having a total width of $b/2$. From Eqs. 2.67 and 2.68 both $\tilde{p}$ and the total power dissipation (over the two narrow strips) will be 1/4 the original values. Thus, it is possible to reduce eddy-current power dissipation to an arbitrarily small value by subdividing the strip. This lamination technique is used widely in power transformers where iron yokes are of iron sheets. Similarly, as we shall see in ***CHAPTERS 5*** and ***7***, superconductors also benefit from subdivision, leading to the universal choice of multifilamentary conductors for magnets.

PROBLEM 2.9: Rogowski coil

A Rogowski coil is an ammeter for time-varying current. It is a toroidal magnetic pickup coil with its integrated output voltage proportional to the total current that passes through the cross sectional area encircled by the Rogowski coil. Figure 2.14a shows a Rogowski coil placed to encircle a current, $I(t)$, to be measured. As indicated in Fig. 2.14a, a Rogowski coil is comprised of N small circular loops connected in series. The center of each loop of radius c is located radially R from the current center, which in this drawing points out of the paper. Figure 2.14b defines the x-y coordinates of one loop.

a) Show that for the case in which $c \ll R$, the total flux linkage, $\Phi(t) = N\Phi_1(t)$, to a Rogowski coil containing N circular loops is given by:

$$\Phi(t) \simeq \frac{\mu_\circ N c^2}{2R} I(t) \tag{2.69}$$

where $\Phi_1(t)$ is the total flux linked to one loop.

b) Show that an exact expression for $\Phi(t)$ is given by:

$$\Phi(t) = \mu_\circ N \left(R - \sqrt{R^2 - c^2}\right) I(t) \tag{2.70}$$

Place one of the N loops centered on the x-y coordinates to compute $\Phi(t)$.

c) Show that in the limit $(c/R)^4 \ll 1$, Eq. 2.70 reduces to Eq. 2.69.

d) Show that $\Phi(t)$ given by Eq. 2.70 is valid even if the Rogowski coil's axis is off-center of the current axis.

e) For a Rogowski coil with $N = 3600$; $c = 3\,\text{mm}$; $R = 0.5\,\text{m}$, compute the volt-seconds generated across its terminal for $\Delta I(t) = 1\,\text{MA}$.

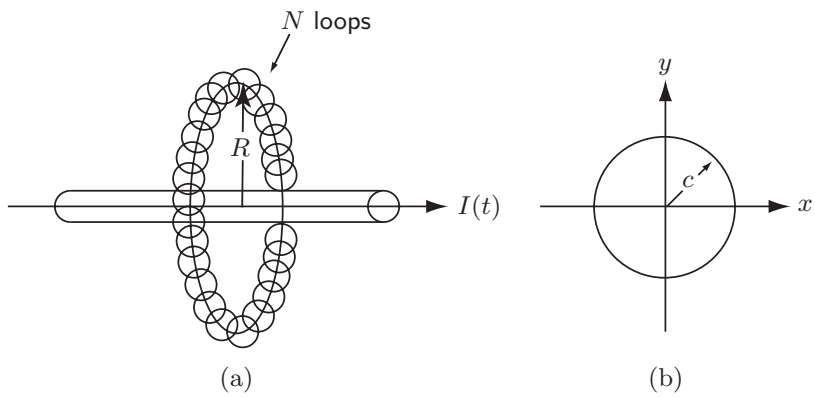

Fig. 2.14 (a) Rogowski coil comprised of N circular loops, each of diameter $2c$, encircling a time-varying current, $I(t)$, to be measured; (b) Cross-sectional view of one loop (radius c), centered on the x-y coordinates, with the loop center located radially R from the center of the current.

Solution to PROBLEM 2.9

a) The magnetic field $H_\phi(t)$ generated by the current $I(t)$ is directed azimuthally relative to the current. $H_\phi(t)$ at R in the radial direction from the center of the current is given by:

$$H_\phi(t) = \frac{I(t)}{2\pi R} \tag{S9.1}$$

For $c \ll R$, $H_\phi(t)$ given by Eq. S9.1 is nearly valid over each loop's cross sectional area, πc^2. Because there are N such loops in a Rogowski coil, we have:

$$\Phi(t) \simeq \frac{\mu_\circ N c^2}{2R} I(t) \tag{2.69}$$

The Rogowski coil output voltage, $V(t)$, is thus given by:

$$V(t) = \frac{d\Phi(t)}{dt} = \frac{\mu_\circ N c^2}{2R} \frac{dI(t)}{dt} \tag{S9.2}$$

b) Because $H_\phi(t)$ is not really constant over each loop, the total flux enclosed by one loop, $\Phi_1(t)$, should be integrated over the area encircled by the loop. Noting that $x^2+y^2=c^2$, with the loop's center at (0,0), $\Phi_1(t)$ is given by:

$$\Phi(t) = \frac{\mu_\circ I(t)}{2\pi} \int_{-c}^{c} \int_{-\sqrt{c^2-y^2}}^{\sqrt{c^2-y^2}} \frac{1}{R+y}\, dx\, dy$$

$$= \frac{\mu_\circ I(t)}{\pi} \int_{-c}^{c} \frac{\sqrt{c^2-y^2}}{R+y}\, dy \tag{S9.3}$$

Equation S9.3 may be solved in a closed form with a new variable, $\xi \equiv R+y$ (note that $d\xi = dy$). Thus, we have:

$$\Phi_1(t) = \frac{\mu_\circ I(t)}{\pi} \int_{R-c}^{R+c} \frac{\sqrt{c^2 - R^2 + 2R\xi - \xi^2}}{\xi}\, d\xi$$

$$= \mu_\circ \left(R - \sqrt{R^2-c^2}\right) I(t) \tag{S9.4}$$

The total flux linked to a Rogowski coil having N loops is given by $\Phi(t) = N\Phi_1(t)$:

$$\Phi(t) = \mu_\circ N \left(R - \sqrt{R^2-c^2}\right) I(t) \tag{2.70}$$

c) Equation 2.70 may be expressed as:

$$\Phi(t) = \mu_\circ N I(t) \left(R - R\sqrt{1 - \frac{c^2}{R^2}}\right) \tag{S9.5}$$

Because for $x \ll 1$, $\sqrt{1-x} \simeq 1-(1/2)x+(1/8)x^2-\cdots$, Eq. S9.5 may be given by:

$$\Phi(t) \simeq \mu_\circ N \left[R - R\left(1 - \tfrac{1}{2}\frac{c^2}{R^2} + \tfrac{1}{8}\frac{c^4}{R^4} - \cdots\right)\right] I(t) \tag{S9.6}$$

$$\Phi(t) \simeq \frac{\mu_\circ N c^2}{2R} I(t) \tag{2.69}$$

Solution to PROBLEM 2.9 (continuation)

d) Figure 2.15 shows a cross sectional view in the plane normal (x-y) to the current direction of a current/Rogowski coil set, in which the Rogowski coil is at the center ($x=0, y=0$) and the current center is off downward by distance δ_i.

Key parameters are defined by Fig. 2.15: r, the radial distance from the Rogowski coil center (0,0) to Point A in one circular loop; θ, the angle between the y-axis and r; s, the radial distance from the *current center* to Point A; and ϵ is the angle formed between r and s. From geometry, s^2 is given by:

$$s^2 = (r\cos\theta + \delta_i)^2 + r^2\sin^2\theta = r^2 + \delta_i^2 + 2r\delta_i\cos\theta \qquad (S9.7)$$

Forming a right triangle (not indicated in Fig. 2.15) by extending r by a length $\delta_i\cos\theta$, we have:

$$\cos\epsilon = \frac{r + \delta_i\cos\theta}{s} \qquad (S9.8)$$

The magnetic field $H_A(t)$ at Point A is given by $H_A(t) = I(t)/2\pi s$; its normal component on the Rogowski coil loop at Point A, $H_{A_\perp}(t)$, is given by:

$$H_{A_\perp}(t) = \frac{I(t)}{2\pi s}\cos\epsilon = \frac{I(t)}{2\pi s}\left(\frac{r + \delta_i\cos\theta}{s}\right) \qquad (S9.9)$$

Combining Eqs. $S9.7$ and $S9.9$, we obtain:

$$H_{A_\perp}(t) = \frac{I(t)}{2\pi}\left(\frac{r + \delta_i\cos\theta}{r^2 + \delta_i^2 + 2r\delta_i\cos\theta}\right) \qquad (S9.10)$$

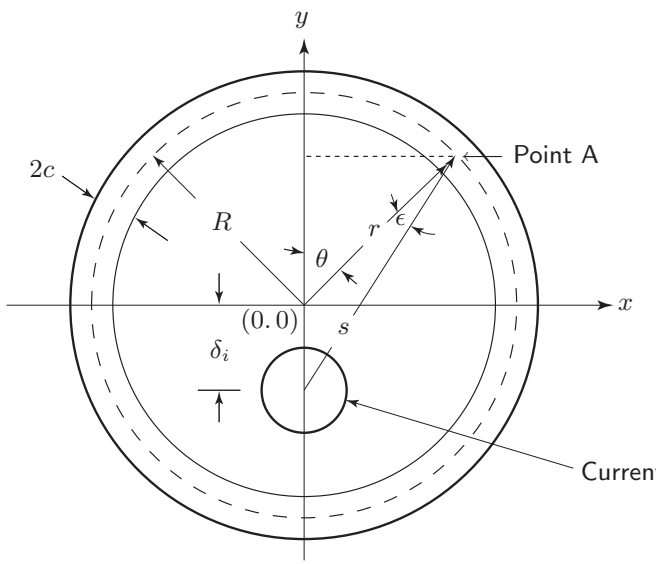

Fig. 2.15 Cross sectional view in the plane normal (x, y) to the azimuthal (current) direction of a current/Rogowski coil set with the Rogowski coil at the center (0, 0) of the plane and the *current center* off downward by distance δ_i.

Solution to PROBLEM 2.9 (continuation)

To compute $\Phi(t)$, Eq. $S9.10$, *multiplied* by $(N/2\pi)2\sqrt{c^2-(r-R)^2}$, must be integrated twice: once with respect to θ from 0 to 2π, at constant radial distance r, to account for N loops, and then with respect to r, from $R-c$ to $R+c$. Note that $2\sqrt{c^2-(r-R)^2}$ is the total segment distance (in the z-direction) of each loop of diameter c at r, which is located at distance $r-R$ from the center of the loop:

$$\Phi(t) = \frac{NI(t)}{2\pi^2}\int_{R-c}^{R+c}\int_0^{2\pi}\left[\frac{(r+\delta_i\cos\theta)\sqrt{c^2-(r-R)^2}}{r^2+\delta_i^2+2r\delta_i\cos\theta}\right]d\theta\,dr \quad (S9.11a)$$

$$= \frac{NI(t)}{\pi}\int_{R-c}^{R+c}\left[0+\frac{\sqrt{c^2-(r-R)^2}}{r}\right]dr \quad (S9.11b)$$

Note that the integration remarkably eliminates δ_i. Now, Eq. $S9.11b$ is integrated over the radial extent of one loop, from $r=R-c$ to $r=R+c$, resulting in:

$$\Phi(t) = \frac{NI(t)}{\pi}\left[\pi(R-\sqrt{R^2-c^2})\right] \quad (S9.11c)$$

Thus, a Rogowski coil measures $I(t)$ accurately regardless of its concentricity to the current that the coil encircles.

e) For $N=3600$, $c=3\,\text{mm}$; $R=0.5\,\text{m}$; and $\Delta I=1\,\text{MA}$, Eq. 2.69 is applicable because $(c/R)^4=1.3\times10^{-9}\ll1$. Thus, from Eq. $S9.2$:

$$\int V(t)\,dt = \frac{\mu_\circ N c^2\Delta I}{2R}$$

$$= \frac{(4\pi\times10^{-7}\,\text{H/m})(3600)(3\times10^{-3}\,\text{m})^2(1\times10^6\,\text{A})}{2(0.5\,\text{m})}$$

$$\simeq 41\,\text{mV s}$$

In a noisy environment such as the one typical in an experimental fusion machine, a signal level of 40-mV s is not easy, but not overwhelmingly difficult, to detect.

"...as we know, there are known knowns; these are things we know we know. We also know there are known unknowns; that is to say we know there are some things we do not know. But there are also unknown unknowns—the ones we don't know we don't know." —Donald Rumsfeld (2002)

"...the answer, my friend, is blowin' in the wind,..." —Bob Dylan (1962)

Chapter 3
Magnets, Fields, and Forces

3.1 Introduction

In this chapter we study key topics related to magnets, fields, and forces. Magnets treated include: 1) solenoids, single and multiple, e.g., comprised of nested coils; 2) Helmholtz coils and high-homogeneity magnets; 3) ideal dipoles; 4) ideal quadrupoles; 5) racetracks; and 6) ideal toroids. Two important solenoidal magnets for the generation of high magnetic fields, "Bitter" and "hybrid," are also discussed. Other issues such as "load lines," minimum volume magnets, superposition techniques, not included in the 1st Edition, are discussed in the **Problems & *Discussions*** that follow this introductory section.

At the present time, field and force computations are generally performed with computer codes that for a given magnet configuration give accurate numerical solutions at any location. These codes can also compute the self and mutual inductances of coils comprising the magnet and Lorentz forces acting on the coils [3.1]. Analytical expressions derived in this chapter give field values only at specialized locations such as the magnet center; however, they illustrate subtle relationships among fields, forces, and magnet parameters.

In this introductory section, we first study the law of Biot-Savart that is basic to computation of a magnetic field generated by a current-carrying element in the absence of magnetic materials. Also presented in this section are rather extensive treatments of: 1) field analysis; 2) axial forces for "rings" and "thin" solenoids; 3) stresses and strains in solenoids; and 4) self and mutual inductances.

3.2 Law of Biot-Savart

The differential magnetic field $d\vec{H}$ produced at point P by a differential current element $I\,d\vec{s}$ located at point O, a distance r away from P, is given by:

$$d\vec{H} = \frac{(I\,d\vec{s} \times \vec{r})}{4\pi r^3} \tag{3.1}$$

Equation 3.1 is known as the law of Biot-Savart (also known as 1st Law of Laplace). It indicates that the magnitude of $d\vec{H}$ at any location decreases inversely as the square of the distance from the differential current element: $|d\vec{H}| \propto 1/r^2$. At a fixed radius, $|d\vec{H}|$ varies as $\sin\theta$, where θ is the angle between the $\vec{s}$ and $\vec{r}$ vectors. We apply Eq. 3.1 to derive an expression for the field along the axis (z) of a loop of radius a located at $z=0$ and carrying current I, as illustrated in Fig. 3.1. The loop's axis defines the z axis; θ, measured from the $z=0$ plane, is defined in Fig. 3.1; φ (not indicated in the figure) is measured in the azimuthal direction.

As seen from Fig. 3.1, the r-component of $\vec{H}$, H_r, at each axial (z) location cancels, leaving only the z-component, $dH_z = |d\vec{H}|\cos\theta$. For this particular case, the $(I\,d\vec{s} \times \vec{r})$ term in Eq. 3.1 simplifies to $(I\,d\vec{s} \times \vec{r})_z = Iar\cos\theta\,d\varphi$, leading to:

$$H_z = \int_0^{2\pi} \frac{Iar\cos\theta}{4\pi r^3} d\varphi = \frac{Ia\cos\theta}{2r^2} \tag{3.2}$$

Y. Iwasa, *Case Studies in Superconducting Magnets: Design and Operational Issues*,
DOI: 10.1007/b112047_3,

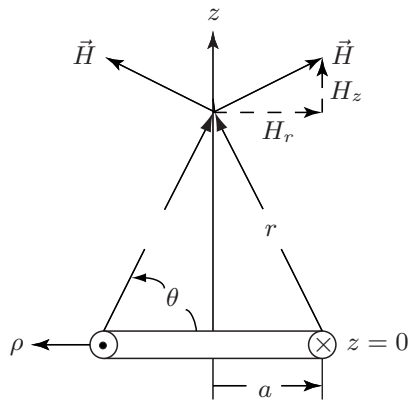

Fig. 3.1 Loop of radius a carrying current I.

With $\cos\theta = a/r$ and $r^2 = a^2 + z^2$, $H_z(z,\rho)$ on the z-axis ($\rho = 0$), $H_z(z,0)$, becomes:

$$H_z(z,0) = \frac{a^2 I}{2r^3} = \frac{a^2 I}{2(a^2+z^2)^{3/2}} \tag{3.3a}$$

In terms of the center ($z = 0, \rho = 0$) field, $H_z(0,0)$, $H_z(z,0)$ may be given by:

$$H_z(z,0) = \frac{H_z(0,0)}{[1+(z/a)^2]^{3/2}} \tag{3.3b}$$

Equation 3.3*a* may be used to derive an expression for the field along the axis of a solenoid of arbitrary winding cross section having any current distribution that is invariant in the φ-direction. **PROBLEM 3.1** and ***DISCUSSION 3.1*** are good examples. From Eq. 3.3*b*, we note that for $z \gg a$ or far from the center, the axial field of a "ring" coil decreases as $1/(z/a)^3$—this is further studied in **PROBLEM *3.11***.

3.3 Lorentz Force and Magnetic Pressure

In the presence of magnetic induction $\vec{B}$, an electric charge q in motion with velocity $\vec{v}$ experiences a force $\vec{F}_L$, called the Lorentz force: $\vec{F}_L = q\vec{v} \times \vec{B}$. For a conductor element carrying current density $\vec{J}$ in the presence of $\vec{B}$, the Lorentz force density, $\vec{f}_L$, is given by:

$$\vec{f}_L = \vec{J} \times \vec{B} \tag{3.4}$$

Equation 3.4 is the basic expression for magnetic forces and stresses in magnets. As stated at the beginning of ***CHAPTER 1***, whether superconducting and operating at a temperature in the range 1.8–80 K, or resistive and operating at room temperature, magnets producing the same field must deal with essentially the same stress level. A magnet's ultimate field is limited by the strength of its structural elements, including the current-carrying conductor. Thus, a 50-T superconducting magnet—if it ever becomes feasible—and a 50-T resistive magnet must both withstand tremendous Lorentz stresses. As illustrated below, a 50-T magnetic induction corresponds to an equivalent magnetic pressure of ~1 GPa (10,000 atm).

Consider an infinitely long, "thin-walled" solenoid (thickness δ) of average diameter $2a$ carrying a uniformly distributed current, which for the sake of computation is lumped into a surface current density K_θ [A/m]. The B_z-component of magnetic induction at (0,0) is given by integration of Eq. 3.3*a* with respect to z:

$$B_z = \frac{\mu_\circ a^2 K_\theta}{2} \int_{-\infty}^{\infty} \frac{dz}{(a^2 + z^2)^{3/2}} = \mu_\circ K_\theta \equiv B_\circ \tag{3.5}$$

The integration is taken over the entire range of z because the current "rings" extend from $z = -\infty$ to $z = \infty$. The application of Ampere's law gives that, for this infinitely long solenoid, $\vec{B}$ outside the solenoid ($r > a$) is zero and that within the solenoid bore ($r < a$) is $B_\circ$, uniform in both z- and r-directions. (From symmetry of the current distribution, the field is also independent of θ. Also note that Eq. 3.3a is valid only for such cases.) That is, the magnetic induction within the bore of an infinitely long solenoid is completely uniform and directed only in the z-direction. A more detailed discussion of axial field analysis is given next.

The B_z field just inside the winding is $B_\circ$ and that just outside the winding is zero, decreasing linearly with r over the winding thickness δ. The average induction, $\tilde{B}_z$, to which the current element in the winding is exposed, is thus $B_\circ/2$, resulting in an r-directed average Lorentz force density $f_{L_r}\vec{\imath}_r$ acting on the winding:

$$f_{L_r}\vec{\imath}_r = \frac{K_\theta}{\delta}\tilde{B}_z\vec{\imath}_r = \frac{K_\theta B_\circ}{2\delta}\vec{\imath}_r \tag{3.6}$$

An r-directed Lorentz force, $F_{L_r}\vec{\imath}_r$ acting on the winding volume element, defined in Fig. 3.2, is equivalent to a magnetic pressure, $p_m\vec{\imath}_r$, acting on the winding surface element, also defined in Fig. 3.2. Thus:

$$F_{L_r}\vec{\imath}_r = f_{L_r}[(a\Delta\theta)\delta\Delta z]\vec{\imath}_r = p_m[(a\Delta\theta)\Delta z]\vec{\imath}_r \tag{3.7}$$

Combining Eqs. 3.5–3.7 and solving for p_m, we obtain:

$$p_m = \frac{B_\circ^2}{2\mu_\circ} \tag{3.8}$$

That is, the magnetic pressure is equal to the magnetic energy density. For $B_\circ$ equal to 1 T, Eq. 3.8 gives a magnetic pressure of 3.98×10^5 Pa or $\sim$4 atm, from which it follows that for $B_\circ = 50$ T, a magnetic pressure of $\sim$1 GPa is reached.

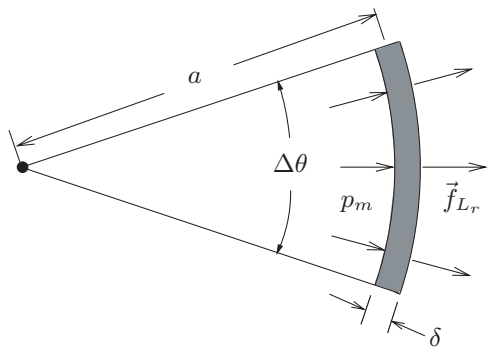

Fig. 3.2 Axial view of a differential element for a "thin-walled" solenoid (thickness δ) of average diameter $2a$. The element is Δz high in the z-direction (out of the paper).

3.4 Field Analysis of Solenoidal Coil

Here, we derive closed-form field expressions useful for analyzing high spatial-field-homogeneity MRI and NMR solenoidal magnets. Also derived are expressions for simple ("long" and "thin") coils; these expressions may be used to "get a feel" for the field homogeneity of a solenoidal coil during the early design stage.

Figure 3.3 shows a cross sectional view of a solenoidal coil of winding i.d., o.d., length (width), respectively, of $2a_1$, $2a_2$, and $2b$. Field lines are drawn to indicate that the magnetic field generated by the coil is chiefly axial in the coil bore, diverging, except along the coil's axis and at the axial midplane, to the radial direction, particularly outside the bore. Two dimensionless parameters used in field analysis of a solenoidal coil are: $\alpha \equiv 2a_2/2a_1 = a_2/a_1$ and $\beta \equiv 2b/2a_1 = b/a_1$, respectively, the winding o.d. and length, normalized to the winding i.d.

In spherical coordinates (r, θ, φ) as indicated in Fig. 3.4, where θ is polar angle and φ is azimuthal angle, the magnetic field in the z-direction, $H_z(r, \theta, \varphi)$, in any source-free space generated by any system of currents and/or magnetized material may be expressed by:

$$H_z(r,\theta,\varphi) = \sum_{n=0}^{\infty} \sum_{m=0}^{n} r^n (n+m+1) P_n^m(u) (A_n^m \cos m\varphi + B_n^m \sin m\varphi) \qquad (3.9)$$

As discussed in ***CHAPTER 2***, $P_n^m(u)$ is the set of Legendre polynomials (for $m=0$) and associated Legendre functions (for $m>0$) with $u = \cos\theta$.

A_n^m and B_n^m are constants. Typically all but A_0^0 and B_0^0 are to be minimized, because they contribute to field nonuniformity. A_n^m and B_n^m may be minimized by adjusting the parameters of each coil in the magnet. These parameters, for each coil, may include winding i.d. ($2a_1$), winding o.d. ($2a_2$), winding length ($2b$), coil midplane location relative to the magnet center, and "overall" current density. As will become clear shortly here, all parameters related to spatial field distribution are functions only of α and β, the two dimensionless parameters defined above.

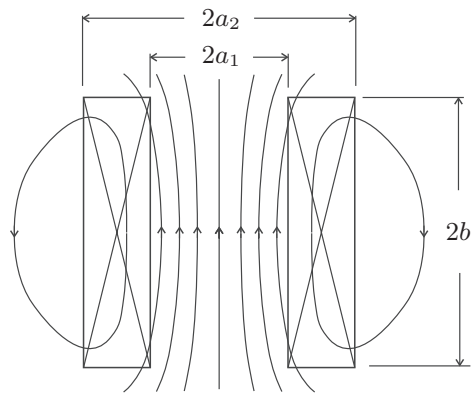

Fig. 3.3 Cross sectional view of a solenoidal coil of winding i.d., o.d., and length (width), respectively, of $2a_1$, $2a_2$, and $2b$. Field lines are drawn to indicate that the magnetic field generated by the coil is chiefly axial in the coil bore, diverging, except along the axial midplane, to the radial direction outside the bore.

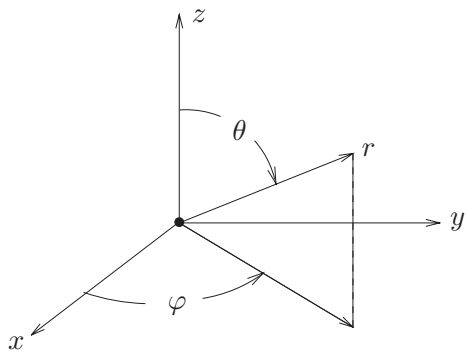

Fig. 3.4 Spherical coordinates.

For solenoidal systems for which all current densities are invariant in φ, i.e., symmetric with respect to the axis, only the $m=0$ terms remain. Along the z-axis ($r=z, \theta=0$), we may simplify Eq. 3.9 for $H_z(z)$ to:

$$H_z(z) = \sum_{n=0}^{\infty} z^n (n+1) A_n^0 \tag{3.10a}$$

Along the x- (or y-) axis ($x, \theta=90°$), at midplane, Eq. 3.9 for solenoids becomes:

$$H_z(x) = \sum_{n=0}^{\infty} \sum_{m=0}^{n} x^n (n+m+1) P_n^m(0) A_n^m \tag{3.10b}$$

Equation 3.10a has no Legendre functions because $P_n^0(1)=P_n(1)=1$. For Eq. 3.10b note that $P_n^m(0)=0$ when n is even and m is odd. Table 2.3 in ***CHAPTER 2*** gives values of $P_n^m(0)$ for even numbers of m up to $m=10$. Using values of $P_n^m(0)$ for n and $m=0$, 2, and 4, we may express $H_z(z)$ and $H_z(x)$ in Cartesian coordinates:

$$H_z(z) = A_0^0 + 3A_2^0 z^2 + 5A_4^0 z^4 + \cdots \tag{3.11a}$$

$$H_z(x) = A_0^0 - (\tfrac{3}{2}A_2^0 - 15A_2^2)x^2 + (\tfrac{15}{8}A_4^0 - \tfrac{105}{2}A_4^2 + 945A_4^4)x^4 + \cdots \tag{3.11b}$$

A_0^0 is the field at the magnet center (0,0,0): $A_0^0 \equiv H_0$. For an "ideal" solenoidal coil, coefficients are zero for $m>0$: $A_n^m=0$ for $m>0$. Coefficients for $n>0, m=0$, A_n^0, are functions of coil parameters—specifically, α and β. Introducing $h_z(\zeta) \equiv H_z(z)/H_0$, where $\zeta \equiv z/a_1$, and $h_z(\xi) \equiv H_z(x)/H_0$, where $\xi \equiv x/a_1$, we obtain:

$$\begin{aligned} h_z(\zeta) = 1 &+ E_2(\alpha,\beta)\zeta^2 + E_4(\alpha,\beta)\zeta^4 \\ &+ E_6(\alpha,\beta)\zeta^6 + E_8(\alpha,\beta)\zeta^8 + E_{10}(\alpha,\beta)\zeta^{10} + \cdots \end{aligned} \tag{3.12a}$$

$$\begin{aligned} h_z(\xi) = 1 &- \tfrac{1}{2}E_2(\alpha,\beta)\xi^2 + \tfrac{3}{8}E_4(\alpha,\beta)\xi^4 \\ &- \tfrac{5}{16}E_6(\alpha,\beta)\xi^6 + \tfrac{35}{128}E_8(\alpha,\beta)\xi^8 - \tfrac{63}{256}E_{10}(\alpha,\beta)\xi^{10} + \cdots \end{aligned} \tag{3.12b}$$

Note that the ξ^2 term coefficient is only half (and of opposite sign) of the ζ^2 coefficient, and the ξ^4 term is 3/8 of the ζ^4 term and of the same sign. Indeed, every coefficient in the plane direction is numerically smaller than that in the z-direction, so that field inhomogeneity tends to be smaller in the x- and y-directions than that in the z-direction.

The center field $H_0\,(\equiv A_0^0)$ is given by:

$$H_0 = \lambda J a_1 F(\alpha,\beta) = \lambda J a_1 \beta \ln\left[\frac{\alpha+\sqrt{\alpha^2+\beta^2}}{1+\sqrt{1+\beta^2}}\right] \tag{3.13a}$$

From Eq. 3.13a, we note that:

$$F(\alpha,\beta) = \beta \ln\left[\frac{\alpha+\sqrt{\alpha^2+\beta^2}}{1+\sqrt{1+\beta^2}}\right] \tag{3.13b}$$

$F(\alpha,\beta)$ is the "field factor" for a uniform-current-density coil [3.2]. Derivation of Eq. 3.13 is left to **PROBLEM 3.1**. Expressions of $E_n(\alpha,\beta)$ in Eq. 3.12 for $n=2$, 4, 6, 8, and 10 are given below as the product of $F(\alpha,\beta)$ and $E_n(\alpha,\beta)$ [3.3].

$$F(\alpha,\beta)E_2(\alpha,\beta) = \frac{1}{2\beta}\left[\frac{1}{(1+\beta^2)^{1.5}} - \frac{\alpha^3}{(\alpha^2+\beta^2)^{1.5}}\right] \tag{3.14a}$$

$$F(\alpha,\beta)E_4(\alpha,\beta) = \frac{1}{24\beta^3}\left[\frac{2+7\beta^2+20\beta^4}{(1+\beta^2)^{3.5}} - \frac{2\alpha^7+7\alpha^5\beta^2+20\alpha^3\beta^4}{(\alpha^2+\beta^2)^{3.5}}\right] \tag{3.14b1}$$

Equation 3.14b1 may be given more concisely as:

$$F(\alpha,\beta)E_4(\alpha,\beta) = -\frac{r^3}{24\beta^3}\left[\frac{2r^4+7r^2\beta^2+20\beta^4}{(r^2+\beta^2)^{3.5}}\right]\Bigg|_{r=1}^{r=\alpha} \tag{3.14b2}$$

This concise format is used below for terms of the 6$^{\text{th}}$, 8$^{\text{th}}$, and 10$^{\text{th}}$ order:

$$F(\alpha,\beta)E_6(\alpha,\beta) = -\frac{r^3}{240\beta^5}\left[\frac{8r^8+44r^6\beta^2+99r^4\beta^4+28r^2\beta^6+280\beta^8}{(r^2+\beta^2)^{5.5}}\right]\Bigg|_{r=1}^{r=\alpha} \tag{3.14c}$$

$$F(\alpha,\beta)E_8(\alpha,\beta) = -\frac{r^3}{896\beta^7}\left[\frac{\begin{array}{r}16r^{12}+120r^{10}\beta^2+390r^8\beta^4+715r^6\beta^6\\ +1080r^4\beta^8-1008r^2\beta^{10}+1344\beta^{12}\end{array}}{(r^2+\beta^2)^{7.5}}\right]\Bigg|_{r=1}^{r=\alpha} \tag{3.14d}$$

$$F(\alpha,\beta)E_{10}(\alpha,\beta) = -\frac{r^3}{11520\beta^9}\left[\frac{\begin{array}{r}128r^{16}+1216r^{14}\beta^2+5168r^{12}\beta^4+12920r^{10}\beta^6+20995r^8\beta^8\\ +19976r^6\beta^{10}+49632r^4\beta^{12}-46464r^2\beta^{14}+21120\beta^{16}\end{array}}{(r^2+\beta^2)^{9.5}}\right]\Bigg|_{r=1}^{r=\alpha} \tag{3.14e}$$

$F(\alpha,\beta)E_n(\alpha,\beta)$ is a recurrence formula; the n^{th} term may be derived from:

$$F(\alpha,\beta)E_n(\alpha,\beta) = \frac{1}{n}\frac{\partial}{\partial\beta}\Big[F(\alpha{=}1,\beta)E_{n-1}(\alpha{=}1,\beta) - F(\alpha,\beta)E_{n-1}(\alpha,\beta)\Big] \tag{3.15a}$$

$F(\alpha,\beta)E_n(\alpha,\beta)$ may also be expressed as:

$$F(\alpha,\beta)E_n(\alpha,\beta) = \frac{1}{M_n\beta^{n-1}}\left[\frac{f_n(\alpha{=}1,\beta)}{(1{+}\beta^2)^{n-0.5}} - \frac{\alpha^3 f_n(\alpha,\beta)}{(\alpha^2{+}\beta^2)^{n-0.5}}\right] \tag{3.15b}$$

where M_n is a constant. From Eqs. 3.14*a*, 3.14*b*1, and 3.15*b*, for example, we find: $f_2(\alpha,\beta){=}1$ and $M_2{=}2$; and $f_4(\alpha,\beta){=}2\alpha^4{+}7\alpha^2\beta^2{+}20\beta^4$ and $M_4{=}24$. Values of M_n and expressions of $f_n(\alpha,\beta)$ for $n = 2, 3, 4, \ldots, 18, 19$, and 20 are given in ***Appendix IB***. In **Problem 3.4**, $f_n(\alpha,\beta)$s for even numbers of n up to 20 are used to solve a field problem.

Henceforth we consider only the z-axis, because, as discussed above (Eqs. 3.12*a* and 3.12*b*), field inhomogeneity of $H_z(z)$, though not always (as in some nested-coil magnets), is greater than those in the plane normal to the z-axis, i.e., $H_z(x)$ and $H_z(y)$. From Eq. 3.12*a*, we obtain:

$$\begin{aligned}\frac{\partial^2 h_z(\zeta)}{\partial\zeta^2} &= [2E_2(\alpha,\beta) + (4)(3)E_4(\alpha,\beta)\zeta^2 + \cdots] \\ &= \sum_{n=1}^{\infty}(2n)(2n{-}1)E_{2n}(\alpha,\beta)\zeta^{2(n-1)}\end{aligned} \tag{3.16a}$$

In general:

$$\frac{\partial^{2k} h_z(\zeta)}{\partial\zeta^{2k}} = \sum_{n=k}^{\infty}(2n)(2n{-}1)(\cdots)(2n{-}2k{+}1)E_{2n}(\alpha,\beta)\zeta^{2(n-k)} \tag{3.16b}$$

At the origin, $\zeta = 0$, Eqs. 3.16*a* and 3.16*b* reduce to simpler expressions because only the first term is nonzero. Thus:

$$\left.\frac{\partial^2 h_z(\zeta)}{\partial\zeta^2}\right|_0 = 2E_2(\alpha,\beta) \tag{3.17a}$$

$$\left.\frac{\partial^{2k} h_z(\zeta)}{\partial\zeta^{2k}}\right|_0 = (2k)!\,E_{2k}(\alpha,\beta) \tag{3.17b}$$

Nested-Coil Magnet

For a magnet comprised of ℓ nested (coaxial and concentric) coils, each of λJ, a_1, α, β, Eq. 3.12*a*, given only up to the ζ^2 term, is generalized:

$$h_z(\zeta) = 1 + \frac{\sum_{j=1}^{\ell}(\lambda J)_j\, a_{1_j} F(\alpha_j,\beta_j)E_2(\alpha_j,\beta_j)}{\sum_{j=1}^{\ell}(\lambda J)_j\, a_{1_j} F(\alpha_j,\beta_j)}\zeta^2 + \cdots \tag{3.18}$$

Before discussing in **3.4.2** errors arising in a two-coil nested magnet, we shall first consider a few special cases for single solenoidal coils.

3.4.1 Simple Coils

Here, we derive for "simple" coils expressions of $E_n(\alpha,\beta)$, and hence $h_z(\zeta)$, up to the 10^{th} order. Each expression of $h_z(\zeta)$ should give the designer, without relying on a field analysis specialist, a "feel" for how the field homogeneity of the coil under consideration is affected by its geometric shape, i.e., α and β.

"Short" Coil

For a short coil ($\beta \to 0$), such as a pancake, $F(\alpha,\beta)$ may be simplified as:

$$F(\alpha,\beta\to 0)=\beta\ln\alpha \tag{3.19}$$

Although *extremely* tedious, expressions for $E_2(\alpha,0),\ldots,E_{10}(\alpha,0)$ may be derived from Eq. 3.14. In the limit $\beta\to 0$, the denominator of each term in $f_n(\alpha,\beta)$, e.g., $(1+\beta^2)^{n-0.5}$, may be expanded in a power series of β^{2k} up to the β^n term, where the integer k runs from 1 to $n/2$.

$$\begin{aligned}\frac{1}{(1+\beta^2)^{n-0.5}}=1-(n-0.5)\beta^2+(n-0.5)(n+0.5)\frac{\beta^4}{2!}\\ -(n-0.5)(n+0.5)(n+1.5)\frac{\beta^6}{3!}+\cdots\\ (-1)^k(n-0.5)(n+0.5)(n+1.5)\cdots(n+k-1.5)\frac{\beta^{2k}}{k!}\end{aligned} \tag{3.20}$$

In the limit of $\beta\to 0$, the terms higher than β^n in the right-hand side of Eq. 3.20 become negligible compared with β^n. Also, remarkably, all the terms below β^n cancel out, leaving only the β^n term in the numerator within the brackets of the right-hand side of Eq. 3.14 with a numerical coefficient, e.g., $-3/4$ for $n=2$.

$E_n(\alpha,0)$ terms, derivable from Eqs. 3.14 and 3.19, may be given by:

$$E_2(\alpha,0)=-\frac{3}{2^2}\cdot\frac{(\alpha^2-1)}{\alpha^2\ln\alpha}=-\frac{3(\alpha^2-1)}{4\alpha^2\ln\alpha} \tag{3.21a}$$

$$E_4(\alpha,0)=\frac{3\cdot5}{2^5}\cdot\frac{(\alpha^4-1)}{\alpha^4\ln\alpha}=\frac{15(\alpha^4-1)}{32\alpha^4\ln\alpha} \tag{3.21b}$$

$$E_6(\alpha,0)=-\frac{5\cdot7}{2^5\cdot3}\cdot\frac{(\alpha^6-1)}{\alpha^6\ln\alpha}=-\frac{35(\alpha^6-1)}{96\alpha^6\ln\alpha} \tag{3.21c}$$

$$E_8(\alpha,0)=\frac{5\cdot7\cdot9}{2^{10}}\cdot\frac{(\alpha^8-1)}{\alpha^8\ln\alpha}=\frac{315(\alpha^8-1)}{1024\alpha^8\ln\alpha} \tag{3.21d}$$

$$E_{10}(\alpha,0)=-\frac{7\cdot9\cdot11}{2^9\cdot5}\cdot\frac{(\alpha^{10}-1)}{\alpha^{10}\ln\alpha}=-\frac{693(\alpha^{10}-1)}{2560\alpha^{10}\ln\alpha} \tag{3.21e}$$

Thus, Eq. 3.12*a* becomes:

$$\begin{aligned}h_z(\zeta)=1-\frac{3(\alpha^2-1)}{4\alpha^2\ln\alpha}\zeta^2+\frac{15(\alpha^4-1)}{32\alpha^4\ln\alpha}\zeta^4-\frac{35(\alpha^6-1)}{96\alpha^6\ln\alpha}\zeta^6\\ +\frac{315(\alpha^8-1)}{1024\alpha^8\ln\alpha}\zeta^8-\frac{693(\alpha^{10}-1)}{2560\alpha^{10}\ln\alpha}\zeta^{10}+\cdots\end{aligned} \tag{3.22}$$

"Thin-Walled" Coil

For a "thin-walled" coil ($\alpha=1$), $F(\alpha,\beta)$ becomes:

$$\lim_{\alpha\to 1} F(\alpha,\beta) = \beta\frac{\epsilon}{\sqrt{1+\beta^2}} \tag{3.23a}$$

$$= \frac{\beta(\alpha-1)}{\sqrt{1+\beta^2}} \tag{3.23b}$$

Combining Eqs. 3.14 and 3.23, we may obtain expressions for $E_n(1,\beta)$:

$$E_2(1,\beta) = -\frac{3}{2(1+\beta^2)^2} \tag{3.24a}$$

$$E_4(1,\beta) = \frac{5(3-4\beta^2)}{2^3(1+\beta^2)^4} \tag{3.24b}$$

$$E_6(1,\beta) = -\frac{7(5-20\beta^2+8\beta^4)}{2^4(1+\beta^2)^6} \tag{3.24c}$$

$$E_8(1,\beta) = \frac{9(35-280\beta^2+336\beta^4-64\beta^6)}{2^7(1+\beta^2)^8} \tag{3.24d}$$

$$E_{10}(1,\beta) = -\frac{11(63-840\beta^2+2016\beta^4-1152\beta^6+128\beta^8)}{2^8(1+\beta^2)^{10}} \tag{3.24e}$$

Thus for a "thin-walled" coil ($\alpha=1,\beta$), we have:

$$\begin{aligned} h_z(\zeta) = 1 &- \frac{3}{2(1+\beta^2)^2}\zeta^2 + \frac{5(3-4\beta^2)}{8(1+\beta^2)^4}\zeta^4 - \frac{7(5-20\beta^2+8\beta^4)}{16(1+\beta^2)^6}\zeta^6 \\ &+ \frac{9(35-280\beta^2+336\beta^4-64\beta^6)}{128(1+\beta^2)^8}\zeta^8 \\ &- \frac{11(63-840\beta^2+2016\beta^4-1152\beta^6+128\beta^8)}{256(1+\beta^2)^{10}}\zeta^{10} \end{aligned} \tag{3.25}$$

"Thin-Walled & Long" Coil

For a "thin-walled & long" coil ($\alpha=1$ and $\beta\to\infty$), Eq. 3.25 simplifies to:

$$h_z(\zeta) = 1 - \frac{1.5}{\beta^4}\zeta^2 - \frac{2.5}{\beta^6}\zeta^4 - \frac{3.5}{\beta^8}\zeta^6 - \frac{4.5}{\beta^{10}}\zeta^8 - \frac{5.5}{\beta^{12}}\zeta^{10} - \cdots - \frac{n+1}{2\beta^{n+2}}\zeta^n \tag{3.26}$$

As may be inferred from Eq. 3.26, note that in the limiting case of $\beta\to\infty$, $E_n(1,\beta)=-(n+1)/2\beta^{(n+2)}$. As expected, homogeneity improves with coil length.

"Ring" Coil

For a "ring" coil ($\alpha=1, \beta=0$), $E_n(\alpha,\beta)$ is derivable from Eq. 3.21 in the limit of $\alpha=1$, or from Eq. 3.25 in the limit $\beta=0$. In Eq. 3.21,

$$\lim_{\alpha\to 1} \frac{\alpha^n - 1}{\alpha^n \ln \alpha} = n \tag{3.27}$$

Thus, we may derive the same expressions by combining Eqs. 3.21 and 3.27 or simply inserting $\beta=0$ in each expression of Eq. 3.24. Either way, we obtain:

$$E_2(1,0) = -\frac{3}{2} = -1.5 \tag{3.28a}$$

$$E_4(1,0) = \frac{3\cdot 5}{2^3} = \frac{3\cdot 5}{2\cdot 4} = 1.875 \tag{3.28b}$$

$$E_6(1,0) = -\frac{5\cdot 7}{2^4} = -\frac{3\cdot 5\cdot 7}{2\cdot 4\cdot 6} \simeq -2.188 \tag{3.28c}$$

$$E_8(1,0) = \frac{5\cdot 7\cdot 9}{2^7} = \frac{3\cdot 5\cdot 7\cdot 9}{2\cdot 4\cdot 6\cdot 8} \simeq 2.461 \tag{3.28d}$$

$$E_{10}(1,0) = -\frac{7\cdot 9\cdot 11}{2^8} = -\frac{3\cdot 5\cdot 7\cdot 9\cdot 11}{2\cdot 4\cdot 6\cdot 8\cdot 10} \simeq -2.707 \tag{3.28e}$$

Thus, for a "ring" coil, $h_z(\zeta)$ is given by:

$$h_z(\zeta) = 1 - \tfrac{3}{2}\zeta^2 + \tfrac{15}{8}\zeta^4 - \tfrac{35}{16}\zeta^6 + \tfrac{315}{128}\zeta^8 - \tfrac{693}{256}\zeta^{10} + \cdots \tag{3.29}$$

Values of $E_{12}(1,0)$, $E_{14}(1,0)$, $E_{16}(1,0)$, $E_{18}(1,0)$, and $E_{20}(1,0)$ are given, respectively, by Eqs. 3.124*a*, 3.124*b*, 3.124*c*, 3.124*d*, and 3.124*e* in **PROBLEM 3.4** (p. 140).

Stronger Magnets (Part 1 of 2 Parts)

—Passage from Francis Bitter's *Magnets: The Education of a Physicist* [3.4]

The strength of a magnetic field may be expressed in a unit called a gauss, *which, like many quantities in physics, is named after a distinguished scientist. Karl Friedrich Gauss, 1777–1855, who devoted himself particularly to mathematics, astronomy, and magnetism, gave his name to this one. For an idea of what this unit means, we might say that a rather weak magnetic field—for example, that existing at the surface of the earth—is somewhat less than a gauss. The field between the poles of little toy horseshoe magnets may be as high as hundreds of gauss, or in really strong ones, such as are used in commercial apparatus, a thousand gauss or so. Between the pole pieces of a big electromagnet, like the one I used for my thesis, one might make fields of the order of 20,000 to 30,000 gauss. Fields somewhat higher than this can be produced by an iron electromagnet, but they are not very useful because they are confined to the very small volumes between the pointed pole pieces of the magnet.*

3.4.2 Harmonic Errors—In a Nested Two-Coil Magnet

Equations 3.12*a* and 3.12*b* indicate that both $h_z(\zeta)$ and $h_z(\xi)$, where $h_z \equiv H_z/H_0$, $\zeta \equiv z/a_1$, and $\xi \equiv x/a_1$, vary only as even-numbered powers of either ζ or ξ. That is, both equations express the spatial variations of the axial field for an "ideal" solenoid or an "ideal" nested set of such solenoids. Here the word "ideal" implies spatial symmetry, uniformity, and invariance in the current density.

Even for a single solenoid, reality is quite different: imperfections in the coil form; conductor dimensions and shape; placement of conductor, for example, result in terms other than those even-numbered. If a magnet consists of nested coils, the number of imperfections multiplies, and many "unwanted" terms will arise. Below, we illustrate the origin of harmonic errors with a two-coil nested magnet.

Consider a two-coil nested magnet of solenoidal Coil 1 of $[2a_1]_1$, α_1, β_1, and $[\lambda J]_1$ in the bore of solenoidal Coil 2 of $[2a_1]_2$, α_2, β_2, and $[\lambda J]_2$. If the two coils are aligned axially and radially, then

$$H_z(z) = [H_z(z)]_1 + [H_z(z)]_2 \tag{3.30}$$

where $[H_z(z)]_1$ and $[H_z(z)]_2$ may be given, from Eq. 3.11*a*:

$$[H_z(z)]_1 = [A_0^0]_1 + 3[A_2^0]_1 z^2 + 5[A_4^0]_1 z^4 + \cdots \tag{3.31a}$$

$$[H_z(z)]_2 = [A_0^0]_2 + 3[A_2^0]_2 z^2 + 5[A_4^0]_2 z^4 + \cdots \tag{3.31b}$$

Note that the total axial field at the center: $H_z(0) = [A_0^0]_1 + [A_0^0]_2 \equiv H_0$.

Coils Misaligned Axially

If Coils 1 and 2 are radially aligned, i.e., coaxial, but their midplanes are misaligned and are, respectively, at $z=0$ and $z=\delta_z$, then $H_z(z)$ of Eq. 3.31 becomes:

$$H_z(z) = H_0 + 3\{[A_2^0]_1 z^2 + [A_2^0]_2 (z-\delta_z)^2\} + 5\{[A_4^0]_1 z^4 + [A_4^0]_2 (z-\delta_z)^4\} + \cdots \tag{3.32a}$$

Expansion of the power terms in Eq. 3.32*a* results in:

$$\begin{aligned} H_z(z) = {} & \{H_0 + 3[A_2^0]_2 \delta_z^2 + 5[A_4^0]_2 \delta_z^4 + \cdots\} \\ & - \{6[A_2^0]_2 \delta_z + 20[A_4^0]_2 \delta_z^3 + \cdots\} z \\ & + \{3[A_2^0]_1 + 3[A_2^0]_2 + 30[A_4^0]_2 \delta_z^2 + \cdots\} z^2 \\ & - \{20[A_4^0]_2 \delta_z + \cdots\} z^3 \\ & + \{5[A_4^0]_1 + 5[A_4^0]_2 \cdots\} z^4 \end{aligned} \tag{3.32b}$$

As may be observed from Eq. 3.32*b* an axial misalignment of Coils 1 and 2 by δ_z not only perturbs the coefficient of each even-numbered z-term but, more importantly, gives rise to odd-numbered z-terms which make $H_z(z)$ axially asymmetric.

In a *real* NMR magnet consisting of many nested coils an axial misalignment is inevitable. The z-term, for example, either results in the broadening of the NMR spectral lines or creates "dips" at each peak in the spectrum. The z^3-term also broadens the spectrum, chiefly at frequencies away from the central frequency.

Axial Shim Coils

These unwanted terms are minimized by "shim" coils that are added to the superconducting magnet, located outside of its "correction" coils; further shimming is achieved by room-temperature shim coils located in the radial gap between the probe and the cryostat room-temperature bore.

A shim coil that minimizes an even-numbered z-term is essentially a "Helmholtz" coil, the basic principle of which is studied in **PROBLEM 3.3**; a shim coil that minimizes an odd-numbered z-term is also of Helmholtz type but with one of its coils of opposite polarity, to generate an axially antisymmetric field.

Coils Misaligned Radially

To study the spatial variation of a two-coil nested magnet misaligned radially, we first express $H_z(x, y, z)$ of a single solenoid in Cartesian coordinates. From Eq. 3.11 and Table 2.4 for Legendre functions of $n=0$, $n=2$, and $n=4$, we have:

$$H_z(x,y,z) = A_0^0 + 3A_2^0\left[z^2 - \tfrac{1}{2}(x^2+y^2)\right] + 5A_4^0\left\{z^4 - 3(x^2+y^2)\left[z^2 - \tfrac{1}{8}(x^2+y^2)\right]\right\} \qquad (3.33a)$$

When Coil 2 is misaligned radially with respect to Coil 1, in the x-direction by δ_x and in the y-direction by δ_y, we substitute $x-\delta_x$ for x and $y-\delta_y$ for y in Eq. 3.33a:

$$\begin{aligned} H_z(x,y,z) = H_0 &+ 3\left([A_2^0]_1[z^2-\tfrac{1}{2}(x^2+y^2)] + [A_2^0]_2\left\{z^2-\tfrac{1}{2}[(x-\delta_x)^2+(y-\delta_y)^2]\right\}\right) \\ &+ 5[A_4^0]_1\left\{z^4-3(x^2+y^2)[z^2-\tfrac{1}{8}(x^2+y^2)]\right\} \\ &+ [A_4^0]_2\left(z^4-3\left[(x-\delta_x)^2+(y-\delta_y)^2\right]\left\{z^2-\tfrac{1}{8}\left[(x-\delta_x)^2+(y-\delta_y)^2\right]\right\}\right) \end{aligned} \qquad (3.33b)$$

Expansion of Eq. 3.33b results in many terms, including x, x^2, x^3, x^4, y, y^2, y^3, y^4, xy, xy^2, x^2+y^2, $(x^2+y^2)^2$, z^2, z^2x, z^2y, and $z^2(x^2+y^2)$.

An x-shim coil consists often of a pair of flat (one or a few conductors thick), rectangular-shaped coils, "saddled" to conform to the magnet's outer cylindrical surface, with the axis along the $\varphi = 0$ (x) direction. It generates a z-directed field that increases with x, being zero at the z-axis ($x=0$). Similarly, y-shim and xy-shim coil pairs are placed, respectively, along the $\varphi=90°$ (y) and $\varphi=45°$ axes. Each coil generates a z-directed field that increases away from the z-axis.

Coils Misaligned Axially & Radially

When nested coils are misaligned both axially and radially—an inevitable consequence in a *real* NMR— xz, yz, xyz, and many more error harmonics can result.

3.5 Axial Forces

We present here useful analytical expressions for axial forces, F_z, among coaxially aligned "ring" coils and "thin-walled" solenoids, all derived from the original expressions given by Garrett [3.5]. Approximate expressions for limiting cases, e.g., coils far apart, are useful to make quick numerical checks; others may be used as the building blocks to create one's own computer code. In all cases, current flows in the same direction; reversing either current reverses the force.

3.5.1 Axial Force between Two "Ring" Coils

Figure 3.5 shows two "ring" coils ($\alpha = 1,\ \beta = 0$) coaxially ($\vec{\imath}_z$) separated by a distance ρ. Coils A and B are, respectively, of diameters $2a_A$ and $2a_B$ and total ampere turns of $N_A I_A$ and $N_B I_B$. The axial ($\vec{\imath}_z$) field generated by each coil points in the same direction. The axial force, $F_{zA}(\rho)$ on Coil A due to Coil B is given by:

$$F_{zA}(\rho) = \frac{\mu_\circ}{2}(N_A I_A)(N_B I_B)\frac{\rho\sqrt{(a_A + a_B)^2 + \rho^2}}{(a_A - a_B)^2 + \rho^2} \times \Big\{k^2 K(k) + (k^2 - 2)[K(k) - E(k)]\Big\} \tag{3.34}$$

$F_{zA}(\rho)$ is $+z$-directed or towards Coil B; i.e., $F_{zA}(\rho)$ is attractive. If the two currents flow in opposite directions, the sign changes to minus, and $F_{zA}(\rho)$ becomes repulsive. In Eq. 3.34, $K(k)$ and $E(k)$ are the complete elliptic integrals, respectively, of the first and second kinds, defined below.

$$K(k) = \int_0^{\pi/2} \frac{d\theta}{\sqrt{1 - k^2 \sin^2\theta}} \tag{3.35a}$$

$$E(k) = \int_0^{\pi/2} \sqrt{1 - k^2 \sin^2\theta}\, d\theta \tag{3.35b}$$

The modulus, k, of the elliptic integrals for this system is given by:

$$k^2 = \frac{4a_A a_B}{(a_A + a_B)^2 + \rho^2} \tag{3.36}$$

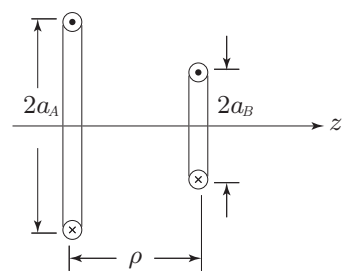

Fig. 3.5 "Ring" coils A and B coaxially aligned and separated by a distance ρ.

Table 3.1: Complete Elliptic Integrals of the First and Second Kinds: $K(k)$ and $E(k)$ for Selected Values of k^2 and k

k^2	k	$K(k)$	$E(k)$	k^2	k	$K(k)$	$E(k)$
0	0	$\pi/2$	$\pi/2$	0.7	0.8367	2.0754	1.2417
0.1	0.3162	1.6124	1.5308	0.8	0.8944	2.2572	1.1785
0.2	0.4472	1.6596	1.4890	0.90	0.9487	2.5781	1.1048
0.3	0.5477	1.7139	1.4454	0.95	0.9747	2.9083	1.0605
0.4	0.6325	1.7775	1.3994	0.98	0.9899	3.3541	1.0286
0.5	0.7071	1.8541	1.3506	0.99	0.9950	3.6956	1.0160
0.6	0.7746	1.9496	1.2984	1	1	∞	1

Table 3.1 gives $K(k)$ and $E(k)$ for selected values of k^2 and k. Note that $K(0)=E(0)=\pi/2$; also obvious are $K(1)=\infty$ and $E(1)=1$, i.e., $K(k)$ increases with k, whereas $E(k)$ decreases with k. For example, if $k^2=0.5$, $K(k=0.7071)=1.8541$.

$K(k)$ and $E(k)$ may be expressed by power series in k^2:

$$K(k)=\frac{\pi}{2}\left[1+\left(\frac{1}{2}\right)^2k^2+\left(\frac{1\cdot3}{2\cdot4}\right)^2k^4+\left(\frac{1\cdot3\cdot5}{2\cdot4\cdot6}\right)^2k^6+\left(\frac{1\cdot3\cdot5\cdot7}{2\cdot4\cdot6\cdot8}\right)^2k^8+\cdots\right] \qquad (3.37a)$$

$$E(k)=\frac{\pi}{2}\left[1-\left(\frac{1}{2}\right)^2k^2-\left(\frac{1\cdot3}{2\cdot4}\right)^2\frac{k^4}{3}-\left(\frac{1\cdot3\cdot5}{2\cdot4\cdot6}\right)^2\frac{k^6}{5}-\left(\frac{1\cdot3\cdot5\cdot7}{2\cdot4\cdot6\cdot8}\right)^2\frac{k^8}{7}-\cdots\right] \qquad (3.37b)$$

For $k^2\ll1$, the two integrals and their difference may be approximated by:

$$K(k)\simeq\frac{\pi}{2}\left(1+\tfrac{1}{4}k^2+\tfrac{9}{64}k^4+\tfrac{25}{256}k^6+\tfrac{1225}{16384}k^8\right) \qquad (3.38a)$$

$$E(k)\simeq\frac{\pi}{2}\left(1-\tfrac{1}{4}k^2-\tfrac{3}{64}k^4-\tfrac{5}{256}k^6-\tfrac{175}{16384}k^8\right) \qquad (3.38b)$$

$$K(k)-E(k)\simeq\frac{\pi}{4}\left(k^2+\tfrac{3}{8}k^4+\tfrac{15}{64}k^6+\tfrac{175}{1024}k^8\right) \qquad (3.38c)$$

Stronger Magnets (Part 2 of 2 Parts)

—Passage from Francis Bitter's *Magnets: The Education of a Physicist*

The reason for this limitation is not hard to find. An electromagnet consists of an iron core surrounded by coils of wire. The current in the wire magnetizes the iron and the magnetized iron produces a field at the gap between the poles. In the last chapter we discussed magnetic saturation—the condition achieved when all the little ferromagnetic domains are pointing in the same direction. In iron at room temperature this is in the vicinity of 20,000 gauss, and it is roughly the maximum field that you can produce with iron core magnets. The slight increase to 30,000 gauss or so is due to an effect that we already have mentioned. There is a tendency for a magnetic field to be concentrated near corners or points. By having pointed pole pieces rather than flat ones larger fields may be obtained. (See **PROBLEM 2.7**).

Special Case 1: Two Ring Coils Far Apart

When two ring coils are far apart, i.e., $\rho^2 \gg (a_A+a_B)^2$, then $k^2 \ll 1$ and approximations of Eqs. 3.38a and 3.38c may be used to simplify Eq. 3.34. Equation 3.34 may first be simplified to:

$$F_{zA}(\rho) \simeq \frac{\mu_\circ}{2}(N_A I_A)(N_B I_B)\Big\{k^2 K(k) + (k^2-2)[K(k)-E(k)]\Big\} \tag{3.39a}$$

Now, in applying Eqs. 3.38a and 3.38c, although $k^2 \ll 1$, we must include terms up to k^4 when expanding the $K(k)-E(k)$ term because it is multiplied not only by k^2 but also by -2.

$$\begin{aligned} F_{zA}(\rho) &\simeq \frac{\mu_\circ}{2}(N_A I_A)(N_B I_B) \\ &\qquad \times \left[k^2\left(\frac{\pi}{2}+\frac{\pi}{8}k^2\right) + (k^2-2)\left(\frac{\pi}{4}k^2+\frac{3\pi}{32}k^4\right)\right] \\ &\simeq \frac{\mu_\circ}{2}(N_A I_A)(N_B I_B)\left(\frac{3\pi}{16}k^4\right) \end{aligned} \tag{3.39b}$$

In the second approximation step, the k^6 term is neglected. Finally, we have a simple expression in the limit $\rho^2 \gg (a_A+a_B)^2$:

$$F_{zA}(\rho) = \frac{3\mu_\circ}{2\pi}\left(\frac{\pi a_A^2 N_A I_A}{\rho^2}\right)\left(\frac{\pi a_B^2 N_B I_B}{\rho^2}\right) \tag{3.39c}$$

Equation 3.39c states that this axial force is proportional to the product of two "magnetic moments," i.e., $\pi a_A^2 N_A I_A$ and $\pi a_B^2 N_B I_B$, each reduced by ρ^2. In ***Discussion 3.17*** (p. 213), Eq. 3.39c is derived from an expression of mutual inductance.

Special Case 2: Two Adjacent Ring Coils of the Same Diameter

When two ring coils have the same diameter $a_A = a_B = a$ and are very close to each other, i.e., $\rho \ll 2a$, hence $k^2 \to 1$ and $K(k) \to \infty$ and $E(k) \to 1$, then Eq. 3.34 may be transformed to an expression much simpler than Eq. 3.34:

$$F_{zA}(\rho) \simeq \mu_\circ (N_A I_A)(N_B I_B)\left(\frac{a}{\rho}\right) \tag{3.39d}$$

We may derive Eq. 3.39d as the product of Ring A circumference ($2\pi a$), Ring A total current ($N_A I_A$), and the radial field (B_r) on Ring A, generated by Ring B axially ρ from Ring A, given approximately by $\mu_\circ N_B I_B/(2\pi\rho)$ for $\rho \ll a$—note that two rings $\rho \ll a$ apart may be modeled as two straight lines ρ apart. Thus:

$$\begin{aligned} F_{zA}(\rho) &\simeq (2\pi a)\times(N_A I_A)\times\left(\frac{\mu_\circ N_B I_B}{2\pi\rho}\right) \\ &= \mu_\circ (N_A I_A)(N_B I_B)\left(\frac{a}{\rho}\right) \end{aligned} \tag{3.39d}$$

TRIVIA 3.1 A legend has it that one of the mathematicians below advanced his argument for the existence of God by using an irrelevant algebraic equation: "Sir, $(a+b)^n/n = x$; hence God exists, answer please!" Who (and to whom)?

i) Euler; ii) Gauss; iii) Laplace; iv) Legendre.

3.5.2 Axial Force Within a "Thin-Walled" Solenoid

Consider a thin-walled ($\alpha=1$) solenoid of $2a$ diameter and $2b$ length with a uniform surface current density of $NI/2b$ with its midplane at $z=0$. For this solenoid the axial force at a location $z\geq 0$ from the midplane, $F_z(z)$, may be given by:

$$F_z(z) = -\frac{\mu_\circ}{2}\left(\frac{NI}{2b}\right)^2 \Big\{(b-z)\sqrt{4a^2+(b-z)^2}\left[K(k_{b_-})-E(k_{b_-})\right] + (b+z)\sqrt{4a^2+(b+z)^2}\left[K(k_{b_+})-E(k_{b_+})\right] - 2b\sqrt{4a^2+4b^2}\left[K(k_{2b})-E(k_{2b})\right]\Big\} \tag{3.40}$$

The elliptic integral moduli, k_{b_-}, k_{b_+}, and k_{2b}, are given by:

$$k_{b_-}^2 = \frac{4a^2}{4a^2+(b-z)^2}; \qquad k_{b_+}^2 = \frac{4a^2}{4a^2+(b+z)^2}; \qquad k_{2b}^2 = \frac{4a^2}{4a^2+4b^2}$$

Special Case 3: End Force

At $z=b$, because $k_{b_+}=k_{2b}$, we have, from Eq. 3.40, $F_z(b)=0$. That is, as expected, the axial force at each end of an isolated solenoid is zero.

Special Case 4: Midplane Force

By inserting $z=0$ into Eq. 3.40, we obtain an expression for the axial force at the midplane ($z=0$), $F_z(0)$.

$$F_z(0) = -\frac{\mu_\circ}{2}\left(\frac{NI}{2b}\right)^2 \Big\{2b\sqrt{4a^2+b^2}\left[K(k_b)-E(k_b)\right] - 2b\sqrt{4a^2+4b^2}\left[K(k_{2b})-E(k_{2b})\right]\Big\} \tag{3.41a}$$

where the modulus k_{2b} is the same as given above and k_b is given by:

$$k_b^2 = \frac{4a^2}{4a^2+b^2}$$

The axial *compressive* force at z in an isolated solenoid increases from 0 at $z=b$ to the maximum at the midplane, $F_z(0)$, given by Eq. 3.41a.

Special Case 5: Midplane Force for a "Long" Thin-Walled Solenoid

For a "long" ($\beta\gg 1$ or $k^2\ll 1$) thin-walled solenoid, Eq. 3.41a, with the approximation of Eq. 3.38c, reduces to a simple expression for $F_z(0)$.

$$F_z(0) \simeq -\frac{\mu_\circ}{2}\left(\frac{NI}{2b}\right)^2 \pi a^2 \tag{3.41b}$$

Equation 3.41b states that $F_z(0)$ is *independent* of coil length for a constant value of surface current density $NI/2b$. Because for a long solenoid, $NI/2b=H_z(0,0)$, the axial center field (see **PROBLEM 3.1**), we have:

$$F_z(0) \simeq -\tfrac{1}{2}\mu_\circ H_z^2(0,0)\times\pi a^2 \tag{3.41c}$$

$F_z(0)$ is thus equal to the magnetic pressure times the area of the coil bore. Indeed, it will be seen below that *every* expression of the axial force derived here begins with this magnetic pressure term, i.e., $\mu_\circ(NI/2b)^2$ or its equivalent form.

3.5.3 Axial Force Between a Thin-Walled Solenoid and Ring Coil

Figure 3.6 shows a thin-walled solenoid ($2a_s$, $2b_s$, $N_SI_S/2b_S$) coaxial with a ring coil ($2a_R$ and N_RI_R). The right-hand end of the solenoid is at distance ρ *left* of the ring coil. The axial field generated by each coil points in the same direction. The axial force on the solenoid, $F_{zS}(\rho)$, is given by:

$$F_{zS}(\rho) = -\frac{\mu_\circ}{2}(N_RI_R)\left(\frac{N_SI_S}{2b_S}\right)\times$$
$$\left(\sqrt{(a_R+a_S)^2+(\rho+2b_S)^2}\left\{2\big[K(k_S)-E(k_S)\big]-k_S^2K(k_S)\right\}\right.$$
$$\left.-\sqrt{(a_R+a_S)^2+\rho^2}\left\{2\big[K(k_R)-E(k_R)\big]-k_R^2K(k_R)\right\}\right) \qquad (3.42)$$

The moduli k_S and k_R are given by:

$$k_S^2 = \frac{4a_Sa_R}{(a_S+a_R)^2+(2b_S+\rho)^2}; \qquad k_R^2 = \frac{4a_Sa_R}{(a_S+a_R)^2+\rho^2}$$

In the right-hand side of Eq. 3.42 the second term is greater than the third term, so $F_{zS}(\rho)$ is positive; i.e., the axial interaction force is attractive.

Special Case 6: Thin-Walled Solenoid and Ring Coil Far Apart

When these two coils are far apart such that $k_S^2 \ll 1$ and $k_R^2 \ll 1$, we obtain:

$$F_{zS}(\rho) \simeq \frac{\mu_\circ}{2\pi}(\pi a_R^2N_RI_R)\left(\frac{\pi a_S^2N_SI_S}{2b_s}\right)\left[\frac{1}{\rho^3}-\frac{1}{(\rho+2b_S)^3}\right] \qquad (3.43a)$$

Again as with the two ring coils treated above, $F_{zS}(\rho)$, $+z$-directed (towards the ring), is proportional to the product of two "magnetic moments."

Special Case 7: Thin-Walled Solenoid and Ring Coil Farther Apart

When these two coils are so far apart that $\rho \gg 2b_s$, the second term within the brackets in Eq. 3.43*a* may be expanded, and we obtain:

$$F_{zS}(\rho) \simeq \frac{\mu_\circ}{2\pi}(\pi a_R^2N_RI_R)\left(\frac{\pi a_S^2N_SI_S}{2b_S}\right)\frac{6b_S}{\rho^4} \qquad (3.43b)$$

Note that, as expected, Eq. 3.43*b* is equivalent to Eq. 3.39*c*.

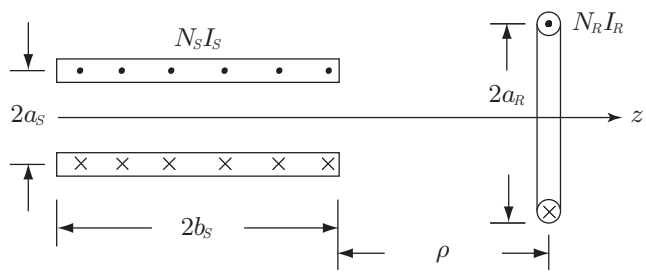

Fig. 3.6 "Thin-walled" solenoid and a ring coil coaxially aligned and separated by ρ.

3.5.4 Axial Force between Two Thin-Walled Solenoids

Here, we derive an equation for the axial force between two thin-walled solenoids; it is based on, but expanded considerably from, the original formulation by Garrett [3.5]. The equation becomes the basis for the axial forces between solenoids that are generally *not* thin-walled, presented next in **3.5.5**.

Consider two coaxial thin-walled solenoids, A ($2a_A$; $2b_A$; $N_AI_A/2b_A$) and B ($2a_B$; $2b_B$; $N_BI_B/2b_B$). As shown in Fig. 3.7, the right-hand end of Solenoid A is at distance ρ *left* of the left-hand end of Solenoid B. The axial field generated by each solenoid points in the same direction.

Axial Force on Solenoid A by Solenoid B

For Solenoid A, the axial force due to Solenoid B, $F_{z_{AB}}$, may be given by:

$$
\begin{aligned}
F_{z_{AB}}(\rho) = \frac{\mu_\circ}{2}\left(\frac{N_AI_A}{2b_A}\right)\left(\frac{N_BI_B}{2b_B}\right)\times \\
\left(\frac{2b_A+\rho}{\sqrt{a_T^2+(2b_A+\rho)^2}}\left\{\left[a_T^2+(2b_A+\rho)^2\right]\left[K(k_A)-E(k_A)\right]-\Upsilon(c^2,k_A)\right\}\right. \\
+\frac{2b_B+\rho}{\sqrt{a_T^2+(2b_B+\rho)^2}}\left\{\left[a_T^2+(2b_B+\rho)^2\right]\left[K(k_B)-E(k_B)\right]-\Upsilon(c^2,k_B)\right\} \\
-\frac{2b_T+\rho}{\sqrt{a_T^2+(2b_T+\rho)^2}}\left\{\left[a_T^2+(2b_T+\rho)^2\right]\left[K(k_T)-E(k_T)\right]-\Upsilon(c^2,k_T)\right\} \\
\left.-\frac{\rho}{\sqrt{a_T^2+\rho^2}}\left\{\left(a_T^2+\rho^2\right)\left[K(k_\rho)-E(k_\rho)\right]-\Upsilon(c^2,k_\rho)\right\}\right) \qquad (3.44)
\end{aligned}
$$

where $a_T = a_A + a_B$ and $b_T = b_A + b_B$. The moduli, k_A, k_B, k_T, and k_ρ, are given by:

$$
k_A^2 = \frac{4a_Aa_B}{a_T^2+(2b_A+\rho)^2}; \qquad k_B^2 = \frac{4a_Aa_B}{a_T^2+(2b_B+\rho)^2}
$$

$$
k_T^2 = \frac{4a_Aa_B}{a_T^2+(2b_T+\rho)^2}; \qquad k_\rho^2 = \frac{4a_Aa_B}{a_T^2+\rho^2}
$$

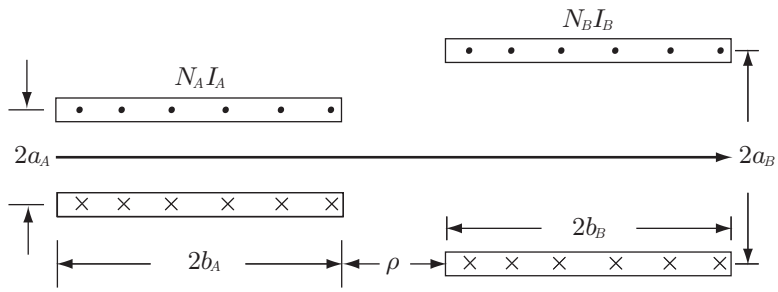

Fig. 3.7 Thin-walled Solenoids, A and B, with the two nearest ends separated by ρ.

In Eq. 3.44, $\Upsilon(c^2,k)$ is defined by:

$$\Upsilon(c^2,k) \equiv (a_A - a_B)^2[\Pi(c^2,k) - K(k)] \tag{3.45}$$

$\Pi(c^2,k)$ is the complete elliptic integral of the third kind, defined by:

$$\Pi(c^2,k) = \int_0^{\pi/2} \frac{d\theta}{(1-c^2\sin^2\theta)\sqrt{1-k^2\sin^2\theta}} \tag{3.46}$$

As evident from Eq. 3.46, $\Pi(c^2,k)$ has two moduli, $c^2 \le 1$ and $k \le 1$. The modulus c^2 in the cases considered here is given by:

$$c^2 = \frac{4a_Aa_B}{a_T^2} = \frac{4a_Aa_B}{(a_A+a_B)^2} \tag{3.47}$$

$\Pi(0,k) = K(k)$ and $\Pi(1,k) = \infty$. $\Pi(c^2,k)$ may be expressed in a power series in c^2 and k^2:

$$\Pi(c^2,k) = \frac{\pi}{2}\sum_{m=0}^{\infty}\sum_{j=0}^{m} \frac{(2m)!\,(2j)!\,k^{2j}\,c^{2(m-j)}}{4^m\,4^j\,(m!)^2\,(j!)^2} \tag{3.48}$$

Low-order terms are:

$$\Pi(c^2,k) = \frac{\pi}{2}\Big(1+\tfrac{1}{2}c^2+\tfrac{1}{4}k^2+\tfrac{3}{8}c^4+\tfrac{3}{16}c^2k^2+\tfrac{9}{64}k^4+ \\ +\tfrac{5}{16}c^6+\tfrac{5}{32}c^4k^2+\tfrac{15}{128}c^2k^4+\tfrac{25}{256}k^6+\cdots\Big) \tag{3.49a}$$

$$\Pi(c^2,0) = \frac{\pi}{2}\Big(1+\tfrac{1}{2}c^2+\tfrac{3}{2^3}c^4+\tfrac{5}{2^4}c^6+\tfrac{5\cdot7}{2^7}c^8+\tfrac{7\cdot9}{2^8}c^{10}+\tfrac{3\cdot7\cdot11}{2^{10}}c^{12} \\ +\tfrac{3\cdot11\cdot13}{2^{11}}c^{14}+\tfrac{5\cdot9\cdot11\cdot13}{2^{15}}c^{16}+\tfrac{5\cdot11\cdot13\cdot17}{2^{16}}c^{18}+\tfrac{11\cdot13\cdot17\cdot19}{2^{18}}c^{20}+\cdots\Big) \tag{3.49b}$$

Note that when $c^2 = 0$, Eq. 3.49*a* becomes identical to Eq. 3.38*a*, because as noted above, $\Pi(0,k) = K(k)$. However, for most problems of interest c^2 is generally close to 1, in which case neither expansion of Eq. 3.49 is very useful, since rapid convergence requires $c^2 \ll 1$. Later, in discussing mutual inductance, we shall use Eq. 3.49*b*. Table 3.2 gives $\Pi(c^2,k)$ for selected values of c^2 and k^2. Mathcad and a number of other software programs can evaluate $K(k)$, $E(k)$, and $\Pi(c^2,k)$.

Special Case 8: Total Midplane Force on Solenoid A

Let us first consider the case in which Solenoids A and B each have the same length ($2b$) and surface current density ($NI/2b$) but different diameters. By making the following substitutions to Eq. 3.44, $2b_A = 2b_B = 2b$, $N_AI_A/2b_A = N_BI_B/2b_B = NI/2b$, and $\rho = 0$ (no gap between the two nearest ends of Solenoids A and B), we obtain an expression for the total midplane force on Solenoid A, $F_{z_A}(0)$, which becomes useful when we consider a solenoid that is *not* "thin-walled."

$$F_{z_A}(0) = \frac{\mu_\circ}{2}\left(\frac{NI}{2b}\right)^2 \times \left(\frac{4b}{\sqrt{a_T^2+4b^2}}\Big\{[a_T^2+4b^2]\big[K(k_{2b})-E(k_{2b})\big]-\Upsilon(c^2,k_{2b})\Big\}\right. \\ \left. -\frac{4b}{\sqrt{a_T^2+16b^2}}\Big\{[a_T^2+16b^2]\big[K(k_{4b})-E(k_{4b})\big]-\Upsilon(c^2,k_{4b})\Big\}\right) \tag{3.50}$$

Table 3.2: Complete Elliptic Integral of the Third Kind $\Pi(c^2,k)$
For Selected Values of c^2 and k $[\,\Pi(0,0)=\pi/2;\ \Pi(1,k)=\infty;\ \Pi(c^2,1)=\infty\,]$

c^2	$k=0$	0.1	0.2	0.3	0.4	0.5	0.6	0.7	0.8	0.9	0.999
0.1	1.6558	1.6600	1.6732	1.6961	1.7307	1.7803	1.8509	1.9541	2.1173	2.4295	4.8804
0.2	1.7562	1.7609	1.7752	1.8002	1.8380	1.8923	1.9696	2.0829	2.2625	2.6077	5.3514
0.4	2.0279	2.0336	2.0513	2.0822	2.1290	2.1963	2.2925	2.4343	2.6604	3.1001	6.7100
0.6	2.4836	2.4913	2.5148	2.5561	2.6187	2.7090	2.8389	3.0315	3.3418	3.9550	9.2511
0.8	3.5124	3.5246	3.5622	3.6283	3.7290	3.8751	4.0867	4.4042	4.9246	5.9821	16.070
0.9	4.9673	4.9863	5.0448	5.1480	5.3056	5.5355	5.8710	6.3796	7.2263	8.9943	27.895
0.92	5.5536	5.5754	5.6426	5.7610	5.9421	6.2069	6.5939	7.1824	8.1667	10.239	33.280
0.94	6.4127	6.4387	6.5186	6.6597	6.8758	7.1921	7.6557	8.3633	9.5535	12.086	41.737
0.95	7.0248	7.0537	7.1429	7.3002	7.5414	7.8948	8.4135	9.2071	10.547	13.414	48.138
0.96	7.8540	7.8869	7.9886	8.1681	8.4435	8.8475	9.4417	10.353	11.897	15.227	57.268
0.97	9.0690	9.1079	9.2280	9.4403	9.7662	10.245	10.951	12.036	13.884	17.905	71.507
0.98	11.107	11.156	11.308	11.575	11.986	12.592	13.486	14.867	17.233	22.440	97.397
0.99	15.708	15.780	16.002	16.395	17.001	17.894	19.219	21.277	24.832	32.789	163.12
0.991	16.558	16.634	16.869	17.286	17.927	18.874	20.279	22.462	26.239	34.711	176.15
0.992	17.562	17.643	17.894	18.338	19.022	20.033	21.532	23.864	27.903	36.986	191.85
0.993	18.775	18.862	19.131	19.609	20.345	21.431	23.045	25.557	29.914	39.735	211.22
0.994	20.279	20.374	20.667	21.185	21.985	23.167	24.923	27.658	32.409	43.151	235.80
0.995	22.214	22.319	22.642	23.214	24.096	25.400	27.339	30.362	35.623	47.552	268.26
0.996	24.836	24.954	25.318	25.962	26.956	28.426	30.613	34.027	39.978	53.523	313.54
0.997	28.679	28.816	29.239	29.989	31.147	32.860	35.412	39.400	46.365	62.286	382.16
0.998	35.124	35.294	35.817	36.745	38.178	40.300	43.464	48.416	57.088	77.009	502.08
0.999	49.673	49.916	50.666	51.996	54.050	57.096	61.643	68.776	81.309	110.30	787.66

where $a_T=a_A+a_B$ and the moduli k_{2b} and k_{4b} are given by:

$$k_{2b}^2=\frac{4a_Aa_B}{a_T^2+4b^2};\qquad\qquad k_{4b}^2=\frac{4a_Aa_B}{a_T^2+16b^2}$$

Because $c^2\simeq 1$, though always $c^2<1$, for most problems of our interest, Eq. 3.50 cannot be approximated even for "long" coils ($\beta\gg 1$).

Derivation of Eq. 3.50 from Eq. 3.44

If we make Solenoids A and B identical in diameter and surface current density but each one half the length of the original, for $\rho=0$ the two solenoids are transformed into one solenoid of length $2b$. Next, if the following substitutions, i.e., $2a_A=2a_B=2a$, $N_AI_A/2b_A=N_BI_B/2b_B=NI/2b$, and $2b_A=2b_B=b$, are made in Eq. 3.44, the modified equation is reduced to Eq. 3.50.

Answer to TRIVIA 3.1 i). The Swiss mathematician Leonhard Euler (1707–1783) to the French encyclopedist Denis Diderot (1713–1784). This anecdote is disputed by Dirk Struik, who states in *A Concise History of Mathematics* (Dover Publications, 1948) that "... no reason exists to think that the thoughtful Euler would have behaved in the asinine way." The great Pierre Simon de Laplace (1749–1827), once asked by Napoleon why his monumental five-volume *Celestial Mechanics* had no mention of God, replied, "I had no need of that hypothesis."

3.5.5 "Thick-Walled" Solenoid—Midplane Axial Force

When a solenoid cannot be treated as "thin-walled," it may be divided radially into many "thin-walled" subsolenoids. Here, we consider the simplest case for treating a solenoid of $\alpha > 1$: the solenoid divided into two "thin-walled" Subsolenoids A (inner) and B (outer), each of the same radial build and length $2b$. Subsolenoids A and B have diameters respectively of $2a_A$ and $2a_B > 2a_A$ and a current per unit length of $\frac{1}{2}(NI/2b)$. $F_{zA}(0)$, the total axial force on one half of Subsolenoid A comprises two components, one due to its other half, $F_{zAA}(0)$ given by Eq. 3.41a, and the other due to Subsolenoid B, $F_{zAB}(0)$. Figure 3.8 shows the arrangement of two subsolenoids appropriate for derivation of an expression for the midplane axial force on Subsolenoid A.

Comparing Figs. 3.7 and 3.8, we note that Eq. 3.44 is applicable if we make the following substitutions for the main parameters: $2b_A = b$; $2b_B = 2b$; and $\rho = -2b$. With these parameters and c^2 given by Eq. 3.47, Eq. 3.44 becomes:

$$F_{zAB}(0) = -\frac{\mu_\circ}{2}\left(\frac{NI}{4b}\right)^2 \times \left(\frac{2b}{\sqrt{a_T^2+b^2}}\left\{[a_T^2+b^2]\big[K(k_b)-E(k_b)\big]-\Upsilon(c^2,k_b)\right\} - \frac{2b}{\sqrt{a_T^2+4b^2}}\left\{[a_T^2+4b^2]\big[K(k_{2b})-E(k_{2b})\big]-\Upsilon(c^2,k_{2b})\right\}\right) \tag{3.51}$$

where $a_T = a_A + a_B$. The moduli, k_b and k_{2b}, are given by:

$$k_b^2 = \frac{4a_Aa_B}{a_T^2+b^2}; \qquad k_{2b}^2 = \frac{4a_Aa_B}{a_T^2+4b^2}$$

$F_{zAA}(0)$, the midplane axial force by Subsolenoid A on itself, is given by Eq. 3.41a with $(NI/4b)$ in place of $(NI/2b)$. Similarly, $F_{zB}(0)$ is the total midplane axial force on Subsolenoid B comprised of $F_{zBB}(0)$ and $F_{zBA}(0)$:

$$F_{zA}(0) = F_{zAA}(0)+F_{zAB}(0) \tag{3.52a}$$

$$F_{zB}(0) = F_{zBB}(0)+F_{zBA}(0) \tag{3.52b}$$

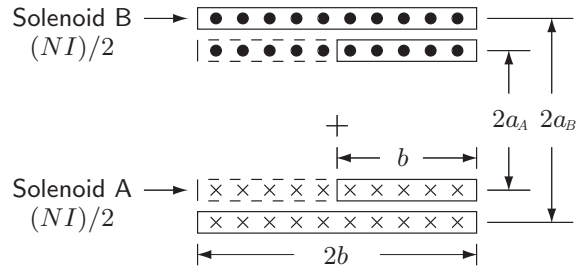

Fig. 3.8 Arrangement of Subsolenoids A and B for computation of the midplane axial force on Subsolenoid A.

Thus:

$$F_{z_A}(0) = -\frac{\mu_\circ}{2}\left(\frac{NI}{4b}\right)^2 \times \left(\left\{2b\sqrt{4a_A^2+b^2}\left[K(k_{b_A})-E(k_{b_A})\right]-2b\sqrt{4a_A^2+4b^2}\left[K(k_{2b_A})-E(k_{2b_A})\right]\right\} + \frac{2b}{\sqrt{a_T^2+b^2}}\left\{\left[a_T^2+b^2\right]\left[K(k_b)-E(k_b)\right]-\Upsilon(c^2,k_b)\right\} - \frac{2b}{\sqrt{a_T^2+4b^2}}\left\{\left[a_T^2+4b^2\right]\left[K(k_{2b})-E(k_{2b})\right]-\Upsilon(c^2,k_{2b})\right\}\right) \qquad (3.53a)$$

Again c^2 is given by Eq. 3.47. The moduli k_{b_A}, k_{2b_A}, k_{b_B}, and k_{2b_B} are given by:

$$k_{b_A}^2 = \frac{4a_A^2}{4a_A^2+b^2}; \quad k_{2b_A}^2 = \frac{4a_A^2}{4a_A^2+4b^2}; \quad k_{b_B}^2 = \frac{4a_B^2}{4a_B^2+b^2}; \quad k_{2b_B}^2 = \frac{4a_B^2}{4a_B^2+4b^2}$$

In this case, because $2b_A = 2b_B = 2b$ and $N_A I_A = N_B I_B$, $F_{z_{AB}}(0) = F_{z_{BA}}(0)$. Thus:

$$F_{z_B}(0) = -\frac{\mu_\circ}{2}\left(\frac{NI}{4b}\right)^2 \times \left(\left\{2b\sqrt{4a_B^2+b^2}\left[K(k_{b_B})-E(k_{b_B})\right]-2b\sqrt{4a_B^2+4b^2}\left[K(k_{2b_B})-E(k_{2b_B})\right]\right\} + \frac{2b}{\sqrt{a_T^2+b^2}}\left\{\left(a_T^2+b^2\right)\left[K(k_b)-E(k_b)\right]-\Upsilon(c^2,k_b)\right\} - \frac{2b}{\sqrt{a_T^2+4b^2}}\left\{\left(a_T^2+4b^2\right)\left[K(k_{2b})-E(k_{2b})\right]-\Upsilon(c^2,k_{2b})\right\}\right) \qquad (3.53b)$$

The total midplane axial force of a solenoid $F_{z_T}(0)$, divided into two thin-walled subsolenoids, is the sum of $F_{z_A}(0)$ and $F_{z_B}(0)$. We thus obtain:

$$F_{z_T}(0) = -\frac{\mu_\circ}{2}\left(\frac{NI}{4b}\right)^2 \times \left(2b\sqrt{4a_A^2+b^2}\left[K(k_{b_A})-E(k_{b_A})\right]-2b\sqrt{4a_A^2+4b^2}\left[K(k_{2b_A})-E(k_{2b_A})\right] + 2b\sqrt{4a_B^2+b^2}\left[K(k_{b_B})-E(k_{b_B})\right]-2b\sqrt{4a_B^2+4b^2}\left[K(k_{2b_B})-E(k_{2b_B})\right] + \frac{4b}{\sqrt{a_T^2+b^2}}\left\{\left(a_T^2+b^2\right)\left[K(k_b)-E(k_b)\right]-\Upsilon(c^2,k_b)\right\} - \frac{4b}{\sqrt{a_T^2+4b^2}}\left\{\left(a_T^2+4b^2\right)\left[K(k_{2b})-E(k_{2b})\right]-\Upsilon(c^2,k_{2b})\right\}\right) \qquad (3.54)$$

Note that when a solenoid is divided into two thin-walled subsolenoids, $F_{zT}(0)$ requires computation of four terms in Eq. 3.54. When a solenoid is divided into $m > 2$ thin-walled subsolenoids, it will require computation of $2(m!)/[(m-2)!]$ terms to obtain $F_{zT}(0)$. For $m=3$ an expression of $F_{zT}(0)$ thus will contain *twelve* terms and *18 moduli*, clearly too tedious for hand computation.

To create a computer code that will accurately compute the midplane axial force of a "practical" solenoidal coil, i.e., a thick-walled solenoid, one has to extend Eq. 3.54 to a set of expressions applicable to m thin-walled subsolenoids. To ensure that each subsolenoid is thin-walled, m may have to be 10 or even greater.

Note that because in most cases c^2 is close to 1, it is not possible to approximate the $\Pi(c^2,k)$ term contained in each $\Upsilon(c^2,k)$ even for "long" ($\beta \gg 1$) solenoids.

Special Case 9: Midplane Force for a "Long" Thick-Walled Solenoid

Because in most of our applications $c^2 \simeq 1$, each $\Pi(c^2,k)$ in the $\Upsilon(c^2,k)$ terms in Eq. 3.54 cannot be approximated by the first few terms of the series expansion in k^2 and c^2. The remaining terms in Eq. 3.54, however, can be expanded for $\beta \gg 1$, as was done above in *Special Case 5* (Eq. 3.41*b*). Thus:

$$F_{zT}(0) \simeq -\mu_\circ \left(\frac{NI}{4b}\right)^2 \left\{ \pi(a_A^2+a_B^2) - (a_A-a_B)^2 \left[2\Pi(c^2,k_b) - \Pi(c^2,k_{2b})\right] \right\}$$

$$\simeq -\mu_\circ \left(\frac{NI}{4b}\right)^2 \pi(a_A^2+a_B^2) \left\{ 1 - \frac{(a_A-a_B)^2}{\pi(a_A^2+a_B^2)} \left[2\Pi(c^2,k_b) - \Pi(c^2,k_{2b})\right] \right\} \quad (3.55)$$

Note that when $a_A = a_B$, Eq. 3.55 reduces to Eq. 3.41*b*. In the second form of Eq. 3.55, the last term within the braces may be considered a correction term.

Kapitza's Magnets (Part 1 of 3 Parts)

—Passage from Francis Bitter's *Magnets: The Education of a Physicist* [3.4]

One project that appealed to me was to make a stronger magnetic field than could be made with iron core magnets. The alternative was not to use iron at all, but to concentrate on the effective use of copper for carrying a current. A current passing through a coil of wire will produce a magnetic field at its center. The larger the current, the stronger the magnetic field. There is no saturation effect here. So far as we know, this increase of field with increasing current continues indefinitely. If you double the current, you double the magnetic field in the middle of the coil. The problem was to discover how far it was practically possible to go. I remember discussing these matters at some length in Cambridge with Peter Kapitza, a brilliant Russian scientist who came to England, became an important part of the scientific community there, had a laboratory built for him, did some pioneering work in developing new ways of producing strong magnetic fields, and then returned to Russia.

3.5.6 Axial Forces in a Nested Two-Coil Magnet

In a magnet comprised of several nested solenoids, all coaxially aligned, it is sometimes important to compute in each solenoid the midplane axial compressive force, which in a large nested-coil magnet such as an MRI magnet can become substantial. Here we consider the simplest nested-coil magnet comprised of two thin-walled solenoids, A and B, shown in Fig. 3.9. Solenoid A (inner) has parameters of $2a_A$, $2b_A$, and $N_AI_A/2b_A$; Solenoid B (outer) similarly has $2a_B$, $2b_B$, and $N_BI_B/2b_B$.

Midplane Axial Force on Solenoid A

The total midplane axial force on the right-hand half of Solenoid A, $F_{z_A}(0)$, is the sum of $F_{z_{AA}}(0)$ and $F_{z_{AB}}(0)$, where $F_{z_{AA}}(0)$ is the midplane axial force due to its own left-hand half, while $F_{z_{AB}}(0)$ is that due to Solenoid B. $F_{z_{AA}}(0)$ is given by Eq. 3.41a with the subscript A inserted appropriately. $F_{z_{AB}}(0)$ is given by Eq. 3.44, with the following substitutions: b_A for $2b_A$ and $-(b_A+b_B)$ for ρ; $2b_B$ in Eq. 3.44 remains the same, and c^2 is still given by Eq. 3.47.

$$
\begin{aligned}
F_{z_A}(0) = -\frac{\mu_\circ}{2}\Bigg[&\left(\frac{N_AI_A}{2b_A}\right)^2 \times \\
&\left\{2b_A\sqrt{4a_A^2+b_A^2}\left[K(k_{b_A})-E(k_{b_A})\right] - 2b_A\sqrt{4a_A^2+4b_A^2}\left[K(k_{2b_A})-E(k_{2b_A})\right]\right\} \\
&+\left(\frac{N_AI_A}{2b_A}\right)\left(\frac{N_BI_B}{2b_B}\right)\Bigg(\frac{2b_B}{\sqrt{a_T^2+b_B^2}}\left\{[a_T^2+b_B^2]\left[K(k_B)-E(k_B)\right]-\Upsilon(c^2,k_B)\right\} \\
&\qquad -\frac{b_D}{\sqrt{a_T^2+b_D^2}}\left\{[a_T^2+b_D^2]\left[K(k_D)-E(k_D)\right]-\Upsilon(c^2,k_D)\right\} \\
&\qquad -\frac{b_T}{\sqrt{a_T^2+b_T^2}}\left\{[a_T^2+b_T^2]\left[K(k_T)-E(k_T)\right]-\Upsilon(c^2,k_T)\right\}\Bigg)\Bigg]
\end{aligned}
\tag{3.56}
$$

Note that $a_T = a_A + a_B$, $b_D = b_B - b_A$, and $b_T = b_A + b_B$. k_{b_A}, k_{2b_A}, k_A, k_B, and k_{AB} are:

$$
k_{b_A}^2 = \frac{4a_A^2}{4a_A^2+b_A^2};\quad k_{2b_A}^2 = \frac{4a_A^2}{4a_A^2+4b_A^2};\quad k_B^2 = \frac{4a_Aa_B}{a_T^2+b_B^2};\quad k_D^2 = \frac{4a_Aa_B}{a_T^2+b_D^2};\quad k_T^2 = \frac{4a_Aa_B}{a_T^2+b_T^2}
$$

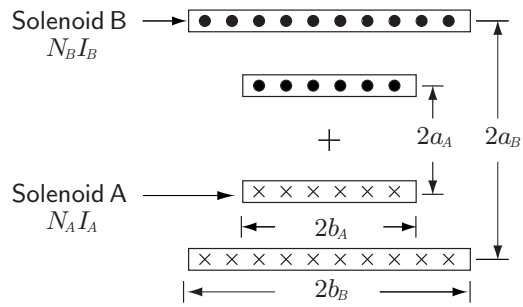

Fig. 3.9 Nested two-coil magnet comprised of Solenoids A and B.

Special Case 10: Midplane Force on Solenoid A—"Long" Solenoids

When both solenoids are "long," i.e., $b_A^2 \gg 4a_A^2$ and $b_B^2 \gg a_T^2$, and of differing lengths so that $b_D^2 \gg a_T^2$, Eq. 3.56 may be simplified to:

$$F_{zA}(0) \simeq -\frac{\mu_\circ}{2}\left\{\left(\frac{N_A I_A}{2b_A}\right)^2 \pi a_A^2 + \left(\frac{N_A I_A}{2b_A}\right)\left(\frac{N_B I_B}{2b_B}\right)\times \right.$$
$$\left. (a_A - a_B)^2\left[\Pi(c^2,k_D)+\Pi(c^2,k_T)-2\Pi(c^2,k_B)\right]\right\} \qquad (3.57a)$$

The second term in the right-hand side of Eq. 3.57*a* represents F_{zAB}. Physically this is due to Solenoid B's B_r on Solenoid A at the axial location near each end of Solenoid B. Note that as $b_A \to \infty$ and $b_B \to \infty$, the second term becomes zero.

Special Case 11: Midplane Axial Force on Solenoid A—
Both Solenoids "Long" & Solenoid B Much Longer than Solenoid A

When both Solenoids are "long" as in *Special Case 10 and* Solenoid B is much longer than Solenoid A, i.e., $b_D \to b_B$ and $b_T \to b_B$, Eq. 3.57*a* is further simplified to:

$$F_{zA}(0) \simeq F_{zAA}(0) \simeq -\frac{\mu_\circ}{2}\left(\frac{N_A I_A}{2b_A}\right)^2 \pi a_A^2 \qquad (3.57b)$$

That $F_{zAB}(0) \to 0$ as $b_A/b_B \to 0$ physically makes sense, because as Solenoid B becomes much longer than Solenoid A, Solenoid B's B_r, a key ingredient of $F_{zAB}(0)$, given by the second term in the right-hand side of Eq. 3.57*a*, becomes zero within its bore where Solenoid A is located.

Midplane Axial Force on Solenoid B

Expressions for the midplane axial forces on Solenoid B are very similar to those derived on Solenoid A. We may therefore derive these expressions from the previous section by making appropriate substitutions. The total midplane axial force in Solenoid B, $F_{zB}(0)$, is the sum of $F_{zBB}(0)$ and $F_{zBA}(0)$, where $F_{zBB}(0)$ is the midplane axial force due to its own left-hand half, while $F_{zBA}(0)$ is that due to Solenoid A.

$$F_{zB}(0) = -\frac{\mu_\circ}{2}\left[\left(\frac{N_B I_B}{2b_B}\right)^2 \times \right.$$
$$\left\{2b_B\sqrt{4a_B^2+b_B^2}\left[K(k_{b_B})-E(k_{b_B})\right]-2b_B\sqrt{4a_B^2+4b_B^2}\left[K(k_{2b_B})-E(k_{2b_B})\right]\right\}$$
$$+\left(\frac{N_B I_B}{2b_B}\right)\left(\frac{N_A I_A}{2b_A}\right)\left(\frac{2b_A}{\sqrt{a_T^2+b_A^2}}\left\{[a_T^2+b_A^2]\left[K(k_A)-E(k_A)\right]-\Upsilon(c^2,k_A)\right\}\right.$$
$$+\frac{b_D}{\sqrt{a_T^2+b_D^2}}\left\{[a_T^2+b_D^2]\left[K(k_D)-E(k_D)\right]-\Upsilon(c^2,k_D)\right\}$$
$$\left.\left.-\frac{b_T}{\sqrt{a_T^2+b_T^2}}\left\{[a_T^2+b_T^2]\left[K(k_T)-E(k_T)\right]-\Upsilon(c^2,k_T)\right\}\right)\right] \qquad (3.58)$$

Here too c^2 is given by Eq. 3.47. The moduli k_{2b_B} and k_A are given by:

$$k^2_{2b_B} = \frac{a_B^2}{4a_B^2 + 4b_B^2}; \qquad k_A^2 = \frac{4a_A a_B}{a_T^2 + b_A^2}$$

The other moduli are the same as those given above for Eq. 3.56.

Special Case 12: Midplane Axial Force on Solenoid B— Both Solenoids "Long" & Solenoid B Much Longer than Solenoid A

When both inner and outer coils are "long" and Solenoid B is much longer than Solenoid A, as in *Special Case 11*, we obtain:

$$F_{z_B}(0) \simeq -\frac{\mu_\circ}{2}\left\{\left(\frac{N_B I_B}{2b_B}\right)^2 \pi a_B^2 + \left(\frac{N_B I_B}{2b_B}\right)\left(\frac{N_A I_A}{2b_A}\right)\left[\pi(a_A^2 + a_B^2) - (a_A - a_B)^2\left[2\Pi(c^2, k_A) + \Pi(c^2, k_D) - \Pi(c^2, k_T)\right]\right]\right\} \qquad (3.59a)$$

As in *Special Case 11*, the second term in Eq. 3.59*a* represents $F_{z_{BA}}$, which is nonnegligible because Solenoid A's B_r impinges on Solenoid B at the axial location near each end of Solenoid A.

Special Case 13: Midplane Axial Force on Solenoid B— Both Solenoids "Long" & Solenoid B Much Shorter than Solenoid A

When both Solenoids are "long" ($b_B^2 \gg a_T^2$ and $b_A^2 \gg a_T^2$) but Solenoid B is much shorter than Solenoid A ($b_D^2 \to b_A^2 \gg a_T^2$), Eq. 3.58 is simplified to:

$$F_{z_B}(0) \simeq -\frac{\mu_\circ}{2}\left(\frac{N_B I_B}{2b_B}\right)^2 \pi a_B^2 \qquad (3.59b)$$

Equation 3.59*b* is analogous to Eq. 3.57*b* of *Special Case 11*; the same physical interpretation used there applies here too.

Kapitza's Magnets (Part 2 of 3 Parts)

—Passage from Francis Bitter's *Magnets: The Education of a Physicist*

The first and main difficulty to overcome in attempting to produce strong magnetic fields by passing very large currents through a coil is that strong enough currents tend to heat the coil, melt it, squeeze it out of shape, and destroy it. Kapitza's solution was to pass currents through a coil for only such a short time that there would not be sufficient energy liberated to heat it to a dangerous extent. Kapitza, however, was not only a scientist but also an engineer. He succeeded in designing novel equipment for producing pulsed magnetic fields of this kind, and also devices for measuring the properties of matter during the small fractions of a second when the fields were reasonably constant and steady.

Kapitza made great progress in developing this trick to overcome the objectionable heating of the coil, but in the end he ran into another limitation, the strength of the coil. You all know that passing a current through a magnetic field results in the application of a force on the conductor of a coil producing its own magnetic field. The parts are squeezed (axially) *and pushed* (radially) *until finally the coil gives way. It was necessary to build a very strong coil, as well as equipment to produce and switch enormous currents on and off in a very short time.*

3.5.7 Axial Restoring Force on Axially Off-Centered Solenoids

When the axial field of each solenoid points in the same direction and when the axial centers of Solenoids A and B mismatch by a distance of ρ, an axial restoring force, $F_{zR}(\rho)$, is generated to align the axial centers. $F_{zR}(\rho)$ may be given by:

$$\begin{aligned} F_{zR}(\rho) = &- \frac{\mu_\circ}{2}\left(\frac{N_A I_A}{2b_A}\right)\left(\frac{N_B I_B}{2b_B}\right)\times \\ &\left(\frac{b_T-\rho}{\sqrt{a_T^2+(b_T-\rho)^2}}\left\{[a_T^2+(b_T-\rho)^2]\big[K(k_{T-})-E(k_{T-})\big]-\Upsilon(c^2,k_{T-})\right\}\right. \\ &+\frac{b_D+\rho}{\sqrt{a_T^2+(b_D+\rho)^2}}\left\{[a_T^2+(b_D+\rho)^2]\big[K(k_{D+})-E(k_{D+})\big]-\Upsilon(c^2,k_{D+})\right\} \\ &-\frac{b_T+\rho}{\sqrt{a_T^2+(b_T+\rho)^2}}\left\{[a_T^2+(b_T+\rho)^2]\big[K(k_{T+})-E(k_{T+})\big]-\Upsilon(c^2,k_{T+})\right\} \\ &\left.-\frac{b_D-\rho}{\sqrt{a_T^2+(b_D-\rho)^2}}\left\{[a_T^2+(b_D-\rho)^2]\big[K(k_{D-})-E(k_{D-})\big]-\Upsilon(c^2,k_{D-})\right\}\right) \end{aligned} \tag{3.60}$$

where $a_T = a_A + a_B$, $b_T = b_A + b_B$, and $b_D = b_A - b_B$; k_{T+}, k_{T-}, k_{D+}, and k_{D-} are given by:

$$k_{T+}^2 = \frac{4a_A a_B}{a_T^2+(b_T+\rho)^2}; \qquad k_{T-}^2 = \frac{4a_A a_B}{a_T^2+(b_T-\rho)^2}$$

$$k_{D+}^2 = \frac{4a_A a_B}{a_T^2+(b_D+\rho)^2}; \qquad k_{D-}^2 = \frac{4a_A a_B}{a_T^2+(b_D-\rho)^2}$$

Special Case 14: No Axial Misalignment

When $\rho = 0$, $k_{T+}^2 = k_{T-}^2$ and $k_{D+}^2 = k_{D-}^2$, and thus $F_{zR}(\rho) = 0$, as expected physically.

Special Case 15: "Small" Axial Misalignment

For a small misalignment, defined as $\rho \ll \sqrt{a_T^2+b_D^2}$, $F_{zR}(\rho)$ is proportional to ρ:

$$F_{zR}(\rho) \propto -\left(\frac{N_A I_A}{2b_A}\right)\left(\frac{N_B I_B}{2b_B}\right)\rho \tag{3.61}$$

Equation 3.61 is later used to derive an expression of $M_{AB}(\rho)$, the mutual inductance between Solenoids A and B misaligned by a small distance ($\rho \ll \sqrt{a_T^2+b_D^2}$).

Special Case 16: Either Solenoid "Long"

If either Solenoid A or Solenoid B is "long," the longer solenoid's axial field becomes uniform, its B_r becomes small and the solenoid generates little axial force on the shorter solenoid even if the solenoid centers are misaligned considerably. This can be seen because the first two +terms and the last two −terms in Eq. 3.60 cancel out when $b_T^2 \gg a_T^2$ and $b_D^2 \gg a_T^2$, resulting in $F_{zR}(\rho) \to 0$.

3.6 Stresses and Strains in Solenoid under Magnetic Force

We study here stresses and strains on a superconductor, induced principally by Lorentz forces, in a solenoidal magnet [3.6]. The analytic expressions derived and graphs presented here of magnetic stresses are for "simple" properties of the winding materials under a "simple" field distribution.

3.6.1 Stress and Strain Equations

The stresses, radial, $\sigma_r(r,z)$; hoop, $\sigma_\theta(r,z)$; axial, $\sigma_z(r,z)$; and shear, $\tau_{rz}(r,z)$ in the winding of a solenoid subjected to a magnetic force density generated by the interaction of λJ and the axial magnetic field (induction), $B_z(r,z)$, are found from the solution of the equilibrium equations:

$$\frac{\partial \sigma_r}{\partial r} + \frac{\sigma_r - \sigma_\theta}{r} + \frac{\partial \tau_{rz}}{\partial z} = -\lambda J B_z(r,z) \tag{3.62a}$$

$$\frac{\partial \tau_{rz}}{\partial r} - \frac{\tau_{rz}}{r} + \frac{\partial \sigma_z}{\partial z} = -\lambda J B_r(r,z) \tag{3.62b}$$

with boundary conditions: $\sigma_r(r=a_1,z)=0$; $\sigma_r(r=a_2,z)=0$; $\sigma_z(r,z=\pm b)=0$; $\tau_{rz}(r=a_1,z)=0$; $\tau_{rz}(r=a_2,z)=0$; and $\tau_{rz}(r,z=\pm b)=0$. Note that the shear stress τ_{rz} is the only variable that couples Eqs. 3.62*a* and 3.62*b*. Most composite superconductors, LTS and HTS, may be considered orthotropic: Hooke's law is applicable. An orthotropic material has mechanical properties, e.g., Young's modulus, Poisson's ratio, that are different in, but symmetric about, three orthogonal directions. The strains, ϵ_r, ϵ_θ, ϵ_z, respectively, in the r, θ, and z directions, and the shear strain, γ_{rz}, in the r-z plane, are related to the stresses by:

$$\epsilon_r = \frac{1}{E_r}\sigma_r - \frac{\nu_{\theta r}}{E_\theta}\sigma_\theta - \frac{\nu_{zr}}{E_z}\sigma_z + \epsilon_{T_r} \tag{3.63a}$$

$$\epsilon_\theta = -\frac{\nu_{r\theta}}{E_r}\sigma_r + \frac{1}{E_\theta}\sigma_\theta - \frac{\nu_{z\theta}}{E_z}\sigma_z + \epsilon_{T_\theta} \tag{3.63b}$$

$$\epsilon_z = -\frac{\nu_{rz}}{E_r}\sigma_r - \frac{\nu_{\theta z}}{E_\theta}\sigma_\theta + \frac{1}{E_z}\sigma_z + \epsilon_{T_z} \tag{3.63c}$$

$$\gamma_{rz} = \frac{1}{G_{rz}}\tau_{rz} \tag{3.63d}$$

E_r, E_θ, and E_z are Young's moduli, respectively, in the r, θ, and z directions. $\nu_{12} \equiv -\epsilon_2/\epsilon_1$ is the Poisson's ratio for transverse strains in two orthogonal directions when the material is stressed in the 1-direction (σ_1; $\sigma_2 = \sigma_3 = 0$). G_{rz} is the shear modulus. ϵ_{T_r}, ϵ_{T_θ}, and ϵ_{T_z} are integrated coefficients of thermal expansion between room temperature (300 K) and operating temperature (T_{op}).

$$\epsilon_{T_r} = \int_{300\,\mathrm{K}}^{T_{op}} \alpha_{T_r}(T)\,dT; \quad \epsilon_{T_\theta} = \int_{300\,\mathrm{K}}^{T_{op}} \alpha_{T_\theta}(T)\,dT; \quad \epsilon_{T_z} = \int_{300\,\mathrm{K}}^{T_{op}} \alpha_{T_z}(T)\,dT \tag{3.63e}$$

$\alpha_{T_r}(T)$, $\alpha_{T_\theta}(T)$, and $\alpha_{T_z}(T)$ are temperature-dependent coefficients of thermal expansion parallel to the major axes. Note that because these coefficients are positive and because the integration is from 300 K to $T_{op} < 300$ K, the thermal strains in Eqs. 3.63*a*–3.63*c* are negative, i.e., compressive.

The following conditions among ν's and E's also apply:

$$\frac{\nu_{r\theta}}{E_\theta} = \frac{\nu_{\theta r}}{E_r}; \qquad \frac{\nu_{\theta z}}{E_z} = \frac{\nu_{z\theta}}{E_\theta}; \qquad \frac{\nu_{zr}}{E_r} = \frac{\nu_{rz}}{E_z} \tag{3.63f}$$

In the case of an axisymmetric body, e.g., an ideal solenoid, the strains and displacements, u_r and u_z, respectively, in the r and z directions, are related by:

$$\epsilon_r = \frac{\partial u_r}{\partial r}; \qquad \epsilon_\theta = \frac{u_r}{r}; \qquad \epsilon_z = \frac{\partial u_z}{\partial z}; \qquad \gamma_{rz} = \frac{\partial u_r}{\partial z} + \frac{\partial u_z}{\partial r} \tag{3.63g}$$

Note that because of axial symmetry, all variables in Eq. 3.62 are independent of θ, and $u_\theta = 0$ too. In general, there is no closed-form simultaneous solution for σ_r (Eq. 3.62a) and σ_z (Eq. 3.62b). In a "long" solenoid, such as that typically used in a spatially high-field-homogeneity NMR magnet, the $B_z(r, z)$ variation in the z-direction, at least over most of the solenoid axial length about the midplane, is quite insignificant. The origin of the shear stress τ_{rz} is the variation in the z-direction of the radial load on the coil generated by $B_z(r, z)$. Therefore, in a long solenoid, we can justifiably simplify Eq. 3.62a by assuming that all variables are independent of z, including u_r, i.e., $\partial u_r/\partial z = 0$. Because in high-field-homogeneity magnets $\partial B_r(r, z)/\partial z \simeq 0$, we may also safely assume that over most of the magnet axial length $\partial u_r/\partial z = 0$, which, together with $\partial u_z/\partial r = 0$, leads to $\gamma_{rz} = \tau_{rz} = 0$, which in turn decouples Eqs. 3.62a and 3.62b.

Combining Eq. 3.62 and Eq. 3.63, with the assumption $\tau_{rz} = 0$, and solving for σ_r and σ_θ in terms of u_r, we obtain a differential equation for u_r:

$$\frac{d^2u_r}{dr^2} + \frac{1}{r}\frac{du_r}{dr} - \zeta^2\frac{u_r}{r^2} = -\frac{1 - \nu_{r\theta}\nu_{\theta r}}{E_r}\lambda J B_z(r) + \frac{F}{r} \tag{3.64a}$$

where

$$\zeta = \sqrt{\frac{E_\theta}{E_r}}; \qquad F = -(\zeta^2 - \nu_{r\theta})\epsilon_{T_\theta} + (1 - \nu_{\theta r}\zeta^2)\epsilon_{T_r} \tag{3.64b}$$

The general solution to Eq. 3.64a is given by:

$$u_r = C_1 r^\zeta + \frac{C_2}{r^\zeta} + u_r^L + u_r^T \tag{3.65}$$

where C_1 and C_2 are constants to be determined from boundary conditions at $r = a_1$ and $r = a_2$. u_r^L and u_r^T (the superscripts L and T stand, respectively, for Lorentz and thermal) are particular solutions corresponding to the "source" terms, given in the right-hand side of Eq. 3.64a. The thermal term u_r^T is given by:

$$u_r^T = \frac{Fr}{1 - \zeta^2} \tag{3.66}$$

For an isotropic material ($E_\theta = E_r$, and thus $\zeta = 1$), u_r^T is given by:

$$u_r^T(\zeta = 1) = \tfrac{1}{2}Fr\ln r \tag{3.67}$$

In general $B_z(r)$ may be given by a power series in r:

$$B_z(r) = \sum_{k=0}^{n} b_k r^k \tag{3.68}$$

Then, the Lorentz term u_r^L may be given by:

$$u_r^T = \frac{1 - \nu_{r\theta}\nu_{\theta r}}{E_r}\lambda J \sum_{k=0}^{n} \frac{b_k r^{k+2}}{\zeta^2 - (k+2)^2} \tag{3.69}$$

3.6.2 Stress and Strain Equations in Isotropic Solenoid

We derive radial and hoop stresses in an isotropic solenoid with the winding current density of λJ. The axial magnetic field in the winding varies linearly with r, from $B_z(r=a_1) \equiv B_1$ to $B_z(r=a_2) \equiv B_2$. Note that both B_1 and B_2 can include a "uniform" background field, generated by "long" coils, in a nested-coil magnet, located outside of this solenoid. We define two nondimensional parameters: $\kappa \equiv B_2/B_1$ and $\rho = r/a_1$. In a high-field NMR magnet, κ for the innermost coil can exceed 0.9; for a stand-alone coil it is roughly -0.1; and for an infinitely long stand-alone coil, $\kappa = 0$. Equation 3.62a for this solenoid is modified to:

$$\frac{d\sigma_\rho}{d\rho} + \frac{\sigma_\rho - \sigma_\theta}{\rho} = -\frac{\lambda J B_1 a_1}{\alpha - 1}[\alpha - \kappa - (1-\kappa)\rho] \tag{3.70}$$

For an isotropic material, strains, with thermal strain ϵ_T included, are given by:

$$\epsilon_\rho = \frac{1}{E}(\sigma_\rho - \nu\sigma_\theta) + \epsilon_T \tag{3.71a}$$

$$\epsilon_\theta = \frac{1}{E}(\sigma_\theta - \nu\sigma_\rho) + \epsilon_T \tag{3.71b}$$

We may solve Eq. 3.71 for σ_ρ and σ_θ:

$$\sigma_\rho = \frac{E}{1-\nu^2}\Big[\epsilon_\rho + \nu\epsilon_\theta - (1+\nu)\epsilon_T\Big] \tag{3.72a}$$

$$\sigma_\theta = \frac{E}{1-\nu^2}\Big[\epsilon_\theta + \nu\epsilon_\rho - (1+\nu)\epsilon_T\Big] \tag{3.72b}$$

Strains are related to displacement, u, (here only in the r-direction), by:

$$\epsilon_\rho = \frac{1}{a_1}\frac{du}{d\rho}; \qquad \epsilon_\theta = \frac{1}{a_1}\frac{u}{\rho} \tag{3.72c}$$

Combining Eqs. 3.72a–3.72c, we obtain:

$$\sigma_\rho = \frac{E}{(1-\nu^2)a_1}\left[\frac{du}{d\rho} + \nu\frac{u}{\rho} - a_1(1+\nu)\epsilon_T\right] \tag{3.72d}$$

$$\sigma_\theta = \frac{E}{(1-\nu^2)a_1}\left[\frac{u}{\rho} + \nu\frac{du}{d\rho} - a_1(1+\nu)\epsilon_T\right] \tag{3.72e}$$

Combination of Eq. 3.70 and Eqs. 3.72d and 3.72e yields:

$$\frac{d^2u}{d\rho^2} + \frac{1}{\rho}\frac{du}{d\rho} - \frac{u}{\rho^2} = -\left(\frac{1-\nu^2}{E}\right)\left(\frac{\lambda J B_1 a_1^2}{\alpha - 1}\right)[\alpha - \kappa - (1-\kappa)\rho] \tag{3.73}$$

The general solution of Eq. 3.73 is given by:

$$u = C_1\rho + \frac{C_2}{\rho} - \left(\frac{1-\nu^2}{E}\right)\left(\frac{\lambda J B_1 a_1^2}{\alpha - 1}\right)\left[\frac{(\alpha-\kappa)\rho^2}{3} - \frac{(1-\kappa)\rho^3}{8}\right] \tag{3.74}$$

where C_1 and C_2 are constants determined from boundary conditions at $\rho = 1$ and $\rho = \alpha$, and the last term is the particular solution. Combining Eq. 3.74 and Eqs. 3.72d and 3.72e, we obtain:

$$\sigma_\rho = \frac{E}{(1-\nu^2)a_1}\left[(1+\nu)C_1-(1-\nu)\frac{C_2}{\rho^2}\right] - \left\{\frac{\lambda J B_1 a_1}{\alpha-1}\left[\frac{2+\nu}{3}(\alpha-\kappa)\rho - \frac{3+\nu}{8}(1-\kappa)\rho^2\right]\right\} - \frac{E\epsilon_T}{1-\nu} \tag{3.75a}$$

$$\sigma_\theta = \frac{E}{(1-\nu^2)a_1}\left[(1+\nu)C_1+(1-\nu)\frac{C_2}{\rho^2}\right] - \left\{\frac{\lambda J B_1 a_1}{\alpha-1}\left[\frac{1+2\nu}{3}(\alpha-\kappa)\rho - \frac{1+3\nu}{8}(1-\kappa)\rho^2\right]\right\} - \frac{E\epsilon_T}{1-\nu} \tag{3.75b}$$

With $\sigma_\rho(1)=0$ and $\sigma_\rho(\alpha)=0$, we have expressions for C_1 and C_2:

$$[(1+\nu)C_1-(1-\nu)C_2] = \frac{1-\nu^2}{E}\left(\frac{\lambda J B_1 a_1^2}{\alpha-1}\right)\left[\frac{2+\nu}{3}(\alpha-\kappa) - \frac{3+\nu}{8}(1-\kappa)\right] + a_1(1+\nu)\epsilon_T \tag{3.76a}$$

$$\left[(1+\nu)C_1-(1-\nu)\frac{C_2}{\alpha^2}\right] = \frac{1-\nu^2}{E}\left(\frac{\lambda J B_1 a_1^2}{\alpha-1}\right)\left[\frac{2+\nu}{3}(\alpha-\kappa)\alpha - \frac{(3+\nu)}{8}(1-\kappa)\alpha^2\right] + a_1(1+\nu)\epsilon_T \tag{3.76b}$$

Equations 3.76a and 3.76b may be solved for C_1 and C_2:

$$C_1 = \frac{1-\nu}{E}\left(\frac{\lambda J B_1 a_1^2}{\alpha^2-1}\right)\left[\frac{2+\nu}{3}(\alpha-\kappa)(\alpha^2+\alpha+1) - \frac{3+\nu}{8}(1-\kappa)(\alpha+1)(\alpha^2+1)\right] + a_1\epsilon_T \tag{3.76c}$$

$$C_2 = \frac{1+\nu}{E}\left(\frac{\lambda J B_1 a_1^2\alpha^2}{\alpha^2-1}\right)\left[\frac{2+\nu}{3}(\alpha-\kappa) - \frac{3+\nu}{8}(1-\kappa)(\alpha+1)\right] \tag{3.76d}$$

Substituting Eqs. 3.76c and 3.76d into Eq. 3.75, we obtain:

$$\sigma_\rho = \frac{\lambda J B_1 a_1}{\alpha-1}\left[\frac{2+\nu}{3}(\alpha-\kappa)\left(\frac{\alpha^2+\alpha+1-\alpha^2/\rho^2}{\alpha+1} - \rho\right) - \frac{3+\nu}{8}(1-\kappa)\left(\alpha^2+1-\frac{\alpha^2}{\rho^2}-\rho^2\right)\right] \tag{3.77a}$$

$$\sigma_\theta = \frac{\lambda J B_1 a_1}{\alpha-1}\left\{(\alpha-\kappa)\left[\frac{2+\nu}{3}\left(\frac{\alpha^2+\alpha+1+\alpha^2/\rho^2}{\alpha+1}\right) - \frac{1+2\nu}{3}\rho\right] - (1-\kappa)\left[\frac{3+\nu}{8}\left(\alpha^2+1+\frac{\alpha^2}{\rho^2}\right) - \frac{1+3\nu}{8}\rho^2\right]\right\} \tag{3.77b}$$

"Thin-Walled" Coil

Figures 3.10a and 3.10b show, respectively, plots, for a "thin" coil, here $\alpha = 1.2$, of normalized stresses, hoop, $\varsigma_\theta \equiv \sigma_\theta/(\lambda J B_1 a_1)$, and radial, $\varsigma_r \equiv \sigma_\rho/(\lambda J B_1 a_1)$, as functions of normalized radial distance, $\rho \equiv r/a_1$, at selected "field ratios," $\kappa \equiv B_2/B_1$. Note that $\kappa = -0.1$ is appropriate for a stand-alone solenoid; $\kappa = 0$ for an infinitely long coil; and $\kappa > 0$ for a coil exposed to a uniform background field.

For each field ratio (κ) ς_θ decreases with ρ, while ς_r, being 0 at $r = a_1$ and $r = a_2$, has an extremum (maximum or minimum) radially midway through the winding.

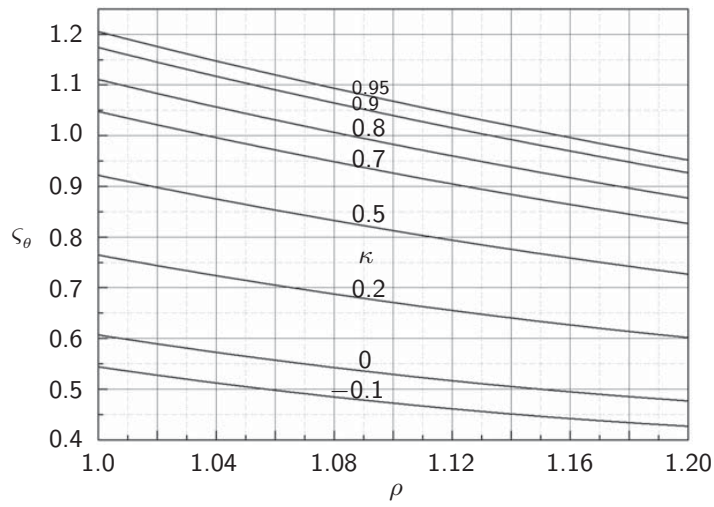

(a)

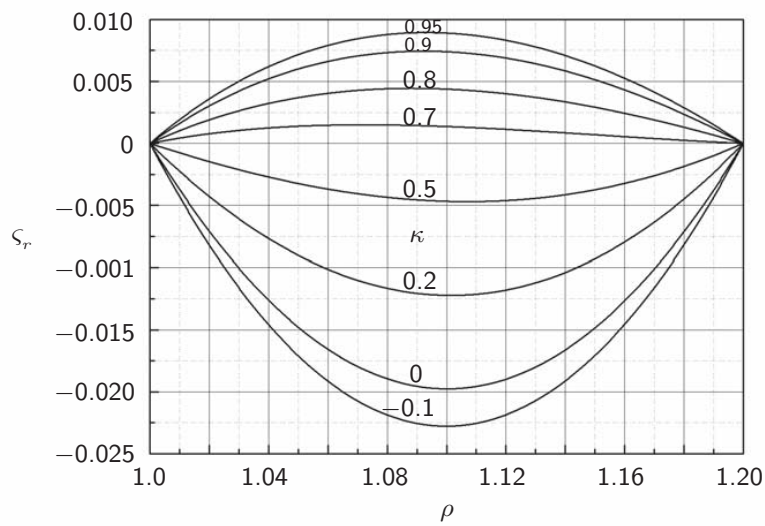

(b)

Fig. 3.10 Plots, at selected $\kappa \equiv B_2/B_1$ values, for a "thin-walled" coil ($\alpha = 1.2$): (a) normalized hoop stress, $\varsigma_\theta \equiv \sigma_\theta/(\lambda J B_1 a_1)$, vs. normalized radial distance, $\rho \equiv r/a_1$; (b) normalized radial stress, $\varsigma_r \equiv \sigma_\rho/(\lambda J B_1 a_1)$, vs. ρ. In each graph κ, from the bottom trace to the top trace: −0.1 (bottom); 0; 0.2; 0.5; 0.7; 0.8; 0.9; and 0.95 (top).

For $\kappa > 0.5$, the winding throughout develops a positive radial stress, which tends to separate turns, a condition that generally should be avoided. The positive effect of winding tension in reducing ς_r is discussed shortly (**3.6.3**).

"Medium-Walled" Coil

Figure 3.11 shows plots similar to those of Fig. 3.10 for a "medium-walled" coil, here $\alpha = 1.8$. In this medium-walled coil, $\varsigma_r > 0$ for $\kappa \approx 0.2$; furthermore, ς_r exceeds 0.1 for $\kappa > 0.8$. That is, an "insert" coil in the bore of a high-field background magnet should be "thin-walled," or otherwise it should be subdivided.

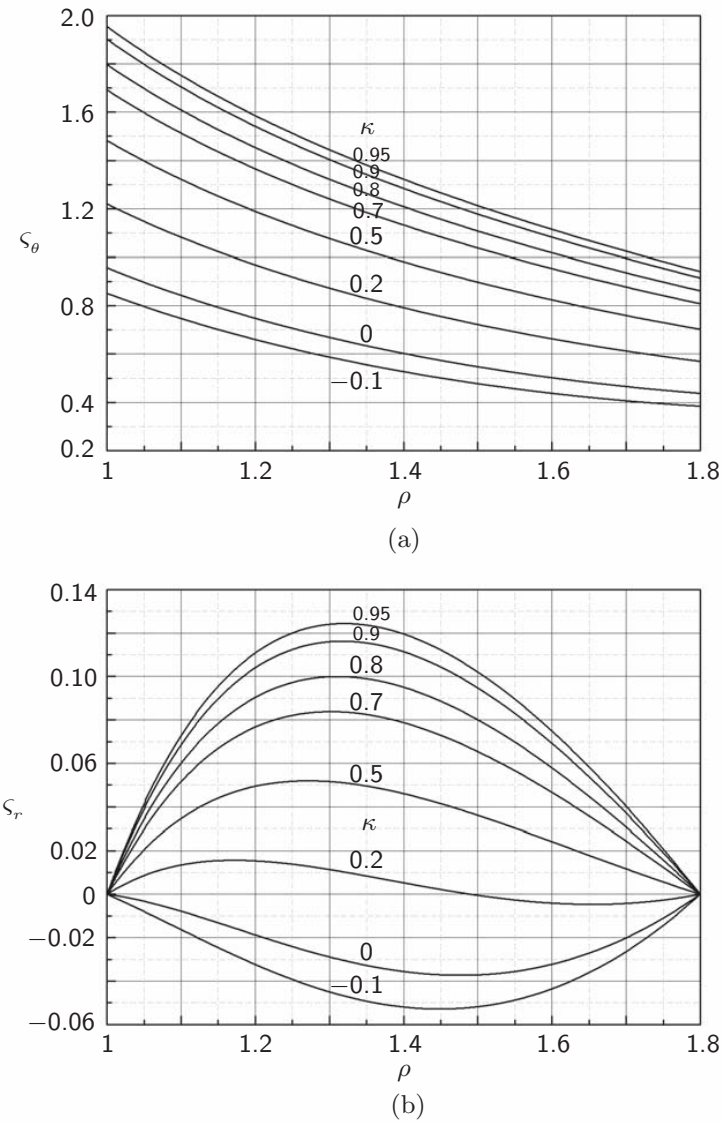

Fig. 3.11 Plots, at selected $\kappa \equiv B_2/B_1$ values, for a "medium-walled" coil ($\alpha = 1.8$): (a) $\varsigma_\theta \equiv \sigma_\theta/(\lambda J B_1 a_1)$ vs. ρ; (b) $\varsigma_r \equiv \sigma_r/(\lambda J B_1 a_1)$ vs. ρ. In each graph κ, from the bottom trace to the top trace: −0.1 (bottom); 0; 0.2; 0.5; 0.7; 0.8; 0.9; and 0.95 (top).

"Thick-Walled" Coil

Figure 3.12 shows plots for a "thick-walled" coil, here $\alpha = 3.6$. Note that ς_θ is roughly twice that for the medium-walled coil. Most significantly, though, in the thick-walled coil normalized radial stress $\sigma_r > 0$ unless κ is sufficiently negative.

There are two practical ways to make σ_r nearly 0 or negative: 1) wind the coil with conductor in tension; and 2) wrap the coil at its outermost layer with a banding wire of high modulus of elasticity. Also, subdividing the coil into thinner coils reduces not only σ_r but also σ_θ.

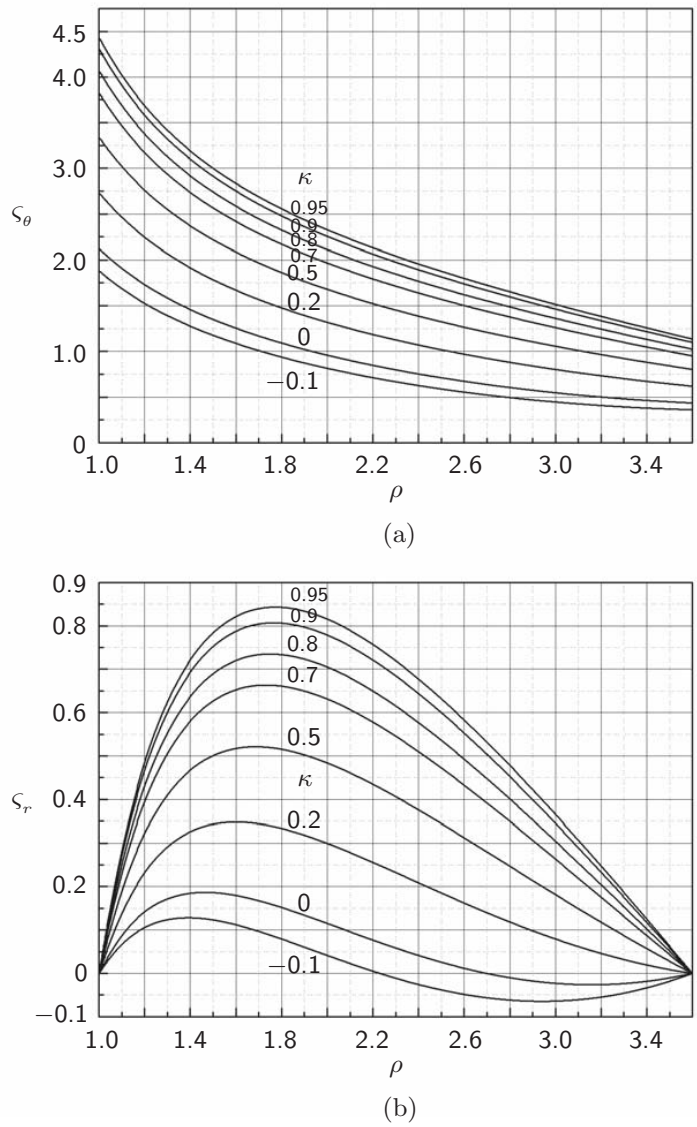

Fig. 3.12 Plots, at selected $\kappa \equiv B_2/B_1$ values, for a "thick-walled" coil ($\alpha = 3.6$): (a) $\varsigma_\theta \equiv \sigma_\theta/(\lambda J B_1 a_1)$ vs. ρ; (b) $\varsigma_r \equiv \sigma_r/(\lambda J B_1 a_1)$vs. ρ. In each graph κ, from the bottom trace to the top trace: −0.1 (bottom); 0; 0.2; 0.5; 0.7; 0.8; 0.9; and 0.95 (top).

3.6.3 Winding Tension to Reduce Radial Stresses

Using an illustrative example, we show here the beneficial effect of winding tension to reduce the radial stress, σ_r, in the winding. As stated above, σ_r should remain *negative* in the winding to keep the layers from separating in the radial direction. Stated simply, when a coil is wound with conductor in tension, the tension generates radial stresses directed inward, reducing the radial stresses within the winding. Even if the winding tension is kept constant during the winding process, the radial variation of the effect of tension within the winding cannot be expressed by an approximate equation as with magnetic body force. In the presence of winding tension, computation of both hoop and radial stresses must be performed through numerical analysis.

Consider an insert coil placed in the bore of a high-field background magnet. The insert has an i.d. ($2a_1$) of 87 mm, an o.d. ($2a_2$) of 156.6 mm: $\alpha = 1.8$, i.e., it is "medium" thick, and in this analysis, as in the above, the coil is assumed "long." Other insert parameters include: $B_z(r=a_1) \equiv B_1 = 28.1\,\mathrm{T}$; $B_z(r=a_2) \equiv B_2 = 24.3\,\mathrm{T}$ or $\kappa \equiv B_2/B_1 = 0.865$; and $\lambda J = 8.26\times10^7\,\mathrm{A/m^2}$. From Fig. 3.11, which gives $\varsigma_r(\rho)$ plots for $\alpha = 1.8$, we find the normalized radial stress, $\varsigma_r \equiv \sigma_r/(\lambda J B_1 a_1)$, has a maximum of 0.11 at $\rho \equiv r/a_1 = 1.3$. The maximum radial stress, $[\sigma_r]_{mx}$, is thus:

$$[\sigma_r]_{mx} = 0.11\lambda J B_1 a_1$$
$$= 0.11(8.26\times10^7\,\mathrm{A/m^2})(28.1\,\mathrm{T})(43.5\times10^{-3}\,\mathrm{m}) = 11.1\,\mathrm{MPa}$$

A radial stress of 11.1 MPa is too large to be tolerated inside the insert. Figure 3.13 presents σ_r vs. r plots for this insert at selected winding tensions, Γ, from 0 to a maximum of 200 N ($\simeq$20 kg). The figure indicates that winding tension of at least 160 N is required to keep σ_r nearly zero or negative. In practice, a winding tension up to 200 N may be applied. For this particular insert a winding tension of 80 N results in a maximum σ_r at ~5 MPa; when a coil is "wet-wound" with epoxy to "glue" adjacent layers, a positive radial stress up to ~5 MPa is tolerable.

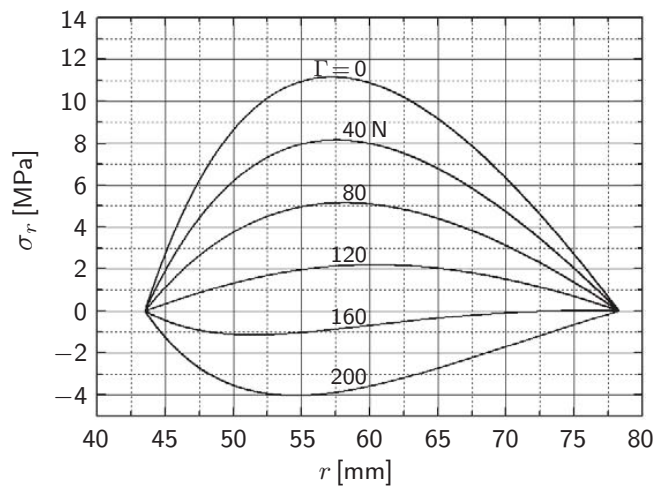

Fig. 3.13 σ_r vs. r plots of a solenoidal coil of $\alpha = 1.8$, with winding tensions, Γ, from 0 (no tension) to 200 N ($\simeq$ 20 kg). With $\Gamma = 0$, σ_r has a peak, at $r \simeq 57.5$ mm, of 11.1 MPa. Only at winding tensions above 160 N ($\simeq$ 16 kg), $\sigma_r \leq 0$ everywhere.

3.7 Self Inductance

Total flux linking a coil, Φ, is proportional to the current I through the coil.

$$\Phi = LI \tag{3.78}$$

The proportionality constant L is the self inductance of the coil. Note that Φ is a "field concept" quantity, while I is a "circuit concept" quantity: L links these two concepts, and because the field concept quantity necessarily involves a volume, L is a geometry-dependent quantity. L is also related to the stored magnetic energy, E_m, of the coil through:

$$E_m = \tfrac{1}{2}LI^2 \tag{3.79}$$

For systems containing no magnetic materials, E_m may be computed by integrating $(1/2)\mu_\circ H^2$ over all space, i.e., E_m is another field-concept quantity; L connects E_m to I through Eq. 3.79.

3.7.1 Self-Inductance of a Circular Loop

An approximate formula for L of a circular loop of radius R of wire of permeability μ and radius a was derived by Maxwell:

$$L = \mu_\circ R\left[\ln\left(\frac{8R}{a}\right) - 2\right] + \tfrac{1}{4}\mu R \tag{3.80a}$$

$$\simeq \mu_\circ R\left[\ln\left(\frac{R}{a}\right) + 0.079\right] + \tfrac{1}{4}\mu R \tag{3.80b}$$

In the right-hand side of each equation above, the first term is the self inductance of the loop due to the flux linked within the circular area ($0 \le r \le R-a$) of the loop and the second term represents, as will be studied in **PROBLEM 3.18** (p. 208), the self inductance of the interior of the wire, $2\pi R$ long. Because the flux linkage outside the wire is frequency independent, the first term is valid for all frequencies, while the second term is frequency dependent. Thus, $(1/4)\mu R$ is valid only at "low" frequencies; the second term reduces to 0 at "high" frequencies. Derivation of the first term of the right-hand side of Eq. 3.80 is quite complex, involving, among others, elliptic integrals.

Kapitza's Magnets (Part 3 of 3 Parts)

—Passage from Francis Bitter's *Magnets: The Education of a Physicist*

In the 1930's, Kapitza completed the construction of a most interesting installation. Fields of the order of magnitude of 300,000 gauss (30 T)*, or about ten times that possible with an iron core magnet, were produced in small coils having about a centimeter inside diameter. Not only did he make and operate these coils; he also performed experiments to show how the properties of matter are influenced by strong magnetic fields. Upon Kapitza's departure from Cambridge this work was stopped and was not picked up again until a few years ago* (early 1950s).

3.7.2 Self Inductance of Solenoidal Coil

For a solenoidal coil containing no ferromagnetic materials and characterized by an inner winding radius a_1, α, β, and total number of turns, N, its self inductance, L, may be given by:

$$L = \mu_o a_1 N^2 \mathcal{L}(\alpha, \beta) \tag{3.81}$$

where $\mathcal{L}(\alpha, \beta)$ is a dimensionless inductance parameter that is a function only of the shape of a coil, represented by α and β.

Figure 3.14 plots $\mathcal{L}(\alpha, \beta)$ plots over the range of $\alpha = 1$ to $\alpha = 5$ and $\beta = 0.04$ to $\beta = 10$ that covers α and β values of solenoidal coils of our interest. For the range $\beta > 1$, which covers most solenoids, important exceptions being "rings" and "pancake" (flat) coils, $\mathcal{L}(\alpha, \beta)$, as seen from the figure, is roughly proportional to α. In fact, when a *rough* ("ball-park") value of L suffices, for example, during the "first-cut" design phase, we might use:

$$\mathcal{L}(\alpha, \beta) \sim \frac{\pi\alpha}{2(\beta + 0.5)} \qquad (\text{for } \beta \to 1 \text{ from } \beta > 1) \tag{3.82a}$$

$$\mathcal{L}(\alpha, \beta) \sim \frac{\pi\alpha}{2\beta} \qquad (\text{for } \beta \to \infty) \tag{3.82b}$$

For a "thin-walled" solenoid, i.e., $\alpha \simeq 1$, in the limit $\beta \to \infty$, Eq. 3.82*b* reduces to $\pi/2\beta$, which will be derived later in **PROBLEM 3.18** (Eq. 3.84*c*, p. 208).

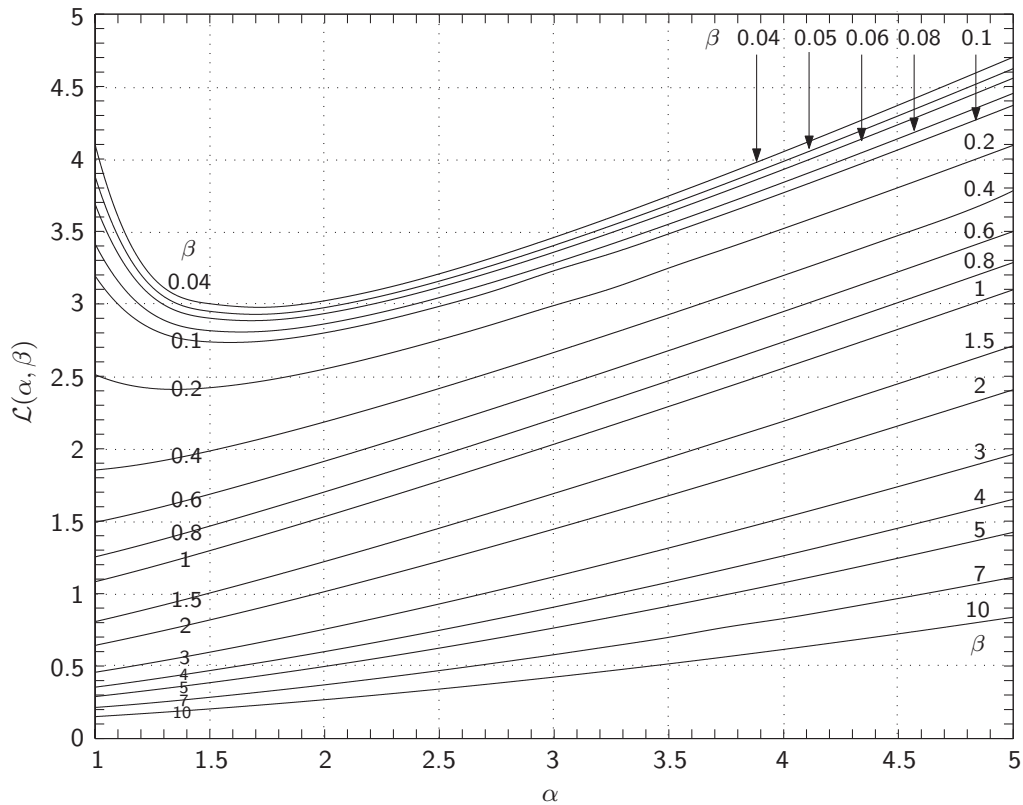

Fig. 3.14 $\mathcal{L}(\alpha, \beta)$ for solenoidal coil of parameters α and β.

3.7.3 Useful Inductance Formulas

Here, useful inductance formulas for coils with nonmagnetic material, i.e., $\mu = \mu_\circ$, are given. Derivations of some of these formulas are revisited in **PROBLEM 3.18**.

Although analytical expressions for coils of "thick" winding build were derived in the past—well before the proliferation of inductance computer codes—and given in engineering reference books, these formulas, mostly not in SI units, are generally tedious to use. Figure 3.14, or even Eq. 3.82, should be sufficient for inductance computation in most applications, particularly during early design stages.

Wire

The interior of a wire of radius a per unit length, L [H/m]:

$$L = \frac{\mu_\circ}{8\pi} \tag{3.83}$$

"Long" Coils

a. A long ($\beta > 0.75$), "thin" coil of i.d. $2a_1$ with N total turns [3.7]:

$$L = \mu_\circ a_1 N^2 \left[\frac{\pi(1+\alpha)^2}{8\beta}\right] \left[1 - \frac{2}{3\pi\beta} + \frac{(1+\alpha)^2}{32\beta^2} \ \cdots\right] \tag{3.84a}$$

For $(\alpha - 1)/(\alpha + 1) \ll 1$ Eq. 3.84*a* reduces to:

$$L = \mu_\circ a_1 N^2 \left(\frac{\pi}{2\beta}\right) \left[1 - \frac{2}{3\pi\beta} + \frac{1}{8\beta^2} \ \cdots\right] \tag{3.84b}$$

b. For a "very long" ($\beta \gg 1$), "thin" ($\alpha \simeq 1$) coil, Eq. 3.84*b* becomes:

$$L = \mu_\circ a_1 N^2 \left(\frac{\pi}{2\beta}\right) \tag{3.84c}$$

Thus, as noted above, for a very long and thin coil, $\mathcal{L}(\alpha, \beta) = \pi/2\beta$.

"Short" Coil

A short ($\beta < 0.75$), thin ($\alpha \simeq 1$) coil of i.d. $2a_1$ with N total turns [3.7]:

$$L \simeq \mu_\circ a_1 N^2 \left(\frac{\alpha+1}{2}\right) \left(\ln\left\{\left[\frac{2(\alpha+1)}{\beta}\right]\left[1 + \frac{\beta^2}{2(1+\alpha^2)}\right]\right\} - \tfrac{1}{2}\left[1 + \frac{\beta^2}{4(1+\alpha^2)}\right]\right) \tag{3.85a}$$

which for $\beta \ll 1$ becomes:

$$L \simeq \mu_\circ a_1 N^2 \left(\frac{\alpha+1}{2}\right) \left\{\ln\left[\frac{2(\alpha+1)}{\beta}\right] - 0.5\right\} \tag{3.85b}$$

"Pancake" (Flat) Coil

A pancake (flat) coil ($\beta \ll 1$) of i.d. $2a_1$ with N total turns [3.7]:

$$L \simeq \mu_\circ a_1 N^2 \left(\frac{\alpha+1}{2}\right)\left\{\ln\left[\frac{4(\alpha+1)}{\alpha-1}\right]\left[1+\tfrac{1}{24}\frac{(\alpha-1)^2}{(\alpha+1)^2}\right] - \tfrac{1}{2}\left[1-\tfrac{43}{144}\frac{(\alpha-1)^2}{(\alpha+1)^2}\right]\right\} \tag{3.86a}$$

For $(\alpha-1)/(\alpha+1) \ll 1$ Eq. 3.86*a* further reduces to:

$$L \simeq \mu_\circ a_1 N^2 \left(\frac{\alpha+1}{2}\right)\left\{\ln\left[\frac{4(\alpha+1)}{\alpha-1}\right]-0.5\right\} \tag{3.86b}$$

Note that for a "ring" ($N=1$), i.e., $a_1(\alpha+1)=2R$ (ring diameter) and $2a_1\beta=2a$ or $a_1(\alpha-1)=2a$ (ring wire diameter), both Eqs. 3.85*b* and 3.86*b* simplify to:

$$L \simeq \mu_\circ R\left[\ln\left(\frac{4R}{a}\right)-0.5\right] = \mu_\circ R\left[\ln\left(\frac{R}{a}\right)+0.886\right] \tag{3.86c}$$

Equation 3.86*c* applies to a ring having a *rectangular* cross sectional area, while Eq. 3.80*a* to a ring of *circular* cross sectional area. For a really fat ($\alpha \gg 1$) pancake, Eq. 3.86*a* further simplifies to:

$$L \simeq 0.5\mu_\circ a_1 \alpha N^2\left\{\ln\left(\frac{25}{6}\right)-\frac{101}{288}\right\} = 0.538\mu_\circ a_1 \alpha N^2$$

$$L \approx 0.5\mu_\circ a_2 N^2 \tag{3.86d}$$

Note that it is a_2, *not* the usual a_1, that appears in Eq. 3.86*d*.

"Ideal" Dipole Magnet

The inductance *per unit length*, L_ℓ [H/m], of an "ideal" dipole (**PROBLEM 3.8**)—infinite in length and "zero" winding thickness—with N total turns:

$$L_\ell = \tfrac{1}{8}\mu_\circ \pi N^2 \tag{3.87}$$

"Ideal" Quadrupole Magnet

The inductance *per unit length*, L_ℓ [H/m], of an "ideal" quadrupole, studied in **PROBLEM 3.9**, infinite in length and "zero" winding thickness with N total turns:

$$L_\ell = \tfrac{1}{16}\mu_\circ \pi N^2 \tag{3.88}$$

Note that for an ideal dipole or quadrupole magnet, the inductance is independent of winding radius, but instead is proportional to length.

"Ideal" Circular Cross Section Toroid

An "ideal" toroidal coil—**PROBLEM 3.10**—zero-winding thickness, major radius R, and circular section of radius a with N total turns:

$$L = \mu_\circ R N^2 \left[1 - \sqrt{1 - \left(\frac{a}{R}\right)^2}\right] \tag{3.89a}$$

In the limit $a \ll R$, L may be approximated by:

$$L = \mu_\circ a N^2 \left(\frac{a}{2R}\right) \left[1 + \tfrac{1}{4}\left(\frac{a}{R}\right)^2 + \tfrac{1}{8}\left(\frac{a}{R}\right)^4 + \cdots\right] \tag{3.89b}$$

$$\simeq \mu_\circ a N^2 \left(\frac{a}{2R}\right) \tag{3.89c}$$

"Ideal" Rectangular Cross Section Toroid

An ideal toroid of major radius R and rectangular section of width (r-axis) $2a$ and height (z-axis) $2b$:

$$L = \mu_\circ b N^2 \left[\frac{1}{\pi} \ln\left(\frac{R+a}{R-a}\right)\right] \tag{3.90a}$$

In the limit $a \ll R$, L may be approximated by:

$$L = \mu_\circ b N^2 \left(\frac{2a}{\pi R}\right) \left[1 + \tfrac{1}{3}\left(\frac{a}{R}\right)^2 + \tfrac{1}{5}\left(\frac{a}{R}\right)^4 + \cdots\right] \tag{3.90b}$$

$$\simeq \mu_\circ b N^2 \left(\frac{2a}{\pi R}\right) \tag{3.90c}$$

My Magnets (Part 1 of 3 Parts)

—Passage from Francis Bitter's *Magnets: The Education of a Physicist* [3.4]

My own thoughts ran in the direction of producing constant magnetic fields. There are many experiments that are extremely difficult or impossible to perform in a hundredth of a second. I wondered whether one might design coils having even larger diameters, so that one might put inside them either a thermos bottle with a liquid gas, like liquid air, for maintaining a low temperature, or a furnace for maintaining a high temperature, and still have room left over for experimentation. Questions then arose. How should one wind the coils so that the available power is used most effectively? How much heat could one take out of the surface of a copper conductor by means of a cooling liquid? What sort of flow would be most suitable? What liquid would be most effective? How should it be introduced so that it would not boil away before completing its function?

The problem of how to design a coil to give the most intense possible magnetic field with a given supply of electric power is an interesting example to tell you about... If one were to wind a coil on a hollow cylinder using different-sized wires for different parts of the coil, was there a best choice of wire sizes? For example, one might use very fine wire for a certain length of the cylinder, then cover this over a longer length with thicker wire... It did not take me long to figure this out and to convince myself that an improvement was possible...

3.8 Mutual Inductance

When two coils, Coil 1 and Coil 2, are near each other, they usually interact inductively. Their coupling may be quantified by means of the mutual inductance, M_{12} or M_{21}. Note that $M_{12} = M_{21} = M$. Thus:

$$M_{12} \equiv N_1 \frac{\Phi_{12}}{I_2} = M_{21} \equiv N_2 \frac{\Phi_{21}}{I_1} \tag{3.91}$$

Φ_{12} is the flux linking the N_1 turns of Coil 1 when Coil 2 carries current I_2; Φ_{21} is the flux linking the N_2 turns of Coil 2 when Coil 1 carries current I_1.

The total magnetic energy, E_m, in a coupled 2-coil system is given by:

$$\begin{aligned} E_m &= \tfrac{1}{2}L_1 I_1^2 + \tfrac{1}{2}L_2 I_2^2 + \tfrac{1}{2}M_{12} I_1 I_2 + \tfrac{1}{2}M_{21} I_1 I_2 \\ &= \tfrac{1}{2}L_1 I_1^2 + \tfrac{1}{2}L_2 I_2^2 + M_{12} I_1 I_2 \end{aligned} \tag{3.92}$$

As with self inductance, there are mutual inductance formulas for selected systems. For systems of our interest, i.e., coupled coaxial solenoidal coils, a code that computes the self inductance of a coil usually can compute the inductance matrix of a multi-coil system.

Series Connected Coils

The effective self inductance, L_s, of a two-coil system of L_1, L_2, and M_{12}, connected in series is given by:

$$L_s = L_1 + L_2 \pm 2M_{12} \tag{3.93}$$

The + is chosen for the M_{12} term if the magnetic fields augment each other and − if they oppose each other.

Parallel Connected Coils

The effective self inductance, L_p, of a two-coil system of L_1, L_2, and M_{12}, connected in parallel is given by:

$$L_p = \frac{L_1 L_2 - M_{12}^2}{L_1 + L_2 \mp 2M_{12}} \tag{3.94}$$

Coupling Coefficient

Mutual inductance M_{12} is related to L_1 and L_2 by:

$$M_{12} = k\sqrt{L_1 L_2} \tag{3.95a}$$

$$k = \frac{M_{12}}{\sqrt{L_1 L_2}} \tag{3.95b}$$

k is called the coupling coefficient; $k = 0$ when the coils are uncoupled, and $k = 1$ when fully coupled. For a tightly nested solenoidal coil pair, in which one coil is in the bore of the other coaxially and concentrically (with the two midplanes coinciding), k ranges 0.3–0.6, being close to 0.6 when their α's and β's are similar and towards 0.3 when they are not.

3.8.1 Mutual Inductances—Selected Analytic Expressions

Because the force and mutual inductance between coils are related, the analytical expression given earlier for axial forces between Coils A and B may be used to derive mutual inductance expressions. From $\vec{F} = I_A I_B \nabla M$, it is evident that expressions for M can be one step more complicated than the axial force expressions given earlier. Therefore only a few simple cases are discussed here.

Mutual Inductance between Two "Ring" Coils

For two coaxially aligned "ring" coils, Coils A (diameter $2a_A$; N_A turns) and B ($2a_B$; N_B), displaced by a distance ρ, the mutual inductance, $M_{AB}(\rho)$, is given by:

$$M_{AB} = \frac{\mu_\circ}{2}(N_A N_B)\sqrt{(a_A + a_B)^2 + \rho^2}\left\{2\big[K(k) - E(k)\big] - k^2 K(k)\right\} \tag{3.96}$$

where the modulus, k^2 for this system is given by:

$$k^2 = \frac{4a_A a_B}{(a_A + a_B)^2 + \rho^2}$$

Special Case 1: Two Ring Coils Far Apart

When the two ring coils are far apart, i.e., $\rho^2 \gg (a_A + a_B)^2$ or $k^2 \ll 1$, Eqs. 3.38*c* and 3.38*a* may be used to simplify Eq. 3.96:

$$M_{AB} \simeq \frac{\mu_\circ}{2\pi}\left[\frac{(\pi a_A^2 N_A)(\pi a_B^2 N_B)}{\rho^3}\right] \tag{3.97}$$

Equation 3.97 states that the mutual inductance is approximately proportional to the product of two "total" winding areas—$\pi a_A^2 N_A$ and $\pi a_B^2 N_B$—reduced by ρ^3.

Mutual Inductance of a "Thin-Walled" Solenoid and a Ring Coil

Here, we consider a coaxially aligned "thin-walled" solenoid ($2a_S$; uniform turn density $N_S/2b_S$) and a ring coil (diameter $2a_R$ and N_R turns). The ring coil is at a distance ρ *right* of the right-hand end of the solenoid, as shown in Fig. 3.6 (p. 87). The mutual inductance, M_{RS}, between the solenoid and the ring coil is given by:

$$\begin{aligned} M_{RS}(\rho) = -\frac{\mu_\circ}{2}\left(\frac{N_R N_S}{2b_S}\right)\times \\ \left(\frac{\rho}{\sqrt{(a_R+a_S)^2+\rho^2}}\left\{\left[(a_R+a_S)^2+\rho^2\right]\big[K(k_R)-E(k_R)\big]-\Upsilon(c^2,k_R)\right\}\right. \\ \left. -\frac{2b_S+\rho}{\sqrt{(a_R+a_S)^2+(2b_S+\rho)^2}}\left\{\left[(a_R+a_S)^2+(2b_S+\rho)^2\right]\big[K(k_S)-E(k_S)\big]-\Upsilon(c^2,k_S)\right\}\right) \end{aligned} \tag{3.98}$$

where k_r, k_s, and c^2 are given by:

$$k_R^2 = \frac{4a_R a_S}{(a_R + a_S)^2 + \rho^2}; \qquad k_S^2 = \frac{4a_R a_S}{(a_R + a_S)^2 + (2b_S + \rho)^2}; \qquad c^2 = \frac{4a_R a_S}{(a_R + a_S)^2}$$

Special Case 2: Thin-Walled Solenoid and Ring Coil Far Apart

When these two coils are far apart such that $k_R^2 \ll 1$, $k_S^2 \ll 1$, and $\rho > b_S$, Eq. 3.98 may be simplified to:

$$M_{RS} = \frac{\mu_\circ}{2}\left(\frac{N_R N_S}{2b_S}\right)\left\{\frac{2\pi(a_R a_S)^2 b_S}{\rho^3}\left(1+\frac{b_S}{\rho}\right) - (a_R - a_S)^2\left[\Pi(c^2,k_R) - \Pi(c^2,k_S)\right]\right\} \tag{3.99}$$

As long as ρ, though much greater than a_R and a_S, is still not much greater than b_S, the "correction" terms, b_S/ρ and that with $\Pi(c^2,k)$s, must be retained in Eq. 3.99.

Special Case 3: Thin-Walled Solenoid and Ring Coil Farther Apart

When these two coils are farther apart so that $\rho \gg b_S$ and the conditions of $k_R \to 0$ and $k_S \to 0$ are satisfied, Eq. 3.99 may be further simplified to:

$$\begin{aligned} M_{RS} &= \frac{\mu_\circ}{2}\left(\frac{N_R N_S}{2b_S}\right)\frac{2\pi(a_R a_S)^2 b_S}{\rho^3} \\ &= \frac{\mu_\circ}{2\pi}(\pi a_R^2 N_R)\left(\frac{\pi a_S^2 N_S}{2b_S}\right)\frac{2b_S}{\rho^3} \end{aligned} \tag{3.100}$$

Ring Coil at the Middle of a Thin-Walled Solenoid

Figure 3.15 shows a schematic arrangement of the two coils, in which the ring coil is at the midplane of a thin-walled solenoid, Note that in this arrangement, $\rho = -b_S$, with ρ defined in Fig. 3.6. Thus by inserting $\rho = -b_S$ into Eq. 3.98, we obtain the simplified expression given below:

$$M_{RS}(\rho = -b_S) \simeq \frac{\mu_\circ}{2}\left(\frac{N_R N_S}{2b_S}\right)\times \frac{2b_S}{\sqrt{(a_R+a_S)^2+b_S^2}}\left\{\left[(a_R+a_S)^2+b_S^2\right]\left[K(k)-E(k)\right] - \Upsilon(c^2,k)\right\} \tag{3.101}$$

where k is given by:

$$k^2 = \frac{4a_R a_S}{(a_R+a_S)^2+b_S^2}$$

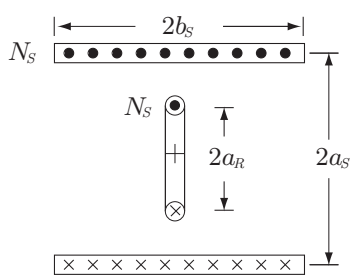

Fig. 3.15 Ring coil at the midplane of a thin-walled solenoid.

Special Case 4: "Long" Thin-Walled Solenoid and Ring Coil

When the thin-walled solenoid is "long," specifically when the conditions $b_S \gg a_S$ and $b_S \gg a_R$ are met, the relative position between the ring coil and the solenoid is no longer important. For a long solenoid, with $k^2 \simeq 4a_R a_S/b_S^2$, Eq. 3.101 becomes:

$$M_{RS} \simeq \frac{\mu_\circ}{2}\left(\frac{N_R N_S}{2b_S}\right)(2)\Big\{b_S^2\big[K(k)-E(k)\big]-\Upsilon(c^2,k)\Big\}$$
$$\simeq \frac{\mu_\circ}{2}\left(\frac{N_R N_S}{2b_S}\right)\pi(a_R^2+a_S^2)\left[1-\frac{2(a_R-a_S)^2}{\pi(a_R^2+a_S^2)}\Pi(c^2,k)\right] \qquad (3.102)$$

The second term within the brackets in Eq. 3.102 may be considered a correction term which becomes negligible in the limit of $a_R \gg a_S$ or $a_R \ll a_S$.

Special Case 5: Ring Coil of Widely Differing Diameter

When the diameter of the ring coil differs greatly from that of the solenoid, the condition $c^2 \to 0$ is satisfied and, as noted earlier (Eq. 3.49*b*), $\Pi(c^2,0)$ may be given by the first few terms of the power expansion in c^2. In the limit $k^2 \to 0$ ($b_S \gg a_R$ and $b_S \gg a_S$), $\Pi(c^2,k) \to \Pi(c^2,0)$ in Eq. 3.102, and using 3.49*b*, we obtain:

$$M_{RS} \simeq \frac{\mu_\circ}{2}\left(\frac{N_R N_S}{2b_S}\right)\pi(a_R^2+a_S^2)\left[1-\frac{(a_R-a_S)^2}{(a_R^2+a_S^2)}\left(1+\tfrac{1}{2}c^2+\tfrac{3}{8}c^4+\tfrac{5}{16}c^6\right)\right]$$
$$\simeq \frac{\mu_\circ}{2}\left(\frac{N_R N_S}{2b_S}\right)\pi(a_R^2+a_S^2)\times$$
$$\left\{1-\frac{(a_R-a_S)^2}{(a_R^2+a_S^2)}\left[1+\frac{2a_R a_S}{(a_R+a_S)^2}+\frac{6(a_R a_S)^2}{(a_R+a_S)^4}+\frac{20(a_R a_S)^3}{(a_R+a_S)^6}\right]\right\} \qquad (3.103)$$

3.8.2 Mutual Inductance and Interaction Force

Using expressions derived in **3.5.7** for axial restoring force on axially off-centered solenoids, we may derive an expression for axial dependance of the mutual inductance between the two solenoids. A net magnetic force, $\vec{F}_{AB}$, between two solenoids, A and B, is related to the total magnetic energy stored in the two solenoids:

$$\vec{F}_{AB} = \nabla E_{AB} \qquad (3.104a)$$

Inserting Eq. 3.92, with the subscripts 1 and 2 replaced, respectively, by A and B in the right-hand side of Eq. 3.104*a*, and noting that $\vec{F}_{AB}$ in the z-direction (with variable ρ) is $F_{zR}(\rho)$, given by Eq. 3.60, we obtain:

$$F_{zR}(\rho) = \frac{\partial E_{AB}}{\partial \rho} = I_A I_B \frac{\partial M_{AB}(\rho)}{\partial \rho} \qquad (3.105b)$$

For small ρ ($\rho \ll \sqrt{a_T^2+b_D^2}$), we may integrate $F_{zR}(\rho)$ given by Eq. 3.61:

$$M_{AB}(\rho) - M_{AB}(0) \propto -\rho^2 \qquad (3.106)$$

For small ρ, $M_{AB}(\rho)$ thus decreases as ρ^2, the square of the off-center distance.

Magnetic Field (H) and Magnetic Induction (B)

Unless otherwise qualified, every magnet in **PROBLEMS & DISCUSSIONS** is air-cored, i.e., the magnetic induction, B, is simply related to the magnetic field, H, by the magnetic permeability of air, which is virtually equal to that of vacuum $\mu_\circ = 4\pi \times 10^{-7}$ H/m: $B = \mu_\circ H$. Often, especially by engineers, the unit of B, tesla [T], is used for the unit of field H, ampere/meter [A/m]. Most likely, this practice of interchanging B and H stems from: 1) B [gauss] and H [oersted] are numerically equal in the cgs (centimeter-gram-second) electromagnetic unit; and 2) gauss is more universally used than oersted. In the 2nd Edition, *most* of field equations originally given in H in the 1st Edition are given in B.

DISCUSSION 3.1: Uniform-Current-Density Solenoids

Here, the basics of a uniform-current-density solenoid, of winding i.d. $2a_1$, winding o.d. $2a_2$, and total winding length $2b$, are first discussed. Figure 3.16 defines the winding cross section—because we are dealing with an axisymmetric solenoid, only the z- and r-axes are considered. The differential magnetic field induction at the center, $dB_z(0,0)$ [T], generated by a current-carrying ring of differential cross section dA [A/m^2] located at (r, z) is given by an equivalent form of Eq. 3.3a:

$$dB_z(0,0) = \frac{\mu_\circ r^2 \lambda J \, dA}{2(r^2 + z^2)^{3/2}} \tag{3.107}$$

where λJ [A/m^2] is the overall current density within the differential cross section. The dimensionless number λ, called the space factor, acknowledges that not all the winding cross section is occupied by current-carrying conductors. Note that λJ in this model is uniform over the winding cross section and given by:

$$\lambda J = \frac{NI}{2b(a_2 - a_1)} \tag{3.108a}$$

$$= \frac{NI}{2a_1^2 \beta(\alpha - 1)} \tag{3.108b}$$

where, once again, $\alpha = a_2/a_1$ and $\beta = b/a_1$. N is the total number of turns, and NI is often called the total ampere-turns.

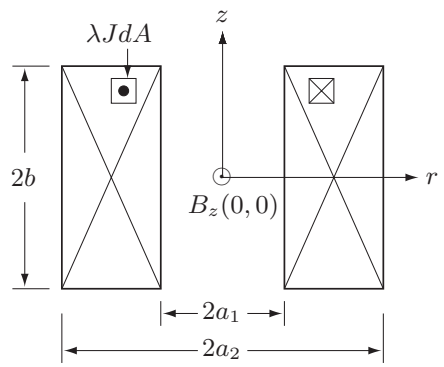

Fig. 3.16 Cross section of a uniform-current-density solenoid.

DISCUSSION 3.1: Uniform-Current-Density Solenoids (continuation)

By integrating Eq. 3.107 from $r=a_1$ to $r=a_2$ and from $z=-b$ to $z=b$, we obtain an expression for $B_z(0,0)$ for the solenoid, given in terms of $H_z(0,0)$ in **3.4** by Eq. 3.13*a* and the field factor $F(\alpha,\beta)$ by Eq. 3.13*b*:

$$B_z(0,0) = \mu_\circ \lambda J a_1 F(\alpha,\beta) \tag{3.109}$$

$$F(\alpha,\beta) = \beta \ln\left(\frac{\alpha+\sqrt{\alpha^2+\beta^2}}{1+\sqrt{1+\beta^2}}\right) \tag{3.13b}$$

As stated earlier, $F(\alpha,\beta)$ is the "field factor" for a uniform-current-density coil and, like the inductance parameter $\mathcal{L}(\alpha,\beta)$ in Eq. 3.81, it depends only on the cross-sectional shape of a solenoidal coil. Three graphs of $F(\alpha,\beta)$ are shown in Fig. 3.17: $F(\alpha,\beta)$ vs. α with constant β lines (dashed) in Fig. 3.17a; $F(\alpha,\beta)$ vs. β with constant α lines (dashed) in Fig. 3.17b; and β vs. α for constant $F(\alpha,\beta)$ lines (dashed) in Fig. 3.17c [3.8].

The total conductor volume in a solenoid, $\mathcal{V}_{cd}=\lambda 2\pi a_1^3(\alpha^2-1)\beta$, depends, for given λ and a_1, only on α and β, as does $F(\alpha,\beta)$: each point on the heavy line in each graph has the *minimum* volume for a given $F(\alpha,\beta)$. Salient features of $F(\alpha,\beta)$ are noted in connection with *special coils* discussed in **PROBLEM 3.1** below.

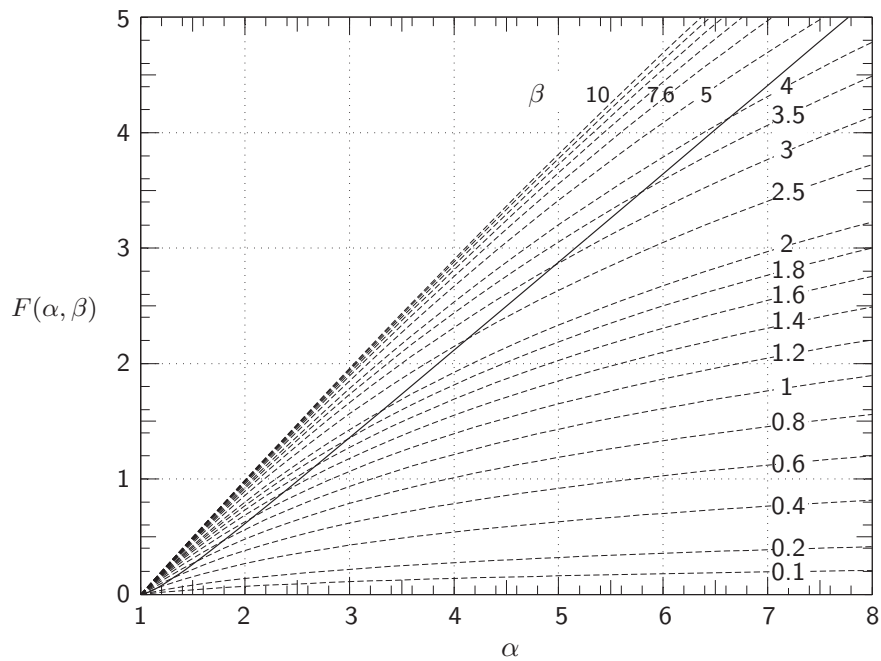

Fig. 3.17a $F(\alpha,\beta)$ vs. α for constant β lines (dashed). The heavy curve represents the minimum conductor volume for a solenoid coil of given $F(\alpha,\beta)$.

DISCUSSION 3.1: Uniform-Current-Density Solenoids (continuation)

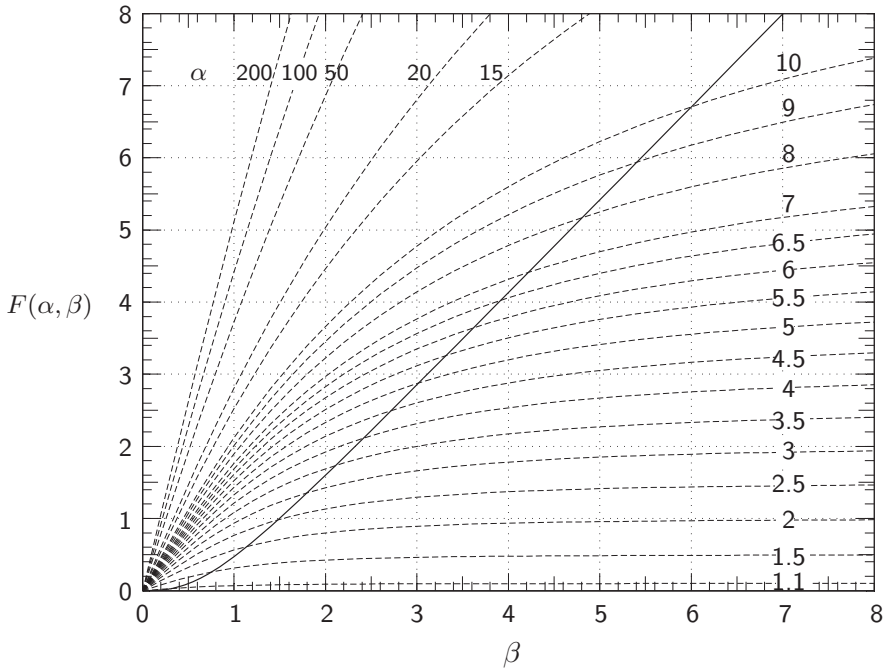

Fig. 3.17b $F(\alpha, \beta)$ vs. β for constant α lines (dashed). The heavy curve represents the minimum conductor volume for a solenoid coil of given $F(\alpha, \beta)$.

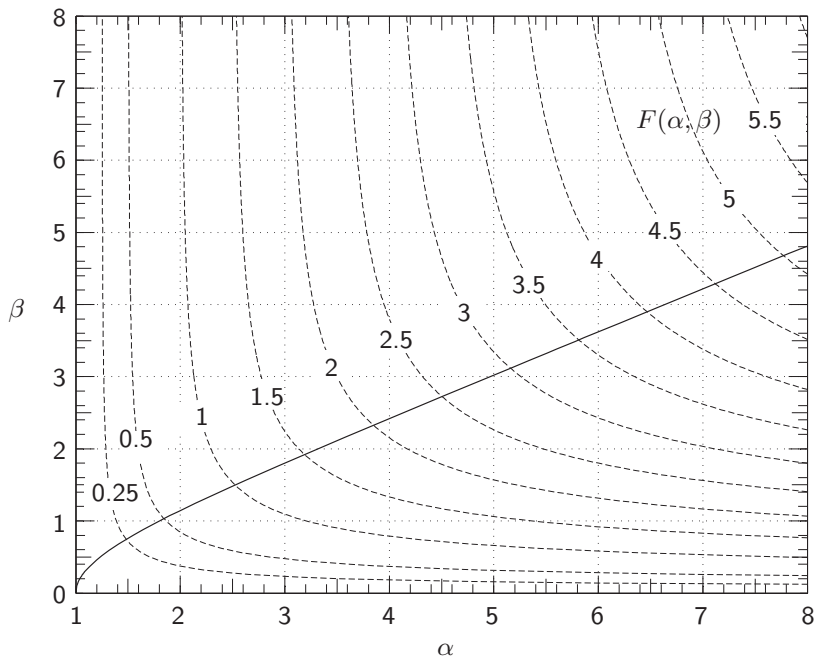

Fig. 3.17c β vs. α for constant $F(\alpha, \beta)$ lines (dashed). The heavy curve represents the minimum conductor volume for a solenoid coil of given $F(\alpha, \beta)$.

PROBLEM 3.1: "Simple" solenoids*

a) Starting with Eq. 3.107, derive Eqs. 3.109 and 3.13*b*.

b) By combining Eqs. 3.108*b* and 3.109 we may also express $B_z(0,0)$ by:

$$B_z(0,0) = \frac{\mu_\circ NI}{2a_1(\alpha-1)} \ln\left(\frac{\alpha+\sqrt{\alpha^2+\beta^2}}{1+\sqrt{1+\beta^2}}\right) \tag{3.110}$$

"Ring" Coil Simplify Eq. 3.110 for a "ring" coil ($\alpha = 1$) of radius a_1 carrying total current NI and reduce it to:

$$B_z(0,0) = \frac{\mu_\circ NI}{2a_1} \tag{3.111a}$$

"Thin-Walled" Solenoid: Show that for a "thin-walled" solenoid ($\alpha \rightarrow 1$) Eq. 3.110 is simplified to:

$$B_z(0,0) = \frac{\mu_\circ NI}{2a_1}\left(\frac{1}{\sqrt{1+\beta^2}}\right) \tag{3.111b}$$

Also show:

$$B_z(0,0) = \mu_\circ \lambda J a_1(\alpha-1)\frac{\beta}{\sqrt{1+\beta^2}} \tag{3.111c}$$

"Long" Solenoid: Simplify Eq. 3.110 for the case of a solenoid that is much longer than its outer winding diameter, i.e., $\beta \gg \alpha$, and reduce it to:

$$B_z(0,0) = \frac{\mu_\circ NI}{2b} \tag{3.111d}$$

Because $NI/2b = K_\theta$, Eq. 3.111*d* is equivalent to Eq. 3.5. Also, show that:

$$B_z(0,0) = \mu_\circ \lambda J a_1(\alpha-1) \tag{3.111e}$$

"Pancake" Coil: Simplify Eq. 3.110 this time for a winding that is very short compared with its outer winding diameter and reduce it to:

$$B_z(0,0) = \frac{\mu_\circ NI}{2a_1}\left(\frac{\ln\alpha}{\alpha-1}\right) \tag{3.111f}$$

Equation 3.111*f* is valid for "pancake" coils (see ***DISCUSSION 3.6***).

c) ***Field vs. Power***: Show that an expression for the center field $B_z(0,0)$ in a *resistive*, e.g., copper, solenoid is related to its power requirement, P, by:

$$B_z(0,0) = \mu_\circ G(\alpha,\beta)\sqrt{\frac{\lambda P}{\rho_{cd} a_1}} \tag{3.112a}$$

$$G(\alpha,\beta) = \sqrt{\frac{\beta}{2\pi(\alpha^2-1)}} \ln\left(\frac{\alpha+\sqrt{\alpha^2+\beta^2}}{1+\sqrt{1+\beta^2}}\right) \tag{3.112b}$$

where ρ_{cd} is the conductor's electrical resistivity. $G(\alpha,\beta)$ is known as the G factor for a uniform-current-density coil [3.2].

---

* Based on **Problem 3.1** in the 1st Edition (Plenum, 1994).

Solution to PROBLEM 3.1

a) By integrating Eq. 3.107 over the appropriate limits for z- and r-coordinates, we have:

$$B_z(0,0) = \frac{\mu_\circ \lambda J}{2} \int_{a_1}^{a_2} \int_{-b}^{b} \frac{r^2\, dz\, dr}{(r^2+z^2)^{3/2}} = \mu_\circ \lambda J \int_{a_1}^{a_2} \int_{0}^{b} \frac{r^2\, dz\, dr}{(r^2+z^2)^{3/2}}$$

From a table of integrals we have:

$$\int_0^b \frac{dz}{(r^2+z^2)^{3/2}} = \left[\frac{z}{r^2\sqrt{r^2+z^2}}\right]_0^b = \frac{b}{r^2\sqrt{r^2+b^2}}$$

Thus:

$$\begin{aligned} B_z(0,0) &= \mu_\circ \lambda J \int_{a_1}^{a_2} \frac{r^2 b\, dr}{r^2\sqrt{r^2+b^2}} = \mu_\circ \lambda J b \left[\ln\left(r+\sqrt{r^2+b^2}\right)\right]_{a_1}^{a_2} \\ &= \mu_\circ \lambda J b \left[\ln\left(a_2+\sqrt{a_2^2+b^2}\right) - \ln\left(a_1+\sqrt{a_1^2+b^2}\right)\right] \\ &= \mu_\circ \lambda J a_1 \left(\frac{b}{a_1}\right) \ln\left[\frac{a_2/a_1+\sqrt{(a_2/a_1)^2+(b/a_1)^2}}{(a_1/a_1)+\sqrt{(a_1/a_1)^2+(b/a_1)^2}}\right] \end{aligned} \qquad (S1.1)$$

With $a_2/a_1 = \alpha$ and $b/a_1 = \beta$, Eq. $S1.1$ becomes:

$$B_z(0,0) = \mu_\circ \lambda J a_1 \beta \ln\left[\frac{\alpha+\sqrt{\alpha^2+\beta^2}}{1+\sqrt{1+\beta^2}}\right] \qquad (S1.2)$$

Thus:

$$B_z(0,0) = \mu_\circ \lambda J a_1 F(\alpha,\beta) \qquad (3.109)$$

$$F(\alpha,\beta) = \beta \ln\left(\frac{\alpha+\sqrt{\alpha^2+\beta^2}}{1+\sqrt{1+\beta^2}}\right) \qquad (3.13b)$$

b) ***"Ring" Coil*** For a ring coil ($\alpha \to 1$; $\beta \to 0$), the logarithmic term in the right-hand side of Eq. 3.110 becomes:

$$\lim_{\beta\to 0} \ln\left(\frac{\alpha+\sqrt{\alpha^2+\beta^2}}{1+\sqrt{1+\beta^2}}\right) = \ln\alpha$$

In the limit $\alpha \to 1$, $\ln\alpha \to \alpha - 1$, because $\ln(1+\epsilon) = \epsilon$ for $|\epsilon| \ll 1$. Thus:

$$B_z(0,0) = \frac{\mu_\circ NI}{2a_1(\alpha-1)}(\alpha-1) = \frac{\mu_\circ NI}{2a_1} \qquad (3.111a)$$

Note that Eq. $3.111a$, except for $\mu_\circ$, is equivalent to Eq. $3.3a$ evaluated at $z = 0$, with a and I replaced, respectively, by a_1 and NI.

Solution to PROBLEM 3.1 (continuation)

"Thin-Walled" Solenoid For a thin-walled solenoid ($\alpha \to 1$), we can combine Eqs. 3.13*b* and 3.23*b* to obtain:

$$\lim_{\alpha\to 1} \ln\left(\frac{\alpha+\sqrt{\alpha^2+\beta^2}}{1+\sqrt{1+\beta^2}}\right) = \frac{\alpha-1}{\sqrt{1+\beta^2}} \qquad (S1.3)$$

Combining Eqs. 3.110 and *S*1.3, we derive Eq. 3.111*b*; and from Eqs. 3.109, 3.13*b*, and *S*1.3, Eq. 3.111*c*:

$$B_z(0,0) = \frac{\mu_\circ NI}{2a_1}\left(\frac{1}{\sqrt{1+\beta^2}}\right) \qquad (3.111b)$$

$$B_z(0,0) = \mu_\circ \lambda J a_1(\alpha-1)\frac{\beta}{\sqrt{1+\beta^2}} \qquad (3.111c)$$

Note that for a "long" solenoid ($\beta \gg 1$), Eq. 3.111*c* becomes Eq. 3.111*e*.

"Long" Solenoid For $\beta \gg \alpha$, we have:

$$\lim_{\beta\gg\alpha} \ln\left(\frac{\alpha+\sqrt{\alpha^2+\beta^2}}{1+\sqrt{1+\beta^2}}\right) = \ln\left(\frac{\alpha+\beta}{1+\beta}\right) = \ln\left(\frac{\alpha/\beta+1}{1/\beta+1}\right)$$

The same approximation in ***"Ring" Coil***, $\ln(1+\epsilon)=\epsilon$ for $|\epsilon| \ll 1$, may be used:

$$\lim_{\beta\gg\alpha} \ln\left(\frac{\alpha/\beta+1}{1/\beta+1}\right) \simeq \frac{\alpha}{\beta} - \frac{1}{\beta} = \frac{\alpha-1}{\beta}$$

In the limit $\beta \gg \alpha$, we thus obtain:

$$B_z(0,0) = \frac{\mu_\circ NI}{2b} \qquad (3.111d)$$

As remarked above, $NI/2b$ may be considered a surface current density. From Eq. 3.108, $NI/(2b) = \lambda J(a_2 - a_1)$, Eq. 3.111*d* may also be expressed as:

$$B_z(0,0) = \mu_\circ \lambda J a_1(\alpha-1) \qquad (3.111e)$$

For a long solenoid, the center field is independent of its length (β)—this virtual independency of $B_z(0,0)$ on β for "large" $\beta\,(>\sim 3)$ and "moderate" $\alpha\,(<\beta)$ is evident from $F(\alpha,\beta)$ vs. β plots (Fig. 3.17b). Also, $B_z(0,0)$ is proportional to the winding build, $(a_2 - a_1)$, which makes perfect sense because the greater the winding build, the greater is the total ampere-turns per unit length—this is evident from $F(\alpha,\beta)$ vs. α plots for large β and moderate $\alpha\,(<\beta)$ shown in Fig. 3.17a.

"Pancake" Coil For a "pancake" coil, the appropriate limit is $\beta \to 0$:

$$\lim_{\beta\to 0} \ln\left(\frac{\alpha+\sqrt{\alpha^2+\beta^2}}{1+\sqrt{1+\beta^2}}\right) = \ln\left(\frac{2\alpha}{2}\right) = \ln\alpha$$

$$B_z(0,0) = \frac{\mu_\circ NI}{2a_1}\left(\frac{\ln\alpha}{\alpha-1}\right) \qquad (3.111f)$$

Note that the central field of a pancake coil is equal to that of a "ring" coil times a factor $\ln\alpha/(\alpha-1)$. In the limit $\alpha \to 1$, Eq. 3.111*f* reduces to Eq. 3.111*a*.

Solution to PROBLEM 3.1 (continuation)

c) Total conductor volume is equal to $\lambda \times$ <winding volume>:

$$<\text{winding volume}> = 2b\pi(a_2^2 - a_1^2) = a_1^3 2\pi\beta(\alpha^2 - 1)$$

And thus:

$$P = \rho_{cd} J^2 \lambda a_1^3 2\pi\beta(\alpha^2 - 1) \tag{3.112}$$

where J is the current density in the conductor only. From Eq. 3.112, we can solve for J in terms of P and other parameters:

$$J = \sqrt{\frac{P}{\rho_{cd}\lambda a_1}} \left[\frac{1}{a_1\sqrt{2\pi\beta(\alpha^2 - 1)}} \right] \tag{S1.4}$$

Combining Eqs. $S1.2$ and $S1.4$, we obtain:

$$B_z(0,0) = \mu_\circ \lambda \sqrt{\frac{P}{\rho_{cd}\lambda a_1}} \left[\frac{1}{a_1\sqrt{2\pi\beta(\alpha^2 - 1)}} \right] a_1 \beta \ln\left(\frac{\alpha + \sqrt{\alpha^2 + \beta^2}}{1 + \sqrt{1 + \beta^2}} \right)$$

$$= \mu_\circ \sqrt{\frac{\lambda P}{\rho_{cd} a_1}} \sqrt{\frac{\beta}{2\pi(\alpha^2 - 1)}} \ln\left(\frac{\alpha + \sqrt{\alpha^2 + \beta^2}}{1 + \sqrt{1 + \beta^2}} \right)$$

Thus:

$$B_z(0,0) = \mu_\circ G(\alpha,\beta) \sqrt{\frac{\lambda P}{\rho_{cd} a_1}} \tag{3.113a}$$

$$G(\alpha,\beta) = \sqrt{\frac{\beta}{2\pi(\alpha^2 - 1)}} \ln\left(\frac{\alpha + \sqrt{\alpha^2 + \beta^2}}{1 + \sqrt{1 + \beta^2}} \right) \tag{3.113b}$$

Equation 3.113a implies that in resistive solenoids the required power P for a given set of α and β, increases *quadratically* with the central magnetic field:

$$P = \frac{\rho_{cu} a_1 B_z^2(0,0)}{\mu_\circ^2 \lambda G^2(\alpha,\beta)} \tag{3.113c}$$

My Magnets (Part 2 of 3 Parts)

—Passage from Francis Bitter's *Magnets: The Education of a Physicist*

. . . By using a variable-size wire in the construction of a coil, I found it possible to increase the magnetic field at the center by a factor of just 1.52 over the best design for a coil with a uniform winding. Therefore, by going into all kinds of practical complications, one could improve the performance of coils only one and a half times or a little more. However, this now was settled; there was no use worrying about it any more. In the end these calculations did show me a practical way of improving the performance of coils by an appreciable amount.

DISCUSSION 3.2 "Bitter" Magnet

Although this book deals primarily with superconducting magnets, here we discuss the iron-free, water-cooled electromagnet. We may call the development of DC high-field, water-cooled ("water") magnet—"Bitter" magnet—that Francis Bitter initiated at M.I.T. in the 1930s as the basis for modern magnet technology. *Passages* from his book *Magnets* [3.4] are placed in this chapter to describe, in his own words, the technical challenges and solutions for high-field magnets, including pulse magnets of Kapitza, and a chronology of Bitter's activities in the 1930s.

Bitter's design employed a conductor in the form of a stack of annular plates, each with a slit and separated by a thin sheet of insulation except over a sector. The slit allows the bare sector to pressure-contact the next plate's bare sector, enabling the current to commutate from one plate to the next in a quasi-helical path as it flows from one end of the stack to the other. Each "Bitter" plate is punched with hundreds of cooling holes. To generate a high field, tens of thousands of amperes of current are pushed through the electrically resistive stack, consuming megawatts of electrical power, which heat the stack. This heat is removed by water forced through the cooling holes at high velocity, $\sim$20 m/s. A silhouette of two nested "Florida-Bitter" plates, developed in the 1990s at the National High Magnetic Field Laboratory (NHMFL), is shown in Fig. 3.18 [3.9]. A radial slit in each plate is clearly visible. Also note that each water passage hole is not circular as in Bitter's plates; the elongated—in the direction of current—shape was first developed by Weggel at M.I.T. in the 1970s. The outer plate of the set here is 148 mm in diameter; plate sizes have been more than 400 mm in diameter. The sixteen large holes are for axially clamping the plates with tie rods. A key feature of the Bitter magnet construction is that it is modular, consisting of many similar plates. Plate thickness, mechanical properties, and electrical properties can be tailored to the axial position to optimize magnet performance.

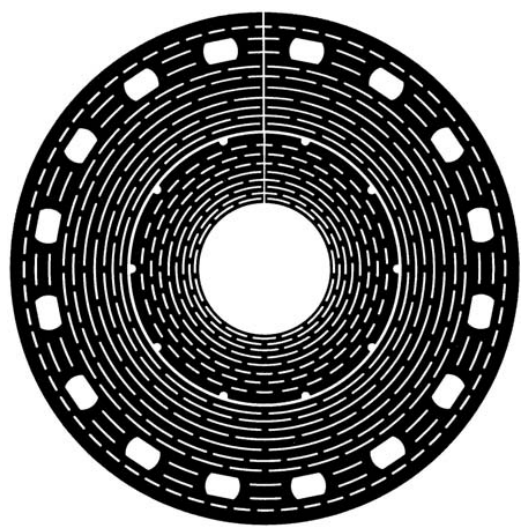

Fig. 3.18 Silhouette of two nested "Florida-Bitter" plates, with an outer plate of 140 mm in diameter, in "water" magnets at the National High Magnetic Field Laboratory [3.9].

DISCUSSION 3.2 Bitter Magnet (continuation)

As evident from Eq. 3.110 (**PROBLEM 3.1**), the smaller the inner winding radius, a_1, the higher the central field, $B_z(0,0)$, for a given total ampere-turns, NI. Also, for the same power consumption, P, reducing a_1 generates a higher $B_z(0,0)$ (Eq. 3.113a). That is, to maximize $B_z(0,0)$ for a given power, it is most efficient to place ampere-turns close to the magnet bore. The Bitter design, in which $J \propto 1/r$ (seen below), is a practical approach to approximate this goal.

A. Current Density, Field, Power

Here we derive expressions for $[J_\theta(r)]_B$ (current density), $[B_z(0,0)]_B$ (center field), $[F(\alpha,\beta)]_B$ (field-factor), and $[G(\alpha,\beta)]_B$ (G-factor) for the Bitter magnet.

Current Density Distribution

We consider a single disk, in which current flows in the θ-direction. The resulting E field gives a voltage V proportional to θ. Because $\vec{E}$ is only θ-directed (E_θ) and it is constant at a given r, $E_\theta 2\pi r = V$. That is, E_θ varies as $1/r$, and because $\vec{J} = \vec{E}/\rho_{cu}$, we have:

$$[J_\theta(r)]_B = \frac{E_\theta}{\rho_{cu}} = \frac{V}{2\pi\rho_{cu} r} = J_0 \frac{a_1}{r} \tag{3.114}$$

where $J_0 = [J_\theta(a_1)]_B = V/(2\pi\rho_{cu} a_1)$. Equation 3.114 shows that in the Bitter magnet current density decreases as $1/r$, with its maximum at $r = a_1$.

Field

We may substitute $J_\theta(r)$ given by Eq. 3.114 for λJ, a constant, in Eq. 3.107 and integrate over appropriate limits:

$$[B_z(0,0)]_B = \mu_\circ \lambda_B J_0 a_1 \int_{a_1}^{a_2}\int_0^b \frac{r\,dr\,dz}{(r^2+z^2)^{3/2}} = \mu_\circ \lambda_B J_0 a_1 \int_1^\alpha\int_0^\beta \frac{\eta\,d\eta\,d\zeta}{(\eta^2+\zeta^2)^{3/2}}$$

where $r/a_1 = \eta$ and $z/a_1 = \zeta$. From a table of integrals, we have:

$$\int_0^\beta \frac{d\zeta}{(\eta^2+\zeta^2)^{3/2}} = \left[\frac{\zeta}{\eta^2\sqrt{\eta^2+\zeta^2}}\right]_0^\beta = \frac{\beta}{\eta^2\sqrt{\eta^2+\beta^2}}$$

Combining the above two equations, we have:

$$[B_z(0,0)]_B = \mu_\circ \lambda_B J_0 a_1 \beta \int_1^\alpha \frac{\eta\,d\eta}{\eta^2\sqrt{\eta^2+\beta^2}} = \mu_\circ \lambda_B J_0 a_1 \beta \left[-\frac{1}{\beta}\ln\left(\frac{\beta+\sqrt{\beta^2+\eta^2}}{\eta}\right)\right]_1^\alpha$$

$$[B_z(0,0)]_B = \mu_\circ \lambda_B J_0 a_1 \ln\left(\alpha\frac{\beta+\sqrt{1+\beta^2}}{\beta+\sqrt{\alpha^2+\beta^2}}\right)$$

We may express the above expression as:

$$[B_z(0,0)]_B = \mu_\circ \lambda_B J_0 a_1 [F(\alpha,\beta)]_B \tag{3.115a}$$

$$[F(\alpha,\beta)]_B = \ln\left(\alpha\frac{\beta+\sqrt{1+\beta^2}}{\beta+\sqrt{\alpha^2+\beta^2}}\right) \tag{3.115b}$$

Note that there is a subtle difference between Eqs. 3.115b and 3.13b.

DISCUSSION 3.2 Bitter Magnet (continuation)

Field and Power

We may derive an expression relating $[H_z(0,0)]_B$ and P_B, the total power in the Bitter magnet, by integrating power density, $\rho_{cu}[J_\theta]_B^2(r)$, over the entire winding volume. Again, using dimensionless parameters, we have:

$$P_B = a_1^3 \int_1^\alpha \int_{-\beta}^{\beta} \rho_{cu}\lambda_B \left(\frac{J_0}{\eta}\right)^2 2\pi\eta \, d\zeta \, d\eta = J_0^2 \rho_{cu}\lambda_B a_1^3 (4\pi\beta \ln\alpha)$$

From the above expression, we may relate J_0 and P_B:

$$J_0 = \frac{1}{a_1\sqrt{4\pi\beta\ln\alpha}}\sqrt{\frac{P_B}{\rho_{cu}\lambda_B a_1}}$$

and combine this with Eqs. 3.115 to relate $[B_z(0,0)]_B$ and P_B:

$$[B_z(0,0)]_B = \mu_\circ [G(\alpha,\beta)]_B \sqrt{\frac{\lambda_B P_B}{\rho_{cu} a_1}} \tag{3.116a}$$

where

$$[G(\alpha,\beta)]_B = \frac{1}{\sqrt{4\pi\beta\ln\alpha}}[F(\alpha,\beta)]_B \tag{3.116b}$$

As in uniform-current-density solenoids, $[B_z(0,0)]_B$ increases as the square root of P_B; P_B is a quadratic function of field. The maximum of $[G(\alpha,\beta)]_B$ occurs when $\alpha \simeq 6.42$ and $\beta \simeq 2.15$: $[G(6.4, 2.15)]_B \simeq 0.166$. $[G(\alpha,\beta)]_B$ is at least 99% of its peak value for $5 \le \alpha \le 9$ and $1.8 \le \beta \le 2.6$. That is, P_B for a given field is within 2% of minimum throughout this range of α and β. However, because field homogeneity for a given value of a_1 improves with $2b$ or β, most Bitter magnets have β values greater than 2.5, as in the magnet considered below.

Illustration We may apply Eq. 3.116 to compute P_B for a Bitter magnet of $2a_1 = 6\,\text{cm}$, $2a_2 = 40\,\text{cm}$, $2b = 22\,\text{cm}$, $\lambda_B = 0.8$, and $\rho_{cu} = 2\times10^{-6}\,\Omega\,\text{cm}$, generating $[B_z(0,0)]_B = 20\,\text{T}$. With $\alpha = (a_2/a_1) = 40/6 = 6.67$; $\beta = (b/a_1) = 22/6 = 3.67$,

$$[G(6.67, 3.67)]_B = \frac{1}{\sqrt{4\pi 3.67 \ln(6.67)}} \ln\left[6.67 \frac{3.67 + \sqrt{1+(3.67)^2}}{3.67 + \sqrt{(6.67)^2 + (3.67)^2}}\right] \simeq 0.159$$

We have an expression of P_B, similar to Eq. 3.113*c*, in terms of $[B_z(0,0)]_B$ and other parameters:

$$P_B = \frac{\rho_{cu} a_1 [B_z(0,0)]_B^2}{\mu_\circ^2 \lambda_B [G(\alpha,\beta)]_B^2}$$

$$= \frac{(2\times10^{-8}\,\Omega\,\text{m})(3\times10^{-2}\,\text{m})(20\,\text{T})^2}{(4\pi\times10^{-7}\,\text{H/m})^2(0.8)(0.159)^2} \simeq 7.5\ \text{MW}$$

This power is typical of 20-T Bitter magnets that were operated at the Francis Bitter National Magnet Laboratory.

DISCUSSION 3.2 Bitter Magnet (continuation)

B. Current Density Distributions Other Than "Bitter"

One important parameter in water-cooled magnets is field efficiency, defined as the square of the field at the magnet center divided by the total power input to the magnet: $[B_z(0,0)]_B^2/\mu_\circ^2 P_B$. As with uniform-current-density magnets, field efficiency defined for Bitter magnets is proportional to λ_B and $[G(\alpha,\beta)]_B^2$ and inversely proportional to a_1 and conductor resistivity ρ_{cu}.

We have considered two current density distributions so far: 1) uniform, $J(r,z) = J_\circ$, and 2) Bitter, $J(r,z) \propto 1/r$. The uniform distribution means J is independent of r and z. Superconducting magnets wound with "graded" conductors have $J(r)$ that changes with r in discrete steps. Those consisting of many nested coils, each of which is wound with a different conductor, also have $J(r)$ distributions that change in discrete steps. We describe here three other current distributions of interest for water-cooled magnets [3.3].

Kelvin Coil

The current density that gives the best field efficiency is known as the Kelvin distribution, $J_K(r,z)$:

$$J_K(r,z) \propto \frac{r}{(r^2+z^2)^{3/2}}$$

Its unique feature is that every portion of the Kelvin coil produces the same field per unit power. In comparison with a Kelvin coil, a uniform-current-density coil for the same total power produces 66% of field at the magnet center; for a Bitter coil, the ratio is 77%. It is not feasible to fabricate coils having the Kelvin current density.

Gaume

The Gaume distribution, $J_G(r,z)$, also gives a good field efficiency:

$$J_G(r,z) \propto \frac{1}{r}\left(\frac{1}{\sqrt{a_1^2+z^2}} - \frac{1}{\sqrt{a_2^2+z^2}}\right)$$

The Gaume coils make each turn produce the same field per unit power as every other turn. A Gaume coil produces 85% of the field of a Kelvin coil. The current distribution of Bitter coils often approximates to a degree the Gaume distribution. This is achieved by using thicker Bitter plates axially away from the magnet midplane: $J_B(r,z) \propto 1/r\delta(z)$, where $\delta(z)$ is the z-dependent plate thickness.

Polyhelix

A polyhelix coil consists of many nested single-layer coils, in which the current density of each layer is adjusted to maximize the field efficiency and/or to match the stress in each layer to its conductor strength:

$$J_P(r,z) \propto f(r)$$

A polyhelix coil of maximum efficiency, with $J_P(r,z) \propto 1/r^2$, generates 92% of a Kelvin coil field. In practice, because of the need to have many electrodes at both ends, polyhelix coils are considered more difficult to manufacture than Bitter coils.

PROBLEM 3.2: Maximum field in a solenoidal coil

Although the axial field at the center of a magnet is one of the parameters often specified by the magnet *user*, an equally important parameter for the *designer* is the maximum field to which the magnet is exposed. In a single solenoidal magnet, as may be inferred from Eq. 3.12*b*, the axial field at the midplane, $H_z(r,0)$, within the bore increases radially away from the axis. Indeed, the maximum field, H_m, axially directed, occurs at the midplane and innermost winding radius point: $H_m = H_z(a_1,0)$. In multi-coil magnets comprised of nested coils, the maximum field in any but the innermost coil, because of the fields generated by the remaining coils, is generally not axially directed and occurs at points away from $(a_1,0)$.

Again, this topic is treated here only to enhance the reader's understanding of field distribution of a simple solenoid. In an actual multi-coil magnet, one must rely on a code to compute the maximum field and its location for each coil.

a) Using expressions in **3.4**, show for a "thin-walled" coil ($\alpha=1$) an expression for $H_z(r,0)/H_z(0,0)=h_z(\xi)$, where $\xi=r/a_1$, is given by:

$$h_z(\xi) = 1 + \frac{3}{4(1+\beta^2)^2}\xi^2 + \frac{15(3-4\beta^2)}{64(1+\beta^2)^4}\xi^4 + \frac{35(5-20\beta^2+8\beta^4)}{256(1+\beta^2)^6}\xi^6 + \frac{315(35-280\beta^2+336\beta^4-64\beta^6)}{16384(1+\beta^2)^8}\xi^8 + \frac{693(63-840\beta^2+2016\beta^4-1152\beta^6+128\beta^8)}{65536(1+\beta^2)^{10}}\xi^{10} \tag{3.117a}$$

b) Also, show that for a "short" coil ($\beta=0$) an expression for $h_z(\xi)$ is given by:

$$h_z(\xi) = 1 + \frac{3(\alpha^2-1)}{8\alpha^2\ln\alpha}\xi^2 + \frac{45(\alpha^4-1)}{256\alpha^4\ln\alpha}\xi^4 + \frac{175(\alpha^6-1)}{1536\alpha^6\ln\alpha}\xi^6 + \frac{11025(\alpha^8-1)}{131072\alpha^8\ln\alpha}\xi^8 + \frac{43659(\alpha^{10}-1)}{655360\alpha^{10}\ln\alpha}\xi^{10} + \cdots \tag{3.117b}$$

c) Similarly, show for a "thin-walled and long" coil, $h_z(\xi)$ is given by:

$$h_z(\xi) \simeq 1 + \frac{3}{4\beta^4}\xi^2 - \frac{15}{16\beta^6}\xi^4 + \frac{35}{32\beta^8}\xi^6 - \frac{315}{256\beta^{10}}\xi^8 + \frac{693}{512\beta^{12}}\xi^{10} - \cdots \tag{3.117c}$$

d) Compute an *approximate* value of $H_m/H_z(0,0) \equiv h_m$ for a "thin-walled" ($\alpha=1$) and relatively short coil with $\beta=0.4$.

e) Calculate h_m for a pancake coil of $\alpha=2$ and $\beta\simeq 0$.

f) Determine h_m for a "thin-walled" and "long" coil of $\alpha=1$ and $\beta=2$.

Note that for a single solenoid of a set of any α and β values, $H_m/H_z(0,0)$ may be given by $h_z(\xi)$ obtained by combining Eqs. 3.12*b* and 3.14.

Solution to PROBLEM 3.2

a) When considering $H_z(r,0)$, which in the midplane is equivalent to $H_z(x,0)$ or $H_z(y,0)$, we use Eq. 3.12*b* where $\xi = x/a_1$, $\xi = y/a_1$, or $\xi = r/a_1$. For a "thin-walled" solenoid, we may then combine Eqs. 3.12*b* and 3.25 to obtain Eq. 3.117*a*.

b) Similarly, Eq. 3.117*b* may be obtained by combining Eqs. 3.12*b* and 3.21.

c) We obtain Eq. 3.117*c* by combining Eqs. 3.12*b* and 3.26. Note that unlike Eq. 3.117*b* in which the signs of the higher terms are all pluses, the signs in Eq. 3.117*c* alternate.

d) Inserting $\beta = 0.4$ and $\xi = 1$ into Eq. 3.117*a*, we obtain:

$$h_m = 1 + 0.5574 + 0.3055 + 0.1125 - 0.0086 - 0.0585 = 1.9082$$

The $H_m/H_z(0,0)$ vs. α plots for constant values of β and $F(\alpha,\beta)$ by Montgomery [3.2], give a value of 1.87.

e) Inserting $\alpha = 2$ and $\xi = 1$ into Eq. 3.117*b*, we obtain:

$$h_m \simeq 1 + 0.4058 + 0.2378 + 0.1618 + 0.1209 + 0.0960 = 2.0222$$

f) Inserting $\beta = 2$ and $\xi = 1$ into Eq. 3.117*a*, we obtain:

$$h_m \simeq 1 + 0.03 - 0.0049 + 0.0005 + 0.0000 - 0.0000 = 1.0256$$

A quicker but less accurate solution may be obtained from Eq. 3.117*c*, which is really valid for $\beta \gg 1$:

$$h_m \simeq 1 + 0.0469 - 0.0146 + 0.0043 - 0.0012 + 0.0003 = 1.0356$$

My Magnets (Part 3 of 3 Parts)

—Passage from Francis Bitter's *Magnets: The Education of a Physicist*

The next point was to estimate how much heat could actually be removed from every square centimeter of surface. And here I ran into a great disappointment. The engineers of that time never had tried to remove a lot of heat from the surface . . . It seemed that water would be a suitable cooling medium. What would happen if the temperature of the pipes or holes through which the water flowed was at the boiling point of water, or above? Would steam layers be formed, such as are formed when you spit on a hot stove? . . . We discovered (from experiments) *that it was possible to take very much more heat out of every square centimeter of surface than had been recorded . . . We found that in turbulent flow any steam layer that is formed is immediately scooped up into the body of the liquid, the steam is condensed, and that heat is transferred to the liquid without the continued existence of the steam layer. An important number for my design was 200 watts per square centimeter . . . Rather than explore the possible limits to discover whether one could go even further, we decided to stop at this point and build magnets based on this figure.*

DISCUSSION 3.3: Load Lines

A. Solenoid Magnet Wound with "Isotropic" Superconductor

Figure 3.19 shows the critical current I_c vs. B curve of an "isotropic" superconductor at a constant temperature $T_\circ$, $I_c(B, T_\circ)$, and two sets of "load lines" for a solenoid magnet wound with the superconductor. Here, the $I_c(B, T_\circ)$ curve is isotropic, i.e., $I_c(B, T_\circ)$ is independent of field direction, the condition generally met with superconductors of circular cross section.

The load lines, solid and dashed, that emerge from the origin $(0, 0)$ correspond to the "self" fields of the magnet energized alone: the solid line corresponds to the axial center field, $B_z(0, 0)$, and the dashed line to the maximum field within the winding, B_{mx}—for a simple solenoid magnet B_{mx} occurs at the winding inside radius ($r = a_1$) and the axial midplane ($z = 0$), $B_{mx} = B_z(a_1, 0)$. The intercept of the $I_c(B, T_\circ)$ point and the dashed load line is the maximum operating current, $I_{op}(B_{mx}, T_\circ)$, achievable by this magnet, still fully superconducting.

When a magnet is placed in the bore of another magnet, the field generated by this "background-field" magnet must be added to the load lines of the inside magnet, the so-called "insert"—in a combined system the two magnets are generally coaxial with the midplanes coincident. The solid load line emerging from $B_{b\circ}$ on the B-axis corresponds to the center field of the combined system, while the dashed line to the maximum insert field—note that the dashed line starts from a field slightly greater than $B_{b\circ}$, because the background field there is greater; the intercept of the $I_c(B, T_\circ)$ point and the dashed line gives the maximum operating current, $I_{op}(B_{mxb}, T_\circ)$, for this combined magnet system.

For various reasons, some of which are discussed in later chapters, a superconducting magnet, alone or in a combined system, is generally designed to operate at a current 50–70% of its maximum possible current.

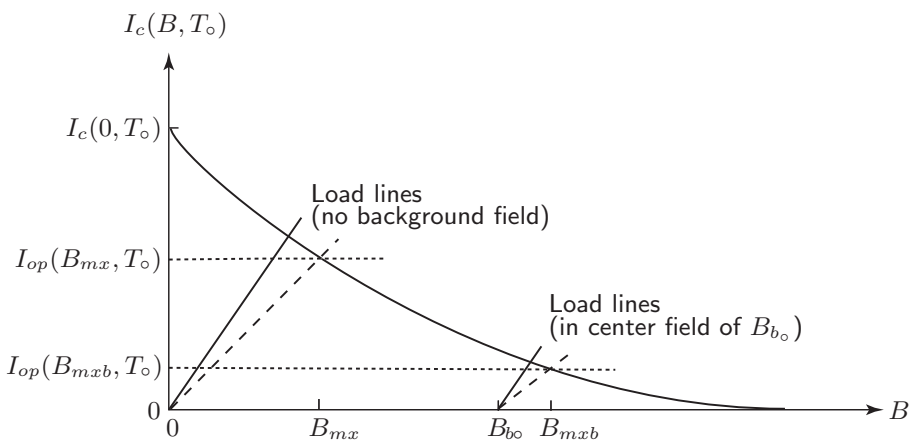

Fig. 3.19 Critical current I_c vs. B curve of an "isotropic" superconductor at a constant temperature $T_\circ$, $I_c(B, T_\circ)$, and two sets of "load lines" for a solenoid magnet, by itself and placed in the bore of another magnet generating a background center field of $B_{b\circ}$.

DISCUSSION 3.3: Load Lines (continuation)

B. Solenoid Magnet Wound with "Anisotropic" Superconductor

For noncircular-cross-section superconductors, $I_c(B, T_\circ)$ is generally "anisotropic," i.e., $I_c(B, T_\circ)$ depends on the field orientation relative to the cross section. Prominent examples of noncircular-cross-section superconductors are high-temperature superconductors, Bi2223 and YBCO, that are available only in tape form.

In ***APPENDIX V*** are presented $I_c(B,T)/I_c(sf, 77\,\mathrm{K})$ plots—$I_c(B,T)$ data normalized to $I_c(sf, 77\,\mathrm{K})$ data—for Bi2223 and YBCO, where sf stands for "self field," the field generated by the transport current alone; for each superconductor two sets of data are given, one in which the applied external field, B, is parallel ($B_\parallel$) to the tape superconductor's "broad" surface normal to the current direction, and the other in which B is perpendicular ($B_\perp$) to the surface. For both Bi2223 and YBCO, $I_c(B, T_\circ)$ decreases more sharply with $B_\perp$ than with $B_\parallel$. Also note that for both superconductors, $I_c(B)$, in both field directions, decreases more sharply with B at higher $T_\circ$.

As may be inferred from the field lines in Fig. 3.3 of a solenoid magnet, the radial component of the field, B_r, which is exactly zero at the solenoid axial midplane ($z=0$), increases in the $\pm z$ and r directions, with a peak radial field, $[B_r(\alpha,\beta)]_{pk}$, occurring at $z = \pm b$ and $a_1 < r < a_2$. No closed-form analytical expression of $[B_r(\alpha,\beta)]_{pk}$ exists. However, for *most* single solenoids, i.e., $1 \le \alpha \le 3.6$ and $0.1 \le \beta \le 10$, and for a preliminary (even before the *first-cut*) design of a tape-based magnet, e.g., a stack of "double-pancake" coils (***DISCUSSION 3.6***), Eq. 3.118 below gives $[B_r(\alpha,\beta)]_{pk}$ to within ±30% of those computed with a code.

$$\frac{[B_r(\alpha,\beta)]_{pk}}{B_z(0,0)} \approx \frac{0.3}{\alpha^2\beta} + \frac{0.6}{\alpha} \tag{3.118}$$

Note that for thin- and medium-walled ($\alpha \le 1.8$) and "short" ($\beta < 1$) solenoids, $[B_r(\alpha,\beta)]_{pk}$ can *exceed* $B_z(0,0)$, e.g., $[B_r(\alpha=1.1, \beta=0.1)]_{pk} \approx 3B_z(0,0)$!

In a tape-wound magnet, therefore, the intercept of a load line corresponding to the maximum perpendicular field, $B_\perp$, i.e., $[B_r(\alpha,\beta)]_{pk}$, and the conductor's $I_c(B_\perp, T_\circ)$ curve may limit its operating current rather than the maximum $B_\parallel$ ($= B_z$) load line corresponding to the $I_c(B_\parallel, T_\circ)$ curve. Also, because $B_\perp$ varies over the height of the tape (tape width) itself in the winding, this variation may have to be included in computing the maximum operating current. Voccio recently formulated an analytical approach to determine the maximum operating current for "pancake coils" wound with Bi2223 and YBCO tapes [3.10].

TRIVIA 3.2 Which one of the cooling water flow rates (liters/min) below is closest for a 31-T (24 MW) water magnet at the NHMFL?

i) 150,000; ii) 15,000; iii) 1,500; iv) 150.

DISCUSSION 3.4: Superposition Technique

The law of Biot-Savart as applied in solving field problems essentially states that a magnetic field at a point in a solenoid is the vector sum (superposition) of fields generated by all current elements within the solenoid. Here we apply a superposition technique to the entire body of a solenoid and compute the axial field at any point on the axis of a solenoid. This technique, though limited to the field on the axis only, is introduced to enhance the reader's general understanding of field generation by a solenoid.

A. End Field

The axial end field of an axially symmetric solenoid is half the *center field* of a solenoid of *identical* composition but twice the length of the original. We may visualize this by considering an axially symmetric solenoid comprised of two identical sections, each of the original length $2b$ (Fig. 3.20). The axial center field of the new solenoid is the sum of two equal fields, generated by the two sections:

$$H(b) = H(\alpha,\beta)|_{z=b} = \tfrac{1}{2}H(\alpha,2\beta)|_{z=0} = \tfrac{1}{2}\lambda J a_1\,[F\,(\alpha,2\beta)] \qquad (3.119)$$

Because $F(\alpha,2\beta) > F(\alpha,\beta)$ (Fig. 3.17*b*), it follows that $H(z=b) > 0.5H(0)$. That is, the end axial field of a solenoid is always greater than half its central field. Note that $H(z=b) \to 0.5H(0)$ in the limit $\beta \to \infty$.

B. Off-Center Axial Fields

The technique may also be applied to compute the axial field at any location along the solenoid axis. Two off-center cases are considered here: 1) $0 < z < b$, i.e., within the solenoid bore; and 2) $z > b$, i.e., outside the bore. Figure 3.21 illustrates the procedure for applying this superposition technique for each case. We thus have:

$$\text{(Case 1: } z<b) \quad H(z) = \tfrac{1}{2}\lambda J a_1 \left[F\left(\alpha,\beta=\frac{b+z}{a_1}\right) + F\left(\alpha,\beta=\frac{b-z}{a_1}\right)\right] \qquad (3.120a)$$

$$\text{(Case 2: } z>b) \quad H(z) = \tfrac{1}{2}\lambda J a_1 \left[F\left(\alpha,\beta=\frac{b+z}{a_1}\right) - F\left(\alpha,\beta=\frac{z-b}{a_1}\right)\right] \qquad (3.120b)$$

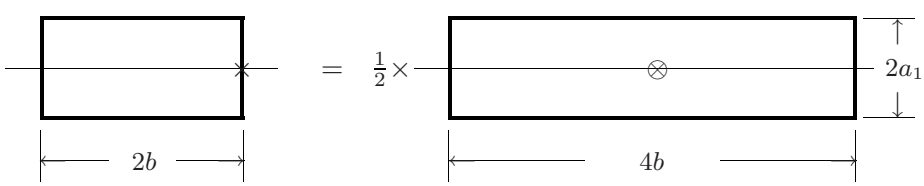

Fig. 3.20 In a superposition technique, the end field of an axially symmetric solenoid of length $2b$ may be computed as half of the center field of a solenoid of the same construction having length $4b$.

DISCUSSION 3.4: Superposition Technique (continuation)

Case 1: $z < b$

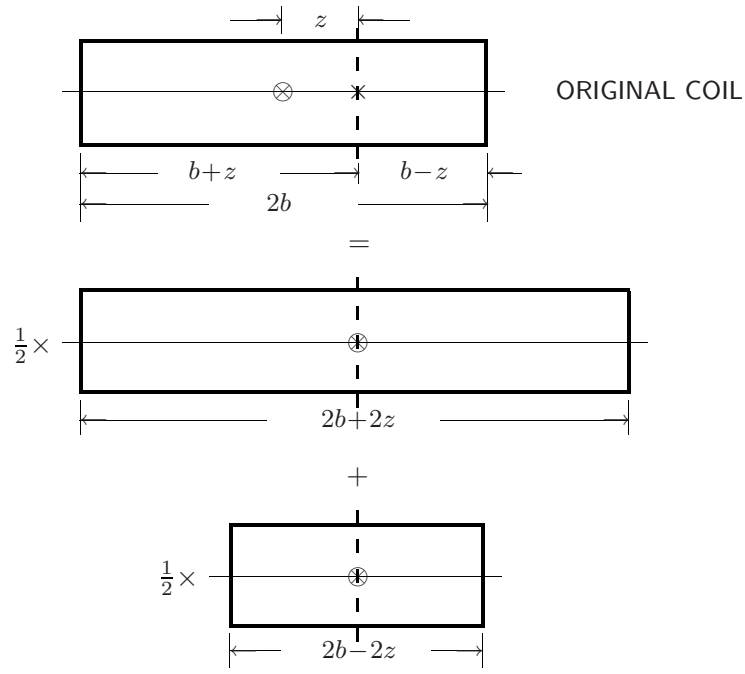

Case 2: $z > b$

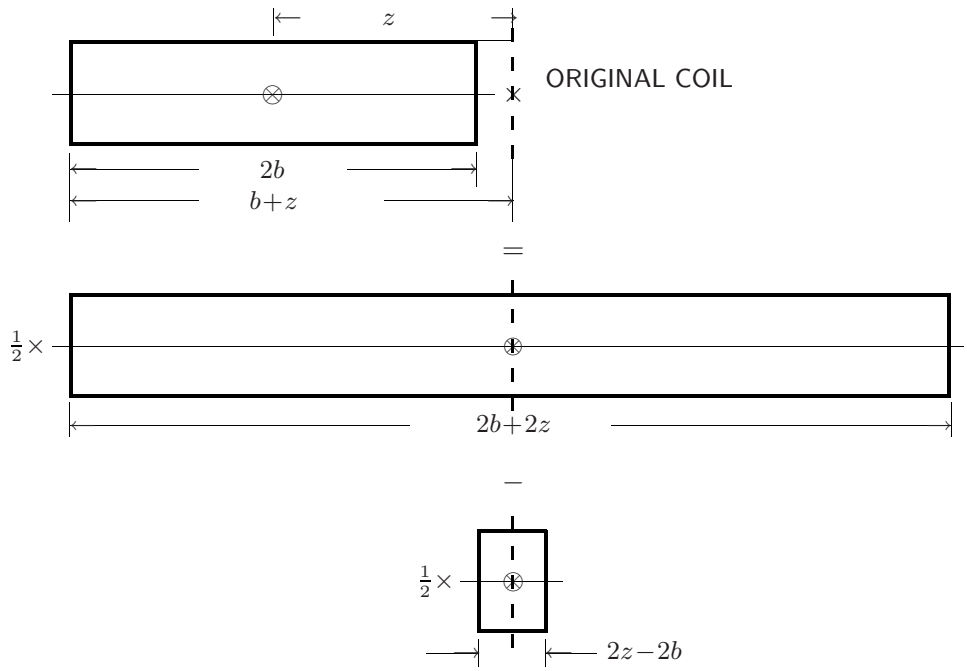

Fig. 3.21 Superposition technique for off-center axial points. Case 1: $z < b$; Case 2: $z > b$.

DISCUSSION 3.5: Hybrid Magnet

A "hybrid" magnet comprises two axially aligned and centered electromagnet "species:" a high-power water-cooled ("water") magnet in the bore of a superconducting magnet (SCM). It was conceived in the mid 1960s by Montgomery and others at the National Magnet Laboratory (NML) as a means to achieve DC fields above ∼25 T [3.11], the highest DC field achievable by Bitter magnets with the power of 9 MW then available. For the next three decades, the Magnet Lab contributed to the development of hybrid magnet technologies by designing, building, and operating several hybrid magnets [3.12–3.18].

A. Selected Hybrid Magnet Facilities

There are several hybrid magnet facilities now operating. Selected hybrid magnets are briefly described below in the chronological order of their operation.

High Field Magnet Laboratory, Radboud University, Nijmegen

Since 1977 the High Field Magnet Laboratory (HFML) at Nijmegen has operated two hybrid magnets, 25.4 T [3.12] and 32 T [3.14, 3.15], powered by a 6-MW supply [3.19]. With its newly installed 20-MW supply [3.20] and advanced "water" magnets [3.21], a 45-T hybrid magnet is scheduled to begin operation in 2012.

High Field Laboratory, Tohoku University, Sendai

In operation since 1983 with a 7.5-MW supply [3.22], the High Field Laboratory has replaced its 23-T "wet" hybrid with a "dry" version that generates 30 T [3.23].

For a *facility* hybrid magnet that must undergo many field-sweep sequences, its SCM should ideally be *dry* and of *HTS*. A dry cryostat avoids loss of liquid cryogen after a trip in its water-cooled magnet; an HTS magnet can tolerate a much greater rise in its operating temperature, caused by AC losses, than its LTS counterpart. ***CHAPTER 4*** discusses two design/operation options that should enable even a *dry* HTS magnet to operate reliably under the facility operation conditions of a hybrid magnet: 1) a volume of solid cryogen in the HTS magnet chamber; and 2) a cryocirculator (***DISCUSSION 4.7***) rather than a cryocooler as the primary cooling source for the SCM.

Grenoble High Magnetic Field Laboratory

The Grenoble Magnet Laboratory began its hybrid magnet operation in 1987 [3.24]. Its latest 24-MW supply [3.25] is for a 40-T hybrid magnet [3.26].

Magnet Laboratory, National Research Institute of Materials Science

In operation since 1995, the Magnet Laboratory at the National Institute of Materials Science at Tsukuba, with its 17-MW supply, operates 30–35 T hybrids [3.27].

National High Magnetic Field Laboratory (NHMFL)

The 45-T hybrid magnet [3.28, 3.29] of the National High Magnetic Field Laboratory (NHMFL) at Florida State University generates the highest DC magnetic field in the world. Currently, the water magnet generates 34 T and the SCM generates 11 T [3.30]. The SCM is discussed in more detail below.

DISCUSSION 3.5: Hybrid Magnet (continuation)

B. NHMFL 45-T Hybrid Magnet

Figure 3.22 shows a cross-sectional view of the "water" magnet, SCM, and some auxiliary components of the 45-T hybrid magnet at the NHMFL [3.31]. The water magnet has four nested coils; it generates a center field of 31 T at 24 MW. The SCM, consisting of three coils, A, B, and C, operated at 1.8 K, initially generated 14 T but now operates at 11 T [3.30]; the water magnet has been redesigned to contribute 34 T at 30 MW. The system includes a superfluid helium supply cryostat, to which the SCM cryostat is connected by a pipe, shown truncated at the right, middle of the figure.

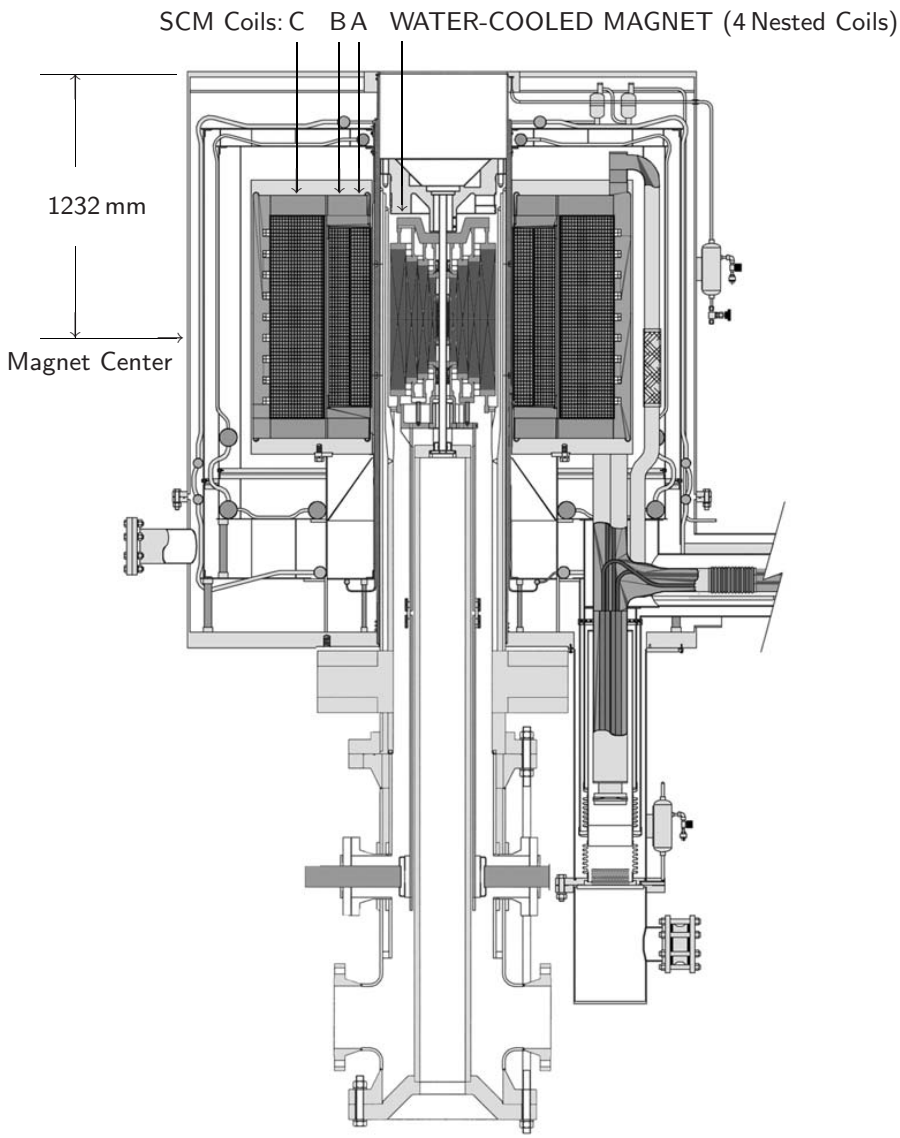

Fig. 3.22 Cross sectional view of the 45-T hybrid magnet at NHMFL [3.31].

DISCUSSION 3.5: Hybrid Magnet (continuation)

Table 3.3: Parameters of 14-T SCM for NHMFL 45-T Hybrid Magnet [3.31]

Coils (each wound with CIC conductor)		*Coil A*	*Coil B*	*Coil C*
Strand composite superconductor		Nb_3Sn		NbTi
Type of winding		Layer		Pancake
Number of layers/double pancakes		6	7	29
Total number of turns		306	378	1015
Winding i.d., $2a_1$	[mm]	710	908	1150
Winding o.d., $2a_2$,	[mm]	888	1115	1680
Winding length, $2b$	[mm]	869	868	992
Operating current, I_{op}	[kA]	10*		
λJ @ I_{op}	[MA/m^2]	39.6*	44.3*	38.6*
Field contribution at center @ I_{op}	[T]	3.3*	3.6*	7.4*
B_{peak} @ I_{op} with water magnet idle	[T]	15.7*	11.7*	8.5*
Combined inductance	[H]	1.96		
Stored energy @ I_{op}	[MJ]	98*		

* Corresponds to operation at 10 kA; currently operated at 8 kA [3.30].

Parameters of the 45-T Hybrid SCM

Table 3.3 presents key parameters of the 45-T hybrid SCM [3.31]. The most notable feature of this SCM is its three coils, each wound with cable-in-conduit (CIC) conductor, which is discussed in ***CHAPTER 6***. The two inner coils, A and B, are layer-wound, while the outer coil, C, is a stack of 29 double-pancake coils.

C. Engineering Challenges of the Hybrid Magnet

Hybrid magnets are rare species, operated at only a half dozen or so major national laboratories. It is not a kind of magnet that is being built regularly, not even at a rate of one a year. It is certainly not a type of magnet that a group of engineers or physicists can or would build in a few months. Because of this rarity few engineers have actually participated in the design, manufacture, and operation of hybrid magnets. Nevertheless, because it combines two species of magnets in close proximity, one operating at room temperature and the other at liquid helium temperature, the two are tightly-coupled, electromagnetically and mechanically. Thus, in addition to engineering issues specific to each magnet, there is an important design and operation challenge unique to the hybrid magnet: transmission of a horrendously large interaction force on the cold SCM to the magnet structure at room temperature with the least heat load to the SCM cryostat. Although a hybrid magnet itself will not be encountered by most of the readers of this textbook, it offers salient design and operational issues that most magnet and cryogenic engineers may find instructive.

Generic topics related to hybrid magnets in the remainder of this chapter as well as in ***CHAPTERS 4, 6, 7,*** and ***8*** are derived chiefly from the 35-T hybrid magnet operated at M.I.T. until 1995 [3.16–3.18].

DISCUSSION 3.5: Hybrid Magnet (continuation)

D. Configuration & Unique Features

In a hybrid magnet, the superconducting magnet is *always* placed outside of its water magnet ("insert") and not the other way around. By this configuration, each component's features are optimized, as given below for each component.

"Water" Magnet

- In ***DISCUSSION 3.2***, it has been shown that the power requirement P_B for Bitter magnets is proportional to a_1 and $[B_z(0,0)]_B^2$ (from Eq. 3.116*a*) , with P_B typically in the 6∼30 MW range. A Bitter magnet is "power hungry," and it is best to minimize its overall volume: use it as an insert in a hybrid. However, because the stronger the field strength, the greater the magnetic stresses in the conductor, the conductor materials must be stronger, which are generally more resistive. Thus, $B_z(0,0) \propto \sqrt{P}$ (Eq. 3.113*a*) and $[B_z(0,0)]_B \propto \sqrt{P_B}$ (Eq. 3.116*a*) both become invalid at higher fields.
- Normal metals such as copper have no "intrinsic" field limit above which they cannot be used to build a magnet. However, as stated above, because those made of stronger materials require greater power, and equally demanding, the cooling that must match this increased Joule dissipation, the range 30–40 T is considered the limit for practical magnet facilities.

Superconducting Magnet

- Superconductors have fairly well-defined upper field limits above which they cannot remain superconducting. Thus it is best to place this magnet in the lower-field part of a hybrid: place it outside the "water" magnet.
- The total energy storage increases with magnet size, but the power required, chiefly for cryogenics, remains insignificant. A 100-MJ magnet does not require a 100-MW power supply; typically 10–100 kW supplies suffice.

Combination of these features makes it natural for a hybrid magnet to consist of a water-cooled insert surrounded by a superconducting magnet.

"We have learned that 'paper' hybrid magnets:
are always built with perfect superconductors;
can be built in perfect confidence with utmost materials;
are not subject to fatigue; never have shorts . . .;
have cryostats closed with zippers and are always vacuum tight;
provide unlimited experimental access; operate themselves;
. . . are always on schedule and within budget." —Mathias J. Leupold

DISCUSSION 3.5: Hybrid Magnet (continuation)

E. Interaction Force

A unique and demanding aspect of a hybrid magnet system arises from interactive forces between the insert magnet and the SCM. If the two magnets are aligned axially and radially, they exert no force on each other. However, relative displacements of their field centers result in forces of increasing magnitude. Axial displacements produce axial restoring forces—the magnets center themselves axially. Radial displacements of the field centers result in forces that increase the displacement, i.e., instability. Normally, forces are modest; careful design and construction can cope with them relatively easily. However, the failure of a necessarily high-performance water-cooled insert must be accepted as inevitable. In such a failure, large forces can suddenly develop from a field displacement created when part of the insert winding becomes shorted and ceases to produce field.

Although less demanding than the structural requirements to contain fault forces, magnet monitoring for electrical protection is also complicated because of magnetic coupling (mutual inductance) of the two systems. Obviously, each magnet and its power system must have electrical protection of some sort to prevent damage or injury if something goes wrong, but there are also strong electrical interactions between the two magnets which would not exist were they separate. **PROBLEMS 8.3** and **8.4** in ***CHAPTER 8*** discuss coil monitoring in more detail for magnets in general and for hybrid magnets in particular.

DISCUSSION 3.6: "Double-Pancake" vs. "Layer-Wound"

Of the two magnet winding techniques, one is commonly known as "double-pancake" or simply "pancake," and the other as "layer-wound." A double-pancake coil is generally wound with flat conductor, e.g., tape, and sometimes with "large" square- or rectangular-cross-sectioned conductor, e.g., CIC. Each is wound with a

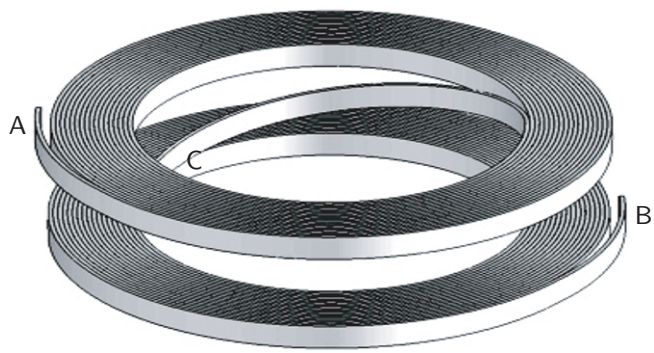

Fig. 3.23 Pictorial view of a double-pancake coil, with the top and bottom pancakes separated axially for clarity. The pancakes in this drawing are wound with a tape conductor. Points A and B indicate the ends of a continuous conductor, with Point C marking the approximate midpoint.

DISCUSSION 3.6: "Double-Pancake" vs. "Layer-Wound" (continuation)

continuous length of conductor. In a double-pancake coil, a schematic drawing of which is shown in Fig. 3.23, the starting point of the winding is the midpoint (approximately point C in Fig. 3.23) of the conductor; in a layer-wound coil, it is one end (A or B) of the conductor. Because the winding height ($2b$) of each double-pancake coil is about twice the conductor height (width in tape), a practical magnet requires multiple double-pancake coils, adjacent coils spliced in the radial space outside the outermost winding diameter ($2a_2$). A layer-wound coil, on the other hand, is wound continuously from one end to the other end of the conductor, layer by layer from the innermost layer to the outermost. Advantages and disadvantages of both techniques are discussed below.

Advantages & Disadvantages

1. For a double-pancake coil, the required length is much less than that for a full, splice-free layer-wound coil. A splice-free length as short as ∼50 m suffices for small coils. Even in a large magnet, a length of ∼1–2 km should be sufficient. In layer-wound coils, on the other hand, splice-free conductor can easily exceed 10 km in a single coil. Because longer conductors are generally more difficult to manufacture than shorter conductors, in terms of conductor length, a pancake coil is preferable to a layer-wound coil.

2. A pancake magnet generally requires many double-pancake coils, each of which ideally is an identical module, to build up the magnet winding height. This *modular* magnet construction approach, together with conductor length requirement stated above, makes manufacturing of a pancake magnet easier (and probably less expensive) than that of a layer-wound counterpart. Also, one catastrophic mistake during the winding process that can potentially render the entire stock unusable in a layer-wound coil will affect only one spool needed for one double-pancake. Because both electromagnetic performance and dimensions of each completed double-pancake can be slightly different, another advantage of the pancake technique is that it enables placement of each double-pancake coil at its most suitable location along the magnet axis.

3. One clear disadvantage of the pancake technique is the unavoidable need for splices between adjacent double-pancakes. Splicing is an added process in the manufacturing, made more difficult than a simple conductor splice because the splice here has to conform to the curvature of the winding. Perhaps more importantly from operation, these splices generate unwanted Joule dissipation, unless they are superconducting. Magnets for NMR and MRI generally require superconducting splices. To make a superconducting splice could be a challenge itself; to ascertain that each splice is indeed superconducting is also not an easy task.

Answer to TRIVIA 3.2 ii). Corresponds to a net temperature rise of ∼25°C. Note that this 17-MW dissipation must obviously be matched by a cooling power of 17 MW. It has been suggested, half in jest, that a water-cooled magnet is a zero-efficiency machine.

PROBLEM 3.3: Helmholtz coil*

Highly uniform magnetic fields are desirable in many applications. An arrangement known as the "Helmholtz coil" achieves a high uniformity of the field over a limited region of space by simple means. It uses two identical coils spaced coaxially a distance d apart (Fig. 3.24a) in the magnet axis (z-direction); the coils are located, respectively, at $z = d/2$ and $z = -d/2$. The spacing d in the Helmholtz coil is adjusted to make at the magnet center ($r = 0, z = 0$):

$$\left.\frac{d^2 H_z(0,z)}{dz^2}\right|_{z=0} = 0 \tag{3.121}$$

a) Idealizing the two coils by two "rings" each of radius a, show that when $d = a$, $dH_z^2(0,z)/dz^2 = 0$ at the magnet center. The solid curve in Fig. 3.24b gives $H_z(0,z)$ of a coil with d that does not satisfy Eq. 3.121.

b) Show that with coils of opposing polarity, a gradient field is generated at the magnet center. Evaluate this dH_z/dz at $z = 0$. (Note that $d^3 H_z(0,z)/dz^3 \neq 0$ when $d = a$; $d^3 H_z(0,z)/dz^3 = 0$ requires $d = \sqrt{3}a$.) This configuration with reverse current is called a Maxwell coil. The dotted curve in Fig. 3.24b gives $H_z(z)$ of a gradient coil.

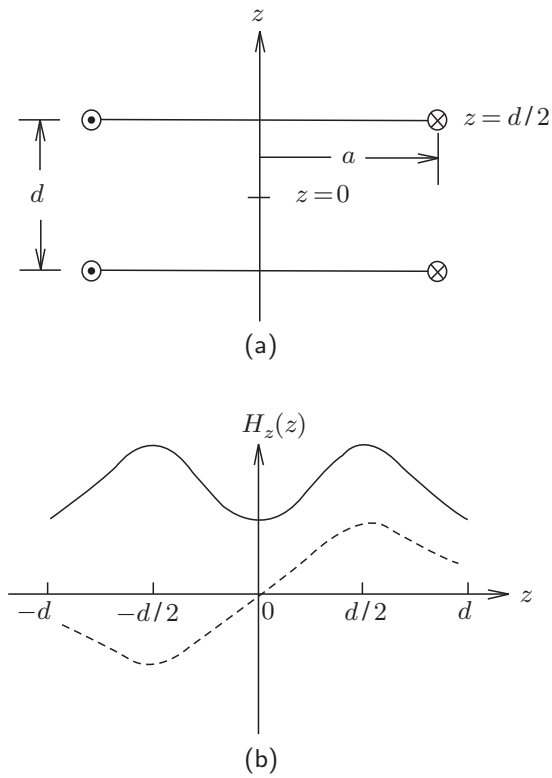

Fig. 3.24 (a) Ideal Helmholtz coil arrangement; (b) $H_z(0,z)$ for a "uniform" field case (solid) and $H_z(0,z)$ for a "gradient" field case (dotted).

* **Problem 3.4** in the 1st Edition (Plenum, 1994).

Solution to PROBLEM 3.3

a) The z-component of magnetic field along the axis ($r=0$) due to the bottom loop, located at $z=-d/2$, may be given by Eq. 3.3a:

$$H_z(0,z) = \frac{a^2 I}{2[a^2+(z+d/2)^2]^{3/2}}$$

Adding the field from the top coil, located at $z=d/2$, we have:

$$H_z(0,z) = \frac{a^2 I}{2}\left\{\frac{1}{[a^2+(z+d/2)^2]^{3/2}} + \frac{1}{[a^2+(z-d/2)^2]^{3/2}}\right\} \qquad (S3.1)$$

Differentiating $H_z(z)$ given by Eq. $S3.1$ with respect to z, we have:

$$\frac{dH_z(0,z)}{dz} = \frac{3a^2 I}{2}\left\{-\frac{(z+d/2)}{[a^2+(z+d/2)^2]^{5/2}} - \frac{(z-d/2)}{[a^2+(z-d/2)^2]^{5/2}}\right\}$$

Note that from symmetry $dH_z(0,z)/dz=0$ at $z=0$ for any value of a.

The second derivative of Eq. $S3.1$ is given by:

$$\frac{d^2H_z(0,z)}{dz^2} = \frac{3a^2 I}{2}\left\{-\frac{a^2-4(z+d/2)^2}{[a^2+(z+d/2)^2]^{7/2}} - \frac{a^2-4(z-d/2)^2}{[a^2+(z-d/2)^2]^{7/2}}\right\}$$

The second derivative is zero at $z=0$ if $d=a$. This technique of locating two identical coils with axial spacing equal to the coil radius to produce a region of field homogeneity, here through the 2nd harmonic order, is one of the design principles used in MRI and other magnets requiring a high spatial field homogeneity.

b) For this system with the current polarity of the bottom coil reversed, we have:

$$H_z(0,z) = \frac{a^2 I}{2}\left\{-\frac{1}{[a^2+(z+d/2)^2]^{3/2}} + \frac{1}{[a^2+(z-d/2)^2]^{3/2}}\right\} \qquad (S3.2)$$

By symmetry, $H_z(z=0)=0$. Differentiating Eq. $S3.2$ with respect to z, we obtain:

$$\frac{dH_z(0,z)}{dz} = \frac{3a^2 I}{2}\left\{\frac{(z+d/2)}{[a^2+(z+d/2)^2]^{5/2}} - \frac{(z-d/2)}{[a^2+(z-d/2)^2]^{5/2}}\right\} \qquad (S3.3)$$

Evaluating Eq. $S3.3$ at $z=0$, we have:

$$\left.\frac{dH_z(0,z)}{dz}\right|_0 = \frac{3a^2 Id}{2[a^2+(d/2)^2]^{5/2}}$$

This method of locating two identical coils having opposite currents to achieve a field gradient is the basic principle used in magnets requiring a gradient field at the midplane. A pulsed magnet used in an MRI system to produce a gradient field (to extract spatial information for imaging) is one example.

PROBLEM 3.4: Analysis of a Helmholtz coil—another method

Here, we analyze the Helmholtz coil of **PROBLEM 3.3**, using Eqs. 3.16*a* and 3.22.

Show that for a Helmholtz pair comprised of two "ring" coils, Coils 1 and 2, each of radius a, located, respectively, at $\zeta(\equiv z/a)=+0.5$ and $\zeta=-0.5$, its axial field 2nd derivative at its center ($\zeta=0$), $d^2h_z(0)/d\zeta^2|_{1/2}$, expressed in a power series in ζ^{2n} converges to 0 as more terms are added. Because each coil is *not* evaluated at its *own* $\zeta=0$, the simplified expression of Eq. 3.17*b* cannot be used here.

Use up to the 20th term to compute $d^2h_z(0)/d\zeta^2|_{1/2}$. Note that $E_2(1,0)\ldots E_{10}(1,0)$ are given by Eq. 3.28. A technique used to derive $E_2(1,0)\ldots E_{10}(1,0)$ may be used to derive $E_{12}(\alpha,0)\ldots E_{20}(\alpha,0)$ from Eq. 3.15*b* and $f_{12}(\alpha,\beta)\ldots f_{20}(\alpha,\beta)$ given in ***APPENDIX IB***. In the limit $\beta\to 0$, the expansion of $1/(1+\beta^2)^{19.5}$ up to the β^{20} term, for example, results in the following expression:

$$\frac{1}{(1+\beta^2)^{19.5}} = 1-\tfrac{39}{2}\beta^2+\tfrac{39}{2}\cdot\tfrac{41}{2}\frac{\beta^4}{2!}-\tfrac{39}{2}\cdot\tfrac{41}{2}\cdot\tfrac{43}{2}\frac{\beta^6}{3!}+\cdots + \tfrac{39}{2}\cdot\tfrac{41}{2}\cdot\tfrac{43}{2}\cdot\tfrac{45}{2}\cdot\tfrac{47}{2}\cdot\tfrac{49}{2}\cdot\tfrac{51}{2}\cdot\tfrac{53}{2}\cdot\tfrac{55}{2}\cdot\tfrac{57}{2}\frac{\beta^{20}}{10!} \tag{3.122}$$

For $E_{12}(\alpha,0)\ldots E_{20}(\alpha,0)$, similar to $E_2(\alpha,0)\ldots E_{10}(\alpha,0)$ as in Eq. 3.21, we have:

$$E_{12}(\alpha,0)=\frac{7\cdot11\cdot13}{2^{12}}\cdot\frac{(\alpha^{12}-1)}{\alpha^{12}\ln\alpha}=\frac{1001(\alpha^{12}-1)}{4096\alpha^{12}\ln\alpha} \tag{3.123a}$$

$$E_{14}(\alpha,0)=-\frac{5\cdot9\cdot11\cdot13}{2^{12}\cdot7}\cdot\frac{(\alpha^{14}-1)}{\alpha^{14}\ln\alpha}=-\frac{6435(\alpha^{14}-1)}{28672\alpha^{14}\ln\alpha} \tag{3.123b}$$

$$E_{16}(\alpha,0)=\frac{5\cdot9\cdot11\cdot13\cdot17}{2^{19}}\cdot\frac{(\alpha^{16}-1)}{\alpha^{16}\ln\alpha}=\frac{109395(\alpha^{16}-1)}{524288\alpha^{16}\ln\alpha} \tag{3.123c}$$

$$E_{18}(\alpha,0)=-\frac{5\cdot11\cdot13\cdot17\cdot19}{2^{17}\cdot3^2}\cdot\frac{(\alpha^{18}-1)}{\alpha^{18}\ln\alpha}=-\frac{230945(\alpha^{18}-1)}{1179648\alpha^{18}\ln\alpha} \tag{3.123d}$$

$$E_{20}(\alpha,0)=\frac{3\cdot7\cdot11\cdot13\cdot17\cdot19}{2^{20}\cdot5}\cdot\frac{(\alpha^{20}-1)}{\alpha^{20}\ln\alpha}=\frac{969969(\alpha^{20}-1)}{5242880\alpha^{20}\ln\alpha} \tag{3.123e}$$

In the limit $\alpha\to 1$, Eqs. 3.123*a*–3.123*e* become:

$$E_{12}(1,0)=\frac{3003}{1024}=\frac{3\cdot7\cdot11\cdot13}{2^{10}}=\frac{3\cdot5\cdot7\cdot9\cdot11\cdot13}{2\cdot4\cdot6\cdot8\cdot10\cdot12}\simeq 2.933 \tag{3.124a}$$

$$E_{14}(1,0)=-\frac{6435}{2048}=-\frac{5\cdot9\cdot11\cdot13}{2^{11}}=-\frac{3\cdot5\cdot7\cdot9\cdot11\cdot13\cdot15}{2\cdot4\cdot6\cdot8\cdot10\cdot12\cdot14}\simeq -3.142 \tag{3.124b}$$

$$E_{16}(1,0)=\frac{109395}{32768}=\frac{5\cdot9\cdot11\cdot13\cdot17}{10^{15}}=\frac{3\cdot5\cdot7\cdot9\cdot11\cdot13\cdot15\cdot17}{2\cdot4\cdot6\cdot8\cdot10\cdot12\cdot14\cdot16}\simeq 3.338 \tag{3.124c}$$

$$E_{18}(1,0)=-\frac{230945}{65536}=\frac{5\cdot11\cdot13\cdot17\cdot19}{10^{16}}=-\frac{3\cdot5\cdot7\cdot9\cdot11\cdot13\cdot15\cdot17\cdot19}{2\cdot4\cdot6\cdot8\cdot10\cdot12\cdot14\cdot16\cdot18}\simeq -3.524 \tag{3.124d}$$

$$E_{20}(1,0)=\frac{969969}{262144}=\frac{3\cdot7\cdot11\cdot13\cdot17\cdot19}{10^{18}}=\frac{3\cdot5\cdot7\cdot9\cdot11\cdot13\cdot15\cdot17\cdot19\cdot21}{2\cdot4\cdot6\cdot8\cdot10\cdot12\cdot14\cdot16\cdot18\cdot20}\simeq 3.700 \tag{3.124e}$$

Solution to PROBLEM 3.4

$d^2h_z(\zeta)/d\zeta^2$ at $\zeta = 0$ due to Coil 1 at $\zeta = +0.5$, $d^2h_z(0)/d\zeta^2|_{1/2}$, is given by Eq. 3.16*a*:

$$\begin{aligned}\left.\frac{d^2h_z(0)}{d\zeta^2}\right|_{1/2} &= 2E_2(1,0) + 12E_4(1,0)\times(0.5)^2 + 30E_6(1,0)\times(0.5)^4 \\ &\quad + 56E_8(1,0)\times(0.5)^6 + 90E_{10}(1,0)\times(0.5)^8 \\ &\quad + 132E_{12}(1,0)\times(0.5)^{10} + 182E_{14}(1,0)\times(0.5)^{12} \\ &\quad + 240E_{16}(1,0)\times(0.5)^{14} + 306E_{18}(1,0)\times(0.5)^{16} \\ &\quad + 380E_{20}(1,0)\times(0.5)^{18} + \cdots \qquad (S4.1)\end{aligned}$$

Because Coil 2 (at $\zeta = -0.5$) gives numerically the same $d^2\zeta_z/d\zeta^2$ at $\zeta = 0.5$ as that of Coil 1 at $\zeta = 0.5$ given by $S4.1$, we have:

$$\begin{aligned}\left.\frac{d^2h_z(0)}{d\zeta^2}\right|_{1/2} &= 4\left(-\frac{3}{2}\right) + 24\left(\frac{15}{8}\right)(0.5)^2 + 60\left(-\frac{35}{16}\right)(0.5)^4 \\ &\quad + 112\left(\frac{315}{128}\right)(0.5)^6 + 180\left(-\frac{693}{256}\right)(0.5)^8 \\ &\quad + 264\left(\frac{3003}{1024}\right)(0.5)^{10} + 364\left(-\frac{6435}{2048}\right)(0.5)^{12} \\ &\quad + 480\left(\frac{109395}{32768}\right)(0.5)^{14} + 612\left(-\frac{230945}{65536}\right)(0.5)^{16} \\ &\quad + 760\left(\frac{969969}{262144}\right)(0.5)^{18} + \cdots \qquad (S4.2)\end{aligned}$$

We compute Eq. $S4.2$ as each higher term is added:

$$\begin{aligned}\left.\frac{d^2h_z(0)}{d\zeta^2}\right|_{1/2} &= -6 && \text{(only } E_2\text{)} \\ &= 5.25 && \text{(through } E_4\text{)} \\ &\simeq -2.9531 && \text{(through } E_6\text{)} \\ &\simeq 1.3535 && \text{(through } E_8\text{)} \\ &\simeq -0.5499 && \text{(through } E_{10}\text{)} \\ &\simeq 0.2062 && \text{(through } E_{12}\text{)} \\ &\simeq -0.0730 && \text{(through } E_{14}\text{)} \\ &\simeq 0.0248 && \text{(through } E_{16}\text{)} \\ &\simeq -0.0081 && \text{(through } E_{18}\text{)} \\ &\simeq 0.0026 && \text{(through } E_{20}\text{)}\end{aligned}$$

From the above, it is clear that $d^2h_z(0)/d\zeta^2|_{1/2} \to 0$ as more higher terms are added. Note that for a single ring coil placed at $\zeta = 0$: $d^2h_z(0)/d\zeta^2 = -3$.

PROBLEM 3.5 Analysis of a spatially homogeneous magnet

Figure 3.25 shows a schematic cross section of a spatially high field homogeneity magnet consisting of three coils, Coils 1–3. Coils 1 and 3 are identical and located below and above the middle coil, Coil 2, to enhance the homogeneity at the center (0,0). Key dimensions (in mm) are indicated in the figure. Each coil has the same $2a_1$ of 100 mm and the same overall current density, $\lambda J = 2.5147 \times 10^8$ A/m^2. Table 3.4 gives field parameters of the magnet computed with a computer code by Bobrov [3.32].

Table 3.4 Field Parameters

Parameters	*Value*
Center field, B_0 [T]	1.000
$d^2B/dz^2\|_0$ [T/cm^2]	0.4658×10^{-6}
$d^4B/dz^4\|_0$ [T/cm^4]	4.8450×10^{-5}
$d^6B/dz^6\|_0$ [T/cm^6]	1.0893×10^{-4}
$d^8B/dz^8\|_0$ [T/cm^8]	1.0789×10^{-4}

Figure 3.26 shows the same magnet represented by three coils, A, B, and C, each centered at (0,0). Coil A extends from Coil 1 to Coil 3, including the two gaps in between. Coil B is identical to Coil 2. Because in the new representation Coil 2 is represented twice, by Coils A and B, Coil C "subtracts" one of the two Coil 2's as well as the two gaps, with its current in the opposite direction from those of Coils A and B.

a) Verify that the coil configuration of Figs. 3.26 gives the same center field of $B_0 = 1.000$ T as the original coil configuration. Coils A, B, and C have the same overall current density, λJ.

$$B_0 = 1.000\,\mathrm{T} = \mu_\circ \lambda J a_1 [F_A(\alpha,\beta) + F_B(\alpha,\beta) - F_C(\alpha,\beta)] \tag{3.125}$$

b) Apply Eqs. 3.14 and 3.17, and using a handheld scientific calculator, compute, $d^2B/dz^2|_0$ and $d^4B/dz^4|_0$ for this magnet. The values should agree with those given in Table 3.4 computed with a code.

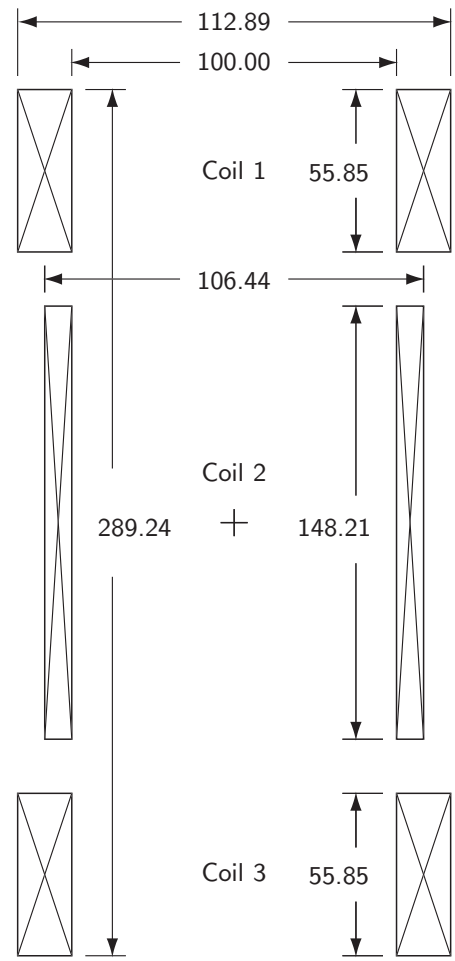

Fig. 3.25 Magnet comprised of 3 coils. Dimensions are in mm.

PROBLEM 3.5: Analysis of a spatially homogenous magnet (continuation)

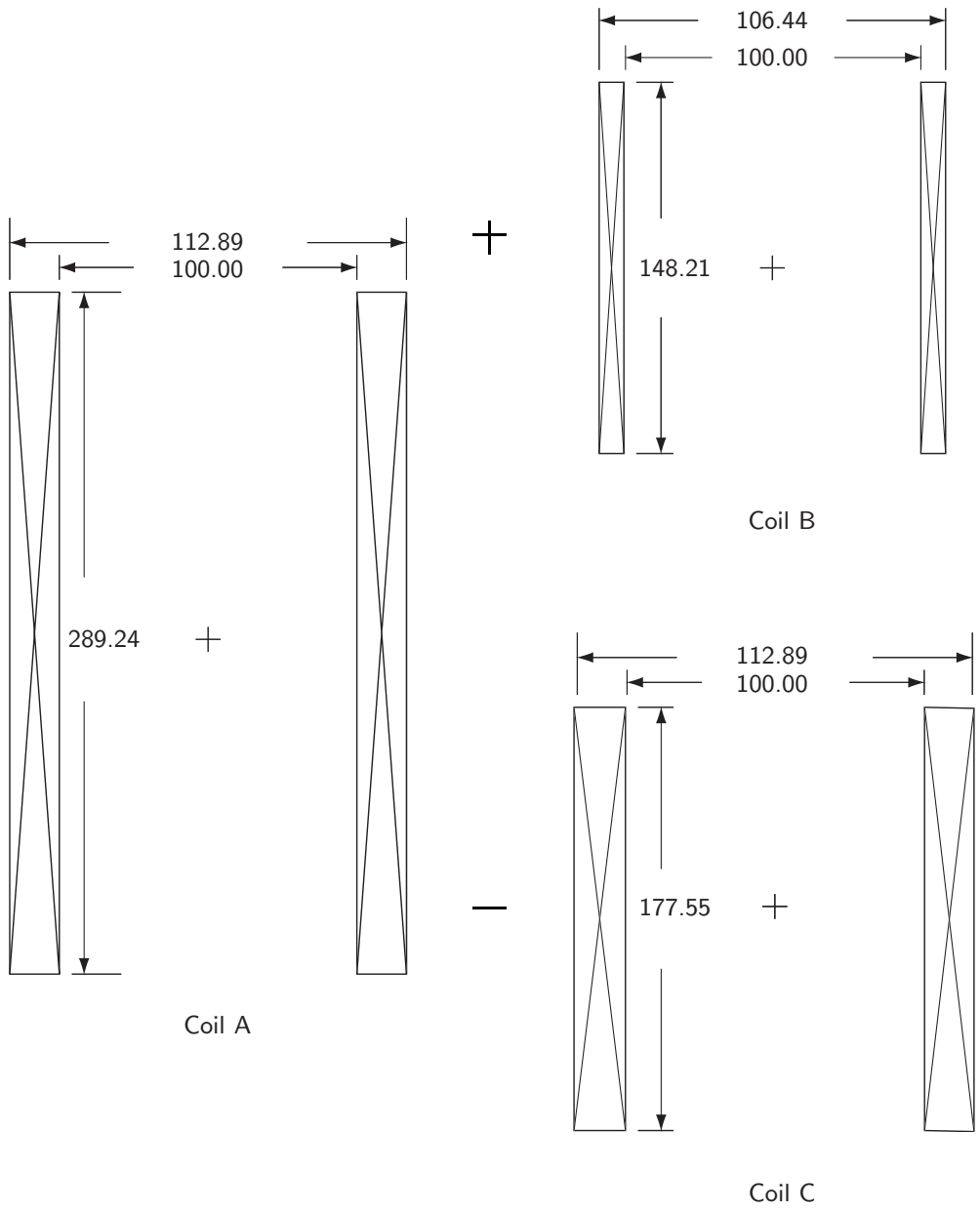

Fig. 3.26 The magnet of Fig. 3.25 represented by Coils A, B, and C, with each center at the magnet center. Note that the minus sign signifies that Coil C carries current in the direction opposite from those in Coils A and B. Dimensions are in mm.

Solution to PROBLEM 3.5

Table 3.5 lists appropriate values of α and β for Coils A, B, and C. Using these values, we obtain:

$$F_A(\alpha,\beta) = 0.12094421$$
$$F_B(\alpha,\beta) = 0.05287933$$
$$F_C(\alpha,\beta) = 0.11053327$$

Table 3.5 Field Parameters

Coils	α	β
A	1.12888	2.89244
B	1.06444	1.48212
C	1.12888	1.77548

a) From Eq. 3.125 we have:

$$B_0 = (4\pi\times10^{-7}\,\mathrm{H/m})(2.5147\times10^{8}\,\mathrm{A/m^2})(5\times10^{-2}\,\mathrm{m}) \times (0.12094421 + 0.05287933 - 0.11053327) = 1.000\,\mathrm{T}$$

b) Inserting α and β into Eqs. 3.14a and 3.14b1, we obtain:

$$F(\alpha,\beta)E_2(\alpha,\beta)_A = -0.002277367; \quad F(\alpha,\beta)E_4(\alpha,\beta)_A = -0.000315757$$
$$F(\alpha,\beta)E_2(\alpha,\beta)_B = -0.007938543; \quad F(\alpha,\beta)E_4(\alpha,\beta)_B = -0.001737981$$
$$F(\alpha,\beta)E_2(\alpha,\beta)_C = -0.010216278; \quad F(\alpha,\beta)E_4(\alpha,\beta)_C = -0.002133593$$

When all coils have the same a_1 and $\lambda J a_1$, Eq. 3.18 becomes:

$$h_\zeta(\zeta) = 1 + \frac{\sum_{j=1}^{k} F(\alpha_j,\beta_j)E_2(\alpha_j,\beta_j)}{\sum_{j=1}^{k} F(\alpha_j,\beta_j)}\zeta^2 + \cdots \qquad (S5.1)$$

$$E_2(\alpha,\beta) = \frac{F(\alpha,\beta)E_2(\alpha,\beta)_A + F(\alpha,\beta)E_2(\alpha,\beta)_B - F(\alpha,\beta)E_2(\alpha,\beta)_C}{F(\alpha,\beta)_A + F(\alpha,\beta)_B - F(\alpha,\beta)_C}$$
$$= \frac{-0.002277367 - 0.007938543 + 0.010216278}{0.120924421 + 0.05287933 - 0.11053327} = 0.000005822$$
$$E_4(\alpha,\beta) = \frac{-0.000315757 - 0.001737981 + 0.002132363}{0.06329027} = 0.001261725$$

We thus have:

$$\left.\frac{d^2B}{dz^2}\right|_0 = 2E_2\left(\frac{B_0}{a_1^2}\right) = 2(0.000005822)\frac{(1.000\,\mathrm{T})}{(5\,\mathrm{cm})^2} = 0.4658\times10^{-6}\,\mathrm{T/cm^2}$$

$$\left.\frac{d^4B}{dz^4}\right|_0 = 24E_4\left(\frac{B_0}{a_1^4}\right) = 24(0.001261725)\frac{(1.000\,\mathrm{T})}{(5\,\mathrm{cm})^4} = 4.8453\times10^{-5}\,\mathrm{T/cm^4}$$

These values are virtually identical with those in Table 3.4, though one must have diligence to compute each figure up to 9 decimal places.

It should be noted that the analysis presented here is useful, though tedious, for computing field gradient terms for a *given* magnet design. The analysis in this present form is impractical for designing a spatially high homogeneity magnet; it can, however, certainly be used as the basis for developing one's own design code.

PROBLEM 3.6: Field expansion in Cartesian coordinates*

In spherical coordinates (r, θ, φ) defined in Fig. 3.4, the magnetic field in the z-direction, H_z, in a source-free space generated by a magnet consisting of nested coils can be expressed by Eq. 3.9.

Show that expressions for $H_z(r, \theta, \varphi)$ in Cartesian coordinates, $H_z(x, y, z)$, for $n = 0$, 1, and 2 are given by:

$$n = 0 \quad H_z(x, y, z) = A_0^0 \tag{3.126a}$$

$$n = 1 \quad H_z(x, y, z) = A_0^0 + 2zA_1^0 + 3(A_1^1\, x + B_1^1\, y) \tag{3.126b}$$

$$\begin{aligned} n = 2 \quad H_z(x, y, z) = {} & A_0^0 + 2zA_1^0 + 3(A_1^1\, x + B_1^1\, y) \\ & + \tfrac{3}{2} A_2^0 (2z^2 - x^2 - y^2) + 12z(A_2^1\, x + B_2^1\, y) \\ & + 15[A_2^2\, (x^2 - y^2) + 2B_2^2\, xy] \end{aligned} \tag{3.126c}$$

---

* Based on **Problem 3.5** in the 1st Edition (Plenum, 1994).

Help from Van (Part 1 of 5 Parts)

—Passage from Francis Bitter's *Magnets: The Education of a Physicist*

And so the design of the first powerful water-cooled coils at M.I.T. gradually evolved. An interesting side light at this point was that a thorough search of the literature revealed that actually we were not the first to attempt to build coils along these lines. During World War I two Frenchmen tried to do the same sort of thing. They designed water-cooled coils and found that the only place they could conveniently get the power to operate them was in the private power station of one of the big department stores in Paris. But they had to stop work because of the war, and for about twenty years it was forgotten. My designs were quite different from theirs, and I decided to follow my own plans. Now I was faced with the same problem as the Frenchmen. If we did build some coils, where could we test them?

Throughout this period and up to the completion of the first magnets the chief person responsible for the realization of my ambitions was Vannevar Bush, at that time the Vice-President of M.I.T. He was interested in what I was doing, and gave it the needed backing. To begin with, after I had made some preliminary designs that looked reasonable, he suggested that I try them out at one of the substations of the Boston Edison Company. They had old-fashioned DC power stations which had spare power during the early hours of the morning. He arranged to have space made available for me to set up a magnet, and to get water cooling from the city water mains.

And so the first magnet was constructed in the basement of the physics building. It was to dissipate about 1000 kilowatts in a magnet having a volume of about one cubic foot (∼30 liters)*. If the water cooling should fail, the 1000 kilowatts dissipated in this volume would melt everything in it in a few seconds. Our water-cooling tests had indicated that the heating would not fail, that steam layers would not form and stop the cooling processes. But it was still an exciting time. When we set up the magnet at the Scotia Street substation of the Edison Company, the engineers were frankly skeptical. But because of Van Bush's backing they were willing enough to give me a chance to prove my ideas.*

Solution to PROBLEM 3.6

The spherical coordinate parameters, r, $u = \cos\theta$, $s = \sin\theta$, $\sin\varphi$, and $\cos\varphi$ are given in terms of x, y, and z:

$$r = \sqrt{x^2 + y^2 + z^2} \tag{S6.1a}$$

$$u = \cos\theta = \frac{z}{\sqrt{x^2 + y^2 + z^2}} \tag{S6.1b}$$

$$s = \sin\theta = \frac{\sqrt{x^2 + y^2}}{\sqrt{x^2 + y^2 + z^2}} \tag{S6.1c}$$

$$\sin\varphi = \frac{y}{\sqrt{x^2 + y^2}} \tag{S6.1d}$$

$$\cos\varphi = \frac{x}{\sqrt{x^2 + y^2}} \tag{S6.1e}$$

Equations 3.9 and $S6.1a$–$S6.1e$ are combined for cases $n = 0$, 1, and 2.

$n = 0$:

$$H_z(x, y, z) = \sum_{m=0}^{0} r^0(1+0)P_0^0(u)(A_0^0\cos 0 + B_0^0\sin 0) \tag{S6.2a}$$

$$= (1)(1)(1)(A_0^0) \tag{S6.2b}$$

For $n=0$, we thus have:

$$H_z(x, y, z) = A_0^0 \tag{3.126a}$$

Note that A_0^0 represents the magnet center field: $H_z(0, 0, 0)$.

$n = 1$:

$$H_z(x, y, z) = \sum_{m=0}^{1} r^1(2+m)P_1^m(A_1^m\cos m\varphi + B_1^m\sin m\varphi) \tag{S6.3a}$$

$$= r^1(2+0)P_1^0(A_1^0) + r^1(2+1)P_1^1(A_1^1\cos\varphi + B_1^1\sin\varphi)$$

$$= 2ruA_1^0 + 3rs(A_1^1\cos\varphi + B_1^1\sin\varphi)$$

$$= 2\sqrt{x^2+y^2+z^2}\,\frac{z}{\sqrt{x^2+y^2+z^2}}A_1^0$$

$$+ 3\sqrt{x^2+y^2+z^2}\,\frac{\sqrt{x^2+y^2}}{\sqrt{x^2+y^2+z^2}}\left(\frac{A_1^1\,x + B_1^1\,y}{\sqrt{x^2+y^2}}\right)$$

$$= 2zA_1^0 + 3(A_1^1\,x + B_1^1\,y) \tag{S6.3b}$$

TRIVIA 3.3 Which of the French mathematicians below chaired a commission to draw up a new system of measurements, out of which came the metric system?

i) Cauchy; ii) Fourier; iii) Lagrange; iv) Poisson.

Solution to PROBLEM 3.6 (continuation)

Thus for n up to 1, we have:

$$H_z(x,y,z) = A_0^0 + 2zA_1^0 + 3(A_1^1\,x + B_1^1\,y) \tag{3.126b}$$

Note that $H_z(x,y,z)$ contains terms up to those varying only as z, x, and y.

$n = 2$:

$$H_z(x,y,z) = \sum_{m=0}^{2} r^2(3+m)P_2^m(A_2^m\cos m\varphi + B_2^m \sin m\varphi) \tag{S6.4}$$

$$\begin{aligned} &= r^2(3+0)P_2^0(A_2^0) + r^2(3+1)P_2^1(A_2^1\cos\varphi + B_2^1\sin\varphi) \\ &\quad + r^2(3+2)P_2^2(A_2^2\cos 2\varphi + B_2^2\sin 2\varphi) \end{aligned}$$

$$\begin{aligned} H_z(x,y,z) &= 3(x^2+y^2+z^2)^{\frac{1}{2}}\left(\frac{2z^2-x^2-y^2}{x^2+y^2+z^2}\right)A_2^0 \\ &\quad + 4(x^2+y^2+z^2)\frac{3z\sqrt{x^2+y^2}}{x^2+y^2+z^2}\left(A_2^1\frac{x}{\sqrt{x^2+y^2}} + B_2^1\frac{y}{\sqrt{x^2+y^2}}\right) \\ &\quad + 5(x^2+y^2+z^2)\frac{3(x^2+y^2)}{x^2+y^2+z^2}\left[A_2^2\left(\frac{2x^2}{x^2+y^2}-1\right) + B_2^2\frac{2xy}{x^2+y^2}\right] \\ &= \tfrac{3}{2}A_2^0(2z^2-x^2-y^2) \\ &\quad + 12z(A_2^1\,x + B_2^1\,y) + 15[A_2^2(x^2-y^2) + 2B_2^2\,xy] \end{aligned} \tag{S6.4b}$$

Summing Eqs. $S6.2b$, $S6.3b$, and $S6.4b$, we have, for n up to 2:

$$\begin{aligned} H_z(x,y,z) &= A_0^0 + 2zA_1^0 + 3(A_1^1\,x + B_1^1\,y) \\ &\quad + \tfrac{3}{2}A_2^0(2z^2-x^2-y^2) + 12z(A_2^1\,x + B_2^1\,y) \\ &\quad + 15[A_2^2(x^2-y^2) + 2B_2^2\,xy] \end{aligned} \tag{3.126c}$$

Note that when evaluated for $n = 0$, 1, and 2, $H_z(x,y,z)$ contains terms varying as x, y, z, z^2, x^2, y^2, zx, zy, and xy.

"Ignorance is like a delicate exotic fruit; touch it and the bloom is gone."
—Lady Bracknell

PROBLEM 3.7: Notched solenoid*

The principle of the Helmholtz coil—to place current-carrying elements symmetrically about the solenoid center to create a spatially homogeneous field in the central zone—is the basis for notched solenoids. Many MRI and NMR magnets are variants of the notched solenoid design.

For a simple solenoid, with winding inner radius a_1, winding outer radius a_2, total winding length $2b$, and overall current density λJ, recall that the axial magnetic field at the center, $H_0 \equiv H_z(0,0)$, is given by Eqs. 3.13*a* and 3.13*b*:

$$H_0 = \lambda J a_1 F(\alpha, \beta) \tag{3.13a}$$

$$F(\alpha, \beta) = \beta \ln\left(\frac{\alpha + \sqrt{\alpha^2 + \beta^2}}{1 + \sqrt{1 + \beta^2}}\right) \tag{3.13b}$$

U**sing* symmetry considerations and the superposition technique presented in ***DISCUSSION 3.4, show that an expression for $H_z(0, z_1)$ of the notched solenoid having a uniform current density λJ shown in Fig. 3.27 is given by:

$$\begin{aligned} H_z(0, z_1) = {} & \tfrac{1}{2}\lambda J a_1 \Big[F(\alpha_1, \beta_1 + \gamma_1) + F(\alpha_1, \beta_1 - \gamma_1)\Big] \\ & - \tfrac{1}{2}\lambda J a_3 \Big[F(\alpha_2, \beta_2 + \gamma_2) + F(\alpha_2, \beta_2 - \gamma_2)\Big] \end{aligned} \tag{3.127}$$

where $\alpha_1 = a_2/a_1$, $\beta_1 = b_1/a_1$, $\gamma_1 = z_1/a_1$, $\alpha_2 = a_2/a_3$, $\beta_2 = b_2/a_3$, and $\gamma_2 = z_1/a_3$. The coil parameters, a_1, a_2, a_3, b_1, and b_2 are defined in Fig. 3.27.

A simple notched solenoid has too few degrees of freedom to zero more than a couple spatial homogeneity coefficients, but it is very good at zeroing those of 2nd and 4th order.

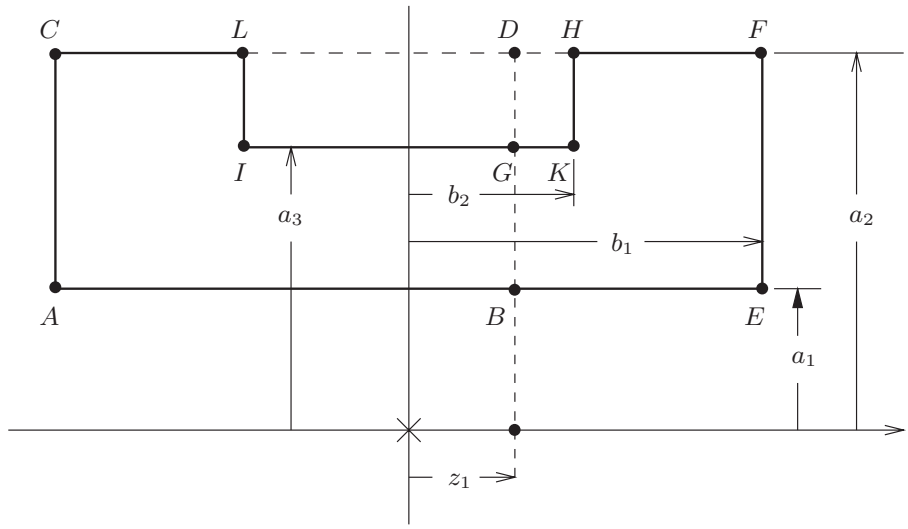

Fig. 3.27 Geometrical arrangement of a notched solenoid.

* **Problem 3.6** in the 1st Edition (Plenum, 1994).

Solution to PROBLEM 3.7

To solve $H_z(0,z_1)$, we may divide the solenoid into four single solenoids whose cross sections are designated by corner points as follows:

Solenoid 1: $ABDC$, with $\alpha_1 = a_2/a_1 = \alpha$ and $\beta_1 = (b_1+z_1)/a_1 = \beta+\gamma$, where $\beta = b_1/a_1$ and $\gamma = z_1/a_1$;

Solenoid 2: $BEFD$, with $\alpha_2 = a_2/a_1 = \alpha$ and $\beta_2 = (b_1-z_1)/a_1 = \beta-\gamma$;

Solenoid 3: $IGDL$, with $\alpha_3 = a_2/a_3 = \alpha'$ and $\beta_3 = (b_2+z_1)/a_3 = \beta'+\gamma'$, where $\beta' = b_2/a_3$ and $\gamma' = z_1/a_3$;

Solenoid 4: $GKHD$, with $\alpha_4 = a_2/a_3 = \alpha'$ and $\beta_4 = (b_2-z_1)/a_3 = \beta'-\gamma'$.

Note that in all solenoids J is of the same magnitude but in Solenoids 3 and 4 is of opposite sign relative to Solenoids 1 and 2. Also note that all solenoids are notchless.

Field from Solenoid 1: $H_z(0,z_1)$ from Solenoid 1, $2b = b_1+z_1$ long, is one-half of the center field of a solenoid, $2b = 2(b_1+z_1)$ long, having the same values of a_1, a_2, and λJ. This may be best seen by noting that the center field $H_z(0,0)$ of a notchless solenoid, $2b$ long, is the sum of the field generated by one-half of the solenoid (from 0 to $z=b$) and that generated by the other half (from $z=-b$ to 0). That is, each half of the solenoid generates 50% of the total field $H_z(0,0)$. Thus:

$$H_z(0,z_1)|_1 = \tfrac{1}{2}\lambda J a_1 F(\alpha, \beta+\gamma) \qquad (S7.1)$$

Field from Solenoid 2: At $(0,z_1)$, H_z from Solenoid 2, $2b = b_1 - z_1$ long, is one-half of the center field of a solenoid, $2b = 2(b_1-z_1)$ long, both solenoids having the same values of a_1, a_2, and λJ.

$$H_z(0,z_1)|_2 = \tfrac{1}{2}\lambda J a_1 F(\alpha, \beta-\gamma) \qquad (S7.2)$$

Field from Solenoid 3: At $(0,z_1)$, H_z from Solenoid 3, $2b = b_2+z_1$ long, is one-half of the center field of a solenoid having $2b = 2(b_2+z_1)$, both solenoids with the same values of a_3, a_2, and λJ. Because J is directed opposite to that of Solenoids 1 and 2, we have:

$$H_z(0,z_1)|_3 = -\tfrac{1}{2}\lambda J a_3 F(\alpha', \beta'+\gamma') \qquad (S7.3)$$

Field from Solenoid 4: At $(0,z_1)$, H_z from Solenoid 4, $2b = b_2 - z_1$ long, is one-half of the center field of a solenoid $2b = 2(b_2-z_1)$ long.

$$H_z(0,z_1)|_4 = -\tfrac{1}{2}\lambda J a_3 F(\alpha', \beta'-\gamma') \qquad (S7.4)$$

Field from the Notched Solenoid

$H_z(0,z_1)$ generated by the original notched solenoid is thus given by the sum of Eqs. $S7.1$–$S7.4$:

$$\begin{aligned} H_z(0,z_1) &= H_z(0,z_1)|_1 + H_z(0,z_1)|_2 + H_z(0,z_1)|_3 + H_z(0,z_1)|_4 \\ &= \tfrac{1}{2}\lambda J a_1 \Big[F(\alpha,\beta+\gamma) + F(\alpha,\beta-\gamma)\Big] \\ &\quad - \tfrac{1}{2}\lambda J a_3 \Big[F(\alpha',\beta'+\gamma') + F(\alpha',\beta'-\gamma')\Big] \end{aligned} \qquad (3.127)$$

DISCUSSION 3.7: Field Analysis of a Pancake-Coil Magnet

Applying the superposition technique of ***DISCUSSION 3.4***, we derive here expressions for axial field that may be used to compute field error coefficients of a solenoidal magnet comprised of $2N$ pancake coils (N double-pancake coils). With Bi2223 and YBCO that are available in tape form, a magnet comprised of pancake coils wound with HTS is a viable design option for spatially homogeneous magnets such as for NMR magnets [3.33, 3.34]. Pancake coils are ideal for conductors of "thin" rectangular cross sectional area.

In this analysis, each pancake is of identical dimensions—$2a_1$; $2a_2$; $2b = w$ (equal to conductor width)—and the same value of λJ in the pancake coil winding. Adjacent pancake coils are separated by a distance δ. Figure 3.28 shows a schematic drawing of the cross section of a magnet comprised of $2N$ single pancake coils.

In deriving field equations, all centered about the magnet origin, we use the following simplified notations. Here, using an abbreviated expression for $F(\alpha, \beta)/\beta$,

$$\frac{F(\alpha,\beta)}{\beta} \equiv \ln(\alpha,\beta) = \ln\left[\frac{\alpha + \sqrt{\alpha^2+\beta^2}}{1+\sqrt{1+\beta^2}}\right] \tag{3.128a}$$

we define a dimensionless axial magnetic field parameter, $\eta(\zeta) \equiv H(z)/(\lambda J a_1)$, where $\zeta \equiv z/a_1$, given by:

$$\eta(\zeta) \equiv \frac{H(z)}{\lambda J a_1} = \beta \ln(\alpha,\beta)\left[1 + \sum_{j=1}^{n} E_{2j}(\alpha,\beta)\zeta^{2j}\right] \tag{3.128b}$$

Because of the use of $\ln(\alpha, \beta)$, Eq. 3.128b is a dimensionless field expression slightly different from that derivable from Eq. 3.13a.

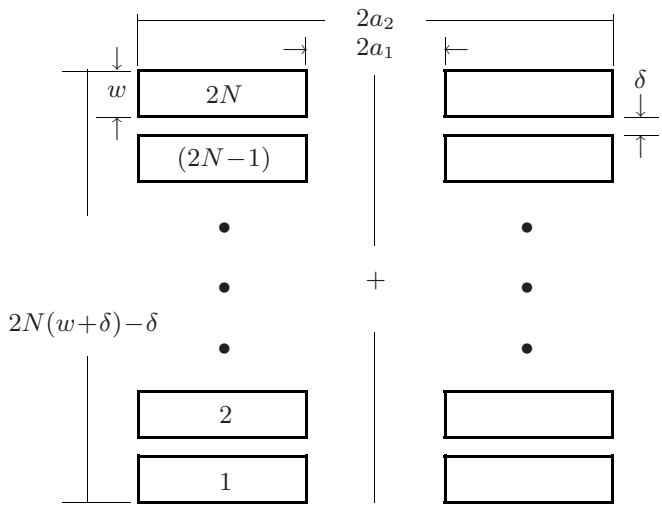

Fig. 3.28 Magnet comprised of $2N$ single pancakes (N double pancakes), each of identical dimensions—$2a_1$; $2a_2$; $2b = w$—and the same λJ.

DISCUSSION 3.7: Field Analysis of Pancake-Coil Magnet (continuation)

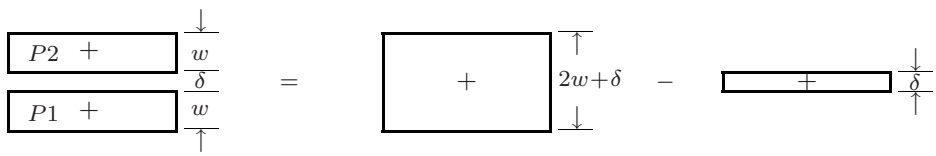

Fig. 3.29 Two-pancake magnet as Coil 2 of $2b = 2w+\delta$ *minus* Coil $2'$ of $2b' = \delta$.

Step 1: Two-Pancake Magnet—Pancake 1 & Pancake 2

Consider first the simplest case: a magnet comprised of two pancake coils, $P1$ and $P2$. Using the superposition technique of ***DISCUSSION 3.4***, the original magnet with a gap of δ (leftmost drawing in Fig. 3.29) is equivalent to two gapless solenoids: Coil 2 (middle) of height $(2b_2 = w + \delta)$ *minus* Coil $2'$ of height $(2b'_2 = \delta)$. The subscript 2 signifies that the magnet under consideration comprises two pancake coils. Note that the cross section of each coil in Fig. 3.29 shows only its height $(2b)$, because this is the only relevant parameter under consideration: thus, Coil 2 has $\beta_2 = (2w+\delta)/2a_1$; and Coil $2'$, $\beta'_2 = \delta/2a_1$.

The dimensionless axial field due to the two coils, $\eta_2(\zeta)$, is given by:

$$\eta_2(\zeta) = [\eta(\zeta)]_2 - [\eta'(\zeta)]_2 \tag{3.129}$$

From Eq. 3.128*b*, we have $[\eta(\zeta)]_2$ and $[\eta'(\zeta)]_2$ given by:

$$[\eta(\zeta)]_2 = \beta_2 \ln(\alpha, \beta_2) \left[1 + \sum_{j=1}^{n} E_{2j}(\alpha, \beta_2) \zeta^{2j} \right] \tag{3.130a}$$

$$[\eta'(\zeta)]_2 = \beta'_2 \ln(\alpha, \beta'_2) \left[1 + \sum_{j=1}^{n} E_{2j}(\alpha, \beta'_2) \zeta^{2j} \right] \tag{3.130b}$$

Combining Eqs. 3.129 and 3.130, we have:

$$\begin{aligned} \eta_2(\zeta) = {} & \left[\beta_2 \ln(\alpha, \beta_2) - \beta'_2 \ln(\alpha, \beta'_2) \right] \\ & + \sum_{j=1}^{n} \left[\beta_2 \ln(\alpha, \beta_2) E_{2j}(\alpha, \beta_2) - \beta'_2 \ln(\alpha, \beta'_2) E_{2j}(\alpha, \beta'_2) \right] \zeta^{2j} \end{aligned} \tag{3.131}$$

Step 2: Four-Pancake Magnet—Addition of Pancakes 3 & 4

Next, we consider a magnet comprised of four pancake coils. As illustrated in Fig. 3.30, the new magnet is the two-pancake magnet considered in *Step 1* with one pancake added to the bottom and another added to the top of the two-pancake magnet. These new pancakes, as indicated in Fig. 3.30, may be modeled as Coil 4 with $2b = 4w+3\delta$ *minus* Coil $4'$ with $2b = 2w+3\delta$. Thus, Coil 4 has $\beta_4 = (4w+3\delta)/2a_1$; and Coil $4'$, $\beta'_4 = (2w+3\delta)/2a_1$.

DISCUSSION 3.7: Field Analysis of Pancake-Coil Magnet (continuation)

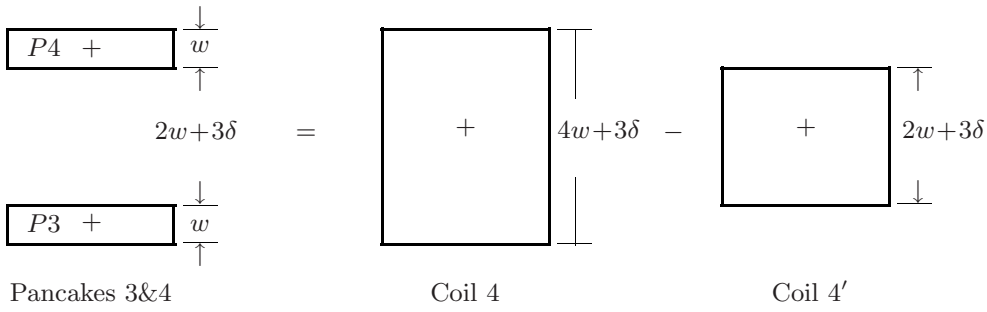

Fig. 3.30 Four-pancake magnet as Coil 4 of $2b = 4w + 3\delta$ *minus* Coil $4'$ of $2b' = 2w + 3\delta$ *added* to the two-pancake magnet shown in Fig. 3.29.

The total dimensionless axial field due to all 4 coils, $\eta_4(z)$ is:

$$\eta_4(z) = [\eta(\zeta)]_2 - [\eta'(\zeta)]_2 + [\eta(\zeta)]_4 - [\eta'(z)]_4 \tag{3.132}$$

where

$$[\eta(\zeta)]_4 = \beta_4 \ln(\alpha, \beta_4) \left[1 + \sum_{j=1}^{n} E_{2j}(\alpha, \beta_4) \zeta^{2j} \right] \tag{3.133a}$$

$$[\eta'(\zeta)]_4 = \beta'_4 \ln(\alpha, \beta'_4) \left[1 + \sum_{j=1}^{n} E_{2j}(\alpha, \beta'_4) \zeta^{2j} \right] \tag{3.133b}$$

From Eqs. 3.130 through 3.133 we obtain:

$$\begin{aligned} \eta_4(\zeta) = {} & \left[\beta_2 \ln(\alpha, \beta_2) + \beta_4 \ln(\alpha, \beta_4)\right] - \left[\beta'_2 \ln(\alpha, \beta'_2) + \beta'_4 \ln(\alpha, \beta'_4)\right] \\ & + \sum_{j=1}^{n} \Big\{ \left[\beta_2 \ln(\alpha, \beta_2) E_{2j}(\alpha, \beta_2) + \beta_4 \ln(\alpha, \beta_4) E_{2j}(\alpha, \beta_4)\right] \\ & - \left[\beta'_2 \ln(\alpha, \beta'_2) E_{2j}(\alpha, \beta'_2) + \beta'_4 \ln(\alpha, \beta'_4) E_{2j}(\alpha, \beta'_4)\right] \Big\} \zeta^{2j} \end{aligned} \tag{3.134}$$

Step 3: 2N-Pancake Coil—Addition of Final Two Pancakes

Figure 3.31 illustrates modeling of the final pancakes, $(2N-1)^{\text{th}}$ and $2N^{\text{th}}$, of the magnet, Coil $2N$ of $2b_N = 2Nw + (2N-1)\delta$ and thus $\beta_{2N} = [2Nw + (2N-1)\delta]/2a_1$ and Coil $2N'$ of $2b'_N = 2(N-1)w + (2N-1)\delta$ and thus $\beta'_{2N} = [2(N-1)w + (2N-1)\delta]/2a_1$.

An expression for the axial field for a $2N$-pancake magnet, which in practice comprises N double-pancake coils, is given by:

$$\eta_{2N}(\zeta) = \sum_{k=1}^{N} \Big\{ [\eta(\zeta)]_{2k} - [\eta'(\zeta)]_{2k} \Big\} \tag{3.135}$$

In this analysis it is assumed that the spacing between pancake coils within each double-pancake coil and those between adjacent double-pancake coils are equal.

DISCUSSION 3.7: Field Analysis of Pancake-Coil Magnet (continuation)

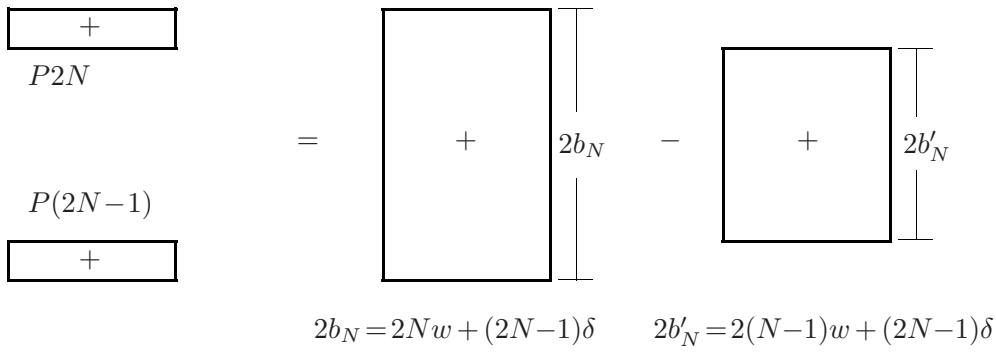

Fig. 3.31 $2N$-pancake magnet as Coil $2N$ of $2b_{2N} = 2Nw + (2N-1)\delta$ *minus* Coil $2N'$ of $2b'_{2N} = 2(N-1)w + (2N-1)\delta$ *added* to the $2(N-1)$-pancake magnet.

We may express Eq. 3.135 in a form similar to Eq. 3.134:

$$\eta_{2N}(\zeta) = \sum_{k=1}^{N} \left\{ \left[\beta_{2k} \ln(\alpha, \beta_{2k}) - \beta'_{2k} \ln(\alpha, \beta'_{2k}) \right] + \sum_{j=1}^{n} \left[\beta_{2k} \ln(\alpha, \beta_{2k}) E_{2j}(\alpha, \beta_{2k}) - \beta'_{2k} \ln(\alpha, \beta'_{2k}) E_{2j}(\alpha, \beta'_{2k}) \right] \right\} \zeta^{2j} \quad (3.136)$$

where

$$\beta_{2k} = \frac{2kw + (2k-1)\delta}{2a_1}$$

$$\beta'_{2k} = \frac{2(k-1)w + (2k-1)\delta}{2a_1}$$

Equation 3.136 may also be expressed as:

$$\frac{\eta_{2N}(\zeta)}{\eta_{2N}(0)} = \left\{ 1 + [E_2]_{2N} \zeta^2 + \cdots + [E_{2n}]_{2N} \zeta^{2n} \right\} \quad (3.137)$$

where $\eta_{2N}(0)$ is the dimensionless center field and $[E_{2n}]_{2N}$ is the n^{th} overall error coefficient. $\eta_{2N}(\zeta = 0)$ and $[E_{2n}]_{2N}$ are given by:

$$\eta_{2N}(0) = \sum_{k=1}^{N} \left[\beta_{2k} \ln(\alpha, \beta_{2k}) - \beta'_{2k} \ln(\alpha, \beta'_{2k}) \right] \quad (3.138a)$$

$$[E_{2n}]_{2N} = \frac{\sum_{k=1}^{N} \left[\beta_{2k} \ln(\alpha, \beta_{2k}) E_{2n}(\alpha, \beta_{2k}) - \beta'_{2k} \ln(\alpha, \beta'_{2k}) E_{2n}(\alpha, \beta'_{2k}) \right]}{\sum_{k=1}^{N} \left[\beta_{2k} \ln(\alpha, \beta_{2k}) - \beta'_{2k} \ln(\alpha, \beta'_{2k}) \right]} \quad (3.138b)$$

Thus Eq. 3.138*b* gives an expression for computation of n^{th} error coefficient comprised of $2N$ identical pancake coils, each of $2a_1$ i.d., $2b = w$, α, and β, and separated from each other by δ.

PROBLEM 3.8: Ideal dipole magnet*

This problem studies an ideal dipole magnet, which is infinitely long (no end effects) and whose fields, directed normal to the dipole axis, are generated by a longitudinal surface current having zero winding thickness. Field and force solutions for real dipole magnets are more complex than those in the ideal dipole; nevertheless, except for complications at the ends, the ideal dipole illustrates most of the key aspects. Dipole magnets are used in systems that require a uniform field directed transverse to the magnet axis, such as in high-energy particle accelerators [3.35–3.40] and electric generators [3.41–3.43].

A long (two-dimensional) dipole magnet of radius R and "zero" winding thickness is energized by a surface current flowing in the z-direction at the dipole shell ($r = R$). The magnetic field within the bore ($r < R$), $\vec{H}_{d1}$, and that outside the shell ($r > R$), $\vec{H}_{d2}$, are given by:

$$\vec{H}_{d1} = H_0(\sin\theta\,\vec{\imath}_r + \cos\theta\,\vec{\imath}_\theta) \tag{3.139a}$$

$$\vec{H}_{d2} = H_0\left(\frac{R}{r}\right)^2(\sin\theta\,\vec{\imath}_r - \cos\theta\,\vec{\imath}_\theta) \tag{3.139b}$$

The 2-D coordinates are defined in Fig. 3.32. The $+z$-direction is out of the paper. In answering the following questions, neglect end effects.

a) Draw neatly the field profile of the dipole for both regions, $r < R$ and $r > R$.

b) Show that an expression for the surface current $\vec{K}_f$ at $r = R$ is given by:

$$\vec{K}_f = -2H_0\cos\theta\,\vec{\imath}_z \tag{3.140}$$

Indicate on a sketch its direction, with circles (o) where $\vec{K}_f$ is $+z$-directed (out of the paper) and with crosses ($\times$) where $\vec{K}_f$ is $-z$-directed.

c) Show that an expression for the Lorentz force density per unit length, $\vec{f}_L$ [N/m^2], acting on a current-carrying element of the shell, is given by:

$$\vec{f}_L = -\mu_\circ H_0^2\sin 2\theta\,\vec{\imath}_\theta \tag{3.141}$$

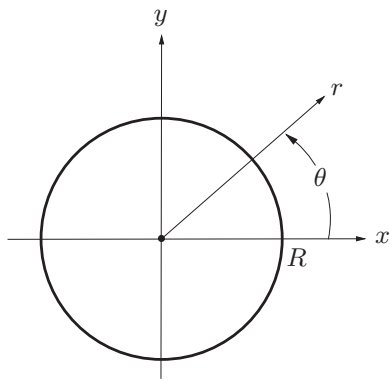

Fig. 3.32 Cylindrical coordinate system; $+z$-direction is out of the paper.

* **Problem 3.7** in the 1st Edition (Plenum, 1994).

PROBLEM 3.8: Ideal dipole magnet (continuation)

d) Show that the net x-directed Lorentz force (per unit dipole length), F_{Lx} [N/m], acting on the right-hand sector ($-90° < \theta < 90°$) is given by:

$$F_{Lx} = \frac{4R\mu_\circ H_0^2}{3} \tag{3.142}$$

e) Show that an expression for the total magnetic energy stored (per unit dipole length), E_m [J/m], is given by:

$$E_m = \frac{\pi R^2 B_0^2}{\mu_\circ} \tag{3.143}$$

Compute E_m for $B_0 = 5\,\mathrm{T}$ and $R = 20\,\mathrm{mm}$. Also, from E_m, compute the inductance, L, of a 10-m long dipole with an operating current, I_{op}, of 5000 A.

To reduce the field outside the dipole, an iron yoke ($\mu = \infty$) of radial thickness d is placed outside the dipole, as shown in Fig. 3.33.

f) Show that the new $\vec{K}_{f1}$ needed to generate the *same* $\vec{H}$ field inside the dipole is exactly one-half that given by Eq. 3.140. Explain this current reduction.

g) In reality, the iron yoke cannot maintain its high μ for an unlimited value of H_0. Show that an expression for the minimum d_m to keep the yoke unsaturated is given by:

$$d_m = R\left(\frac{H_0}{M_{sa}}\right) \tag{3.144}$$

where M_{sa} is the yoke material's saturation magnetization. Compute d_m for the following set: $\mu_\circ H_\circ = 5$ T; $\mu_\circ M_{sa} = 1.2\,\mathrm{T}$; $R = 20\,\mathrm{mm}$.

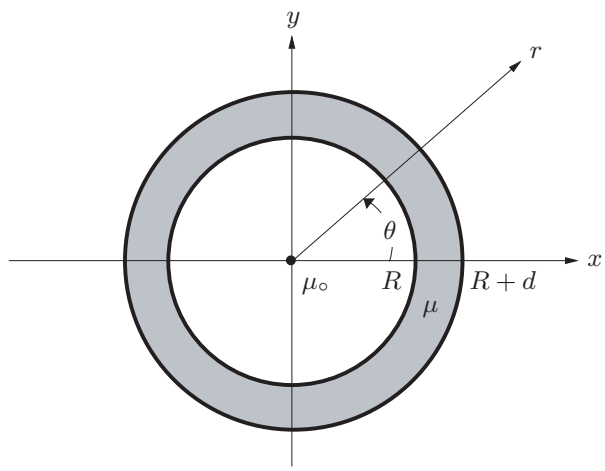

Fig. 3.33 Ideal dipole with an iron yoke of thickness d.

Solution to PROBLEM 3.8

a) The field lines are sketched in Fig. 3.34a for both regions. The normal (r-directed) component of the field is continuous at the boundary ($r = R$).

b) The discontinuity in the tangential (θ-directed) component of the field at $r = R$ is equal to the surface current density ($\vec{K}_f$) flowing there. From Eq. 2.6:

$$\begin{aligned}\vec{K}_f &= \vec{\imath}_r \times (\vec{H}_{d2} - \vec{H}_{d1}) = \vec{\imath}_r \times -2H_0 \cos\theta\, \vec{\imath}_\theta \\ &= -2H_0 \cos\theta\, \vec{\imath}_z \end{aligned} \tag{3.140}$$

As indicated in Fig. 3.34b, $\vec{K}_f$ in the $-90° < \theta < 90°$ segment points in the $-z$-direction, while that in the $90° < \theta < 270°$ segment points in the $+z$-direction.

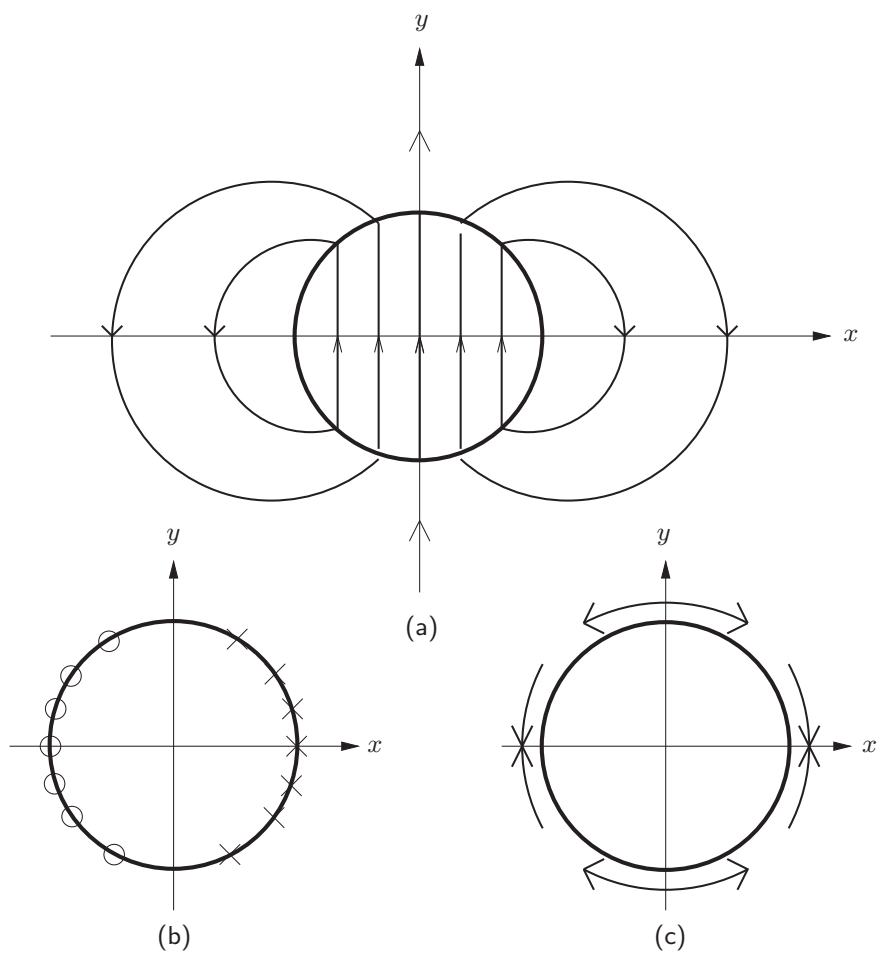

Fig. 3.34 Ideal dipole. a) inside and outside fields; b) surface current density vectors; c) force vectors.

Solution to PROBLEM 3.8 (continuation)

c) $\vec{f}_L$ is given by $\vec{K}_f \times \mu_\circ \vec{H}_d$, where $\mu_\circ \vec{H}_d = \mu_\circ(\vec{H}_{d1} + \vec{H}_{d2})/2$:

$$\vec{f}_L = \vec{K}_f \times \mu_\circ H_0 \sin\theta\, \vec{\imath}_r \qquad (S8.1)$$

$$= -2\mu_\circ H_0^2 \cos\theta\, \sin\theta\, \vec{\imath}_\theta$$

$$= -\mu_\circ H_0^2 \sin 2\theta\, \vec{\imath}_\theta \qquad (3.141)$$

Note that $\vec{f}_L$ has no r-component; it has only a θ-component (Fig. 3.34c). Also the force density is maximum at $\theta = \pi/4 + n\pi/2$ and zero at $\theta = 0 + n\pi/2$, where $n = 0, 1, 2, 3$. The cumulative force, $\propto \int f_L(\theta)\, d\theta$, is maximum at $\theta = 0$ and 180°.

d) It is clear from Fig. 3.34c that the net Lorentz force per unit length [N/m] acting on the right-hand segment of the shell is $+x$-directed. Thus:

$$F_{Ldx} = \int \vec{f}_L \cdot \vec{\imath}_x\, dx = -R \int_{-\pi/2}^{\pi/2} f_{L\theta} \sin\theta\, d\theta \qquad (S8.2a)$$

$$= -2R \int_0^{\pi/2} f_{L\theta} \sin\theta\, d\theta = 4R\mu_\circ H_0^2 \int_0^{\pi/2} \cos\theta \sin^2\theta\, d\theta \qquad (S8.2b)$$

From Eq. $S8.2b$, we obtain:

$$F_{Lx} = \frac{4R\mu_\circ H_0^2}{3} \qquad (3.142)$$

The net Lorentz force on the left-hand segment has the same magnitude as that on the right-hand segment but is $-x$-directed. That is, there is a large force trying to push the two halves of the dipole apart. In fact structural support to withstand these forces is a key design issue for dipole magnets.

e) E_m [J/m] may be computed by integrating $\mu_\circ |H(r,\theta)|^2/2$, the magnetic energy density, over the entire surface, from $r = 0$ to $r = \infty$ and from $\theta = 0$ to $\theta = 2\pi$, transverse to the dipole axis.

$$E_m = \frac{\mu_\circ}{2} \int_0^R |H_{d1}|^2 2\pi r\, dr + \frac{\mu_\circ}{2} \int_R^\infty |H_{d2}|^2 2\pi r\, dr \qquad (S8.3a)$$

$$= \frac{\mu_\circ}{2} H_0^2 \pi R^2 + \frac{\mu_\circ}{2} H_0^2 \pi R^2 \qquad (S8.3b)$$

$$= \mu_\circ \pi R^2 H_0^2 = \frac{\pi R^2 B_0^2}{\mu_\circ} \qquad (3.143)$$

From Eq. $S8.3b$ it is clear that the total stored magnetic energy is divided equally inside and outside the dipole shell. We may imagine that one-half of the current flowing in the dipole is used to create $\vec{H}_{d1}$ and the other half is used to create $\vec{H}_{d2}$. Inserting $\mu_\circ H_0 = B_0 = 5\,\mathrm{T}$ and $R = 0.02\,\mathrm{m}$ into the above expression, we obtain:

$$E_m = \frac{\pi(2\times 10^{-2}\,\mathrm{m})^2 (5\,\mathrm{T})^2}{4\pi \times 10^{-7}\,\mathrm{H/m}} = 25\,\mathrm{kJ/m}$$

Solution to PROBLEM 3.8 (continuation)

For a 5-T dipole, 10-m long, the total magnetic energy becomes 250 kJ. This total energy may be equated to the dipole's total inductive energy:

$$\tfrac{1}{2}LI_{op}^2 = 250\,\text{kJ} \tag{S8.4}$$

Solving Eq. $S8.4$ for L with $I_{op}=5000\,\text{A}$, we have:

$$L = \frac{2(250\times10^3\,\text{J})}{(5000\,\text{A})^2}$$

$$= 20\,\text{mH}$$

In **3.7.3** the inductance per unit length of an ideal dipole is given by:

$$L_\ell = \tfrac{1}{8}\mu_\circ\pi N^2 \tag{3.87}$$

Equating this $L_\ell(=2\,\text{mH/m})$ with 20 mH and solving for N, we find $N\simeq 64$ for $I_{op}=5000\,\text{A}$. Note that if the dipole's operating current is, for example, 1000 A, then the dipole must have an inductance of 0.5 H; it must have five times more winding turns than the 20-mH dipole: $N\simeq 318$.

f) Because $\mu=\infty$, $\vec{H}_{d2}=0$ for $R<r<R+d$ and, if the shield is thick enough to avoid saturation, $\vec{H}_{d2}=0$ also for $r>R+d$. We still have $\vec{H}_{d1}$ as before. Clearly:

$$\vec{K}_{f1} = -H_0\cos\theta\,\vec{\imath}_\theta \tag{S8.5}$$

which is exactly one-half of $\vec{K}_f$ given by Eq. 3.140. Considering the surface current requirements for both cases, we may interpret that of the total surface current needed to generate the bore field, $-2H_\circ\cos\theta$, one half comes from the "surface current" of the iron magnetization.

g) All the flux per unit length [Wb/m] entering the yoke of radial thickness d between 0 and $\theta=90^\circ$ must be equal to or less than $\mu_\circ M_{sa}d$. That is:

$$R\mu_\circ H_0\int_0^{\pi/2}\sin\theta\,d\theta = R\mu_\circ H_0 \le \mu_\circ M_{sa}d \tag{S8.6}$$

The minimum yoke thickness d_m is thus given by:

$$d_m = R\left(\frac{H_0}{M_{sa}}\right) \tag{3.144}$$

With $R=20\,\text{mm}$, $\mu_\circ H_0=5\,\text{T}$, and $\mu_\circ M_{sa}=1.2\,\text{T}$, we obtain:

$$d_m = (20\,\text{mm})\frac{5\,\text{T}}{1.2\,\text{T}} = 83\,\text{mm}$$

Note that from Table 2.5 (p. 50), at $\mu_\circ M = 1.25\,\text{T}$ for as-cast steel, the material has a permeability of $180\mu_\circ$ which, though not ∞, is still large enough for our simple approach based on the assumption that $\mu=\infty$.

PROBLEM 3.9: Ideal quadrupole magnet*

This problem studies an ideal quadrupole magnet, which is infinitely long (no end effects) and whose fields, directed normal to the magnet axis, are generated by a longitudinal surface current having zero winding thickness. Like dipole magnets, quadrupole magnets are chiefly used in particle accelerators [3.35, 3.39, 3.44–3.46]. As discussed below in **f)**, they are used to focus beams of charged particles.

A long quadrupole magnet of radius R and of "zero" winding thickness is energized by a surface current flowing in the z-direction at the quadrupole shell ($r = R$). The magnetic field within the bore ($r < R$), $\vec{H}_{q1}$, and that outside the shell ($r > R$), $\vec{H}_{q2}$, are given by:

$$\vec{H}_{q1} = H_0 \left(\frac{r}{R}\right) (\sin 2\theta\, \vec{\imath}_r + \cos 2\theta\, \vec{\imath}_\theta) \tag{3.145a}$$

$$\vec{H}_{q2} = H_0 \left(\frac{R}{r}\right)^3 (\sin 2\theta\, \vec{\imath}_r - \cos 2\theta\, \vec{\imath}_\theta) \tag{3.145b}$$

In answering the following questions, neglect end effects.

a) Draw *neatly* the field profiles of the quadrupole for both regions.

b) Show that an expression for the surface current $\vec{K}_f$ at $r = R$ is given by:

$$\vec{K}_f = -2H_0 \cos 2\theta\, \vec{\imath}_z \tag{3.146}$$

Indicate neatly on a sketch its direction, with circles (o) where $\vec{K}_f$ is $+z$-directed (out of the paper) and with crosses ($\times$) where $\vec{K}_f$ is $-z$-directed.

c) Show that an expression for the Lorentz force density per unit length [N/m^2], $\vec{f}_L$, acting on a current-carrying element of the shell is given by:

$$\vec{f}_L = -\mu_\circ H_0^2 \sin 4\theta\, \vec{\imath}_\theta \tag{3.147}$$

d) Show that an expression for the "magnetic spring constant," k_{Lx}, in the x-direction for a proton traveling in the $+z$-direction along the center of the magnet with a speed nearly equal to that of light, c, is given by:

$$k_{Lx} \simeq \frac{qc\mu_\circ H_0}{R} \tag{3.148}$$

e) Similarly, show that an expression for the "magnetic spring constant," k_{Ly}, in the y-direction for a proton traveling in the $+z$-direction along the center of the magnet with a speed nearly equal to that of light, c, is given by:

$$k_{Ly} \simeq -\frac{qc\mu_\circ H_0}{R} \tag{3.149}$$

f) By stating whether k_{Lx} and k_{Ly} are unstable or restoring, describe the function of quadrupoles for charged particle accelerators.

---

* **Problem 3.8** in the 1st Edition (Plenum, 1994).

Solution to PROBLEM 3.9

a) The field lines are sketched in Fig. 3.35a. As with the ideal dipole, the r-component of the field is continuous at $r = R$.

b) The discontinuity in the θ-component of the field at the boundary is equal to the surface current density ($\vec{K}_f$) flowing at $r = R$. Thus:

$$\begin{aligned} \vec{K}_f &= \vec{\imath}_r \times (\vec{H}_{q2} - \vec{H}_{q1}) = \vec{\imath}_r \times -2H_0 \cos 2\theta \, \vec{\imath}_\theta \\ &= -2H_0 \cos 2\theta \, \vec{\imath}_z \end{aligned} \tag{3.146}$$

The $\vec{K}_f$ vectors change directions four times around the magnet shell (Fig. 3.35b).

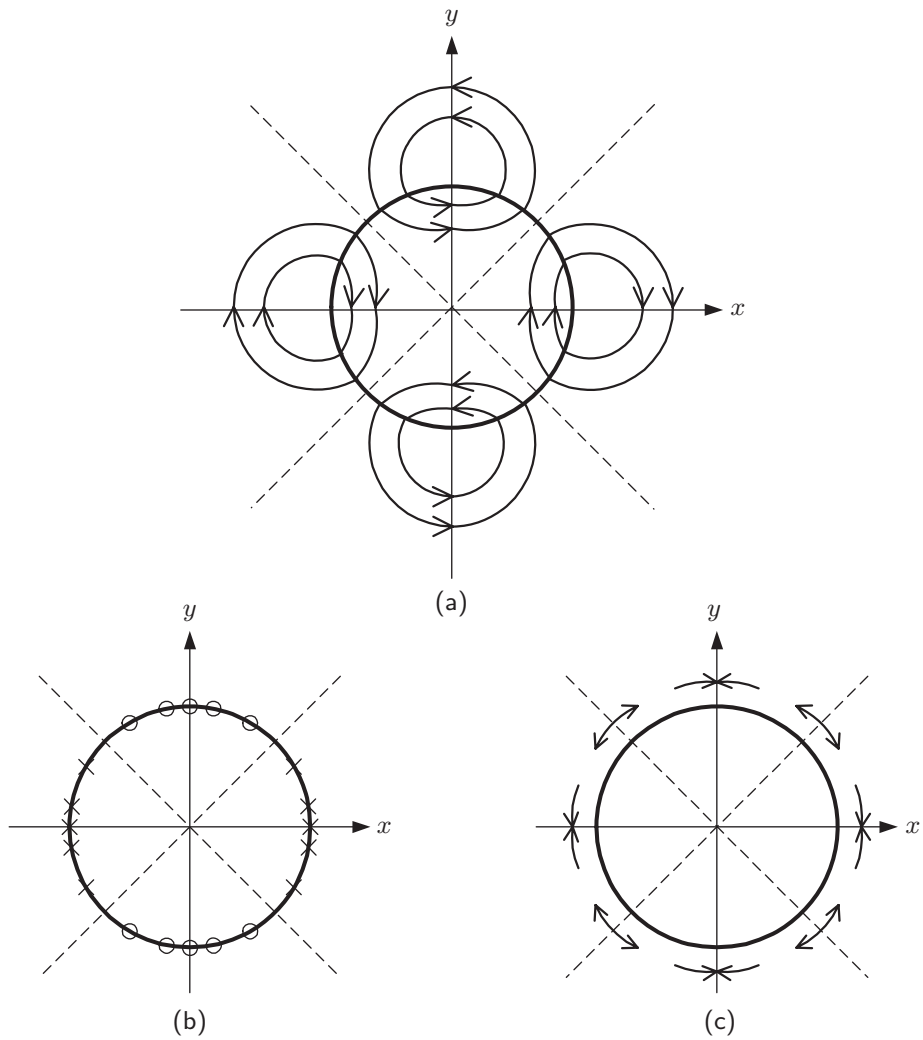

Fig. 3.35 a) Quadrupole fields inside and outside the bore; b) surface current density vectors in the magnet; c) force directions in the magnet.

Solution to PROBLEM 3.9 (continuation)

c) $\vec{f}_L$, is given by the cross-product of $\vec{K}_f$ and $\mu_\circ \vec{H}$ at $r = R$. At $r = R$, the average field, $(\vec{H}_{q1}+\vec{H}_{q2})/2$, is $\vec{H} = H_0 \sin 2\theta\, \vec{\imath}_r$, because the θ-component of $\vec{H}_{q1}$ cancels that of $\vec{H}_{q2}$. Noting that $\vec{K}_f = -2H_0 \cos 2\theta\, \vec{\imath}_z$, we have:

$$\begin{aligned} \vec{f}_L &= -2\mu_\circ H_0^2 \sin 2\theta \cos 2\theta\, \vec{\imath}_\theta \\ &= -\mu_\circ H_0^2 \sin 4\theta\, \vec{\imath}_\theta \end{aligned} \tag{3.147}$$

The $\vec{f}_L$ distribution is sketched in Fig. 3.35c.

d) We may define the magnetic spring constant in the x-direction as:

$$k_{Lx} = -\frac{\partial F_{Lx}}{\partial x} \tag{S9.1}$$

F_{Lx}, the Lorentz force in the x-direction on a proton of electric charge q traveling in the z-direction with a velocity nearly equal to c (speed of light), is given by:

$$\begin{aligned} F_{Lx} &\simeq [q(c\,\vec{\imath}_z) \times \mu_\circ H_{q1}\, \vec{\imath}_\theta]_{\theta=0} \\ &\simeq -qc\mu_\circ H_0 \left(\frac{r}{R}\right) \vec{\imath}_x \end{aligned} \tag{S9.2}$$

k_{Lx} is thus given by:

$$\begin{aligned} k_{Lx} &= -\frac{\partial F_{Lx}}{\partial x} = -\frac{\partial F_{Lx}}{\partial r} \\ &\simeq \frac{qc\mu_\circ H_0}{R} \end{aligned} \tag{3.148}$$

e) In the y-direction (r-direction at $\theta = 90°$), the magnetic force F_{Ly} is given by:

$$\begin{aligned} F_{Ly} &\simeq [q(c\,\vec{\imath}_z) \times \mu_\circ H_{q1}\, \vec{\imath}_\theta]_{\theta=\frac{\pi}{2}} \\ &\simeq qc\mu_\circ H_0 \left(\frac{r}{R}\right) \vec{\imath}_y \end{aligned} \tag{S9.3}$$

k_{Ly} is thus given by:

$$\begin{aligned} k_{Ly} &= -\frac{\partial F_{Ly}}{\partial y} = -\frac{\partial F_{Ly}}{\partial r} \\ &\simeq -\frac{qc\mu_\circ H_0}{R} \end{aligned} \tag{3.149}$$

f) F_{Lx} is restoring, but F_{Ly} is unstable, diverging the beam in the y-direction. In accelerator rings, quadrupole magnets are thus used in pairs, one focusing the beam in the x-direction followed by another focusing the beam in the y-direction; the net effect is focusing in both directions.

Answer to TRIVIA 3.3 iii). Despite his friendship with the royal family, having been lionized by Marie Antoinette, it is said that Joseph Louis Lagrange (1736–1813) survived the *Terror* because of the general respect for his accomplishments in mathematics and his foreign birth (Torino). He was appointed to head this commission in 1793.

DISCUSSION 3.8: Two-"Racetrack" Coil Magnet*

We discuss here a magnet comprised of two parallel long *ideal* "racetrack" coils spaced a distance $2c$ apart in the plane normal to the magnet axis. The name "racetrack" arises because at each end the conductor loops around 180° like the end of a racetrack. Unlike in a dipole winding, its windings remain in a plane, i.e., flat. The flat winding makes it easier to wind a racetrack than a dipole, and thus racetrack coils are preferred over dipole coils in generators and motors [3.47–3.50]. The racetrack magnet is also suitable for Maglev [3.51–3.53].

Figure 3.36 shows a cross sectional view of the winding configuration of a magnet comprised of two long ideal racetracks. A set of two very long racetrack coils, parallel to each other as shown, can sometimes substitute for a dipole magnet. For example, if a long length of a superconductor must be tested in a uniform field directed transverse to its major axis, this magnet configuration could be used; it has the advantage of requiring simpler winding rigs than a dipole magnet. As indicated in Fig. 3.36, each of the two racetracks, $2c$ apart, has a winding outer width of $2a_2$, inner width of $2a_1$, and contains N turns.

The direction of current in the right-hand side of each racetrack coil is in the $+z$ direction (out of the paper), while the direction of current in the left-hand side is in the $-z$ direction. We shall derive expressions of key parameters of the magnet.

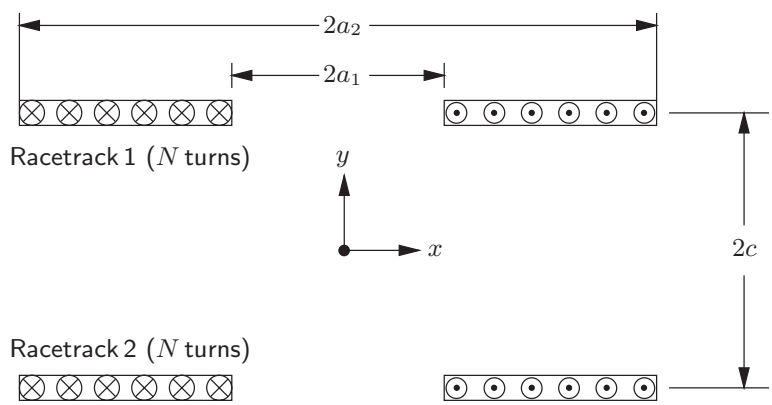

Fig. 3.36 Cross section of a magnet comprised of two ideal racetrack coils.

* **Problem 3.9** in the 1st Edition (Plenum, 1994).

DISCUSSION 3.8: Two-"Racetrack" Coil Magnet (continuation)

A. Field at Magnet Center

By applying the law of Biot-Savart (Eq. 3.1) on a differential surface current, $K\,d\xi$, located at ξ in the right-hand side of racetrack 1 (with $+z$ current) as shown in Fig. 3.37, we obtain an expression for the differential field at $(x,\ y)$, $d\vec{H}_{1+}$:

$$d\vec{H}_{1+} = \frac{K\,d\xi}{2\pi r_1}\,\vec{\imath} \tag{3.150}$$

where the field direction is shown in the figure and $K = NI/(a_2 - a_1)$. The y-component of field, H_{y1+}, contributed by the entire $+z$-surface current, from $\xi = a_1$ to $\xi = a_2$, is given by integration of Eq. 3.151 (below) from $\xi = a_1$ to $\xi = a_2$:

$$H_{y1+} = -\frac{K}{2\pi}\int_{a_1}^{a_2} \frac{\cos\theta_1\,d\xi}{r_1} \tag{3.151}$$

With $r_1 = \sqrt{(\xi - x)^2 + (c-y)^2}$ and $\cos\theta_1 = (\xi - x)/r_1$ into Eq. 3.151, we obtain:

$$H_{y1+} = -\frac{K}{2\pi}\int_{a_1}^{a_2} \frac{(\xi - x)\,d\xi}{(\xi-x)^2+(c-y)^2} = -\frac{K}{4\pi}\ln\left[\frac{(a_2-x)^2+(c-y)^2}{(a_1-x)^2+(c-y)^2}\right] \tag{3.152a}$$

Similarly, the contributions from the remaining current sheets are given by:

$$H_{y1-} = -\frac{K}{2\pi}\int_{a_1}^{a_2} \frac{(\xi + x)\,d\xi}{(\xi+x)^2+(c-y)^2} = -\frac{K}{4\pi}\ln\left[\frac{(a_2+x)^2+(c-y)^2}{(a_1+x)^2+(c-y)^2}\right] \tag{3.152b}$$

$$H_{y2+} = -\frac{K}{2\pi}\int_{a_1}^{a_2} \frac{(\xi - x)\,d\xi}{(\xi-x)^2+(c+y)^2} = -\frac{K}{4\pi}\ln\left[\frac{(a_2-x)^2+(c+y)^2}{(a_1-x)^2+(c+y)^2}\right] \tag{3.152c}$$

$$H_{y2-} = -\frac{K}{2\pi}\int_{a_1}^{a_2} \frac{(\xi + x)\,d\xi}{(\xi+x)^2+(c+y)^2} = -\frac{K}{4\pi}\ln\left[\frac{(a_2+x)^2+(c+y)^2}{(a_1+x)^2+(c+y)^2}\right] \tag{3.152d}$$

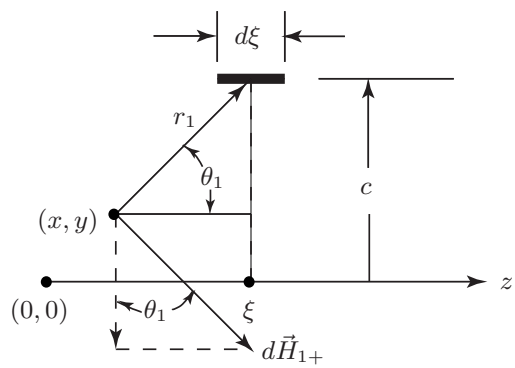

Fig. 3.37 Field produced by a differential current element.

DISCUSSION 3.8: Two-"Racetrack" Coil Magnet (continuation)

Combining these four contributions, we have:

$$H_y(x,y) = -\frac{K}{4\pi}\left\{\ln\left[\frac{(a_2-x)^2+(c-y)^2}{(a_1-x)^2+(c-y)^2}\right]+\ln\left[\frac{(a_2+x)^2+(c-y)^2}{(a_1+x)^2+(c-y)^2}\right]\right.$$
$$\left.+\ln\left[\frac{(a_2-x)^2+(c+y)^2}{(a_1-x)^2+(c+y)^2}\right]+\ln\left[\frac{(a_2+x)^2+(c+y)^2}{(a_1+x)^2+(c+y)^2}\right]\right\} \quad (3.153a)$$

By inserting $x=0$ and $y=0$ into Eq. 3.153a, we obtain:

$$H_y(0,0) = -\frac{K}{\pi}\ln\left(\frac{a_2^2+c^2}{a_1^2+c^2}\right) \quad (3.153b)$$

B. Field Near the Center

We may derive an expression of $H_y(x,y)$ (Eq. 3.153a) as the sum of $H_y(0,0)$ and a term containing H_{y1+} derived above. Equation 3.152a may be expressed as:

$$H_{y1+} = -\frac{K}{4\pi}\ln\left[\frac{(a_2-x)^2+(c-y)^2}{(a_1-x)^2+(c-y)^2}\right]$$
$$= -\frac{K}{4\pi}\left\{\ln[(a_2-x)^2+(c-y)^2]-\ln[(a_1-x)^2+(c-y)^2]\right\} \quad (3.154)$$

The term $\ln[(a_2-x)^2+(c-y)^2]$ may be given as:

$$\ln[(a_2-x)^2+(c-y)^2] = \ln\left[(a_2^2+c^2)\left(1+\frac{x^2+y^2-2a_2x-2cy}{a_2^2+c^2}\right)\right]$$
$$= \ln(a_2^2+c^2)+\ln\left(1+\frac{x^2+y^2-2a_2x-2cy}{a_2^2+c^2}\right)$$

By using $\ln(1+x) \simeq x - x^2/2$ for $|x| \ll 1$, we have:

$$\ln[(a_2-x)^2+(c-y)^2] \simeq \ln(a_2^2+c^2) + \frac{(c^2-a_2^2)(x^2-y^2)-2(a_2^2+c^2)(a_2x+cy)-4a_2cxy}{(a_2^2+c^2)^2}$$

$$\ln[(a_1-x)^2+(c-y)^2] \simeq \ln(a_1^2+c^2) + \frac{(c^2-a_1^2)(x^2-y^2)-2(a_1^2+c^2)(a_1x+cy)-4a_1cxy}{(a_1^2+c^2)^2}$$

Thus, Eq. 3.154 may be expressed as:

$$H_{y1+}(x,y) \simeq -\frac{K}{4\pi}\left[\ln\left(\frac{a_2^2+c^2}{a_1^2+c^2}\right)+\frac{(c^2-a_2^2)(x^2-y^2)-2(a_2^2+c^2)(a_2x+cy)-4a_2cxy}{(a_2^2+c^2)^2}\right.$$
$$\left.-\frac{(c^2-a_1^2)(x^2-y^2)-2(a_1^2+c^2)(a_1x+cy)-4a_1cxy}{(a_1^2+c^2)^2}\right] \quad (3.155a)$$

DISCUSSION 3.8: Two-"Racetrack" Coil Magnet (continuation)

Similarly, H_{y1-}, H_{y2+}, and H_{y2-} may be expressed as:

$$H_{y1-}(x,y) \simeq -\frac{K}{4\pi}\left[\ln\left(\frac{a_2^2+c^2}{a_1^2+c^2}\right)+\frac{(c^2-a_2^2)(x^2-y^2)+2(a_2^2+c^2)(a_2x-cy)+4a_2cxy}{(a_2^2+c^2)^2}\right.$$
$$\left.-\frac{(c^2-a_1^2)(x^2-y^2)+2(a_1^2+c^2)(a_1x-cy)+4a_1cxy}{(a_1^2+c^2)^2}\right] \quad (3.155b)$$

$$H_{y2+}(x,y) \simeq -\frac{K}{4\pi}\left[\ln\left(\frac{a_2^2+c^2}{a_1^2+c^2}\right)+\frac{(c^2-a_2^2)(x^2-y^2)-2(a_2^2+c^2)(a_2x-cy)+4a_2cxy}{(a_2^2+c^2)^2}\right.$$
$$\left.-\frac{(c^2-a_1^2)(x^2-y^2)-2(a_1^2+c^2)(a_1x-cy)+4a_1cxy}{(a_1^2+c^2)^2}\right] \quad (3.155c)$$

$$H_{y2-}(x,y) \simeq -\frac{K}{4\pi}\left[\ln\left(\frac{a_2^2+c^2}{a_1^2+c^2}\right)+\frac{(c^2-a_2^2)(x^2-y^2)+2(a_2^2+c^2)(a_2x+cy)-4a_2cxy}{(a_2^2+c^2)^2}\right.$$
$$\left.-\frac{(c^2-a_1^2)(x^2-y^2)+2(a_1^2+c^2)(a_1x-cy)-4a_1cxy}{(a_1^2+c^2)^2}\right] \quad (3.155d)$$

Combining each term, near $(0,0)$ we have:

$$H_y(x,y) \simeq -\frac{K}{\pi}\left[\ln\left(\frac{a_2^2+c^2}{a_1^2+c^2}\right)-\frac{(a_2^2-a_1^2)[3c^4+(a_2^2+a_1^2)c^2-a_2^2a_1^2]}{(a_2^2+c^2)^2(a_1^2+c^2)^2}(x^2-y^2)\right]$$
$$\simeq H_y(0,0)+K\left[\frac{a_2^2-c^2}{(a_2^2+c^2)^2}-\frac{a_1^2-c^2}{(a_1^2+c^2)^2}\right](x^2-y^2) \quad (3.156a)$$

Note that the 2nd-order inhomogeneity term becomes zero when c^2 satisfies:

$$c^2 = \tfrac{1}{6}\left[\sqrt{(a_2^2+a_1^2)^2+12a_2^2a_1^2}-(a_2^2+a_1^2)\right]$$
$$= \tfrac{1}{6}\left[\sqrt{a_2^4+14a_2^2a_1^2+a_1^4}-(a_2^2+a_1^2)\right] \quad (3.156b)$$

.

C. Center Field from Four Current Elements

We may further simplify the expression for the magnetic field near the center of the racetrack magnet by approximating each of the four current sheets as a current element carrying NI, illustrated in Fig. 3.38. A dot indicates it is in the $+z$-direction and a cross in the $-z$-direction.

In this case, we let $a_1 = a$, $a_2 = a+\epsilon$, and $K\epsilon = K(a_2-a) = NI$. Substituting these parameters into Eq. 3.153b and noting $\ln(1+x)=x$ for $|x|\ll 1$, we have:

$$H_y(0,0) = -\frac{K}{\pi}\ln\left(\frac{a_2^2+c^2}{a_1^2+c^2}\right) \simeq -\frac{K}{\pi}\ln\left(\frac{a^2+c^2+2a\epsilon}{a^2+c^2}\right)$$
$$\simeq -\frac{K2a\epsilon}{\pi(a^2+c^2)} \simeq -\frac{2aNI}{\pi(a^2+c^2)} \quad (3.157a)$$

DISCUSSION 3.8: Two-"Racetrack" Coil Magnet (continuation)

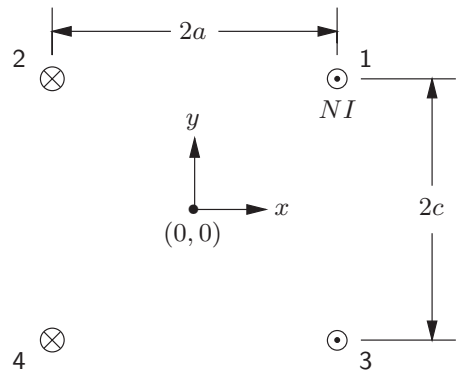

Fig. 3.38 Current distribution model for force calculation.

The quantity $K(a_2^2-a_1^2)=K(a_2+a_1)(a_2-a_1)$ in the second term of the right-hand side of the first line of Eq. 3.156a becomes $2aNI$. Thus:

$$\frac{K(a_2^2-a_1^2)[3c^4+(a_2^2+a_1^2)c^2-a_2^2a_1^2]}{\pi(a_2^2+c^2)^2(a_1^2+c^2)^2}(x^2-y^2)\simeq\frac{2aNI[3c^4+2a^2c^2-a^4]}{\pi(a^2+c^2)^4}(x^2-y^2)$$

$$=-H_y(0,0)\left[\frac{3c^4+2a^2c^2-a^4}{(a^2+c^2)^3}(x^2-y^2)\right]$$

Combining the above equation and Eq. 3.156, we obtain:

$$H_y(x,y)\simeq H_y(0,0)\left[1+\frac{3c^4+2a^2c^2-a^4}{(a^2+c^2)^3}(x^2-y^2)\right] \tag{3.157b}$$

D. Forces on Current Elements

The same 4-current-element model may be used to compute the Lorentz forces (per unit axial length) acting on current element 1, $\vec{F}_1$, as the sum of Lorentz interactions on current element 1 by current elements 2, 3, and 4:

$$\vec{F}_1=\vec{F}_1|_2+\vec{F}_1|_3+\vec{F}_1|_4 \tag{3.158}$$

where $\vec{F}_1|_2$, $\vec{F}_1|_3$, and $\vec{F}_1|_4$ are the force vectors on element 1 by elements, respectively, 2, 3, and 4.

The force, $\vec{F}_1|_2$, on element 1 carrying $I_1=NI$ by element 2 carrying $I_2=NI$, is $+x$-directed and given by:

$$\vec{F}_1|_2=\frac{\mu_\circ I_1I_2}{4\pi a}\,\vec{\imath}_x=\frac{\mu_\circ N^2I^2}{4\pi a}\,\vec{\imath}_x \tag{3.159a}$$

DISCUSSION 3.8: Two-"Racetrack" Coil Magnet (continuation)

Similarly, the force on element 1 by element 3, $\vec{F}_1|_3$, is $-y$-directed and given by:

$$\vec{F}_1|_3 = -\frac{\mu_\circ I_1 I_3}{4\pi c}\,\vec{\imath}_y = -\frac{\mu_\circ N^2 I^2}{4\pi c}\,\vec{\imath}_y \tag{3.159b}$$

The force on element 1 by element 4, $\vec{F}_1|_4$, is directed along both x and y axes:

$$\begin{aligned}\vec{F}_1|_4 &= \frac{\mu_\circ I_1 I_4}{4\pi\sqrt{a^2+c^2}}\left(\frac{a}{\sqrt{a^2+c^2}}\,\vec{\imath}_x + \frac{c}{\sqrt{a^2+c^2}}\,\vec{\imath}_y\right)\\ &= \frac{\mu_\circ N^2 I^2}{4\pi}\left(\frac{a}{a^2+c^2}\,\vec{\imath}_x + \frac{c}{a^2+c^2}\,\vec{\imath}_y\right)\end{aligned} \tag{3.159c}$$

The x- and y-components of the electromagnetic force on element 1 from the three other current elements, F_{1x} and F_{1y}, are thus given, respectively, by:

$$F_{1x} = \frac{\mu_\circ N^2 I^2}{4\pi}\left(\frac{1}{a} + \frac{a}{a^2+c^2}\right) = \frac{\mu_\circ N^2 I^2}{4\pi a}\left(1 + \frac{a^2}{a^2+c^2}\right) \tag{3.160a}$$

$$F_{1y} = \frac{\mu_\circ N^2 I^2}{4\pi}\left(-\frac{1}{c} + \frac{c}{a^2+c^2}\right) = -\frac{\mu_\circ N^2 I^2}{4\pi c}\left(1 - \frac{c^2}{a^2+c^2}\right) \tag{3.160b}$$

E. Interaction Forces Within Racetrack and Between Racetracks

Because $c^2 < a^2 + c^2$, F_{1y} points in the $-y$-direction. The net force between elements 1 and 2, within racetrack 1, is repulsive because their current polarities are opposite. Similarly, that between elements 3 and 4 in racetrack 2 is repulsive. Thus, in the absence of external restraint, each racetrack seeks a circular geometry.

The net force between elements 1 and 3, because their polarities are the same, is attractive. Similarly, that between elements 2 and 4 is attractive. As indicated by Eq. 3.160*b*, the net force between the two racetracks is attractive.

Help from Van (Part 2 of 5 Parts)

—Passage from Francis Bitter's *Magnets: The Education of a Physicist*

I well remember the occasion for the first trial. We were to have the power at some time in the middle of the night, around 1 A.M. Shortly before the appointed hour Van arrived to see how things went. Then, as usual, there were seemingly endless delays. First of all, for some unforeseen reason, the power was not available, and we were told to wait half an hour. Then another hour. Then we went out to get some coffee. I don't remember just how long, in the end, we had to wait.

But finally the moment arrived. Sometime near dawn, when we were all worn out with waiting, we stood around the corner of a wall and watched as the power began to be turned up. At first everything was all right. Then there were slight hissing sounds. They got louder; finally there was a bang. Whereupon the power was shut off. When we went to examine the magnet, we could find nothing much wrong. One of the bolts in the flanges of the case holding the parts together had mysteriously exploded. The magnet had failed for some reason quite different from those we had expected.

PROBLEM 3.10: Ideal toroidal magnet*

This problem deals with an ideal toroidal magnet, i.e., of zero winding thickness, illustrating key features of toroidal magnets.

An ideal circular-cross-section torus of major radius R and minor radius a is energized with a surface current sheet with equivalent total ampere turns NI (Fig. 3.39). Assume that the surface current flows around the torus in the plane perpendicular to the toroidal direction, i.e., zero pitch in the φ-direction.

a) Show that an expression for the toroidal magnetic induction, B_φ, within the torus is given by:

$$B_\varphi(r) = \frac{\mu_\circ NI}{2\pi r} \tag{3.161}$$

Also show that B_φ outside the torus is zero.

b) Assuming that the torus consists of N loops, each carrying a current of I, show that an expression for the net radial Lorentz force F_{L+} acting on a single loop is given by:

$$F_{L+} = \frac{\mu_\circ NI^2}{2}\left(1 - \frac{R}{\sqrt{R^2 - a^2}}\right) \tag{3.162}$$

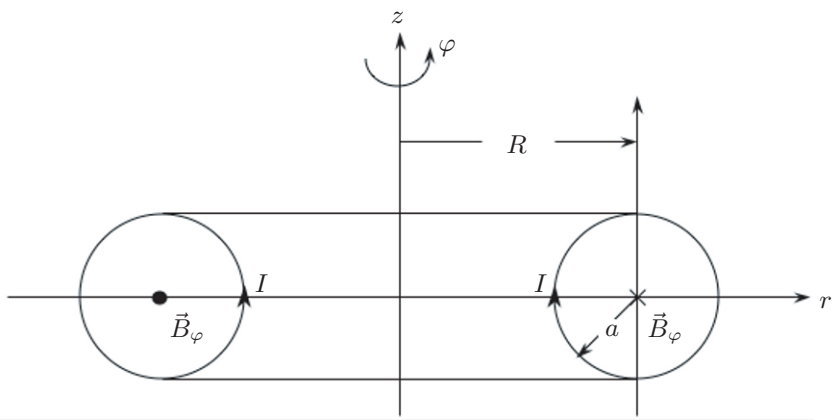

Fig. 3.39 Ideal toroidal magnet comprised of N loops, each carrying current I.

* Based on **Problem 3.10** in the 1st Edition (Plenum, 1994).

TRIVIA 3.4 Of the four pressures below, three are close to the magnetic pressure corresponding to a 1.5-T field, while the other is not. Identify this odd man out.

i) Compressive, on the toes of a ballerina performing a pirouette;

ii) Internal, of an uncorked champagne bottle;

iii) Lift, on the wings of a 747 jet at cruising speed;

iv) Thermal, of the plasma in an experimental Tokamak.

Solution to PROBLEM 3.10

a) Noting that H_φ, from symmetry, is independent of φ, we can apply Ampere's integral law within the torus:

$$\int_0^{2\pi} H_\varphi(r) r \, d\varphi = 2\pi r H_\varphi(r) = NI \tag{S10.1}$$

Because $B_\varphi(r) = \mu_\circ H_\varphi(r)$, we have:

$$B_\varphi(r) = \frac{\mu_\circ NI}{2\pi r} \tag{3.161}$$

Outside the torus, no net current is enclosed when the above integral is performed over the entire circumference. Therefore $H_\varphi(r) = 0$ and $B_\varphi(r) = 0$.

b) Figure 3.40 shows a single loop in which a differential force $d\vec{F}_L$ acts on a differential element $d\vec{s}$ with differential force dF_{Lr} in the r-direction.

$d\vec{F}_L$ is given by:

$$d\vec{F}_L = -I \, ds \, \vec{\imath}_\theta \times \tilde{B}_\varphi(r) \, \vec{\imath}_\varphi \tag{S10.2}$$

where $\tilde{B}_\varphi(r)$ is the average field acting on the surface current. Because this field varies from that given by Eq. 3.161 just inside the surface current to zero just outside, the average field is one half of that given by Eq. 3.161. Thus:

$$d\vec{F}_L = -I \, ds \, \vec{\imath}_\theta \times \tilde{B}_\varphi(r) \, \vec{\imath}_\varphi = \frac{\mu_\circ NI^2 ds}{4\pi r} \, \vec{\imath}_\xi \tag{S10.3}$$

where the vector $\vec{\imath}_\xi$ points in the direction of $\vec{F}_L$ (Fig. 3.40). The r-component of this differential force is given by:

$$dF_{Lr} = \frac{\mu_\circ NI^2 \cos\theta \, ds}{4\pi r} \tag{S10.4}$$

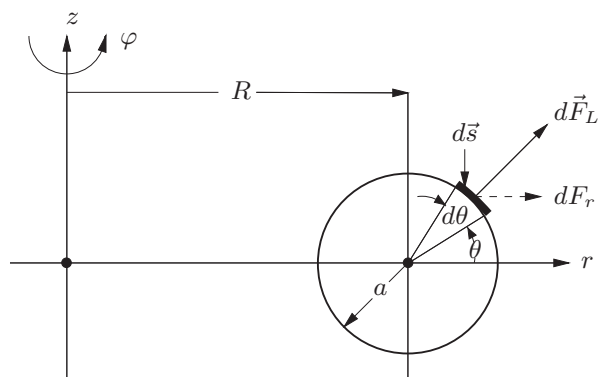

Fig. 3.40 Differential force acting on a single loop.

Solution to PROBLEM 3.10 (continuation)

Because $ds = a\,d\theta$ and $r = R + a\cos\theta$, we can write Eq. $S10.4$ for dF_{Lr} as:

$$dF_{Lr} = \frac{\mu_\circ N I^2 a \cos\theta\, d\theta}{4\pi(R + a\cos\theta)} \qquad (S10.5)$$

By integrating Eq. $S10.5$ for the entire minor circle, we have:

$$F_{Lr} = \frac{\mu_\circ N I^2 a}{4\pi}\int_0^{2\pi} \frac{\cos\theta\, d\theta}{R + a\cos\theta} = \frac{\mu_\circ N I^2 a}{2\pi}\int_0^{\pi} \frac{\cos\theta\, d\theta}{R + a\cos\theta} \qquad (S10.6)$$

Using a table of integrals, we obtain:

$$\begin{aligned} F_{Lr} &= \frac{\mu_\circ N I^2 a}{2\pi}\left(\frac{\theta}{a}\bigg|_0^{\pi} - \frac{R}{a}\int_0^{\pi}\frac{d\theta}{R + a\cos\theta}\right) \\ &= \frac{\mu_\circ N I^2 a}{2\pi}\left\{\frac{\pi}{a} - \frac{2R}{a\sqrt{R^2 - a^2}}\tan^{-1}\left[\sqrt{\frac{R-a}{R+a}}\tan\frac{\theta}{2}\right]_0^{\pi}\right\} \qquad (S10.7a) \end{aligned}$$

$$F_{Lr} = \frac{\mu_\circ N I^2}{2}\left(1 - \frac{R}{\sqrt{R^2 - a^2}}\right) \qquad (3.162)$$

Note that as $R \to \infty$, the torus becomes a straight solenoid of diameter $2a$ and, as expected, $F_{Lr} \to 0$.

DISCUSSION 3.9: Nuclear Fusion and Magnetic Confinement

If nuclei of light elements are confined and heated to a very high temperature ($\sim$100 MK), they fuse. Because the total mass of the fusion products, M_f, is less than the total mass of the original nuclei, M_n, a net energy $E_n = (M_n - M_f)c^2$ is released by the reaction, where c is the speed of light. The sun generates energy through this process. A controlled thermonuclear fusion reactor is a miniature man-made sun. The sun confines unstable hot plasma gravitationally. Magnetic pressure can substitute for gravitational pressure; the technique of using magnetic fields to stabilize a hot plasma is known as magnetic confinement.

Power-generating fusion reactors will most likely use the Tokamak, a toroidal-shaped machine configuration that uses magnetic confinement. The Tokamak was conceived in the 1950s by L.A. Artsimovich and A.D. Sakharov of the Kurchatov Institute of Atomic Energy, Moscow. The International Thermonuclear Experimental Reactor (ITER) project is a joint project of the European Union, Japan, Russia, United States, Korea, China, and India. ITER's goal is to construct a break-even Tokamak based on superconducting magnets. ITER's toroidal magnet, not circular as studied above but D-shaped, will have a major radius (R) of $\sim$8 m and be $\sim$12 m tall ($2a$ in the z-direction); its toroidal magnetic induction (B_φ) is $\sim$6 T, with a peak induction at the conductor of $\sim$13 T. ITER will be built in the French region called Cadarache, $\sim$40 km north of Aix-en-Provence.

PROBLEM 3.11: Fringing field*

This problem deals with fringing fields—unwanted fields outside a magnet system. A fringing field is important because it can be a safety hazard to those near the system; it may also disrupt or distort field-sensitive equipment. For computing the fringing field, $\vec{H}_f$, at locations *far* from the magnet, the magnet can be modeled as a spherical dipole with an effective radius R_e:

$$\vec{H}_f = H_0 \left(\frac{R_e}{r}\right)^3 (\cos\theta\,\vec{\imath}_r + \tfrac{1}{2}\sin\theta\,\vec{\imath}_\theta) \tag{3.163}$$

where $\mu_\circ H_0$ is the central field. We may compute R_e by equating the dipole's far field ($r \gg R_e$) along the z-axis (r-direction at $\theta = 0$), given by Eq. 3.163, and that ($z \gg a$) of a ring of current I and radius a, given by Eq. 3.3a. Thus:

$$H_0 R_e^3 = \tfrac{1}{2} a^2 I \tag{3.164}$$

a) For a solenoidal coil having total ampere-turns of NI, i.d. of $2a_1$ and o.d. of $2a_2$, show, by using a weighted-average, $\tilde{a}^2$, that Eq. 3.164 is modified to:

$$H_0 R_e^3 = \tfrac{1}{2}\tilde{a}^2 NI = \tfrac{1}{6}(a_1^2 + a_2^2 + a_1 a_2)NI \tag{3.165}$$

When Eq. 3.164 is applied to *each layer* of a winding comprising n_ℓ layers, each layer having the *same* total turns per *layer*, $n_{t/\ell}$, we have, given without derivation, an expression, which the reader with extra time may derive:

$$H_0 R_e^3 = \tfrac{1}{2} a_1^2 NI \left[1 + (\alpha - 1)\frac{(n_\ell + 1)}{n_\ell} + (\alpha - 1)^2 \frac{(n_\ell + 1)(2n_\ell + 1)}{6n_\ell^2}\right] \tag{3.166}$$

Note that $N = n_{t/\ell} n_\ell$. For $n_\ell \gg 1$, Eq. 3.166 may be approximated by Eq. 3.165. Because R_e is proportional to the *cube root* of the right-hand side of each equation, in most cases Eq. 3.165 is a good approximation to Eq. 3.166. In any case these equations are valid only for $r \gg R_e$, and thus R_e computed by Eq. 3.165 is independent of magnet length, $2b$, and NI. For a nested-coil magnet comprised of k coils, Eq. 3.165 may be generalized to:

$$H_0 R_e^3 = \tfrac{1}{6} I \sum_{j=1}^{k} (a_{1_j}^2 + a_{2_j}^2 + a_{1_j} a_{2_j}) N_j \tag{3.167}$$

b) By using Eq. 3.167 and parameter values given in Table 3.3, show that $R_e = 0.67\,\text{m}$ for the 45-T SCM. (Because the water magnet's volume is much smaller than the SCM's, the water magnet, despite its central field of 31 T, contributes little to the fringing fields and may be neglected here.)

c) For reasons of safety, people and equipment associated with operation and experiment of this magnet should be outside the 100-gauss contour prolate spheroid of the magnet. Determine the radial distance r_m, at $z = 2.75\,\text{m}$, at which the fringing field magnitude $|\mu_\circ \vec{H}_f|$ is 100 gauss.

---

* Based on **Problem 3.11** in the 1st Edition (Plenum, 1994).

Solution to PROBLEM 3.11

a) The weighted-average $\tilde{a}^2$ of a solenoid of $2a_1$ and $2a_2$ may be given by:

$$\tilde{a}^2 = \frac{1}{(a_2 - a_1)} \int_{a_1}^{a_2} r^2 \, dr = \frac{(a_2^3 - a_1^3)}{3(a_2 - a_1)} = \tfrac{1}{3}(a_1^2 + a_2^2 + a_1 a_2) \qquad (S11.1)$$

Thus:

$$H_0 R_e^3 = \tfrac{1}{2}\tilde{a}^2 NI = \tfrac{1}{6}(a_1^2 + a_2^2 + a_1 a_2)NI \qquad (3.165)$$

b) Applying Eq. 3.167 to the 45-T SCM (Table 3.3) with $H_0 = 14\,\mathrm{T}/\mu_\circ$, we have:

$$\frac{(14\,\mathrm{T})}{(4\pi \times 10^{-7}\,\mathrm{H/m})} R_e^3 = \tfrac{1}{6}(10^4\,\mathrm{A}) \times$$

$$\Big\{ [(0.355\,\mathrm{m})^2 + (0.444\,\mathrm{m})^2 + (0.355\,\mathrm{m})(0.444\,\mathrm{m})] \times 306$$
$$+ [(0.454\,\mathrm{m})^2 + (0.5575\,\mathrm{m})^2 + (0.454\,\mathrm{m})(0.5575\,\mathrm{m})] \times 378$$
$$+ [(0.575\,\mathrm{m})^2 + (0.840\,\mathrm{m})^2 + (0.575\,\mathrm{m})(0.840\,\mathrm{m})] \times 1015 \Big\}$$

$$(11.1408 \times 10^6\,\mathrm{A/m}) R_e^3 = 3.300 \times 10^6\,\mathrm{A\,m^2}$$

$$R_e = 0.667\,\mathrm{m}$$

c) With $\mu_\circ \vec{H}_f = 0.01\,\mathrm{T}$ (100 gauss) at $I_{op} = 10\,\mathrm{kA}$, we have:

$$(0.01\,\mathrm{T}) = (14\,\mathrm{T}) \left(\frac{0.67\,\mathrm{m}}{R\,\mathrm{m}} \right)^3 (\cos\theta\, \vec{\imath}_r + \tfrac{1}{2} \sin\theta\, \vec{\imath}_\theta) \qquad (S11.2a)$$

$$(R\,\mathrm{m}) = \sqrt{(x\,\mathrm{m})^2 + 0 + (2.7\,\mathrm{m})^2} \qquad (S11.2b)$$

$$\theta = \tan^{-1} \left(\frac{x\,\mathrm{m}}{2.7\,\mathrm{m}} \right) \qquad (S11.2c)$$

Solving Eqs. $S11.2a$, $S11.2b$, and $S11.2c$ for x, we find: $x = 6.52\,\mathrm{m}$. For $x = 6.52\,\mathrm{m}$, we find from Eq. $S11.2b$ that $R \simeq 7.05\,\mathrm{m}$ and $\theta \simeq 67.5°$.

Note that this 100-gauss exposure to the experimenters, presumably over a period of a half day or at most a day, is different from the long-term exposure level of 5 gauss sanctioned by the FDA.

Answer to TRIVIA 3.4 iii) 747 (0.06, in atm); 1.5-T field (9) —champagne (6); ballerina toes (8); plasma (10).

DISCUSSION 3.10: Scaling a Solenoidal Magnet

In an early stage of magnet design, it is sometimes convenient, and certainly quick, to scale, up or down, the parameters of a magnet already designed to those of a new magnet. Requirements often imposed in scaling are to preserve the central field, $H_z(0,0)$, or power consumption. Note that all the scaling laws below, though formulated for a solenoidal magnet, are applicable to magnets of any shape.

Thus, the original winding dimensions, $a_{1_\circ} \equiv a_\circ$; $a_{2_\circ} \equiv \alpha_\circ a_\circ$; $b_\circ \equiv \beta_\circ a_\circ$, are scaled up by $\chi > 1$ (or down by $\chi < 1$), where χ is a constant, to new winding dimensions, respectively, $a_{1\chi} = \chi a_\circ$, $a_{2\chi} = \chi \alpha_\circ a_\circ$, and $b_\chi = \chi \beta_\circ a_\circ$. Note that in the following discussion all $\circ$-subscripted parameters are those of the original magnet, while χ-subscripted parameters are those of the scaled magnet.

The parameters of interest are: $H_z(0,0) \equiv H$, the central field; λ, the space factor; J, the overall current density; I, the operating current; A, the conductor cross-sectional area; E, the magnetic energy; ℓ, the total conductor length, and $\mathcal{V}$, the volume in the winding. In this discussion, let us assume that both magnets have the same space factor: $\lambda_\chi = \lambda_\circ = \lambda$.

A. Spatial Homogeneity

As discussed in **3.4**, the spatial field homogeneity of a solenoidal magnet is determined completely by α and β. Therefore, the full-scale magnet will have the same field homogeneity (over the scaled volume) as the model magnet (over the original volume) if α and β are kept the same.

B. Center Field vs. Current Density

From Eq. 3.13*a* (**3.4** and **PROBLEM 3.1**), for the same λ, α, and β, the center field is proportional to $a_1 J$. Because $a_{1\chi} = \chi a_\circ$, J_χ must be scaled by $1/\chi$: $J_\chi = J_\circ/\chi$. Note that because the magnetic pressure is proportional to $H_z^2(0,0)$, it follows that the magnetic pressure of the new magnet remains the same as that of the original magnet. This can also be seen by noting that magnetic pressure is proportional to $a_1 J$, the product of the magnet's radial size and its operating current density, and the product is invariant in this scaling process. As may be inferred from Eq. 3.54, the total axial force at the midplane of the new magnet will be χ^2 times that of the original magnet—in Eq. 3.54, the $(NI/4b)^2$ term remains unchanged; it is the "area" term that increases by χ^2.

C. Conductor Size & Operating Current

The scaled magnet's conductor cross sectional area, $A_\chi \simeq I_\chi/J_\chi$, has to be scaled by χ^2 if I_χ is scaled by χ: $A_\chi = \chi^2 A_\circ$ for $I_\chi = \chi I_\circ$. On the other hand, if the operating current remains unchanged, $I_\chi = I_\circ$, then $A_\chi = \chi A_\circ$.

D. Total Number of Turns

The scaled magnet's number of turns, N_χ, may be given by:

$$N_\chi = \frac{\lambda J_\chi (2\beta a_\chi) a_\chi (\alpha - 1)}{I_\chi} \qquad (3.168a)$$

DISCUSSION 3.10: Scaling a Solenoidal Magnet (continuation)

As with A_χ, and $J_\chi = J_\circ/\chi$, because $H_z(0,0)$ must remain unchanged, N_χ can remain unchanged or must be scaled by χ, as shown below.

$$(\text{for } I_\chi = \chi I_\circ) \qquad N_\chi = \frac{\lambda(J_\circ/\chi)(2\beta\chi a_\circ)\chi a_\circ(\alpha-1)}{\chi I_\circ} = N_\circ \qquad (3.168b)$$

$$(\text{for } I_\chi = I_\circ) \qquad N_\chi = \frac{\lambda(J_\circ/\chi)(2\beta\chi a_\circ)\chi a_\circ(\alpha-1)}{I_\circ} = \chi N_\circ \qquad (3.168c)$$

E. Total Conductor Length, Operating Current & Ampere-Meter

The total conductor length required for the magnet, ℓ_χ, may have two options:

$$(\text{for } I_\chi = \chi I_\circ) \quad \ell_\chi = N_\chi \pi(\alpha a_\chi + a_\chi) = N_\circ \chi \pi a_\circ(\alpha+1) = \chi \ell_\circ \qquad (3.169a)$$

$$(\text{for } I_\chi = I_\circ) \quad \ell_\chi = \chi N_\circ \chi \pi a_\circ(\alpha+1) = \chi^2 \ell_\circ \qquad (3.169b)$$

The total ampere-meter, $I_\chi \ell_\chi$, which is a good indication of the conductor cost, thus is scaled by χ^2 in either case:

$$I_\chi \ell_\chi = \chi^2 I_\circ \ell_\circ \qquad (3.170)$$

F. Total Magnetic Energy

Because the total magnetic energy of a magnet is the magnetic energy density integrated over the entire spatial volume occupied by the field, and because the magnetic energy density remains unchanged, it follows: $E_{m\chi} = \chi^3 E_{m_\circ}$.

Illustrative Example

We have a model magnet of the following parameters: $H_z(0,0) = 1.53\,\text{T}$; $2a_1 = 80\,\text{mm}$; $2a_2 = 130\,\text{mm}$; $2b = 220\,\text{mm}$; total number of turns, $N_\circ = 2976$. The magnet has a self inductance of 0.301 H and generates a center field of 1.53 T at an operating current, $I_\circ$, of 100 A. Now let us consider a "full-scale" magnet with its dimensions scaled by 10 from the model magnet with λ remaining the same. We may compute a few parameters for the full-scale magnets.

Inductance Because $L_\chi = \mu_\circ a_\chi N_\chi^2 \mathcal{L}(\alpha,\beta)$, 1) $L_\chi = \chi L_\circ$ (if $I_\chi = \chi I_\circ$); or 2) $L_\chi = \chi^3 L_\circ$ (if $I_\chi = I_\circ$). Thus: 1) $L_\chi \simeq 3.01\,\text{H}$ if $I_\chi = 1000\,\text{A}$; and 2) $L_\chi = 301\,\text{H}$ if $I_\chi = 100\,\text{A}$.

Let us first compute $\ell_\circ$:

$$\ell_\circ = N_\circ \frac{a_\circ(\alpha+1)}{2}$$

$$= (2976)\frac{(0.04\,\text{m})(1.625+1)}{2} \simeq 156\,\text{m}$$

Thus: 1) $\ell_\chi \simeq 1.56\,\text{km}$ if $I_\chi = 1000\,\text{A}$; or 2) $\ell_\chi = 15.6\,\text{km}$ if $I_\chi = 100\,\text{A}$.

DISCUSSION 3.11: Particle Accelerators

The simple principle that an electric field ($\vec{E}$) accelerates charged particles is the basis for particle accelerators. Early machines of Cockroft-Walton (1928) and Van de Graaff (1930) were linear, accelerating particles along a straight path over a potential ($\int \vec{E} \cdot d\vec{s}$). A large potential is always required to produce highly energetic particles. A linear accelerator thus requires either a large $\vec{E}$ field, a long distance, or a combination of both. The Stanford Linear Accelerator (∼20 GeV) has a beam distance of 2 miles (3.2 km).

In the 1930s E.O. Lawrence developed the cyclotron, a circular accelerator. Modern circular accelerators are variations of Lawrence's cyclotron. In a circular accelerator, charged particles are accelerated by a modest potential each time they circulate around the machine; by circulating them many times it is possible to accelerate them to energy levels well beyond those achievable by linear accelerators. One essential component of a circular accelerator is a set of magnets that supplies a magnetic field (usually in the vertical direction) to bend the particles into a circular trajectory; modern machines use dipole magnets, while Lawrence's first 1.2-MeV cyclotron used magnet polepieces, which sandwiched the beam trajectory.

As studied in **PROBLEM 3.12** below, the particle energy (E_p) in circular accelerators is proportional to the beam trajectory's radius (R_a), beam velocity, and vertical magnetic induction (B_z). For a particle energy of 7 TeV of the newest particle accelerator, Large Hadron Collider (LHC), at CERN, it means a machine radius of nearly 3 km! Compare this with ∼0.1 m, the radius of Lawrence's first cyclotron. If the LHC were to use ∼1 T, the strength of B_z in Lawrence's first cyclotron, the factor of $\sim 3 \times 10^4$ increase in radius (and increase in beam energy) would still bring E_p to only ∼0.8 TeV. In LHC, the additional factor of ∼8 needed to reach the energy level of 7 TeV is achieved through increased field strength, a goal feasible only with superconducting dipole magnets.

PROBLEM 3.12: Circulating proton in an accelerator*

The LHC, the world's largest "atom smasher" (protons), has ∼1250 dipole magnets, each ∼14 m long and generating a field of 8.3 T within a diameter of 56 mm. The LHC will have two counter-circulating beams of protons, each accelerated to an energy (E_p) of 7 TeV.

a) The oblong-shaped main ring comprises two half circles of radius $R_a = 2.8$ km, connected by 4.5-km nearly straight sections for a proton with an energy E_p of 7 TeV. The dipoles occupy the ring's two half-circle sections. Show that a dipole field of 8.3 T generates a Lorentz force, $\vec{F}_L$, that balances the centripetal force, $\vec{F}_{cp}$, on a 7-TeV proton in the circular section. Assume that the proton speed is equal to the speed of light. Note: $1\,\text{eV} = 1.6 \times 10^{-19}$ J.

b) Show that the proton speed at an energy of 7 TeV is nearly the speed of light.

---

* Based on **Problem 3.12** in the 1st Edition (Plenum, 1994).

Solution to PROBLEM 3.12

a) The centripetal force, $\vec{F}_{cp}$, on a circulating proton (mass M_p) is balanced by the Lorentz force, $\vec{F}_L$. The direction of B_z is chosen to make F_L point radially inward because F_{cp} always points radially outward. The two forces are given by:

$$\vec{F}_{cp} = \frac{M_p v^2}{R_a}\,\vec{\imath}_r \simeq \frac{M_p c^2}{R_a}\,\vec{\imath}_r = \frac{E_p}{R_a}\,\vec{\imath}_r \qquad (S12.1a)$$

$$\vec{F}_L = -qcB_z\,\vec{\imath}_r \qquad (S12.1b)$$

Solving for R_a from $\vec{F}_{cp} + \vec{F}_L = 0$, we obtain:

$$R_a = \frac{E_p}{qcB_z} \qquad (S12.2)$$

From Eq. $S12.2$, we have:

$$R_a = \frac{(1.6\times10^{-19}\,\text{J/eV})(7\times10^{12}\,\text{eV})}{(1.6\times10^{-19}\,\text{C})(3\times10^{8}\,\text{m/s})(8.3\,\text{T})}$$
$$\simeq 2.81\times10^{3}\,\text{m} \simeq 2.8\,\text{km}$$

This is less than the actual radius of LHC, which is slightly over 4 km. Note that in the above computation it is assumed that the entire ring is occupied by dipoles; in fact the occupancy rate for the dipoles is ∼60%—quadrupoles, detector magnets occupy most of the rest. The average dipole field along the LHC ring is thus ∼5 T, leading to a computed radius of ∼4 km. Of course, a dipole field of $B_z = 15\,\text{T}$, for example, will nearly halve the ring diameter; superconducting dipole magnets with a field in the range 10–16 T are not out of the question [3.54–3.56].

b) The proton mass M_p, traveling at speed v, is related to its rest mass, $M_{p\circ}$ (1.67×10^{-27} kg), by:

$$M_p = \frac{M_{p\circ}}{\sqrt{1-\left(\frac{v}{c}\right)^2}} = \frac{E_p}{c^2} \qquad (S12.3)$$

Solving for v/c from Eq. $S12.3$, we have:

$$\frac{v}{c} = \sqrt{1-\frac{M_{p\circ}^2 c^4}{E_p^2}} \qquad (S12.4)$$

Because v/c is very close to 1, Eq. $S12.4$ may be approximated by:

$$\frac{v}{c} \simeq 1 - \frac{M_{p\circ}^2 c^4}{2E_p^2} = 1 - \frac{(1.67\times10^{-27}\,\text{kg})^2(3\times10^{8}\,\text{m/s})^4}{2(1.6\times10^{-19}\,\text{J/eV})^2(7\times10^{12}\,\text{eV})^2}$$
$$\simeq 1 - 9\times10^{-9}$$

That is, the proton velocity is within nine parts per billion of the speed of light.

TRIVIA 3.5 If an electron is to circle around the earth at the equator, should it travel eastward or westward? (Note that it will travel at nearly the speed of light.)

PROBLEM 3.13: Two-coil magnet

Figure 3.41 shows a cross sectional view of a magnet consisting of two axially aligned identical coils, A and B, energized in the *same* polarity. The axial field, B_z, is in the horizontal direction. As remarked in **PROBLEM 3.3** (Helmholtz coil), the antisymmetric system (Maxwell coil) generates a "linear" axial field (B_z) at the midpoint ($z=0$). The axial interaction force between coils in the symmetric system is attractive; in the split-pair antisymmetric configuration, repulsive, of identical magnitude.

The winding parameters of each coil are: $2a_1 = 1.5\,\text{m}$; $2a_2 = 2.1\,\text{m}$; $2b = 0.1\,\text{m}$; $N=8900$; and $I=65\,\text{A}$. The left coil is axially centered at $z=0.5\,\text{m}$, while the right coil is at $z=0.5\,\text{m}$—the center-to-center distance is $1\,\text{m}$ (ρ in **3.5**). Each heavy horizontal bar schematically represents a room-temperature structural element that supports the interactive force between the two coils.

Figures 3.42a and 3.42b show, respectively, $B_z(r,z)$ and $B_r(r,z)$ plots for one coil at $I=65\,\text{A}$. Note that here $z=0$ coincides with the axial midpoint of the coil.

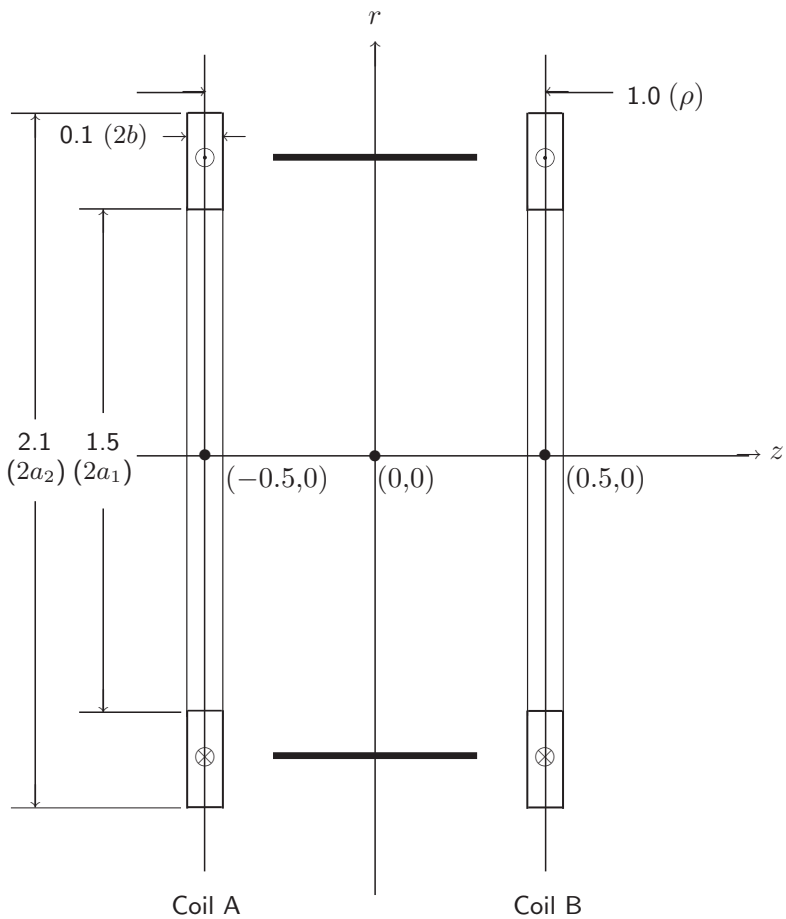

Fig. 3.41 Cross sectional view of a 2-coil magnet consisting of two identical coils, A and B, energized in the same polarity. Dimension in meters.

PROBLEM 3.13: Two-coil magnet (continutation)

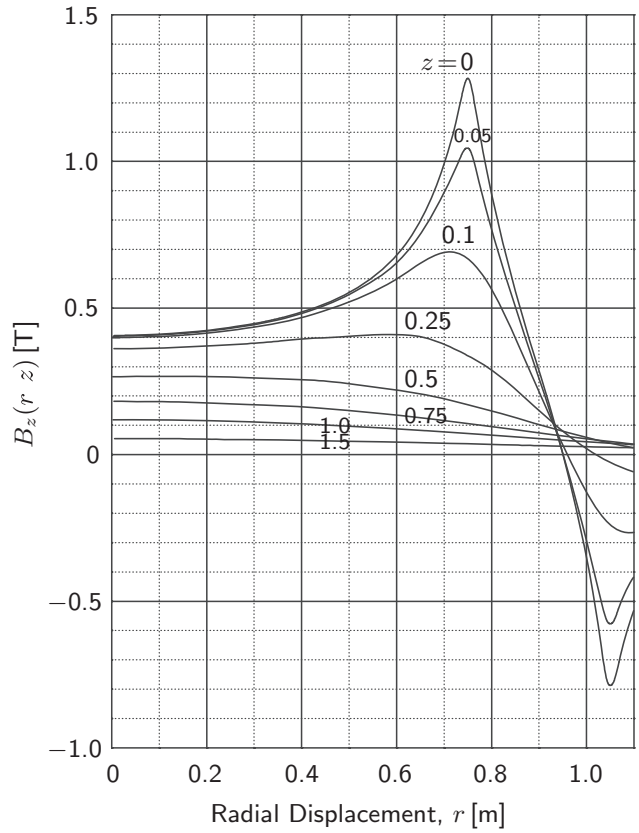

(a)

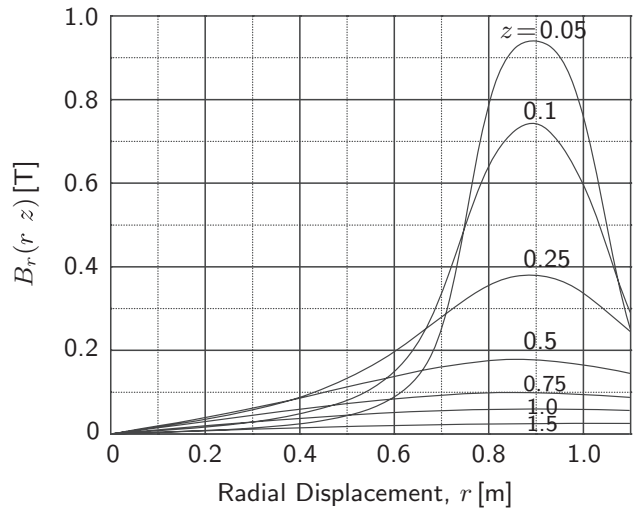

(b)

Fig. 3.42 (a) $B_z(r, z)$ and (b) $B_r(r, z)$ plots for one coil, A *or* B, at $I = 65$ A, with the other coil *unenergized*, at axial (z) locations of the energized coil.

PROBLEM 3.13: Two-coil magnet (continuation)

a) Compute the overall current density of Coil A at $I = 65\,\text{A}$.

b) Compute the total conductor length in the winding of Coil A.

c) Using an appropriate analytical expression, show that B_z at the axial midpoint of Coil A at 65 A, with Coil B *not energized*, is approximately 0.4 T, as given by Fig. 3.42a.

d) Using $\mathcal{L}(\alpha, \beta)$ given by Fig. 3.14 for solenoidal coils and Eq. 3.81, compute the self inductance L of Coil A; a code gives 216.8 H.

f) Show, qualitatively, that the axial force on Coil A, $F_{z_A}(\rho)$, studied in **3.5.1**, when Coil B is energized at 65 A, is $+z$-directed, i.e., the axial force between Coils A and B is attractive.

g) Using appropriate field data of Figs. 3.42a and 3.42b, compute the magnitude of this interactive force, when each coil is energized with a current of 65 A, to within $\pm 20\%$ of $\sim 2 \times 10^5$ N. (A code value is -193 kN, the minus sign indicating that the force is attractive.)

h) Approximating each coil as a "ring coil" (see Fig. 3.5) and using Eq. 3.34, compute the axial force exerted on Coil A, $F_{z_A}(\rho)$, by Coil B. Use $K(k) = 2.10000$ and $E(k) = 1.2000$ with $k = 0.874157$. Note that here $a_A = a_B = 0.9\,\text{m}$ and $\rho = 1.0\,\text{m}$.

i) Compute $F_{z_A}(\rho)$ for $\rho = 5\,\text{m}$.

Table 3.6 gives computed mutual inductance vs. center-to-center distance data, $M_{AB}(\rho)$, for this 2-coil system.

j) Show that the total stored magnetic energy of the system, E_m, for $\rho = 1.0\,\text{m}$ at an operating current of 65 A is approximately 1 MJ. Use $L = 216.8\,\text{H}$.

k) By applying Eq. 3.105*b* on the system, compute $F_{z_A}(\rho)$ from the $M_{AB}(\rho)$ data.

Table 3.6: M_{AB} vs. ρ Data

ρ [m]	M_{AB} [H]	ρ [m]	M_{AB} [H]
0.4	85.230	0.9	34.873
0.5	69.890	1.0	29.826
0.6	57.997	1.1	25.650
0.7	48.585	1.2	22.173
0.8	41.028	1.3	19.258

"Sometimes there is as much magic as science in the explanations of the force. Yet what is a magician but a practicing theorist?" —*Obi Wan Kenobi*

Solution to PROBLEM 3.13

a) From Eq. 3.108a:

$$\lambda J = \frac{NI}{2b(a_2 - a_1)} \tag{3.108a}$$

$$= \frac{(8900)(65\,\mathrm{A})}{(0.1\,\mathrm{m})(1.05\,\mathrm{m} - 0.75\,\mathrm{m})} = 19.3\times10^6\,\mathrm{A/m^2}$$

b) Total conductor length, ℓ, is given by: $\ell = N\pi(a_2+a_1) \simeq 50.3\,\mathrm{km}$. This 2-coil magnet thus contains a total conductor length of $\sim$100 km.

c) We may approximate Coil A (or Coil B) as a "pancake" coil with $\alpha = 1.4$. By applying Eq. 3.111f, we obtain B_{z_A}, the center axial field of Coil A:

$$B_{z_A} \simeq B_z(0,0) = \frac{\mu_\circ NI}{2a_1}\left(\frac{\ln\alpha}{\alpha - 1}\right) \tag{3.111f}$$

$$= \frac{(4\pi\times10^{-7}\,\mathrm{H/m})(8900)(65\,\mathrm{A})}{(1.5\,\mathrm{m})}\left(\frac{0.336}{0.4}\right) = 0.4\,\mathrm{T}$$

d) From Fig. 3.14, we have $\mathcal{L}(\alpha = 1.4, \beta = 0.067) \simeq 2.8$. From Eq. 3.81:

$$L = \mu_\circ a_1 N^2 \mathcal{L}(\alpha,\beta) \tag{3.81}$$

$$= (4\pi\times10^{-7}\,\mathrm{H/m})(0.75\,\mathrm{m})(8900)^2(2.8) = 209\,\mathrm{H}$$

f) $B_r(r,z)$ of Fig. 3.42b is valid for $z \geq 0$, indicating $B_r(r,z)$ is positive, pointing radially outward. When $B_r(r,z)$ generated by Coil B is applied to Coil A, however, because Coil A is located at $z < 0$ relative to the axial midpoint of Coil B, $B_r(r,z)$ of Coil B on Coil A is directed radially inward. If we apply the $I\,\vec{\imath}_\theta \times -B_r(r,z)\vec{\imath}_r$ product to the top winding cross section of Coil A in Fig. 3.41, the axial force on Coil A by Coil B is $+z$-directed, indicating the force, as expected, is attractive.

g) $F_{z_A}(\rho)$ is the Lorentz interaction force, here given by:

$$F_{z_A}(\rho) \simeq (\text{average winding circumference})\times(NI)\times$$
$$(B_r \text{ at the winding cross section center})$$
$$= \pi(1.8\,\mathrm{m})(8900\times65\,\mathrm{A})(0.06\,\mathrm{T}) = 196\,\mathrm{kN}$$

h) $F_{z_A}(\rho)$ on Coil A due to Coil B is given by:

$$F_{z_A}(\rho) = \frac{\mu_\circ}{2}(N_A I_A)(N_B I_B)\frac{\rho\sqrt{(a_A + a_B)^2 + \rho^2}}{(a_A - a_B)^2 + \rho^2}$$
$$\times\Big\{k^2K(k) + (k^2 - 2)[K(k) - E(k)]\Big\} \tag{3.34}$$

where $K(k)$ and $E(k)$ are, respectively, the complete elliptic integrals of the first and second kinds.

$$k^2 = \frac{4a_A a_B}{(a_A + a_B)^2 + \rho^2} \tag{3.36}$$

Solution to PROBLEM 3.13 (continuation)

Here, we have: $N_A = N_B = N = 8900$; $a_A = a_B = (a_1 + a_2)/2 = 0.9\,\text{m}$; and $\rho = 1\,\text{m}$.

$$k^2 = \frac{4(0.9\,\text{m})(0.9\,\text{m})}{(0.9\,\text{m} + 0.9\,\text{m})^2 + (1.0\,\text{m})^2} = 0.764151 \quad \Rightarrow \quad k = 0.874157$$

We have: $K(k) = 2.100000$ and $E(k) = 1.200000$. Thus:

$$\begin{aligned} F_{zA}(1\,\text{m}) = &-\frac{(4\pi \times 10^{-7}\,\text{H/m})}{2}(8900 \times 65\,\text{A})^2 \\ &\times \left[\frac{(1.0\,\text{m})\sqrt{(0.9\,\text{m}+0.9\,\text{m})^2+(1.0\,\text{m})^2}}{(0.9\,\text{m}-0.9\,\text{m})^2+(1.0\,\text{m})^2}\right] \\ &\times \Big\{(0.764151)2.10000+(0.764151-2)(2.10000-1.200000)\Big\} \\ = &\,(210.27 \times 10^7\,\text{N})(2.059)(0.492) \simeq -213.2\,\text{kN} \end{aligned}$$

i) In the limit $\rho^2 \gg (a_A + a_B)^2$, Eq. 3.34 is simplified to:

$$F_{zA}(\rho) = \frac{3\mu_\circ}{2\pi}\left(\frac{\pi a_A^2 N_A I_A}{\rho^2}\right)\left(\frac{\pi a_B^2 N_B I_B}{\rho^2}\right) \tag{3.39c}$$

With $\rho^2 = 25.0\,\text{m}^2$ and $(a_A + a_B)^2 = 3.24\,\text{m}^2$, the condition $\rho^2 \gg (a_A + a_B)^2$ is satisfied. Because $N_A = N_B = N = 8900$, $I_A = I_B = 65\,\text{A}$, $a_A = b_B = 0.9\,\text{m}$, Eq. 3.39*c* becomes:

$$F_{zA}(\rho) = \frac{3(4\pi \times 10^{-7}\,\text{H/m})}{2\pi}\left[\frac{\pi(0.9\,\text{m})^2(8900)(65\,\text{A})}{(5.0\,\text{m})^2}\right]^2 = 2.08\,\text{kN}$$

A force of 2 kN (∼200 kg) is only about 13% the weight of each coil.

j) The total stored magnetic energy of the system, E_m, is given by Eq. 3.92:

$$E_m = \tfrac{1}{2}L_1 I_1^2 + \tfrac{1}{2}L_2 I_2^2 + M_{12} I_1 I_2 \tag{3.92}$$

With $L_1 = L_A = L_2 = L_B \equiv L = 216.8\,\text{H}$, $I_1 = I_A = I_2 = I_B \equiv I = 65\,\text{A}$, and from the table $M_{AB} \simeq 29.8\,\text{H}$, thus:

$$E_m = LI^2 + M_{AB}I^2 = (L + M_{AB})I^2 = (246.6\,\text{H})(65\,\text{A})^2 = 1.04\,\text{MJ}$$

k) Equation 3.105*b* is given by:

$$F_{zR}(\rho) = \frac{\partial E_{AB}}{\partial \rho} = I_A I_B \frac{\partial M_{AB}(\rho)}{\partial \rho} \tag{3.105b}$$

From the table, $M_{AB}(\rho = 0.9\,\text{m}) = 34.873\,\text{H}$ and $M_{AB}(\rho = 1.1\,\text{m}) = 25.650\,\text{H}$. Thus:

$$\frac{\partial M_{AB}(\rho)}{\partial \rho} \simeq \frac{(25.650\,\text{H} - 34.873\,\text{H})}{(1.1\,\text{m} - 0.9\,\text{m})} = -46.115\,\text{H/m} \tag{S17.1}$$

Inserting Eq. *S*17.1 into Eq. 3.105*b* with $I_A = I_B = I = 65\,\text{A}$, we have:

$$F_{zR}(\rho) \simeq (65\,\text{A})^2(-46.115\,\text{H/m}) = -194.8\,\text{kN}$$

Not surprisingly, this agrees quite well with the −193 kN computed by a code.

PROBLEM 3.14: Midplane axial force in a solenoid

In this problem, we shall apply some of the expressions derived in **Sec. 3.5** for a solenoid of $2a_1 = 10\,\text{cm}$; $2a_2 = 14\,\text{cm}$; $2b = 25\,\text{cm}$; $NI = 1.5\times10^6\,\text{A}$, shown in Fig. 3.43a.

a) Although this solenoid ($\alpha = 1.4$, $\beta = 2.5$) is really neither "thin-walled" nor "long," use Eq. 3.111*d* to compute $B_z(0,0)$.

b) Treating the solenoid as "thin-walled," apply Eq. 3.41*a* to compute the axial midplane force, $F_z(0)$, which by a code is $-187.8\,\text{kN}$. Use $2a = 10\,\text{cm}$.

c) Use Eq. 3.41*b*, valid for a "long" coil, to compute $F_z(0)$. Choose: 1) $2a = 10\,\text{cm}$; 2) $2a = 12\,\text{cm}$, the solenoid average diameter.

d) Now, divide the solenoid into two subsolenoids, A and B, as illustrated in Fig. 3.43b, each of an equal radial build of 1 cm, with $2a_A = 10\,\text{cm}$, $2a_B = 12\,\text{cm}$, and $NI = 0.75\times10^6\,\text{A}$. Compute $B_z(0,0)$.

e) Apply Eq. 3.54 and compare with $F_{zT}(0) = -187.8\,\text{kN}$, computed by a code.

f) Apply Eq. 3.55, valid for a "long" coil, and compute $F_{zT}(0)$.

g) Applying the condition $\nabla\cdot\vec{B} = 0$ over the surfaces of one half of a "thin-wall" and "long" coil $(2a, 2b)$ having a uniform surface current density $NI/2b$, derive Eq. 3.41*b*. Note that the surfaces to be considered are the coil's x-y-plane cross-sectional areas at $z = 0$ (midplane) and $z = b$, each πa^2, and the cylindrical surface area at $r = a$ from $z = 0$ to $z = b$, i.e., $2\pi ab$.

h) For a long ($\beta \gg 1$) coil, explain why its axial force over most of its length, from the midplane to near its end, is constant and given by that corresponding to the midplane value. Try estimating the z location over one half of this long solenoid at which B_z begins to plummet from $B_z(0,0)$.

Table 3.7 on the next page gives values of appropriate complete elliptic integrals.

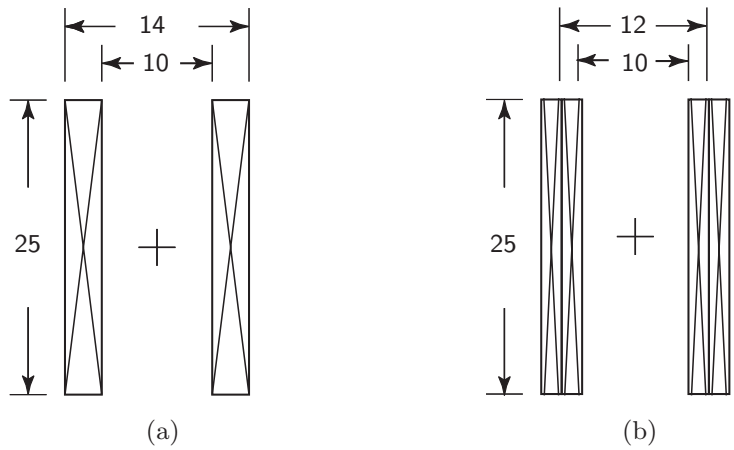

Fig. 3.43 (a) Solenoid with $2a_1 = 10\,\text{cm}$; $2a_2 = 14\,\text{cm}$; $2b = 25\,\text{cm}$. (b) Solenoid subdivided into subsolenoids A and B, with $2a_A = 10\,\text{cm}$; $2a_B = 12\,\text{cm}$; $2b = 25\,\text{cm}$.

Solution to PROBLEM 3.14

Table 3.7: Values of Appropriate Complete Elliptic Integrals for **b)** and **e)**

k^2	$K(k)$	$E(k)$	k^2	$K(k)$	$E(k)$
0.137931	1.62961	1.51514	0.390244	1.77081	1.40400
0.160858	1.64041	1.50558	0.432822	1.80099	1.38373
0.187256	1.65325	1.49445	0.479600	1.83717	1.36084
c^2	k	$\Pi(c^2,k)$	c^2	k	$\Pi(c^2,k)$
0.991736	0.401071	18.7227	0.991736	0.657892	22.3701

a) Applying Eq. 3.111d we have:

$$B_z(0,0) = \frac{\mu_\circ NI}{2b} \qquad (3.111d)$$
$$= \frac{(4\pi\times10^{-7}\,\mathrm{H/m})(1.5\times10^{6}\,\mathrm{A})}{(0.25\,\mathrm{m})} = 7.5\,\mathrm{T}$$

Equation 3.109 for this solenoid of $\alpha = 1.4$ and $\beta = 2.5$, gives $B_z(0,0) = 6.8\,\mathrm{T}$. Equation 3.111$d$ thus errs by ∼10%, not too bad considering its simplicity.

b) Equation 3.41a is given here once more.

$$F_z(0) = -\frac{\mu_\circ}{2}\left(\frac{NI}{2b}\right)^2 \Big\{2b\sqrt{4a^2+b^2}\,\big[K(k_b)-E(k_b)\big] - 2b\sqrt{4a^2+4b^2}\,\big[K(k_{2b})-E(k_{2b})\big]\Big\} \qquad (3.41a)$$

with moduli given by:

$$k_b^2 = \frac{4a^2}{4a^2+b^2} = \frac{4(5\,\mathrm{cm})^2}{4(5\,\mathrm{cm})^2+(12.5\,\mathrm{cm})^2} \simeq 0.390244$$
$$k_{2b}^2 = \frac{4a^2}{4a^2+(2b)^2} = \frac{4(5\,\mathrm{cm})^2}{4(5\,\mathrm{cm})^2+(25\,\mathrm{cm})^2} \simeq 0.137931$$

With values of appropriate $K(k)$ and $E(k)$ given in Table 3.7:

$$F_z(0) = -\frac{(4\pi\times10^{-7}\,\mathrm{H/m})}{2}\left(\frac{1.5\times10^{6}\,\mathrm{A}}{0.25\,\mathrm{m}}\right)^2\times$$
$$\Big\{(0.25\,\mathrm{m})\sqrt{4(0.05\,\mathrm{m})^2+(0.125\,\mathrm{m})^2}\,(1.77081-1.40400)$$
$$-\,(0.25\,\mathrm{m})\sqrt{4(0.05\,\mathrm{m})^2+4(0.125\,\mathrm{m})^2}\,(1.62961-1.51514)\Big\}$$
$$= -(2.262\times10^{7}\,\mathrm{N/m^2})(14.680\times10^{-3}\,\mathrm{m^2} - 7.705\times10^{-3}\,\mathrm{m^2})$$
$$\simeq -157.8\,\mathrm{kN}$$

$F_z(0)\simeq-157.8\,\mathrm{kN}$ is 84% of $-187.8\,\mathrm{kN}$ computed by a code.

Solution to PROBLEM 3.14 (continuation)

c) Equation 3.41*b* is given by:

$$F_z(0) \simeq -\frac{\mu_\circ}{2}\left(\frac{NI}{2b}\right)^2 \pi a^2 \tag{3.41b}$$

Applying Eq. 3.41*b* with $a = 5\,\text{cm}$ and $a = 6\,\text{cm}$, we obtain:

1) $$F_z(0) \simeq -\frac{(4\pi\times10^{-7}\,\text{H/m})}{2}\left(\frac{1.5\times10^6\,\text{A}}{0.25\,\text{m}}\right)^2 \pi(5\times10^{-2}\,\text{m})^2 = -177.7\,\text{kN}$$

2) $$F_z(0) \simeq -\frac{(4\pi\times10^{-7}\,\text{H/m})}{2}\left(\frac{1.5\times10^6\,\text{A}}{0.25\,\text{m}}\right)^2 \pi(6\times10^{-2}\,\text{m})^2 = -255.8\,\text{kN}$$

Equation 3.41*b* underestimates the code value by ∼5% with $a = 5\,\text{cm}$, while it overestimates the code value by 36% with $a = 6\,\text{cm}$. These results appear to suggest that it is better to equate $2a$ with the solenoid i.d. However, this may not be valid for other values of α.

d) Apply Eq. 3.111*d* to each subsolenoid; we find that $B_z(0,0)$ remains the same.

$$\begin{aligned} B_z(0,0) &= B_{z_A}(0,0) + B_{z_B}(0,0) \\ &= (4\pi\times10^{-7}\,\text{H/m})\left[\frac{(0.75\times10^6\,\text{A})}{(0.25\,\text{m})} + \frac{(0.75\times10^6\,\text{A})}{(0.25\,\text{m})}\right] = 7.5\,\text{T} \end{aligned}$$

e) Equation 3.54 is given below once again:

$$\begin{aligned} F_{z_T}(0) = -\frac{\mu_\circ}{2}\left(\frac{NI}{4b}\right)^2 \times \\ \Bigg(& 2b\sqrt{4a_A^2+b^2}\left[K(k_{b_A})-E(k_{b_A})\right] - 2b\sqrt{4a_A^2+4b^2}\left[K(k_{2b_A})-E(k_{2b_A})\right] \\ &+ 2b\sqrt{4a_B^2+b^2}\left[K(k_{b_B})-E(k_{b_B})\right] - 2b\sqrt{4a_B^2+4b^2}\left[K(k_{2b_B})-E(k_{2b_B})\right] \\ &- \frac{4b}{\sqrt{a_T^2+b^2}}\Big\{(a_T^2+b^2)\left[K(k_b)-E(k_b)\right] - \Upsilon(c^2,k_b)\Big\} \\ &+ \frac{4b}{\sqrt{a_T^2+4b^2}}\Big\{(a_T^2+4b^2)\left[K(k_{2b})-E(k_{2b})\right] - \Upsilon(c^2,k_{2b})\Big\}\Bigg) \end{aligned} \tag{3.54}$$

with c^2 and the other moduli given by:

$$c^2 = \frac{4a_A a_B}{(a_A+a_B)^2} = \frac{4(5\,\text{cm})(6\,\text{cm})}{(5\,\text{cm}+6\,\text{cm})^2} \simeq 0.991736$$

$$k_{b_A}^2 = \frac{4a_A^2}{4a_A^2+b^2} = \frac{4(5\,\text{cm})^2}{4(5\,\text{cm})^2+(12.5\,\text{cm})^2} \simeq 0.390244$$

$$k_{2b_A}^2 = \frac{4a_A^2}{4a_A^2+(2b)^2} = \frac{4(5\,\text{cm})^2}{4(5\,\text{cm})^2+(25\,\text{cm})^2} \simeq 0.137931$$

$$k_{b_B}^2 = \frac{4a_B^2}{4a_B^2+b^2} = \frac{4(6\,\text{cm})^2}{4(6\,\text{cm})^2+(12.5\,\text{cm})^2} \simeq 0.479600$$

Solution to PROBLEM 3.14 (continuation)

$$k_{2b_B}^2 = \frac{4a_B^2}{4a_B^2 + (2b)^2} = \frac{4(6\,\mathrm{cm})^2}{4(6\,\mathrm{cm})^2 + (25\,\mathrm{cm})^2} \simeq 0.187256$$

$$k_b^2 = \frac{4a_A a_B}{(a_A + a_B)^2 + b^2} \simeq 0.432822 \Longrightarrow k_b \simeq 0.657892$$

$$k_{2b}^2 = \frac{4a_A a_B}{(a_A + a_B)^2 + 4b^2} \simeq 0.160858 \Longrightarrow k_{2b} \simeq 0.401071$$

Inserting these and other appropriate values into Eq. 3.54, we obtain:

$$\begin{aligned}
F_z(0) = &-\frac{(4\pi\times10^{-7}\,\mathrm{H/m})}{2}\left(\frac{1.5\times10^6\,\mathrm{A}}{0.5\,\mathrm{m}}\right)^2\times \\
&\Big[(0.25\,\mathrm{m})\sqrt{4(0.05\,\mathrm{m})^2+(0.125\,\mathrm{m})^2}\,(1.77081-1.40400) \\
&-(0.25\,\mathrm{m})\sqrt{4(0.05\,\mathrm{m})^2+4(0.125\,\mathrm{m})^2}\,(1.62961-1.51514) \\
&+(0.25\,\mathrm{m})\sqrt{4(0.06\,\mathrm{m})^2+(0.125\,\mathrm{m})^2}\,(1.83717-1.36084) \\
&-(0.25\,\mathrm{m})\sqrt{4(0.06\,\mathrm{m})^2+4(0.125\,\mathrm{m})^2}\,(1.65325-1.49445) \\
&+\frac{4(0.125\,\mathrm{m})}{\sqrt{(0.11\,\mathrm{m})^2+(0.125\,\mathrm{m})^2}}\Big\{[(0.11\,\mathrm{m})^2+(0.125\,\mathrm{m})^2](1.80099-1.38373) \\
&\qquad -(0.05\,\mathrm{m}-0.06\,\mathrm{m})^2(22.3701-1.8010)\Big\} \\
&-\frac{4(0.125\,\mathrm{m})}{\sqrt{(0.11\,\mathrm{m})^2+4(0.125\,\mathrm{m})^2}}\Big\{[(0.11\,\mathrm{m})^2+4(0.125\,\mathrm{m})^2](1.64041-1.50558) \\
&\qquad -[(0.05\,\mathrm{m}-0.06\,\mathrm{m})^2(18.7227-1.6404)\Big\}\Big] \\
= &-(5.655\times10^7\,\mathrm{N/m^2})\times\Big(14.680\times10^{-3}\,\mathrm{m^2}-7.705\times10^{-3}\,\mathrm{m^2} \\
&\qquad +20.634\times10^{-3}\,\mathrm{m^2}-11.009\times10^{-3}\,\mathrm{m^2} \\
&\qquad +34.739\times10^{-3}\,\mathrm{m^2}-6.177\times10^{-3}\,\mathrm{m^2} \\
&\qquad -18.413\times10^{-3}\,\mathrm{m^2}+3.127\times10^{-3}\,\mathrm{m^2}\Big) \\
\simeq &-(5.655\times10^7\,\mathrm{N/m^2})\times(29.875\times10^{-3}\,\mathrm{m^2}) \\
\simeq &-168.9\,\mathrm{kN}
\end{aligned}$$

The computation still underestimates the code value ($-187.8\,\mathrm{kN}$), but now it is 90%. Although Eq. 3.54 gives a value more accurate than Eq. 3.41*a*, as seen here, it is extremely tedious and thus not recommended as a means to make a quick estimate of the force. Clearly, dividing a solenoid into two subsolenoids and applying Eq. 3.54 is the limit of manual computation with a pocket calculator.

Note that the remarkable result of Eq. 3.41*b* with $a = 5\,\mathrm{cm}$ seen above is most likely coincidental rather than a general rule.

Solution to PROBLEM 3.14 (continuation)

f) Applying Eq. 3.55 with $a_A = 5\,\text{cm}$ and $a_B = 6\,\text{cm}$, we obtain:

$$F_z(0) \simeq -(4\pi\times10^{-7}\,\text{H/m})\left(\frac{1.5\times10^6\,\text{A}}{0.5\,\text{m}}\right)^2 \pi[(0.05\,\text{m})^2 + (0.06\,\text{m})^2]$$

$$\times\left\{1 - \frac{(0.05\,\text{m} - 0.06\,\text{m})^2(2\times22.3701 - 18.7227)}{\pi[(0.05\text{m})^2 + (0.06\,\text{m})^2]}\right\}$$

$$\simeq -(216.7\,\text{kN})(1 - 0.136) = -187.3\,\text{kN}$$

Equation 3.55, which is much simpler to compute than Eq. 3.54, also turns out to give, at least in this particular example, a better result than Eq. 3.54.

g) The differential force acting on one complete turn at $z \geq 0$ carrying a differential current of dI is given by:

$$dF_z(z \geq 0) = -2\pi a B_r(z)\, dI$$

The negative sign indicates this force is directed towards the midplane. Substituting $dI = (NI/2b)\, dz$ and integrating over the entire half length of the solenoid, from $z = 0$ to $z = b$, we have:

$$F_z(0) = -\int_0^b 2\pi a B_r(z)\frac{NI}{2b}\, dz = -\frac{NI}{2b}\int_0^b 2\pi a B_r(z)\, dz \qquad (S14.1)$$

The integral $\int_0^b 2\pi a B_r(z) dz$ is the total radial flux leaving this half of the solenoid. From $\nabla\cdot\vec{B} = 0$ this is equal to the difference between the total axial flux entering into this half of the solenoid over the circular plane at the midplane ($z = 0$) and that leaving the solenoid over the circular plane at $z = b$. Namely,

$$\int_0^b 2\pi a B_r(z)\, dz = \pi a^2[B_z(0) - B_z(b)] \qquad (S14.2)$$

Note that it is assumed that for a "long" coil ($k^2 \ll 1$ or $\beta \gg 1$), for which Eq. 3.41*b* is valid, $B_z(0,0)$ and $B_z(0,b)$ may be assumed constant over the circular plane of area πa^2. For this long solenoid, it is also true that $B_z(0,b) \simeq 0.5B_z(0,0)$ (see ***DISCUSSION 3.4***), thus Eq. $S14.2$ may be given by:

$$\int_0^b 2\pi a B_r(z)\, dz \simeq \frac{\pi a^2}{2} B_z(0) \qquad (S14.3)$$

For a long coil, $B_z(0,0) = \mu_\circ NI/2b$ (Eq. 3.111), thus:

$$\int_0^b 2\pi a B_r(z)\, dz \simeq \frac{\pi a^2}{2}\times\frac{\mu_\circ NI}{2b} \qquad (S14.4)$$

Combining Eqs. $S14.1$ and $S14.4$, we have:

$$F_z(0) \simeq -\frac{NI}{2b}\times\frac{\pi a^2}{2}\times\frac{\mu_\circ NI}{2b} \simeq -\frac{\mu_\circ}{2}\left(\frac{NI}{2b}\right)^2 \pi a^2 \qquad (3.41b)$$

Solution to PROBLEM 3.14 (continuation)

h) For a "long" solenoid, $B_z(z)$ is constant with z, and from the requirement of $\nabla\cdot\vec{B}=0$ the radial component $B_r(z)$ is virtually zero. Because $F_z(z)$ is generated by $B_r(z)$ (Eq. S14.1), $dF_z(z)=0$ over most of the coil length. $F_z(z)$ thus remains constant until z approaches $z=b$, at which point flux lines begin to diverge away from the magnet axis, giving rise to $B_r(z)$, which generates $F_z(z)$. For $4b^2 \gg 4a^2$ and $(b+z)^2 \gg 4a^2$, it can be shown that the 2nd and 3rd lines within the braces in Eq. 3.40 cancel out, leaving only the first term for $F_z(z\simeq b)$, given by:

$$F_z(z\simeq b) \simeq -\frac{\mu_\circ}{2}\left(\frac{NI}{2b}\right)^2 \left\{(b-z)\sqrt{4a^2+(b-z)^2}\left[K(k_{b-})-E(k_{b-})\right]\right\} \qquad (S14.5)$$

Because z is close to b, $k_{b-}^2 = 4a^2/[4a^2+(b-z)^2] \not\ll 1$ and thus $K(k_{b-})-E(k_{b-})$ cannot be approximated in k_{b-}^2. Let us simply guess the location of z near b at which point $F_z(z\sim b)$ is close to that given by Eq. 3.41b. If we guess $z=b$–$2a$, then:

$$F_z(z=b-2a) \simeq -\frac{\mu_\circ}{2}\left(\frac{NI}{2b}\right)^2 \left\{2a\sqrt{4a^2+4a^2}\left[K(k_{b-})-E(k_{b-})\right]\right\} \qquad (S14.6)$$

where $k_{b-}^2 = 4a^2/8a^2 = 0.5$, which gives, from Table 3.1, $K(k_{b-}=0.7071)=1.8541$ and $E(k_{b-})=1.3506$. Inserting these values into Eq. S14.6, we obtain:

$$\begin{aligned} F_z(z=b-2a) &\simeq -\frac{\mu_\circ}{2}\left(\frac{NI}{2b}\right)^2 4a^2\sqrt{2}(0.5035) \\ &= -\frac{\mu_\circ}{2}\left(\frac{NI}{2b}\right)^2 2.85a^2 \end{aligned} \qquad (S14.7)$$

Because 2.85 is $\sim 90\%$ of π, $F_z(z)$ indeed approaches the midplane force at a distance within $\sim 2a$ from each end of a long solenoid. This constant $F_z(z)$ over most of the axial length of a long solenoid also implies that $B_z(z)$ remains nearly $B_z(0,0)$ over the same axial length, $\sim(2b-4a)$, of the solenoid.

Help from Van (Part 3 of 5 Parts)

—Passage from Francis Bitter's *Magnets: The Education of a Physicist*

It was too late for us to do any more about it that night, but we had made some progress although we had not reached the maximum power input into that magnet by a big factor. Then came a period of taking the magnet apart, finding out what had gone wrong, putting it together, trying again. Finally it became clear that there was nothing fundamentally wrong with the design, but that many little details hard to foresee had to be looked after. The usual expression for this sort of thing is getting the 'bugs' out of the apparatus. When we got the bugs out, the magnet behaved just as had been calculated. It was a success.

PROBLEM 3.15: Midplane axial forces in a nested 2-coil magnet

In this problem we compute the axial compressive forces of Solenoids A and B that comprise a nested 2-coil magnet, as shown in Fig. 3.44; the axial fields of both solenoids point in the z-direction. The coil parameters are as follows: $2a_A = 10\,\text{cm}$; $2b_A = 50\,\text{cm}$; $N_A I_A = 3\times10^6$ A; $2a_B = 14\,\text{cm}$; $2b_B = 100\,\text{cm}$; $N_B I_B = 8\times10^6$ A. Each solenoid has a radial winding build of 1 cm.

a) Treating each solenoid "thin-walled" ($\alpha = 1$) and "long" ($\beta \gg 1$), compute the center field generated by each solenoid, $B_{z_A}(0,0)$ and $B_{z_B}(0,0)$. Show that the center field of this nested magnet is ~17.5 T (exact value: 17.31 T).

b) Using Eq. 3.57b, compute $F_{z_A}(0)$, the total midplane axial force on Solenoid A. A code gives $F_{z_A}(0) = -200.9\,\text{kN}$.

c) Using Eq. 3.57a, recompute $F_{z_A}(0)$. The computed value should be closer to $-200.9\,\text{kN}$ than that computed in **b)** with Eq. 3.57b.

d) Using Eq. 3.59a compute $F_{z_B}(0)$, the total midplane axial force on Solenoid B. A code gives $F_{z_B} = -1207.5\,\text{kN}$.

e) Explain why the maximum total field within the winding of Solenoid A, $B_{T_A} = \sqrt{B_{z_A}^2 + B_{r_A}^2}$, is likely to be at $r = a_A$ (winding's innermost radius) and $z = 0$.

f) Explain why the maximum total field within the winding of Solenoid B, $B_{T_B} = \sqrt{B_{z_B}^2 + B_{r_B}^2}$, likely will not be at or even near $z = 0$. Where will it likely be?

Table 3.8 on next page gives values of $\Pi(c^2, k)$

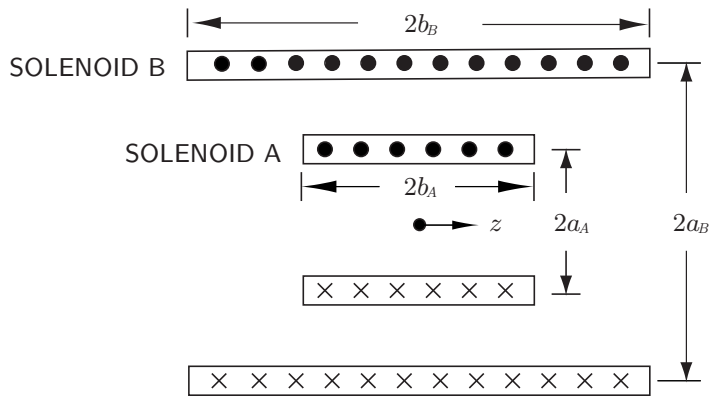

Fig. 3.44 Drawing of a nested 2-coil magnet comprised of two "thin-walled" ($\alpha = 1$) solenoids. Solenoid A (inner) $2a_A = 10\,\text{cm}$; $2b_A = 50\,\text{cm}$. Solenoid B (outer) $2a_B = 14\,\text{cm}$; $2b_B = 100\,\text{cm}$.

Solution to PROBLEM 3.15

Table 3.8: Values of $\Pi(c^2=0.992222,k)$ for **c)** and **d)**

k	$\Pi(c^2,k)$	k	$\Pi(c^2,k)$	k	$\Pi(c^2,k)$
0.155782	9.5245	0.230109	9.6468	0.426679	10.2692

a) From $B_z(0,0)=\mu_\circ H_z(0,0)$ and Eq. 3.111d, we have:

$$B_{z_A}(0,0) = (4\pi\times10^{-7}\,\mathrm{H/m})\frac{(3\times10^6\,\mathrm{A})}{(0.5\,\mathrm{m})} \simeq 7.5\,\mathrm{T}$$

$$B_{z_B}(0,0) = (4\pi\times10^{-7}\,\mathrm{H/m})\frac{(8\times10^6\,\mathrm{A})}{(1.0\,\mathrm{m})} \simeq 10.0\,\mathrm{T}$$

$$B_z(0,0) = B_{z_A}(0,0) + B_{z_B}(0,0) \simeq 17.5\,\mathrm{T}$$

As noted in the question statement, the exact central field value is 17.32 T.

b) Equation 3.57b is given below:

$$F_{z_A}(0) \simeq F_{z_{AA}}(0) \simeq -\frac{\mu_\circ}{2}\left(\frac{N_A I_A}{2b_A}\right)^2 \pi a_A^2 \qquad (3.57b)$$

Inserting appropriate values into Eq. 3.57b, we have:

$$F_{z_A} \simeq -\frac{(4\pi\times10^{-7}\,\mathrm{H/m})}{2}\left(\frac{3\times10^6\,\mathrm{A}}{0.5\,\mathrm{m}}\right)^2 \pi(0.05\,\mathrm{m})^2 \simeq -177.7\,\mathrm{kN}$$

Thus Eq. 3.57b gives a value that is 88% of that computed by a code; some of the discrepancy is because Eq. 3.57b does not include the $F_{z_{AB}}(0)$ contribution.

c) Equation 3.57a is given below:

$$F_{z_A}(0) \simeq -\frac{\mu_\circ}{2}\left\{\left(\frac{N_A I_A}{2b_A}\right)^2 \pi a_A^2 + \left(\frac{N_B I_B}{2b_B}\right)\left(\frac{N_A I_A}{2b_A}\right)\times \right.$$
$$\left. (a_A-a_B)^2\left[\Pi(c^2,k_D)+\Pi(c^2,k_T)-2\Pi(c^2,k_B)\right]\right\} \qquad (3.57a)$$

where

$$c^2 = \frac{4a_A a_B}{(a_A+a_B)^2} = \frac{4(5\,\mathrm{cm})(7\,\mathrm{cm})}{(5\,\mathrm{cm}+7\,\mathrm{cm})^2} = 0.972222$$

$$k_B^2 = \frac{4a_A a_B}{a_T^2+b_B^2} = \frac{4(5\,\mathrm{cm})(7\,\mathrm{cm})}{(12\,\mathrm{cm})^2+(50\,\mathrm{cm})^2} = 0.052950 \Longrightarrow k_B \simeq 0.230109$$

$$k_D^2 = \frac{4a_A a_B}{a_T^2+b_D^2} = \frac{4(5\,\mathrm{cm})(7\,\mathrm{cm})}{(12\,\mathrm{cm})^2+(25\,\mathrm{cm})^2} = 0.182055 \Longrightarrow k_D \simeq 0.426679$$

$$k_T^2 = \frac{4a_A a_B}{a_T^2+b_T^2} = \frac{4(5\,\mathrm{cm})(7\,\mathrm{cm})}{(12\,\mathrm{cm})^2+(75\,\mathrm{cm})^2} = 0.024268 \Longrightarrow k_T \simeq 0.155781$$

Solution to PROBLEM 3.15 (continuation)

Inserting appropriate values into Eq. 3.57a, we have:

$$F_{z_A} \simeq -\frac{(4\pi\times10^{-7}\,\mathrm{H/m})}{2}\left\{\left(\frac{3\times10^6\,\mathrm{A}}{0.5\,\mathrm{m}}\right)^2\pi(0.05\,\mathrm{m})^2+\left[\left(\frac{8\times10^6\,\mathrm{A}}{1.0\,\mathrm{m}}\right)\left(\frac{3\times10^6\,\mathrm{A}}{0.5\,\mathrm{m}}\right)\right.\right.$$
$$\left.\left.\times(0.05\,\mathrm{m}-0.07\,\mathrm{m})^2(10.2692+9.5245-2\times9.6468)\right]\right\}$$
$$\simeq -(177.7\,\mathrm{kN}+6.0\,\mathrm{kN})\simeq -183.7\,\mathrm{kN}$$

This is 91% of −200.9 kN; as expected, an improvement from **b)**, though not enough to justify the increased complexity.

d) Equation 3.59a is given by:

$$F_{z_A}(0) \simeq -\frac{\mu_\circ}{2}\left\{\left(\frac{N_BI_B}{2b_B}\right)^2\pi a_B^2+\left(\frac{N_BI_B}{2b_B}\right)\left(\frac{N_AI_A}{2b_A}\right)\left[\pi(a_A^2+a_B^2)\right.\right.$$
$$\left.\left.-(a_A-a_B)^2\left[2\Pi(c^2,k_A)+\Pi(c^2,k_D)-\Pi(c^2,k_T)\right]\right]\right\} \qquad (3.59a)$$

where c^2, k_D^2, and k_T^2 are given above; for this case, because $b_A=b_D$, $k_A^2=k_D^2$. Thus:

$$F_{z_B} \simeq -\frac{(4\pi\times10^{-7}\,\mathrm{H/m})}{2}\left\{\left(\frac{8\times10^6\,\mathrm{A}}{1.0\,\mathrm{m}}\right)^2\pi(0.07\,\mathrm{m})^2\right.$$
$$+\left(\frac{8\times10^6\,\mathrm{A}}{1.0\,\mathrm{m}}\right)\left(\frac{3\times10^6\,\mathrm{A}}{0.5\,\mathrm{m}}\right)\left[\pi[(0.05\,\mathrm{m})^2+(0.07\,\mathrm{m})^2]\right.$$
$$\left.\left.-(0.05\,\mathrm{m}-0.07\,\mathrm{m})^2(2\times10.2692+10.2692-9.5245)\right]\right\}$$
$$\simeq -(619.0\,\mathrm{kN}+444.4\,\mathrm{kN})\simeq -1063.4\,\mathrm{kN}$$

This is 88% of the code value.

e) Because $(2b_B)^2 \gg (2b_A)^2$, within the bore of Solenoid A the fields generated by Solenoid B and Solenoid A are both uniform and point only axially. Thus the maximum field within Solenoid A, close to 17.5 T, occurs at its innermost radius at $z=0$. According to the same code, a maximum field of 17.32 T occurs at ($r=5$ cm, $z=0$).

f) Again because $(2b_B)^2 \gg (2b_A)^2$, the radial field component of Solenoid A impinges on Solenoid B away from its center point where the axial field of Solenoid B is still essentially the same as that at its midplane. Therefore, it is quite likely that the field maximum in Solenoid B can exceed 10.0 T, the midplane field of Solenoid B (9.94 T by code), and occur at an axial distance $\sim\pm b_A$ from the center. The code shows that the maximum field in Solenoid B is 9.96 T ($B_r=\pm1.70$ T; $B_z=9.81$ T) and it occurs at ($r=7$ cm, $z=\pm25$ cm). Note that $b_A=25$ cm.

PROBLEM 3.16: Stresses in an epoxy-impregnated solenoid*

This problem deals with simple but approximate stress computations applicable for epoxy-impregnated magnets. We will use a 500-MHz (12 T) NMR superconducting magnet built in the late 1970s at FBNML as an example [3.57]. The magnet consists of a high-field insert, a main coil, and several correction and shim coils. The main coil's winding inner radius (a_1) is 72.6 mm, the winding outer radius (a_2) is 102 mm, and the winding length ($2b$) is 488 mm. The main coil is wound with a Nb-Ti multifilamentary conductor; the volumetric ratio of copper to Nb-Ti is 2.1. The composite wire has diameters of 0.63 mm bare (D_{cd}) and 0.71 mm insulated (D_{ov}). The winding has a close-packed hexagonal configuration. The space between the wires is filled with epoxy resin. Figure 3.45 shows three neighboring wires in a close-packed hexagonal winding configuration.

When all the coils are energized, the axial (z) component of the magnetic induction, B_z, decreases linearly with radial distance (r) through the build of the main coil. At the midplane ($z = 0$) of the main coil, B_z varies from 8.22 T at $r = a_1$ to -0.21 T at $r = a_2$. This linear decrease of B_z is quite accurate at $z = 0$. The overall operating current density (λJ) in the main coil is 248 MA/m^2.

The analytic solution for an anisotropic cylinder loaded with body forces was used to calculate the stresses at the midplane of the main coil. The hoop stresses at the inner and outer radii were found to be, respectively, 105 MPa and 65 MPa; the hoop stress decreases roughly linearly from the inner radius to the outer radius.

a) Using simple force equilibrium considerations, show that these stress values are consistent with the loading situation.

b) Assuming the winding pattern is a close-packed (wires touching) hexagonal configuration, compute the area fraction for each of the three constituents, Nb-Ti, copper, and organic materials (epoxy plus insulation).

c) Based on these area fractions and approximate Young's moduli for these materials at 4.2 K ($E_{sc} = 85$ GPa; $E_{cu} = 100$ GPa; $E_{in} = 30$ GPa), find the hoop stresses in the Nb-Ti and copper at the innermost layer of the winding.

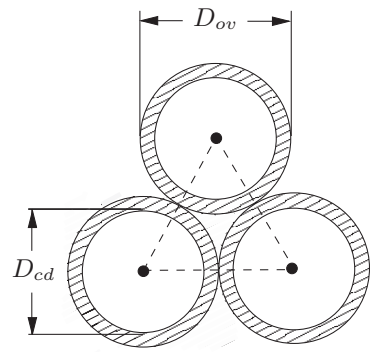

Fig. 3.45 Three neighboring conductors in a close-packed hexagonal winding.

* **Problem 3.17** in the 1st Edition (Plenum, 1994).

Solution to PROBLEM 3.16

a) The average hoop stress in the winding is given by:

$$\tilde{\sigma} = \frac{\sigma_i + \sigma_o}{2} = \frac{105\,\text{MPa} + 65\,\text{MPa}}{2} \qquad (S16.1)$$
$$= 85\,\text{MPa}$$

The mean winding radius, $\tilde{R} = (a_1 + a_2)/2$ is 87.3 mm; the mean magnetic induction, $\tilde{B}_z = (B_i + B_o)/2$, is 4.0 T. The mean hoop stress in the winding may thus be given by:

$$\tilde{\sigma} = \tilde{R}(\lambda J)\tilde{B}_z = (87.3\times10^{-3}\,\text{m})(248\times10^{6}\,\text{A/m}^2)(4.0\,\text{T}) \qquad (S16.2)$$
$$= 86.6\,\text{MPa}$$

which is nearly identical to $\tilde{\sigma}$, the mean of σ_i and σ_o, computed above (Eq. $S16.1$).

b) See Fig. 3.45 for the close-packed hexagonal configuration. The triangular area, A_{tr}, defined by the dotted lines is given in terms of the overall conductor diameter, D_{ov}, by: $A_{tr} = \sqrt{3}D_{ov}^2/4$. The conductor area, A_{cd}, within the triangle is given by: $A_{cd} = \pi D_{cd}^2/8$, of which 2.1/3.1 is copper area, A_{cu}, and 1/3.1 is Nb-Ti area, A_{sc}. The epoxy and insulation area, A_{in}, within the triangle is given by: $A_{in} = A_{tr} - A_{cd}$. Thus:

$$f_{cu} = \frac{A_{cu}}{A_{tr}} = \frac{\frac{2.1}{3.1}\frac{\pi D_{cd}^2}{8}}{\frac{\sqrt{3}}{4}D_{ov}^2} = \frac{(2.1)(\pi)(4)(0.63\,\text{mm})^2}{(3.1)(\sqrt{3})(8)(0.71\,\text{mm})^2} = 0.484 \qquad (S16.3a)$$

$$f_{sc} = \frac{A_{sc}}{A_{tr}} = \frac{1}{2.1}\frac{A_{cu}}{A_{tr}} = 0.230 \qquad (S16.3b)$$

$$f_{in} = \frac{A_{in}}{A_{tr}} = 1 - \frac{A_{cu} + A_{sc}}{A_{tr}} = 1 - 0.484 - 0.230 = 0.286 \qquad (S16.3c)$$

c) The Young's modulus for the composite, $\tilde{E}$, may be given from the parallel mixture rule:

$$\tilde{E} = f_{cu}E_{cu} + f_{sc}E_{sc} + f_{in}E_{in} \qquad (S16.4)$$
$$= (0.48)(100\,\text{GPa}) + (0.23)(85\,\text{GPa}) + (0.29)(30\,\text{GPa})$$
$$\simeq 76\,\text{GPa}$$

We may calculate the stress of each component at the innermost winding radius:

$$\sigma_{cu} = \sigma_i\frac{E_{cu}}{\tilde{E}} = (105\,\text{MPa})\frac{100\,\text{GPa}}{76\,\text{GPa}} \simeq 137\,\text{MPa} \qquad (S16.5a)$$

$$\sigma_{sc} = \sigma_i\frac{E_{sc}}{\tilde{E}} = (105\,\text{MPa})\frac{85\,\text{GPa}}{76\,\text{GPa}} \simeq 117\,\text{MPa} \qquad (S16.5b)$$

$$\sigma_{in} = \sigma_i\frac{E_{sc}}{\tilde{E}} = (105\,\text{MPa})\frac{30\,\text{GPa}}{76\,\text{GPa}} \simeq 41\,\text{MPa} \qquad (S16.5b)$$

These values ignore residual stresses, which in fact may be very large.

PROBLEM 3.17: Stresses and axial force in an HTS magnet

We present here a stress analysis performed on an 1.75-T (75 MHz) HTS "insert" solenoid, a stack of 48 double-pancake (DP) coils [3.58], each DP coil wound with high-strength HTS tape. The HTS insert, operated at 86.7 A, is combined with a 14.1-T (600 MHz) all-LTS background NMR magnet to form a 675 MHz LTS/HTS NMR magnet—later the insert was operated at 115.95 A to achieve a combined field of 16.26 T (692.2 MHz) [3.59]. Table 3.9 gives key parameters of the insert and the HTS tape, a composite of Bi2223/Ag and two stainless steel strips. The mixture rules used are based on the mechanical properties of silver and stainless steel. The axial field values, B_z and B_r, in the table are for the DP coils, flanking the midplane ($z=0$), that experience the largest stresses and hoop strains.

Stress & Strain Equations

The stresses, radial, $\sigma_r(r,z)$; hoop, $\sigma_\theta(r,z)$; axial, $\sigma_z(r,z)$; and shear, $\tau_{rz}(r,z)$ in the winding of a solenoid are found from the equilibrium equations of Eq. 3.62:

$$\frac{\partial \sigma_r}{\partial r} + \frac{\sigma_r - \sigma_\theta}{r} + \frac{\partial \tau_{rz}}{\partial z} = -\lambda J B_z(r,z) \tag{3.62a}$$

$$\frac{\partial \tau_{rz}}{\partial r} - \frac{\tau_{rz}}{r} + \frac{\partial \sigma_z}{\partial z} = -\lambda J B_r(r,z) \tag{3.62b}$$

with boundary conditions: $\sigma_r(r=a_1,z)=0$; $\sigma_r(a_2,z)=0$; $\sigma_z(r,z=\pm b)=0$; $\tau_{rz}(r,\pm b)=0$; $\tau_{rz}(a_2,\pm b)=0$. The HTS composite may be considered orthotropic, and Hooke's law, with no thermal strains included, is given by:

$$\epsilon_r = \frac{1}{E_r}\sigma_r - \frac{\nu_{rh}}{E_h}\sigma_\theta - \frac{\nu_{rz}}{E_z}\sigma_z \tag{3.171a}$$

$$\epsilon_\theta = -\frac{\nu_{hr}}{E_r}\sigma_r + \frac{1}{E_h}\sigma_\theta - \frac{\nu_{hz}}{E_z}\sigma_z \tag{3.171b}$$

$$\epsilon_z = -\frac{\nu_{zr}}{E_r}\sigma_r - \frac{\nu_{zh}}{E_h}\sigma_\theta + \frac{1}{E_z}\sigma_z \tag{3.171c}$$

where $\nu_{\xi\eta}$ is the Poisson's ratio that gives ϵ_ξ due to σ_η, where ξ and η can be, respectively, θ- (hoop-), r-, or z-direction.

Table 3.9: Parameters of 48-Double-Pancake-Coil Solenoid [3.32, 58]

Winding i.d.($2a_1$); o.d.($2a_2$); length ($2b$)	[mm]	78.2; 126.6; 406.6
Interturn insulation thickness/pancake-pancake space	[mm]	0.038/0.178
Total number of turns		6816
Operating current (I_{op}); λJ_{op}	[A; A/mm^2]	86.7; 66.31
$B_z(r=a_1)$; $B_z(r=a_2)$ @86.7 A	[T]	15.86; 13.97
Tape overall width; thickness	[mm]	4.10; 0.30
Thickness: Stainless steel (ss) strips; solder lamination	[μm]	40 (×2); 10 (×2)
Volumetric ratio (without ss strips): Ag/non-Ag	[mm]	1.5
Equivalent Young's Moduli (mixture rule): E_r; E_θ; E_z	[GPa]	62.8; 81.3; 70.6
Equivalent Poisson's Ratios (mixture rule): ν_{rh}; ν_{hr}; ν_{zr}		0.31; 0.29; 0.26

PROBLEM 3.17: Stresses & axial force in an HTS magnet (continuation)

Table 3.10: Stresses (σ) & Strains (ϵ) in HTS Insert Midplane Pancake Coil [3.32] (Operating at 86.7 A in a Background Field of 14.1 T)

r [mm]	σ_r	Average $\bar{\sigma}_\theta$ [MPa]	Silver σ_θ [MPa]	Steel σ_θ [MPa]	Silver σ_z [MPa]	Silver $\sigma_T{}^*$ [MPa]	Tape ϵ_θ [%]
39.10	0	62.3	54.3	152.9	−2.1	56.4	0.030
51.19	2.6	44.9	39.2	110.3	−2.1	41.3	0.028
63.29	0	33.6	29.3	82.4	−2.1	31.4	0.026

* Tresca stress: $\sigma_T = \sigma_\theta - \sigma_z$.

Table 3.10 gives values of stresses and hoop strains at three radial locations, innermost, midpoint, and outermost, in one of the midplane pancakes [3.32]. The midplane axial force is −16 kN. Note that the highest stresses occur at the innermost ($a_1 = 39.10$ mm) winding. The maximum combined stress, Tresca stress, σ_T ($= \sigma_\theta - \sigma_z$), in silver is 56.4 MPa, which is less than the allowable stress, $\sigma_{allow} = 2\sigma/3$ (0.2%): for silver at 77 K, $\sigma_{allow} \simeq 120$ MPa.

Stresses and strains may be computed by solving Eqs. 3.62 and 3.171. However, some of the equations derived in **3.5** may be applied to estimate the midplane axial force. As noted above, the HTS magnet at its midplane will have a computed axial force of −16.2 kN (i.e., compressive), which as discussed in **3.5**, arises from the self field of the HTS magnet and from the interaction of the HTS and the LTS magnet. Here, we compute approximate values of the midplane force in the HTS magnet by its own field *alone*. The above analysis gives a value of −8.6 kN [3.32].

a) Treating the HTS magnet as "thin-walled," apply Eq. 3.41*a* to compute $F_z(0)$. Choose $a = 39.1$ mm, $b = 203.3$ mm, and $NI = 5.91 \times 10^6$ A.

b) Apply Eq. 3.41*b* to compute $F_z(0)$ with 1) $a = 39.1$ mm, the "a_1" of the HTS magnet and 2) $a = 51.2$ mm, which is the average winding radius.

c) Now treat the HTS magnet as two "thin-walled" and "long" subsolenoids, A and B, of the same winding thickness, and apply Eq. 3.55 to compute $F_{zT}(0)$. Choose $a_A = 39.1$ mm and $a_B = 51.2$ mm.

d) The 14.1-T LTS magnet that surrounds this HTS insert consists of nested coils. Model the LTS magnet as a thin-walled solenoid of $a_B = 191.3$ mm; $b_B = 337.5$ mm; $N_B I_B = 7.535$ MA; the HTS insert as a thin-walled solenoid of $a_A = 51.2$ mm; $b_A = 203.3$ mm; $N_A I_A = 0.591$ MA. By applying Eq. 3.57*a*, compute the total midplane axial force for the HTS insert magnet: $F_{zA}(0)$, which is −16.2 kN. Explain why Eq. 3.57*a* does *not* give the correct value.

e) Using the same models for both magnets and applying Eq. 3.60, compute an axial restoring force on the HTS insert when it is off-center by 5 mm ($\rho = 5$ mm in Eq. 3.60). A code gives a value of −2.1 kN.

In the following pages, appropriate elliptic integral values are given, Tables 3.11 through 3.14.

Solution to PROBLEM 3.17

Table 3.11: Values of $K(k)$ and $E(k)$ for **a)**

k^2	$K(k)$	$E(k)$
0.128888	1.625445	1.518888
0.035670	1.585092	1.556694

a) We have Eq. 3.41a:

$$F_z(0) = -\frac{\mu_\circ}{2}\left(\frac{NI}{2b}\right)^2 \Big\{2b\sqrt{4a^2+b^2}\,\big[K(k_b)-E(k_b)\big] - 2b\sqrt{4a^2+4b^2}\,\big[K(k_{2b})-E(k_{2b})\big]\Big\} \qquad (3.41a)$$

where k_b and k_{2b} are the moduli determined by a and b. For this case, in which $a=39.1\,\text{mm}$ and $b=203.3\,\text{mm}$, we have:

$$k_b^2 = \frac{4a^2}{4a^2+b^2} = \frac{4(39.1\,\text{mm})^2}{4(39.1\,\text{mm})^2+(203.3\,\text{mm})^2} = 0.128888$$

$$k_{2b}^2 = \frac{4a^2}{4a^2+(2b)^2} = \frac{4(39.1\,\text{mm})^2}{4(39.1\,\text{cm})^2+(406.6\,\text{mm})^2} = 0.035670$$

Appropriate complete elliptic integral values are given in Table 3.11. By applying Eq. 3.38c up to the k^6 term, we may compute $K(k)-E(k)$ for $k^2 \ll 1$. Thus:

$$K(k_{2b})-E(k_{2b}) \simeq \frac{\pi}{4}\big[(0.128888)+\tfrac{3}{8}(0.128888)^2+\tfrac{15}{64}(0.128888)^3\big] = 0.106515$$

which is essentially identical (0.04% error) to the $K(k)$–$E(k)=0.106557$, computed from values of $K(k)$ and $E(k)$ given in Table 3.11.

With $NI=0.591\times10^6\,\text{A}$, and other values inserted in Eq. 3.41a, we have:

$$\begin{aligned} F_z(0) &= -(2\pi\times10^{-7}\,\text{H/m})\left[\frac{(0.591\times10^6\,\text{A})}{(0.4066\,\text{m})}\right]^2 \times \\ &\quad \Big\{[(0.4066\,\text{m})\sqrt{4(0.0391\,\text{m})^2+(0.2033\,\text{m})^2}\,(1.625445-1.518888) \\ &\quad -(0.4066\,\text{m})\sqrt{4(0.0391\,\text{m})^2+4(0.2033\,\text{m})^2}\,(1.585092-1.556694)\Big\} \\ &= -(2\pi\times10^{-7}\,\text{H/m})(2.11\times10^{12}\,\text{A}^2/\text{m}^2)(9.44\times10^{-3}\,\text{m}^2-4.78\times10^{-3}\,\text{m}^2) \\ &= -6.2\,\text{kN} \end{aligned}$$

This computation underestimates the code value by 28%.

Solution to PROBLEM 3.17 (continuation)

Table 3.12: Values of $\Pi(c^2,k)$ for **c)**

c^2	k	$\Pi(c^2,k)$
0.982045	0.402269	12.66889
0.982045	0.214848	11.96934

b) Equation 3.41*b* is given by:

$$F_z(0) \simeq -\frac{\mu_\circ}{2}\left(\frac{NI}{2b}\right)^2 \pi a^2 \tag{3.41b}$$

$$\simeq -\frac{(4\pi\times10^{-7}\,\mathrm{H/m})}{2}\left[\frac{(5.91\times10^5\,\mathrm{A})}{0.4066\,\mathrm{m}}\right]^2 \pi(0.0391\,\mathrm{m})^2$$

$$= -6.4\,\mathrm{kN}$$

This is 74% of the code value. The average radius of 51.2 mm instead of 39.1 mm results in a force of 10.9 kN, 27% greater than the code value.

c) If the magnet is modeled by two "thin-walled" and "long" solenoids, Eq. 3.55 applies:

$$F_{z\,T}(0) \simeq -\mu_\circ\left(\frac{NI}{4b}\right)^2 \pi(a_A^2+a_B^2)\left\{1-\frac{(a_A-a_B)^2}{\pi(a_A^2+a_B^2)}[2\Pi(c^2,k_b)-\Pi(c^2,k_{2b})]\right\} \tag{3.55}$$

The moduli, k_b, k_{2b}, and c^2, with $a_T = a_A + a_B$, $a_A = 39.1\,\mathrm{mm}$, $a_B = 51.2\,\mathrm{mm}$, $b = 203.3\,\mathrm{mm}$, $a_T = 90.3\,\mathrm{mm}$, are given by:

$$c^2 = \frac{4a_Aa_B}{a_T^2} = \frac{4(39.1\,\mathrm{mm})(51.2\,\mathrm{mm})}{(90.3\,\mathrm{mm})^2} = 0.982045$$

$$k_b^2 = \frac{4a_Aa_B}{a_T^2+b^2} = \frac{4(39.1\,\mathrm{mm})(51.2)\,\mathrm{mm}}{(90.3\,\mathrm{mm})^2+(203.3\,\mathrm{mm})^2} = 0.161820 \Rightarrow k_b = 0.402269$$

$$k_{2b}^2 = \frac{4a_Aa_B}{a_T^2+4b^2} = \frac{4(39.1\,\mathrm{mm})(51.2)\,\mathrm{mm}}{(90.3\,\mathrm{mm})^2+4(203.3\,\mathrm{mm})^2} = 0.046160 \Rightarrow k_{2b} = 0.214848$$

Thus:

$$F_z(0) = -(4\pi\times10^{-7}\,\mathrm{H/m})\left[\frac{(0.591\times10^6\,\mathrm{A})}{(0.8132\,\mathrm{m})}\right]^2 \pi[(0.0391\,\mathrm{m})^2+(0.0512\,\mathrm{m})^2]$$

$$\times\left\{1-\frac{(0.0391\,\mathrm{m}-0.0512\,\mathrm{m})^2}{\pi[(0.0391\,\mathrm{m})^2+(0.0512\,\mathrm{m})^2]}[2(12.66889)-11.96934]\right\}$$

$$= -(4\pi\times10^{-7}\,\mathrm{H/m})(5.28\times10^{11}\,\mathrm{A^2/m^2})(1.304\times10^{-2}\,\mathrm{m^2})(1-0.150)$$

$$= -7.4\,\mathrm{kN}$$

This underestimates the code by 15%.

Solution to PROBLEM 3.17 (continuation)

Table 3.13: Values of $\Pi(c^2,k)$ for **d)**

c^2	k	$\Pi(c^2,k)$
0.666226	0.333965	2.822156
0.666226	0.476278	2.046996
0.666226	0.714162	3.382637

d) Equation 3.57a is given below:

$$F_{z_A}(0) \simeq -\frac{\mu_\circ}{2}\left\{\left(\frac{N_A I_A}{2b_A}\right)^2 \pi a_A^2 + \left(\frac{N_B I_B}{2b_B}\right)\left(\frac{N_A I_A}{2b_A}\right)\times \right.$$
$$\left.(a_A - a_B)^2\left[\Pi(c^2,k_D)+\Pi(c^2,k_T)-2\Pi(c^2,k_B)\right]\right\} \qquad (3.57a)$$

Parameter values other than those given in question **d)** are: $a_T = a_A + a_B = 242.5\,\text{mm}$; $b_T = b_A + b_B = 540.8\,\text{mm}$; $b_D = b_A - b_B = -134.2\,\text{mm}$; and

$$c^2 = \frac{4a_A a_B}{a_T^2} = \frac{4(51.2\,\text{mm})(191.3\,\text{mm})}{(242.5\,\text{mm})^2} = 0.666226$$

$$k_D^2 = \frac{4a_A a_B}{a_T^2 + b_D^2} = \frac{4(51.2\,\text{mm})(191.3)\,\text{mm}}{(242.5\,\text{mm})^2 + (-134.2\,\text{mm})^2} = 0.510028 \Rightarrow k_D = 0.714162$$

$$k_T^2 = \frac{4a_A a_B}{a_T^2 + b_T^2} = \frac{4(51.2\,\text{mm})(191.3)\,\text{mm}}{(242.5\,\text{mm})^2 + (540.8\,\text{mm})^2} = 0.111533 \Rightarrow k_T = 0.333965$$

$$k_B^2 = \frac{4a_A a_B}{a_T^2 + b_B^2} = \frac{4(51.2\,\text{mm})(191.3)\,\text{mm}}{(242.5\,\text{mm})^2 + (337.5\,\text{mm})^2} = 0.226841 \Rightarrow k_B = 0.476278$$

Inserting appropriate values into Eq. 3.57a, we have:

$$F_{z_A}(0) \simeq -\frac{(4\pi\times 10^{-7}\,\text{H/m})}{2}\left\{\left(\frac{5.91\times 10^5\,\text{A}}{0.4066\,\text{m}}\right)^2 \pi(0.0512\,\text{m})^2 \right.$$
$$+\left[\left(\frac{7.535\times 10^6\,\text{A}}{0.675\,\text{m}}\right)\left(\frac{5.91\times 10^5\,\text{A}}{0.4066\,\text{m}}\right)\right.$$
$$\left.\left.\times(0.0512\,\text{m}-0.1913\,\text{m})^2(3.3826+2.8222-2\times 2.0470)\right]\right\}$$
$$\simeq -(1.09\,\text{kN} + 42.2\,\text{kN}) \simeq -43.3\,\text{kN}$$

This is 2.7 times the code value of 16.2 kN. The major source of error comes from the approximation of Eq. 3.57a involving the interaction force, $F_{z_{AB}}$. In order for Eq. 3.57a to be valid, as remarked in its derivation, the conditions $b_A^2 \gg 4a_A^2$, $b_B^2 \gg a_T^2$, $b_D^2 \gg a_T^2$, must be satisfied. In this particular case, we have: $b_A^2/4a_T^2 = 0.176$; $b_B^2/a_T^2 = 1.94$; and $b_D^2/a_T^2 = 0.306$. That is, none of the conditions necessary for Eq. 3.57a to be valid is satisfied in this particular case.

Solution to PROBLEM 3.17 (continuation)

Table 3.14: Values of $K(k)$, $E(k)$, and $\Pi(c^2,k)$ for **e)**

k^2	$K(k)$	$E(k)$	k^2	$K(k)$	$E(k)$
0.109834	1.616815	1.526733	0.113269	1.618355	1.525324
0.501110	1.855016	1.350085	0.518925	1.870449	1.341054

c^2	k	$\Pi(c^2,k)$	c^2	k	$\Pi(c^2,k)$
0.666226	0.331412	2.820467	0.666226	0.336555	2.823887
0.666226	0.707891	3.364664	0.666226	0.720364	3.400959

e) Equation 3.60 is given below:

$$
\begin{aligned}
F_{z_R}(\rho) = &-\frac{\mu_\circ}{2}\left(\frac{N_A I_A}{2b_A}\right)\left(\frac{N_B I_B}{2b_B}\right)\times \\
&\left(\frac{b_T-\rho}{\sqrt{a_T^2+(b_T-\rho)^2}}\Big\{[a_T^2+(b_T-\rho)^2]\big[K(k_{T-})-E(k_{T-})\big]-\Upsilon(c^2,k_{T-})\Big\}\right. \\
&+\frac{b_D+\rho}{\sqrt{a_T^2+(b_D+\rho)^2}}\Big\{[a_T^2+(b_D+\rho)^2]\big[K(k_{D+})-E(k_{D+})\big]-\Upsilon(c^2,k_{D+})\Big\} \\
&-\frac{b_T+\rho}{\sqrt{a_T^2+(b_T+\rho)^2}}\Big\{[a_T^2+(b_T+\rho)^2]\big[K(k_{T+})-E(k_{T+})\big]-\Upsilon(c^2,k_{T+})\Big\} \\
&\left.-\frac{b_D-\rho}{\sqrt{a_T^2+(b_D-\rho)^2}}\Big\{[a_T^2+(b_D-\rho)^2]\big[K(k_{D-})-E(k_{D-})\big]-\Upsilon(c^2,k_{D-})\Big\}\right)
\end{aligned}
\tag{3.60}
$$

Parameter values other than those given in question **e)** are: $a_T = a_A + a_B = 242.5\,\text{mm}$; $b_T = b_A + b_B = 540.8\,\text{mm}$; $b_D = b_A - b_B = -134.2\,\text{mm}$; and

$$c^2 = \frac{4a_A a_B}{a_T^2} = \frac{4(51.2\,\text{mm})(191.3\,\text{mm})}{(242.5\,\text{mm})^2} = 0.666226$$

$$k_{T+}^2 = \frac{4a_A a_B}{a_T^2+(b_T+\rho)^2} = \frac{4(51.2\,\text{mm})(191.3)\,\text{mm}}{(242.5\,\text{mm})^2+(545.8\,\text{mm})^2} = 0.109834 \Rightarrow k_{T+} = 0.331412$$

$$k_{T-}^2 = \frac{4a_A a_B}{a_T^2+(b_T-\rho)^2} = \frac{4(51.2\,\text{mm})(191.3)\,\text{mm}}{(242.5\,\text{mm})^2+(535.8\,\text{mm})^2} = 0.113269 \Rightarrow k_{T-} = 0.336554$$

$$k_{D+}^2 = \frac{4a_A a_B}{a_T^2+(b_D+\rho)^2} = \frac{4(51.2\,\text{mm})(191.3)\,\text{mm}}{(242.5\,\text{mm})^2+(-129.2\,\text{mm})^2} = 0.518925 \Rightarrow k_{D+} = 0.720364$$

$$k_{D-}^2 = \frac{4a_A a_B}{a_T^2+(b_D-\rho)^2} = \frac{4(51.2\,\text{mm})(191.3)\,\text{mm}}{(242.5\,\text{mm})^2+(-139.2\,\text{mm})^2} = 0.501110 \Rightarrow k_{D-} = 0.707891$$

Solution to PROBLEM 3.17 (continuation)

Table 3.15: Values of Terms in Eq. 3.60 for **e)**

$\dfrac{b_T-\rho}{\sqrt{a_T^2+(b_T-\rho)^2}}$	$\dfrac{(0.5358\,\mathrm{m})}{\sqrt{(0.2425\,\mathrm{m})^2+(0.5358\,\mathrm{m})^2}}$	0.911035
$a_T^2+(b_T-\rho)^2$	$(0.2425\,\mathrm{m})^2+(0.5358\,\mathrm{m})^2$	$0.345888\,\mathrm{m}^2$
$K(k_{T-})-E(k_{T-})$	$1.618355-1.525324$	0.093031
$(a_A-a_B)^2$	$(0.0512\,\mathrm{m}-0.1913\,\mathrm{m})^2$	$0.019628\,\mathrm{m}^2$
$(a_A-a_B)^2[\Pi(c^2,k_{T-})-K(k_{T-})]$	$(0.019628\,\mathrm{m}^2)(2.823887-1.618355)$	$0.023662\,\mathrm{m}^2$
$\dfrac{b_D+\rho}{\sqrt{a_T^2+(b_D+\rho)^2}}$	$\dfrac{(-0.1292\,\mathrm{m})}{\sqrt{(0.2425\,\mathrm{m})^2+(-0.1292\,\mathrm{m})^2}}$	-0.470210
$a_T^2+(b_D+\rho)^2$	$(0.2425\,\mathrm{m})^2+(-0.1292\,\mathrm{m})^2$	$0.075499\,\mathrm{m}^2$
$K(k_{D+})-E(k_{D+})$	$1.870449-1.341054$	0.529395
$(a_A-a_B)^2[\Pi(c^2,k_{D+})-K(k_{D+})]$	$(0.019628\,\mathrm{m}^2)(3.400959-1.870449)$	$0.030041\,\mathrm{m}^2$
$\dfrac{b_T+\rho}{\sqrt{a_T^2+(b_T+\rho)^2}}$	$\dfrac{(0.5458\,\mathrm{m})}{\sqrt{(0.2425\,\mathrm{m})^2+(0.5458\,\mathrm{m})^2}}$	0.913860
$a_T^2+(b_T+\rho)^2$	$(0.2425\,\mathrm{m})^2+(0.5458\,\mathrm{m})^2$	$0.356704\,\mathrm{m}^2$
$K(k_{T+})-E(k_{T+})$	$1.616815-1.526733$	0.090082
$(a_A-a_B)^2[\Pi(c^2,k_{T+})-K(k_{T+})]$	$(0.019628\,\mathrm{m}^2)(2.820467-1.616815)$	$0.023625\,\mathrm{m}^2$
$\dfrac{b_D-\rho}{\sqrt{a_T^2+(b_D-\rho)^2}}$	$\dfrac{(-0.1392\,\mathrm{m})}{\sqrt{(0.2425\,\mathrm{m})^2+(-0.1392\,\mathrm{m})^2}}$	-0.497833
$a_T^2+(b_D-\rho)^2$	$(0.2425\,\mathrm{m})^2+(-0.1392\,\mathrm{m})^2$	$0.078183\,\mathrm{m}^2$
$K(k_{D-})-E(k_{D-})$	$1.855016-1.350085$	0.504931
$(a_A-a_B)^2[\Pi(c^2,k_{D-})-K(k_{D-})]$	$(0.019628\,\mathrm{m}^2)(3.364664-1.855016)$	$0.029632\,\mathrm{m}^2$

Applying these values in Table 3.15 into Eq. 3.60, we compute:

$$F_{zR}(\rho) = -2.2\,\mathrm{kN}$$

This overestimates the code value (2.1 N) by ∼4%; the − sign implies that the force is restoring. The "spring constant" between the magnets is ∼400 kN/m.

Formula for Radial Build of a Close-Packed Hexagonal Winding

With a round-wire conductor, many solenoids are wound in a close-packed hexagonal configuration. Figure 3.45, with three neighboring round wires of overall diameter D_{ov}, is a cross sectional view of such a winding. The radial build, a_2-a_1, of a solenoid (i.d. $2a_1$ and o.d. $2a_2$) with a close-packed hexagonal winding containing N_ℓ layers is given by:

$$a_2 - a_1 = \left[1 + \frac{\sqrt{3}}{2}(N_\ell - 1)\right] D_{ov} \tag{3.172}$$

Note that when $N_\ell = 1$, as expected, $a_2 - a_1 = D_{ov}$.

DISCUSSION 3.12: Magnetic Force on an Iron Sphere*

For safety considerations, it is very important to keep ferromagnetic objects away from a large magnet. Using the 45-T hybrid as an example, we derive here magnetic force expressions for an iron sphere (Fig. 3.46) *"far"* from the hybrid. The fringing (*far*) field of a solenoid, as discussed in **PROBLEM 3.11**, is given by a dipole field:

$$\vec{H}_f = H_0 \left(\frac{R_e}{r}\right)^3 (\cos\theta\,\vec{\imath}_r + \tfrac{1}{2}\sin\theta\,\vec{\imath}_\theta) \tag{3.163}$$

When a magnetic object, such as an iron sphere, is in a spatially varying magnetic field, it will be subjected to a magnetic force density, $\vec{f}_m$, given by:

$$\vec{f}_m(r,\theta) = \nabla e_m \tag{3.173}$$

where ∇ is the grad operator in spherical coordinates and e_m is the magnetic energy density stored in the iron due to its magnetization. For a ferromagnetic sphere with $\mu/\mu_\circ \gg 1$, the magnetic induction inside the sphere, $\vec{B}_{sp}$, is three times the "uniform" applied magnetic induction: $\vec{B}_{sp} \simeq 3\mu_\circ \vec{H}_f = 3\vec{B}_f$ (**PROBLEM 2.1**). For a sphere of a diameter much smaller than the distance from the magnet center to the sphere, $\vec{B}_f$ may be assumed uniform over the sphere. Thus:

$$e_m = \frac{\vec{B}_{sp}\cdot\vec{B}_f}{2\mu_\circ} = \frac{3|\vec{B}_f|^2}{2\mu_\circ} \tag{3.174}$$

When the iron is saturated with magnetization $\vec{M}_{sa}$, its magnetic induction is approximately equal to $\vec{B}_{sa}$ $(= \mu_\circ \vec{M}_{sa})$, which is constant and aligned with $\vec{B}_f$. Its energy density e_{ms} is thus given by:

$$e_{ms} \simeq \frac{\vec{B}_{sa}\cdot\vec{B}_f}{2\mu_\circ} \tag{3.175}$$

In Eqs. 3.174 and 3.175, it is assumed that the impinging field is "uniform" for energy density computation, but nonuniform for force density computation.

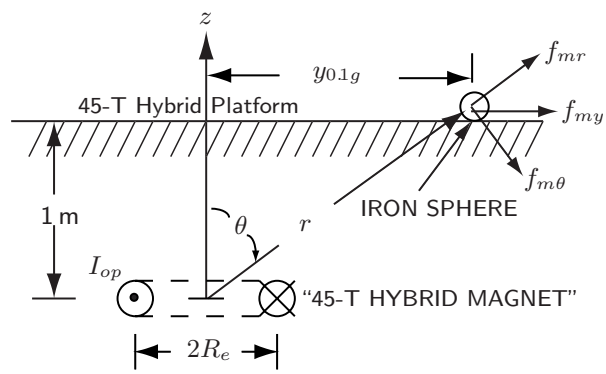

Fig. 3.46 Iron sphere on the 45-T hybrid platform.

* Based on **Problem 3.13** in the 1st Edition (Plenum, 1994).

DISCUSSION 3.12: Magnetic Force on an Iron Sphere (continuation)

A. Force on Unsaturated Sphere

To derive an expression of $\vec{f}_m(r,\theta)$ for an unsaturated iron sphere, we first compute $|\vec{B}_f|^2$ from Eq. 3.163:

$$|\vec{B}_f|^2 = \mu_\circ^2 H_0^2 \left(\frac{R_e}{r}\right)^6 (\cos^2\theta + \tfrac{1}{4}\sin^2\theta)$$

Combining the above expression with Eq. 3.174 and using the grad operator in spherical coordinates (Eq. 2.36a) on Eq. 3.173, we obtain:

$$\begin{aligned}\vec{f}_m(r,\theta) &= \frac{3\mu_\circ H_0^2}{2}\left[(\cos^2\theta + \tfrac{1}{4}\sin^2\theta)\frac{\partial}{\partial r}\left(\frac{R_e}{r}\right)^6 \vec{\imath}_r \right.\\ &\qquad \left. + \frac{1}{r}\left(\frac{R_e}{r}\right)^6 \frac{\partial}{\partial\theta}\left(\cos^2\theta + \tfrac{1}{4}\sin^2\theta\right)\vec{\imath}_\theta\right]\\ &= \frac{3\mu_\circ H_0^2}{2R_e}\left(\frac{R_e}{r}\right)^7 \left[-6(\cos^2\theta + \tfrac{1}{4}\sin^2\theta)\,\vec{\imath}_r - \tfrac{3}{2}\sin\theta\cos\theta\,\vec{\imath}_\theta\right]\end{aligned}$$

which may be simplified to:

$$\vec{f}_m(r,\theta) = -\frac{9\mu_\circ H_0^2}{4R_e}\left(\frac{R_e}{r}\right)^7 [(1+3\cos^2\theta)\,\vec{\imath}_r + \sin\theta\cos\theta\,\vec{\imath}_\theta] \qquad (3.176a)$$

Note that $\vec{f}_m(r,\theta)$ varies as $1/r^7$ and, as expected for any ferromagnetic object, the r-component of $\vec{f}_m(r,\theta)$ is directed *towards* the magnet center.

B. Force on Saturated Sphere

The magnetic energy density of Eq. 3.175 is given by:

$$e_{ms} = \mu_\circ M_{sa} H_0 \left(\frac{R_e}{r}\right)^3 \sqrt{\cos^2\theta + \tfrac{1}{4}\sin^2\theta}$$

Performing a similar grad operation on e_m, we obtain:

$$\begin{aligned}\vec{f}_{ms}(r,\theta) &= -\frac{3\mu_\circ M_{sa} H_0}{2R_e}\left(\frac{R_e}{r}\right)^4\\ &\qquad \times\left(\sqrt{1+3\cos^2\theta}\;\vec{\imath}_r + \frac{\sin\theta\cos\theta}{\sqrt{1+3\cos^2\theta}}\,\vec{\imath}_\theta\right)\end{aligned} \qquad (3.176b)$$

The magnetic force thus varies as $1/r^4$ when the iron sphere is saturated. Note also that because it is $-r$-directed, as in the unsaturated case, the iron sphere is attracted to the magnet center.

DISCUSSION 3.12: Magnetic Force on an Iron Sphere (continuation)

Illustration For the 45-T hybrid magnet (only the SCM field is considered), for which $B_0 = 14\,\mathrm{T}$ and $R_e = 0.67\,\mathrm{m}$ (see **PROBLEM 3.11**), we may compute $y_{0.1g}$, the y-axis distance from the magnet center on the platform ($z = 2.75\,\mathrm{m}$) at which f_{my}, the y-component of the magnetic force density on an unsaturated iron sphere of density ϱ, is $0.1\varrho g$ (an acceleration of 0.1 that of gravity) f_{my} is given by:

$$f_{my} = f_{mr}\sin\theta + f_{m\theta}\cos\theta \tag{3.177}$$

where f_{mr} and $f_{m\theta}$ are, respectively, the r- and θ-components of the magnetic force. Combining Eqs. 3.176a and 3.177, we have:

$$\begin{aligned} f_{my} &= \frac{9\mu_\circ H_0^2}{4R_e}\left(\frac{R_e}{r}\right)^7 [-(1+3\cos^2\theta)\sin\theta - \sin\theta\cos^2\theta] \\ &= -\frac{9\mu_\circ H_0^2}{4R_e}\left(\frac{R_e}{r}\right)^7 (1+4\cos^2\theta)\sin\theta \end{aligned} \tag{3.178}$$

The minus sign in Eq. 3.178 indicates f_{my} actually points in the direction opposite from that indicated in Fig. 3.46. r, $\sin\theta$, and $\cos\theta$ for the case $x = 0$ are given by:

$$r = \sqrt{y_{0.1g}^2 + z^2}; \qquad \sin\theta = \frac{y_{0.1g}}{\sqrt{y_{0.1g}^2 + z^2}}; \qquad \cos\theta = \frac{z}{\sqrt{y_{0.1g}^2 + z^2}}$$

Combining the above expressions and Eq. 3.178, and with $f_{my} = 0.1\varrho g$ we have:

$$0.1\varrho g = \frac{9(\mu_\circ H_0)^2 R_e^6}{4\mu_\circ}\left(\frac{1}{y_{0.1g}^2 + z^2}\right)^{3.5}\left(1 + \frac{4z^2}{y_{0.1g}^2 + z^2}\right)\frac{y_{0.1g}}{\sqrt{y_{0.1g}^2 + z^2}}$$

By inserting appropriate values in the above expression, with $z = 2.75\,\mathrm{m}$, we have:

$$\begin{aligned} 0.1(8000\,\mathrm{kg/m^3})(9.81\,\mathrm{m/s^2}) = {} & \frac{9(14\,\mathrm{T})^2(0.67\,\mathrm{m})^6}{4(4\pi\times10^{-7}\,\mathrm{H/m})}\left[\frac{1}{y_{0.1g}^2 + (2.75\,\mathrm{m})^2}\right]^{3.5} \\ & \times\left[1 + \frac{4(2.75\,\mathrm{m})^2}{y_{0.1g}^2 + (2.75\,\mathrm{m})^2}\right]\frac{y_{0.1g}}{\sqrt{y_{0.1g}^2 + (2.75\,\mathrm{m})^2}} \end{aligned}$$

Solving the above equation for $y_{0.1g}$, we find: $y_{0.1g} \simeq 2.42\,\mathrm{m}$.

We may compute the total field on the sphere and see if the sphere is indeed unsaturated as assumed in the computation. With $r_{0.1g} = \sqrt{(2.42\,\mathrm{m})^2 + (2.75\,\mathrm{m})^2} \simeq 3.66\,\mathrm{m}$ and $\theta = \tan^{-1}(2.42\,\mathrm{m}/2.75\,\mathrm{m}) = 41.3^\circ$ substituted into Eq. 3.163, we have:

$$\begin{aligned} |\mu_\circ\vec{H}_f| &= (14.0\,\mathrm{T})\left(\frac{0.67\,\mathrm{m}}{3.66\,\mathrm{m}}\right)^3\sqrt{\cos^2 41.3^\circ + \tfrac{1}{4}\sin^2 41.3^\circ} \\ &= (14.0\,\mathrm{T})(6.1\times10^{-3})(0.82) = 0.070\,\mathrm{T} \quad (\vec{M} = 3\mu_\circ\vec{H}_f = 0.21\,\mathrm{T}) \end{aligned}$$

DISCUSSION 3.13: Radial Force in Two-Coil Magnet

Figure 3.47 shows an arrangement of a two-coil magnet, in which the axis of Coil 1 (inner) is displaced radially in the plane normal to the z-axis—$+\Delta x$ in the x-direction in the figure—with respect to Coil 2 (outer). The axial field of each coil points upward ($+z$ direction) and the midplane of each coil is at $z=0$.

When Coils 1 and 2 are concentric, i.e., $\Delta x=0$ and $\Delta y=0$, the $J_\theta \times B_z$ interaction force on a unit winding volume is r-directed and from symmetry it cancels out: the net radial force is zero. If Coil 1 is displaced, as shown in the figure, by $+\Delta x$, then B_{z2} on one half (180° arc on the $+x$ side of the x-y plane) of its winding volume is on average greater than B_{z2} on the other half (180° arc mostly on the $-x$ side of the x-y plane) of the winding volume. The resulting net unbalanced force, F_{x1}, may be given approximately by:

$$F_{x1} \simeq 4\pi \Delta x \int_0^b \int_{a_1}^{a_2} J_{\theta 1} \frac{\partial B_{z2}(r,z)}{\partial r} r\, dr\, dz \tag{3.179}$$

where B_{z2} is the axial field generated by Coil 2. As indicated by Eq. 3.12*b* and also by Eqs. 3.117*a*–3.117*c* (**PROBLEM 3.2**), B_{z2} increases with displacement in the x-y plane, i.e., $\partial B_{z2}/\partial r > 0$. Thus, F_{x1} is positive and increasing in the x-direction; Coil 1's displacement gets even greater: the system is unstable.

Another way of looking at this is to recognize that an energized coil is always attracted to the highest field region. Thus, if Coil 1 is displaced radially, it continues to move radially towards Coil 2 because, as noted above, B_{z2} increases with displacement in the x-y plane; B_{z2} is maximum at the innermost winding radius of Coil 2. The same argument may be used to explain why displacement in the z-direction, on the other hand, is stable: if Coil 1 is displaced axially by Δz, because the axial field of each coil is maximum at the midplane ($z=0$), Coil 1 seeks to align its maximum field region with that of Coil 2, resulting in a stable condition for displacement in the z-direction.

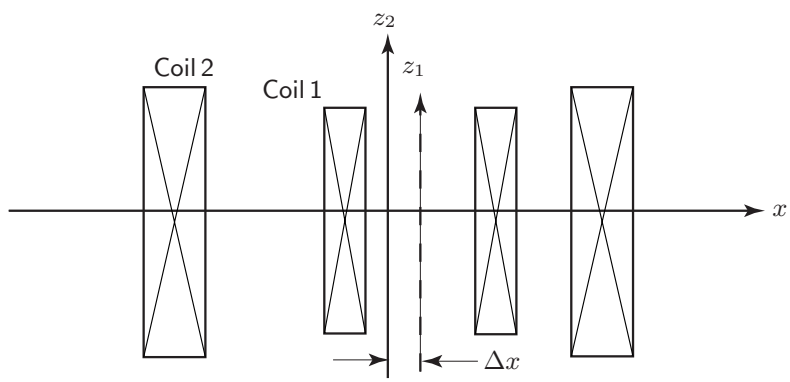

Fig. 3.47 Two nested solenoidal coils, one displaced radially from the other.

Answer to TRIVIA 3.5 Eastward. The *current* must point westward to make a resultant magnetic force on the electron directed toward the earth center.

DISCUSSION 3.14: Mechanical Support in the 45-T Hybrid*

The 45-T Hybrid was designed with potential for upgrade later to 50-T operation with higher power resistive inserts—35 MW vs. 24 MW. A key element in the design is the structure for transmitting fault forces between the insert and the SCM. Especially critical is the structural component that provides thermal stand-off inside the cryostat. In the 45-T Hybrid, this component is a single cylindrical steel column, coaxial to the SCM, with heat intercepts at ∼80 K and ∼20 K. To compute an upper bound on the potential fault load on the support column during an insert failure, the analysis described below was carried out for a 50-T upgrade.

1. This analysis was performed by taking the dimensions of the 45-T resistive insert, with uniform current density in each sub-coil at the peak value, and adjusting the current level in each sub-coil to the 50 T field. The analysis gives an insert that has inherently higher magnetic energy and higher misalignment forces relative to the SCM than coils with $1/r$ current distribution.

2. Based on this configuration, a worst-case fault was postulated corresponding to a short suddenly appearing at the midplane of each sub-coil, resulting in doubling the current (constant voltage assumption) and an axial shift of each sub-coil's magnetic center by a distance b_i (the half-height of the i^{th} coil). For the sub-coil geometries assumed, this hypothetical fault resulted in forces in Coils A, B, and C, respectively, of ∼1.7 MN, ∼1.8 MN, and ∼2.5 MN, i.e., a total of ∼6 MN on the SCM. The wall thickness of the support column was chosen so that the mean stress during a fault would not exceed 2/3 yield. The wall thicknesses of the 1.8–20 K, 20–80 K, and 80–300 K sections were graded to match the temperature-dependance of the yield stress of austenitic steel. The resultant conduction heat input is a small portion of the system's total cryogenic load. The resultant support-column design has the added advantage of being very stiff against both axial and transverse loads. Consequently, relative deflection between insert and outsert for typical misalignment forces are quite minimal.

* John Miller (NHMFL, 2004).

Help from Van (Part 4 of 5 Parts)

—Passage from Francis Bitter's *Magnets: The Education of a Physicist*

The Edison Company was getting rather fed up with the time-consuming experiments. While they were willing enough to make it possible to test out a brand-new piece of equipment, they were not exactly eager to go on interrupting their own schedules and having their people work overtime on a project of no interest to them. So we called a halt to these tests, and Van set out to find some money for me to get a power station of my own at M.I.T. and to construct some new magnets using the experience gained in the preliminary tests. In due course the money was made available. The sum was perhaps a tenth of what was required ten or fifteen years later to duplicate the installation, but luckily in those days (the mid-1930's) secondhand equipment could be had.

*DISCUSSION 3.15: Stresses in Composite Nb_3Sn Conductor**

Here we shall discuss the stress state in a composite Nb_3Sn conductor, focusing on the stress relationships among bronze, copper, and Nb_3Sn—the three major constituents of the composite [3.60]. Because the critical current densities of superconductors (LTS and HTS), are degraded when strained, particularly in tension, the maximum strain level on the superconductor is a key magnet design specification. Effects of strain, particularly on Nb-Ti and Nb_3Sn composite superconductors, are quite well documented [3.61, 3.62]; data are now also available for HTS [3.63, 3.64].

When a Nb_3Sn composite is cooled to 4.2 K, each constituent experiences a temperature reduction of ∼1000 K, from the reaction temperature of ∼1000 K to the operating temperature of 4.2 K. Because each constituent has a different coefficient of thermal contraction, residual stress arises in each constituent.

Figure 3.48 shows, schematically, strain states for three cases of interest: a) the composite at a reaction temperature ∼1000 K, b) at 4.2 K if the three constituents can contract *individually*, c) the composite at 4.2 K. Though exaggerated, the figure indicates the relative sizes of the individual thermal contractions of bronze, copper, and Nb_3Sn, given respectively by ϵ_{br_0}, ϵ_{cu_0}, ϵ_{s_0}, after cooldown from ∼1000 K to 4.2 K. Correspondingly, their residual strains, ϵ_{br_r}, ϵ_{cu_r}, ϵ_{s_r}, in the composite at 4.2 K are as shown in the figure. That is, both bronze and copper will be in *tension*, while Nb_3Sn will be in *compression*. In the figure E and A refer, respectively, to Young's modulus and cross section, with subscripts indicating constituents. Here, these strains as drawn in Fig. 3.48 are *scalar* quantities.

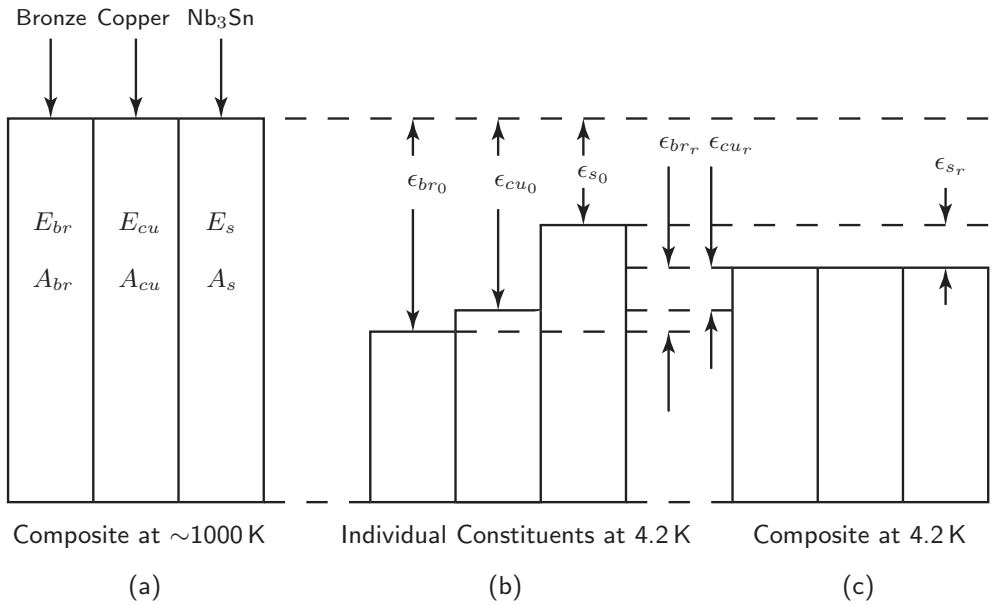

Fig. 3.48 Schematic strain states in the Nb_3Sn composite after cooldown.

* **Problem 3.18** in the 1st Edition (Plenum, 1994).

DISCUSSION 3.15: Stresses in Composite Nb_3Sn Conductor (continuation)

A. Equilibrium Equations

The stress and strain equilibrium equations for the composite at 4.2 K are:

$$\epsilon_{br_r} A_{br} E_{br} + \epsilon_{cu_r} A_{cu} E_{cu} - \epsilon_{s_r} A_s E_s = 0 \tag{3.180a}$$

$$+\epsilon_{br_r} + \epsilon_{s_r} = \epsilon_{br_0} - \epsilon_{s_0} \tag{3.180b}$$

$$-\epsilon_{cu_r} + \epsilon_{s_r} = \epsilon_{cu_0} - \epsilon_{s_0} \tag{3.180c}$$

$$-\epsilon_{cu_r} + \epsilon_{br_r} = \epsilon_{cu_0} - \epsilon_{br_0} \tag{3.180d}$$

Equation 3.180*a* states that the net internal force is zero. Equations 3.180*b* –3.180*d* give the strain compatibilities for, respectively, the bronze/Nb_3Sn, copper/Nb_3Sn, and copper/bronze. Be aware that Eq. 3.180 implicitly assumes that each constituent is in its elastic range, which usually is not the case.

B. Residual Strains

From Eqs. 3.180*b* and 3.180*c*, we may obtain expressions for ϵ_{s_r} and ϵ_{cu_r}:

$$\epsilon_{s_r} = \epsilon_{br_0} - \epsilon_{s_0} - \epsilon_{br_r}$$

$$\epsilon_{cu_r} = \epsilon_{br_r} - \epsilon_{br_0} + \epsilon_{cu_0}$$

Combining the above expressions with Eq. 3.180, we obtain:

$$\epsilon_{br_r} A_{br} E_{br} + (\epsilon_{br_r} - \epsilon_{br_0} + \epsilon_{cu_0}) A_{cu} E_{cu} + (\epsilon_{br_r} - \epsilon_{br_0} + \epsilon_{s_0}) A_s E_s = 0$$

Solving the above equation for ϵ_{br_r}, we have:

$$\epsilon_{br_r} = \frac{(\epsilon_{br_0} - \epsilon_{cu_0}) A_{cu} E_{cu} + (\epsilon_{br_0} - \epsilon_{s_0}) A_s E_s}{A_{cu} E_{cu} + A_{br} E_{br} + A_s E_s} \tag{3.181a}$$

Similarly, from Eqs. 3.180*b*–3.180*d* we may obtain expressions for ϵ_{s_r} and ϵ_{br_r}:

$$\epsilon_{s_r} = \epsilon_{cu_0} - \epsilon_{s_0} - \epsilon_{cu_r}$$

$$\epsilon_{br_r} = \epsilon_{br_0} - \epsilon_{cu_0} + \epsilon_{cu_r}$$

Thus,

$$(\epsilon_{br_0} - \epsilon_{cu_0} + \epsilon_{cu_r}) A_{br} E_{br} + \epsilon_{cu_r} A_{cu} E_{cu} + (\epsilon_{cu_r} - \epsilon_{cu_0} + \epsilon_{s_0}) A_s E_s = 0$$

Solving for ϵ_{cu_r} from the above equations, we have:

$$\epsilon_{cu_r} = \frac{(\epsilon_{cu_0} - \epsilon_{br_0}) A_{br} E_{br} + (\epsilon_{cu_0} - \epsilon_{s_0}) A_s E_s}{A_{cu} E_{cu} + A_{br} E_{br} + A_s E_s} \tag{3.181b}$$

Also,

$$\epsilon_{br_r} = \epsilon_{br_0} - \epsilon_{s_0} - \epsilon_{s_r}$$

$$\epsilon_{cu_r} = \epsilon_{cu_0} - \epsilon_{s_0} - \epsilon_{s_r}$$

Thus,

$$(\epsilon_{br_0} - \epsilon_{s_0} - \epsilon_{s_r}) A_{br} E_{br} + (\epsilon_{cu_0} - \epsilon_{s_0} - \epsilon_{s_r}) A_{cu} E_{cu} - \epsilon_{s_r} A_s E_s = 0$$

Solving for ϵ_{s_r} from the above equations, we have:

$$\epsilon_{s_r} = \frac{(\epsilon_{cu_0} - \epsilon_{s_0}) A_{cu} E_{cu} + (\epsilon_{br_0} - \epsilon_{s_0}) A_{br} E_{br}}{A_{cu} E_{cu} + A_{br} E_{br} + A_s E_s} \tag{3.181c}$$

DISCUSSION 3.15: Stresses in Composite Nb_3Sn Conductor (continuation)

Numerical Values By using Eqs. 3.181*a* — 3.181*c* and the values given in Table 3.16 for each constituent, we may compute values of ϵ_{br_r}, ϵ_{cu_r}, and ϵ_{s_r}.

$$\epsilon_{br_r} = \frac{(1.66-1.62)(0.62)(100\,\text{GPa})+(1.66-0.72)(0.14)(165\,\text{GPa})}{(0.24)(100\,\text{GPa})+(0.62)(100\,\text{GPa})+(0.14)(165\,\text{GPa})}$$
$$= \left(\frac{24.19\,\text{GPa}}{109.1\,\text{GPa}}\right)\% \simeq 0.22\% \quad \text{(from Fig. 3.48, } \textit{tensile}\text{)}$$

$$\epsilon_{cu_r} = \frac{(1.62-1.66)(0.24)(100\,\text{GPa})+(1.62-0.72)(0.14)(165\,\text{GPa})}{62.9\,\text{GPa}}$$
$$= \left(\frac{19.83\,\text{GPa}}{109.1\,\text{GPa}}\right)\% \simeq 0.18\% \quad \text{(from Fig. 3.48, } \textit{tensile}\text{)}$$

$$\epsilon_{s_r} = \frac{(1.62-0.72)(0.62)(100\,\text{GPa})+(1.66-0.72)(0.24)(100\,\text{GPa})}{62.9\,\text{GPa}}$$
$$= \left(\frac{78.36\,\text{GPa}}{109.1\,\text{GPa}}\right)\% \simeq 0.72\% \quad \text{(from Fig. 3.48, } \textit{compressive}\text{)}$$

Note that both matrix materials are in tension, while Nb_3Sn is in compression; ϵ_{s_r} of 0.72% is too severe and would certainly damage the conductor. However, when the magnet is energized, the conductor is subjected mostly to a tensile stress, which tends to place ϵ_{s_r} towards zero strain; usually, the Lorentz stresses are sufficient to put Nb_3Sn in tensile strain when the magnet is energized.

C. Stresses in Bronze and Copper

From ϵ_{br_r} and ϵ_{cu_r} computed above, we may compute the corresponding stresses in the bronze and copper. We have:

$$\sigma_{br_r} = \epsilon_{br_r} E_{br} \simeq (2.2\times10^{-3})(100\times10^{9}\,\text{Pa}) \simeq 220\,\text{MPa}$$
$$\sigma_{cu_r} = \epsilon_{cu_r} E_{cu} \simeq (1.8\times10^{-3})(100\times10^{9}\,\text{Pa}) \simeq 180\,\text{MPa}$$

The yield stresses of annealed bronze, σ_{br_y}, and annealed copper, σ_{cu_y}, are both only ∼100 MPa; both bronze and copper thus yield plastically during cooldown.

Table 3.16: Properties of Bronze, Copper, and Nb_3Sn at 4.2 K
—Approximate Values—

Constituent	ϵ_0^* [%]	E [GPa]	$A^\dagger$
bronze	1.66	100	0.24
copper	1.62	100	0.62
Nb_3Sn	0.72	165	0.14

* Thermal contraction strain from ∼1000 to 4.2 K.

† Fraction of the total composite cross section.

PROBLEM 3.18: Self inductances of selected systems

Derive the "low" frequency self inductance formulas given in **3.7.3**.

a) Equation 3.83, for the interior of the wire of radius a per unit length:

$$L = \frac{\mu_\circ}{8\pi} \tag{3.83}$$

b) Equation 3.84c, for a "very long" ($\beta \gg \alpha$) and thin coil with N total turns:

$$L = \mu_\circ a_1 N^2 \left(\frac{\pi}{2\beta}\right) \tag{3.84c}$$

c) Equation 3.87, for the unit length of an "ideal" dipole with N total turns:

$$L = \tfrac{1}{8}\mu_\circ \pi N^2 \tag{3.87}$$

Derive Eq. 3.87 using two expressions: 1) $L = 2E_m/I^2$; and 2) $L = N\Phi$.

d) For the unit length of an "ideal" quadrupole with N total turns, Eq. 3.88:

$$L = \tfrac{1}{16}\mu_\circ \pi N^2 \tag{3.88}$$

Derive Eq. 3.88 using two expressions: 1) $L = 2E_m/I^2$; and 2) $L = N\Phi$.

e) Equation 3.89a, for an "ideal" toroidal coil of major radius R and circular section of radius a with N total turns.

$$L = \mu_\circ R N^2 \left[1 - \sqrt{1 - \left(\frac{a}{R}\right)^2}\right] \tag{3.89a}$$

f) Equation 3.89b, for the ideal toroidal coil of **e)** in the limit $a \ll R$.

$$L = \mu_\circ a N^2 \left(\frac{a}{2R}\right)\left[1 + \tfrac{1}{4}\left(\frac{a}{R}\right)^2 + \tfrac{1}{8}\left(\frac{a}{R}\right)^4 \cdots\right] \tag{3.89b}$$

g) Equation 3.90a, for an ideal toroid of major radius R and rectangular section of width (r-axis) $2a$, height (z-axis) $2b$, and N total turns.

$$L = \mu_\circ b N^2 \left[\frac{1}{\pi}\ln\left(\frac{R+a}{R-a}\right)\right] \tag{3.90a}$$

h) Equation 3.90b, for the ideal toroidal coil of **g)** in the limit $a \ll R$.

$$L = \mu_\circ b N^2 \left(\frac{2a}{\pi R}\right)\left[1 + \tfrac{1}{3}\left(\frac{a}{R}\right)^2 + \tfrac{1}{5}\left(\frac{a}{R}\right)^4 \cdots\right] \tag{3.90b}$$

Solution to PROBLEM 3.18

a) For a wire of radius a carrying current I distributed uniformly over its cross section, the interior magnetic field is given by:

$$H_\theta(r) = \frac{I}{2\pi a^2} r \tag{S18.1}$$

Magnetic energy per unit wire length stored in the wire interior, e_m, is given by:

$$e_m = \tfrac{1}{2}\mu_\circ \int_0^a 2\pi H_\theta^2(r) r\, dr \tag{S18.2}$$

Combining Eqs. $S18.1$ and $S18.2$, we obtain:

$$e_m = \frac{\mu_\circ}{16\pi} I^2 \tag{S18.3}$$

Combining Eqs. 3.79 ($E_m = LI^2/2$; $e_m = LI^2/2$ on a unit length basis) and $S18.3$ and solving for the self inductance of the wire interior, L, we have:

$$L = \frac{\mu_\circ}{8\pi} \tag{3.83}$$

b) From Eq. $3.111d$, the center field, $B_z(0,0)$, of a long solenoid ($\beta \gg \alpha$) is given by $\mu_\circ NI/2b$. As may be inferred from Eq. $3.117c$, the field in a "thin-walled" and "long" solenoid is uniform in both axial and radial directions and equal to the center field. Thus the total flux linked by N turns of the solenoid is given by:

$$\Phi = \int_0^{a_1} 2\pi r H_z(0,0)\, dr = N\left(\frac{\pi a_1^2 \mu_\circ NI}{2b}\right) \tag{S18.4}$$

Combining Eqs. 3.78 ($\Phi = LI$) and $S18.4$, we obtain:

$$L = \mu_\circ a_1 N^2 \left(\frac{\pi}{2\beta}\right) \tag{3.84c}$$

c) ***Method 1: Energy*** The total ampere-turns (NI) in an ideal dipole, as studied in **PROBLEM 3.8**, is given by:

$$NI = \int_{-\pi/2}^{\pi/2} K_f R\, d\theta \tag{S18.5}$$

where R is the dipole radius. Combining Eqs. 3.140 (for $\vec{K}_f$) and $S18.5$, we have:

$$NI = \int_{-\pi/2}^{\pi/2} 2H_0 R\cos\theta\, d\theta = 4H_0 R \tag{S18.6}$$

The total magnetic energy E_m *per unit length* of the dipole is given by Eq. 3.143:

$$E_m = \frac{\pi R^2 B_0^2}{\mu_\circ} \tag{3.143}$$

From $S18.6$, we compute $H_0 R = NI/4$. Now combining this, Eqs. 3.143 and 3.79, and solving for L_ℓ (L per unit length), we have:

$$L_\ell = \tfrac{1}{8}\mu_\circ \pi N^2 \tag{3.87}$$

Solution to PROBLEM 3.18 (continuation)

Method 2: Flux Linkage First, because the surface current density, $\vec{K}_f$, is not uniform over the dipole winding, i.e., $\vec{K}_f = -2H_0 \cos\theta \, \vec{\imath}_z$ (Eq. 3.140), for a "uniform" I in the winding, the "turn density," $n(\theta)$, must vary with θ as:

$$n(\theta) = \tfrac{1}{2} N \cos\theta \tag{S18.7}$$

Because the dipole has a uniform field of H_0, the total flux linkage by the N turns of the dipole is given by:

$$\begin{aligned} N\Phi &= \int_{-\pi/2}^{\pi/2} n(\theta) \mu_\circ H_0 (2R\cos\theta)\, d\theta = \mu_\circ N H_0 R \int_{-\pi/2}^{\pi/2} \cos\theta^2 \, d\theta \\ &= \tfrac{1}{2}\mu_\circ \pi N H_0 R = \tfrac{1}{8}\mu_\circ \pi N^2 I \end{aligned} \tag{S18.8}$$

Combining Eqs. S18.8 and 3.78, we obtain:

$$L_\ell = \tfrac{1}{8}\mu_\circ \pi N^2 \tag{3.87}$$

d) ***Method 1: Energy*** The total ampere-turns (NI) in an ideal quadrupole (**PROBLEM 3.9**) is given by:

$$NI = 2\times \int_{-\pi/4}^{\pi/4} K_f R \, d\theta \tag{S18.9}$$

R is the quadrupole radius. The integral is multiplied by 2 because, as may be seen from Fig. 3.35(b), the current distribution is divided in two regions—we are considering only one polarity. Combining Eqs. 3.146 (for $\vec{K}_f$) and S18.9, we have:

$$NI = 2\times \int_{-\pi/4}^{\pi/4} 2H_0 R \cos 2\theta \, d\theta = 4H_0 R \tag{S18.10}$$

The total magnetic energy E_m *per unit length* of the quadrupole is obtained by integrating $\mu_\circ |H(r,\theta)|^2/2$ over the entire surface. $|H(r,\theta)|^2$, from Eq. 3.145, is independent of θ, because $\sin^2 2\theta + \cos^2 2\theta = 1$.

$$\begin{aligned} E_m &= \tfrac{1}{2}\mu_\circ \left(\frac{H_0}{R}\right)^2 \int_0^R 2\pi r^3 \, dr + \tfrac{1}{2}\pi\mu_\circ H_0^2 R^6 \int_R^\infty \frac{2\pi \, dr}{r^5} \\ &= \tfrac{1}{2}\mu_\circ \pi H_0^2 R^2 \end{aligned} \tag{S18.11}$$

Combining Eqs. 3.79, S18.10, and S18.11, we obtain:

$$L_\ell = \tfrac{1}{16}\mu_\circ \pi N^2 \tag{3.88}$$

That E_m of an ideal quadrupole is 1/2 that of an ideal dipole is reasonable because the quadrupole field varies from 0 to H_0 within the bore rather than uniform as for a dipole and decays as $1/r^3$ outside rather than as $1/r^2$ for a dipole field.

Solution to PROBLEM 3.18 (continuation)

Method 2: Flux Linkage As with the dipole treated above, the "turn density," $n(\theta)$, in the quadrupole also must vary with θ, here, as:

$$n(\theta) = \tfrac{1}{2} N \cos 2\theta \qquad (S18.12)$$

Note that the integral of Eq. $S18.12$ over one quadrant, e.g., from to $-45°$ to $+45°$, gives, as it must, the total number of turns in that quadrant: $N/2$. For the ideal quadrupole, the total flux linkage, Φ, is given by:

$$N\Phi = 2 \times \int_{-\pi/4}^{\pi/4} n(\theta)\phi(R,\theta)\, d\theta \qquad (S18.13a)$$

Because $H_{1r} = H_0(r/R)\sin 2\theta$ (Eq. 3.145a), we have:

$$\phi(R,\theta) = 2\mu_\circ H_0 R \int_0^\theta \sin 2\omega\, d\omega = \mu_\circ H_0 R \cos 2\theta \qquad (S18.13b)$$

Therefore:

$$N\Phi = \mu_\circ N H_0 R \int_{-\pi/4}^{\pi/4} \cos^2 2\theta\, d\theta$$

$$= \tfrac{1}{4}\mu_\circ \pi N H_0 R = \tfrac{1}{16}\mu_\circ \pi N^2 I \qquad (S18.14)$$

Combining Eqs. 3.78 and $S18.14$, we obtain:

$$L_\ell = \tfrac{1}{16}\mu_\circ \pi N^2 \qquad (3.88)$$

e) As discussed in **PROBLEM 3.10**, the field within the circular section of an ideal toroid, $H(r)$, is in the azimuthal (φ) direction and, from Eq. 3.161, given by:

$$H_\varphi(r) = \frac{NI}{2\pi r} \qquad (S18.15)$$

The total flux linked by the toroid, Φ, is thus given by:

$$\Phi = \mu_\circ N \int_{R-a}^{R+a} \int_{z=-a}^{z=+a} H(r)\, dz\, dr \qquad (S18.16)$$

The equation of the circle that defines the cross section is given by:

$$z^2 + (R-r)^2 = a^2 \qquad (S18.17)$$

Solving z from Eq. $S18.17$ for the limits of z in the integral of Eq. $S18.16$ in terms of r and constants, and after combining with Eq. $S18.15$, we have:

$$\Phi = \frac{\mu_\circ N^2}{2\pi} \int_{R-a}^{R+a} \int_{-\sqrt{a^2-(R-r)^2}}^{\sqrt{a^2-(R-r)^2}} \frac{dz\, dr}{r}$$

$$= \frac{\mu_\circ N^2 I}{\pi} \int_{R-a}^{R+a} \frac{\sqrt{a^2 - R^2 + 2Rr - r^2}}{r}\, dr \qquad (S18.18)$$

Solution to PROBLEM 3.18 (continuation)

$$\Phi = \frac{\mu_\circ N^2 I}{\pi}\left| R\sin^{-1}\left(\frac{2r-2R}{2a}\right) + \frac{(a^2-R^2)}{\sqrt{R^2-a^2}}\sin^{-1}\left(\frac{2Rr+2a^2-2R^2}{2ra}\right)\right|_{R-a}^{R+a}$$

$$= \frac{\mu_\circ N^2 I}{\pi}\left(R\pi + \pi\frac{a^2-R^2}{\sqrt{R^2-a^2}}\right) = \mu_\circ N^2 RI\left[1-\sqrt{1-\left(\frac{a}{R}\right)^2}\right] \qquad (S18.19)$$

Combining Eqs. 3.78 and $S18.19$, we obtain:

$$L = \mu_\circ RN^2\left[1-\sqrt{1-\left(\frac{a}{R}\right)^2}\right] \qquad (3.89a)$$

f) For $a \ll R$, we have:

$$\sqrt{1-\left(\frac{a}{R}\right)^2} = 1 - \tfrac{1}{2}\left(\frac{a}{R}\right)^2 - \tfrac{1}{8}\left(\frac{a}{R}\right)^4 - \tfrac{1}{16}\left(\frac{a}{R}\right)^6 \cdots \qquad (S18.20)$$

From Eqs. $3.89a$ and $S18.20$,

$$L = \mu_\circ RN^2\left[\tfrac{1}{2}\left(\frac{a}{R}\right)^2 + \tfrac{1}{8}\left(\frac{a}{R}\right)^4 + \tfrac{1}{16}\left(\frac{a}{R}\right)^6 \cdots\right]$$

Thus:

$$L = \frac{\mu_\circ a^2 N^2}{2R}\left[1 + \tfrac{1}{4}\left(\frac{a}{R}\right)^2 + \tfrac{1}{8}\left(\frac{a}{R}\right)^4 \cdots\right] \qquad (3.89b)$$

g) The field within the rectangular section of this ideal toroid is the same as that in the circular section of the toroid studied above. Thus:

$$N\Phi = \frac{\mu_\circ N^2 I}{2\pi}\int_{R-a}^{R+a}\int_{z=-b}^{z=+b}\frac{1}{r}\,dz\,dr$$

$$= \frac{\mu_\circ N^2 bI}{\pi}\ln\left(\frac{R+a}{R-a}\right) \qquad (S18.21)$$

Combining Eqs. 3.78 and $S18.21$, we obtain:

$$L = \frac{\mu_\circ bN^2}{\pi}\ln\left(\frac{R+a}{R-a}\right) \qquad (3.90a)$$

h) For $a \ll R$, we may expand $\ln(1\pm a/R)$ as:

$$\ln\left(1\pm\frac{a}{R}\right) = \pm\frac{a}{R} - \tfrac{1}{2}\left(\frac{a}{R}\right)^2 \pm \tfrac{1}{3}\left(\frac{a}{R}\right)^3 - \tfrac{1}{4}\left(\frac{a}{R}\right)^4 \pm \tfrac{1}{5}\left(\frac{a}{R}\right)^5 \cdots \qquad (S18.22)$$

Combining Eqs. $3.90a$ and $S18.22$, we obtain:

$$L = \frac{\mu_\circ bN^2}{\pi}\left[2\left(\frac{a}{R}\right) + \tfrac{2}{3}\left(\frac{a}{R}\right)^3 + \tfrac{2}{5}\left(\frac{a}{R}\right)^5 \cdots\right]$$

$$L = \frac{2\mu_\circ abN^2}{\pi R}\left[1 + \tfrac{1}{3}\left(\frac{a}{R}\right)^2 + \tfrac{1}{5}\left(\frac{a}{R}\right)^4 \cdots\right] \qquad (3.90b)$$

DISCUSSION 3.16: Mutual Inductance of Rogowski Coil

The Rogowski coil was studied in **PROBLEM 2.11** and an expression was derived for total flux linked to the Rogowski coil:

$$\Phi(t) \simeq \frac{\mu_\circ N c^2}{2R} I(t) \tag{2.69}$$

where R is the radius of the Rogowski coil and c is the radius of each of N loops. Equation 2.69 is valid for $(c/R)^4 \ll 1$, which is generally satisfied by most Rogowski coils. The mutual inductance, M_{ri}, between the current element and the Rogowski coil is thus given by:

$$M_{ri} \equiv \frac{\Phi}{I} \simeq \frac{\mu_\circ N c^2}{2R} \tag{3.182}$$

DISCUSSION 3.17: Force vs. Mutual Inductance

From $\vec{f}_m(r,\theta) = \nabla e_m$ (Eq. 3.173) given in ***DISCUSSION 3.12*** (p. 200), we may re-derive an expression, e.g., for the axial force between two "ring" coils $F_{z_A}(\rho)$ from the mutual inductance between them, M_{AB}, or vice versa. Here, we study a simple case in which two "ring" coils are "far apart" in which case, $F_{z_A}(\rho)$ is given by Eq. 3.39*c* and M_{AB} is given by Eq. 3.97. Thus:

$$F_{z_A}(\rho) = \frac{3\mu_\circ}{2\pi}\left(\frac{\pi a_A^2 N_A I_A}{\rho^2}\right)\left(\frac{\pi a_B^2 N_B I_B}{\rho^2}\right) \tag{3.39c}$$

and

$$M_{AB} \simeq \frac{\mu_\circ}{2\pi}\left[\frac{(\pi a_A^2 N_A)(\pi a_B^2 N_B)}{\rho^3}\right] \tag{3.97}$$

For this system, we have:

$$e_m = I_A I_B M_{AB} \tag{3.183}$$

Applying Eq. 3.173 in the ρ-direction and combining Eqs. 3.97 and 3.182, we have:

$$F_{z_B}(\rho) = I_A I_B \frac{dM_{AB}}{d\rho} \tag{3.184a}$$

$$= I_A I_B \frac{d}{d\rho}\left\{\frac{\mu_\circ}{2\pi}\left[\frac{(\pi a_A^2 N_A)(\pi a_B^2 N_B)}{\rho^3}\right]\right\} \tag{3.184b}$$

$$= -\frac{3\mu_\circ}{2\pi}\left(\frac{\pi a_A^2 N_A I_A}{\rho^2}\right)\left(\frac{\pi a_B^2 N_B I_B}{\rho^2}\right) \tag{3.184c}$$

Note that in the $d/d\rho$ operation in Eq. 3.184*a*, it is Coil B (right-hand side of two coils in Fig. 3.5, p. 83) that is moved by a distance of $\partial\rho$, and thus $F_{z_B}(\rho)$ points in the negative direction of ρ. That is,

$$F_{z_A}(\rho) = -F_{z_B}(\rho)$$

$$= \frac{3\mu_\circ}{2\pi}\left(\frac{\pi a_A^2 N_A I_A}{\rho^2}\right)\left(\frac{\pi a_B^2 N_B I_B}{\rho^2}\right) \tag{3.39c}$$

DISCUSSION 3.17: Force vs. Mutual Inductance (continuation)

Clearly, the above process may be reversed to obtain an expression of M_{AB} from a known expression of $F_{zA}(\rho)$. Again, we must watch out for the sign.

$$M_{AB} = -\frac{1}{I_A I_B}\int_0^\rho F_{zA}(y)\,dy \tag{3.185}$$

$$= \frac{\mu_\circ}{2\pi}\left[\frac{(\pi a_A^2 N_A)(\pi a_B^2 N_B)}{\rho^3}\right] \tag{3.97}$$

Help from Van (Part 5 of 5 Parts)

—Passage from Francis Bitter's *Magnets: The Education of a Physicist*

After inquiring here and there, I found that the place to look for big secondhand generators was in New Jersey, out beyond Jersey City. It was a peculiar feeling, going shopping for big secondhand electrical machinery, about which I knew very little. But I found something that looked suitable. It had a central motor, and on each end of the shaft a generator capable of delivering up to 5000 amps at 170 volts. It was an impressive object—much bigger than any magnet I had seen—about 12 feet (∼4 m) *high and 20 feet* (∼6 m) *long. When I reported my findings to Van, he suggested that we employ a firm of consulting engineers to check on the condition of the motor generator and then to design a proper installation . . . and before long we had a 1.7 megawatt (million-watt) motor generator which could deliver power at any voltage from zero to 170 volts. This was very valuable, since gradual starting and stopping were necessary. By means of the voltage control we were able to connect the magnet to the power line without drawing current, and then slowly build up the current and increase the power drawn from the power mains.*

For about three years we had three or four magnets in more or less continuous operation, providing facilities for a considerable range of experiments. There were first of all some low-temperature experiments which, as I pointed out in Chapter III, might be expected to lead to particularly interesting results in high magnetic fields . . .

*. . .Some years after the war was over, and we were continuing work with our battered twenty-year old magnets, a colleague asked what I felt about the possibility of making even better and stronger magnets. I told him that it seemed to me that our experiments with heat transfer were inconclusive, . . . That is, it seemed possible to remove heat from the copper not at the rate of 200 watts per square centimeter, as I had designed it, but at approximately 2000 watts per square centimeter. The design of such a magnet would lead to even more critical cooling conditions, and in the event that something went wrong the magnet might literally explode. But such magnets are being built. The bugs are being taken out of the new designs, and more and more powerful magnets are becoming available for scientific investigations.**

* In the 1930s Francis Bitter (1902–1967) built 10-T "Bitter" magnets [3.65] to perform research in high magnetic fields [3.66]. His magnet laboratory in the basement of an M.I.T. physics building led to the establishment in 1960 of the National Magnet Laboratory (NML) at M.I.T., the first major facility in the world dedicated to high magnetic field sciences and technologies. The NML in turn led to the creation of high magnetic field facilities in Europe (England, Netherlands, France, Germany, Poland, Russia) and Asia (Japan, China). Currently, the largest and most extensive is the National High Magnetic Field Laboratory, in operation since 1995 on the campus of Florida State University. In 1995 the NML, by then the Francis Bitter National Magnet Laboratory, named in his honor in 1968, became the Francis Bitter Magnet Laboratory, as before, an M.I.T. laboratory.

REFERENCES

[3.1] Many codes are available, created by individuals and institutions, e.g., SOLDESIGN (M.I.T.), and by commercial outfits, e.g., COMSOL, ANSYS, ANSOFT.

[3.2] D. Bruce Montgomery, *Solenoid Magnet Design* (Robert Krieger Publishing, New York, 1980).

[3.3] R.J. Weggel (personal communication, 1999).

[3.4] Francis Bitter, *Magnets: The Education of a Physicist* (Doubleday, New York, 1959).

[3.5] Milan Wayne Garrett, "Calculation of fields, forces, and mutual inductances of current systems by elliptical integrals," *J. Appl. Phys.* **34**, 2567 (1963).

[3.6] Based on a reformulation with new materials by Emanuel Bobrov (FBML) in 2005, with additional contribution by Seung-Yong Hahn (FBML), of a paper by E.S. Bobrov and J.E. Williams, "Stresses in superconducting solenoid" *Mechanics of Superconducting Structures*, F.C. Moon, Ed. (ASME, New York, 1980), 13–41.

[3.7] *Standard Handbook for Electrical Engineers*, Ed. Archer E. Knowlton (McGraw-Hill Book, 1949).

[3.8] Benjamin J. Haid (personal communication, 2003).

[3.9] Hans-J. Schneider-Muntau and Mark Bird (personal communication, 2004).

[3.10] John Peter Voccio,"Qualification of Bi-2223 high-temperature superconducting (HTS) coils for generator applications" (Ph.D. Thesis, Department of System Design Engineering, Keio University, 2007).

[3.11] D.B. Montgomery, J.E.C. Williams, N.T. Pierce, R. Weggel, and M.J. Leupold, "A high field magnet combining superconductors with water-cooled conductors," *Adv. Cryogenic Eng.* **14**, 88 (1969).

[3.12] M.J. Leupold, R.J. Weggel and Y. Iwasa, "Design and operation of 25.4 and 30.1 tesla hybrid magnet systems," *Proc. 6th Int. Conf. Magnet Tech. (MT-6)* (ALFA, Bratislava), 400 (1978).

[3.13] M.J. Leupold, J.R. Hale, Y. Iwasa, L.G. Rubin, and R.J. Weggel, "30 tesla hybrid magnet facility at the Francis Bitter National Magnet Laboratory," *IEEE Trans. Magn.* **MAG-17**, 1779 (1981).

[3.14] M.J. Leupold, Y. Iwasa and R.J. Weggel, "32 tesla hybrid magnet system," *Proc. 8th Int. Conf. Magnet Tech. (MT-8)* (*J. Physique Colloque C1, supplément to* **45**), C1-41 (1984).

[3.15] M.J. Leupold, Y. Iwasa, J.R. Hale, R.J. Weggel, and K. van Hulst, "Testing a 1.8 K hybrid magnet system," *Proc. 9th Int. Conf. Magnet Tech. (MT-9)* (Swiss Institute for Nuclear Research, Villigen), 215 (1986).

[3.16] M.J. Leupold, Y. Iwasa, and R.J. Weggel, "Hybrid III system," *IEEE Trans. Magn.* **MAG-24**, 1070 (1988).

[3.17] Y. Iwasa, M.J. Leupold, R.J. Weggel, J.E.C. Williams, and Susumu Itoh, "Hybrid III: the system, test results, the next step," *IEEE Trans. Appl. Superconduc.* **3**, 58 (1993).

[3.18] Y. Iwasa, M.G. Baker, J.B. Coffin, S.T. Hannahs, M.J. Leupold, E.J. McNiff, and R.J. Weggel, "Operation of Hybrid III as a facility magnet," *IEEE Trans. Magn.* **30**, 2162 (1994).

[3.19] K. van Hulst and J.A.A.J. Perenboom, "Status and development at the High Field Magnet Laboratory of the University of Nijmegen," *IEEE Trans. Magn.* **24**, 1397 (1988).

[3.20] Jos A.A.J. Perenboom, Stef A.J. Wiegers, Jan-Kees Maan, Paul H. Frings, "First operation of the 20 MW Nijmegen High Field Magnet Laboratory," *IEEE Trans. Appl. Superconduc.* **14**, 1276 (2004).

[3.21] S.A.J. Wiegers, J. Rook, J.A.A.J. Perenboom, and J.C. Maan, "Design of a 50 mm bore 31^+ T resistive magnet using a novel cooling hole shape," *IEEE Trans. Appl. Superconduc.* **16**, 988 (2006).

[3.22] Y. Nakagawa, K. Noto, A. Hoshi, S. Miura, K. Watanabe and Y. Muto, "Hybrid magnet project at Tohoku University," *Proc. 8th Int. Conf. Magnet Tech. (MT-8)* (*Supplément au Journal de Physique, FASC. 1*), C1-23 (1984).

[3.23] K. Watanabe, G. Nishijima, S. Awaji, K. Takahashi, K. Koyama, N. Kobayashi, M. Ishizuka, T. Itou, T. Tsurudome, and J. Sakuraba, "Performance of a cryogen-free 30 T-class hybrid magnet," *IEEE Trans. Appl. Superconduc.* **16**, 934 (2006).

[3.24] H.-J. Schneider-Muntau and J.C. Vallier, "The Grenoble hybrid magnet," *IEEE Trans. Magn.* **MAG-24**, 1067 (1988).

[3.25] G. Aubert, F. Debray, J. Dumas, K. Egorov, H. Jongbloets, W. Joss, G. Martinez, E. Mossang, P. Petmezakis, Ph. Sala, C. Trophime, and N. Vidal, "Hybrid and giga-NMR projects at the Grenoble High Magnetic Field," *IEEE Trans. Appl. Superconduc.* **14**, 1280 (2004).

[3.26] A. Bonito Oliva, M.N. Biltcliffe, M. Cox, A. Day, S. Fanshawe, G. Harding, G. Howells, W. Joss, L. Ronayette, and R. Wotherspoon, "Preliminary results of final test of the GHMFL 40 T hybrid magnet," *IEEE Trans. Appl. Superconduc.* **15**, 1311 (2005).

[3.27] K. Inoue, T. Takeuchi, T. Kiyoshi, K. Itoh, H. Wada, H. Maeda, T. Fujioka, S. Murase, Y. Wachi, S. Hanai, T. Sasaki, "Development of 40 tesla class hybrid magnet system," *IEEE Trans. Magn.* **28**, 493 (1992).

[3.28] John R. Miller, "The NHMFL 45-T hybrid magnet system: past, present, and future," *IEEE Trans. Appl. Superconduc.* **13**, 1385 (2003).

[3.29] M. Bird, S. Bole, I. Dixon, Y. Eyssa, B. Gao, and H. Schneider-Muntau, "The 45T hybrid insert: recent achievement," *Phys.* **B**, 639 (2001).

[3.30] J.R. Miller, Y.M. Eyssa, S.D. Sayre and C.A. Luongo, "Analysis of observations during operation of the NHMFL 45-T hybrid magnet systems," *Cryogenics* **43**, 141 (2003).

[3.31] J.R. Miller (Personal communication, 2003).

[3.32] E.S. Bobrov (Personal communication, 2003).

[3.33] Juan Bascuñán, Emanuel Bobrov, Haigun Lee, and Yukikazu Iwasa, "A low- and high-temperature superconducting (LTS/HTS) NMR magnet: design and performance results," *IEEE Trans. Appl. Superconduc.* **13**, 1550 (2003).

[3.34] Haigun Lee, Juan Bascuñán, and Yukikazu Iwasa, "A high-temperature superconducting (HTS) insert comprised of double pancakes for an NMR magnet," *IEEE Trans. Appl. Superconduc.* **13**, 1546 (2003).

[3.35] J. Allinger, G. Danby, and J. Jackson, "High field superconducting magnets for accelerators and particle beams," *IEEE Trans. Magn.* **MAG-11**, 463 (1975).

[3.36] A.D. McInturff, W.B. Sampson, K.E. Robins, P.F. Dahl, R. Damm, D. Kassner, J. Kaugerts, and C. Lasky, "ISABELLE ring magnets," *IEEE Trans. Magn.* **MAG-13**, 275 (1977).

[3.37] W.B. Fowler, P.V. Livdahl, A.V. Tollestrup, B.F. Strauss, R.E. Peters, M. Kuchnir, R.H. Flora, P. Limon, C. Rode, H. Hinterberger, G. Biallas, K. Koepke, W. Hanson, and R. Borcker, "The technology of producing reliable superconducting dipoles at

Fermilab," *IEEE Trans. Magn.* **MAG-13**, 275 (1977).

[3.38] G. Ambrosio, N. Andreev, E. Barzi, P. Bauer, D.R. Chichili, K. Ewald, S. Feher, L. Imbasciati, V.V. Kashikhin, P.J. Limon, L. Litvinenko, I. Novitski, J.M. Rey, R.M. Scanlan, S. Yadav, R. Yamada, and A.V. Zlobin, "R&D for a single-layer Nb_3Sn common coil dipole using the react-and-wind fabrication technique," *IEEE Trans. Appl. Superconduc.* **12**, 39 (2002).

[3.39] L. Rossi, "The LHC main dipoles and quadrupoles towards series production," *IEEE Trans. Appl. Superconduc.* **13**, 1221 (2003).

[3.40] L. Bottura, D. Leroy, M. Modena, M. Pojer, P. Pugnat, L. Rossi, S. Sanfilippo, A. Siemko, J. Vlogaert, L. Walckiers, and C. Wyss, "Performance of the first LHC pre-series superconducting dipoles," *IEEE Trans. Appl. Superconduc.* **13**, 1235 (2003).

[3.41] T Doi, H. Kimura, S. Satō, K. Kuroda, H. Ogata, M. Kudō, and U. Kawabe, "Superconducting saddle shaped magnets," *Cryogenics* **8**, 290 (1968).

[3.42] J.L. Smith, Jr., J.L. Kirtley, Jr., P. Thullen, "Superconducting rotating machines," *IEEE Trans. Magn.* **MAG-11**, 128 (1975).

[3.43] T. Ohara, H. Fukuda, T. Ogawa, K. Shimizu, R. Shobara, M. Ohi, A. Ueda, K. Itoh, and H. Taniguchi, "Development of 70MW class superconducting generators," *IEEE Trans. Magn.* **27**, 2232 (1991).

[3.44] J. Kerby, A.V. Zlobin, R. Bossert, J. Brandt, J. Carson, D. Chichili, J. Dimarco, S. Feher, M.J. Lamm, P.J. Limon, A. Makarov, F. Nobrega, I. Novitski, D. Orris, J.P. Ozelis, B. Robotham, G. Sabbi, P. Schlabach, J.B. Strait, M. Tartaglia, J.C. Tompkins, S. Caspi, A.D. McInturff, and R. Scanlan, "Design, development and test of 2 m quadrupole model magnets for the LHC inner triplet," *IEEE Trans. Appl. Superconduc.* **9**, 689 (1999).

[3.45] T. Nakamoto, T. Orikasa, Y. Ajima, E.E. Burkhardt, T. Fujii, E. Hagashi, H. Hirano, T. Kanahara, N. Kimura, S. Murai, W. Odajima, T. Ogitsu, N. Ohuchi, O. Oosaki, T. Shintomi, K. Sugita, K. Tanaka, A. Terashima, K. Tsuchiya, and A. Yamamoto, "Fabrication and mechanical behavior of a prototype for the LHC low-beta quadrupole magnets," *IEEE Trans. Appl. Superconduc.* **12**, 174 (2002).

[3.46] R. Burgmer, D. Krischel, U. Klein, K. Knitsch, P. Schmidt, T. Trtschanoff, K. Schirm, M. Durante, J.M. Rifflet, and F. Simon, "Industrialization of LHC main quadrupole cold masses up to series production," *IEEE Trans. Appl. Superconduc.* **14**, 169 (2004).

[3.47] S.H. Minnich, T.A. Keim, M.V.K. Chari, B.B. Gamble, M.J. Jefferies, D.W. Jones, E.T. Laskaris, P.A. Rios, "Design studies of superconducting generators," *IEEE Trans. Magn.* **MAG-15**, 703 (1979).

[3.48] A.S. Ying, P.W. Eckels, D.C. Litz, W.G. Moore, "Mechanical and thermal design of the EPRI/Westinghouse 300 MVA superconducting generator," *IEEE Trans. Magn.* **MAG-17**, 894 (1981).

[3.49] W. Nick, G. Nerowski, H.-W. Neumüller, M. Frank, P. van Hasselt, J. Frauenhofer, and F. Steinmeyer, "380 kW synchronous machine with HTS rotor windings—development at Siemens and first test results," *Physica C: Superconductivity* **372–376**, 1470 (2002).

[3.50] Greg Snitchler, Bruce Gamble, and Swarn S. Kalsi, "The performance of a 5 MW high temperature superconductor ship propulsion motor," *IEEE Trans. Appl. Superconduc.* **15**, 2206 (2005).

[3.51] H. Ichikawa and H. Ogiwara, "Design considerations of superconducting magnets as a Maglev pad," *IEEE Trans. Magn.* **MAG-10**, 1099 (1974).

[3.52] Bruce Gamble, David Cope, and Eddie Leung, "Design of a superconducting magnet system for Maglev applications," *IEEE Trans. Appl. Superconduc.* **3**, 434 (1993).

[3.53] Kenji Tasaki, Kotaro Marukawa, Satoshi Hanai, Taizo Tosaka, Toru Kuriyama, Tomohisa Yamashita, Yasuto Yanase, Mutuhiko Yamaji, Hiroyuki Nako, Motohiro Igarashi, Shigehisa Kusada, Kaoru Nemoto, Satoshi Hirano, Katsuyuki Kuwano, Takeshi Okutomi, and Motoaki Terai, "HTS magnet for Maglev applications (1)—coil characteristics," *IEEE Trans. Appl. Superconduc.* **16**, 2206 (2006).

[3.54] A. den Ouden, W.A.J. Wessel, G.A. Kirby, T. Taylor, N. Siegel, and H.H.J. ten Kate, "Progress in the development of an 88-mm bore 10 T Nb_3Sn dipole magnet," *IEEE Trans. Appl. Superconduc.* **11**, 2268 (2001).

[3.55] G. Ambrosio, N. Andreev, S. Caspi, K. Chow, V.V. Kashikhin, I. Terechkine, M. Wake, S. Yadav, R. Yamada, A.V. Zlobin, "Magnet design of the Fermilab 11 T Nb_3Sn short dipole model," *IEEE Trans. Appl. Superconduc.* **10**, 322 (2000).

[3.56] A.R. Hafalia, S.E. Bartlett, S. Caspi, L. Chiesa, D.R. Dietderich, P. Ferracin, M. Goli, S.A. Gourlay, C.R. Hannaford, H. Higley, A.F. Lietzke, N. Liggins, S. Mattafirri, A.D. McInturff, M. Nyman, G.L. Sabbi, R.M. Scanlan, and J. Swanson, "HD 1: design and fabrication of a 16 tesla Nb_3Sn dipole magnet" *IEEE Trans. Appl. Superconduc.* **14**, 283 (2004).

[3.57] J.E.C. Williams, L.J. Neuringer, E.S. Bobrov, R. Weggel, and W.G. Harrison, "Magnet system of the 500 MHz spectrometer at the FBNML: 1. Design and development of the magnet," *Rev. Sci. Instrum.* **52**, 649 (1981).

[3.58] Haigun Lee, Emanuel S. Bobrov, Juan Bascuñán, Seung-yong Hahn and Yukikazu Iwasa, "An HTS insert for Phase 2 of a 3-phase 1-GHz LTS/HTS NMR magnet," *IEEE Trans. Appl. Superconduc.* **15**. 1299 (2005).

[3.59] Juan Bascuñán, Wooseok Kim, Seungyong Hahn, Emanuel S. Bobrov, Haigun Lee, and Yukikazu Iwasa, "An LTS/HTS NMR magnet operated in the range 600–700 MHz," *IEEE Tran. Appl. Superconduc.* **17**, 1446 (2007).

[3.60] D.S. Easton, D.M. Kroeger, W. Specking, and C.C. Koch, "A prediction of the stress state in Nb_3Sn superconducting composites," *J. Appl. Phys.* **51**, 2748 (1980).

[3.61] J.W. Ekin, "Strain scaling law for flux pinning in practical superconductors. Part 1: Basic relationship and application to Nb_3Sn conductors," *Cryogenics* **20**, 611 (1980).

[3.62] J.W. Ekin, "Four-dimensional J-B-T-ϵ critical surface for superconductors," *J. Appl. Phys.* **54**, 303 (1983).

[3.63] S.L. Bray, J.W. Ekin, and C.C. Clickner, "Transverse compressive stress effects on the critical current of Bi-2223/Ag tapes reinforced with pure Ag and oxide-dispersion-strengthened Ag, *J. Appl. Phys.* **88**, 1178 (2000).

[3.64] J.W. Ekin, S.L. Bray, N. Cheggour, C.C. Clickner, S.R. Foltyn, P.N. Arendt, A.A. Polyanskii, D.C. Larbalestier and C.N. McCowan, "Transverse stress and fatigue effects in Y-Ba-Cu-O coated IBAD tapes," *IEEE Trans. Appl. Superconduc.* **11**, 3389 (2001).

[3.65] F. Bitter, "The design of powerful electromagnets Part IV. The new magnet laboratory at M.I.T.," *Rev. Sci. Inst.* **10**, 373 (1939).

[3.66] George R. Harrison and Francis Bitter, "Zeeman effects in complex spectra at fields up to 100,000 gauss," *Phys. Rev.* **57**, 15 (1940).

Chapter 4
Cryogenics

4.1 Introduction

Cryogenics is essential for superconductivity. This reliance of superconductivity on cryogenics has been a major hindrance to the widespread use of superconductivity for applications such as electric power. It is, however, important to put cryogenics in perspective and not *overemphasize* its role. From cryogenics alone, it is clearly more efficient to operate a superconducting magnet at the highest permissible temperature, but if this superconducting magnet is a part of a system, the impact of this operating temperature on the overall system must be evaluated. The question of "What is the best operating temperature for a superconducting magnet?" becomes a real, and extremely important, design/operation issue, particularly with HTS magnets. To generate the same field an HTS magnet operating at 77 K, for example, unquestionably requires considerably more superconductor than one at 20 K; the savings in cryogenics may be insufficient to offset the increased superconductor cost.

Also not to be overlooked is the mandatory requirement of thermal insulation for *every* superconducting system: the best thermal insulation is vacuum. A thermally "effective" vacuum is relatively easy to achieve in a cryostat when the cold temperature is below 20 K, at which point hydrogen condenses. Hydrogen, outgassed from the "evacuated" cryostat surfaces, is the primary heat transfer medium within the cryostat. Thus, for the *overall* HTS magnet system it might be more cost effective to operate the magnet below, rather than above, 20 K. Alternatively, if we can select an operating temperature high enough, e.g., above ∼70 K, arguably most people's preferred option, we may be able to eliminate vacuum insulation altogether from the cryogenic system, making it one step closer to *less intrusive*.

In this introductory section, the cryogenic design/operation issues of superconducting magnets are briefly discussed : 1) two cooling methods for superconducting magnets, "wet" and "dry;" 2) cooling sources, heating sources, and cryogenic measurements; 3) cryogens for wet magnets; and 4) solid cryogens that may become useful for dry magnets. Details of some of these topics are further studied and covered in **Problems & *Discussions*** which follow this section.

4.2 "Wet" and "Dry" Magnets

Until around 1990, *all* superconducting magnets were operated "wet," i.e., cooled by liquid helium. The discovery of HTS, coupled with advances in cryocooler technology, spurred, beginning in the early 1990s, development of "dry" (cryogen-free) magnets "cryocooled," i.e., cooled by a cryocooler, with both LTS [4.1–4.11] and HTS [4.12–4.18]. Because a dry cryogenic system is less cumbersome to operate and maintain, and equally important, because it is easier to make it less *intrusive* than its "wet" counterpart, the dry magnet is the preferred option in most applications, provided that the magnet generates virtually no dissipations of its own, e.g., AC losses, under normal operating conditions.

Y. Iwasa, *Case Studies in Superconducting Magnets: Design and Operational Issues*,
DOI: 10.1007/b112047_4,

Cooling Methods for Superconducting Magnets

As summarized in Table 4.1, superconducting magnets can employ any of five cooling methods, four wet and one dry. Although the terms "cryostable," "adiabatic," and "quasi-stable" used here are discussed in more detail in ***CHAPTER 6***, qualitatively these terms should be understandable to the reader. Each method is briefly discussed below in the context primarily of cryogenics.

Bath-Cooled Cryostable Magnets built before the early 1980s were chiefly bath-cooled and cryostable. A key cryogenic feature of these magnets is "ventilation" of the windings to facilitate cryogen penetration, making virtually every part of the winding exposed to liquid cryogen. Here, convective heat transfer, discussed qualitatively below, is important; some data are presented in ***CHAPTER 6***.

Bath-Cooled Adiabatic To achieve high performance, bath-cooled "adiabatic" magnets began to be developed in the early 1980s. Here, the winding pack is dense, with virtually no cryogen penetration, resulting in overall current densities in the winding that are significantly greater than those of bath-cooled cryostable magnets. The winding pack is cooled only at its outer surfaces.

Force-Cooled Cryostable To keep cryogen in one phase, which is not generally the case in bath-cooled magnets, and more importantly to reinforce winding with conductor itself, the so-called "cable-in-conduit" (CIC) conductor was developed in the early 1970s, particularly for "large" magnets. Cooling and winding are well-coupled here. Important heat transfer data are those of forced convective flow, typical heat transfer data for which are presented in ***CHAPTER 6***.

Force-Cooled Quasi-Stable Here, to make it robust, the winding is not ventilated. To achieve better stability than in bath-cooled adiabatic magnets, however, the coolant is forced through the winding, not through the conductor, but only in close proximity to the conductor pack. As in the adiabatic winding the bulk of the conductor is cooled by conduction.

Cryocooled Here the magnet is connected to a cryocooler; cooling within the winding is primarily by conduction. As discussed in more detail in ***CHAPTER 6***, LTS magnets operate quasi-stably, while, HTS magnets operate quite stably. As pointed out in ***DISCUSSION 4.7*** (p. 247), a *"cryocirculator"* is actually preferable to a cryocooler for the cooling source of a dry magnet, particularly LTS.

Table 4.1: Cooling Methods for Wet and Dry Superconducting Magnets

Wet Magnets		
Cooling Method	*Cooling-Conductor Coupling*	*Heat Transfer*
Bath-cooled, "cryostable"	Good; entire conductor	Convective
Bath-cooled, "adiabatic"	Essentially nonexistent	Conductive*
Force-cooled, "cryostable"	Good; entire conductor	Convective
Force-cooled, "quasi-stable"	Close proximity, but indirect	Conductive
Dry Magnets		
Cryocooled, "quasi-stable"	Indirect	Conductive

* To the surfaces of the magnet winding pack.

4.3 Cryogenics Issues—Cooling; Heating; Measurement

For superconducting magnet technology, three basic cryogenics issues are relevant: 1) cooling sources; 2) heat sources; and 3) measurement. These issues are briefly discussed in this introductory section, with more detailed discussion on specific topics in **PROBLEMS & *DISCUSSIONS***, as well as in later chapters.

4.3.1 Cooling Sources

As summarized in Table 4.1, a superconducting magnet is cooled to and maintained at its operating temperature by either a cryogen or a cryocooler. Cryogens are briefly discussed below. As for the cryocooler only the basic thermodynamics (**PROBLEM 4.1**) and performance data (***DISCUSSION 4.1***) are presented.

4.3.2 Heat Sources

Generally there are five principal sources of heat in the cold environment of a cryostat housing a superconducting magnet: 1) radiation between the cryostat walls; 2) convection in the "evacuated" space between the cryostat walls; 3) conduction through the magnet support and cryostat structural elements; 4) combination of conduction and Joule dissipation of current leads; 5) dissipation within the magnet. Radiation, convection, and current leads are discussed later in the **PROBLEMS & *DISCUSSIONS***. Dissipation in magnets is discussed in ***CHAPTER 7***.

4.3.3 Measurement

In the operation of superconducting magnets, cryogenic parameters generally measured include: 1) temperature; 2) pressure (cryostat vacuum or cryogen pressure); 3) cryogen flow rate (force-cooled wet magnets); and 4) vapor flow rate (current leads in wet magnets). In this book, only temperature measurement is discussed briefly in ***DISCUSSION 4.13*** (p. 264).

4.4 Liquid Cryogens—for "Wet" Magnets

Until the early 1990s, only liquid helium (LHe) was suitable for operation of superconducting magnets. Liquid nitrogen (LN_2) is used to intercept heat in some LHe cryostats; it also precools LHe-cooled magnets to economize on LHe consumption as the magnet is cooled down from room temperature to 4.2 K (***DISCUSSION 4.2***).

Six cryogens with atmospheric saturation (boiling) temperatures below 100 K are oxygen (90.18 K); argon (87.28 K); nitrogen (77.36 K); neon (27.09 K); hydrogen (20.39 K); and helium (4.22 K). For "wet" HTS magnets and devices, cryogens called upon, in order of likelihood, are nitrogen, neon, and possibly hydrogen. For wet LTS magnets and LTS/HTS magnets, e.g., high-field NMR magnets that consist of both LTS and HTS coils, liquid helium still dominates. Boiling heat transfer parameters of five liquids—helium, hydrogen, neon, nitrogen, and, for comparison, water—are briefly discussed below.

> ***TRIVIA 4.1*** Of the important events below for helium, which is said to have been achieved for the first time on February 29?
>
> i) Discovery; ii) Liquefaction; iii) Solidification; iv) Superfluidity.

Table 4.2: Boiling Heat Transfer Parameters

Liquid	T_s [K]	h_ℓ [J/cm^3]	q_{pk} [W/cm^2]	ΔT_{pk} [K]	q_{fm} [W/cm^2]
Helium	4.22	2.6	∼1	∼1	∼0.3
Hydrogen	20.39	31.3	∼10	∼5	∼0.5
Neon	27.09	104	∼15	∼10	∼1
Nitrogen	77.36	161	∼25	∼15	∼2
Water	373.15	2255	∼100	∼30	∼10

Boiling Heat Transfer Parameters

In a wet superconducting magnet, particularly bath-cooled and cryostable, cooling relies on nucleate boiling heat transfer. Because in nucleate boiling heat transfer, cooling is achieved by vaporization of liquid, the liquid's *volumetric* heat of vaporization, h_ℓ, is a key parameter. It also implies that a plot of boiling heat transfer flux, g_q vs. temperature, shown in Fig. 4.1 with both axes generally in log scales, looks similar for most liquids. Here the x-axis is the difference between the surface temperature, T, of the object exposed to liquid and the liquid saturation temperature, T_s: $T - T_s (= \Delta T)$. Other key parameters of the plot are: q_{pk}, the peak nucleate boiling heat transfer flux; ΔT_{pk}, the ΔT at which q_{pk} occurs; and q_{fm}, the minimum film boiling heat flux. Table 4.2 presents values of T_s under atmospheric pressure and h_ℓ, together with *typical* values of q_{pk}, ΔT_{pk}, and q_{fm} for helium, hydrogen, neon, nitrogen, and, for comparison, water.

From Table 4.2, we can easily conclude that liquid helium, the only cryogen suitable for LTS magnets, is the least effective coolant, absorbing the least energy density when vaporized. Although an HTS magnet is best operated dry, if it is to be operated wet, hydrogen, neon, or nitrogen can cover the temperature range for most HTS magnets. One outcome of fuel cell application in the automotive industry is advancement in liquid hydrogen (LH_2) technology, including safety aspects, that may prove useful for LH_2-cooled HTS magnets.

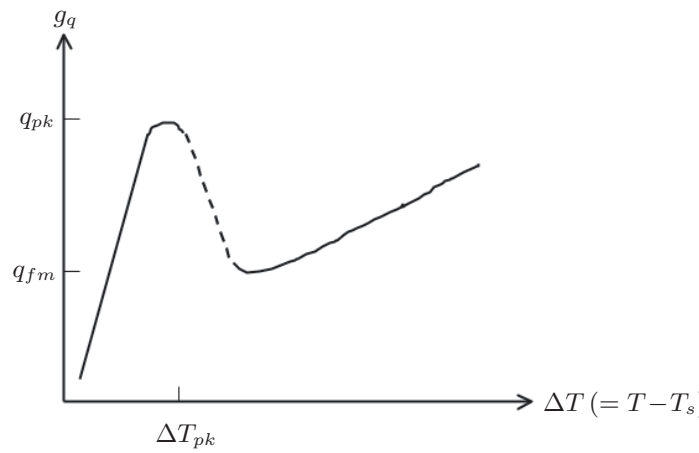

Fig. 4.1 Boiling heat transfer flux vs. temperature (difference between the surface temperature and liquid saturation temperature, T_s) for a typical liquid.

4.5 Solid Cryogens—for "Dry" Magnets

As stated earlier, dry LTS magnets, particularly those with operating currents below ~1 kA, are likely to gradually replace wet, low-current LTS magnets. With one, two, or even all three of the HTS currently being developed (i.e., BSCCO, coated YBCO, and MgB_2) expected to become full-fledged "magnet-grade-conductors" in the near future, dry HTS magnets may not only replace dry LTS magnets but also find other applications that are possible only with HTS magnets.

4.5.1 "Wet" LTS Magnets vs. "Dry" HTS Magnets—Heat Capacities

One positive aspect of a "wet" LTS magnet often overlooked is the large heat capacity of the "cold body," provided by a volume of liquid helium that is an integral part of every wet LTS magnet. The "large" enthalpy density of liquid helium at 4.2 K of 2.6 J/cm^3—"large" in comparison with copper's enthalpy density, say, from 4.2 K to 4.5 K of ~0.0003 J/cm^3, ~10,000 times greater than copper's—essentially "anchors" the magnet at its operating temperature *most* of the time.

Every "dry" magnet also should be provided with a large temperature-anchoring heat capacity: solid cryogen is an excellent candidate for this purpose. Figure 4.2 presents heat capacity, C_p, vs. T plots of solid cryogens—neon (SNe), nitrogen (SN_2), and argon (SAr)—and metals, lead (Pb), silver (Ag), and copper (Cu). (Solid hydrogen is excluded because of its low heat capacity, ~0.2 J/cm^3 K at 13.96 K.) Lead is used often as a heat capacity enhancer in cryogenic equipment, copper is the most widely used matrix metal in LTS, and silver is the matrix metal associated with BSCCO.

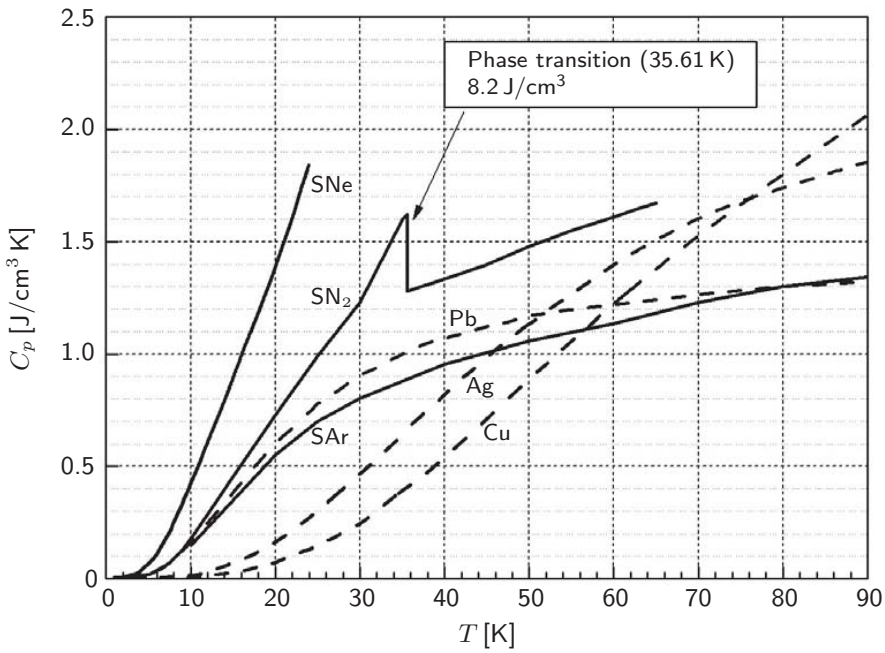

Fig. 4.2 Heat capacity, C_p, vs. temperature, T, plots for SNe, SN_2 and SAr (solid lines); and Pb, Ag, and Cu (dashed lines). Note that SN_2 has a solid-to-solid phase transition at 35.61 K, absorbing an energy density of 8.2 J/cm^3.

4.5.2 Solid Cryogens—Neon, Nitrogen, and Argon

Three solid cryogens—neon, nitrogen, and argon—that are likely to be used with dry HTS magnets are briefly described below. Selected thermodynamic properties of helium, nitrogen, neon, and argon are given in ***APPENDIX II.***

Although high heat capacity is what makes solid cryogens excellent impregnant materials, there are two other properties that make solid cryogens, in some applications, preferable to epoxy: 1) thermal conductivity; and 2) mechanical strength. Over the temperature range 10–15 K, for example, SN_2 is more effective than epoxy to make the temperature over an HTS winding uniform. Also SN_2 makes the winding more robust than epoxy.

Solid Nitrogen (SN_2) Because it remains solid up to 64.2 K and is inexpensive, lighter (∼1/10 the density of lead), and electrically insulating, solid nitrogen (SN_2) can be an effective heat capacity enhancer for a dry HTS magnet that operates in the temperature range below 64 K. For example, a BSCCO or YBCO magnet may operate anywhere in the range 20–60 K. For an MgB_2 magnet this could be 10-15 K or even 20–30 K. As seen in Fig. 4.2 SN_2 undergoes a solid-solid phase transition at 35.61 K, absorbing an additional energy density of 8.2 J/cm^3. Because its heat capacity is ∼1.5 J/cm^3 K near this transition temperature, an additional 8.2 J/cm^3 energy absorption is equivalent to more than 5 K in temperature rise, a significant "temperature reserve" for an HTS magnet operating in this range.

Solid Neon (SNe) The heat capacity data of Fig. 4.2 show that solid neon (SNe), which on a volume basis is ∼200 times more expensive than SN_2, would be the best heat capacity enhancer, among those in the figure, for applications in the range 4–10 K. However, above ∼10 K, SN_2 should suffice for most cases. Although there are other substances, e.g., Er_3Ni, that enhance the system heat capacity better than solid neon in the temperature range 4–24 K, for magnets, solid neon, like solid nitrogen and solid argon, is more suitable. The only drawback, aside from cost, is its relatively (compared with SN_2) low melting temperature of 24.6 K, which limits the operating range of SNe systems to below this temperature.

Solid Argon (SAr) Being the most abundant inert gas in the atmosphere, argon is at least an order of magnitude less expensive than neon, though still more expensive than nitrogen. Solid argon will likely be used only for dry magnets operating in the temperature range above 64.2 K (melting point of SN_2) and below 83.8 K (melting point of SAr).

In the **PROBLEMS & *DISCUSSIONS*** that follow this introductory section, cryogenic topics relevant to wet and dry magnets are studied; they are followed by a brief discussion on temperature measurement. In the last section, a rather extensive treatment is given, by means of **PROBLEMS & *DISCUSSIONS***, on current leads, all vapor-cooled, except one "dry" lead. This is because "large" magnet systems, particularly those operating at currents above 1 kA, are still dominated by wet LTS magnets that require vapor-cooled current leads.

"The perpetual motion? Nonsense! It can never be discovered. It is a dream that may delude men whose brains are mystified with matter, but not me."—Owen Warland

PROBLEM 4.1: Carnot refrigerator

Because superconductivity occurs at very low temperatures, refrigeration is required to achieve and maintain the cryogenic environment. Using a Carnot refrigerator, shown schematically in Fig. 4.3, we study the most efficient thermodynamic cycle for cooling. The Carnot cycle is composed of two reversible adiabatic (isentropic) and two reversible isothermal processes, in which a working fluid operates between two thermal reservoirs to produce refrigeration (or work) with the highest efficiency. Although Carnot efficiency can never be attained in practice, it sets an upper bound on what is possible.

a) Draw a Carnot cycle on a T vs. S plot. Use the following notation indicated in Fig. 4.3—T_{op}: the cold reservoir temperature, which is generally equal to the magnet operating temperature; S_{cl}: the entropy of the mass flow leaving the cold reservoir; T_{wm}: the warm reservoir temperature; and S_{wm}: the entropy of the mass flow entering the warm reservoir. Both reservoir temperatures, T_{op} and T_{wm}, are maintained constant.

b) Show that for an ideal Carnot refrigerator, the work input W_{ca} required to extract heat Q from the reservoir at T_{op} and release it to the reservoir at T_{wm} is given by:

$$W_{ca} = Q\left(\frac{T_{wm}}{T_{op}} - 1\right) \tag{4.1}$$

c) Show that for a Carnot refrigerator with $T_{wm} = 300\,\mathrm{K}$, $W_{ca}/Q \simeq 70$ for $T_{op} = 4.2\,\mathrm{K}$ and $W_{ca}/Q \simeq 3$ for $T_{op} = 77\,\mathrm{K}$.

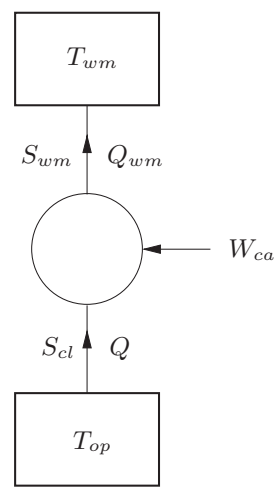

Fig. 4.3 Carnot refrigerator operating between two heat reservoirs.

* Based on **Problem 4.1** in the 1st Edition (Plenum, 1994).

Solution to PROBLEM 4.1

a) The Carnot refrigerator operates between two reservoirs, the lower one at T_{op} and the higher one at T_{wm}, extracting heat Q at T_{op} and releasing heat Q_{wm} at T_{wm}. As illustrated in Fig. 4.3, work W_{ca} is needed to run the refrigerator.

The Carnot refrigeration cycle consists of four reversible processes performed on a working fluid, as shown in the T vs. S plot of Fig. 4.4:

- An isentropic compression of working fluid, starting at State 1 (S_{wm}, T_{op});
- An isothermal compression, starting at State 2 (S_{wm}, T_{wm});
- An isentropic expansion, starting at State 3 (S_{cl}, T_{wm});
- An isothermal expansion, starting at State 4 (S_{cl}, T_{op}) and ending at State 1.

b) From the first law of thermodynamics, we have:

$$Q_{wm} = Q + W_{ca} = 0 \tag{S1.1}$$

W_{ca} is the work input to the refrigerator, equal to the area enclosed on the T-S diagram. (When the directions of W_{ca}, Q, and Q_{wm} in Fig. 4.3 are reversed, this Carnot cycle represents an *ideal* working machine and the area enclosed on the T-S diagram represents the work output.) Because each process is reversible, $Q = T_{op}(S_{wm} - S_{cl})$ and $Q_{wm} = T_{wm}(S_{wm} - S_{cl})$, and thus:

$$S_{wm} - S_{cl} = \frac{Q}{T_{op}} \tag{S1.2a}$$

$$S_{wm} - S_{cl} = \frac{Q_{wm}}{T_{wm}} \tag{S1.2b}$$

Equating Eqs. $S1.2a$ and $S1.2b$, we obtain:

$$\frac{Q}{T_{op}} = \frac{Q_{wm}}{T_{wm}} \tag{S1.3}$$

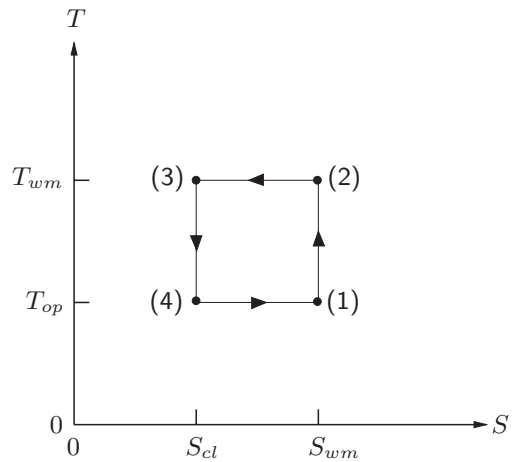

Fig. 4.4 Temperature vs. entropy plot for the Carnot refrigerator.

Solution to PROBLEM 4.1 (continuation)

Combining Eqs. $S1.1$ and $S1.3$, we have:

$$\frac{Q}{T_{op}} = \frac{Q + W_{ca}}{T_{wm}} \tag{S1.4}$$

By solving Eq. $S1.4$ for W_{ca}, we obtain:

$$W_{ca} = Q\left(\frac{T_{wm}}{T_{op}} - 1\right) \tag{4.1}$$

c) ***Temperature range 4.2–300 K***: With $T_{op} = 4.2\,\text{K}$ and $T_{wm} = 300\,\text{K}$, $W_{ca}/Q \simeq 70$ from Eq. 4.1; i.e., for each 1 W of cooling at 4.2 K, the cryocooler requires 70 W of work input. In real cryocoolers, the "performance" ratio, W_{cp}/Q, where W_{cp} is the compressor work, improves with Q, from ~10,000 for small units ($Q = 1\,\text{W}$) to ~300 for large units ($Q \sim 100\,\text{kW}$)—see ***DISCUSSION 4.1*** below.

Temperature range 77~300 K: With $T_{op} = 77\,\text{K}$ and $T_{wm} = 300\,\text{K}$ inserted into Eq. 4.1, we find $W_{ca}/Q \simeq 3$. In real cryocoolers, the performance ratio ranges from ~50 for small (1 W) units to ~10 for large (100 kW) units.

DISCUSSION 4.1: Cryocooler Performance

Here, we shall briefly examine the cryocooler's performance in two different ways: 1) cryocoolers rated at one refrigeration power and at different operating temperatures (Q/T_{op}); and 2) a cryocooler rated at one combination of refrigeration power and operating temperature but operating at different temperatures.

A. Specific Cooling Powers at Specific Temperatures

Figure 4.5 shows W_{cp}/Q vs. T_{op} plots for cryocoolers of specific cooling powers, Q in [W], listed in the figure legend [4.19]; the symbol ⊗ is the Carnot cycle.

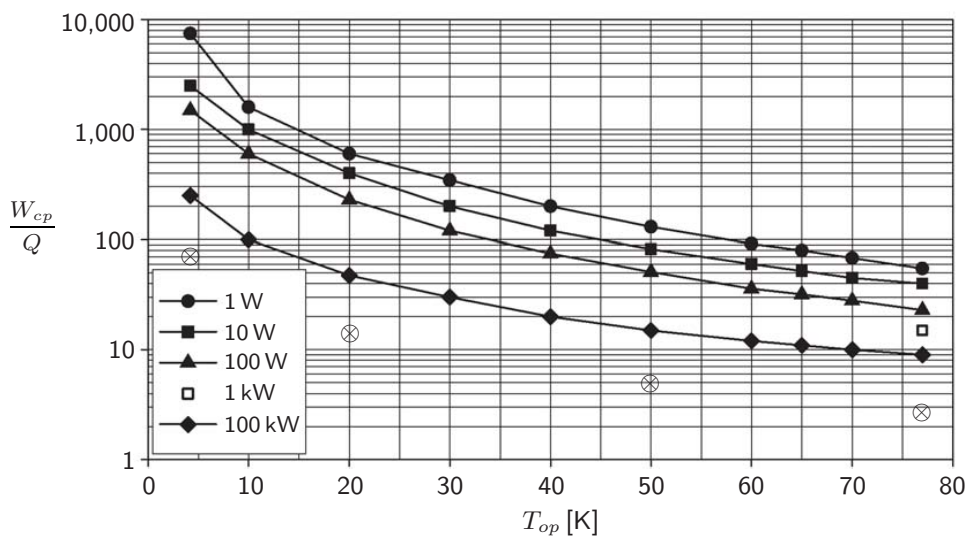

Fig. 4.5 W_{cp}/Q vs. T_{op} plots for cryocoolers at specified levels of Q [W] (inset) [4.19]. The symbol ⊗ is for the Carnot cycle at selected T_{op}, computed for $T_{wm} = 300\,\text{K}$.

DISCUSSION 4.1: "Cryocooler" Performance (continuation)

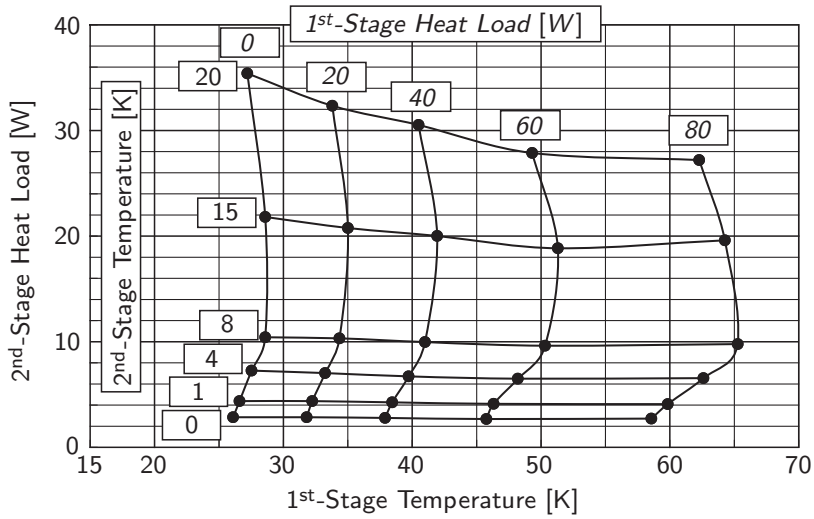

Fig. 4.6 Performance data of a 2-stage cryocooler.

Thus, 1-W cryocoolers (solid circles) have W_{cp}/Q ratios, for example, of 7500 for a unit designed for $T_{op} = 4.2$ K and 600 for a 1-W unit with $T_{op} = 20$ K. As discussed below, its W_{cp}/Q ratios at different levels of T_{op} are different from a cryocooler optimized at specific temperatures of 4.2 K and 20 K.

B. Operation at Temperatures Other Than the Design Temperature

Figure 4.6 shows performance (1st- and 2nd-stage refrigeration powers) data for a 2-stage cryocooler (Sumitomo Heavy Industries: Model RDK-408D2), as functions of the 1st-stage and 2nd-stage operating temperatures. Its nominal lowest 2nd-stage operating temperature is 4.2 K at a cooling power (Q) of 1 W with a compressor power (W_{cp}) of 7.5 kW: $W_{cp}/Q = 7500$. The data show that the cryocooler's 2nd-stage power/temperature rating—for this same compressor power—ranges from 0 W at 3 K, i.e., $W_{cp}/Q = \infty$, to 15 W at 20 K, i.e., $W_{cp}/Q = 500$. (Note that Fig. 4.5 indicates a 15-W/20-K unit optimized at 20 K has a W_{cp}/Q ratio of ∼350.) The nearly horizontal 2nd-stage cooling lines, each at a given 2nd-stage temperature of up to ∼20 K, indicate that the 2nd-stage cooling power is almost independent of the 1st-stage temperature over a range from ∼25 K to ∼60 K.

Because this cryocooler runs at the same compressor power of 7.5 kW irrespective of the 1st- and 2nd-stage loads, to keep the 2nd-stage temperature at a desired level, the *total* heat load, at least at the 2nd-stage, must *match* its cooling power. Thus, if a 2nd-stage operating temperature of 20 K is desired—at a 1st stage operating condition of 40 W/42 K—and if the *actual* heat load at the 2nd stage is, for example, 5 W, an additional heat load of 10 W must be supplied to the 2nd stage, because, as seen from Fig. 4.6, the 2nd stage provides a cooling power of 15 W at 20 K. This extra heating load of 10 W is generally supplied by a heater, attached to the 2nd-stage coldhead, making this system even less efficient.

DISCUSSION 4.2: Cooling Modes for Wet Magnets*

Because on a volume basis LHe not only is at least one order of magnitude more expensive than LN_2 but also has only ~1/60 the latent heat of vaporization, a LHe-cooled magnet often undergoes a two-step cooldown procedure: 1) with LN_2, cool down the magnet to 77 K; and 2) flush out the LN_2 from the cryostat and immediately start cooling down with LHe. For a large magnet (>1 ton), the liquid nitrogen in Step 2 may be pumped down to a pressure of 109 torr (0.14 atm) to bring its temperature, and thus the magnet's, to 64 K.

A. "Perfect" Cooldown Mode

Under a "perfect" cooldown mode, the magnet is cooled by a series of infinitesimal perfect energy exchanges with cold helium. At the n^{th} step, the magnet at temperature T_n is cooled to $T_n - \Delta T$ by helium of mass ΔM_{he}, which is vaporized and heated to T_n. Note that the available enthalpy of helium vapor between T_n and room temperature is not used in cooling the magnet. If M_{he} is the mass of helium required to cool a magnet of mass M_{mg} from T_i to 4.2 K, M_{he}/M_{mg} is given by:

$$\frac{M_{he}}{M_{mg}} = \int_{4.2\,\text{K}}^{T_i} \frac{c_{cu}(T)\,dT}{h_{he}(T) - h_{he}(4.2\,\text{K, liq.})} \tag{4.2}$$

where $c_{cu}(T)$ is the specific heat of copper (representing all the materials in the winding) and $h_{he}(T)$ is the specific enthalpy of helium.

This cooling mode may be approached, but never realized in practice, by having liquid helium introduced in the cryostat space *underneath* the magnet at a very *slow* rate. However, the cooling rate cannot be arbitrarily slow, because it would take too long, consuming lots of LHe to cope with heat leakage into the cryostat.

B. "Dunk" Mode

An extreme mode of cooldown is to "dunk" the whole magnet initially at T_i into a bath of liquid helium boiling at 4.2 K. $[M_{he}/M_{mg}]_{dk}$ to cool down the magnet from T_i to 4.2 K by this "dunk" mode is given by:

$$\left[\frac{M_{he}}{M_{mg}}\right]_{dk} = \frac{[h_{cu}(T_i) - h_{cu}(4.2\,\text{K})]}{h_L} \tag{4.3}$$

where h_L [kJ/kg] is the specific heat of vaporization of LHe at 4.2 K. $h_{cu}(T_i)$ and $h_{cu}(4.2\,\text{K})$ are the specific enthalpies of copper, respectively, at T_i and 4.2 K.

C. Cooldown with Liquid Neon (LNe) or Liquid Nitrogen (LN_2)

With a cryocooled HTS magnet operating at $T_{op} \geq 10$ K, sometimes it is required to initially cool down the magnet from room temperature to T_{op} much faster than would be possible with the cryocooler alone. We may meet this requirement in two steps: 1) by deploying liquid neon (LNe) to reach 27 K, if $T_{op} < 27$ K, or LN_2 to 77 K, if $27\,\text{K} < T_{op} < 77\,\text{K}$; and 2) with the cryocooler to T_{op}. The required amount of LNe or LN_2, by either cooling mode, may be computed with Eq. 4.2 or Eq. 4.3 with the enthalpies of Ne or N_2 in the equations.

---

* Based on **Problem 4.2** in the 1st Edition (Plenum, 1994).

DISCUSSION 4.2: Cooling Modes for Wet Magnets (continuation)

Table 4.3 presents liquid cryogen (LHe, LNe, LN_2) volumes (in liters) required, by *"Perfect"* and *"Dunk"* modes, to cool a 1000-kg copper block from T_i to 4.2 K (LHe), 27 K (LNe), or 77 K (LN_2). Copper specific enthalpy ($h_{p_{cu}}$) data are also included. From Table 4.3 it is clear that for a LHe-cooled magnet, LN_2 precooling results in a great saving of LHe. The large differences in volumetric heats of vaporization among these cryogens—2.6 [J/cm^3] for LHe; 104 [J/cm^3] for LNe; 161 [J/cm^3] for LN_2—are evident in the volume requirements.

Table 4.3: Liquid Cryogens (LHe, LNe, LN_2) Required to Cool a 1000-kg Copper Block from T_i to 4.2 K (LHe), 27 K LNe), and 77 K (LN_2)

		LHe Required [liter]		*LNe Required* [liter]		*LN_2 Required* [liter]	
T_i [K]	$h_{p_{cu}}$ [kJ/kg]	*"Perfect"* (Eq. 4.2)	*"Dunk"** (Eq. 4.3)	*"Perfect"* (Eq. 4.2)†	*"Dunk"** (Eq. 4.3)†	*"Perfect"* (Eq. 4.2)†	*"Dunk"** (Eq. 4.3)†
300	79.6	800	30,000	290	770	300	460
280	72.0	760	28,000	270	700	270	420
240	56.9	670	22,000	230	550	230	320
200	42.4	570	16,000	190	410	170	230
180	35.3	520	14,000	170	340	150	190
160	28.5	460	11,000	140	280	120	140
140	22.1	390	8,500	120	210	90	100
120	16.1	320	6,200	90	160	60	66
100	10.6	240	4,100	66	100	31	33
90	8.22	200	3,200	53	78	17	17
77	5.90	150	2,100	37	51	0	0
70	4.13	130	1,600	29	39	—	—
60	2.58	90	1,000	19	24	—	—
50	1.40	57	550	11	12	—	—
40	0.61	31	240	4.4	4.8	—	—
30	0.196	13	77	0.7	0.7	—	—
27	0.124	9.0	50	0	0	—	—
20	0.034	3.4	13	—	—	—	—
15	0.0107	1.3	4.0	—	—	—	—
10	0.0024	0.4	0.9	—	—	—	—

* Rounded to two significant figures.

† Eqs. 4.2 and 4.3 applied to neon for T_i between 27 K and 300 K; and to nitrogen for T_i between 77 K and 300 K.

Answer to TRIVIA 4.1 iii). In 1928 (a leap year), by a colleague of Kamerlingh Onnes, the Dutch physicist Willem Keesom (1876–1956), who in 1927 also discovered the phenomenon of superfluidity in liquid helium. The element was first observed in 1868 by the French astronomer Pierre Jules César Janssen (1824–1907) as a spectral line in the sun (*hēlios*) during a total eclipse in India. The Scottish chemist Sir William Ramsay (1852–1916) in 1895 discovered the element on earth in America from samples of gas obtained from a uranium mineral.

DISCUSSION 4.3: "Cryocooling" HTS Magnet

In this discussion we study a dry HTS magnet as it is "cryocooled" (cooled by a cryocooler) from an initial temperature T_i to its operating temperature T_{op} over a total cooldown period of τ_{cn}. The cooling power of the 2nd stage of this cryocooler, $Q_r(T)$, vs. its temperature, T, is shown in Fig. 4.7. Note that the cooling power of this cryocooler is rated 10 W at 10 K. (Its 1st stage is used to cool the radiation shields that surround the magnet.)

To simplify the discussion, let us consider an adiabatic control volume consisting only of the magnet and the cryocooler with no additional heat input to the system during the cooldown. Also let us assume that the magnet mass is represented by copper mass M_{cu}. A plot of copper heat capacity, $C_{cu}(T)$ [kJ/m^3], is given in ***APPENDIX III***, based on a constant copper density, ϱ_{cu}, of 8960 kg/m^3. Assume furthermore that the cooling rate is sufficiently slow to make the copper (magnet) temperature, T_{cu}, uniform over the entire winding and equal to the cryocooler temperature, T, at all times during the cooldown, i.e., $T_{cu} = T$.

Applying the 1st law of thermodynamics on the control volume containing the cryocooler and the copper mass M_{cu}, and noting $T_{cu} = T$, we have:

$$-Q_r(T) = \left(\frac{M_{cu}}{\varrho_{cu}}\right) C_{cu}(T) \frac{dT}{dt} \tag{4.4}$$

The minus sign for $Q_r(T)$ in Eq. 4.4 signifies that the cryocooler is providing refrigeration: the magnet (copper mass) is cooling, i.e., $dT/dt < 0$.

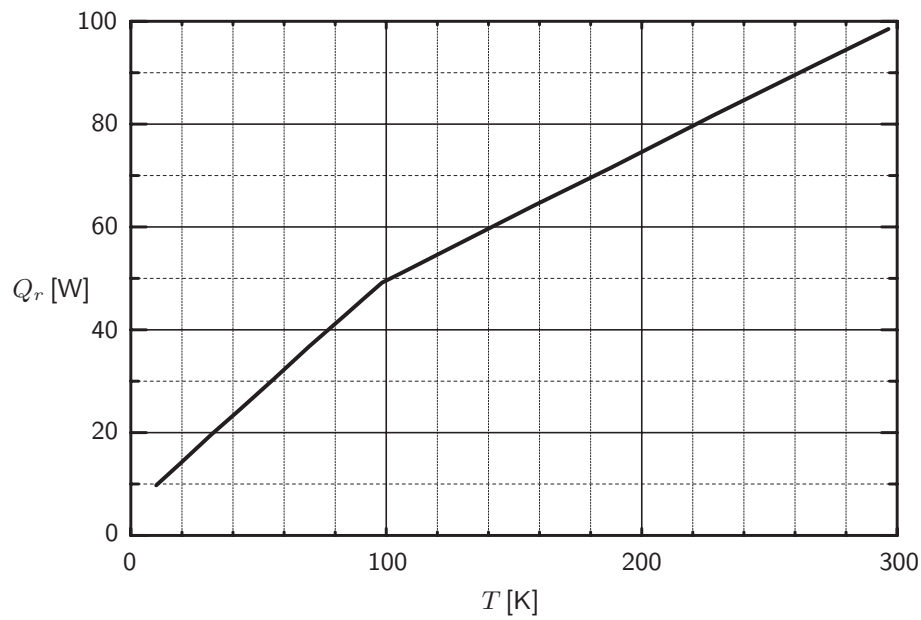

Fig. 4.7 $Q_r(T)$ curve for the magnet cryocooler.

DISCUSSION 4.3: "Cryocooling" an HTS Magnet (continuation)

Table 4.4: $Q_r(T)$, $C_{cu}(T)$, and $\mathcal{K}(T) \equiv C_{cu}(T)/Q_r(T)$

T [K]	$Q_r(T)$ [W]	$C_{cu}(T)$ [J/m^3 K]	$\mathcal{K}(T)$ [s/m^3 K]
300	100	3.44×10^6	3.44×10^4
250	87	3.32×10^6	3.82×10^4
200	75	3.17×10^6	4.23×10^4
150	63	2.87×10^6	4.56×10^4
100	50	2.26×10^6	4.52×10^4
77	40	1.75×10^6	4.38×10^4
50	28	0.88×10^6	3.14×10^4
30	19	0.24×10^6	1.26×10^4
20	15	0.69×10^5	0.46×10^4
10	10	0.08×10^5	0.08×10^4

Table 4.4 lists $Q_r(T)$, $C_{cu}(T)$, and $\mathcal{K}(T) \equiv C_{cu}(T)/Q_r(T)$ at selected temperatures. We may integrate Eq. 4.4 to solve for τ_{cn} for a set of T_i, T_{op}, $Q_r(T)$, and M_{cu}:

$$\tau_{cn} = \frac{M_{cu}}{\varrho_{cu}} \int_{T_{op}}^{T_i} \frac{C_{cu}(T)}{Q_r(T)}\, dT = \frac{M_{cu}}{\varrho_{cu}} \int_{T_{op}}^{T_i} \mathcal{K}(T)\, dT \tag{4.5a}$$

$$M_{cu} = \frac{\varrho_{cu}\tau_{cn}}{\displaystyle\int_{T_{op}}^{T_i} \mathcal{K}(T)\, dT} \tag{4.5b}$$

In some applications, τ_{cn} is the primary design specification, which, as may be seen from Eq. 4.5*b*, limits the copper mass (here representing the magnet mass), $\tilde{M}_{cu}$, to be cooled within τ_{cn}. Note that for a given combination of T_i and T_{op}, $\tilde{M}_{cu}$ is proportional to τ_{cn}. Table 4.5 lists $\tilde{M}_{cu}$ for combinations of τ_{cn}, T_i, and T_{op}, with $Q_r(T)$ given by Fig. 4.7. Thus, if a magnet is to be cooled down from 300 K to 30 K in a time period of 4 h, for example, its mass is limited to 11.6 kg.

The results shown in Table 4.5 clearly indicate that for a given τ_{cn} we may dramatically increase $\tilde{M}_{cu}$ by first cooling down the mass to 77 K. Table 4.3 may be used to estimate the amount of LN_2 required to accomplish this.

Table 4.5: $\tilde{M}_{cu}$ for τ_{cn}, T_i, T_{op}, with $Q_r(T)$ given by Fig. 4.7

T_i [K]	T_{op} [K]	$\tilde{M}_{cu}$ [kg]							
τ_{cn} [*hour*/**day**]→		*1*	*2*	*4*	*12*	***1***	***2***	***10***	***20***
300	77	3.4	6.8	13.6	41	82	164	820	1640*
	50	3.0	6.1	12.1	36	73	147	735	1470*
	30	2.9	5.8	11.6	35	70	140	700	1400*
	10	2.9	5.7	11.5	34	69	139	695	1390*
77	50	29	58	118	352	704	1410*	7040*	14100*
	30	20	40	80	242	484	968	4840*	9680*
	10	19	38	76	227	453	906	4530*	9060*

* Up to 3 significant figures.

DISCUSSION 4.4: Superfluidity

Figure 4.8 shows the phase diagram of ordinary helium (He^4), in which two forms of liquid are present, He I and He II [4.20]. Because of its unique properties of extremely high effective thermal conductivity (k) and low viscosity (ν), He II is known as superfluid helium; superfluidity has been compared to superconductivity. As may be inferred from the phase diagram, ordinary liquid helium (He I) boiling at 4.22 K can readily be transformed to He II simply by pumping on the liquid. When the saturation pressure of 5 kPa (37.8 torr) is reached, the liquid, at 2.18 K, becomes "superfluid." The temperature 2.18 K is known as the λ-point and designated by T_λ. According to the "two-fluid" model, the fraction of superfluid, zero at T_λ, increases monotonically as temperature is lowered. The extraordinary thermal conductivity and viscosity of superfluid helium may be appreciated by comparing these properties of He II with those of common materials (Table 4.6).

A. Transport Properties

Because of its extremely high thermal conductivity superfluid helium is sometimes used as a coolant for superconducting magnets, generally operated at ~1.8 K ($<T_\lambda$). (Although we use the classical definition of thermal conductivity here, i.e., heat conduction $\propto$ temperature difference, in He II the smaller the temperature difference, the greater becomes the "equivalent" conductivity, which also varies with heat flux.) The high thermal conductivity of He II does not allow a temperature gradient in the liquid sufficient for creation of vapor. Thus, unlike the winding of a 4.2-K He I cooled cryostable magnet, the "bubbleless" winding of a 1.8-K He II cooled cryostable magnet does not require ventilation. However, this does not mean that He II can transport unlimited heat fluxes through narrow channels. Analogous to the critical current density in superconductors, He II has a critical heat flux.

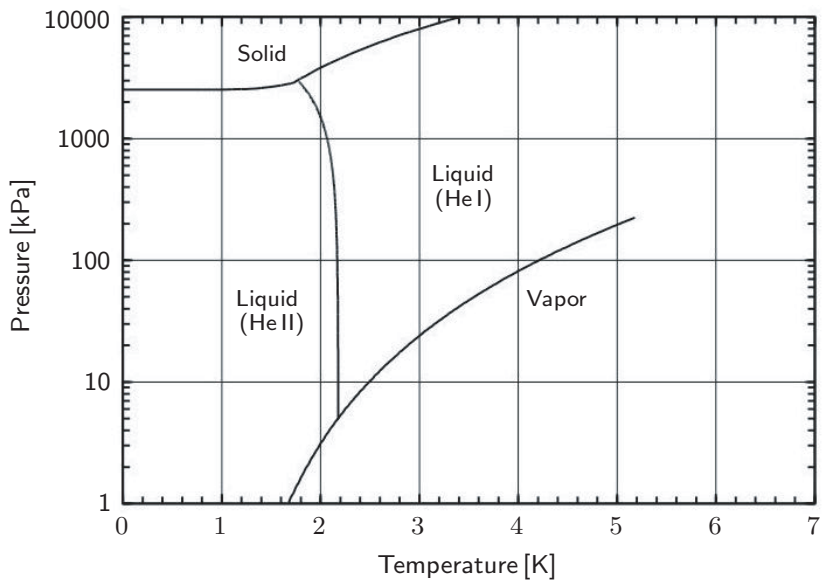

Fig. 4.8 Phase diagram of ordinary helium (He^4) [4.20].

DISCUSSION 4.4: Superfluidity (continuation)

Table 4.6: Thermal Conductivities and Viscosities of He II, He I, Copper, Water, Air

Material	k [W/m K]	ν [μPa s]
He II	∼100,000*	0.01∼0.1
He I (4.2 K, liq.)	0.02	∼3
Copper (4.2 K)	∼400	—
Water (293 K)	∼1	∼1,000
Air (293 K)	∼0.05	∼20

* "Equivalent" k at a *specified* temperature difference and heat flux.

Bon Mardion, Claudet, and Seyfert studied heat flux in He II through narrow channels [4.21]. Figure 4.9 presents their results in the form of a parameter $X(T)$ defined by them; it is given by:

$$X(T_{cl}) - X(T_{wm}) = q^{3.4}L \tag{4.6a}$$

where T_{cl} [K] is the cold-end temperature and T_{wm} [K] is the warm-end temperature. q [W/cm^2] is the heat flux through a channel L [cm] long between the two ends, one end at T_{cl} and the other at T_{wm}. Equation 4.6a is applicable for the case with no additional heating introduced to the liquid from the channel itself. Under normal operating conditions, $T_{cl} = T_b$, where T_b is the bath temperature; T_{wm} is the liquid temperature adjacent to a heated region within the winding, which cannot exceed T_λ. When $T_{wm} = T_\lambda$, from Fig. 4.9, $X(T_{wm}) = 0$, and we can simplify Eq. 4.6a to:

$$X(T_b) = q_c^{3.4}L \tag{4.6b}$$

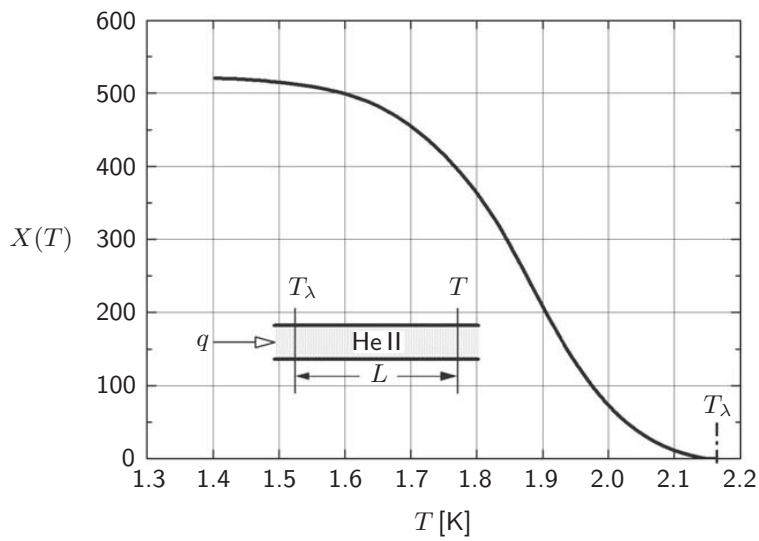

Fig. 4.9 Bon Mardion-Claudet-Seyfert plot of $X(T)$ for a channel of length L [cm] filled with 1-atm, superfluid helium conducting heat flux q. [4.21].

DISCUSSION 4.4: Superfluidity (continuation)

For $T_{wm} > T_\lambda$ the heat flux from the surface of the heated region will be limited by q_{pk} which, for He I as given in Table 4.2, is $\sim$1 W/cm^2. The limit implied by Eq. 4.6*b* will exceed 1 W/cm^2 in magnets whose characteristic size is less than 1 m as long as $T_b < 2$ K. In designing channel configuration and dimensions, we must make sure that the operating heat flux, q_{op}, through the channel does not exceed q_c given by Eq. 4.6*b*.

Heated Channel

When heating is uniformly introduced over the entire length L of the channel, rather than at the hot end as discussed above, Eq. 4.6*b* is modified [4.22]:

$$X(T_b) = \frac{q_c^{3.4}}{4.4} L \tag{4.6c}$$

B. Heat Transfer—Kapitza Resistance

Heat transfer between a metal or other thermally conductive material and He II is limited by Kapitza resistance. Heat transfer flux, q_k [W/cm^2], between a metal whose surface is at T_{cd} [K] and liquid helium at T_b [K] is given by:

$$q_k = a_k (T_{cd}^{n_k} - T_b^{n_k}) \tag{4.7}$$

Table 4.7 gives typical values of a_k and n_k.

Table 4.7: Approximate Values for Kapitza Resistance*

Metal (surface)	a_k [W/cm^2 K^{n_k}]	n_k
Aluminum (polished)	0.05	3.4
Copper (polished)	0.02	4.0
Copper† (polished)	0.02	3.8
Copper (as-received)	0.05	2.8
Copper (solder-coated)	0.08	3.4
Copper (varnish-coated)	0.07	2.1
Silver (polished)	0.06	3.0

* Based on values given in references [4.23, 4.24].

† Annealed.

TRIVIA 4.2 Of the four contemporary chemists (born 1870–1881) below, who first produced neon lights?

i) Claude; ii) Fischer; iii) Hahn; iv) Langmuir.

*DISCUSSION 4.5: Subcooled 1.8-K Cryostat**

Here we discuss a cryostat for a superconducting magnet operated in a bath of subcooled superfluid helium at 1 atm and 1.8 K. Performance of a magnet improves significantly as the operating temperature is decreased from 4.2 K to 1.8 K, particularly in bath-cooled NbTi magnets [4.25], because of significant improvements in: 1) critical current density; and 2) heat transfer between conductor and coolant.

Figure 4.10 shows a schematic of the subcooled 1.8-K cryostat for the Hybrid III magnet system [4.26]. A pump, located outside the cryostat, drives the helium flow, at a mass flow rate of $\dot{m}_h$, required by the 1.8-K evaporator ("ice cube") housed in the magnet vessel. The 1.8-K/1-atm magnet vessel is connected hydraulically to the 4.2-K/1-atm reservoir located above through a narrow channel sufficient both to keep the magnet vessel at 1 atm (subcooled) and to minimize conduction heat input by helium from the reservoir to the magnet vessel. The current leads pass through the 4.2-K reservoir and then enter the magnet vessel through current links connecting the two liquid vessels. Components such as structural elements not directly related to the refrigeration cycle are not included in Fig. 4.10.

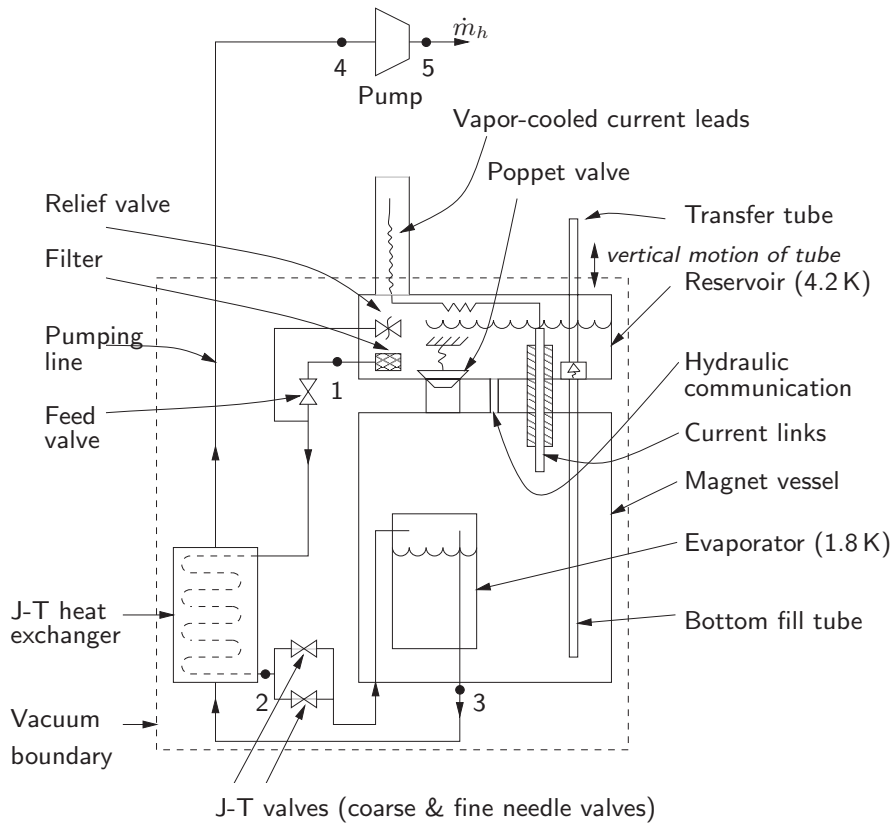

Fig. 4.10 Schematic of a subcooled 1.8-K cryostat [4.26].

* Based on **Problem 4.6** in the 1st Edition (Plenum, 1994).

DISCUSSION 4.5: Subcooled 1.8-K Cryostat (continuation)

From Point 1, just outside the reservoir, filtered 4.2-K/1-atm (760 torr) liquid helium is cooled by the J-T heat exchanger and then flows through the J-T valves. The valves reduce the helium pressure isenthalpically from 760 torr to 12.3 torr—more about Joule-Thomson (J-T) process in ***DISCUSSION 4.6***—and creates a mixture of liquid and vapor, both at 1.8 K and 12.3 torr. The 1.8-K liquid enters the evaporator and cools the 1-atm liquid in the magnet vessel, as would an ice cube in a glassful of water. On its return path the 1.8-K vapor leaves the evaporator and cools the incoming 4.2-K liquid in the J-T heat exchanger.

Upon leaving the pump, the helium gas is purified and stored in a pressure tank. The exhaust helium gas from the 4.2-K reservoir is funneled through the vapor-cooled current leads, and it too is stored in the tank. Helium from the tank is liquefied and transferred into a 500-liter storage dewar, from which it is continuously transferred to the 4.2-K reservoir to maintain the reservoir's liquid level. This 1.8-K cryostat thus is a closed system.

Under normal operating conditions, the 1.8-K/12.3-torr superfluid helium in the evaporator is kept at a nearly constant level. The total combined heat load on the magnet vessel, $Q_{1.8}$, is thus matched by refrigeration produced by the evaporator. $Q_{1.8}$ enters into the evaporator from the vessel through the evaporator wall.

A. Refrigeration Power at 1.8 K

Refrigeration power at 1.8 K, $Q_{1.8}$, provided by the evaporator may be derived from the first law of thermodynamics applied to the control volume (c.v.) enclosing the evaporator, schematically shown in Fig. 4.11. In the figure, $\dot{m}_h$ is the mass flow rate entering and leaving the control volume. Under the steady-state condition, the difference between the total heat output, Q_{out} and total input, Q_{in}, to the evaporator, is equal to $Q_{1.8}$. Thus:

$$Q_{out} - Q_{in} = Q_{1.8} \tag{4.8}$$

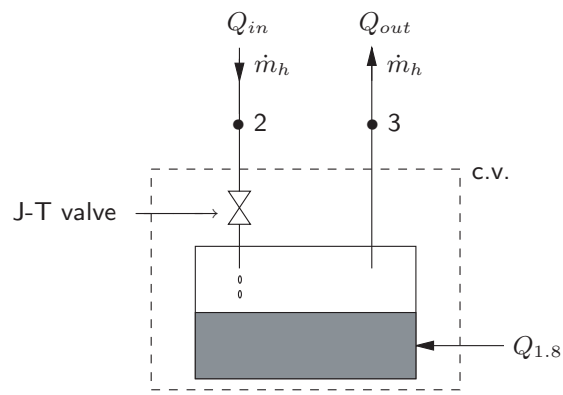

Fig. 4.11 Heat balance for the evaporator. See Fig. 4.10 for locations of Points 2 and 3 in the cryostat.

DISCUSSION 4.5: Subcooled 1.8-K Cryostat (continuation)

Note that $Q_{1.8}$ is also equal to the refrigeration load to the evaporator. $Q_{1.8}$ consists principally of:

- Dissipation within the magnet—splice losses and AC losses during field change; these losses are discussed in ***CHAPTER 7***.
- Heat input to the magnet vessel—conduction: through structural supports and by current leads between the 4.2-K reservoir and the 1.8-K vessel; superfluid conduction through the pressure communication channel; radiation as well as residual convection on the vessel surfaces.

Heat output, Q_{out}, from the control volume is given by $Q_{out} = \dot{m}_h h_3$, where h_3 is the helium (vapor) enthalpy at Point 3. Similarly, $Q_{in} = \dot{m}_h h_2$, where h_2 is the helium (liquid) enthalpy at Point 2. Solving Eq. 4.8 for $Q_{1.8}$, we obtain:

$$Q_{1.8} = \dot{m}_h (h_3 - h_2) \tag{4.9}$$

Point 1 is at 4.2 K, while Point 3 is at 1.8 K. To maximize $Q_{1.8}$ at a given helium flow rate, as seen from Eq. 4.9, $(h_3 - h_2)$ must be maximized: the helium temperature at Point 2 must be as close to 1.8 K as possible. The J-T heat exchanger cools down the incoming 4.2-K/760-torr liquid with the outgoing 1.8-K/12.3-torr vapor.

Illustration We may determine $\dot{m}_h$ [g/s] to make $Q_{1.8} = 20$ W for the following parameters: $P_2 = 1$ atm; $T_2 = 3.0$ K; $P_3 = 12.3$ torr and $T_3 = 1.8$ K. From ***APPENDIX II***, $h_3(1.8\,\text{K}, 12.3\,\text{torr};\ \text{vapor}) = 24.02$ J/g and $h_2(3.0\,\text{K},\ 1\,\text{atm};\ \text{liquid}) = 5.64$ J/g, and solving for $Q_{1.8}$ (Eq. 4.9), we obtain:

$$Q_{1.8} = \dot{m}_h (24.02\,\text{J/g} - 5.64\,\text{J/g}) = 20\,\text{W}$$

Solving the above equation for $\dot{m}_h$, we obtain $\dot{m}_h = 1.09$ g/s, which corresponds to a supply rate of liquid helium (at 4.2 K, 1 atm) of 31 liter/h. Note that in addition to this 31 liter/h liquid replenishment rate, it is necessary to transfer liquid into the reservoir to remove the heat from current leads and other sources.

B. Refrigeration Pumping Power Requirement

Assuming the pumping process to be isentropic and helium vapor to be a perfect gas, we may compute the minimum input power (between Points 4 and 5 in Fig. 4.10) required to pump helium at a mass flow rate $\dot{m}_h = 1$ g/s from Point 4 (12.3 torr/300 K) to Point 5 (760 torr). For an isentropic pump, the pump power requirement, $\mathbb{P}_s$, is given by:

$$\mathbb{P}_s = \dot{m}_h \left(\frac{\gamma}{\gamma - 1}\right) (P_4 v_4) \left[\left(\frac{P_5}{P_4}\right)^{\frac{\gamma-1}{\gamma}} - 1\right] \tag{4.10}$$

$\gamma = C_p/C_v$ for a perfect gas is 5/3; v_4 is the specific volume at Point 4, which for helium at 300 K and 12.3 torr is 371 m^3/kg. With $P_4 = 12.3\,\text{torr} = 1.64 \times 10^3$ Pa, $P_5/P_4 = 61.8$, and $\dot{m}_h = 0.001$ kg/s (1 g/s), we obtain: $\mathbb{P}_s = 6400$ W (or $\sim$9 hp, horsepower). Note that this is for an ideal case; the power requirement for a real pump is roughly 20 kW.

DISCUSSION 4.5: Subcooled 1.8-K Cryostat (continuation)

Line Pressure Drop It is important to keep the pressure drop between Points 3 and 4 much less than 12.3 torr, the operating pressure at Point 3. Note that the lower P_4 gets—below 12.3 torr to keep $P_3 = 12.3$ torr—the more $\mathbb{P}_s$ is needed. For the Hybrid III system, the plumbing outside the cryostat consists of a pipe of 15-cm i.d. and 13-m length, having five 90° bends and one shut-off valve. It handles a mass flow rate up to ∼2 g/s with a total pressure drop less than 1 torr.

Also, precautions should be taken not to introduce contaminants into the evaporator. Such contaminants tend to freeze out at the narrowest passage areas, e.g., J-T valves, and block the line. In Hybrid III each J-T valve has a heater attached to melt away frozen contaminants.

C. Heat Leakage Through Hydraulic Communication

For the Hybrid III cryostat, the hydraulic communication has an effective area of 2.6 mm^2 to keep the magnet vessel at 1 atm. Its effective length, L, connecting the helium in the reservoir and that in the magnet vessel is 10 cm. Using the Bon Mardion-Claudet-Seyfert plot of $X(T)$ given in Fig. 4.9, and assuming the helium temperature at the bottom of the reservoir to be T_λ and at the magnet vessel to be 1.8 K, we may compute the heat input into the 1.8-K magnet vessel from the 4.2-K reservoir, conducted by the superfluid helium in the channel.

For narrow channels filled with 1-atm superfluid helium, as discussed in **4.4 A**, we may apply Eq. 4.6*a* which relates $X(T)$ for two end temperatures, T_{wm} (warm) and T_{cl} (cold), to conduction heat flux q [W/cm^2], and channel length L [cm]. With $T_{wm} = T_\lambda$, $T_{cl} = 1.8$ K, and $L = 10$ cm, we have, from Fig. 4.9: $X(T_\lambda) = 0$, and $X(1.8) = 360$ (in appropriate units). Inserting these values into Eq. 4.6*a*, we obtain: $360 = q^{3.4}10$, which results in: $q = 2.87$ W/cm^2. With the channel cross sectional area of 2.6 mm^2, total conduction heat input to the 1.8-K magnet vessel through the hydraulic communication channel becomes ∼75 mW.

Carbon resistors are placed in the bottom area of the reservoir to measure liquid temperature in that area. Although measurement indicated that the liquid temperature in this particular reservoir bottom was ∼3 K, generally in this type of 1.8-K cryostat, the liquid at the reservoir bottom would be closer to $T_\lambda (= 2.18$ K). Because 2.6 mm^2 is an insufficient flow area to limit the overpressure in the 1.8-K vessel in the event of a magnet quench, the cryostat has a "poppet" valve of 40-mm^2 cross section. Under normal conditions the poppet valve is kept shut by a spring; the valve is opened when pressure builds up in the magnet vessel.

D. Replenishment of 4.2-K Liquid

One of the final steps in the "cool-down mode" of the Hybrid III magnet involves cooling the liquid helium in the magnet vessel from 4.2 K to 1.8 K. The cooling is provided by the evaporator, which is continuously fed with liquid, initially at 4.2 K in the reservoir and cooled by the J-T heat exchanger before entering the evaporator, and then pumped. For a liquid volume in the magnet vessel of 250 liters, we may estimate the total volume of "replenishment" liquid for the magnet vessel as the liquid is cooled from 4.2 K to 1.8 K.

DISCUSSION 4.5: Subcooled 1.8-K Cryostat (continuation)

The liquid densities at 1 atm are 125 kg/m^3 at 4.2 K and 147 kg/m^3 at 1.8 K. Thus for Hybrid III, the 250-liter vessel starts with about 31 kg of liquid at 4.2 K and ends up with about 37 kg of liquid at 1.8 K. That is, about 6 kg of liquid must be supplied to the vessel. In terms of volume at 4.2 K, this translates to ∼50 liters.

Although the cross section of 2.6 mm^2 provided by the hydraulic communication channel is adequate to transport this additional mass of liquid over a cooldown period of ∼2 hr, the poppet valve with a total flow passage area of 40 mm^2 is kept open until the liquid in the vessel reaches T_λ.

E. Current Leads Between 4.2-K Reservoir and 1.8-K Vessel

The current leads must reach from the bottom of the reservoir to the terminals of the magnet in the 1.8-K vessel. It is customary to use a composite superconductor for current leads. In this application the cross section occupied by normal metal (copper) must be small enough to minimize heat conduction by the metal from the reservoir to the vessel but sufficient to stabilize the composite superconductor. The "dry" lead criterion, to be studied in ***DISCUSSION 4.15*** (p. 274), is applicable here, because between the two ends the lead is essentially insulated—in the Hybrid III cryostat, the vertical gap separating the reservoir and 1.8-K vessel is in vacuum.

We may show that the peak steady-state temperature in the normal-state lead carrying I_t occurs at the lead's reservoir end. By choosing the "current-sharing temperature" (T_{cs}) of composite superconductor in the lead to be well above T_λ, the helium temperature at the reservoir bottom, we may ensure stable operation of the current leads—see ***CHAPTER 6*** for discussion of T_{cs}.

An expression for the steady-state temperature profile along the normal-state lead is derived from Eq. 4.52 given in ***DISCUSSION 4.15***:

$$T(z) = -\frac{\tilde{\rho} I_t^2}{2A^2\tilde{k}} z^2 + \left[\frac{(T_\ell - T_0)}{\ell} + \frac{\tilde{\rho} I_t^2 \ell}{2A^2\tilde{k}} \right] z + T_0 \tag{4.11}$$

In Eq. 4.11, the composite's $z=0$ is at the 1.8-K vessel and $z=\ell$ is at the reservoir. $\tilde{\rho}$ and $\tilde{k}$ are, respectively, the composite normal metal's resistivity and thermal conductivity. A and ℓ are the lead's cross sectional area and length separating the cold and warm ends, respectively, at T_0 (1.8 K) and T_ℓ ($\simeq T_\lambda$). According to ***DISCUSSION 4.15***, a dry lead rated at $I_t = I_\circ$ satisfies the following condition:

$$\left(\frac{I_\circ \ell}{A} \right)_{dr} = \sqrt{\frac{2\tilde{k}(T_\ell - T_0)}{\tilde{\rho}}} \tag{4.12}$$

Combining the above two equations and defining a new variable $\xi \equiv z/\ell$, we have:

$$T(\xi) = -(T_\ell - T_0)\xi^2 + 2(T_\ell - T_0)\xi + T_0 \tag{4.13}$$

At $\xi = 1$, where $dT/d\xi = 0$, the temperature peak occurs. Since this location is at $\xi = 1$, it implies that the peak temperature is $T_\ell \simeq T_\lambda$. That is, even if the lead is driven normal, if the lead satisfies the criterion given by Eq. 4.12, the conduction cooling is sufficient to limit the peak lead temperature to T_λ, no greater than the warm-end temperature of the lead when it is superconducting.

DISCUSSION 4.6: Joule-Thomson Process

In the Joule-Thomson (J-T) process, a gas expands adiabatically with no work involved (isenthalpic) through a restricted passage, e.g., a J-T (needle) valve to a lower pressure, changing its temperature in the process. Whether the change is positive, negative, or zero depends on the gas properties, the starting temperature, and initial and final pressures. For helium at initial and final pressures of 10 atm and 1 atm, respectively, liquefaction results if the initial temperature is below ∼7.5 K. Because the process is irreversible, liquefaction by the J-T process always results in a smaller portion of liquid produced than if the gas had been expanded isentropically. For example, at a starting temperature of 6 K and a pressure of 10 atm—typical values for liquefiers—the following isenthalpic relationship may be used to compute the fraction of helium liquefied (x_ℓ) at 4.2 K and 1 atm:

$$h_g(6\,\mathrm{K}, 10\,\mathrm{atm}) = x_\ell h_\ell(4.2\,\mathrm{K}, 1\,\mathrm{atm}) + (1 - x_\ell)h_g(4.2\,\mathrm{K}, 1\,\mathrm{atm}) \tag{4.14}$$

From Eq. 4.14 we find $x_\ell = 0.47$. If the same gas is expanded isentropically, an entropy relationship similar to the enthalpy relationship of Eq. 4.14 gives $x_\ell = 0.85$. Despite this reduction in liquid production efficiency, the J-T expansion, because of its mechanical simplicity, is used in the final stage of many helium liquefiers.

James Prescott Joule (1818–1889)

—Passage from Isaac Asimov's *Asimov's Biographical Encyclopedia of Science and Technology* [4.27]

Joule was son of a wealthy brewer, which meant he had the means to devote himself to a life of research... Joule was almost a fanatic on the subject of measurement, and even on his honeymoon he took time out to devise a special thermometer to measure the temperature of the water at the top and bottom of a scenic waterfall his wife and he were to visit... He went on to devote a decade to measuring the heat produced by every process he could think of... Even his honeymoon measurement of the waterfall temperature was based on the thought that the energy of falling water should be converted to heat once it was stopped so that the temperature at the bottom of the waterfall should be higher than that at the top...

In all those cases he calculated the amount of work that had entered the system and the amount of heat that came out and he found, as Rumford had maintained fully half a century before, that the two were closely related. A particular quantity of work always produced a particular quantity of heat. In fact, 41,800,000 ergs of work produced one calorie of heat. This is called the "mechanical equivalent of heat."

His original statement of this discovery was rejected by various learned journals and he was forced to present it at a public lecture in Manchester and then get his speech published in full by a reluctant Manchester newspaper. A few months later he finally managed to present it before an unsympathetic scientific gathering and his presentation would have passed almost unnoticed but for a twenty-three-old in the audience. His name was William Thomson, and he was later to be known as Lord Kelvin. His comments on Joule's work were shrewd enough and logical enough to rouse interest and even enthusiasm, and Joule's reputation was made.

---

* Although for many years until his death a faculty member of Boston University, the biochemist Isaac Asimov (1920–1992) devoted his life writing for the general public on virtually every subject conceivable. In the sci-fi genre his books include the *Galactic Empire* series (*Pebble in the Sky*, 1950) and the *Robot* series (*I, Robot*, 1950).

PROBLEM 4.2: Cryocooler-based "mini" helium liquefier

With proliferation of cryocoolers, as stated at the outset of this chapter, most "DC" superconducting magnets, LTS and HTS, will likely be operated "dry" (cryogen-free) with cooling provided by a cryocooler. In some applications, unlike most cryocooled magnets in which the cryocooler/magnet assembly is housed within the same cryostat, the magnet and its cryocooler are housed in separate cryostats. A schematic drawing of one such system is shown in Fig. 4.12 for a slow "magic angle spinning" (MAS) NMR magnet. In such a magnet, its principal field is directed 54.73° from the magnet axis (see **PROBLEM 2.5**) as the magnet is spun about its axis. As indicated in Fig. 4.12, the primary cooling source for the magnet may be provided by a stationary cryocooler placed ∼1 m away from the magnet. Each numbered component of the system is given in the figure caption.

Stated briefly, the system permits the magnet/cryostat assembly (component 2 in Fig. 4.12) to be spun as a flow of liquid helium is continuously transferred to the magnet cryostat, through the spinning shaft, at a mass flow rate of $\dot{m}_{he}$ from a "mini" helium liquefier, whose primary source of refrigeration is a cryocooler housed in the second cryostat (14). The thermodynamics of this cryocooler-based mini liquefier is the focus of this problem.

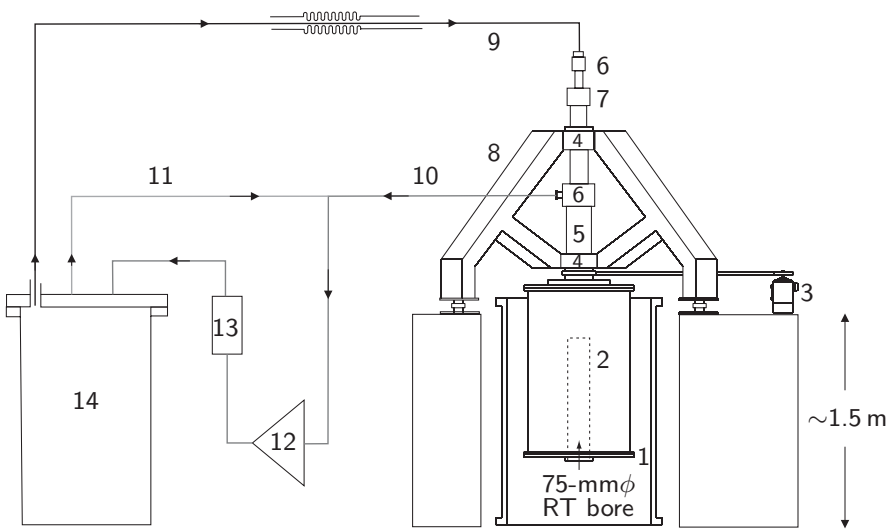

Fig. 4.12 Schematic of a superconducting magnet system that incorporates a cryocooler-based "mini" helium liquefier, here, as applied to a slow MAS (magic angle spinning) NMR system, in which a persistent-mode superconducting magnet that generates a magnetic field directed 54.73° (magic angle) from the axis of rotation is cooled by liquid helium, continuously transferred, from the cryocooled-based mini liquefier, to the rotating magnet/cryostat assembly. 1: earth field compensation coils (stationary); 2: magnet/cryostat assembly; 3: driving motor; 4: bearing(s); 5: shaft; 6: swivel joint(s); 7: slip ring; 8: supporting triple; 9: LHe transfer line; 10: He recovery line; 11: warm helium return; 12: compressor; 13: cold trap; 14: cryocooled-based mini liquefier.

PROBLEM 4.2: Cryocooler-based "mini" helium liquefier (continuation)

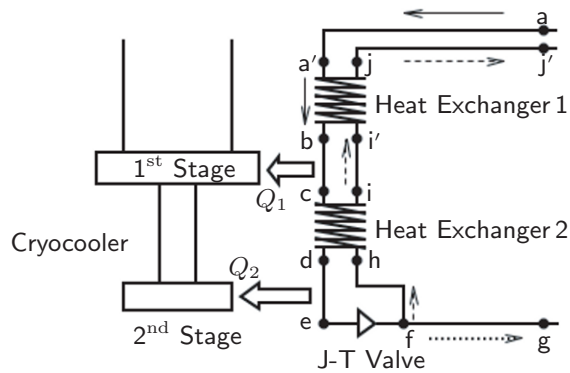

Fig. 4.13 Schematic drawing of a cryocooler-based mini helium liquefier.

Figure 4.13 shows schematic details of the mini liquefier, comprising the warm-to-cold stream (mass flow rate $\dot{m}_{he}$; pressure 10 atm) and cold-to-warm helium vapor stream ($\dot{m}_v$; 1 atm), and the 1st and 2nd stages of a cryocooler as cooling sources. The processes are assumed "ideal," e.g., no pressure drop; perfect heat exchange with no temperature difference between the two streams.

Warm-to-Cold Helium Stream—Indicated by solid arrows in Fig. 4.13

Point a. Mini Liquefier entrance, from Cold trap (13 in Fig. 4.12): $T_a = 295\,\text{K}$; $P_a = 10\,\text{atm}$ (1 MPa).

Point a′. Heat Exchanger 1 entrance: thermodynamically identical to Point a.

Point b. Heat Exchanger 1 exit (1st Stage entrance): T_b.

Point c. Heat Exchanger 2 entrance (1st Stage exit): T_c. Between Points b and c, the 1st Stage extracts Q_1 from the helium stream.

Point d. Heat Exchanger 2 exit (2nd Stage entrance): T_d.

Point e. 2nd Stage exit (J-T Valve entrance): T_e. Between Points d and e, the 2nd Stage extracts Q_2 from the helium stream.

Point f. J-T Valve exit: $T_f = 4.22\,\text{K}$; $P_f = 1\,\text{atm}$; $\dot{m}_v$; $\dot{m}_{\ell p}$ (liquefaction mass rate). LHe to Point g, indicated by the dotted arrow.

Cold-to-Warm Helium Stream—Indicated by dashed arrows in Fig. 4.13

Point g. To LHe transfer line (9 in Fig. 4.12): $T_g = 4.22\,\text{K}$; $P_g = 1\,\text{atm}$; $\dot{m}_\ell$.

Point h. Heat Exchanger 2 entrance: $T_h = 4.22\,\text{K}$; $P_h = 1\,\text{atm}$; $\dot{m}_v$ and $\dot{m}_{\ell r} = \dot{m}_{\ell p} - \dot{m}_\ell$ (LHe return mass rate).

Point i. Heat Exchanger 2 exit: $T_i = T_c$; $P_i = 1\,\text{atm}$.

Point i′. Heat Exchanger 1 entrance: thermodynamically identical to Point i.

Point j. Heat Exchanger 1 exit: $T_j = 295\,\text{K}$; $P_j = 1\,\text{atm}$.

Point j′. To warm helium exit line (10 in Fig. 4.12).

PROBLEM 4.2: Cryocooler-based "mini" helium liquefier (continuation)

a) Show that to achieve a helium liquefaction rate, $\dot{m}_{\ell p} \simeq 0.202\,\text{g/s}$ with $\dot{m}_{he} = 1.0\,\text{g/s}$ through the J-T process, $T_e = 7\,\text{K}$ (and $P_e = 10\,\text{atm}$) at Point e.

b) For $T_d = 8\,\text{K}$ (and $P_d = 10\,\text{atm}$), compute Q_2 (at 7 K), the 2nd stage refrigeration power of the cryocooler. Note that $T_e = 7\,\text{K}$ (and $P_e = 10\,\text{atm}$).

c) For a cryocooler with Q_2 (at 7 K), what would its Q_2 at 4.22 K be?

d) For $T_b = 46\,\text{K}$ and $T_c = 30\,\text{K}$ (and $P_b = P_c = 10\,\text{atm}$), compute Q_1 (at 30 K), the 1st stage refrigeration power.

e) Assuming that Heat Exchanger 2 is "ideal," i.e., no heat loss to its environment and the heat transfer between the warm-to-cold stream (of $\dot{m}_{he} = 1.0\,\text{g/s}$) and the cold-to-warm stream (of $\dot{m}_v$ and $\dot{m}_{\ell r}$) is perfect, show that $\dot{m}_{\ell r} = 0.158\,\text{g/s}$ and hence $\dot{m}_\ell = 0.044\,\text{g/s}$. Assume $T_c = T_d = 30\,\text{K}$.

f) Similarly, show that the perfect heat transfer in Heat Exchanger 1 between the two streams is consistent with $\dot{m}_{\ell r} = 0.158\,\text{g/s}$. Assume that $T_b = 46\,\text{K}$, $T_{i'} = 30\,\text{K}$, and $T_{a'} = T_j = 295\,\text{K}$.

g) Applying Eq. 4.10, compute the *isentropic* (constant entropy) power requirement, $\mathbb{P}_s$, of Compressor (12, Fig. 4.12) to boost the warm helium flow of $\dot{m}_{he} = 1.0\,\text{g/s}$ from $P_j = 1\,\text{atm}$ to $P_a = 10\,\text{atm}$.

Sir James Dewar (1842–1923)

— Passage from Isaac Asimov's *Asimov's Biographical Encyclopedia of Science and Technology* [4.27]

His interest (in the field of extremely low temperatures) *was kindled in the 1870s, when Cailletet and Pictet simultaneously and independently announced the liquefaction of gasses such as oxygen, nitrogen, and carbon monoxide and attained temperatures less than eighty degrees above the absolute zero.*

In 1892 he constructed double-walled flasks with a vacuum between the walls. The vacuum would not transmit heat by conduction or by the convection of air currents. It would do so only by radiation. By silvering the walls so that radiation heat would be reflected rather than absorbed, Dewar cut down on that variety of heat transmission as well. . . .Such flasks are called Dewar flasks and have been adapted to everyday uses, for keeping hot coffee hot during trips, for instance, or keeping cold milk cold (since heat transfer is barred in either direction). The home variety of the Dewar flask is better known as a Thermos bottle.

Dewar then began to experiment with hydrogen, which still resisted liquefaction. He made use of the Joule-Thomson effect (see ***DISCUSSION 4.6***)*, first discovered by Joule and Kelvin to produce low temperatures, as Cailletet and Pictet had done, but used the system of regeneration that Linde had introduced. He built a large-scale machine in which this process could be carried out more extensively and efficiently than ever before. . . .hydrogen was liquefied in 1898 and solidified in 1899. In this way Dewar reached a temperature of only fourteen degrees above absolute zero.*

At this temperature, all substances were reduced to a solid state, except for a new gas, helium, that had just been discovered (on earth) *by Ramsay and that, at that temperature, was not even liquefied. It resisted all efforts at liquefaction for another decade, when Kamerlingh-Onnes finally succeeded* (in 1908).

Solution to PROBLEM 4.2

a) Because in a J-T process, enthalpy remains constant, the following enthalpy equality relationship holds:

$$h_{he}(7\,\text{K},10\,\text{atm}) = x_\ell h_\ell(4.22\,\text{K},1\,\text{atm}) + (1-x_\ell)h_v(4.22\,\text{K},1\,\text{atm}) \qquad (S2.1)$$

where $h_{he}(7\,\text{K},10\,\text{atm}) = 26.00\,\text{J/g}$ is helium enthalpy at 7 K and 10 atm; x_ℓ is the liquid mass fraction at 4.22 K and 1 atm; $h_\ell(4.22\,\text{K},1\,\text{atm}) = 9.71\,\text{J/g}$ is liquid helium enthalpy at 4.22 K and 1 atm; and $h_v(4.22\,\text{K},1\,\text{atm}) = 30.13\,\text{J/g}$ is vapor helium enthalpy at 4.22 K and 1 atm. Solving Eq. $S2.1$, we find:

$$x_\ell = \frac{h_{he}(7\,\text{K},10\,\text{atm}) - h_v(4.22\,\text{K},1\,\text{atm})}{h_\ell(4.22\,\text{K},1\,\text{atm}) - h_v(4.22\,\text{K},1\,\text{atm})}$$

$$= \frac{(26.00\,\text{J/g} - 30.13\,\text{J/g})}{(9.71\,\text{J/g} - 30.13\,\text{J/g})} = 0.202 \qquad (S2.2)$$

With $x_\ell = 0.202$, $\dot{m}_{\ell p} = 0.202\,\text{g/s}$ and $\dot{m}_v = 0.798\,\text{g/s}$ for $\dot{m}_{he} = 1.0\,\text{g/s}$.

b) The following power equation applies between Points d and e:

$$\dot{m}_{he}h_{he}(8\,\text{K},10\,\text{atm}) = Q_2 + \dot{m}_{he}h_{he}(7\,\text{K},10\,\text{atm}) \qquad (S2.3)$$

Solving Eq. $S2.3$ for Q_2, we find:

$$Q_2 = \dot{m}_{he}[h_{he}(8\,\text{K},10\,\text{atm}) - h_{he}(7\,\text{K},10\,\text{atm})]$$

$$= (1\,\text{g/s})(33.44\,\text{J/g} - 26.00\,\text{J/g}) = 7.44\,\text{W}$$

c) The performance data of a 2-stage cryocooler shown in Fig. 4.6, indicate that this cryocooler with a refrigeration capacity of 1 W at 4.2 K delivers a cooling power of 4 W at 7 K. Thus a cryocooler with a capacity of 7.44 W at 7 K would most likely deliver a cooling power of ∼2 W at 4.2 K. Cryocoolers with a cooling power of ∼2 W at 4.22 K are expected to be commercially available by ∼2010.

d) An equation similar to Eq. $S2.3$ may be applied between Points b and c:

$$\dot{m}_{he}h_{he}(46\,\text{K},10\,\text{atm}) = Q_1 + \dot{m}_{he}h_{he}(30\,\text{K},10\,\text{atm}) \qquad (S2.4)$$

From Eq. $S2.4$ we find:

$$Q_1 = \dot{m}_{he}[h_{he}(46\,\text{K},10\,\text{atm}) - h_{he}(30\,\text{K},10\,\text{atm})]$$

$$= (1\,\text{g/s})(252\,\text{J/g} - 168\,\text{J/g}) \simeq 84\,\text{W}$$

The performance data of Fig. 4.6 indicate that $Q_1 \simeq 84\,\text{W}$ is not achievable with a cryocooler having the performance data of Fig. 4.6 even if its 4.22-K performance is increased to 2 W. A cryocooler with an enhanced 2nd stage refrigeration power will be required.

e) The total enthalpy decrease of the warm-to-cold stream from Points c to d must be equal to the total enthalpy increase of the cold-to-warm stream from Points h to i:

$$\dot{m}_{he}[h_{he}(30\,\text{K},10\,\text{atm}) - h_{he}(8\,\text{K},10\,\text{atm})]$$

$$= (\dot{m}_v + \dot{m}_{\ell r})h_v(30\,\text{K},1\,\text{atm}) - \left[\dot{m}_v h_v(4.22\,\text{K},1\,\text{atm}) + \dot{m}_{\ell r}h_l(4.22\,\text{K},1\,\text{atm})\right] \qquad (S2.5)$$

Solution to PROBLEM 4.2 (Continuation)

Solving Eq. $S2.5$ for $\dot{m}_{\ell r}$, we find:

$$\dot{m}_{\ell r} = \frac{\left\{\begin{matrix}\dot{m}_{he}[h_{he}(30\,\mathrm{K},10\,\mathrm{atm}) - h_{he}(8\,\mathrm{K},10\,\mathrm{atm})] \\ -\dot{m}_v[h_v(30\,\mathrm{K},1\,\mathrm{atm}) - h_v(4.22\,\mathrm{K},1\,\mathrm{atm})]\end{matrix}\right\}}{h_v(30\,\mathrm{K},1\,\mathrm{atm}) - h_l(4.22\,\mathrm{K},1\,\mathrm{atm})}$$

$$= \frac{(1\,\mathrm{g/s})(168.4\,\mathrm{J/g} - 33.44\,\mathrm{J/g}) - (0.798\,\mathrm{g/s})(170.2\,\mathrm{J/g} - 30.13\,\mathrm{J/g})}{(170.2\,\mathrm{J/g} - 9.71\,\mathrm{J/g})} \simeq 0.144\,\mathrm{g/s}$$

Because $\dot{m}_\ell = \dot{m}_{\ell p} - \dot{m}_{\ell r}$, we find: $\dot{m}_\ell \simeq 0.202\,\mathrm{g/s} - 0.144\,\mathrm{g/s} = 0.058\,\mathrm{g/s}$, which translates to a liquid volume rate of ∼1.7 liters/h and a cooling power of 1.2 W.

f) The thermal power loss of the warm-to-cold stream from Points a′ to b equals the thermal power increase of the cold-to-warm stream from Points i′ to j:

$$\dot{m}_{he}[h_{he}(295\,\mathrm{K},10\,\mathrm{atm}) - h_{he}(46\,\mathrm{K},10\,\mathrm{atm})]$$
$$= (\dot{m}_v + \dot{m}_{\ell r})\Big[h_v(295\,\mathrm{K},1\,\mathrm{atm}) - h_v(30\,\mathrm{K},1\,\mathrm{atm})\Big] \qquad (S2.6)$$

The left-hand side of Eq. $S2.6$ is given by:

$$\dot{m}_{he}[h_{he}(295\,\mathrm{K},10\,\mathrm{atm}) - h_{he}(46\,\mathrm{K},10\,\mathrm{atm})] = (1\,\mathrm{g/s})(1550.0\,\mathrm{J/g} - 253.9\,\mathrm{J/g})$$
$$\simeq 1296\,\mathrm{W} \qquad (S2.7a)$$

Similarly, the right-hand side of Eq. $S2.6$ is given by:

$$(\dot{m}_v + \dot{m}_{\ell r})[h_{he}(295\,\mathrm{K},1\,\mathrm{atm}) - h_{he}(30\,\mathrm{K},1\,\mathrm{atm})]$$
$$\simeq (0.798\,\mathrm{g/s} + 0.144\,\mathrm{g/s})(1547.0\,\mathrm{J/g} - 170.2\,\mathrm{J/g})$$
$$\simeq 1297\,\mathrm{W/s} \qquad (S2.7b)$$

Equations. $S2.7a$ and $S2.7b$ are equal, within round-off errors of ∼0.1 %.

g) Applying Eq. 4.10, we obtain an ideal compressor power requirement, $\mathbb{P}_s$:

$$\mathbb{P}_s = \dot{m}_h \left(\frac{\gamma}{\gamma - 1}\right)(P_j v_j)\left[\left(\frac{P_a}{P_j}\right)^{\frac{\gamma-1}{\gamma}} - 1\right] \qquad (S2.8)$$

$\gamma = C_p/C_v$ for a perfect gas is 5/3; v_i is the specific volume at the compressor inlet of $P_j = 1$ atm, which for helium at 295 K is $\simeq 6\,\mathrm{m^3/kg}$. With $P_j = 1\,\mathrm{atm} \simeq 1{\times}10^5$ Pa, $P_a/P_j = 10$, and $\dot{m}_h = 0.001\,\mathrm{kg/s}$ (1 g/s), we obtain: $\mathbb{P}_s = 2.3\,\mathrm{kW}$ (or ∼3 hp, horsepower). Note that this is for an ideal case; the power requirement for a real pump would be roughly 7 kW.

Of course in a *real* mini helium liquefier, the liquid yield, because chiefly of "imperfection" of the heat exchangers and pressure drops in both the warm-to-cold and cold-to-warm helium streams, would be smaller than that of an "ideal" liquefier: $\dot{m}_{\ell p}$ (and thus $\dot{m}_\ell$) will be off by a factor of perhaps as much as two, respectively, from 0.202 g/s (∼6 liters/h) and 0.058 g/s (∼1.7 liter/h) computed above.

DISCUSSION 4.7: Cryocooler vs. "Cryocirculator"

Two cooling sources for "dry" (cryogen-free) magnets are discussed here.

Cryocooler Currently, *all* dry (cryogen-free) magnets, LTS or HTS, are cryocooled, i.e., cooled by a cryocooler, whose coldhead is attached to one end of the cryostat assembly of the magnet. Figure 4.14 shows a schematic drawing of a cryocooled dry magnet: the 1st stage of the coldhead is thermally attached to the radiation shield and the 2nd stage to the magnet chamber. For "large" dry LTS magnets, it will be a challenge to satisfy the tenet of LTS magnet stability, i.e., $\Delta T_{op}/T_{op} \simeq 0$, where ΔT_{op} is the temperature difference between the coldest spot (near the 2nd stage) and the warmest spot (furthest from the 2nd stage).

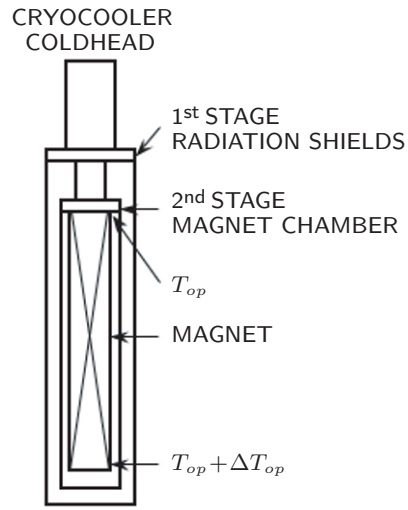

Fig. 4.14 Schematic drawing of a cryocooled dry magnet.

"Cryocirculator" To keep the magnet temperature uniform, $\Delta T_{op}/T_{op} \simeq 0$, a "cryocirculator" is preferable to a cryocooler for dry superconducting magnets. As illustrated schematically in Fig. 4.15, a cryocirculator is a 2-stage cryocooler equipped with a cold helium circulator for each stage. Each circulator forces a stream of cold, high-pressure helium through a cooling coil (sometimes embossed, as illustrated in Fig. 4.15) over the surface of a radiation shield wall or magnet chamber walls. The cryocirculator has two advantages over the cryocooler: 1) it provides cooling over most of the magnet chamber surface area, enabling a magnet, *regardless* of *its size*, to satisfy the condition of $\Delta T_{op}/T_{op} \simeq 0$, though for HTS magnets, ΔT_{op} may easily exceed 1 K; and 2) the cooling source and the magnet cryostat, connected by flexible helium lines, may easily be decoupled.

One early application of a cryocirculator is the Hybrid III magnet [3.14]. The radiation shields of its cryostat are maintained at their operating temperatures, one circulator keeping one set of embossed radiation shields at 90 K and the other circulator keeps another set—for the 1.8-K magnet cryostat—at 20 K.

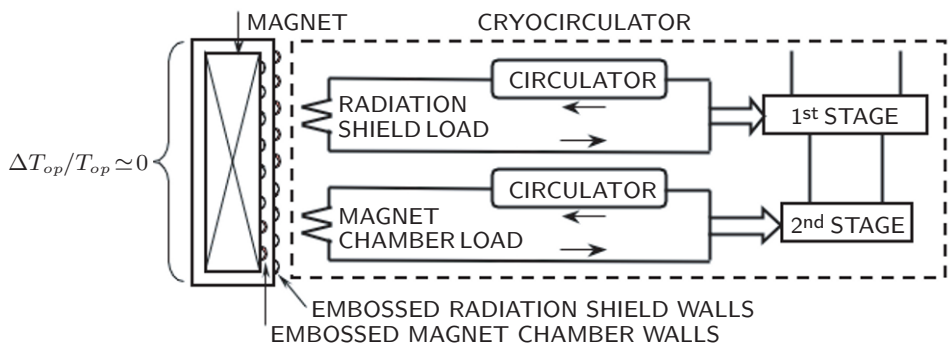

Fig. 4.15 Schematic drawing of a cryocirculator-cooled magnet.

DISCUSSION 4.8: Radiative Heat Transfer*

Here, we discuss heat input to a cryostat by radiation. The Hybrid III cryostat is used as an example. The theory of radiative heat transfer begins with the Stefan-Boltzmann equation:

$$q_r = \epsilon_r \sigma T^4 \tag{4.15}$$

q_r is the radiative heat flux [W/m^2] from a surface at temperature T [K]. ϵ_r is the total emissivity at T. σ is the Stefan-Boltzmann constant, 5.67×10^{-8} W/m^2 K^4. What makes computation of radiation heat input to a cryostat usually less straightforward than suggested by Eq. 4.15 is the task of determining the correct value of ϵ_r for each of the two surfaces that are radiating heat. For a configuration of parallel plates with emissivities of ϵ_{cl} and ϵ_{wm}, respectively, with one surface at cold temperature T_{cl} and the other at warm temperature T_{wm}, the effective total emissivity, ϵ_r, is given by:

$$\epsilon_r = \frac{\epsilon_{cl}\epsilon_{wm}}{\epsilon_{cl} + \epsilon_{wm} - \epsilon_{cl}\epsilon_{wm}} \tag{4.16}$$

Although theory distinguishes among "parallel-plate," "cylindrical," and "spherical" configurations, in most cryostat applications the parallel-plate equations suffice for all three geometries. (Nonparallel-plate configurations usually have surfaces of different areas.) This is because: 1) in most cryostats, the distance separating the two surfaces is generally much less than dimensions along the surface; and 2) the error that would be introduced in an estimate of radiative heat input through this geometric approximation is still likely to be considerably less than that introduced by uncertainties associated with the emissivities of the surfaces in question. Equation 4.15 is thus modified to:

$$q_r = \epsilon_r \sigma (T_{wm}^4 - T_{cl}^4) \tag{4.17}$$

Table 4.8 gives "typical" values of ϵ_r and q_r for combinations of materials and two temperature ranges, from T_{wm} to T_{cl}: $T_{wm} \rightarrow T_{cl}$.

Illustration Here we first compute the total heat input to the Hybrid III magnet vessel at 4.2 K by radiation from the 20-K and 80-K shields. The magnet vessel surface areas, both of mechanically polished stainless steel, are: 1) 7.3 m^2 facing the 20-K radiation shields; 2) 2.8 m^2 facing the 80-K radiation shields.

To simplify the computation, we apply the parallel-plate model of Eq. 4.17 and use the same cold-temperature surface areas for respective warm-temperature areas. Using appropriate values of q_r given in Table 4.8 for the mechanically polished stainless steel surface, we have:

20-K panels to vessel: $Q_r \simeq (0.4\times10^{-3}\,\mathrm{W/m^2})(7.3\,\mathrm{m^2}) \simeq 3\,\mathrm{mW}$

80-K panels to vessel: $Q_r \simeq (162\times10^{-3}\,\mathrm{W/m^2})(2.8\,\mathrm{m^2}) = 454\,\mathrm{mW}$

---

* Based on **Problem 4.8** in the 1st Edition (Plenum, 1994).

DISCUSSION 4.8: Radiative Heat Transfer (continuation)

Table 4.8: Typical Values of Radiative Heat Flux [4.28]

Material	$T_{wm} \rightarrow T_{cl}$ [K]	ϵ_r	q_r [mW/m^2]
Copper			
as received	20 → 4	0.03	0.3
	80 → 4	0.06	140
	300 → 80	0.12	55,000
mechanically	20 → 4	0.01	0.1
polished	80 → 4	0.02	46
	300 → 80	0.06	27,000
Stainless steel			
as received	20 → 4	0.06	0.54
	80 → 4	0.12	280
	300 → 80	0.34	155,000
mechanically	20 → 4	0.04	0.4
polished	80 → 4	0.07	162
	300 → 80	0.12	55,000
electropolished	20 → 4	0.03	0.3
	80 → 4	0.06	140
	300 → 80	0.10	46,000
Aluminum			
as received	20 → 4	0.04	0.4
	80 → 4	0.07	162
	300 → 80	0.49	224,000
mechanically	20 → 4	0.03	0.3
polished	80 → 4	0.06	140
	300 → 80	0.10	46,000
electropolished	20 → 4	0.02	0.2
	80 → 4	0.03	70
	300 → 80	0.08	37,000
Superinsulation	20 → 4	≤ 10*	2†‡
	80 → 20	40*	40†
	300 → 80	60*	2,500†

* Number of layers in a 25-mm "vacuum" gap.

† Measured values (Bascuñán [4.19]).

‡ In the 4–20 K range, layers of superinsulation are not effective—in comparison, see $q_r = 0.2\,\mathrm{mW/m^2}$ for electropolished aluminum listed 3 lines above. A 250-Å thick aluminum coating on each side of superinsulation is too thin compared with the wave lengths of radiation in the 4–20 K range for superinsulation layers to be effective. Instead, one layer of aluminum foil, ∼100-μm thick, may be used to emulate an electropolished aluminum surface.

Answer to TRIVIA 4.2 The French chemist Georges Claude (1870–1960) showed that electric discharge through inert gases could produce light, the start of neon lights, making him rich; now more well-known as the developer of an eponymous refrigeration cycle.

DISCUSSION 4.8: Radiative Heat Transfer (continuation)

We may also compute the heat input to the 80-K radiation shield facing the 300-K surface; the total area of the 80-K panels facing the 300-K surface is $11.7\,\mathrm{m}^2$. Again, we assume the parallel-plate geometry, i.e., the total 300-K surface facing the 80-K panels is also $11.7\,\mathrm{m}^2$.

Using appropriate values of q_r given in Table 4.8 for the mechanically polished stainless steel surface, we have:

300-K to 80-K panels: $Q_r \simeq (55\,\mathrm{W/m}^2)(11.7\,\mathrm{m}^2) = 644\,\mathrm{W}$

A. Effect of Superinsulation Layers

As may be noted from Table 4.8, the largest radiative heat load to a cryostat is from the 80-K shield, which receives heat from the 300-K surface. Thus, it is customary to place a number of 0.5-μm aluminum coated Mylar sheets—superinsulation—in the vacuum space ($< 10^{-4}\,\mathrm{torr}$) between the 80-K and 300-K surfaces. The presence of N_i superinsulation layers modifies Eq. 4.17 roughly to:

$$q_r = \frac{\epsilon_r}{N_i + 1}\sigma(T_{wm}^4 - T_{cl}^4) \tag{4.18}$$

Equation 4.18 indicates that even one superinsulation layer reduces q_r by a factor of two. A rule of thumb is to use about 10–20 layers for each 1-cm spacing. Also, to minimize solid conduction paths, each superinsulation sheet should be installed either crinkled or, if smooth, with thin insulating spacers between adjacent layers of superinsulation. (The bottom three rows of Table 4.8 give *measured* values of q_r for layers of superinsulation in the three temperature ranges.)

B. Practical Considerations of Emissivity

It is important to note that radiation is an electromagnetic phenomenon: emissivity ϵ_r increases with "surface" electrical resistivity of the material. The material's emissivity is thus affected in the same way as the material's surface electrical resistivity. Thus, we may list the following rules of thumb on emissivity:

- For the same temperature range, ϵ_r values of copper are smaller than those of aluminum, which in turn are smaller than those of stainless steel.
- For the same surface, ϵ_r decreases with temperature; ϵ_r for copper decreases more markedly than for stainless steel.
- ϵ_r of metal is more sensitive to surface contamination than that of nonconductive material. Contamination includes oxidation and alloying.
- Mechanical polishing sometimes improves (decreases) ϵ_r and sometimes degrades (increases) ϵ_r. If an oxide layer on a conductive metal's surface is removed by mechanical polishing, the result is an improvement. If the metal's resistivity is increased by work-hardening, the result is degradation.

"We may not arrive at our port within a calculable period, but we would preserve the true course." —Henry D. Thoreau

*DISCUSSION 4.9: Convective Heat Transfer by Residual Gas**

Residual gas transfers heat within the "vacuum" space of a cryostat. In cryostats for LTS magnets, the only residual gas is helium. In cryostats for HTS magnets operating above 20 K, hydrogen, outgassed from the surfaces of the structural components of the cryostats, metals and nonmetals, is the chief residual gas.

A. "High" Pressure Limit

When the pressure of a gas is sufficiently high, its mean free path (λ_g) is much shorter than the typical distance (d) separating the two surfaces at different temperatures in a cryostat. Under this condition of $\lambda_g \ll d$, the thermal conductivity of a gas (k_g), according to the kinetic theory, is proportional only to the mean velocity ($\bar{v}$) of the molecules, which in turn varies as $\sqrt{T}$. The important point here is that when $\lambda_g \ll d$, k_g is independent of gas pressure, P_g.

The kinetic theory also shows that $\lambda_g \propto \eta/P_g$, where η is the gas viscosity. At $T = 300$ K and $P_g = 760$ torr (1 atm), $\lambda_g \simeq 0.2\,\mu$m for helium and $\simeq 0.1\,\mu$m for hydrogen. Thus, the condition $\lambda_g \ll d$ is clearly satisfied in this "high" pressure limit. At a "vacuum" pressure of $P_g <\sim 10^{-4}$ torr, however, the condition $\lambda_g \ll d$ is violated by both gases.

B. "Low" Pressure Limit

At P_g of $\sim 10^{-4}$ torr or less, k_g becomes directly proportional to P_g. For a parallel-plate configuration of a cold plate at T_{cl} and a warm plate at T_{wm}, the heat flux, q_g, by a "residual" gas at pressure P_g may be given by [4.29]:

$$q_g = \eta_g P_g (T_{wm} - T_{cl}) \tag{4.19}$$

η_g depends not only on T_{wm} and T_{cl} but also on accommodation coefficients, which range from 0.3 for He and H_2 at 300 K to 1 for He at 4.2 K and 0.6 for H_2 at 20 K. Table 4.9 presents values of η_g and q_g for He and H_2 at $P_g = 10^{-5}$ torr (1.33 mPa) across two parallel plates at T_{cl} and T_{wm} [4.29].

Illustration The principal surface areas, approximated at 4.2 K (T_{cl}), of the magnet vessel of Hybrid III are 7.3 m^2 facing the 20-K (T_{wm}) radiation shields, and 2.8 m^2 facing the 80-K (T_{wm}) radiation shields. Using the "parallel-plates" approximation, we may compute the total heat input into the Hybrid III magnet vessel by residual helium gas of pressure 10^{-5} torr in the vacuum space.

For a magnet vessel surface at 4.2 K exposed to 20-K radiation shields, q_g at $P_g = 10^{-5}$ torr is, from Table 4.9, 27 mW/m^2. Thus, for a surface area of 7.3 m^2 under the parallel-plates approximation, the total heat input becomes $\approx$300 mW. Similarly, for a magnet vessel surface at 4.2 K exposed to 80-K radiation shields, q_g is, from Table 4.9, 86 mW/m^2, or a total heat input of $\approx$240 mW for a surface area of 2.8 m^2. Thus the combined heat input to the magnet vessel becomes $\approx$540 mW, which for this system would be excessive; a vacuum level of 10^{-6} torr should be maintained. It is therefore important to keep the cryostat vacuum pressure to better (i.e., less) than $\sim 10^{-5}$ torr.

---

* Based on **Problem 4.7** in the 1st Edition (Plenum, 1994).

DISCUSSION 4.9: Convective Heat Transfer by Residual Gas (continuation)

Table 4.9: Heat Conduction by
Residual He and H_2 Gases at P_g of 10^{-5} Torr [4.29]

Helium			*Hydrogen*		
$T_{wm} \rightarrow T_{cl}$ [K]	η_g [W/m^2 Pa K]	q_g [mW/m^2]	$T_{wm} \rightarrow T_{cl}$ [K]	η_g [W/m^2 Pa K]	q_g [mW/m^2]
$20 \rightarrow 4$	1.27	27	—	—	—
$80 \rightarrow 4.2$	0.85	86	$80 \rightarrow 20$	2.20	176
$300 \rightarrow 4.2$	0.64	251	$300 \rightarrow 20$	1.32	494
$300 \rightarrow 80$	0.44	129	$300 \rightarrow 80$	1.02	298

DISCUSSION 4.10: Vacuum Pumping System

Figure 4.16 shows a schematic diagram of a typical vacuum system used in the operation of a superconducting magnet. The cryostat vacuum space outlet is connected to a turbomolecular pump, which in the past decade has begun replacing the once widely used diffusion pump/cold trap combination. The turbomolecular pump is the only purely mechanical vacuum pump that can function down to a pressure range of 10^{-10} torr without requiring a trap. Although the "turbo" pump is equipped with its own mechanical pump, in most magnet applications where the cryostat vacuum space can be quite large, a separate mechanical pump is added, as shown in the figure. The procedure used to evacuate the cryostat vacuum space is to start with the mechanical pumps(s) to reach a vacuum of ∼5 torr, and then to turn on the turbo pump (or a diffusion/cold trap), to reach 10^{-5}–10^{-6} torr.

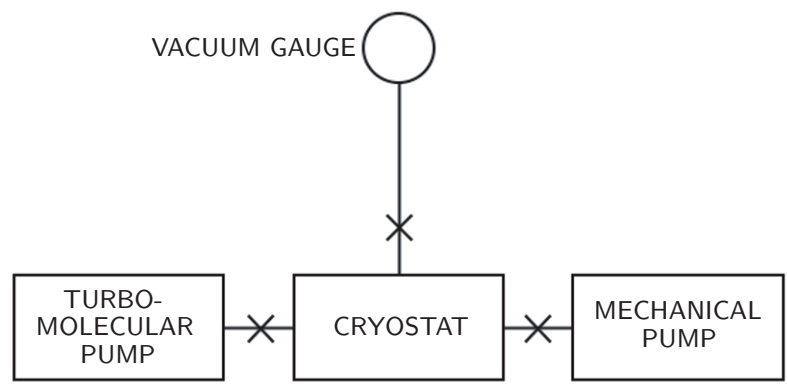

Fig. 4.16 Schematic diagram of a typical pumping vacuum system used in the operation of a superconducting magnet.

DISCUSSION 4.10: Vacuum Pumping System (continuation)

Vacuum Gauges

Two types of vacuum gauges are commonly used for cryostats: 1) thermocouple; and 2) ionization. Below is a brief description of each type.

Thermocouple: The thermocouple gauge relies on the pressure dependance of the gas thermal conductivity, valid in the "low" pressure limit discussed above. The thermocouple junction is situated in a tube connected to the vacuum space to be measured, and its temperature is set by a heater. The gas provides cooling, which varies with the gas pressure; the change in the induced current through the junction circuit is a measure of the vacuum pressure. The gauge's range of applicability is 10^{-3}∼1 torr, the range covered by mechanical pumps.

Ionization: For the vacuum range between $\sim 10^{-6}$ and $\sim 10^{-3}$ torr, the operating range in most cryostats, the ionization gauge is used most widely. There are two versions: 1) hot-cathode; and 2) cold-cathode.

Hot-Cathode: This gauge consists of a heated filament (hot cathode), an anode, and a negatively biased ion collector plate, all housed in a tube that connects to the vacuum space to be measured. The electrons flowing from the filament to the anode collide with gas molecules, creating ionized molecules that are drawn to the collector plate and measured as a current through the measurement circuit. Because the molecules are ionized by electrons, the ion current depends also on the number of electrons bombarding the molecules: accurate pressure measurement thus requires careful control of filament current. The hot-cathode gauge used in the Hybrid III cryostat is turned off during magnet operation to minimize "filament fatigue" caused by the filament's oscillating motion that results from the Lorentz interaction of the filament supply current (60 Hz) and the magnet's fringing field.

Cold-Cathode: Known as the Philips (or Penning) gauge, it uses a cold cathode and two parallel anode plates with a magnetic field applied in the direction normal to the anode plates, which are turned on (∼2 kV) one at a time. The small number of electrons produced by the cold cathode are thus made to travel in a helical path alternately toward one of the two plates. This configuration effectively increases the collision chances between the small number of electrons and gas molecules. Unlike hot filaments, cold cathodes do not contaminate the gas nor are they destroyed in the event of a loss of vacuum, but they are less accurate than hot-cathodes.

TRIVIA 4.3 Of the four contemporary physicists (born 1602–1627) below, who first achieved, in 1650, a vacuum by means of an air pump?

i) Boyle; ii) Guericke; iii) Pascal; iv) Torricelli.

DISCUSSION 4.11: Cryocooled Solid Cryogen/Magnet

A. Design and Operation Concept

Generally, a superconducting magnet, LTS or HTS, remains fully superconducting and operates "stably" over a temperature range from its nominal operating temperature T_{op} to a maximum operating temperature. Chiefly because of a much greater critical temperature, T_c, of HTS compared with that of LTS, this range, ΔT_{op}, is an order of magnitude greater for an HTS magnet than an LTS magnet of comparable size and field performance: typically $\Delta T_{op} > 1\,\mathrm{K}$ for HTS, while $\Delta T_{op} < 1\,\mathrm{K}$ for LTS. (This concept of "temperature margin" for LTS and HTS magnets is discussed in ***CHAPTER 6***.)

A design/operation concept developed at FBML recognizes this large ΔT_{op} of HTS magnets and combines it with the large heat capacity of solid cryogen [4.30–4.32]. In this design/operation concept, ΔT_{op} is no longer considered a transitory excursion permitted in LTS magnets, but a *new opportunity* for a magnet.

This combination of an expanded operating range, possible primarily with HTS but not altogether impossible with LTS, and an enhanced heat capacity offers operating options, an example of which is described below, that are infeasible with "conventional" design/operation concepts, i.e., "dry," cryocooled but without solid cryogen, or "wet," immersed in a bath of cryogen or force-cooled by cryogen. Note that even for a solid cryogen-cooled magnet, the primary cooling source is a cryocooler or a cryocirculator (***DISCUSSION 4.7***). Typically, such a magnet is surrounded by a volume of solid cryogen and housed in a magnet chamber.

Application to Persistent-Mode Magnets

One application of this design/operation concept is in constant-field magnets such as for NMR and MRI that normally operate in persistent mode. With the magnet's operating temperature designed to span a "large" range, this concept enables such a magnet to maintain a constant operating field over a design-specified period of time even after its primary cooling source is turned off and thermally decoupled from the cold body. The cooling source may be turned off intentionally, e.g., to create a measurement environment free of the cooling source vibration or for cooling source maintenance, or under fault mode, e.g., a power outage.

B. Thermal Diffusion in Solid

In a homogeneous isotropic solid (density, ϱ, thermal conductivity, k, and specific heat, c_p) the rate of thermal diffusion through the solid is characterized by its thermal diffusivity, D_{th} [$\mathrm{m^2/s}$], given by:

$$D_{th} = \frac{k}{\varrho c_p} \tag{4.20}$$

The time scale required for transient heating applied at one location to "reach" a distance δ_{sd} in the solid thus is given by:

$$\tau_{sd} = \frac{1}{D_{th}} \left(\frac{\delta_{sd}}{\pi} \right)^2 \tag{4.21}$$

DISCUSSION 4.11: Cryocooled Solid Cryogen/Magnet (continuation)

Table 4.10: Approximate Values of D_{th} and τ_{sd} (for $\delta_{sd}=10\,\text{mm}$) Solid Neon (SNe), Solid Nitrogen (SN_2), Copper (Cu) in the 4–60 K Range

	D_{th} [mm^2/s]			τ_{sd} [s] for $\delta_{sd}=10\,\text{mm}$		
T [K]	*SNe*	SN_2	*Cu*	*SNe*	SN_2	*Cu*
5	35	157	0.36×10^{6}	0.29	0.06	27×10^{-6}
10	22	70	0.17×10^{6}	0.46	0.14	60×10^{-6}
20	0.27	0.58	0.29×10^{5}	38	17	0.3×10^{-3}
30	—	0.22	8000	—	46	1.3×10^{-3}
34*	—	0.16	5000	—	63	2×10^{-3}
37*	—	0.18	3500	—	56	3×10^{-3}
40	—	0.17	2800	—	60	4×10^{-3}
50	—	0.13	1200	—	78	8×10^{-3}
60	—	0.12	600	—	84	17×10^{-3}

* At 35.61 K, as described in **4.5**, SN_2 undergoes a solid-to-solid phase transition and $D_{th}=0$, because at this temperature the SN_2's heat capacity approaches infinity.

Table 4.10 lists *approximate* values of D_{th} and corresponding τ_{sd} for $\delta_{sd}=10\,\text{mm}$ for solid neon (SNe), solid nitrogen (SN_2), and copper (Cu) in the range 4–60 K, based on $\varrho(T)$, $c_p(T)$, and $k(T)$ data [4.33–4.35]. Over this temperature range thermal diffusivities of SN_2 are 3 to 5 orders of magnitude less than those of copper—heat penetrates into SN_2 much more slowly than into copper. For example, at 30 K, as given in Table 4.10 for $\delta_{sd}=10\,\text{mm}$, $\tau_{sd}=46\,\text{s}$ in SN_2, whereas it is only 1.3 ms for Cu. However, SN_2 can absorb much more heat per unit volume than Cu.

"Slow" Heating

If the heat required to be absorbed by a volume of solid cryogen of a "reasonable" thermal diffusion distance can be absorbed gradually, over a period of time much longer than τ_{sd}, the entire solid will remain nearly uniform in temperature. Indeed, as noted above, solid cryogen appears best applied to magnets that are generally operated in persistent mode such as those for MRI and NMR. As studied in **PROBLEM 4.3** below, in a solid-cryogen-cooled magnet which has a heating time of hours over a diffusion distance of 1–2 cm, the entire solid-nitrogen volume may be assumed to be at a uniform temperature.

Transient Heating

Under rapid transient conditions only a very thin layer of solid cryogen—note that $\delta_{sd} \propto \sqrt{\tau_{sd}}$ (from Eq. 4.21)—is effective in absorbing heat that would otherwise heat the magnet winding. Even with this limitation, and despite the probable occurrence of "thermal dry-out" (below), SN_2 has proven effective in suppressing temperature rises in HTS test samples subjected to transient heating [4.36, 4.37].

Recently, a group in Kyoto University has shown that a phenomenon they term "thermal dry-out" occurs, creating a "large" temperature gap across the contact between the transiently heated surface and solid nitrogen [4.38–4.40]. Thermal dry-out and a solution to overcome this phenomenon are discussed below.

DISCUSSION 4.12: Cryocooled Solid Cryogen/Magnet (continuation)

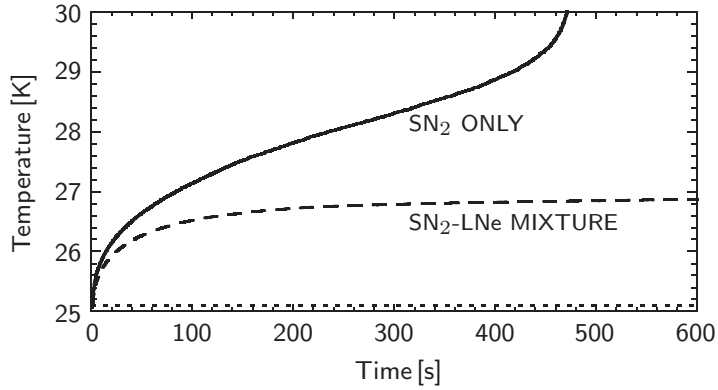

Fig. 4.17 Temperature vs. time plots of an HTS strip under over-current disturbances. Solid curve: with the HTS strip cooled by SN_2 only; dashed: with the strip cooled by an SN_2-LNe mixture; dotted: initial temperature at 25.1 K [4.38–4.40].

C. "Thermal Dry-Out"

Nakamura and his colleagues in Kyoto University have experimentally demonstrated that when the surface in thermal contact with SN_2 is subjected to a "large" heating flux, thermal dry-out occurs [4.38–4.40]. For solid nitrogen at 60 K, for example, a thermal dry-out begins at a power flux of $\sim$1.5 W/cm^2. Apparently, a thin vapor layer at the interface is responsible for this temperature discontinuity.

Figure 4.17 shows temperature vs. time plots for an HTS strip under over-current disturbances, each disturbance lasting up to $\sim$600 s. The solid curve corresponds to a typical run for the strip in contact with solid nitrogen only. The dotted horizontal line, at 25.1 K, indicates the initial temperature of both the strip and solid nitrogen. Beyond $\sim$400 s, at which the heat flux is 14.3 W/cm^2 with a temperature difference (ΔT) in excess of 3 K, a thermal runaway occurs that, were the over-current to persist, would lead to conductor damage.

Solid Nitrogen-Liquid Neon Mixture To Suppress Thermal Dry-Out

The Kyoto group has demonstrated that a mixture of solid nitrogen and liquid neon—liquid neon occupying $\sim$1% of the total volume—is quite effective in suppressing this thermal dry-out. Of course the use of LNe restricts operation to a narrow range, between 24.5 and 27.1 K under atmospheric pressure. The dashed curve in Fig. 4.17 corresponds to a typical run for the strip in contact with an SN_2-LNe mixture. Even after repeated over-current runs, it was observed that the strip temperature remained at 26.9 K, anchored by LNe. Note that here $\Delta T < 2$ K; more importantly, at least for up to 600 s, there appears to be no imminent thermal runaway. (Note that in both sets of measurements, the "cold body" was continuously cooled by a cryocooler, which acted as the system's cold sink.)

For applications in the liquid nitrogen temperature range, perhaps a mixture of solid argon (SAr) and subcooled liquid nitrogen operating in the range 65–77 K may be an effective option to improve the solid cryogen's inherently poor thermal contact characteristics. Argon melts at 83.8 K and boils at 87.3 K.

PROBLEM 4.3: Solid cryogen cooled magnet

Here, we deal with issues on solid cryogen cooled magnets.

a) Using C_p vs. T plots shown in Fig. 4.2, make $T(t)$ plots of volumes, each 1 liter, of Cu, Pb, SNe, and SN_2, under 1-W heat input for an initial temperature of 4 K and a final temperature of 60 K, except for SNe, 25 K. Assume uniformity of temperature within each volume during the warm-up.

b) Using the $T(t)$ plot for SN_2 of **a)**—or straight from Fig. 4.2—show that it takes ∼30 hours for a 15-liter volume of SN_2 to warm up from 10 K to 15 K under a constant heat input of 0.25 W. Neglect heat capacities of other materials, including that of the magnet, in the cold body and assume temperature uniformity within the solid nitrogen during the warm-up.

As discussed in ***DISCUSSION 4.11***, it is desirable for a solid cryogen cooled magnet to be able to operate over a temperature range considerably greater than the ∼1 K (or even less) typical for LTS magnets. In an SN_2-cooled HTS magnet operating in persistent mode, for example, a typical operating mode might be to operate at a nominal temperature of 10 K with its cooling source running. When the cooling source is shut off, either purposely to eliminate its noise or accidentally by a power outage, and it is thermally decoupled from the cold body, the magnet will start warming up slowly, keeping its operating field over a temperature rise of ΔT_{op}, which is 5 K for this particular magnet. Note that in order to take full advantage of this large heat capacity of solid cryogen available in the cold body, it is required to design the system to have the cold body automatically decoupled thermally from the cooling source whenever it is turned off.

c) This 15-liter volume of solid nitrogen is to be placed inside the cold body to encircle a magnet of 896-mm winding o.d. (860-mm i.d.) and 300-mm winding length. Let the nitrogen be in the shape of a cylinder, ≈896-mm i.d., 300-mm long, and Δr_{N2} thick. (Because the cold body is constructed of copper sheets of sufficient thickness, most heat entering the cold body from the i.d. side of the magnet flows through the walls of the cold body by conduction to the outer wall.) Compute Δr_{N2} for this 15-liter SN_2 and, assuming that heat entering the cold body flows through the solid nitrogen layer only in the radial direction from the outer wall of the cold body, show that the thermal diffusion time corresponding to this layer thickness is ∼0.6 s, which is much smaller than the 30-h warm-up time from 10 K to 15 K.

d) Show that the 15-liter volume of cryogen in the cold body filled with solid nitrogen in **b)** may be *halved* if it is filled with solid neon. (Because the volumetric price of SN_2 is at least ∼200 times less than that of SNe, nitrogen is preferred to neon unless neon is absolutely necessary.)

e) Show that it takes this 15-liter SN_2 another ∼80 hours to warm up from 15 K to 60 K. Over the 15–60 K temperature range, take an average heat input to the cold body of 3.3 W. Neglect the magnetic energy stored in the magnet that would presumably be converted into thermal energy when the magnet becomes warm enough to lose its superconductivity.

PROBLEM 4.3: Solid cryogen cooled magnet (continuation)

f) During this warm-up process beyond 15 K, when the highest field part of the winding reaches, say 20 K, the magnet begins losing superconductivity and its field decays. For this magnet with a winding volume of 15,000 cm^3 and a stored energy of 75 kJ, compute its final temperature for an initial temperature of 20 K, assuming that during this transient the entire magnetic energy is converted to heat within the winding only. Assume that the winding is at a uniform temperature at the end of energy conversion and its enthalpy may be approximated by copper's. Note that because a total thermal energy of ∼1 MJ is absorbed by the solid nitrogen from 15 K to 60 K, it is reasonable to neglect the additional thermal energy of 75 kJ in **e)** above.

Although the magnet is at uniform temperature except during the brief period of field decay and shortly thereafter, because the field within the winding is not uniform, quenching is not initiated simultaneously within the winding. Nevertheless, the field decay is expected to last only a few seconds—this is based on a quench analysis of a real HTS magnet.

g) Show that it takes the same HTS magnet system ∼3 hours from an initial operating temperature of 30 K to a final temperature of 35 K for a constant heat input of 10 W. Assume the other assumptions in **b)** are valid.

h) Repeat **g**) for the range 35–40 K for the same constant heat input of 10 W, and demonstrate that the extra enthalpy of the phase transition at 35.61 K doubles the warm-up time over the same temperature increment of 5 K.

Solid nitrogen may also be used to *stabilize* an HTS winding subjected to *transitory* disturbances. Experiments have demonstrated that a thin layer (∼0.5 mm) of SN_2 in contact with a Bi2223 tape indeed suppressed the conductor's temperature rise when it was driven to the normal state by an over-current pulse imposed upon a constant transport current [4.36, 4.37]. It is because of the poor thermal diffusivity of solid nitrogen that only a thin layer (∼0.5 mm) is effective in absorbing transient power dissipation.

i) Using Eq. 4.21 given in ***DISCUSSION 4.11***, show that a transient heating of constant amplitude (square wave) and ∼0.1-s duration diffuses through a 0.4-mm thick layer of SN_2, initially at 30 K, over this heating period. Although the solid nitrogen layer temperature rises during heating, use a constant value of $D_{th} = 2.4 \times 10^{-3}$ cm^2/s at 30 K ($D_{th} = 0.24$ mm^2/s in Table 4.10).

j) For this 0.1-s transient heating of **i)**, show that a power flux of 4.2 W/cm^2 could be absorbed by this SN_2 layer as it is heated to 35 K.

k) Discuss the effectiveness of a thin layer of solid nitrogen subjected to transient heating when the heated layer must pass through the solid-to-solid phase transition at 35.61 K. As footnoted in Table 4.10, D_{th} of solid nitrogen at 35.61 K is theoretically 0.

l) Discuss to what extent the expansion of a magnet may impact the spatial field homogeneity as the magnet warms up over its permitted operating temperature range, here between 10 K and 15 K.

Solution to PROBLEM 4.4

a) Figure 4.18 shows $T(t)$ plots of 1-liter volumes of Cu, Pb, SNe, and SN_2, subjected to a constant heat input of 1 W with an initial temperature of 4.2 K and a final temperature of 60 K (25 K for SNe)—it also includes a dotted horizontal line at 4.2 K showing the duration required to boil off 1 liter of 4.2-K liquid helium (LHe). The figure clearly demonstrates that among these substances, at least on a *volume basis* SNe in the range 4–25 K and SN_2 in the range 25–60 K are the best heat capacity enhancers. Because specific densities of SNe (1.25 g/cm^3 at 25 K) and SN_2 (1 g/cm^3 at 25 K) are an order of magnitude less than those of Pb (11.4 g/cm^3) and Cu (8.96 g/cm^3), for the same extra volume in the cold body occupied by a heat capacity enhancer substance, either of these solid cryogens not only performs its task well but also is only a modest extra mass to the system.

Because the entire warm-up (4.2 K–60 K) takes, for example, ∼18 hours for SN_2, we may safely conclude that the assumption of uniform temperature throughout the 1-liter volume of solid with a diffusion distance of ∼10 cm—$(1000\,\text{cm}^3)^{1/3}$—is valid. The uniform temperature assumption is clearly valid for copper and lead.

b) From Fig. 4.18 we note that for 1-liter SN_2, $T(t \simeq 400\,\text{s}) = 10\,\text{K}$ and $T(t \simeq 2{,}150\,\text{s}) = 15\,\text{K}$. For 1-liter SN_2, we have the warm-up period from 10 K to 15 K with 1-W heat input: $[\Delta t(10\,\text{K} \to 15\,\text{K})]^{1\,\text{W}}_{1\,\text{liter}} \simeq 1{,}750\,\text{s} = 0.486\,\text{h}$. For 15-liter solid nitrogen with 0.25-W heat input, the 10-15 K warm-up period, $[\Delta t(10\,\text{K} \to 15\,\text{K})]^{0.25\,\text{W}}_{15\,\text{liter}}$, is given by:

$$[\Delta t(10\,\text{K}\to 15\,\text{K})]^{0.25\,\text{W}}_{15\,\text{liter}} = \left(\frac{1\,\text{W}}{0.25\,\text{W}}\right)\left(\frac{15\,\text{liter}}{1\,\text{liter}}\right)[\Delta t(10\,\text{K}\to 15\,\text{K})]^{1\,\text{W}}_{1\,\text{liter}}$$
$$\simeq (4)(15)(0.486\,\text{h}) = 29\,\text{h} \sim 30\,\text{h}$$

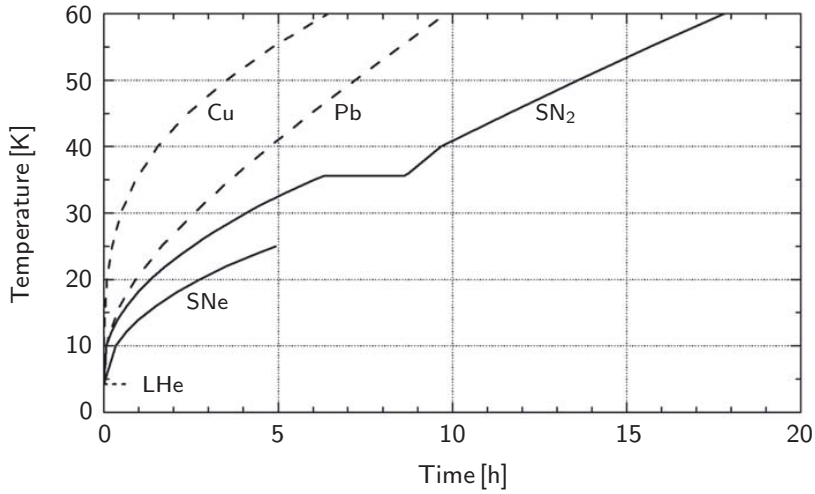

Fig. 4.18 $T(t)$ plots with an initial temperature of 4.2 K and a final temperature of 60 K (25 K, SNe) for a 1-liter volume each of Cu, Pb, SNe, and SN_2 subjected to a constant heat input of 1 W. The duration required to boil off 1 liter of liquid helium (LHe), ∼0.7 h, is indicated by the dotted horizontal line at 4.2 K.

Solution to PROBLEM 4.3 (continuation)

Alternatively, we may directly use Fig. 4.2 and compute $h(15\,\mathrm{K})-h(10\,\mathrm{K})\,[\mathrm{J/cm^3}]$ by performing the $\int C_p(T)\,dT$ for SN_2 between 10 K and 15 K:

$$\begin{aligned} h(15\,\mathrm{K})-h(10\,\mathrm{K}) &\simeq \frac{C_p(10\,\mathrm{K})+C_p(15\,\mathrm{K})}{2}(15\,\mathrm{K}-10\,\mathrm{K}) \\ &\simeq \frac{(0.175\,\mathrm{J/cm^3\,K}+0.475\,\mathrm{J/cm^3\,K})}{2}\,(5\,\mathrm{K}) \\ &\simeq 1.625\,\mathrm{J/cm^3} \end{aligned}$$

Thus the 10–15 K warm-up time for 15-liter solid nitrogen with 0.25-W heat input, $[\Delta t(10\,\mathrm{K}\rightarrow 15\,\mathrm{K})]^{0.25\,\mathrm{W}}_{15\,\mathrm{liter}}$ may be given by:

$$[\Delta t(10\,\mathrm{K}\rightarrow 15\,\mathrm{K})]^{0.25\,\mathrm{W}}_{15\,\mathrm{liter}} = \frac{(15000\,\mathrm{cm^3})(1.625\,\mathrm{J/cm^3})}{(0.25\,\mathrm{W})(3600\,\mathrm{s/h})} \simeq 27.1\,\mathrm{h} \sim 30\,\mathrm{h}$$

c) The volume of solid nitrogen, $\mathcal{V}_{N2}$, in a cylinder of i.d. D, length ℓ, and layer thickness $\Delta r_{N2} \ll D$, is:

$$\mathcal{V}_{N2} = \pi D \ell \Delta r_{N2} \qquad (S3.1)$$

With $\mathcal{V}_{N2}=15000\,\mathrm{cm^3}$, $D=90\,\mathrm{cm}$, $\ell = 30\,\mathrm{cm}$ inserted in Eq. $S3.1$, we have:

$$\Delta r_{N2} = \frac{\mathcal{V}_{N2}}{\pi D \ell} = \frac{(15000\,\mathrm{cm^3})}{\pi(90\,\mathrm{cm})(30\,\mathrm{cm})} = 1.8\,\mathrm{cm}$$

We may equate $\Delta r_{N2}=1.8\,\mathrm{cm}$ to δ_{sd} of Eq. 4.21 and with $D_{th}\simeq 55\times 10^{-2}\,\mathrm{cm^2/s}$, a rough average value between 10 K and 15 K, solve Eq. 4.21 for τ_{sd}:

$$\begin{aligned} \tau_{sd} &= \frac{1}{D_{th}}\left(\frac{\delta_{sd}}{\pi}\right)^2 \qquad (4.21) \\ &= \frac{1}{(55\times 10^{-2}\,\mathrm{cm^2/s})}\left(\frac{1.8\,\mathrm{cm}}{\pi}\right)^2 \sim 0.6\,\mathrm{s} \end{aligned}$$

The diffusion time of ∼0.6 s is much less than the 30-h warm-up time. Thus, the assumption of uniform temperature within this 15-liter SN_2 is valid.

d) We reverse the order of the two approaches to the solution given in **b)**. Thus, using the $C_p(T)$ data for solid neon given in Fig. 4.2 and by taking the area underneath the $C_p(T)$ curve for SNe between 10 K and 15 K, we have:

$$\begin{aligned} h(15\,\mathrm{K})-h(10\,\mathrm{K}) &\simeq \frac{C_p(10\,\mathrm{K})+C_p(15\,\mathrm{K})}{2}(15\,\mathrm{K}-10\,\mathrm{K}) \\ &\simeq \frac{(0.400\,\mathrm{J/cm^3\,K}+0.875\,\mathrm{J/cm^3\,K})}{2}\,(5\,\mathrm{K}) \\ &\simeq 3.2\,\mathrm{J/cm^3} \end{aligned}$$

Solution to PROBLEM 4.3 (continuation)

For the same warm-up time from 10 K to 15 K with 0.25-W heat input for 15-liter solid nitrogen, $[\Delta t(10\,\mathrm{K}\rightarrow 15\,\mathrm{K})]_{15\,\mathrm{liter}}^{0.25\,\mathrm{W}} \simeq 27.1\,\mathrm{h}$ computed in **b)**, the volume of solid neon, $\mathcal{V}_{Ne}(10\,\mathrm{K}\rightarrow 15\,\mathrm{K})$, is given by:

$$\mathcal{V}_{Ne}(10\,\mathrm{K}\rightarrow 15\,\mathrm{K}) = \frac{(27.1\,\mathrm{h})(3600\,\mathrm{s/h})(0.25\,\mathrm{W})}{(3.2\,\mathrm{J/cm^3})(1000\,\mathrm{cm^3/liter})}$$

$$\simeq 7.6\,\mathrm{liter} \sim \tfrac{1}{2} \times 15\,\mathrm{liter}$$

From Fig. 4.18 we note that for 1-liter solid neon, $T(t \simeq 0.33\,\mathrm{h}) = 10\,\mathrm{K}$ and $T(t \simeq 1.22\,\mathrm{h}) = 15\,\mathrm{K}$, resulting in $[\Delta t(10\,\mathrm{K}\rightarrow 15\,\mathrm{K})]_{1\,\mathrm{liter}}^{1\,\mathrm{W}} \simeq 0.89\,\mathrm{h}$ for SNe; for 1-liter SN_2: $[\Delta t(10\,\mathrm{K}\rightarrow 15\,\mathrm{K})]_{1\,\mathrm{liter}}^{1\,\mathrm{W}} \simeq 0.486\,\mathrm{h}$. We thus have:

$$\mathcal{V}_{Ne}(10\,\mathrm{K}\rightarrow 15\,\mathrm{K}) = \frac{(0.486\,\mathrm{h})}{(0.89\,\mathrm{h})}(15\,\mathrm{liter}) \simeq 8.2\,\mathrm{liter} \sim \tfrac{1}{2} \times (15\,\mathrm{liter})$$

e) From Fig. 4.18 we note that for 1-liter solid nitrogen, $T(t \simeq 0.6\,\mathrm{h}) = 15\,\mathrm{K}$ and $T(t \simeq 17.75\,\mathrm{h}) = 60\,\mathrm{K}$, or $[\Delta t(15\,\mathrm{K}\rightarrow 60\,\mathrm{K})]_{1\,\mathrm{liter}}^{1\,\mathrm{W}} \simeq 17.15\,\mathrm{h}$. For an average heat input of 3.3 W and 15-liter SN_2, we have:

$$[\Delta t(15\,\mathrm{K}\rightarrow 60\,\mathrm{K})]_{15\,\mathrm{liter}}^{3.3\,\mathrm{W}} = \left(\frac{15\,\mathrm{liter}}{1\,\mathrm{liter}}\right)\left(\frac{1\,\mathrm{W}}{3.3\,\mathrm{W}}\right)[\Delta t(15\,\mathrm{K}\rightarrow 60\,\mathrm{K})]_{1\,\mathrm{liter}}^{1\,\mathrm{W}}$$

$$\simeq (15)(0.303)(17.15\,\mathrm{h})$$

$$= 78\,\mathrm{h} \sim 80\,\mathrm{h}$$

f) In this transition, an energy density of $5\,\mathrm{J/cm^3} [= (75\,\mathrm{kJ})/(15{,}000\,\mathrm{cm^3})]$ is injected into copper at an initial temperature of 20 K. Thus, we may determine the final temperature T_f from the following equation:

$$\int_{20\,\mathrm{K}}^{T_f} [C_p(T)]_{cu}\, dT = 5\,\mathrm{J/cm^3} \qquad (S3.2)$$

From Fig. 4.2, we find Eq. $S3.2$ is satisfied with $T_f \simeq 40\,\mathrm{K}$.

g) Using the $C_p(T)$ data for SN_2 given in Fig. 4.2 and by taking the area underneath the $C_p(T)$ curve from 30 K to 35 K, we have:

$$h(35\,\mathrm{K}) - h(30\,\mathrm{K}) \simeq \frac{C_p(30\,\mathrm{K}) + C_p(35\,\mathrm{K})}{2}(35\,\mathrm{K} - 30\,\mathrm{K})$$

$$\simeq \frac{(1.24\,\mathrm{J/cm^3\,K} + 1.55\,\mathrm{J/cm^3\,K})}{2}(5\,\mathrm{K})$$

$$\simeq 7.0\,\mathrm{J/cm^3}$$

Answer to TRIVIA 4.3 ii). The German physicist Otto von Guericke (1602–1686) of "Magdeburg hemispheres" fame was the first with a pump, though the Italian physicist Evangelista Torricelli (1608–1647) achieved, in 1643, the first man-made vacuum by using a glass tube and a dish full of mercury.

Solution to PROBLEM 4.3 (continuation)

We thus have:

$$[\Delta t(30\,\mathrm{K}\rightarrow 35\,\mathrm{K})]_{15\,\mathrm{liter}}^{10\,\mathrm{W}} = \frac{(15{,}000\,\mathrm{cm}^3)(7.0\,\mathrm{J/cm}^3)}{(10\,\mathrm{W})(3{,}600\,\mathrm{s/h})}$$
$$\simeq 2.9\,\mathrm{h} \sim 3\,\mathrm{h}$$

h) We proceed as in **g)** except here an energy absorption at 35.61 K, $\Delta h(35.61\,\mathrm{K})$ of $8.2\,\mathrm{J/cm}^3$, must be added. Also, the enthalpy area computation must be performed over two temperature ranges, 35–35.61 K and 35.61–40 K. Thus:

$$\begin{aligned} h(40\,\mathrm{K}) - h(35\,\mathrm{K}) &\simeq \frac{C_p(35\,\mathrm{K}) + C_p(35.61\,\mathrm{K})}{2}(35.61\,\mathrm{K} - 35\,\mathrm{K}) \\ &\quad + \Delta h(35.61\,\mathrm{K}) + \frac{C_p(35.61\,\mathrm{K}) + C_p(40\,\mathrm{K})}{2}(40\,\mathrm{K} - 35.61\,\mathrm{K}) \\ &\simeq \frac{(1.60\,\mathrm{J/cm^3\,K} + 1.62\,\mathrm{J/cm^3\,K})}{2}(0.6\,\mathrm{K}) \\ &\quad + 8.2\,\mathrm{J/cm}^3 + \frac{(1.29\,\mathrm{J/cm^3\,K} + 1.33\,\mathrm{J/cm^3\,K})}{2}(4.39\,\mathrm{K}) \\ &\simeq 0.98\,\mathrm{J/cm}^3 + 8.2\,\mathrm{J/cm}^3 + 5.75\,\mathrm{J/cm}^3 \simeq 14.9\,\mathrm{J/cm}^3 \end{aligned}$$

$$[\Delta t(30\,\mathrm{K}\rightarrow 35\,\mathrm{K})]_{15\,\mathrm{liter}}^{10\,\mathrm{W}} = \frac{(15{,}000\,\mathrm{cm}^3)(14.9\,\mathrm{J/cm}^3)}{(10\,\mathrm{W})(3{,}600\,\mathrm{s/h})}$$
$$\simeq 6.2\,\mathrm{h} \sim 6\,\mathrm{h}$$

Thus the contribution of the extra enthalpy at 35.61 K more than doubles (2.1 times) the warm-up time for the same temperature increment of 5 K.

i) Equation 4.21 is used to compute τ_{sd} for $D_{th} = 2.4 \times 10^{-3}\,\mathrm{cm}^2/\mathrm{s}$ and $\delta_{sd} = 0.04\,\mathrm{cm}$ and demonstrate that this τ_{sd} indeed is ∼0.1 s. Thus:

$$\tau_{sd} = \frac{1}{D_{th}}\left(\frac{\delta_{sd}}{\pi}\right)^2 \tag{4.21}$$
$$= \frac{1}{(2.4\times 10^{-3}\,\mathrm{cm}^2/\mathrm{s})}\left(\frac{0.04\,\mathrm{cm}}{\pi}\right)^2 \simeq 0.067\,\mathrm{s}$$
$$\sim 0.1\,\mathrm{s}$$

j) The maximum power flux, p_{sd}, that may inject energy in 0.067 s into a 0.04-mm thick layer of SN_2 from 30 K to 35 K may be given by:

$$p_{sd} = [h(35\,\mathrm{K}) - h(30\,\mathrm{K})]\frac{\delta_{sd}}{\tau_{sd}}$$
$$= (7.0\,\mathrm{J/cm}^3)\frac{(0.04\,\mathrm{cm})}{(0.067\,\mathrm{s})} = 4.2\,\mathrm{W/cm}^2$$

Solution to PROBLEM 4.3 (continuation)

k) As footnoted in Table 4.10, $D_{th} = 0$ for solid nitrogen at 35.61 K, because energy, instead of being diffused through, is absorbed by the solid—8.2 J/cm^3—as it undergoes the phase transition, i.e., SN_2 heat capacity effectively approaches infinity. However, results of transient experiments [4.36, 4.37] have demonstrated an undiminished effectiveness of solid nitrogen in absorbing transient energy even over a range that spans this phase transition temperature.

l) Because the impact of a winding's temperature rise on the magnet's spatial field homogeneity is potentially quite important for NMR and MRI applications, it is presented below in ***DISCUSSION 4.12***.

DISCUSSION 4.12: Temperature Rise vs. Field Homogeneity

For an NMR or MRI magnet spatial field homogeneity is a key design/operation issue. In this discussion, we shall qualitatively inquire to what extent a rise in an operating temperature may impact the magnet's field spatial homogeneity as it warms up over a permitted range. Here, the range 10–15 K is used for computation.

The coefficient of linear thermal expansion, $\alpha(T)$, is defined by:

$$\alpha(T) = \frac{1}{L_\circ}\left(\frac{\partial L}{\partial T}\right)_P \tag{4.22}$$

where $L_\circ$ is the initial length. The subscript P implies a constant pressure process. At low temperatures, $\alpha(T)$ may be given by:

$$\alpha(T) = aT + bT^3 \tag{4.23}$$

Based on an experimental $\alpha(T)$ plot of copper in the range $0 \leq T \leq 50$ K, we find a and b for copper: $a_{cu} = 5\times10^{-9}\,\mathrm{K}^{-2}$ and $b_{cu} = 3\times10^{-11}\,\mathrm{K}^{-4}$. For $\Delta T_{op} = 5$ K, between 10 K and 15 K, we may compute $\Delta L/L_\circ$ for copper, $(\Delta L/L_\circ)_{cu}$, by integrating Eq. 4.23 between 10 K and 15 K. Here copper is selected as representative of the winding materials. As may be deduced from Table A3.4 in ***APPENDIX III***, which lists mean linear thermal expansion data of selected metals and nonmetals, *percentage changes* in expansion between 20 K and 80 K, for example, are about the same order of magnitude among these materials. We are thus justified here in choosing copper to quantitatively estimate $\Delta L/L$. Thus:

$$\left(\frac{\Delta L}{L_\circ}\right)_{cu} = \int_{10\,\mathrm{K}}^{15\,\mathrm{K}} (5\times10^{-9}T + 3\times10^{-11}T^3)dT = 0.62\times10^{-6} \tag{4.24}$$

This *linear* change occurs in three dimensions. If the windings were to expand equally in all directions, there would be no deterioration of homogeneity. In reality, because every winding is anisotropic, a degradation of the field homogeneity is expected but to what extent depends on how much the medium is anisotropic, and consequently this amplitude cannot accurately be predicted.

Note that $(\Delta L/L_\circ)$ in *all* materials increases not only with ΔT_{op} but also with initial temperature. Therefore, because of this potential field homogeneity degradation during an operating temperature excursion, for solid cryogen cooled magnets applied to NMR and MRI, it may be prudent to keep their initial operating temperatures to below ~20 K and ΔT_{op} no greater than 10 K.

DISCUSSION 4.13: Low-Temperature Thermometers

Temperature plays a dominant role in the key design/operation issues—conductor, cryogenics, mechanical, protection, stability—of superconducting magnets, as may be inferred from Fig. 1.6. Temperature measurement is thus one of the requirements in the operation of and experiments on superconducting magnets. It is a large subject, with a book devoted to it [4.41] or a whole chapter [4.42]. Rubin presents, with nearly 500 papers cited, a thorough review of progress in cryogenic thermometry over the period 1982–1997 [4.43]. Here our coverage, at only an introductory level and extent, is limited to thermometers, not thermometry. Specifically, we discuss temperature sensors that are *readily available* and *commonly used* in superconducting magnets; not included here are instrumentation and calibration techniques, important topics in thermometry. Because we deal with sensors only for superconducting magnets and related experiments, our discussion on thermometers covers the temperature range 2–300 K.

A. Kelvin Scale

In 1854 Kelvin proposed to take absolute zero as the starting point of a thermodynamic temperature scale. In 1954, the kelvin (K) was adopted as the unit of thermodynamic temperature, defined as 1/273.16 of water's triple point temperature (0.0100°C). Accordingly, 0°C, water's melting point on the Celsius scale, is equal to 273.15 K. Note that K stands by itself as the unit of temperature scale: it is thus *not* 4.2°K or 4.2 degrees Kelvin, but 4.2 K or 4.2 kelvins.

B. Requirements

As for any sensor, there are a number of requirements for a temperature sensor. These (listed here in no particular order of importance) with the desired quality given in parentheses, include: 1) signal level (high); 2) sensitivity (high); 3) response time (fast, to detect transitory events); 4) size (small); 5) magnetic field effect (minimal); 6) DC offset (zero); and 7) cost (low). Also desirable are reproducibility, stability, and linearity. Although every sensor is a *linear* function of any variable over a small range, clearly it cannot be expected to remain linear over an arbitrarily large range. With the proliferation of computer-based data acquisition techniques, linearity is not as pressing as it once was.

C. Types of Thermometers

Three types of thermometers are used in superconducting magnets and related experiments: 1) diodes; 2) resistors; and 3) thermocouples. Gas and vapor pressure thermometers, once quite common, particularly in the laboratory setup, are rarely used now. Each of the three types of thermometers is described briefly below.

Diode Thermometers The junction voltage of a semiconductor device, such as a diode, forward-biased at a constant current, increases with decreasing temperature. Most widely used diode thermometers are based on Si and GaAlAs junctions; many commercial thermometers, both calibrated and uncalibrated, are available. Calibrated versions are as little as ∼1/2 (some Si diodes) or as much as ∼4 times more expensive than uncalibrated versions, the cost differential dictated chiefly by the sensor's operating temperature range.

DISCUSSION 4.13: Low-Temperature Thermometers (continuation)

Resistance Thermometers Resistance thermometers are available with either temperature coefficient sign: negative if based on semiconductors and positive if based on metals (generally pure to maximize the sensor's sensitivity, ohm/kelvin).

The negative temperature coefficient sensors include germanium, carbon resistors, carbon-glass (primarily for use in magnetic fields), and ruthenium oxide. The positive temperature coefficient sensors include platinum, platinum alloys, and rhodium-iron. Becoming increasingly popular is the zirconium oxynitride thermometer under the name Cernox, manufactured by Lake Shore Cryotronics, Inc. Among metal-based sensors, the one based on pure platinum is the most prominent and everyone's choice when highest-accuracy is required; indeed the standard platinum resistance thermometer defines the International Temperature Standard from 13.8033 K, the triple point of hydrogen, up to well beyond 300 K.

Temperature Spectrum

Figure 4.19 shows a temperature spectrum over the range from 100 picokelvins (100 pK) to 1 gigakelvin (1 GK). Note that superconducting magnets operate over a temperature span that extends less than 2 log scales, 1 K–100 K.

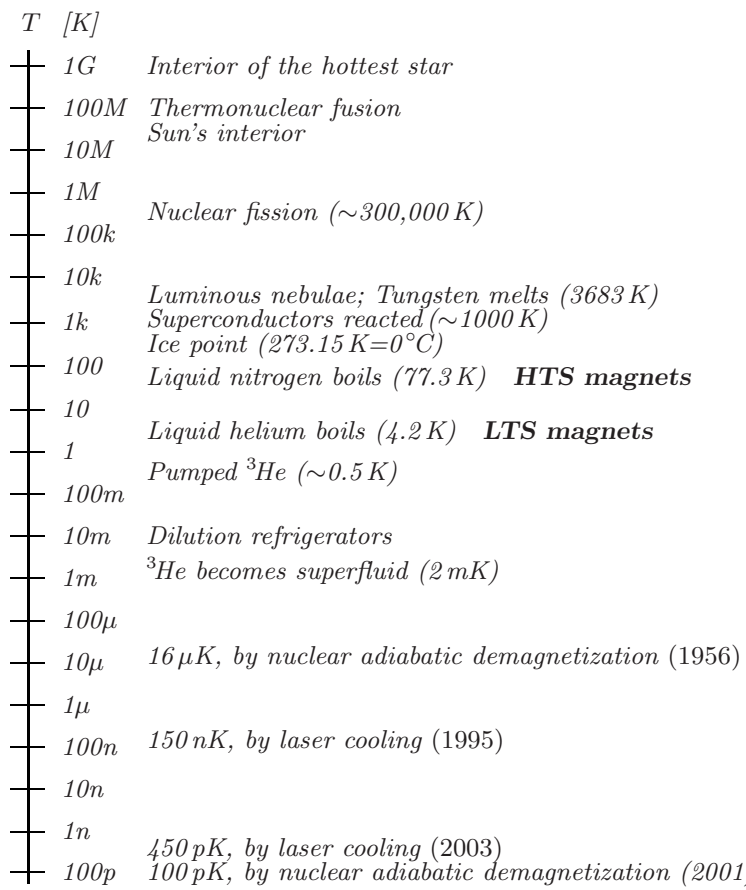

Fig. 4.19 Temperature spectrum covering 19 orders of magnitude.

DISCUSSION 4.13: Low-Temperature Thermometers (continuation)

Thermocouples For cryogenic applications that tolerate uncertainties of temperature up to 5%—for example, 1 K at 20 K—thermocouples are widely used. This is chiefly because they can meet some of the requirements listed earlier—small size and fast response time—more readily than the diode and resistance thermometers. Also, thermocouples are the least expensive among the three types.

D. Signal Levels and Sensitivities of Selected Thermometers

Table 4.11 presents *approximate* values of signal level (V) and sensitivity ($\delta V/\delta T$) at selected temperatures in the 2–300 K range for six commonly used thermometers, two from each of the three types: diodes [4.44], resistances [4.44]; and thermocouples [4.45]. Note that these values are given here to demonstrate that both signal levels and sensitivities vary over a wide range among thermometers and as a "guide" in the selection process for appropriate sensors. Commercial sources of these sensors generally supply accurate "general" data for these sensors; each *calibrated* sensor is provided with its own specific data. Each thermometer in Table 4.11 is briefly discussed below, including magnetic field effects.

Additional Remarks, Including Magnetic Field Effects

Diode Diode thermometers, such as silicon and GaAlAs, have the highest sensitivity among the three types over the entire temperature range of our interest. Also as may be deduced from Table 4.11, the sensor's $V(T)$ curve is quite linear, i.e., V decreasing roughly linearly with T, in the 50–300 K range. Also attractive is that for most applications in which temperature uncertainties up to 5% are acceptable, uncalibrated sensors that rely only on the manufacturer's standard calibration curve may be used. The only negative is its unsuitability in the presence of a magnetic field, particularly in the temperature range below 60 K [4.45].

Table 4.11: *Approximate* Values of Signal Level (V) and Sensitivity ($\delta V/\delta T$) of Selected Thermometers of Diodes [4.44]; Resistances [4.44]; and Thermocouples [4.45]

Sensor		2 K	4 K	10 K	20 K	50 K	100 K	200 K	300 K
Silicon	V [V]	1.69	1.63	1.42	1.21	1.07	0.98	0.76	0.52
	$\delta V/\delta T$ [mV/K]	−21	−33	−29	−18	−1.8	−2.0	−2.3	−2.4
GaAlAs	V [V]	5.5	5.1	4.1	2.7	1.5	1.4	1.1	0.9
	$\delta V/\delta T$ [mV/K]	−210	−210	−145	−110	−30	−1.5	−2.6	−2.7
Cernox	V [mV]	12	14	17	28	13	20	33	20
	$\delta V/\delta T$ [mV/K]	−10	−3.5	−1.5	−1.2	−0.24	−0.18	−0.18	−0.07
@ Current	[μA]	1	3	10	30	30	100	300	300
Platinum	V [mV]	NA	NA	NA	2.4	10	31	77	114
	$\delta V/\delta T$ [mV/K]	NA	NA	NA	0.086	0.35	0.41	0.39	0.38
@ Current	[mA]	—	—	—	1	1	1	1	1
Type E	V [μV]	1.3	4.6	24.9	91	504	1775	5871	11445
	$\delta V/\delta T$ [μV/K]	1.15	2.09	4.65	8.51	18.7	31.4	49.3	61
AuFe(0.07%)-	V [μV]	17.2	39.6	124.9	286.6	768.6	1647	3667	5864
Chromel	$\delta V/\delta T$ [μV/K]	10.0	12.2	15.6	16.3	16.4	18.7	21.4	22.8

DISCUSSION 4.13: Low-Temperature Thermometers (continuation)

GaAlAs There are two important aspects of GaAlAs that are different from Si: 1) greater nonlinearity of $V(T)$; and 2) insensitivity to magnetic fields up to ∼5 T.

Cernox Although not as sensitive as diode thermometers, second to Si, Cernox is widely used. Unlike Si, it is quite insensitive to a magnetic field. Data of Lake Shore Cryotronics [4.44], the manufacturer of Cernox, show that at 20 K the sensor's $\delta T/T$ uncertainty due to magnetic field is less than 0.2% up to a field of 20 T; the error increases with decreasing temperature, reaching ∼5% at 2 K.

Platinum A platinum sensor is quite insensitive to magnetic field at temperatures above ∼40 K: for example, at 40 K and 5 T, $\delta T/T$ is 1.5%, which, at 80 K and 5 T, decreases by a factor of 10 [4.44].

Type E Thermocouple Both Type E and Chromel-Au0.07%Fe have the smallest signal levels and sensitivities compared with the other four sensors. Note that with the ice-point (0°) reference, Type E, at 20 K, for example, has an offset voltage of ∼11 mV, while its sensitivity is only ∼10 μV/K. However, its accuracy is much improved when only *changes* in temperature from a specific operating point are to be measured. Also, if temperature uncertainties up to ∼5% can be tolerated and many sensors are required, Type E is an excellent choice. Field sensitivity is quite modest, e.g., 2% at 20 K and <1% at 45 K, both in a field of 8 T [4.44].

AuFe(0.07%)-Chromel Among all thermocouples, chromel-AuFe(0.07%) gives the highest sensitivity, and thus is most suitable, at temperatures below ∼20 K. Its $V(T)$ values, however, can easily deviate from the published values [4.45] when the AuFe(0.07%) wire is strained—it must be handled very carefully. Its sensitivity to magnetic field is roughly one order of magnitude greater than that of Type E.

Capacitance Thermometers

Though not included in the above discussion, capacitance thermometers such as strontium titanate sensors are used because of their very low magnetic field dependence. Several other types based on glass or plastic materials are popular for temperatures below 1 K.

Fahrenheit Scale

—Passage from Linus Pauling's *College Chemistry* [4.46]

The Fahrenheit scale was devised by Gabriel Daniel Fahrenheit (1686–1736), a natural philosopher who was born in Danzig (now Gdańsk) *and settled in Holland. He invented the mercury thermometer in 1714; before then alcohol had been used as the liquid in thermometers. As the zero point on his scale he took the temperature produced by mixing equal quantities of snow and ammonium chloride. His choice of 212° for the boiling point of water was made in order that the temperature of his body should be 100°F. The normal temperature of the human body is 98.6°F* (37.0°C)*; perhaps Fahrenheit had a slight fever while he was calibrating his thermometer.*

DISCUSSION 4.14: Vapor-Cooled Copper Current Lead*

For a superconducting magnet immersed in a bath of liquid helium at 4.2 K, a vapor-cooled copper current lead can be a large heat load on the system cryogenics. The basic design concept for an optimum vapor-cooled copper lead is to make the Joule heating and conduction heating about equal and to remove the heat by funneling cold helium vapor through the lead. Work on vapor-cooled leads began in the 1960s and continues [4.47–4.52]. Vapor-cooled leads are now *commercially* available in the current range 100 A–75 kA. Recently, it has reached the 100-kA level [4.53]. Here we present analytical expressions for key parameters of a lead.

A. Power Density Equation

The total power Q_{in} flowing into and generated within a differential volume $A\Delta z$ of a vapor-cooled lead (Fig. 4.20) carrying the lead's rated current $I_\circ$ is given by:

$$Q_{in} = \left[Ak(T)\frac{dT}{dz}\right]_{z+\Delta z} + \dot{m}_I c_p(T)T + \frac{\rho(T)I_\circ^2}{A}\Delta z \tag{4.25}$$

where z is the axial distance along the lead, and $z=0$ at the lead's cold end. $k(T)$, A, and $\rho(T)$ are, respectively, the thermal conductivity, active cross sectional area, and electrical resistivity of the lead (usually copper). $\dot{m}_I$ and $c_p(T)$ are, respectively, the helium mass flow rate and specific heat. The heat transfer between the helium and the lead is assumed perfect; T is the temperature of both the lead and helium at z. The total power Q_{out} flowing out of the differential volume of $A\Delta z$ is given by:

$$Q_{out} = \left[Ak(T)\frac{dT}{dz}\right]_{z} + \dot{m}_I c_p(T)(T+\Delta T) \tag{4.26}$$

In the steady-state condition, we have $Q_{in} = Q_{out}$. Thus:

$$\left[Ak(T)\frac{dT}{dz}\right]_{z+\Delta z} - \left[Ak(T)\frac{dT}{dz}\right]_{z} - \dot{m}_I c_p(T)\Delta T + \frac{\rho(T)I_\circ^2}{A}\Delta z = 0 \tag{4.27}$$

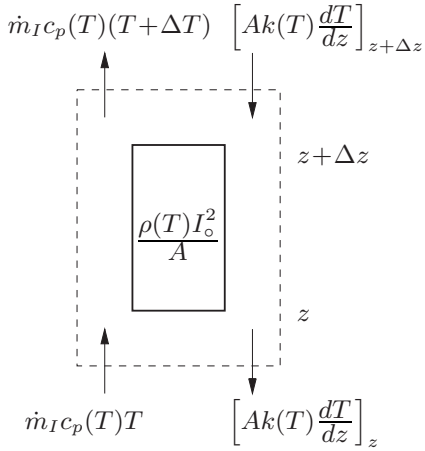

Fig. 4.20 Heat balance for a differential volume of a vapor-cooled lead.

* Based on **Problem 4.3** in the 1st Edition (Plenum, 1994).

DISCUSSION 4.14: Vapor-Cooled Copper Current Lead (continuation)

Dividing Eq. 4.27 by Δz and letting $\Delta z \to 0$, we obtain:

$$\frac{d}{dz}\left[Ak(T)\frac{dT}{dz}\right] - \dot{m}_I c_p(T)\frac{dT}{dz} + \frac{\rho(T)I_\circ^2}{A} = 0 \tag{4.28}$$

B. Cold-End Heat Input & Boil-Off Rate

In the "high" current limit, i.e., $|d[Ak(T)dT/dz]/dz| \ll \rho(T)I_\circ^2/A$, Eq. 4.28 evaluated at $z = 0$, where $T(0) = T_0$, is simplified to:

$$-\dot{m}_I c_{p0}\left.\frac{dT}{dz}\right|_{z=0} + \frac{\rho_0}{A}I_\circ^2 \simeq 0 \tag{4.29a}$$

where $c_{p0} = c_p(T_0)$ and $\rho_0 = \rho(T_0)$. From Eq. 4.29*a*, we can solve for $(dT/dz)_{z=0}$:

$$\left.\frac{dT}{dz}\right|_{z=0} \simeq \frac{\rho_0 I_\circ^2}{A\dot{m}_I c_{p0}} \tag{4.29b}$$

Because $Q_{I_\circ}$ at $z = 0$ is purely by conduction, we have, with $k_0 = k(T_0)$:

$$Q_{I_\circ} = Ak(T_0)\left.\frac{dT}{dz}\right|_{z=0} = \frac{k_0\rho_0 I_\circ^2}{\dot{m}_I c_{p0}} \tag{4.30}$$

The power input $Q_{I_\circ}$ into the liquid boils off the liquid at a rate $\dot{m}_I$ given by:

$$\dot{m}_I = \frac{Q_{I_\circ}}{h_L} \tag{4.31a}$$

where h_L is the liquid helium's latent heat of vaporization [J/kg]. Combining Eqs. 4.30 and 4.31*a* and solving for $\dot{m}_I$, we obtain:

$$\dot{m}_I = I_\circ\sqrt{\frac{k_0\rho_0}{c_{p0}h_L}} \tag{4.31b}$$

Inserting $\dot{m}_I$ given by Eq. 4.31*b* into Eq. 4.30 and solving for $Q_{I_\circ}/I_\circ$, we derive:

$$\frac{Q_{I_\circ}}{I_\circ} = \sqrt{\frac{h_L k_0\rho_0}{c_{p0}}} \tag{4.32a}$$

Note that $Q_{I_\circ}$ depends neither on ℓ, the lead active length between the bottom end $(z = 0)$ and top end $(z = \ell)$, nor on A, the lead conductor cross section. It is, however, directly proportional to $I_\circ$, the lead's rated current. Note that if the lead carries $I < I_\circ$, the cold-end heat input will *not* be $(I/I_\circ)Q_{I_\circ}$.

Throughout this discussion T_0 is the cold-end temperature of a vapor-cooled lead, assumed below to be $T_0 = 6$ K. However, in a *real* vapor-cooled lead, this cold end $(z = 0)$ may be located high above the top of the magnet (and minimum liquid level)—in some cases 25 cm or even higher, because it is often desirable to provide a reservoir of liquid helium above the magnet. The cold end is then electrically and thermally connected to a superconductor-shunted copper extension, the other end $(z < 0)$ of which penetrates into the liquid. The superconductor shunt (often of copper/NbTi composite) carries $I_\circ$ to the magnet, and the copper conducts $Q_{I_\circ}$ to the liquid. The copper extension must have enough cross sectional area to conduct $Q_{I_\circ}$, even when exposed out of liquid helium over its entire span, without raising T_0 too high, thus enabling the superconductor shunt to carry $I_\circ$ superconductively.

DISCUSSION 4.14: Vapor-Cooled Copper Current Lead (continuation)

With $h_L = 20.7\times10^3\,\text{J/kg}$ and $c_{p0} \simeq 5.26\times10^3\,\text{J/kg K}$ for liquid helium; $k_0 = 600\,\text{W/m K}$ and $\rho_0 \simeq 2.5\times10^{-10}\,\Omega\,\text{m}$ for copper, we obtain:

$$\frac{Q_{I_\circ}}{I_\circ} \simeq \sqrt{\frac{(20.7\times10^3\,\text{J/kg})(600\,\text{W/m K})(2.5\times10^{-10}\,\Omega\,\text{m})}{5.26\times10^3\,\text{J/kg K}}}$$

$$= 7.7\times10^{-4}\,\text{W/A} = 0.77\,\text{mW/A} \sim 1\,\text{mW/A} \qquad (4.32b)$$

For an optimum vapor-cooled lead, 1 mW/A is a rule-of-thumb value useful for estimating the heat input into liquid helium. For a single 10-kA lead operating at 10 kA ($=I_\circ$), the heat load will be ∼10 W, or ∼20 W for a pair of such leads.

C. Optimal Current-Lead Parameters

The high-current approximation of Eq. 4.28 is given by:

$$-\dot{m}_I c_p(T)\frac{dT}{dz} + \frac{\rho(T)I_\circ^2}{A} = 0 \qquad (4.33)$$

Solving for $dT/\rho(T)$ from Eq. 4.33 with $c_p(T) \simeq \tilde{c}_p$, a temperature-averaged (from T_0 to T_ℓ) heat capacity of helium, and integrating both sides over appropriate limits (T_0 at $z = 0$ and T_ℓ at $z = \ell$) we obtain:

$$\int_{T_0}^{T_\ell}\frac{dT}{\rho(T)} = \int_0^\ell \frac{I_\circ^2\,dz}{A\dot{m}_I\tilde{c}_p} = \frac{I_\circ^2\ell}{A\dot{m}_I\tilde{c}_p} \qquad (4.34a)$$

For copper, the integral $\int_{T_0}^{T_\ell} dT/\rho(T)$is given approximately by:

$$\int_{T_0}^{T_\ell}\frac{dT}{\rho(T)} \simeq 1.2\times10^{11}\,\text{K/}\Omega\,\text{m} \qquad (4.34b)$$

for $T_0 = 6\,\text{K}$ and $T_\ell = 273\,\text{K}$. Inserting $\dot{m}_I$ (Eq. 4.31*b*) in Eq. 4.34*a* and assuming $\tilde{c}_p \simeq c_{p0}$, a valid assumption for helium, we obtain:

$$\int_{T_0}^{T_\ell}\frac{dT}{\rho(T)} \simeq \left(\frac{I_\circ^2\ell}{Ac_{p0}}\right)\frac{1}{I_\circ}\sqrt{\frac{c_{p0}h_L}{k_0\rho_0}} \qquad (4.34c)$$

We express the optimal-current-lead parameter ratio, $(I_\circ\ell/A)_{ot} \equiv \zeta_\circ$, in terms of its rated current ($I_\circ$), lead active length (ℓ), and cross sectional area (A):

$$\left(\frac{I_\circ\ell}{A}\right)_{ot} \equiv \zeta_\circ \simeq \left[\int_{T_0}^{T_\ell}\frac{dT}{\rho(T)}\right]\sqrt{\frac{c_{p0}k_0\rho_0}{h_L}} \qquad (4.35a)$$

Inserting appropriate values for the parameters in the above equation, we can numerically solve for $\zeta_\circ$:

$$\zeta_\circ \simeq (1.2\times10^{11}\,\text{K/}\Omega\,\text{m})\sqrt{\frac{(5.26\times10^3\,\text{J/kg K})(600\,\text{W/m K})(2.5\times10^{-10}\,\Omega\,\text{m})}{20.7\times10^3\,\text{J/kg}}}$$

Thus:

$$\left(\frac{I_\circ\ell}{A}\right)_{ot} \simeq 2.3\times10^7\,\text{A/m} \qquad (4.35b)$$

For $I_\circ = 6\,\text{kA}$ and $\ell = 38\,\text{cm}$, for example, Eq. 4.35*b* gives: $A \simeq 1\,\text{cm}^2$.

DISCUSSION 4.14: Vapor-Cooled Copper Current Lead (continuation)

D. Standing Heat Input

The liquid helium boil-off rate when the optimized lead carries no current—called the "standing" boil-off rate, $\dot{m}_0$—is due to heat input into the helium by conduction only. With $I_\circ = 0$ inserted into Eq. 4.28, we have:

$$A\tilde{k}\frac{d^2T}{dz^2} - \dot{m}_0\tilde{c}_p\frac{dT}{dz} = 0 \tag{4.36}$$

where $\tilde{k}$ is the average thermal conductivity and $\tilde{c}_p$ is the average specific heat of helium, both in the temperature range, T_0 to T_ℓ.

$$\tilde{k} = \frac{1}{T_\ell - T_0}\int_{T_0}^{T_\ell} k(T)\,dT \tag{4.37}$$

Table 4.18 (p. 307) presents values of $\tilde{k}$ for four materials (G-10, stainless steel 304, brass, and copper) over three common temperature ranges in cryogenic applications: 4–80 K; 4–300 K; and 80–300 K.

With the boundary conditions, $T(z=0) = T_0$ and $A\tilde{k}(dT/dz)_{z=0} = \dot{m}_0 h_L$, $T(z)$ may be given by:

$$T(z) = T_0 + \frac{h_L}{\tilde{c}_p}\left[\exp\left(\frac{\dot{m}_0\tilde{c}_p z}{A\tilde{k}}\right) - 1\right] \tag{4.38a}$$

Thus:

$$T(\ell) \equiv T_\ell = T_0 + \frac{h_L}{\tilde{c}_p}\left[\exp\left(\frac{\dot{m}_0\tilde{c}_p \ell}{A\tilde{k}}\right) - 1\right] \tag{4.38b}$$

Solving Eq. 4.38*b* for $\dot{m}_0\tilde{c}_p\ell/A\tilde{k}$, we have:

$$\frac{\dot{m}_0\tilde{c}_p\ell}{A\tilde{k}} = \ln\left[\frac{\tilde{c}_p(T_\ell - T_0)}{h_L} + 1\right] \tag{4.39a}$$

From Eq. 4.39*a* we may solve for $\dot{m}_0$. Thus:

$$\dot{m}_0 = \frac{\tilde{k}}{\tilde{c}_p}\left(\frac{A}{\ell}\right)\ln\left[\frac{\tilde{c}_p(T_\ell - T_0)}{h_L} + 1\right] \tag{4.39b}$$

Combining Eq. 4.39*b* and $Q_0 = \dot{m}_0 h_L$, we obtain:

$$Q_0 = \frac{\tilde{k}h_L}{\tilde{c}_p}\left(\frac{A}{\ell}\right)\ln\left[\frac{\tilde{c}_p(T_\ell - T_0)}{h_L} + 1\right] \tag{4.40a}$$

For an optimal lead, $(I_\circ\ell/A)_{ot} = \zeta_\circ$, we thus obtain:

$$Q_0 = \frac{\tilde{k}h_L}{\tilde{c}_p}\left(\frac{I_\circ}{\zeta_\circ}\right)\ln\left[\frac{\tilde{c}_p(T_\ell - T_0)}{h_L} + 1\right] \tag{4.40b}$$

DISCUSSION 4.14: Vapor-Cooled Copper Current Lead (continuation)

For an optimum vapor-cooled copper lead, the ratio of Q_0 to $Q_{I_\circ}$ is given by:

$$\frac{Q_0}{Q_{I_\circ}} = \frac{\tilde{k}}{\tilde{c}_p \zeta_\circ} \sqrt{\frac{h_L c_{p0}}{k_0 \rho_0}} \ln \left[\frac{\tilde{c}_p (T_\ell - T_0)}{h_L} + 1 \right] \tag{4.41}$$

With $\tilde{k} = 660\,\mathrm{W/m\,K}$ (Table 4.18); $\tilde{c}_p \simeq 5.2\,\mathrm{kJ/kg\,K}$; $T_\ell = 300\,\mathrm{K}$; $T_0 = 4\,\mathrm{K}$ and $\zeta_\circ \simeq 2.3 \times 10^7\,\mathrm{A/m}$ inserted into Eq. 4.41, we obtain:

$$\frac{Q_0}{Q_{I_\circ}} \simeq 0.69 \tag{4.42}$$

That is, the standing boil-off rate of a vapor-cooled lead is roughly 70% of the boil-off rate of the lead carrying its rated current.

E. Voltage Drop Across an Optimal Lead

The voltage drop $V_\circ$ over the entire length of the copper lead at $I_\circ$ is given by:

$$V_\circ = \frac{I_\circ}{A} \int_0^\ell \rho_{cu}\, dz \tag{4.43a}$$

Integration over the lead length ℓ is necessary because ρ_{cu}, the electrical resistivity of copper, is temperature-dependent and thus varies with z. Equation 4.43*a* may be expressed as:

$$V_\circ = \tilde{\rho}_{cu} \left(\frac{I_\circ \ell}{A} \right)_{ot} = \tilde{\rho}_{cu} \zeta_\circ \tag{4.43b}$$

where

$$\tilde{\rho}_{cu} = \frac{1}{\ell} \int_0^\ell \rho_{cu}\, dz \simeq \frac{1}{T_\ell - T_0} \int_{T_0}^{T_\ell} \rho_{cu}(T)\, dT \tag{4.44}$$

Equation 4.44 assumes a linear temperature gradient along the current lead. Combining Eqs. 4.43*b*, where $\tilde{\rho}_{cu}$ is given in the unit of $\Omega\,\mathrm{m}$, and Eq. 4.35*b*, we have:

$$V_\circ \simeq 2.3 \times 10^7 \tilde{\rho}_{cu}\,\mathrm{V} \tag{4.45}$$

That is, V_{ot} is the same among leads optimized for any rated current.

For copper, ρ_{cu} is $\sim 2.5 \times 10^{-10}\,\Omega\,\mathrm{m}$ (below $\sim 50\,\mathrm{K}$) and varies linearly with temperature above $\sim 50\,\mathrm{K}$, being $1.75 \times 10^{-8}\,\Omega\,\mathrm{m}$ at $273\,\mathrm{K}$. From Eq. 4.44, we have: $\tilde{\rho}_{cu} \simeq 0.4 \times 10^{-8}\,\Omega\,\mathrm{m}$. The voltage drop across an optimum lead at its rated current is *independent of rated current*; for a copper lead it is $\sim 100\,\mathrm{mV}$. Thus, $V_\circ \sim 100\,\mathrm{mV}$ at 100 A for a 100-A lead and at 10 kA for a 10-kA lead; when the warm end is "cool," which often happens in vapor-cooled leads, $V_\circ$ can be less than 100 mV. This conclusion agrees, within an order of magnitude, with experimental data for vapor-cooled copper leads in the 1 kA–30 kA range [4.54].

TRIVIA 4.4: List the temperatures below in descending order.

i) Critical, of superconductor MgB_2;
ii) Curie, of ferromagnet $CrBr_3$;
iii) Phase transition, of solid N_2;
iv) Surface, of the "planet" Pluto.

DISCUSSION 4.14: Vapor-Cooled Copper Current Lead (continuation)

F. Heating Upon Flow Stoppage

When a cooling gas flow stoppage occurs, the steady-state solution on which the design of optimum leads is based is no longer valid. If the lead continues to carry its rated current $I_\circ$ without cooling, "flow stoppage meltdown" of the lead may occur, most often near the warm end. The time-dependent power equation [W/m] for a differential element of an optimum lead is given by:

$$AC_{cu}(T)\frac{dT}{dt} = \frac{d}{dz}\left[Ak(T)\frac{dT}{dz}\right] - \dot{m}_I c_p(T)\frac{dT}{dz} + \frac{\rho_{cu}(T)}{A}I_\circ^2 \tag{4.46}$$

where $C_{cu}(T)$ is the volumetric heat capacity of the lead metal (copper). With no cooling ($\dot{m}_I = 0$) and the conduction term set equal to zero (conservative assumption), Eq. 4.46 becomes:

$$AC_{cu}(T)\frac{dT}{dt} = \frac{\rho_{cu}(T)}{A}I_\circ^2 \tag{4.47}$$

An optimum lead satisfies $(I_\circ \ell/A) = \zeta_\circ = 2.3\times10^7$ A/m. Thus:

$$C_{cu}(T)\frac{dT}{dt} = \frac{\rho_{cu}(T)\zeta_\circ^2}{\ell^2} \tag{4.48}$$

Because flow stoppage meltdown usually happens near the warm end, we replace $C_{cu}(T)$ with $C_\circ$ (a constant) and $\rho_{cu}(T) = \rho_\circ + \gamma_{cu}T$ ($\rho_\circ$ and γ_{cu} both constants):

$$\frac{dT}{dt} = \frac{\rho_\circ\zeta_\circ^2}{C_\circ\ell^2} + \frac{\gamma_{cu}\zeta_\circ^2}{C_\circ\ell^2}T = \frac{\rho_\circ}{\gamma_{cu}\tau_\ell} + \frac{T}{\tau_\ell} \tag{4.49}$$

The thermal time constant of the lead, τ_ℓ, is given by:

$$\tau_\ell = \frac{C_\circ\ell^2}{\gamma_{cu}\zeta_\circ^2} \tag{4.50}$$

The solution to Eq. 4.49 is given by:

$$T(t) = Ke^{t/\tau_\ell} - \frac{\rho_\circ}{\gamma_{cu}} \tag{4.51}$$

where K is a constant. Equation 4.51 states that upon gas flow stoppage $T(t)$ rises exponentially with a time constant of τ_ℓ. Because τ_ℓ is proportional to ℓ^2, a longer optimum lead takes longer to reach the metal's meltdown temperature than does a shorter optimum lead. Note that because $\zeta_\circ = (I_\circ\ell/A)$, we may also conclude that for the same rated current a thicker optimum lead is safer than a thinner optimum lead against a flow stoppage incident.

For an optimum 10-kA lead with $\ell = 1$ m, for example, with $C_\circ = 3.5\times10^6$ J/m^3 K, $\gamma_{cu} = 68\times10^{-12}\,\Omega$ m/K, and $(I_\circ\ell/A) \equiv \zeta_\circ = 2.3\times10^7$ A/m, we obtain:

$$\tau_\ell = \frac{(3.5\times10^6\ \text{J/m}^3\,\text{K})(1\ \text{m})^2}{(68\times10^{-12}\,\Omega\,\text{m/K})(2.5\times10^7\ \text{A/m})^2} \sim 90\ \text{s}$$

Note that τ_ℓ is doubled for an optimum 10-kA lead having $\ell = 1.4$ m.

DISCUSSION 4.15: "Dry" Leads—Normal Metal & HTS*

For a dry superconducting magnet, current leads must generally operate in a vacuum environment. Here we discuss two types of leads rated at $I_\circ$: 1) normal metal [4.55]; and 2) HTS over its usable temperature range [4.56].

A. Normal Metal

The steady-state power differential equation over a unit lead length is given by:

$$A\tilde{k}\frac{d^2T}{dz^2} + \frac{\tilde{\rho}I_\circ^2}{A} = 0 \tag{4.52}$$

where A is the lead active cross sectional area; $\tilde{k}$ and $\tilde{\rho}$ are, respectively, the metal's T-averaged thermal conductivity and electrical resistivity. Solving Eq. 4.52 with the boundary conditions $T(z=0) = T_0$ and $T(z=\ell) = T_\ell$, we obtain Eq. 4.11 (p. 240), from which the heat input at the cold end, $Q_{I_\circ}$ may be derived:

$$Q_{I_\circ} = A\tilde{k}\frac{dT}{dz}\bigg|_{z=0} = \tilde{k}(T_\ell - T_0)\left(\frac{A}{\ell}\right) + \frac{\tilde{\rho}I_\circ^2}{2}\left(\frac{\ell}{A}\right) \tag{4.53}$$

Differentiating Eq. 4.53 with respect to ℓ/A and setting it to 0 for $(I_\circ\ell/A)_{dr}$, we obtain $(I_\circ\ell/A)_{dr}$ for an optimal dry lead that minimizes $[Q_{I_\circ}]_{dr}$ (Eq. 4.12, p. 240):

$$\left(\frac{I_\circ\ell}{A}\right)_{dr} = \sqrt{\frac{2\tilde{k}(T_\ell - T_0)}{\tilde{\rho}}} \tag{4.12}$$

From Eqs. 4.12 and 4.53, we obtain an expression for $[Q_{I_\circ}]_{dr}$:

$$[Q_{I_\circ}]_{dr} = I_\circ\sqrt{2\tilde{k}\tilde{\rho}(T_\ell - T_0)} \tag{4.54}$$

With $\tilde{k} = 460\,\mathrm{W/m\,K}$ and $\tilde{\rho} = 1\times10^{-8}\,\Omega\,\mathrm{m}$ (for copper in the range 80–300 K), Eq. 4.54 gives: $[Q_{I_\circ}]_{dr}/I_\circ \simeq 45\,\mathrm{mW/A}$; for brass, Eq. 4.54 gives 32 mW/A [4.19]. That is, for a conduction-cooled lead, brass is preferable to copper.

B. HTS Extension

After the discovery of YBCO, HTS lead "extensions" were built for the cold portion (below ~80 K) of a normal metal lead [4.57, 4.58]. The heat input to the magnet environment at T_0 by an HTS extension, $[Q_{I_{hts}}]_{dr}$, of "average" thermal conductivity k_{hts}, cross sectional area A_{hts}, length ℓ_{hts}, and warm-end temperature $T_{w_{hts}}$ is *ideally* by conduction, for which:

$$[Q_{I_{hts}}]_{dr} = k_{hts}A_{hts}\frac{(T_{w_{hts}} - T_0)}{\ell_{hts}} \tag{4.55}$$

In a real normal-metal/HTS lead, the normal metal heat at its cold end, given by Eq. 4.54 with $T_0 \simeq T_{w_{hts}}$, generally is absorbed by the 1st stage of a cryocooler, the 2nd stage of which maintains the magnet at T_0. Also, the HTS lead, whether of bulk or tape, must be protected; protection of Bi2223 tape current lead is discussed in ***DISCUSSION 8.5***. Besides the HTS lead considered here, there also are vapor-cooled HTS versions, as studied in **PROBLEMS 4.4–4.6**.

---

* Based on **Problem 4.4** in the 1st Edition (Plenum, 1994).

PROBLEM 4.4: Vapor-cooled HTS current lead —*F*ully *S*uperconducting *V*ersion (FSV)

Together with conduction-cooled HTS current leads, vapor-cooled HTS current leads were also among the earliest practical, and successful, HTS devices. Started in 1989, the work is still continuing [4.59–4.73]. HTS leads now reach rated currents of 60 kA [4.69] and 70 kA [4.74].

Here, we study a vapor-cooled current lead incorporating HTS, specifically that in the form of tape, in which the HTS's warm end is thermally anchored at 77–80 K; at this point the HTS lead is connected to a vapor-cooled normal-metal lead, to reach the room-temperature termination. Hull has classified altogether 11 types of current leads [4.60]. Among these is a fully-superconducting version (FSV) of a vapor-cooled HTS lead, i.e., that operates fully superconducting over the entire temperature range, between 4.2 K and 77–80 K. Because such a lead relies on convective cooling by the effluent helium vapor, it is appropriate primarily for superconducting magnets that operate immersed in a bath of liquid helium.

Figure 4.21 shows the basic configuration of the vapor-cooled HTS lead studied here, comprised of N_{fs} paralleled HTS tapes, each of active length ℓ. The HTS lead, rated at current $I_\circ$, operates between its cold end ($z=0$) at temperature T_0 and its warm end ($z=\ell$), at T_ℓ. The HTS lead conducts heat, Q_{in}, into liquid helium, generating effluent vapor, of mass flow rate $\dot{m}_h$, that absorbs the heat over the lead length ℓ.

Between T_ℓ and room temperature, any vapor-cooled HTS lead must be coupled to an optimal vapor-cooled lead of normal metal, generally copper, rated at the same current of $I_\circ$. Because Q_{in} of the HTS lead is necessarily smaller than that of the copper counterpart—this reduction in Q_{in} is the *only* reason for incorporating the HTS lead—the helium flow rate $\dot{m}_h$ generated by the HTS section is insufficient for the normal metal section. Therefore extra coolant is introduced at the cold-end of the normal-metal vapor-cooled lead, as indicated in Fig. 4.21.

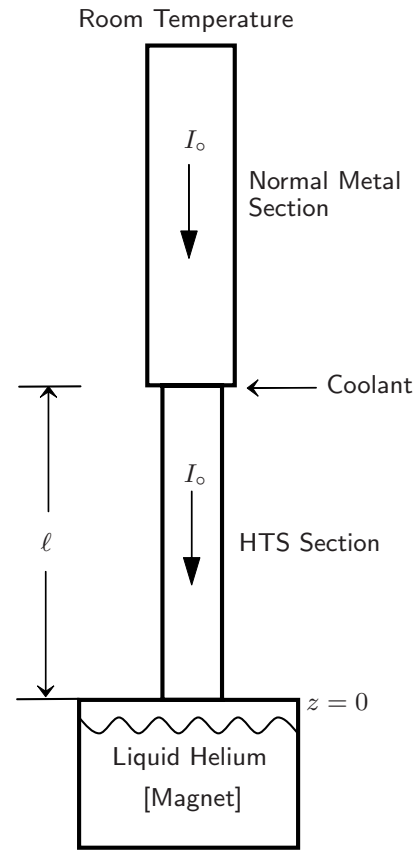

Fig. 4.21 Basic configuration of a vapor-cooled HTS lead coupled to an optimal vapor-cooled lead of normal metal. The HTS lead extends from $z=0$, generally at 4.2 K, to $z=\ell$, e.g., at 77–80 K. An extra flow of coolant is introduced at $z=\ell$.

PROBLEM 4.4: Vapor-cooled HTS current lead—FSV (continuation)

The steady-state time-independent power equation for a differential element of an HTS current lead cooled by the effluent helium vapor is given by:

$$\frac{d}{dz}\left[[A_m]_{fs}k_m(T)\frac{dT}{dz}\right] - [\dot{m}_h]_{fs}c_p(T)\frac{dT}{dz} = 0 \tag{4.56}$$

It is assumed here that heat transfer between the lead and helium vapor is perfect, with zero temperature difference between the two.

In Eq. 4.56, $[A_m]_{fs}$ is the total cross sectional area in the FSV lead of HTS matrix (normal) metal, e.g., Ag-Au in Bi2223 tape: $[A_m]_{fs} = N_{fs}a_m$, where a_m is the matrix cross sectional area of an individual tape; N_{fs} is the number of parallel HTS tapes; $k_m(T)$ is the thermal conductivity of the matrix metal; $[\dot{m}_h]_{fs}$ is the helium flow rate; and $c_p(T)$ is the specific heat of helium. We linearize Eq. 4.56 by making $k_m(T) = \tilde{k}$ and $c_p(T) = \tilde{c}_p$, both constants, respectively, temperature-averaged $k_m(T)$ and $c_p(T)$ over the range from T_0 at $z=0$ to T_ℓ at $z=\ell$, Thus:

$$[A_m]_{fs}\tilde{k}\frac{d^2T}{dz^2} - [\dot{m}_h]_{fs}\tilde{c}_p\frac{dT}{dz} = 0 \tag{4.57}$$

Equation 4.57 may be solved for $T(z)$:

$$T(z) = T_0 + \left(\frac{T_\ell - T_0}{e^{[\alpha]_{fs}} - 1}\right)\left[e^{[\alpha]_{fs}(z/\ell)} - 1\right] \tag{4.58}$$

where, $[\alpha]_{fs}$, a dimensionless quantity, is given by:

$$[\alpha]_{fs} = \frac{[\dot{m}_h]_{fs}\tilde{c}_p\ell}{\tilde{k}[A_m]_{fs}} \tag{4.59}$$

a) Show that $[Q_{in}]_{fs}$, the heat input to the helium bath ($z=0$), is given by:

$$[Q_{in}]_{fs} = \frac{\tilde{k}[A_m]_{fs}h_L}{\tilde{c}_p\ell}\ln\left[\frac{\tilde{c}_p(T_\ell - T_0)}{h_L} + 1\right] \tag{4.60}$$

where h_L is the latent heat of vaporization of helium. Note that $[Q_{in}]_{fs}$, unlike $Q_{I_\circ} \propto I_\circ$ (from Eq. 4.32*a*) for the vapor-cooled copper lead, is proportional not to current but to N_{fs} through $[A_m]_{fs} = N_{fs}a_m$.

b) Show that the difference between $[Q_{in}]_{fs}$ and $[Q_\ell]_{fs}$, the heat conducted into the FSV lead from the copper lead at $z = \ell$, is equal to the difference in enthalpy energy of the effluent helium vapor at $z=\ell$ (T_ℓ) and $z=0$ (T_0):

$$[Q_\ell]_{fs} - [Q_{in}]_{fs} = [\dot{m}_h]_{fs}\tilde{c}_p(T_\ell - T_0) \tag{4.61}$$

Answer to TRIVIA 4.4: Pluto (~40, in K); MgB_2 (39); $CrBr_3$ (37); N_2 (35.6).

Solution to PROBLEM 4.4

a) From Eq. 4.58, we may first solve for $dT/dz|_0$ (dT/dz at $z=0$). Then, $[Q_{in}]_{fs}$:

$$[Q_{in}]_{fs} = \tilde{k}[A_m]_{fs}\left.\frac{dT}{dz}\right|_0 = [\dot{m}_h]_{fs}h_L \tag{S4.1}$$

Evaluating $dT/dz|_0$ from Eq. 4.58 and inserting $[\alpha]_{fs}$ given by Eq. 4.59, we obtain:

$$\begin{aligned}\tilde{k}[A_m]_{fs}\left.\frac{dT}{dz}\right|_0 &= \tilde{k}[A_m]_{fs}\left(\frac{T_\ell - T_0}{e^{[\alpha]_{fs}}-1}\right)\frac{[\alpha]_{fs}}{\ell} \\ &= \left(\frac{T_\ell - T_0}{e^{[\alpha]_{fs}}-1}\right)[\dot{m}_h]_{fs}\tilde{c}_p = [\dot{m}_h]_{fs}h_L \end{aligned}\tag{S4.2}$$

Solving Eq. $S4.2$ for $e^{[\alpha]_{fs}}$, we have:

$$e^{[\alpha]_{fs}} = \frac{\tilde{c}_p(T_\ell - T_0)}{h_L} + 1 \tag{S4.3a}$$

$$[\alpha]_{fs} = \ln\left[\frac{\tilde{c}_p(T_\ell - T_0)}{h_L} + 1\right] \tag{S4.3b}$$

Combining Eqs. 4.59 and $S4.3b$, we have:

$$[\dot{m}_h]_{fs} = \frac{\tilde{k}[A_m]_{fs}}{\tilde{c}_p\ell}\ln\left[\frac{\tilde{c}_p(T_\ell - T_0)}{h_L} + 1\right] \tag{S4.4}$$

Substituting Eq. $S4.4$ into $S4.1$, we obtain:

$$[Q_{in}]_{fs} = \frac{\tilde{k}[A_m]_{fs}h_L}{\tilde{c}_p\ell}\ln\left[\frac{\tilde{c}_p(T_\ell - T_0)}{h_L} + 1\right] \tag{4.60}$$

Strictly, Eq. 4.60 is valid only when the system bath is continuously replenished so that its liquid level is kept constant; if it is not, a correction factor of $(1-\varrho_v/\varrho_\ell)$ is needed for $[\dot{m}_h]_{fs}h_L$ [4.63], where ϱ_v and ϱ_ℓ are respectively the densities of vapor and liquid at saturation. At 4.2 K the density ratio is 0.135: $(1-\varrho_v/\varrho_\ell)=0.865$.

b) Conduction heat into the lead at $z=\ell$ from above, $[Q_\ell]_{fs}$, is given by:

$$[Q_\ell]_{fs} = \tilde{k}[A_m]_{fs}\left.\frac{dT}{dz}\right|_\ell = [\dot{m}_h]_{fs}\tilde{c}_p\left(\frac{T_\ell - T_0}{e^{[\alpha]_{fs}}-1}\right)e^{[\alpha]_{fs}} \tag{S4.5a}$$

$$\begin{aligned}&= [\dot{m}_h]_{fs}h_L\left[\frac{\tilde{c}_p(T_\ell - T_0)}{h_L} + 1\right] \\ &= [\dot{m}_h]_{fs}\tilde{c}_p(T_\ell - T_0) + [\dot{m}_h]_{fs}h_L \end{aligned}\tag{S4.5b}$$

Combining the outboard terms of Eq. $S4.1$ and Eq. $S4.5b$, we note that:

$$[Q_\ell]_{fs} - [Q_{in}]_{fs} = [\dot{m}_h]_{fs}\tilde{c}_p(T_\ell - T_0) \tag{4.61}$$

Equation 4.61 shows that the three power terms are balanced. Namely, the difference in heat entering the lead at $z=\ell$ and that leaving the lead at $z=0$ is exactly equal to the gain in thermal power of the effluent helium vapor.

PROBLEM 4.5: Vapor-cooled HTS current lead —*C*urrent-*S*haring *V*ersion (CSV)

We study here a vapor-cooled HTS current lead in which a short section at the warm (T_ℓ) end is designed to operate in the so-called "current-sharing" mode [4.75–4.77]—current sharing is studied in ***CHAPTER 6***. This current-sharing version (CSV) of a vapor-cooled HTS lead has the same rated current as its FSV counterpart studied in **PROBLEM 4.4**. Figure 4.22 shows a linearized $I_c(T)$ plot for the superconductor in the lead, with critical currents of I_{c0} at T_0 ($z=0$) and $I_{c\ell}$ at T_ℓ ($z=\ell$). Also shown by the dotted horizontal line is the rated transport current $I_\circ$ of the lead. As indicated in the figure, $I_c(T_{cs})=I_\circ$ at T_{cs}, the temperature at which current sharing begins. The dashed line indicates the portion of $I_\circ$ in the superconductor's normal metal matrix. At T_ℓ the superconductor carries $I_{c\ell}$, and the matrix $I_\circ - I_{c\ell}$. This short section of the HTS lead dissipates Joule heat, which must be removed by the effluent helium.

Advantage of CSV

For the *same* rated transport current, the CSV lead contains fewer (N_{cs}) *expensive* HTS tapes than its FSV counterpart ($N_{cs} < N_{fs}$). Furthermore, as discussed in **PROBLEM 4.6** for 6-kA leads, the cold-end heat input of the CSV lead, despite its Joule dissipation near the warm end, is less than that of the FSV counterpart.

Analysis of Superconducting Section ($0 \le z \le \ell_{cs}$)

We first analyze the superconducting section of this CSV lead. It spans between $z=0$ at T_0 and $z=\ell_{cs}$ at T_{cs}. The temperature $T(\xi)$, with z normalized to ℓ ($\xi \equiv z/\ell$) and constant materials properties, is similar to Eq. 4.58. Thus:

$$T(\xi) = \left(\frac{T_{cs}-T_0}{e^{[\alpha_\ell]_{cs}\xi_{cs}}-1}\right)\left(e^{[\alpha_\ell]_{cs}\xi} + \frac{e^{[\alpha_\ell]_{cs}\xi_{cs}}T_0 - T_{cs}}{T_{cs}-T_0}\right) \quad (0 \le z \le \ell_{cs}) \tag{4.62}$$

With $[A_m]_{cs} = N_{cs}a_m$, $[\alpha_\ell]_{cs}$ is given by:

$$[\alpha_\ell]_{cs} \equiv \frac{[\dot{m}_h]_{cs}\tilde{c}_p\ell}{\tilde{k}[A_m]_{cs}} \tag{4.63}$$

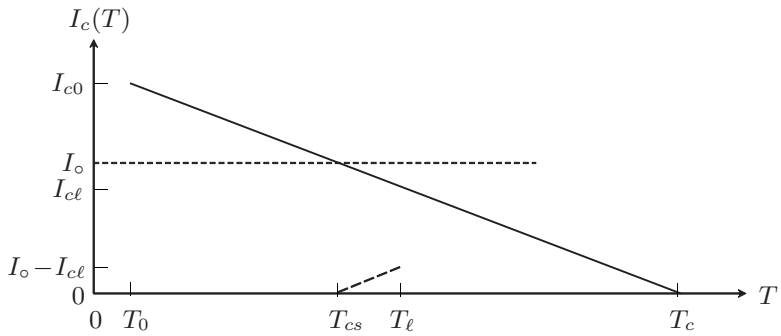

Fig. 4.22 $I_c(T)$ plot (solid line), approximated to be linear with temperature for HTS. The dotted horizontal line is the lead's rated current, $I_\circ$. The dashed line indicates the current through the matrix, $I_\circ - I_c(T)$, in the current-sharing region.

PROBLEM 4.5: Vapor-cooled HTS current lead—CSV (continuation)

a) Show, from Eq. 4.62, that $T(\xi=0)=T_0$ and $T(\xi=\xi_{cs})=T_{cs}$.

b) Show that $[Q_{in}]_{cs}$, the heat input at $z=0$ in the CSV lead, is given by:

$$[Q_{in}]_{cs} = \frac{\tilde{k}[A_m]_{cs}h_L}{\tilde{c}_p\ell_{cs}} \ln\left[\frac{\tilde{c}_p(T_{cs}-T_0)}{h_L}+1\right] \tag{4.64}$$

In practice, as we shall see in **PROBLEM 4.6**, which deals with a numerical example, ℓ_{cs} and $T_{cs}-T_0$ are, respectively, nearly equal to ℓ and $T_\ell-T_0$ of the FSV counterpart. Thus, $[Q_{in}]_{cs}<[Q_{in}]_{fs}$ comes mainly from $[A_m]_{cs}<[A_m]_{fs}$. In the process of deriving Eq. 4.64, show also that $[\alpha_\ell]_{cs}$ is given by:

$$e^{[\alpha_\ell]_{cs}\xi_{cs}} = \frac{\tilde{c}_p(T_{cs}-T_0)}{h_L}+1 \tag{4.65a}$$

$$[\alpha_\ell]_{cs} = \frac{1}{\xi_{cs}} \ln\left[\frac{\tilde{c}_p(T_{cs}-T_0)}{h_L}+1\right] \tag{4.65b}$$

Analysis of Current-Sharing Section $(\ell_{cs}\le z\le\ell)$

In the current-sharing region, between $z=\ell_{cs}$ at T_{cs} and $z=\ell$ at T_ℓ, the power per conductor length equation, with the material properties constant, is given by:

$$\tilde{k}[A_m]_{cs}\frac{d^2T}{dz^2} - [\dot{m}_h]_{cs}\tilde{c}_p\frac{dT}{dz} + \frac{\tilde{\rho}_x I_\circ(I_\circ-I_{c\ell})}{[A_m]_{cs}(T_\ell-T_{cs})}(T-T_{cs}) = 0 \qquad (\ell_{cs}\le z\le\ell) \tag{4.66}$$

The third term in Eq. 4.66 gives the Joule dissipation that takes place over this section of the CSV lead that operates in the current-sharing mode. $\tilde{\rho}_x$ is the temperature-averaged electrical resistivity of the lead over this section. With the boundary conditions, $T(\ell_{cs})=T_{cs}$ and $T(\ell)=T_\ell$, and normalizing z with ℓ, $\xi\equiv z/\ell$, we obtain in the range $\xi_{cs}\le\xi\le 1$:

$$T(\xi) = T_{cs} + \frac{(T_\ell-T_{cs})}{e^{\frac{[\alpha_\ell]_{cs}}{2}}\sin\beta_{cs}(1-\xi_{cs})} e^{\frac{[\alpha_\ell]_{cs}}{2}\xi}\sin\beta_{cs}(\xi-\xi_{cs}) \tag{4.67}$$

where, β_{cs}, another dimensionless quantity, is given by:

$$\beta_{cs} = \sqrt{\frac{\tilde{\rho}_x I_\circ(I_\circ-I_{c\ell})\ell^2}{\tilde{k}[A_m]_{cs}^2(T_\ell-T_{cs})} - \tfrac{1}{4}\left(\frac{[\dot{m}_h]_{cs}\tilde{c}_p\ell}{\tilde{k}[A_m]_{cs}}\right)^2} \tag{4.68a}$$

Combining Eqs. 4.68*a* and 4.63, we have:

$$\beta_{cs} = \sqrt{\frac{\tilde{\rho}_x I_\circ(I_\circ-I_{c\ell})\ell^2}{\tilde{k}[A_m]_{cs}^2(T_\ell-T_{cs})} - \tfrac{1}{4}[\alpha_\ell]_{cs}^2} \tag{4.68b}$$

Combining Eqs. 4.68*b* and 4.65*b*, we also have:

$$\beta_{cs} = \sqrt{\frac{\tilde{\rho}_x I_\circ(I_\circ-I_{c\ell})\ell^2}{\tilde{k}[A_m]_{cs}^2(T_\ell-T_{cs})} - \tfrac{1}{4}\left\{\frac{1}{\xi_{cs}}\ln\left[\frac{\tilde{c}_p(T_{cs}-T_0)}{h_L}+1\right]\right\}^2} \tag{4.68c}$$

PROBLEM 4.5: Vapor-cooled HTS current lead—CSV (continuation)

c) By equating conduction heat derivable from Eq. 4.62 and that derivable from Eq. 4.67, both at $\xi_{cs}=\ell_{cs}/\ell$, show that ξ_{cs} may be given by:

$$[\alpha_\ell]_{cs}e^{\frac{[\alpha_\ell]_{cs}(1+\xi_{cs})}{2}}=\frac{\beta_{cs}}{\sin\beta_{cs}(1-\xi_{cs})}\left[\frac{\tilde{c}_p(T_\ell-T_{cs})}{h_L}\right] \tag{4.69}$$

Combining Eqs. 4.65*a*, 4.65*b*, and 4.69, and noting that:

$$e^{\frac{[\alpha_\ell]_{cs}}{2}}=\left[\frac{\tilde{c}_p(T_{cs}-T_0)}{h_L}+1\right]^{1/(2\xi_{cs})} \tag{4.70a}$$

$$e^{\frac{[\alpha_\ell]_{cs}\xi_{cs}}{2}}=\left[\frac{\tilde{c}_p(T_{cs}-T_0)}{h_L}+1\right]^{1/2} \tag{4.70b}$$

We obtain:

$$\frac{1}{\xi_{cs}}\left[\frac{h_L}{\tilde{c}_p(T_\ell-T_{cs})}\right]\ln\left[\frac{\tilde{c}_p(T_{cs}-T_0)}{h_L}+1\right]\left[\frac{\tilde{c}_p(T_{cs}-T_0)}{h_L}+1\right]^{\frac{1+\xi_{cs}}{2\xi_{cs}}}=\frac{\beta_{cs}}{\sin\beta_{cs}(1-\xi_{cs})} \tag{4.71}$$

Note that for a set of parameters of a CSV lead—$\tilde{\rho}_x$, $\tilde{k}$, $[A_m]_{cs}$, $I_\circ$, $I_{c\ell}$—the only unknown parameter in Eq. 4.71 is ξ_{cs}, because the only unknown in β_{cs} (Eq. 4.68*c*) is also ξ_{cs}: ξ_{cs} must satisfy both Eqs. 4.68*c* and 4.71.

d) Show that over the fully superconducting section ($0\le z\le\ell_{cs}$) of this CSV lead, the three power terms are balanced:

$$[Q_{\ell_{cs}}]_{cs}-[Q_{in}]_{cs}=[\dot{m}_h]_{cs}\tilde{c}_p(T_{cs}-T_0) \tag{4.72}$$

where $[Q_{\ell_{cs}}]_{cs}$ is the conduction heat entering the fully superconducting section at $z=\ell_{cs}$.

e) Show that in the current-sharing region, the four power terms—$[Q_\ell]_{cs}$, the conduction into the CSV lead at $z=\ell$; Q_j, the total Joule dissipation generated within the region; $[Q_{\ell_{cs}}]_{cs}$, the conduction out of the lead at $z=\ell_{cs}$; and convective cooling, $\dot{m}_h\tilde{c}_p(T_\ell-T_{cs})$—are balanced.

$$[Q_\ell]_{cs}+Q_j-[Q_{\ell_{cs}}]_{cs}=[\dot{m}_h]_{cs}\tilde{c}_p(T_\ell-T_{cs}) \tag{4.73}$$

f) Show that:

$$[Q_\ell]_{cs}+Q_j-[Q_{in}]_{cs}=[\dot{m}_h]_{cs}\tilde{c}_p(T_\ell-T_0) \tag{4.74}$$

That is, over the entire CSV lead, power is balanced.

Solution to PROBLEM 4.5

a) By inserting $\xi=0$ into Eq. 4.62, we obtain:

$$T(0) = \left(\frac{T_{cs}-T_0}{e^{[\alpha_\ell]_{cs}\xi_{cs}}-1}\right)\left(1+\frac{e^{[\alpha_\ell]_{cs}\xi_{cs}}T_0-T_{cs}}{T_{cs}-T_0}\right)$$
$$= \left(\frac{T_{cs}-T_0}{e^{[\alpha_\ell]_{cs}\xi_{cs}}-1}\right)\left[\frac{T_0(e^{[\alpha_\ell]_{cs}\xi_{cs}}-1)}{T_{cs}-T_0}\right] = T_0 \qquad (S5.1)$$

Similarly, by inserting $\xi=\xi_{cs}$ into Eq. 4.62, we obtain:

$$T(\xi_{cs}) = \left(\frac{T_{cs}-T_0}{e^{[\alpha_\ell]_{cs}\xi_{cs}}-1}\right)\left(e^{[\alpha_\ell]_{cs}\xi_{cs}}+\frac{e^{[\alpha_\ell]_{cs}\xi_{cs}}T_0-T_{cs}}{T_{cs}-T_0}\right)$$
$$= \left(\frac{T_{cs}-T_0}{e^{[\alpha_\ell]_{cs}\xi_{cs}}-1}\right)\left[\frac{T_{cs}(e^{[\alpha_\ell]_{cs}\xi_{cs}}-1)}{T_{cs}-T_0}\right] = T_{cs} \qquad (S5.2)$$

b) We have:

$$[Q_{in}]_{cs} = \frac{\tilde{k}[A_m]_{cs}}{\ell}\left.\frac{dT}{d\xi}\right|_{\xi=0} \qquad (S5.3)$$

where $dT/d\xi$ is evaluated from $T(\xi)$ given by Eq. 4.62. Thus:

$$[Q_{in}]_{cs} = \frac{\tilde{k}[A_m]_{cs}}{\ell}\left(\frac{T_{cs}-T_0}{e^{[\alpha_\ell]_{cs}\xi_{cs}}-1}\right)[\alpha_\ell]_{cs} = [\dot{m}_h]_{cs}h_L \qquad (S5.4)$$

Combining $[\alpha_\ell]_{cs}$ given by Eqs. 4.63 and $S5.4$, we obtain:

$$e^{[\alpha_\ell]_{cs}\xi_{cs}} = \frac{\tilde{c}_p(T_{cs}-T_0)}{h_L}+1 \qquad (4.65a)$$

$$[\alpha_\ell]_{cs} = \frac{1}{\xi_{cs}}\ln\left[\frac{\tilde{c}_p(T_{cs}-T_0)}{h_L}+1\right] \qquad (4.65b)$$

Finally, by combining Eqs. $S5.3$ and $4.65b$, and noting $\xi_{cs}\ell=\ell_{cs}$, we have:

$$[Q_{in}]_{cs} = \frac{\tilde{k}[A_m]_{cs}h_L}{\tilde{c}_p\ell_{cs}}\ln\left[\frac{\tilde{c}_p(T_{cs}-T_0)}{h_L}+1\right] \qquad (4.64)$$

Although $\ell_{cs}<\ell$, $[Q_{in}]_{cs}<[Q_{in}]_{fs}$, given by Eq. 4.60 for FSV, because $[A_m]_{cs}/\ell_{cs}$ is generally less, at most ~80% of $[A_m]_{fs}/\ell$ for FSV. Also note that $T_{cs}-T_0<T_\ell-T_0$, which also contributes to making $[Q_{in}]_{cs}<[Q_{in}]_{fs}$.

Solution to PROBLEM 4.5 (continuation)

c) We can solve for ξ_{cs} by equating the temperature slope derivable from Eq. 4.62 and that derivable from Eq. 4.67, both at $\xi_{cs}=\ell_{cs}/\ell$.

$$\text{(from Eq. 4.62)} \qquad \left.\frac{dT}{d\xi}\right|_{\ell_{cs}} = \frac{[\alpha_\ell]_{cs}e^{[\alpha_\ell]_{cs}\xi_{cs}}(T_{cs}-T_0)}{(e^{[\alpha_\ell]_{cs}\xi_{cs}}-1)} \tag{S5.5a}$$

$$\text{(from Eq. 4.67)} \qquad \left.\frac{dT}{d\xi}\right|_{\ell_{cs}} = \frac{\beta_{cs}e^{\frac{[\alpha_\ell]_{cs}\xi_{cs}}{2}}(T_\ell-T_{cs})}{e^{\frac{[\alpha_\ell]_{cs}}{2}}\sin\beta_{cs}(1-\xi_{cs})} \tag{S5.5b}$$

Equating Eqs. $S5.5a$ and $S5.5b$, we obtain:

$$\frac{[\alpha_\ell]_{cs}e^{[\alpha_\ell]_{cs}\xi_{cs}}(T_{cs}-T_0)}{(e^{[\alpha_\ell]_{cs}\xi_{cs}}-1)} = \frac{\beta_{cs}e^{\frac{[\alpha_\ell]_{cs}\xi_{cs}}{2}}(T_\ell-T_{cs})}{e^{\frac{[\alpha_\ell]_{cs}}{2}}\sin\beta_{cs}(1-\xi_{cs})} \tag{S5.6}$$

Equation $S5.6$ may be rearranged and combined with Eqs. 4.70 to obtain Eq. 4.71.

d) From Eq. $S5.5a$, we may compute $[Q_{\ell_{cs}}]_{cs}$:

$$\begin{aligned}[Q_{\ell_{cs}}]_{cs} &= \frac{\tilde{k}[A_m]_{cs}}{\ell}\left.\frac{dT}{d\xi}\right|_{\ell_{cs}} \\ &= \tilde{k}[A_m]_{cs}\frac{[\alpha_\ell]_{cs}e^{[\alpha_\ell]_{cs}\xi_{cs}}(T_{cs}-T_0)}{\ell(e^{[\alpha_\ell]_{cs}\xi_{cs}}-1)}\end{aligned} \tag{S5.7}$$

With $[\alpha_\ell]_{cs}$ given by Eq. 4.63 and $e^{[\alpha_\ell]_{cs}\xi_{cs}}$ derivable from Eq. 4.70b, we obtain:

$$\begin{aligned}[Q_{\ell_{cs}}]_{cs} &= \tilde{k}[A_m]_{cs}\frac{[\dot{m}_h]_{cs}\tilde{c}_p\ell}{\tilde{k}[A_m]_{cs}}\times\frac{\left[\frac{\tilde{c}_p(T_{cs}-T_0)}{h_L}+1\right](T_{cs}-T_0)}{\ell\left[\frac{\tilde{c}_p(T_{cs}-T_0)}{h_L}\right]} \\ &= [\dot{m}_h]_{cs}h_L\left[\frac{\tilde{c}_p(T_{cs}-T_0)}{h_L}+1\right]\end{aligned} \tag{S5.8}$$

Because $[Q_{in}]_{cs}=[\dot{m}_h]_{cs}h_L$, combining this with Eq. $S5.8$, we have:

$$[Q_{\ell_{cs}}]_{cs} - [Q_{in}]_{cs} = [\dot{m}_h]_{cs}\tilde{c}_p(T_{cs}-T_0) \tag{4.72}$$

That is, within the fully superconducting section of a CSV lead, power is balanced.

e) $[Q_\ell]_{cs}$, the conduction into the lead at $z=\ell$ may be evaluated from Eq. 4.67:

$$\begin{aligned}[Q_\ell]_{cs} = \frac{\tilde{k}[A_m]_{cs}}{\ell}\left.\frac{dT}{d\xi}\right|_{\ell} &= \frac{\tilde{k}[A_m]_{cs}(T_\ell-T_{cs})}{\ell e^{[\alpha_\ell]_{cs}}\sin\beta_{cs}(1-\xi_{cs})} \\ &\quad\times e^{[\alpha_\ell]_{cs}}\left[\tfrac{1}{2}[\alpha_\ell]_{cs}\sin\beta_{cs}(1-\beta_{cs})+\beta_{cs}\cos\beta_{cs}(1-\xi_{cs})\right] \\ &= \frac{\tilde{k}[A_m]_{cs}(T_\ell-T_{cs})}{\ell}\left[\tfrac{1}{2}[\alpha_\ell]_{cs}+\beta_{cs}\cot\beta_{cs}(1-\xi_{cs})\right]\end{aligned} \tag{S5.9}$$

Solution to PROBLEM 4.5 (continuation)

$[Q_{\ell_{cs}}]_{cs}$, the conduction out of the lead at $z=\ell_{cs}$ may be evaluated from Eq. $S5.5b$:

$$[Q_{\ell_{cs}}]_{cs} = \frac{\tilde{k}[A_m]_{cs}}{\ell}\frac{dT}{d\xi}\bigg|_{\ell_{cs}} = \frac{\tilde{k}[A_m]_{cs}(T_\ell - T_{cs})}{\ell}\left[\beta_{cs}\frac{e^{\frac{[\alpha_\ell]_{cs}\xi_{cs}}{2}}}{e^{\frac{[\alpha_\ell]_{cs}}{2}}\sin\beta_{cs}(1-\xi_{cs})}\right] \quad (S5.10)$$

By inserting $T(\xi)$, given by Eq. 4.67 (with $\xi = z/\ell$), into the last term of the left-hand side of Eq. 4.66 and integrating from $\xi=\xi_{cs}$ to $\xi=1$, we evaluate Q_j:

$$Q_j = \frac{\tilde{\rho}_x I_\circ (I_\circ - I_{c\ell})\ell}{[A_m]_{cs}e^{\frac{[\alpha_\ell]_{cs}}{2}}\sin\beta_{cs}(1-\xi_{cs})}\int_{\xi_{cs}}^{1} e^{\frac{[\alpha_\ell]_{cs}}{2}\xi}\sin\beta_{cs}(\xi-\xi_{cs})\,d\xi \quad (S5.11)$$

Making $x=\xi-\xi_{cs}$, we can integrate Eq. $S5.11$ and obtain:

$$Q_j = \frac{4\tilde{\rho}_x I_\circ (I_\circ - I_{c\ell})\ell e^{\frac{[\alpha_\ell]_{cs}\xi_{cs}}{2}}}{[A_m]_{cs}e^{\frac{[\alpha_\ell]_{cs}}{2}}\sin\beta_{cs}(1-\xi_{cs})\,([\alpha_\ell]_{cs}^2+4\beta_{cs}^2)} \times \left| e^{\frac{[\alpha_\ell]_{cs}}{2}x}\left(\frac{[\alpha_\ell]_{cs}}{2}\sin\beta_{cs}x - \beta_{cs}\cos\beta_{cs}x\right)\right|_0^{1-\xi_{cs}} \quad (S5.12a)$$

$$= \frac{4\tilde{\rho}_x I_\circ (I_\circ - I_{c\ell})\ell}{[A_m]_{cs}e^{\frac{[\alpha_\ell]_{cs}}{2}}\sin\beta_{cs}(1-\xi_{cs})\,([\alpha_\ell]_{cs}^2+4\beta_{cs}^2)} \times \left[\frac{[\alpha_\ell]_{cs}}{2}e^{\frac{[\alpha_\ell]_{cs}}{2}}\sin\beta_{cs}(1-\xi_{cs}) - \beta_{cs}e^{\frac{[\alpha_\ell]_{cs}}{2}}\cos\beta_{cs}(1-\xi_{cs}) + \beta_{cs}e^{\frac{[\alpha_\ell]_{cs}\xi_{cs}}{2}}\right] \quad (S5.12b)$$

From Eq. 4.68b we may derive:

$$[\alpha_\ell]_{cs}^2 + 4\beta_{cs}^2 = \frac{4\tilde{\rho}_x I_\circ (I_\circ - I_{c\ell})\ell^2}{\tilde{k}[A_m]_{cs}^2(T_\ell - T_{cs})} \quad (S5.13)$$

Combining Eqs. $S5.12b$ and $S5.13$, we obtain:

$$Q_j = \frac{\tilde{k}[A_m]_{cs}(T_\ell - T_{cs})}{\ell} \times \left[\frac{1}{2}[\alpha_\ell]_{cs} - \beta_{cs}\cot\beta_{cs}(1-\xi_{cs}) + \beta_{cs}\frac{e^{\frac{[\alpha_\ell]_{cs}\xi_{cs}}{2}}}{e^{\frac{[\alpha_\ell]_{cs}}{2}}\sin\beta_{cs}(1-\xi_{cs})}\right] \quad (S5.14)$$

Combining Eqs. $S5.9$, $S5.10$, and $S5.14$, we obtain:

$$[Q_\ell]_{cs} + Q_j - [Q_{\ell_{cs}}]_{cs} = \frac{\tilde{k}[A_m]_{cs}(T_\ell - T_{cs})}{\ell}[\alpha_\ell]_{cs} \quad (S5.15)$$

And from Eqs. $S5.15$ and 4.63:

$$[Q_\ell]_{cs} + Q_j - [Q_{\ell_{cs}}]_{cs} = [\dot{m}_h]_{cs}\tilde{c}_p(T_\ell - T_{cs}) \quad (4.73)$$

f) By adding Eqs. 4.72 and 4.73, we obtain:

$$[Q_\ell]_{cs} + Q_j - [Q_{in}]_{cs} = [\dot{m}_h]_{cs}\tilde{c}_p(T_\ell - T_0) \quad (4.74)$$

Thermal Conductivity & Electrical Resistivity Data of Ag-Au Alloys

Figures 4.23 and 4.24 present, respectively, thermal conductivity and electrical resistivity data of Ag-Au alloys [4.78]. Although "pure" silver used in Bi2223 has an advantage of very small electrical resistivity, its thermal conductivity is too great for current leads. A compromise has been to replace pure Ag with Ag-Au in Bi2223 manufactured specifically for use in current leads.

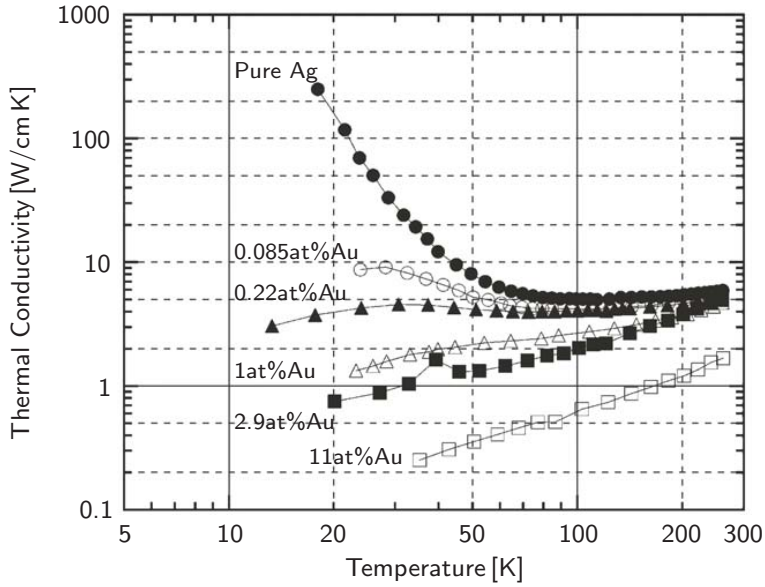

Fig. 4.23 Thermal conductivity vs. temperature data of selected Ag-Au alloys [4.78].

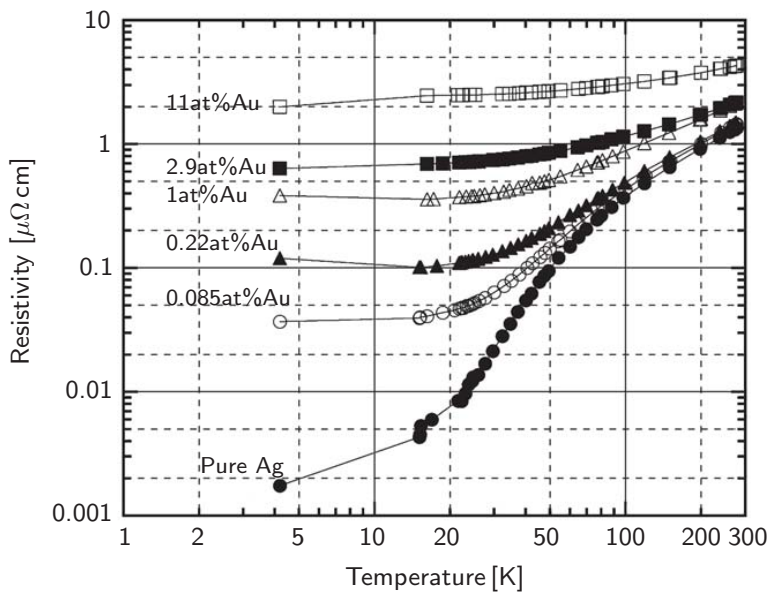

Fig. 4.24 Electrical resistivity vs. temperature data of selected Ag-Au alloys [4.78].

DISCUSSION 4.16: Protection of FSV and CSV Current Leads

Because each HTS tape (Bi2223/Ag-Au in **PROBLEM 4.5**) in either an FSV or a CSV lead has a relatively large $i_c(T_\ell)$ with a relatively small a_m, when driven normal it generates a large Joule dissipation in comparison with the available convective cooling: neither lead is capable of surviving an episode of even a short period of flow stoppage. To protect against such a fault-mode incident, the lead must be paralleled with normal-metal tapes that not only reduce Joule dissipation but also increase the cooling surface area.

FSV $[Q_{in}]_{fs}$ for an FSV lead will be modified to $[Q_{in}]^n_{fs}$, given by:

$$[Q_{in}]^n_{fs} = \frac{[\widetilde{kA}]^n_{fs} h_L}{\tilde{c}_p \ell} \ln\left[\frac{\tilde{c}_p(T_\ell - T_0)}{h_L} + 1\right] \tag{4.75}$$

where

$$[\widetilde{kA}]^n_{fs} = \tilde{k}[A_m]_{fs} + \tilde{k}_n[A_n]_{fs} \tag{4.76}$$

$\tilde{k}_n$ and $[A_n]_{fs}$ are, respectively, the thermal conductivity and total cross sectional area of the normal metal tapes paralleled to the HTS tapes. Note that for the sake of protection, heat input to the liquid helium is increased because $[Q_{in}]^n_{fs} > [Q_{in}]_{fs}$, as given by Eq. 4.60. $[\alpha]_{fs}$, given by Eq. 4.59, is modified to:

$$[\alpha_\ell]^n_{fs} = \frac{[\dot{m}_h]^n_{fs} \tilde{c}_p \ell}{[\widetilde{kA}]^n_{fs}} \tag{4.77a}$$

$$= \ln\left[\frac{\tilde{c}_p(T_\ell - T_0)}{h_L} + 1\right] \tag{4.77b}$$

where $[\dot{m}_h]^n_{fs}$ is the effluent helium mass flow rate for an FSV lead paralleled with normal metal tapes.

$$[Q_\ell]_{cs} + Q_j - [Q_{in}]_{cs} = \dot{m}_h \tilde{c}_p (T_\ell - T_0) \tag{4.74}$$

CSV For a CSV lead, $[Q_{in}]_{cs}$, given by Eq. 4.64, is modified to $[Q_{in}]^n_{cs}$:

$$[Q_{in}]^n_{cs} = \frac{[\widetilde{kA}]^n_{cs} h_L}{\tilde{c}_p \ell_{cs}} \ln\left[\frac{\tilde{c}_p(T_{cs} - T_0)}{h_L} + 1\right] \tag{4.78}$$

$$[\widetilde{kA}]^n_{cs} = \tilde{k}[A_m]_{cs} + \tilde{k}_n[A_n]_{cs} \tag{4.79}$$

where $[A_n]_{cs}$ is the total cross sectional area of normal metal tapes used in a CSV lead. Note that ℓ_{cs} remains the same whether the CSV lead is paralleled with normal metal tapes or not. Note also that because $[A_m]_{fs}$ and $[A_m]_{cs}$ are different, $[A_n]_{fs}$ and $[A_n]_{cs}$ can be different. $[\alpha_\ell]_{cs}$ also is different:

$$[\alpha_\ell]^n_{cs} = \frac{[\dot{m}_h]^n_{cs} \tilde{c}_p \ell}{[\widetilde{kA}]^n_{cs}} \tag{4.80a}$$

$$= \frac{1}{\xi_{cs}} \ln\left[\frac{\tilde{c}_p(T_{cs} - T_0)}{h_L} + 1\right] \tag{4.80b}$$

where $[\dot{m}_h]^n_{cs}$ and $\xi_{cs} (= \ell_{cs}/\ell)$ are, respectively, the helium mass flow rate and dimensionless length from $z = 0$ at which the current-sharing region starts for a CSV lead paralleled with normal metal tapes.

DISCUSSION 4.16: Protection of FSV and CSV Leads (continuation)

For the CSV lead, β_{cs} also is modified:

$$\beta_{cs}^{n} = \sqrt{\frac{\tilde{\rho}_x \tilde{\rho}_n I_\circ (I_\circ - I_{c\ell}) \ell^2}{[\widetilde{kA}]_{cs}^{n} [\widetilde{\rho A}]_{cs}^{n} (T_\ell - T_{cs})} - \tfrac{1}{4} ([\alpha_\ell]_{cs}^{n})^2} \tag{4.81}$$

where

$$[\widetilde{\rho A}]_{cs}^{n} = \tilde{\rho}_x [A_n]_{cs} + \tilde{\rho}_n [A_m]_{cs} \tag{4.82}$$

Equation 4.71 is modified as given below:

$$\frac{1}{\xi_{cs}} \left[\frac{h_L}{\tilde{c}_p (T_\ell - T_{cs})} \right] \ln \left[\frac{\tilde{c}_p (T_{cs} - T_0)}{h_L} + 1 \right] \left[\frac{\tilde{c}_p (T_{cs} - T_0)}{h_L} + 1 \right]^{\frac{1+\xi_{cs}}{2\xi_{cs}}} = \frac{\beta_{cs}^{n}}{\sin \beta_{cs}^{n} (1 - \xi_{cs})} \tag{4.83}$$

Electricity

—Passage from Helen Davis' *The Chemical Elements* [4.79]

Among the special uses for certain elements, none is more remarkable than the dependence of electrical industry upon copper. Its softness and ductility allow the metal to be drawn into wire which carries the electric current, and its electrical conductivity is greater than that of any other suitable metal except silver [and now, obviously, superconductors].

Alessandro Volta (1745–1827) *in 1800 wrote to Sir Joseph Banks,* describing a piece of apparatus he had built: "The apparatus of which I speak to you, and which without doubt will surprise you, is only the assemblage of a number of good conductors of different sorts, arranged in a certain number, 30, 40, 60 pieces, preferably, of copper, or better silver, each touching a piece of tin, or, which is better, of zinc, and an equal number of layers of water, or some other liquid which should be a better conductor than simple water like salt water, lye solution, etc., or pieces of cardboard, leather, etc., well soaked in these liquids; of which pads interposed between each couple or combination of the two different metals, alternating with each set, and always in the same order, of the three sorts of conductors; that is all there is to my new instrument."*

Volta drew sparks from his battery, felt light shocks in the wrists of both hands when he touched the top and bottom plates with wet fingers, and admired the way it would, after each discharge, re-establish itself—"an inexhaustible charge, a perpetual effect." He did not notice the slight corrosion of the metal which accounts for the source of the electric current.

* The English botanist Sir Joseph Banks (1743–1820) was "that convenient but rare phenomenon, a scientist of great independent wealth who spends that wealth liberally in the support of science. While still a student at Oxford he financed a lectureship in botany, which is how the subject came to be taught there for the first time." [4.27]

DISCUSSION 4.17: HTS Current Lead—Copper Extension

Because *all* HTS current leads, at least those currently available, are usable only up to $T_\ell \sim 80\,\mathrm{K}$, every HTS lead, vapor-cooled or not, must be connected to a normal-metal lead to reach the room-temperature terminal. For any vapor-cooled HTS current lead, an optimal vapor-cooled copper lead is the logical choice. However, as mentioned earlier, Q_{in} at 4.2 K of any of these HTS current leads is necessarily smaller than that of an optimal vapor-cooled copper lead rated for the same $I_\circ$. That is, the helium flow rate generated by the HTS lead is insufficient for the copper lead. Extra coolant (see Fig. 4.21) must be introduced at the cold end of the copper lead. Here, the effluent helium vapor of the HTS section is not mixed with the new coolant to be introduced at ∼80 K; it is diverted away, cold. Basically there are two choices for the new coolant: 1) cold gas (helium or nitrogen); and 2) liquid nitrogen boiling at 77.3 K.

A. Coolant Fluid Flow Rate

To determine the minimum coolant flow rate to be introduced at the cold end of the copper lead, we analyze here an optimal vapor-cooled copper current lead in the temperature range ∼80 K–300 K. For a copper lead carrying $I_\circ$ and cooled with fluid mass flow rate, $\dot{m}_{fl}$, the steady-state ($dT/dt = 0$) power equation, with $\zeta \equiv z/\ell_{cu}$, for a differential element of the copper current lead is given by:

$$\frac{\tilde{k}_{cu} A_{cu}}{\ell_{cu}^2} \frac{d^2T}{d\zeta^2} - \frac{\dot{m}_{fl} \tilde{c}_{fl}}{\ell_{cu}} \frac{dT}{d\zeta} + \frac{I_\circ^2 \gamma_{cu}}{A_{cu}} (T - T_\circ) + \frac{I_\circ^2 \rho_\circ}{A_{cu}} = 0 \tag{4.84}$$

In Eq. 4.84 $\tilde{k}_{cu}$ and $\tilde{c}_{fl}$ are, respectively, the T-averaged copper thermal conductivity and the fluid specific heat; γ_{cu} and $\rho_\circ$ are, respectively, the resistivity temperature coefficient and resistivity at the cold-end temperature, $T_\circ$ (here 77 K). Because over most of the 77–293 K range the last term in the left-hand side of Eq. 4.84 is negligible compared with the third term, Eq. 4.84 may be simplified to:

$$\frac{d^2T}{d\zeta^2} - \left(\frac{\dot{m}_{fl} \tilde{c}_{fl} \ell_{cu}}{\tilde{k}_{cu} A_{cu}} \right) \frac{dT}{d\zeta} + \left(\frac{I_\circ^2 \gamma_{cu} \ell_{cu}^2}{\tilde{k}_{cu} A_{cu}^2} \right) (T - T_\circ) = 0 \tag{4.85}$$

With $T(\zeta = 1) \equiv T_{\ell_{cu}}$, $T(0) \equiv T_\circ$, and $\theta(\zeta) \equiv T(\zeta) - T_\circ$, $\theta(\zeta)$ may be given by:

$$\theta(\zeta) = \frac{T_{\ell_{cu}} - T_\circ}{e^{\alpha_{cu}} \sin \beta_{cu}} e^{\alpha_{cu} \zeta} \sin \beta_{cu} \zeta \tag{4.86}$$

where

$$\alpha_{cu} = \frac{\dot{m}_{fl} \tilde{c}_{fl} \ell_{cu}}{2 \tilde{k}_{cu} A_{cu}} \tag{4.87a}$$

$$\beta_{cu} = \sqrt{\frac{I_\circ^2 \gamma_{cu} \ell_{cu}^2}{\tilde{k}_{cu} A_{cu}^2} - \left(\frac{\dot{m}_{fl} \tilde{c}_{fl} \ell_{cu}}{2 \tilde{k}_{cu} A_{cu}} \right)^2} \tag{4.87b}$$

$$= \sqrt{\frac{I_\circ^2 \gamma_{cu} \ell_{cu}^2}{\tilde{k}_{cu} A_{cu}^2} - \alpha_{cu}^2} \tag{4.87c}$$

DISCUSSION 4.17: HTS Current Lead—Copper Extension (continuation)

We may force θ_{mx} to occur at $\zeta=1$ by setting $d\theta/d\zeta|_{\zeta=1}=0$ and obtain:

$$\alpha_{cu}\sin\beta_{cu}+\beta_{cu}\cos\beta_{cu}=0 \tag{4.88a}$$

$$\alpha_{cu}+\beta_{cu}\cot\beta_{cu}=0 \tag{4.88b}$$

For a given set of lead parameters, i.e., A_{cu}, ℓ_{cu}, $I_\circ$, $\tilde{c}_{fl}$, γ_{cu}, there is a unique set of α_{cu} and β_{cu} (and thus, from Eq. 4.87*a* or 4.87*b*, a value of $\dot{m}_{fl}$) that satisfies Eq. 4.86. Note that $\cot\beta_{cu}$ must be negative, and therefore θ_{mx} must be greater than $\pi/2$, as we will see later in **PROBLEM 4.6D**.

B. Cold-End Heat Input & Power Balance

The cold-end heat input, $Q_\circ$, is given by:

$$Q_\circ=\frac{\tilde{k}_{cu}A_{cu}}{\ell_{cu}}\frac{d\theta(\zeta)}{d\zeta}\bigg|_0=\frac{\tilde{k}_{cu}A_{cu}\theta_{\ell_{cu}}\beta_{cu}}{\ell_{cu}e^{\alpha_{cu}}\sin\beta_{cu}}\simeq 0 \tag{4.89}$$

$Q_\circ\simeq 0$ because of the large value of $e^{\alpha_{cu}}$. This will indeed be the case in **PROBLEM 4.6D**, in which a 6-kA copper lead is studied.

The warm-end conduction heat, $Q_{\ell_{cu}}$ is, by definition, zero (Eq. 4.88*a*). Therefore, because no heat enters or leaves the lead by conduction from either end, the coolant is used entirely to remove the Joule dissipation, Q_j, generated in the lead:

$$\begin{aligned}Q_j&=\frac{I_\circ^2\gamma_{cu}}{A_{cu}}\int_0^{\ell_{cu}}\theta(z)\,dz\\&=\frac{I_\circ^2\gamma_{cu}\ell_{cu}}{A_{cu}}\int_0^1\theta(\zeta)\,d\zeta\end{aligned} \tag{4.90}$$

Combining Eqs. 4.86 and 4.90, and then invoking Eq. 4.87*c*, we obtain:

$$\begin{aligned}Q_j&=\frac{I_\circ^2\gamma_{cu}\ell_{cu}(T_{\ell_{cu}}-T_\circ)}{A_{cu}e^{\alpha_{cu}}\sin\beta_{cu}}\int_0^1 e^{\alpha_{cu}\zeta}\sin\beta_{cu}\zeta\,d\zeta\\&=\frac{I_\circ^2\gamma_{cu}\ell_{cu}(T_{\ell_{cu}}-T_\circ)}{A_{cu}(\alpha_{cu}^2+\beta_{cu}^2)}(\alpha_{cu}-\beta_{cu}\cot\beta_{cu})\\&\quad+(\text{terms containing } e^{-\alpha_{cu}})\\&\simeq\frac{\tilde{k}_{cu}A_{cu}}{\ell_{cu}}(T_{\ell_{cu}}-T_\circ)(\alpha_{cu}-\beta_{cu}\cot\beta_{cu})\end{aligned} \tag{4.91a}$$

Combined with Eq. 4.88*b*, Eq. 4.91*a* becomes:

$$Q_j=\frac{\tilde{k}_{cu}A_{cu}}{\ell_{cu}}(T_{\ell_{cu}}-T_\circ)(\alpha_{cu}+\alpha_{cu}) \tag{4.91b}$$

Next, combined with Eq. 4.87*a*, Eq. 4.91*b* becomes:

$$Q_j=\dot{m}_{fl}\tilde{c}_{fl}(T_{\ell_{cu}}-T_\circ) \tag{4.92}$$

Note that, as expected, Eq. 4.92 states that the Joule dissipation generated over the entire length of the copper lead is balanced by the cooling power of fluid introduced at the cold end of the lead.

DISCUSSION 4.17: HTS Current Lead—Copper Extension (continuation)

C. Liquid Nitrogen Mass Flow Rate

When 77-K liquid nitrogen is introduced at the cold end at a mass flow rate of $\dot{m}_{fl}$, it generates a cooling power, $Q_{n2} = \dot{m}_{fl} h_{n2}$, at the cold end, where $h_{n2} = 199\,\mathrm{J/g}$ is the liquid's latent heat of vaporization at 77 K.

When a vapor-cooled copper lead is operated down to the liquid helium environment, Q_{in} is matched by $\dot{m}_h h_L$, where $h_L = 20.7\,\mathrm{J/g}$ is the helium heat of vaporization; $\dot{m}_h$ of helium vapor is sufficient to keep the entire lead stable. Because $Q_\circ \simeq 0$, as remarked above, the cooling power of liquid nitrogen, $\dot{m}_{fl} h_{n2}$, cannot be matched at the cold end. What actually happens is that $\dot{m}_{fl} h_{n2}$ soaks up the Joule dissipation generated over the lower portion of the copper lead, from the cold end to a distance of $\ell_{\ell q}$. That is, the 77-K point instead of being anchored at the cold end now extends from $z = 0$ to $z = \ell_{\ell q}$. This extended 77-K portion of the lead, because it is resistive, generates Joule dissipation $Q_{j_{\ell q}}$, which is matched by $\dot{m}_{fl} h_{n2}$. Noting that the last term in the left-hand side of Eq. 4.84, neglected in Eq. 4.85, cannot be neglected at 77 K, we have:

$$Q_{j_{\ell q}} = \frac{\rho_\circ I_\circ^2 \ell_{\ell q}}{A_{cu}} = \dot{m}_{fl} h_{n2} \tag{4.93}$$

$\ell_{\ell q}$ and $\dot{m}_{fl}$ in Eq. 4.93 are not yet known.

With the lower portion of the lead ($z = \ell_{\ell q}$ long) at 77 K, the effective vapor-cooled length of the lead is shortened to $(\ell_{cu} - \ell_{\ell q})$, and Eq. 4.88*b* thus becomes:

$$\alpha'_{cu} + \beta'_{cu} \cot \beta'_{cu} = 0 \tag{4.94}$$

where

$$\alpha'_{cu} = \frac{\dot{m}_{fl} \tilde{c}_{fl} (\ell_{cu} - \ell_{\ell q})}{2 \tilde{k}_{cu} A_{cu}} \tag{4.95a}$$

$$\beta'_{cu} = \sqrt{\frac{I_\circ^2 \gamma_{cu} (\ell_{cu} - \ell_{\ell q})^2}{\tilde{k}_{cu} A_{cu}^2} - (\alpha'_{cu})^2} \tag{4.95b}$$

There is a unique combination of $\dot{m}_{fl}$ and $\ell_{\ell q}$ that satisfies both Eqs. 4.93 and 4.94.

Conversion from Wt% to At%

In the thermal conductivity and electrical resistivity data of Ag-Au (metal A–metal B) alloys shown in Figs. 4.23 and 4.24, the gold contents are given in X_{at} at%Au—an atomic weight (mole) %. However, superconductor manufacturers often express the gold content in X_{wt} wt%Au—a weight (mass) %, as in Table 4.12 next page.

The conversion from X_{wt}%B to X_{at}%B of metal B of atomic weight W_B alloyed in metal A of atomic weight W_A is given by:

$$X_{at}\%B = \frac{100 X_{wt}\%B \times W_A}{(100 - X_{wt}\%B) \times W_B + X_{wt}\%B \times W_A}$$

PROBLEM 4.6: 6-kA vapor-cooled HTS current lead

In **PROBLEM 4.6**, the design concepts discussed in **PROBLEMS 4.4** and **4.5** are applied for three types of 6-kA vapor-cooled HTS leads: A) FSV, with no parallel normal metal tapes; B) FSV, with 120 parallel normal metal tapes; and C) CSV also with the same number of normal metal tapes. Table 4.12 shows key parameters of Bi2223/Ag-Au tape. In the table, a_m is the cross sectional area of Ag-Au matrix in one tape: thus, $[A_m]_{fs} = N_{fs} a_m$; $I_c(T_\ell) = N_{fs} i_c(T_\ell)$; and $I_c(T_0) = N_{fs} i_c(T_0)$. Each tape is assumed to be exposed to a normal field of 0.2 T over its entire active length. $\tilde{k}$ and $\tilde{\rho}_x$ are, respectively, the average thermal conductivity and electrical resistivity of Ag-Au over the temperature range indicated in Table 4.12. Table 4.13 shows key parameters of brass tape.

PROBLEM 4.6A: FSV, with no parallel normal metal tapes

a) Show that $N_{fs} = 75$ for this 6-kA vapor-cooled FSV lead.

b) Show that $[Q_{in}]_{fs} = 0.0786$ W for this lead with $\ell = 20$ cm. Here, ℓ must be "long" on one hand to ensure good heat exchange with effluent vapor, while "short" on the other to limit the cost of the Bi2223/Ag-Au tapes.

c) Verify that Eq. 4.61 is satisfied for this lead by computing each power term.

Table 4.12: Parameters of Bi2223/Ag-Au Tape

Parameters		*Value*
Overall width	[mm]	4.2
Overall thickness	[mm]	0.228
Bi2223 filling (volume)	[%]	42
Au content	[wt%]	5.3
Ag-Au cross section, a_m	[mm^2]	0.555
Tape cross section	[mm^2]	0.958
$i_c(T_\ell)$ (@77.3 K @$B_\perp = 0.2$ T)	[A]	80*
$i_c(T_0)$ (@4.2 K @$B_\perp = 0.2$ T)	[A]	445.5†
$\tilde{k}$ (4.2–77 K)	[W/cm K]	0.327
$\tilde{\rho}_x$ (T_ℓ–77 K)	[$\mu\Omega$ cm]	1.0

* 1-μV/cm criterion.

† At 4.2 K the effect of $B_\perp = 0.2$ T is negligible.

Table 4.13: Parameters of Normal Metal (Brass) Tape

Parameters		*Value*
Width (each tape)	[mm]	4.203
Thickness (each tape)	[mm]	0.344
Total # of paralleled tapes		120
$[A_n]_{fs}$ and $[A_n]_{cs}$	[cm^2]	1.735
$\tilde{k}_n$ (4.2–77 K)	[W/cm K]	0.350
$\tilde{\rho}_n$ (4.2–77 K)	[$\mu\Omega$ cm]	2.25

Solution to PROBLEM 4.6A

a) Because $I_\circ = N_{fs} i_c(T_\ell)$, we have: $N_{fs} = 6{,}000\,\text{A}/80\,\text{A} = 75$.

b) With $\tilde{k} = 0.327\,\text{W/cm K}$; $[A_m]_{fs} = N_{fs} a_m = 0.416\,\text{cm}^2$; $h_L = 20.7\,\text{J/g}$; $\tilde{c}_p = 5.28\,\text{J/g K}$ (averaged between 4.2 K and 77 K) ; $T_\ell = 77.3\,\text{K}$; $T_0 = 4.2\,\text{K}$, and $\ell = 20\,\text{cm}$ into Eq. 4.60, we obtain:

$$[Q_{in}]_{fs} = \frac{\tilde{k}[A_m]_{fs} h_L}{\tilde{c}_p \ell} \ln\left[\frac{\tilde{c}_p(T_\ell - T_0)}{h_L} + 1\right] \tag{4.60}$$

$$= \frac{(0.327\,\text{W/cm K})(0.416\,\text{cm}^2)(20.7\,\text{J/g})}{(5.28\,\text{J/g K})(20\,\text{cm})} \times \ln\left[\frac{(5.28\,\text{J/g K})(77.3\,\text{K} - 4.2\,\text{K})}{(20.4\,\text{J/g})} + 1\right]$$

$$= 0.0798\,\text{W}$$

As studied in ***DISCUSSION 4.14*** (Eq. 4.32*b*), a copper vapor-cooled 6-kA lead would have had $Q_{in} \simeq 6\,\text{W}$; thus, $\sim$0.08 W is indeed an impressive improvement.

c) With $[Q_{in}]_{fs} = 0.0798\,\text{W}$, we obtain $[\dot{m}_h]_{fs} = [Q_{in}]_{fs}/h_L = 0.00385\,\text{g/s}$. Heat input at $z = \ell$ is given by the first form of Eq. *S*4.5*b*:

$$[Q_\ell]_{fs} = [\dot{m}_h]_{fs} h_L \left[\frac{\tilde{c}_p(T_\ell - T_0)}{h_L} + 1\right]$$

$$= (0.00385\,\text{g/s})(20.7\,\text{J/g}) \left[\frac{(5.28\,\text{J/g K})(77.3\,\text{K} - 4.2\,\text{K})}{(20.7\,\text{J/g})} + 1\right]$$

$$= 1.566\,\text{W}$$

Thus: $[Q_\ell]_{fs} - [Q_{in}]_{fs} = 1.486\,\text{W}$, which essentially equals $[\dot{m}_h]_{fs} \tilde{c}_p (T_\ell - T_0) = 1.487\,\text{W}$.

TRIVIA 4.5 Of the statements below on bismuth, which is *incorrect*?

i) A diamagnet with an usually large susceptibility;

ii) Like water, expands upon freezing;

iii) One of the four elements familiar to the medieval alchemist;

iv) A superconductor with a critical temperature of 0.83 K.

PROBLEM 4.6B: FSV, with parallel normal metal tapes

Here, we study an FSV lead with 120 normal metal tapes, $[A_n]_{fs} = 1.735\,\text{cm}^2$ (Table 4.13), paralleled to the FSV lead of **PROBLEM 4.6A**. Although not demonstrated here, for this lead a normal metal of 1.735-cm^2 cross section is sufficient against flow stoppage incidents that may occur in typical operating conditions.

a) Using Eq. 4.75, compute $[Q_{in}]^n_{fs}$. Because of the presence of normal metal tapes, $[A_n]_{fs} \gg [A_m]_{fs}$, $[Q_{in}]^n_{fs} \gg [Q_{in}]_{fs} = 0.0798\,\text{W}$ computed above.

b) Verify numerically that the power terms are balanced for this lead too.

Solution to PROBLEM 4.6B

a) First, we compute $[\widetilde{kA}]^n_{fs}$ using Eq. 4.76. Note that again $[A_m]_{fs} = 0.416\,\text{cm}^2$.

$$\begin{aligned}[\widetilde{kA}]^n_{fs} &= (0.327\,\text{W/cm K})(0.416\,\text{cm}^2) + (0.350\,\text{W/cm K})(1.735\,\text{cm}^2)\\ &= 0.136\,\text{W cm/K} + 0.607\,\text{W cm/K} = 0.743\,\text{W cm/K}\end{aligned}$$

From Eq. 4.75, we have:

$$[Q_{in}]^n_{fs} = \frac{[\widetilde{kA}]^n_{fs} h_L}{\tilde{c}_p \ell} \ln\left[\frac{\tilde{c}_p(T_\ell - T_0)}{h_L} + 1\right] \tag{4.75}$$

$$= \frac{(0.743\,\text{W cm/K})(20.7\,\text{J/g})}{(5.28\,\text{J/g K})(20\,\text{cm})} \times \ln\left[\frac{(5.28\,\text{J/g K})(77.3\,\text{K} - 4.2\,\text{K})}{(20.7\,\text{J/g})} + 1\right] = 0.4337\,\text{W}$$

Note that although indeed $[Q_{in}]^n_{fs} \gg [Q_{in}]_{fs}$, 0.4337 W is still only ∼1/14 of the copper counterpart (∼6 W). Also note, from Eq. 4.35*b*, that for an optimal vapor-cooled copper lead rated at 6 kA with 20-cm active length (ℓ), $A = 0.480\,\text{cm}^2$, ∼30% of $[A_n]_{fs} = 1.735\,\text{cm}^2$. Despite this large $[A_n]_{fs}$ the reason $[Q_{in}]^n_{fs}$ is still ∼1/14 of $Q_{I_\circ}$ (Eq. 4.32*a*) is principally because $\tilde{k}_n \ll k_0$, where k_0 is the copper thermal conductivity near 4.2 K, i.e., 0.350 W/cm K ($\tilde{k}_n$) vs. 6 W/cm K (k_0). Also note that this lead generates no Joule dissipation over this part (ℓ) of the lead.

b) With $[Q_{in}]^n_{fs} = 0.4337\,\text{W}$, we obtain $[\dot{m}_h]^n_{fs} = [Q_{in}]^n_{fs}/h_L \simeq 0.021\,\text{g/s}$. Heat input at $z = \ell$, $[Q_\ell]^n_{fs}$, though not derived, is *similar* to Eq. *S*4.5*b*. Thus:

$$[Q_\ell]^n_{fs} = [\dot{m}_h]^n_{fs} h_L \left[\frac{\tilde{c}_p(T_\ell - T_0)}{h_L} + 1\right]$$

$$\simeq (0.021\,\text{g/s})(20.7\,\text{J/g})\left[\frac{(5.28\,\text{J/g K})(77.3\,\text{K} - 4.2\,\text{K})}{(20.7\,\text{J/g})} + 1\right] = 8.540\,\text{W}$$

We have thus: $[Q_\ell]^n_{fs} - [Q_{in}]^n_{fs} = 8.106\,\text{W} \simeq [\dot{m}_h]^n_{fs}\tilde{c}_p(T_\ell - T_0) = 8.105\,\text{W}$.

PROBLEM 4.6C: CSV, with parallel normal metal tapes

Here, we shall consider an example of a CSV lead with $N_{cs} = (2/3)N_{fs} = 50$ and the same number (120) of normal metal tapes added as in the FSV studied above.

a) Show that $T_{cs} = 69.3\,\mathrm{K}$ for this CSV lead. Assume that $i_c(T)$ is a linear function of T, with $i_c(T_0) = 445.5\,\mathrm{A}$ and $i_c(T_\ell) = 80\,\mathrm{A}$, as given in Table 4.12.

b) For $\ell = 20\,\mathrm{cm}$ (same value as the FSV counterparts), determine ξ_{cs} for this CSV for a special—simple—case in which:

$$\sin\beta_{cs}^n(1-\xi_{cs}) = 1 \tag{4.96a}$$

$$\beta_{cs}^n(1-\xi_{cs}) = \pi/2 \tag{4.96b}$$

You may determine ξ_{cs} iteratively, first guessing a value of ξ_{cs}, compute β_{cs}^n from Eq. 4.96*b*, then insert ξ_{cs} and β_{cs}^n into Eq. 4.83 to see if Eq. 4.83 is indeed satisfied. Because $i_c(T)$ is assumed a linear function of T, an appropriate starting value of ξ_{cs} into Eq. 4.96*b* may be 0.9 ($\simeq 69.3/77.3$).

c) Verify that β_{cs}^n found in **b)** agrees with β_{cs}^n computed by Eq. 4.81.

d) Compute $[Q_{in}]_{cs}^n$, the heat input to liquid helium at $z=0$, given by Eq. 4.78.

e) Numerically compute each term appearing in the following power balance equation and demonstrate that power is balanced.

$$[Q_\ell]_{cs}^n + [Q_j]_{cs}^n - [Q_{in}]_{cs}^n = [\dot{m}_h]_{cs}^n \tilde{c}_p(T_\ell - T_0) \tag{4.97}$$

$[Q_\ell]_{cs}^n$ is the heat into the lead at $z=\ell$; $[Q_j]_{cs}^n$ is the Joule dissipation within the current-sharing region; and $[Q_{\ell_{cs}}]_{cs}$ is the heat out of the lead at $z=\ell_{cs}$. $[Q_\ell]_{cs}^n$ and $[Q_j]_{cs}^n$ are given by *modified* forms of Eq. $S5.9$ and Eq. $S5.14$:

$$[Q_\ell]_{cs}^n = \frac{[\widetilde{kA}]_{cs}^n(T_\ell - T_{cs})}{\ell}\left[\tfrac{1}{2}[\alpha_\ell]_{cs}^n + \beta_{cs}^n\cot\beta_{cs}^n(1-\xi_{cs})\right] \tag{4.98}$$

$$[Q_j]_{cs}^n = \frac{[\widetilde{kA}]_{cs}^n(T_\ell - T_{cs})}{\ell}\left[\tfrac{1}{2}[\alpha_\ell]_{cs}^n - \beta_{cs}^n\cot\beta_{cs}^n(1-\xi_{cs}) + \beta_{cs}^n\frac{e^{\frac{[\alpha_\ell]_{cs}^n\xi_{cs}}{2}}}{e^{\frac{[\alpha_\ell]_{cs}^n}{2}}\sin\beta_{cs}^n(1-\xi_{cs})}\right] \tag{4.99}$$

Note that because $\beta_{cs}^n(1-\xi_{cs}) = \pi/2$ here, Eqs. 4.98 and 4.99 are simplified:

$$[Q_\ell]_{cs}^n = \frac{[\widetilde{kA}]_{cs}^n(T_\ell - T_{cs})}{\ell} \times \tfrac{1}{2}[\alpha_\ell]_{cs}^n \tag{4.100}$$

$$[Q_j]_{cs}^n = \frac{[\widetilde{kA}]_{cs}^n(T_\ell - T_{cs})}{\ell}\left[\tfrac{1}{2}[\alpha_\ell]_{cs}^n + \beta_{cs}^n e^{\frac{[\alpha_\ell]_{cs}^n(\xi_{cs}-1)}{2}}\right] \tag{4.101}$$

Solution to PROBLEM 4.6C

a) Because $I_c(T_\ell) = N_{cs} i_c(T_\ell)$, with $N_{cs} = 50$ and, from Table 4.12, $i_c(T_\ell) = 80\,\text{A}$, we have: $I_c(T_\ell) = 50 \times 80\,\text{A} = 4{,}000\,\text{A}$ at $T_\ell = 77.3\,\text{K}$; similarly, $I_c(T_0) = 22{,}275\,\text{A}$ at $T_0 = 4.2\,\text{K}$. Thus, this particular set of Bi2223/Ag-Au tapes has the following $I_c(T)$ between 77.3 K and 4.2 K:

$$I_c(T) = 23{,}325 - 250T \;\;[\text{A}] \qquad (S6C.1)$$

where T is in kelvins. This equation gives $T_c = 93.3\,\text{K}$. From Eq. $S6C.1$, we can solve for T_{cs} at which $I_c(T_{cs}) = 6{,}000\,\text{A}$: $T_{cs} = 69.3\,\text{K}$.

b) As shown in Table 4.14 below, $\xi_{cs} = 0.94505$, which gives $\beta^n_{cs} = 28.586$.

c) $[A_m]_{cs} = N_{cs} a_m = 50 \times 0.555\,\text{mm}^2 (\text{from Table 4.12}) = 0.2775\,\text{cm}^2$; and $[A_n]_{cs} = [A_n]_{fs} = 1.735\,\text{cm}^2$ (Table 4.13) and thus, from Eqs. 4.79, 4.82, and 4.80b:

$$\begin{aligned}
[\widetilde{kA}]^n_{cs} &= \tilde{k}[A_m]_{cs} + \tilde{k}_n[A_n]_{cs} \qquad (4.79)\\
&= (0.327\,\text{W/cm K})(0.2775\,\text{cm}^2) + (0.350\,\text{W/cm K})(1.735\,\text{cm}^2)\\
&= 0.0907\,\text{W cm/K} + 0.607\,\text{W cm/K} = 0.698\,\text{W cm/K}
\end{aligned}$$

$$\begin{aligned}
[\widetilde{\rho A}]^n_{cs} &= \tilde{\rho}_x[A_n]_{cs} + \tilde{\rho}_n[A_m]_{cs} \qquad (4.82)\\
&= (1\,\mu\Omega\,\text{cm})(1.735\,\text{cm}^2) + (2.25\,\mu\Omega\,\text{cm})(0.2775\,\text{cm}^2)\\
&= 1.735\,\mu\Omega\,\text{cm}^3 + 0.624\,\mu\Omega\,\text{cm}^3 = 2.359\,\mu\Omega\,\text{cm}^3
\end{aligned}$$

$$\begin{aligned}
[\alpha_\ell]^n_{cs} &= \frac{1}{\xi^n_{cs}} \ln\left[\frac{\tilde{c}_p(T_{cs} - T_0)}{h_L} + 1\right] \qquad (4.80b)\\
&= \frac{1}{0.94505} \ln\left[\frac{(5.28\,\text{J/g K})(69.3\,\text{K} - 4.2\,\text{K})}{(20.7\,\text{J/g})} + 1\right]\\
&= \frac{1}{0.94505} \ln(17.605) = 3.035
\end{aligned}$$

Thus, $([\alpha_\ell]^n_{cs})^2/4$, required to compute Eq. 4.81 is given by:

$$\tfrac{1}{4}([\alpha_\ell]^n_{cs})^2 = 2.303$$

Table 4.14: Determination of ξ^n_{cs} and β^n_{cs}

Guess Value of ξ_{cs}	*Eq. 4.96b* β^n_{cs}*	*Left-Hand Side Eq. 4.83*
0.9	15.708	32.3975
0.95	31.4159	28.2120
0.94	26.1799	28.9759
0.945	28.5599	28.5898
0.9451	28.6120	28.5821
0.94505	28.5859 $\simeq$ 28.5860	

* $\sin\beta^n_{cs}(1 - \xi_{cs}) = 1$ and thus β^n_{cs} is equal to the left-hand side of Eq. 4.83.

Solution to PROBLEM 4.6C (continuation)

Inserting appropriate values into Eq. 4.81, we obtain:

$$\beta_{cs}^{n} = \sqrt{\frac{\tilde{\rho}_x \tilde{\rho}_n I_\circ (I_\circ - I_{c\ell})\ell^2}{[\widetilde{kA}]_{cs}^{n}[\widetilde{\rho A}]_{cs}^{n}(T_\ell - T_{cs})} - \tfrac{1}{4}([\alpha_\ell]_{cs}^{n})^2} \tag{4.81}$$

$$28.586 = \sqrt{\frac{(1\,\mu\Omega\,\text{cm})(2.25\,\mu\Omega\,\text{cm})(6\,\text{kA})(6\,\text{kA}-4\,\text{kA})(20\,\text{cm})^2}{(0.698\,\text{W cm/K})(2.359\,\mu\Omega\,\text{cm}^3)(77.3\,\text{K}-69.3\,\text{K})} - 2.303}$$

$$28.586 \simeq \sqrt{817.58} = 28.593$$

d) With $\xi_{cs} = 0.94505$ and $\ell = 20\,\text{cm}$: $\ell_{cs} = 18.9\,\text{cm}$. The current-sharing region for this CSV lead thus spans 1.1 cm, from $z = 18.9\,\text{cm}$ to $z = 20\,\text{cm}$. From Eq. 4.78:

$$[Q_{in}]_{cs}^{n} = \frac{[\widetilde{kA}]_{cs}^{n} h_L}{\tilde{c}_p \ell_{cs}} \ln\left[\frac{\tilde{c}_p(T_{cs} - T_0)}{h_L} + 1\right] \tag{4.78}$$

$$= \frac{(0.698\,\text{W cm/K})(20.7\,\text{J/g})}{(5.28\,\text{J/g K})(18.9\,\text{cm})} \ln\left[\frac{(5.28\,\text{J/g K})(69.3\,\text{K}-4.2\,\text{K})}{(20.7\,\text{J/g})} + 1\right]$$

$$= (0.1448\,\text{W})(2.868) = 0.4153\,\text{W}$$

Thus, as expected $[Q_{in}]_{cs}^{n} = 0.4153\,\text{W} < [Q_{in}]_{fs}^{n} = 0.4296\,\text{W}$; $[Q_{in}]_{cs}^{n}$ is $\sim 1/15$ that of a copper counterpart. From $[Q_{in}]_{cs}^{n} = 0.4153\,\text{W}$, $[\dot{m}_h]_{cs}^{n} = 0.02006\,\text{g/s}$.

e) Applying Eqs. 4.100 and 4.101, we have:

$$[Q_\ell]_{cs}^{n} = \frac{[\widetilde{kA}]_{cs}^{n}(T_\ell - T_{cs})}{\ell}\left(\frac{[\alpha_\ell]_{cs}^{n}}{2}\right) \tag{4.100}$$

$$= \frac{(0.698\,\text{W cm/K})(77.3\,\text{K}-69.3\,\text{K})}{(20\,\text{cm})}\left(\frac{3.035}{2}\right) = 0.4237\,\text{W}$$

$$[Q_j]_{cs}^{n} = \frac{[\widetilde{kA}]_{cs}^{n}(T_\ell - T_{cs})}{\ell}\left[\frac{[\alpha_\ell]_{cs}^{n}}{2} + \beta_{cs}^{n} e^{\frac{[\alpha_\ell]_{cs}^{n}(\xi_{cs}-1)}{2}}\right] \tag{4.101}$$

$$= \frac{[\widetilde{kA}]_{cs}^{n}(T_\ell - T_{cs})}{\ell}\left[\left(\frac{3.035}{2}\right) + (28.586)e^{\frac{3.035(0.945-1)}{2}}\right]$$

$$= \frac{(0.698\,\text{W cm/K})(77.3\,\text{K}-69.3\,\text{K})}{(20\,\text{cm})}\left[\left(\frac{3.035}{2}\right) + 26.30\right] = 7.7658\,\text{W}$$

With $[\dot{m}_h]_{cs}^{n}\tilde{c}_p(T_\ell - T_0) = (0.02006\,\text{g/s})(5.28\,\text{J/g K})(77.3\,\text{K}-4.2\,\text{K}) = 7.7743\,\text{W}$ and $[Q_{in}]_{cs}^{n} = 0.4153\,\text{W}$, we obtain:

$$[Q_\ell]_{cs}^{n} + [Q_j]_{cs}^{n} - [Q_{in}]_{cs}^{n} = [\dot{m}_h]_{cs}^{n}\tilde{c}_p(T_\ell - T_0) \tag{4.97}$$

$$0.4237\,\text{W} + 7.7658 - 0.4153 = 7.7742\,\text{W}$$

$$\simeq 7.7743\,\text{W}$$

DISCUSSION 4.18: "Optimal" CSV Lead

As we have seen from the numerical power check in **e)** of **PROBLEM 4.6C**, the largest power component is $[Q_j]^n_{cs} = 7.7659\,\text{W}$, yet $[Q_{in}]^n_{cs} = 0.4153\,\text{W}$ is very nearly the same as $[Q_{in}]^n_{fs} = 0.4337\,\text{W}$ for the FSV counterpart.

Thus, despite the large value of $[Q_j]^n_{cs}$, the only way this CSV lead can have $[Q_{in}]^n_{cs}$ comparable with $[Q_{in}]^n_{fs}$ is to have $[Q_\ell]^n_{cs} \ll [Q_\ell]^n_{fs}$. This is indeed the case, as may be seen from Solution **b)** of **PROBLEM 4.6B**, which shows: $[Q_\ell]^n_{fs} = 8.540\,\text{W}$, while Solution **e)** of **PROBLEM 4.6C** shows: $[Q_\ell]^n_{cs} = 0.4237\,\text{W}$. How can this be? The answer may be seen from Eq. 4.98, given again here:

$$[Q_\ell]^n_{cs} = \frac{[\widetilde{kA}]^n_{cs}(T_\ell - T_{cs})}{\ell}\left[\tfrac{1}{2}[\alpha_\ell]^n_{cs} + \beta^n_{cs}\cot\beta^n_{cs}(1-\xi_{cs})\right] \tag{4.98}$$

It is possible to make $[Q_\ell]^n_{cs} = 0$ by a suitable choice of β^n_{cs} and ξ_{cs} in the bracketed term of the right-hand side of Eq. 4.98. For $\beta^n_{cs}(1-\xi_{cs}) > \pi/2$, $\cot\beta^n_{cs}(1-\xi_{cs}) < 0$, and there indeed exists a set of β^n_{cs} and ξ_{cs} that not only makes $[Q_\ell]^n_{cs} = 0$ but also satisfies Eq. 4.83. Such a set in fact minimizes $[Q_{in}]^n_{cs}$, giving rise to an "optimal" CSV lead that is loaded with normal metal to satisfy a protection criterion.

Heike Kamerlingh Onnes (1853–1926)

—Passage from K. Mendelssohn's *The Quest for Absolute Zero* [4.80]

In 1882 the University of Leiden appointed to the chair of physics a young man of only twenty nine whose early work had already given great promise. He came from an old family in Groningen in the north of Holland,... Two years earlier [Kamerlingh] *Onnes had been much impressed by one of van der Waals' papers which dealt with the concept of corresponding states... was particularly intrigued by the prediction of the critical points of as yet unliquefied gases which could be made on the basis of the van der Waals equation...*

Although he was deeply interested in the great revolution of physical concepts and theories which was to take place during his lifetime, his main preoccupation was with the measurements from which these new ideas were to arise. He was essentially an experimentalist with a keen sense for the engineering problems involved in the perfection and proper use of scientific instruments. Without ever becoming a perfectionist, he was acutely aware of the importance of careful planning and organisation for the success of an experiment and he used these ideas on a scale which had never previously been attempted in a physical laboratory. Quite apart from the decisive role which his laboratory played in the development of low-temperature research, it also served as the model for the research institutions of the twentieth century. Kamerlingh Onnes was not only a master of organisational genius, he was also a good and patient diplomatist and a wise man. His great strength was to plan not for tomorrow but for the day after. The secret of the steady output of brilliant work which issued from his institute lay in the fact that each experiment had been thoroughly thought out and prepared long before work on it was begun.

[Kamerlingh] *Onnes was probably the first scientist to realise that the complexity of modern research techniques would require a reliable supply of skilled and specially trained assistants. He sensed that the time of the amateur professor was over, who could go into the laboratory and discover the secrets of nature in odd afternoons with the aid of string and sealing wax...*

PROBLEM 4.6D: Copper section (~80 K–300 K)

Here, we study a 6-kA vapor-cooled copper current lead that may be coupled to either the FSV lead studied in **PROBLEM 4.6B** or the CSV lead studied in **PROBLEM 4.6C**. We shall determine values of three fluid flow rates: 1) gaseous helium; 2) gaseous nitrogen; and 3) liquid nitrogen. For the liquid nitrogen case, we shall also determine the value of $\ell_{\ell q}$. Table 4.15 lists values of key parameters for a 6-kA vapor-cooled copper lead. Note that the cold end ($z = 0$) is at 77.3 K and the warm end ($z = \ell_{cu}$) is at 293 K.

a) Determine $\dot{m}_{fl}$ when the coolant is gaseous helium entering the cold-end ($z = 0$) point at 77.3 K.

b) As discussed in connection with Eq. 4.89, demonstrate here that $Q_\circ$, the cold-end conduction heat input, is indeed negligibly small.

c) Determine $\dot{m}_{fl}$ when the coolant is gaseous nitrogen entering the cold-end ($z = 0$) point at 77.3 K.

d) Determine $\dot{m}_{fl}$ when the coolant is liquid nitrogen entering the cold-end ($z = 0$) point at 77.3 K. Also determine $\ell_{\ell q}$.

Table 4.15: Parameters of 6-kA Vapor-Cooled Copper Lead

Parameters		*Value*
Operating range ($T_\circ$–$T_{\ell_{cu}}$)	[K]	77.3–300
Active area, A_{cu}	[cm^2]	1.19
Active length, ℓ_{cu}	[cm]	38
Area exposed to coolant	[cm^2]	12,650
$\tilde{k}_{cu}$ (77–300 K)	[W/cm K]	4
$\tilde{c}_{fl}$ (77–300 K): helium	[J/g K]	5.28
$\tilde{c}_{fl}$ (77–300 K): nitrogen	[J/g K]	1.04
h_{n2} (77.3 K)	[J/g]	199
$\rho_\circ$ (77 K)	[$\mu\Omega$ cm]	0.22
γ_{cu} (77–300 K)	[nΩ cm/K]	7.01

Answer to TRIVIA 4.5 iv). Although itself a nonsuperconductor (even at 0.83 K), Element 83 is a key constituent of HTS. The other three substances of the alchemist: antimony (Sb); arsenic (As); and zinc (Zn).

Solution to PROBLEM 4.6D

a) Inserting parameter values from Table 4.15 into Eq. 4.87*c*, we have:

$$\beta_{cu} = \sqrt{\frac{I_\circ^2 \gamma_{cu} \ell_{cu}^2}{\tilde{k}_{cu} A_{cu}^2} - \alpha_{cu}^2} = \sqrt{\frac{(6\,\text{kA})^2 (7.01\,\text{n}\Omega\,\text{cm/K})(38\,\text{cm})^2}{(4\,\text{W/cm K})(1.19\,\text{cm}^2)^2} - \alpha_{cu}^2}$$

$$= \sqrt{64.333 - \alpha_{cu}^2} \qquad (S6D.1)$$

There is a set of β_{cu} and α_{cu} that satisfies both Eqs. 4.88*b* and *S*6*D*.1. These two equations may be solved iteratively; Table 4.16 gives results of the iteration. From Table 4.16, we note that $\beta_{cu} = 2.786750 \simeq 2.786885$, and thus $\alpha_{cu} = 7.521055$. Solving $\dot{m}_{fl}$ from Eq. 4.87*a*, we have:

$$\dot{m}_{fl} = \frac{2\alpha_{cu} \tilde{k}_{cu} A_{cu}}{\tilde{c}_{fl} \ell_{cu}} \qquad (S6D.2)$$

$$= \frac{2(7.521)(4\,\text{W/cm K})(1.19\,\text{cm}^2)}{(5.28\,\text{J/g K})(38\,\text{cm})} = 0.357\,\text{g/s}$$

A helium mass flow rate of 0.357 g/s computed here is very close to the boiling liquid helium mass flow rate $\dot{m}_h$ corresponding to an AMI 6-kA vapor-cooled copper lead, i.e., $Q_{in} \sim 7.2\,\text{W}$: $\dot{m}_h \sim 0.35\,\text{g/s}$ ($\sim 7.2\,\text{W}/20.4\,\text{J/g}$). Note that the total cooling power between 77.3 K and 293 K is 407 W, given by $\dot{m}_{fl} \tilde{c}_{fl} (T_{\ell_{cu}} - T_\circ)$.

b) Inserting $e^{\alpha_{cu}} = e^{7.521055} = 1846$, $\sin(159.669°) = 0.3474$, $\theta_{\ell_{cu}} = 293\,\text{K} - 77\,\text{K} = 216\,\text{K}$, and other parameter values into Eq. 4.89, we obtain:

$$Q_\circ = \frac{\tilde{k}_{cu} A_{cu}}{\ell_{cu}} \frac{d\theta(\zeta)}{d\zeta}\bigg|_0 = \frac{\tilde{k}_{cu} A_{cu} \theta_{\ell_{cu}} \beta_{cu}}{\ell_{cu} e^{\alpha_{cu}} \sin \beta_{cu}} \simeq 0 \qquad (4.89)$$

$$= \frac{(4\,\text{W/cm K})(1.19\,\text{cm}^2)(216\,\text{K})(2.787)}{(38\text{cm})(1846)(0.3474)} \simeq 0.118\,\text{W} \simeq 0$$

c) The values of β_{cu} and α_{cu} determined in **a)** are also valid for gaseous nitrogen entering the cold-end ($z = 0$) at 77.3 K. The only difference between helium and nitrogen is $\tilde{c}_{fl}$, which for the latter is 1.04 J/g K. Thus: $\dot{m}_{fl} = 1.812\,\text{g/s}$.

Table 4.16: Determination of β_{cu} and α_{cu}

Eq. 4.88*b*			Eq. 4.88*b*	Eq. 4.87*c*
β_{cu} [degree]	$-\cot \beta_{cu}$	β_{cu}	α_{cu}	β_{cu}
150	1.732051	2.617994	4.534498	6.615990
160	2.747477	2.792527	7.672404	2.338207
159	2.605089	2.775074	7.229314	3.474194
159.5	2.674621	2.783800	7.445612	2.982594
159.6	2.688919	2.785545	7.490106	2.869026
159.7	2.703351	2.787291	7.535026	2.748887
159.65	2.696118	2.786418	7.512513	2.809832
159.67	2.699007	2.786767	7.521505	2.785671
159.669	2.698863	**2.786**750	7.521055	**2.786**885

Solution to PROBLEM 4.6D (continuation)

d) Here, we have to determine the value of $\ell_{\ell q}$ that satisfies Eqs. 4.93, 4.94, and 4.95 for given parameter values of $\rho_\circ$, γ_{cu}, $I_\circ$, and $\tilde{k}_{cu}$, and A_{cu}. Again, it is simplest to determine $\ell_{\ell q}$ iteratively. Thus we proceed along the following steps:

Step 1 Guess $\ell_{\ell q}$ (1^{st} column in Table 4.17);

Step 2 Compute $\dot{m}_{fl}$ from Eq. 4.93 (2^{nd} column);

Step 3 Insert $\ell_{\ell q}$ and $\dot{m}_{fl}$ into Eq. 4.95*a*, and compute α'_{cu} (3^{rd} column);

Step 4 With this α'_{cu} inserted into Eq. 4.95*b*, compute β'_{cu} (4^{th} column);

Step 5 Express this β'_{cu} in degrees (5^{th} column): it must be between 90° and 180°;

Step 6 Compute $-\cot\beta'_{cu}$ (6^{th} column);

Step 7 Compute α'_{cu} using Eq. 4.94 (7^{th} column).

If α'_{cu} computed in *Step 7* agrees with that computed in *Step 3*, the iteration process is complete and $\ell_{\ell q}$ guessed at the outset of this iteration is correct. Table 4.17 gives results of the above iteration, and it shows that $\ell_{\ell q} = 26.98\,\text{cm}$ ($\simeq 27\,\text{cm}$) and $\dot{m}_{fl} = 0.902\,\text{g/s}$ are the desired values.

Thus, with liquid nitrogen in the lower section of the copper lead, specifically over a length of $\simeq 27\,\text{cm}$, and soaked by a mixture of liquid and gaseous nitrogen, this section is at 77.3 K. Only the remaining section, extending from $z \simeq 27\,\text{cm}$ to $z = 38\,\text{cm}$ is cooled by a flow of gaseous nitrogen; its temperature rises from 77.3 K at $z \simeq 27\,\text{cm}$ to 293 K at $z = 38\,\text{cm}$.

In comparing with $\dot{m}_{fl} = 1.812\,\text{g/s}$ found in **c)** with 77.3-K gaseous nitrogen, we note that liquid nitrogen requires less ($\sim 1/2$) mass flow rate. This is because liquid nitrogen contributes a large dose of cooling upon vaporization at 77.3 K, i.e., 199 J/g, which with $\tilde{c}_{fl} = 1.04\,\text{J/g K}$ of nitrogen, is equivalent to a temperature rise of gaseous nitrogen of nearly 200 K. If the coolant to be introduced at the cold end of the copper current lead is to be 77.3-K nitrogen, the results of **c)** and **d)** suggest that 77.3-K liquid is likely preferable to 77.3-K gas.

Table 4.17: Determination of $\ell_{\ell q}$, β'_{cu}, and α'_{cu}

Eq. 4.93		Eq. 4.95*a*	Eq. 4.95*b*		Eq. 4.94	
$\ell_{\ell q}$ [cm]	$\dot{m}_{fl}$ [g/s]	α'_{cu}	β'_{cu}	β'_{cu} [degree]	$-\cot\beta'_{cu}$	α'_{cu}
10	0.3334453	1.023033	5.820835	333.5	*no solution*	
20	0.668891	1.315298	3.564382	204.2	*no solution*	
26	0.869558	1.139925	2.261869	129.595532	0.827141	1.870884
27	0.903002	1.085120	2.052632	117.607165	0.522947	1.073417
26.9	0.898304	1.089288	2.074294	118.848308	0.550853	1.142631
26.98	0.902334	1.086289	2.056789	117.845335	0.528252	1.086503
26.9805	0.902350	1.086259	2.056686	117.839402	0.528119	1.086175
26.9802	0.902340	1.086277	2.056748	117.842976	0.528199	1.086373
26.9804	0.902347	**1.0862**65	2.056706	117.840594	0.528146	**1.0862**41

PROBLEM 4.7: Vapor-cooled brass current lead

Vapor-cooled current leads for a superconducting magnet operated in a bath of liquid helium may be entirely of copper (***DISCUSSION 4.14***) or superconducting over the lower cold section (**PROBLEMS 4.4–4.6**), extended to the room-temperature terminal by a copper lead rated at the same current.

In some applications, current leads carry a rated current only occasionally or even rarely during the life of a magnet [4.81–4.84]. Examples of occasional use include magnets of low duty cycle in which the magnets are energized periodically, each time for a short duration. When the total duration of "off-current" operation far exceeds that of "on-current" operation, it may be possible to reduce the long-term consumption of helium with vapor-cooled leads having a $Q_0/Q_{I_\circ}$ ratio (Eq. 4.42) significantly smaller than the ∼0.6 achievable with copper leads.

Because $Q_0 \propto \tilde{k}$ (Eq. 4.40), such low-Q_0 leads should be of an alloy (e.g., brass), rather than pure copper. It necessarily implies that such an alloy lead would have Joule dissipation rate greater than its copper counterpart. Because the effluent helium flow rate would remain roughly the same, to be effective, the alloy lead must operate in overcurrent mode, and the thermal behavior of such a lead in overcurrent mode becomes an important design and operation issue [4.85].

For the questions below, use the following property values for brass: thermal conductivity, $[k_0]_{br} = 22\,\mathrm{W/m\,K}$, and resistivity, $[\rho_0]_{br} = 21\,\mathrm{n\Omega\,m}$, both at T_0, and $\int_{T_0}^{T_\ell} dT/\rho_{br}(T) = 0.97\times10^{10}\,\mathrm{K/\Omega\,m}$ [4.86].

a) Show that for brass leads ($I_\circ \ell/A$), which is approximately $2.3\times10^7\,\mathrm{A/m}$ for copper (Eq. 4.35*b*), is given by:

$$\left[\frac{I_\circ \ell}{A}\right]_{br} \equiv [\zeta_\circ]_{br} \simeq 0.35\times10^7\ \mathrm{A/m} \tag{4.102}$$

That is, a brass lead having the same ℓ and A as those of a copper lead will have its optimal rated current ∼1/7 that of the copper lead.

b) Show that $[Q_{I_\circ}/I_\circ]_{br}$, the ratio of the cold-end heat input to rated current for the brass lead, is given by:

$$\left[\frac{Q_{I_\circ}}{I_\circ}\right]_{br} \simeq 1.25\,\mathrm{mW/A} \tag{4.103}$$

This ratio is 0.77 mW/A for copper leads (Eq. 4.32*b*). Note that for the brass lead, despite its much greater resistivity—by a factor of ∼100—than copper's at 4.2 K, $[Q_{I_\circ}/I_\circ]_{br}$ is only ∼60% greater than $Q_{I_\circ}/I_\circ$ (for copper).

c) Show that $[Q_0/Q_{I_\circ}]_{br}$, the ratio of cold-end heat input of a brass lead with no current ($I = 0$) to that of the lead at $I_\circ$ is given by:

$$\left[\frac{Q_0}{Q_{I_\circ}}\right]_{br} \simeq 0.21 \tag{4.104}$$

Use $\tilde{k}_{br} = 55\,\mathrm{W/m\,K}$ (Table 4.18); $\tilde{c}_p = 5.2\,\mathrm{kJ/kg\,K}$; and $c_{p0} = 6.0\,\mathrm{kJ/kg\,K}$.

PROBLEM 4.7: Vapor-cooled brass current lead (continuation)

Overcurrent Mode

As stated above, brass leads are suitable for low-duty-cycle applications. Consider a brass current lead in the overcurrent mode carrying a *constant* current $I > I_\circ$, the nominal rated current. The power equation may be given by:

$$AC_{br}(T)\frac{dT}{dt} = \frac{d}{dz}\left[Ak_{br}(T)\frac{dT}{dz}\right] - \dot{m}_{br}(I)c_p(T)\frac{dT}{dz} + \frac{\rho_{br}(T)}{A}I^2 \qquad (4.105)$$

where $C_{br}(T)$, $k_{br}(T)$, and $\rho_{br}(T)$ are, respectively, the temperature-dependent heat capacity, thermal conductivity, and electrical resistivity of brass, and $\dot{m}_{br}(I)$ is the vapor flow rate, which depends on current. For an optimal brass lead at $I > I_\circ$ in stable operation, $dT/dt = 0$: the temperature of a differential element of the lead, though it depends on z, is constant with time.

To solve Eq. 4.105 at $I > I_\circ$, we make the following assumptions.

1. The entire lead is treated as a single entity with an average temperature of $\tilde{T}$, which is further assumed to be at the midpoint ($z = \ell/2$) temperature. $C_{br}(T)$ and $c_p(T)$ are also assumed constants, respectively, $\tilde{C}_{br}$ and $\tilde{c}_p$.
2. dT/dz appearing in Eq. 4.105 is assumed constant, $\tilde{T}/(\ell/2) = 2\tilde{T}/\ell$.
3. For $I > I_\circ$ $\dot{m}_{br}(I) = \nu_{br} I[1 + \eta_{br}(I - I_\circ)]$, where ν_{br} and η_{br} are constants.
4. $\rho_{br}(T) = [\rho_0]_{br} + \gamma_{br}(\tilde{T} - \tilde{T}_\circ)$, where $\tilde{T}_\circ$ is the initial midpoint temperature (when $I = I_\circ$); for brass, $[\rho_0]_{br} = 21\,\mathrm{n\Omega\,m}$ and $\gamma_{br} = 74\,\mathrm{p\Omega\,m/K}$ [4.86].

With these assumptions, Eq. 4.105 becomes:

$$A\tilde{C}_{br}\frac{d\tilde{T}(t)}{dt} = -\nu_{br} I[1 + \eta_{br}(I - I_\circ)]\tilde{c}_p\frac{\tilde{T}(t)}{(\ell/2)} + \frac{[\rho_0]_{br}}{A}I^2 + \frac{\gamma_{br}}{A}[\tilde{T}(t) - \tilde{T}_\circ]I^2 \quad (4.106)$$

Inserting $\theta(t) = \tilde{T}(t) - \tilde{T}_\circ$ to Eq. 4.106, we have $d\theta(t)/dt$ and solution $\theta(t)$:

$$\frac{d\theta(t)}{dt} = \frac{1}{A^2\ell\tilde{C}_{br}}\left(\left\{2\nu_{br}\tilde{c}_p AI[1 + \eta_{br}(I - I_\circ)] - \gamma_{br}\ell I^2\right\}\theta(t) + \left\{2\nu_{br}\tilde{c}_p A\tilde{T}_\circ I[1 + \eta_{br}(I - I_\circ)] - [\rho_0]_{br}\ell I^2\right\}\right) \quad (4.107a)$$

$$\theta(t) = \Delta\theta(I)\left[1 - e^{-t/\tau_j(I)}\right] \qquad (4.107b)$$

$\Delta\theta(I)$ and $\tau_j(I)$, both I-dependent constants, are, respectively, the temperature rise and response time, which is assumed to be much longer than the period during which the condition $I > I_\circ$ is established. Solving for $\Delta\theta(I)$ and $\tau_j(I)$, we have:

$$\Delta\theta(I) = \frac{[\rho_0]_{br}\ell I^2 - 2\nu_{br}\tilde{c}_p A\tilde{T}_\circ I[1 + \eta_{br}(I - I_\circ)]}{2\nu_{br}\tilde{c}_p AI[1 + \eta_{br}(I - I_\circ)] - \gamma_{br}\ell I^2} \qquad (4.108a)$$

$$\tau_j(I) = \frac{A^2\tilde{C}_{br}\ell}{2\nu_{br}\tilde{c}_p AI[1 + \eta_{br}(I - I_\circ)] - \gamma_{br}\ell I^2} \qquad (4.108b)$$

PROBLEM 4.7: Vapor-cooled brass current lead (continuation)

d) Show that ν_{br} is given by:

$$\nu_{br} = \frac{[\rho_0]_{br}\ell I_\circ}{2\tilde{c}_p A\tilde{T}_\circ} \tag{4.109}$$

e) Show that in the overcurrent region, $[Q_I]_{br}$, the heat input is given by:

$$[Q_I]_{br} = h_L\nu_{br}I[1+\eta_{br}(I-I_\circ)] \tag{4.110}$$

f) Show that $[I_\circ\ell/A]_{br}$, given by Eq. 4.102, is also given by:

$$\left[\frac{I_\circ\ell}{A}\right]_{br} = \frac{2\tilde{c}_p\tilde{T}_\circ}{[\rho_0]_{br}}\sqrt{\frac{[k_0]_{br}[\rho_0]_{br}}{h_L c_{p0}}} \tag{4.111}$$

where c_{p0} is the helium specific heat at the cold-end temperature.

g) The voltage across the entire lead, $V_{br}(t)$ is given by:

$$V_{br}(t) = V_\circ(\tilde{T}_\circ) + \Delta V(I)(1-e^{-t/\tau_j(I)}) \tag{4.112}$$

where $V_\circ(\tilde{T}_\circ)$ is the steady-state lead voltage when the lead is carrying $I_\circ$. Show that $\Delta V(I)$, a constant at I, is given by:

$$\Delta V(I) = \frac{\gamma_{br}\ell}{A}\left\{\frac{[\rho_0]_{br}\ell I^2 - 2\nu_{br}\tilde{c}_p A\tilde{T}_\circ I[1+\eta_{br}(I-I_\circ)]}{2\nu_{br}\tilde{c}_p AI[1+\eta_{br}(I-I_\circ)]-\gamma_{br}\ell I^2}\right\}I \tag{4.113}$$

h) Consider a vapor-cooled brass lead rated at 25 kA under a cyclic operation in which it is subjected to an overcurrent of 75 kA ($=3\times I_\circ$) over a 5-min period, followed by a 30-min off-current period. As may become evident from experimental results performed on a 40-A brass lead [4.87], presented later in Figs. 4.25 and 4.26, the 40-A brass lead can operate stably at an overcurrent of up to nearly 200 A ($= 5\times I_\circ$) over an indefinite period of time—in the experiment the overcurrent condition at a given I lasts only up to 500 s.

Determine $I_\circ$ of a vapor-cooled copper lead that when operated at $I_\circ$ continuously results in the same cold-end heat input as that of the 25-kA brass lead operated in the mode described above. Use $\nu_{br} = 6.13\times10^{-8}$ kg/s A, determined in the experiment [4.87], and $\eta_{br} = 2.2\times10^{-5}$ A^{-1}, scaled to a 25-kA lead from the experiment ($\eta_{br} = 0.0138$ A^{-1} at $I_\circ = 40$ A). For the copper lead, use $Q_{I_\circ}/I_\circ = 1$ mW/A.

TRIVIA 4.6 List the metals below in the descending order of their electrical resistivities.

i) Aluminum 1100 at 4.2 K; ii) Copper (RRR $\simeq$ 20,000) at 100 K;

iii) Copper (RRR $\simeq$ 100) at 50 K; iv) Copper (RRR $\simeq$ 100) at 4.2 K in a 20-T field.

Solution to PROBLEM 4.7

a) From Eq. 4.35, $[I_\circ \ell/A]_{br}$ for brass leads is:

$$\left[\frac{I_\circ \ell}{A}\right]_{br} = \sqrt{\frac{c_{p0}[k_0]_{br}[\rho_0]_{br}}{h_L}} \int_{T_0}^{T_\ell} \frac{dT}{\rho_{br}(T)} \tag{S7.1}$$

With $c_{p0} = 6.0\,\text{kJ/kg K}$ and other property values inserted into Eq. $S7.1$, we have:

$$\left[\frac{I_\circ \ell}{A}\right]_{br} = \sqrt{\frac{(6.0\,\text{kJ/kg K})(22\,\text{W/m K})(21\,\text{n}\Omega\,\text{m})}{(20.7\,\text{kJ/kg})}}(0.97\times 10^{10}\,\text{K/}\Omega\,\text{m})$$

Thus:

$$\left[\frac{I_\circ \ell}{A}\right]_{br} \equiv [\zeta_\circ]_{br} \simeq 0.35\times 10^7\ \text{A/m} \tag{4.102}$$

b) From Eq. 4.32a, which is for copper leads, we obtain:

$$\left[\frac{Q_{I_\circ}}{I_\circ}\right]_{br} = \sqrt{\frac{h_L[k_0]_{br}[\rho_0]_{br}}{c_{p0}}} = \sqrt{\frac{(20.4\,\text{kJ/kg})(22\,\text{W/m K})(21\,\text{n}\Omega\,\text{m})}{(6.0\,\text{kJ/kg K})}} \tag{S7.2}$$

Thus:

$$\left[\frac{Q_{I_\circ}}{I_\circ}\right]_{br} \simeq 1.25\,\text{mW/A} \tag{4.103}$$

c) From Eq. 4.41 with $\tilde{k}_{br} = 55\,\text{W/m K}$ (Table 4.18) and other values, including $\ln[\tilde{c}_p(T_\ell - T_0)/h_L + 1] \simeq 4.32$, we have:

$$\left[\frac{Q_0}{Q_{I_\circ}}\right]_{br} = \frac{\tilde{k}_{br}}{\tilde{c}_p[\zeta_\circ]_{br}} \sqrt{\frac{h_L c_{p0}}{[k_0]_{br}[\rho_0]_{br}}} \times \ln\left[\frac{\tilde{c}_p(T_\ell - T_0)}{h_L} + 1\right] \tag{S7.3}$$

$$\simeq \frac{(55\,\text{W/m K})}{(5.2\,\text{kJ/kg K})(0.36\times 10^7\,\text{A/m})} \sqrt{\frac{(20.7\,\text{kJ/kg})(6.0\,\text{kJ/kg K})}{(22\,\text{W/m K})(21\,\text{n}\Omega\,\text{m})}} \times (4.32)$$

Thus:

$$\left[\frac{Q_0}{Q_{I_\circ}}\right]_{br} \simeq 0.21 \tag{4.104}$$

d) Because $\Delta\theta(I_\circ) = 0$ (no overcurrent), from Eq. 4.107a we have:

$$[\rho_0]_{br}\ell I_\circ^2 - 2\nu_{br}\tilde{c}_p A \tilde{T}_\circ I_\circ = 0 \tag{S7.4}$$

From Eq. $S7.4$, we obtain:

$$\nu_{br} = \frac{[\rho_0]_{br}\ell I_\circ}{2\tilde{c}_p A \tilde{T}_\circ} \tag{4.109}$$

Solution to PROBLEM 4.7 (continuation)

e) From $[Q_{I_\circ}]_{br} = \dot{m}_{br} h_L$ and with $\dot{m}_{br}(I) = \nu_{br} I[1+\eta_{br}(I-I_\circ)]$ (assumption *3*):

$$[Q_{I_\circ}]_{br} = h_L \nu_{br} I[1 + \eta_{br}(I - I_\circ)] \tag{4.110}$$

f) With $[I_\circ \ell/A]_{br}$ from Eq. 4.109 and $[Q_{I_\circ}]_{br}$ from Eq. 4.110 at $I = I_\circ$:

$$\left[\frac{I_\circ \ell}{A}\right]_{br} = \nu_{br} \frac{2\tilde{c}_p \tilde{T}_\circ}{[\rho_0]_{br}} \tag{S7.5a}$$

$$[Q_{I_\circ}]_{br} = h_L \nu_{br} I_\circ \tag{S7.5b}$$

Combining Eqs. $S7.5a$ and $S7.5b$, we have:

$$\left[\frac{I_\circ \ell}{A}\right]_{br} = \left[\frac{Q_{I_\circ}}{I_\circ}\right]_{br} \frac{2\tilde{c}_p \tilde{T}_\circ}{h_L [\rho_0]_{br}} \tag{S7.6}$$

Inserting $[Q_{I_\circ}/I_\circ]_{br}$ from Eq. $S7.2$ into Eq. $S7.6$, we obtain:

$$\left[\frac{I_\circ \ell}{A}\right]_{br} = \frac{2\tilde{c}_p \tilde{T}_\circ}{[\rho_0]_{br}} \sqrt{\frac{[k_0]_{br}[\rho_0]_{br}}{h_L c_{p0}}} \tag{4.111}$$

We may determine the value of $\tilde{T}_\circ$, the only unknown parameter in Eq. 4.111:

$$\tilde{T}_\circ = \frac{[\rho_0]_{br}}{2\tilde{c}_p} \left[\frac{I_\circ \ell}{A}\right]_{br} \sqrt{\frac{h_L c_{p0}}{[k_0]_{br}[\rho_0]_{br}}} \tag{S7.7}$$

$$= \frac{(21\,\mathrm{n\Omega\,m})}{2(5.19\,\mathrm{kJ/kg\,K})} (0.358 \times 10^7\,\mathrm{A/m}) \sqrt{\frac{(20.7\,\mathrm{kJ/kg})(6.0\,\mathrm{kJ/kg\,K})}{(22\,\mathrm{W/m\,K})(21\,\mathrm{n\Omega\,m})}}$$

$$\simeq 120\,\mathrm{K}$$

This value of 120 K is quite reasonable because $\tilde{T}_\circ$ is assumed to be the steady-state *average* temperature of the entire lead at $I_\circ$, i.e., ∼4 K at the cold end and ∼293 K at the warm end, which gives a linear average value of 149 K.

g) An increase in the lead voltage, $\Delta V(I)$, at a given level of overcurrent I comes from an increase in the brass resistivity, $\Delta\rho_{br}(I)$, which in turn is caused by an increase in the lead temperature, $\Delta\theta(I)$. Thus:

$$\Delta V(I) = \frac{\ell \Delta\rho_{br}(I)}{A} I = \frac{\gamma_{br} \ell \Delta\theta(I)}{A} I \tag{S7.8}$$

Inserting the expression of $\Delta\theta(I)$ given by Eq. 4.108a, we obtain:

$$\Delta V(I) = \frac{\gamma_{br}\ell}{A} \left\{ \frac{[\rho_0]_{br} \ell I^2 - 2\nu_{br}\tilde{c}_p A \tilde{T}_\circ I[1+\eta_{br}(I-I_\circ)]}{2\nu_{br}\tilde{c}_p A I[1+\eta_{br}(I-I_\circ)] - \gamma_{br}\ell I^2} \right\} I \tag{4.113}$$

Solution to PROBLEM 4.7 (continuation)

h) For a vapor-cooled 25-kA brass lead at an overcurrent of $I = 75\,\text{kA}$, we have $[Q_{I_\circ}]_{br}$, with $h_L = 20.7\,\text{kJ/kg}$; $\nu_{br} = 6.13\times10^{-8}\,\text{kg/s A}$; $\eta_{br} = 2.2\times10^{-5}\,\text{A}^{-1}$; and $I_\circ = 25\,\text{kA}$, inserted into Eq. 4.110:

$$[Q_{I_\circ}]_{br} = h_L \nu_{br} I[1 + \eta_{br}(I - I_\circ)] \tag{4.110}$$

$$= (20.7\,\text{kJ/kg})(6.13\times10^{-8}\,\text{kg/s A})(75\,\text{kA}) \times [1 + (2.2\times10^{-5}\,\text{A}^{-1})(75\,\text{kA} - 25\,\text{kA})] \simeq 200\,\text{W}$$

At $I_\circ = 25\,\text{kA}$, we have, from Eq. 4.103, $[Q_{I_\circ}]_{br} = 31.5\,\text{W}$. When carrying no current, this 25-kA brass lead has, from Eq. 4.104, $[Q_0]_{br} \simeq 0.21[Q_{I_\circ}]_{br} \simeq 6.6\,\text{W}$. Thus, a total energy injected into the cold bath, E_{br}, over a 300-s period at 75 kA and over a 1800-s period at 25 kA, is given by:

$$E_{br} \simeq (300\,\text{s})(200\,\text{W}) + (1{,}800\,\text{s})(6.6\,\text{W}) \tag{S7.10}$$

$$\simeq 72\,\text{kJ}$$

Over this 2100-s period, a copper lead would have required a cold-end heat input of 33.8 W, to match the total energy $E_{br} = 72\,\text{kJ}$. For a vapor-cooled copper lead operating continuously at $I_\circ$, this translates to a current rating of ~35 kA (<75 kA). Although no detailed study is available for vapor-cooled *copper* leads in overcurrent mode, it is quite possible that a copper lead too can be operated safely with an overcurrent up to a "reasonable" value of $I/I_\circ$.

Experimental Results of a Vapor-Cooled Brass Lead

Here we present experimental results of a pair of vapor-cooled brass leads [4.87]. Each lead has the same active length ($\ell = 54\,\text{cm}$) and cross sectional area ($A = 0.0613\,\text{cm}^2$) as those of an optimal vapor-cooled copper lead rated at 280 A. As inferred from Eq. 4.102, this brass counterpart thus is rated at $[I_\circ]_{br}$ given by:

$$[I_\circ]_{br} = \frac{[\zeta_\circ]_{br}}{\zeta_\circ} I_\circ$$

$$\simeq \frac{(0.35\times10^7\,\text{A/m})}{(2.3\times10^7\,\text{A/m})}(280\,\text{A}) \sim 40\,\text{A}$$

Figure 4.25 shows a measured heat input vs. I plot of this brass lead in the current ranges of 0 to its nominally rated current of 40 A, and 40 A to 90 A (overcurrent). As expected, the results show that the heat input is linear with I up to ~40 A, while beyond 40 A, the results agree well with the solid curve given by Eq. 4.110.

Figure 4.26 shows $\Delta V(I)$ vs. t plots for three constant overcurrent levels, 130 A, 150 A, and 203 A. The solid curves are experimental, while the dotted curves are analytical, given by Eq. 4.113. The experimental curve at 203 A shows that at this level of overcurrent ($I \sim 5\times I_\circ$), the lead eventually—after ~400 s—enters into an unstable (overheated) region. The results indicate that it is safe to operate the lead up to an overcurrent level ~4 times the rated current.

Solution to PROBLEM 4.8 (continuation)

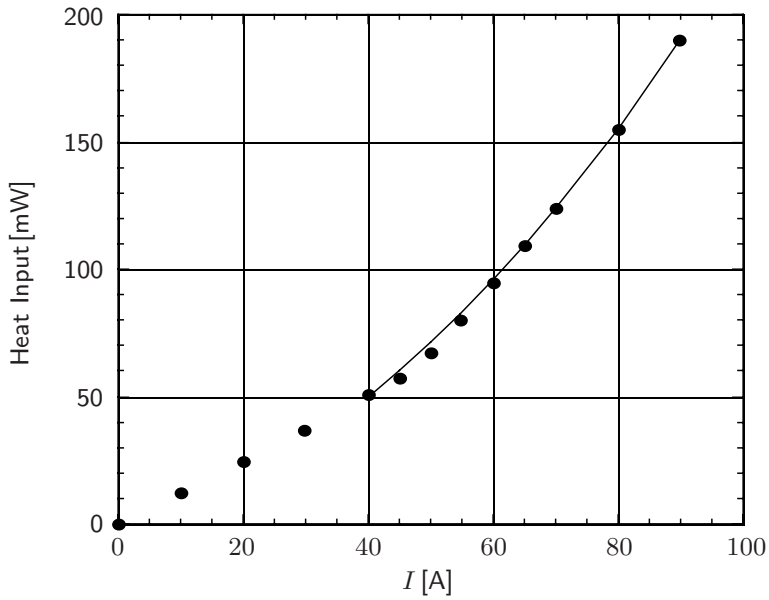

Fig. 4.25 Measured heat input vs. I plot for a vapor-cooled brass lead ($I_\circ = 40\,\mathrm{A}$) [4.87]. Solid curve: based on Eq. 4.110, with $\nu_{br} = 6.13 \times 10^{-8}\,\mathrm{kg/s\,A}$; and $\eta_{br} = 0.0138\,\mathrm{A}^{-1}$.

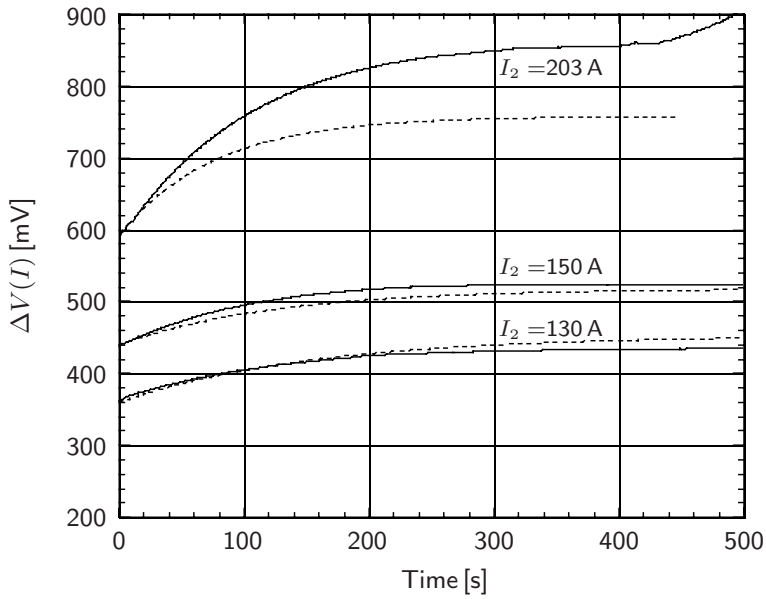

Fig. 4.26 $\Delta V(I)$ vs. t plots for over-current levels of 130, 150, and 203 A [4.87]. Solid curves: experimental; Dotted curves: based on τ_j given by Eq. 4.108b and $\Delta V(I)$ by Eq. 4.113, with $A = 0.0613\,\mathrm{cm}^2$; $\ell = 54\,\mathrm{cm}$; $c_{p_\circ} = 5.19\,\mathrm{J/g\,K}$; and $b = 7.4\,\mathrm{n\Omega\,cm/K}$.

Answer to TRIVIA 4.6

Cu @100 K (2, in nΩ m); Cu @4.2 K, 20 T (1); Al (0.8); Cu @50 K (0.6)

DISCUSSION 4.19: Vapor-Cooled Support Rods*

Structural supports inside a cryostat represent a conductive heat load on the cryogenic environment. Like the vapor-cooled copper current lead in ***DISCUSSION 4.14***, the effluent helium vapor may be used to cool a support rod of active length ℓ and cross sectional area A spanning two temperatures (T_0 at the cold end and T_ℓ at the warm end) and thus greatly to reduce the conductive heat loss.

Assuming that the rod material's thermal conductivity is temperature-independent and given by $\tilde{k}$ and that heat transfer between the helium and the rod is perfect, we may show that the ratio of conduction heat input through the rod from T_ℓ to T_0 *without* helium cooling, $Q_{\overline{vp}}$, to that *with* helium cooling, Q_{vp}, is given by:

$$\frac{Q_{\overline{vp}}}{Q_{vp}} = \frac{c_{p0}(T_\ell - T_0)}{h_L \ln\left[\dfrac{c_{p0}(T_\ell - T_0)}{h_L} + 1\right]} \tag{4.114}$$

Note that $Q_{\overline{vp}}/Q_{vp}$ is independent of the rod's dimensions and thermal conductivity. With $c_{p0} = 6.0\,\text{J/g K}$, $h_L = 20.4\,\text{J/g}$, $T_0 = 4\,\text{K}$, $T_\ell = 300\,\text{K}$, Eq. 4.114 gives:

$$\frac{Q_{\overline{vp}}}{Q_{vp}} = \frac{(6.0\,\text{J/g K})(296\,\text{K})}{(20.4\,\text{J/g})\ln(88)} = 19.4 \sim 20$$

That is, it is possible to greatly reduce the conduction heat input through structural elements by an effective use of cold effluent helium vapor.

DISCUSSION 4.20: Structural Materials for Cryogenics

Structural materials for cryogenic applications must withstand large stresses, while conducting very little heat flux over a temperature range. A material property that can be used to quantify the suitability for cryogenic applications is $\tilde{k}/\sigma_U$, the ratio of the temperature-averaged thermal conductivity (over a specific span) to its ultimate tensile strength. *Both* $Q_{\overline{vp}}$ and Q_{vp} are proportional to $\tilde{k}$.

Table 4.18 presents values for G-10, stainless steel 304, brass, and copper to gauge their suitability as structural materials for cryogenic applications; copper is included to demonstrate its unsuitability. Based on $\tilde{k}/\sigma_U$, G-10 is better than stainless steel; however, stainless steel has a virtue of weldability.

Table 4.18: "Structural Data" for G-10, Stainless Steel 304, Brass, and Copper

Material	$\tilde{k}$ [W/m K]			σ_U [MPa]	$\tilde{k}/\sigma_U$ [m^2/K s]†
	4–80 K	4–300 K	80–300 K	295 K	(80–300 K)
G-10	0.25	0.50	0.56	280	2×10^{-9}
Stainless Steel 304	4.5	11	13	1300	10×10^{-9}
Brass	24	55	65	400	2×10^{-7}
Copper	1300	660	460	250	2×10^{-6}

† Approximate values.

* Based on **Problem 4.5** in the 1st Edition (Plenum, 1994).

REFERENCES

[4.1] E. Trifon Laskaris, Kenneth G. Herd and Bijan Dorri, "A compact 0.8 T superconducting MRI magnet," *Cryogenics* **34**, 635 (1994).

[4.2] Toru Kuriyama, Masami Urata, Takashi Yazawa, Kazutaka Yamamoto, Yasumi Ohtani, Kei Koyanagi, Tamaki Masegi, Yutaka Yamada, Shunji Nomura, Hideaki Maeda, Hideki Nakagome and Osamu Horigami, "Cryocooler directly cooled 6 T NbTi superconducting magnet system with 180 mm room temperature bore," *Cryogenics* **34**, 643 (1994).

[4.3] Lisa Cowey, Peter Cetnik, Kevin Timums, Peter Daniels, John Mellors and Ian McDougall, "Cryogen free Nb_3Sn magnet, operated at 9.5 K with high Tc BiSrCaCuO (2212) current leads," *IEEE Trans. Appl. Superconduc.* **5**, 825 (1995).

[4.4] Weijun Shen, M. Coffey, W. McGhee, "Development of 9.5 T NbTi cryogen-free magnet," *IEEE Trans. Appl. Superconduc.* **11**, 2619 (2001).

[4.5] C.H. Chang, F.Z. Hsiao, C.S. Hwang, M.H. Huang, and C.T. Chen, "Design of a 7.5 T superconducting quadrupole magnet for magnetic circular dichroism experiments," *IEEE Trans. Appl. Superconduc.* **12**, 718 (2002).

[4.6] Achim Hobl, Detlef Krischel, Michael Poier, Ruediger Albrecht, Ralf Bussjaeger, and Uwe Konopka, "Design, manufacture, and test of a large bore cryogen-free magnet," *IEEE Trans. Appl. Superconduc.* **13**, 1569 (2003).

[4.7] R. Hirose, S. Hayashi, S. Fukumizu, Y. Muroo, H. Miyata, Y. Okui, A. Itoki, T. Kamikado, O. Ozaki, Y. Nunoya, and K. Okuno, "Development of 15 T cryogen-free superconducting magnets," *IEEE Trans. Appl. Superconduc.* **16**, 953 (2006).

[4.8] Yingming Dai, Luguang Yan, Baozhi Zhao, Shousen Song, Yuanzhong Lei, and Quiliang Wang, "Tests on a 6 T conduction-cooled superconducting magnet," *IEEE Trans. Appl. Superconduc.* **16**, 961 (2006).

[4.9] M.A. Daugherty, J.Y. Coulter, W.L. Hults, D.E. Daney, D.D. Hill, D.E. McMurry, M.C. Martinez, I.G. Phillips, J.O. Willis, H.J. Boenig, F.C. Prenger, A.J. Rodenbush and S. Young "HTS high gradient magnetic separation system," *IEEE Trans. Appl. Superconduc.* **7**, 650 (1997).

[4.10] K. Watanabe, S. Awaji, K. Takahashi, G. Nishijima, M. Motokawa, Y. Sasaki, Y. Ishikawa, K. Jikihara, J. Sakuraba, "Construction of the cryogen-free 23 T hybrid magnet," *IEEE Trans. Appl. Superconduc.* **12**, 678 (2002).

[4.11] J. Good and R. Mitchell, "A desktop cryogen free magnet for NMR and ESR," *IEEE Trans. Appl. Superconduc.* **16**, 1328 (2006).

[4.12] G. Snitchler, S.S. Kalsi, M. Manlief, R.E. Schwall, A. Sidi-Yekhlef, S. Ige and R. Medeiros, "High-field warm-bore HTS conduction cooled magnet," *IEEE Trans. Appl. Superconduc.* **9**, 553 (1999).

[4.13] K. Sato, T. Kato, K. Ohkura, S. Kobayashi, K. Fujino, K. Ohmatsu and K. Hayashi, "Performance of all high-T_c superconducting magnets generating 4 T and 7 T at 20 K," *Supercond. Sci. Technol.* **13**, 18 (2000).

[4.14] Hitoshi Kitaguchi, Hiroaki Kumakura, Kazumasa Togano, Michiya Okada, Katsunori Azuma, Hiroshi Morita, Jun-ichi Sato, "Cryocooled Bi-2212/Ag solenoid magnet system generating 8 T in 50 mm room temperature bore; design and preliminary test," *IEEE Trans. Appl. Superconduc.* **10**, 495 (2000).

[4.15] R. Musenich, P. Fabbricatore, S. Farinon, C. Ferdeghini, G. Grasso, M. Greco, A. Malagoli, R. Marabotto, M. Modica, D. Nardelli, A.S. Siri, M. Tassisto, and A. Tumino, "Behavior of MgB_2 react & wind coils above 10 K," *IEEE Trans. Appl. Superconduc.* **15**, 1452 (2005).

[4.16] L'ubomír Kopera, Pavol Kováč, and Tibor Melišek, "Compact design of cryogen-

free HTS magnet for laboratory use," *IEEE Trans. Appl. Superconduc.* **16**, 1415 (2006).

[4.17] Richard McMahon, Stephen Harrison, Steve Milward, John Ross, Robin Stafford Allen, Claude Bieth, Saïd Kantas, and Gerry Rodrigues, "Design and manufacture of high temperature superconducting magnets for an electron cyclotron resonance ion source," *IEEE Trans. Appl. Superconduc.* **14**, 608 (2004).

[4.18] Kaoru Nemoto, Motoaki Terai, Motohiro Igarashi, Takeshi Okutomi, Satoshi Hirano, Katsuyuki Kuwano, Shigehisa Kusada, Tomohisa Yamashita, Yasuto Yanse, Toru Kuriyama, Taizo Tosaka, Kenji Tasaki, Kotaro Marukawa, Satoshi Hanai, Mutsuhiko Yamaji, and Hiroyuki Nakao, "HTS magnet for Maglev applications (2)—magnet structure and performance," *IEEE Trans. Appl. Superconduc.* **16**, 1104 (2006).

[4.19] Juan Bascuñán (Personal communication, 2002).

[4.20] Luca Bottura (Personal communication, 2004).

[4.21] G. Bon Mardion, G. Claudet, and P. Seyfert, "Practical data on steady state heat transport in superfluid helium at atmospheric pressure," *Cryogenics* **29**, 45 (1979).

[4.22] Steven W. Van Sciver (personal communication, 1993).

[4.23] G. Claudet, C. Mwueia, J. Parain, and B. Turck, "Superfluid helium for stabilizing superconductors against local disturbances," *IEEE Trans. Magn.* **MAG-15**, 340 (1979).

[4.24] Steven W. Van Sciver, *Helium Cryogenics*, (Plenum Press, New York, 1986), 182.

[4.25] See, for example, C. Taylor, R. Althaus, S. Caspi, W. Gilbert, W. Hassenzahl, R. Meuser, J. Reschen, R. Warren, "Design of epoxy-free superconducting dipole magnets and performance in both helium I and pressurized helium II," *IEEE Trans. Magn.* **MAG-17**, 1571 (1981).

[4.26] M.J. Leupold and Y. Iwasa, "A subcooled superfluid helium cryostat for a hybrid magnet system," *Cryogenics* **26**, 579 (1986).

[4.27] Isaac Asimov, *Asimov's Biographical Encyclopedia of Science and Technology* (Doubleday, New York, 1964).

[4.28] Takashi Noguchi, "Vacuum insulation for a cryostat," *Cryogenic Engineering* (in Japanese) **28**, 355 (1993).

[4.29] Randall F. Barron, *Cryogenic Systems* 2nd Ed., (Clarendon University Press, Oxford, 1985).

[4.30] Yukikazu Iwasa, "A 'permanent' HTS magnet system: key design & operational issues," *Advances in Superconductivity X* (Springer-Verlag, Tokyo, 1998), 1377.

[4.31] Benjamin J. Haid, "A 'permanent' high-temperature superconducting magnet operated in thermal communication with a mass of solid nitrogen," *Ph.D. thesis, Department of Mechanical Engineering, M. I. T., Cambridge, MA* (June, 2001).

[4.32] Benjamin J. Haid, Haigun Lee, Yukikazu Iwasa, Sang-Soo Oh, Young-Kil Kwon, and Kang-Sik Ryu, "Design analysis of a solid heat capacitor cooled 'Permanent' high-temperature superconducting magnet system," *Cryogenics* **42**, 617 (2002).

[4.33] L.A. Koloskova, I.N. Krupskii, V.G. Manzhelii, and B.Ya. Gorodilov, "Thermal conductivity of solid nitrogen and carbon monoxide," *Sov. Phys. Solid State* **15**, 1278 (1973).

[4.34] T.A. Scott, "Solid and liquid nitrogen," *Physics Reports (Section C of Physics Letters* **27**, 89 (1976).

[4.35] V.A. Rabinovich, A.A. Vasserman, V.I. Nedostup, L.S. Veksler, *Thermophysical*

Properties of Neon, Argon, Krypton, and Xenon (Hemisphere Publishing Corp., New York, 1988).

[4.36] Akira Sugawara, Hisashi Isogami, Benjamin J. Haid, and Yukikazu Iwasa, "Beneficial effects of solid nitrogen on a BSCCO-2223/Ag composite subjected to local heating," *Physica* **C**, 1443 (2002).

[4.37] Hisashi Isogami, Benjamin Haid, and Yukikazu Iwasa, "Thermal behavior of a solid nitrogen impregnated high-temperature superconducting pancake test coil under transient heating," *IEEE Trans. Appl. Superconduc.* **11**, 1852 (2001).

[4.38] T. Nakamura, I. Muta, K. Okude, A. Fujio, and T. Hoshino, "Solidification of nitrogen refrigerant and its effect on thermal stability of HTSC tape," *Physica C*, **372-376**, 1434 (2002).

[4.39] T. Nakamura, K. Higashikawa, I. Muta, A. Fujio, K. Okude, and T. Hoshino, "Improvement of dissipative property in HTS coil impregnated with solid nitrogen," *Physica C* **386**, 415 (2003).

[4.40] T. Nakamura, K. Higashikawa, I. Muta, and T. Hoshino, "Performance of conduction-cooled HTS tape with the aid of solid nitrogen-liquid neon mixture," *Physica C* **412–414**, 1221 (2004).

[4.41] Frank Pobell, *Matter and Methods at Low Temperature*, 2nd Ed. (Springer Verlag, New York, 1996).

[4.42] Jack W. Ekin, *Experimental Techniques for Low Temperature Measurements* (Oxford University Press, Oxford, 2006).

[4.43] L.G. Rubin, "Cryogenic thermometry: a review of progress since 1982," *Cryogenics* **37**, 341 (1997).

[4.44] *Temperature Measurement and Control* (*Lake Shore Cryotronics, Inc., Westerville, OH 43082-8888*).

[4.45] G.W. Burns, M.G. Scroger, G.F. Strouse, M.C. Croarkin, and W.F. Guthrie, "Temperature-Electromotive Force Reference Functions and Tables for the Letter-Designated Thermocouple Types Based on the ITS-90" (*NIST Monograph 175, 1993*).

[4.46] Linus Pauling, *College Chemistry*, 2nd Ed. (W.H. Freeman, San Francisco, 1955).

[4.47] J.E.C. Williams, "Counterflow current leads for cryogenic applications," *Cryogenics* **3**, 234 (1963).

[4.48] V.E. Keilin and E.Y. Klimenko, "Investigation into high current leads in liquid helium application," *Cryogenics* **6**, 222 (1966).

[4.49] K.R. Efferson, "Helium vapor cooled current leads," *Rev. Sci. Instru.* **38**, 1776 (1967).

[4.50] Yu. L. Buyanov, A.B. Fradkov and I. Yu. Shebalin, "A review of current leads for cryogenic devices," *Cryogenics* **15**, 193 (1975).

[4.51] H. Katheder, L. Schappals, "Design and test of a 10 kA gas-cooled current-lead for superconducting magnets," *IEEE Trans. Magn.* **17**, 2071 (1981).

[4.52] Ho-Myung Chang, Jung Joo Byun, Hong-Beom Jin, "Effect of convection heat transfer on the design of vapor-cooled current leads," *Cryogenics* **46**, 324 (2006).

[4.53] Yuenian Huang, G. William Foster, Seog-Whan Kim, Peter O. Mazur, Andrew Oleck, Henryk Piekarz, Roger Rabehl, and Masayoshi Wake, "The development of 100 kA current leads for a superconducting transmission line magnet," *IEEE Trans. Appl. Superconduc.* **16**, 457 (2006).

[4.54] E. Tada, Y. Takahashi, T. Ando and S. Shimamoto, "Experiences on high current leads for superconducting magnets; seven types from 1 kA to 30 kA," *Cryogenics*

24, 200 (1984).

[4.55] Richard McFee, "Optimum input leads for cryogenic apparatus," *Rev. Sci. Instr.* **30**, 98 (1959).

[4.56] Ho-Myung Chang and Steven W. Van Sciver, "Thermodynamic optimization of conduction-cooled HTS current leads," *Cryogenics* **38**, 729 (1998).

[4.57] D.U. Gubser, M.M. Miller, L. Toth, R. Rayne, S. Lawrence, N.McN. Alford, and T.W. Button, "Superconducting current leads of YBCO and Pb-BSCCO," *IEEE Trans. Magn.* **27**, 1854 (1991).

[4.58] B. Dorri, K. Herd, E.T. Laskaris, J.E. Tkaczyk, and K.W. Lay, "High temperature superconducting current leads for cryogenic applications in moderate magnetic fields," *IEEE Trans. Magn.* **27**, 1858 (1991).

[4.59] A. Matrone, G. Rosatelli, R. Vaccarone, "Current leads with high Tc superconductor bus bars," *IEEE Trans. Magn.* **25**, 1742 (1989).

[4.60] J.R. Hull, "High temperature superconducting current leads for cryogenic apparatus," *Cryogenics* **29**, 1116 (1989).

[4.61] F. Grivon, A. Leriche, C. Cottevieille, J.C. Kermarrec, A. Petitbon, A. Février, "YBaCuO current lead for liquid helium temperature applications," *IEEE Trans. Magn.* **27**, 1866 (1991).

[4.62] J.L. Wu, J.T. Dederer, P.W. Eckels, S.K. Singh, J.R. Hull, R.B. Poepple, C.A Youngdahl, J.P. Singh, M.T. Lanagan, and U. Balachandran, "Design and testing of a high temperature superconducting current lead," *IEEE Trans. Mag.* **27**, 1861 (1991).

[4.63] Y.S. Cha, R.C. Niemann, and J.R. Hull, "Thermodynamic analysis of helium boil-off experiments with pressure variations," *Cryogenics* **33**, 675 (1993).

[4.64] K. Ueda, T. Bohno, K. Takita, K. Mukae, T. Uede, I. Itoh, M. Mimura, N. Uno, T. Tanaka, "Design and testing of a pair of current leads using bismuth compound," *IEEE Trans. Appl. Superconduc.* **3**, 400 (1993).

[4.65] P.F. Herrmann, C. Albrecht, J. Bock, C. Cottevieille, S. Elschner, W. Herkert, M.-O. Lafon, H. Lauvray, A. Leriche, W. Nick, E. Preisler, H. Salzburger, J.-W. Tourre, T. Verhaege, "European project for the development of high T_c current leads," *IEEE Trans. Appl. Superconduc.* **3**, 876 (1993).

[4.66] Y. Yamada, T. Yanagiya, T. Hasebe, K. Jikihara, M. Ishizuka, S. Yasuhara, M. Ishihara, "Superconducting current leads of Bi-based oxide," *IEEE Trans. Appl. Superconduc.* **3**, 923 (1993).

[4.67] R. Wesche and A.M. Fuchs, "Design of superconducting current leads," *Cryogenics* **34**, 145 (1994).

[4.68] B. Zeimetz, S.X. Dou, H.K. Liu, "Vapour cooled high current leads utilizing Bi-2223/Ag tapes," *Supercond. Sci. Technol.* **11**, 1091 (1998).

[4.69] Q.L. Wang, D.Y. Jeong, S.S. Oh, H.J. Kim, J.W. Cho and K.C. Seong, "Design of Bi-based superconducting current lead for SMES," *IEEE Trans. Appl. Superconduc.* **9**, 499 (1999).

[4.70] A. Ballarino, "High temperature superconducting current leads for the large hadron collider," *IEEE Trans. Appl. Superconduc.* **9**, 523 (1999).

[4.71] Andrew V. Gavrilin, Victor E. Keilin, Ivan A. Kovalev, Sergei L. Kruglov, Vladimir I. Shcherbakov, Igor I. Akimov, Dmitry K. Rokov, and Alexander K. Shikov, "Optimized HTS current leads," *IEEE Trans. Appl. Superconduc.* **9**, 531 (1999).

[4.72] Darren M Spiller, C Beduz, M K Al-Mosawi, C M Friend, P Thacker and A Ballarino, "Design optimization of 600 A-13 kA current leads for the Large Hadron Collider project at CERN," *Supercond. Sci. Technol.* **14**, 168 (2001).

[4.73] T. Isono, K. Kawano, K. Hamada, K. Matsui, Y. Nunoya, E. Hara, T. Kato, T. Ando, K. Okuno, T. Bohno, A. Tomioka, Y. Sanuki, K. Sakaki, M. Konno and T. Uede, "Test results of 60-kA HTS current lead for fusion application," *Physica C: Superconductivity* **392–396**, 1219 (2003).

[4.74] R. Heller, W.H. Fietz, R. Lietzow, V.L. Tanna, A. Vostner, R. Wesche, G.R. Zahn, "70 kA high temperature superconductor current lead operation at 80 K," *IEEE Trans. Appl. Superconduc.* **16**, 823 (2006).

[4.75] Yukikazu Iwasa and Haigun Lee, "High-temperature superconducting current lead incorporating operation in the current-sharing mode," *Cryogenics* **40**, 209 (2000).

[4.76] Haigun Lee, Paul Arakawa, Kenneth R. Efferson, Robert Fielden, and Yukikazu Iwasa, "AMI-MIT 1-kA leads with high-temperature superconducting sections—design concept and key parameters," *IEEE Trans. Appl. Superconduc.* **11**, 2539 (2001).

[4.77] M. Lakrimi, J. Brown, P. Cetnik, M. Wilkinson, D. Clapton, R. Fair, K. Smith, and P. Noonan, "Low boil-off HTS current lead," *IEEE Trans. Appl. Superconduc.* **17**, 2270 (2007).

[4.78] H. Fujishiro, M. Ikebe, K. Noto, T. Sasaoka, and K. Nomura, "Thermal and electrical properties of Ag-Au and Ag-Cu alloy tapes for metal stabilizers of oxide superconductors," *Cryogenics* **33**, 1086 (1993). Additional data by H. Fujishiro (Iwate University)—private communication (2004).

[4.79] Helen Miles Davis, *The Chemical Elements* (Ballantine Books, New York, 1964).

[4.80] K. Mendelssohn, *The Quest for Absolute Zero* (World University Library, New York, 1966).

[4.81] M.N. Wilson and G.J. Homer, "Low loss heavy current leads for intermittent use," *Cryogenics* **13**, 672 (1973).

[4.82] Yu. L. Buyanov and I. Yu. Shebalin, "Current leads to a cryostat working under short-term load conditions," *Cryogenics* **15**, 611 (1975).

[4.83] R.F. Berg and G.G. Ihas, "Simple 100 A current leads for low duty cycle use," *Cryogenics* **23**, 437 (1983).

[4.84] Sangkwon Jeong and Schwan In, "Investigation on vapor-cooled current leads operating in a pulse mode," *Cryogenics* **44**, 241 (2004).

[4.85] Andrew V. Gavrilin, Victor E. Keilin, "Overload current leads," *MT-15 proceedings* (Beijing, China: Science Press), 1254 (1998).

[4.86] A.F. Clark, G.E. Childs, and G.H. Wallace, "Electrical resistivity of some engineering alloys at low temperatures," *Cryogenics* **10**, 295 (1970).

[4.87] Haigun Lee, Paul Arakawa, Kenneth Efferson, and Yukikazu Iwasa, "Helium vapor-cooled brass current leads: experimental and analytical results," *Cryogenics* **41**, 485 (2001).

Chapter 5
Magnetization

5.1 Introduction

In this chapter we study the magnetization of Type II superconductors by using a phenomenological theory of magnetization developed in 1962 by Bean [5.1]. As remarked in ***Chapter 1***, over the field range of interest (above ~0.5 T) for most magnet applications, a Type II superconductor is in the mixed state, consisting of normal-state islands in a sea of superconductivity. When a Type II superconductor is subjected to a time-varying magnetic field or transport current, dissipation takes place in these islands and manifests either as "flux jumping," a transitory phenomenon, or AC losses. Known as Bean's *critical state model*, the theory, pertinent to LTS and HTS, has been successfully applied to formulate requirements in closed-form expressions to eradicate flux jumping and minimize AC losses.

Today, well-established methods of producing LTS wires and cables that virtually eradicate flux jumps are available. As we will study in this chapter, flux jumping is not an overriding concern with HTS as it is for LTS. Thus, if magnetization were important only for eradication of flux jumping, for HTS applications, it might be appropriate to regard it as a minor topic. However, because it also plays a crucial role in AC losses in both LTS and HTS, we are devoting an entire chapter here to study magnetization; AC losses will be addressed in more detail in ***Chapter 7***.

5.2. Bean's Theory For a Type II Superconductor

5.2.1 No Transport Current

Bean's theory treats magnetization of a superconductor under assumptions that enable, like many successful theories, simple mathematics to derive closed-form expressions that agree remarkably well with experimental results [5.2–5.5]. In the Bean model the superconductor has the simplest geometry—a slab of width $2a$ (in the x-direction) and infinite lengths in the y- and z-directions. Here, magnetic field quantities (H, B, M) point in the y-direction, while current, I, and current density, J, flow in the z-direction. Also in the Bean model, $J = J_c$, the critical current density, which is assumed independent of magnetic field and temperature.

Vector Eq. 2.15 relating $\vec{B}$, $\vec{H}$, and $\vec{M}$ may thus be simplified to define magnetization M in terms of B and H:

$$M = \frac{B}{\mu_\circ} - H \tag{5.1}$$

According to the Bean model, magnetic induction B is *not* zero within the interior of the hard superconductor but is equal to the superconductor's volumetric average of $\mu_\circ H_s$, where H_s is the magnetic field within the superconductor.

Figure 5.1 shows a Type II superconducting slab infinitely high (in the y-direction) and deep (in the z-direction), and $2a$ wide (in the x-direction). An external field H_e, applied parallel to a slab previously unexposed to a magnetic field ("virgin" slab), creates $H_s(x)$ within the slab. With Ampere's law $\nabla \times \vec{H} = \vec{J} = \vec{J_c}$ applied

Y. Iwasa, *Case Studies in Superconducting Magnets: Design and Operational Issues*,
DOI: 10.1007/b112047_5,

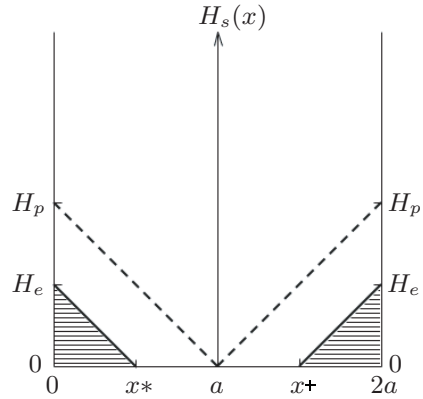

Fig. 5.1 Slab of Type II superconductor exposed to an external field.

to the slab, we obtain the magnetic field within the superconductor, $H_s(x)$:

$$H_s(x) = \begin{cases} 0 & (x* \le x \le x+) \quad (5.2a) \\ H_e - J_c x & (0 \le x \le x*) \quad (5.2b) \\ H_e + J_c(x - 2a) & (x+ \le x \le 2a) \quad (5.2c) \end{cases}$$

Note that the slope of $H_s(x)$ is equal to J_c, positive where J_c is positive (z-directed, out of the paper) and negative where J_c is negative. $x*$ (and $2a - x+$) gives the extent of the field penetration in the slab; in terms of H_e and J_c:

$$x* = \frac{H_e}{J_c} \quad (5.3a)$$

At $H_e = H_p \equiv J_c a$, $x* = x+ = a$, and the entire slab is in the critical state; H_p is known as the penetration field:

$$H_p \equiv J_c a \quad (5.3b)$$

The average magnetic induction within the slab, $\tilde{B}_s$, is thus given by

$$\tilde{B}_s = \frac{\mu_\circ}{2a}\int_0^{2a} H_s(x)\,dx = \frac{\mu_\circ}{2a} \times \text{<shaded area in Fig. 5.1>} \quad (5.4a)$$

$$= 2 \times \frac{\mu_\circ}{2a} \times \frac{H_e x*}{2} = \frac{\mu_\circ H_e^2}{2aJ_c} \quad (5.4b)$$

$$= \frac{\mu_\circ H_e^2}{2H_p} \quad (5.4c)$$

From the definition, $M = \tilde{B}_s/\mu_\circ - H_e$, we have:

$$-M = H_e - \frac{H_e^2}{2H_p} \qquad (0 \le H_e \le H_p) \quad (5.5)$$

The superconductor is diamagnetic; $-M$ is the magnitude of its magnetization.

As the external field is increased further, the field eventually penetrates the slab completely ($H_e \ge H_p$), and $\tilde{B}_s = H_e - H_p/2$, and thus:

$$-M = \tfrac{1}{2}H_p = \tfrac{1}{2}J_c a \qquad (H_e \ge H_p) \quad (5.6)$$

The dashed magnetization profile in Fig. 5.1 corresponds to $H_e = H_p$.

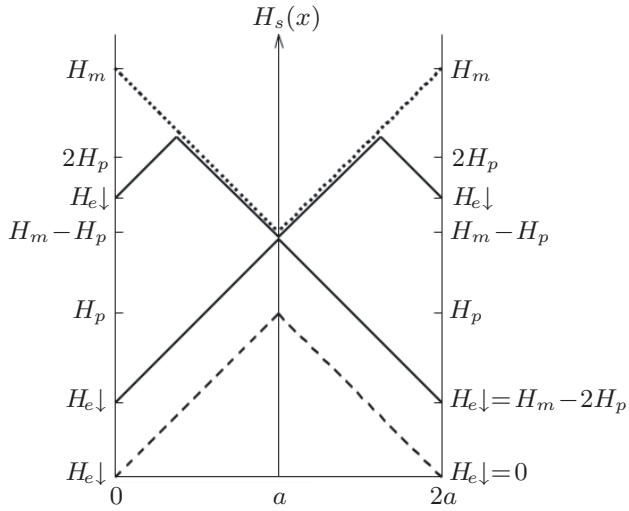

Fig. 5.2 $H_s(x)$ during a return field sequence: $H_e\downarrow = H_m \to 0$.

The dotted lines in Fig. 5.2 represent $H_s(x)$ at $H_e = H_m > 2H_p$, where H_m is the maximum external field applied in this field sweep sequence.

As H_e is reduced from H_m towards 0, $H_s(x)$ changes as indicated by the solid lines in Fig. 5.2. When $H_e = H_m - 2H_p$, $-M$ becomes $-H_p/2$, as may be inferred from Fig. 5.2, because $H_s(x)$ is a perfect mirror image of that at H_m. It can be shown that for the return field sweep from H_m to $H_e\downarrow = 0$, $-M(H_e)$ is given by:

$$-M(H_e) = \tfrac{1}{2}H_p - (H_m - H_e) + \frac{(H_m - H_e)^2}{4H_p} \qquad (H_e\downarrow = H_m \to H_m - 2H_p) \quad (5.7a)$$

$$= -\tfrac{1}{2}H_p \qquad (H_e\downarrow = H_m - 2H_p \to 0) \quad (5.7b)$$

Note that $-M$ is a quadratic function of H_e, as is the case when an external field is applied to the virgin slab; also $-M(H_e) = -H_p/2$ when H_e returns to 0. This "remanent" magnetization is indicated by the dashed lines in Fig. 5.2. Once exposed to an external magnetic field, a Type II superconductor will thus become magnetized. This remanent magnetization cannot be removed by means of the external field; one way to remove it is to heat the superconductor, raising its temperature to above T_c.

Figure 5.3 gives $-M$ vs. H_e plots for the entire positive field sweep sequence from 0 to $H_m = H_{c2}$ and back to 0, where H_{c2} is the upper critical field. The solid curve is based on Eqs. 5.5–5.7 derived with Bean's assumption that J_c is field-independent. The dashed curve qualitatively corrects for more realistic cases [5.2–5.5] in which J_c decreases with field, becoming 0 at H_{c2}. Note that magnetization is hysteretic, and its magnitude within the range $H_p < H_e < H_m - 2H_p$, $\Delta M = -M(H_e\uparrow) + M(H_e\downarrow)$, is equal to $H_p = J_c a$. A magnetization measurement is thus sometimes performed to obtain $J_c(H_e)$ data—see ***DISCUSSION 5.4*** (p. 331).

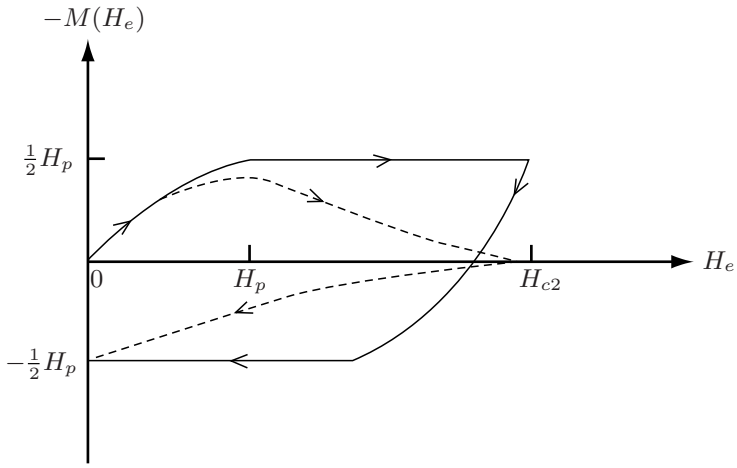

Fig. 5.3 Magnetization vs. field traces for a hard superconducting slab subjected to an external field sequence of $0 \rightarrow H_{c2} \rightarrow 0$. The solid curve presents the case $J_c =$ constant; the dashed curve qualitatively presents the case $J_c(H_e)$, with $J_c = 0$ at H_{c2} [5.2–5.5].

Figure 5.4 shows the current distribution within the slab corresponding to the field distribution of Fig. 5.1. Note that $J_c = H_p/2a$. The net current *per unit length* in the y-direction [A/m] flowing through the slab in the z-direction is given by:

$$I = \int_0^{2a} J(x)\, dx = 0 \tag{5.8}$$

As expected, $I = 0$ in the absence of transport current.

5.2.2 Effect of Transport Current on Magnetization

When a transport current I_t (*per unit length* in the y-direction) flows in the slab in the $+z$-direction (out of the paper), we see an increase in magnetic field of $I_t/2$ at $x = 2a$ and a decrease in magnetic field of $I_t/2$ at $x = 0$.

Because the shielding current within the slab builds up from each surface into the interior, the field distribution $H_s(x)$ within the slab will be that shown in Fig. 5.5. In Fig. 5.5, $x*$ and $x+$ are given by:

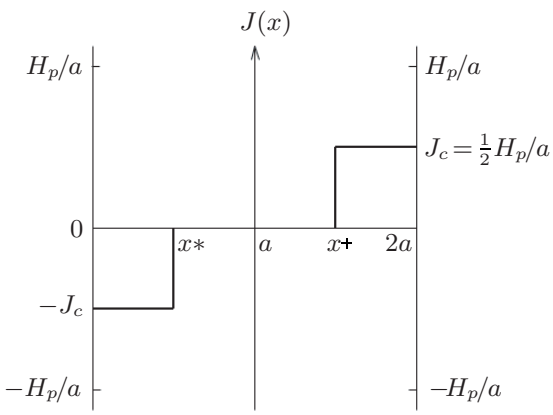

Fig. 5.4 $J(x)$ corresponding to $H_s(x)$ given in Fig. 5.1.

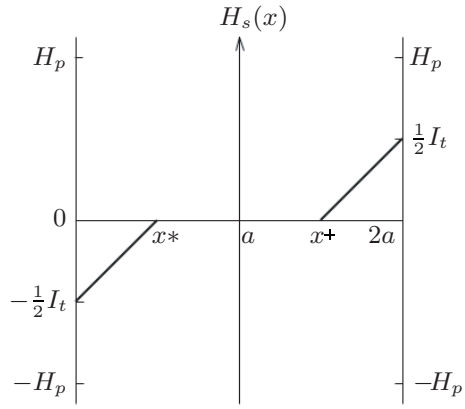

Fig. 5.5 $H_s(x)$ with transport current I_t in the slab.

$$-\tfrac{1}{2}I_t + J_c x* = 0 \tag{5.9a}$$

$$J_c(x+ - 2a) + \tfrac{1}{2}I_t = 0 \tag{5.9b}$$

$$x* = \frac{I_t}{2J_c} \quad \text{and} \quad x+ = 2a - \frac{I_t}{2J_c} \tag{5.9c}$$

Figure 5.6 shows current distribution $J(x)$ in the slab. By integrating $J(x)$ across the slab width, we can show that the net current flowing in the slab is indeed I_t:

$$I = \int_0^{2a} J(x)\,dx = J_c x* + J_c(2a - x+) \tag{5.10a}$$

$$= \tfrac{1}{2}I_t + \tfrac{1}{2}I_t = I_t \tag{5.10b}$$

As expected, the net current in the slab is the current supplied by the external source. Note that the presence of an external field $H_e\,\vec{\imath}_y$, when applied *after* I_t, does not fundamentally change the distributions shown in Figs. 5.5 and 5.6; but if $H_e\,\vec{\imath}_y$ is applied *before* I_t, different $H_s(x)$ and $J(x)$ would emerge. In ***Discussion 5.1*** the effects of transport current on magnetization are studied in detail.

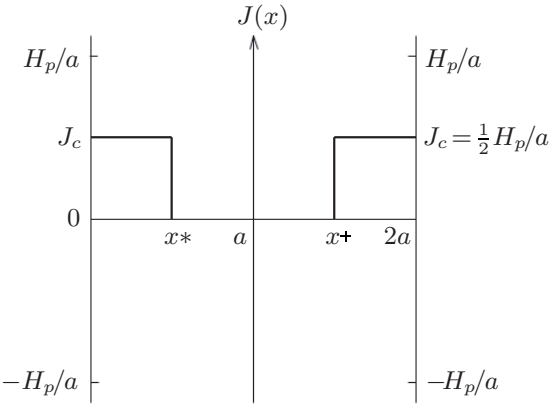

Fig. 5.6 $J(x)$ corresponding to $H_s(x)$ given in Fig. 5.5.

5.3 Measurement Technique

We describe here the technique most widely used to measure magnetization. Figure 5.7 presents the key components of this technique [5.6]: 1) a primary search coil; 2) a secondary search coil; and 3) a balancing potentiometer. Not shown in the figure but equally essential is an integrator that converts the bridge output voltage, $V_{bg}(t)$, to a voltage that is directly proportional to $M(H_e)$. The test sample is placed within the primary search coil set. When the primary and secondary search coils are subjected to a time-varying external magnetic field $H_e(t)$ which is nearly uniform over the space occupied by each search coil, voltages, $V_{pc}(t)$ and $V_{sc}(t)$, are induced across the terminals of each search coil:

$$V_{pc}(t) = \mu_\circ N_{pc} A_{pc} \left[\frac{dM}{dt} + \left(\frac{d\tilde{H}_e}{dt} \right)_{pc} \right] \tag{5.11a}$$

$$V_{sc}(t) = \mu_\circ N_{sc} A_{sc} \left(\frac{d\tilde{H}_e}{dt} \right)_{sc} \tag{5.11b}$$

The subscripts pc and sc refer to the primary and secondary search coils, respectively. N is the number of turns of each search coil and A is the effective area of each turn in the coil through which $H_e(t)$ is coupled. $\tilde{H}_e$ is the space-averaged field over each search coil.

The bridge output voltage $V_{bg}(t)$ is given by:

$$V_{bg}(t) = (k-1)V_{pc}(t) + kV_{sc}(t) \tag{5.12}$$

where k is a constant (from 0 to 1) that expresses the fraction of the potentiometer resistance (R) appearing in the primary side of the search coil in Fig. 5.7. Combining Eqs. 5.11 and 5.12, we obtain:

$$V_{bg}(t) = (k-1)\mu_\circ N_{pc} A_{pc} \frac{dM}{dt} + (k-1)\mu_\circ N_{pc} A_{pc} \left(\frac{d\tilde{H}_e}{dt} \right)_{pc} + k\mu_\circ N_{sc} A_{sc} \left(\frac{d\tilde{H}_e}{dt} \right)_{sc} \tag{5.13}$$

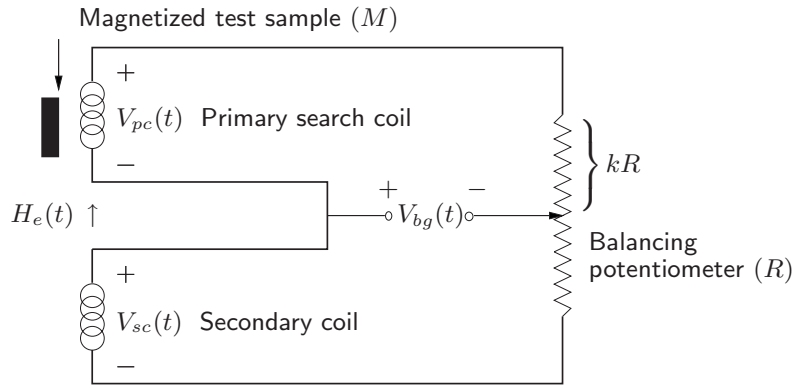

Fig. 5.7 Schematic of a magnetization measurement technique.

Now, it is possible to adjust k of the potentiometer to satisfy the following condition and make $V_{bg}(t)$ proportional to dM/dt:

$$(k-1)\mu_\circ N_{pc}A_{pc}\left(\frac{d\tilde{H}_e}{dt}\right)_{pc} + k\mu_\circ N_{sc}A_{sc}\left(\frac{d\tilde{H}_e}{dt}\right)_{sc} = 0 \tag{5.14a}$$

$$V_{bg}(t) = (k-1)\mu_\circ N_{pc}A_{pc}\frac{dM}{dt} \tag{5.14b}$$

Although in practice the condition required by Eq. 5.14a is not always satisfied over a wide frequency range, Eq. 5.14b is a good approximation for most cases. Generally k is close to 0.5. $V_{bg}(t)$ is fed into an integrator, and its output, $V_{mz}(t)$, is proportional to M. Specifically, if the test sample is in the virgin state ($M=0$) and $H_e(t)$ is *increased* ($H_e\uparrow$) from 0 (at $t=0$) to H_e (at $t=t_1$), then we have:

$$\begin{aligned} V_{mz}(H_e\uparrow) &= \frac{1}{\tau_{it}}\int_0^{t_1} V_{bg}(t)\,dt \\ &= \frac{(k-1)\mu_\circ N_{pc}A_{pc}}{\tau_{it}}M(H_e) \end{aligned} \tag{5.15}$$

where τ_{it} is the effective integrator time constant. If $H_e > H_p$, then $M(H_e) = -H_p/2 = -J_c a/2$ (Eq. 5.6), and Eq. 5.15 simplifies to:

$$V_{mz}(H_e\uparrow > H_p) = -f_m\frac{(k-1)\mu_\circ N_{pc}A_{pc}}{\tau_{it}}\left(\frac{J_c a}{2}\right) \tag{5.16a}$$

The factor f_m is the ratio of magnetic material volume to the total test sample volume. This factor is needed because generally a test sample does not consist entirely of magnetic material for which magnetization is measured; in the case of a multifilamentary conductor, for example, the test sample consists not only of superconducting filaments but also of a matrix metal and other nonmagnetic materials, e.g., insulator. If an external field excursion is $0 \rightarrow H_m > H_p \rightarrow H_e\downarrow < H_m - 2H_p$, then we have:

$$V_{mz}(H_e\downarrow < H_m - 2H_p) = f_m\frac{(k-1)\mu_\circ N_{pc}A_{pc}}{\tau_{it}}\left(\frac{J_c a}{2}\right) \tag{5.16b}$$

$\Delta V_{mz} = V_{mz}(H_e\uparrow > H_p) - V_{mz}(H_e\downarrow < H_m - 2H_p)$ is thus proportional to the "width" of magnetization curve at H_e:

$$\Delta V_{mz} = -f_m\frac{(k-1)\mu_\circ N_{pc}A_{pc}}{\tau_{it}}J_c a \tag{5.16c}$$

From Eq. 5.16c we note that ΔV_{mz} is directly proportional to J_c and a.

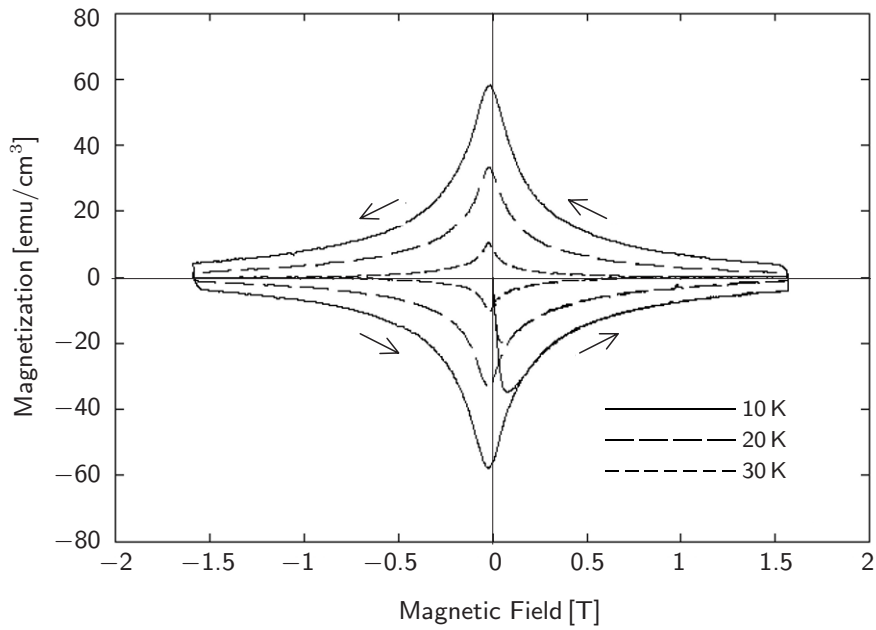

Fig. 5.8 Magnetization vs. field (in tesla) traces of MgB_2 at 10 K, 20 K, and 30 K [5.7].

Figure 5.8 shows magnetization vs. field (here given in the unit of tesla) traces of MgB_2 at 10 K, 20 K, and 30 K, each completing a field cycle, from 0 to +1.7 T, back to 0, to −1.7 T, and finally to 0 [5.7]. Note that unlike Fig. 5.3 which shows $-M(H_e)$ plots, these are $+M(H_e)$ plots. Because the traces are not tilted along the x (field) axis, we may conclude that the primary and secondary coils used in this measurement are well balanced.

The hysteretic nature of its magnetization clearly indicates that MgB_2 is a Type II superconductor. Note that the diamagnetic nature of this superconductor is evident in the first part of each trace when the field is increased from 0 towards 1.7 T, magnetization enters into the negative quadrant.

As may be inferred from $H_p = J_c a$ of Bean's model, magnetization is directly proportional to the superconductor's J_c. However, unlike in Bean's model, J_c is a decreasing function of not only field but temperature. Dependence on J_c and T are clearly evident in Fig. 5.8. Here, the magnetization is in emu/cm^3, a non-SI unit. In ***Discussion 5.1***, we shall apply Bean's model to the magnetization data of Fig. 5.8 to compute the material's J_c at 10 K in zero field.

*DISCUSSION 5.1: Magnetization with Transport Current**

As stated at the outset, magnetization in the presence of transport current depends on the order in which the external field and transport current are applied. Here we examine three cases: A) field and then transport current; B) transport current and then magnetic field; and C) field and then current, which is subsequently changed.

A. Field and then Transport Current

Figure 5.9 shows the field profiles inside a Bean slab of thickness $2a$, $H_s(x)$, after specific field-current sequences given below.

1. Initially, $H_{s1}(x)$, with $H_e = 2.5H_p$ and no transport current—dotted lines.
2. Next, $H_{s2}(x)$, after application of transport current $I_t = J_c a = I_c/2$, with the external field held constant—solid lines. Note that $J_c a = H_p$.
3. Finally, $H_{s3}(x)$, after transport current is increased further to $2J_c a = I_c$, with $H_e = 2.5H_p$, resulting in $H_{s3}(0) = 1.5H_p$ and $H_{s3}(2a) = 3.5H_p$—dashed line.

$H_{s1}(x)$ and $H_{s3}(x)$ are quite straightforward. $H_{s2}(x)$ consists of three piece-wise functions, $H_{s2_1}(x)$, $H_{s2_2}(x)$, and $H_{s2_3}(x)$:

$$H_{s2_1}(x) = 2H_p + J_c x = 2J_c a + J_c x \qquad (0 \le x \le x*)$$

$$H_{s2_2}(x) = 2.5H_p - J_c x = 2.5J_c a - J_c x \qquad (x* \le x \le x+)$$

$$H_{s2_3}(x) = H_p + J_c x = J_c a + J_c x \qquad (x+ \le x \le 2a)$$

where $x*$ and $x+$ are given by two intersections of $H_{s1}(x)$ and $H_{s2}(x)$. Namely, $H_{s1}(x*) = H_{s2_1}(x*)$ and $H_{s1}(x+) = H_{s2_3}(x+)$: $x* = 0.25a$ and $x+ = 0.75a$.

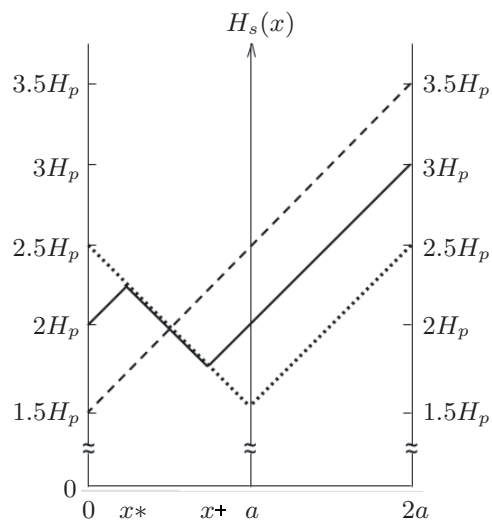

Fig. 5.9 Field profiles in the presence of $H_e = 2.5H_p$, first with $I_t = 0$ (dotted lines), then $I_t = J_c a = I_c/2$ (solid), and finally $I_t = 2J_c a = I_c$ (dashed).

* **Problems 5.1–3** in the 1st Edition (Plenum, 1994).

DISCUSSION 5.1: Magnetization with Transport Current (continuation)

Figure 5.10 shows $H_s(x)$ for the general case in the presence of I_t as piece-wise solid lines of $H_{s2_1}(x)$, $H_{s2_2}(x)$, and $H_{s2_3}(x)$. As noted in **5.2.2**, I_t (z-axis) is the transport current per unit y-axis length. Here, we define a dimensionless transport current, i: $i \equiv I_t/I_c$, where $I_c = 2aJ_c$. For $\int H_s(x)\,dx$ integration, the slab in Fig. 5.10 is divided into three areas, A_1, A_2, and A_3, as partitioned by the vertical dashed lines in Fig. 5.10. Note that $I_t = iI_c = 2iaJ_c = 2iH_p$.

The solid field line in area A_1 $(0 \le x \le x*)$, $H_{s2_1}(x)$, that in A_2 $(x* \le x \le x+)$, $H_{s2_2}(x)$, and that in A_3 $(x+ \le x \le 2a)$, $H_{s2_3}(x)$, are given by:

$$H_{s2_1}(x) = \left(H_e - \tfrac{1}{2}I_t\right) + J_c x \qquad (0 \le x \le x*)$$

$$H_{s2_2}(x) = H_e - J_c x \qquad (x* \le x \le x+)$$

$$H_{s2_3}(x) = \left(H_e + \tfrac{1}{2}I_t\right) + J_c(x - 2a) \qquad (x+ \le x \le 2a)$$

We solve for $x*$ and $x+$, and determine $H_{s2_2}(x*)$ and $H_{s2_2}(x+)$:

$$H_{s2_1}(x*) = H_{s2_2}(x*)$$

$$H_e - H_p i + J_c x* = H_e - J_c x* \quad \Longrightarrow \quad x* = \frac{H_p}{2J_c} i = \tfrac{1}{2}ai$$

$$H_{s2_2}(x*) = H_e - \tfrac{1}{2}aJ_c i = H_e - \tfrac{1}{2}H_p i$$

and

$$H_{s2_2}(x+) = H_{s2_3}(x+)$$

$$H_e - J_c x+ = H_e + H_p i + J_c(x+ - 2a) \quad \Longrightarrow \quad x+ = a\left(1 - \tfrac{1}{2}i\right)$$

$$H_{s2_2}(x+) = H_e - H_p + \tfrac{1}{2}H_p i$$

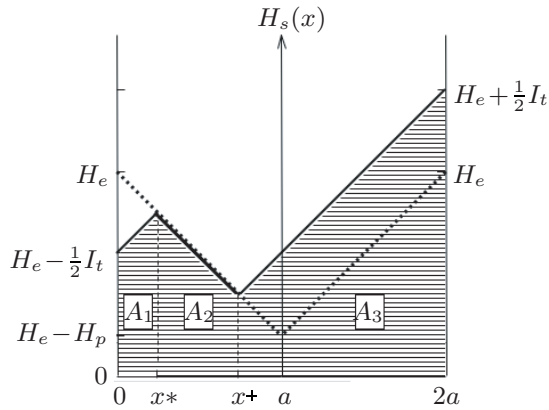

Fig. 5.10 Field profile with transport current (solid) for computation of magnetization. The vertical dashed lines partition three areas, A_1, A_2, and A_3.

DISCUSSION 5.1: Magnetization with Transport Current (continuation)

M is proportional to the size of the "shaded area," shown in Fig. 5.10, which is the sum of three partitioned areas A_1, A_2, and A_3.

The area of each trapezoid is its (base)×(height$_1$+height$_2$)/2.

$$\begin{aligned} A_1 &= \tfrac{1}{2}x*[H_{s1}(0) + H_{s2}(x*)] = \tfrac{1}{4}ai\left[(H_e - H_p i) + \left(H_e - \tfrac{1}{2}H_p i\right)\right] \\ &= \tfrac{1}{4}ai\left(2H_e - \tfrac{3}{2}H_p i\right) \\ &= a\left(\tfrac{1}{2}H_e i - \tfrac{3}{8}H_p i^2\right) \end{aligned}$$

$$\begin{aligned} A_2 &= \tfrac{1}{2}(x+ - x*)[H_{s2}(x*) + H_{s2}(x+)] \\ &= \tfrac{1}{2}(a - ai)\left(H_e - \tfrac{1}{2}H_p i + H_e - H_p + \tfrac{1}{2}H_p i\right) \\ &= \tfrac{1}{2}a(1-i)(2H_e - H_p) \\ &= a\left(H_e - H_e i - \tfrac{1}{2}H_p + \tfrac{1}{2}H_p i\right) \end{aligned}$$

$$\begin{aligned} A_3 &= \tfrac{1}{2}(2a - x+)[H_{s2}(x+) + H_{s3}(2a)] \\ &= \tfrac{1}{2}\left(a + \tfrac{1}{2}ai\right)(H_e - H_p + \tfrac{1}{2}H_p i + H_e + H_p i) \\ &= a\left(1 + \tfrac{1}{2}i\right)(H_e - \tfrac{1}{2}H_p + \tfrac{3}{4}H_p i) \\ &= a\big(H_e + \tfrac{1}{2}H_e i - \tfrac{1}{2}H_p - \tfrac{1}{4}H_p i + \tfrac{3}{4}H_p i + \tfrac{3}{8}H_p i^2\big) \end{aligned}$$

By combining these three areas, we may compute the shaded area:

$$\begin{aligned} \text{Shaded area} &= A_1 + A_2 + A_3 \\ &= a\big(\tfrac{1}{2}H_e i - \tfrac{3}{8}H_p i^2 + H_e - H_e i - \tfrac{1}{2}H_p + \tfrac{1}{2}H_p i \\ &\qquad + H_e + \tfrac{1}{2}H_e i - \tfrac{1}{2}H_p - \tfrac{1}{4}H_p i + \tfrac{3}{4}H_p i + \tfrac{3}{8}H_p i^2\big) \\ &= a(2H_e - H_p + H_p i) \end{aligned}$$

With the shaded area known, M can be computed quickly:

$$\begin{aligned} -M(i) &= H_e - \frac{1}{2a}\times(\text{Shaded area}) \\ &= H_e - H_e + \tfrac{1}{2}H_p - \tfrac{1}{2}H_p i \\ &= \tfrac{1}{2}H_p(1-i) && (5.17a) \\ &= -M(0)f_1(i) && (5.17b) \end{aligned}$$

where $f_1(i) = 1 - i$. $-M(i)$ decreases linearly with i, becoming 0 at $i = 1$.

DISCUSSION 5.1: Magnetization with Transport Current (continuation)

B. Transport Current and then Field

Here, the order is reversed for introducing external magnetic field and transport current to the slab. Specifically, a transport current of $J_c a = (I_c/2)\,\vec{\imath}_z$ (out of the paper) is introduced into the slab initially in the virgin state. Next, while I_t is held constant, an external magnetic field of $2H_p$ is applied in the $+y$-direction.

In Fig. 5.11 the dotted lines present $H_s(x)$ after a transport current of $J_c a$ $(=H_p/2)$ but before H_e of $2H_p$ is introduced; the solid lines present $H_s(x)$ after the field $H_e = 2H_p$ is introduced. In both cases the net current in the slab is $J_c a$.

Initially with $H_e = 0$:

$$I_t = \int_0^{2a} J(x)\,dx = J_c(0.5a) + J_c(2a - 1.5a) = J_c a$$

Next, with $H_e = 2H_p$:

$$I_t = \int_0^{2a} J(x)\,dx = -J_c(0.5a) + J_c(2a - 0.5a) = J_c a$$

To determine the magnetization in the slab for the general case of arbitrary current $(I < I_c)$, we must first find $x*$ (Fig. 5.12), which can be determined from the solid line in Region I, $H_{s1}(x)$ $(0 \le x \le x*)$ and that in Region II, $H_{s2}(x)$ $(x* \le x \le 2a)$.

$$H_{s1}(x) = (H_e - H_p i) - J_c x \qquad (0 \le x \le x*)$$

$$H_{s2}(x) = (H_e + H_p i) + J_c(x - 2a) \qquad (x* \le x \le 2a)$$

Because $H_{s1}(x*) = H_{s2}(x*)$, we may solve for $x*$ from the above expressions:

$$x* = a - ai = a(1 - i)$$

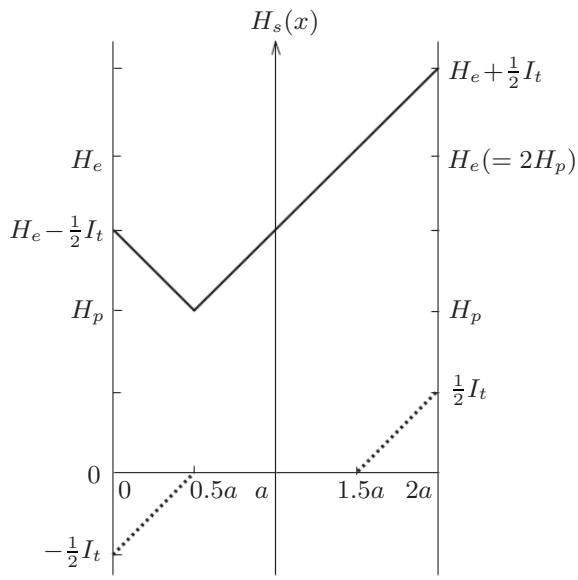

Fig. 5.11 Field profiles, with current only (dotted) and with current and field (solid).

DISCUSSION 5.1: Magnetization with Transport Current (continuation)

Once $x*$ is determined, we can compute $H_{s1}(x*)$:

$$H_{s1}(x*) = H_e - H_p i - J_c a(1-i) = H_e - H_p$$

We can now compute the shaded area, which is the sum of two areas, A_1 and A_2, partitioned by the vertical dashed line in Fig. 5.12.

$$\begin{aligned} A_1 &= \tfrac{1}{2}a(1-i)(H_e - H_p i + H_e - H_p) \\ &= a(1-i)\big(H_e - \tfrac{1}{2}H_p - \tfrac{1}{2}H_p i\big) \\ &= a\big(H_e - H_e i - \tfrac{1}{2}H_p + \tfrac{1}{2}H_p i^2\big) \end{aligned}$$

$$\begin{aligned} A_2 &= \tfrac{1}{2}(2a - a + ai)(H_e + H_p i + H_e - H_p) \\ &= a(1+i)\big(H_e - \tfrac{1}{2}H_p + \tfrac{1}{2}H_p i\big) \\ &= a\big(H_e + H_e i - \tfrac{1}{2}H_p + \tfrac{1}{2}H_p i^2\big) \end{aligned}$$

$$\begin{aligned} \text{Shaded area} &= A_1 + A_2 \\ &= a(2H_e - H_p + H_p i^2) \end{aligned}$$

Once the shaded area is known, we have M:

$$\begin{aligned} -M(i) &= H_e - \tfrac{1}{2}(2H_e - H_p + H_p i^2) \\ &= \tfrac{1}{2}H_p(1 - i^2) \qquad (5.18a) \\ &= -M(0) f_2(i) \qquad (5.18b) \end{aligned}$$

where $f_2(i) = 1 - i^2$. This magnetization is a parabolic function of i.

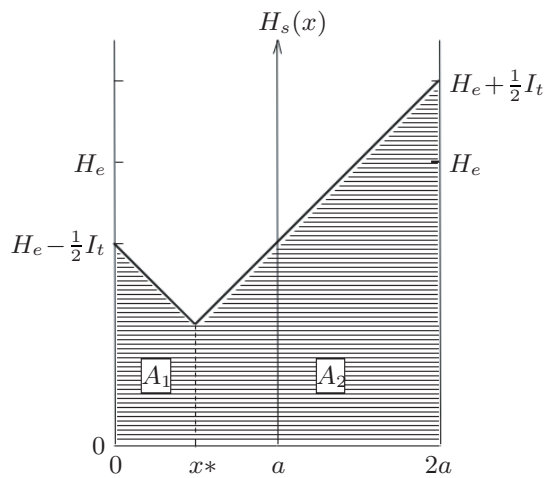

Fig. 5.12 Field profile with transport current and field for computation of magnetization. The vertical dashed line partitions areas A_1 and A_2.

DISCUSSION 5.1: Magnetization with Transport Current (continuation)

C. Field and then Current Changes

Finally, we shall consider $H_s(x)$ and $-M(i)$ for the slab when the following sequence of field and transport current is applied.

Step 1: Starting with a virgin state and $I_t = 0$ initially, the external magnetic field, $H_e = 2H_p$, is applied in the $+y$-direction.

Step 2: While H_e remains at $2H_p$, a transport current $I_t = 2H_p i$, where $i = I_t/I_c$, is introduced into the slab in the z-direction (out of the paper).

Step 3: With H_e remaining at $2H_p$, I_t is reduced to zero.

Step 4: I_t is now reversed and $|2H_p i|$ is introduced into the slab in the $-z$-direction (into the paper).

Step 5: I_t is again reduced to zero; H_e still remains at $2H_p$.

Figure 5.13 shows the field profile $H_s(x)$ after Step 5, consisting of five piece-wise solid lines, the second and third of which, useful to compute $M(i)$, are given below.

$$H_{s2}(x) = H_e + H_p i - J_c x \qquad (x* \le x \le a)$$
$$H_{s3}(x) = H_e + H_p i + J_c(x - 2a) \qquad (a \le x \le x+)$$

where $x*$ and $x+$ may be solved from: $H_{s2}(x*) = H_{s3}(x+) = H_e$. Thus:

$$H_{s2}(x*) = H_e \Longrightarrow H_e + H_p i - J_c x*$$
$$x* = \frac{H_p i}{J_c} = ai$$
$$H_{s3}(x+) = H_e \Longrightarrow H_e + H_p i + J_c(x+ - 2a)$$
$$x+ = 2a - \frac{H_p}{J_c} i = 2a - ai$$

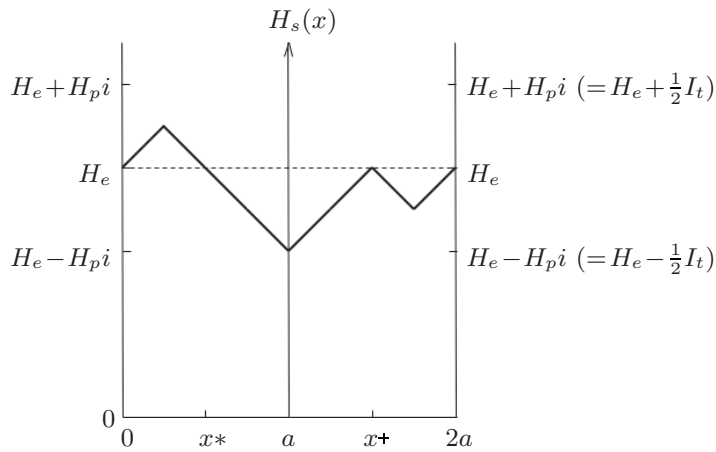

Fig. 5.13 Field profile after Step 5.

DISCUSSION 5.1: Magnetization with Transport Current (continuation)

The magnetization is computed from appropriate areas, shown in Fig. 5.14, in which the slab is divided into four "white" areas, from left to right, designated A_1 (rectangle), A_2 (trapezoid), A_3 (trapezoid), and A_4 (rectangle minus "triangle"). In the figure, "base" and "height" are given by:

$$\begin{aligned}\text{base} &= x+ - x* = (2a - ai) - ai = 2a(1-i)\\ \text{height} &= H_e - H_{s2}(a) = H_e - (H_e + H_p i - J_c a)\\ &= J_c a - H_p i = H_p(1-i)\end{aligned}$$

The two "dotted" areas in Fig. 5.14 are equal in magnitude but have "opposite" signs, hence they cancel out when we perform the area integral. The sum of the areas, A_1, A_2, A_3, and A_4, is given by:

$$\begin{aligned}\sum_{j=1}^{4} A_j &= 2aH_e - \text{crossed area}\\ \text{crossed area} &= \tfrac{1}{2}(\text{base})\times(\text{height})\\ \sum_{j=1}^{4} A_j &= 2aH_e - \tfrac{1}{2}2a(1-i)H_p(1-i)\\ &= 2aH_e - aH_p(1-i)^2\end{aligned}$$

The magnetization, $-M(i)$, is thus given by:

$$\begin{aligned}-M(i) &= H_e - \frac{1}{2a}[2aH_e - aH_p(1-i)^2]\\ &= \tfrac{1}{2}H_p(1-i)^2\\ -M(i) &= -M(0)(1-i)^2 \qquad (5.19a)\\ &= -M(0)f_3(i) \qquad (5.19b)\end{aligned}$$

where $f_3(i) = (1-i)^2$.

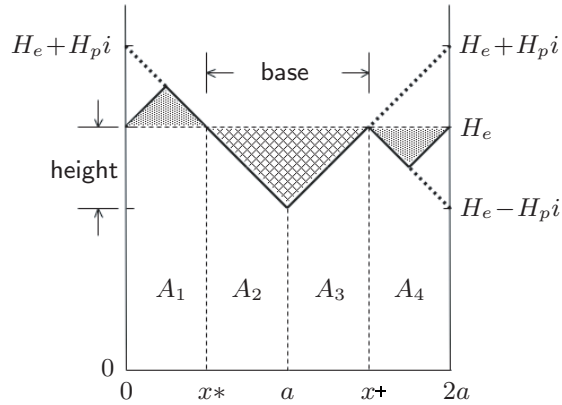

Fig. 5.14 Field profile (after Step 5) for computation of magnetization.

DISCUSSION 5.1: Magnetization with Transport Current (continuation)

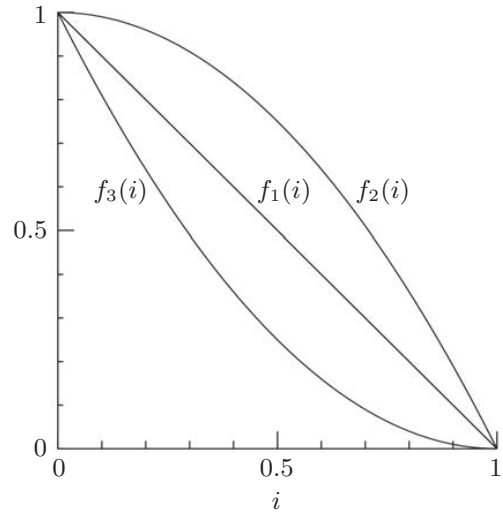

Fig. 5.15 Three normalized magnetization vs. normalized transport current functions studied in ***DISCUSSION 5.1***.

Magnetization Functions—Summary

Figure 5.15 presents three normalized magnetization functions, $f_1(i)$, $f_2(i)$, and $f_3(i)$, where $i = I_t/I_c$. It is interesting to note how different sequences of transport current and external field applications affect $M(i)$. These $f(i)$ functions were validated with experimental results [5.3, 5.4], thereby making Bean's model accepted quite quickly after its formulation.

DISCUSSION 5.2: SQUID for Magnetization Measurement

A SQUID (Superconducting Quantum Interference Device), based on the principle of the Josephson effect, is an electronic device that can be used to measure changes in magnetic field with extremely high resolution—individual flux quanta of magnitude 2.0×10^{-15} Wb (T m^2).

A typical SQUID magnetization measurement setup consists of a test sample, at a constant temperature, placed in a uniform field. The test sample is moved back and forth in the uniform field; during each cycle it cuts through measurement coils, one located at one end of the test sample and the other located at the other end. The induced current in each measurement coil is measured by the SQUID in terms of the field generated by the current, which, in turn, is a measure of the test sample's magnetization. Because SQUIDs operate best in low-field environments (perhaps no higher than ∼100 oersted or ∼0.01 T), they are usually shielded from the high-field environment of the test sample.

To do is to be. —Immanuel Kant
To be is to do. —Jean-Paul Sartre
Do be do be do. —Frank Sinatra

DISCUSSION 5.3: Magnetization in a "Bean Filament" Part 1: Field Parallel to the Filament's Axis

For an infinitely long superconducting filament of diameter d_f subjected to an external magnetic field parallel to the filament's axis (z), $H_e\,\vec{\imath}_z$, we may use the same assumptions as Bean to derive expressions for its magnetization. For an infinitely long filament exposed to $H_e\,\vec{\imath}_z$, Ampere's law (Eq. 2.5) is given by:

$$\frac{dH_z}{dr}\,\vec{\imath}_\theta = -J_c\,\vec{\imath}_\theta \tag{5.20}$$

Equation 5.20 states that an axially (z) directed magnetic field within the filament, $H_s(r)$, is a linear function of r with a slope of J_c.

A. Initial State

For $H_e \le H_p$, where H_p is the critical-state field, the field within the filament, $H_s(r)$, is zero from $r=0$ to $r*=(d_f/2-H_e/J_c)$ and varies as $J_c r$ from $r*$ to $d_f/2$:

$$H_s(r) = H_e\frac{r-r*}{d_f/2-r*} \qquad (r \ge r*) \tag{5.21}$$

Note that $r*=0$ when $H_e=H_p$, where H_p is the critical-state field:

$$H_p = \tfrac{1}{2}J_c d_f \tag{5.22}$$

Using steps similar to those taken with Eq. 5.4, we may compute the average magnetic induction within the filament, $\tilde{B}_s$:

$$\begin{aligned}\tilde{B}_s &= \frac{4\mu_\circ}{\pi {d_f}^2}\int_{r*}^{d_f/2} H_e\frac{r-r*}{d_f/2-r*}(2\pi r)\,dr \\ &= \frac{8\mu_\circ H_e}{d_f^2(d_f/2-r*)}\left(\tfrac{1}{24}d_f^3 - \tfrac{1}{8}d_f^2 r* + \tfrac{1}{6}{r*}^3\right)\end{aligned} \tag{5.23}$$

Unlike in the case of a slab, where the integration may be performed geometrically from $H_s(x)$, here the "area" integration must be performed mathematically. By inserting $r*=(d_f/2-H_e/J_c)$ into Eq. 5.23 and noting that $H_p=J_c d_f/2$, we obtain:

$$\frac{\tilde{B}_s}{\mu_\circ} = \frac{2H_e^2}{d_f J_c} - \frac{4H_e^3}{3(d_f J_c)^2} = \frac{H_e^2}{H_p} - \frac{H_e^3}{3H_p^2} \tag{5.24}$$

From the definition $M=\tilde{B}_s/\mu_\circ - H_e$, we have:

$$-M = H_e - \frac{H_e^2}{H_p} + \frac{H_e^3}{3H_p^2} \qquad (0 \le H_e \le H_p) \tag{5.25}$$

Note that Eq. 5.25 is similar to, but clearly different from, Eq. 5.5 for the slab.

B. Critical State and Beyond

For $H_e \ge H_p$ the filament is in the critical state, and its magnetization is constant and given from Eq. 5.25 with $H_e=H_p$:

$$-M = \tfrac{1}{3}H_p = \tfrac{1}{3}\left(\frac{J_c d_f}{2}\right) \qquad (H_e \ge H_p) \tag{5.26}$$

The "magnetization factor" for the filament is 1/3; for the slab it is 1/2 (Eq. 5.6).

DISCUSSION 5.3: Magnetization in a "Bean Filament" (continuation)

Part 2: Field Perpendicular to the Filament's Axis

When the applied external field is perpendicular to the axis of a filament of diameter d_f, the current distribution within the filament is complicated for $H_e \leq H_p$, the critical field. For $H_e \geq H_p$, a total current of $J_c \pi d_f^2/8$ is induced flowing in the $+z$-direction, and the same magnitude in the $-z$-direction. Figure 5.16 shows the current distributions for: a) a Bean slab ($2a$); and b) a filament of diameter d_f.

We may compute the magnetization, M, by integrating the magnetic moment, $\mathbf{m_A}$, per unit volume. Here, we derive expressions for the critical state magnetization for a Bean slab of width $2a$ and a filament of diameter d_f.

A. Bean Slab

For a Bean slab in the critical state, the magnetic moment $\mathbf{m_A}$ per unit length in both z- and y-directions, from $J_c(x)$ shown in Fig. 5.16a, is given by:

$$\mathbf{m_A} = \int_0^a 2x J_c(x)\, dx = J_c a^2 \tag{5.27a}$$

The conductor volume per unit length in both z- and y-directions is $2a$. Thus:

$$M = \frac{\mathbf{m_A}}{2a} = \tfrac{1}{2} J_c a \tag{5.27b}$$

M given by Eq. 5.27b, except for the sign, is identical to that given by Eq. 5.6.

B. Filament

For a filament of diameter d_f, the magnetic moment $\mathbf{m_A}$ per unit length in the z-direction, from $J_c(x, y)$ shown in Fig. 5.16b, is given by:

$$\mathbf{m_A} = \int_{-d_f/2}^{d_f/2} \int_0^{\sqrt{(d_f/2)^2 - y^2}} 2x J_c(x, y)\, dx\, dy = \tfrac{1}{6} J_c d_f^3 \tag{5.28}$$

The conductor volume per unit length in the z-direction is $\pi d_f^2/4$. Thus:

$$M = \frac{4\mathbf{m_A}}{\pi {d_f}^2} = \left(\frac{4}{3\pi}\right) J_c \left(\frac{d_f}{2}\right) \simeq 0.424 J_c \left(\frac{d_f}{2}\right) \sim 0.5 J_c a \tag{5.29a}$$

$$H_p = \left(\frac{8}{3\pi}\right) J_c \left(\frac{d_f}{2}\right) \tag{5.29b}$$

This is nearly the same ($8/3\pi \sim 1$) as that for a Bean slab of thickness d_f.

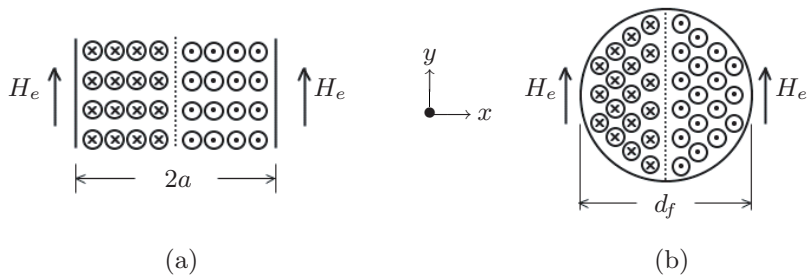

Fig. 5.16 Induced current distributions in a) Bean slab of width $2a$ and b) an infinitely long filament of diameter d_d, both subjected to an external field H_e in the y-direction.

DISCUSSION 5.4: J_c from Magnetization

We demonstrate here how critical current density (J_c) data may be extracted from magnetization (M) data. This method of extracting J_c data from M data is quite useful when dealing with superconductor test samples too short for a standard voltage vs. current measurement technique. Test samples too small for $V(I)$ measurement were common in the early days of HTS, and Bean's model discussed above was extremely useful.

In a $V(I)$ measurement the sample must be "long" to: 1) generate a detectable voltage with the very low electric field that defines the superconducting-to-normal transition—the typical criterion is between 0.1 to 1 μV/cm; and 2) keep the contact resistance to the lead wires at each end of the test sample "low," thereby preventing excessive heating at the ends which might cause a premature normal transition. The test samples should normally be at least 10 mm long; perhaps under certain circumstances they can be as short as 5 mm, but not much shorter than this. It depends largely on the level of critical current.

Figure 5.8 presented the magnetization vs. applied field traces at 10 K, 20 K, and 30 K of a short length (15 mm) of copper/MgB_2 composite wire of an equivalent circular diameter of 1.038 mm[5.7]; the MgB_2 itself has a diameter of 0.531 mm. Here, the unit of magnetization is given in emu/cm^3 corresponding to the *total* wire diameter of 1.038 mm. The external field is along the wire axis, i.e., the same configuration as in ***DISCUSSION 5.3 Part 1***. To compute the superconductor's J_c, for example, at 10 K in zero field, we treat the wire as a Bean rod of infinite length and 0.531 mm diameter. First, we convert emu/cm^3 into the SI unit equivalent, A/m, by multiplying it by 1000. (See Appendix I.)

At 10 K in zero field, the magnetization, from Fig. 5.8, is 60 emu/cm^3 or 60 kA/m. To translate this to M corresponding to the volume of just the MgB_2, we must multiply 60 kA/m by $(1.038/0.531)^2 = 4.0$. Solving Eq. 5.26 for J_c with $M = 240$ kA/m and $d_f = 5.31\times10^{-4}$ m, we obtain:

$$\begin{aligned} J_c(0\,\mathrm{T};10\,\mathrm{K}) &= \frac{6M(0\,\mathrm{T};10\,\mathrm{K})}{d_f} \\ &= \frac{6(240\times10^3\ \mathrm{A/m})}{(0.531\times10^{-3}\ \mathrm{m})} \\ &= 2.7\times10^9\ \mathrm{A/m^2} \end{aligned}$$

TRIVIA 5.1 Fill in the blank in a poetic couplet about one of the poet's contemporaries below. *God said, Let ____ be! and all was light.*

i) Bach; ii) Halley; iii) Newton; iv) Wren.

PROBLEM 5.1: Magnetization measurement*

This problem applies the magnetization measurement technique discussed in **5.4** to one of the four superconductors used in the Hybrid III SCM, to confirm that there would be no flux jumping. The absence of flux jumping is one of the necessary conditions for magnets that are not "cryostable"—this point will be discussed in more detail in ***CHAPTER 6***.

Table 5.1 presents specifications of the superconductor, a bare NbTi composite strip with overall dimensions of 9.2 mm width and 2.6 mm thickness. (Not all parameters in the table, e.g., twist pitch, are relevant for this problem.)

The test sample consisted of 52 (13×4) 100-mm long strips assembled in a rectangular solid of square cross section, 38 mm×38 mm, as shown in Fig. 5.17. Each bare strip was electrically insulated with a thin tape. In the orientation shown in Fig. 5.17a, each strip presents its narrow surface to the external magnetic induction B_e; in the orientation shown in Fig. 5.17b, each strip is broadside to B_e. The test sample assembly was placed inside a rectangular-bore (cross section 107 mm×42 mm) search coil set containing a primary search coil and two secondary coils (Fig. 5.17c). The test assembly midplane coincided with that of the primary search coil, whose midplane coincided with that of an external magnet generating B_e. The midplane-to-midplane distance between the primary and one of the secondary coils was 70 mm. The primary coil had 500 turns of fine copper wire over an axial distance of 40 mm centered on its midplane; each secondary search coil had 280 turns, extending an axial distance of 20 mm centered on its midplane. The turn density in the axial direction in each search coil was uniform.

When an external magnetic induction B_e was swept at a rate of 0.05 T/s between 0 and 5 T with the test sample at 4.2 K with its orientation as in Fig. 5.17a, a plot of $-M$ (given in V_{mz}) vs. B_e plot similar to that shown in Fig. 5.8 was obtained. $+V_{mz}$ is the integrator output proportional to $-M$, the negative of the test sample magnetization. The effective integration time, τ_{it}, was 1 s; the balancing potentiometer's constant k was 0.5. Assume negligible voltage drift.

Table 5.1: Specifications for a Hybrid III NbTi Conductor

Overall width, a	[mm]	9.2	Cu/Sc ratio, $\gamma_{c/s}$		3
Overall thickness, b	[mm]	2.6	T_c @ 10 T	[K]	4.7
Filament diameter†	[μm]	100	I_c @ 1.8 K, 10 T	[A]	6000
Twist pitch length, ℓ_p	[mm]	100	J_c @ 4.2 K, 5 T	[GA/m^2]	2.0
Insulation		none	—		—

† Computed value for filaments of circular cross section.

* Based on **Problem 5.5** in the 1st Edition (Plenum, 1994).

PROBLEM 5.1: Magnetization measurement (continuation)

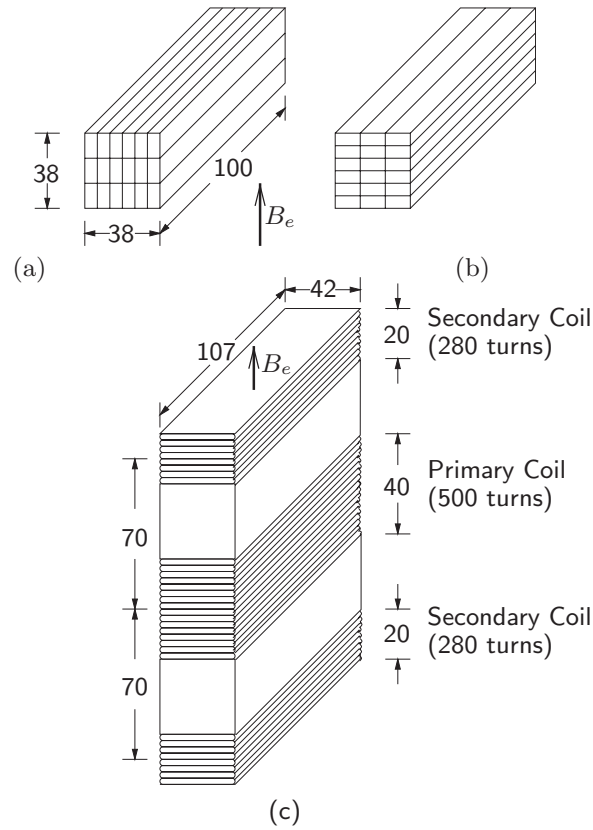

Fig. 5.17 Magnetization measurement details, dimensions in mm. (a) Each strip presents its narrow surface to the external magnetic induction, B_e; (b) Each strip is broadside to B_e; (c) Search coil setup.

a) Make a *ballpark* estimate of ΔV_{mz} at $B_e \sim 2.5\,\mathrm{T}$ (magnetization trace "width" in Fig. 5.8, given in volts). Note that $\tau_{it} = 1\,\mathrm{s}$ and $k = 0.5$. Assume $d_f = 2a$, where d_f is the filament diameter and $2a$ is the width of the Bean slab.

b) A 1.8-K measurement was performed by pumping on the cryostat and reducing the liquid helium bath pressure to 12.6 torr. The technician who controlled the cryostat pressure noticed that pressure control was more difficult, because of an increased liquid boil-off rate, when the test sample orientation was as in Fig. 5.17b rather than as in Fig. 5.17a. Is this an aberration or does his observation make sense? Explain.

c) The z-component of the external induction B_e over the radial space occupied by the search coil may be approximated to vary as:

$$B_e(z) \simeq B_e(0)\left[1 - c\left(\frac{z}{z_\circ}\right)^2\right] \tag{5.30}$$

where $z_\circ = 75\,\mathrm{mm}$. Based on information you have, compute the value of c.

Solution to PROBLEM 5.1

a) Equation 5.13 indicates that search coils need to be balanced; otherwise, a term proportional to the applied field contributes to the apparent magnetization. Since the $-M(H)$ trace shown in Fig. 5.8 is not tilted, the search coils are balanced. From Eq. 5.14*b*:

$$V_{bg}(t) = (k-1)\mu_\circ N_{pc} A_{pc} \frac{dM}{dt} \tag{5.14b}$$

We have from Eq. 5.16*c*:

$$\Delta V_{mz} = -f_m \frac{(k-1)\mu_\circ N_{pc} A_{pc}}{\tau_{it}} J_c a \tag{5.16c}$$

We have: $k = 0.5$; $\tau_{it} = 1\,\mathrm{s}$; $N_{pc} = 500$; $A_{pc} = (13)(0.1\,\mathrm{m})(2.6\times10^{-3}\,\mathrm{m}) = 3.38{\times}10^{-3}\,\mathrm{m}^2$ [also acceptable is $(0.1\,\mathrm{m}){\times}(38{\times}10^{-3}\,\mathrm{m}) = 3.8{\times}10^{-3}\,\mathrm{m}^2$]; f_m =(NbTi volume)/total composite volume)= $1/(\gamma_{c/s}+1) = 0.25$.

Estimate of J_c (4.2 K, 2.5 T)

From Table 5.1 we have J_c at 4.2 K and 5 T of $2.0\times10^9\,\mathrm{A/m^2}$. It is generally accepted that for a given temperature, $J_c(B_e)$ may be approximated, based on Eq. 1.3, by:

$$J_c = \frac{J_0 B_0}{B_e + B_0} \tag{S1.1}$$

where for NbTi, $B_0 \sim 0.3\,\mathrm{T}$. J_0 is the zero-field critical current density, which is usually difficult to measure. Thus from the J_c value at 5 T and $B_0 = 0.3\,\mathrm{T}$, we can first solve for $J_0 B_0$:

$$2.0{\times}10^9\,\mathrm{A/m^2} = \frac{J_0 B_0}{5\,\mathrm{T} + 0.3\,\mathrm{T}} \Longrightarrow J_0 B_0 = 10.6{\times}10^9\,\mathrm{A\,T/m^2}$$

Once $J_0 B_0$ is known, then J_c may be solved at 2.5 T. Thus:

$$J_c(2.5\,\mathrm{T}) = \frac{10.6{\times}10^9\,\mathrm{A\,T/m^2}}{2.8\,\mathrm{T}} = 3.8{\times}10^9\,\mathrm{A/m^2}$$

Inserting appropriate values into Eq. 5.16*c*, we have:

$$\begin{aligned}\Delta V_{mz} &= -0.25\frac{(-0.5)(4\pi{\times}10^{-7}\,\mathrm{H/m})(500)(3.38{\times}10^{-3}\,\mathrm{m^2})}{1\,\mathrm{s}} \\ &\quad \times(3.8{\times}10^9\,\mathrm{A/m^2})(50{\times}10^{-6}\,\mathrm{m}) \\ &\simeq 50\,\mathrm{mV}\end{aligned}$$

Solution to PROBLEM 5.1 (continuation)

Because the strip is flattened from a round conductor by a process that squeezes the conductor between rollers, the projected diameter of filaments in the direction parallel to B_e would be actually slightly less than the equivalent circular-area radius, $a = 50\,\mu$m, which is used in the above computation for ΔV_{mz}. If a radius less than $50\,\mu$m is used, ΔV_{mz} would be less than 50 mV.

b) The anisotropic shape of the NbTi filaments makes magnetization in the orientation of Fig. 5.17b greater than that in the orientation of Fig. 5.17a—the "effective" a is greater. Thus there will be more magnetization loss.

If the aspect ratio of the filaments is the same as for the conductor, eddy current loss will be proportional to $(a\dot{H}_e)^2$ in the orientation of Fig. 5.17b and $(b\dot{H}_e)^2$ in the orientation Fig. 5.17a—review **PROBLEM 2.8**. Thus eddy current loss is greater by a factor of $(9.2/2.6)^2 = 12.5$ for Fig. 5.17b than for Fig. 5.17a.

The increased heat load on the helium due to higher magnetization and eddy current losses causes a higher liquid helium boil-off rate; thus the technician's observation makes sense.

c) With balanced search coils, we have:

$$N_{pc}A_{pc}\left(\frac{d\tilde{B}_e}{dt}\right)_{pc} = N_{sc}A_{sc}\left(\frac{d\tilde{B}_e}{dt}\right)_{sc} \qquad (S1.2)$$

Because $A_{pc} = A_{sc}$, we have: $N_{pc}[\tilde{B}_e]_{pc} = N_{sc}[\tilde{B}_e]_{sc}$. From symmetry, we consider only the upper half (the unit mm is omitted in the following equations):

$$[\tilde{B}_e]_{pc} = \frac{B_e(0)}{20}\int_0^{20}\left[1 - c\left(\frac{z}{z_0}\right)^2\right]dz \qquad (S1.3a)$$

$$[\tilde{B}_e]_{sc} = \frac{B_e(0)}{20}\int_{60}^{80}\left[1 - c\left(\frac{z}{z_0}\right)^2\right]dz \qquad (S1.3b)$$

The $N_{pc}[\tilde{B}_e]_{pc} = N_{sc}[\tilde{B}_e]_{sc}$ equality gives:

$$\frac{250}{20}\int_0^{20}\left[1 - c\left(\frac{z}{z_0}\right)^2\right]dz = \frac{280}{20}\int_{60}^{80}\left[1 - c\left(\frac{z}{z_0}\right)^2\right]dz \qquad (S1.4)$$

$$250\left[20 - \frac{c}{3}\frac{(20)^3}{(75)^2}\right] = 280\left[80 - \frac{c}{3}\frac{(80)^3}{(75)^2} - 60 + \frac{c}{3}\frac{(60)^3}{(75)^2}\right]$$

$$5000 - 118.5c = 22400 - 8495.4c - 16800 + 3584c$$

$$c \simeq \frac{600}{4793} \simeq 0.125$$

DISCUSSION 5.5: Magnetic and Thermal Diffusion*

Before studying the flux jump criterion next in **PROBLEM 5.2**, we derive here basic equations of magnetic and thermal diffusion to identify two diffusivities: magnetic diffusivity, D_{mg}, and thermal diffusivity, D_{th}. The relative sizes of these two diffusivities are quite different for electrically conductive normal metals ($D_{th} \gg D_{mg}$) and for Type II superconductors ($D_{th} \ll D_{mg}$). This condition of $D_{th} \ll D_{mg}$ in Type II superconductors makes the penetration of flux into a superconductor an adiabatic process, leading, as we shall study in **PROBLEM 5.2**, to the criterion for flux jumping.

To derive the magnetic diffusion equation, the applicable Maxwell's equations are Ampere's law and Faraday's law, both in differential forms:

$$\text{Ampere's law:} \qquad \nabla \times \vec{H} = \vec{J}_f \tag{2.5}$$

$$\text{Faraday's law:} \qquad \nabla \times \vec{E} = -\frac{\partial \vec{B}}{\partial t} \tag{2.8}$$

For the slab (width $2a$) geometry, we can express Eqs. 2.5 and 2.8 as:

$$\text{Ampere's law:} \qquad \frac{\partial H_y}{\partial x} = J_z = \frac{E_z}{\rho_e} \tag{5.31}$$

$$\text{Faraday's law:} \qquad \frac{\partial E_z}{\partial x} = \frac{\partial B_y}{\partial t} = \mu_\circ \frac{\partial H_y}{\partial t} \tag{5.32}$$

where ρ_e is the material's electrical resistivity. From Eqs. 5.31 and 5.32, we obtain:

$$\rho_e \frac{\partial^2 H_y}{\partial x^2} = \mu_\circ \frac{\partial H_y}{\partial t}$$

$$\frac{\rho_e}{\mu_\circ} \frac{\partial^2 H_y}{\partial x^2} \equiv D_{mg} \frac{\partial^2 H_y}{\partial x^2} = \frac{\partial H_y}{\partial t} \tag{5.33}$$

Equation 5.33 is a magnetic diffusion equation, for which:

$$D_{mg} = \frac{\rho_e}{\mu_\circ} \tag{5.34}$$

Similarly, the one-dimensional thermal diffusion equation having constant thermal properties is given by:

$$k \frac{\partial^2 T}{\partial x^2} = C \frac{\partial T}{\partial t} \tag{5.35a}$$

where k and C are, respectively, the material's thermal conductivity and heat capacity. Dividing both sides of Eq. 5.35a by C, we obtain:

$$\frac{k}{C} \frac{\partial^2 T}{\partial x^2} \equiv D_{th} \frac{\partial^2 T}{\partial x^2} = \frac{\partial T}{\partial t} \tag{5.35b}$$

Equation 5.35b is a thermal diffusion equation, for which:

$$D_{th} = \frac{k}{C} \tag{5.36}$$

Note that Eq. 5.36 and 4.20 are equivalent, because $C = \varrho c_p$.

---

* Based on **Problems 6.5** in the 1st Edition (Plenum, 1994).

DISCUSSION 5.5: Magnetic and Thermal Diffusion (continuation)

Table 5.2: Diffusivities* of Stainless Steel and Copper at 4 K and 80 K

Metal		ρ_e [nΩ m]	k [W/m K]	C [J/m^3 K]	*Diffusivity* [m^2/s] D_{mg}	D_{th}
Stainless Steel	@4 K	500	0.2	3×10^{3}	0.4	7×10^{-5}
	@80 K	500	8	1.5×10^{6}	0.4	5×10^{-6}
Copper	@4 K	0.2	400	800	1.6×10^{-4}	0.5
	@80 K	2	600	1.8×10^{6}	1.6×10^{-3}	3×10^{-4}

* Property values are approximate.

Table 5.2 presents *approximate* values of electrical and thermal properties and corresponding diffusivities at 4 K and 80 K for stainless steel and copper. From Table 5.2 we can clearly see that stainless steel, a stand-in for normal-state superconductors, and copper are opposite with respect to magnetic and thermal diffusivities. Specifically, changes in magnetic field propagate quickly through stainless steel, whereas temperature gradients are relatively slow to propagate; hence, large nonuniform temperature distributions can be created in stainless steel during changing magnetic fields. Physically, it means that magnetic heating happens essentially adiabatically in Type II superconductors. In copper, the reverse is true: the magnetic field diffuses very slowly, while any nonuniformity in temperature is quickly "evened out." Therefore, copper in intimate contact with Type II superconductor can alleviate field-motion-induced instability in Type II superconductors. This thinking is the essence of dynamic stability, one of the stability criteria developed during the 1960s and 1970s [5.8] and applied also to HTS in the late 1980s [5.9].

Answer to TRIVIA 5.1 iii). The *Principia Mathematica* of Sir Isaac Newton (1642–1727) is regarded as a dominant force ushering in the *Age of Reason.* The complete couplet of the English poet Alexander Pope (1688–1744): *Nature and Nature's laws lay hid in night/God said, Let Newton be! and all was light.*

PROBLEM 5.2: Criterion for flux jumping*

This problem deals with the derivation of the critical conductor size above which flux jumping will occur. Flux jumping was once a major source of instabilities in the first superconducting magnets of engineering significance in the early 1960s [5.10]. Flux jumping is a thermal instability peculiar to a Type II superconductor that permits the magnetic field to penetrate its interior. A time-varying magnetic field, $\dot{H}_e$, at the conductor surface induces an electric field $\vec{E}$ in the conductor, which interacts with the supercurrent (density J_c). This $\vec{E}\cdot\vec{J}_c$ interaction heats the conductor. Since J_c decreases with temperature, the field (flux) penetrates further into the conductor, generating more heat, which further decreases J_c. The field penetration and temperature rise can cascade until the conductor loses its superconductivity. This thermal runaway event is called a flux jump.

a) Using the Bean model and computing the $\vec{E}\cdot\vec{J}_c$ interaction over the positive half ($0 \le x \le a$) of the slab, show that an expression for the dissipative energy density, e_ϕ [J/m^3], generated within the slab when the critical current density J_c is suddenly *decreased* by $|\Delta J_c|$ is given by:

$$e_\phi = \frac{\mu_\circ J_c |\Delta J_c| a^2}{3} \tag{5.37}$$

Note that the entire slab is in the critical state with its surface ($\pm a$) exposed to an external field of $H_e\,\vec{\imath}_y$.

b) Derive Eq. 5.37 by computing the Poynting energy flow into the slab at $x = a$ and equating it with the change in magnetic energy storage and dissipation energy $\mathcal{E}_\phi$ in the positive half of the slab.

c) To relate ΔJ_c to an equivalent temperature rise in the conductor, we may assume a linear temperature dependence for $J_c(T)$:

$$J_c(T) = J_{c_\circ}\left(\frac{T_c - T}{T_c - T_{op}}\right) \tag{5.38}$$

where $J_{c_\circ}$ is the critical current density at the operating temperature T_{op}. T_c is the critical temperature at a given magnetic induction $B_\circ$. From Eq. 5.38, ΔJ_c in Eq. 5.37 may be related to an equivalent temperature rise ΔT:

$$\Delta J_c = -J_{c_\circ}\left(\frac{\Delta T}{T_c - T_{op}}\right) \tag{5.39}$$

Now, by requiring that $\Delta T_s = e_\phi/\tilde{C}_s \le \Delta T$, where $\tilde{C}_s$ is the superconductor's average heat capacity [J/m^3 K] in the range from T_{op} to T_c, show thermal stability implies a critical slab half width a_c of:

$$a_c = \sqrt{\frac{3\tilde{C}_s(T_c - T_{op})}{\mu_\circ J_{c_\circ}^2}} \tag{5.40}$$

---

* Based on **Problem 5.6** in the 1st Edition (Plenum, 1994).

Solution to PROBLEM 5.2

a) Because of symmetry about $x = 0$, we shall consider only one half of the slab, between $x = 0$ and $x = a$. As illustrated in Fig. 5.18, the solid line corresponds to $H_{s1}(x)$, which gives the initial field distribution within the slab, with $J = J_c$. The dotted line corresponds to $H_{s2}(x)$ for the slab carrying $J_c - |\Delta J_c|$. Note that the field at the surface is H_e in both cases. We thus have:

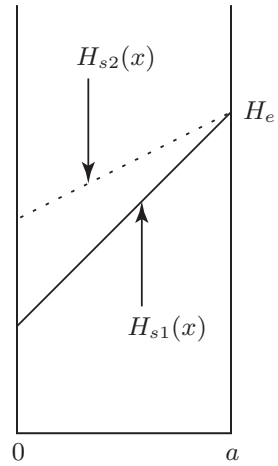

Fig. 5.18 Field profiles.

$$H_{s1}(x) = H_e + J_c(x - a) \qquad (S2.1a)$$

$$H_{s2}(x) = H_e + (J_c - |\Delta J_c|)(x - a) \qquad (S2.1b)$$

Because there is a change in magnetic field within the slab, an electric field $\vec{E}$ is generated, which from Faraday's law of induction is given by:

$$\oint_{\mathcal{C}} \vec{E} \cdot d\vec{s} = -\mu_\circ \int_{\mathcal{S}} \frac{\Delta H_s(x)\, \vec{\imath}_y \cdot d\vec{\mathcal{A}}}{\Delta t} \qquad (S2.2)$$

From symmetry we have $\vec{E}(x = 0) = 0$ and $\vec{E}$ points in the z-direction. $\Delta H_s(x)$ is given by:

$$\begin{aligned} \Delta H_s(x) &= H_{s2}(x) - H_{s1}(x) \\ &= |\Delta J_c|(a - x) \end{aligned} \qquad (S2.3)$$

Combining Eqs. $S2.2$ and $S2.3$, we obtain:

$$\begin{aligned} E_z(x) &= \mu_\circ \frac{|\Delta J_c|}{\Delta t} \int_0^x (a - x)\, dx \\ &= \mu_\circ \frac{|\Delta J_c|}{\Delta t} \left(ax - \frac{x^2}{2} \right) \end{aligned} \qquad (S2.4)$$

Dissipation power density, $p(x)$, is given by $E_z(x)J_c$; the total energy density per unit length dissipated in the slab or per unit slab surface area in the y-z plane, $\mathcal{E}_\phi$ [J/m^2], is given by:

$$\begin{aligned} \mathcal{E}_\phi &= \int_0^a p(x)\Delta t\, dx \\ &= \mu_\circ J_c |\Delta J_c| \int_0^a \left(ax - \frac{x^2}{2} \right) dx = \frac{\mu_\circ J_c |\Delta J_c| a^3}{3} \end{aligned} \qquad (S2.5)$$

The average dissipation energy density, e_ϕ, is given by $\mathcal{E}_\phi / a$:

$$e_\phi = \frac{\mu_\circ J_c |\Delta J_c| a^2}{3} \qquad (5.37)$$

Solution to PROBLEM 5.2 (continuation)

b) The Poynting energy flux [J/m^2] in the y-z plane into the slab (in the $-x$-direction) at $x = a$ is equal to the change in magnetic energy storage flux ΔE_m [J/m^2] and dissipation energy flux $\mathcal{E}_\phi$ in the slab. Thus:

$$\int S_x(a)\,dt = \Delta E_m + \mathcal{E}_\phi \tag{S2.6}$$

We can verify the direction of $\vec{S}$ by computing $\vec{S} = \vec{E}\times\vec{H}$ at $x = a$. At $x = a$, $\vec{H} = H_e\,\vec{\imath}_y$; from $E_z(x)$ derived in Eq. S2.4:

$$E_z(a) = \mu_\circ \frac{|\Delta J_c|a^2}{2\Delta t} \tag{S2.7}$$

Thus:

$$\vec{S}(a) = \mu_\circ \frac{|\Delta J_c|a^2}{2\Delta t}\,\vec{\imath}_z \times H_e\,\vec{\imath}_y = -\mu_\circ \frac{H_e|\Delta J_c|a^2}{2\Delta t}\,\vec{\imath}_x \tag{S2.8}$$

As expected, $\vec{S}(a)$ points in the $-x$-direction; energy indeed flows into the slab. Thus:

$$\int S_x(a)\,dt = \mu_\circ \frac{H_e|\Delta J_c|a^2}{2} \tag{S2.9}$$

The difference in magnetic energy flux ΔE_m in the slab is given by:

$$\begin{aligned}\Delta E_m &= \frac{\mu_\circ}{2}\int_0^a [H_{s2}^2(x) - H_{s1}^2(x)]\,dx \qquad (S2.10)\\ &= \frac{\mu_\circ}{2}\int_0^a \{[H_e + (J_c - |\Delta J_c|)(x-a)]^2 - [H_e + J_c(x-a)]^2\}\,dx\\ &= \frac{\mu_\circ}{2}\int_0^a [-2H_e|\Delta J_c|(x-a) - 2J_c|\Delta J_c|(x-a)^2 + |\Delta J_c|^2(x-a)^2]\,dx\end{aligned}$$

Neglecting the $|\Delta J_c|^2$ term in the above integral, we obtain:

$$\Delta E_m = \mu_\circ\left(\frac{H_e|\Delta J_c|a^2}{2} - \frac{J_c|\Delta J_c|a^3}{3}\right) \tag{S2.11}$$

From Eq. S2.6, we have:

$$\mathcal{E}_\phi = \int S_x(a)\,dt - \Delta E_m \tag{S2.12}$$

Combining Eqs. S2.9, S2.11, and S2.12, we obtain:

$$\begin{aligned}\mathcal{E}_\phi &= \mu_\circ \frac{H_e|\Delta J_c|a^2}{2} - \mu_\circ\left(\frac{H_e|\Delta J_c|a^2}{2} - \frac{J_c|\Delta J_c|a^3}{3}\right)\\ &= \mu_\circ \frac{J_c|\Delta J_c|a^3}{3} \qquad (S2.13)\end{aligned}$$

Equation S2.13 leads directly to Eq. 5.37:

$$e_\phi = \frac{\mathcal{E}_\phi}{a} = \frac{\mu_\circ J_c|\Delta J_c|a^2}{3} \tag{5.37}$$

Solution to PROBLEM 5.2 (continuation)

c) As given by Eq. 5.38, $J_c(T)$ is a decreasing function of temperature. We thus have:

$$\Delta J_c = -J_{c_\circ}\left(\frac{\Delta T}{T_c - T_{op}}\right) \tag{5.39}$$

From Eq. 5.39, we have:

$$|\Delta J_c| = \frac{J_{c_\circ}\Delta T}{T_c - T_{op}} \tag{S2.14}$$

Replacing J_c with $J_{c_\circ}$ in Eq. 5.37 and combining it with Eq. $S2.14$, we obtain:

$$e_\phi = \frac{\mu_\circ J_{c_\circ}^2 \Delta T a^2}{3(T_c - T_{op})} \tag{S2.15}$$

Note that e_ϕ is proportional not only to ΔT but also, more importantly, to a^2. Under adiabatic conditions, the dissipation energy density e_ϕ increases the superconductor's temperature by ΔT_s, given by:

$$\Delta T_s = \frac{e_\phi}{\tilde{C}_s} > 0 \tag{S2.16}$$

$\tilde{C}_s$ is the superconductor's average heat capacity [J/m^3 K] in the temperature range from T_{op} to T_c. Combining Eqs. $S2.15$ and $S2.16$, and requiring $\Delta T_s < \Delta T$ for thermal stability, we have:

$$\frac{\Delta T_s}{\Delta T} < \frac{\mu_\circ J_{c_\circ}^2 a^2}{3\tilde{C}_s(T_c - T_{op})} \tag{S2.17}$$

For a given superconducting material and operating temperature, a is the only parameter that can be varied by the magnet designer to satisfy Eq. $S2.17$. That is, thermal stability can be satisfied only if the slab half-width a is less than the critical size a_c, given by:

$$a_c = \sqrt{\frac{3\tilde{C}_s(T_c - T_{op})}{\mu_\circ J_{c_\circ}^2}} \tag{5.40}$$

Equation 5.40 is applied to compute approximate values of a_c for NbTi (LTS) operating at 4.2 K and YBCO (HTS) operating at 77.3 K. Table 5.3 lists approximate values of parameters appearing in Eq. 5.40 for both superconductors.

We may conclude that for a circular filament of NbTi, $a_c = 140\,\mu$m means a critical diameter of $\sim 300\,\mu$m (Eq. 5.29) and a coated YBCO tape of width 8 mm.

Table 5.3: Application of Eq. 5.40 to NbTi and YBCO

Superconductor	T_{op} [K]	T_c [K]	$J_{c_\circ}$ [A/m^2]	$\tilde{C}_s$ [J/m^3 K]	a_c [mm]
NbTi	4.2	9.8	2×10^9	6×10^3	0.14
YBCO	77.3	93	2×10^9	2×10^6	4

PROBLEM 5.3: Flux jumps*

The magnetization vs. ambient field trace shown in Fig. 5.19 was obtained with a monofilament Nb-Zr wire (0.5 mm ϕ) at 4.2 K carrying *no* transport current. (In the early 1960s, superconductors based on alloys of niobium and zirconium, Nb-Zr, preceeded Nb-Ti. Shortly after a composite superconductor became the standard form for magnet-grade superconductors in the mid 1960s, Nb-Ti (now more commonly designated NbTi), being much easier to co-process with copper than Nb-Zr, replaced Nb-Zr.) Note that both ordinate (magnetization) and abscissa (field) are given in non-SI units. Use Bean's model and treat the wire, of diameter d_f, as a slab of thickness $2a$.

a) Show that the field interval, ΔH_f, indicated in the trace, is consistent with the measured magnitude of magnetization.

b) Estimate the dissipation energy density, e_ϕ [J/m^3], resulting from the flux jump labeled A in Fig. 5.19. First, show that e_ϕ is given by:

$$e_\phi = \frac{(\mu_\circ H_p)^2}{6\mu_\circ} \tag{5.41}$$

c) Estimate the temperature rise for flux jump A. Assume the heat capacity of Nb-Zr to be independent of temperature and equal to 6 kJ/m^3 K.

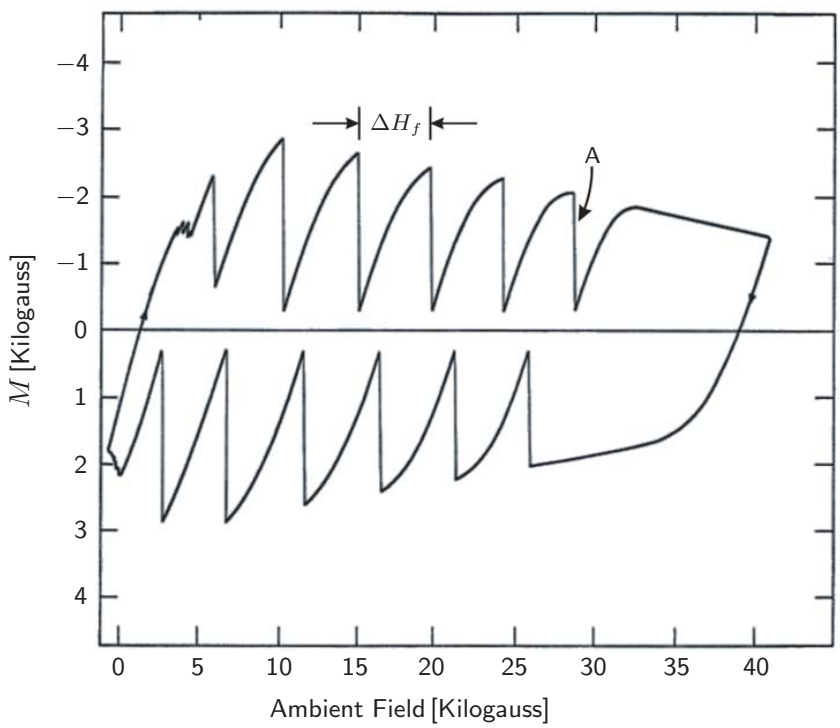

Fig. 5.19 Magnetization vs. ambient field trace for a 0.5-mm dia. Nb-Zr monofilament.

* Based on **Problem 5.7** in the 1st Edition (Plenum, 1994).

Solution to PROBLEM 5.3

a) From Bean's model, flux jumping can occur every H_p. Clearly, $H_p = \Delta H_f$, where ΔH_f is indicated in Fig. 5.19. Also, full magnetization for a slab is $H_p/2$.

From Fig. 5.19, $\Delta H_f \simeq 5\,\text{kilogauss}$, $\mu_\circ \Delta H_f = 0.5\,\text{T}$. Also from Fig. 5.19, $H_p/2 \simeq 2.5\,\text{kilogauss}$, which is (1/2) ΔH_f. They are consistent.

b) We can derive the flux jump energy density, e_ϕ, using the Poynting energy balance: $e_s = e_\phi + \Delta e_m$, where e_s is the Poynting energy density entering the superconductor at $x = a$, and Δe_m is its change in stored magnetic energy density. Let's consider only $0 \le x \le a$. $\Delta H(x)$ within the slab is given by:

$$\Delta H(x) = H_p \frac{(a-x)}{a} \tag{S3.1}$$

From Eq. $S3.1$, we have:

$$E(x) = \mu_\circ \frac{H_p}{\Delta t} \int_0^x \frac{a-x}{a}\, dx = \frac{\mu_\circ H_p}{a \Delta t} \left(ax - \frac{x^2}{2} \right) \tag{S3.2}$$

$\vec{S}$ at $x = a$ is thus given by:

$$\vec{S}(a) = -\frac{\mu_\circ}{2\Delta t} H_p a H_e\, \vec{\imath}_x \tag{S3.3}$$

$\vec{S}(a)$ is directed towards the slab, and the Poynting energy density e_s is given by:

$$e_s = \frac{\int S_x(a)\, dt}{a} = \frac{\mu_\circ}{2} H_p H_e \tag{S3.4}$$

The stored magnetic energy density after flux jumping (e_{m2}) is $\mu_\circ H_e^2/2$. The stored magnetic energy density before flux jumping, e_{m1}, is given by:

$$e_{m1} = \frac{\mu_\circ}{2a} \int_0^a [H_e + J_c(x-a)]^2\, dx \tag{S3.5}$$

$$= \frac{\mu_\circ}{2a} \left(H_e^2 a - H_e J_c a^2 + \frac{J_c^2 a^3}{3} \right) = \frac{\mu_\circ}{2} H_e^2 - \frac{\mu_\circ}{2} H_e H_p + \frac{\mu_\circ}{6} H_p^2 \tag{S3.6}$$

$$\Delta e_m = e_{m2} - e_{m1} = \frac{\mu_\circ}{2} H_e H_p - \frac{\mu_\circ}{6} H_p^2 \tag{S3.7}$$

Because $e_\phi = e_s - \Delta e_m$, we obtain:

$$e_\phi = \frac{\mu_\circ}{2} H_p H_e - \frac{\mu_\circ}{2} H_e H_p + \frac{\mu_\circ}{6} H_p^2 = \frac{\mu_\circ}{6} H_p^2 \tag{S3.8}$$

Equation $S3.8$ may be expressed as:

$$e_\phi = \frac{(\mu_\circ H_p)^2}{6\mu_\circ} \tag{5.41}$$

Inserting $\mu_\circ H_p = 0.5\,\text{T}$ into Eq. 5.41:

$$e_\phi \simeq \frac{(0.5\text{T})^2}{(6)(4\pi \times 10^{-7}\,\text{H/m})} \simeq 33 \times 10^3 \text{J/m}^3$$

c) $e_\phi = C_s \Delta T_s$; $33 \times 10^3 = 6 \times 10^3 \Delta T_s$. Solving for ΔT_s, we obtain: $\Delta T_s = 5.5\,\text{K}$, sufficient to drive the superconductor normal.

PROBLEM 5.4: Wire twisting*

As discussed in **PROBLEM 5.2**, to avoid flux jumping requires a conductor diameter less than $2a_c$, which for NbTi is $\sim 250\,\mu$m. With $J_{c_\circ}$ typically 2×10^9 A/m^2 (at 4.2 K and 5 T), a 250-μm diameter NbTi filament has a critical current of only $\sim$100 A—insufficient for most magnet applications if used singly. The idea of using many filaments, each small enough to avoid flux jumping, in a matrix of normal metal, emerged in the late 1960s to build conductors with critical currents as high as 1000 A. Today, 50-kA conductors are available.

In early (c. 1969) "multifilamentary" conductors, wires were untwisted. Coupling between filaments caused the wire as a whole to flux jump, despite each filament being small enough to satisfy the size criterion (Eq. 5.40). **PROBLEM 5.5** deals with such conductors. Results of a study of multifilamentary conductors, analytical and experimental, by Wilson and others at the Rutherford Laboratory in the late 1960s launched a new era of multifilamentary conductors [5.11].

Simply stated, when filaments are embedded in a conductive metal (e.g., copper) and subjected to a time-varying magnetic field, the filaments are electrically coupled according to Faraday's law. They then act as a single entity with an effective conductor diameter nearly as great as that of the entire conductor. The basic premise of the flux jumping criterion for isolated filaments is thus violated in an untwisted multifilamentary conductor. In order to eliminate flux jumping in multifilamentary conductors, filaments must be decoupled. Twisting of the wires, or more ideally transposition of the filaments (or strands of a multi-strand conductor), can do the trick of filament decoupling.

Consider a two-dimensional conductor model comprised of two Bean slabs, each d_f wide, separated by a copper slab of width $2w$ and electrical resistivity ρ_{cu}. Figure 5.20 shows the conductor as seen looking down the z-axis. Note that unlike the one-dimensional Bean slab which extends into infinity in both the y- and z-directions, this conductor is 2ℓ long in the y-direction.

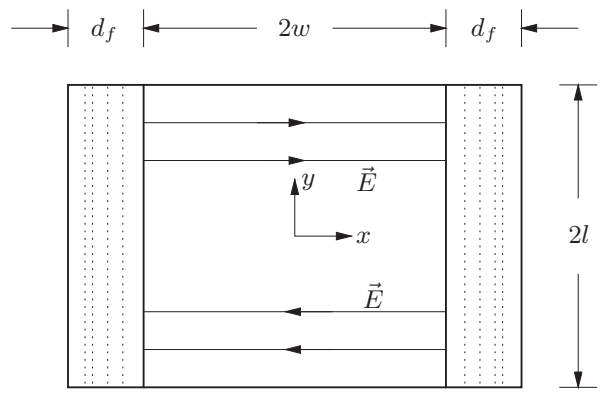

Fig. 5.20 Two-dimensional conductor consisting of a normal metal slab sandwiched between two Bean slabs.

* Based on **Problem 5.8** in the 1st Edition (Plenum, 1994).

PROBLEM 5.4: Wire twisting (continuation)

Suppose the conductor is subjected to a spatially uniform, time-varying magnetic field pointed in the z-direction, $\dot{H}_{0z}\vec{\imath}_z$.

a) Show that the x-directed electric field within the copper slab, E_{1x}, varies with y as given by:

$$E_{1x} = \mu_\circ \dot{H}_{0z} y \tag{5.42}$$

Assume the electric field in each superconducting slab to be zero—strictly speaking it is not, but compared with that in the copper, it is extremely small; hence the approximation of zero $\vec{E}$ field is valid. Also assume the field to be quasi-static. Under these assumptions, it is apparent that the $\vec{E}$ field in the copper, as indicated in Eq. 5.42, has only an x component.

b) Show that the net current flowing through the copper (per unit conductor depth in the z-direction), I_{cp} [A/m], from one superconducting slab to the other superconducting slab, over one half conductor length (from $y = 0$ to $y = \ell$), is given by:

$$I_{cp} = \int_0^\ell J_{cu}\, dy = \frac{\mu_\circ \dot{H}_{0z}}{\rho_{cu}} \int_0^\ell y\, dy = \frac{\mu_\circ \dot{H}_{0z} \ell^2}{2\rho_{cu}} \tag{5.43}$$

c) At a critical length ℓ_c, the net current I_{cp} given by Eq. 5.43, becomes equal to $J_c d_f$, the slab's critical current (per unit conductor depth). Show that the critical length ℓ_c is:

$$\ell_c = \sqrt{\frac{2\rho_{cu} J_c d_f}{\mu_\circ \dot{H}_{0z}}} \tag{5.44}$$

d) Multifilamentary superconductors for 60-Hz power applications must have a filament size (d_f) that is extremely small, in the range 0.1∼0.5 μm, which is even smaller than the wavelength of visible light (∼0.7 μm). This extremely small size is required to keep "manageable" the hysteresis energy, generated within each filament every time a magnetic field is cycled. (As will be discussed in ***CHAPTER 6***, hysteresis loss per cycle of field excitation is proportional to filament diameter.)

Compute ℓ_c for a typical "submicron" superconductor having the following parameters: $\rho_m = 30\,\text{n}\Omega\,\text{m}$; $J_c = 2\,\text{GA/m}^2$; $d_f = 0.2\,\mu\text{m}$; $\mu_\circ \dot{H}_{0z} = 2\,\text{kT/s}$ (equivalent to a sinusoidal excitation of 5-T amplitude magnetic induction at 60 Hz). ρ_m is the electric resistivity of the matrix, which is generally a copper-nickel alloy.

e) Compute the number of filaments required for a submicron multifilamentary conductor with a filament diameter of 0.2 μm having a critical current of 100 A. Use the same values of parameters given in **d)**.

Solution to PROBLEM 5.4

a) From Faraday's law, applied under the quasi-static assumption, we have:

$$\frac{\partial E_{1y}}{\partial x} - \frac{\partial E_{1x}}{\partial y} = -\mu_\circ \dot{H}_{0z} \qquad (S4.1)$$

Because $\vec{E}$ is zero in the superconducting slabs, $E_y = 0$ at $x = \pm w$, forcing $E_{1y} = 0$ everywhere in the copper slab. Thus:

$$E_{1x} = \mu_\circ \dot{H}_{0z} y \qquad (5.42)$$

b) Once the E field is known, the current density J_{cu} in the copper slab is given by: $J_{cu} = E_{1x}/\rho_{cu}$. The net current flowing in the copper from one superconducting slab to the other over half the conductor length is given by:

$$I_{cp} = \int_0^\ell J_{cu}\, dy = \frac{\mu_\circ \dot{H}_{0z}}{\rho_{cu}} \int_0^\ell y\, dy = \frac{\mu_\circ \dot{H}_{0z} \ell^2}{2\rho_{cu}} \qquad (5.43)$$

c) Equating I_{cp} given by Eq. 5.43 with $J_c d_f$ and solving for ℓ_c, we have:

$$\ell_c = \sqrt{\frac{2\rho_{cu} J_c d_f}{\mu_\circ \dot{H}_{0z}}} \qquad (5.44)$$

d) Inserting appropriate values into Eq. 5.44, we obtain:

$$\ell_c = \sqrt{\frac{2(3\times10^{-8}\,\Omega\,\mathrm{m})(2\times10^{9}\,\mathrm{A/m^2})(0.2\times10^{-6}\,\mathrm{m})}{2\times10^{3}\,\mathrm{T/s}}}$$

$$= 1.1\times10^{-4}\,\mathrm{m} = 110\,\mu\mathrm{m}$$

In typical submicron strands, the twist pitch length is thus $\sim$100 μm. This means that the diameter of such strands, by mechanical requirements, should be $\sim$1 μm; actually a thermal-magnetic stability criterion, similar to the flux jump criterion, requires it to be even smaller than 1 μm. This is because the strands, to reduce coupling losses, use Cu-Ni alloys as the matrix materials, resulting in a magnetic diffusion time constant that is smaller than the thermal diffusion time constant.

e) Critical current (I_c), critical current density (J_c), filament number (N_f) and diameter (d_f) in a multifilamentary conductor are related by:

$$I_c = N_f \frac{\pi d_f^2}{4} J_c \qquad (S4.2)$$

Solving for N_f from Eq. $S4.2$ with appropriate values of parameters, we obtain:

$$N_f = \frac{4I_c}{\pi d_f^2 J_c} = \frac{4(100\,\mathrm{A})}{\pi(0.2\times10^{-6}\,\mathrm{m})^2(2\times10^{9}\,\mathrm{A/m^2})}$$

$$= 1.6\times10^{6}$$

In submicron strands, the number of filaments may approach ten million.

PROBLEM 5.5: Magnetization of conductors*

This problem illustrates the effect of filament size and twisting on magnetization. In the late 1960s, three NbTi composite superconductors of equal volume were subjected to magnetization measurements [5.12]. Conductors 1, 2, and 3, respectively, are: twisted multifilamentary wire with a twist pitch length ℓ_{p1}; twisted multifilamentary wire with a twist pitch length $\ell_{p2} > \ell_{p1}$; and a monofilament.

Figure 5.21 presents three magnetization curves, labeled A, B, and C, for the three NbTi composite conductors. Each conductor was subjected to field pulses indicated by arrows in the figure. Traces A, B, and C do not necessarily correspond to Conductors 1, 2, and 3, respectively. Note that Traces B (B_1, B_2, B_3) show a dependence on field sweep rate; Trace C is independent of field sweep rate; Trace A also is independent of field sweep rate, but shows "partial" flux jumps induced by the field pulses.

a) Identify which magnetization trace corresponds to which conductor.

b) Estimate the ratio of filament diameter in the monofilament conductor to that in the multifilament conductors.

c) Estimate the value of ℓ_{p2}. Take $J_c d_f = 4\times10^4$ A/m for Conductors 1 and 2. Also comment on ℓ_{p1}.

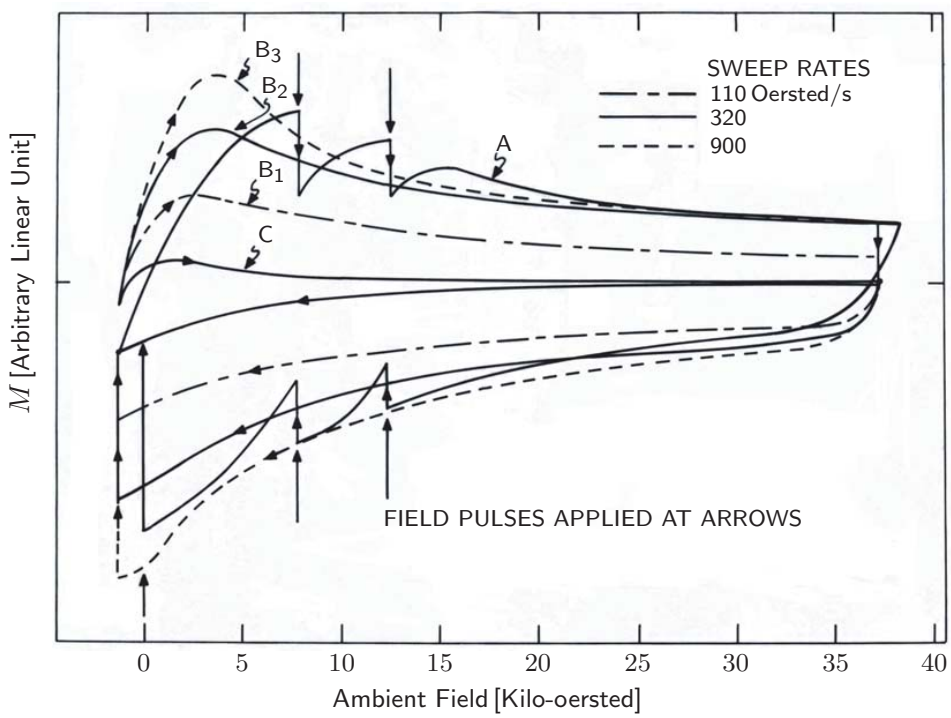

Fig. 5.21 Magnetization traces for Conductors 1, 2, and 3 [5.12].

* Based on **Problem 5.9** in the 1st Edition (Plenum, 1994).

Solution to PROBLEM 5.5

a) Note that Traces A and C are independent of field sweep rate and that the corresponding magnetization—an indication of filament diameter—is much greater for Trace A than that for Trace C. We therefore conclude that Trace A is for Conductor 3 (monofilament) and that Trace C is for Conductor 1 (ℓ_{p1}). That leaves Trace B for Conductor 2 (ℓ_{p2}). (Remember that each conductor has the same volume of NbTi superconductor, and thus its measured magnetization should be directly proportional to filament diameter.)

b) The ratio of magnetization width, $(M(H_e \uparrow) - M(H_e \downarrow))$ of Conductor 3 (monofilament, Trace A) to that of Conductor 1 (Trace C), is roughly 10 for $\mu_\circ H_e$ below $\sim$1 T (10 kilo-oersted). Therefore, we conclude that the filament diameter ratio is roughly 10.

c) Because a field sweep-rate of 900 oersted/sec ($\mu_\circ \dot{H}_{0z} = 0.09\,\mathrm{T/s}$) makes the magnetization of Conductor 2 (Trace B_3) nearly equal to that of Conductor 3 (Trace A), we may conclude that this sweep rate makes Conductor 2's filament twist pitch length ℓ_{p2} critical. Thus from Eq. 5.44:

$$\ell_{p2} = 2\sqrt{\frac{2\rho_{cu} J_c d_f}{\mu_\circ \dot{H}_{0z}}} \qquad (S5.1)$$

With $\rho_{cu} = 2\times10^{-10}\,\Omega\,\mathrm{m}$; $J_c d_f = 4\times10^4\,\mathrm{A/m}$; and $\mu_\circ \dot{H}_{0z} = 0.09\,\mathrm{T/s}$, we obtain:

$$\ell_{p2} = 2\sqrt{\frac{(2)(2\times10^{-10}\,\Omega\,\mathrm{m})(4\times10^4\,\mathrm{A/m})}{0.09\,\mathrm{T/s}}}$$

$$= 2.7\times10^{-2}\,\mathrm{m} = 27\,\mathrm{mm}$$

This value is close enough to the actual twist pitch of 10 mm. Because the magnetization of Conductor 1 (Trace C) at a sweep rate of 320 oersted/sec is considerably smaller than that of Conductor 2 for the same field sweep rate, we conclude that ℓ_{p1} is significantly shorter than ℓ_{p2}.

DISCUSSION 5.6: Twisting

An important implication of the condition $I_{cp} = J_c d_f$, used to derive Eq. 5.44 (**PROBLEM 5.4**), is that the two superconducting slabs are electrically coupled. Were the conductor length substantially shorter than $2\ell_c$, on the other hand, the two would be decoupled. In reality, these slabs may be decoupled, even if each one is much longer than $2\ell_c$, if they are alternated in their positions with a pitch length less than $2\ell_c$. In multifilamentary conductors, we can achieve partial decoupling by twisting the wires with a pitch length $\ell_p \ll 2\ell_c$; $2\ell_c$ must be small when $\dot{H}_{0z}$ is large. Note that in a twisted conductor each filament remains at a fixed radial distance from the strand axis. By contrast, in a cable of *transposed* strands, more complete decoupling is possible, because when strands are transposed each strand is made to occupy every radial position across the cable diameter as it spirals along the cable's transposition length.

DISCUSSION 5.7: Flux Jumping in HTS?

A. Size Criterion for "Complete" Flux Jumping

The conductor size criterion (Eq. 5.40) was originally derived for LTS in the limit $\Delta e_\phi/\Delta T = C_s$, where C_s is the superconductor heat capacity per unit volume, assumed constant. Because in LTS, the temperature excursion in a complete flux jump, i.e., $T_c - T_{op}$, is small, this size criterion is adequate.

A general condition for suppression of flux jumping, under *adiabatic* conditions, is that the superconductor's magnetic energy must be less than its thermal density. Under *adiabatic* conditions a flux jump can proceed to *completion* only if the *initial* magnetic energy density at T_{op}, $e_\phi(T_{op})$, exceeds the thermal energy density required to heat the superconductor from T_{op} to T_c:

$$e_\phi(T_{op}) \geq h_s(T_c) - h_s(T_{op}) \tag{5.45}$$

where $h_s(T_c)$ and $h_s(T_{op})$ are the superconductor enthalpies, respectively, at T_c and T_{op}. Because $e_\phi(T_{op}) = [\mu_\circ H_p(T_{op})]^2/6\mu_\circ$, and for Bean slab, $H_p(T_{op}) = aJ_c(T_{op})$, the conductor size criterion, a_c, for suppressing *complete* flux jumping is given by:

$$a_c = \sqrt{\frac{6[h_s(T_c) - h_s(T_{op})]}{\mu_\circ J_c^2(T_{op})}} \tag{5.46}$$

Comparing these two size criteria (Eqs. 5.40 and 5.46), we may conclude that under adiabatic conditions, a flux jump may initiate if the conductor size is greater than that specified by Eq. 5.40, but it may be only "partial" if the size does not exceed that of Eq. 5.46. Thus, flux jumps will be only partial in a superconductor that either violates the size criterion of Eq. 5.40 but not Eq. 5.46, or the process is not adiabatic. Note that even those flux jumps seen in Fig. 5.19 are, strictly speaking, not complete, most probably because the process was not perfectly adiabatic.

B. Flux Jumping in HTS

Because T_c is ∼100 K in HTS, under adiabatic conditions the energy condition of Eq. 5.45 is unlikely to be satisfied. *Flux jumping is unlikely in HTS.*

For YBCO with $T_{op} = 77$ K and $T_c = 93$ K (zero field and current), for example, the enthalpy difference is $\approx 20\,\mathrm{MJ/m^3}$ (60% of the enthalpy difference for copper—from C_p differences of the two materials at 120 K), and with $J_c(T_{op}) = 10^{10}\,\mathrm{A/m^2}$, we compute, from Eq. 5.46: $a_c \simeq 1$ mm (∼2 mm diameter). Note that a YBCO wire of 2-mm diameter will have a "Bean" magnetization, $\mu_\circ M = \mu_\circ a J_c(T_{op}) \sim 2$ T.

Despite our expectation for HTS, flux jumps, not merely partial but also complete, have been observed in HTS, for example, in "thin" crystals, $2a = 4.2$ mm, with a y-axis extent of 0.2 mm (thus "thin" rather than ∞ as in a Bean slab) of BSCCO-2212 [5.13] and thin (∼100-μm) films of Type II superconductors including YBCO [5.14]. Nevertheless, in a *real* magnet-grade-superconductor, even of HTS, because it must satisfy many requirements, including limiting AC losses, the requirement that imposes, among other conditions, a severe size restriction, flux jumping should be one of the least troubling aspects for HTS magnets.

REFERENCES

[5.1] C.P. Bean, "Magnetization of hard superconductors," *Phys. Rev. Lett.* **8**, 250 (1962).

[5.2] Y.B. Kim, C.F. Hempstead, and A.R. Strnad, "Magnetization and critical supercurrents," *Phys. Rev.* **129**, 528 (1963).

[5.3] M.A.R. LeBlanc, "Influence of transport current on the magnetization of a hard superconductor," *Phys. Rev. Lett.* **11**, 149 (1963).

[5.4] Kō Yasukōchi, Takeshi Ogasawara, Nobumitsu Usui, and Shintaro Ushio, "Magnetic behavior and effect of transport current on it in superconducting Nb-Zr wire," *J. Phys. Soc. Jpn.* **19**, 1649 (1964).

Kō Yasukōchi, Takeshi Ogasawara, Nobumitsu Usui, Hisayasu Kobayashi, and Shintaro Ushio, "Effect of external current on the magnetization of non-ideal Type II superconductors," *J. Phys. Soc. Jpn.* **21**, 89 (1966).

[5.5] H.T. Coffey,"Distribution of magnetic fields and currents in Type II superconductors," *Cryogenics* **7**, 73 (1967).

[5.6] W.A. Fietz, "Electronic integration technique for measuring magnetization of hysteretic superconducting materials," *Rev. Sci. Instr.* **36**, 1621 (1965).

[5.7] Figure 5.8, modified for use here by Mohit Bhatia (Ohio State University), from the work of M.D. Sumption, E.W. Collings, E. Lee, X.L. Wang, S. Soltanina, S.X. Dou, and M.T. Tomsic, "Real and apparent loss suppression in MgB_2 superconducting composite," *Physica C*, 98 (2002).

[5.8] H.R. Hart, Jr., "Magnetic instabilities and solenoid performance: Applications of the critical state model," *Proc. 1968 Summer Study on Superconducting Devices and Accelerators*, (Brookhaven National Laboratory, Upton, NY, 1969), 571.

[5.9] T. Ogasawara, "Conductor design issues for oxide superconductors. Part 2: exemplification of stable conductors," *Cryogenics* **29**, 6 (1989).

[5.10] See, for example, M.S. Lubell, B.S. Chandrasekhar, and G.T. Mallick, "Degradation and flux jumping in solenoids of heat-treated Nb-25% Zr wire," *Appl. Phys. Lett.* **3**, 79 (1963).

[5.11] Superconducting Applications Group (Rutherford Laboratory), "Experimental and theoretical studies of filamentary superconducting composites," *J. Phys.* **D3**, 1517 (1970).

[5.12] Y. Iwasa, "Magnetization of single-core, multi-strand, and twisted multi-strand superconducting composite wires," *Appl. Phys. Lett.* **14**, 200 (1969).

[5.13] A. Nabiałek, M. Niewczas, H. Dabkowska, A. Dabkowski, J.P. Castellan, and B. D. Gaulin, "Magnetic flux jumps in textured $Bi_2Sr_2CaCu_2O_{8+\delta}$," *Phys. Rev. B* **67**, 024518 (2003).

[5.14] Igor S. Aranson, Alex Guerevich, Marco S. Welling, Rinke J. Wijngaarden, Vitalii K. Vlasko-Vlasov, Valerii M. Vinokur, and Ulrich Welp, "Dendritic flux avalanches and nonlocal electrodynamics in thin superconducting films," *Phys. Rev. Lett.* **94**, 037002 (2005).

Chapter 6
Stability

6.1 Introduction

Reliability is one of the major requirements that all devices must meet, superconducting magnets included. Historically, reliability has been one of the most troubling, and therefore most challenging, aspects of superconducting magnet technology. As illustrated in Fig. 1.5, superconductivity exists within a phase volume bounded by three parameters: current density (J), magnetic field (H), and temperature (T).

Of these parameters, as examined in ***Chapter 3***, the designer can define, and more importantly control, current density and magnetic field quite well, at least under normal operating conditions. Even under a complex fault-mode condition such as that involving more than one solenoid in a hybrid or nested multi-coil magnet, the current density and magnetic field are tractable: the magnet designer has firm control of these two parameters. This is not strictly the case with temperature: it is the least tractable of the three. The magnitude of its excursion from the operating point could vary unpredictably in time and, more intractably, in space within the winding. The energy stored in the magnet, both magnetic and mechanical, can easily be converted into heat, raising the conductor temperature to above its critical value at one or more locations in the winding. Indeed, virtually every "stability problem" of a superconducting magnet may be traceable to the magnet designer's inability to keep the winding temperature intact at its operating point.

In this chapter we shall consider: 1) basic physics controlling temperature in a superconducting winding; and 2) stability evaluation methods to quantify the likelihood of an unscheduled temperature rise within the winding. ***Chapters 7*** and *8* also deal with temperature rise in the winding under different contexts: ***Chapter 7*** on causes or sources of temperature rises; and ***Chapter 8*** on methods to protect magnets subsequent to unscheduled temperature rises. First, there is a striking difference in this stability issue between LTS and HTS magnets.

LTS vs. HTS

As remarked in reference to Fig. 1.6, difficulty or cost of stability decreases with increasing operating temperature. In a discussion below, we will compare "stability margins" of LTS and HTS magnets and show that an HTS magnet is indeed very stable. That is, *every HTS* magnet will reach its operating current without any "premature quench." Such incidents often still afflict "high-performance" (i.e., "adiabatic" and "high" overall current density) LTS magnets.

This means stability is no longer as pressing a design/operation issue for HTS magnets as it is for LTS magnets. Nevertheless, stability remains a key issue for HTS magnets [6.1–6.8].

Y. Iwasa, *Case Studies in Superconducting Magnets: Design and Operational Issues*,
DOI: 10.1007/b112047_6,

6.2 Stability Theories and Criteria

We will discuss the thermal stability of a superconducting magnet carrying operating current I_{op} by examining the power density equation governing the temperature, T, of a unit superconductor volume:

$$C_{cd}(T)\frac{\partial T}{\partial t} = \nabla\cdot[k_{cd}(T)\nabla T] + \rho_{cd}(T)J^2_{cd_\circ}(t) + g_d(t) - \left(\frac{f_p\mathcal{P}_D}{A_{cd}}\right)g_q(T) \qquad (6.1)$$

In Eq. 6.1, the left-hand side represents the time rate of change of thermal energy density of the conductor, where $C_{cd}(T)$ is the heat capacity per unit volume of the conductor, which, after the development in 1964 by Stekly [6.9] of "composite" superconductors, consists of superconductor and normal-metal matrix. For complete steady-state stability, this term must remain zero at all times; in practice a modest temperature excursion, ΔT_{op} from the operating point, T_{op}, is permitted during operation in most windings, even "adiabatic" ones. Because this permissible ΔT_{op} is generally much greater in HTS magnets than in LTS magnets, as stated at the outset, stability is almost a non-issue for HTS magnets. This point is elaborated a bit more below.

In the right-hand side, each on a per unit volume basis, the first term describes thermal conduction into the composite superconductor element, where $k_{cd}(T)$ is the thermal conductivity of the composite. The second term is Joule heating, where $\rho_{cd}(T)$ is the composite's electrical resistivity (zero in the superconducting state), and $J_{cd_\circ}(t)$ is the current density at operating current $I_{op}(t)$, which can depend on time. $g_d(t)$ describes non-Joule heat generation, primarily magnetic and mechanical in origin. The last term represents cooling, where f_p is the fraction of the composite perimeter, $\mathcal{P}_D$, exposed to cryogen, A_{cd} is the composite cross sectional area, and $g_q(T)$ is the convective heat transfer flux for the cryogen.

The history of the development of theories and concepts for stability (and protection to be discussed in ***CHAPTER 8***) has evolved around solutions to simplifications of Eq. 6.1. Table 6.1 lists various concepts derived from Eq. 6.1 under special conditions. In the table, a parameter labeled 0 signifies that it is negligible or not considered in the equation; $\surd$ signifies inclusion. Before discussing each term of Eq. 6.1, we briefly discuss the concepts listed in Table 6.1.

Table 6.1: Concepts Derived from Power Density Equation (Eq. 6.1)

$C_{cd}(T)(\partial T/\partial t)$	$\nabla\cdot[k_{cd}(T)\nabla T]$	$\rho_{cd}(T)J^2_{cd}(t)$	$g_d(t)$	$g_q(T)$	*Concept*
$\surd$	0	0	$\surd$	0	Flux jump
0	0	$\surd$	0	$\surd$	Cryostability
$\surd$	$\surd$	$\surd$	0	$\surd$	Dynamic stability
0	$\surd$	$\surd$	0	$\surd$	"Equal area"
0	$\surd$	$\surd$	0	0	MPZ*
$\surd$	0	$\surd$	0	0	Protection
$\surd$	$\surd$	$\surd$	0	0	Adiabatic NZP†

* Minimum propagating zone.

† Normal zone propagation.

6.2.1 Concepts Derived from Equation 6.1

Each concept derived from Eq. 6.1 and listed in Table 6.1 is briefly discussed below.

Flux Jumping

As examined in ***CHAPTER 5***, criteria have been developed to eradicate most instances of flux jumping, which generally afflicts LTS.

Cryostability

The basic concept of cryostability was developed in the mid 1960s as an engineering solution to achieve reliable magnet operation [6.9]. In a "cryostable" composite conductor, a superconductor is co-processed with a highly conductive matrix metal [6.10], and a large portion of the conductor surface is exposed to cryogen to ensure "local" cooling. As shown by Table 6.1, the terms other than the Joule heating and cooling terms may be neglected. Many successful magnets in the 1970s are cryostable [6.11, 6.12]; it is now applied only to "large" LTS magnets. As we shall see later, it is not applied to HTS magnets. The cryostable concept is further studied in this chapter's **PROBLEMS & *DISCUSSIONS***.

Dynamic Stability

As studied in ***CHAPTER 5***, when the magnetic diffusivity is much greater than the thermal diffusivity, as in Type II superconductors, flux jumping can occur when the conductor size criterion to suppress it cannot be readily met, e.g., a tape conductor. By loading the superconductor with a high thermal diffusivity material, e.g., copper, we may balance the two diffusivities and achieve stable operation free of flux jumping. Tape-LTS is now rarely used; flux jumping is unlikely in HTS tapes (***DISCUSSION 5.7***). This criterion is not discussed further in this chapter.

Equal Area

The "equal-area" criterion is a special case of cryostability in which the thermal conduction term $(\nabla \cdot [k_{cd}(T)\nabla T])$ in Eq. 6.1 is included to improve the overall current density at which the magnet may be cryostable. This will be further discussed in the **PROBLEMS & *DISCUSSIONS***.

MPZ

The concept of MPZ (minimum propagating zone) considers the effect on coil performance of a local disturbance, $g_d(t)$ in Eq. 6.1, in the winding [6.13]. The MPZ concept shows that it is possible for a magnet to remain superconducting even in the presence of a small normal-state region in its winding, provided that the normal-zone volume is smaller than a critical size defined by the MPZ theory. Its importance in adiabatic magnets was recognized by Wilson in the late 1970s [1.27], and it has since become an indispensable concept for analyzing the stability of adiabatic magnets. The MPZ concept will be further studied in the **PROBLEMS & *DISCUSSIONS***.

Nonsteady Cases

The last two cases in Table 6.1 concern the non-steady-state thermal behavior of the winding. Both are treated in ***CHAPTER 8***.

6.2.2 Thermal Energy

Long-term stability requires $\partial T/\partial t \simeq 0$; for a given heat input, this is inversely proportional to $C_{cd}(T)$, which varies by orders of magnitude over the temperature range, 2–90 K, in which superconducting magnets may be operated. Table 6.2 gives approximate heat capacities of substances, over relevant temperature ranges of NbTi (LTS), MgB_2 (HTS), and YBCO (HTS), that constitute the winding, or the immediate vicinity of the winding, of superconducting magnets, cooled by methods discussed in ***CHAPTER 4***.

In the table, operating ranges of NbTi, MgB_2, and YBCO are set, respectively, 2–10 K, 2–30 K, and 2–90 K. For stability, the most influential substances in the table are copper (that represents here an electrically conductive normal "matrix" metal; others: aluminum and silver) and the superconductor itself. Because $C_p(T)$ of copper in the 10–20 K range (the likely range for MgB_2) is several orders of magnitude greater than at 2–4 K (NbTi), and at 50–90 K (YBCO) is another order of magnitude greater still, it is quite clear, in terms of stability, that YBCO, followed by MgB_2, presents the easiest challenges to the magnet engineer. We may conclude that stability is of real concern only for LTS.

6.2.3 Thermal Conduction

The thermal conduction term is neglected altogether in cryostability. In "adiabatic" *LTS* magnets, it plays a subtle role in that it determines the MPZ (minimum propagating zone) size, which in turn determines to what extent the adiabatic winding can permit "localized" disturbances. As will be studied in the **PROBLEMS & DISCUSSIONS** of this chapter, this term also determines the level of steady-state dissipation density, e.g., AC losses, that can be tolerated in the cryocooled winding of an adiabatic magnet to limit the maximum temperature. Table 6.3, similar to Table 6.2 for $C_p(T)$, gives approximate values of thermal conductivity, $k(T)$.

Table 6.2: Heat Capacities of Substances in Superconducting Magnets

Superconductor Operating Temperature Range	⟸ NbTi($T_c = 9.8$ K) ⟹						
	⟸ MgB_2 ($T_c = 39$ K) ⟹						
	⟸ YBCO ($T_c = 93$ K) ⟹						
	$C_p(T)$ [J/cm^3 K]						
Material	2 K	4 K	10 K	20 K	30 K	50 K	90 K
Copper	0.00025	0.00089	0.0076	0.067	0.236	0.857	2.07
NbTi	0.00018	0.0014	0.022	—	—	—	—
MgB_2	0.000040	0.00032	0.00181	0.0081	0.0242	—	—
YBCO	0.000086	0.0007			0.120	0.454	1.12
Stainless steel	0.0014	0.003	0.01	0.04	0.1	0.4	1.5
Epoxy	0.00008	0.00066	0.014	0.080			
Helium @3 atm	—	0.47*	0.095*	—	—	—	—
Solid Neon	0.003	0.027	0.42	1.39	—	—	—
Solid Nitrogen	0.007	0.031	0.17	0.71	1.21	1.51	—

* Liquid (4 K) & vapor (10 K).

Table 6.3: Thermal Conductivities of Substances in Superconducting Magnets
Electrical Resistivity of Copper and Stainless Steel

Superconductor	⟸ NbTi($T_c = 9.8\,\mathrm{K}$) ⟹						
Operating	⟸ MgB_2 ($T_c = 39\,\mathrm{K}$) ⟹						
Temperature	⟸ YBCO ($T_c = 93\,\mathrm{K}$) ⟹						
Range	$k(T)$ [W/cm K]						
Material	2 K	4 K	10 K	20 K	30 K	50 K	90 K
Copper	2	4.2	8.5	15	15	9	5
NbTi	0.0006	0.0017	0.0057	—	—	—	—
MgB_2			0.024	0.068	0.110	—	—
YBCO	0.020	0.080	0.120	0.225	0.250	0.240	0.125
Stainless steel	0.001	0.0027	0.009	0.02	0.035	0.057	0.088
Epoxy	0.0001	0.0003	0.0012	0.0027	0.004	0.006	0.007
Helium @3 atm	0.00017*	0.0002	0.00018	—	—	—	—
Solid Neon	0.030	0.038	0.0095	0.004	—	—	—
Solid Nitrogen	0.09	0.057	0.016	0.0042	0.003	0.002	—
Material	$\rho(T)$ [$\mu\Omega$ cm]						
Copper (RRR=100)	0.015	0.015	0.015	0.017	0.02	0.07	0.3
Stainless steel (316)	54	54	54	54	55	56	57

* At 2.5 K

Unlike its heat capacity, the thermal conductivity of each substance in the table varies much less dramatically with temperature. Copper has the most remarkable thermal conductivity. It is much greater than those of the rest, making it, particularly for stability (this chapter) and protection (***CHAPTER 8***), unquestionably indispensable in any winding, LTS or HTS. As discussed in ***CHAPTER 7***, because of Joule dissipation from eddy currents in copper windings subjected to time-varying electromagnetic fields, the presence of copper can present operational difficulties, which are generally circumvented or minimized by a complex configuration for the composite superconductor.

6.2.4 Joule Heating

Under normal operating conditions, the Joule heating term is zero in a superconducting magnet. Because Type II superconductors are, with the exception of niobium, all some alloy or compound of elements, the normal-state electrical resistivity of Type II superconductors is generally much greater than electrical resistivities of matrix metals such as copper. This point was already studied in ***DISCUSSION 5.5*** (magnetic and thermal diffusion). One component of Stekly's stability theory is to provide a highly conductive passage, in the form of a normal metal shunt, to a highly resistive superconductor when it is not superconducting. (The other is to provide sufficient cooling to remove this Joule dissipation.) Table 6.3 also lists electrical resistivities, $\rho(T)$, of copper and stainless steel, which may be used to approximate a normal-state superconductor, except, as discussed later in the **PROBLEMS & *DISCUSSIONS***, when the effects of flux flow must be considered in the vicinity of the critical current.

6.2.5 Disturbance Spectra

The term $g_d(t)$ in Eq. 6.1 represents the so-called disturbance or heating density, other than the Joule heating density that could arise within the winding. The disturbance may be characterized in both time, i.e., transitory (and a disturbance given in energy) vs. continuous (power), and space, i.e., localized (energy or power) vs. global (energy density or power density). A sudden slippage of conductor—wire motion—is a good example of a transitory and localized disturbance that can best be quantified in terms of the total energy released in the winding by the slippage. Perhaps the best example of continuous and global disturbances may be AC losses that would invariably be released in the winding of an AC electric power device. A design issue for an adiabatic winding subjected to a continuous and global heating density is studied in the **PROBLEMS & *DISCUSSIONS***.

Figure 6.1 shows the disturbance spectra of six prominent sources compiled over the years for LTS magnets [6.14]. Of these sources, flux jumping, wire motion, and AC losses are "intrinsic" in that they originate within the winding; heat leaks are linked to the way the winding is coupled to the outside world; particle showers and nuclear heat are device-specific and negligible in most magnets.

As discussed in ***CHAPTER 5***, flux jumping may now be considered benign in LTS and certainly in HTS. Wire motion and other mechanical events can *still* afflict *adiabatic LTS* magnets. However, as studied here even adiabatic HTS magnets are generally immune from these disturbances. Because Type II superconductors are dissipative under time-varying electromagnetic fields, making HTS as vulnerable to AC losses as LTS, how well AC losses are minimized will unquestionably make or break HTS in the vast area of electric power applications.

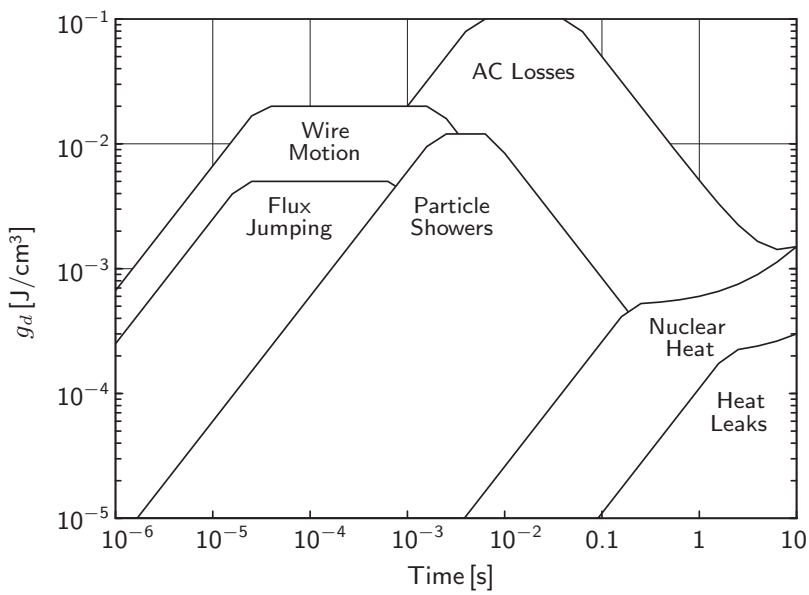

Fig. 6.1 Spectra of $g_d(t)$ compiled for LTS magnets [6.14].

6.2.6 "Stability Margin" vs. Disturbance Energy

The so-called "stability margin" or simply "energy margin" is a useful design parameter especially for an adiabatic superconducting magnet. It is the maximum energy density, Δe_h, that a composite superconductor—cooled or adiabatic—carrying operating (transport) current, I_{op} (I_t), can absorb and still remain *fully* superconducting. Unless the cooling balances this Δe_h, the composite is heated and its temperature is raised above the operating temperature T_{op}; it remains completely superconducting until it is heated to the I_{op}-dependent "current-sharing" temperature, $T_{cs}(I_{op})$. Figure 6.2 shows a critical current vs. temperature plot, $I_c(T)$, of a Type II superconductor, defining $T_{cs}(I_{op})$—here, $I_c(T)$ is approximated by a straight line connecting $I_c(T_{op}) \equiv I_{c_\circ}$, the critical current at T_{op}, and $I_c(T_c) = 0$. The solid circle defines $T_{cs}(I_{op})$ as the intersecting point of the $I_c(T)$ line and the dashed line at I_{op}. Note that $T_{cs}(I_{op})$ is the maximum temperature to which a composite, carrying I_{op}, can remain completely superconducting even under *adiabatic* conditions. Beyond $T_{cs}(I_{op})$ the matrix normal metal begins to "share" the current, generating Joule dissipation. In an adiabatic winding, the transition from $T_{cs}(I_{op})$ to the critical temperature, T_c, can be almost instantaneous, and at T_c and beyond the matrix carries virtually the entire current. Also defined in the figure is $[\Delta T_{op}(I_{op})]_{st} = T_{cs}(I_{op}) - T_{op}$, the temperature excursion limit that a composite can tolerate from T_{op} and still remain fully superconducting. Sometimes instead of Δe_h, a "temperature margin," $[\Delta T_{op}(I_{op})]_{st}$, is used to quantify the degree of stability. Under *adiabatic* conditions, Δe_h is given by:

$$\Delta e_h = \int_{T_{op}}^{T_{cs}(I_{op})} C_{cd}(T)\, dT = \int_{T_{op}}^{T_{op}+[\Delta T_{op}(I_{op})]_{st}} C_{cd}(T)\, dT \tag{6.2}$$

Note that Δe_h depends not only on $C_{cd}(T)$, T_{op}, and $T_{cs}(I_{op})$ or $[\Delta T_{op}(I_{op})]_{st}$ but also on I_{op} relative to $I_{c_\circ}$, i.e., $i_{op} \equiv I_{op}/I_{c_\circ}$. Specifically, for the simple straight line approximation of $I_c(T)$ of Fig. 6.2, $[\Delta T_{op}(I_{op})]_{st}$ is given by:

$$[\Delta T_{op}(I_{op})]_{st} = (T_c - T_{op})(1 - i_{op}) \tag{6.3}$$

From Eq. 6.3 we may conclude that for an adiabatic magnet its current-sharing temperature must be greater than its operating temperature, $T_{cs} > T_{op}$, i.e., its I_{op} (I_t) should be below the conductor's lowest $I_{c_\circ}$ in the winding, because $I_{c_\circ}$ depends on magnetic field, which varies in the winding. Table 6.4 lists selected values of T_{op} and ΔT_{op} typical for LTS and HTS magnets, and corresponding values of Δe_h.

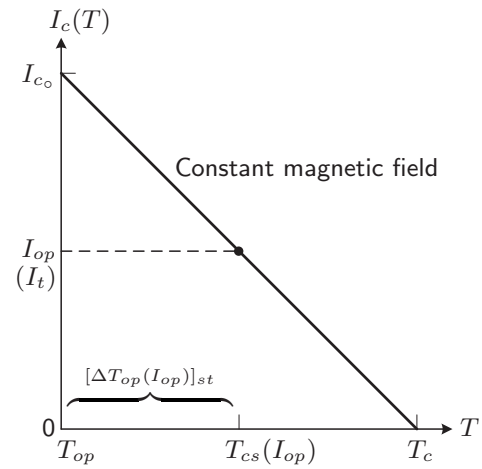

Fig. 6.2 Straight line approximation of $I_c(T)$ plot of a Type II superconductor.

Table 6.4: Selected Values of T_{op}, ΔT_{op}, and Δe_h for LTS and HTS

LTS			*HTS*		
T_{op} [K]	$[\Delta T_{op}(I_{op})]_{st}$ [K]	Δe_h [J/cm^3]	T_{op} [K]	$[\Delta T_{op}(I_{op})]_{st}$ [K]	Δe_h [J/cm^3]
2.5	0.3	1.2×10^{-4}	4.2	25	1.6
4.2	0.5	0.6×10^{-3}	10	20	1.8
4.2	2	4.3×10^{-3}	30	10	3.7
10	1	9×10^{-3}	70	5	8.1

LTS Comparison of energy margins in Table 6.4 with disturbance energy densities in Fig. 6.1 clearly indicates that LTS magnets are very much susceptible to quenching induced by a disturbance, the energy density of which is represented by $g_d(t)$ in Eq. 6.1. Aptly, techniques have been developed over the years to suppress these disturbances, e.g., wire motion and flux jumping, or minimize AC losses for *most* "DC" LTS adiabatic magnets to make them operate stably *most* of the time. Techniques to minimize or eradicate mechanical disturbances, e.g., wire motion, important only to LTS magnets, discussed more extensively in the 1st Edition, are *briefly* discussed in ***CHAPTER 7*** of this Edition.

HTS With the exception of AC losses, the disturbance energy spectra for HTS magnets should be those given in Fig. 6.1. Referring to Δe_h values in Table 6.4, we may conclude that HTS magnets, at least under DC conditions, are *absolutely* stable: *every* DC HTS magnet should thus be designed to operate adiabatically.

6.2.7 Cooling

Although cooling is required for operation of every superconducting magnet, as discussed in ***CHAPTER 4***, only bath-cooled, cryostable magnets require cryogen cooling *within the winding*. The $-g_q(T)$ term in Eq. 6.1 thus refers to cooling present only within the winding; cooling exterior to the winding, which every superconducting magnet requires, is literally peripheral; it does not enter Eq. 6.1. As discussed above, HTS magnets can, and really should always, be operated adiabatically. Furthermore most HTS magnets, except those coupled to LTS magnets and which therefore must operate at liquid helium temperature, operate at temperatures above ∼20 K. Therefore, liquid helium heat transfer data are no longer as essential for the design of HTS magnets as for bath-cooled cryostable LTS magnets; even liquid nitrogen heat transfer data are not essential for HTS magnets, which are adiabatic, because liquid nitrogen is not present in the winding.

Bottura has summarized helium heat transfer coefficient, h_q, vs. ΔT plots (Fig. 6.3) for various cooling regimes [6.14]; here ΔT is the temperature difference between the heated surface and the helium at 4.2 K, except where noted otherwise. The plots include: 1) nucleate boiling and film boiling, including peak nucleate boiling point (h_{pk}) of 1.23 W/cm^2 K; 2) transient nucleate; 3) Kapitza at 1.8 K (superfluid) and at 4.2 K; 4) forced-flow at 3.5 atm, 4.5 K, and Reynolds numbers of 10^4 and 10^5. Of these plots, the nucleate boiling plot, including $h_{pk} = 1.23$ W/cm^2 K, is for bath-cooled and cryostable magnets; the Kapitza (1.8 K) plot is for superfluid-cooled cryostable magnets; forced-flow plots are for cryostable magnets wound with cable-in-conduit (CIC) conductor.

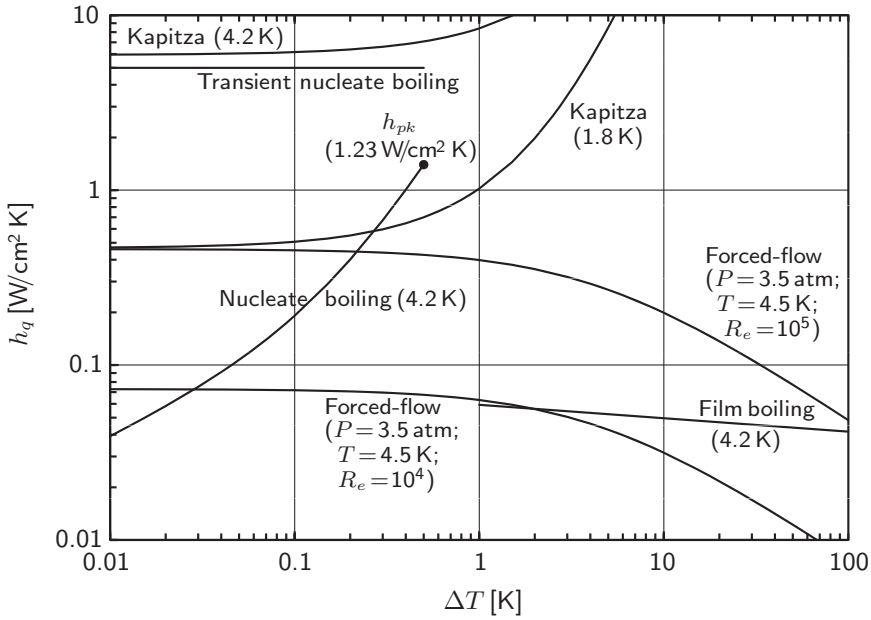

Fig. 6.3 Helium heat transfer coefficient, h_q, vs. ΔT plots [6.14].

6.3 Current Densities

For computation of the magnetic field generated by a magnet, one key parameter is λJ, the overall current density (Eq. 3.108), given by the total ampere-turns, NI, divided by the magnet's winding cross sectional area, which includes not only the current-carrying conductor but also non-current-carrying elements in the winding. Figure 6.4a shows components that comprise cross-sectional areas of "composite superconductor." Figure 6.4b does the same for the winding pack. Each figure defines the symbol "commonly" used for each component.

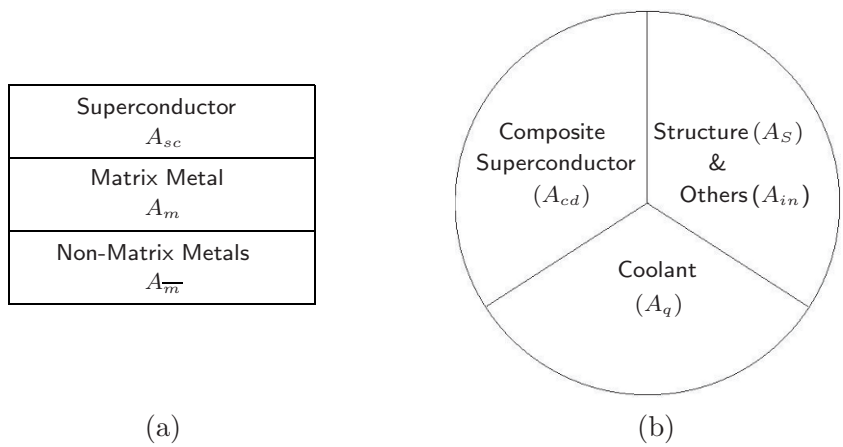

Fig. 6.4 Schematic cross sectional area drawings of: (a) composite superconductor; and (b) winding pack, showing their components and respective area symbols.

6.3.1 Cross Sectional Areas

As illustrated in Fig. 6.4, there are at least seven separate cross-sectional areas in the winding of a superconducting magnet that are used to define various current densities: A_{sc}, A_m, and $A_{\overline{m}}$, identified in Fig. 6.4a for the composite superconductor; and A_{cd}, A_S, A_{in}, and A_q identified in Fig. 6.4b for the winding pack. $A_{\overline{m}}$, non-matrix metals, is zero in alloys such as NbTi, but in compound superconductors such as Nb_3Sn and YBCO it is not negligible. Note that the cross section occupied by other materials such as insulator is not included in the total composite superconductor cross section. A_S is generally the cross sectional area occupied by metallic reinforcing elements, while A_{in} includes those occupied by insulator and organic filling material such as epoxy. Except in cable-in-conduit (CIC) conductors, discussed below, A_S and A_{in} may generally be combined as the structural element. Two total cross sections, for the composite (A_{cd}) and winding pack (A_{wd}) are:

$$A_{cd} = A_{sc} + A_m + A_{\overline{m}} \tag{6.4a}$$

$$A_{wd} = A_{cd} + A_S + A_{in} + A_q \tag{6.4b}$$

6.3.2 Composite Superconductor

Three common current densities for a composite are defined and described below.

Superconductor Critical Current Density

Superconductor critical density, J_c, is defined by the superconductor's critical current, I_c at a given temperature and field, divided by either A_{sc} (for materials such as NbTi and YBCO, in which A_{sc} is clearly quantified) or else $A_{sc}+A_{\overline{m}}$ (for conductors such as Nb_3Sn, in which non-matrix metal is an integral part). Thus:

$$J_c \equiv \frac{I_c}{A_{sc}} \tag{6.5a}$$

$$J_c \equiv \frac{I_c}{A_{sc}+A_{\overline{m}}} \tag{6.5b}$$

During the materials development stage (*Stage 1* in Table 1.4), J_c, especially $J_c \equiv I_c/A_{sc}$, together with H_{c2} and T_c, is the most suitable, and useful, parameter to characterize the superconductor performance.

Engineering (or Conductor) Critical & Operating Current Densities

Engineering (or conductor) critical density, J_e (or J_{cd}), recognizes the manufacturing and magnet requirements that $A_{\overline{m}}$ and A_m are both crucial components of a *magnet-grade superconductor*:

$$J_e = J_{cd} \equiv \frac{I_c}{A_{cd}} = \frac{I_c}{A_{sc} + A_m + A_{\overline{m}}} \tag{6.6}$$

In a cable-in-conduit (CIC) conductor (see ***DISCUSSION 6.6***), the areas of other components such as structural element (A_S) and coolant (A_q) are integral parts of the conductor and thus these are sometimes included in A_{cd}. For a conductor at its operating current, I_{op}, we may also define engineering (or conductor) *operating current* density: $J_{e_\circ} = J_{cd_\circ} \equiv I_{op}/A_{cd}$. $J_{cd_\circ}(t)$ implies $I_{op}(t)$ can vary with time.

Matrix Current Density

Matrix current density, J_m, is an important parameter for stability and protection of a magnet wound with a composite superconductor. J_m is defined by the current through the matrix, I_m, divided by A_m:

$$J_m \equiv \frac{I_m}{A_m} \quad \text{or} \quad J_m(t) \equiv \frac{I_m(t)}{A_m} \tag{6.7a}$$

Note that I_m is a part or all of the operating (transport) current, I_{op} (or I_t), depending on whether the superconductor is superconducting or not:

$$I_{op} = I_t = I_m + I_s \quad \text{or} \quad I_{op}(t) = I_t(t) = I_m(t) + I_s(t) \tag{6.7b}$$

where I_s is the current through the superconductor. Because the most relevant matrix current is the normal operating current, I_{op}, i.e., when $I_s = 0$, another matrix current density based on I_{op} is often used:

$$J_{m_\circ} \equiv \frac{I_{op}}{A_m} \qquad \text{or} \quad J_{m_\circ}(t) \equiv \frac{I_{op}(t)}{A_m} \tag{6.7c}$$

6.3.3 Current Density in Winding Pack

As studied in ***Chapter 3*** and briefly restated above, the magnetic field generated by a magnet is directly proportional to the magnet winding's overall current density. We may define this current density by using two currents: I, which represents any current; and I_{op}, which represents the magnet operating current. Thus:

$$\lambda J \equiv \frac{I}{A_{wd}} \tag{6.8a}$$

$$\lambda J_{op} \equiv \frac{I_{op}}{A_{wd}} \quad \text{or} \quad \lambda J_{op}(t) \equiv \frac{I_{op}(t)}{A_{wd}} \tag{6.8b}$$

Because λJ_{op} determines the field generated by a magnet, among the current densities discussed here, it affects most directly the cost of the magnet. Therefore, for a magnet to be competitive in the marketplace, λJ_{op} must be as large as possible but still consistent with the magnet's design/operation requirements. (In ***Chapter 3***, chiefly for the sake of simplicity, λJ is used in place of λJ_{op}.)

Current Density for Cable-In-Conduit (CIC) Conductor

Cable-in-conduit (CIC) conductor, as will be described in ***Discussion 6.6***, is used in "large" and "high-field" magnets. Because in CIC conductor, the conductor and winding pack are essentially combined, we make a special definition of "conductor" current density, $J_{\text{cic}_\circ}$, for CIC conductor at operating current I_{op}:

$$J_{\text{cic}_\circ} \equiv \frac{I_{op}}{A_{\text{cic}}} \quad \text{or} \quad J_{\text{cic}_\circ}(t) \equiv \frac{I_{op}(t)}{A_{\text{cic}}} \tag{6.9a}$$

where

$$A_{\text{cic}} \equiv A_{cd} + A_S + A_q \tag{6.9b}$$

"Mendel's epoch-making discovery required little previous knowledge; what it needed was a life of elegant leisure spent in a garden." —Bertrand Russell

DISCUSSION 6.1: Cryostability—Circuit Model*

We discuss here the theory of cryostability. A circuit model is used to study the behavior of a composite superconductor comprised of a superconductor (generally comprising many filaments) embedded in a matrix of copper.

Figure 6.5a shows an "ideal" R_s vs. I plot for a length of the superconductor, where R_s is the superconductor's resistance—this plot, quite applicable to most LTS is not applicable to most HTS, as discussed later. The plot is ideal in the sense that for $I_s < I_c$, $R_s = 0$, where I_c is the superconductor's critical current. For $I_s > I_c$, $R_s = R_n$, where R_n is the superconductor's resistance in the normal state; at $I_s = I_c$, $0 \le R_s \le R_n$, i.e., it satisfies conditions imposed by the circuit. Figure 6.5b shows a circuit model for the composite superconductor carrying a transport current I_t at temperature T. I_s is the current through the superconductor, and R_m is the matrix metal resistance; generally $R_m \ll R_n$.

$I_t \le I_c$ Range Here, the superconductor carries the entire transport current, $I_s = I_t \le I_c$ and, from Fig. 6.5a, $R_s = 0$, and from Fig. 6.5b, $V_{cd} = 0$, where V_{cd} is the voltage across the composite. The total Joule dissipation, G_j, is zero.

$I_t > I_c$ Range When $I_t > I_c$, almost all excess current greater than I_c now flows through the copper matrix because $R_m \ll R_n$. That is, $I_m \simeq I_t - I_c$ and $I_s \simeq I_c$. I_m is the current flowing through the matrix. We thus have:

$$V_{cd} = R_m I_m \simeq R_m (I_t - I_c) \tag{6.10a}$$

$$G_j = V_{cd} I_t \tag{6.10b}$$

Combining Eqs. 6.10*a* and 6.10*b*, we obtain:

$$G_j \simeq R_m I_t (I_t - I_c) \tag{6.11}$$

Note that G_j is temperature-independent as long as R_m and I_c remain independent of temperature. Because the resistivity of matrix metal such as copper is nearly temperature-independent for the temperature range from 4 to ∼30 K (*APPENDIX IV*), R_m is always assumed constant in a stability analysis of LTS.

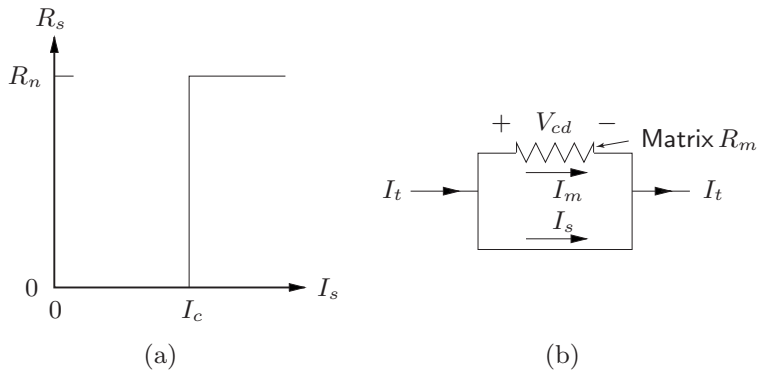

Fig. 6.5 (a) R_s vs. I_s plot for superconducting filaments alone. (b) Circuit model for a composite superconductor.

* Based on **Problem 6.1** in the 1st Edition (Plenum, 1994).

PROBLEM 6.1: Cryostability—temperature dependence*

We shall now investigate the temperature dependence of G_j, the total Joule dissipation in the unit composite superconductor length considered in ***DISCUSSION 6.1*** and given by Eq. 6.11. Figure 6.6 (same as Fig. 6.2) shows an I_c vs. T plot often used to approximate a superconductor's $I_c(T)$ function at a constant magnetic field. (Equation 5.38 gives the same linear approximation for critical current density.) Note that $I_c(T_{op}) = I_{c_\circ}$ and $I_c(T_c) = 0$. The net transport current through the composite, I_t, remains constant as the conductor temperature is varied. The current sharing temperature, T_{cs}, is given by $I_t = I_c(T_{cs})$, as indicated in the plot.

a) With $I_c(T)$ of the superconductor approximated by:

$$I_c(T) = I_{c_\circ}\left(\frac{T_c - T}{T_c - T_{op}}\right) \qquad (T_{op} \le T \le T_c) \tag{6.12}$$

show that $G_j(T)$ depends on temperature as:

$$G_j(T) = 0 \qquad (T_{op} \le T \le T_{cs}) \tag{6.13a}$$

$$G_j(T) = R_m I_t^2\left(\frac{T - T_{cs}}{T_c - T_{cs}}\right) \qquad (T_{cs} \le T \le T_c) \tag{6.13b}$$

$$G_j(T) = R_m I_t^2 \qquad (T \ge T_c) \tag{6.13c}$$

Assume R_m to be temperature-independent.

b) Make a plot of Eq. 6.13 for the temperature range from T_{op} to $T > T_c$.

c) Give a physical explanation of $G_j(T)$ given by Eq. 6.13*b*.

d) Discuss qualitatively how Eq. 6.13*b* must be modified above ~30 K, at which point R_m becomes temperature-dependent, $R_m(T)$, as may be the case with a composite HTS.

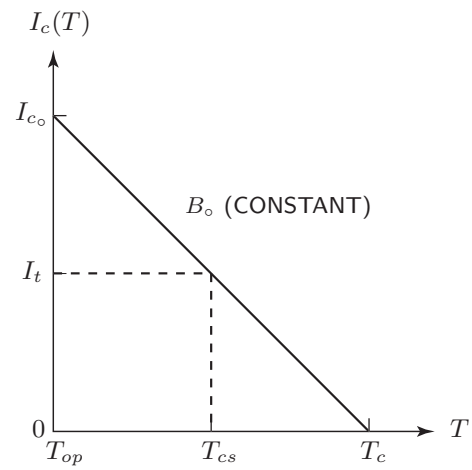

Fig. 6.6 Linear approximation of I_c vs. T (Eq. 6.12) for the superconductor.

* Based on **Problem 6.2** in the 1st Edition (Plenum, 1994).

Solution to PROBLEM 6.1

a) Because $I_c(T) \geq I_t$ for $T_{op} \leq T \leq T_{cs}$ (Fig. 6.6), we have:

$$G_j(T) = 0 \qquad (T_{op} \leq T \leq T_{cs}) \tag{6.13a}$$

By inserting $I_c(T)$ given by Eq. 6.12 into G_j given by Eq. 6.11, we obtain:

$$G_j(T) = R_m I_t \left[I_t - I_{c_\circ} \left(\frac{T_c - T}{T_c - T_{op}} \right) \right] \qquad (T_{cs} \leq T \leq T_c) \tag{S1.1}$$

Setting $I_t = I_c(T_{cs})$ and inserting this into Eq. 6.12, we can solve for $I_{c_\circ}$:

$$I_{c_\circ} = I_t \left(\frac{T_c - T_{op}}{T_c - T_{cs}} \right) \tag{S1.2}$$

where $I_{c_\circ} \equiv I_c(T_{op})$. Combining Eqs. $S1.1$ and $S1.2$, we obtain:

$$G_j(T) = R_m I_t^2 \left(\frac{T - T_{cs}}{T_c - T_{cs}} \right) \qquad (T_{cs} \leq T \leq T_c) \tag{6.13b}$$

$$G_j(T) = R_m I_t^2 \qquad (T \geq T_c) \tag{6.13c}$$

b) Equation 6.13 is plotted in Fig. 6.7.

c) Clearly, as long as $I_t \leq I_c(T)$, all the transport current flows through the superconductor, and $V_{cd} = 0$, making $G_j(T) = 0$. At T_{cs}, the current-sharing temperature, when $I_t = I_c$, the superconductor is carrying its maximum possible current as a superconductor; beyond T_{cs} the current begins to "spill over" to the copper matrix, and Joule heating is generated in the composite. This spilling continues monotonically with T until T_c is reached, at which point, under the condition $R_m \ll R_n$, which is generally valid, virtually the entire transport current has shifted to the matrix. Because R_m is constant, the variation of G_j with T is *linear* between T_{cs} and T_c, and *constant* beyond T_c. This constant R_m assumption is valid for most matrix metals such as copper for T_{op} up to $\sim$30 K.

d) The assumption of constant R_m is invalid for matrix metals if $T_{op} > \sim 30$ K. That is, for most HTS loaded with matrix metal with $R_m(T)$, Eqs. 6.13*b* and 6.13*c* are modified accordingly.

$T_{cs} \leq T \leq T_c$:

$$G_j(T) = R_m(T) I_t^2 \left(\frac{T - T_{cs}}{T_c - T_{cs}} \right) \tag{6.14a}$$

$T \geq T_c$:

$$G_j(T) = R_m(T) I_t^2 \tag{6.14b}$$

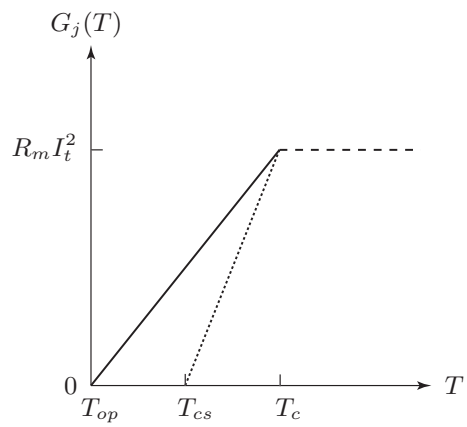

Fig. 6.7 $G_j(T)$ plots for the composite superconductor, with R_m constant.

DISCUSSION 6.2: Stekly Cryostability Criterion

As remarked in **6.2.1** the so-called Stekly cryostability criterion balances the Joule heating generated by the composite superconductor with cooling provided by the coolant penetrating into the well-ventilated winding. Thus, Eq. 6.1 reduces to:

$$C_{cd}(T)\frac{\partial T}{\partial t} = \underset{\wr\wr\ 0}{\nabla\cdot[k_{cd}(T)\nabla T]} + \underset{\wr\wr\ 0}{\rho_{cd}(T)J_{cd}^2(t)} + g_d(t) - \underset{\wr\wr\ 0}{\left(\frac{f_p\mathcal{P}_D}{A_{cd}}\right)g_q(T)} \qquad (6.15)$$

where $\mathcal{P}_D$ is the total conductor perimeter; the constant f_p quantifies the fraction of $\mathcal{P}_D$ exposed to cryogen. Stekly first developed his theory by choosing $I_t = I_{c_\circ}$, i.e., I_t equal to the superconductor's critical current at T_{op}. (Note that I_t also stands for operating current, I_{op}.) The choice of $I_t = I_{op} = I_{c_\circ}$ makes $T_{cs} = T_{op}$, and Eq. 6.13*b* becomes:

$$G_j(T) = R_m I_{c_\circ}^2\left(\frac{T - T_{op}}{T_c - T_{op}}\right) \qquad (T_{op} \le T \le T_c) \qquad (6.16a)$$

$$\rho_{cd}(T)J_{cd}^2(t) = \frac{\rho_m I_{c_\circ}^2}{A_{cd}A_m}\left(\frac{T - T_{op}}{T_c - T_{op}}\right) \qquad (T_{op} \le T \le T_c) \qquad (6.16b)$$

Historically, Stekly's choice of $I_t = I_{c_\circ}$ in developing his criterion was not for stability of a superconducting magnet but for that of a superconductor test sample as its current was pushed beyond $I_{c_\circ}$ during V vs. I measurement. Nowadays, the operating current for *every* LTS magnet is chosen less than $I_{c_\circ}$. For HTS *magnets*, stability is not an important design issue; but as with LTS *test samples*, it is for HTS *test samples* too. Stability as related to V vs. I characteristics is studied in more detail in **PROBLEM 6.5**.

Stekly's choice for cooling was one that is linear with temperature:

$$g_q(T) = h_q(T - T_b) \simeq h_q(T - T_{op}) \qquad (6.17)$$

T is the conductor surface temperature. T_b is the bath (cryogen) temperature, assumed equal to T_{op}: $T_b \simeq T_{op}$.

The Stekly cryostability criterion requires, from Eq. 6.15, that $(f_p\mathcal{P}_D/A_{cd})g_q(T) \ge \rho_{cd}(T)J_{cd}^2(t)$. From Eqs. 6.16*b* and 6.17, we obtain:

$$\frac{f_p\mathcal{P}_D h_q(T - T_{op})}{A_{cd}} \ge \frac{\rho_m I_{c_\circ}^2}{A_{cd}A_m}\left(\frac{T - T_{op}}{T_c - T_{op}}\right)$$

$$\frac{\rho_m I_{c_\circ}^2}{f_p\mathcal{P}_D A_m h_q(T_c - T_{op})} \le 1 \qquad (6.18)$$

The Stekly stability parameter, α_{sk}, is given by Eq. 6.18:

$$\alpha_{sk} = \frac{\rho_m I_{c_\circ}^2}{f_p\mathcal{P}_D A_m h_q(T_c - T_{op})} \qquad (6.19)$$

Note that α_{sk}, a dimensionless number, expresses the ratio of Joule dissipation density to cooling density. Operation is thus stable when $\alpha_{sk} \le 1$ (sufficient cooling) and unstable when $\alpha_{sk} > 1$ (insufficient cooling.)

DISCUSSION 6.2: Stekly Cryostability Criterion (continuation)

Most large magnets built and *reliably* operated in the late 1960s and early 1970s were "cryostable," based on Stekly's cryostability criterion. Equation 6.19 states $\alpha_{sk} \propto 1/A_m$ and implies that for a given cooling condition stability (or reliability) is directly linked to A_m and vice versa:

$$A_m = \frac{\rho_m I_{c_\circ}^2}{\alpha_{sk} f_p \mathcal{P}_D h_q (T_c - T_{op})} \tag{6.20}$$

To achieve a greater degree of stability for given cooling conditions, it is necessary to increase A_m in a bath-cooled cryostable magnet. The composite superconductor's current density at operating current, J_{op}, is given by:

$$J_{op} = \frac{I_{op}}{A_{sc} + A_{\overline{m}} + A_m} \tag{6.6}$$

$$= \left(\frac{\gamma_{m/s}}{\gamma_{m/s} + 1}\right) J_{m_\circ} \tag{6.21a}$$

where the area ratio, $\gamma_{m/s}$, is defined as:

$$\gamma_{m/s} \equiv \frac{A_m}{(A_{sc} + A_{\overline{m}})} \tag{6.21b}$$

$\gamma_{m/s}$ is known as the matrix-to-superconductor ratio as in composite NbTi ($A_{\overline{m}} = 0$) or matrix-to-nonmatrix ratio as in composite Nb_3Sn ($A_{\overline{m}} \neq 0$). Note that for $\gamma_{m/s} \gg 1$, $J_{op} \simeq J_{m_\circ}$

Clearly, in these early "large" magnets, reliability was unquestionably favored over efficiency. This philosophy continues to this day, particularly with large magnets in which another issue is dominant, perhaps more so than stability: large electromagnetic forces. Required reinforcement elements, A_S, incorporated in the winding of a large cryostable LTS magnet are even more a factor than is matrix metal, A_m, in limiting the winding's overall current density.

Table 6.5 lists current parameters—I_c, I_{op}, $\gamma_{m/s}$, $J_c(= I_c/A_{sc})$, $J_e(= I_c/A_{cd})$, $J_{m_\circ}(= I_{op}/A_m)$, and $\lambda J_{op}(= I_{op}/A_{wd})$—for two cryostable LTS magnets, a "bubble chamber" NbTi magnet of the late 1960s [6.12] and a more recent CIC Nb_3Sn magnet [3.24]. Compared with the NbTi magnet, the Nb_3Sn magnet has a $\gamma_{m/s}$ significantly smaller, resulting in a much improved λJ_{op}. This improvement arises in part due to a better understanding of stability and protection issues gained over nearly 40 years of building *real* magnets, as well as to pressure to keep the cost down even among these one-of-a-kind magnets dedicated solely for research use.

Table 6.5: Current Parameters in Cryostable Magnets

Composite	$\gamma_{m/s}$	I_c [kA]	I_{op} [kA]	J_c [MA/m^2]	J_e [MA/m^2]	$J_{m_\circ}$ [MA/m^2]	λJ_{op} [MA/m^2]
NbTi*	24	4.0[a)]	2.2	800	32.0	18.3	7.8
Nb_3Sn†	21.5	15.8[b)]	10.0	627[c)]	74.4	184	39.2

* "Bubble chamber" magnet [6.12]. $B = 2.5$ T; $T_{op} = 4.2$ K; *a*): measured (specified: 3.0 kA).

† NHMFL 45-T Hybrid [3.24]. Coil A (CIC Nb_3Sn; see ***DISCUSSION 6.6***), $B = 15.7$ T; $T_{op} = 1.8$ K; *b*): extrapolated from measurements; *c*): here $J_c = I_c/(A_{sc} + A_{\overline{m}})$ *not* $J_c = I_c/A_{sc}$.

DISCUSSION 6.3: Composite Superconductors

Magnet-grade superconductors are generally available in two types, one known as "monolithic" and the other known as "built-up."

A. Monolith

The superconductor and the normal metal form one entity, achieved chiefly through metallurgical processes. By visual inspection, it is impossible to distinguish, except through the conductor cross section, the existence of more than one constituent in a monolith. Most round composite superconductors are monolithic. For values of $\gamma_{m/s}$ above ∼10, however, it is difficult to manufacture monolithic superconductors without breaking filaments in the metal forming processes, particularly for those having filaments less than ∼100-μm diameter.

B. Built-Up

A built-up conductor is comprised of a monolithic superconductor having a $\gamma_{m/s}$ close to 1 and normal-metal stabilizer parts that are generally soldered to the monolith after the monolith has been prepared. Mechanical properties of the stabilizer parts are therefore unaffected by manufacturing processes of the monolith, making it sometimes easier to satisfy conductor specifications. The CIC conductor is a variant of built-up conductors.

PROBLEM 6.2: Cryostability—nonlinear cooling curves*

The parameter α_{sk} derived in ***DISCUSSION 6.2*** is based on a heat transfer coefficient h_q that is temperature independent. In reality, cooling curves are quite nonlinear, even in the nucleate boiling heat transfer regime where these cryostable magnets generally operate; see for example, Fig. 4.1. It is thus more accurate to incorporate the heat transfer flux curve, $q(T)$ [W/cm^2 or W/m^2], directly in the derivation of the cryostability criterion.

a) Show that an expression for $[J_{m_\circ}]_{sk}$, the matrix current density at I_{op} satisfying a variation of Stekly cryostability criterion that incorporates the heat transfer flux curve $q(T)$, may be given by:

$$[J_{m_\circ}]_{sk} = \sqrt{\frac{f_p \mathcal{P}_D q_{fm}}{\rho_m A_m}} \tag{6.22}$$

where q_{fm} is the minimum heat transfer flux in the film boiling regime.

b) For $I_{op} = I_{c_\circ}$, where $I_{c_\circ}$ is the superconductor's I_c at T_{op}, draw qualitatively, on the same plot, a $q(T)$ curve and a dimensionally consistent generation curve, and indicate on the plot the region of stable operation.

c) Generalize **b)** for the case $I_{op} < I_{c_\circ}$ on the same plot used in **b)**. Show also that for this case ($I_{op} < I_{c_\circ}$), $g_j(T_c)$ and $d\hat{g}_j(T)/dT$ in the current-sharing temperature range are less than those corresponding to the case $I_{op} = I_{c_\circ}$.

---

* Based on **Problem 6.4** in the 1st Edition (Plenum, 1994).

Solution to PROBLEM 6.2

a) In most applications where cryostability is applied, we must assume that the conductor may operate in the fully normal state. Then, it is safest to use the minimum heat flux (q_{fm} in Table 4.2) in the film boiling regime. We thus have:

$$\frac{\rho_m I_{c_\circ}^2}{A_m} = f_p \mathcal{P}_D q_{fm} \tag{S2.1}$$

Solving for $[J_{m_\circ}]_{sk}$, we obtain:

$$[J_{m_\circ}]_{sk} = \sqrt{\frac{f_p \mathcal{P}_D q_{fm}}{\rho_m A_m}} \tag{6.22}$$

b) Figure 6.8 presents a typical plot of $q(T)$ for liquid helium. Plotted also is a curve of $\hat{g}_j(T) \equiv (A_{cd}/f_p\mathcal{P}_D) g_j(T)\,[\mathrm{W/m^2}]$. Parameters are chosen to make $\hat{g}_j(T_c) = (A_{cd}/f_p\mathcal{P}_D) g_j(T_c)$ slightly less than q_{fm}.

c) The dotted line in Fig. 6.8 presents the case in which $I_t < I_{c_\circ}$. Note that in the temperature range $T_{op} \le T \le T_{cs}$ the conductor is fully superconducting. Because $G_j(T_{op}) = R_m I_t^2$, clearly, it is less for $I_t < I_{c_\circ}$. From Eq. $S1.2$ of **PROBLEM 6.1**:

$$I_t = I_{c_\circ} \left(\frac{T_c - T_{cs}}{T_c - T_{op}} \right) \tag{S1.2}$$

Combining Eqs. 6.13*b* and $S1.2$, we have:

$$g_j(T) = \left(\frac{A_{cd}}{f_p \mathcal{P}_D} \right) R_m I_t^2 = \left(\frac{A_{cd}}{f_p \mathcal{P}_D} \right) R_m I_{c_\circ}^2 \frac{(T_c - T_{cs})^2 (T - T_{cs})}{(T_c - T_{op})^3}$$

$$\frac{dg_j(T)}{dT} = \left(\frac{A_{cd}}{f_p \mathcal{P}_D} \right) R_m I_{c_\circ}^2 \frac{(T_c - T_{cs})^2}{(T_c - T_{op})^3}$$

Thus, $G_j(T_c)$ for $I_t = I_{c_\circ}$ $(T_{cs} = T_{op})$ is greater than that for $I_t < I_{c_\circ}$ $(T_{cs} > T_{op})$.

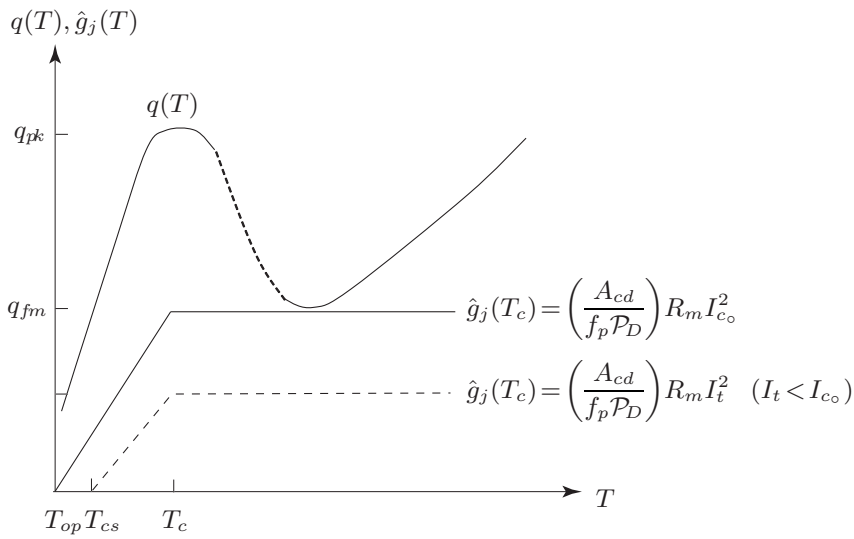

Fig. 6.8 Qualitative plots of $q(T)$ for liquid helium and $\hat{g}_j(T)$ for the case $I_{op} = I_{c_\circ}$ (solid straight lines) and $I_{op} < I_{c_\circ}$ (dashed straight lines).

DISCUSSION 6.4: "Equal-Area" Criterion

The "equal-area" criterion of Maddock, James, and Norris [6.15], a variant to the cryostability criterion, retains the thermal conduction term, $\nabla \cdot [k_{cd}(T)\nabla T]$, in Eq. 6.1. Thus, the equal-area criterion works only when Joule dissipation is not spread globally over the entire winding. While in Stekly's cryostability criterion Joule dissipation is *locally* and entirely balanced by the cooling term, $g_q(T)$, in the equal-area criterion thermal conduction along the conductor axis aids the local cooling to remove the Joule dissipation. Because the criterion applies to a bath-cooled cryostable magnet, it is chiefly applicable to liquid helium cooled LTS magnets. The equal-area criterion requires the following condition be satisfied:

$$\int_{T_{op}}^{T_{eq}} \left[g_q(T) - \left(\frac{A_{cd}}{f_p \mathcal{P}_D} \right) g_j(T) \right] dT = \int_{T_{op}}^{T_{eq}} [g_q(T) - \hat{g}_j(T)] \, dT = 0 \qquad (6.23)$$

where T_{eq} is the temperature above T_{op} at which $g_q(T) = \hat{q}_j(T)$. $g_q(T)$ [W/m^2] is the convective heat flux; $g_j(T)$ [W/m^3], the Joule dissipation density, may be derived from G_j [W] of Eq. 6.13 for which $T_{cs} = T_{op}$ (or Eq. 6.14 for which $T_{cs} > T_{op}$) with $J_{m_\circ} = I_{op}/A_m$. Thus:

$$g_j(T) = \rho_m(T) J_{m_\circ}^2 \left(\frac{T - T_{op}}{T_c - T_{op}} \right) \qquad (T_{op} \le T \le T_c) \qquad (6.24a)$$

$$g_j(T) = \rho_m(T) J_{m_\circ}^2 \qquad (T \ge T_c) \qquad (6.24b)$$

Figure 6.9 shows one example of $\hat{g}_j(T)$ curves satisfying the "equal area" criterion. In this example, Eq. 6.23 is satisfied by having two cross-lined areas in Fig. 6.9 equal, the one bounded by the $g_q(T) > \hat{g}_j(T)$ and $\hat{g}_j(T)$ curves and the other bounded by the $\hat{g}_j(T) > g_q(T)$ and $g_q(T)$ curves. Physically, the "excess" heating in the "warmer" region where the conductor temperature ranges from $\sim T_c$ to T_{eq} is conducted to the "cooler" region where the conductor temperature ranges between T_{op} and $\sim T_c$; this cooler region thus provides "excess" cooling. Figure 6.9 clearly shows that the Joule dissipation line, $\hat{g}_j(T \ge T_c)$, for the composite satisfying the equal-area criterion is greater than that given by the Stekly cryostability criterion.

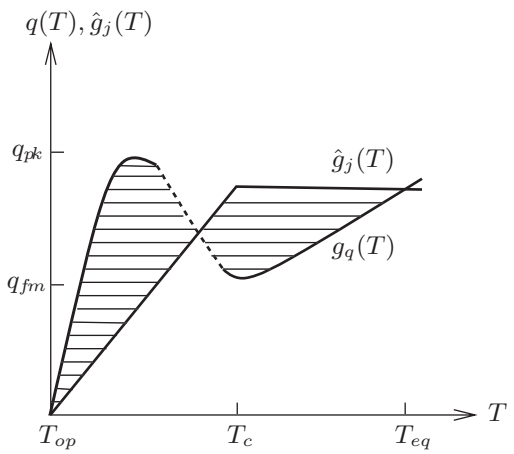

Fig. 6.9 Example of $\hat{g}_j(T)$ curves satisfying the "equal area" criterion. The cross-lined area bounded by the $g_q(T) > \hat{g}_j(T)$ and $\hat{g}_j(T)$ curves is equal to the other cross-lined area bounded by the $\hat{g}_j(T) > g_q(T)$ and $g_q(T)$ curves.

Wilson extended this 1-D equal-area criterion to the 2-D equal-area criterion [6.16]; the 2-D criterion was verified by an experiment conducted on pancake test coils.

DISCUSSION 6.5: Superconductor "Index" (n)

The voltage vs. current characteristic of a superconductor, "real" or "ideal," may be expressed by the following "phenomenological" relationship:

$$V_s = V_c \left(\frac{I_s}{I_c}\right)^n \tag{6.25a}$$

where V_s and I_s are, respectively, the superconductor voltage (over a unit axial length) and current; I_c is the critical current at a specified criterion voltage V_c; and n is the superconductor *index*. Equation 6.25*a* may be expressed in terms of the superconductor electric field, E_s, and current density, J_s:

$$E_s = E_c \left(\frac{J_s}{J_c}\right)^n \tag{6.25b}$$

Obviously, E_c represents a specified critical electric field, generally 1×10^{-4} V/m (1×10^{-6} V/cm) for HTS and one or two orders of magnitude smaller for LTS.

An "ideal" superconductor, i.e., zero resistance below I_c as assumed in **DISCUSSION 6.1**, may be characterized with $n=\infty$. Among magnet-grade-superconductors, real and potential, e.g., NbTi, Nb_3Sn, Bi2223, Bi2212, and coated YBCO, n ranges from ~30 to ~80 for LTS and from ~10 to ~40 for HTS.

As stated at the outset, Eq. 6.25*a* (or Eq. 6.25*b*) is phenomenological. It is based solely on experimental V_s vs. I_s data: n is computed to curve-fit V_s vs. I_s data in the vicinity of I_s. There is no theoretical basis to predict n, though poor quality of a superconductor, e.g., nonuniform filament diameter, may be responsible for low indices [6.17]. Because of practical difficulties in measuring V_s—nanovolts or less—for I_s below ~$0.8I_c$, it is difficult to examine the validity of Eq. 6.25*a* below ~$0.8I_c$ [6.18]. This "index" issue on HTS has been studied [6.19], with the results applied for the design of a YBCO coil [6.20].

Figure 6.10 shows V_s vs. I_s plots based on Eq. 6.25*a* for three indices: $n_1=5$, $n_2=50$, and $n_3=\infty$ at and in the vicinity of I_c for criterion voltage V_c. The R_s vs. I_s plot of Fig. 6.5 thus corresponds to an ideal superconductor ($n=\infty$).

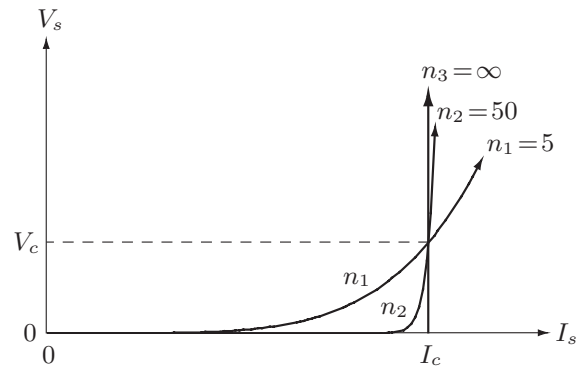

Fig. 6.10 V_s vs. I_s plots for three indexes, $n_1=5$, $n_2=50$, and $n_3=\infty$ in the vicinity of I_c, the critical current at a criterion voltage of V_c.

PROBLEM 6.3: Composite superconductor (n)—circuit model

For a composite superconductor in which the superconductor is characterized by Eq. 6.25a, the equivalent circuit of Fig. 6.5b is modified, as shown in Fig. 6.11. It consists of an ideal voltage source (zero internal resistance) V_S in series with a differential resistance, $R_{dif} \equiv \partial V_s / \partial I_s$, where V_s is the voltage across the superconductor. As in Fig. 6.5b the matrix is represented by a resistor R_m.

a) Show, with $R_c \equiv V_c / I_c$, that $R_s \equiv V_s / I_s$ and R_{dif} are given by:

$$R_s = R_c \left(\frac{I_s}{I_c} \right)^{(n-1)} \tag{6.26a}$$

$$R_{dif} = nR_c \left(\frac{I_s}{I_c} \right)^{(n-1)} \tag{6.26b}$$

Note that $R_{dif} = nR_s$. For a superconductor of $n = 1$, its V-I curve becomes similar to a regular resistor's and, as may be expected, $R_s = R_c = R_{dif}$.

b) For a 10-cm long and 1-cm wide composite superconductor with $I_c = 100$ A at 77.3 K, $V_c = 10\,\mu$V, $n = 15$, a matrix resistance of $R_m = 0.3\,\text{m}\Omega$, and assuming, for simplicity, that the composite, cooled by boiling nitrogen, always remains at 77.3 K, compute: 1) I_m and I_s; 2) total voltage across the 10-cm long composite; 3) total Joule dissipation in the composite; 4) Joule heat flux over the composite cooling surface area of 10 cm^2 (10 cm$\times$1 cm); and 5) R_{dif}, at transport currents, I_t, of 90 A; 100 A; 120 A; 150 A; 300 A; and 500 A.

c) Discuss the assumption of constant temperature of 77.3 K and discuss, qualitatively, how results are modified if the composite superconductor's temperature increases with increasing Joule dissipation.

d) Repeat **b)**, except with $n = 30$.

e) Repeat **b)**, now with $n = 60$.

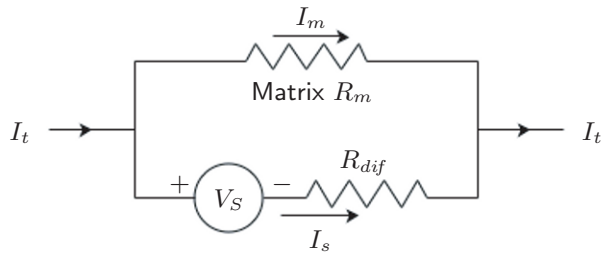

Fig. 6.11 Circuit model for a composite superconductor with a superconductor of the V_s vs. I_s characteristic (Eq. 6.25a), shunted by a matrix resistance R_m. The superconductor consists of V_S, an ideal voltage source, in series with R_{dif}, the differential resistor.

TRIVIA 6.1 List the items below in descending order of length.

i) Charles river; ii) Interstate 90 (I-90);

iii) NbTi/Cu composite wire in an actively-shielded whole-body 1.5-T MRI magnet;

iv) Thread in a silkworm cocoon.

Solution to PROBLEM 6.3

a) From the definition of R_s and using Eq. 6.25a for V_s, we have:

$$R_s = \frac{V_s}{I_s} = \frac{V_c}{I_s}\left(\frac{I_s}{I_c}\right)^n = \frac{V_c}{I_c}\left(\frac{I_s}{I_c}\right)^{(n-1)} \qquad (S3.1)$$

With $R_c = V_c/I_c$, Eq. $S3.1$ becomes:

$$R_s = R_c\left(\frac{I_s}{I_c}\right)^{(n-1)} \qquad (6.26a)$$

R_{dif} represents the superconductor's differential resistance at I_s, hence:

$$R_{dif} = \frac{\partial V_s}{\partial I_s} = \frac{nV_c}{I_c}\left(\frac{I_s}{I_c}\right)^{(n-1)} \qquad (S3.2)$$

$$R_{dif} = nR_c\left(\frac{I_s}{I_c}\right)^{(n-1)} \qquad (6.26a)$$

The partial differentiation is performed in Eq. $S3.2$ because in realistic situations the temperature dependance of I_c, i.e., $I_c(T)$, must be included in the analysis in the range $I_s > I_c$, where the composite is expected to be heated, here above 77.3 K.

b) The circuit must satisfy the following current and voltage equations:

$$I_t = I_m + I_s \qquad (S3.3a)$$

$$V_m = R_m I_m = V_s = V_c\left(\frac{I_s}{I_c}\right)^n \qquad (S3.3b)$$

As an illustration, let us compute I_m for $I_t = 90$ A. From Eq. $S3.3a$, we have: $I_s = 90\,\text{A} - I_m$. Inserting this into Eq. $S3.3b$, we obtain:

$$3\times10^{-4}\,\Omega\times I_m\,[\text{A}] = 10^{-5}\,\text{V}\left(\frac{90\,\text{A} - I_m\,[\text{A}]}{100\,A}\right)^{15} \qquad (S3.3c)$$

From Eq. $S3.3c$: $I_m = 0.00686$ A and hence $I_s = 89.99314$ A.

The total power dissipation in the composite superconductor, P_{cd}, is given by:

$$P_{cd} = R_m I_m I_t = V_s I_t \qquad (S3.4)$$

The Joule dissipation flux, g_{jcd} is given simply by P_{cd} divided by the composite's total cooling surface, here 10 cm^2.

Table 6.5a gives a summary of solution to **b)**.

Table 6.5a: Summary of Solution to **b)** ($n = 15$)

I_t [A]	I_m [A]	I_s [A]	$R_m I_m$ [V]	P_{cd} [W]	g_{jcd} [W/cm^2]	R_{dif} [Ω]
90	0.00686	89.99314	2.06×10^{-6}	185×10^{-6}	18.5×10^{-6}	0.343×10^{-6}
100	0.0332	99.967	9.95×10^{-6}	995×10^{-6}	99.5×10^{-6}	1.49×10^{-6}
120	0.483	119.517	145×10^{-6}	17.4×10^{-3}	1.74×10^{-3}	18.2×10^{-6}
150	7.07	142.93	2.12×10^{-3}	318×10^{-3}	31.8×10^{-3}	223×10^{-6}
300	126.75	173.25	38.0×10^{-3}	11.4	1.14	3.29×10^{-3}
500	315.88	184.12	94.8×10^{-3}	47.4	4.74	7.72×10^{-3}

Solution to PROBLEM 6.3 (continuation)

c) Even when the composite is well-cooled by boiling cryogen, its temperature must rise to transfer Joule dissipation to the cryogen. With liquid nitrogen boiling at 77.3 K, this rise, which increases with heat flux, can be as high as ∼10 K in the nucleate boiling range. The most obvious temperature-dependent parameter in Eq. 6.25*a* is I_c, which decreases with increasing temperature; the temperature-dependence of n is not well-documented, LTS or HTS—in an analysis of this nature, we may assume n to be constant. In the equivalent circuit, R_m, if it is a matrix of pure metal, remains constant at low temperatures and increases nearly linearly with temperature beyond ∼30 K. I_c on the other hand may be assumed to decrease linearly with T. The $(I_s/I_c)^n$ term thus increases sharply with temperature as does, consequently, Joule dissipation. Next, in **PROBLEM 6.4**, we will perform a circuit analysis in which I_c and R_m are T-dependent.

d) Results for $n=30$ are summarized in Table 6.5b.

e) Table 6.5b also gives a summary of results with $n=60$.

Note that for $I_t > I_c = 100$ A the smaller the n, the smaller are I_m, $R_m I_m = V_s(I_s)$, P_{cd}, g_{jcd}, and R_{dif}; for $I_t < 100$ A, the opposite is true. This could pose practical problems in a real situation. For instance, at $I_t = 150$ A, $R_m I_m = 2.12$ mV for an $n=15$ composite, while it is 11.3 mV for an $n=60$ composite: clearly for detection of a resistive voltage, the $n=60$ composite is preferable to the $n=15$ composite.

Table 6.5b: Summary of Solution to **d)**, and **e)**

I_t [A]	I_m [A]	I_s [A]	$R_m I_m$ [V]	P_{cd} [W]	g_{jcd} [W/cm^2]	R_{dif} [Ω]
$n=30$						
90	0.00141	89.9986	0.424×10^{-6}	38.1×10^{-6}	3.81×10^{-6}	0.127×10^{-6}
100	0.0330	99.967	9.90×10^{-6}	990×10^{-6}	99.0×10^{-6}	2.97×10^{-6}
120	3.37	116.63	1.01×10^{-3}	121×10^{-3}	12.1×10^{-3}	260×10^{-6}
150	25.27	124.73	7.58×10^{-3}	1.14	114×10^{-3}	1.82×10^{-3}
300	167.16	132.8	50.1×10^{-3}	15.0	1.50	11.32×10^{-3}
500	363.67	136.33	109×10^{-3}	54.6	5.46	24.0×10^{-3}
$n=60$						
90	0.00006	89.99994	0.018×10^{-6}	1.62×10^{-6}	0.162×10^{-6}	0.012×10^{-6}
100	0.0327	99.9673	9.81×10^{-6}	981×10^{-6}	98.1×10^{-6}	5.89×10^{-6}
120	10.02	109.98	3.01×10^{-3}	361×10^{-3}	36.1×10^{-3}	1.64×10^{-3}
150	37.57	112.43	11.3×10^{-3}	1.69	169×10^{-3}	6.02×10^{-3}
300	184.55	115.45	55.4×10^{-3}	16.6	1.66	28.8×10^{-3}
500	383.14	116.86	114.9×10^{-3}	57.5	5.75	59.0×10^{-3}

PROBLEM 6.4: Composite YBCO under a current pulse

Here, we consider a sample of a 10-mm wide YBCO composite tape, cooled by liquid nitrogen boiling at 77 K. Figure 6.12a shows a schematic drawing of the composite cross section. The composite is insulated on one side by a G-10 strip; on the other side a copper strip is soldered over the silver layer, with a total Cu/Ag layer thickness of 55 μm; the Cu surface is exposed to boiling liquid nitrogen (LN_2). A transport current, $I_t(t)$, is passed through the composite. As indicated by the dashed trace in Fig. 6.12b, it begins at 100 A, then increases quickly to 300 A, remains at 300 A for the next 0.31 s, and returns to 100 A. The conductor voltage, $V_{cd}(t)$, over a distance of 5 cm is shown by the solid trace in Fig. 6.12b.

Although a real HTS magnet is very likely operated adiabatically, for measurements such as V_s vs. I_s plots it is always desirable to keep the test sample, LTS or HTS, at a constant temperature in a well-cooled environment, which for HTS is most easily achieved by immersion in a bath of liquid cryogen.

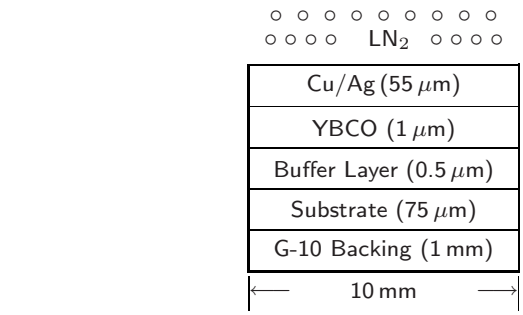

(a)

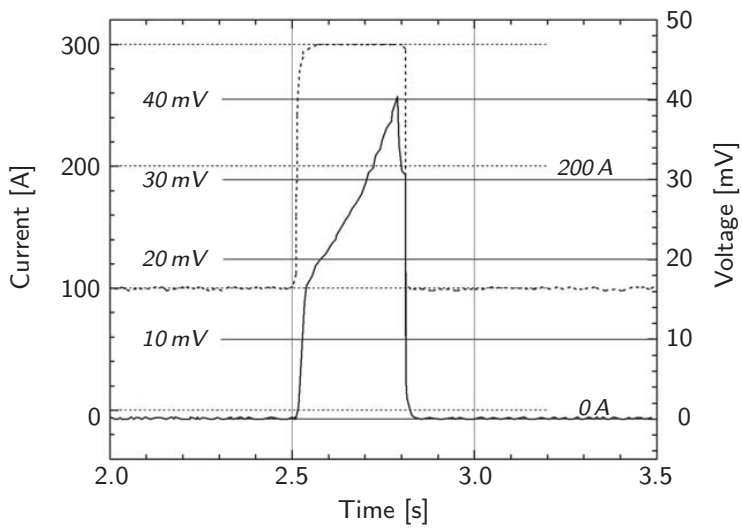

(b)

Fig. 6.12 (a) Schematic drawing of the cross section of a 10-mm wide composite YBCO; the Cu/Ag side is exposed to boiling LN_2. (b) Transport current (dashed) and voltage (solid) vs. time traces recorded with an over-current pulse applied to the composite.

PROBLEM 6.4: Composite YBCO under a current pulse (continuation)

We may use the following T-dependent normal metal matrix resistance over a composite distance of 5 cm, $R_m(T)$, $I_c(T)$, and V_s for this YBCO:

$$R_m(T) = 0.190 + 1.530\left(\frac{T-77}{293-77}\right) \quad [\text{m}\Omega] \tag{6.27a}$$

$$I_c(T) = 100\left(\frac{93-T}{93-77}\right) \quad [\text{A}] \tag{6.27b}$$

$$V_s(T) = 5\left[\frac{I_s(T)}{I_c(T)}\right]^{10} \quad [\mu\text{V}] \tag{6.27c}$$

where T is in kelvins. Equation 6.27a is valid for the range 77–293 K; Eqs. 6.27b and 6.27c, only in the range ∼77–93 K.

a) Referring to Fig. 6.12b, very early in the current pulse ($t \simeq 2.54$ s and $I_t = 290$ A), when it is safe to assume that the composite is still at 77 K, we have: $V_{cd}(t = 2.54\,\text{s}) \simeq 18$ mV. By satisfying the voltage and current requirements of the circuit model shown in Fig. 6.11, compute: 1) I_s; 2) I_m; and 3) V_{cd}.

Is V_{cd} computed here equal to the 18 mV measured?

b) Among V_{cd} ($=V_s$ or $R_m I_m$), I_s, and n measured in the experiment, n is the least accurate. Show that $n = 12.24$ in Eq. 6.27c gives $V_{cd} = 18$ mV in **a)**.

c) During the pulse, $V_{cd}(t)$ continues to increase and reaches a peak value of 40 mV—the drop in $V_{cd}(t)$ that occurs just before the end of the pulse is believed to be caused by a sudden improvement in cooling. Compute the heat flux, p_{cd} [W/cm^2], at the composite surface when $V_{cd}(t = 2.79\,\text{s}) = 40$ mV.

d) Assuming that the Cu-Ag and YBCO layers are at the same temperature, compute the temperature when $V_{cd} = 40$ mV ($t \simeq 2.79$ s). Use $n = 12.24$.

Answer to TRIVIA 6.1

ii) I-90 (5000, in km); Charles (100); MRI magnet (50); cocoon (1).

Solution PROBLEM 6.4

a) The circuit must satisfy both current and voltage requirements:

$$I_t = I_s + I_m \tag{S4.1a}$$

$$R_m I_m = V_s(I_s) \tag{S4.1b}$$

Inserting appropriate values, we obtain:

$$I_s = (290\,\text{A}) - I_m \tag{S4.2a}$$

$$(0.19\times10^{-3}\,\Omega)I_m = (5\times10^{-6}\,\text{V})\left(\frac{290\,\text{A} - I_m}{100\,\text{A}}\right)^{10} \tag{S4.2b}$$

Solving for I_m from Eq. $S4.2b$, we obtain: 1) $I_m = 70\,\text{A}$. Once I_m is known, I_s and $V_{cd} \equiv R_m I_m = V_s(I_s)$ may be computed easily: 2) $I_s = 220\,\text{A}$; and 3) $V_{cd} = 13.3\,\text{mV}$. That is, 13.3 mV, computed, does not quite agree with the 18 mV measured.

b) At 77 K, we know $R_m = 0.19\,\text{m}\Omega$. Thus, solving for I_m with $R_m I_m = 18\,\text{mV}$, we obtain: $I_m = 94.74\,\text{A}$; hence: $I_s = 290\,\text{A} - 94.74\,\text{A} = 195.26\,\text{A}$. Inserting these values of I_m and I_s into Eq. 6.27c with 10 replaced with an unknown n, we have:

$$(18\times10^{-3}\,\text{V}) = (5\times10^{-6}\,\text{V})\left(\frac{195.26\,\text{A}}{100\,\text{A}}\right)^{n} \tag{S4.3}$$

Solving Eq. $S4.3$ for n, we have: $n = 12.24$. An *apparent* error in the measured n of ∼20% from the computed n is not unreasonable considering that n measured is extracted from the measured V_s vs. I_s plot. However, even a small error, because n is an exponent, can make a significant error in other parameters.

c) The total power dissipation over a 5-cm section of the composite, P_{cd}, is given by: $P_{cd} = V_{cd} I_t$. Hence: $P_{cd} = (40\,\text{mV})(300\,\text{A}) = 12\,\text{W}$. Because the total matrix area exposed to liquid nitrogen, with the thin edge areas neglected, is $5\,\text{cm}^2$, we have a heat flux, p_{cd}, of $2.4\,\text{W/cm}^2$, well below the peak nucleate boiling heat flux for liquid nitrogen of $\sim10\,\text{W/cm}^2$.

d) The circuit requirements are the same as those in **a)**, except now T is no longer at 77 K. The only known parameter: $V_{cd} = 40\,\text{mV}$. Thus for the matrix:

$$V_{cd} = 40\times10^{-3}\,\text{V} = R_m(T)I_m \tag{S4.4}$$

Combining Eq. $S4.4$ with Eq. 6.27a and solving for I_m, we have:

$$40\times10^{-3}\,\text{V} = \left\{\left[0.190+1.530\left(\frac{T-77}{293-77}\right)\right]\times10^{-3}\,\Omega\right\}I_m(T) \tag{S4.5a}$$

$$I_m(T) = \frac{40\times10^{-3}\,\text{V}}{\left[0.190+1.530\left(\frac{T-77}{293-77}\right)\right]\times10^{-3}\,\Omega} \tag{S4.5b}$$

$$= \frac{40}{\left[0.190+1.530\left(\frac{T-77}{293-77}\right)\right]}\,\text{A} \tag{S4.5c}$$

Solution PROBLEM 6.4 (continuation)

The superconductor side has the same V_{cd}, thus:

$$40\times10^{-3}\,\mathrm{V} = (5\times10^{-6}\,\mathrm{V})\left[\frac{300\,\mathrm{A} - I_m(T)}{I_c(T)}\right]^{12.24} \qquad (S4.6)$$

With $I_m(T)$ and $I_c(T)$ given, respectively, by Eq. $S4.5c$ and $6.27b$, we obtain:

$$40\times10^{-3}\,\mathrm{V} = (5\times10^{-6}\,\mathrm{V})\left[\frac{300\,\mathrm{A} - \dfrac{40\,\mathrm{A}}{\left[0.190+1.530\left(\dfrac{T-77}{293-77}\right)\right]}}{(100\,\mathrm{A})\left(\dfrac{93-T}{93-77}\right)}\right]^{12.24} \qquad (S4.7)$$

Equation $S4.7$ is simplified to the following algebraic equation for T:

$$8000 = \left[\frac{16(406200T - 28027799)}{(93-T)(135400T - 6793895)}\right]^{12.24} \qquad (S4.8)$$

Solving for T in Eq. $S4.8$, we obtain: $T = 83.125\,\mathrm{K}$. This translates to a temperature difference of $\sim 6\,\mathrm{K}$ between the composite surface and liquid nitrogen boiling at 77.3 K (in Eqs. $6.27a$, $6.27b$, and in subsequent equations the liquid temperature is set at 77 K); for LN_2 this is well within the nucleate boiling regime. Figure 6.13 shows heat transfer flux data for liquid nitrogen boiling at 77.3 K. The data point corresponding to 6.4 **c)** and **d)** is indicated by the solid circle in the figure.

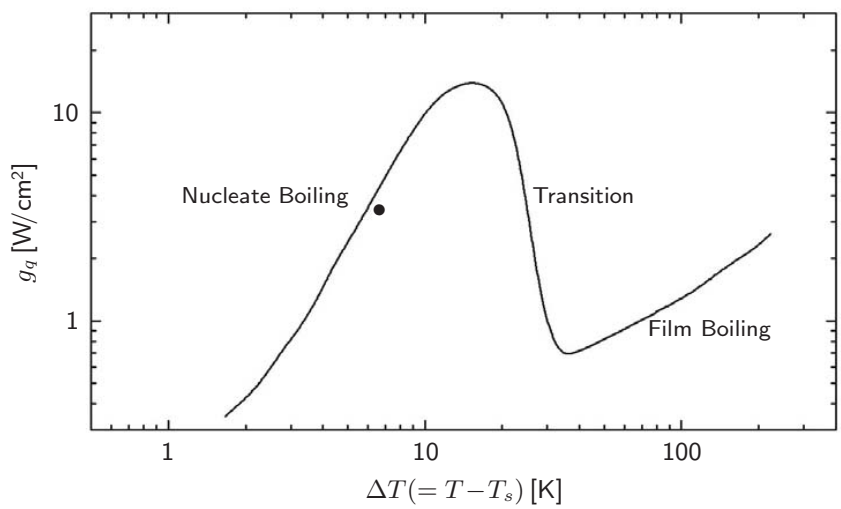

Fig. 6.13 Typical heat transfer flux data for liquid nitrogen boiling at 77.3 K. The data point corresponding to **c)** and **d)** is indicated by the solid circle in the figure.

DISCUSSION 6.6: Cable-in-Conduit (CIC) Conductors

It was through consideration of stability and the desire to find an alternative to bath-cooling that the concept of cable-in-conduit (CIC) conductors was proposed by Hoenig and Montgomery in the early 1970s [6.21]. Indeed, this desire to find an alternative to bath-cooling in the form of forced-cooling for a superconducting magnet was proposed in the mid 1960s by Morpurgo [6.22], who developed a conductor with a cooling hole, similar to water-cooled copper conductor in some resistive magnets. In terms of heat transfer, CIC conductor is superior to a single-holed conductor because the cable can provide a much larger cooling area than the interior wall of a single hole with the same coolant cross section. The idea is thus to encase a cable of superconducting strands in a leak-tight conduit through which supercritical helium is forced, guaranteeing a nearly complete penetration of cryogen throughout the winding. Figure 6.14 presents sketches of CIC conductors. There are *many* variations to these basic conduit-cable designs.

It is only after the initial development of CIC conductor that its second feature, which was at first overlooked, has become recognized as its second asset: built-in-reinforcement. Magnets which are "large" (winding i.d. $>\sim$1 m) and high field ($>\sim$10 T) now use CIC conductor almost exclusively. A large, high-field magnet is generally expensive. Furthermore it often is a component of an even larger and more expensive device, e.g., a fusion reactor; the magnet must be *absolutely* stable. Because a stable magnet must have cooling well-coupled to every part of the conductor in the winding, CIC conductor, by virtue of its configuration, turns out to quite naturally meet both stability and strength requirements.

A. Power Density Equations

The basic power density equation for composite temperature T is essentially the same as given by Eq. 6.1, except here the cooling term is more specific than the general form given in Eq. 6.1. Thus:

$$C_{cd}(T)\frac{\partial T}{\partial t} = \nabla\cdot[k_{cd}(T)\nabla T]+\rho_{cd}(T)J^2_{cd_\circ}(t)+g_d(t)-\left(\frac{f_p\mathcal{P}_D}{A_{cd}}\right)h_{he}(T-T_{he}) \quad (6.28a)$$

where h_{he} and T_{he} are, respectively, the heat transfer coefficient and temperature of helium forced through the conduit. At present, every CIC conductor is based on LTS and cooled by helium, hence the use of h_{he} and T_{he} in Eq. 6.28a. The power density equation for T_{he} is given by:

$$C_{he}(T_{he})\frac{\partial T_{he}}{\partial t} = \left(\frac{f_p\mathcal{P}_D}{A_{cd}}\right)h_{he}(T-T_{he}) \quad (6.28b)$$

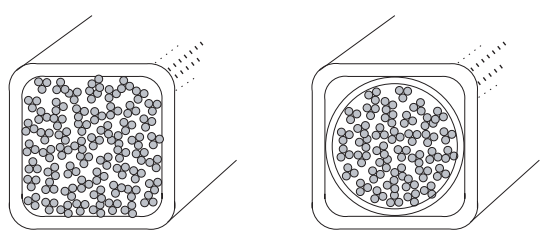

Fig. 6.14 Examples of CIC conductors.

DISCUSSION 6.6: Cable-in-Conduit (CIC) Conductors (continuation)

B. Components of CIC Conductor

As we may infer from Fig. 6.14, the CIC conductor includes: 1) cable; 2) helium; and 3) conduit. Each is briefly described.

Cable

The cable basically consists of many strands, each a composite of diameter ∼1 mm or smaller containing many filaments of 10–100 μm diameter superconductor, NbTi or Nb_3Sn; often copper strands of the same diameter as that of either NbTi or Nb_3Sn strands are substituted for the superconducting strands either to enhance the overall matrix metal cross sectional area, reduce the cable cost or both. Generally three or seven strands are "bundled" to form what we call here a "basic cable." The 3-strand basic cables may be deciphered from each of the CIC conductors illustrated in Fig. 6.14. A typical CIC conductor is at least one cm or two across—for fusion magnets this can exceed 5 cm—and therefore operates at a high current, with an operating current, I_{op}, of at least 10 kA and, for some fusion magnets, close to 100 kA. To meet this high I_{op} requirement, the bundling process continues, in which generally 3, 5, or 7 basic cables are bundled to form the 2nd-step cable, and so forth to additional steps, as required.

Table 6.6 lists three CIC conductors: Coils A and C of the 45-T Hybrid Magnet at NHMFL; and a proposed CIC conductor for an ITER toroidal-field coil design. The 45-T Hybrid Magnet is operating, while the ITER coil is still in the design stage, though many model versions have been operated. The first part of Table 6.6 lists parameters of the cables for these coils.

Helium

Helium in supercritical state, i.e., its pressure above the critical pressure, 227.5 kPa (2.25 atm), is forced through the windings at a nominal operating pressure P_{op} ∼3–5 atm. The operating temperature, T_{op}, though, is generally maintained below its critical temperature (5.2 K), by having the circulating helium cooled to typically 4.3–4.5 K, before it enters the winding. In the 45-T Hybrid the helium is subcooled superfluid, at a nominal P_{op} of 1 atm and a nominal T_{op} of 1.8 K. The remarkable properties of superfluidity (high thermal conductivity and low viscosity) enable this system to rely simply on "natural convection," rather than forced flow, to transport dissipation to a heat exchanger located outside the winding. The helium parameters for the three coils are in the middle part of Table 6.6.

For forced-flow helium, its heat transfer coefficient, h_{he} [W/cm^2 K], is based on the so-called Dittus-Boelter-Giarratano-Yaskin correlation [6.23]:

$$h_{he} = 0.0259 \left(\frac{k_{he}}{D_{hy}}\right) \mathrm{Re}^{0.8}\mathrm{Pr}^{0.4} \left(\frac{T_{he}}{T_{cd}}\right)^{-0.716} \tag{6.29}$$

In Eq. 6.29 k_{he}, Re, and Pr are, respectively, the thermal conductivity of helium, Reynolds number, and Prandtl number; D_{hy} is the hydraulic diameter; and T_{cd} is the conductor temperature. Heat transfer fluxes, g_q, at 3.5 atm and 4.5 K, for $\mathrm{Re} = 10^4$ and $\mathrm{Re} = 10^5$ are given in Fig. 6.3.

DISCUSSION 6.6: Cable-in-Conduit (CIC) Conductors (continuation)

Table 6.6: Examples of CIC Conductors

CIC Conductor Coil	45-T Hybrid Magnet		ITER
Parameters	Coil A	Coil C	TF Coil
Nominal I_{op} [kA]	10		50
Total area ($A_{\rm cic}$) [mm^2]	209.94	196.29	2601
Basic Cable # strands	6 Nb_3Sn/Cu+1 Cu	3 NbTi/Cu	6 Nb_3Sn/Cu
Strand diameter, d_{st} [mm]	0.433	0.810	0.810
Cable Patterns	$7\times3\times5\times5$	$3\times3\times3\times5$	$3\times(4^3)\times6$
Total strand number, N_{st}	525	135	1152
Conductor area, A_{cd} [mm^2]	79.44*	70.49*	593.6
$A_{sc}+A_{\overline{m}}$ [mm^2]	25.19	11.25	94.74
A_m [mm^2]	54.25	59.14	498.05
$A_{cd}/A_{\rm cic}$	0.38	0.36	0.23
Helium	Superfluid†		Supercritical
Nominal P_{op} [atm]	1		5
Nominal T_{op} [K]	1.8		4.5
Nominal flow rate [g/s]	not-forced; natural convection		10
D_{hy}‡ [mm]	227.3	109.4	933.1
Flow area†† (A_q) [mm^2]	50.30	36.50	276
$A_q/A_{\rm cic}$	0.24	0.19	0.106
Conduit Material	Stainless steel‡‡		Incoloy
Area (A_S) [mm^2]	80.20	89.30	1466.9
height×width [mm×mm]	16.22×13.71	15.85×13.74	51×51
wall thickness [mm]	1.64	2.00	2.86
outer corner radius [mm]	3.40	4.77	
$A_S/A_{\rm cic}$	0.38	0.45	0.56

* Greater than the cross sectional area given by $N_{st}(\pi d_{st}^2/4)$, due to cabling.

† Forced, during cooldown to 4.5 K.

‡ Computed wetted perimeter, given by $N_{st}d_{st}$.

†† Often expressed by void fraction: $A_q/(A_{cd}+A_q)$.

‡‡ Coil A: modified 316LN (low carbon/high nitrogen); Coil C: pancakes near the ends, 316L; pancakes near the center, standard 316LN.

Conduit

The conduit encases a bundle of cabled strands and provides space for coolant, which is generally forced supercritical helium but can be stagnant if the coolant is superfluid helium, like the superconducting coils of the 45-T Hybrid Magnet. For composite Nb_3Sn strands, which are brittle and must not be strained more than ∼0.3%, the final heat treatment for Nb_3Sn reaction must be performed after the unreacted strands are first encased in the conduit and wound into the coil. In the 1980s a nickel-iron based superalloy, Incoloy 908, was the preferred conduit metal, but recently most conduits use stainless steel grade 316LN—the designation LN indicates 316 stainless steel with low carbon and high nitrogen contents.

DISCUSSION 6.6: Cable-in-Conduit (CIC) Conductors (continuation)

C. Stability

From the very beginning in the early 1970s, much attention was given to the stability of CIC conductors. One of the important results from this early era was the observation in 1977 of "recovery" in CIC conductor even in the absence of a net coolant flow through the conductor [6.24]. Apparently, heating-induced high-velocity local coolant flow in the heated region is responsible for supplying the cooling necessary for recovery.

An important milestone early in the stability work for CIC conductors is the discovery by Lue, Miller, and Dresner in 1979 of multivalued stability margins that can exist under certain operating conditions [6.25]. Here the energy margin, Δe_h, is defined as the maximum dissipative energy density pulse (per unit strand volume) to which a conductor can be exposed and still remain superconducting when it is carrying a given transport current. Figure 6.15 presents a typical Δe_h vs. $I_t/I_{c_\circ}$ for constant values of operating temperature (T_{op}), field (B_0), and coolant flow rate. Here, I_t is the transport current and $I_{c_\circ}(T_{op}, B_0)$ is the critical current. The "dual stability" regime, characterized by multivalued stability margins, occurs near $I_t/I_{c_\circ} \sim 0.5$. The regime below the dual stability regime is referred to as "well-cooled" and that above as "ill-cooled" [6.26].

In the face of the requirement to *guarantee* stable operation of large superconducting magnets such as for fusion reactors, ITER magnets are designed to operate in the well-cooled regime, i.e., I_t below I_{lim}, given by:

$$I_{lim} = \sqrt{\frac{A_m f_p \mathcal{P}_D h_{he}(T_c - T_{op})}{\rho_m}} \tag{6.30}$$

Note that I_{lim} satisfies the Stekly criterion, i.e., $I_{lim} = I_{c_\circ}$ with $\alpha_{sk} = 1$ in Eq. 6.19.

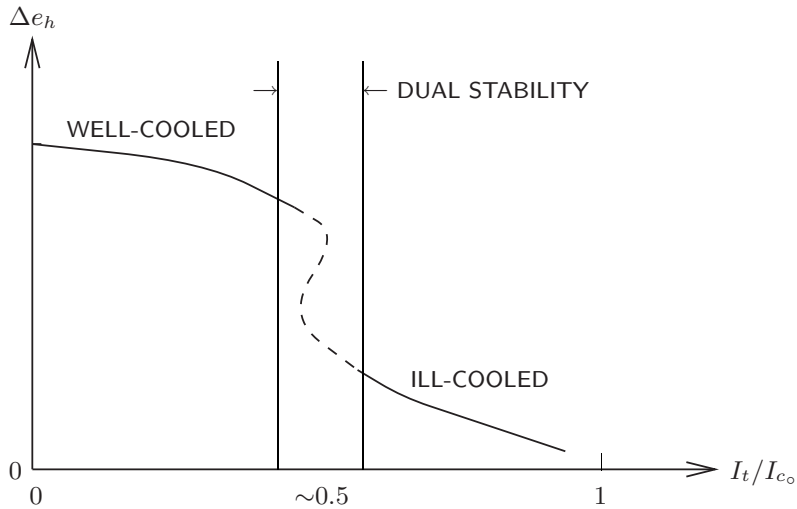

Fig. 6.15 General energy margin vs. normalized transport current plot for a CIC conductor [6.25].

DISCUSSION 6.6: Cable-in-Conduit (CIC) Conductors (continuation)

D. Other Issues

AC Losses

Because superconducting magnets in fusion reactors are subjected to time-varying magnetic fields, AC losses occur within CIC conductors. How to deal with AC losses is a major topic in the design of CIC conductors [6.27–6.50]. AC losses are discussed in ***CHAPTER 7***.

Joint

A CIC conductor handles both strands that carry current and the conduit that carries coolant. Therefore, joining of two CIC conductors is much more difficult than joining two composites unconfined in a conduit. Several techniques have been developed to deal with this issue [6.51–6.57].

Ramp-Rate Limitation

A conductor such as CIC conductor that is comprised of cabled composite strands sometimes suffers from a phenomenon known as "ramp-rate limitation," a form of instability that quenches the conductor below its designated operating current. The instability phenomenon occurs only when the current ramp rate exceeds a critical rate or for a conductor carrying a constant current but exposed to a rapid change in the background magnetic field. Clearly, nonuniform sharing of transport current within the cabled strands is due chiefly to inequalities in inductances and resistances of strands in the cable. The problem has been studied extensively in the past decade [6.58–6.62]. Because the ramp-rate-limitation does not occur in cabled strands that operate at currents below I_{lim}, perhaps it is another reason for these large magnets to operate at the conservative level set by I_{lim}.

"In this very spot there are whole forests which were buried millions of years ago; now they have turned to coal, and for me they are an inexhaustible mine."
—*Captain Nemo* (c. 1870)

"The seas of this planet contain 100,000,000,000,000,000 tons of hydrogen and 20,000,000,000,000 tons of deuterium. Soon we will learn to use these simplest of all atoms to yield unlimited power." —Arthur C. Clarke (c. 1960)

PROBLEM 6.5: V vs. I traces of a cooled composite conductor*

This problem investigates V vs. I traces of a composite superconductor immersed in a bath of 4.2-K liquid helium; we will generate V vs. I traces for three different cooling conditions. The conductor parameters are as follows: $I_{c_\circ} = 1000\,\text{A}$, the critical current at $T_{op} = 4.2\,\text{K}$; $\rho_m = 4\times10^{-10}\,\Omega\,\text{m}$, the electrical resistivity of the matrix metal; $A_m = 2\times10^{-5}\,\text{m}^2$, the total matrix cross section; $P_{cd} = 2\times10^{-2}\,\text{m}$, the total conductor perimeter (that exposed to liquid helium: $f_p P_{cd}$); and $h_q = 10^4\,\text{W/m}^2\,\text{K}$, the heat transfer coefficient. V is measured across a conductor length $\ell = 0.1\,\text{m}$. In deriving V vs. I traces, assume that $I_c(T)$ is given by Eq. 6.12.

a) For $I < I_{c_\circ}$, we have $V = 0\,\text{V}$. For $I \geq I_{c_\circ}$, show that V is given by the following expression:

$$V = \frac{R_m(I - I_{c_\circ})}{1 - \dfrac{R_m I I_{c_\circ}}{f_p P_{cd}\ell h_q(T_c - T_{op})}} \tag{6.31}$$

where $R_m = \rho_m\ell/A_m$. Assume that the composite is in thermal equilibrium, i.e., the resistive dissipation balanced by the cooling with the composite at $T_{op}+\Delta T$. Note that $I_m = I - I_s$, where I_m is the matrix current and I_s is the superconductor current at $T = T_{op} + \Delta T$, as given by Eq. 6.12.

b) By defining two additional dimensionless parameters, $v \equiv V/R_m I_{c_\circ}$, $i \equiv I/I_{c_\circ}$, and also using α_{sk}, the Stekly parameter (Eq. 6.19), show that dimensionless voltage, $v(i)$, is given by:

$$v(i) = \frac{i - 1}{1 - \alpha_{sk} i} \tag{6.32}$$

c) *Condition 1:* $f_p = 1$ ($\alpha_{sk} = 0.1$). For $T_c = 5.2\,\text{K}$ (and $T_{op} = 4.2\,\text{K}$), compute v at $i = 1$, 1.1, 1.5, and 2.

d) *Condition 2:* $f_p = 0.1$ ($\alpha_{sk} = 1$). Show that v is indeterminate at $i = 1$.

e) *Condition 3:* $f_p = 0.05$ ($\alpha_{sk} = 2$). Here, the surface area is nearly insulated from liquid helium, the composite will behave unstably, and as observed by Stekly in his experiment using a *real* supply, the supply momentarily drops its current from the designated level, matching the positive load voltage, before settling back to the original current and the corresponding voltage on the $v = i$ line [6.63]. Although Eq. 6.32, derived from Eq. 6.31 based on the premise that $v = 0$ for $i < 1$, is not valid for $i > 1$ under the *steady-state conditions*, you may use the equation to find values of v for for $i = 1$, 0.9, 0.8, 0.75, and 0.707.

f) Plot $v(i)$ traces for the three conditions studied above. Plot $v = i$ with a solid line. Label $\alpha_{sk} = 0.1$ for the curve corresponding to *Condition 1*; $\alpha_{sk} = 1$ for the *Condition 2* curve; $\alpha_{sk} = 2$ for the *Condition 3* curve.

---

* Based on **Problem 6.9** in the 1st Edition (Plenum, 1994).

Solution to PROBLEM 6.5

a) For $I > I_{c_\circ}$, V across the voltage taps is given by $R_m(I - I_s)$ where I_s is the current in the superconductor, i.e., $I_s = I_c(T)$. Joule heat generation $G_j(T_{op}+\Delta T)$ in the composite is thus given by:

$$G_j(T_{op} + \Delta T) = VI = R_m \left\{ I - I_{c_\circ} \left[\frac{T_c - (T_{op} + \Delta T)}{T_c - T_{op}} \right] \right\} I$$

$$= R_m I \left[(I - I_{c_\circ}) + \frac{I_{c_\circ} \Delta T}{T_c - T_{op}} \right] \qquad (S5.1)$$

$G_j(T_{op} + \Delta T)$ is matched by the cooling, which is given by $f_p P_{cd} \ell h_q (T - T_{op}) = f_p P_{cd} \ell h_q \Delta T$. Equating these two powers and solving for ΔT, we obtain:

$$\Delta T = \frac{R_m I (I - I_{c_\circ})(T_c - T_{op})}{f_p P_{cd} \ell h_q (T_c - T_{op}) - R_m I_{c_\circ} I} \qquad (S5.2)$$

Combining Eqs. $S5.1$ and $S5.2$ and solving for V, we obtain:

$$V = R_m \left\{ (I - I_{c_\circ}) + \frac{I_{c_\circ}}{(T_c - T_{op})} \left[\frac{R_m I (I - I_{c_\circ})(T_c - T_{op})}{f_p P_{cd} \ell h_q (T_c - T_{op}) - R_m I_{c_\circ} I} \right] \right\} \qquad (S5.3a)$$

$$= R_m (I - I_{c_\circ}) + \frac{R_m^2 I_{c_\circ} I (I - I_{c_\circ})}{f_p P_{cd} \ell h_q (T_c - T_{op}) - R_m I_{c_\circ} I} \qquad (S5.3b)$$

From Eq. $S5.3b$ we obtain:

$$V = \frac{R_m (I - I_{c_\circ})}{1 - \dfrac{R_m I I_{c_\circ}}{f_p P_{cd} \ell h_q (T_c - T_{op})}} \qquad (6.31)$$

b) By substituting R_m/ℓ for ρ_m/A_m in α_{sk} (Eq. 6.19), we can rewrite Eq. 6.31:

$$V = \frac{R_m (I - I_{c_\circ})}{1 - \alpha_{sk} (I/I_{c_\circ})} \qquad (S5.4)$$

From which, we obtain:

$$v(i) = \frac{i - 1}{1 - \alpha_{sk} i} \qquad (6.32)$$

c) $R_m = \rho_m \ell / A_m = 2 \times 10^{-6}\,\Omega$. With $f_p = 1$, we have α_{sk}:

$$\alpha_{sk} = \frac{\rho_m I_{c_\circ}^2}{f_p P_{cd} A_m h_q (T_c - T_{op})}$$

$$= \frac{(4 \times 10^{-10}\,\Omega\,\mathrm{m})(1000\,\mathrm{A})^2}{(1)(2 \times 10^{-2}\,\mathrm{m})(2 \times 10^{-5}\,\mathrm{m}^2)(10^4\,\mathrm{W/m^2\,K})(5.2\,\mathrm{K} - 4.2\,\mathrm{K})} = 0.1$$

Thus, Eq. 6.32 is given by:

$$v(i) = \frac{10(i - 1)}{10 - i} \qquad (S5.5)$$

Values of $v(i)$ at selected values of i are given in Table 6.7.

Solution to PROBLEM 6.5 (continuation)

Table 6.7: v vs. i for $\alpha_{sk}=0.1$

i	1	1.1	1.5	2
v	0	0.11	0.59	1.25

Table 6.8: i vs. v for α_{sk}=2*

i	1	0.9	0.8	0.75	0.725	0.707	$\leq$0.707
v	0	0.125	0.333	0.5	0.611	0.707	0

* This is not under the steady-state conditions.

d) When $f_p=0.1$, α_{sk} becomes 1. For $i<1$, by definition, $v=0$. For $i>1$, from Eq. 6.32, $v(i)=i$. At $i=1$, $v(i)$ is really indeterminate; physically, as pointed out in ***DISCUSSION 6.1***, this means that v can be any point on the vertical line at $i=1$. Note that at $i=1$ ($I=I_{c_o}$), $V=0$ according to Eq. 6.31.

e) Here, with $f_p = 0.05$, $\alpha_{sk} = 2$, we may compute $v(i)$ using Eq. 6.32. As remarked above, Stekly observed [6.63] that $v(i)$ is double-valued between $i=0.707$ (as computed here) and $i=1$, i.e., $v=0$ as i is increased from 0 to $i=1$, at which point v suddenly appears, forcing i to drop (because the power supply, set at a minimal voltage needed in the current range from $i=0$ and $i=1$, cannot sustain the current at $i=1$). First, v traces the curved line, labeled $\alpha_{sk}=2$, shown in Fig. 6.16 from $i=1$ to $i=0.707$, known as the "recovery" current (normalized) for $\alpha_{sk}=2$. Subsequently, v returns to 0 as i is decreased below 0.707.

f)

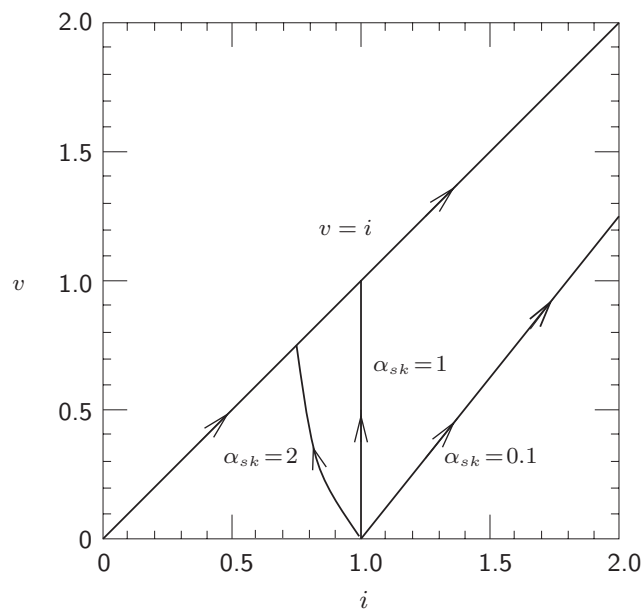

Fig. 6.16 Normalized voltage vs. normalized current traces for $\alpha_{sk}=0.1$, 1, and 2.

PROBLEM 6.6: Stability analysis of Hybrid III SCM*

This problem deals with the cryostability of the Hybrid III's NbTi coil, whose conductor specifications are given in Table 5.1 of **PROBLEM 5.1**. (The NbTi coil in Hybrid III actually employs two grades of NbTi composite conductors; here it is simplified to use only one grade.)

The NbTi coil consists of a stack of 32 double-pancake coils, with a total overall winding height of 640 mm. Each pancake coil is of 658-mm winding i.d. and 907-mm o.d. Figure 6.17 shows important details of the winding. As is evident from the figure, each turn is separated by a thin insulator strip. The two pancakes in each double-pancake unit are separated by a sheet of 0.5-mm thick insulator bonded with epoxy resin. Between adjacent double pancakes are 1.0-mm thick insulating strips extending radially from the inside radius to space the coils to provide cooling. The spacer strips cover, on the average, 60% of the flat surface of each coil exposed to liquid helium. Note that in each double-pancake set, helium wets the top surface (40%) of the top pancake and the bottom surface of the bottom pancake. Because the liquid helium is superfluid at 1.8 K, there are no helium bubbles to impair the cooling of each bottom pancake facing downward.

The NbTi coil (and Nb_3Sn coil) is designed to be operated while immersed in a bath of 1-atm subcooled 1.8-K superfluid helium. Assume the cooling to be domi-

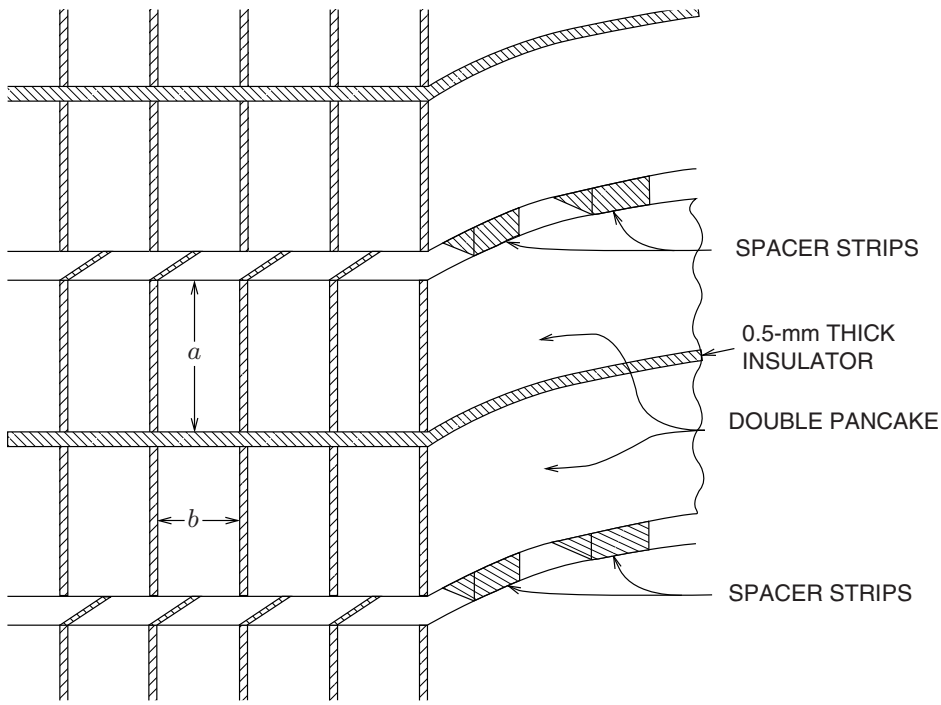

Fig. 6.17 Winding details for the NbTi pancakes.

* Based on **Problem 6.10** in the 1st Edition (Plenum, 1994).

PROBLEM 6.6: Stability analysis of Hybrid III SCM (continuation)

nated by Kapitza resistance; therefore q_k given by Eq. 4.7 should be used for cooling, $q(T)$:

$$q_k = a_k(T_{cd}^{n_k} - T_b^{n_k}) \tag{4.7}$$

T_{cd} [K] is the conductor temperature (really the temperature of the conductor surface, which is of matrix metal copper) and T_b [K] is the bath temperature. You may take $a_k = 0.02\,\mathrm{W/cm^2\,K^4}$ and $n_k = 4.0$ (Table 4.7). At an operating temperature T_{op} of 1.8 K ($T_{op} = T_b$), the coil carries a transport current I_{op} of 2100 A and is exposed to a maximum magnetic induction of ∼10 T. Table 5.1 gives useful data.

a) Make an appropriate $I_c(T)$ plot for this conductor covering the temperature range, from 1.8 K, the nominal operating temperature, to 4.1 K, the critical temperature at 10 T. Determine, from the plot, the current sharing temperature T_{cs} for a transport current I_t of 2100 A. Indicate T_{cs} in the plot.

b) Make, and label, power flux [W/cm^2] vs. temperature [K] plots for both cooling and heat generation at 10 T when $T_{op} = T_b = 1.8$ K, $I_{op} = 2100$ A. Based on the plots, state whether the pancakes are stable, and, if so, by which criterion. If not, explain why they are not stable. For the purpose of answering this question you may assume that: 1) $q(T)$ given above is valid over the *entire* temperature range of interest and that 2) heat generated within each pancake is transported freely through the 1-mm high radial channels.

c) In the pancake coils in previous hybrid magnets built at the FBNML, each turn in these windings was separated by thin (∼0.4 mm thick) spacers to make the windings "ventilated" and thus cryostable. In the early phase of the Hybrid III project, pancake designs with such turn-to-turn cooling spacers were seriously considered but were abandoned in favor of a spacerless winding design, because turn-to-turn spacers reduce the radial stiffness of the winding. Assuming turn-to-turn cooling channels are present in the Hybrid III NbTi pancakes, draw again neatly on another graph power flux [W/cm^2] vs. temperature [K] plots for both cooling and heat generation at 10 T when $T_b = 1.8$ K, $I_{op} = 2100$ A. For this case, assume 50% of the total conductor perimeter is exposed directly to liquid helium. Again, based on these plots, comment on the stability of the pancakes.

"...there must be discipline. For many things are not as they appear. Discipline must come from trust and confidence." —*Robert Jordan*

Solution to PROBLEM 6.6

a) Figure 6.18 presents the $I_c(T)$ plot for this conductor, constructed by joining two points: one at 6000 A at 1.8 K and 10 T (Table 5.1) and the other at 0 A at 4.7 K (T_c at 10 T; Table 5.1; also indicated in Fig. 6.18). The current sharing temperature T_{cs} is given by 2100 A = $I_c(T_{cs})$: it is 3.7 K.

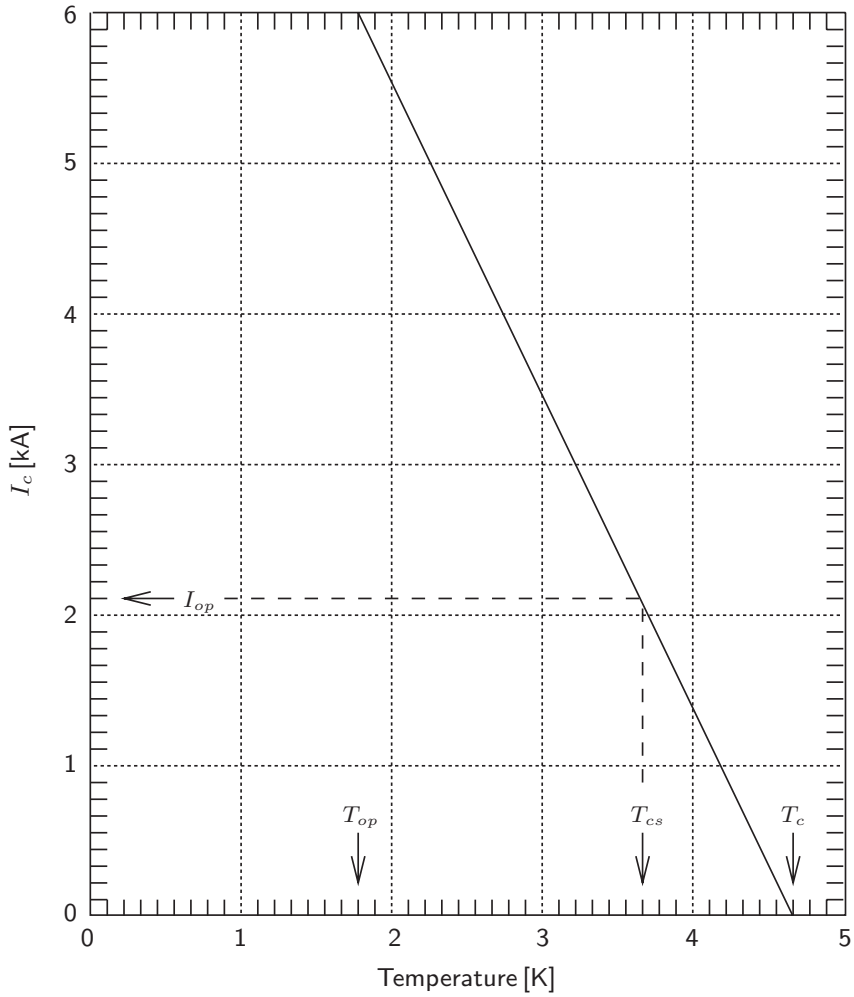

Fig. 6.18 I_c vs. T plot (solid) for a Hybrid III Nb-Ti conductor at 10 T. The intersection of the line at $I_c = 0$ determines $T_c = 4.7$ K. $I_t = 2100$ A is given by the dashed line, which intersects the solid line at $T_{cs} = 3.7$ K.

TRIVIA 6.2 List the items below in the descending order of their surface heat fluxes.

i) Bottom wet surface, of a heated teapot keeping the water at 373 K;

ii) LED bulb, of a lit Christmas tree miniature decoration light;

iii) Normal-state composite HTS, cryostabilized by boiling liquid nitrogen at 77 K;

iv) Sunlight over Mars.

Solution to PROBLEM 6.6 (continuation)

b) Let us first compute $\hat{g}_j$ in the normal state valid for $T \geq T_c = 4.7\,\text{K}$. Unlike $g_j(T_c) = \rho_m I_{op}^2 / A_m A_{cd}\,[\text{W/m}^3]$, $\hat{g}_j(T_c)$ is the normal-state generation flux (per unit of conductor surface exposed to liquid helium). That is, $\hat{g}_j(T_c) = (A_{cd}/f_p P_{cd}) g_j(T)$, where $f_p P_{cd}$ is the conductor perimeter exposed to liquid helium. A_{cd} and A_m are the cross sectional areas, respectively, of the overall conductor and matrix metal. We have: $A_{cd} = ab$, where a and b are the overall conductor width and thickness, respectively; and $A_m = ab\gamma_{c/s}/(\gamma_{c/s}+1)$, where $\gamma_{c/s}$ is the copper-to-superconductor ratio. We thus have: $\hat{g}_j(T_c) = \rho_m I_{op}^2 (\gamma_{c/s}+1)/\gamma_{c/s} ab f_p P_{cd}$.

With $I_t = 2100\,\text{A}$, $\rho_m = 4.5 \times 10^{-10}\,\Omega\,\text{m}$, $a = 9.2 \times 10^{-3}\,\text{m}$, $b = 2.6 \times 10^{-3}\,\text{m}$, $\gamma_{c/s} = 3$, $f_p P_{cd} = (0.4)(2.6 \times 10^{-3}\,\text{m}) = 1.04 \times 10^{-3}\,\text{m}$, we obtain: $\hat{g}_j = 1.06 \times 10^5\,\text{W/m}^2$.

$\hat{g}_j(T)$ is zero for $1.8\,\text{K} \leq T \leq T_{cs}$ (3.7 K), and starting at T_{cs} it rises linearly with T until T_c (4.7 K), at which point $\hat{g}_j(T_c) = 1.06 \times 10^5\,\text{W/m}^2$.

Figure 6.19 shows $\hat{g}_j(T)$ and $q(T)$ plots. From the plots, it is clear that the pancakes are almost cryostable; they certainly satisfy the equal area criterion.

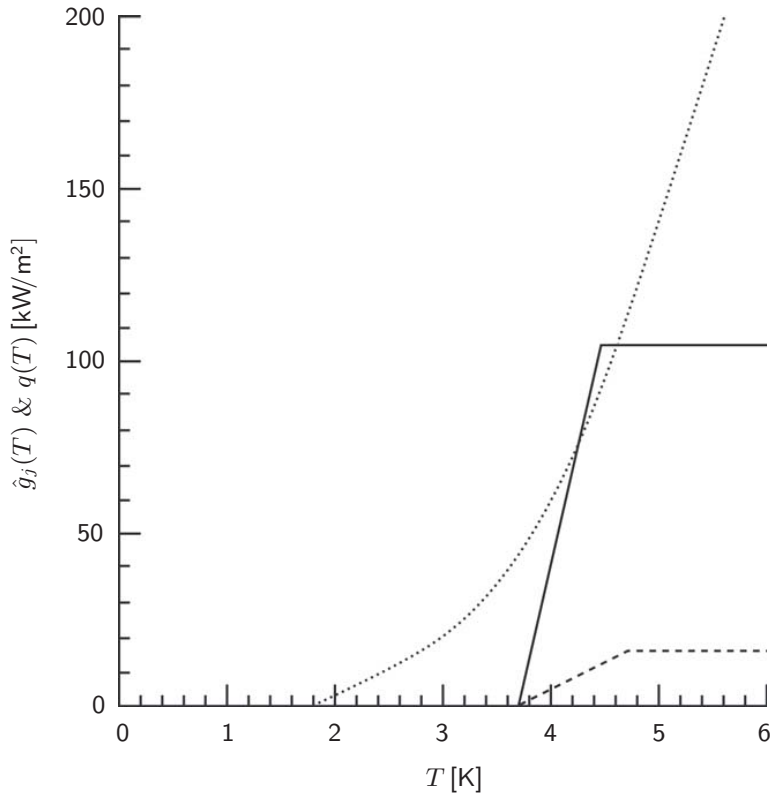

Fig. 6.19 $\hat{g}_j(T)$ plot (solid) and $q(T)$ plot (dotted); $\hat{g}_j(T)$ (dashed) corresponds to question **c)**.

Solution to PROBLEM 6.6 (continuation)

c) Both $g_j(T)$ and $q(T)$ are the same as those computed in **b)**. The area exposed to helium per unit conductor length will of course be much greater in this case than in the spacerless winding. For this case, $f_p P_{cd} = (0.5)(23.6 \times 10^{-3}\,\text{m}) = 11.8 \times 10^{-3}\,\text{m}$ and $\hat{g}_j(T_c) = 9.34\,\text{kW/m}^2$.

The dashed curve in Fig. 6.19 shows the $\hat{g}_j(T)$ plot; the same $q(T)$ used in the previous case is valid. From the plots, it is clear that the pancakes are cryostable.

DISCUSSION 6.7: Cryostable vs. Quasi-Adiabatic Magnets

As described in **PROBLEM 6.6**, the double pancakes of the Hybrid III NbTi coil have no cooling channels between turns. The decision to make these double pancakes "quasi-adiabatic" (QA) was to reduce stresses. The term "quasi-adiabatic" was used because it was thought that the NbTi coil, without cooling channels, would not be cryostable but would approximate adiabatic performance—later, when the stability analysis presented above was performed as an exercise for students, the coil was found to be stable. An internal (unpublished) study performed at FBML in 1986 to examine the effects of mechanical disturbances on coil operation concluded that the NbTi coil, under quasi-adiabatic condition, would, and indeed did, perform satisfactorily.)

Figure 6.20 shows an example of hoop stress (σ_h) vs. winding radius (r) plots of the NbTi conductors, High-Field (HF) grade and Low-Field (LF) grade for cryostable and QA windings [3.14]. For cryostable windings, because of the presence of structurally "soft" turn-to-turn insulating strips, σ_h vs. r traces the local $(r \times J \times B_z)$ stresses. (A jump in the stress at the HF-LF transition is due to the reduction in conductor cross section.) For the QA winding, because the winding is much more rigid in the radial direction (no spacers), radial expansion of the inner turns is supported by the outer turns, decreasing stresses in the inner turns. The net result is a more uniform stress distribution. (In the analysis it was assumed that both sections had the same conductor cross sectional area.) Equally important is a substantial reduction in the overall size of the NbTi coil, from a winding o.d. of 1.06 m to an o.d. of ∼0.9 m.

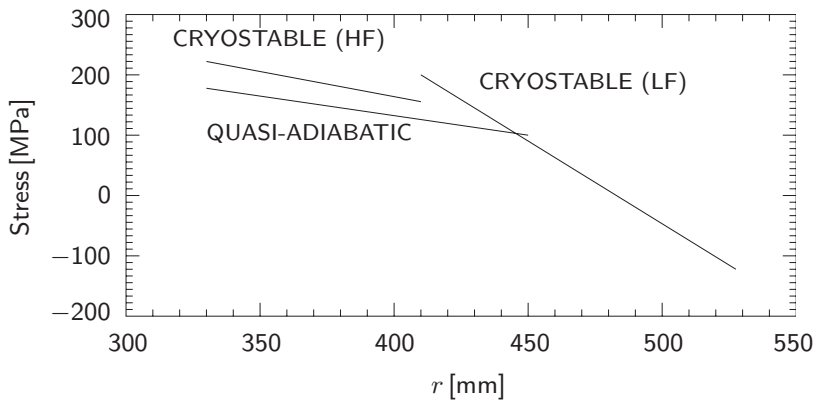

Fig. 6.20 Hoop stress vs. radius plots for cryostable and quasi-adiabatic windings.

DISCUSSION 6.8: The MPZ Concept*

As briefly stated in **6.2.1**, the MPZ (minimum propagating zone) concept has played a key role in advancing our understanding of "disturbances" that occur within a magnet winding and their effects on the performance of virtually every kind of magnet, adiabatic as well as cooled [1.27, 6.14]. The concept showed the minuteness of disturbances degrading the performance of *LTS* magnets [6.64, 6.65].

Consider an isotropic winding geometry of infinite radial extent (Fig. 6.21) operating at I_{op}, which in a spherical region 1 ($r \leq R_{mz}$) is fully normal and dissipating Joule heating density of $\rho_m J_m^2$, where ρ_m is the temperature-independent matrix resistivity and $J_m = I_{op}/A_m$; region 2 ($r \geq R_{mz}$) is superconducting; far away from R_{mz}, the winding temperature is T_{op}. Assuming that the winding is characterized by a uniform and temperature-independent thermal conductivity k_{wd}, we may derive, under time-independent and "adiabatic" conditions, with no dissipation other than Joule dissipation, i.e., $C_{cd}\partial T/\partial t = 0$, $g_d(t) = 0$, and $g_q(T) = 0$, in Eq. 6.1, an expression for R_{mz}:

$$R_{mz} = \sqrt{\frac{3k_{wd}(T_c - T_{op})}{\rho_m J_m^2}} \tag{6.33}$$

If we insert values of k_{wd}, T_c, T_{op}, ρ_m, and J_m typical for an LTS magnet operating at liquid helium temperature, R_{mz} is 0.1–10 mm. (If k_{wd} is anisotropic but orthotropic, as within a real winding, the MPZ shape will be an ellipsoid, not a sphere.) The MPZ volume is minute compared with the winding volume, but it is possible to sustain a minute amount of $g_d(t)$ even within an adiabatic winding, provided its extent is limited to less than R_{mz}.

Although $(T_c - T_{op})$ in Eq. 6.33 can be an order of magnitude greater for an HTS winding than an LTS winding, because ρ_m increases with T_{op} and k_{wd} remains relatively constant, the MPZ size of an HTS winding at $T_{op} = 77.3$ K is about the same as that for an LTS magnet operating at $T_{op} = 4.2$ K. A parameter that dramatically increases with T_{op} is the enthalpy densities of the winding materials, making it virtually impossible, as stated at the outset of this chapter, to drive any HTS magnet above its critical temperature with disturbance energies such as those originating from mechanical events, e.g., wire motion and epoxy cracking, that still, though rarer than in the early 1980s, continue to afflict high-performance LTS magnets for high-energy physics accelerators, NMR, and MRI.

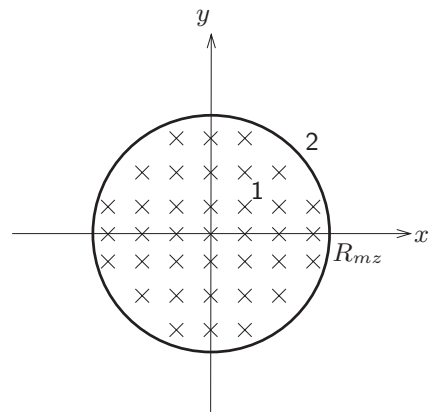

Fig. 6.21 Isotropic winding where in region 1 ($r \leq R_{mz}$) the winding is generating Joule heating and in region 2 ($r \geq R_{mz}$) the winding is superconducting.

* Based on **Problem 6.8** in the 1st Edition (Plenum, 1994).

PROBLEM 6.7: Dissipation density in adiabatic winding

Consider an infinitely long solenoid of winding i.d. $2a_1$ and o.d. $2a_2$. The magnet, cryocooled and maintained at operating temperature T_{op} at the magnet boundaries, i.e., i.d. and o.d. of the winding, experiences a uniformly distributed dissipation within the winding. This model approximates a cryocooled magnet subjected to AC losses within the epoxy-impregnated winding. Under steady-state conditions in which the winding temperature $T(r)$ is time-independent and the composite superconductor is fully superconducting, i.e., no Joule dissipation, the power density equation applied to the thermally isotropic winding is an extreme simplification of Eq. 6.1:

$$0 = \nabla\cdot[k_{wd}(T)\nabla T] + g_d(t) \tag{6.34}$$

where $k_{wd}(T)$ is the "average" thermal conductivity of the winding.

a) Show that under the condition that $k_{wd}(T) = k_{wd}$ is constant, the temperature, $T(\rho)$, in the winding, $1 \le \rho \le \alpha$, where $\rho \equiv r/a_1$, subjected to a spatially uniform and constant dissipation density, $g_d(t) = g_d$, is given by:

$$T(\rho) = \frac{a_1^2 g_d}{4k_{wd}}\left[(1-\rho^2) + \left(\frac{\alpha^2-1}{\ln\alpha}\right)\ln\rho\right] + T_{op} \tag{6.35}$$

b) Show that the maximum winding temperature, T_{mx}, occurs at ρ_{mx}:

$$\rho_{mx} = \sqrt{\frac{\alpha^2-1}{2\ln\alpha}} \tag{6.36}$$

c) Show that the critical dissipation density, g_{d_c}, at which the maximum temperature rise within the winding from T_{op}, $\Delta T_{mx} \equiv T_{mx} - T_{op}$, is given by:

$$g_{d_c} = \frac{4k_{wd}\Delta T_{mx}}{a_1^2\left\{1 + \dfrac{\alpha^2-1}{2\ln\alpha}\left[\ln\left(\dfrac{\alpha^2-1}{2\ln\alpha}\right) - 1\right]\right\}} \tag{6.37a}$$

Note that g_{d_c} is proportional to $\Delta T_{mx} \equiv T_{mx} - T_{op}$.

We may express Eq. 6.37*a* as:

$$g_{d_c} = \left(\frac{k_{wd}\Delta T_{mx}}{a_1^2}\right)\gamma_{d_c}(\alpha) \tag{6.37b}$$

where the dimensionless parameter $\gamma_{d_c}(\alpha)$ is given by:

$$\gamma_{d_c}(\alpha) \equiv \frac{4}{1 + \dfrac{\alpha^2-1}{2\ln\alpha}\left[\ln\left(\dfrac{\alpha^2-1}{2\ln\alpha}\right) - 1\right]} \tag{6.37c}$$

d) Construct a graph of $\gamma_{d_c}(\alpha)$ given by Eq. 6.37*c* in the α range 1.25–5.

Solution to PROBLEM 6.7

a) Equation 6.34 in 2-D cylindrical coordinates with $k_{wd}(T)$ assumed constant, k_{wd}, is given by:

$$\frac{k_{wd}}{r}\frac{d}{dr}\left(r\frac{dT}{dr}\right)+g_d=0 \tag{S7.1a}$$

Substituting $\rho\equiv r/a_1$, we have:

$$\frac{k_{wd}}{\rho}\frac{d}{d\rho}\left(\rho\frac{dT}{d\rho}\right)+g_d a_1^2=0 \tag{S7.1b}$$

Integrating Eq. $S7.1b$ twice with respect to ρ, we obtain:

$$T(\rho)=-\frac{g_d a_1^2}{4k_{wd}}\rho^2+A\ln\rho+B \tag{S7.2}$$

With boundary conditions $T(1)=T_{op}$ and $T(\alpha)=T_{op}$, we have:

$$T(\rho)=\frac{a_1^2 g_d}{4k_{wd}}\left[(1-\rho^2)+\left(\frac{\alpha^2-1}{\ln\alpha}\right)\ln\rho\right]+T_{op} \tag{6.35}$$

b) Differentiating Eq. 6.35 with respect to ρ and setting the resultant expression equal to zero, we obtain:

$$\frac{dT}{d\rho}=\frac{g_d a_1^2}{4k_{wd}}\left[-2\rho+\left(\frac{\alpha^2-1}{\ln\alpha}\right)\frac{1}{\rho}\right]=0 \tag{S7.3}$$

Solving for ρ, we have:

$$\rho_{mx}=\sqrt{\frac{\alpha^2-1}{2\ln\alpha}} \tag{6.36}$$

c) At $\rho=\rho_{mx}$, $T(\rho_{mx})=T_{mx}$. Thus, from Eq. 6.35, T_{mx} is given by:

$$T(\rho_{mx})\equiv T_{mx}=\frac{a_1^2 g_d}{4k_{wd}}\left[(1-\rho_{mx}^2)+\left(\frac{\alpha^2-1}{\ln\alpha}\right)\ln\rho_{mx}\right]+T_{op} \tag{S7.4}$$

Noting that $\Delta T_{mx}=T_{mx}-T_{op}$ and $g_d=g_{d_c}$ at T_{mx}, and combining Eqs. 6.36 and $S7.4$, we obtain:

$$\Delta T_{mx}=\frac{g_{d_c}a_1^2}{4k_{wd}}\left\{1+\frac{\alpha^2-1}{2\ln\alpha}\left[\ln\left(\frac{\alpha^2-1}{2\ln\alpha}\right)-1\right]\right\} \tag{S7.5}$$

Solving Eq. $S7.5$ for g_{d_c}, we have:

$$g_{d_c}=\frac{4k_{wd}\Delta T_{mx}}{a_1^2\left\{1+\frac{\alpha^2-1}{2\ln\alpha}\left[\ln\left(\frac{\alpha^2-1}{2\ln\alpha}\right)-1\right]\right\}} \tag{6.37a}$$

d) A graph of $\gamma_{d_c}(\alpha)$ for the α range of 1.25–5 is shown in Fig. 6.22.

Answer to TRIVIA 6.2 Teapot (50, in W/cm^2); HTS (10); LED bulb (0.2); Mars (0.05).

Solution to PROBLEM 6.7 (continuation

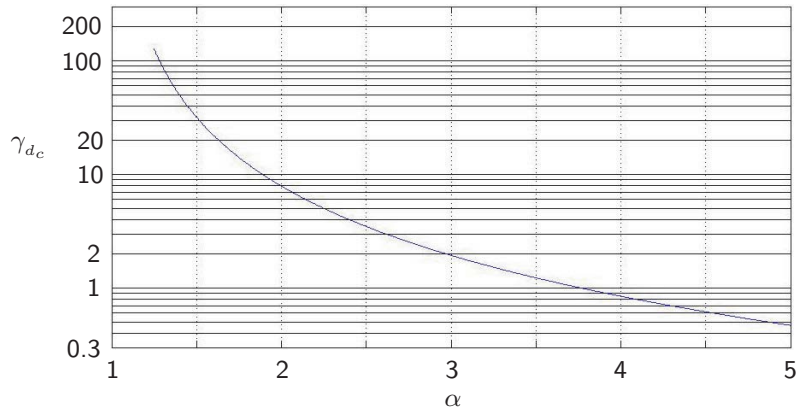

Fig. 6.22 $\gamma_{d_c}(\alpha)$ for the α range of 1.25–5.

Illustration Let us consider a few examples that may approximate real cases. ***Case 1*** Here we consider $\alpha = 2$; $a_1 = 10\,\text{cm}$; $k_{wd} = 0.01\,\text{W/cm K}$ (a "typical" winding at ∼30 K, consisting of metal and insulator); and $\Delta T_{mx} = 3\,\text{K}$. Because $\gamma_{d_c}(2) = 7.9$, applying Eq. 6.37*b*, we obtain:

$$g_{d_c} = \left(\frac{k_{wd}\Delta T_{mx}}{a_1^2}\right)\gamma_{d_c}(\alpha) \tag{6.37b}$$

$$= \frac{(0.01\,\text{W/cm K})(3\,\text{K})}{(10\,\text{cm})^2}(7.9) \simeq 2.4\times10^{-3}\,\text{W/cm}^3 \simeq 2.4\times10^{3}\,\text{W/m}^3$$

For this HTS solenoid, of $a_1 = 10\,\text{cm}$ and $a_2 = 20\,\text{cm}$ (and of infinite axial length), in which the winding is kept at ∼30 K and cooled by conduction from its i.d. and o.d., a uniform dissipation density, for example by AC losses, up to $2.4\,\text{kW/m}^3$ ($2.4\,\text{mW/cm}^3$) within the winding will not destroy superconductivity, provided the superconductor has a temperature margin, ΔT_{mx}, of at least 3 K. Note that this upper limit of dissipation density increases proportionately with ΔT_{mx}. Of course, even if the HTS can remain fully superconducting under a dissipation density of $2.4\,\text{kW/m}^3$, the system cryogenic load may be prohibitively high.

As studied in ***CHAPTER 7***, for an HTS tape of width w and thickness δ exposed to a cyclic magnetic field of (amplitude H_m), directed *parallel* to the tape's width (see Fig. 7.1d), hysteresis energy density, e_{hy}, one of three major AC losses in multifilamentary superconductor composite, for example, is given by: $e_{hy} \simeq \mu_\circ J_c \delta H_m$ (Eq. 7.29*d*), where J_c is the superconductor critical current density. For YBCO at 30 K and 2 T, $J_c \approx 2\times10^9\,\text{A/m}^2$ and $\delta \approx 1\times10^{-6}\,\text{m}$; thus for $\mu_\circ H_m = B_m = 2\,\text{T}$, we find: $e_{hy} = 4\,\text{kJ/m}^3 = 4\,\text{mJ/cm}^3$. This dissipation energy density translates to a power density, at 60 Hz, of $240\,\text{kW/m}^3$, 100 times greater than the maximum permissible level computed above! To limit the hysteresis dissipation power density to $2.4\,\text{kW/m}^3$, for the same J_c, B_m has to be limited to 0.02 T. Note that this is for the field *parallel* to the tape.

Case 2 Here, we consider a thinner solenoid: $\alpha = 1.25$, with the other parameters the same. With $\gamma_{d_c}(1.25) \simeq 128$, we have: $g_{d_c} \simeq 38\,\text{kW/m}^3$.

Solution to PROBLEM 6.7 (continuation)

Case 3 For a "thick" solenoid, e.g., $\alpha = 4$, $\gamma_{d_c}(4) \simeq 0.85$: $g_{d_c} \simeq 260\,\mathrm{W/m^3}$. This critical dissipation density may be too low for HTS tape—a magnetic field of 0.01 T at 60 Hz has a magnetic power density of $1200\,\mathrm{W/m^3}$! We may increase g_{d_c}, though obviously at increased cryogenic loads, by enhancing k_{wd}, or subdividing the winding into thin-walled coils, each cooled at its i.d. and o.d.

REFERENCES

[6.1] E.W. Collings, "Design considerations for high T_c ceramic superconductors," *Cryogenics* **28**, 724 (1988).

[6.2] Y. Iwasa, "Design and operational issues for 77-K superconducting magnets," *IEEE Trans. Mag.* **MAG-24**, 1211 (1988).

[6.3] L. Ogasawara, "Conductor design issues for oxide superconductors Part I: criteria of magnetic stability," *Cryogenics* **29**, 3 (1989).

[6.4] L. Dresner, "Stability and protection of Ag/BSCCO magnets operated in the 20–40 K range," *Cryogenics* **33**, 900 (1993).

[6.5] L.Y. Xiao, S. Han, L.Z. Lin, and H.M. Wen, "Stability study on composite conductors for HTSC superconducting magnets," *Cryogenics* **34**, 785 (1994).

[6.6] J.W. Lue, L. Dresner, S.W. Schwenterly, D. Aized, J.M. Campbell, and R.E. Schwall, "Stability measurements on a 1-T high temperature superconducting magnet," *IEEE Appl. Superconduc.* **5**, 230 (1995).

[6.7] Yu. A. Ilyin, V.S. Vysotsky, T. Kiss, M. Takeo, H. Okamoto and F. Irie, "Stability and quench development study in small HTS magnet," *Cryogenics* **41**, 665 (2001).

[6.8] T. Obana, K. Tasaki, T. Kuriyama, and T. Okamura, "Thermal stability analysis of conduction-cooled HTS coil," *Cryogenics* **43**, 603 (2003).

[6.9] A.R. Kantrowitz and Z.J.J. Stekly, "A new principle for the construction of stabilized superconducting coils," *Appl. Phys. Lett.* **6**, 56 (1965). Also see, Z.J.J. Stekly, R. Thome, and B. Strauss, "Principles of stability in cooled superconducting magnets," *J. Appl. Phys.* **40**, 2238 (1969).

[6.10] J. Wong, D.F. Fairbanks, R.N. Randall, and W.L. Larson, "Fully stabilized superconducting strip for the Argonne and Brookhaven bubble chambers," *J. Appl. Phys.* **39**, 2518 (1968).

[6.11] G. Bogner, C. Albrecht, R. Maier, and P. Parsch, "Experiments on copper- and aluminum-stabilized Nb-Ti superconductors in view of their application in large magnets," *Proc. 2nd Int'l Cryo. Eng. Conf.* (Iliffe Science and Technology Publication, Surrey, 1968), 175.

[6.12] J.R. Purcell, "The 1.8 tesla, 4.8 m i.d. bubble chamber magnet," *Proc. 1968 Summer Study on Superconducting Devices and Accelerators* (Brookhaven National Laboratory, Upton New York, 1969), 765.

[6.13] A.P. Martinelli and S.L. Wipf, "Investigation of cryogenic stability and reliability of operation of Nb_3Sn coils in helium gas environment," *Proc. Appl. Superconduc. Conf.* (IEEE Pub. 72CHO682-5-TABSC), 331 (1977).

[6.14] L. Bottura [Private communication, 2004].

[6.15] B.J. Maddock, G.B. James, and W.T. Norris, "Superconductive composites: heat transfer and steady state stabilization," *Cryogenics* **9**, 261 (1969).

[6.16] M.N. Wilson and Y. Iwasa, "Stability of superconductors against localized disturbances of limited magnitude," *Cryogenics* **18**, 17 (1978).

[6.17] J.E.C. Williams, E.S. Bobrov, Y. Iwasa, W.F.B. Punchard, J. Wrenn, A. Zhukovsky, "NMR magnet technology at MIT," *IEEE Trans. Magn.* **28**, 627 (1992).

[6.18] Y. Iwasa and V.Y. Adzovie, "The index number (n) below 'critical' current in Nb-Ti superconductors," *IEEE Trans. Appl. Superconduc.* **5**, 3437 (1995).

[6.19] K. Yamafuji and T. Kiss, "Current-voltage characteristics near the glass-liquid transition in high-T_c superconductors," *Physica C* **290**, 9 (1997).

[6.20] Kohei Higashikawa, Taketsune Nakamura, Koji Shikimachi, Naoki Hirano, Shigeo Nagaya, Takenobu Kiss, and Masayoshi Inoue, "Conceptual design of HTS coil for SMES using YBCO coated conductor," *IEEE Trans. Appl. Superconduc.* **17**, 1990 (2007).

[6.21] Mitchell O. Hoenig and D. Bruce Montgomery, "Dense supercritical-helium cooled superconductors for large high field stabilized magnets," *IEEE Trans. Magn.* **MAG -11**, 569 (1975).

[6.22] M. Morpurgo, "A large superconducting dipole cooled by forced circulation of two phase helium," *Cryogenics* **19**, 411 (1979).

[6.23] P.J. Giarratano, V.D. Arp and R.V. Smith, "Forced convection heat transfer to supercritical helium," *Cryogenics* **11**, 385 (1971).

[6.24] Y. Iwasa, M.O. Hoenig, and D.B. Montgomery, "Cryostability of a small superconducting coil wound with cabled hollow conductor," *IEEE Trans. Magn.* **MAG-13**, 678 (1977).

[6.25] J.W. Lue, J.R. Miller, and L. Dresner, "Stability of cable-in-conduit superconductors," *J. Appl. Phys.* **51**, 772 (1980).

[6.26] L. Bottura, "Stability, protection and ac loss of cable-in-conduit conductors – a designer's approach," *Fusion Eng. and Design* **20**, 351 (1993).

[6.27] J.V. Minervini, M.M. Steeves, and M.O. Hoenig, "Calorimetric measurement of AC loss in ICCS conductors subjected to pulsed magnetic fields," *IEEE Trans. Magn.* **MAG-23**, 1363 (1980).

[6.28] T. Ando, K. Okuno, H. Nakajima, K. Yoshida, T. Hiyama, H. Tsuji, Y. Takahashi, M. Nishi, E. Tada, K. Koizumi, T. Kato, M. Sugimoto, T. Isono, K. Kawano, M. Konno, J. Yoshida, H. Ishida, E. Kawagoe, Y. Kamiyauchi, Y. Matsuzaki, H. Shirakata, S. Shimamoto, "Experimental results of the Nb_3Sn demo poloidal coil (DPC-EX)," *IEEE Trans. Magn.* **27** 2060 (1991).

[6.29] G.B.J. Mulder, H.H.J. ten Kate, A. Nijhuis and L.J.M. van de Klundert, "A new test setup to measure the AC losses of the conductors for NET," *IEEE Trans. Magn.* **27**, 2190 (1991).

[6.30] R. Bruzzese, S. Chiarelli, P. Gislon, and M. Spadoni, and S. Zannella, "Critical currents and AC losses on subsize cables of the NET-EM/LMI 40-kA Nb_3Sn cable-in-conduit conductor prototype," *IEEE Trans. Magn.* **27**, 2198 (1991).

[6.31] D. Ciazynski, J.L. Duchateau, B. Turck, "Theoretical and experimental approach to AC losses in a 40 kA cable for NET," *IEEE Trans. Magn.* **27**, 2194 (1991).

[6.32] P. Bruzzone, L. Bottura, J. Eikelboom, A.J.M. Roovers, "Critical currents and AC losses on subsize cables of the NET-EM/LMI 40-kA Nb_3Sn cable-in-conduit conductor prototype," *IEEE Trans. Magn.* **27**, 2198 (1991).

[6.33] S.A. Egorov, A. Yu. Koretskij and E.R. Zapretilina, "Interstrand coupling AC losses in multistage cable-in-conduit superconductors," *Cryogenics* **32**, 439 (1992).

[6.34] Naoyuki Amemiya, Takayuki Kikuchi, Tadayoshi Hanafusa and Osami Tsukamoto, "Stability and AC loss of superconducting cables—Analysis of current imbalance and inter-strand coupling losses," *Cryogenics* **34**, 559 (1994).

[6.35] B.J.P. Baudouy, K. Bartholomew, J. Miller and S.W. Van Sciver, "AC loss measurement of the 45-T hybrid/CIC conductor," *IEEE Trans. Appl. Superconduc.* **5**, 668 (1995).

[6.36] B. Blau, I. Rohleder, G. Vecsey, "AC behaviour of full size, fusion dedicated cable-in-conduit conductors in SULTAN III under applied pulsed field," *IEEE Trans. Appl. Superconduc.* **5**, 697 (1995).

[6.37] Arend Nijhuis, Herman H.J. ten Kate, Pierluigi Bruzzone and Luca Bottura, "First results of a parametric study on coupling loss in subsize NET/ITER Nb_3Sn cabled specimen," *IEEE Trans. Appl. Superconduc.* **5**, 992 (1995).

[6.38] M. Ono, S. Hanawa, Y. Wachi, T. Hamajima, M. Yamaguchi, "Influence of coupling current among superconducting strands on stability of cable-in-conduit conductor," *IEEE Trans. Magn.* **32**, 2842 (1996).

[6.39] K. Kwasnitza and St. Clerc, "Coupling current loss reduction in cable-in-conduit superconductors by thick chromium oxide coating," *Cryogenics* **38**, 305 (1998).

[6.40] Toshiyuki Mito, Kazuya Takahata, Akifumi Iwamoto, Ryuji Maekawa, Nagato Yanagi, Takashi Satow, Osamu Motojima, Junya Yamamoto, EXSIV Group, Fumio Sumiyoshi, Shuma Kawabata and Naoki Hirano, "Extra AC losses for a CICC coil due to the non-uniform current distribution in the cable," *Cryogenics* **38**, 551 (1998).

[6.41] P.D. Weng, Y.F. Bi, Z.M. Chen, B.Z. Li and J. Fang, "HT-7U TF and PF conductor design," *Cryogenics* **40**, 531 (2000).

[6.42] Soren Prestemon, Stacy Sayre, Cesar Luongo and John Miller, "Quench simulation of a CICC model coil subjected to longitudinal and transverse field pulses," *Cryogenics* **40**, 511 (2000).

[6.43] Kazutaka Seo, Katuhiko Fukuhara and Mitsuru Hasegawa, "Analyses for inter-strand coupling loss in multi-strand superconducting cable with distributed resistance between strands," *Cryogenics* **41**, 511 (2001).

[6.44] Yoshikazu Takahashi, Kunihiro Matsui, Kenji Nishi, Norikiyo Koizumi, Yoshihiko Nunoya, Takaaki Isono, Toshinari Ando, Hiroshi Tsuji, Satoru Murase, and Susumu Shimamoto, "AC loss measurement of 46 kA-13 T Nb_3Sn conductor for ITER," *IEEE Trans. Appl. Superconduc.* **11**, 1546 (2001).

[6.45] Qiuliang Wang, Cheon Seong Yoon, Sungkeun Baang, Myungkyu Kim, Hyunki Park, Yongjin Kim, Sangil Lee and Keeman Kim, "AC losses and heat removal in three-dimensional winding pack of Samsung superconducting test facility under pulsed magnetic field operation," *Cryogenics* **41**, 253 (2001).

[6.46] S. Egorov, I. Rodin, A. Lancetov, A. Bursikov, M. Astrov, S. Fedotova, Ch. Weber, and J. Kaugerts, "AC loss and interstrand resistance measurement for NbTi cable-in-conduit conductor," *IEEE Trans. Appl. Superconduc.* **12**, 1607 (2002).

[6.47] A. Nijhuis, Yu. Ilyin, W. Abbas, B. ten Haken and H.H.J. ten Kate, "Change of interstrand contact resistance and coupling loss in various prototype ITER NbTi conductors with transverse loading in the Twente Cryogenic Cable Press up to 40,000 cycles," *Cryogenics* **44**, 319 (2004).

[6.48] S. Lee, Y. Chu, W.H. Chung, S.J. Lee, S.M. Choi, S.H. Park, H. Yonekawa, S.H. Baek, J.S. Kim, K.W. Cho, K.R. Park, B.S. Lim, Y.K. Oh, K. Kim, J.S. Bak, and G.S. Lee, "AC loss characteristics of the KSTAR CSMC estimated by pulse test," *IEEE Trans. Appl. Superconduc.* **16**, 771 (2006).

[6.49] Y. Yagai, H. Sato, M. Tsuda, T. Hamajima, Y. Nunoya, Y. Takahashi, and K. Okuno, "Irregular loops with long time constants in CIC conductor," *IEEE Trans. Appl. Superconduc.* **16**, 835 (2006).

[6.50] P. Bruzzone, B. Stepanov, R. Wesche, A. Portone, E. Salpietro, A. Vostner, and A. della Corte, "Test results of a small size CICC with advanced Nb_3Sn strands," *IEEE Trans. Appl. Superconduc.* **16**, 894 (2006).

[6.51] R.D. Blaugher, M.A. Janocko, P.W. Eckels, A. Patterson, J. Buttyan and E.J. Sestak, "Experimental test and evaluation of the Nb_3Sn joint and header region," *IEEE Trans. Magn.* **MAG-17**, 467 (1981).

[6.52] M.M. Steeves and M.O. Hoenig, "Lap joint resistance of Nb_3Sn cable terminations for the ICCS-HFTF 12 tesla coil program," *IEEE Trans. Magn.* **MAG-19**, 378 (1983).

[6.53] A. Bonito Oliva, P. Fabbricatore, A. Martin, R. Museich, S. Patrone, R. Penco, N. Valle, "Development and tests of electrical joints and terminations for CICC Nb_3Sn, 12 tesla solenoid," *IEEE Trans. Appl. Superconduc.* **3**, 468 (1993).

[6.54] D. Ciazynski, B. Bertrand, P. Decool, A. Martinez, L. Bottura, "Results of the European study on conductor joints for ITER coils," *IEEE Trans. Magn.* **32**, 2332 (1996).

[6.55] P. Bruzzone, N. Mitchell, D. Ciazynski, Y. Takahashi, B. Smith, M. Zgekamskij, "Design and R&D results of the joints for the ITER conductor," *IEEE Trans. Appl. Superconduc.* **7**, 461 (1997).

[6.56] Philip C. Michael, Chen-Yu Gung, Raghavan Jayakumar, and Joseph V. Minervini, "Qualification of joints for the inner module of the ITER CS model coil," *IEEE Trans. Appl. Superconduc.* **9**, 201 (1999).

[6.57] M.M. Steves, M. Takayasu, T.A. Painter, M.O. Hoenig, T. Kato, K. Okuno, H. Nakajima, and H. Tsuji, "Test results from the Nb_3Sn US-demonstration poloidal coil," *Adv. Cryo. Engr.* **37A**, 345 (1992).

[6.58] L. Krempasky and C. Schmidt, "Theory of 'supercurrents' and their influence on field quality and stability of superconducting magnets," *J. Appl. Phys.* **78** 5800 (1995).

[6.59] S. Jeong, J.H. Schultz, M. Takayasu, V. Vysotsky, P.C. Michael, W. Warnes, and S. Shen, "Ramp-rate limitation experiments using a hybrid superconducting cable," *Cryogenics* **36**, 623 (1996).

[6.60] Vitaly S. Vysotsky, Makoto Takayasu, Sangkwon Jeong, Philip C. Michael, Joel H. Schultz, and Joseph V. Minervini, "Measurements of current distribution in a 12-strand Nb3Sn cable-in-conduit conductor," *Cryogenics* **37**, 431 (1997).

[6.61] N. Amemiya, "Overview of current distribution and re-distribution in superconducting cables and their influence on stability," *Cryogenics* **38**, 545 (1998).

[6.62] Sangkwon Jeong, Seokho Kim and Tae Kuk Ko, "Experimental investigation to overcome the ramp-rate limitation of CICC superconducting magnet," *IEEE Trans. Applied Superconduc.* **11**, 1689 (2001).

[6.63] Z.J.J. Stekly, "Behavior of superconducting coil subjected to steady local heating within the windings," *J. Appl. Phys.* **37**, 324 (1966).

[6.64] A.Vl. Gurevich and R.G Mints, "Self-heating in normal metals and superconductors," *Rev. Mod. Phys.* **59**, 117 (1987).

[6.65] Michael J. Superczynski, "Heat pulses required to quench a potted superconducting magnet," *IEEE Trans. Magn.* **MAG-15**, 325 (1979).

Chapter 7
AC and Other Losses

7.1 Introduction

Although the perfect conductivity of superconductors is what makes superconductivity perpetually fascinating for scientists and enticing to engineers and entrepreneurs, Type II superconductors, suitable for magnets, operate in the *mixed* state and, as seen in ***Chapter 5***, are magnetically hysteretic. They are *intrinsically dissipative* under time-varying conditions of magnetic field, transport current, or both. Furthermore, when a Type II superconductor is processed into a composite conductor in the form of multifilaments embedded in a normal metal matrix, other magnetic losses besides hysteresis come into play. These magnetic losses are commonly known as AC losses. In addition, the magnet is subjected to other dissipations, the sources of which include: 1) conductor splices; 2) Lorentz-force induced conductor, and even winding, motion, which results in frictional heating; and 3) Lorentz-force induced cracking in the winding impregnants, which also results in dissipation. Although not discussed here, there is another source of dissipation in fusion magnets: neutron radiation.

The dissipation power density, expressed by g_d in Eq. 6.1 of ***Chapter 6***, lumps all these chiefly non-Joule heating dissipation densities. Generally, its size is miniscule compared with the Joule dissipation density, $\rho_{cd}(T)J^2_{cd_\circ}(t)$ of Eq. 6.1. Despite its small magnitude, it can play a critical role in *adiabatic* superconducting magnets, particularly LTS, because the steady-state dissipation base line for LTS magnets is zero or nearly so. As seen in ***Chapter 6***, an adiabatic *HTS* magnet, on the other hand, can remain "superconducting" despite a large dissipation density within its winding—as much as $\sim 400\,\mathrm{kW/m^3}$ in an illustrative case, though at a great cryogenic load. For comparison, the dissipation density base line for water-cooled magnets can be tens of $\mathrm{GW/m^3}$; dissipations other than Joule heating are completely negligible.

In ***Chapter 7*** we discuss and study three types of the disturbance term g_d: 1) magnetic (AC losses); 2) electrical (splice resistance); and 3) mechanical (frictional and epoxy cracking). For LTS magnets AC losses have proven devastating: only LTS magnets having windings "locally" cooled with liquid helium—*cryostable*—can tolerate AC losses, limiting their applications (e.g., "research" and fusion) and essentially excluding commercially relevant applications, where, for efficiency, "adiabatic" windings are preferred. Only those in which AC losses may be reduced at will (i.e., for "DC" applications, e.g., NMR and MRI), are adiabatic LTS magnets usable and applied successfully. With AC losses controllable and remedies against mechanical disturbances in place, *most* adiabatic *LTS* NMR/MRI magnets nowadays operate successfully *most* of the time. Remarkably, as noted on the disturbance spectra of Fig. 6.1, there are no major "intractable" disturbances, *except* AC losses, in *HTS* magnets. ***Chapter 7*** thus focuses chiefly on AC losses; splice dissipation and mechanical disturbances are treated as "other losses."

Y. Iwasa, *Case Studies in Superconducting Magnets: Design and Operational Issues*,
DOI: 10.1007/b112047_7,

7.2 AC Losses

Following the basic philosophy of this book, only those cases amenable to analytical expressions with which to compute *ballpark* figures of AC losses are considered; i.e., only a few "simple" cases are presented and studied. Thus a complex "real-world" case may have to be either simplified to an analytically solvable model—a recommended approach for *every* problem—or computed head-on with a code at the outset, an unattractive and much less revealing approach.

Three distinguishable AC loss energy densities $[\mathrm{J/m^3}]$ in a multifilamentary composite conductor or strand are: 1) hysteresis, e_{hy}; 2) coupling, e_{cp}; and 3) eddy-current, e_{ed}. AC losses in the conductor are generated by a magnetic field and/or transport current, with one or both varying in time; here only selected field-current excitations are considered. Subjected to one of these field-current excitations, AC losses in the conductor generally depend on 1) the conductor cross-section shape—considered here are "Bean" slab, cylinder, tape—and 2) the magnetic field direction with respect to the conductor axis—either longitudinal, parallel to the broad face (if any), or perpendicular to it.

AC losses within a magnet winding add to the system cryogenic load and, because an HTS magnet can operate at temperatures much higher than 4.2 K, it can tolerate "some" AC losses. Still, for any "AC" superconducting magnet to compete with a room-temperature magnet, its total AC losses *multiplied by* the ratio of compressor power input to heat load at operating temperature (W_{cp}/Q) must be less than those of a room-temperature counterpart. Note that, as shown in Fig. 4.5, the range of W_{cp}/Q is 250–8000 at 4.2 K and 10–50 at 77 K. These ratios alone make the task of enabling an AC superconducting magnet to succeed in the marketplace daunting.

Work on AC losses for Type II superconductors as applied to magnets started in the late 1960s and has continued to date. The bases for the work were established in the 1970s and early 1980s [1.27, 7.1–7.16]. More recent articles are cited where appropriate, including those on HTS.

Superconductor Orientations Relative to External Field

As stated above, superconductor cross sections considered for computation of AC losses are: Bean slab; circle (as in round wire); and rectangle (represented often by tape). Figure 7.1 shows these conductors exposed to a *spatially uniform* time-varying magnetic field, $H_e(t)$, vector: a) Bean slab of width $2a$; b) and c) wire of diameter d_f; d) and e) tape of width w and thickness δ. Note that the external field $H_e(t)$ may be in any of three directions with respect to the wire or tape orientation: longitudinal, $H_{e\|}(t)$ for wire; parallel, $H_{e/\!/}(t)$, for tape; and perpendicular, $H_{e\perp}(t)$, for wire and tape. For Bi2223 and YBCO conductors, available only in tape, AC losses are a serious issue.

In each superconductor, transport current flows along the superconductor axis. The transport current is limited to the superconductor critical current, I_c, where for the Bean slab I_c [A/m] is per unit slab length along the field direction—note that the Bean slab is infinite in the field direction (y-axis) and in the current direction (z-axis), with the width ($2a$) in the x direction.

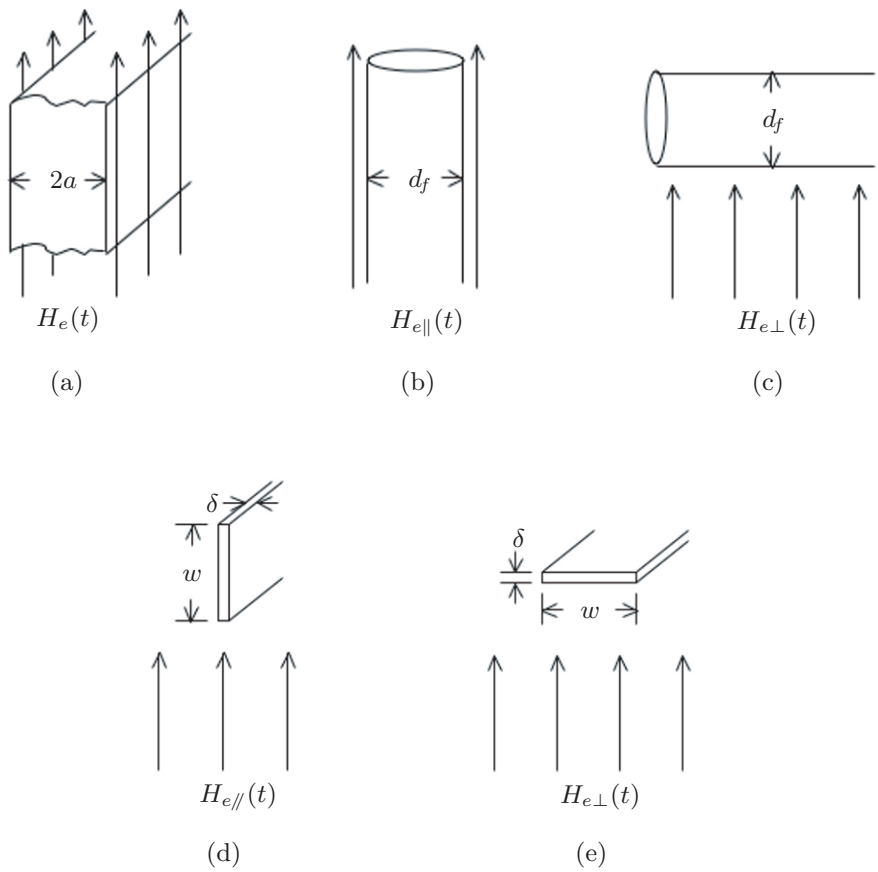

Fig. 7.1 Superconductors exposed to a spatially uniform, time-varying magnetic field, $H_e(t)$, directed as indicated by the arrowed lines. a) Bean slab of width $2a$; b) and c) circular wire of diameter d_f; d) and e) tape of width w and thickness δ.

Time-Varying Magnetic Field

For computation of AC losses we may, most of the time, characterize a time function of magnetic field (and transport current) by its maximum extent or amplitude, H_m for field and I_m for current, and its frequency f or period τ_m—if more than one frequency is involved, f is assigned its dominant frequency. AC losses in "real-world" situations are so complex that even with a code it is virtually impossible to accurately simulate the problem and thus expect a high-degree of accuracy in AC loss computation. Characterizing most time-functions with a single frequency or period is thus quite adequate, certainly for a *ballpark* estimate.

Tables for Energy Densities of AC Losses

The closed-form analytic expressions of AC loss energy densities are summarized in Tables 7.3–7.9 (pages 439–443), presented in **Problems & *Discussions*** which follow this introductory section. The expressions are valid only for the superconductor configurations and field directions shown in Fig. 7.1; those corresponding to a Bean slab (Fig. 7.1a) are derived in this chapter.

7.2.1 Hysteresis Loss

As noted in ***CHAPTER 2***, dissipation within a volume may be treated as the flow of Poynting vector $\vec{S}$ (Eq. 2.20). In integral form, neglecting the electric energy term, Eq. 2.20 may be expressed by:

$$\int \left[-\int_{\mathcal{S}} \vec{E} \times \vec{H} \cdot d\vec{\mathcal{A}} \right] dt = \int_{\mathcal{V}} \left[\int \vec{E} \cdot \vec{J}\, dt + \tfrac{1}{2}\mu_\circ H^2 + \mu_\circ \int \vec{H} \cdot d\vec{M} \right] d\mathcal{V} \qquad (7.1)$$

Although the definition $\vec{B} = \mu_\circ(\vec{H} + \vec{M})$ is used by Bean in his purely *phenomenological* ("critical-state") model of the magnetic behavior of Type II superconductors, as discussed in ***CHAPTER 5***, B is *computed* as the "average" magnetic induction, B_s (Eq. 5.4*a*), based on the *magnetic field* distribution within the superconductor, $H_s(x)$, i.e., $B_s(x) = \mu_\circ H_s(x)$. Because the Bean slab is finite in only one dimension (x), $H_s(x)$ and the supercurrent density induced in the slab, J_c, field-independent in the Bean model, varies only in the x direction. J_c is established by the $\vec{E}$ field, which in turn is induced by $d\vec{B}(t)/dt$, which, for the Bean slab, is equal to $\mu_\circ d\vec{H}_e(t)/dt$, the time rate of change of the uniform external magnetic field.

Hysteresis Loss for Bean Slab

Therefore, in the Bean critical state model for Type II superconductors $\vec{M}$ is really represented by $\vec{H}_s(x)$, which in turn is represented by $\vec{J}_c$. Accordingly, Eq. 7.1 for a Bean slab of width $2a$ is modified:

$$\int \left[-\int_{\mathcal{S}} \vec{E}(x) \times \vec{H}_e \cdot d\vec{\mathcal{A}} \right] dt = \int_0^{2a} \left[\int \vec{E}(x) \cdot \vec{J}_c(x)\, dt + \tfrac{1}{2}\mu_\circ H_s^2(x) \right] dx \qquad (7.2)$$

where the integration is performed from $x = 0$ to $x = 2a$ (or from $x = -a$ to $x = a$). Because $\vec{J}_c(x)$ is induced by $\vec{E}(x)$, it is parallel to the E field. The $\int \vec{E}(x) \cdot \vec{J}_c(x)\, dt$ term in Eq. 7.2 represents dissipation, and this dissipation is known as hysteresis loss. Hysteresis loss energy density, e_{hy} [W/m^3], for the Bean slab is given by:

$$e_{hy} = \frac{1}{2a} \int_0^{2a} \left[\int J_c E(x)\, dt \right] dx \qquad (7.3a)$$

By combining Eqs. 7.2 and 7.3*a*, we have another expression for e_{hy}:

$$e_{hy} = \frac{1}{2a} \left\{ \int \left[-\int_{\mathcal{S}} \vec{E}(x) \times \vec{H}_e \cdot d\vec{\mathcal{A}} \right] dt - \tfrac{1}{2}\mu_\circ \int_0^{2a} H_s^2(x)\, dx \right\} \qquad (7.3b)$$

Equation 7.3*b* states that the hysteresis energy density in the slab is equal to the total energy density supplied by the Poynting energy density to the slab minus the magnetic energy density in the slab.

When the external field $\vec{H}_e$ makes one complete cycle in which the initial and final fields, respectively, $\vec{H}_{e_i}$ and $\vec{H}_{e_f}$ *as well as* magnetizations, $\vec{M}(\vec{H}_{e_i})$ and $\vec{M}(\vec{H}_{e_f})$, are identical, e_{hy} may also be given by:

$$e_{hy} = \mu_\circ \oint \vec{H}_e \, d\vec{M}_e(\vec{H}_e) \tag{7.4a}$$

Equation 7.4*a* may be algebraically given by:

$$e_{hy} = -\mu_\circ \oint M(H_e) \, dH_e \tag{7.4b}$$

In Eq. 7.4*b*, the vector symbols are dropped because each vector parameter points in only one direction: H_e and M in the y direction.

Bean Slab under External Field Time Sequences

In **Problems 7.1–7.4** and ***Discussions 7.1–7.2***, hysteresis energy densities are studied for a Bean slab subjected to an external magnetic field, $H_e(t)$, of different time sequences (Cases). Cases 1–6 and Cases 1*i*–6*i*, respectively, in the absence and presence of DC transport current in the slab, are identified in Eq. 7.5 below.

$$H_e(t) = \overbrace{\underbrace{\overbrace{0^*(\text{Virgin slab}) \rightarrow \underbrace{H_m}_{\text{CASES 1 (AND 1}i\text{)}} \rightarrow 0}^{\text{CASES 2 (AND 2}i\text{)}} \rightarrow -H_m \rightarrow \overbrace{0 \rightarrow \underbrace{H_m}_{\text{CASES 4 (AND 4}i\text{)}} \rightarrow 0}^{\text{CASES 5 (AND 5}i\text{)}} \rightarrow -H_m \rightarrow 0}_{\text{CASES 3 (AND 3}i\text{)}}}^{\text{CASES 6 (AND 6}i\text{)}} \tag{7.5}$$

Each time sequence of $H_e(t)$ of Eq. 7.5 is briefly described below.

Case 1	$H_e(t)$ is increased from 0^* to H_m, where 0^* denotes the slab is virgin, i.e., no supercurrent density, J_c, in the slab.
Case 2	This is a field-decreasing sequence that follows Case 1: $H_e(t) = H_m \rightarrow 0$.
Case 3	This is a combination of Cases 1 and 2: $H_e(t) = 0^* \rightarrow H_m \rightarrow 0$.
Case 4	Similar to Case 1, but the slab is no longer virgin.
Case 5	Similar to Case 2, but it follows Case 4: $H_e(t) = H_m \rightarrow 0$.
Case 6	Starting with a non-virgin slab, $H_e(t)$ makes one complete cycle.
Cases 1*i*–6*i*	Each of these, in the presence of DC transport current, is identical to the zero-current counterpart described above.

$H_s(x)$ plots for Cases 1, 2, and 4 are shown, respectively, in Figs. 7.2–7.4. In the absence of transport current the magnetic behavior of a slab (of width $2a$) is symmetric about its midpoint ($x = a$); therefore, $H_s(x)$ plots are shown only for ($0 \leq x \leq a$). $H_s(t)$ plots for selected Cases 1*i*–6*i* are shown later.

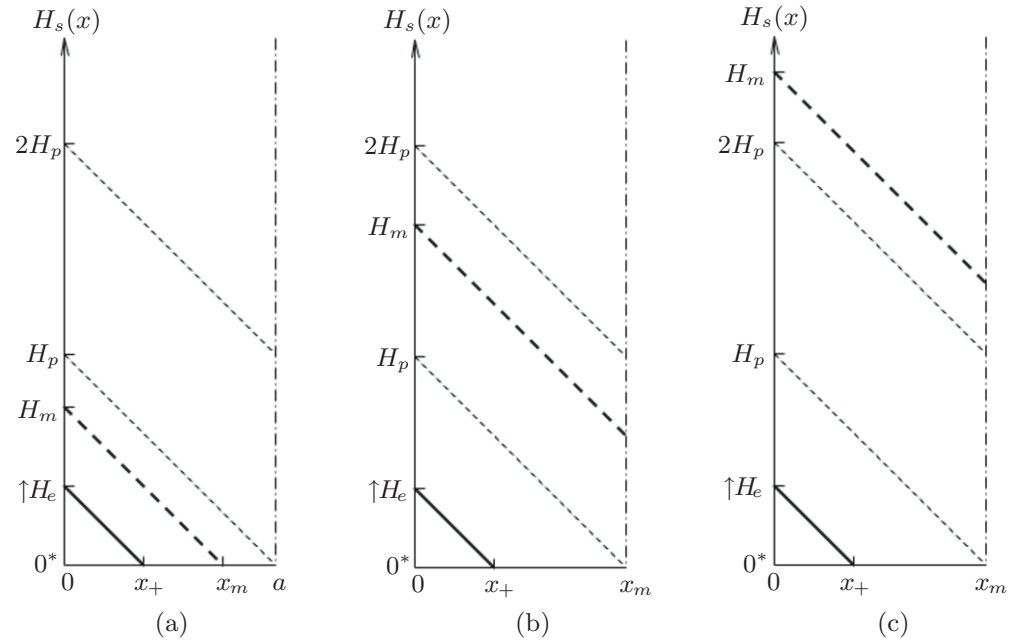

Fig. 7.2 Field profiles for Case 1, $H_e = 0^* \to H_m$, at $0^* < H_e < H_m$ (solid lines) and at H_m (heavy dashes): (a) "small" field ($H_m \le H_p$); (b) "medium" ($H_p \le H_m \le 2H_p$); and (c) "large" ($H_m \ge 2H_p$). $\uparrow H_e$ indicates that H_e is increasing. In each graph, $x_+ = H_e/J_c$ and $x_m = H_m/J_c$, which becomes $x_m = a$ for (b) and (c).

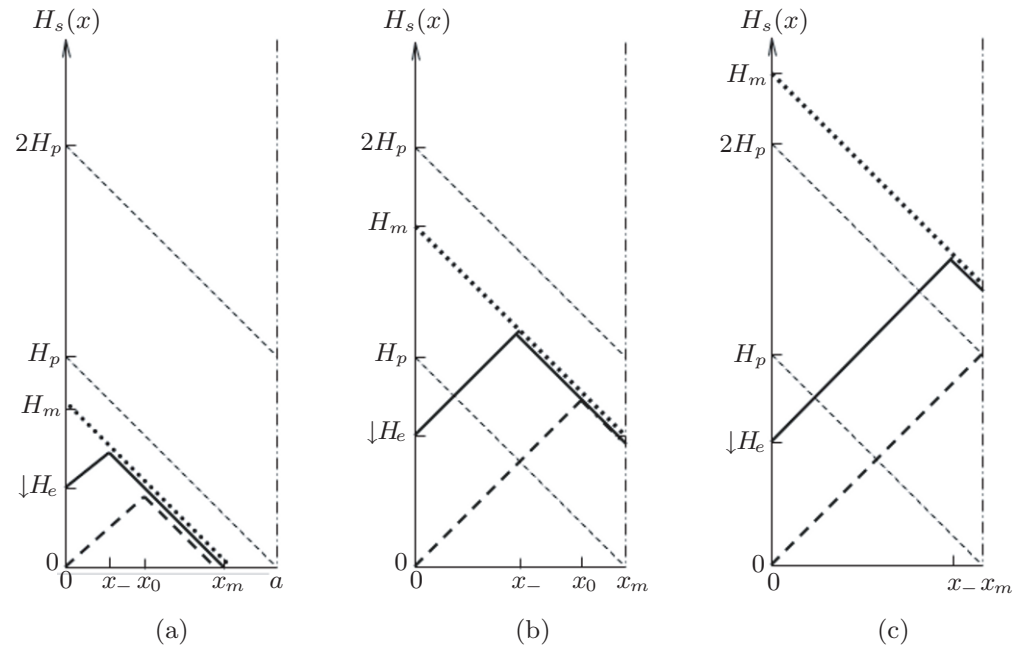

Fig. 7.3 Field profiles for Case 2, $H_e = H_m \to 0$: $\downarrow H_e$ (the arrow indicating H_e is decreasing) between H_m and 0 (solid lines) and when H_e returns to 0 (heavy dashes). (a) "small" field ($H_m \le H_p$); (b) "medium" ($H_p \le H_m \le 2H_p$); and (c) "large" ($H_m \ge 2H_p$). In each graph, the heavy dotted line represents the field profile at H_m, the start of Case 2; $x_- = (H_m - H_e)/2J_c$; and $x_0 = H_m/2J_c$, which becomes $x_0 = x_m = a$ for (c).

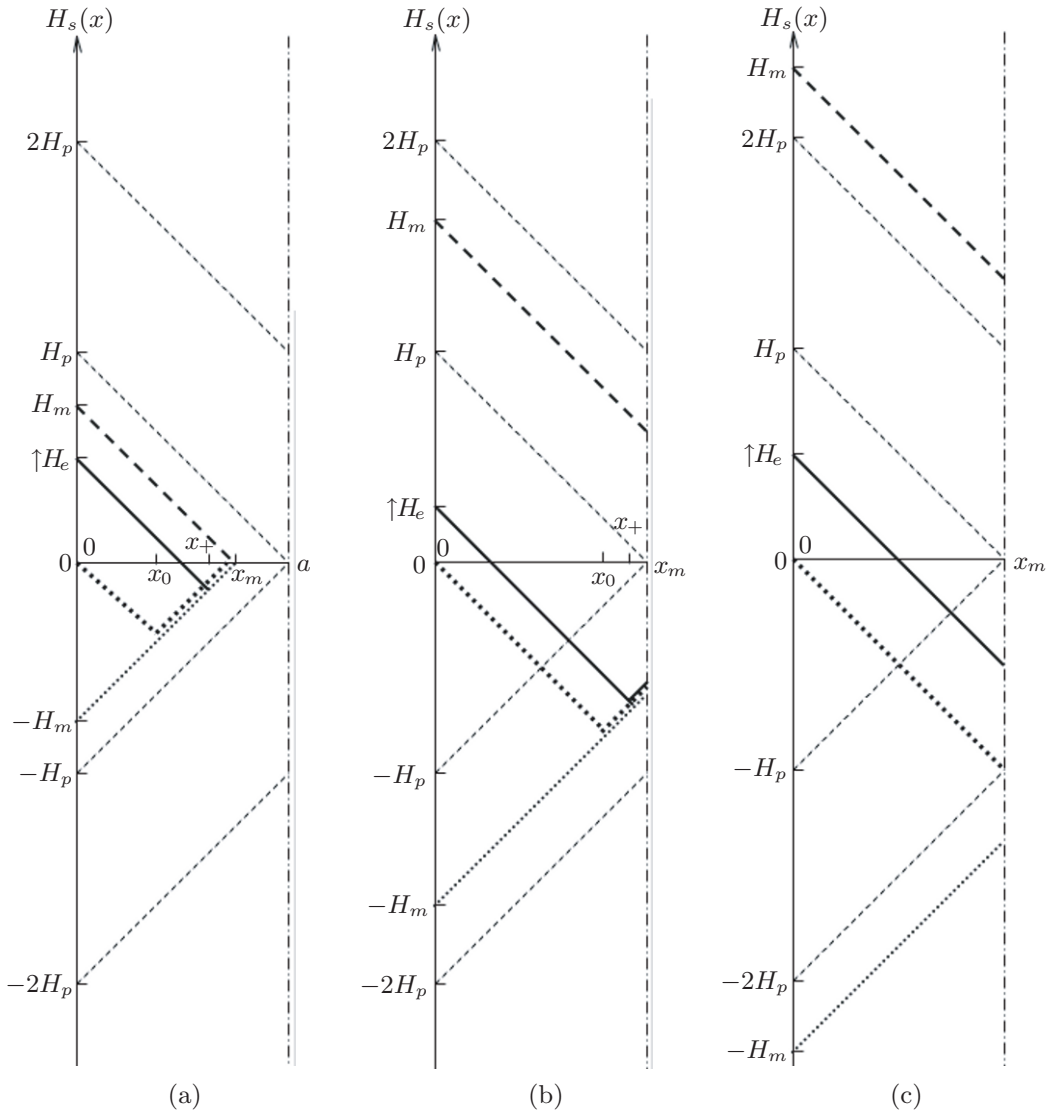

Fig. 7.4 Field profiles for Case 4, in each graph, starting at $H_e = 0$ (heavy "square-dots") after H_e returns from $-H_m$; i.e., the slab is no longer virgin at the start of Case 4: $\uparrow H_e$ (the arrow indicates H_e is increasing) between 0 and H_m (solid lines) and at $H_e = H_m$ (heavy dashes). (a) "small" field ($H_m \le H_p$); (b) "medium" ($H_p \le H_m \le 2H_p$); and (c) "large" ($H_m \ge 2H_p$). Note that $x_0 = H_m/2J_c$, $x_+ = (H_m + H_e)/2J_c$, and $x_m = a$ for (b) and $x_m = x_0 = x_+ = a$ for (c).

Trivia 7.1 List the items below in descending order of energy.

i) Caloric, of a grain of granulated sugar;

ii) Kinetic, of a snail crawling at a speed of 0.01 mph (mile per hour);

iii) Minimum quenching, in a high-performance LTS magnet at 4.2 K;

iv) Potential, of a flea atop the Empire State Building.

7.2.2 Coupling Loss in Multifilamentary Composite

Coupling loss is another form of Joule heat dissipation within a multifilamentary composite. It results from the inter-filament (coupled) current induced in the multifilamentary composite exposed to a time-varying magnetic field. Because the coupling current flows through the resistive matrix metal, it decays with time which, for the sake of simplicity, is characterized generally by an exponential with a single "coupling" time constant, τ_{cp}. Clearly, the larger the τ_{cp}, the longer the coupling current flows through the matrix metal, and thus the greater will be e_{cp}, coupling energy loss density. τ_{cp} is the ratio of the inductance L and resistance R of the coupling current path; L/R decreases with increasing tightness of "twist pitch" length, ℓ_p, of a multifilamentary composite and decreases with increasing matrix metal resistivity. Figure 7.5 shows a schematic drawing of a two-filament composite. The complex geometry of a multifilamentary conductor, with "transposed" filaments as one source of complications, makes analysis based on the Bean slab model nearly impossible.

Coupling Time Constant

The key parameter for e_{cp} is the coupling time constant, τ_{cp}. It defines the decay time constant of inter-filament (coupled) currents induced in the multifilamentary composite when it is exposed to a time-varying magnetic field. In reality, the current decay function contains many time constants, not just the dominant one. Experimentally, however, only the dominant term can be determined, and it is used in most of the "phenomenological" approaches. τ_{cp} is given by:

$$\tau_{cp} = \frac{\mu_\circ \ell_p^2}{8\pi^2 \rho_{ef}} \tag{7.6}$$

where ℓ_p is the "twist pitch" length of filaments and ρ_{ef} is the effective matrix resistivity for inter-filament currents. Because, as stated above, the longer the coupled currents last, the greater the energy dissipated, the greater τ_{cp} is, the greater will be e_{cp}. As Wilson points out [1.27], e_{cp} may be viewed as a *fraction* of the total magnetic field energy density in the composite, $\mu_\circ H_m^2/2$, and as $\tau_{cp} \to 0$, $e_{cp} \to 0$. As stated above, useful formulas for e_{cp} are presented later in Table 7.8; it includes formulas of e_{cp} for multifilamentary wire under four time functions of external magnetic field: 1) sinusoidal; 2) exponential; 3) triangular; and 4) trapezoidal. Key time parameters for these functions are defined in Fig. 7.18.

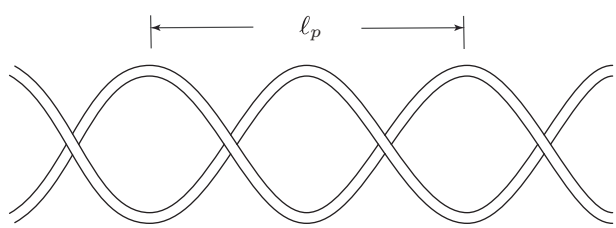

Fig. 7.5 Two-filament model of a multifilamentary composite, defining twist pitch length ℓ_p used in Eq. 7.6.

Effective Matrix Resistivity

We shall briefly discuss the resistivity, ρ_{ef}, appearing in Eq. 7.6. It represents the matrix's effective resistivity for the flow of current *perpendicular* to the axis of filamentary conductors. Two models have been proposed by Carr for ρ_{ef} [7.18]:

$$\rho_{ef_0} = \frac{1-\lambda_f}{1+\lambda_f}\rho_m \tag{7.7a}$$

$$\rho_{ef_\infty} = \frac{1+\lambda_f}{1-\lambda_f}\rho_m \tag{7.7b}$$

where λ_f is the volumetric fraction of the superconducting filaments in the composite superconductors and ρ_m is the matrix resistivity.

Equations 7.7*a* and 7.7*b* are based on the two limiting current distributions shown in Fig. 7.6: in (a) the contact resistance at the filament surface is *zero* and current is drawn into the filaments as shown schematically, making the "apparent" cross section and distance for the passage of current, respectively, large and small, and hence Eq. 7.7*a*; in (b) the opposite is true and Eq. 7.7*b*. Neither expression has been tested rigorously, analytically or experimentally. In practice, Eqs. 7.7*a* and 7.7*b* are applied to composite superconductors, respectively, of Nb_3Sn and NbTi.

7.2.3 Eddy-Current Loss

The basics of eddy-current loss have been discussed in **PROBLEM 2.7**. The formulas for its energy density, e_{ed}, in the "low" frequency limit, for wire (Figs. 7.1b and 7.1c) and tape (Figs. 7.1d and 7.1e) are summarized in Table 7.9.

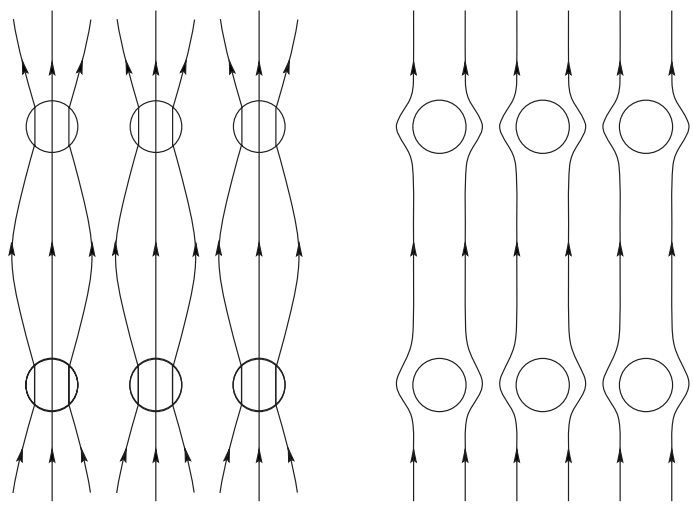

Fig. 7.6 Current distributions in a multifilamentary composite conductor *perpendicular* to the conductor axis. (a) Contact resistance between filament and matrix is zero—Eq. 7.7*a*; (b) Contact resistance is infinite—Eq. 7.7*b*.

7.3 Other Losses

There are two other sources of dissipation: 1) splice—or joint—resistance; and 2) mechanical disturbances. For "dry" magnets in driven mode, LTS and HTS, dissipation generated at resistive joints, for obvious reasons, must be minimized—it directly adds to the thermal load on the cryocooler. Clearly, it is not an issue for persistent-mode magnets in which each splice resistance is virtually zero, i.e., in the order of pico-ohms. Mechanical disturbances—those occurring within the winding in the form of conductor motion or epoxy cracking in epoxy-impregnated windings—are important only for "adiabatic" LTS magnets; for well-cooled LTS magnets in which the biggest dissipation is Joule heating of the composite superconductor itself, mechanical disturbances may be ignored entirely. For a different reason, as stated in ***CHAPTER 6***, HTS magnets, well-cooled or "adiabatic," are immune from these mechanical disturbances.

7.3.1 Splice Resistance

A resistive splice becomes a design issue only when: 1) it must be confined within a restricted space or conform to a specific configuration; 2) it is located deep inside the winding where there is limited or zero "local" cooling; 3) it must withstand large forces; 4) there are so many of them that the cumulative dissipation can tax the system's refrigeration capacity. 5) it is not in direct contact with coolant, such as in cryocooler-cooled magnets.

There are basically two types of joint, lap and butt. For most applications, a lap joint is better than a butt joint for three reasons: 1) it is easier to make than a butt joint; 2) splice resistance may be arbitrarily reduced by simply increasing the lap length; and 3) it is generally easier than a butt joint to meet strength requirements. Here, we discuss the lap splice.

Lap Splice (Joint)

A "hand-shake" lap splice, shown in Fig. 7.7, is the most widely used splice design; it is also quite suitable even for use within the winding. The splice between Conductor A and Conductor B is electrically joined by a solder layer of overlap length ℓ_{sp}, width a, and thickness δ_{sd}. The solder layer resistance, R_{sd}, with solder resistivity of ρ_{sd} is given by:

$$R_{sd} = \frac{\rho_{sd}\delta_{sd}}{a\ell_{sp}} \tag{7.8}$$

Generally, a is equal to the width of the conductors being spliced.

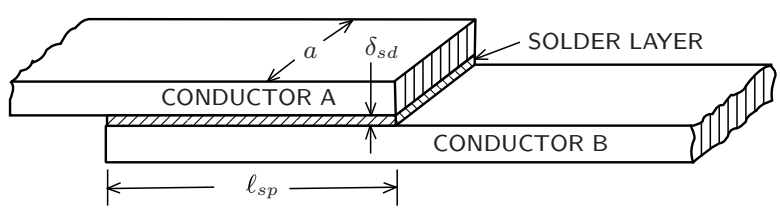

Fig. 7.7 Sketch of a typical "hand-shake" lap splice of a solder layer of length ℓ_{sp}, width a, and thickness δ_{sd}

Contact Resistance

The splice resistance, R_{sp}, is the sum of three components:

$$R_{sp} = R_{cA} + R_{sd} + R_{cB} \tag{7.9a}$$

$$= \frac{R_{ct}}{A_{ct}} \tag{7.9b}$$

where R_{cA} is the contact resistance between Conductor A and the solder layer and R_{cB} is that between Conductor B and the solder layer. R_{ct} is the contact resistance in the unit of $[\Omega\,\mathrm{m}^2]$, and $A_{ct} = a\ell_{sp}$ is the contact area. If the solder "wets" the surface of each conductor, it is reasonable to assume $R_{cA} \simeq R_{cB} \simeq 0$ or at least $R_{cA} \simeq R_{cB} \ll R_{sd}$:

$$R_{sp} = \frac{R_{ct}}{A_{ct}} \simeq R_{sd} \tag{7.9c}$$

Note that R_{sp} can be made arbitrarily small by making ℓ_{sp} sufficiently long. Combining Eqs. 7.8 and 7.9*c*, we obtain:

$$R_{ct} \simeq \rho_{sd}\delta_{sd} \tag{7.10}$$

Thus, we may achieve "small" R_{ct} by selecting a low-resistivity solder and, equally important, by minimizing δ_{sd}, certainly no thicker than 10–50 μm. Indeed, if a "superconducting" solder is used, R_{ct} becomes zero, provided such a splice is placed in a low field region and enough area ($a\ell_{sp}$) provided for current passage. With a superconducting solder, it is possible to create an essentially superconducting joint with a resistance in the range of pico-ohms. Such a joint must be in a very low-field ($\leq$1 T) and cold ($\leq$9 K) environment, with the contact area large enough to keep the solder superconducting as the joint carries the operating current.

Table 7.1 presents values of R_{ct} for selected tin-lead solders. R_{ct} is magnetic field-dependent, increasing linearly with B. In some data, a nonlinearity is observed between zero and 1 T. These data are presented only as a general guide. In projects involving large magnets and where splice resistance is an important design issue, it is prudent to rely on actual measurements.

Table 7.1: Solder Contact Resistances at 4.2 K

Solder	R_{ct} [pΩ m^2]			
	0 T	1 T	2 T	9 T
60Sn-40Pb	3.0*	3.3*	3.6*	5.5*
(2nd set of data)	1.1*	1.6*	2.0*	5.3*
50Sn-50Pb]	0.8	1.5*	1.7*	2.9*
(2nd set of data)	1.8	3.3*	3.7*	6.8*
50Sn-50Pb [7.19]	$\rho_{sd} = 5.90(1 + 0.0081B)$ nΩ m (B in [T])			
60Sn-40Pb [7.19]	$\rho_{sd} = 5.40(1 + 0.0089B)$			
USW† [7.20]	0.45 ($B = 0$ T)			
60Sn-40Pb‡	$R_{sd}(B)/R_{sd}(0) = 1 + 0.57B$ (B in [T])			

* Linear with B in this range.
† Between two scarfed copper surfaces ultrasonically welded.
‡ Splice resistance between two CIC conductors.

Table 7.2: Electrical Resistivities of Solder Alloys at Selected Temperatures [7.21]

Solder Alloy				Resistivity [nΩ m] (Cu: 18 nΩ m @293 K)							
	T_{sl} [℃]	T_{lq} [℃]	T_c [K]	4.2 K	10 K	20 K	50 K	77 K	100 K	200 K	293 K
100In	157	157	3.41	0.3	0.3	1.6	9.3	17	23	54	87
50In-50Pb	184	210	6.35	0	162	164	175	187	196	236	290
52In-48Sn	118	118	≈7.5	0	62	63	71	79	87	123	169
63Sn-37Pb	183	183	≈7	0	4.0	6.5	24	36	48	105	162
60Sn-40Pb	183	191	≈7.1	0	2.8	4.5	18	33	44	99	152
50Sn-50Pb	183	212	≈7.1	0	8.3	11	26	42	54	112	169
40Sn-60Pb	183	238	≈7.1	0	9.5	13	27	44	57	118	177

Table 7.2 presents zero-field electrical resistivity vs. temperature data, by Fujishiro [7.21], of indium (In) and six "common" solder alloys of In, lead (Pb), and tin (Sn), listed in the table, where T_{sl} and T_{lq} are, respectively, solidus and liquidus temperatures. (The smaller the differences in these temperatures, the easier the soldering; when $T_{sl}=T_{lq}$, an alloy has a well-defined melting point.) As indicated in the table, these common solder alloys are superconducting above 4.2 K; T_c is the zero-field critical temperature [4.41, 4.42, 7.20].

Mechanical-Contact Switch

For some applications it is advantageous to use a mechanical-contact switch rather than a heater-activated persistent-current switch (PCS). Resistances of mechanical contacts between copper or indium-coated copper surfaces, though small, are not superconducting even at 4.2 K [7.22]. Recently, mechanical contacts between HTS bulk disks operating at 77 K have been explored by Sawa and others to build mechanical-contact switches [7.23, 7.24]. Although obviously not superconducting at 77 K, if operated below ∼10 K and with HTS bulk disks coated with a *superconducting* solder, it may be possible to achieve a *superconducting* disk-to-disk contact for a *superconducting* mechanical-contact switch.

7.3.2 Mechanical Disturbances

Until the mid 1970s, most magnets (all LTS, of course) were built according to the Stekly stability criterion, i.e., well-(and locally-)cooled and thus low-λJ_{op} magnets, and therefore mechanical disturbances were not a great concern—the windings were designed to deal with the much greater Joule dissipation. Only when it became necessary to make magnets operate at high λJ_{op} ($\geq 100\,\mathrm{A/mm^2}$), in dipole and quadrupole magnets of high-energy physics particle accelerators and "commercially viable" NMR and MRI magnets—did mechanical disturbances become a critical design issue. One obvious way to enhance λJ_{op} is to abolish the space occupied by coolant and replace it with field-generating conductor or load-bearing material—the birth of *adiabatic* LTS magnets. These magnets are susceptible to quench with a minuscule level of g_d. Through the use of an acoustic emission (AE) technique described below, it was established by the mid 1980s that a mechanical disturbance event, primarily either conductor motion or fracture of the impregnated filling material, was responsible for virtually every incident of "premature quench" in these adiabatic LTS magnets.

The absence of cooling makes adiabatic magnets prone to quench prematurely, sometimes at currents well below their intended operating currents. Fortunately, these mechanical events usually obey what is known in acoustic emission as the "Kaiser effect." It describes mechanical behavior observed during a sequence of cyclic loading in which mechanical disturbances such as conductor motion and epoxy fracture appear only when the loading responsible for events exceeds the maximum level achieved in any previous loading sequence. Thus an adiabatic magnet suffering premature quenches generally "trains" and improves its performance progressively to the point where it may finally reach its intended operating current. Obviously, the goal in designing an adiabatic magnet is to make it reach the operating current on the first try; such a remarkable feat is achieved *occasionally*, e.g., a 750-MHz (17.6 T) NMR magnet [7.25].

Remedies against these mechanical disturbances have been introduced since the mid 1980s and nowadays, as remarked at the outset, *most* adiabatic LTS magnets now escape these menacing episodes *most* of the time. Conductor motion and fracture of the filler material, and remedies against these mechanical disturbances, are briefly described below.

Conductor Motion and Remedy

Even if the conductor is wound "tightly" in a perfectly ordered arrangement, e.g., close-packed hexagonal, the winding would still be sufficiently loose for the conductor to move against a frictional force under the action of Lorentz forces. We may estimate the extent of the frictional displacement needed to adiabatically drive a unit conductor volume normal in a typical operating condition and show that this displacement is indeed likely. For example, a conductor at $r = 0.2\,\mathrm{m}$, exposed to a z-directed field, B_z, of 5 T and carrying a current density (over conductor cross section) in the θ direction of $J_\theta = 200 \times 10^6\,\mathrm{A/m^2}$, experiences an r-directed Lorentz force density $f_{L_r} = J_\theta B_z$ of $2 \times 10^8\,\mathrm{N/m^3}$. Suppose that the conductor slides against the frictional force opposing this f_{L_r} by a distance Δr_f; a frictional energy density, e_f, of this motion over a unit conductor volume may be given by:

$$e_f = \mu_f f_{L_r} \Delta r_f \tag{7.11}$$

where μ_f is the frictional coefficient. Inserting values of $\mu_f = 0.3$ and $e_f = 1300\,\mathrm{J/m^3}$, which is copper's enthalpy difference between 4.2 K and 5.2 K, and $f_{L_r} = 2 \times 10^8\,\mathrm{N/m^3}$, and solving Eq. 7.11 for Δr_f, we find:

$$\Delta r_f = \frac{e_f}{\mu_f f_{L_r}} = \frac{(1300\,\mathrm{J/m^3})}{(0.3)(2 \times 10^8\,\mathrm{N/m^3})} \simeq 20 \times 10^{-6}\,\mathrm{m} = 20\,\mu\mathrm{m}$$

Sliding of such a small distance is nearly impossible to avoid even in tight, orderly-packed windings. Slips as small as $\sim 10\,\mu$m are sufficient to trigger a quench, as observed in a series of experiments [7.26–7.31].

A remedy to eliminate these microslips is impregnation of the winding with an insulating material, which is usually fluid when filling up the void space but later becomes solid. The impregnation transforms the entire winding into a monolithic structural element. Today, virtually every adiabatic LTS magnet is impregnated with a filling material, ranging from paraffin wax to epoxy, some mixed with fine powder to "strengthen" it and/or improve its thermal conductivity.

Fracture of Filler Material and Remedy

Although conductor motion may be absent in the impregnated windings, two problems still remain. First, by the action of Lorentz forces, the entire winding body—in solenoidal magnets—tries to become barrel-shaped. Unless the winding is firmly anchored to the coil form to prevent this barrel-shaped deformation, interface motion occurs between the winding and the coil form; this motion generates heating, which may result in a premature quench. It is possible to decouple the conductor from such frictional heating by means of a low-thermal-conductivity sheet bonded to the inner surface of the winding [7.32]. Second, if the winding is firmly held to the coil form, high stresses are developed in the winding, and the impregnant may fracture, resulting in another source of thermal disturbance.

In impregnated windings, there are two possible approaches to prevent a premature quench caused by a fracture of the filler material: 1) minimize the amount of energy induced by the fracture; and 2) eliminate fracture incidents altogether. Although there have been attempts to measure fracture-induced energies at cryogenic temperatures [7.33, 7.34], our understanding of the fracture mechanisms is not sufficiently advanced to permit this approach to be useful.

Great progress has been achieved in the second remedy for eliminating the fracture incidents. The techniques developed include: 1) graded pretensioning of the conductor during the winding process [7.35]; and 2) allowing the winding section to "float" in the coil form [7.35, 7.36]. Maeda has pushed to the limit this floating winding concept and achieved successful performance with "coilformless" solenoids [7.37]. Today, most impregnated windings "float" in the coil form, enabling adiabatic LTS operating at 4.2 K or below to achieve their operating currents, perhaps not at the very first try but usually after a few training premature quenches.

Some Consequences of Friction

—Passage from Ernest Rabinowicz's *Friction and Wear of Materials**

In walking, the forward foot comes into contact with the floor surface at a low speed, typically 30 mm/sec. To avoid slipping, the kinetic friction coefficient f_k between foot and floor (measured at a speed of about 30 mm/sec) should be above 0.25... When the kinetic friction coefficient drops below 0.20, people walking at a full stride begin to feel that the floor is slippery. However, because people carry in their brains a built-in warning and servo system based on the nature of the contact between foot and floor, they adjust readily and rapidly on encountering a low friction surface. They slow down and change their stride, and in this way they are able to walk even when the friction coefficient is as low as 0.10 or lower. Most falls occur when people first step onto a low-friction surface (e.g., a highly waxed floor), or when they encounter a low-friction patch on an otherwise high-friction surface (the infamous banana peel). Then slipping occurs before the warning system can be activated.

* John Wiley & Sons, Inc., New York, 1995. For many years until his retirement in 1993, Ernest Rabinowicz (1927–2006) taught mechanical engineering at M.I.T. While still a student in Cambridge University, he once handed back a crystal radio, restored *by his friend*, to the great English physicist Paul Andrien Maurice Dirac (1902-1984), who thanked and commended him, "You're a promising young man."

7.4 Acoustic Emission Technique

7.4.1 Detection of Mechanical Events—LTS Magnets

Generally, time-varying strains create AE signals in a superconducting magnet when it is being stressed (or being unstressed) by magnetic forces. Beginning in the late 1970s [7.38–7.40], it was established in the 1980s that the two principal mechanical events afflicting high-performance *LTS* magnets—conductor motion and epoxy fracture—could be detected by the AE technique [7.41–7.54]. The most effective use of AE for superconducting magnets is the AE/voltage technique first reported by Brechna and Turowski in 1978 [7.40]. Because a sudden conductor motion event generates an AE signal—which travels within the winding at speeds typically 2–5 km/s—and at the same time induces a voltage spike across the magnet terminals, the simultaneous detection of AE and voltage signals at the time of a quench shows that it is induced by conductor motion—a sudden shift in the position of a short length of the conductor in the presence of a magnetic field generates, through Faraday's law, a voltage pulse across the terminals of the winding. The AE technique can also be used to demonstrate that a quench accompanied by an AE signal but *not* by a voltage spike is caused most likely by other mechanical events such as epoxy cracking. Figure 7.8 shows a premature quench of a Nb_3Sn coil; AE signals appearing at the onset of the voltage pulse that precedes the resistive quench voltage strongly suggest that this premature quench was triggered by conductor motion [7.54].

7.4.2 Application to HTS Magnets

Besides magnetic forces, another important source of time-varying strains in a superconducting magnet is a time-varying *nonuniform* temperature distribution. Abundant AE signals are in fact generated as a magnet is cooled down (or warmed up). Indeed, AE signals have been observed in LTS magnets in which time-varying nonuniform temperature distributions are primary sources [7.55, 7.56]. Figure 7.9 presents one oscillogram recorded on a dipole reaching its critical current [7.57]. Because the quench was "natural," no AE signals were triggered at the onset of the quench. However, as registered by SENSOR 1, ∼5 ms after the quench onset,

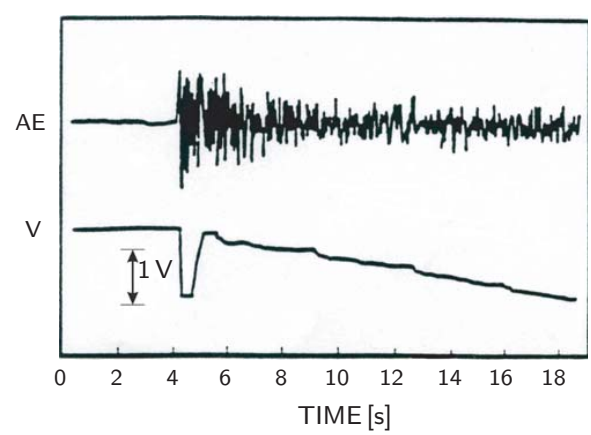

Fig. 7.8 AE and voltage signals from an Nb_3Sn coil prematurely quenching [7.57].

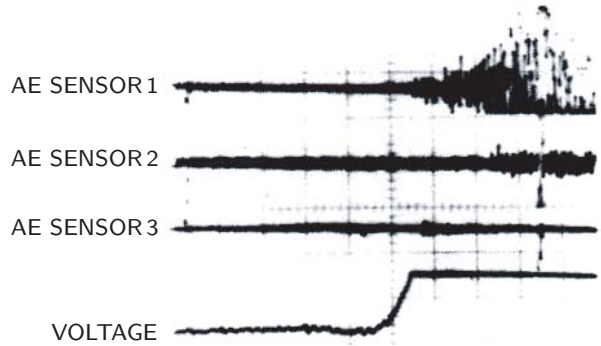

Fig. 7.9 Oscillogram traces of AE signals and voltage from a "natural" quench of a superconducting magnet at its critical current (time scale: 2 ms/div) [7.57].

AE signals appear. It is likely that the signals were caused by a *nonuniform temperature* distribution created by the quench, which, though "naturally" triggered, was localized to the high-field region.

AE signals could become useful complements to voltage signals for detecting the onset of overheating in HTS magnets, particularly as the resistive voltage of HTS, owing chiefly to its low index, does not rise with current as sharply as that of LTS. Woźny and others recorded the AE signals generated by the temperature rise at the superconducting-normal transition in YBCO bulk samples [7.58]; Arai detected heating-induced AE signals in a test pancake coil wound with Bi2223 [7.59]. Further work towards making AE signals complement voltage signals for protection of HTS magnets is in progress [7.60].

"Time, time, what is time?
Swiss manufacture it.
French hoard it.
Italians squander it.
Americans say it is money.
Hindus say it does not exist . . ." —O'Hara

"We can know the time, we can know a time. We can never know Time." —Ada

PROBLEM 7.1: Hysteresis energy density—"Virgin" Bean slab Under "small" field sequences (Cases 1–3)

Consider a "virgin" Bean slab of width $2a$ first subjected to an increasing-field sequence, Case 1 (Eq. 7.5), $H_e = 0^* \rightarrow H_m \leq H_p$ ("small" field), where 0^* denotes that the Bean slab is virgin, and $H_p = J_c a$. It is then subjected to a decreasing-field sequence, Case 2, $H_e = H_m \rightarrow 0$. The field sequence for Case 3 is Case 1 followed by Case 2. $-M(H_e)$ for Case 1 is given by Eq. 5.5 and that for Case 2 by a modified form of Eq. 5.7. Thus:

$$-M(H_e) = H_e - \frac{H_e^2}{2H_p} \qquad (H_e = 0^* \rightarrow H_m \leq H_p) \qquad (5.5)$$

$$-M(H_e) = H_e + \frac{H_e^2 - 2H_m H_e - H_m^2}{4H_p} \qquad (H_e = H_m \rightarrow 0) \qquad (7.12)$$

Figure 7.10 shows $-M(H_e)$ as given by Eqs. 5.5 and 7.12.

a) Applying Eq. 7.3a for one half of the slab $(0 \leq x \leq a)$, show that e_{hy} for Case 1, $H_e = 0^* \rightarrow H_m$, is given by:

$$e_{hy} = \frac{\mu_\circ H_m^3}{6H_p} \qquad (0 \leq H_m \leq H_p) \qquad (7.13a)$$

b) Similarly, applying Eq. 7.3a for one half of the slab $(0 \leq x \leq a)$, show that e_{hy} for Case 2, $H_e = H_m \rightarrow 0$, is given by:

$$e_{hy} = \frac{\mu_\circ H_m^3}{24H_p} \qquad (0 \leq H_m \leq H_p) \qquad (7.14a)$$

c) Using Eq. 7.3b, show that e_{hy} for Case 3, $H_e = 0^* \rightarrow H_m \rightarrow 0$, which is obviously the sum of Eqs. 7.13a and 7.14a, is given by:

$$e_{hy} = \frac{5\mu_\circ H_m^3}{24H_p} \qquad (0 \leq H_m \leq H_p) \qquad (7.15a)$$

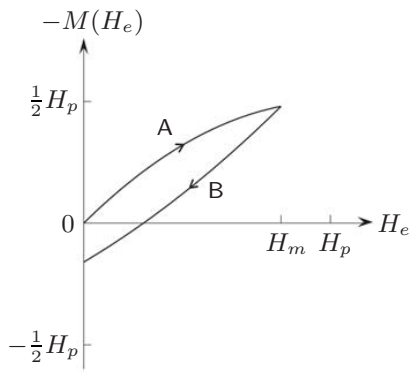

Fig. 7.10 $-M(H_e)$ for "small" field excitation $(H_m \leq H_p)$. Case 1: Trace A; Case 2: Trace B; Case 3: Traces A and B. Sequence A begins at the origin (0,0), with a "virgin" Bean slab.

Solution to PROBLEM 7.1

a) In an increasing-field sequence, $H_e = 0^* \rightarrow H_m$, let us first find an expression for $E_z(x)dt$ when the external field is increasing. $H_s(x)$ within the slab is shown by the solid line in Fig. 7.2a. Within the slab between $x=0$ and $x=x_+(=H_e/J_c)$, $E_z(x)$ due to this field change, dH_e/dt, may be given by:

$$E_z(x) = \mu_\circ \frac{dH_e}{dt}(x_+ - x) \qquad (S1.1a)$$

$$E_z(x)\,dt = \mu_\circ (x_+ - x)\,dH_e \qquad (S1.1b)$$

Applying Eqs. 7.3*a* for the first half of the slab, and $S1.1b$, we have:

$$e_{hy} = \frac{1}{a}\int_0^a \left[\int J_c E(x)\,dt\right] dx \qquad (S1.2a)$$

$$= \frac{\mu_\circ J_c}{a}\int_0^{H_m}\left[\int_0^{x_+}(x_+ - x)\,dx\right] dH_e \qquad (S1.2b)$$

Note that in Eq. $S1.2b$ the order of integration is reversed from that of Eq. $S1.2a$ because x_+ depends on H_e. Equation $S1.2b$ leads to:

$$e_{hy} = \frac{\mu_\circ J_c}{a}\int_0^{H_m}\left(x_+^2 - \frac{x_+^2}{2}\right) dH_e \qquad (S1.2c)$$

$$= \frac{\mu_\circ J_c}{a}\int_0^{H_m}\frac{H_e^2}{2J_c^2}\,dH_e = \frac{\mu_\circ H_m^3}{6aJ_c} \qquad (S1.2d)$$

$$e_{hy} = \frac{\mu_\circ H_m^3}{6H_p} \qquad (H_m \le H_p) \qquad (7.13a)$$

Note that $e_{hy} \propto H_m^3$; i.e., in a "small" field excitation e_{hy} increases as the 3rd power of H_m; this has been verified by many experiments.

b) Similarly in a decreasing-field sequence, $H_e = H_m \rightarrow 0$, $E_z(x)\,dt$ is given by:

$$E_z(x)\,dt = \mu_\circ (x - x_-)\,dH_e \qquad (S1.3)$$

where $x_- = (H_m - H_e)/2J_c$, as indicated in Fig. 7.3a. Thus e_{hy} is given by:

$$e_{hy} = \frac{\mu_\circ J_c}{a}\int_{H_m}^0\left[\int_0^{x_-}\left[(x - x_-)\,dx\right] dH_e = \frac{\mu_\circ J_c}{a}\int_{H_m}^0\left(\frac{x_-^2}{2} - x_-^2\right) dH_e \right. \qquad (S1.4)$$

$$= -\frac{\mu_\circ J_c}{a}\int_{H_m}^0 \frac{(H_m - H_e)^2}{8J_c^2}\,dH_e = \frac{\mu_\circ H_m^3}{24aJ_c}$$

$$e_{hy} = \frac{\mu_\circ H_m^3}{24H_p} \qquad (0 \le H_m \le H_p) \qquad (7.14a)$$

Note that in the decreasing-field sequence, e_{hy} is 1/4 that of the increasing-field sequence. This is, as may be evident from Figs. 7.2a and 7.3a, because E_z induced within the slab in Case 1 is between $x=0$ and $x_m = H_m/J_c$ (Fig. 7.2a), while in Case 2 it is between $x=0$ and $x_0 = H_m/2J_c$ (Fig. 7.3a); again, $e_{hy} \propto H_m^3$.

Solution to PROBLEM 7.1 (continuation)

c) The E-field in the slab, as may be noted by its subscript z, points in the z direction, specifically in the $-z$ direction when $H_e(t)$ points in the $+y$ direction. Thus at the slab surface ($x = 0$), the Poynting vector $\vec{S}(= \vec{E} \times \vec{H})$ points, as expected, in the $+x$ direction, because during the first field sequence, $H_e = 0^* \rightarrow H_m$, energies, dissipated and stored, flow to the slab from the external source. In the first field sequence, $E_z(0)$ is given by Eq. $S1.1b$, with $x_+ = H_e/J_c$:

$$E_z(0) = \mu_\circ \frac{H_e}{J_c} \left(\frac{dH_e}{dt} \right) \tag{S1.5a}$$

The first term of the right-hand side of Eq. 7.3b, the Poynting energy density in Case 1, e_{py1}, thus may be expressed as:

$$e_{py1} \equiv \frac{1}{a} \int \left[-\int_{\mathcal{S}} \vec{E}(x) \times \vec{H}_e \cdot d\vec{\mathcal{A}} \right] dt = \frac{\mu_\circ}{aJ_c} \int_0^{H_m} H_e^2 \, dH_e$$

$$e_{py1} = \frac{\mu_\circ H_m^3}{3H_p} \tag{S1.6a}$$

In Case 2, $E_z(0)$ is given by Eq. $S1.3$, with $x_- = (H_m - H_e)/2J_c$:

$$E_z(0) = -\mu_\circ \left(\frac{H_m - H_e}{2J_c} \right) \frac{dH_e}{dt} \tag{S1.5b}$$

The Poynting energy density in Case 2, e_{py2}, thus is given by:

$$e_{py2} = \frac{\mu_\circ}{2aJ_c} \int_{H_m}^0 (H_m - H_e) H_e \, dH_e$$

$$e_{py2} = -\frac{\mu_\circ H_m^3}{12H_p} \tag{S1.6b}$$

The $-$sign in Eq. $S1.6b$ indicates that e_{py2} was returned to the source. At the end of the full field sequence, $H_e = 0^* \rightarrow H_m \rightarrow 0$ (Case 3), as may be inferred from Eq. 7.12, $-M(0) = -H_m^2/4H_p$: the slab stores magnetic (or magnetization) energy density, e_{m_f}, through $H_s(x)$, which, with $x_0 = H_m/2J_c$, is given by:

$$H_s(x) = J_c x \qquad (0 \le x \le x_0) \tag{S1.7a}$$

$$H_s(x) = H_m - J_c x \qquad (x_0 \le x \le H_m/J_c) \tag{S1.7b}$$

Using Eqs. $S1.7a$ and $S1.7b$, we may evaluate e_{m_f}:

$$e_{m_f} = \frac{\mu_\circ}{2a} \int_0^a H_s^2(x) \, dx = \frac{\mu_\circ}{2a} \left(2 \times \int_0^{\frac{H_m}{2J_c}} J_c^2 x^2 \, dx \right)$$

$$e_{m_f} = \frac{\mu_\circ H_m^3}{24H_p} \tag{S1.8}$$

Solution to PROBLEM 7.1 (continuation)

Combining Eqs. 7.3*b*, *S*1.6*a*, *S*1.6*b*, and *S*1.8, we obtain e_{hy} for Case 3:

$$\begin{aligned} e_{hy} &= e_{py1} + e_{py2} - e_{m_f} \\ &= \frac{\mu_\circ H_m^3}{3H_p} - \frac{\mu_\circ H_m^3}{12H_p} - \frac{\mu_\circ H_m^3}{24H_p} \\ e_{hy} &= \frac{5\mu_\circ H_m^3}{24H_p} \qquad (0 \le H_m \le H_p) \end{aligned} \tag{7.15a}$$

Energy Flow

Here, let us check the energy flow from the source to the slab during each field sequence. In each sequence, the energy densities must be balanced:

$$e_{py} = e_{hy} + e_{m_f} - e_{m_i} \tag{S1.9}$$

where e_{m_f} and e_{m_i} are the magnetic energy densities in the slab, respectively, at the final and initial states. Note that Eq. *S*1.9 is essentially the same as Eq. 7.2.

For the first field sequence, $e_{py} = e_{py1}$ (Eq. *S*1.6*a*), e_{hy} (Eq. 7.13*a*), $e_{m_i} = 0$ (because the slab is in the virgin state), and $e_{m_{f1}}$ may be evaluated from $H_s(x) = H_m - J_c x$:

$$\begin{aligned} e_{m_{f1}} &= \frac{\mu_\circ}{2a}\int_0^a H_s^2(x)\,dx \\ &= \frac{\mu_\circ}{2a}\left[\int_0^{\frac{H_m}{J_c}} (H_m - J_c x)^2\,dx\right] \\ e_{m_{f1}} &= \frac{\mu_\circ H_m^3}{6H_p} \end{aligned} \tag{S1.10}$$

Inserting Eqs. 7.13*a* and *S*1.10 into the right-hand side of Eq. *S*1.9, we obtain:

$$e_{py1} = \frac{\mu_\circ H_m^3}{6H_p} + \frac{\mu_\circ H_m^3}{6H_p} = \frac{\mu_\circ H_m^3}{3H_p} \tag{S1.11a}$$

e_{py1} of Eq. *S*1.11*a* is identical to Eq. *S*1.6*a*, demonstrating that the energy density flow in the first field sequence is balanced.

We may also check the energy balance during the second field sequence, $H_e = H_m \to 0$. During this sequence, appropriate energy densities in the right-hand side of Eq. *S*1.9 are: e_{hy} (Eq. 7.14*a*), e_{m_f} (Eq. *S*1.8), and $e_{m_i} = e_{m_{f1}}$ (Eq. *S*1.10):

$$e_{py2} = \frac{\mu_\circ H_m^3}{24H_p} + \frac{\mu_\circ H_m^3}{24H_p} - \frac{\mu_\circ H_m^3}{6H_p} = -\frac{\mu_\circ H_m^3}{12H_p} \tag{S1.11b}$$

e_{py2} of Eq. *S*1.11*b* indeed equals e_{py2} given by Eq. *S*1.6*b*, once again demonstrating that the energy balance of Eq. *S*1.9 is valid in the second field sequence. The $-$sign indicates, as remarked above, a net flow of energy *back* to the external source during the second field sequence: this energy density plus the hysteresis energy density are "paid" for by a net reduction in the magnetic energy storage in the slab.

PROBLEM 7.2: Hysteresis energy density—"Virgin" Bean slab Under "medium" field sequences (Cases 1–3)

Here Cases 1–3 are studied for a "medium" field excitation, specifically, $H_p \le H_m \le 2H_p = 2J_c a$. In the increasing-field, $H_e = 0^* \to H_m$ sequence (Cases 1 and 3), e_{hy} is independent of H_m for $H_m \ge H_p$—this is, of course, because J_c in the Bean critical-state model is field-independent. $-M(H_e)$ functions for the increasing-field and decreasing-field sequences are given by:

$$-M(H_e) = H_e - \frac{H_e^2}{2H_p} \qquad (H_e = 0^* \to H_p) \qquad (5.5)$$

$$= \tfrac{1}{2} H_p \qquad (H_e = H_p \to H_m) \qquad (5.6)$$

$$-M(H_e) = \tfrac{1}{2} H_p - (H_m - H_e) + \frac{(H_m - H_e)^2}{4H_p} \qquad (H_e = H_m \to 0) \qquad (5.7a)$$

Figure 7.11 shows $-M(H_e)$ plots given by Eqs. 5.5, 5.6, and 5.7*a*.

a) Applying Eq. 7.3*a* for one half of the slab ($0 \le x \le a$), show that e_{hy} for Case 1 is given by:

$$e_{hy} = \tfrac{1}{2}\mu_\circ H_p H_m \left(1 - \frac{2H_p}{3H_m}\right) \qquad (H_p \le H_m \le 2H_p) \qquad (7.13b)$$

b) For Case 2, explain why e_{hy} is still given by Eq. 7.14*a* (p. 415).

c) Using Eq. 7.3*b*, show that e_{hy} for Case 3, which is obviously the sum of Eqs. 7.13*b* and 7.14*a*, is given by:

$$e_{hy} = \tfrac{1}{2}\mu_\circ H_p H_m \left[1 - \frac{2H_p}{3H_m} + \tfrac{1}{12}\left(\frac{H_m}{H_p}\right)^2\right] \qquad (H_p \le H_m \le 2H_p) \qquad (7.15b)$$

d) Show that for $H_m = H_p$, Eqs. 7.15*a* (p. 415) and 7.15*b* give the same e_{hy}.

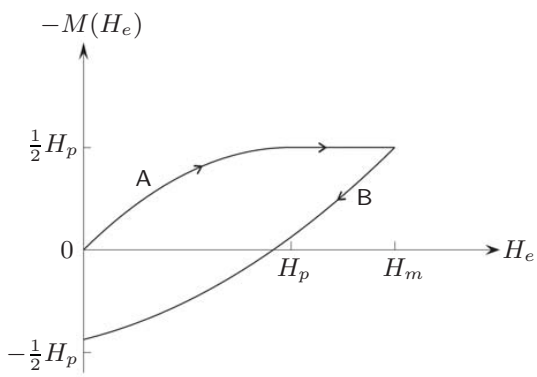

Fig. 7.11 $-M(H_e)$ for "medium" field excitation. Case 1: Trace A; Case 2: Trace B; Case 3: Traces A and B. Note that $H_p \le H_m \le 2H_p = 2J_c a$.

Solution to PROBLEM 7.2

a) For the first part of Case 1, $H_e = 0^* \rightarrow H_p$, we obtain hysteresis energy density, $e_{hy\,1'}$, by inserting $H_m = H_p$ into Eq. 7.13*a* (p. 415):

$$e_{hy\,1'} = \tfrac{1}{6}\mu_\circ H_p^2 \qquad (H_e = 0 \rightarrow H_p) \tag{S2.1}$$

For the second part of Case 1, $H_e = H_p \rightarrow H_m$, field penetrates the entire slab (here, invoking symmetry, we show only half the slab, from $x = 0$ to $x = a$), as shown by the dashed line in Fig. 7.2b. $E_z(x)$ due to dH_e/dt may be given by:

$$E_z(x) = \mu_\circ \frac{dH_e}{dt}(a - x) \tag{S2.2}$$

From Eqs. 7.3*a* and *S*2.2, applied to one half of the slab ($0 \le x \le a$), we have $e_{hy\,1''}$:

$$e_{hy\,1''} = \frac{1}{a}\int_0^a \left[\int J_c E(x)\, dt\right] dx = \frac{\mu_\circ J_c}{a}\int_0^a \left[\int_{H_p}^{H_m} (a - x)\, dH_e\right] dx \tag{S2.3a}$$

$$= \mu_\circ J_c (H_m - H_p)\int_0^a \frac{a-x}{a}\, dx = \tfrac{1}{2}\mu_\circ H_p (H_m - H_p) \tag{S2.3b}$$

Adding $e_{hy\,1'}$ and $e_{hy\,1''}$ given respectively by Eqs. *S*2.1 and *S*2.3*b*, we obtain e_{hy} for Case 1:

$$e_{hy} = \tfrac{1}{6}\mu_\circ H_p^2 + \tfrac{1}{2}\mu_\circ H_p (H_m - H_p)$$

$$= \tfrac{1}{2}\mu_\circ H_p H_m - \tfrac{1}{3}\mu_\circ H_p^2$$

$$e_{hy} = \tfrac{1}{2}\mu_\circ H_p H_m \left(1 - \frac{2H_p}{3H_m}\right) \quad (H_p \le H_m \le 2H_p) \tag{7.13b}$$

b) For Case 2, $H_e = H_m \rightarrow 0$, $H_s(x)$ at $0 < H_e < H_m$, given by the solid lines in Fig. 7.3b, is essentially identical to that given by the solid lines of Fig. 7.3a—each covers the slab from $x = 0$ to $x = x_0$. Thus, $E_z(x)\, dt$ for this field sequence is identical to Eq. *S*1.3, leading to the same e_{hy} given by Eq. 7.14*a*.

c) For the first part of this field sequence, the Poynting energy density, $e_{py\,1'}$, is given by Eq. *S*1.6*a* with $H_m = H_p$:

$$e_{py\,1'} = \tfrac{1}{3}\mu_\circ H_p^2 \tag{S2.4a}$$

In the second part of the field sequence, $H_e = H_p \rightarrow H_m$, $E_z(0)$ is given by Eq. *S*2.2:

$$E_z(0) = \mu_\circ a \frac{dH_e}{dt} \tag{S2.5}$$

The first part of the right-hand side of Eq. 7.3*b*, the Poynting energy density, $e_{py\,1''}$, thus may be expressed as:

$$e_{py\,1''} \equiv \frac{1}{a}\int \left[-\int_{\mathcal{S}} \vec{E}(x) \times \vec{H}_e \cdot d\vec{\mathcal{A}}\right] dt = \mu_\circ \int_{H_p}^{H_m} H_e\, dH_e$$

$$e_{py\,1''} = \tfrac{1}{2}\mu_\circ (H_m^2 - H_p^2) \tag{S2.4b}$$

Solution to PROBLEM 7.2 (continuation)

In the second field sequence, $H_e = H_m \to 0$, $E_z(0)$ is the same as given by Eq. $S1.5b$; the corresponding Poynting energy density, e_{py2}, thus is given by Eq. $S1.6b$:

$$e_{py2} = -\frac{\mu_\circ H_m^3}{12H_p} \qquad (S1.6b)$$

Again the $-$sign indicates that e_{py2} was returned to the source. At the end of the full field sequence (Case 3), as may be inferred from Fig. 7.11, the slab stores magnetic (or magnetization) energy density, e_{m_f}, through $H_s(x)$, which, with $x_0 = H_m/2J_c$, is again given by Eq. $S1.7$. Using Eq. $S1.7$, we may evaluate e_{m_f}. Here, unlike in the previous integration (Eq. $S1.8$), where the integration from $x = 0$ to $x = x_0 = H_m/2J_c$ is doubled to compute e_{m_f}, the integration must be performed separately for the two ranges, $x = 0 \to x_0$ and $x_0 \to a$ (Fig. 7.3b):

$$e_{m_f} = \frac{\mu_\circ}{2a}\int_0^a H_s^2(x)\,dx = \frac{\mu_\circ}{2a}\left[\int_0^{\frac{H_m}{2J_c}} J_c^2 x^2\,dx + \int_{\frac{H_m}{2J_c}}^a (H_m - J_c x)^2\,dx\right]$$

$$e_{m_f} = \tfrac{1}{2}\mu_\circ H_m^2 - \frac{\mu_\circ H_m^3}{8H_p} - \tfrac{1}{2}\mu_\circ H_m H_p + \tfrac{1}{6}\mu_\circ H_p^2 \qquad (S2.7)$$

Combining Eqs. $7.3b$, $S2.4a$, $S2.4b$, $S1.6b$, and $S2.7$ we obtain e_{hy} for Case 3:

$$\begin{aligned} e_{hy} &= e_{py1'} + e_{py1''} + e_{py2} - e_{m_f} \\ &= \tfrac{1}{3}\mu_\circ H_p^2 + \tfrac{1}{2}\mu_\circ (H_m^2 - H_p^2) - \frac{\mu_\circ H_m^3}{12H_p} \\ &\quad - \left(\tfrac{1}{2}\mu_\circ H_m^2 - \frac{\mu_\circ H_m^3}{8H_p} - \tfrac{1}{2}\mu_\circ H_m H_p + \tfrac{1}{6}\mu_\circ H_p^2\right) \\ &= -\tfrac{1}{3}\mu_\circ H_p^2 + \frac{\mu_\circ H_m^3}{24H_p} + \tfrac{1}{2}\mu_\circ H_p H_m \end{aligned} \qquad (S2.8)$$

Equation $S2.8$ is equivalent to Eq. $7.15b$:

$$e_{hy} = \tfrac{1}{2}\mu_\circ H_p H_m\left[1 - \frac{2H_p}{3H_m} + \tfrac{1}{12}\left(\frac{H_m}{H_p}\right)^2\right] \quad (H_p \le H_m \le 2H_p) \qquad (7.15b)$$

d) At $H_m = H_p$, e_{hy} may be given by either Eqs. $7.15a$ (p. 415) or $7.15b$:

$$e_{hy} = \frac{5\mu_\circ H_m^3}{24H_p} \qquad (H_m \le H_p) \qquad (7.15a)$$

$$= \tfrac{5}{24}\mu_\circ H_p^2$$

$$e_{hy} = \tfrac{1}{2}\mu_\circ H_p H_m\left[1 - \frac{2H_p}{3H_m} + \tfrac{1}{12}\left(\frac{H_m}{H_p}\right)^2\right] \quad (H_p \le H_m \le 2H_p) \qquad (7.15b)$$

$$= \tfrac{1}{2}\mu_\circ H_p^2\left[1 - \frac{2}{3} + \frac{1}{12}\right] = \tfrac{5}{24}\mu_\circ H_p^2$$

PROBLEM 7.3: Hysteresis energy density—"Virgin" Bean slab Under "large" field sequences (Cases 1–3)

For a "large" field excitation, specifically, $H_m \geq 2H_p = 2J_c a$, the magnetization curve in the increasing-field sequence, $H_e = 0^* \rightarrow H_m$, is essentially identical to that for a "medium" field excitation studied in **PROBLEM 7.2**, and therefore e_{hy} in the increasing-field range for Cases 1 and 3 is given by Eq. 7.13*b* (p. 419).

$-M(H_e)$ for Case 2 is given by Eqs. 5.7*a* and 5.7*b*, respectively, in the first field range, $H_e = H_m \rightarrow (H_m - 2H_p)$, and in the second field range, $H_e = (H_m - 2H_p) \rightarrow 0$. Figure 7.12 shows $-M(H_e)$ over the entire field range.

a) Show that $e_{hy2'}$, the hysteresis energy density in the first part of Case 2, $H_e = H_m \rightarrow (H_m - 2H_p)$, is given by:

$$e_{hy2'} = \tfrac{1}{3}\mu_\circ H_p^2 \tag{7.16a}$$

b) Show that $e_{hy2''}$, the hysteresis energy density in the second part of Case 2, $H_e = (H_m - 2H_p) \rightarrow 0$, is given by:

$$e_{hy2''} = \tfrac{1}{2}\mu_\circ H_p H_m \left(1 - \frac{2H_p}{H_m}\right) \tag{7.16b}$$

c) Show that e_{hy} for Case 2, $H_e = H_m \rightarrow 0$, is given by:

$$e_{hy} = \tfrac{1}{2}\mu_\circ H_p H_m \left(1 - \frac{4H_p}{3H_m}\right) \qquad (H_m \geq 2H_p) \tag{7.14b}$$

d) Show that e_{hy} for Case 3, $H_e = 0^* \rightarrow H_m \rightarrow 0$, is given by:

$$e_{hy} = \mu_\circ H_p H_m \left(1 - \frac{H_p}{H_m}\right) \qquad (H_m \geq 2H_p) \tag{7.15c}$$

e) Show that Eqs. 7.15*b* (p. 419) and 7.15*c* agree at $H_m = 2H_p$.

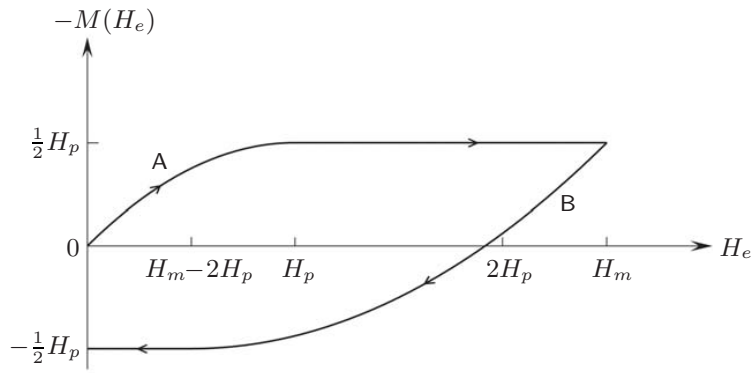

Fig. 7.12 $-M(H_e)$ for "large" field excitation. Case 1: Trace A; Case 2: Trace B; Case 3: Traces A and B. Note that $H_m \geq 2H_p = 2J_c a$.

Solution to PROBLEM 7.3

a) As in the "small" field sequence, $E_z(x)$ is given by Eq. $S1.3$, where, once again, $x_- = (H_m - H_e)/2J_c$. Thus, $e_{hy2'}$ is given by Eq. $S1.4$, except that here the field range is from H_m to $H_m - 2H_p$. Thus:

$$e_{hy2'} = \frac{\mu_\circ J_c}{a}\int_{H_m}^{H_m-2H_p}\left[\int_0^{x_-}\left[(x-x_-)\,dx\right]\right]dH_e = -\frac{\mu_\circ J_c}{2a}\int_{H_m}^{H_m-2H_p} {x_-}^2\,dH_e$$

$$= -\frac{\mu_\circ}{8H_p}\int_{H_m}^{H_m-2H_p}(H_m-H_e)^2\,dH_e = -\frac{\mu_\circ}{8H_p}\int_{H_m}^{H_m-2H_p}(H_m^2-2H_mH_e+H_e^2)\,dH_e$$

$$e_{hy2'} = \tfrac{1}{3}\mu_\circ H_p^2 \tag{7.16a}$$

b) Again, $E_z(x)$ is given by Eq. $S1.3$ and $e_{hy2''}$ by Eq. $S1.4$ with $x_- = a$:

$$e_{hy2''} = \frac{\mu_\circ J_c}{a}\int_{H_m-2H_p}^{0}\left[\int_0^{a}\left[(x-a)\,dx\right]\right]dH_e = -\frac{\mu_\circ J_c}{2a}\int_{H_m-2H_p}^{0} a^2\,dH_e$$

$$e_{hy2''} = \tfrac{1}{2}\mu_\circ H_p H_m\left(1-\frac{2H_p}{H_m}\right) \tag{7.16b}$$

c) Adding $e_{hy2'}$ and $e_{hy2''}$, we obtain:

$$e_{hy} = e_{hy2'} + e_{hy2''}$$

$$= \tfrac{1}{3}\mu_\circ H_p^2 + \tfrac{1}{2}\mu_\circ H_p H_m\left(1-\frac{2H_p}{H_m}\right)$$

$$e_{hy} = \tfrac{1}{2}\mu_\circ H_p H_m\left(1-\frac{4H_p}{3H_m}\right) \qquad (H_m \geq 2H_p) \tag{7.14b}$$

d) We may simply add Eq. 7.13*b* (e_{hy} for $H_e = 0 \rightarrow H_m$) and Eq. 7.14*b*:

$$e_{hy} = \tfrac{1}{2}\mu_\circ H_p H_m\left(1-\frac{2H_p}{3H_m}\right) + \tfrac{1}{2}\mu_\circ H_p H_m\left(1-\frac{4H_p}{3H_m}\right)$$

$$e_{hy} = \mu_\circ H_p H_m\left(1-\frac{H_p}{H_m}\right) \qquad (H_m \geq 2H_p) \tag{7.15c}$$

e) At $H_m = 2H_p$, e_{hy} may be given by either Eqs. 7.15*b* (p. 419) or 7.15*c*:

$$e_{hy} = \tfrac{1}{2}\mu_\circ H_p H_m\left[1-\frac{2H_p}{3H_m}+\tfrac{1}{12}\left(\frac{H_m}{H_p}\right)^2\right] \tag{7.15b}$$

$$= \mu_\circ H_p^2\left(1-\frac{1}{3}+\frac{4}{12}\right) = \mu_\circ H_p^2$$

$$e_{hy} = \mu_\circ H_p H_m\left(1-\frac{H_p}{H_m}\right) \tag{7.15c}$$

$$= 2\mu_\circ H_p^2\left(1-\frac{1}{2}\right) = \mu_\circ H_p^2$$

DISCUSSION 7.1: Hysteresis Energy Density—Magnetized Bean Slab (Cases 4–6)

Once exposed to an external field, a virgin Bean slab is magnetized even after the field is reduced to 0—see the "square-dot" lines in Figs. 7.4a, 7.4b, and 7.4c.

For a magnetized Bean slab in Case 4, $H_e = 0 \rightarrow H_m$. $-M(H_e)$ is given by:

"Small" $(H_e = 0 \rightarrow H_m)$

$$-M(H_e) = H_e - \frac{H_e^2 + 2H_m H_e - H_m^2}{4H_p} \tag{7.17a}$$

"Medium" $(H_e = 0 \rightarrow 2H_p - H_m)$

$$-M(H_e) = -\tfrac{1}{2}H_p + (H_m + H_e) - \frac{(H_m + H_e)^2}{4H_p} \tag{7.17b}$$

"Medium" $(H_e = 2H_p - H_m \rightarrow H_m)$ ***&*** ***"Large"*** $(H_e = 0 \rightarrow H_m)$

$$-M(H_e) = \tfrac{1}{2}H_p \tag{5.6}$$

Similarly, for Case 5, $H_e = H_m \rightarrow 0$, $-M(H_e)$ is one of the functions below:

"Small" $(H_e = H_m \rightarrow 0)$

$$-M(H_e) = H_e + \frac{H_e^2 + 2H_m H_e - H_m^2}{4H_p} \tag{7.18}$$

"Medium" $(H_e = H_m \rightarrow 0)$ ***&*** ***"Large"*** $(H_e = H_m \rightarrow H_m - 2H_p)$

$$-M(H_e) = \tfrac{1}{2}H_p - (H_m - H_e) + \frac{(H_m - H_e)^2}{4H_p} \tag{5.7a}$$

"Large" $(H_e = H_m - 2H_p \rightarrow 0)$

$$-M(H_e) = -\tfrac{1}{2}H_p \tag{5.7b}$$

Figure 7.13 shows $-M(H_e)$ plots over the field range from $-H_m$ to H_m. The dash-dotted, dashed, and solid lines correspond, respectively, to "small," "medium," and "large" field excursions, each applicable to Case 6.

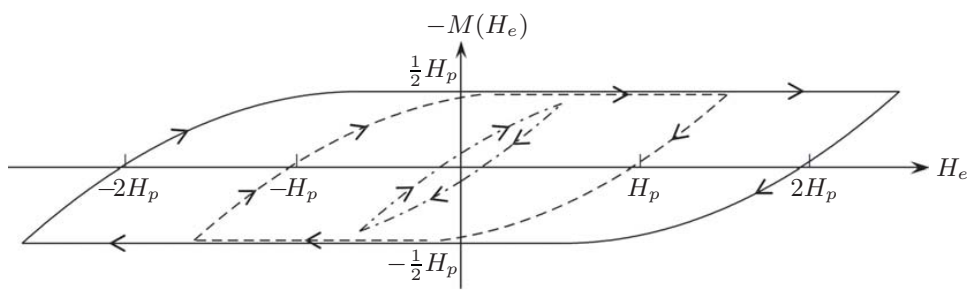

Fig. 7.13 $-M(H_e)$ plots from $-H_m$ to H_m: dash-dotted; dashed; and solid lines correspond, respectively, to "small," "medium," and "large" field excursions.

DISCUSSION 7.1: Hysteresis Energy Density—Magnetized Bean Slab (Cases 4–6) (continuation)

Case 4—"Small" The same approach used in **PROBLEM 7.1** may be used here, where $E_z(x)\,dt$ is given by Eq. $S1.1b$:

$$E_z(x)\,dt = \mu_\circ(x_+ - x)\,dH_e \qquad (S1.1b)$$

Here, as noted in the Fig. 7.4 caption, $x_+ = (H_m + H_e)/2J_c$, rather than $x_+ = H_e/J_c$ as in **PROBLEM 7.1**. Equation $S1.1b$ leads to Eq. $S1.2c$:

$$e_{hy} = \frac{\mu_\circ J_c}{a}\int_0^{H_m}\left(x_+^2 - \frac{x_+^2}{2}\right)dH_e \qquad (S1.2c)$$

Then, inserting $x_+ = (H_m + H_e)/2J_c$ into Eq. $S1.2c$, we have:

$$e_{hy} = \frac{\mu_\circ J_c}{2a}\int_0^{H_m}\left(\frac{H_m + H_e}{2J_c}\right)^2 dH_e$$

$$= \frac{\mu_\circ}{8H_p}\int_0^{H_m}(H_m^2 + 2H_mH_e + H_e^2)\,dH_e$$

$$e_{hy} = \frac{7\mu_\circ H_m^3}{24H_p} \qquad (0 \le H_m \le H_p) \qquad (7.19a)$$

Case 4—"Medium" As may be inferred from Fig. 7.4b, when H_e reaches such that $H_e + H_m = 2H_p$, i.e., $H_e = 2H_p - H_m$ (remember here $H_p \le H_m \le 2H_p$), $H_s(x) = H_e - J_c x$ throughout the slab (of course, from $x = 0$ to $x = a$) and $E_z(x)$ is given simply by Eq. $S2.2$ of **Solution to PROBLEM 7.2**:

$$E_z(x) = \mu_\circ\frac{dH_e}{dt}(a - x) \qquad (S2.2)$$

Until $H_e = 2H_p - H_m$, as may be inferred from Fig. 7.4b, H_e penetrates only to x_+. Thus, e_{hy} must be computed over two field ranges, $H_e = 0 \to 2H_p - H_m$ and $H_e = 2H_p - H_m \to H_m$, with $E_z(x)\,dt$ given, respectively, by Eq. $S1.1b$ and Eq. $S2.2$:

$$e_{hy} = \frac{\mu_\circ J_c}{2a}\left[\int_0^{2H_p - H_m}\left(\frac{H_m + H_e}{2J_c}\right)^2 dH_e + \int_{2H_p - H_m}^{H_m} a^2\,dH_e\right]$$

$$= \frac{\mu_\circ}{8H_p}\int_0^{2H_p - H_m}(H_m^2 + 2H_mH_e + H_e^2)\,dH_e + \tfrac{1}{2}\mu_\circ H_p\int_{2H_p - H_m}^{H_m} dH_e$$

$$= \left(\tfrac{1}{3}\mu_\circ H_p^2 - \frac{\mu_\circ H_m^3}{24H_p}\right) + (\mu_\circ H_pH_m - \mu_\circ H_p^2)$$

Thus:

$$e_{hy} = \mu_\circ H_pH_m\left[1 - \frac{2H_p}{3H_m} - \tfrac{1}{24}\left(\frac{H_m}{H_p}\right)^2\right] \qquad (H_p \le H_m \le 2H_p) \qquad (7.19b)$$

Note that Eqs. 7.19a and 7.19b, as expected, agree at $H_m = H_p$: $e_{hy} = 7\mu_\circ H_p^2/24$.

DISCUSSION 7.1: Hysteresis Energy Density—Magnetized Bean Slab (Cases 4–6) (continuation)

Case 4—"Large" As may be inferred from Fig. 7.4c, the field penetrates the slab completely over the entire field range. Thus:

$$e_{hy} = \frac{\mu_\circ J_c}{2a}\left(\int_0^{H_m} a^2\, dH_e\right) = \tfrac{1}{2}\mu_\circ H_p \int_0^{H_m} dH_e$$

$$e_{hy} = \tfrac{1}{2}\mu_\circ H_p H_m \qquad (H_m \geq 2H_p) \tag{7.19c}$$

Note that Eqs. 7.19*b* and 7.19*c*, as expected, agree at $H_m = 2H_p$: $e_{hy} = \mu_\circ H_p^2$.

Case 5 Comparing Fig. 7.4 with Fig. 7.3 for Case 2, we note that the $H_s(x)$ profiles for Case 5 for "small," "medium," and "large" fields are identical to the respective $H_s(x)$ profiles for Case 2; therefore, the e_{hy}'s for Case 5 are identical to the Case 2 counterparts, given, respectively, by Eq. 7.14*a* (p. 415) for "small" and "medium," and Eq. 7.14*b* (p. 422) for "large."

Case 6—"Small" e_{hy} is obviously twice the sum of the e_{hy}'s given by Eqs. 7.19*a* and 7.14*a* (p. 415) valid for Case 2, "small." Thus, we have:

$$e_{hy} = 2 \times \left(\frac{7\mu_\circ H_m^3}{24H_p} + \frac{\mu_\circ H_m^3}{24H_p}\right)$$

$$e_{hy} = \frac{2\mu_\circ H_m^3}{3H_p} \qquad (0 \leq H_m \leq H_p) \tag{7.20a}$$

Of course, because here the field goes through one complete cycle, we may derive e_{hy} of Eq. 7.20*a* by applying Eq. 7.4*b*. Because $-M(H_e)$ is antisymmetric, the integral between $-H_m$ and H_m is equal to twice the integral between 0 and H_m. Thus:

$$e_{hy} = \mu_\circ \oint -M(H_e)\, dH_e \tag{7.4b}$$

$$= 2\mu_\circ \int_0^{H_m} -M(H_e)\, dH_e$$

$$= 2\mu_\circ \int_0^{H_m} \Big\{ -[M(H_e)]_{H_e=0\to H_m} + [M(H_e)]_{H_e=H_m\to 0} \Big\}\, dH_e \tag{7.21}$$

Inserting $M(H_e)$ given by Eqs. 7.17*a* and 7.18 into Eq. 7.21, we have:

$$e_{hy} = 2\mu_\circ \int_0^{H_m} \left[\left(H_e - \frac{H_e^2 + 2H_m H_e - H_m^2}{4H_p}\right) - \left(H_e + \frac{H_e^2 - 2H_m H_e - H_m^2}{4H_p}\right)\right] dH_e$$

$$= 2\mu_\circ \int_0^{H_m} \left(-\frac{H_e^2}{2H_p} + \frac{H_m^2}{2H_p}\right) dH_e = 2\mu_\circ \left(-\frac{H_m^3}{6H_p} + \frac{H_m^3}{2H_p}\right)$$

Hence:

$$e_{hy} = \frac{2\mu_\circ H_m^3}{3H_p} \qquad (0 \leq H_m \leq H_p) \tag{7.20a}$$

DISCUSSION 7.1: Hysteresis Energy Density—Magnetized Bean Slab (Cases 4–6) (continuation)

Case 6—"Medium" Similarly, e_{hy} is twice the sum of e_{hy}'s given by Eqs. 7.19*b* valid for Case 4 and 7.14*a* (p. 415) valid for Case 2 (and Case 5):

$$e_{hy} = 2 \times \left\{ \mu_\circ H_p H_m \left[1 - \frac{2H_p}{3H_m} - \tfrac{1}{24} \left(\frac{H_m}{H_p} \right)^2 \right] + \frac{\mu_\circ H_m^3}{24 H_p} \right\}$$

$$e_{hy} = 2\mu_\circ H_p H_m \left(1 - \frac{2H_p}{3H_m} \right) \quad (H_p \le H_m \le 2H_p) \tag{7.20b}$$

We may also derive Eq. 7.20*b* above from Eq. 7.21, the equivalent of Eq. 7.4*a*.

$$e_{hy} = -2\mu_\circ \int_0^{H_m} \Big\{ [M(H_e)]_{H_e=0\to H_m} - [M(H_e)]_{H_e=H_m\to 0} \Big\}\, dH_e \tag{7.21}$$

Because $-M(H_e)$ is given by Eq. 7.17*b* for $H_e = 0 \to 2H_p - H_m$ and by Eq. 5.6 for $H_e = 2H_p - H_m \to H_m$, the $M(H_e)\, dH_e$ integral of Eq. 7.21 consists of three components. With Eqs. 7.17*b*, 5.6, and 5.7*a* into Eq. 7.21, we have:

$$\begin{aligned}
e_{hy} &= 2\mu_\circ \left\{ \int_0^{2H_p - H_m} \left[-\tfrac{1}{2} H_p + (H_m + H_e) - \frac{(H_m + H_e)^2}{4H_p} \right] dH_e \right. \\
&\qquad \left. + \int_{2H_p - H_m}^{H_m} \tfrac{1}{2} H_p \, dH_e - \int_0^{H_m} \left[\tfrac{1}{2} H_p - (H_m - H_e) + \frac{(H_m - H_e)^2}{4H_p} \right] \right\} dH_e \\
&= 2\mu_\circ \left\{ \int_0^{2H_p - H_m} \left[-\tfrac{1}{2} H_p + H_m + H_e - \frac{H_m^2}{4H_p} - \frac{H_m H_e}{2H_p} - \frac{H_e^2}{4H_p} \right] dH_e \right. \\
&\qquad \left. + H_p(H_m - H_p) - \int_0^{H_m} \left[\tfrac{1}{2} H_p - H_m + H_e + \frac{H_m^2}{4H_p} - \frac{H_m H_e}{2H_p} + \frac{H_e^2}{4H_p} \right] \right\} dH_e \\
&= 2\mu_\circ \left[\left(\tfrac{1}{3} H_p^2 + \tfrac{1}{2} H_p H_m - \tfrac{1}{2} H_m^2 + \frac{H_m^3}{12 H_p} \right) \right. \\
&\qquad \left. + H_p(H_m - H_p) - \left(\tfrac{1}{2} H_p H_m - \tfrac{1}{2} H_m^2 + \frac{H_m^3}{12 H_p} \right) \right] \\
&= 2\mu_\circ \left(-\tfrac{2}{3} H_p^2 + H_p H_m \right)
\end{aligned}$$

Thus:

$$e_{hy} = 2\mu_\circ H_p H_m \left(1 - \frac{2H_p}{3H_m} \right) \quad (H_p \le H_m \le 2H_p) \tag{7.20b}$$

DISCUSSION 7.1: Hysteresis Energy Density—Magnetized Bean Slab (Cases 4–6) (continuation)

Case 6—"Large" Here too e_{hy} is twice the sum of the e_{hy}'s given by Eqs. 7.19*c* valid for Case 4 and 7.14*b* (p. 422) valid for Case 2 (and Case 5):

$$e_{hy} = 2 \times \left[\tfrac{1}{2}\mu_\circ H_p H_m + \tfrac{1}{2}\mu_\circ H_p H_m \left(1 - \frac{4H_p}{3H_m}\right)\right]$$

$$e_{hy} = 2\mu_\circ H_p H_m \left(1 - \frac{2H_p}{3H_m}\right) \quad (H_m \geq 2H_p) \tag{7.20c}$$

Equation 7.20*c* may also be derived from Eq. 7.21. Here too, although $-M(H_e)$ is given by Eq. 5.6 for the entire field range in the increasing-field sequence (Case 4), because in the decreasing-field sequence (Case 5) $-M(H_e)$ is given by Eq. 5.7*a* in the range $H_e = H_m \rightarrow H_m - 2H_p$ and by Eq. 5.7*b* in the range $H_e = H_m - 2H_p \rightarrow 0$, the $M(H_e)\,dH_e$ integral (Eq. 7.21) consists of three components:

$$e_{hy} = 2\mu_\circ \int_0^{H_m} \Big\{ -[M(H_e)]_{H_e=0\rightarrow H_m} + [M(H_e)]_{H_e=H_m\rightarrow 0} \Big\}\, dH_e \tag{7.21}$$

$$= 2\mu_\circ \Bigg\{ \int_0^{H_m} \tfrac{1}{2}H_p\, dH_e$$

$$- \int_{H_m-2H_p}^{H_m} \left[\tfrac{1}{2}H_p - (H_m - H_e) + \frac{(H_m - H_e)^2}{4H_p}\right] - \int_0^{H_m-2H_p} \left(-\tfrac{1}{2}H_p\right) \Bigg\}\, dH_e$$

$$= 2\mu_\circ \Bigg[H_p(H_m - H_p)$$

$$+ \int_{H_m-2H_p}^{H_m} \left(-\tfrac{1}{2}H_p + H_m - \frac{H_m^2}{4H_p} - H_e + \frac{H_m H_e}{2H_p} - \frac{H_e^2}{4H_p}\right) dH_e \Bigg]$$

$$= 2\mu_\circ \left[H_p(H_m - H_p) + \tfrac{1}{3}H_p^2 \right]$$

$$e_{hy} = 2\mu_\circ H_p H_m \left(1 - \frac{2H_p}{3H_m}\right) \quad (H_m \geq 2H_p) \tag{7.20c}$$

Note that for $H_m \gg H_p$, the condition which is generally met in most applications, e_{hy} is proportional to H_m; because $H_p = J_c a$, e_{hy} also increases with J_c and a:

$$e_{hy} = 2\mu_\circ H_p H_m \qquad (H_m \gg H_p) \tag{7.20d}$$

$$= 2\mu_\circ J_c a H_m \qquad (H_m \gg H_p) \tag{7.20e}$$

Answer to TRIVIA 7.1

Sugar (1, in J); flea (10^{-2}); LTS magnet (10^{-5}); snail (10^{-7}).

DISCUSSION 7.2: Bean Slab Carrying DC Current

When transport current, I_t, flows uniformly in the z direction in a Bean slab of $2a$ width, the y-directed magnetic field distribution within the slab, $H_s(x)$, no longer has mirror symmetry about the slab's midpoint, as illustrated in Fig. 5.5 (*CHAPTER 5*). Note that I_t is the current per unit length in the y direction; it has the unit of ampere/meter [A/m]. Define i as the normalized transport current: $i = I_t/I_c$, where $I_c = 2aJ_c$ [A/m]. We shall examine $H_s(x)$ distributions in a current-carrying Bean slab exposed to an external magnetic field, $H_e(t)$.

Cases 1i and 2i

We begin with time sequences Cases 1i and 2i—given by Eq. 7.5. Graphs of $H_x(t)$ plots for selected instances in Cases 1i and 2i are shown in Figs. 7.14(a)–(d). In

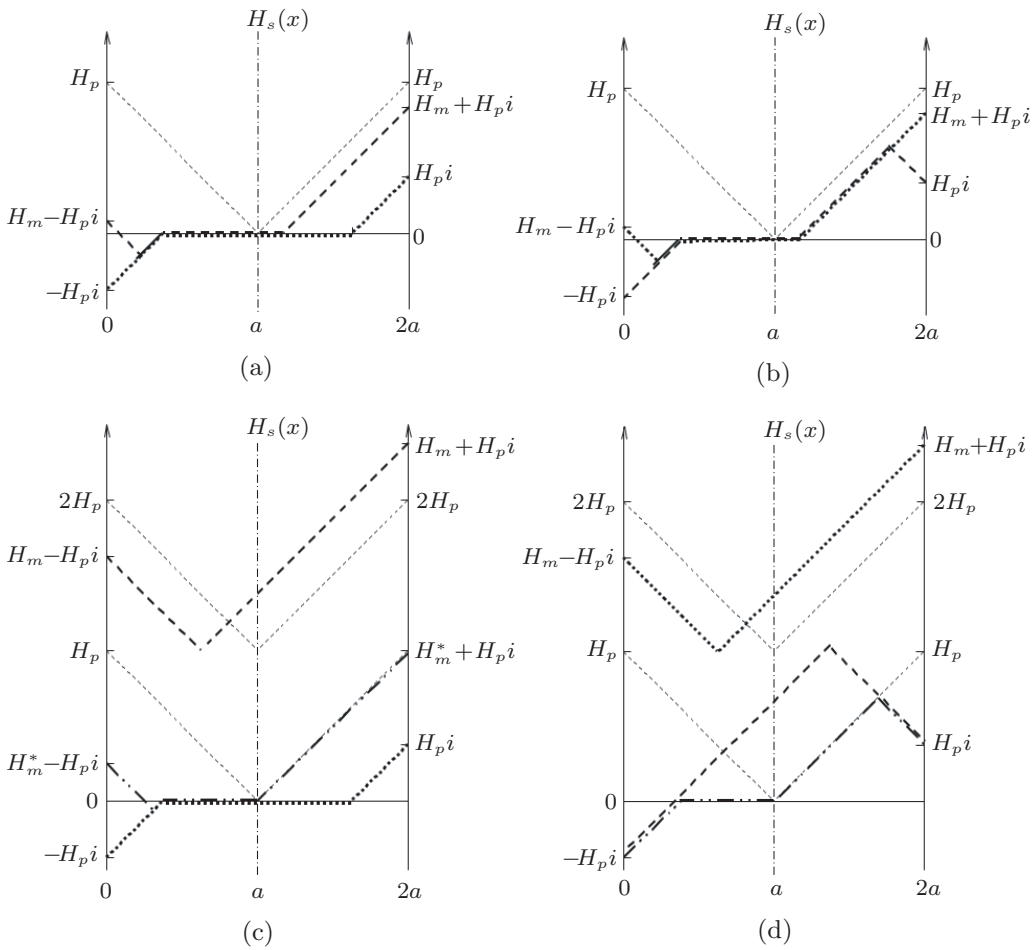

Fig. 7.14 Graphs of $H_s(x)$ plots for a Bean slab of width $2a$ carrying DC transport current of $I_t(=2iH_p)$, subjected to $H_e(t)$ of Cases 1i and 2i, where H_m is the maximum external field. In each graph, the dotted and dashed lines correspond, respectively, to $H_s(x)$ at the start and the end of a field sequence. Graphs (a) and (b), respectively Cases 1i and 2i, are for $H_m < H_p(1-i)$; graphs (c) and (d), respectively Cases 1i and 2i, are $H_m \geq H_p(1-i)$. The dash-dot-dot lines in (c) and (d) represent $H_s(x)$ at the *end* of a field sequence when $H_m = H_p(1-i) \equiv H^*_m$.

DISCUSSION 7.2: Bean Slab Carrying DC Current (continuation)

each graph the dotted and dashed lines correspond to $H_s(x)$, respectively, at the start ($H_e = 0$) and the end ($H_e = H_m$) of each field sequence. Note that the dotted lines in graphs (a) and (b) give $H_s(x)$ after the application of I_t to a *virgin* slab; the light dashes are $H_s(x)$ plots at $H_e(t) = H_p$ and $2H_p$ in the *absence* of transport current. Graphs (a)–(d) are for Cases 1*i* and 2*i*; graphs (a) and (b) are for $H_m < H_p(1-i)$, while graphs (c) and (d) are for $H_m > H_p(1-i)$. The dash-dot-dot lines in (c) and (d) correspond to $H_s(x)$ at the *end* of each sequence when $H_m = H_p(1-i) \equiv H_m^*$.

Cases 4i and 5i—"Small" Field Excitation

We now examine $H_s(x)$ plots for Cases 4*i* and 5*i*, shown in Fig. 7.15, in which H_m, the maximum amplitude of external field $H_e(t)$, is "small," specifically, $H_m \le H_p(1-i)$. Note that, as evident from the figure, because the field distribution is asymmetric with respect to the midpoint of the slab, later when hysteresis energy densities are computed, the horizontal distance is measured from either the left-hand end, $x = 0$ (x-axis) or the right-hand end $\xi = 0$ (ξ-axis), which is $x = 2a$—either way the field distribution is designated by $H_x(x)$. Graph (a) is for Case 4*i*, in which the external field is increasing ($\uparrow H_e$), i.e., $H_e(t) = 0 \rightarrow H_m$, *after* the field sequence $H_e(t) = -H_m \rightarrow 0$; graph (b) is for Case 5*i*, in which the external field is decreasing ($\downarrow H_e$), i.e., $H_e(t) = H_m \rightarrow 0$. In each graph, the dotted and dashed lines correspond to $H_s(x)$, respectively, at the start and the end of a field sequence; the solid lines are for $H_s(x)$ at $0 < \uparrow H_e < H_m$ (Case 4*i*) or $H_s(x)$ at $H_m > \downarrow H_e > 0$ (Case 5*i*).

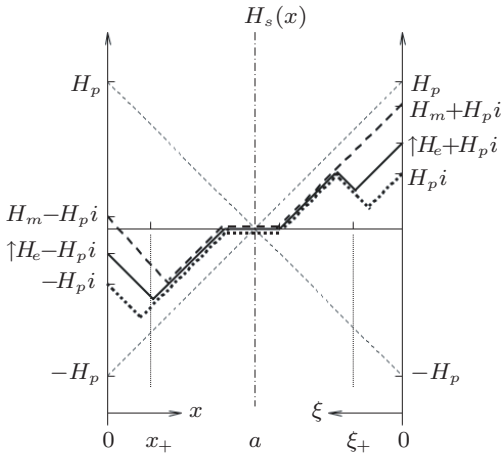

(a)

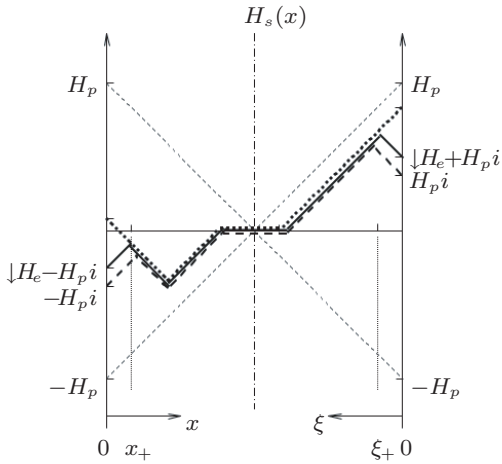

(b)

Fig. 7.15 $H_s(x)$ plots for Cases 4*i* and 5*i*, in which $H_m \le H_p(1-i)$. Graph (a) is for Case 4*i*, i.e., $H_e(t) = 0 \rightarrow H_m$, *after* the field sequence from $-H_m$ to 0; graph (b) is for Case 5*i*, i.e., $H_e(t) = H_m \rightarrow 0$. In each graph the dotted and dashed lines correspond to $H_s(x)$, respectively, at the start and end of each sequence; the solid lines correspond to $H_s(x)$ for $\uparrow H_e$ (Case 4*i*) or $\downarrow H_e$ (Case 5*i*) between 0 and H_m. Note that the horizonal coordinate is either x or ξ, measured, respectively, from the left-hand end or the right-hand end of the slab.

DISCUSSION 7.2: Bean Slab Carrying DC Current (continuation)

Cases 4i and 5i—"Large" Field Excitation

Next, we examine $H_s(x)$ plots for Cases 4*i* and 5*i*, shown in Fig. 7.16, in which H_m is "large," i.e., $H_m \geq 2H_p(1-i)$. Again, both x- and ξ-axes are used. In each graph, the dotted and dashed lines correspond to $H_s(x)$, respectively, at the start and end of a field sequence. Graph (a) is for Case 4*i* *after* the field sequence $H_e(t) = -H_m \rightarrow 0$. From the beginning field penetrates the slab fully, from both sides, $H_m > H_p(1-i)$. Here, $\ell^* = a(1-i)$ on the x-axis or $\ell^* = a(1+i)$ on the ξ-axis; the solid lines are for $H_s(x)$ at $0 < \uparrow H_e < H_m$, and this field distribution remains the same for $0 \leq H_e \leq H_m$.

Graph (b) is for Case 5*i*, a decreasing field sequence, in which $\downarrow H_e$ does not penetrate the slab fully until it is decreased from H_m to H_m^*, which is given by: $H_m^* = H_m - 2H_p(1-i)$. $H_s(x)$ at $\downarrow H_e = H_m^*$ is drawn by the dash-dot-dot lines; $H_s(0) = H_m^* - H_p i$, and $H_s(\xi = 0) = H_m^* + H_p i$; the dash-dot lines in the graph correspond to $H_s(x)$ for $H_m^* \leq H_e \leq H_m$.

For $\downarrow H_e^* \equiv H_e \leq H_m^*$, the field penetration is full, and the solid lines correspond to $\downarrow H_e^*$ for the remainder of the field sequence. Here, as may be inferred from graph (b), $\ell^* = a(1+i)$ on the x-axis, and $\ell^* = a(1-i)$ on the ξ-axis.

Note that $H_s(x)$ under full field penetration in Case 5*i* is a mirror image of that in Case 4*i*.

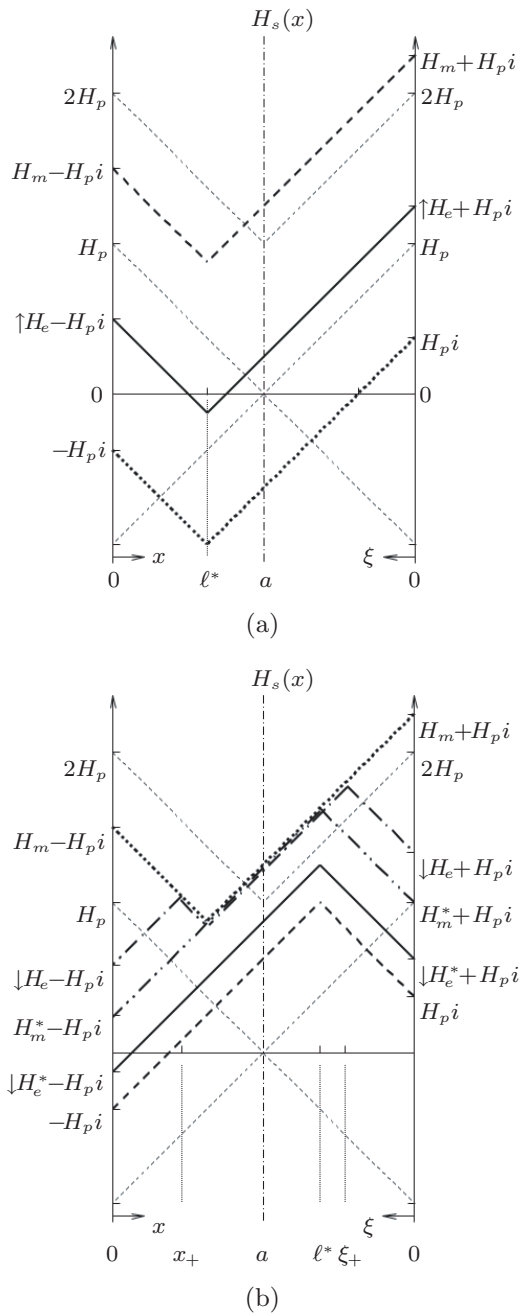

Fig. 7.16 $H_s(x)$ plots for Cases 4*i* and 5*i*, in which $H_m \geq 2H_p(1-i)$. Graph (a) for Case 4*i*, i.e., $H_e(t) = 0 \rightarrow H_m$, *after* the field sequence $H_e(t) = -H_m \rightarrow 0$; graph (b) for Case 5*i*, i.e., $H_e(t) = H_m \rightarrow 0$. In each graph the dotted and dashed lines correspond to $H_s(x)$, respectively, at the start and end of a field sequence. Note that in Case 5*i* field penetration is not full from H_m to $H_m^* \equiv H_m - 2H_p(1-i)$; it is full for the remainder of the decreasing field sequence.

PROBLEM 7.4: Hysteresis energy density—Bean slab with DC transport current (Cases 4*i*–6*i*)

Here we study hysteresis energy dissipation of a Bean slab carrying DC transport current I_t (per unit length in the y direction) subjected to a uniform magnetic field, $H_e(t)$, applied in the y direction, under time sequences of Cases 4*i*–6*i*. As discussed above, I_t may also be expressed as $H_p i$, where $i \equiv I_t/I_c$. Use the $J_c E(x)\,dt$ approach, i.e., Eq. 7.3*a*, for deriving e_{hy} expressions below.

a) Show that the hysteresis energy density for Case 4*i*, $H_e = 0 \rightarrow H_m$, for a "small" field excursion, i.e., $H_m \leq H_p(1-i)$, is given by:

$$e_{hy} = \frac{7\mu_\circ H_m^3}{24 H_p} \qquad [0 \leq H_m \leq H_p(1-i)] \tag{7.22a}$$

b) Show that the hysteresis energy density for Case 5*i*, $H_e = H_m \rightarrow 0$, after a "small" field excursion, i.e., $H_m \leq H_p(1-i)$, is given by:

$$e_{hy} = \frac{\mu_\circ H_m^3}{24 H_p} \qquad [0 \leq H_m \leq H_p(1-i)] \tag{7.22b}$$

c) Show that the hysteresis energy density for Case 6*i*, $H_e = 0 \rightarrow H_m \rightarrow 0 \rightarrow -H_m \rightarrow 0$, after a "small" field excursion, i.e., $H_m \leq H_p(1-i)$, is given by:

$$e_{hy} = \frac{2\mu_\circ H_m^3}{3 H_p} \qquad [0 \leq H_m \leq H_p(1-i)] \tag{7.22c}$$

Note that e_{hy} given by Eq. 7.22*c* is identical to e_{hy} given by Eq. 7.20*a* (p. 426) for a slab carrying no transport current: for a "small" field excursion, transport current has no effect on hysteresis dissipation.

d) Show that the hysteresis energy density for Case 4*i*, $H_e = 0 \rightarrow H_m$, for a "large" field excursion, i.e., $H_m \geq 2H_p(1-i)$, is given by:

$$e_{hy} = \tfrac{1}{2}\mu_\circ H_p H_m (1 + i^2) \qquad [H_m \geq 2H_p(1-i)] \tag{7.23a}$$

e) Show that the hysteresis energy density for Case 5*i*, $H_e = H_m \rightarrow 0$, after a "large" field excursion, i.e., $H_m \geq 2H_p(1-i)$, is given by:

$$e_{hy} = \tfrac{1}{2}\mu_\circ H_p H_m (1 + i^2) - \tfrac{2}{3}\mu_\circ H_p^2 (1 - i^3) \quad [H_m \geq 2H_p(1-i)] \tag{7.23b}$$

f) Show that the hysteresis energy density for Case 6*i*, $H_e = 0 \rightarrow H_m \rightarrow 0 \rightarrow -H_m \rightarrow 0$, after a "large" field excursion, i.e., $H_m \geq 2H_p(1-i)$, is given by:

$$e_{hy} = 2\mu_\circ H_p H_m (1 + i^2) - \tfrac{4}{3}\mu_\circ H_p^2 (1 - i^3) \quad [H_m \geq 2H_p(1-i)] \tag{7.23c}$$

g) Show that Eq. 7.23*c* with $i = 0$—zero transport current—reduces to Eq. 7.20*c* (p. 428), an expression for e_{hy} with no transport current in the slab.

Solution to PROBLEM 7.4

a) We first derive e_{hyx}, the hysteresis energy density in the "x" side of the slab, $H_s(x)$; $H_s(0) = \uparrow H_e - H_p i$, as shown in Fig. 7.15a. Inside the slab between $x = 0$ and $x = x_+$, with $x_+ = (H_m + H_e)/2J_c$, $E_z(x)$ due to this field change, dH_e/dt, may be given by:

$$E_z(x) = \mu_\circ \frac{dH_e}{dt}(x_+ - x) \tag{S4.1a}$$

$$E_z(x)\, dt = \mu_\circ (x_+ - x)\, dH_e \tag{S4.1b}$$

Combining Eqs. $S4.1b$ and $7.3a$, we have for the half-slab, $0 \le x \le a$:

$$e_{hyx} = \frac{1}{2a}\int_0^a \left[\int J_c E(x)\, dt\right] dx \tag{7.3a}$$

$$= \frac{\mu_\circ J_c}{2a}\int_0^{H_m}\left[\int_0^{x_+}(x_+ - x)\, dx\right] dH_e \tag{S4.2a}$$

Inserting $x_+ = (H_m + H_e)/2J_c$ into Eq. $S4.2a$ and performing the integration, we obtain:

$$e_{hyx} = \frac{7\mu_\circ H_m^3}{48 H_p} \tag{S4.2b}$$

Next, we derive $e_{hy\xi}$, the hysteresis energy density in the "ξ" side of the slab, $H_s(\xi)$; $H_s(0) = \uparrow H_e + H_p i$, as shown in Fig. 7.15a. With $\xi_+ = (H_m + H_e)/2J_c$, it is quite clear that $e_{hy\xi} = e_{hyx}$ and hence $e_{hy} = 2e_{hyx}$. Thus:

$$e_{hy} = \frac{7\mu_\circ H_m^3}{24 H_p} \qquad [0 \le H_m \le H_p(1 - i)] \tag{7.22a}$$

b) We consider the "x" side of the slab. Similar to Eq. $S4.2a$, e_{hyx} is given by:

$$e_{hyx} = \frac{\mu_\circ J_c}{2a}\int_{H_m}^0 \left[\int_0^{x_+}(x - x_+)\, dx\right] dH_e \tag{S4.3a}$$

where, in this decreasing field sequence, $x_+ = (H_m - H_e)/2J_c$. Thus:

$$e_{hyx} = -\frac{\mu_\circ J_c}{4a}\int_{H_m}^0 x_+^2\, dH_e = -\frac{\mu_\circ}{16 H_p}\int_{H_m}^0 (H_m - H_e)^2 dH_e \tag{S4.3b}$$

$$= \frac{\mu_\circ H_m^3}{48 H_p} \tag{S4.3c}$$

Again, the hysteresis energy density in the ξ side of the slab, $e_{hy\xi}$, is the same as e_{hyx}. Therefore e_{hy} for this case is *twice* e_{hyx} given by Eq. $S4.3c$:

$$e_{hy} = \frac{\mu_\circ H_m^3}{24 H_p} \qquad [0 \le H_m \le H_p(1 - i)] \tag{7.22b}$$

Solution to PROBLEM 7.4 (continuation)

c) e_{hy} for Case 6*i* is the sum of e_{hy} for Case 4*i* and e_{hy} for Case 5*i* *multiplied by 2* to include those for the field sequences $H_e(t)=0\rightarrow -H_m$ and $H_e(t)=-H_m\rightarrow 0$:

$$e_{hy} = 2\times\left(\frac{7\mu_\circ H_m^3}{24H_p}+\frac{\mu_\circ H_m^3}{24H_p}\right) \qquad (S4.4)$$

From Eq. *S*4.4 we obtain:

$$e_{hy} = \frac{2\mu_\circ H_m^3}{3H_p} \qquad [0\le H_m\le H_p(1-i)] \qquad (7.22c)$$

Note that, as stated above, for a "small" field excursion, i.e., $H_m\le H_p(1-i)$, e_{hy} is independent of transport current flowing in the slab.

d) We first consider the "x" side of the slab. Similar to Eq. *S*4.2*a*, we have:

$$e_{hyx} = \frac{\mu_\circ J_c}{2a}\int_0^{H_m}\left[\int_0^{\ell^*}(\ell^*-x)\,dx\right]dH_e \qquad (S4.5a)$$

where, measured from $x=0$, $\ell^*=a(1-i)$. Thus:

$$e_{hyx} = \frac{\mu_\circ J_c a^2(1-i)^2}{4a}\int_0^{H_m} dH_e = \tfrac{1}{4}\mu_\circ H_p H_m(1-i)^2 \qquad (S4.5b)$$

Next, we consider the "ξ" side of the slab. Similar to Eq. *S*4.2*a*, we have:

$$e_{hy\xi} = \frac{\mu_\circ J_c}{2a}\int_0^{H_m}\left[\int_0^{\ell^*}(\ell^*-\xi)\,d\xi\right]dH_e \qquad (S4.6a)$$

where, measured from $\xi=0$, $\ell^*=a(1+i)$. Thus:

$$e_{hy\xi} = \frac{\mu_\circ J_c a^2(1+i)^2}{4a}\int_0^{H_m} dH_e = \tfrac{1}{4}\mu_\circ H_p H_m(1+i)^2 \qquad (S4.6b)$$

Because $e_{hy}=e_{hyx}+e_{hy\xi}$, combining Eqs. *S*4.5*b* and *S*4.6*b*, we obtain:

$$e_{hy} = \tfrac{1}{2}\mu_\circ H_p H_m(1+i^2) \qquad [H_m\ge 2H_p(1-i)] \qquad (7.23a)$$

e) For a decreasing field sequence, Case 5*i*, we first consider the range between H_m and $H_m{*}\equiv H_m-2H_p(1-i)$. Considering the "$x$" side of the slab, we have:

$$e_{hyx} = \frac{\mu_\circ J_c}{2a}\int_{H_m}^{H_m^*}\left[\int_0^{x_+}(x-x_+)\,dx\right]dH_e \qquad (S4.7a)$$

where, in this decreasing field sequence, $x_+=(H_m-H_e)/2J_c$. Thus:

$$\begin{aligned} e_{hyx} &= \frac{\mu_\circ J_c}{4a}\int_{H_m^*}^{H_m}\left(\frac{H_m-H_e}{2J_c}\right)^2 dH_e \qquad (S4.7b)\\ &= \frac{\mu_\circ}{16H_p}(H_m^2H_e - H_mH_e^2+\tfrac{1}{3}H_e^3)\Big|_{H_m-2H_p(1-i)}^{H_m}\\ &= \tfrac{1}{6}\mu_\circ H_p^2(1-i)^3 \end{aligned}$$

Solution to PROBLEM 7.4 (continuation)

From Fig. 7.16a it is quite clear that $e_{hyx} = e_{hy\xi}$, and thus for $H_e = H_m \rightarrow H_m - 2H_p(1-i)$, e_{hy} is given by:

$$e_{hy} = \tfrac{1}{3}\mu_\circ H_p^2(1-i)^3 \qquad (S4.7c)$$

Next, we consider the sequence $H_e = H_m^* \rightarrow 0$. In the "$x$" side, we have:

$$e_{hyx} = \frac{\mu_\circ J_c}{2a}\int_{H_m^*}^{0}\left[\int_0^{x_+}(x-x_+)\,dx\right]dH_e = -\frac{\mu_\circ H_p(1+i)^2}{4}\int_{H_m^*}^{0} dH_e$$

$$= \tfrac{1}{4}\mu_\circ H_p(1+i)^2[H_m - 2H_p(1-i)]$$

$$= \tfrac{1}{4}\mu_\circ H_p H_m(1+i)^2 - \tfrac{1}{2}\mu_\circ H_p^2(1+i)^2(1-i) \qquad (S4.8a)$$

In the ξ side we find $e_{hy\xi}$ to be very similar to that given by Eq. $S4.8a$:

$$e_{hy\xi} = \tfrac{1}{4}\mu_\circ H_p H_m(1-i)^2 - \tfrac{1}{2}\mu_\circ H_p^2(1-i)^3 \qquad (S4.8b)$$

In the range from $H_m - 2H_p(1-i)$ to 0, we have: $e_{hy} = e_{hyx} + e_{hy\xi}$; combining Eqs. $S4.8a$ and $S4.8b$, we obtain:

$$e_{hy} = \tfrac{1}{2}\mu_\circ H_p H_m(1+i^2) - \mu_\circ H_p^2(1-i)(1+i^2) \qquad (S4.8c)$$

e_{hy} for Case $5i$ is given by the sum of those given by Eqs. $S4.7c$ and $S4.8c$:

$$e_{hy} = \tfrac{1}{2}\mu_\circ H_p H_m(1+i^2) - \tfrac{2}{3}\mu_\circ H_p^2(1-i^3) \quad [H_m \geq H_p(1-i)] \qquad (7.23b)$$

f) e_{hy} for Case $6i$, $H_m \geq H_p(1-i)$, is the sum of e_{hy} for Case $4i$ and e_{hy} for Case $5i$ *multiplied by 2* to include those for the field sequences $H_e(t) = 0 \rightarrow -H_m$ and $H_e(t) = -H_m \rightarrow 0$:

$$e_{hy} = 2 \times \left[\tfrac{1}{2}\mu_\circ H_p H_m(1+i^2) + \tfrac{1}{2}\mu_\circ H_p H_m(1+i^2) - \tfrac{2}{3}\mu_\circ H_p^2(1-i^3)\right] \qquad (S4.9)$$

From Eq. $S4.9$ we obtain:

$$e_{hy} = 2\mu_\circ H_p H_m(1+i^2) - \tfrac{4}{3}\mu_\circ H_p^2(1-i^3) \quad [H_m \geq H_p(1-i)] \qquad (7.23c)$$

g) By inserting $i = 0$ to Eq. $7.23c$, we find:

$$e_{hy} = 2\mu_\circ H_p H_m - \tfrac{4}{3}\mu_\circ H_p^2 \qquad (S4.10)$$

We note that Eq. $S4.10$ is equivalent to Eq. $7.20b$:

$$e_{hy} = 2\mu_\circ H_p H_m\left(1 - \frac{2H_p}{3H_m}\right) \qquad (7.20b)$$

PROBLEM 7.5: Self-field hysteresis energy density—Bean slab

When a Bean slab carries a cyclic AC transport current, $I(t)$, it dissipates energy because of a cyclic AC surface (external) field, $H_e(t)$, generated on the slab by the transport current. This dissipation, per unit volume, is known as self-field hysteresis energy density, e_{sf}. The current-time sequence is given by:

$$I(t) = 0^*(\text{Virgin slab}) \rightarrow I_m \rightarrow 0 \rightarrow -I_m \rightarrow \overbrace{0 \rightarrow \underbrace{I_m \rightarrow 0}_{\text{CASE 2}sf} \rightarrow -I_m \rightarrow 0}^{\text{CASE 1}sf} \qquad (7.25)$$

$$\underbrace{\qquad\qquad\qquad\qquad\qquad\qquad\qquad\qquad}_{\text{CASE 3}sf}$$

In Eq. 7.25 I_m is the amplitude of the cyclic AC current. Note that in Cases 1*sf*–3*sf* considered here the slab is no longer virgin. Figure 7.17 shows $H_s(x)$ plots for a Bean slab of width $2a$, in which graphs (a) and (b) correspond, respectively, to Cases 1*sf*, $i(t) = 0 \rightarrow i_m$, and 2*sf*, $i(t) = i_m \rightarrow 0$, where $i \equiv I/I_c \leq i_m \equiv I_m/I_c \leq 1$. As seen in each graph, $H_s(x)$ is antisymmetric about the slab's midpoint: to derive expressions of e_{hy} below, consider only one half of the slab, from $x = 0$ to $x = a$.

a) Applying Eq. 7.3*a* (p. 402), show that e_{sf} for Case 1*sf* is given by:

$$e_{sf} = \tfrac{7}{24}\mu_\circ H_p^2 i_m^3 \qquad (7.26a)$$

b) Applying Eq. 7.3*a*, show that e_{sf} for Case 2*sf* is given by:

$$e_{sf} = \tfrac{1}{24}\mu_\circ H_p^2 i_m^3 \qquad (7.26b)$$

c) Applying Eq. 7.3*a*, show that e_{sf} for Case 3*sf* is given by:

$$e_{sf} = \tfrac{2}{3}\mu_\circ H_p^2 i_m^3 \qquad (7.26c)$$

d) Derive Eq. 7.26*c* from Eq. 7.20*a* (p. 426), e_{hy} valid for Case 6 ("small").

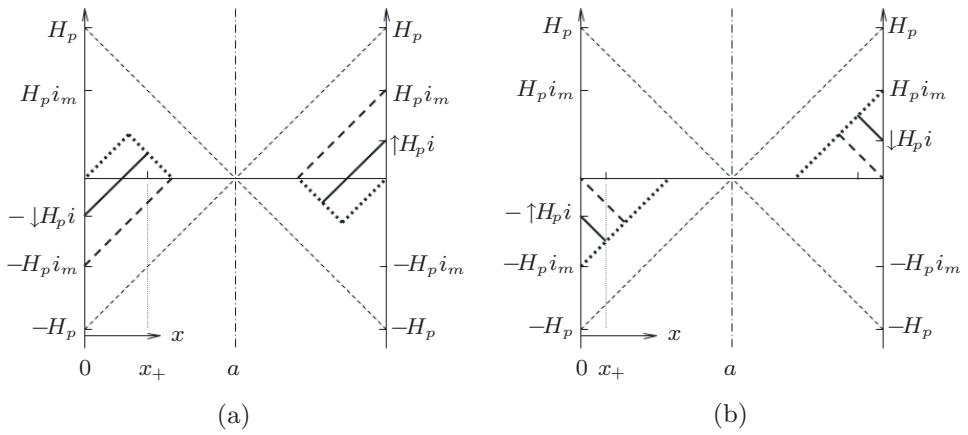

Fig. 7.17 $H_s(x)$ plots for Cases 1*sf* and 2*sf*, in which $i \equiv I/I_c \leq i_m \equiv I_m/I_c \leq 1$. Graph (a) for Case 1*sf*; graph (b) for Case 2*sf*. In each graph the dotted and dashed lines correspond to $H_s(x)$, respectively, at the start and end of a current sequence.

Solution to PROBLEM 7.5

a) For Case 1*sf* we apply Eq. 7.3*a* to one half of the slab, $0 \le x \le a$, as transport current is increased from 0 to i_m and the self field at $x=0$, H_{sf}, is *decreased* from 0 to $-H_p i_m$:

$$e_{sf\,x} = \frac{\mu_\circ J_c}{2a} \int_0^{-H_p i_m} \left[\int_0^{x_+} (x - x_+)\, dx \right] dH_{sf} \tag{S5.1a}$$

$$= \frac{\mu_\circ J_c}{4a} \int_0^{-H_p i_m} (-x_+^2)\, dH_{sf} \tag{S5.1b}$$

Substituting $H_{sf} = -H_p i$ into Eq. *S*5.1*b* and, with $x_+ = H_p(i_m + i)/2J_c$, we obtain:

$$e_{sf\,x} = \frac{\mu_\circ H_p^2}{16} \int_0^{i_m} (i_m^2 + 2 i_m i + i^2) di \tag{S5.2a}$$

$$= \tfrac{7}{48} \mu_\circ H_p^2 i_m^3 \tag{S5.2b}$$

Because the same dissipation energy density is generated over the other half of the slab, $a \le x \le 2a$, e_{sf} for Case 1*sf* is twice $e_{sf\,x}$:

$$e_{sf} = \tfrac{7}{24} \mu_\circ H_p^2 i_m^3 \tag{7.26a}$$

b) Similarly to Case 1*sf*, for Case 2*sf* we have, with $x_+ = H_p(i_m - i)/2J_c$:

$$e_{sf\,x} = \frac{\mu_\circ J_c}{2a} \int_{-H_p i_m}^{0} \left[\int_0^{x_+} (x_+ - x)\, dx \right] dH_{sf} \tag{S5.3a}$$

$$= \frac{\mu_\circ H_p^2}{16} \int_{i_m}^{0} (i_m^2 - 2 i_m i + i^2) di \tag{S5.3b}$$

$$= \tfrac{1}{48} \mu_\circ H_p^2 i_m^3 \tag{S5.3c}$$

Thus, e_{sf} for Case 2*sf* is twice $e_{sf\,x}$ given by Eq. *S*5.3*c*:

$$e_{sf} = \tfrac{1}{24} \mu_\circ H_p^2 i_m^3 \tag{7.26b}$$

c) For Case 3*sf* e_{hy} is the sum of those of Cases 1*sf* and 2*sf* multiplied by 2, because Case 3*sf* covers a full cycle, $i(t) = 0 \to i_m \to 0 \to -i_m \to 0$:

$$e_{sf} = 2 \times \left(\tfrac{7}{24} \mu_\circ H_p^2 i_m^3 + \tfrac{1}{24} \mu_\circ H_p^2 i_m^3 \right) \tag{S5.4}$$

Equation *S*5.4 reduces to:

$$e_{sf} = \tfrac{2}{3} \mu_\circ H_p^2 i_m^3 \tag{7.26c}$$

Solution to PROBLEM 7.5 (continuation)

d) For hysteresis energy density computations the field profiles shown in Fig. 7.17 are identical with those shown in Fig. 7.4a, which correspond to Case 4 ("small" field), when $H_p i_m$ in Fig. 7.17 is substituted for H_m. Thus:

$$e_{hy} = \frac{2\mu_\circ H_m^3}{3H_p} \tag{7.20a}$$

$$= \frac{2\mu_\circ (H_p i_m)^3}{3H_p}$$

$$= \tfrac{2}{3}\mu_\circ H_p^2 i_m^3 \tag{7.26c}$$

Tables Summarizing Formulas for AC Losses

Expressions of AC energy density derived above, in **PROBLEMS 7.1–7.5** and ***DISCUSSIONS 7.1*** and ***7.2***, for Bean slab of width $2a$ (Fig. 7.1a) as well as those available in the literature for circular-cross-section conductor (Figs. 7.1b and 7.1c) and tape (Figs. 7.1d and 7.1e) are summarized in the tables below. *Italic equation numbers* are those equations derived by others [1.27, 7.3, 7.5, 7.13, 7.15].

Table 7.3A: Hysteresis energy density, e_{hy}, for Bean slab, no transport current.

Table 7.3B: e_{hy} for Bean slab, with DC transport current.

Table 7.4: Self-field energy density, e_{sf}, for Bean slab.

Table 7.5: e_{hy}, for wire and tape, no transport current.

Table 7.6: e_{sf} for wire and tape.

Table 7.7: Energy density, e_{ih}, for Bean slab, with sinusoidal in-phase current and field excitation.

Table 7.8: Coupling energy density, e_{py}, for multifilamentary wire under sinusoidal, exponential, triangular, or trapezoidal field excitation, as defined and illustrated in Fig. 7.18.

Table 7.9: Eddy-current energy density, e_{ed}, for wire and tape.

Sinusoidal: $H_e(t) = H_m \sin(2\pi t/\tau_m)$ Exponential: $H_e(t) = H_m \exp(-t/\tau_m)$

Triangular: Trapezoidal:

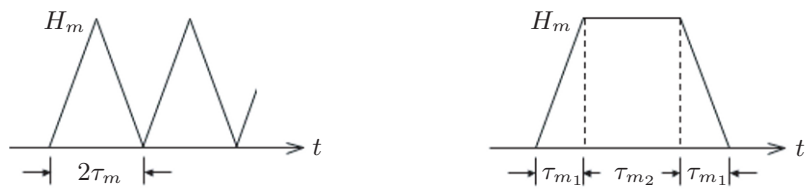

Fig. 7.18 $H_e(t)$ functions for coupling and eddy-current energy densities.

Table 7.3A: Hysteresis Energy Density, e_{hy} [J/m^3]—Bean Slab (Width: $2a$)
No Transport Current

$$H_e(t) = \overbrace{\underbrace{0^*(\text{Virgin slab}) \rightarrow \underbrace{H_m \rightarrow 0}_{\text{CASE 2}}}_{\text{CASE 3}} \rightarrow -H_m \rightarrow \overbrace{\underbrace{0 \rightarrow \underbrace{H_m \rightarrow 0}_{\text{CASE 5}}}_{\text{CASE 6}} \rightarrow -H_m \rightarrow 0}^{\text{CASE 4}}}^{\text{CASE 1}} \tag{7.5}$$

Case 1

$$e_{hy} = \frac{\mu_\circ H_m^3}{6H_p} \qquad (0 \le H_m \le H_p) \tag{7.13a}$$

$$e_{hy} = \tfrac{1}{2}\mu_\circ H_p H_m \left(1 - \frac{2H_p}{3H_m}\right) \qquad (H_m \ge H_p) \tag{7.13b}$$

Cases 2 ***and*** 5

$$e_{hy} = \frac{\mu_\circ H_m^3}{24H_p} \qquad (0 \le H_m \le 2H_p) \tag{7.14a}$$

$$e_{hy} = \tfrac{1}{2}\mu_\circ H_p H_m \left(1 - \frac{4H_p}{3H_m}\right) \qquad (H_m \ge 2H_p) \tag{7.14b}$$

Case 3

$$e_{hy} = \frac{5\mu_\circ H_m^3}{24H_p} \qquad (0 \le H_m \le H_p) \tag{7.15a}$$

$$e_{hy} = \tfrac{1}{2}\mu_\circ H_p H_m \left[1 - \frac{2H_p}{3H_m} + \tfrac{1}{12}\left(\frac{H_m}{H_p}\right)^2\right] \qquad (H_p \le H_m \le 2H_p) \tag{7.15b}$$

$$e_{hy} = \mu_\circ H_p H_m \left(1 - \frac{H_p}{H_m}\right) \qquad (H_m \ge 2H_p) \tag{7.15c}$$

Case 4

$$e_{hy} = \frac{7\mu_\circ H_m^3}{24H_p} \qquad (0 \le H_m \le H_p) \tag{7.19a}$$

$$e_{hy} = \mu_\circ H_p H_m \left[1 - \frac{2H_p}{3H_m} - \tfrac{1}{24}\left(\frac{H_m}{H_p}\right)^2\right] \qquad (H_p \le H_m \le 2H_p) \tag{7.19b}$$

$$e_{hy} = \tfrac{1}{2}\mu_\circ H_p H_m \qquad (H_m \ge 2H_p) \tag{7.19c}$$

Case 6

$$e_{hy} = \frac{2\mu_\circ H_m^3}{3H_p} \qquad (0 \le H_m \le H_p) \tag{7.20a}$$

$$e_{hy} = 2\mu_\circ H_p H_m \left(1 - \frac{2H_p}{3H_m}\right) \qquad (H_p \le H_m \le 2H_p) \tag{7.20b}$$

$$e_{hy} = 2\mu_\circ H_p H_m \left(1 - \frac{2H_p}{3H_m}\right) \qquad (H_m \ge 2H_p) \tag{7.20c}$$

$$e_{hy} = 2\mu_\circ H_p H_m \qquad (H_m \gg H_p) \tag{7.20d}$$

$$e_{hy} = 2\mu_\circ J_c a H_m \qquad (H_m \gg H_p) \tag{7.20e}$$

Table 7.3B: Hysteresis Energy Density, e_{hy} [J/m^3]—Bean Slab (Width: $2a$)
With DC Transport Current I_t $(i = I_t/I_c)$

$$H_e(t) = \overbrace{\underbrace{0^*(\text{Virgin slab}) \to \overbrace{H_m \to 0}^{\text{CASE 2}i} \to -H_m \to 0 \to \overbrace{H_m \to 0}^{\text{CASE 5}i} \to -H_m \to 0}_{\text{CASE 6}i}}^{\text{CASE 4}i}}^{\text{CASE 1}i \text{ CASE 3}i} \qquad (7.5)$$

Cases 1i–3i

Only $H_s(x)$ profiles for Cases 1i and 2i are studied—see Figs. 7.14 and 7.15.

Case 4i

$$e_{hy} = \frac{7\mu_\circ H_m^3}{24 H_p} \qquad [0 \le H_m \le H_p(1-i)] \qquad (7.22a)$$

$$e_{hy} = \tfrac{1}{2}\mu_\circ H_p H_m (1 + i^2) \qquad [H_m \ge 2H_p(1-i)] \qquad (7.23a)$$

Case 5i

$$e_{hy} = \frac{\mu_\circ H_m^3}{24 H_p} \qquad [0 \le H_m \le H_p(1-i)] \qquad (7.22b)$$

$$e_{hy} = \tfrac{1}{2}\mu_\circ H_p H_m (1 + i^2) - \tfrac{2}{3}\mu_\circ H_p^2 (1 - i^3) \qquad [H_m \ge 2H_p(1-i)] \qquad (7.23b)$$

Case 6i

$$e_{hy} = \frac{2\mu_\circ H_m^3}{3 H_p} \qquad [0 \le H_m \le H_p(1-i)] \qquad (7.22c)$$

$$e_{hy} = 2\mu_\circ H_p H_m (1 + i^2) - \tfrac{4}{3}\mu_\circ H_p^2 (1 - i^3) \qquad [H_m \ge 2H_p(1-i)] \qquad (7.23c)$$

Table 7.4: Self-Field Hysteresis Energy Density, e_{sf} [J/m^3]
Bean Slab (Width: $2a$)

$$I_t(t) = 0^*(\text{Virgin slab}) \to I_m \to 0 \to -I_m \to \underbrace{0 \to \overbrace{I_m \to 0}^{\text{CASE 2}sf} \to -I_m \to 0}_{\text{CASE 3}sf}^{\text{CASE 1}sf} \qquad (7.25)$$

$i_m = I_m/I_c$

Case 1sf

$$e_{sf} = \tfrac{7}{24}\mu_\circ H_p^2 i_m^3 \qquad (7.26a)$$

Case 2sf

$$e_{sf} = \tfrac{1}{24}\mu_\circ H_p^2 i_m^3 \qquad (7.26b)$$

Case 3sf

$$e_{sf} = \tfrac{2}{3}\mu_\circ H_p^2 i_m^3 \qquad [0 \le H_m \le H_p(1-i)] \qquad (7.26c)$$

Table 7.5: Hysteresis Energy Density, e_{hy} [J/m^3]—*No Transport Current*
Wire (Diameter: d_f) [1.27, 7.14] & Tape (Width: w; Thickness: δ) [1.27, 7.13]

$$H_{e\parallel}(t) \text{ or } H_{e\perp}(t) = \underbrace{Virgin\, 0^* \rightarrow H_m \rightarrow 0 \rightarrow -H_m \rightarrow}_{\text{HISTORY}}\ \underbrace{0 \rightarrow H_m \rightarrow 0 \rightarrow -H_m \rightarrow 0}_{\text{LOSS CYCLE}}$$

Wire

Field Parallel to Wire Axis (Fig. 7.1b): $H_p \equiv J_c(d_f/2)$

$$e_{hy} = \tfrac{4}{3}\frac{\mu_\circ H_m^3}{H_p} - \tfrac{2}{3}\frac{\mu_\circ H_m^4}{H_p^2} \qquad (0 \le H_m \le H_p) \tag{7.27a}$$

$$e_{hy} = \tfrac{4}{3}\mu_\circ H_p H_m - \tfrac{2}{3}\mu_\circ H_p^2 \qquad (H_m \ge H_p) \tag{7.27b}$$

$$e_{hy} \simeq \tfrac{4}{3}\mu_\circ H_p H_m \qquad (H_m \gg H_p) \tag{7.27c}$$

Field Perpendicular to Wire Axis (Fig. 7.1c): $H_p \equiv J_c(4d_f/3\pi)$

$$e_{hy} = \tfrac{8}{3}\frac{\mu_\circ H_m^3}{H_p} - \tfrac{4}{3}\frac{\mu_\circ H_m^4}{H_p^2} \qquad (0 \le H_m \le H_p) \tag{7.28a}$$

$$e_{hy} = \tfrac{8}{3}\mu_\circ H_p H_m - \tfrac{4}{3}\mu_\circ H_p^2 \qquad (H_m \ge H_p) \tag{7.28b}$$

$$e_{hy} \simeq \tfrac{8}{3}\mu_\circ H_p H_m \qquad (H_m \gg H_p) \tag{7.28c}$$

Tape

Field Parallel to Tape Surface (Fig. 7.1d):* $H_p \equiv J_c(\delta/2)$

*same as Bean Slab ***Case 1*** (Table 7.3A)

$$e_{hy} = \tfrac{2}{3}\frac{\mu_\circ H_m^3}{H_p} \qquad (0 \le H_m \le H_p) \tag{7.29a}$$

$$e_{hy} = 2\mu_\circ H_p H_m \left(1 - \frac{2H_p}{3H_m}\right) \qquad (H_m \ge H_p) \tag{7.29b}$$

$$e_{hy} \simeq 2\mu_\circ H_p H_m \qquad (H_m \gg H_p) \tag{7.29c}$$

$$e_{hy} \simeq \mu_\circ J_c \delta H_m \qquad (H_m \gg H_p) \tag{7.29d}$$

Field Perpendicular to Tape Surface (Fig. 7.1e): $H_p \equiv J_c(w/2)$

$$e_{hy} = \mu_\circ H_m H_p \left(\frac{w}{\delta}\right)\left[\frac{2}{\theta}\ln(\cosh\theta) - \tanh\theta\right] \quad (\theta \equiv H_m/H_p) \tag{7.30a}$$

$$e_{hy} \simeq \tfrac{1}{6}\mu_\circ H_m H_p \left(\frac{w}{\delta}\right)\theta^3 \simeq \tfrac{1}{6}\mu_\circ H_m^2 \left(\frac{H_m}{H_p}\right)^2\left(\frac{w}{\delta}\right) \quad (0 \le H_m \ll H_p) \tag{7.30b}$$

$$\simeq \mu_\circ H_p \left(\frac{w}{\delta}\right)(H_m - 2H_p \ln 2) \simeq \mu_\circ H_m H_p \left(\frac{w}{\delta}\right) \quad (H_m \gg H_p) \tag{7.30c}$$

TRIVIA 7.2 Which of the contemporary American engineers (born 1846–1856) below was a pigeon fancier?

i) Bell; ii) Edison; iii) Tesla; iv) Westinghouse.

Table 7.6: Self-Field Energy Density, e_{sf} [J/m^3]—Wire & Tape [1.27, 7.14]

$$I_t(t) = \underbrace{Virgin\, 0^* \rightarrow I_m \rightarrow 0 \rightarrow -I_m \rightarrow}_{\text{HISTORY}}\ \underbrace{0 \rightarrow I_m \rightarrow 0 \rightarrow -I_m \rightarrow 0}_{\text{LOSS CYCLE}} \qquad (i_m \equiv I_m/I_c)$$

Wire (Diameter: d_f; Figs. 7.1b & 7.1c)

$$e_{sf} = \frac{\mu_\circ I_c J_c}{\pi}\left[i_m - \tfrac{1}{2}i_m^2 + (1-i_m)\ln(1-i_m)\right] \tag{7.31a}$$

$$\simeq \frac{\mu_\circ I_c J_c}{\pi}\left(\frac{i_m^3}{6} + \frac{i_m^4}{12}\right) \simeq \frac{\mu_\circ J_c I_m^3}{6\pi I_c^2} \propto \frac{I_m^3}{J_c d_f^4} \qquad (0 \le i_m \ll 1) \tag{7.31b}$$

Tape (Width: w; Thickness: δ; Figs. 7.1d & 7.1e)

$$e_{sf} = \frac{\mu_\circ I_c J_c}{\pi}\left[(1-i_m)\ln(1-i_m) + (1+i_m)\ln(1+i_m) - i_m^2\right] \tag{7.32a}$$

$$\simeq \frac{\mu_\circ I_c J_c}{\pi}\left(\frac{i_m^4}{6} + \frac{i_m^6}{15}\right) \simeq \frac{\mu_\circ I_c J_c}{\pi}\left(\frac{i_m^4}{6}\right) \propto \frac{I_m^4}{J_c^2 w^3 \delta^3} \quad (0 \le i_m \ll 1) \tag{7.32b}$$

$$I_t(t) = \underbrace{Virgin\, 0^* \rightarrow I_m \rightarrow}_{\text{HISTORY}}\ \underbrace{0 \rightarrow I_m \rightarrow 0}_{\text{LOSS CYCLE}}$$

Wire (Diameter: d_f; Figs. 7.1b & 7.1c)

$$e_{sf} = \frac{\mu_\circ I_c J_c}{\pi}\left[4i_m - i_m^2 + 4(2-i_m)\ln\left(\frac{2-i_m}{2}\right)\right] \tag{7.33a}$$

$$\simeq \frac{\mu_\circ I_c J_c}{\pi}\left(\frac{i_m^3}{6} + \frac{i_m^4}{24}\right) \simeq \frac{\mu_\circ J_c I_m^3}{6\pi I_c^2} \propto \frac{I_m^3}{J_c d_f^4} \qquad (0 \le i_m \ll 1) \tag{7.33b}$$

Table 7.7: Energy Density, e_{ih} [J/m^3]—Bean Slab (Width: $2a$) [7.5]
In-Phase Sinusoidal Transport Current & Field
$I_t(t) = I_m \sin(2\pi f t)$; $\quad H_e(t) = H_m \sin(2\pi f t)$

$$e_{ih} = 2\mu_\circ H_p^2\left(\frac{H_p^2 i_m^3}{2H_m^2} + i_m\right) \qquad (0 \le H_m \le H_p) \tag{7.34a}$$

$$\simeq \frac{\mu_\circ H_p^4}{H_m^2} i_m^3 \propto \frac{I_m^3 I_c}{H_m^2} \qquad (0 \le H_m \ll H_p) \tag{7.34b}$$

$$e_{ih} = 2\mu_\circ H_p^2\left(\frac{H_m}{3H_p} + \frac{H_p i_m^2}{H_m}\right) \qquad (0 \le H_m \le H_p) \tag{7.35a}$$

$$e_{ih} = 2\mu_\circ H_p^2\left[\frac{H_p(3+i_m^2)}{3H_m} - \frac{2H_p^2(1-i_m^3)}{3H_m^2} + \frac{6H_p^3 i_m^2(1-i_m)^2}{3H_m^2(H_m - H_p i_m)}\right.$$
$$\left. + \frac{6H_p^3 i_m^2(1-i_m)^2}{3H_m^2(H_m - H_p i_m)} - \frac{4H_p^4 i_m^2(1-i_m)^3}{3H_m^2(H_m - H_p i_m)^2}\right] \qquad (H_m \ge H_p) \tag{7.35b}$$

$$\simeq \frac{2\mu_\circ H_p^3}{3H_m}(3+i_m^2) \propto \frac{I_c^3}{H_m}(3+i_m^2) \qquad (H_m \gg H_p) \tag{7.35c}$$

Table 7.8: Coupling Energy Density Over One Period, e_{cp} [J/m^3] [7.16]
Wire of Outermost Diameter, D_{mf}, Enclosing Multifilaments

$$e_{cp} = 2\mu_\circ H_m^2 \left[1+\tfrac{1}{4}\left(\frac{\pi D_{mf}}{\ell_p}\right)^2\right]\Gamma \qquad (7.36)$$

Sinusoidal: $$\Gamma = \frac{2\pi^2\tau_m\tau_{cp}}{\tau_m^2+4\pi^2\tau_{cp}^2} \qquad (7.37a)$$

$$\Gamma \simeq \frac{\tau_m}{2\tau_{cp}} \quad (\tau_m \ll \tau_{cp}) \qquad (7.37b); \qquad \Gamma \simeq \frac{2\pi^2\tau_{cp}}{\tau_m} \quad (\tau_m \gg \tau_{cp}) \qquad (7.37c)$$

Exponential: $$\Gamma = \frac{\tau_{cp}}{2(\tau_m+\tau_{cp})} \qquad (7.38)$$

Triangular: $$\Gamma = \frac{2\tau_{cp}}{\tau_m}\left[1-\frac{2\tau_{cp}}{\tau_m}\tanh\left(\frac{\tau_m}{2\tau_{cp}}\right)\right] \qquad (7.39a)$$

$$\Gamma \simeq \frac{\tau_m}{4\tau_{cp}} \quad (\tau_m \ll \tau_{cp}) \qquad (7.39b); \qquad \Gamma \simeq \frac{2\tau_{cp}}{\tau_m} \quad (\tau_m \gg \tau_{cp}) \qquad (7.39c)$$

Trapezoidal:

$$\Gamma = \frac{\tau_{cp}}{\tau_{m_1}}\left\{2+\frac{\tau_{cp}}{\tau_{m_1}}\left[1-e^{-\frac{\tau_{m_1}}{\tau_{cp}}}\right]\left[e^{-\frac{(\tau_{m_1}+\tau_{m_2})}{\tau_{cp}}}-e^{-\frac{\tau_{m_2}}{\tau_{cp}}}-2\right]\right\} \qquad (7.40a)$$

$$\Gamma \simeq 1-e^{-\frac{\tau_{m_2}}{\tau_{cp}}} \quad (\tau_{m_1} \ll \tau_{cp}) \quad (7.40b); \qquad \Gamma \simeq \frac{2\tau_{cp}}{\tau_{m_1}} \quad (\tau_{m_1} \gg \tau_{cp}) \qquad (7.40c)$$

Trapezoidal, Cyclic With a Period of $2(\tau_{m_1}+\tau_{m_2})$

$$\Gamma = \frac{2\tau_{cp}}{\tau_{m_1}}\left\{1-\frac{\left(1+e^{-\frac{\tau_{m2}}{\tau_{cp}}}\right)\left(1-e^{-\frac{\tau_{m1}}{\tau_{cp}}}\right)}{\frac{\tau_{m_1}}{\tau_{cp}}\left[1+e^{-\frac{(\tau_{m1}+\tau_{m2})}{\tau_{cp}}}\right]}\right\} \qquad (7.41a)$$

$$\Gamma \simeq 1-\frac{\tau_{m_1}}{3\tau_{cp}} \quad \begin{pmatrix}\tau_{m_1} \ll \tau_{cp}\\ \tau_{m_2} \gg \tau_{cp}\end{pmatrix} \qquad (7.41b); \qquad \Gamma \simeq \frac{2\tau_{cp}}{\tau_{m_1}} \quad \begin{pmatrix}\tau_{m_1} \gg \tau_{cp}\\ \tau_{m_2} \ll \tau_{cp}\end{pmatrix} \qquad (7.41c)$$

Table 7.9: Eddy-Current Energy Density, e_{ed} and $<e_{ed}>^*$ [J/m^3]

Wire (Diameter: d), Under $\vec{H}_e(t)=\vec{H}_{m\parallel}\sin(2\pi t/\tau_m)$ or $\vec{H}_e(t)=\vec{H}_{m\perp}\sin(2\pi t/\tau_m)$

$$<e_{ed}> = \frac{\pi^2 d^2(\mu_\circ H_{m\parallel})^2}{4\rho_m\tau_m} \qquad (7.42a); \qquad <e_{ed}> = \frac{\pi^2 d^2(\mu_\circ H_{e\perp})^2}{12\rho_m\tau_m} \qquad (7.42b)$$

Tape (Width: w; Thickness: δ; Figs. 7.1d & 7.1e); $\lambda\mathcal{H}_m \equiv \sqrt{(\delta H_{m\parallel})^2+(wH_{m\perp})^2}$

Sinusoidal: $<e_{ed}> = \dfrac{4\pi^2(\mu_\circ\lambda\mathcal{H}_m)^2}{24\rho_m\tau_m}$ (7.43a); Exponential: $e_{ed} = \dfrac{(\mu_\circ\lambda\mathcal{H}_m)^2}{24\rho_m\tau_m}$ (7.43b)

Triangular (time-averaged) & Trapezoidal: $$e_{ed} = \frac{(\mu_\circ\lambda\mathcal{H}_m)^2}{12\rho_m\tau_m} \qquad (7.43c)$$

* Time-averaged.

DISCUSSION 7.3: AC Losses for the Whole Magnet

The closed-form analytical expressions of AC loss energy densities, summarized in Tables 7.3–7.9, are valid for only the simplest superconductor configurations and conditions. First, the superconductor is an *isolated* single Bean slab, and its J_c is field-independent. Second, the external magnetic field applied is *uniform* and points in a special direction: parallel to the surfaces of a Bean slab that define its thickness ($2a$). Third, if a transport current is present, it too is under the simplest condition: DC current already present when the magnetic field is applied.

It is not possible with a closed-form analytical expression to *accurately* compute AC losses for a whole magnet. If the total AC losses of a magnet must be known, for instance, to estimate the system cryogenic load, it is best to resort to a computational technique that sums up space-dependent "local" AC losses. For a *ballpark* estimate of AC losses, e.g., the Hybrid III SCM (**PROBLEM 7.7**), the expressions in Tables 7.3–7.9 may be used, though the conductor configurations and field/current conditions are far more complicated than those used in deriving these expressions. With both time-varying field and transport current present, the expressions are not really applicable. For short samples and whole coils, the surest approach is measurement, often accompanied with numerical analysis [7.1, 7.2, 7.4, 7.61–7.85].

It should be noted, however, that the vast majority of superconducting magnets in operation now, and likely in the immediate future, are adiabatic. An adiabatic magnet, LTS or HTS, tolerates only limited AC losses that can be thermally conducted away to its surrounding surfaces with a peak winding temperature rise *less* than $[\Delta T_{op}(I_{op})]_{st}$, the temperature margin (**6.2.6**), which is generally greater in an HTS magnet than in an LTS magnet. To estimate this peak temperature, it usually is sufficient to compute the AC losses over the small winding volume where they are likely to be greatest. For this type of computation, for which great accuracy is not required, the expressions in Tables 7.3–7.9 may be applied.

DISCUSSION 7.4: Techniques to Measure AC Losses

As discussed above, *accurate* computation of AC losses for *real* superconductors, short samples as well whole magnets, is nearly impossible: the only recourse is measurement [7.61–7.103]. Basically, there are three methods for measuring AC losses: 1) magnetic; 2) calorimetric; and 3) electrical. The magnetic method is useful only for hysteresis loss of "short" samples (Eq. 7.4*b*) carrying *no* transport current (next in **PROBLEM 7.6**). In the calorimetric method, a test sample (a short length of conductor or even a whole coil) is immersed in a bath of liquid cryogen—helium for LTS and generally nitrogen for HTS—and AC losses, often under cyclic field and/or transport current conditions, are deduced from the vapor boil-off rate of the cryogen that surrounds the test sample; in a variation of this method, a slight temperature rise caused by AC losses may be used to determine the losses. In the electrical method, applicable when a test sample is subjected to a time-varying transport current, $I_t(t)$, the time-integral, $\int V(t) I_t(t)\, dt$, is measured, where $V(t)$ is the voltage across the test sample. In practice great caution must be exercised in placing voltage taps to measure $V(t)$ [7.98].

Figure 7.19 shows a schematic drawing of a cross section, based on the original drawing [7.87], of a calorimetric setup for measuring total AC dissipation of a superconducting Test Coil. In this technique Calibration Heater, placed inside Calorimeter Housing with Test Coil, is controlled to keep the rate of the boil-off vapor, measured by Vapor Flow Meter, constant as Test Coil, carrying either AC or DC transport current, is exposed to a time-varying external field, generated by Bitter Magnet. The variation in Calibration Heater input is related to the *total* AC dissipation of Test Coil. To stabilize the cryostat pressure, liquid helium is not transferred during measurement. The effluent helium vapor of Test Coil and

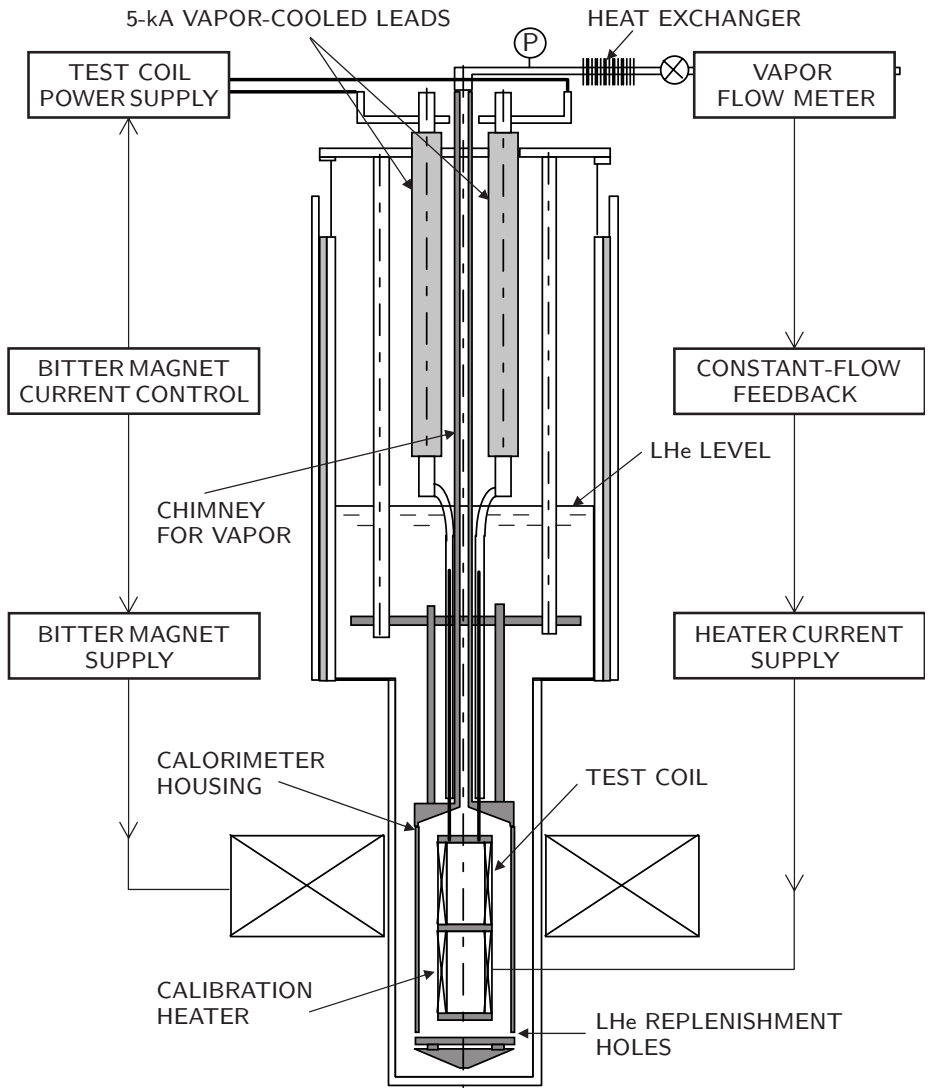

Fig. 7.19 Schematic drawing of a cross section, based on the original drawing [7.87], of a calorimeter setup for measuring total AC dissipation of a superconducting Test Coil carrying either AC or DC current and subjected to a time-varying magnetic field.

Calibration Heater, guided through Chimney, is measured, at room temperature, by Vapor Flow Meter. A set of holes at the bottom of Calorimeter Housing replenishes liquid helium to keep it filled with the liquid and at the cryostat pressure.

Illustration Total AC losses for this Test Coil were 100–500 mW [7.87, 7.88]. For the latent heat of vaporization of liquid helium at 4.22 K, $h_L = 20.9\,\text{kJ/kg}\,(\text{J/g})$; a dissipation of 100 mW at 4.22 K, for example, evaporates helium at a mass rate of 4.8 mg/s or a volumetric *liquid* (density: $0.125\,\text{g/cm}^3$) evaporation rate of $0.038\,\text{cm}^3/\text{s}$. Because under atmospheric pressure helium expands, from 4.22-K liquid to 273-K (0°C) vapor, by a factor of 700 (Table A2.1, ***APPENDIX II***), the volumetric flow rate measured by Vapor Flow Meter (Fig. 7.19) will be $28.6\,\text{cm}^3/\text{s}$ or 1596 SCCM—Standard (1 atm, 0°C) Cubic Centimeter per Minute.

DISCUSSION 7.5: AC Losses in CIC Conductors

A CIC conductor, unlike a conductor with its strands embedded in a conductive matrix, is suitable for AC applications, because its strands may be magnetically and electrically decoupled. (In this respect, so is the Rutherford cable, because its strands, mounted on a high-strength strip, may likewise be decoupled.)

As in all AC-applicable strands, the superconducting multifilaments in each strand of a CIC conductor are transposed, and each filament in turn is surrounded by a thin layer of "resistive" metal (generally Nb or Cu-Ni) barrier to minimize coupling currents that are induced under time-varying conditions. The greater the barrier resistance, the smaller will be both the "effective Bean slab thickness" and the inter-filament coupling time constant, τ_{cp} (Eq. 7.6), which result in smaller, respectively, hysteresis energy density, e_{hy}, and coupling energy density e_{cp}.

The effective matrix resistivity, ρ_{ef} (Eq. 7.7), determines the *inter-filament* coupling time constant. Similarly the *inter-strand* resistivity determines the *inter-strand* coupling time constant that in turn determines the inter-strand coupling energy density. For CIC conductors both the inter-strand resistivity (or resistance) and coupling time constant require measurement [7.104–7.107].

DISCUSSION 7.6: AC Losses in HTS

It is worth emphasizing that the mechanisms of AC losses in HTS are the same as those of AC losses in LTS. Thus, to minimize AC losses, HTS size must be minimized (hysteresis loss); superconducting filaments magnetically and electrically decoupled (coupling loss); and conductive matrix added sparingly in the superconductor (eddy-current loss), while still satisfying other requirements.

Tape is the least desirable conductor configuration to minimize hysteresis loss: Bi2223, YBCO, and MgB_2 (available in wire too) thus are not ideally suited for some AC applications. Although Bi2223 and MgB_2 tapes comprise many "mini" tapes to reduce their effective size ($2a$ of Bean slab), because these mini tapes are not twisted, let alone transposed, AC losses remain a critical issue; for YBCO ingenious, but perhaps difficult to economically achieve, conductor designs have been proposed to reduce the effective size and decouple mini tapes [7.108–7.113]. For some AC applications, HTS wires, e.g., Bi2212 and MgB_2, may fare better.

PROBLEM 7.6: Hysteresis loss in Nb_3Sn filament

In this problem we consider a Nb_3Sn conductor presently manufactured for a fusion project. Figure 7.20 shows $\mu_\circ M$ vs. $\mu_\circ H$ plots, measured at 4.2 K, for Nb_3Sn/Cu composite wires of overall bare diameters 1.0, 0.8, 0.6, 0.4, and 0.3 mm [7.114].

a) The 0.3-mmϕ wire (labeled 0.3 in Fig. 7.20) has a critical current density at 3 T and 4.2 K, $J_c(3\,\mathrm{T}, 4.2\,\mathrm{K})$, of $0.72\times10^{10}\,\mathrm{A/m^2}$. Show that within $\pm10\%$ uncertainty, its J_c at 0 T, $J_c(0\,\mathrm{T}, 4.2\,\mathrm{K})$, is $2.8\times10^{10}\,\mathrm{A/m^2}$. Note that for Nb_3Sn it is customary to assume $J_c = J_{noncu}$, the critical current density over non-copper cross sectional area.

b) Assuming filaments in these wires are of circular cross section, compute the *effective* filament diameter, d_{eff}, for the 0.3-mm wire. You may equate d_{eff} to the width $2a$ of a Bean slab.

c) The wires of diameters 0.8-mm, 0.6-mm, 0.4-mm, and 0.3-mm were all drawn from the 1.0-mm diameter wire and thus have the same number of filaments. Explain qualitatively and, if you so choose, quantitatively two important differences in magnetization curves among these wires shown in Fig. 7.20.

d) Compute the hysteresis energy density, e_{hy} [J/m^3] for the 0.3-mmϕ wire over one complete field cycle between -3 T and $+3$ T. Assume $B_p \ll 3$ T.

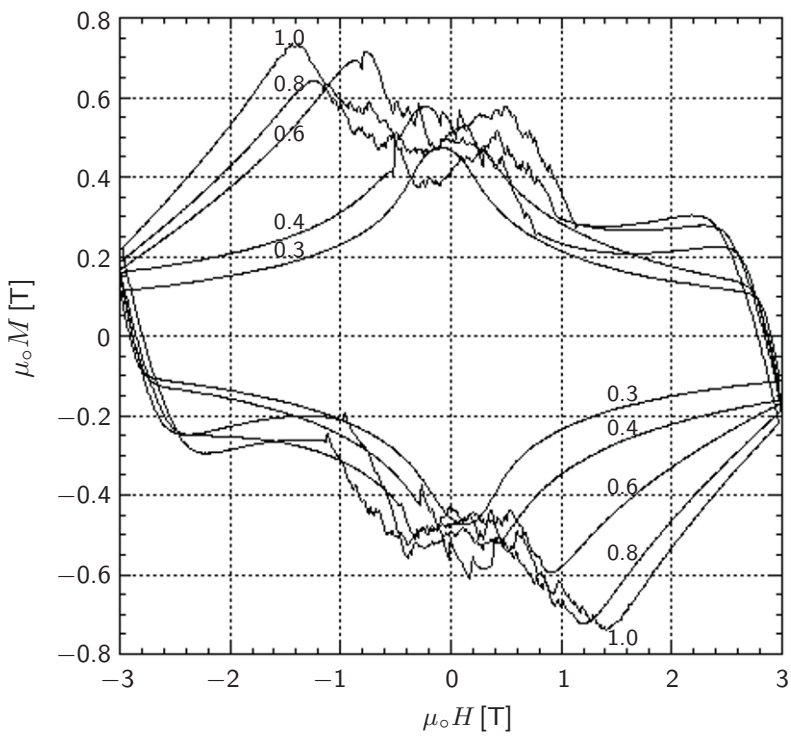

Fig. 7.20 $\mu_\circ M$ vs. $\mu_\circ H$ plots, measured at 4.2 K, for Nb_3Sn/Cu composite wires of diameters 1.0, 0.8, 0.6, 0.4, and 0.3 mm [7.114].

Solution to PROBLEM 7.6

a) The envelope of a flux-jump free $M(\mu_\circ H, T)$ curve, as illustrated in Fig. 5.3, is proportional to $J_c(\mu_\circ H, T)$. From Fig. 7.20 for the 0.3-mmϕ wire, we have: $|\mu_\circ M(0\,\mathrm{T}, 4.2\,\mathrm{K})| \simeq 0.47\,\mathrm{T}$ and $|\mu_\circ M(3\,\mathrm{T}, 4.2\,\mathrm{K})| \simeq 0.12\,\mathrm{T}$. Thus:

$$\begin{aligned} J_c(0\,\mathrm{T}, 4.2\,\mathrm{K}) &= J_c(3\,\mathrm{T}, 4.2\,\mathrm{K}) \times \left| \frac{M(0\,\mathrm{T}, 4.2\,\mathrm{K})}{M(3\,\mathrm{T}, 4.2\,\mathrm{K})} \right| \\ &\simeq J_c(3\,\mathrm{T}, 4.2\,\mathrm{K}) \times \frac{(0.47\,\mathrm{T})}{(0.12\,\mathrm{T})} \simeq J_c(3\,\mathrm{T}, 4.2\,\mathrm{K}) \times 3.92 \\ &\simeq 2.8 \times 10^{10}\,\mathrm{A/m^2} \end{aligned}$$

b) From the Bean model, for $H \geq H_p = J_c a$, $M(H) = H_p/2$, and using $a = d_{\mathit{eff}}/2$, where d_{eff} is the filament diameter, we have:

$$M(H) = \tfrac{1}{2} H_p = \tfrac{1}{2}(d_{\mathit{eff}}/2) J_c(H)$$

From Fig. 7.20 and question **a)** we have, respectively: $\mu_\circ M(0\,\mathrm{T}) \simeq 0.47\,\mathrm{T}$ and $J_c(0\,\mathrm{T}) \simeq 2.8 \times 10^{10}\,\mathrm{A/m^2}$. Thus:

$$d_{\mathit{eff}} = \frac{4\mu_\circ M(0\,\mathrm{T})}{\mu_\circ J_c(0\,\mathrm{T})} \simeq \frac{4(470 \times 10^{-3}\,\mathrm{T})}{(4\pi \times 10^{-7}\,\mathrm{H/m})(2.8 \times 10^{10}\,\mathrm{A/m^2})} = 53\,\mu\mathrm{m}$$

Note that d_{eff} may be computed at any value of H at which both $M(H)$ and $J_c(H)$ are known.

c) As may be inferred from the positive magnitudes of magnetization at $\mu_\circ H = -2\,\mathrm{T}$, the magnitude, $\propto d_{\mathit{eff}} J_c$, is nearly proportional to the overall wire size. It implies that d_{eff} decreases with wire diameter though perhaps not exactly in proportion to it. The critical size, a_c, for a Bean slab is given by Eq. 5.40:

$$a_c = \sqrt{\frac{3\tilde{C}_s(T_c - T_{op})}{\mu_\circ J_{c_\circ}^2}} \tag{5.40}$$

To avoid flux jumping, the product aJ_c must satisfy the following condition:

$$aJ_{c_\circ} \leq \sqrt{\frac{3\tilde{C}_s(T_c - T_{op})}{\mu_\circ}} \tag{S6.1}$$

The presence of partial flux jumps in the range $-1.5\,\mathrm{T} \leq \mu_\circ H \leq 1.5\,\mathrm{T}$ in these wires, except that of 0.3-mmϕ, implies that the flux jump criterion, as expressed by Eq. *S*6.1 is not satisfied by these wires, except the 0.3-mmϕ wire.

PROBLEM 7.7: AC losses in Hybrid III SCM*

This problem deals with AC losses in the Hybrid III SCM (superconducting magnet). A typical sequence of its operation is described below.

Step 1: The SCM is charged from 0 to 800 A in a period of 1200 s. This charging rate corresponds to a field sweep rate at the innermost winding radius at the magnet midplane of 4 mT/s. During this sequence, a significant dissipation apparently takes place, resulting in a net rise in bath temperature of ∼0.1 K, from 1.70 to 1.80 K.

Step 2: The SCM is charged from 800 to 1800 A in a period of 900 s. No measurable increase in bath temperature is observed.

Step 3: In the final leg of the charging sequence, SCM goes from 1800 to 2100 A in a period of 600 s, again with negligible increase in bath temperature. The SCM is now generating 12.3 T at the magnet center.

Step 4: With SCM held at 2100 A, the insert is energized and discharged at a constant rate to an induction, typically between 0 and 22.7 T. Again, during this charging-discharging sequence, no measurable increase in bath temperature is observed.

Panic: In the event of an insert malfunction, the insert is "tripped," forcing its field to decay from 22.7 to 0 T in about 0.3 s. Because of large AC dissipations expected in the SCM under this emergency condition, the SCM is automatically "dumped," resulting in a decay of its current from 2100 to 0 A with a time constant of ∼10 s.

As noted above, AC losses are important only during Step 1. Because of a rapid decrease in the insert's fringing field during *Panic*, the SCM, particularly the NbTi coil, is driven normal, forcing the SCM to dump. Table 7.10 gives pertinent conductor parameters of the Hybrid III SCM.

Table 7.10: Pertinent Conductor Parameters

Parameter		*Nb_3Sn Coil*†	*NbTi Coil*†
Overall width/thickness, a/b	[mm]	9.50/4.50	9.20/2.60
Filament diameter, d_f	[μm]	50	75
Twist pitch length, ℓ_p	[mm]	100	100
Filament #, N_f		1000	2500
Total conductor length, ℓ_{cd}	[m]	1700	8100
J_c @ 0∼5 T, 1.8 K	[GA/m^2]	5	3
$B_p = \mu_\circ H_p = \mu_\circ J_c d_f/2$ @ 1.8 K	[T]	0.16	0.14
ρ_m @ 0∼8 T, 1.8 K	[nΩ m]	0.5	0.5

† For the purpose of this problem, each coil is approximated by one grade of conductor.

* Based on **Problem 7.7** in the 1st Edition (Plenum, 1994).

PROBLEM 7.7: AC losses in Hybrid III SCM (continuation)

a) Justify a temperature increase of ∼0.1 K (from 1.70 to 1.80 K at 1 atm) as the SCM is charged from 0 to 800 A, at which point it is generating a center field of 4.8 T. For computation of hysteresis losses in the Nb_3Sn and NbTi coils, respectively Coils 1 and 2, assume that the *entire* Nb_3Sn conductor in Coil 1 is exposed to a field that increases from 0 to 3.8 T (B_{m1}) and the NbTi conductor in Coil 2 to a field that increases from 0 to 2.4 T (B_{m2}). Note that the magnet vessel contains 250 liters of superfluid liquid helium and, as illustrated in ***DISCUSSION 4.5*** (p. 236), the 1.8-K helium is refrigerated at a cooling rate of 20 W.

b) Show that the narrow cooling channels provided in each double pancake are sufficient to transport AC losses generated in the double pancake to annular spaces at the i.d. and o.d. Note that there are 32 double pancakes in the NbTi coil, each double pancake having cooling channels of 1-mm height and occupying ∼40% of the pancake surface area (Fig. 6.17). The pancake i.d. and o.d. are, respectively, 658 mm and 907 mm.

c) During *Panic* each coil is subjected to a rapid decrease in the insert's fringing field. For the NbTi conductor at the innermost turn at the magnet midpoint ($r = 329$ mm, $z = 0$), $\Delta|B_e|$ is estimated to be ∼1 T, taking place in a time period of 0.3 s, or $\Delta|\dot{B}_e| \sim 3$ T/s. Show that the average temperature of a unit combined volume (conductor and liquid helium adjacent to it) located at the innermost radius at the magnet midplane will exceed T_λ. In applying equations given in Table 7.8, which is really for multifilamentary *wire* of outermost diameter of D_{mf}, assume $D_{mf} = b = 2.60$ mm (Table 7.10).

"Burst Disk" and Diffuser for Hybrid III Cryostat

As discussed in ***CHAPTER 3***, the major fault condition in hybrid magnets is triggered by an insert burnout; the Hybrid III SCM is designed to be discharged quickly in the event of an insert burnout—the event described above as *Panic*. (This fast discharge mode is discussed further in ***CHAPTER 8***.)

One critical consequence of this fast discharge is a rapid rise in the cryostat pressure. The Hybrid III cryostat is equipped with a "burst disk" to limit the pressure increase in the cryostat to 1 atm; a 40-μm thick aluminum foil disk, with an active diameter of 70 mm, is placed in vacuum fittings (Fig. 7.21). When an overpressure of 1 atm is reached in the cryostat, the foil ruptures, relieving the cryostat pressure. As indicated in the figure, a diffuser is placed at the burst disk exit to minimize the exit pressure loss of the emerging vapor.

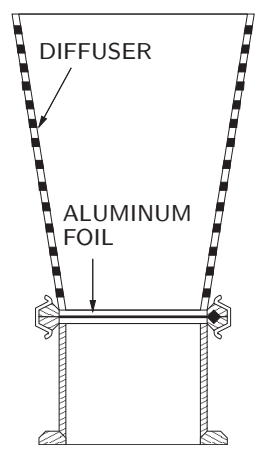

Fig. 7.21 Burst disk (with diffuser) arrangement for Hybrid III cryostat.

Solution to PROBLEM 7.7

a) The major source of dissipation during Step 1 is hysteresis loss. We compute these losses for the Nb_3Sn coil, E_{hy1} and NbTi coil, E_{hy2}. Although there is transport current present (up to 800 A), we use Eq. 7.28*c* ($H_m \gg H_p$) for each coil.

$$e_{hy} \simeq \tfrac{8}{3}\mu_\circ H_p H_m \qquad (7.28c)$$

$$\simeq \frac{8B_pB_m}{3\mu_\circ} \qquad (S7.1)$$

where $B_p = \mu_\circ H_p$ and $B_m = \mu_\circ H_m$. The total energy dissipated in the Nb_3Sn coil, E_{hy1} and that in the NbTi coil, E_{hy2}, are given by:

$$E_{hy1} = \mathcal{V}_{f1} e_{hy} \qquad (S7.1a)$$

$$E_{hy2} = \mathcal{V}_{f2} e_{hy} \qquad (S7.1b)$$

where $\mathcal{V}_{f1}$ and $\mathcal{V}_{f2}$ are the total volumes of the filaments, respectively, of the Nb_3Sn coil and NbTi coil, given by:

$$\mathcal{V}_{f1} = N_{f1}\ell_{cd1}\left(\frac{\pi d_{f1}^2}{4}\right) \qquad (S7.2a)$$

$$\mathcal{V}_{f2} = N_{f2}\ell_{cd2}\left(\frac{\pi d_{f2}^2}{4}\right) \qquad (S7.2b)$$

where N_f, ℓ_{cd}, and d_f are, respectively, the total number of filaments in the conductor, total conductor length, and filament diameter, with subscripts 1 and 2 for, respectively, the Nb_3Sn and NbTi coils.

Inserting appropriate values given in Table 7.10 into Eq. *S*7.2*a* and *S*7.2*b*, with $B_{m1} = 4.3\,\mathrm{T}$ and $B_{m2} = 1.8\,\mathrm{T}$, we obtain:

$$\begin{aligned} E_{hy1} &= (1000)(1700\,\mathrm{m})\frac{\pi(50\times10^{-6}\,\mathrm{m})^2}{4} \\ &\quad\times\left(\frac{8}{3}\right)\times\frac{(0.16\,\mathrm{T})(4.3\,\mathrm{T})}{(4\pi\times10^{-7}\,\mathrm{H/m})} \\ &= (3.3\times10^{-3}\,\mathrm{m}^3)(1.46\times10^6\,\mathrm{J/m}^3) \simeq 4.9\,\mathrm{kJ} \end{aligned} \qquad (S7.3a)$$

$$\begin{aligned} E_{hy2} &= (2500)(8100\,\mathrm{m})\frac{\pi(75\times10^{-6}\,\mathrm{m})^2}{4} \\ &\quad\times\left(\frac{8}{3}\right)\times\frac{(0.14\,\mathrm{T})(1.8\,\mathrm{T})}{(4\pi\times10^{-7}\,\mathrm{H/m})} \\ &= (89.4\times10^{-3}\,\mathrm{m}^3)(0.53\times10^6\,\mathrm{J/m}^3) \simeq 48\,\mathrm{kJ} \end{aligned} \qquad (S7.3b)$$

The total hysteresis loss released into the liquid is thus ∼53 kJ.

Answer to TRIVIA 7.2 iii). The Croatian-American Nikola Tesla (1856–1943) bred pigeons on whom, it is said, he lavished all the affection he was unable to give humans. With George Westinghouse (1846–1914), he fought and prevailed over Thomas Alva Edison (1847–1931) for the utilities' adoption of AC power.

Solution to PROBLEM 7.7 (continuation)

The mass of 250 liters of liquid helium at 1.70 K is 37 kg. The enthalpy of 1-atm helium at 1.70 K is 1280 J/kg and that at 1.80 K is 1530 J/kg (***APPENDIX II***), or a net change in enthalpy of 250 J/kg. With a total mass of 37 kg, an increase in bath temperature from 1.70 to 1.80 K requires a net energy input of ∼10 kJ; during this 1200-s period, the refrigerator running at 20 W removes ∼25 kJ from the liquid: a total energy of ∼35 kJ is required to raise the liquid from 1.7 K to 1.8 K. Our computed dissipation energy of ∼53 kJ thus overestimates the dissipation energy by a factor of about two, not too bad considering the above analysis is expected to give a *ball park* figure; it certainly demonstrates hysteresis loss is the major source of dissipation.

b) With a total hysteresis energy dissipation in the NbTi coil of ∼30 kJ (5/8 of ∼48 kJ, as corrected above), released in 1200 s, the overall hysteresis dissipation rate is ∼25 W. For each of 32 double-pancake coils in Coil 2, the dissipation rate would be ∼0.8 W. Under the most conservative condition, the total channel cross section for each double pancake would be ∼4 cm^2 (40% of the circumference corresponding to the innermost diameter of 658 mm times a channel height of 0.5 mm—note that the 1-mm high channel is shared by two pancakes), or a heat flux of ∼0.2 W/cm^2. Since heat can flow radially both inward and outward, an appropriate value for the channel length is one quarter the difference between o.d. and i.d., or ∼6 cm.

Because dissipation is taking place over the entire channel length, Eq. 4.6*c* (p. 235) is applicable. Thus:

$$X(T_b) = \frac{q_c^{3.4}}{4.4} L \tag{4.6c}$$

From Fig. 4.9, we have: $X(T_b = 1.8\,\mathrm{K}) = 350$. With $L = 6$ cm, solving Eq. 4.6*c* for q_c, gives: $q_c = 5.1$ W/cm^2, which is much greater than the minimum required value of ∼0.2 W/cm^2. That is, the channels are ample to remove the hysteresis dissipation during a charge up from 0 to 800 A. This conclusion has been validated by actual runs.

c) In a rapidly changing field, the most important losses are coupling (e_{cp}) and eddy (e_{ed}). We shall consider here only e_{cp}, because it is sufficient to drive the conductor-helium unit volume to T_λ, even without any contribution from e_{ed}.

We shall first compute τ_{cp}, the coupling time constant, for the NbTi conductor.

$$\tau_{cp} = \frac{\mu_\circ \ell_p^2}{8\pi^2 \rho_{ef}} \tag{7.6}$$

For NbTi composite, ρ_{ef} given by Eq. 7.7*b* is generally used. In terms of $\gamma_{c/s}$, the copper-to-superconductor ratio, ρ_{ef} is given by:

$$\rho_{ef} = \frac{1+\lambda_f}{1-\lambda_f}\rho_m \tag{7.7b}$$

$$= \frac{\gamma_{c/s}+2}{\gamma_{c/s}}\rho_m \tag{S7.4}$$

Solution to PROBLEM 7.7 (continuation)

With $\gamma_{c/s} = 2.2$ (deducible from the conductor parameters given in Table 7.10) and inserting appropriate values into Eq. 7.6, we obtain: $\tau_{cp} \simeq 0.17 \sim 0.2\,\text{s}$, comparable with $\tau_m = 0.3\,\text{s}$ for the insert discharge.

Applying Eqs. 7.36 and 7.39*a* (triangular) of Table 7.8, with a factor of 1/2 (for discharge only) and $H_m = B_m/\mu_\circ$ and $D_{mf} = b$ inserted in Eq. 7.36, we obtain:

$$e_{cp} = \tfrac{1}{2} \times 2 \frac{B_m^2}{\mu_\circ} \left[1 + \tfrac{1}{4}\left(\frac{\pi b}{\ell_p}\right)^2\right] \times \frac{2\tau_{cp}}{\tau_m}\left[1 - \frac{2\tau_{cp}}{\tau_m}\tanh\left(\frac{\tau_m}{2\tau_{cp}}\right)\right] \qquad (S7.5a)$$

$$= \frac{2B_m^2 \tau_{cp}}{\mu_\circ \tau_m}\left[1 + \tfrac{1}{4}\left(\frac{\pi b}{\ell_p}\right)^2\right]\left[1 - \frac{2\tau_{cp}}{\tau_m}\tanh\left(\frac{\tau_m}{2\tau_{cp}}\right)\right] \qquad (S7.5b)$$

Inserting appropriate values in Eq. *S*7.5*b*, we obtain:

$$e_{cp} \simeq \frac{2(1\,\text{T})^2(0.2\,\text{s})}{(4\pi \times 10^{-7}\,\text{H/m})(0.3\,\text{s})} \times \left\{1 + \tfrac{1}{4}\left[\frac{\pi(2.6 \times 10^{-3}\,\text{m})}{0.1\,\text{m}}\right]^2\right\}\left\{1 - \frac{2(0.2\,\text{s})}{(0.3\,\text{s})}\tanh\left[\frac{(0.3\,\text{s})}{2(0.2\,\text{s})}\right]\right\}$$

$$\simeq (1.05 \times 10^6\,\text{J/m}^3)(1)(0.15) \sim 0.16 \times 10^6\,\text{J/m}^3$$

Consider a unit length (1 cm) of conductor. Because its cross section is $(0.92 \times \text{cm}) \times (0.26\,\text{cm}) = 0.24\,\text{cm}^2$, the conductor has volume $\mathcal{V}_{cd}$ of $0.24\,\text{cm}^3$. Over this conductor length, helium occupies 0.4 cm length (40% filling) and 0.5 mm channel depth (1-mm deep channel is shared by conductors of the top and bottom pancakes) over the conductor width of 2.6 mm. Thus for a unit conductor length, helium occupies a volume $\mathcal{V}_{he}$ of $5.2 \times 10^{-3}\,\text{cm}^3$. The total dissipation energy over the unit conductor length, E_{cp}, will thus be given by:

$$E_{cp} = e_{cp}\mathcal{V}_{cd} \qquad (S7.9)$$

$$\sim (0.16\,\text{J/cm}^3) \times (0.24\,\text{cm}^3) \sim 38\,\text{mJ}$$

The total thermal energy, ΔE_{th} needed to raise the unit conductor (and accompanying liquid helium) from 1.8 K to T_λ is given by:

$$E_{th} = [h_{cu}(T_\lambda) - h_{cu}(1.8\,\text{K})]\mathcal{V}_{cd} + [h_{he}(T_\lambda) - h_{he}(1.8\,\text{K})]\mathcal{V}_{he} \qquad (S7.10)$$

Inserting $\Delta h_{cu} \simeq 0.1\,\text{mJ/cm}^3$ and $\Delta h_{he} \sim 290\,\text{mJ/cm}^3$ into Eq. *S*7.10, we have:

$$E_{th} = (0.1\,\text{mJ/cm}^3)(0.24\,\text{cm}^3) + (290\,\text{mJ/cm}^3)(5.2 \times 10^{-3}\,\text{cm}^3) \qquad (S7.11)$$

$$\simeq 2\,\text{mJ}$$

Because $E_{cp} \gg E_{th}$, the entire helium surrounding the unit conductor will be heated to well above T_λ, making it unlikely for the conductor to recover.

"Oh figures! You can make figures do whatever you want." —Ned Land

DISCUSSION 7.7: Splice Dissipation in Hybrid III NbTi Coil*

The Hybrid III NbTi coil consists of 32 double pancakes, each wound with two grades of 9.2-mm wide NbTi composite strip. In each single pancake, a "hand-shake" splice (Fig. 7.7) between the high-field (HF) grade conductor and low-field (LF) grade conductor occurs at $r = 378\,\text{mm}$ along a 90° arc; in each double pancake there are thus two such splices. In addition, there is another splice in each double pancake, at $r = 455\,\text{mm}$ over a 90° arc, to connect the double pancake to the next double pancake. Altogether the Hybrid III NbTi coil has a total of 64 splices at $r = 378\,\text{mm}$ and 32 splices at $r = 455\,\text{mm}$. To make a conservative estimate, we shall use R_{ct} data having the higher values of R_{ct} for 50Sn-50Pb (2nd set of data in Table 7.1): R_{ct} of $3.3\times10^{-12}\,\Omega\,\text{m}^2$ at 1 T and $4.1\times10^{-12}\,\Omega\,\text{m}^2$ at 3 T.

A. Splice Resistances

Applying Eq.7.9*b*, we compute the resistance at $r = 378\,\text{mm}$, R_{sp1}:

$$R_{sp} = \frac{R_{ct}}{A_{ct}} \qquad (7.9b)$$

$$R_{sp1} = \frac{R_{ct}}{a\ell_{sp1}}$$

In the above equation, $a\ell_{sp1} = A_{ct}$, a is the conductor width, and ℓ_{sp} is the splice overlap length, given by $\pi r_{sp1}/2$, where r_{sp1} is the winding radius at which the splice takes place. Inserting $R_{ct} = 4.1\times10^{-12}\,\Omega\,\text{m}^2$, $a = 9.2\times10^{-3}\,\text{m}$, $\pi/2 = 1.57$ (90° arc), and $r_{sp1} = 0.378\,\text{m}$, we have:

$$R_{sp1} = \frac{(4.1\times10^{-12}\,\Omega\,\text{m}^2)}{(9.2\times10^{-3}\,\text{m})(1.57\times0.378\,\text{m})} = 0.75\,\text{n}\Omega$$

Similarly, the splice resistance at $r = 455\,\text{mm}$, R_{sp2}, is given by:

$$R_{sp2} = \frac{(3.3\times10^{-12}\,\Omega\,\text{m}^2)}{(9.2\times10^{-3}\,\text{m})(1.57\times0.455\,\text{m})} = 0.50\,\text{n}\Omega$$

Total splice resistance, R_{sp}, thus is given by:

$$R_{sp} = 64R_{sp1} + 32R_{sp2} = 48\,\text{n}\Omega + 16\,\text{n}\Omega = 64\,\text{n}\Omega$$

B. Total Splice Dissipation

Total splice dissipation at $I_{op} = 2100\,\text{A}$, P_{sp}, is given by:

$$P_{sp} = R_{sp}I_{op}^2 = (64\times10^{-9}\,\Omega)(2.1\times10^3\,\text{A})^2 = 0.28\,\text{W} \qquad (S8.5)$$

This fraction-of-a-watt of splice dissipation at 2100 A is consistent with data obtained from Hybrid III runs. When the system was allowed to reach the lowest possible temperature with no transport current, the bath temperature reached 1.65 K. The same was true at 2100 A. That is, the splice dissipation rate was negligible compared with the quiescent refrigeration load at 1.65 K, a shade less than 20 W at 1.80 K, computed in ***DISCUSSION 4.4*** in ***CHAPTER 4***.

---

* Based on **Problem 7.9** in the 1st Edition (Plenum, 1994).

DISCUSSION 7.8: Persistent-Mode Operation & "Index"

Here we discuss the key issues related to operation of a persistent-mode magnet such as those used for NMR or MRI. Generation by a superconducting magnet of a persistent, *i.e.*, *permanent*, field much greater than that possible with permanent magnets unquestionably qualifies as one of the unique features of superconductivity. This is clearly reflected by a proliferation of commercially available NMR and MRI superconducting magnets.

However, a *real* persistent-mode magnet contains a small but *nonzero* circuit resistance, one of the subjects here, causing the field to decay. Generally, a field decay is permitted even in these magnets if its decay rate is no greater than ∼0.01 ppm/h (0.01 *p*art *p*er *m*illion per hour). This decay rate translates to an equivalent decay time constant of 10^8 h, or ∼10,000 years. For a magnet with an inductance of 360 H, a decay rate of 0.01 ppm/h implies a total nonzero circuit resistance of $10^{-9}\,\Omega$ (1 nΩ).

A. Circuit & Operation

Circuit

Figure 7.22 presents the basic elements of a persistent-mode magnet circuit with L representing the magnet. In a real persistent-mode NMR magnet, for example, studied in **PROBLEM 8.6** (p. 530), the circuit would contain many inductors, each representing one of many coils in the magnet, and each coil would be shunted by a resistor. r is the total circuit resistance, ideally $r = 0$ but, as stated above, not quite zero in real magnets. As shown in the figure, a persistent-current switch, PCS, shunts the magnet terminals, the black dots in the figure; these joints must ideally be superconducting; if not superconducting, the joint resistance at each terminal becomes a part of r. The two power diodes, in opposite polarities, shunting the PCS protect the switch in the event of a magnet quench [7.115]. When operated at

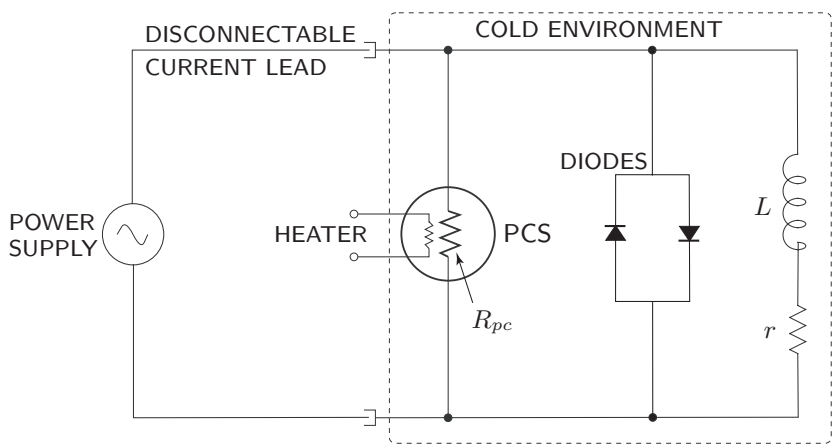

Fig. 7.22 Basic circuit diagram for a persistent-mode superconducting magnet.

* Based on **Problem 7.11** in the 1st Edition (Plenum, 1994).

DISCUSSION 7.8: Persistent-Mode Operation & "Index" (continuation)

4.2 K, the "forward" threshold voltage of a power diode increases from ≤ 1 V at room temperature to $\sim$10 V, making the forward diode in the circuit effectively open for magnet energizing voltages below $\sim$10 V. For a *persistent-mode HTS* magnet operating well above 4.2 K, this threshold voltage will be small. However, at a higher operating temperature the switch may also be able to survive a magnet quench without the diode protection.

Operation

With the PCS closed (and superconducting, i.e., $R_{pc} = 0$), short-circuiting the magnet terminals, it is impossible to energize the magnet (**PROBLEM 1.2**). To energize the magnet by a power supply via "disconnectable" current leads, the PCS must become resistive (i.e., $R_{cp} \neq 0$), achieved with a heater. The elements enclosed by the dashed lines in the figure are within the cold operating environment.

When the operating current is reached, the heater current may be turned off and the switch becomes superconducting. The circuit is now fully (if $r = 0$) or nearly (if $r \simeq 0$) superconducting; the supply current may be reduced to zero—note that the magnet, now shunted by the PCS, is isolated from the supply. To minimize the conduction heat input to the cold environment from the idle current leads, the current leads are usually disconnected at the magnet terminals. In some instances, the leads are removed altogether from the cryostat.

B. Design of PCS

There are three issues for designing a PCS: 1) normal-state resistance; 2) stability and protection; and 3) thermal insulation.

Normal State Resistance

Ideally, the switch's normal-state resistance should be infinite ($R_{pc} = \infty$); in reality it should be large enough to make the current through the resistive switch, I_{pc}, no greater than $\sim$10% of I_{op}, the magnet operating current. When the magnet consists of many coils, each shunted by a resistor, as in the circuit shown in Fig. 8.27 (p. 531), then R_{pc} must be greater than the sum of the shunt resistors, because $I_{pc} = V_{ch}/R_{pc}$, where V_{ch} is the charging voltage applied across the magnet terminals. A combination of R_{pc} and I_{pc} of course dissipates power in the switch, $R_{pc}I_{pc}^2 = V_{ch}^2/R_{pc}$, which is *in addition* to the heater power. There are thus two requirements for a PCS: 1) $V_{ch}/R_{pc} < \sim 0.1 I_{op}$ (or R_{pc} should be equal to or greater than the sum of the resistors shunting the coils in a multi-coil magnet); and 2) V_{ch}^2/R_{pc} preferably 1 W or less, or at any case no greater than a few watts.

In practice, an LTS switch made of NbTi/Cu composite wire is unsuitable, because copper is too conductive in the cold environment of the magnet; a special composite NbTi wire with Cu-Ni alloy matrix is generally used. At 4.2 K the electrical resistivity of Cu-Ni is $\sim$1000 times greater than that of copper (***APPENDIX IV***). Similarly, an HTS made of Bi2223/Ag is unsuitable, because pure Ag is too conductive to meet the requirements of R_{pc} given above. For PCS, Ag-Au alloy should be substituted for pure Ag. According to data shown in Fig. 4.24 (p. 284), at 30 K pure Ag is $\sim$40 times less resistive than Ag-2.9at%Au (Ag-5wt%Au).

DISCUSSION 7.8: Persistent-Mode Operation & "Index" (continuation)

Stability and Protection

Because a PCS is usually located in a low-field region of the magnet, the superconductor in the switch, even without being "oversized," has a temperature margin much greater than those of the superconductors in the windings. For protection, the "backward" diode (Fig. 7.22) shunts the resistive PCS. In a multi-coil magnet with a shunt resistor across each coil, the switch may remain superconducting during the entire period the magnet is quenching. In the event a switch is damaged, it simply needs to be replaced, as a burnt out light bulb would be. The switch is likely to be the least expensive component in a multi-coil magnet.

Thermal Insulation

Heating injected into the switch to maintain it resistive is a cryogenic load to the cryostat. The more thermally-insulated the switch is from the cold environment, the less the cryogenic load.

C. Index Loss

As given by Eq. 6.25*b*, for magnet-grade superconductors the electric field E and current density J_s may be approximated by:

$$E_s = E_c \left(\frac{J_s}{J_c}\right)^n \tag{6.25b}$$

Consider a persistent-mode superconducting magnet wound with a superconductor of index n. Because field strength decreases away from the maximum field region, located in the vicinity of the magnet midplane at the innermost winding radius, the conductor's J_c also increases, and J_{op}/J_c decreases away from the maximum field region. Therefore, it is necessary to consider the index voltage only in the maximum field region. Let ℓ_{mx} be the total conductor length in this region.

By integrating E field over a conductor length ℓ_{mx}, we obtain the total index-induced voltage, V_n, at I_{op} given by:

$$V_n = E\ell_{mx} = E_c \left(\frac{I_{op}}{I_c}\right)^n \ell_{mx} \tag{7.44}$$

This resistive voltage causes a current decay in the magnet of inductance L_m:

$$\frac{dI_{op}}{dt} = -\frac{V_n}{L_m} = -\frac{E_c}{L_m}\left(\frac{I_{op}}{I_c}\right)^n \ell_{mx} \tag{7.45}$$

Because I_{op} and $H_\circ$ are proportional, we have:

$$\frac{dH}{dt} \equiv -\left(\frac{\Delta H}{\tau_p}\right) \propto -\frac{E_c}{L_m}\left(\frac{I_{op}}{I_c}\right)^n \ell_{mx}$$

$$\left(\frac{\Delta H}{H_\circ \tau_p}\right) = \frac{E_c}{L_m I_{op}}\left(\frac{I_{op}}{I_c}\right)^n \ell_{mx} \tag{7.46}$$

"Clocks are slow on Sundays." — Holly Golightly

DISCUSSION 7.8: Persistent-Mode Operation & "Index" (continuation)

Solving for I_{op}/I_c from Eq. 7.46, we obtain:

$$\frac{I_{op}}{I_c} \leq \left[\frac{L_m I_{op}}{E_c \ell_{mx}}\left(\frac{\Delta H}{H_\circ \tau_p}\right)\right]^{1/n} \tag{7.47a}$$

By inserting $\Delta H/(H_\circ \tau_p) = 10^{-8}/\text{hr} = 2.78\times10^{-12}/\text{s}$ and other parameter values into Eq. 7.47*a*, we have:

$$\frac{I_{op}}{I_c} = \left[\frac{(300\,\text{A})(100\,\text{H})}{(10^{-7}\,\text{V/cm})(10^5\,\text{cm})}(2.78\times10^{-12}/\text{s})\right]^{1/n} \tag{7.47b}$$

From Eq. 7.47*b*, we have: $I_{op}/I_c = 0.31$ for $n = 10$; $I_{op}/I_c = 0.56$ for $n = 20$; $I_{op}/I_c = 0.68$ for $n = 30$; and $I_{op}/I_c = 0.79$ for $n = 50$.

These values indicate that for a conductor of $n = 10$, I_{op} must be kept below 31% of I_c—a rather inefficient use of the conductor; for $n = 50$, I_{op} may be increased to 79% of I_c. The results of a recent experimental study [6.18] show that n, determined from a V *vs* I plot at and *above* I_c, instead of remaining constant actually *increases* for currents *below* I_c. In one test conductor, n was found to increase from ∼30 at I_c to as much as 145 at $I/I_c = 0.75$. That is, as long as I_{op} is chosen not too close to I_c, even conductors with $n\sim20$ at I_c may be usable for persistent-mode magnets.

New techniques are being developed to enable even a *slightly resistive* NMR magnet to operate effectively in persistent mode. These include a "digital flux injector" that periodically injects a metered and precisely controllable flux [7.116–7.121], a flux pump [7.122–7.124], and a current supply arrangement [7.125] to a dissipative part of an NMR magnet. A digital flux injector which pumps microamperes of current into an NMR magnet is the *reverse* of a flux pump originally conceived to pump thousands of amperes of current into a magnetic circuit.

D. Experimental Determination of Index

The technique widely used to determine the index n of a superconductor is through the superconductor's V *vs* I plot such as shown in Fig. 7.23. Thus:

$$n = \frac{\ln(V_2/V_1)}{\ln(I_2/I_1)} \tag{7.48}$$

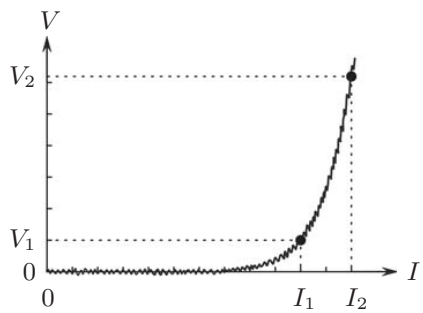

Fig. 7.23 Typical V vs. I trace from which to determine an index number.

References

[7.1] Donald J. Hanrahan, *A Theoretical and Experimental Study of the AC Losses of a High Field Superconductor and the Implications for Power Applications* (Naval Research Laboratory, Washington DC, 1969).

[7.2] J.J. Rabbers, *AC Loss in Superconducting Tapes and Coils* (Doctoral Thesis, University of Twente, 1970).

[7.3] W.T. Norris, "Calculation of hysteresis losses in hard superconductors carrying ac: isolated conductors and edge of thin sheets," *J. Phys.* D**3**, 489 (1970).

[7.4] G. Ries and H. Brechna, *AC Losses in Superconducting Pulsed Magnets* (KFK Report 1372, Gesellschaft für Kernforschung m.b.H. Karlsruhe, 1972).

[7.5] Marijin Pieter Oomen, *AC Loss in Superconducting Tapes and Cables* (Doctoral Thesis, University of Twente, 1972).

[7.6] W.J. Carr, Jr., "ac loss in a twisted filamentary superconducting wire. II," *J. Appl. Phys.* **45**, 935 (1974).

[7.7] K. Kwasnitza, "Scaling law for the ac losses of multifilament superconductors," *Cryogenics* **17**, 616 (1977).

[7.8] F. Sumiyoshi, F. Irie and K. Yoshida, "Magnetic field dependence of ac losses in multi-filamentary superconducting wires," *Cryogenics* **18**, 209 (1978).

[7.9] J.D. Thompson, M.P. Maley, John R. Clem, "Hysteretic losses of a type II superconductor in parallel ac and dc magnetic fields of comparable magnitude," *J. Appl. Phys.* **50**, 3531 (1979).

[7.10] J.P. Soubeyrand and B. Turck, "Losses in superconducting composite under high rate pulsed transverse field," *IEEE Trans. Magn.* **MAG-15**, 248 (1979).

[7.11] T. Ogasawara, Y. Takahashi, K. Kanbara, Y. Kubota, K. Yasohama and K. Yasukochi, "Alternating field losses in superconducting wires carrying dc transport currents. Part 1: single core conductors," *Cryogenics* **19**, 736 (1979).

[7.12] T. Ogasawara, Y. Takahashi, K. Kanbara, Y. Kubota, K. Yasohama and K. Yasukochi, "Alternating field losses in superconducting wires carrying dc transport currents. Part 2: multifilamentary composite conductors," *Cryogenics* **21**, 97 (1981).

[7.13] I. Hlásnik, "Review on AC losses in superconductors," *IEEE Trans. Magn.* **MAG-17**, 2261 (1981).

[7.14] E.H. Brandt and M. Indenbom, "Type-II superconductor strip with current in a perpendicular magnetic field," *Phys. Rev.* B **48**, 12893 (1993).

[7.15] John R. Clem and Alvaro Sanchez, "Hysteretic ac losses and susceptibility of thin superconducting disks," *Phys. Rev.* B **50**, 9355 (1993).

[7.16] Kazuo Funaki and Fumio Sumiyoshi, **多芯線と導体** (*"Multifilaments and Conductors"* in Japanese) (ISBN: 4782857527, 1995).

[7.17] W.J. Carr, Jr., *AC Loss and Macroscopic Theory of Superconductors* 2nd Ed. (Taylor & Francis, London, 2001).

[7.18] W.J. Carr, Jr., "Conductivity, permeability, and dielectric constant in a multifilament superconductor," *J. Appl. Phys.* **46**, 4043 (1975).

[7.19] R.W. Fast, W.W. Craddock, M. Kobayashi, and M.T. Mruzek, "Electrical and mechanical properties of lead/tin solders and splices for superconducting cables," *Cryogenics* **28**, 7 (1988).

[7.20] J.W. Hafstrom, D.H. Killpatrick, R.C. Niemann, J.R. Purcell, and H.R. Thresh, "Joining NbTi superconductors by ultrasonic welding," *IEEE Trans. Magn.* **MAG-**

13, 94 (1977).

[7.21] Hiroyuki Fujishiro (unpublished data, 2006).

[7.22] Jean-Marie Noterdaeme, "Demountable resistive joint design for high current superconductors," (M.S. Thesis, MIT Dept. Nuclear Engineering, May 1978).

[7.23] K. Sawa, M. Suzuki, M. Tomita and M. Murakami, "A fundamental behavior on mechanical contacts of YBCO bulks," *Physica C: Superconduc.* **378**, 803 (2002).

[7.24] Hiroyuki Fujita, Katsuya Fukuda, Koichiro Sawa, Masaru Tomita, Masato Murakami, Naomichi Sakai, Izumi Hirabayashi, "Contact resistance characteristics of high temperature superconducting bulk – Part V," *Proc. 52*nd *IEEE Holm Conf. Electrical Contacts*, 124 (2006).

[7.25] Y. Kawate, R. Ogawa, and R. Hirose (personal communication, 1994).

[7.26] R.S. Kensley and Y. Iwasa, "Frictional properties of metal insulator surfaces at cryogenic temperatures," *Cryogenics* **20**, 25 (1980).

[7.27] R.S. Kensley, H. Maeda, and Y. Iwasa, "Transient slip behavior of metal/insulator pairs at 4.2 K," *Cryogenics* **21**, 479 (1981).

[7.28] H. Maeda, O. Tsukamoto, and Y. Iwasa, "The mechanism of friction motion and its effect at 4.2 K in superconducting magnet winding models, " *Cryogenics* **22**, 287 (1982).

[7.29] A. Iwabuchi and T. Honda, "Temperature rise due to frictional sliding of SUS316 vs SUS316L and SUS316 vs polyimide at 4 K," *Proc. 11th Int. Conf. Magnet Tech. (MT11)* (Elsevier Applied Science, London), 686 (1990).

[7.30] P.C. Michael, E. Rabinowicz, and Y. Iwasa, "Friction and wear of polymeric materials at 293, 77, and 4.2 K," *Cryogenics* **31**, 695 (1991).

[7.31] T. Takao and O. Tsukamoto, "Stability against the frictional motion of conductor in superconducting windings," *IEEE Trans. Magn.* **27**, 2147 (1991).

[7.32] Y. Iwasa, J.F. Maguire, and J.E.C. Williams, "The effect on stability of frictional decoupling for a composite superconductor," *Proc. 8th Symp. on Engr. Problems of Fusion Research,* (IEEE Publication 79CH1441-5, 1979), 1407.

[7.33] Y. Yasaka and Y. Iwasa, "Stress-induced epoxy cracking energy release at 4.2 K in epoxy-coated superconducting wires," *Cryogenics* **24**, 423 (1984).

[7.34] S. Fuchino and Y. Iwasa, "A cryomechanics technique to measure dissipative energies of ∼10 nJ," *Exp. Mech.* **30**, 356 (1990).

[7.35] E.S. Bobrov and J.E.C. Williams, "Direct optimization of the winding process for superconducting solenoid magnets (linear programming approach)," *IEEE Trans. Magn.* **MAG-17**, 447 (1981).

[7.36] E.S. Bobrov, J.E.C. Williams, and Y. Iwasa, "Experimental and theoretical investigation of mechanical disturbances in epoxy-impregnated superconducting coils. 2. Shear stress-induced epoxy fracture as the principal source of premature quenches and training—theoretical analysis," *Cryogenics* **25**, 307 (1985).

[7.37] H. Maeda, M. Urata, H. Ogiwara, S. Miyake, N. Aoki, M. Sugimoto, and J. Tani, "Stabilization for wind and react Nb_3Sn high field insert coil," *Proc. 11th Int. Conf. Magnet Tech. (MT-11)* (Elsevier Applied Science, London, 1990), 1114.

[7.38] H. Nomura, K. Takahisa, K. Koyama, and T. Sakai, "Acoustic emission from superconducting magnets," *Cryogenics* **17**, 471 (1977).

[7.39] Curt Schmidt and Gabriel Pasztor, "Superconductors under dynamic mechanical stress," *IEEE Trans. Magn.* **MAG-13**, 116 (1977).

[7.40] H. Brechna and P. Turowski, "Training and degradation phenomena in superconducting magnets," *Proc. 6th Int. Conf. Magnet Tech. (MT-6)* (ALFA, Bratislava, Czechoslovakia, 1978), 597.

[7.41] O. Tsukamoto, J.F. Maguire, E.S. Bobrov, and Y. Iwasa, "Identification of quench origins in a superconductor with acoustic emission and voltage measurements," *Appl. Phys. Lett.* **39**, 172 (1981).

[7.42] O. Tsukamoto and Y. Iwasa, "Sources of acoustic emission in superconducting magnets," *J. Appl. Phys.* **54**, 997 (1983).

[7.43] S. Caspi and W.V. Hassenzahl, "Source, origin and propagation of quenches measured in superconducting dipole magnets," *IEEE Trans. Magn.* **MAG-19**, 692 (1983).

[7.44] Markus Pappe, "Discussion of acoustic emission of a superconducting solenoid," *IEEE Trans. Magn.* **MAG-19**, 1086 (1983).

[7.45] H. Iwasaki, S. Nijishima, and T. Okada, "Application of acoustic emission method to the monitoring system of superconducting magnet," *Proc. 9th Int. Conf. Magnet Tech. (MT-9)* (Swiss Institute for Nuclear Research, Villigen, 1985), 830 (1985).

[7.46] Y. Iwasa, E.S. Bobrov, O. Tsukamoto, T. Takaghi, and H. Fujita, "Experimental and theoretical investigation of mechanical disturbances in epoxy-impregnated superconducting coils. 3. Fracture-induced premature quenches," *Cryogenics* **25**, 317 (1985).

[7.47] K. Yoshida, M. Nishi, H. Tsuji, Y. Hattori, and S. Shimamoto, "Acoustic emission measurement on large coils at JAERI," *Adv. Cryogenic Eng.* **31**, 277 (1986).

[7.48] O.O. Ige, A.D. McInturff, and Y. Iwasa, "Acoustic emission monitoring results from a Fermi dipole," *Cryogenics* **26**, 131 (1986).

[7.49] J. Chikaba, F. Irie, K. Funaki, M. Takeo, and K. Yamafuji, "Instabilities due to mechanical strain energy in superconducting magnets," *IEEE Trans. Magn.* **MAG-23**, 1600 (1987).

[7.50] K. Ikizawa, N. Takasu, Y. Murayama, K. Seo, S. Nishijima, K. Katagiri, and T. Okada, "Instability of superconducting racetrack magnets," *IEEE Trans. Magn.* **27**, 2128 (1991).

[7.51] T. Ogitsu, K. Tsuchiya, and A. Devred, "Investigation of wire motion in superconducting magnets," *IEEE Trans. Magn.* **27**, 2132 (1991).

[7.52] Kazuaki Arai, Hiroshi Yamaguchi, Katsuyuki Kaiho, Hiroshi Fuji, Nobuyuki Sadakata, and Takashi Saitoh, "Acoustic emission occurrence induced from a NbTi superconducting coil under alternating current operation," *IEEE Trans. Appl. Superconduc.* **9**, 4648 (1999).

[7.53] A. Ninomiya, K. Arai, K. Takano, T. Ishigohka, K. Kaiho, H. Nakajima, H. Tsuji, K. Okuno, N. Martovetsky, and I. Rodin, "Diagnosis of ITER's large scale superconducting coils using acoustic emission techniques," *IEEE Trans. Appl. Superconduc.* **13**, 1408 (2003).

[7.54] H. Maeda, A. Sato, M. Koizumi, M. Urata, S. Murase, I. Takano, N. Aoki, M. Ishihara, E. Suzuki, "Application of acoustic emission technique to a multi-filamentary 15.1 tesla superconducting magnet system," *Adv. Cryogenic Eng.* **31**, 293 (1986).

[7.55] T. Ishigohka, O. Tsukamoto, and Y. Iwasa, "Method to detect a temperature rise in superconducting coils with piezoelectric sensors," *Appl. Phys. Lett.* **43**, 317 (1983).

[7.56] O. Tsukamoto and Y. Iwasa, "Correlation of acoustic emission with normal zone occurrence in epoxy-impregnated windings: an application of acoustic emission diagnostic technique to pulse superconducting magnets," *Appl. Phys. Lett.* **44**,

922 (1984).

[7.57] Oluwasegun Olubunmi Ige, "Mechanical disturbances in high-performance superconducting dipoles," (Ph.D. Thesis, MIT Dept. Mechanical Engineering, 1989).

[7.58] L. Woźny, P. Lubicki, and B. Mazurek, "Acoustic emission from high T_c superconductors during current flow," *Cryogenics* **33**, 825 (1993).

[7.59] Kazuaki Arai and Yukikazu Iwasa, "Heating-induced acoustic emission in an adiabatic high-temperature superconducting winding," *Cryogenics* **37**, 473 (1997).

[7.60] Haigun Lee, Ho Min Kim, Joseph Jankowski, Yukikazu Iwasa, "Detection of 'hot spots' in HTS coils and test samples with acoustic emission signals," *IEEE Trans. Appl. Superconduc.* **14**, 1298 (2004).

[7.61] P.F. Dahl, G.H. Morgan, and W.B. Sampson, "Loss measurements on twisted multifilamentary superconducting wires," *J. Appl. Phys.* **40**, 2083 (1969).

[7.62] K. Kwasnitza and I. Horvath, "Measurement of ac losses in multifilament superconducting wires at frequencies between 1 and 100 Hz," *Cryogenics* **14**, 71 (1974).

[7.63] W. David Lee, J. Thomas Broach, "60 Hz AC losses in superconducting solenoids," *IEEE Trans. Magn.* **MAG-13**, 542 (1977).

[7.64] W.J. Carr, Jr., Ben Clawson, and Wayne Vogen, "AC losses in superconducting solenoids," *IEEE Trans. Magn.* **MAG-14**, 617 (1978).

[7.65] M.S. Walker, J.G. Declerq, B.A. Zeitlin, J.D. Scudiere, M.J. Ross, M.A. Janocko, S.K. Singh, E.A. Ibrahim, P.W. Eckels, J.D. Rogers, and J.J. Wollan, "Superconductor design and loss analysis for a 20 MJ induction heating coil," *IEEE Trans. Magn.* **MAG-17**, 908 (1981).

[7.66] D. Ito, Y. Nakayama, and T. Ogasawara, "Losses in superconducting magnets under fast ramp rate operation," *IEEE Trans. Magn.* **MAG-17**, 971 (1981).

[7.67] K. Kwasnitza and I. Horvath, "AC loss behaviour of the high-current NbTi superconductor for the Swiss LCT fusion coil," *IEEE Trans. Magn.* **MAG-17**, 2278 (1981).

[7.68] Kunishige Kuroda, "ac losses of superconducting solenoidal coils," *J. Appl. Phys.* **53**, 578 (1982).

[7.69] A. Lacaze, Y. Laumond, J.P. Tavergnier, A. Fevrier, T. Verhaege, B. Dalle, A. Ansart, "Coils performances of superconducting cables for 50/60 Hz applications," *IEEE Trans. Magn.* **27**, 2178 (1991).

[7.70] T. Ando, Y. Takahashi, K. Okuno, H. Tsuji, T. Hiyama, M. Nishi, E. Tada, K. Yoshida, K. Koizumi, H. Nakajima, T. Kato, M. Sugimoto, T. Isono, K. Kawano, M. Konno, J. Yoshida, H. Ishida, E. Kawagoe, Y. Kamiyauchi and S. Shimamoto, "AC loss results of the Nb3Sn Demo Poloidal Coil (DPC-EX)," *IEEE Trans. Magn.* **28**, 206 (1992).

[7.71] F. Sumiyoshi, S. Kawabata, Y. Kanai, T. Kawashima, T. Mito, K. Takahata and J. Yamamoto, "Losses in cable-in-conduit superconductors used for the poloidal coil system of the Large Helical Device," *IEEE Trans. Appl. Superconduc.* **3**, 476 (1993).

[7.72] J.P. Ozelis, S. Delchamps, S. Gourlay, T. Jaffery, W. Kinney, W. Koska, M. Kuchnir, M.J. Lamm, P.O. Mazur, D. Orris, J. Strait, M. Wake, J. Dimarco, J. Kuzminski, and H. Zheng, "AC loss measurements of model and full size 50 mm SSC collider dipole magnets at Fermilab," *IEEE Trans. Appl. Superconduc.* **3**, 678 (1993).

[7.73] Z. Ang, I. Bejar, L. Bottura, D. Richter, M. Sheahan, L. Walckiers, R. Wolf, "Measurement of AC loss and magnetic field during ramps in the LHC model dipoles,"

IEEE Trans. Appl. Superconduc. **9**, 742 (1999).

[7.74] T. Honjo, T. Hasegawa, K. Kaiho, H. Yamaguchi, K. Arai, M. Yamaguchi, S. Fukui, K. Kato and K. Itagaki, "AC losses of HTS coils carrying transport current," *IEEE Trans. Appl. Superconduc.* **9**, 829 (1999).

[7.75] T. Hamajima, S. Hanai, Y. Wachi, M. Kyoto, M. Shimada, M. Ono, K. Shimada, L. Kushida, M. Tezuka, N. Martovetsky, J. Zbasnik, J. Moller, Y. Takahashi, K. Matsui, T. Isono, M. Yamamoto, I. Takano, T. Himeno, N. Hirano, K. Shinoda, T. Satow, "AC loss performance of the 100 kWh SMES model coil," *IEEE Trans. Appl. Superconduc.* **10**, 812 (2000).

[7.76] Charles E. Oberly, Larry Long, Gregory L. Rhoads and W. James Carr Jr., "AC loss analysis for superconducting generator armatures wound with subdivided Y-Ba-Cu-O coated tape," *Cryogenics* **41**, 117 (2001).

[7.77] Masataka Iwakuma, Kazuo Funaki, Kazuhiro Kajikawa, Hideki Tanaka, Takaaki Bohno, Akira Tomioka, Hisao Yamada, Shinichi Nose, Masayuki Konno, Yujiro Yagi, Hiroshi Maruyama, Takenori Ogata, Shigeru Yoshida, Kouichi Ohashi, Katsuya Tsutsumi and Kazuo Honda, "AC loss properties of a 1 MVA single-phase HTS power transformer," *IEEE Trans. Appl. Superconduc.* **11**, 1482 (2001).

[7.78] Emmanuel Vinot, Guillaume Donnier-Valentin, Pascal Tixador, and Gérard Meunier, "AC losses in superconducting solenoids," *IEEE Trans. Appl. Superconduc.* **12**, 1790 (2002).

[7.79] B. Péerez, A. Álvarez, P. Suárez, D. Cáceres, J.M. Ceballos, X. Obradors, X. Granados, and R. Bosch, "AC losses in a toroidal superconducting transformer," *IEEE Trans. Appl. Superconduc.* **13**, 2341 (2003).

[7.80] K. Tasaki, M. Ono, and T. Kuriyama, "Study on AC losses of a conductive cooled HTS coil," *IEEE Trans. Appl. Superconduc.* **13**, 1565 (2003).

[7.81] M.N. Wilson, M. Anerella, G. Ganetis, A.K. Ghosh, P. Joshi, A. Marone, C. Muehle, C. Muratore, J. Schmalzle, R. Soika, R. Thomas, P. Wanderer, J. Kaugerts, G. Moritz, and W.V. Hassenzahl, "Measured and calculated losses in model dipole for GSI's heavy ion synchrotron," *IEEE Trans. Appl. Superconduc.* **14**, 306 (2004).

[7.82] Kenji Tasaki, Toru Kuriyama, Shunji Nomura, Yukihiro Sumiyoshi, Hidemi Hayashi, Hironobu Kimura, Masataka Iwakuma, and Kazuo Funaki, "AC operating test results for a conduction-cooled HTS coil," *IEEE Trans. Appl. Superconduc.* **14**, 731 (2004).

[7.83] Hirofumi Kasahara, Fumio Sumiyoshi, Akifumi Kawagoe, Kazuto Kubota, and Shirabe Akita, "AC losses in long Bi-2223 tapes wound into a solenoidal-coil," *IEEE Trans. Appl. Superconduc.* **14**, 1078 (2004).

[7.84] Jong-Tae Kim, Woo-Seok Kim, Sung-Hoon Kim, Kyeong-Dal Choi, Jin-Ho Han, Gye-Won Hong, and Song-Yop Hahn, "Analysis of AC losses in HTS pancake windings for transformer according to the operating temperature," *IEEE Trans. Magn.* **41**, 1888 (2005).

[7.85] Myung-Jin Park, Sang-Yeop Kwak, Woo-Seok Kim, Seoung-Wook Lee, Ji-Kwang Lee, Jin-Ho Han, Kyeong-Dal Choi, Hyun-Kyo Jung, Ki-Chul Seong, and Song-yop Hahn, "AC Loss and Thermal Stability of HTS Model Coils for a 600 kJ SMES," *IEEE Trans. Appl. Superconduc.* **17**, 2418 (2007).

[7.86] A.J.M. Roovers, W. Uijttewaal, H.H.J. ten Kate, B. ten Haken and L.J.M. van de Klundert, "A loss measurement system in a test facility for high-current superconducting cables and wires," *IEEE Trans. Magn.* **24**, 1174 (1988).

[7.87] M. Takayasu, C.Y. Gung, M.M. Steeves, B. Oliver, D. Reisner and M.O. Hoenig, "Calorimetric measurement of AC loss in Nb_3Sn superconductors," *Proc. 11*$^{\text{th}}$*Int.*

Conf. Magnet Tech. (MT-11), 1033 (1990).

[7.88] C.Y. Gung, M. Takayasu, M.M. Steeves, and M.O. Hoenig, "AC loss measurements of Nb_3Sn wire carrying transport current," *IEEE Trans. Magn.* **27**, 2162 (1991).

[7.89] E.N. Aksenova and P.V. Aksenova, "New equipment for calorimetric measurement of AC losses in superconducting samples," *Cryogenics* **32**, 223 (1992).

[7.90] S. Fleshler, L.T. Cronis, G.E. Conway, A.P. Malozemoff, T. Pe, J. McDonald, J.R. Clem, G. Vellego, P. Metra, "Measurement of the AC power loss of $(Bi,Pb)_2Sr_2Ca_2Cu_3O_x$ composite tapes using the transport technique," *Appl. Phys. Lett.* **67**, 3189 (1995).

[7.91] S. Fukui, O. Tsukamoto, N. Amemiya, I. Hlásnik, "Dependence of self field AC losses in AC multifilamentary composites on phase of external AC magnetic field," *IEEE Trans. Appl. Superconduc.* **5**, 733 (1995).

[7.92] Hervé Daffix, Pascal Tixador, "Electrical AC loss measurements in superconducting coils," *IEEE Trans. Appl. Superconduc.* **7**, 286 (1997).

[7.93] G. Snitchler, J. Campbell, D. Aized, A. Sidi-Yekhlef, S. Fleshler, S. Kalsi, and R. Schwall, "Long length calorimetric measurement of AC losses of Bi-2223 with external field oriented perpendicular to the tape width," *Appl. Superconduc.* **7**, 290 (1997).

[7.94] D.E. Daney, H.J. Boenig, M.P. Maley, D.E. McMurry, and B.G. DeBlanc, "Ac loss calorimeter for three-phase cable," *IEEE Trans. Appl. Superconduc.* **7**, 310 (1997).

[7.95] S.P. Ashworth and M. Suenaga, "Measurement of ac losses in superconductors due to ac transport currents in applied ac magnetic fields," *Physica C: Superconduc.* **313**, 175 (1999).

[7.96] Kazuhiro Kajikawa, Masataka Iwakuma, Kazuo Funaki, Mitsuo Wada and Atsushi Takenaka, "Influences of geometrical configuration on AC loss measurement with pickup-coil method," *IEEE Trans. Appl. Superconduc.* **9**, 746 (1999).

[7.97] Curt Schmidt, "Calorimetric ac-loss measurement of high T_c-tapes at 77 K, a new measuring technique," *Cryogenics* **40**, 137 (2000).

[7.98] O. Tsukamoto, J. Ogawa, M. Ciszek, D. Miyagi, I. Okazaki, Y. Niidome and S. Fukui, "Origins of errors in AC transport current loss measurements of HTS tapes and methods to suppress errors," *IEEE Trans. Appl. Superconduc.* **11**, 2208 (2001).

[7.99] Michael Staines, Stephan Rupp, David Caplin, Dingan Yu, and Steven Fleshler, "Calibration of Hall sensor AC loss measurements," *IEEE Trans. Appl. Superconduc.* **11**, 2224 (2001).

[7.100] S. W. Schwenterly, A. Demko, J.W. Lue, M.S. Walker, C.T. Reis, D.W. Hazelton, Xin Shi, and M.T. Gardner, "AC loss measurements with a cryocooled sample," *IEEE Trans. Appl. Superconduc.* **11**, 4027 (2001).

[7.101] R.J. Soulen, Jr., M.S. Osofsky, M. Patten, and T. Datta, "A new technique for the measurement of AC loss in second-generation HTS tapes," *IEEE Trans. Appl. Superconduc.* **12**, 1607 (2002).

[7.102] Jeffrey O. Willis, Martin P. Maley, Heinrich J. Boenig, Giacomo Coletta, Renata Mele, and Marco Nassi, "AC losses in prototype multistrand conductors for warm dielectric cable designs," *IEEE Trans. Appl. Superconduc.* **13**, 1960 (2003).

[7.103] IEC61788-8 Superconductivity–Part 8: AC loss measurements—Total AC loss measurement of Cu/NbTi composite superconducting wires exposed to a trans-

verse alternating magnetic field by a pickup coil method, First edition, April 2003.

[7.104] Arend Nijhuis, Herman H.J. ten Kate, Pierluigi Bruzzone, Luca Bottura, "Parametric study on coupling loss in subsize ITER Nb_3Sn cabled specimen," *IEEE Trans. Magn.* **4**. 2743 (1996).

[7.105] Arend Nijhuis, Herman H.J. ten Kate, Victor Pantsyrny, Alexander K. Shikov, Marco Santini, "Interstrand contact resistance and AC loss of a 48-strands Nb3 Sn CIC conductor with a Cr/Cr-oxide coating," *IEEE Trans. Appl. Superconduc.* **10**, 1090 (2000).

[7.106] S. Egorov, I. Rodin, A. Lancetov, A. Bursikov, M. Astrov, S. Fedotova, Ch. Weber, and J. Kaugerts, "AC loss and interstrand resistance measurement for NbTi cable-in-conduit conductor," *IEEE Trans. Appl. Superconduc.* **12**, 1607 (2002).

[7.107] Takataro Hamajima, Naoyuki Harada, Takashi Satow, Hiroshi Shimamura, Kazuya Takahata, and Makoto Tsuda, "Long time constants of irregular AC coupling losses in a large superconducting coil," *IEEE Trans. Appl. Superconduc.* **12**, 1616 (2002).

[7.108] H. Eckelmann, M. Quilitz, C. Schmidt, W. Goldacker, M. Oomen, M. Leghissa, "AC losses in multifilamentary low AC loss Bi(2223) tapes with novel interfilamentary resistive carbonate barriers," *IEEE Trans. Appl. Superconduc.* **9**, 762 (1999).

[7.109] Naoyuki Amemiya, Keiji Yoda, Satoshi Kasai, Zhenan Jiang, George A. Levin, Paul N. Barnes, and Charles E. Oberly, "AC loss characteristics of multifilamentary YBCO coated conductors," *IEEE Trans. Appl. Superconduc.* **15**, 1637 (2005).

[7.110] Mike D. Sumption, Paul N. Barnes, and Edward W. Collings, "AC losses of coated conductors in perpendicular fields and concepts for twisting," *IEEE Trans. Appl. Superconduc.* **15**, 2815 (2005).

[7.111] M. Majoros, B.A. Glowacki, A.M. Campbell, G.A. Levin, P.N. Barnes, and M. Polak, "AC losses in striated YBCO coated conductors," *IEEE Trans. Appl. Superconduc.* **15**, 2819 (2005).

[7.112] Osami Tsukamoto, Naoki Sekine, Marian Ciszek, and Jun Ogawa, "A method to reduce magnetization losses in assembled conductors made of YBCO coated conductors," *IEEE Trans. Appl. Superconduc.* **15**, 2823 (2005).

[7.113] K. Osamura, N. Wada, T. Ogawa, and F. Nakao, "Formation of submicron-thick oxide barrier for reducing AC loss in multifilamentary Bi2223 tape," *IEEE Trans. Appl. Superconduc.* **15**, 2875 (2005).

[7.114] Kunihiko Egawa (personal communication, 2003).

[7.115] Shunji Yamamoto, Tadatoshi Yamada and Masatoshi Iwamoto, "Quench protection of persistent current switches using diodes in cryogenic temperature," *19th Annual IEEE Power Electronics Specialists Conf.* **1**, 321 (1988).

[7.116] Yukikazu Iwasa, "Microampere flux pumps for superconducting NMR magnets Part 1: Basic concept and microtesla flux measurement," *Cryogenics* **41**, 384 (2001).

[7.117] S. Jeong, H. Lee, and Y. Iwasa, "Superconducting flux pump for high temperature superconducting insert coils of NMR magnets," *Adv. Cryo. Engr.* **47**, 441 (2002).

[7.118] Haigun Lee, Homin Kim, and Yukikazu Iwasa, "A flux pump for NMR magnets," *IEEE Trans. Appl. Superconduc.* **13**, 1640 (2003).

[7.119] Rocky Mai, Seung-yong Hahn, Haigun Lee, Juan Bascuñán, and Yukikazu Iwasa,

"A digital flux injector for NMR Magnets," *IEEE Trans. Appl. Superconduc.* **15**, 2348 (2005).

[7.120] M. Lakrimi, P. Bircher, G. Dunbar, and P. Noonan, "Flux injector for NMR magnets," *IEEE Trans. Appl. Superconduc.* **17**, 1438 (2007).

[7.121] Weijun Yao, Woo-Seok Kim, Seungyong Hahn, J. Bascuñán, Hai-Gun Lee, and Yukikazu Iwasa, "A digital flux injector operated with a 317-MHz NMR magnet," *IEEE Trans. Appl. Superconduc.* **17**, 1450 (2007).

[7.122] Yoondo Chung, Itsuya Muta, Tsutomu Hoshino, and Taketsune Nakamura, "Performance of a linear type magnetic flux pump for compensating a little decremented persistent current of HTS magnets," *IEEE Trans. Appl. Superconduc.* **14**, 1723 (2004).

[7.123] Marijin Oomen, Martino Leghissa, Guenter Ries, Norbert Proelss, Heinz-Werner Neumueller, Florian Steinmeyer, Markus Vester, and Frank Daview, "HTS flux pump for cryogen-free HTS magnets," *IEEE Trans. Appl. Superconduc.* **15**, 1465 (2005).

[7.124] Yoondo Chung, Tsutomu Hoshino, and Taketsune Nakamura, "Current pumping performance of linear-type magnetic flux pump with use of feedback control circuit system," *IEEE Trans. Appl. Superconduc.* **16**, 1638 (2006).

[7.125] W. Denis Markiewicz, "Current injection for field decay compensation in NMR spectrometer magnets," *IEEE Trans. Appl. Superconduc.* **12**, 1886 (2002).

Chapter 8
Protection

8.1 Introductory Remarks

Protection is one of the five key design and operation issues—the others are stability; mechanical integrity; cryogenics; conductor. As qualitatively shown in Fig. 1.6, the difficulty or cost of magnet protection increases with operating temperature, while that of stability decreases. For HTS, protection can become a real challenge, while stability is benign, as discussed in ***Chapter 6***. The question most often asked concerning protection of HTS is this: "If HTS is so stable, why is it necessary to worry about protecting it?" The answer comes down to the cost of an HTS device vs. the cost of its protection and the probability of a system failure mode that needs protection. To protect or not to protect an "inherently stable" HTS magnet is a dilemma. This question is revisited in ***Discussion 8.7***.

Our focus is protection of the magnet winding; other parts of the magnet—mechanical, electrical, and cryogenic—are not addressed, except in passing. The issues included here are: 1) overheating; 2) overstraining (thermal and mechanical); 3) high internal voltage; and 4) protection techniques. **Problems & *Discussions*** also cover other relevant topics. Protection of course has been a key topic for superconducting magnets and has been addressed by many since the 1960s [1.27, 8.1–8.6], updated periodically [8.7–8.11]; other references are cited later where appropriate.

8.1.1 Thermal Energy vs. Magnetic Energy Densities

Unless a winding is protected, it is not uncommon for a small section of a magnet winding, a "hot spot," to absorb most of the magnetic energy stored in the winding, thereby becoming heated excessively and damaged permanently. However, the thermal energy density to melt a unit winding volume of a superconducting magnet is much greater than the stored magnetic energy density of the magnet.

To heat up copper, a good representative material of the winding, from 4 K (or even from 80 K) to its melting temperature of 1356 K entirely by the adiabatic conversion to heat, with enthalpy density, $h_{cu}(T)$, of copper, of the magnetic energy stored only within its *own* volume, the initial magnetic induction, B_0, would have to be ∼115 T:

$$\frac{B_0^2}{2\mu_\circ} = h_{cu}(1356\,\mathrm{K}) - h_{cu}(4\,\mathrm{K}\,\text{or}\,80\,\mathrm{K}) \simeq 5.2\times10^9\,\mathrm{J/m^3} \tag{8.1}$$

$$B_0 \simeq \sqrt{2(4\pi\times10^{-7}\,\mathrm{H/m})(5.2\times10^9\,\mathrm{J/m^3})} \simeq 115\,\mathrm{T}$$

That a magnet of even modest field, e.g., 3 T, has been permanently damaged by overheating demonstrates that a catastrophic energy concentration can occur in *real* magnets. If only the *local* magnetic energy density were converted *locally* into heat, field energy density to enthalpy density computation similar to Eq. 8.1 gives temperatures below 200 K for fields up to ∼25 T; for fields above ∼25 T, see ***Illustration*** in the next section.

Y. Iwasa, *Case Studies in Superconducting Magnets: Design and Operational Issues*,
DOI: 10.1007/b112047_8,

8.1.2 Hot Spot and Hot-Spot Temperature

A magnet quench is often initiated over a small winding volume, the so-called hot spot. As remarked above, the entire stored energy of the magnet may be dissipated over this hot spot, leading to permanent damage of the magnet.

Here, we study adiabatic absorption in a hot spot of the entire magnetic energy stored in the solenoid, E_m, and the resultant final temperature, T_f, the hot-spot temperature. The goal of any magnet protection is to limit T_f to ∼200 K or below, and definitely not above 300 K. The stored magnetic energy, E_m, of a solenoid of self inductance L at current I is given by:

$$E_m = \tfrac{1}{2} L I^2 \tag{3.79}$$

Equation 3.81 (p. 107) gives the inductance L of a solenoid (a_1, α, β) with a total number of turns N:

$$L = \mu_\circ a_1 \mathcal{L}(\alpha, \beta) N^2 \tag{3.81}$$

Figure 3.14 shows $\mathcal{L}(\alpha, \beta)$, which depends only on the winding parameters α and β. The axial center field, $B_\circ$, is given by:

$$B_\circ = \frac{\mu_\circ N I}{2a_1(\alpha - 1)\beta} F(\alpha, \beta) \tag{8.2}$$

where $F(\alpha, \beta)$ is given by:

$$F(\alpha, \beta) = \beta \ln \left(\frac{\alpha + \sqrt{\alpha^2 + \beta^2}}{1 + \sqrt{1 + \beta^2}} \right) \tag{3.13b}$$

From Eq. 8.2 we may express NI in terms of a_1, α, β, and $B_\circ$:

$$NI = \frac{2a_1(\alpha - 1)\beta B_\circ}{\mu_\circ F(\alpha, \beta)} \tag{8.3}$$

Thus, for a solenoid of α and β, its E_m may be related to its $B_\circ$ by:

$$E_m = \frac{4a_1^3(\alpha - 1)^2 \beta^2 \mathcal{L}(\alpha, \beta)}{F^2(\alpha, \beta)} \left(\frac{B_\circ^2}{2\mu_\circ} \right) \tag{8.4}$$

The total winding volume, V_w, is given by:

$$V_w = 2\pi a_1^3 (\alpha^2 - 1)\beta \tag{8.5}$$

Note that V_w includes all winding materials, conductor as well as non-conductors. The total volume of the hot spot (resistive zone), V_r, is given by:

$$V_r = f_r V_w = f_r 2\pi a_1^3 (\alpha^2 - 1)\beta \tag{8.6}$$

where f_r is the fraction of the hot-spot volume in the winding. If the magnet's total magnetic energy, E_m, is converted to heat adiabatically in the hot spot only, the average thermal energy density, e_{mr}, of the hot spot is given by:

$$e_{mr} \equiv \frac{E_m}{V_r} = \frac{2(\alpha - 1)\beta \mathcal{L}(\alpha, \beta)}{f_r \pi (\alpha + 1) F^2(\alpha, \beta)} \left(\frac{B_\circ^2}{2\mu_\circ} \right) \tag{8.7}$$

Note that e_{mr} does *not* depend on magnet volume, but on f_r, α, and β, and, of course, on $B_\circ$. However, the *actual* hot-spot volume required to limit its temperature T_f increases with winding volume. What must be the minimum size of a hot spot volume in a solenoid to meet a requirement of $T_f \leq$200 K is a key question of protection issue: this is discussed in ***Illustration*** presented below.

Table 8.1: Hot Spot Volume Fraction, f_r, vs. Hot-Temperature, T_f
Solenoid ($\alpha = 1.5$, $\beta = 2.0$) of $B_\circ$ 1.5 T–30 T

$f_r = 1(100\%)$		$T_i = 4\,\mathrm{K}$		$T_i = 80\,\mathrm{K}$	
$B_\circ$	e_{mr}	$T_f = 200\,\mathrm{K}$	$T_f = 300\,\mathrm{K}$	$T_f = 200\,\mathrm{K}$	$T_f = 300\,\mathrm{K}$
[T]	[J/cm^3]	f_r (%)		f_r (%)	
1.5	1.02	0.27	0.14	0.31	0.15
3.0	4.06	1.1	0.57	1.2	0.62
6.0	16.2	4.3	2.3	5.0	2.5
12	65.0	17	9.1	20	9.9
20	180	48	25	55	27
25	282	74	40	87	43
30	406	107	57	125	62

Illustration Table 8.1 presents the hot-spot volume fractions, f_r (%), of a solenoid ($\alpha = 1.5, \beta = 2.0$), in the range of $B_\circ$, 1.5–30 T, required to limit the final hot-spot temperature, T_f, to 200 K and 300 K for two initial winding temperatures, T_i, 4 K and 80 K. Here, the entire winding is assumed copper (density: 8.96 g/cm^3), and T_f is computed from $e_{mr} = h_{cu}(T_f) - h_{cu}(T_i)$, where e_{mr} is given by Eq. 8.7. The table indicates that for this solenoid ($\alpha = 1.5, \beta = 2.0$) generating, for example, 1.5 T, a hot spot can be a fraction (<1%) of the winding volume for two limits of T_f, 200 K and 300 K. This small f_r to meet the $T_f \leq 200\,\mathrm{K}$ requirement has a practical benefit for "detect-and-activate-the-heater" active protection: for most solenoids, a *cumbersome* "protection heater," discussed in **8.8.4**, planted within the winding needs to convert (and expand) only a fraction of the winding to a hot spot. However, as evident from Table 8.1, though $f_r \leq 1\,(100\%)$ for solenoids of $B_\circ$ up to ∼25 T, for ≥ 30 T, f_r exceeds 1 (100%), i.e., a portion of the stored energy must be dissipated *outside* the solenoid, i.e., into a dump resistor (**8.8.3**).

8.1.3 Temperature Data for Winding Materials

Table 8.2 lists "permissible" limits of hot-spot T_f for selected winding materials in magnets, LTS and HTS. Each entry in Table 8.2 is briefly discussed below.

Below 200 K It is generally agreed that resistive zones, even those confined to a small volume of the winding, may safely warm to as much as 200 K, because differential thermal strains in a winding with one segment at 200 K and the rest at an initial temperature of as low as 4.2 K will be less than ∼0.1%, which is safe for most magnet-grade conductors.

320 K (47°C) Lowest melting point among indium alloys.

335 K No I_c-degradation of a Cu-laminated YBCO sample ($I_c = 161$ A @77.3 K), heated by a 60-ms current pulse of 1.23 kA [8.12].

370 K A slight I_c-degradation (161 A→157 A) of the same Cu-laminated YBCO sample as above, heated by a 60-ms current pulse of 1.36 kA [8.12].

380 K Formvar insulation and Stycast 2850, organic materials often employed in windings, lose their usefulness beyond this temperature.

Table 8.2: "Permissible" Limits of T_f for Selected Materials

T [K]	*Remarks*
≤200	Considered acceptable for LTS and HTS winding
320	Lowest melting point among indium solders
335	Cu-laminated YBCO: *no* I_c-degradation [8.12]
370	Cu-laminated YBCO: *slight* I_c-degradation [8.12]
380	Limits of Formvar insulation and Stycast 2850
400	Paraffin melts
430	Indium melts
493	50Sn-50Pb solder melts
720	Bi2223-Ag: *no* I_c-degradation [8.12]
800	Bi2223-Ag: I_c-degradation [8.12]

400 K and 430 K At ∼400 K, paraffin melts; at 430 K, indium melts.

456 K (183°C) A solder widely used in magnets, 63Sn-37Pb, melts.

720 K No I_c-degradation of a Bi2223-Ag test sample ($I_c = 119$ A @77.3 K), heated by a 320-ms current pulse of 450 A [8.12].

800 K A major degradation of I_c ($I_c = 119$ A→50 A) in the same Bi2223-Ag test sample, heated by a 330-ms current pulse of 450 A [8.12].

8.1.4 Safe, Risky, and Very Risky Ranges of T_f

We may divide the above temperature range into three T_f ranges for the winding: 1) safe; 2) risky; and 3) very risky. Each range is specified below.

Safe T_f below 200 K is a safe upper limit for the normal zone. Note that there is no basic difference in this regard between LTS and HTS windings. However, in some applications, the recovery time to normal operating temperature is important and lower T_f's are desirable.

Risky The range 200–300 K may be regarded "cautious." If T_f is kept in this range, no winding materials are heated dangerously high and thus damaged, except possibly by thermal strains, which are briefly discussed below.

Very Risky T_f above 300 K is very risky for the winding, LTS or HTS.

8.1.5 Temperature-Induced Strains

Overheating, in addition to damaging the winding thermally, may also do so mechanically, by inducing strains. Table 8.3 presents linear thermal expansion (actually, contraction) data referenced to 293 K, $[L(T)–L(293\,\text{K})]/L(293\,\text{K})$, for selected magnet winding materials. Consider a pancake coil, and assume that the inner half of the coil build is heated to 140 K, while the outer half of the pancake coil remains at 80 K. The data in Table 8.3 indicate that a tensile strain induced in the innermost layer of the outer half would not exceed ∼0.1%, which should be safe. If the inner half of the winding build were to be heated to 300 K, while the outer half remains at 80 K, then induced strains could exceed 0.2%, a dangerous

Table 8.3: Mean Linear Thermal Expansion Data
— $[L(T)-L(293\,\mathrm{K})]/L(293\,\mathrm{K})$ in 10^{-3} —

Material	$[L(T)-L(293\,\mathrm{K})]/L(293\,\mathrm{K})$ in 10^{-3}
Copper	−3.00 (80 K); −2.34 (140 K)
Nickel	−2.11 (80 K); −1.71 (140 K)
Silver	−3.60 (80 K); −2.7 (140 K)
Sn50-Pb50 solder	−4.98 (80 K); −3.65 (140 K)
Stainless steel 304	−2.81 (80 K); −2.22 (140 K)
Epoxy	−10 (80 K); −9 (140 K)
Nb_3Sn	−1.41 (80 K); −1.02 (140 K)
NbTi	−1.67 (80 K); −1.24 (140 K)
Bi2223, *a-b* plane	−1.37 (80 K); −1.11 (140 K) [8.13]
Bi2223-Ag (tape)*	
roll (axial)/transverse (width)	each, -2.4 ± 0.3 (77 K) [8.14, 8.15]
Bi2223-Ag (3-ply tape)†	
roll (axial)/transverse (width)	each, -2.8 ± 0.3 (77 K) [8.14, 8.15]
YBCO	−2.23 (80 K); −1.82 (140 K) [8.16]

* 4.1-mm wide tape.

† 4.8-mm wide tape, with stainless steel strips sandwiching Bi2223-Ag.

level for Nb_3Sn and HTS. However, even if a *uniform* temperature is maintained during heating, because a magnet winding consists of materials of different thermal expansion coefficients (Table 8.3), uniform heating can still induce overstraining in a superconductor. It is generally safest to keep T_f below 200 K.

8.2 Adiabatic Heating

One of the major forms of permanent damage in a superconducting magnet is excessive heating ("overheating") of its composite conductor. If it is severe, the overheating may melt the composite or create thermal gradients in the winding that overstrain the superconductor, permanently degrading its J_c performance. Overheating has been studied, with experiment and analysis, since the 1960s.

Even if the magnet is isolated from its power supply and operating in persistent mode, as demonstrated above, overheating in a superconducting magnet may occur by dissipation within a small volume of the winding of the total magnetic energy stored in the magnet. In a powered magnet, overheating may also occur by resistive heating by the power supply, after the magnet is driven to the normal state; this heating can be localized or global, encompassing the entire winding volume. We may analyze adiabatic heating of a unit composite volume by modifying Eq. 6.1 with the conduction, disturbance, and cooling terms neglected:

$$C_{cd}(T)\frac{dT}{dt} \simeq \rho_{cd}(T)J^2_{cd_\circ}(t) \tag{8.8a}$$

$$\simeq \rho_m(T)J^2_{cd_\circ}(t) \tag{8.8b}$$

In Eq. 8.8*b* the conductor electrical resistivity, ρ_{cd}, is approximated by the matrix resistivity, ρ_m, as in the circuit model of Fig. 6.5 (or $n = \infty$ in Eq. 6.25). Note that Eq. 8.8 would be in the 7th row (Protection) of Table 6.1 in ***CHAPTER 6***.

8.2.1 Adiabatic Heating Under Constant-Current Mode

First, we study adiabatic heating under constant-current mode, as illustrated in Fig. 8.1: a resistive zone, $r(T)$, within a superconducting magnet (inductance L) connected to a constant-current supply that keeps the magnet operating current, I_{op}, constant. With the above assumption that the resistive zone carries the *entire* I_{op}, Eq. 8.8*b*, in the power density equation per *unit conductor length*, becomes:

$$A_{cd}C_{cd}(T)\frac{dT}{dt} = \frac{\rho_m(T)}{A_m}I_{op}^2(t) \tag{8.9a}$$

Inserting $I_{op}/A_m = J_{m_\circ}$ (Eq. 6.7*c*) into Eq. 8.9*a*, $C_{sc}(T) \approx C_{\overline{m}}(T) \approx C_m(T)$ and $A_m/A_{cd} = \gamma_{m/s}/(\gamma_{m/s}+1)$, where $\gamma_{m/s} \equiv A_m/(A_{sc}+A_{\overline{m}})$ (Eq. 6.21*b*), we obtain:

$$C_m(T)\frac{dT}{dt} = \left(\frac{A_m}{A_{cd}}\right)\rho_m(T)J_{m_\circ}^2 = \left(\frac{\gamma_{m/s}}{1+\gamma_{m/s}}\right)\rho_m(T)J_{m_\circ}^2 \tag{8.9b}$$

We may rearrange Eq. 8.9*b* and integrate between the initial values, $T = T_i$ and $t = 0$, and final values, $T = T_f$ and $t = \tau_{ah}$:

$$\int_{T_i}^{T_f}\frac{C_m(T)}{\rho_m(T)}\,dT = \left(\frac{A_m}{A_{cd}}\right)J_{m_\circ}^2\tau_{ah} \tag{8.9c}$$

$$= \left(\frac{\gamma_{m/s}}{1+\gamma_{m/s}}\right)J_{m_\circ}^2\tau_{ah} \tag{8.9d}$$

The temperature integral on the left-hand side of Eqs. 8.9*c* and 8.9*d* depends monotonically on T; we define a $Z(T_f, T_i)$ function:

$$Z(T_f, T_i) \equiv \int_{T_i}^{T_f}\frac{C_m(T)}{\rho_m(T)}\,dT \tag{8.10a}$$

For "alloy" matrix metals with $\rho_m(T)$ sufficiently constant to be approximated by a temperature-averaged resistivity, $\tilde{\rho}_m$, Eq. 8.10*a* may be simplified to:

$$Z(T_f, T_i) \simeq \frac{1}{\tilde{\rho}_m}\int_{T_i}^{T_f}C_m(T_f)\,dT = \frac{H_m(T_f) - H_m(T_i)}{\tilde{\rho}_m} \tag{8.10b}$$

where $H_m(T)$ is the matrix metal volumetric enthalpy at T.

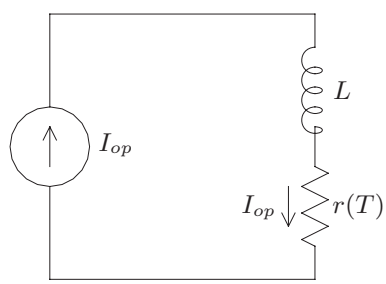

Fig. 8.1 Circuit representing a superconducting magnet of inductance L with a normal zone of T-dependent resistance $r(T)$, connected to a supply of constant-current I_{op}.

Figure 8.2 gives $Z(T,0)$ plots for silver (RRR = 1000, the ratio of electrical resistivities at 0°C and 4.2 K; 100); copper (200; 100; 50); aluminum (grade: 1100); and brass (70Cu-30Zn). The dashed line (barely discernable) is for brass with $\tilde{\rho}_m = 5.5\times10^{-8}\,\Omega\,\mathrm{m}$ (Eq. 8.10*b*). Note that for any combination of T_i and T_f:

$$Z(T_f,T_i) = Z(T_f,0) - Z(T_i,0) = Z(T_f) - Z(T_i) \tag{8.11}$$

For any combination of T_f and T_i, there is a heating duration $\tau^i_{dh}(T_f,T_i)$—the superscript i denotes under *constant-current* (at $J_{m_\circ}$) heating—given by:

$$\tau^i_{dh}(T_f,T_i) = \left(\frac{1+\gamma_{m/s}}{\gamma_{m/s}}\right)\frac{Z(T_f,T_i)}{J^2_{m_\circ}} \tag{8.12a}$$

Similarly, for any combination of T_f and T_i, there is a matrix current density, $J^i_{m_\circ}(T_f,T_i)$, under *constant-current* heating of duration τ_{dh}, given by:

$$J^i_{m_\circ}(T_f,T_i) = \sqrt{\left(\frac{1+\gamma_{m/s}}{\gamma_{m/s}}\right)\frac{Z(T_f,T_i)}{\tau_{dh}}} \tag{8.12b}$$

Because above ~300 K $C_m(T)$ approaches an asymptote, while $\rho_m(T)$ continues to increase with T, the integrand $C_m(T)/\rho_m(T)$ diminishes with T, and therefore a small additional increase in $Z(T_f,T_i)$ results in a drastic increase in T_f that in most instances damages the winding: keep T_f less than 200 K.

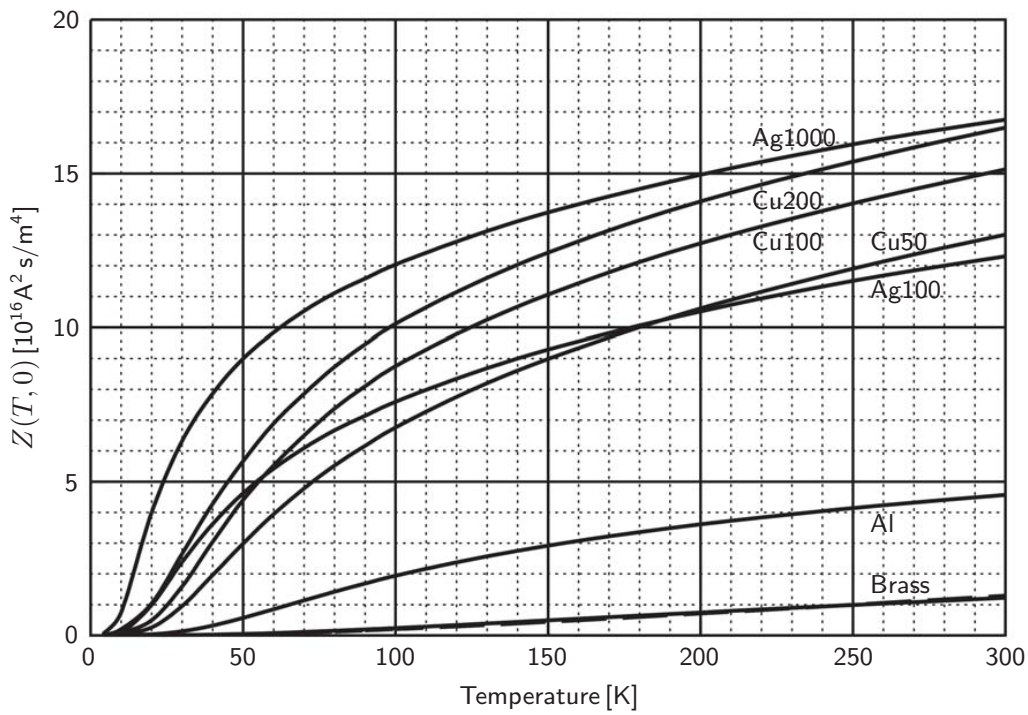

Fig. 8.2 $Z(T,0)$ plots. Ag1000 (RRR:1000); Ag100; Cu200; Cu100; Cu50; Al (Grade 1100); Brass (70Cu-30Zn)—also dashed line (Eq. 8.10*b*, with $\tilde{\rho}_m = 5.5\times10^{-8}\,\Omega\,\mathrm{m}$).

8.2.2 Adiabatic Heating Under Current-Discharge Mode

Here, we study adiabatic heating of a normal zone of resistance $r(t)$—or it can be of $r(T)$—within a superconducting magnet (L) under current-discharge mode, which is encountered quite often in the protection of superconducting magnets. Practical examples are illustrated later in **PROBLEMS & DISCUSSIONS**.

The magnet is initially ($t=0$) energized at current I_{op} and shunted by a "dump" (discharge) resistor (R_D). Figure 8.3 shows the circuit diagram, in which $I_m(t)$ is the time-dependent matrix metal current. $V_D \equiv R_d I_m(0) = R_d I_{op}$ is the "dump" (discharge) voltage across the dump resistor at $t=0$.

Under adiabatic heating with the same assumption used in expressing Eq. 8.9*a* by Eq. 8.9*b*, but $J_{m_\circ} = I_{op}/A_m$ (constant) replaced by $J_m(t) \equiv I_m(t)/A_m$, we have:

$$C_m(T)\frac{dT}{dt} = \left(\frac{A_m}{A_{cd}}\right)\rho_m(T)J_m^2(t) \tag{8.13}$$

The circuit equation for $I_m(t)$ is given by:

$$L\frac{dI_m(t)}{dt} + [R_D + r(t)]I_m(t) = 0 \tag{8.14}$$

We now invoke a simplifying assumption valid in most cases: $R_D \gg r(t)$. Equation 8.14 then may be solved for $I_m(t)$, and thus $J_m(t)$, with $\tau_{dg} = L/R_D$:

$$J_m(t) = J_{m_\circ} e^{-t/\tau_{dg}} \tag{8.15}$$

where $J_{m_\circ} \equiv J_m(t=0)$. Combining Eqs. 8.13 and 8.15 and using the definition for $Z(T_f, T_i)$, we obtain:

$$Z(T_f, T_i) = \left(\frac{A_m}{A_{cd}}\right)\int_0^\infty J_{m_\circ}^2 e^{-2t/\tau_{dg}}\,dt = \left(\frac{A_m}{A_{cd}}\right)J_{m_\circ}^2 \times \tfrac{1}{2}\tau_{dg} \tag{8.16a}$$

$$= \left(\frac{A_m}{A_{cd}}\right)J_{m_\circ}^2\left(\frac{L}{2R_D}\right) \tag{8.16b}$$

$$= \left(\frac{\gamma_{m/s}}{1+\gamma_{m/s}}\right)J_{m_\circ}^2\left(\frac{L}{2R_D}\right) \tag{8.16c}$$

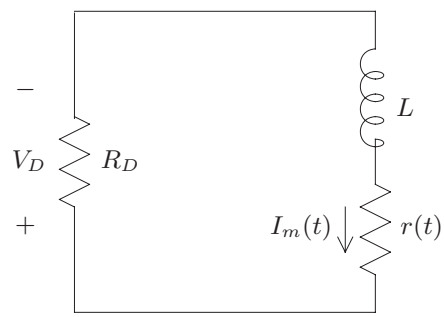

Fig. 8.3 Circuit representing a superconducting magnet of inductance L with a normal zone of $T(t)$-dependent resistance, $r(t)$, heated adiabatically under current-discharge mode. A "dump" resistor of R_D shunts the magnet terminals. $V_D \equiv R_d I_m(0)$ is the dump voltage across R_D at $t=0$.

The magnet inductance L and the dump resistance R_D may be expressed in terms, respectively, of the initial stored magnetic energy, E_m, of the magnet and the initial discharge voltage V_D across R_D. Thus:

$$L = \frac{2E_m}{I_{op}^2} \tag{8.17a}$$

$$R_D = \frac{V_D}{I_{op}} \tag{8.17b}$$

Combining Eqs. 8.16*b*, 8.17*a*, and 8.17*b*, we obtain:

$$Z(T_f, T_i) = \left(\frac{A_m}{A_{cd}}\right) \frac{J_{m_\circ}^2 E_m}{V_D I_{op}} \tag{8.18a}$$

Equation 8.18*a* shows that T_f is higher for combinations of greater $J_{m_\circ}$ and/or E_m and smaller V_D and/or I_{op}. We may consider the ratio $E_m/V_D I_{op}$ to be an effective discharge period, where $V_D I_{op}$ is the effective discharge power. Noting that $J_{m_\circ} = I_{op}/A_m$, we may reduce Eq. 8.18*a* to:

$$Z(T_f, T_i) = \frac{J_{m_\circ} E_m}{A_{cd} V_D} \tag{8.18b}$$

Under this discharge current mode, there is a maximum matrix current density, $J_{m_\circ}^D$, for any winding temperature limit T_f:

$$J_{m_\circ}^D = \frac{A_{cd} V_D Z(T_f, T_i)}{E_m} \tag{8.19}$$

Equation 8.19 gives a criterion for $J_{m_\circ}$ that is entirely different from the cryostability criterion of Eq. 6.22.

8.2.3 Adiabatic Heating in Magnet with Shorted Terminals

Let us assume a magnet (L) with its terminals shorted, in which at $t = 0$ a small normal zone is developed within its winding, as shown in Fig. 8.4; the current, $I_m(t)$, flows in the matrix metal in the normal zone of resistance $r(T)$.

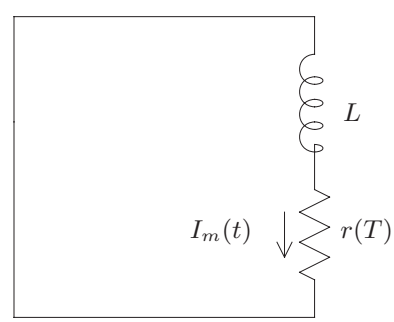

Fig. 8.4 Circuit representing a shorted superconducting magnet of inductance L with a normal zone of T-dependent resistance $r(T)$, heated adiabatically. The current in the normal zone is $I_m(t)$.

The matrix metal current $I_m(t)$ is governed by:

$$L\frac{dI_m(t)}{dt} + r(T)I_m(t) = 0 \tag{8.20}$$

$r(T)$, expressed as T-dependent, obviously increases with time for two reasons: 1) magnetic energy is being converted to thermal energy to raise the normal zone temperature; and 2) the normal zone itself is spreading in the winding. For the purpose of our analysis here, the *simplest* assumption is used: a constant normal-zone resistance, $r(T) = R_{nz}$, given by:

$$R_{nz} = \frac{\rho_m(T_f)\ell_{nz}}{4A_m} \tag{8.21}$$

where $\rho_m(T_f)$ is the matrix resistivity at the normal zone's final temperature; ℓ_{nz} is the total conductor length in the resistive state when the current has decayed to zero. The factor of 4 in the denominator accounts for "averaging," both in time (factor of 2) and space (another factor of roughly 2), of the normal zone temperature, from T_i to T_f. Note that Eq. 8.21 also assumes $\rho_m(T_f) \gg \rho_m(T_i)$, which may not be valid for some combinations of T_f and T_i, but the uncertainty introduced by this simplification is considered small compared with that arising from the basic assumption of Eq. 8.21. For R_{nz} constant, $J_m(t) = I_m(t)/A_m$, with $J_m(t=0) = I_{op}/A_m = J_{m_\circ}$, is given by:

$$J_m(t) = J_{m_\circ} e^{-t/(L/R_{nz})} \tag{8.22}$$

Under adiabatic heating, we obtain:

$$Z(T_f, T_i) = \left(\frac{A_m}{A_{cd}}\right)\int_0^\infty J_{m_\circ}^2 e^{-2t/(L/R_{nz})}dt \tag{8.23a}$$

$$Z(T_f, T_i) = \tfrac{1}{2}\left(\frac{A_m}{A_{cd}}\right)J_{m_\circ}^2\left(\frac{L}{R_{nz}}\right) \tag{8.23b}$$

$$= \tfrac{1}{2}\left(\frac{A_m}{A_{cd}}\right)J_{m_\circ}^2\tau_{dg} \tag{8.23c}$$

where $\tau_{dg} = L/R_{nz}$ is the effective discharge time constant. For a solenoid of a_1, α, and total number of turns N, the total length of the composite driven to the normal state, ℓ_{nz}, may be given by:

$$\ell_{nz} = f_r \pi a_1(\alpha + 1)N \tag{8.24}$$

where f_r is the fraction of the winding volume in the resistive state, as in Eq. 8.6. Combining Eqs. 8.21 and 8.24, we obtain:

$$R_{nz} = f_r\frac{\rho_m(T_f)\pi a_1(\alpha+1)N}{4A_m} \tag{8.25}$$

We may express N in terms of L and other magnet parameters (Eq. 3.81):

$$N = \sqrt{\frac{L}{\mu_\circ a_1 \mathcal{L}(\alpha, \beta)}} \tag{8.26}$$

R_{nz} may thus be given by:

$$R_{nz} = f_r \frac{\pi(\alpha+1)\rho_m(T_f)}{4A_m} \sqrt{\frac{a_1 L}{\mu_\circ \mathcal{L}(\alpha, \beta)}} \tag{8.27}$$

Thus, we may obtain the discharge time constant, τ_{dg}:

$$\tau_{dg} = \frac{L}{R_{nz}} = \frac{4A_m}{f_r \pi(\alpha+1)\rho_m(T_f)} \sqrt{\frac{\mu_\circ \mathcal{L}(\alpha, \beta) L}{a_1}} \tag{8.28a}$$

Noting that $J_{m_\circ} = I_{op}/A_m$ and $L = 2E_m/I_{op}^2$, where E_m is the initial magnetic energy stored by the magnet, we may express Eq. 8.28*a* as:

$$\tau_{dg} = \frac{4}{f_r \pi(\alpha+1)\rho_m(T_f) J_{m_\circ}} \sqrt{\frac{2\mu_\circ \mathcal{L}(\alpha, \beta) E_m}{a_1}} \tag{8.28b}$$

Combining Eqs. 8.23*c* and 8.28*b*, we obtain:

$$\rho_m(T_f) Z(T_f, T_i) = \left(\frac{A_m}{A_{cd}}\right) \frac{2J_{m_\circ}}{f_r \pi(\alpha+1)} \sqrt{\frac{2\mu_\circ \mathcal{L}(\alpha, \beta) E_m}{a_1}} \tag{8.29}$$

Equation 8.29 may be solved for T_f. As noted in **8.1.2** above, T_f is critically dependent on f_r, which is generally unknown, but for the illustrative examples given in **8.1.2**, to keep T_f below 200 K when $B_\circ \geq 5$ T, f_r should be at least ~0.1. This condition can be difficult to meet for HTS with a small normal zone propagation (NZP) speed, discussed in **8.4**.

Although f_r is unknown, for a given combination of T_f and T_i there is a maximum matrix current density, $J_{m_\circ}^{sh}$, that limits overheating for a shorted magnet:

$$J_{m_\circ}^{sh} = \tfrac{1}{2}\left(\frac{A_{cd}}{A_m}\right) f_r \pi(\alpha+1)\rho_m(T_f) Z(T_f, T_i) \sqrt{\frac{a_1}{2\mu_\circ \mathcal{L}(\alpha, \beta) E_m}} \tag{8.30a}$$

As expected $J_{m_\circ}^{sh}$ increases with combinations of greater f_r and T_f and smaller E_m. Because $E_m = \mu_\circ a_1 \mathcal{L}(\alpha, \beta) N^2 I_{op}^2/2$, $J_{m_\circ}^{sh}$ may also be given by:

$$J_{m_\circ}^{sh}(T_f, T_i) = \tfrac{1}{2}\left(\frac{A_{cd}}{A_m}\right) \frac{f_r \pi(\alpha+1)\rho_m(T_f) Z(T_f, T_i)}{\mu_\circ \mathcal{L}(\alpha, \beta) N I_{op}} \tag{8.30b}$$

Equation 8.30*b* states that a solenoid of large ampere-turns (NI_{op}) must operate at smaller $J_{m_\circ}^{sh}$.

8.2.4 Adiabatic Heating Under Constant-Voltage Mode

Finally, consider a superconducting magnet that is resistive over its entire winding of total composite conductor length ℓ_{cd}, $R_m(T)$, connected to a constant-voltage supply, as shown in Fig. 8.5. Here, the entire winding is at $T(t)$. The power density equation, similar to Eq. 8.9a, is given, with $R_m(T) = \rho_m(T)\ell_{cd}/A_m$, by:

$$A_{cd}\ell_{cd}C_{cd}(T)\frac{dT}{dt} = \frac{V_{op}^2}{R_m(T)} = \frac{V_{op}^2 A_m}{\rho_m(T)\ell_{cd}}$$

$$C_m(T)\frac{dT}{dt} \simeq \left(\frac{A_m}{A_{cd}}\right)\frac{V_{op}^2}{\rho_m(T)\ell_{cd}^2} \tag{8.31a}$$

We may express Eq. 8.31a as Eq. 8.9c:

$$\int_{T_i}^{T_f} C_m(T)\rho_m(T)\,dT = \left(\frac{A_m}{A_{cd}}\right)\frac{V_{op}^2}{\ell_{cd}^2}\tau_{ah} \tag{8.31b}$$

where τ_{ah} is the heating duration under constant-voltage mode. As with $Z(T_f, T_i)$, we may define a function $Y(T_f, T_i)$:

$$Y(T_f, T_i) \equiv \int_{T_i}^{T_f} C_m(T)\rho_m(T)\,dT \tag{8.32a}$$

which, for alloy matrix metals, may be simplified, as Eq. 8.10b, by:

$$Y(T_f, T_i) \simeq \tilde{\rho}_m[H_m(T_f) - H_m(T_i)] \tag{8.32b}$$

Similarly to $Z(T_f, T_i)$, $Y(T_f, T_i)$ is given by:

$$Y(T_f, T_i) = Y(T_f) - Y(T_i) \tag{8.32c}$$

Figure 8.6 presents $Y(T, 0)$ plots for the same metals as those for $Z(T, 0)$ in Fig. 8.2. Note that metal purity, which greatly influences ρ_m for temperatures below $\sim$50 K and thus has a large impact on $Z(T, 0)$, has little impact on $Y(T, 0)$ for $T > \sim$100 K.

From Eq. 8.31b we may derive, similar to Eq. 8.9c:

$$Y(T_f, T_i) = \left(\frac{A_m}{A_{cd}}\right)\frac{V_{op}^2\tau_{ah}}{\ell_{cd}^2} \tag{8.33}$$

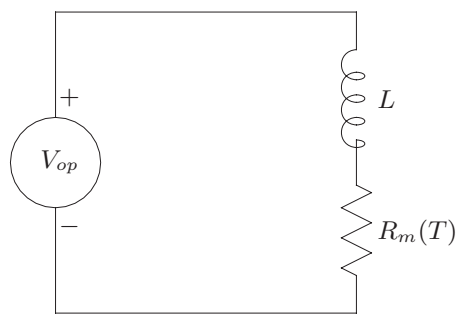

Fig. 8.5 Circuit for a superconducting magnet (L) with the *entire* winding in the normal state, $R_m(T)$, under constant-voltage (V_{op}) heating mode.

Noting that ℓ_{cd} for a solenoidal coil is given by Eq. 8.24 with $f_r = 1$, and using Eq. 8.26, we find:

$$\ell_{cd} = \pi(\alpha+1)\sqrt{\frac{a_1 L}{\mu_\circ \mathcal{L}(\alpha,\beta)}} \tag{8.34}$$

Inserting Eq. 8.34 for ℓ_{cd} into Eq. 8.33, we obtain:

$$Y(T_f, T_i) = \left(\frac{A_m}{A_{cd}}\right)\frac{\mu_\circ \mathcal{L}(\alpha,\beta) V_{op}^2 \tau_{dh}}{\pi^2(\alpha+1)^2 a_1 L} \tag{8.35}$$

For any combination of T_f and T_i, there is a duration limit, τ_{dh}^v, under *constant-voltage* heating, given by:

$$\tau_{dh}^v = \left(\frac{A_{cd}}{A_m}\right)\frac{\pi^2(\alpha+1)^2 a_1 L}{\mu_\circ \mathcal{L}(\alpha,\beta)}\left[\frac{Y(T_f,T_i)}{V_{op}^2}\right] \tag{8.36}$$

Because $\rho_m(T)$ increases with T, the $Y(T,0)$ plots continue to increase with T beyond 300 K. Since the total resistance of this superconducting magnet in the normal state, $R_m(T)$, is proportional to $\rho_m(T)\ell_{cd}$, the heating current through the magnet, given by $V_{op}/R_m(T)$, decreases with T. This implies that τ_{dh}^v increases more rapidly than T_f; i.e., under constant-voltage heating mode, thermal runaway is less likely than under constant-current mode. For heating a superconducting magnet, therefore, the constant-voltage mode is safer than the constant-current mode. This is further studied in **PROBLEM 8.1**.

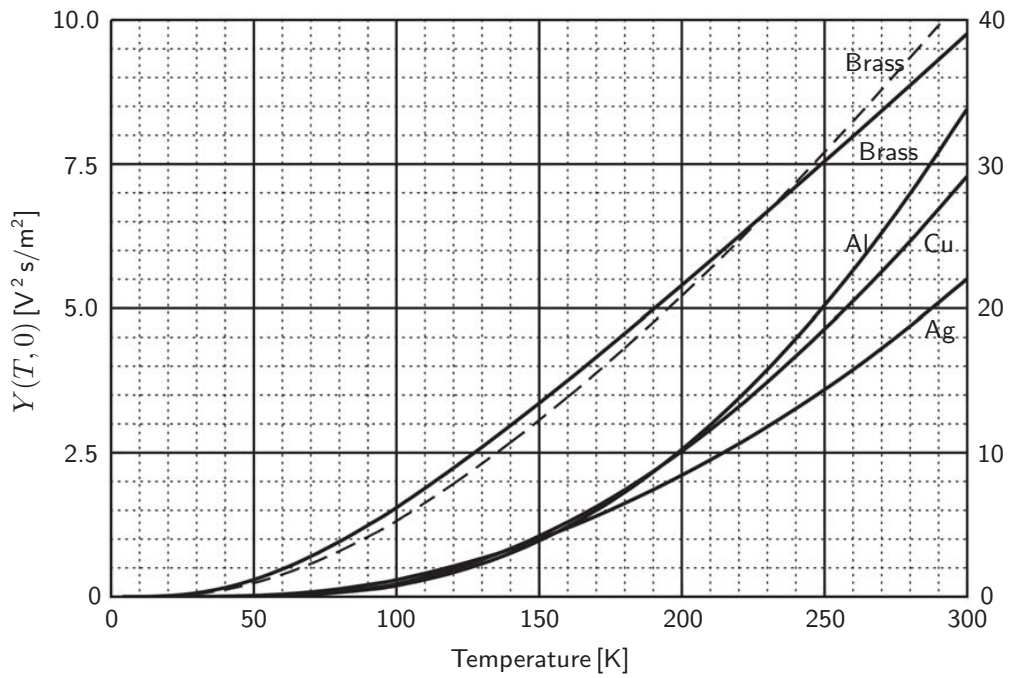

Fig. 8.6 $Y(T,0)$ plots. *Left-hand vertical* scale: Ag (100 to 1000); Cu (50 to 200); Al (Grade: 1100). *Right-hand vertical* scale: brass (Cu70-Zn30)—also dashed line (Eq. 8.32*b* with $\tilde{\rho}_m = 5.5\times10^{-8}\,\Omega\,\mathrm{m}$). Especially for temperatures above ∼100 K, $Y(T,0)$ is nearly independent of the purity of Ag and Cu.

8.3 High Voltage

One attractive feature of most superconducting magnets is the "low" voltage required for energization, i.e., ∼10 V, compared with >100 V for normal-metal magnets generating the same field strength. Magnet operation consists of three time regimes: 1) charge-up; 2) quiescent, at a fixed field; and 3) discharge. Unfortunately, this low-voltage sufficiency generally is guaranteed only during the first two time regimes; Regime 3 may entail very high voltages, particularly if it is in fault mode. Of course Regime 3 may abruptly begin during Regime 1 or Regime 2, initiated by a magnet quench. Because a superconducting magnet is an inductor, its terminal voltage contains an inductive component given by:

$$V = L\frac{dI}{dt} \tag{8.37a}$$

Noting that $L = 2E_m/I_\circ^2$, where $I_\circ$ is the magnet current at the beginning of Regime 3, and because in this regime the total drop in magnet current, ΔI, often is equal to $I_\circ$, we may express Eq. 8.37*a* as:

$$V = \frac{2E_m}{I_\circ^2}\left(\frac{\Delta I}{\Delta t}\right) \approx \frac{2E_m}{I_\circ \Delta t} \tag{8.37b}$$

Protection becomes a serious business chiefly for those magnets with E_m above ∼100 kJ; magnets storing less energy than this are dispensable or at least unlikely to cause severe hardship. If we specify the dangerous-voltage level to be 1 kV in a "real-world" superconducting magnet, then from Eq. 8.37*b*, with $E_m = 100$ kJ, any combination of $I_\circ \Delta t$ of less than 200 A s will generate more than 1 kV, with ample energy in the magnet to do severe damage. For example, a 100-kJ magnet operating at $I_\circ = 1$ kA will generate 1 kV if the current is discharged in a time scale of ∼200 ms. The problem becomes worse as the stored energy increases [8.17].

From Eq. 8.37*b* we can also see that the current leads must withstand high discharge voltages. Anishchenko, Heller, and others [8.18] and Gerhold [8.19] have developed current leads designed to withstand high voltages.

8.3.1 Arcing Environments

A superconducting winding may be in an environment where the designer has options to choose from, for example: 1) vacuum vs. nonvacuum; 2) liquid vs. vapor; and/or 3) helium vs. nitrogen. For resistance to arcing, vacuum, except near the Paschen pressure (see below), is preferred to nonvacuum; liquid to vapor; and nitrogen to helium. However, a discharge can upset the designer's choice of environment. Heating in the winding initiated by the fault can upset the design condition: 1) it may accelerate outgasing in the system, which may make it difficult for the system to maintain high vacuum; or 2) it may locally convert the environment from liquid to vapor.

Useful data on dielectric breakdown of cryogens have been collected since the early 1970s [8.20, 8.21]. Gerhold presents dielectric breakdown data for nitrogen and helium [8.22]. There are many design issues that affect arcing in a superconducting magnet, with no clear-cut data that can be applied for general discussion. Schultz covers this large topic concisely, with figures and data [1.28, 8.11].

Table 8.4: Data of Minimum Arcing Voltage, V_{mn}, and Pd at V_{mn} for Gases at Room Temperature [8.23]

Gas	V_{mn} [V]	Pd @V_{mn} [torr mm]
Air	327	5.67
Ar	137	9
H_2	273	11.5
He	156	40
N_2	251	6.7

8.3.2 Paschen Voltage Test

Table 8.4 presents minimum arcing voltage V_{mn} and Pd at V_{mn} data for gases at *room temperature* [8.23]. P is the gas pressure and d is the distance over which V_{mn} is applied. Note that V_{mn} is greater for diatomic gases than noble gases.

A Paschen voltage test is routinely performed for superconducting magnets with a discharge voltage above ∼1 kV. The test subjects the cryostat accesses (penetrations) such as current leads and measurement cables to a voltage, starting with the cryostat evacuated to a pressure, e.g., of $P \sim 10^{-3}$ torr. If no leakage current is observed as voltage is increased up to V_{mn}, the measurement is repeated at successive levels of pressure, from $P \sim 10^{-2}$ torr to atmospheric pressure (of, *not helium*, but air). The system must pass this simple test before more elaborate high-voltage tests are conducted.

8.3.3 Peak Internal Voltage Within a Quenching Magnet

Using a simple model and invoking additional simplifying assumptions, we study the peak internal voltage that can arise within a quenching superconducting magnet with its terminals shorted [1.27; 8.25]. For two common modes of superconducting magnet operation the shorted-terminals condition is quite valid over at least a short period of time: 1) during Regime 1, when the magnet is connected to a constant-voltage current source and the magnet current is increasing towards its Regime 2 level; 2) when the magnet, in Regime 2, is shunted with a persistent-mode switch. In either mode, when a fault develops the magnet shifts to Regime 3, either forced (active protection) or automatically (passive protection), and the terminals can no longer be considered shorted. However, by this time, especially when the magnet is actively protected, because of a delay in execution, damage already may have occurred.

Internal Voltage Distribution

In a shunted magnet in which a normal zone is spreading, there is a distribution of internal voltage that depends on the normal zone volume within the winding volume. Figure 8.7 shows voltage distributions within a magnet, in which the winding is wound from one grounded terminal to the other grounded terminal. The inductance per unit conductor length is assumed constant. In Fig. 8.7a, 10% ($f_r = 0.1$) of the winding, starting from one terminal, has gone resistive; in Fig. 8.7b, 20%; in Fig. 8.7c, 50%; and in Fig. 8.7d, 100%.

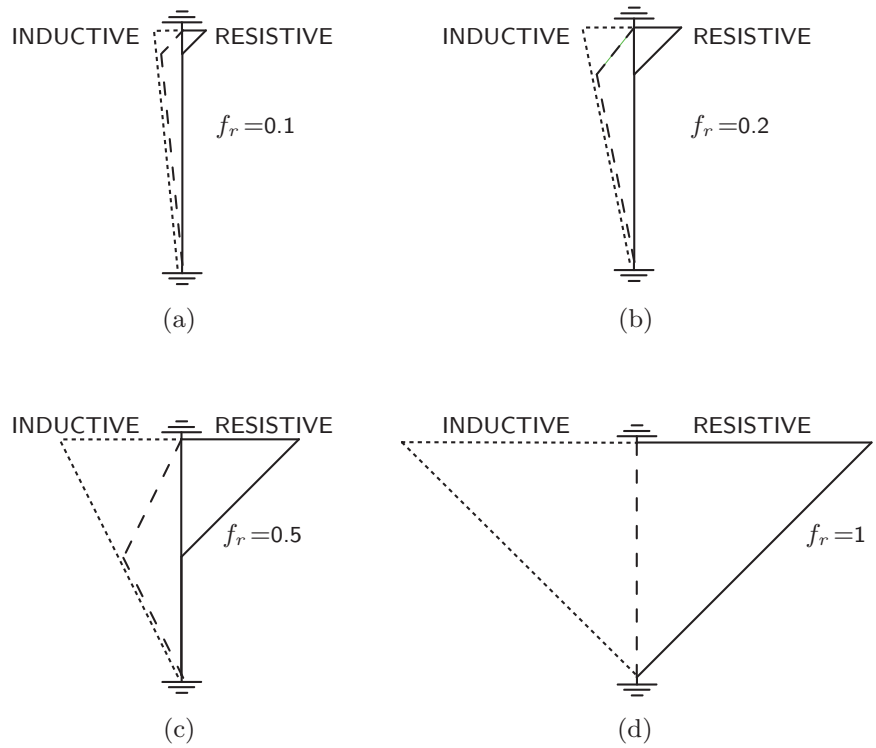

Fig. 8.7 Voltage distributions, at constant current, for different normal zone sizes within a quenching superconducting magnet, both terminals grounded and unwound from one end of the conductor to the other end. Within the resistive zone the conductor resistivity is assumed constant. (a) 10% ($f_r = 0.1$) of the winding is in the resistive state; (b) 20% ($f_r = 0.2$); (c) 50% ($f_r = 0.5$); (d) 100% ($f_r = 1$). The solid lines represent the resistive voltage; the short dashed lines the inductive voltage; and the long dashed lines the total internal voltage, given by the sum of the resistive and inductive voltages.

In each set of voltage distributions shown in Fig. 8.7, the solid line represents the resistive voltage; the short dashed line the inductive voltage; and the long dashed line the total internal voltage, given by the sum of the resistive and inductive voltages. In each figure, the magnet current remains constant at I_{op}. In reality, the current is decreasing with time; the effect of this decrease is included later.

The maximum resistive voltage, $[V_r]_{mx}$, occurs at one terminal of the magnet, and because the terminal is grounded, it is matched exactly by an inductive voltage of the same magnitude as that of $[V_r]_{mx} = R_{nz} I_{op}$, where R_{nz} is the total normal-zone resistance, given by Eq. 8.25.

From Fig. 8.7, we note that the maximum *internal* voltage, $[V_{in}]_{mx}$ is given by:

$$[V_{in}]_{mx} = f_r(1 - f_r) R_{nz} I_{op} \tag{8.38}$$

where f_r, as noted first with Eq. 8.6, is the fraction of the winding volume driven to the resistive state. Note that the magnet current remains at I_{op}. Equation 8.38 shows that $[V_{in}]_{mx} \to 0$ as $f_r \to 0$ or $f_r \to 1$. The equation also shows that $[V_{in}]_{mx}$ peaks at $f_r = 0.5$.

Combining Eqs. 8.25 and 8.38, we obtain:

$$[V_{in}]_{mx} = f_r(1-f_r)\frac{\pi(\alpha+1)\rho_m(T_f)a_1}{4A_m}NI_{op} \tag{8.39}$$

Voltage Criterion for Matrix Current Density

The maximum internal voltage occurs when either the normal zone spreads out to occupy 50% ($f_r = 0.5$) of the winding with the magnet current remaining at I_{op}, or 50% of the winding is driven normal initially.

We may obtain an expression, $J^V_{m_\circ}$, the matrix current density that limits the internal voltage induced within a shunted solenoid to a breakdown value of V_{bk}. Combining Eq. 8.39 and Eq. 8.3, we have:

$$J^V_{m_\circ} = \frac{2}{f_r(1-f_r)}\left[\frac{F(\alpha,\beta)}{\pi(\alpha^2-1)\beta}\right]\left[\frac{\mu_\circ V_{bk} I_{op}}{a_1^2\rho_m(T_f)B_\circ}\right] \tag{8.40a}$$

Similarly, we may obtain an expression that directly shows the dependence on E_m:

$$J^V_{m_\circ} = \frac{2}{f_r(1-f_r)}\left[\frac{\sqrt{\mathcal{L}(\alpha,\beta)}}{\pi(\alpha+1)}\right]\left[\frac{V_{bk} I_{op}}{\rho_m(T_f)}\sqrt{\frac{2\mu_\circ}{a_1 E_m}}\right] \tag{8.40b}$$

Note that $J^V_{m_\circ}$ increases with the product of V_{bk} and I_{op}. Most importantly here, $J^V_{m_\circ}$ improves with the normal metal's electrical *conductivity*. Also, a higher V_{bk} implies a higher $J^V_{m_\circ}$, but the winding pack density at I_{op}, λJ_{op} (**6.3.3**), could be lower because of the need for more insulation.

TRIVIA 8.1 Of the contemporary physicists (born 1821–1831) below, who was the first to show that an electrical impulse moves at the speed of light?

i) Helmholtz; ii) Kelvin; iii) Kirchhoff; iv) Maxwell.

8.4 Normal-Zone Propagation (NZP)

For protection, most LTS magnets of "practical" size must rely on one type or another of active techniques, some of which are discussed later. However, because of the inevitable delay between the detection of a non-recovering normal zone and the current dump by any active protection technique, it is desirable to make the magnet's normal-zone propagation (NZP) velocities "fast," thereby to enlarge its f_r, which in turn limits e_{mr} (Eq. 8.7) and enhances both $J_{m_\circ}^{sh}$ (Eq. 8.30) and $J_{m_\circ}^{V}$ (Eq. 8.40). A magnet with fast NZP velocities (in three directions) may become "self-protecting;" more detailed requirements for self-protection are discussed later. Because NZP velocity generally is much less in an HTS winding than that in its LTS counterpart, the prospect of a "self-protecting" HTS magnet is virtually zero: *all* HTS magnets must rely on active protection.

8.4.1 Longitudinal (Axial) NZP Velocity

The normal-zone propagation (NZP) velocity in the longitudinal direction (along the conductor axis), U_ℓ, is one of the subjects that has been studied extensively since the 1960s, under adiabatic, quasi-adiabatic, and cooled conditions, with test samples, model windings, and magnets, both LTS and HTS [8.1, 8.2, 8.25–8.75]. It is an important parameter for protection of high-performance (adiabatic) magnets. In these adiabatic or quasi-adiabatic windings, NZP is not confined only along the conductor axis but spreads out three-dimensionally: $U_t \propto U_\ell$, where U_t is the "transverse" propagation velocity.

NZP Under Adiabatic Condition

Figure 8.8 shows a schematic drawing of a conductor, under adiabatic conditions, carrying current I, with the normal-superconducting boundary, at $x=0$, moving at a constant velocity, U_ℓ, along the $+x$-direction. The power density equation for the normal-state superconductor is given by a one-dimensional (x) form of Eq. 6.1 with both disturbance and cooling terms zero:

$$C_n(T)\frac{\partial T_n}{\partial t} = \frac{\partial}{\partial x}\left[k_n(T)\frac{\partial T_n}{\partial x}\right] + \rho_n(T)J^2 \qquad (8.41a)$$

where $C_n(T)$, $k_n(T)$, and $\rho_n(T)$ are, respectively, the heat capacity, thermal conductivity, and electrical resistivity of the superconductor in the normal state.

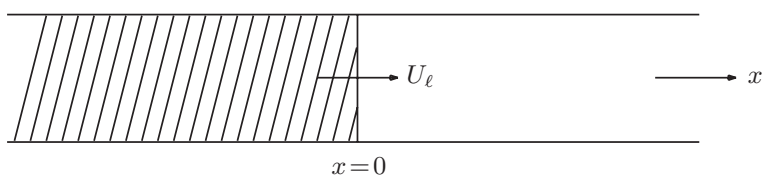

Fig. 8.8 One-dimensional normal-to-superconducting boundary ($x=0$) moving at a constant velocity U_ℓ along the longitudinal (axial) direction. The shaded side ($x<0$) is normal, and the unshaded side ($x>0$) is superconducting.

Similarly, a power density equation in the x-direction for the adiabatic case in the superconducting region is given by:

$$C_s(T)\frac{\partial T_s}{\partial t} = \frac{\partial}{\partial x}\left[k_s(T)\frac{\partial T_s}{\partial x}\right] \tag{8.41b}$$

where $C_s(T)$ and $k_s(T)$ are the superconducting-state heat capacity and thermal conductivity. When the normal-superconducting boundary moves at a constant velocity U_ℓ in the $+x$-direction, we may transform the x-coordinate to z-coordinate: $z = x - U_\ell t$. The term $\partial T_n/\partial t$ may be expressed by:

$$\frac{\partial T_n}{\partial t} = \frac{\partial T}{\partial z}\frac{\partial z}{\partial t} = -U_\ell \frac{dT}{dz} \tag{8.42}$$

We may thus express Eq. 8.41 as:

$$-C_n(T)U_\ell \frac{dT_n}{dz} = \frac{d}{dz}\left[k_n(T)\frac{dT_n}{dz}\right] + \rho_n(T)J^2 \tag{8.43a}$$

$$-C_s(T)U_\ell \frac{dT_s}{dz} = \frac{d}{dz}\left[k_s(T)\frac{dT_s}{dz}\right] \tag{8.43b}$$

Rearranging Eqs. 8.43a and 8.43b, we have the following power density equations for the superconductor in the normal ($z<0$) and superconducting ($z>0$) regions:

$$(z<0) \qquad \frac{d}{dz}\left[k_n(T)\frac{dT_n}{dz}\right] + C_n(T)U_\ell \frac{dT_n}{dz} + \rho_n(T)J^2 = 0 \tag{8.44a}$$

$$(z>0) \qquad \frac{d}{dz}\left[k_s(T)\frac{dT_s}{dz}\right] + C_s(T)U_\ell \frac{dT_s}{dz} = 0 \tag{8.44b}$$

With $k_n(T)$, $C_n(T)$, $k_s(T)$, and $C_s(T)$ constant, each given respectively, by k_n, C_n, k_s, and C_s, and assuming $d^2T_n/dz^2 \simeq 0$, we can rewrite Eq. 8.44:

$$(z<0) \qquad C_n U_\ell \frac{dT_n}{dz} + \rho_n J^2 = 0 \tag{8.45a}$$

$$(z>0) \qquad k_s \frac{d^2T_s}{dz^2} + C_s U_\ell \frac{dT_s}{dz} = 0 \tag{8.45b}$$

$T_s(z)$ may be solved directly from Eq. 8.45b:

$$T_s(z) = Ae^{-cz} + T_{op} \tag{8.46a}$$

where T_{op} is the operating temperature far away from $z = 0$, i.e., $z \gg 0$, and $c = C_s U_\ell / k_s$. We also know that $T_s = T_t$ at $z = 0$, where T_t is the *transition temperature* for the superconductor carrying I. Thus:

$$T_s(z) = (T_t - T_{op})\exp\left(-\frac{C_s U_\ell}{k_s}z\right) + T_{op} \tag{8.46b}$$

Another boundary condition is that the $k(dT/dz)$ of each region should be equal at $z = 0$—heat flow must be continuous across the boundary:

$$k_n \frac{dT_n}{dz}\bigg|_0 = k_s \frac{dT_s}{dz}\bigg|_0 \tag{8.47a}$$

Combining Eqs. 8.45a, 8.46b, and 8.47a, we have:

$$-\frac{k_n \rho_n J^2}{C_n U_\ell} = -C_s U_\ell (T_t - T_{op}) \tag{8.47b}$$

Solving Eq. 8.47b for U_ℓ, we obtain:

$$U_\ell = J\sqrt{\frac{\rho_n k_n}{C_n C_s (T_t - T_{op})}} \tag{8.48}$$

Important points to be noted from Eq. 8.48 are that U_ℓ is directly proportional to current density J and inversely proportional to the "geometric" average of the heat capacities in the two regions, $\sqrt{C_n C_s}$. U_ℓ given by Eq. 8.48 is valid for a bare superconductor under adiabatic conditions. Although it is rarely necessary to use an exact expression of U_ℓ for which material properties are temperature dependent, it is given below for the sake of completeness [8.47]:

$$U_\ell = J\sqrt{\frac{\rho_n(T_t)k_n(T_t)}{\left[C_n(T_t) - \dfrac{1}{k_n(T_t)}\dfrac{dk_n}{dT}\bigg|_{T_t}\displaystyle\int_{T_{op}}^{T_t} C_s(T)dT\right]\displaystyle\int_{T_{op}}^{T_t} C_s(T)\,dT}} \tag{8.49}$$

Equation 8.49 has been found to agree well with U_ℓ values measured for short samples of coated YBCO tape in the temperature range 45–77 K [8.66].

For constant material properties, we may note that Eq. 8.49 reduces to Eq. 8.48. Also for the case $C_n = C_s = C_\circ$, Eq. 8.48 may be written as:

$$U_\ell = \frac{J}{C_\circ}\sqrt{\frac{\rho_n k_n}{(T_t - T_{op})}} \tag{8.50a}$$

For $(T_t - T_{op})/T_{op} \ll 1$, a condition generally applicable to LTS but not HTS, we may modify Eq. 8.50a to include the effects of T-dependent $C_\circ$, ρ_n, and k_n:

$$U_\ell = \frac{J}{C_\circ(\tilde{T})}\sqrt{\frac{\rho_n(\tilde{T})k_n(\tilde{T})}{(T_t - T_{op})}} \tag{8.50b}$$

where $\tilde{T} = (T_t + T_{op})/2$. Equations 8.48 through 8.50 are valid for superconductors having no matrix metal; in reality magnet-grade-conductors are composites, and we may approximate the material properties by those of the matrix metal.

Composite Superconductor

For a composite conductor with matrix metal of cross section A_m, again for $(T_t - T_{op})/T_{op} \ll 1$ (thus valid only for LTS), with T-dependent properties, we may generalize, with $\tilde{T} = (T_t + T_{op})/2$, Eq. 8.50*b* to:

$$U_\ell = \frac{J_m}{C_{cd}(\tilde{T})} \sqrt{\frac{\rho_m(\tilde{T}) k_m(\tilde{T})}{T_t - T_{op}}} \tag{8.51a}$$

where $C_{cd}(\tilde{T})$ is the conductor's volumetric heat capacity averaged over the range from T_{op} to T_t, and J_m is the current density over the matrix metal's cross section. Because ρ_m (the matrix metal's electrical resistivity) is much smaller than ρ_n, and k_m (the matrix metal's thermal conductivity) is much greater than k_n, $k_m(\tilde{T})$ and $\rho_m(\tilde{T})$ in Eq. 8.51*a* are quite appropriate. In Eq. 8.51*a* a transition temperature, $T_t \equiv (T_{cs} + T_c)/2$, as suggested by Joshi [8.45], or simply $T_t = T_{cs}$, may be used. This subtle difference is difficult to verify with experimental data. Based on the same approximation used in Eq. 8.9*b*, we may replace $C_{cd}(\tilde{T})$ in Eq. 8.51*a* with $C_{cd}(\tilde{T}) \simeq C_m(\tilde{T})$:

$$U_\ell \simeq \frac{J_m}{C_m(\tilde{T})} \sqrt{\frac{\rho_m(\tilde{T}) k_m(\tilde{T})}{T_t - T_{op}}} \tag{8.51b}$$

The general validity of Eqs. 8.48–8.51 has been amply demonstrated by many experiments, with LTS and more recently with HTS.

Experimental Determination of Longitudinal NZP Velocity

The basic setup to experimentally determine U_ℓ is simple. Generally, "local" voltage signals are measured for a short length (10–20 cm) of a straight test sample, as shown in Fig. 8.9; in some instances local temperatures are also monitored. If the test sample is in the bore of a magnet, the sample may be circular or helical rather than straight. With the test sample carrying current I, a localized normal zone is created, e.g., by a heater, and its progression is monitored by voltage signals V_1, V_2, and V_3, and also $V_\Sigma = V_1 + V_2 + V_3$; Clearly, U_ℓ may be computed from the distance separating neighboring voltage (and/or temperature) signals and their arrival times. Figure 8.9b shows an oscillogram displaying voltage traces, V_1, V_2, V_3, and V_Σ recorded in a 10-cm long Nb_3Sn tape [8.55].

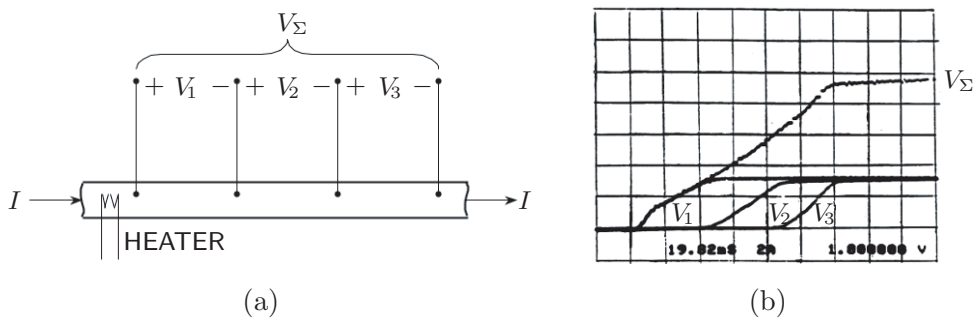

Fig. 8.9 (a) Schematic drawing of a setup to experimentally measure longitudinal NZP velocity. (b) Oscillogram showing voltages traces recorded during an NZP event [8.55].

Experiments with techniques similar to those used for LTS tests, one example of which is described above, have been performed since the early 2000s. Here, without any details of experimental setups, we present in Fig. 8.10 four sets of traces, voltage (Figs. 8.10a–8.10c) and temperature (Fig. 8.10d), recorded to determine NZP velocities in YBCO tapes: a), b) and c) are $V(t)$ traces for test samples of lengths, respectively, 20 cm [8.65], 15 cm [8.70], and 18 cm [8.74]. In the 20-cm long YBCO tape [8.65], creation of a local normal zone in the test sample, initially at 50 K, relied on the *nonuniform* distribution of critical current over the 20-cm long tape. An over-current pulse of 72 A (shown in Figs. 8.10a and Fig. 8.10d) triggered a quench in zone 5 (respectively, V_5 and T_5), inducing an NZP at a constant current of 30 A (Fig. 8.10a); the time scales of $V(t)$ traces in a) and of a companion set, the $T(t)$ traces in d), agree well. The $V(t)$ traces shown in b), were recorded with the 15-cm long tape at 60 K [8.70], and in c), with the 18-cm long tape at 70 K [8.74]. The measured NZP velocities ranged 2–10 mm/s, as summarized in Table 8.5.

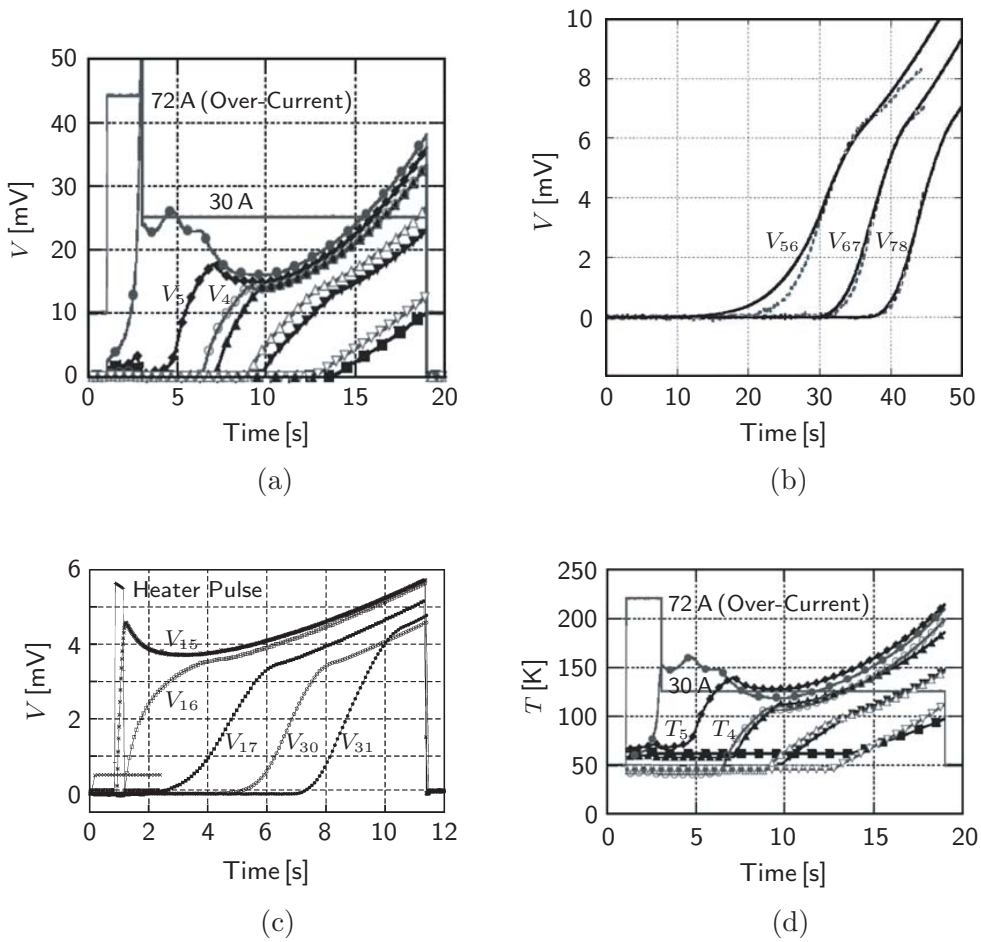

Fig. 8.10 Longitudinal NZP signals from YBCO test samples: a), b), and c) are $V(t)$ traces recorded for test samples of lengths, respectively, 20 cm [8.67], 15 cm [8.70], and 18 cm [8.74]. $T(t)$ traces shown in d) are a companion set to the $V(t)$ traces shown in a) [8.67]. Except the signal traces, the labeling style in each figure has been modified.

Table 8.5: Selected Measured U_ℓ for LTS and HTS, Bare and Composite

Superconductor	Environment	T_{op} [K]	B_{ex} [T]	J [A/mm^2]	U_ℓ [mm/s]
Nb-Zr [8.26] (single strand; no matrix metal)	Liquid helium	4.2	0	100*	933
				1000*	9330
			6	100*	5345
		8.8	0	100*	1215
NbTi [8.36] (multifilamentary composite)	Liquid helium	4.2	0	420†	"Recovery"
				840†	6800
			4	420†	4660
				840†	18600
Nb_3Sn [8.39] (multifilamentary composite)	Adiabatic	4.2	0	630†	1830
			6	315†	1490
				630†	3720
Nb_3Sn [8.55] (tape)	Quasi-adiabatic	12	0	700†	510
		5.5	5	470†	525
Bi2223-Ag [8.55]	Quasi-adiabatic	40	0	230†	2
YBCO [8.64] (coated) [8.69] [8.73]	Adiabatic	46	0	10–15†	2–8
	Adiabatic	77	0	3–15†	3–10
	Adiabatic	77	0	65†	2.5
				115†	9
		40	0	115†	38
MgB_2 [8.70] (single strand; iron matrix)	Quasi-adiabatic	4.2	4	26†	No NZP
				78†	930
				212†	6000

* I/(conductor cross section).

† I/(matrix metal cross section).

Table 8.5 lists measured values of U_ℓ for LTS and HTS. Although cooled by liquid helium, $U_\ell \propto J$ for the Nb-Zr single strand [8.26] because in the absence of matrix metal (pre-Stekly era superconductor) the normal-state Joule heating completely overwhelms the cooling. Generally, these data show that NZP velocities for HTS (Bi2223-Ag; coated YBCO) are about two to four orders of magnitude less than those of LTS. "Recovery" for the NbTi [8.36] is discussed in **8.4.2** below. As for MgB_2 with iron matrix [8.70], the velocities are comparable with those of LTS, chiefly because of the absence of conductive matrix metal. Here at an overall conductor current density (J_{cd}) of 26 A/mm^2 or below, no NZP takes place: the "normal-state" superconductor is not generating "full" Joule heating, chiefly because of its low index ($n \approx 15$). Similar no-NZP behaviors were observed with both Bi2223-Ag tape [8.55] and YBCO tapes [8.64, 8.69, 8.73].

8.4.2 NZP in "Cooled" Conditions

Although for protection NZP is not as important with "cooled" magnets as it is with adiabatic magnets, NZP in the presence of cooling has also been extensively studied. As observed in the NbTi composite shown in Table 8.5, there is in fact a "recovery" current, below which a normal zone shrinks rather than grows.

8.4.3 Transverse (Turn-To-Turn) Velocity

We now turn our attention to transverse (turn-to-turn) NZP velocity, U_t, focusing on superconductors in the form of tape. Although once quite popular, Nb_3Sn tape is no longer available. Now the most widely used composite tape superconductors are HTS: Bi2223-Ag and YBCO, both wound into pancake coils. The windings of these HTS magnets, though cooled by liquid cryogen or cryocooled, are essentially adiabatic and the adiabatic analysis of U_ℓ may be used to derive U_t [8.57]:

$$U_t = U_\ell \sqrt{\tfrac{1}{2}\left(\frac{\delta_{cd}}{\delta_i}\right)\left[\frac{k_i(\tilde{T})}{k_m(\tilde{T})}\right]} \tag{8.52}$$

$k_i(\tilde{T})$ is the temperature-averaged thermal conductivity of the insulating layer of thickness δ_i between adjacent composite tapes, each of thickness δ_{cd}. In Eq. 8.52, generally $\delta_{cd} > \delta_i$ perhaps by a factor of from ~3 to as much as ~10, but $k_m \gg k_i$ by a factor of ~1000 or more, even at 77 K; therefore, U_t is at least one to two orders of magnitude less than U_ℓ. Measurements with model windings of Bi2223-Ag and YBCO indeed have shown U_t is at least one order of magnitude less than U_ℓ. Because U_ℓ itself is only one to tens of mm/s for HTS with conductive matrix, U_t will be small indeed. As discussed below, contact thermal resistance can reduce even further the *effective* U_t in 2-D and 3-D windings.

Contact Thermal Resistance

Because $U_t \propto \sqrt{k_i}$, it is tempting to try to increase U_t by using a thermally conductive material for turn-to-turn insulation. One such material is diamond; the bulk thermal conductivity of diamond in the liquid nitrogen temperature range is 10–100 times greater than that of copper's [8.54]. However, Eq. 8.52 ignores the contact thermal resistance between the conductor and the insulator. Actually, there are two contact thermal resistances, $R_{th^1_{ct}}$ and $R_{th^2_{ct}}$, from a conductor to an adjacent conductor, separated by one insulating spacer. Thus, k_i in Eq. 8.52 should be replaced by k'_i, given by:

$$\frac{1}{k'_i} = \frac{1}{k_i} + R_{th^1_{ct}} + R_{th^2_{ct}} \tag{8.53}$$

Replacing k_i in Eq. 8.52 by k'_i, given by Eq. 8.53, we obtain:

$$U_t = U_\ell \sqrt{\tfrac{1}{2}\left(\frac{\delta_{cd}}{\delta_i}\right)\frac{k_i}{k_m[1 + k_i(R_{th^1_{ct}} + R_{th^2_{ct}})]}} \tag{8.54}$$

Equation 8.54 indicates that when contact thermal resistance is dominant, i.e., $k_i(R_{th^1_{ct}} + R_{th^2_{ct}}) \gg 1$, k_i cancels out in Eq. 8.54, making the insulator's thermal conductivity irrelevant in determining U_t. Thus, for $k_i(R_{th^1_{ct}} + R_{th^2_{ct}}) \gg 1$:

$$U_t = U_\ell \sqrt{\tfrac{1}{2}\left(\frac{\delta_{cd}}{\delta_i}\right)\frac{1}{k_m(R_{th^1_{ct}} + R_{th^2_{ct}})}} \tag{8.55}$$

Measurements of U_t with 250-μm spacers between Bi2223-Ag tapes have essentially confirmed the validity of Eq. 8.55; similar results have been observed with Nomex and Mylar spacers between YBCO tapes [8.74, 8.75].

Experimental Results

Despite the condition $U_t \ll U_\ell$ for LTS and HTS, in most *LTS* windings the dominant direction of NZP is still transverse to the conductor axis, because in most windings the conductor length, ℓ_{cd}, is much greater than the winding dimensions, e.g., $a_2 - a_1$ for a solenoid: the condition $(a_2 - a_1)/U_t \ll \ell_{cd}/2U_\ell$ is generally met in both LTS and HTS windings. However, as further discussed in **8.6**, this condition does not necessarily guarantee protection of a magnet, LTS or HTS.

Figure 8.11 shows four sets of transverse NZP signals for YBCO test assemblies at 77 K: a) measured $V(t)$ traces for two winding models, insulated with 38-μm thick Nomex spacers—"dry" spacers (solid traces) and epoxied (dashed) [8.75]; b) $V(t)$ traces for the same epoxied winding model, experiment [solid; the same as dashed in a)] and simulation (dashed), with $R_{th^1_{ct}} = R_{th^2_{ct}} = 0$; c) $V(t)$ traces and d) $T(t)$ traces predicted for a model pancake coil of 100 mm i.d., 120 mm o.d., and 10 layers, epoxy-impregnated—the transport current was shut off at $t = 20$ s [8.76].

The data give U_t in the range 0.1–1 mm/s, at least one order of magnitude less than U_ℓ. In the dry winding packs [8.75], measured U_t ranges from ∼0.1 mm/s at a contact pressure of 10 MPa to ∼0.2 mm/s at a contact pressure of 25 MPa, while with the epoxied winding packs, the transverse velocity is 1 mm/s.

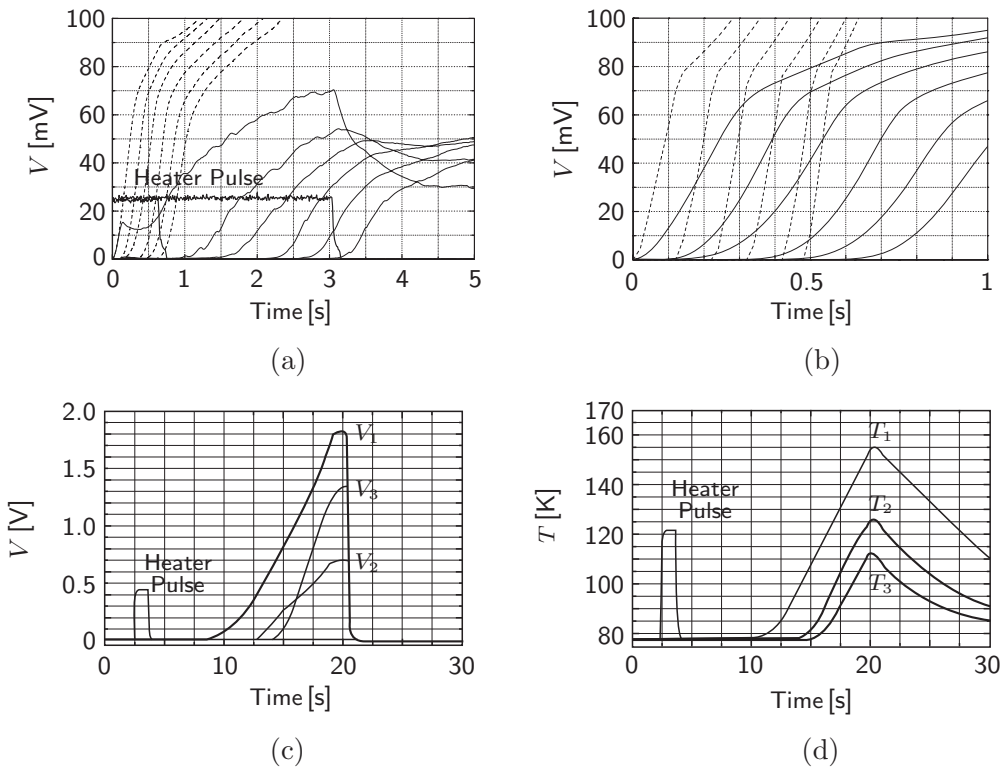

Fig. 8.11 Transverse NZP signals from YBCO test assemblies at 77 K, each event triggered by a heater pulse: a) $V(t)$ traces for winding models insulated with 38-μm thick Nomex spacers—"dry" spacers (solid traces) and epoxied spacers (dashed); b) experimental, epoxied (solid) and simulation (dashed), for the same winding model [8.75]; c) $V(t)$ traces and d) $T(t)$ traces for an epoxy-impregnated model pancake coil [8.76].

8.4.4 Thermal-Hydraulic Quenchback (THQB)

Applicable to CIC conductors cooled by forced-flow helium, the phenomenon of thermal-hydraulic quenchback (THQB) occurs when a local normal zone propagates at a velocity greater than that of the helium flow. Initially studied by Luongo and others [8.76–8.78; 1.23] and as a phenomenon related to other phenomena arising from a quench in a CIC conductor (e.g., internal pressure rise, helium expulsion from the ends of the conductor), it generally occurs when a CIC conductor is operated at high matrix current density, J_m, and close to the conductor's critical current. Because, as discussed in ***DISCUSSION 6.6***, for the most important and large-scale application of CIC conductor, fusion magnets, the CIC conductors are designed to operate in the "well-cooled" regime, i.e., below I_{lim} (Eq. 6.30), THQB should not be a serious protection issue.

8.4.5 AC-Losses-Assisted NZP

So far we have considered Joule dissipation as the only source of NZP in an adiabatic winding. When a non-recovering normal zone is created and a fault mode sets in, the magnet current decays with time, creating a time-varying magnetic field, dB/dt, within the winding—in an NMR magnet studied in **PROBLEM 8.6**, the magnitude of this current decay rate is $\sim$100 A/s. AC losses are thus generated; i.e., $g_d(t) \neq 0$ in Eq. 6.1. In the absence of "local" cooling, this dB/dt-induced $g_d(t)$ leads to $\Delta T_{op} > 0$ in the winding. The greater the $g_d(t)$, the greater will be this ΔT_{op}, though, as discussed in **6.2.6**, even an adiabatic winding can tolerate a limited ΔT_{op}, specifically up to $[\Delta T_{op}]_{mx}$, the temperature margin. Because of this $g_d(t)$ heating, some NMR magnets are energized at a *slow* rate, taking up, in some cases, a week to reach the operating current, to ensure that the adiabatic stability condition of $\Delta T_{op} < [\Delta T_{op}]_{mx}$ is met.

This dB/dt-induced heating, therefore, makes the "apparent" values of U_ℓ and U_t greater than those in which Joule dissipation is the only driving force for NZP. The dB/dt-induced heating can be *designed* to accelerate NZP in the event of a fault, when it is desirable to quickly enlarge the normal zone and also bring down the current quickly [8.79–8.81]. For the sake of protection, some NMR (and MRI) magnets use multifilamentary conductors with a twist pitch length purposely chosen "long" to *promote* coupling losses.

At much greater magnitudes of current decay rate, $\sim$0.01–1 MA/s, though clearly not possible with highly inductive MRI and NMR magnets but possible with resistive devices such as fault current limiters, Vysotsky and others find faster NZP velocities approaching 1 km/s [8.82]; under these high rates of current change, quenching becomes global rather than propagated from a local zone.

TRIVIA 8.2 List the items below in descending order of speed.

i) Average, of a commuter car stuck in an evening rush hour gridlock;

ii) Fastball, of Daisuke Matsuzaka of the Boston Red Sox on September 28, 2007;

iii) NZP (longitudinal), in HTS tape at 77 K;

iv) Tsunami.

8.5 Computer Simulation

Because of the coupled nature of quench processes in adiabatic magnets, particularly those with more than one coil, quench analysis is best performed with the aid of a computer. From Wilson's early attempt in 1968 [8.83], quench simulation work (some accompanied with experimental results) continues [1.5–1.23; 8.84–8.100], some of which is obviously for HTS windings.

Here we briefly describe the quench simulation codes for adiabatic, solenoidal windings that have evolved at FBNML, starting in 1985 with Williams' work [8.101]. The simplifying postulate of the FBNML codes is that the complex thermal diffusion process that controls normal-zone propagation within a winding may be reduced to a single parameter U_t, the transverse propagation velocity, that depends on magnetic field, temperature, and matrix current density. The complex effects of the winding's thermal properties are lumped into U_t, and the codes are simplified immensely without much sacrifice in accuracy [8.45, 8.101]. As discussed in **8.4.3**, U_t is related to the longitudinal propagation velocity, U_ℓ; U_t thus depends both on time and location within the winding.

Figure 8.12 pictorially shows quench propagation within an adiabatic solenoidal winding, which in this case is a close-packed-hexagonal arrangement of round wire, impregnated with epoxy resin. Note that quenching in the figure is initiated at the innermost radius of the winding midplane. The turn-to-turn transit time by transverse propagation velocity (U_t) generally is shorter than the circumferential transit time by longitudinal velocity U_ℓ because of the following condition, valid in most windings:

$$\frac{d_{cd}}{U_t} \ll \frac{2\pi a_1}{U_\ell} \tag{8.56}$$

where a_1 is the innermost winding radius and d_{cd} is the conductor diameter.

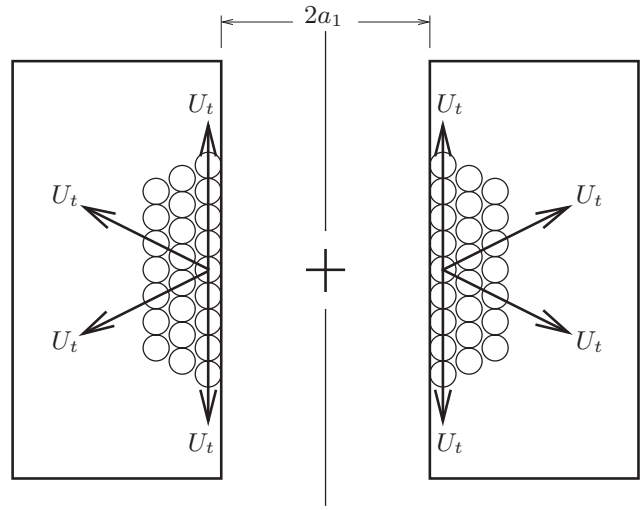

Fig. 8.12 Quenching in an adiabatic, solenoidal winding.

8.6 Self-Protecting Magnets

A superconducting magnet is said to be *self-protecting* if it can be protected, without reliance on any external intervention, against overheating by having its normal zone spread out quickly over enough of its winding volume. According to **8.1.2**, for most "adiabatic" magnets at least ∼10% of the winding should absorb the total magnetic energy, to keep the maximum temperature below ∼200 K. How fast this process takes place may be gauged by the NZP velocity. Self-protecting magnets generally must have "high" NZP velocities, and as shown qualitatively below, must be "small." However, as discussed later, a magnet, though self-protecting against overheating, may not be so against overstraining.

8.6.1 Size Limit

As seen from Table 8.1 in **8.1.2**, if a magnet's initial stored magnetic energy is dissipated totally as heat in the winding, in order to keep T_f below ∼200 K it is necessary that a fraction of the winding, f_r, of at least ∼0.1 must turn to the normal state within the current decay time, τ_{dg}, and absorb the energy.

If a small normal zone is created at the innermost radius, i.e., a_1, of the magnet, then we may need to satisfy the following "ideal" requirement on the magnet's winding radial build, $a_1(\alpha-1)$, to ensure that f_r is sufficiently large to make the magnet self-protecting:

$$\frac{a_1(\alpha-1)}{U_t} < \tau_{dg} \tag{8.57}$$

Equation 8.57 states that the propagation time over the entire radial build, given by $a_1(\alpha-1)/U_t$, must be less than τ_{dg}. Actually, as stated above, a rather modest percentage of the winding volume may be sufficient to keep T_f below ∼200 K. Here in this "order of magnitude" discussion, we use the ideal condition of Eq. 8.57.

Size Limit Under Constant-Current Heating

In adiabatic, constant-current heating mode (**8.2.1**), we have $\tau_{dg} = \tau^i_{ah}(T_f, T_i)$, where $\tau^i_{ah}(T_f, T_i)$, given by Eq. 8.12*a*, is the maximum duration under adiabatic, constant-current ($J_{m_\circ}$) heating. Combining Eqs. 8.57 and 8.12*a*, we obtain:

$$\frac{a_1(\alpha-1)}{U_t} = \frac{Z(T_f, T_i)}{J^2_{m_\circ}} \tag{8.58}$$

Combining Eqs. 8.51*b*, 8.52, and 8.58 with $J_m = J_{m_\circ}$, we obtain a size limit, $[a_1(\alpha-1)]^i_{ah}$, for the winding build of a self-protecting magnet under adiabatic, constant-current heating condition:

$$[a_1(\alpha-1)]^i_{ah} = \frac{Z(T_f, T_i)}{J_{m_\circ} C_m(\tilde{T})} \sqrt{\frac{\rho_m(\tilde{T}) k_i(\tilde{T}) \delta_{cd}}{2\delta_i (T_t - T_{op})}} \tag{8.59}$$

Equation 8.59 states that the permissible magnet size, as expected, decreases with $J_{m_\circ}$ and $C_m(\tilde{T})$ and increases with $Z(T_f, T_i)$. It also shows that the size limit expands with $\rho_m(\tilde{T})$ and $k_i(\tilde{T})$, and shrinks with $(T_t - T_{op})$. The $C_m(\tilde{T})$ and $(T_t - T_{op})$ dependences imply that for the same $J_{m_\circ}$ and T_f, a self-protecting HTS magnet, if such a magnet of practical utility can indeed exist, would have to be more compact than its LTS counterpart.

Size Limit in Magnet with Shorted Terminals

From the protection point of view, it is desirable to make a magnet with shorted terminals self-protecting. Indeed, most NMR and MRI magnets are designed to self-protect themselves, not necessarily by NZP to spread the normal zone, but by induced AC losses and also, as discussed later, by diodes and resistors connected across the magnet terminals.

Here, we consider the size limit for a magnet with shorted terminals to self-protect by NZP alone: the adiabatic heating of a magnet with shorted terminals was discussed in **8.2.3**. For this case, $\tau_{dg} = R_{nz}/L$, where R_{nz} is given Eq. 8.27 (or Eq. 8.25). Combining Eqs. 8.57 and Eq. 8.27, with U_t given by Eqs. 8.52 and 8.51*b*, and solving for the size limit, $[a_1(\alpha–1)]^{sh}_{ah}$, for the winding build of a self-protecting magnet with shorted terminals under adiabatic heating, we obtain:

$$[a_1(\alpha-1)]^{sh}_{ah} = U_t\left(\frac{L}{R_{nz}}\right) \tag{8.60a}$$

$$= \frac{J_{m_\circ}}{C_m(\tilde{T})}\sqrt{\frac{\rho_m(\tilde{T})k_i(\tilde{T})\delta_{cd}}{2\delta_i(T_t-T_{op})}}\left(\frac{L}{R_{nz}}\right) \tag{8.60b}$$

$$= \frac{J_{m_\circ}}{C_m(\tilde{T})}\sqrt{\frac{\rho_m(\tilde{T})k_i(\tilde{T})\delta_{cd}}{2\delta_i(T_t-T_{op})}}\times \frac{4A_m}{f_r\pi(\alpha+1)\rho_m(T_f)}\sqrt{\frac{\mu_\circ\mathcal{L}(\alpha,\beta)L}{a_1}} \tag{8.60c}$$

or in terms of E_m:

$$[a_1(\alpha-1)]^{sh}_{ah} = \frac{1}{C_m(\tilde{T})}\sqrt{\frac{\rho_m(\tilde{T})k_i(\tilde{T})\delta_{cd}}{2\delta_i(T_t-T_{op})}}\times \frac{4}{f_r\pi(\alpha+1)\rho_m(T_f)}\sqrt{\frac{2\mu_\circ\mathcal{L}(\alpha,\beta)E_m}{a_1}} \tag{8.60d}$$

Again, as with the constant-current heating case treated above, because both $C_m(\tilde{T})$ and $T_t - T_{op}$ appear in the denominator of Eqs. 8.60*c* and 8.60*d*, for the same operating parameters a self-protecting HTS magnet must be considerably smaller than its LTS counterpart operating at liquid helium temperature.

Answer to TRIVIA 8.1 iii). The German physicist Gustav R. Kirchhoff (1824–1887) taught the young Kamerlingh Onnes (1853–1926) in Heidelberg (c. 1870); most noted as the developer, with R.W. von Bunsen (1811–1899), of the first spectroscope; identified a half dozen elements, including gold, in the sun. Once asked by his banker, unimpressed by his claim of a spectroscope's ability to find gold in the sun, "Of what use is gold in the sun if I cannot bring it down to earth?"

8.7 Passive Protection of "Isolated" Magnets*

A passive protection technique is generally used for persistent-mode superconducting magnets, e.g., MRI and NMR. Unlike the active protection technique discussed next in **8.8**, it generally does not rely on devices located outside the cryostat.

Figure 8.13 presents a circuit for a persistent-mode magnet, which is represented by two inductors in series. It models, in the simplest way, a real magnet that often has many "nested" coils. The magnet is shunted by a persistent-current switch (PCS), whose state is either "normal," with the heater current on, or superconducting (heater off). (The circuit does not include the diodes that protect the PCS, as in a more complete circuit shown in Fig. 7.22. The basic features and operation of a persistent-mode circuit, including the use of diodes for protection, are described in ***Discussion 7.8***.) In this model, each coil is shunted with a resistor (R_1 or R_2), a key element for protection of an isolated magnet.

For this simple system the self inductance of each coil is identical: $L_1 = L_2 = L$; and the mutual inductance $M = k\sqrt{L_1 L_2} = kL$, where k is the coupling coefficient; also $R_1 = R_2 = R$. Initially, each coil is carrying a constant transport current I_0. At time $t = 0$, a small normal zone is formed in Coil 1; it is represented by a resistor r (not included in Fig. 8.13), which for this analysis is constant.

The total magnetic energy of the system is: $E_m = (L+M)I_0^2$. The ratio E_r/E_m, where E_r is the total energy dissipated in resistor r, is given, with $\zeta = r/R$, by:

$$\frac{E_r}{E_m} = \frac{0.5\zeta(1-k) + (1+k)}{\zeta + (1+k)} \tag{8.61}$$

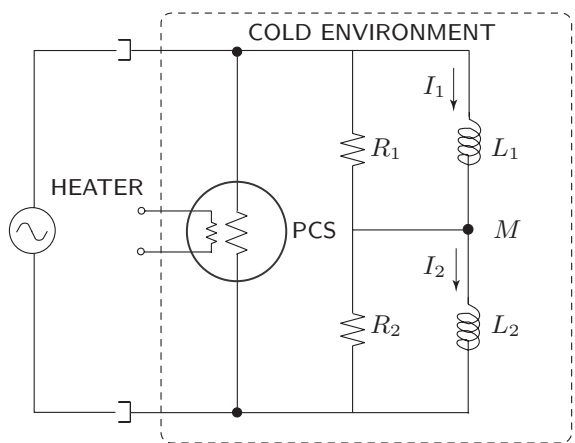

Fig. 8.13 Circuit for an "isolated," persistent-mode 2-coil magnet.

"*. . . gold outweighs a thousand arguments.*"—*Medea*

* Based on **Problem 8.9** in the 1st Edition (Plenum, 1994).

For $r \gg R(1+k)$—a condition that can be met in most high-performance coils—the analysis also gives expressions for $I_1(t)$ and $I_2(t)$:

$$\frac{I_1(t)}{I_0} = \frac{R(1+k)^2}{2r}\exp\left(-\frac{Rt}{2L}\right) + \left[1 - \frac{R(1+k)^2}{2r}\right]\exp\left[-\frac{rt}{(1-k^2)L}\right] \quad (8.62a)$$

$$\frac{I_2(t)}{I_0} = (1+k)\exp\left(-\frac{Rt}{2L}\right) - k\exp\left[-\frac{rt}{(1-k^2)L}\right] \quad (8.62b)$$

From Eq. 8.62 we may make the following observation.

- Equation 8.61 implies that as $r \to 0$, $E_r/E_m \to 1$. This is because to transfer energy into the shunt resistors—the only other elements capable of absorbing dissipative energy—it is necessary to create a voltage across each shunt resistor. If the normal zone r is very small, the voltage appearing across shunt resistor R_1 will be very small. As $r \to 0$, infinitesimal voltage appears across either shunt resistor, and the *entire* magnetic energy is dissipated by the normal zone, giving rise to $E_r/E_m \to 1$; fortunately this does not happen in "adiabatic" windings, because once a normal zone is created in the "adiabatic" windings, r rapidly increases, providing a sufficient voltage across each shunt resistor.

- Equation 8.61 also states $E_r/E_m \to 0.5(1-k)$ as $r \to \infty$, which for $k = 1$ means $E_r/E_m = 0$. Under this condition, a large voltage appears across each shunt resistor and most of the total energy is dissipated in the shunt resistors. If the two coils are well coupled ($k \to 1$), the energy stored in Coil 1 is transferred to Coil 2 and then dissipated through the shunt resistors.

  Note that because the total voltage across the two shunt resistors must remain 0 throughout, *equal* (but opposite-polarity) current always flows through each shunt resistor; the two dissipations are identical. That is, each shunt resistor dissipates an identical amount of energy if $R_1 = R_2$.

- Equation 8.62*b* indicates that when $r/R \gg (1-k^2)/2$, $I_2(t)$, the current in Coil 2, that is still superconducting, initially increases. The appearance of r in Coil 1 forces current to flow through shunt resistor R_1. Because the voltage across the magnet terminals must remain zero—the PCS is superconducting—an equal but opposite current must flow in shunt resistor $R_2(=R_1)$. The current flowing in each shunt resistor ends up in Coil 2, increasing $I_2(t)$ and decreasing $I_1(t)$ by the same amount, preserving flux in the magnet.

- The increase in $I_2(t)$ can continue until it reaches the critical current of the conductor at the innermost winding radius of the coil midplane, *inducing* a quench in Coil 2, thus contributing to a rapid expansion of the normal zone. This process is further explored in the next problem, in which a real coil situation is studied in more detail.

- A large increase in $I_2(t)$, beneficial in triggering a quench, may spell trouble because, as mentioned above, the flux remains essentially constant, and thus there will be a large increase in stresses in the winding. This means that in designing coils that are to be protected by shunt resistors, they must be designed to withstand the maximum stress that might appear during quenching. An important parameter here is $I_2(t) \times B_2(t)$ during quenching.

Two-Coil Magnet

A 2-coil magnet, with its circuit in Fig. 8.14 [8.45], is studied here as an illustrative case. The two coils, each wound (close-packed hexagonal) with an insulated NbTi composite wire and shunted with a 0.5-Ω resistor, are connected in series. The power supply may be modeled as a constant current source for voltages up to 10 V.

In the analysis, it is assumed that the normal-zone propagation is dominated by transverse heat conduction. The normal-zone growth is three dimensional—axial and radial over the entire circumference. Although $U_\ell \gg U_t$, because $2\pi a_{1_1} U_\ell \ll d_1 U_t$, where a_{1_1} and d_1 are, respectively, the inner winding radius and conductor diameter of Coil 1, transverse propagation predominates in both sections.

Table 8.6 gives the coil's appropriate parameters. The total inductance is 1.52 H. Because Coil 2 is wound directly over Coil 1, the two coils are in good thermal contact at the interface: the entire coil may be considered as one homogeneous thermal unit. (Note that, as indicated in Table 8.6, the two coils are wound with conductors of different diameters, and thus the NZP velocities are different.)

A heater, placed at the midplane of the innermost radius of Coil 1, is used to initiate a quench. We may thus assume that the normal zone starts as a ring at the midplane of the innermost radius of Coil 1 and spreads as depicted in Fig. 8.12.

Figure 8.15 shows current and voltage vs. time traces for a heater-driven quench in which the magnet is initially at 100 A; the power supply voltage limit is 10 V. Both current and voltage plots consist of four traces: the solid traces (experiment) and dashed traces (simulation). For both current and voltage traces, the curves labeled 1 are for Section 1 and the curves labeled 2 are for Section 2. In answering the following questions, you may ignore the analytical curves.

- The following observations may be made from the traces shown in Fig. 8.15:

  1. I_1 decreases initially because Section 1 is where the quench is initiated.

  2. I_2 increases initially to keep the flux constant.

  3. The behaviors of I_1 and I_2 are also reflected in V_1 and V_2. V_1 increases because ΔI_1, not flowing through Section 1, is now flowing through R_1.

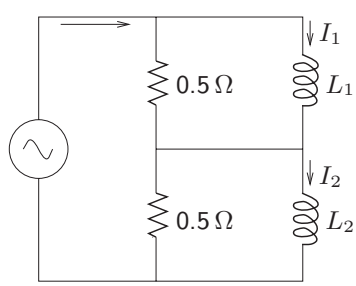

Fig. 8.14 2-Coil Magnet circuit.

Table 8.6: Coil Parameters

Parameter	Coil 1	Coil 2
Winding i.d. [mm]	76	112
Winding o.d. [mm]	112	134
Winding length [mm]	71	71
Self inductance [H]	0.20	0.72
Mutual inductance [H]	0.30	
Wire diameter [mm]	0.90	0.70
Wire length, ℓ_d [m]	530	1010
Cu/NbTi ratio	2	3

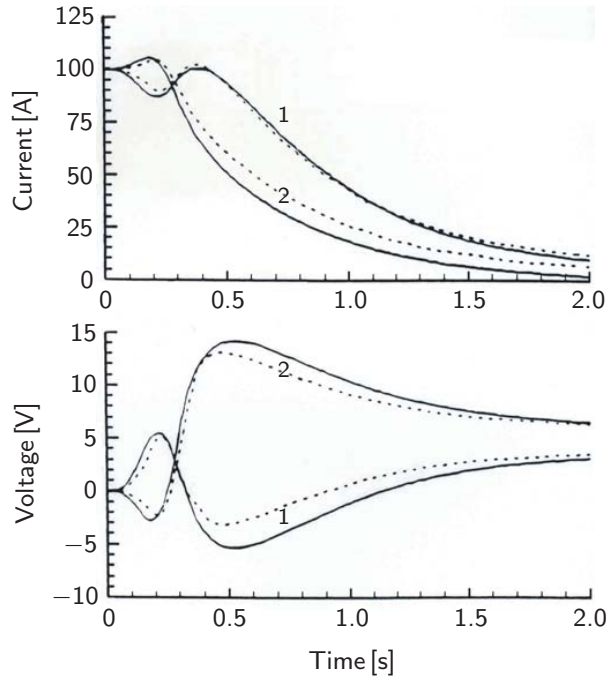

Fig. 8.15 Current and voltage vs. time traces of Coil 1 (labeled 1): experiment (solid lines) and simulation (dashed); and Coil 2 (labeled 2) for a quench with the magnet initially at 100 A [8.45].

4. To keep the terminal voltage zero (at least initially), V_2 swings negative. These initial responses are consistent with results discussed in **PROBLEM 8.9**. Eventually $V_1 + V_2$ climbs up to 10 V, the power supply limit.
5. At $t \sim 0.2$ s, V_2 starts climbing up, a definite indication that a normal zone has been induced in or has reached Coil 2.
6. I_2 thus begins to drop, and I_1 increases, trying to keep the flux constant.
7. At $t \sim 0.4$ s, $V_1 + V_2$ reaches 10 V, and I_1 must start decreasing.
8. $V_1 + V_2 = 10$ V for $t > 0.4$ s.

- The total energy dissipated in the magnet, E_d, may be given by:

$$E_d = E_m + E_s - E_{R1} - E_{R2} \tag{8.63}$$

where E_m is the total energy stored in the magnet initially, E_s is the energy supplied by the power supply between $t = 0$ and $t = 2$ s, and E_{R1} and E_{R2} are, respectively, energies dissipated in resistor R_1 and R_2. E_m is 7600 J [$= (0.5)(1.52\,\text{H})(100\,\text{A})^2$]. E_s is given by $V_s(t)I_s(t)$ integrated for $0 \le t \le 2$ s. $V_s(t)$ and $I_s(t)$ are, respectively, the power supply voltage and current. The power supply may be modeled as a constant current supply (100 A) for $0 \le t \le 0.4$ s and a constant voltage supply (10 V) for $t \ge 0.4$ s. We have, for $0 \le t \le 0.4$ s, $V_s(t) = V_1(t) + V_2(t)$ and, for $t \ge 0.4$ s, $I_s(t) = I_1(t) + V_1(t)/R_1$. (A proof of a relationship similar to this involving more coils is a question in **PROBLEM 8.11**.)

Using traces shown in Fig. 8.15, we can compute E_s, E_{R1}, and E_{R2}:

$$E_s = (100\,\mathrm{A})\int_0^{0.4\,\mathrm{s}} [V_1(t) + V_2(t)]\,dt + (10\,\mathrm{V})\int_{0.4\,\mathrm{s}}^{2\,\mathrm{s}} \left[I_1(t) + \frac{V_1(t)}{R_1}\right] dt$$

$$\simeq 200\,\mathrm{J} + 650\,\mathrm{J} \simeq 850\,\mathrm{J}$$

$$E_{R1} = \frac{1}{R_1}\int_0^{2\,\mathrm{s}} V_1(t)^2\,dt \simeq 50\,\mathrm{J} \qquad E_{R2} = \frac{1}{R_2}\int_0^{2\,\mathrm{s}} V_2(t)^2\,dt \simeq 300\,\mathrm{J}$$

The total energy dissipated in the magnet is thus about 5500 J.

- If $I_0 = 50\,\mathrm{A}$ the normal zone should reach Coil 2 at ∼0.4 s or later because $U_t \propto U_\ell \propto I_t$. Also B is halved or T_c is raised, making the arrival time even later than 0.4 s. The terminal voltage should reach 10 V later than 0.4 s, perhaps as late as ∼0.8 s, because shunt voltages will be lower by a factor of 2 and it takes longer for the terminal voltage to reach 10 V.
- The total winding volume (conductor and epoxy filler) is $694\,\mathrm{cm}^3$. Assuming the entire winding heat capacity, C_{wd}, is of copper, we have:

$$\mathcal{V}_{cd}[h_{cu}(T_f) - h_{cu}(T_{op}] \simeq (694\,\mathrm{cm}^3)[h_{cu}(T_f)] = 5500\,\mathrm{J}$$

  where $\mathcal{V}_{cd}$ is winding volume and h_{cu} is copper's volumetric enthalpy. For $T_f > T_{op} = 4.2\,\mathrm{K}$, $h_{cu}(T_f) \gg h_{cu}(T_{op})$. From Fig. A3.3, we find $T_f \simeq 50\,\mathrm{K}$, which roughly agrees with a simulation value of 47 K (see Fig. 8.16).
- When aluminum is substituted for copper, Fig. A3.3 gives $T_f = 75\,\mathrm{K}$. A simulation gives a temperature of 57 K.

Figure 8.16 shows spatially averaged temperature plots for Section 1 and Section 2 of this magnet. The solid curves correspond to Nb-Ti/copper wires, while the dotted curves correspond to Nb-Ti/aluminum wires [8.46].

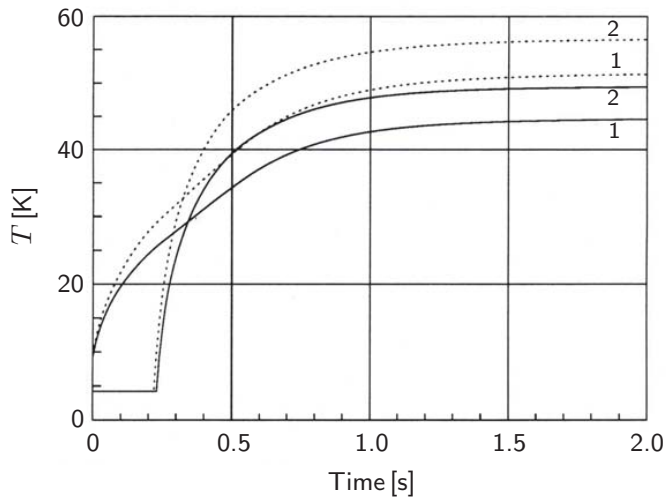

Fig. 8.16 Spatially averaged temperature vs. time plots for Coils 1 and 2. Solid curves: NbTi/copper wires; dotted curves: NbTi/aluminum wires [8.45].

8.8 Active Protection

8.8.1 Overheating

Most superconducting magnets, except some used in electric power applications, are low-voltage devices, capable of storing large amounts of energy in their magnetic fields. Protection thus generally means to keep its total energy from being converted into heat in small winding volumes, which in turn generally means keeping the maximum temperature reached in the energy absorbing regions to a level considered safe, i.e., below 200 K.

As discussed above, a self-protecting magnet can achieve this protection goal by having NZP velocities large to enable the winding to expand its energy absorbing volume to a significant portion of its winding volume within the time scale of the energy conversion. However, as discussed above, there is a size limit for a self-protecting magnet even for high-performance LTS magnets with fast NZP velocities. Because of very low NZP velocities, HTS magnets are not self-protecting.

An important goal of magnet protection is to limit the maximum T_f in the winding, as discussed in **8.1**, to below 200 K. A self-protecting magnet achieves this goal by itself, without any active intervening steps provided in the system specifically for this purpose. In contrast to active protection, we may call the protection of a self-protecting magnet *passive*.

The basic approach for active protection is to either 1) transfer most of the stored magnetic energy, E_m, to a mass outside the winding or 2) distribute the energy over a large portion, $f_r \geq \sim 0.1$, of the winding volume. Either approach achieves the goal of $T_f < 200$ K, which may be seen from Eq. 8.7, given here once again:

$$e_{mr} \equiv \frac{E_m}{V_r} = \frac{2(\alpha-1)\beta\mathcal{L}(\alpha,\beta)}{f_r\pi(\alpha+1)F^2(\alpha,\beta)}\left(\frac{B_\circ^2}{2\mu_\circ}\right) \tag{8.7}$$

Thus, in approach 1), the effective E_m converted into heating in the winding is decreased even when f_r remains small; in approach 2), the effective E_m remains the same as the original stored energy, but f_r is increased. Each thus lowers e_{mr}.

8.8.2 Overstraining in a Multi-Coil Magnet

Although so far not discussed at all, there is another important goal in protection which is applicable only to a multi-coil magnet in which the coils are inductively coupled. Here, a quench-induced decay in one coil can induce a large current in another coil, causing the strain limit to be exceeded in the coil, damaging it. (Note that this current-induced overstraining is different from temperature-induced overstraining.)

We have seen this in our 2-coil magnet studied above. As given by Eq. 8.62*b*, $I_2(t)/I_0$ (current in Coil 2, which remains superconducting when Coil 1 goes normal) initially rises above I_0, and as discussed above, this may lead to overstraining the conductor in Coil 2—this increase in $I_2(t)$ is also seen from the current traces shown in Fig. 8.15 recorded for a 2-coil system. An active protection technique that minimizes this current increase is discussed later in this section.

8.8.3 Active Protection Technique: Detect-and-Dump

This so-called "detect-and-dump" technique is widely used in large magnet systems. Originally proposed by Maddock and James in 1968 [8.3], its basic premise is to protect the magnet by transferring most of the stored energy into a "dump" resistor connected across the magnet terminals. Thus, even for "large" E_m, f_r may remain small. Figure 8.17 presents the basic circuit for this detect-and-dump technique. The magnet is represented by inductance L; the dump resistor, connected across the magnet terminals and usually located outside the cryostat, is represented by R_D. Switch S is opened when a nonrecovering normal zone, represented by $r(t)$, appears within the magnet. The stored magnet energy, E_m, at the magnet's operating current I_{op} is given by $LI_{op}^2/2$. Note that once the switch S opens, the circuit becomes identical to the one shown in Fig. 8.3 for **8.2.2**, which discusses relevant points of this technique.

Thus, with most of the potentially dangerous energy dissipated elsewhere, the normal zone created within the winding is heated only over the brief period of time during which the magnet current decays to zero. Thus, it is possible to limit T_f to a safe level: the faster the current decay rate, the lower the hot-spot temperature. To achieve this fast rate of current discharge, however, the magnet terminals have to withstand high voltages. Thus, the magnet designer tries to limit simultaneously T_f and the terminal discharge voltage, V_D: two competing requirements, as is often the case. The relationship between T_f, in the form of $Z(T_f, T_i)$, and V_D (and other key parameters) has already been discussed in **8.2.2** and expressed by Eq. 8.18*b*:

$$Z(T_f, T_i) = \frac{J_{m_\circ} E_m}{A_{cd} V_D} \tag{8.18b}$$

where $J_{m_\circ}$ is the matrix metal current density at I_{op}.

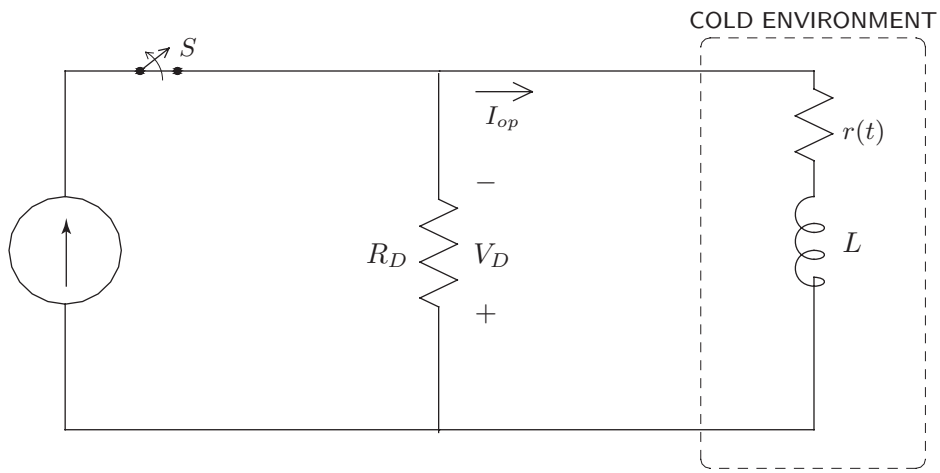

Fig. 8.17 Magnet circuit for detect-and-dump active protection.

What all this leads to is an overheating criterion for matrix metal current density at operating current, $J^D_{m_\circ}$, already derived and given by Eq. 8.19:

$$J^D_{m_\circ} = \frac{A_{cd} Z(T_f, T_i) V_D}{E_m} \tag{8.19}$$

This active protection technique requires two sequentially executed actions: 1) detection of the non-recovering normal zone, which may be very small; and 2) opening of the switch S that forces the magnet to discharge through the dump resistor. The drawback of the technique is that both actions may be unreliable. Detection of this normal zone is not easy, being obscured by large inductive voltages, because the action is usually needed while the magnet is being charged, rather than after it has been charged to I_{op} and is in the quiescent state. A quench-voltage detection method useful for this protection technique is discussed later in this section.

Options to Improve $J^D_{m_o}$ Equation 8.19 indicates that, for given values of $\gamma_{m/s}$, T_f, and E_m, there are two options to improve $J^D_{m_\circ}$: increase A_{cd} and/or V_D. An increased A_{cd} leads to an increased I_{op}. From Fig. 8.2, we note that among the matrix metals selected in Fig. 8.2, Ag1000 gives the largest $Z(T_f, T_i)$. To improve $J^D_{m_\circ}$, copper and silver matrix metals are preferable to aluminum and brass.

Increased A_{cd} (and Increased I_{op}): The following consequences need to be assessed for this option.

1. Large conductor, which, for a given kA-m (kiloampere-meter), is generally more expensive than small conductor.
2. Large current leads, which result in a greater heat input into the cryostat.
3. Large $\vec{B} \times \vec{I}$ forces, e.g., current leads, bus-bar systems.
4. For a given power rating, VI, high-I supplies are generally more expensive than low-I supplies.

Increased V_D: This will obviously increase susceptibility to sparking incidents for LHe-immersed magnets, particularly when V_D exceeds $\sim$700 V.

Discharge Voltage: V_D

For a given $Z(T_f, T_i)$, as may be inferred, for example, from Eq. 8.18, there are five design parameters: $J_{m_\circ}$; E_m; $\gamma_{m/s}$; V_D; and I_{op}. V_D is thus given by:

$$V_D = \frac{J_{m_\circ} E_m}{A_{cd} Z(T_f, T_i)} \tag{8.65}$$

Equation 8.65 states that V_D increases linearly with E_m and $J_{m_\circ}$ and decreases inversely with A_{cd} (and hence I_{op}) and $Z(T_f, T_i)$.

Answer to TRIVIA 8.2 Tsunami (200, in m/s); fastball (42.2); car (2); NZP (0.01).

Switching Delay

Equations 8.18 and 8.19 are both based on the assumption that the current discharge begins at the instant a non-recovering normal zone is created. In realty, there is a delay, τ_{dl}, between the creation of this normal zone and the start of the current discharge: τ_{dl} is the sum of the delay in the normal zone detection and the circuit delay for the switch to actually open. During this period the current will remain at its initial value, I_{op}. Thus, to compute T_f, through $Z(T_f, T_i)$, we shall combine Eq. 8.12a, with τ_{dl} substituted for $\tau^i_{ah}(T_f, T_i)$), and Eq. 8.16a:

$$Z(T_f, T_i) = \left(\frac{A_m}{A_{cd}}\right)(J^2_{m_\circ}\tau_{dl} + \tfrac{1}{2}J^2_{m_\circ}\tau_{dg}) \tag{8.66a}$$

$$= \left(\frac{A_m}{A_{cd}}\right)(\tau_{dl} + \tfrac{1}{2}\tau_{dg})J^2_{m_\circ} \tag{8.66b}$$

8.8.4 Active Protection Technique: Detect-and-Activate-the-Heater

This "detect-and-activate-the-heater" technique is widely used in large magnets [8.102–8.110]. Upon the detection of a resistive zone in a magnet, most, or at least a large portion, of the rest of the winding still in the superconducting state is driven normal with a "protection heater," implanted within the winding, that forcibly increases f_r. As shown in Table 8.1, for most magnets the goal of $T_f < 200$ K may be achieved with $f_r < 0.1$, which would make it less cumbersome to plant a protection heater in the winding than if f_r were close to 1. Also note that this protection heater may be planted in a *convenient* location in the winding, *irrespective* of the quench spot or its initial size [8.75, 8.111]. This concept of implanting a protection heater in a convenient location is further studied in ***Discussion 8.6***.

Passive Activate-the Heater

Figure 8.18 shows a circuit diagram of a 2-coil persistent-mode ("isolated") magnet

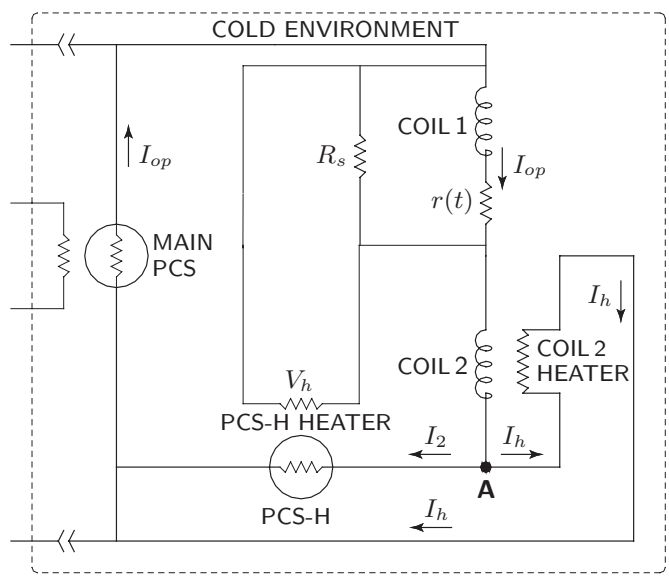

Fig. 8.18 Magnet circuit with *passive* activate-the-heater protection.

with *passive* activate-the-heater protection. The circuit is a simplified version of a persistent-mode NMR magnet [8.101]—in an actual nested-coil magnet each coil is shunted by a resistor; here for the sake of simplicity, the circuit shows only one shunt resistor, R_s. In this 2-coil version, Coil 2 (insert to Coil 1) is wrapped with a heater wire (Coil 2 Heater). Under normal operating conditions, $r(t)=0$ in Coil 1: $I_2 = I_{op}$; $I_h = 0$; and $V_h = 0$, where I_h is the current for Coil 2 Heater. When Coil 1 quenches, $r(t) \neq 0$, and voltage V_h is developed across PCS-H Heater, and PCS-H "opens," i.e., becomes resistive. At point **A** most of the magnet current, I_{op}, is then diverted to flow through Coil 2 Heater, i.e., $I_h > 0$ (with $I_2 + I_h = I_{op}$), initiating a normal zone over the outermost layer of Coil 2.

Suitable for persistent-mode magnets, this is a *passive* version of the detect-and-activate-the-heater protection, in which voltage-based quench detection is not possible and not required. There are many variations to the detect-and-activate-the-heater technique.

8.8.5 Quench-Voltage Detection Technique—Basic Bridge Circuit

One key sequence in the execution of active protection is detection of a *nonrecovering* quench. The active protection generally forces the magnet discharge, which disrupts the entire operation: *false-alarm* discharges must be avoided. Detection of a *genuine* quench voltage can be challenging in "noisy" real-world environments [8.112, 8.113].

Figure 8.19 shows the basic bridge circuit containing two coils, Coil 1 and Coil 2, connected in series. The two coils can really be one coil divided into two parts. L_1 is Coil 1's self inductance and L_2 is Coil 2's self inductance. (In this model, with the two coils are connected in series, the mutual inductance between the two coils can be included in the self inductances.) r represents the resistance of a small normal zone created in Coil 1 upon its quench. R_1 and R_2 are the bridge circuit resistors, and $V_{out}(t)$ represents the bridge output.

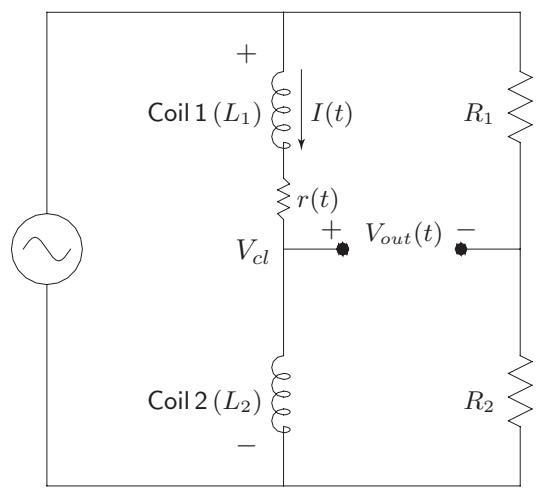

Fig. 8.19 Bridge circuit voltage detection technique.

In the following analysis, we assume that all circuit elements, including r, are constant; also we assume that R_1 and R_2 are sufficiently large so that they do not "load" the bridge circuit.

For the case when R_1 and R_2 are "large," the total voltage across the two coils, $V_{cl}(t)$, is given by:

$$V_{cl}(t) = L_1 \frac{dI(t)}{dt} + rI(t) + L_2 \frac{dI(t)}{dt} \tag{8.67a}$$

For the same condition, the current through the resistors R_1 and R_2, $i_R(t)$, is given by:

$$i_R(t) = \frac{V_{cl}(t)}{R_1 + R_2} \tag{8.67b}$$

From the circuit shown in Fig. 8.19, we have:

$$V_{out}(t) = L_1 \frac{dI(t)}{dt} + rI(t) - R_1 i_R(t) \tag{8.67c}$$

Combining Eqs. 8.67*a*–8.67*c*, we obtain:

$$\begin{aligned} V_{out}(t) &= L_1 \frac{dI(t)}{dt} + rI(t) \\ &\quad - \frac{R_1}{R_1 + R_2} \left[L_1 \frac{dI(t)}{dt} + rI(t) + L_2 \frac{dI(t)}{dt} \right] \\ &= \left(\frac{R_2}{R_1 + R_2} \right) L_1 \frac{dI(t)}{dt} \\ &\quad - \left(\frac{R_1}{R_1 + R_2} \right) L_2 \frac{dI(t)}{dt} + \left(\frac{R_2}{R_1 + R_2} \right) rI(t) \end{aligned} \tag{8.68}$$

To make $V_{out}(t)$ proportional only to $rI(t)$, the first two terms in the right-hand side of Eq. 8.68 must sum to zero:

$$\left(\frac{R_2}{R_1 + R_2} \right) L_1 \frac{dI(t)}{dt} - \left(\frac{R_1}{R_1 + R_2} \right) L_2 \frac{dI(t)}{dt} = 0 \tag{8.69}$$

Equation 8.69 is simplified to give the required condition: $R_2 L_1 = R_1 L_2$. With the first two terms in the right-hand side of Eq. 8.68 eliminated, Eq. 8.68 becomes:

$$V_{out}(t) = \left(\frac{R_2}{R_1 + R_2} \right) rI(t) \tag{8.70}$$

As we shall see in ***DISCUSSION 8.1***, the condition in real hybrid magnets is far from ideal: it is generally very difficult to achieve, in *real* magnets, the condition $R_2 L_1 = R_1 L_2$ independent of $I(t)$ and dI/dt.

In the following **PROBLEMS & *DISCUSSIONS*** selected topics discussed above are further studied, including some finer points.

"ACCIDENT, n. An inevitable occurrence due to the action of immutable natural laws." —Ambrose Bierce

PROBLEM 8.1: Warming up a large superconducting magnet

In the course of testing a superconducting magnet, it is often necessary to warm up the magnet from, say, 4.2 K, to room temperature. If this cryogen-immersed magnet is "small," we may simply leave it in the cryostat unattended with the liquid cryogen depleted from the cryostat, and in a few hours to a day, the magnet will warm up to room temperature.

In this problem we consider two methods of warming up "large" magnets, first a magnet after it has been operated in a bath of liquid helium at 4.2 K, and next an HTS magnet operated in a bath of liquid nitrogen at 77 K. For a large LHe-immersed magnet, a method often used is to heat up the magnet by connecting its terminals to a power supply. Here we consider two power-supply options: 1) constant current (**8.2.1**); and 2) constant voltage (**8.2.4**).

The warming sequence may be described by either of the following differential equations, in which T is the magnet temperature.

$$\mathcal{V}_{cd} C_{cd}(T) \frac{dT}{dt} = \frac{\rho_m(T)\ell_{cd}}{A_m} I_\circ^2 \qquad \text{(Constant Current)} \qquad (8.71a)$$

$$= \frac{A_m}{\rho_m(T)\ell_{cd}} V_\circ^2 \qquad \text{(Constant Voltage)} \qquad (8.71b)$$

where $\mathcal{V}_{cd}$ is the total conductor volume in the magnet, here assumed that thermal energy is stored only by the conductor; $C_{cd}(T)$ is the conductor heat capacity, here set equal to that of copper, i.e., $C_{cd}(T) = C_{cu}(T)$; $\rho_m(T)$ is copper electrical resistivity, i.e., $\rho_m(T) = \rho_{cu}(T)$; ℓ_{cd} is the total conductor length in the magnet; A_m is the copper cross sectional area; $I_\circ$ is the current from a constant-current supply; and $V_\circ$ is the voltage from a constant-voltage supply.

Assume that there are no other sources of heat input to the magnet during either heating mode. (Sometimes, the cryostat vacuum is broken to accelerate the warm-up process, but this practice is not generally recommended: it causes frosting over the surfaces of the cryostat, not a neat sight. In a CIC-magnet, helium gas may be circulated through the winding to facilitate the warm-up process.)

For this particular magnet: $\mathcal{V}_{cd} = 0.4\,\text{m}^3$; $\ell_{cd} = 10^4\,\text{m}$; and $A_m = 1.5 \times 10^{-5}\,\text{m}^2$. (Note that in most magnets, wound with graded conductors, A_m is not constant throughout the winding as assumed here.)

a) Compute an approximate (within ±20% uncertainty) magnet warm-up time from 10 K to 300 K when heated with a constant-current supply of $I_\circ = 25\,\text{A}$.

b) Compute an approximate (within ±20% uncertainty) magnet warm-up time from 10 K to 300 K when heated with a constant-voltage supply of $V_\circ = 25\,\text{V}$.

c) Discuss a practical case in which neither a constant-current nor constant-voltage heating is possible over the entire temperature range because of limitations of *real* power supplies.

d) Repeat **a)**, except with an initial temperature of 80 K.

e) Repeat **b)**, except with an initial temperature of 80 K.

Solution to PROBLEM 8.1

a) We may use Eq. 8.71*a* to solve for $\Delta t_w^I|_{10\,\mathrm{K}}^{300\,\mathrm{K}}$, the warm-up time from 10 K to 300 K under constant-current heating:

$$\Delta t_w^I|_{10\,\mathrm{K}}^{300\,\mathrm{K}} = \frac{\mathcal{V}_{cd} A_m}{\ell_{cd} I_\circ^2} \int_{10\,\mathrm{K}}^{300\,\mathrm{K}} \frac{C_{cu}(T)}{\rho_{cu}(T)}\, dT$$

$$= \frac{\mathcal{V}_{cd} A_m}{\ell_{cd} I_\circ^2} Z(T_f = 300\,\mathrm{K}, T_i = 10\,\mathrm{K}) \qquad (S1.1)$$

For copper RRR = 100, $Z(T_f, T_i)$ is given in Fig. 8.2: $Z(T_f = 300\,\mathrm{K}, T_i = 10\,\mathrm{K}) = 15.1 \times 10^{16}\,\mathrm{A^2\,s/m^4}$. Solving for $\Delta t_w^I|_{10\,\mathrm{K}}^{300\,\mathrm{K}}$, we obtain:

$$\Delta t_w^I|_{10\,\mathrm{K}}^{300\,\mathrm{K}} = \frac{(0.4\,\mathrm{m^3})(1.5 \times 10^{-5}\,\mathrm{m^2})(15.1 \times 10^{16}\,\mathrm{A^2\,s/m^4})}{(1 \times 10^4\,\mathrm{m})(25\,\mathrm{A})^2}$$

$$\simeq 1.45 \times 10^5\,\mathrm{s} \simeq 40\,\mathrm{h} \simeq 1\tfrac{2}{3}\,\mathrm{days} \qquad (S1.2)$$

With a constant-current supply feeding 25 A into the magnet, the magnet warms up from 10 K to 300 K in slightly less than two days.

b) We may use Eq. 8.71*b* to solve for $\Delta t_w^V|_{10\,\mathrm{K}}^{300\,\mathrm{K}}$, the warm-up time from 10 K to 300 K under constant-voltage heating:

$$\Delta t_w^V|_{10\,\mathrm{K}}^{300\,\mathrm{K}} = \frac{\mathcal{V}_{cd}\, \ell_{cd}}{A_m V_\circ^2} \int_{10\,\mathrm{K}}^{300\,\mathrm{K}} C_{cu}(T) \rho_{cu}(T)\, dT$$

$$= \frac{\mathcal{V}_{cd}\, \ell_{cd}}{A_m V_\circ^2} Y(T_f = 300\,\mathrm{K}, T_i = 10\,\mathrm{K}) \qquad (S1.3)$$

For copper RRR = 100, $Y(T_f, T_i)$ is given in Fig. 8.6: $Y(T_f = 300\,\mathrm{K}, T_i = 10\,\mathrm{K}) = 7.25\,\mathrm{V^2 s/m^2}$. Solving for $\Delta t_w^V|_{10\,\mathrm{K}}^{300\,\mathrm{K}}$, we obtain:

$$\Delta t_w^V|_{10\,\mathrm{K}}^{300\,\mathrm{K}} = \frac{(0.4\,\mathrm{m^3})(1 \times 10^4\,\mathrm{m})(7.25\,\mathrm{V^2 s/m^2})}{(1.5 \times 10^{-5}\,\mathrm{m^2})(25\,\mathrm{V})^2}$$

$$= 3.1 \times 10^6\,\mathrm{s} \simeq 860\,\mathrm{h} \simeq 36\,\mathrm{days} \qquad (S1.4)$$

With a constant-voltage supply of 25 V across the magnet, the magnet warms up from 10 K to 300 K in roughly 36 days.

It may be computed that the magnet resistance is about 0.32 Ω at 10 K and 17.2 Ω at 300 K. It means that with a 25-A supply, the voltage and corresponding power are, respectively, 8 V and 200 W at 10 K; 430 V and ∼11 kW at 300 K. Similarly, with a 25-V supply, they are 78 A and ∼2 kW at 10 K; ∼1.5 A and ∼35 W at 300 K.

Most constant-current supplies do not deliver unlimited voltage; constant-voltage supplies do not deliver unlimited current. Therefore, a 25-A mode may require a warm-up period considerably longer than the ∼2 days computed above, and a 25-V mode considerably longer than 36 days.

Solution to PROBLEM 8.1 (continuation)

c) Most power supplies generally permit operation in either a constant-current or a constant-voltage mode. However, there is a limit of voltage for constant-current mode operation and a limit of current for constant-voltage mode operation. Let us assume that the power supply considered in this problem has limits of 100 A and 100 V; i.e., it is a 10-kW supply that matches a load of 1 Ω. Because the magnet resistance, as discussed above, varies from 0.32 Ω at 10 K to 17.2 Ω at 300 K, it is not possible for this supply to deliver its maximum possible power of 10 kW during the entire warm-up process.

The quickest *real* warm-up time is achieved by setting the initial current at 100 A ($V = 1.6$ V), letting the supply warm up the magnet at 100-A mode until its resistance reaches 1 Ω; then switching to a 100-V mode until the magnet reaches 300 K. Let us compute this warm-up time.

10–50 K The temperature at which the magnet has a resistance of 1 Ω, 1/17.2 that at 300 K (from Fig. A4.1), is 50 K. Thus, $\Delta t_w^I|_{10\text{K}}^{50\text{K}}$, the 10 K→50 K warm-up time under a 100-A mode, with $Z(50\,\text{K}, 10\,\text{K}) = 4.5\times10^{16}\,\text{A}^2\,\text{s/m}^4$, is given by:

$$\Delta t_w^I|_{10\text{K}}^{50\text{K}} = \frac{(0.4\,\text{m}^3)(1.5\times10^{-5}\,\text{m}^2)(4.5\times10^{16}\,\text{A}^2\,\text{s/m}^4)}{(1\times10^4\,\text{m})(100\,\text{A})^2}$$

$$\simeq 2.7\times10^3\,\text{s} = 45\,\text{min.} \qquad (S1.5)$$

50–300 K From 50 K to 300 K, a 100-V heating mode is used with. With $Y(300\,\text{K}, 50\,\text{K}) = 7.25\,\text{J}\,\Omega/\text{m}^2$, $\Delta t_w^V|_{50\text{K}}^{300\text{K}}$, the 50 K→300 K warm-up time under a 100-V heating mode, is given by:

$$\Delta t_w^V|_{50\text{K}}^{300\text{K}} = \frac{(0.4\,\text{m}^3)(1\times10^4\,\text{m})(7.25\,\text{J}\,\Omega/\text{m}^2)}{(1.5\times10^{-5}\,\text{m}^2)(100\,\text{V})^2}$$

$$= 1.93\times10^5\,\text{s} = 54\,\text{h} \qquad (S1.6)$$

A total warm-up time of ∼55 h is required for this combined heating mode. Because as the magnet warms up, a constant-voltage mode delivers less and less power, it is safer (though generally slower) than a constant-current mode.

d) If we consider a magnet mass to be thermally equivalent to its matrix metal mass, there is no distinction between a magnet of LTS and a magnet of HTS, except of course T_i. With $T_i = 80$ K and $Z(300\,\text{K}, 80\,\text{K}) = 7.7\times10^{16}\,\text{A}^2\,\text{s/m}^4$ used in Eq. $S1.1$, we obtain:

$$\Delta t_w^I|_{80\text{K}}^{300\text{K}} \simeq 0.7\times10^5\,\text{s} \sim 20\,\text{h} \qquad (S1.7)$$

e) With $T_i = 80$ K and $Y(300\,\text{K}, 80\,\text{K}) = 7\,\text{A}^2\text{s/m}^4$ used in Eq. $S1.4$, we obtain:

$$\Delta t_w^I|_{80\text{K}}^{300\text{K}} \simeq 3\times10^6\,\text{s} \simeq 830\,\text{h} \simeq 35\,\text{days} \qquad (S1.8)$$

Note that because there is not much thermal energy stored between 10 K and 80 K, the warm-up times for the constant-voltage mode are nearly identical for $T_i = 10$ K and $T_i = 80$ K.

PROBLEM 8.2: Protection of 6-kA vapor-cooled HTS lead

This problem addresses protection of a 6-kA vapor-cooled HTS current lead studied in **PROBLEM 4.6B**, which states that "... for this lead a normal metal of 1.735-cm^2 cross section is sufficient against flow stoppage incidents that may occur..."

Consider the following fault scenario. A pair of these vapor-cooled leads is connected to a superconducting magnet (inductance L) operated in a bath of liquid helium at 4.2 K. Upon the detection of a fault—here a flow stoppage in one of the leads—the magnet is discharged through a dump resistor (resistance R_D) connected across the magnet terminals at the warm end of each vapor-cooled lead; i.e., the system—magnet and leads—is protected by the detect-and-dump technique. Here, there are two important time sequences: 1) between the detection of the fault and the opening of a switch that initiates the magnet current discharge, from $I_{op}=6$ kA, and 2) the current discharge itself. The first sequence is characterized by a delay time of τ_{dl} and the second by a discharge time constant $\tau_{dg}=L/R_D$.

a) Show that $A_m=1.735\,\text{cm}^2$ will limit T_f for this 6-kA lead to 180 K in case of a flow stoppage for $\tau_{dl}=5$ s and $\tau_{dg}=15$ s. Note that in **PROBLEM 4.6B** special symbols for lead cross sections, $[A_n]_{fs}$ and $[A_n]_{cs}$, are used for A_m, the matrix metal cross section in the composite superconductor. Assume that after the flow stoppage, the entire current is carried by the matrix metal alone and Joule heating is adiabatic. Also assume that $T_i=80$ K and $\gamma_{m/s}=2$.

b) Compute the maximum delay time, $\tau_{dl}|_{mx}$, so that $T_f=300$ K. (Unlike within the winding, here it is assumed that T_f can exceed 200 K safely.)

Solution to PROBLEM 8.2

a) Similar to the Detect-and-Dump protection technique with Switching Delay, discussed in **8.8.3**, the Joule heating of matrix metal here consists of two modes: 1) constant-current during τ_{dl}; and 2) current-discharge with a time constant τ_{dg}. Thus, applying Eq. 8.66*b*, we obtain:

$$Z(T_f,T_i)=\left(\frac{A_m}{A_{cd}}\right)(\tau_{dl}+\tfrac{1}{2}\tau_{dg})J_{m_\circ}^2 \tag{8.66b}$$

With $A_m/A_{cd}=\gamma_{m/s}/(\gamma_{m/s}+1)$, we have:

$$Z(T_f,T_i)=\left(\frac{\gamma_{m/s}}{1+\gamma_{m/s}}\right)(\tau_{dl}+\tfrac{1}{2}\tau_{dg})J_{m_\circ}^2 \tag{S2.1}$$

With $\tau_{dl}=5$ s, $\tau_{dg}=15$ s, $J_{m_\circ}=(6000\,\text{A})/(1.735\times10^{-4}\,\text{m}^2)=3.46\times10^7\,\text{A/m}^2$, and $\gamma_{m/s}=2$ inserted into Eq. *S*2.1, $Z(T_f,T_i)$ becomes:

$$Z(T_f,T_i)=(12.5\,\text{s})\left(\frac{2}{3}\right)(3.46\times10^7\,\text{A/m}^2)^2\simeq1\times10^{16}\,\text{A}^2\,\text{s/m}^4$$

From Fig. 8.2, we find $Z(T_f,T_i=80\,\text{K})=1\times10^{16}\,\text{A}^2\,\text{s/m}^4$ for *brass* corresponds to $T_f=250$ K, which is well within the safe limit of this 6-kA HTS current lead.

b) With $Z(300\,\text{K},80\,\text{K})\simeq1.1\times10^{16}\,\text{A}^2\,\text{s/m}^4$ (Fig. 8.2) for brass into Eq. *S*2.1 and solving it for τ_{dl}, we find: $\tau_{dl}+\tau_{dg}/2\simeq14$ s; $\tau_{dl}\simeq6.5$ s.

PROBLEM 8.3: Protection of a cryostable NbTi magnet*

Consider a cryostable magnet wound with NbTi composite strip, $a = 10\,\text{mm}$, $b = 3\,\text{mm}$, and $\gamma_{m/s} = 4$ (copper matrix metal of RRR = 50). For $f_p = 0.5$ and $q_{fm} = 0.36\,\text{W/cm}^2$, Eq. 6.22 gives: $[J_{m_\circ}]_{Sk} = 6.25\times10^7\,\text{A/m}^2$, the matrix metal current density at I_{op} satisfying the Stekly cryostability criterion. The magnet is protected with a detect-and-dump method.

a) First show $I_{op} = 1500\,\text{A}$ and then compute V_D for $E_m = 10\,\text{MJ}$ and $T_f = 100\,\text{K}$. To make it easier to recool a magnet to 4.2 K after a dump, T_f is sometimes set, as here, well below the overstraining limit temperature of 200 K. Note that here $J^D_{m_\circ} = [J_{m_\circ}]_{Sk}$.

b) Repeat **a)** for V_D for $E_m = 100\,\text{MJ}$ and $T_f = 100\,\text{K}$.

Solution to PROBLEM 8.3

a) With $I_{op} = [J_{m_\circ}]_{Sk} A_m$, where $A_m = (a\times b)\gamma_{m/s}/(1+\gamma_{m/s})$, the matrix metal cross section in the composite, we compute:

$$I_{op} = (6.25\times10^7\,\text{A/m}^2)\frac{(10\times10^{-3}\,\text{m})(3\times10^{-3}\,\text{m})4}{(1+4)} = 1500\,\text{A}$$

From Eq. 8.19, we solve for V_D:

$$V_D = \frac{J_{m_\circ} E_m}{A_{cd} Z(T_f, T_i)} \tag{8.72}$$

Inserting $J^D_{m_\circ} = [J_{m_\circ}]_{Sk} = J_{m_\circ}$, $E_m = 10\times10^6\,\text{J}$, $A_{cd} = (10\times10^{-3}\,\text{m})\times(3\times10^{-3}\,\text{m}) = 3\times10^{-5}\,\text{m}^2$, and $Z(100\,\text{K}, 4.2\,\text{K}) = 6.7\times10^{16}\,\text{A}^2\,\text{s/m}^4$ into Eq. 8.72, we obtain:

$$V_D = \frac{(6.25\times10^7\,\text{A/m}^2)^2(10\times10^6\,\text{J})}{(3\times10^{-5}\,\text{m}^2)(6.7\times10^{16}\,\text{A}^2\,\text{s/m}^4)} \tag{S3.1}$$

$$\simeq 310\,\text{V}$$

A discharge voltage of 310 V is safe and should not pose any undue difficulties.

b) With $E_m = 100\,\text{MJ}$ substituted into Eq. 8.72, we obtain: $V_D = 3100\,\text{V}$, a very dangerous level within a cryostat environment. One method widely used to reduce the voltage between a magnet and its cryostat is to center-tap the magnet dump resistor to ground, the level to which most cryostats are also anchored. This will limit the relative voltage to $\pm1550\,\text{V}$. This of course does not reduce the voltage across the magnet terminals. For some large magnets, such as for Tokamak fusion, discharge voltages as high as 5 kV–20 kV are considered unavoidable. As remarked in **8.8.3A**, one way to reduce V_D is to increase A_{cd} and thus I_{op}. This is the reason that large fusion magnets operate in the range 50 kA–100 kA. Note that if $I_{op} = 15\,\text{kA}$ (10 times the original A_{cd}) is chosen for this magnet ($E_m = 100\,\text{MJ}$ and $T_f = 100\,\text{K}$), $V_D = 310\,\text{V}$.

---

* Based partly on **Problem 8.1** in the 1st Edition (Plenum, 1994).

PROBLEM 8.4: Hot-spot temperatures in Hybrid III SCM*

This problem deals with protection of the Hybrid III SCM (superconducting magnet). Table 8.7 lists appropriate conductor parameters. The magnet relies on the detect-and-dump protection method discussed in **8.8.3A**.

The dump resistor R_D for Hybrid III is $0.3\,\Omega$. The inductance, L, of the SCM is 8.0 H. At 2230 A (the highest operating current used), the SCM stores a magnetic energy of 19.9 MJ. (The system's nominal operating current is 2100 A.)

a) Compute the final temperature, T_f, of the hot spot, where a quench occurred, for each grade of Nb_3Sn and NbTi composite when the SCM is dumped from 2230 A, assuming that each conductor remains superconducting during the dump except at the hot spot in each of the four conductors, and that adiabatic conditions prevail at each hot spot. Assume further that each hot spot contributes negligible electrical resistance to the circuit. Use the Z-function for copper (RRR =50) in Fig. 8.2.

What actually happens when the SCM dump is initiated at $t=0$ is that the entire SCM is driven normal essentially at $t=0$, primarily because of AC heating generated by the rapid field change within the winding. The winding is subsequently heated further by Joule dissipation. It is therefore more realistic to include $r(t)$ in the analysis of current decay. For the sake of simplicity, let us express $r(t)$ by:

$$r(t) = r_0 + \eta t \tag{8.73}$$

where r_0 and η are both constants.

b) Show that the SCM current $I(t)$ during the dump ($t \geq 0$) may be given by:

$$I(t) = I_{op} \exp\left[-\frac{(R_D + r_0)}{L}t - \frac{\eta}{2L}t^2\right] \tag{8.74}$$

Note that $I(t=0) = I_{op}$.

c) Using the above model, compute the total energy dissipated in the SCM, E_{sm}, for the following set of values: $I_{op} = 2230$ A; $L = 8$ H; $R_D = 0.3\,\Omega$; $r_0 = 0.3\,\Omega$; $\eta = 0.04\,\Omega$/s. Unlike, as discussed in **8.4.2** under cryostable conditions, a normal zone here expands rather than shrinks, thus, $\eta > 0$, because a dump induces dB/dt heating that creates vapor in the winding, upsetting the cooling conditions that otherwise prevail in cryostable windings.

Table 8.7: Hybrid III SCM Conductor Parameters

Superconductor	*Nb_3Sn*		*NbTi*	
Conductor Grade	*HF*	*LF*	*HF*	*LF*
Overall width, a [mm]	9.49	9.10	9.20	9.20
Overall thickness, b [mm]	4.52	4.47	2.60	2.00
$\gamma_{m/s}\,[=A_m/(A_{sc}+A_{\overline{m}})]$	4.1	5.3	3.0	10

* Based on **Problem 8.2** in the 1st Edition (Plenum, 1994).

Solution to PROBLEM 8.4

a) In general, when the discharge time constant, τ_{dg}, is determined completely by the magnet inductance L and dump resistor R_D, we have, from Eq. 8.16*c*:

$$Z(T_f, T_i) = \left(\frac{\gamma_{m/s}}{1+\gamma_{m/s}}\right) J_{m_\circ}^2 \left(\frac{L}{2R_D}\right) \tag{8.16c}$$

$J_{m_\circ}$ is given by:

$$J_{m_\circ} = \frac{I_{op}}{A_m} = \left(\frac{\gamma_{m/s}+1}{\gamma_{m/s}}\right) \frac{I_{op}}{ab} \tag{S4.1}$$

Nb_3Sn HF: We have:

$$J_{m_\circ} = \left(\frac{5.1}{4.1}\right) \frac{(2230\,\mathrm{A})}{(9.49\times10^{-3}\,\mathrm{m})(4.52\times10^{-3}\,\mathrm{m})}$$

$$= 6.47\times10^{7}\,\mathrm{A/m^2} \tag{S4.2}$$

Combining Eqs. 8.16*c* and *S*4.2, we have:

$$Z(T_f, 4\,\mathrm{K}) = \left(\frac{4.1}{5.1}\right) (6.47\times10^{7}\,\mathrm{A/m^2})^2 \left(\frac{8\,\mathrm{H}}{2\times0.3\,\Omega}\right)$$

$$Z(T_f, 4\,\mathrm{K}) = 4.5\times10^{16}\,\mathrm{A^2\,s/m^4}$$

From Fig. 8.2 (copper RRR = 50), we find $T_f \sim 65\,\mathrm{K}$ for the hot spot.

Table 8.8 presents a summary for the four conductors. From Table 8.8 we note that because of excessive hot-spot temperatures both grades of the NbTi conductors may be damaged severely.

b) The circuit differential equation for $t \geq 0$ is given by:

$$L\frac{dI(t)}{dt} + (R_D + R_0 + \eta t)I(t) = 0 \tag{S4.3}$$

Equation *S*4.3 may be solved as:

$$\frac{dI(t)}{I(t)} = -\frac{(R_D + R_0 + \eta t)}{L}\,dt \tag{S4.4}$$

$$\ln\left[\frac{I(t)}{I_{op}}\right] = -\frac{(R_D + R_0)}{L}t - \frac{\eta}{2L}t^2 \tag{S4.5}$$

Table 8.8: $Z(T_f, 4\,\mathrm{K})$ and T_f Values for Hybrid III Conductors

Conductor	A_m [$10^{-6}\,\mathrm{m^2}$]	$J_{m_\circ}$ [$\mathrm{MA/m^2}$]	$Z(T_f, 4\,\mathrm{K})$ [$10^{16}\,\mathrm{A^2\,s/m^4}$]	T_f [K]
Nb_3Sn HF	34.5	64.7	4.5	$\sim$65
Nb_3Sn LF	34.2	65.2	4.7	$\sim$70
NbTi HF	17.9	124.3	15.4	$\gg 300$
NbTi LF	16.7	121.4	17.8	$\gg 300$

Solution to PROBLEM 8.4 (continuation)

Solving Eq. $S4.5$ for $I(t)$, we obtain:

$$I(t) = I_{op} \exp\left[-\frac{(R_D + R_0)}{L}t - \frac{\eta}{2L}t^2\right] \tag{8.74}$$

c) There are two methods to solve this problem.

Method 1: The easiest and quickest way to compute E_{sm} is to estimate an average value of $r(t)$ during the current decay, $\tilde{r}$, and use a simple "voltage divider" method to determine the energy dissipated in the SCM: $E_{sm} = E_m\tilde{r}/(\tilde{r} + R_D)$, where in this case $E_m = 19.9\,\text{MJ}$.

Without $r(t)$, the circuit time constant, τ_D, is given by L/R_D, which is $\sim$27 s. From Eq. 8.73 we have: $r(0) = 0.3\,\Omega$; $r(5\,\text{s}) = 0.5\,\Omega$; $r(10\,\text{s}) = 0.7\,\Omega$; $r(15\,\text{s}) = 0.9\,\Omega$; $r(20\,\text{s}) = 1.1\,\Omega$.

The average of $r(t)$ over this time period is $0.7\,\Omega$, or a new dump time constant of $\sim$8 s $[= L/(R_D + 0.7\,\Omega)]$. This means the time average should be taken between 0 and $\sim$10 s, or a new average value of $\tilde{r}$ of $0.5\,\Omega$. That is, $\sim$63% $[= 0.5/(0.3 + 0.5)]$ of 19.9 MJ is dissipated in the SCM: $E_{scm} \simeq 12.4\,\text{MJ}$.

Method 2: A more rigorous way to determine E_{sm} is to integrate $r(t)I^2(t)$. That is:

$$E_{sm} = \int_0^\infty r(t) I_0^2 \exp\left[-\frac{2(R_D + r_0)}{L}t - \frac{\eta}{L}t^2\right] dt \tag{S4.6}$$

Equation $S4.6$ involves *erf* functions. Alternatively, it can be integrated graphically; results are presented in Table 8.9. Integrating $r(t)I^2(t)$ over the period from $t = 0$ to $t = 20\,\text{s}$, we obtain: $E_{sm} \simeq 12.2\,\text{MJ}$, which is $\sim$60% of the energy initial stored energy; 12.2 MJ is essentially identical to the 12.4 MJ computed above.

$Z(T_f)$ for *HF* NbTi now becomes $\sim 8 \times 10^{16}\,\text{A}^2\,\text{s/m}^4$, giving $T_f \sim 125\,\text{K}$; $Z(T_f)$ for *LF* NbTi becomes $\sim 9 \times 10^{16}\,\text{A}^2\,\text{s/m}^4$, giving $T_f \sim 150\,\text{K}$, both below the safe limit of $\sim$200 K.

Table 8.9: Energy Dissipated in Hybrid III SCM

t [s]	$r(t)$ [Ω]	$I(t)$ [A]	$r(t)I^2(t)$ [MW]	$\int_0^t r(t)I^2(t)\,dt$ [MJ]
0	0.3	2230	1.49	0
5	0.5	1440	1.04	6.5
10	0.7	820	0.47	10.2
15	0.9	413	0.15	11.7
20	1.1	183	0.04	12.2

*DISCUSSION 8.1: Quench-Voltage Detection—A Variation**

Figure 8.20 represents a schematic model for Hybrid II, another hybrid magnet once operated at FBNML [3.17]. The superconducting magnet is a NbTi coil comprised of 22 double pancakes (DP). In addition to the NbTi coil, the water-cooled insert and copper radiation plates are included in the figure to emphasize that in a "real" system, magnetic coupling is not confined just to double pancakes; all components are coupled. The magnetic coupling between these components complicates the "balancing" of the bridge circuit discussed in **8.8.5**.

Two quench-voltage-detection techniques are used for the Hybrid II, whose SCM is divided into four sections: section B′ (DP 1 through 7); section A′ (DP 8 through 11); section A (DP 12 through 15); and B (DP 16 through 22).

A. Technique I

In this technique, the magnet is divided into A′+A and B′+B. Although inductive voltage canceling achieved by this technique is slightly better than that achieved by a more conventional technique that divides the magnet into B′+A′ and A+B, it is still not entirely satisfactory. The technique cannot completely eliminate all inductive voltages that are developed whenever either the water-cooled insert or the NbTi coil is energized.

B. Technique II

The second technique, developed by Ishigohka [8.114], employs voltage taps on all 22 double pancakes, and combines them into two major components: one that contains odd-numbered double pancakes, $V_{2n-1}(t)$, and the other that contains

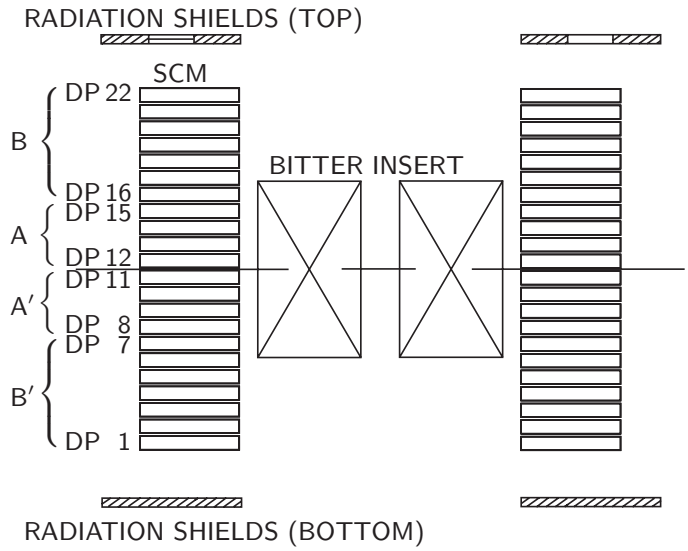

Fig. 8.20 Schematic arrangement of Hybrid II with a Bitter insert, a 22-DP SCM (superconducting magnet), and radiation shields [3.17].

* Based on **Problem 8.4** in the 1st Edition (Plenum, 1994).

DISCUSSION 8.1: Quench-Voltage Detection—A Variation (continuation)

even-numbered double pancakes, $V_{2n}(t)$. By adjusting the gain of each of 22 separate amplifiers, we can adjust the voltage from each double pancake to minimize $V_{out}(t)$ in the absence of a resistive voltage. Thus:

$$V_{out}(t) = \sum_{n=1}^{11} [\alpha_{2n-1} V_{2n-1}(t) - \alpha_{2n} V_{2n}(t)] \tag{8.75}$$

where α_{2n-1} is the amplifier gain for the $(2n-1)^{\text{th}}$ double pancake, and α_{2n} is the amplifier gain for the $2n^{\text{th}}$ double pancake.

How successfully we can eliminate inductive voltages in Technique I ($A+A'$ vs. $B+B'$) depends on the closeness of inductive voltages of the two parts irrespective of current level or current sweep rate. In Hybrid II, because the cryostat housing the NbTi coil was not symmetric about the coil's midplane, voltage balancing could not be maintained irrespective of current level or current sweep rate.

Also, more seriously, a bridge circuit setting optimized for charging the NbTi coil alone is not optimized when the insert is charged, and the optimized setting shifts with self-field sweep rate as well as with insert sweep rate.

Technique II (odd-numbered vs. even-numbered pancakes) greatly reduces the asymmetry of the entire system, which includes the coil itself, insert, radiation shields, and other parts of the cryostat. This makes the total unbalanced inductive voltages orders of magnitude smaller than those of the midplane/ends case.

Figure 8.21 shows three "balanced" voltages, $V_{AA'}$, $V_{BB'}$, and the odd-even difference voltage, V_δ for an insert trip from 25 kA [8.114]. Note that the peak value of $V_{BB'} - V_{AA'}$ is about ∼100 times greater than the peak value of V_δ.

V_δ is thus a much more sensitive method for monitoring *only* the operating condition of the superconducting coil. The cost of improved sensitivity is the large number of differential amplifiers required, each of which, of course, must not fail.

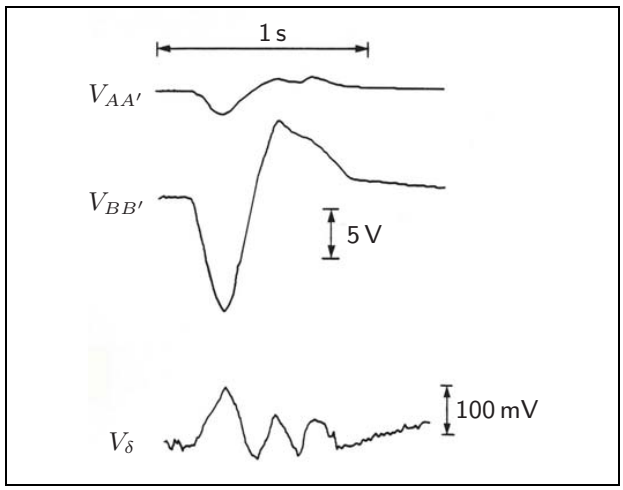

Fig. 8.21 Measured unbalanced voltages from an insert trip in Hybrid II [8.114].

PROBLEM 8.5: Design of a dump resistor

Here, we study design criteria for the dump resistor R_D used in active protection [8.115, 8.116]. Two parameters are important: 1) the value of R_D itself; and 2) the stored magnetic energy, E_m. E_m is important because in virtually every dump, the resistor must absorb most of E_m; clearly a prudent design assumption is that *100%* of E_m is adiabatically absorbed by the resistor. As illustrated in Fig. 8.22, let us here assume that our resistor is a bar, ℓ long, with a rectangular cross section of width w and thickness δ.

Because a dump resistor is often subjected to a dump voltage far above 100 V and absorbs an energy much greater than 1 MJ, in the process heated to 200 K or even higher above room temperature, its location in the magnet site must be carefully selected with safety as the most important criterion. Often the dump resistor is placed in a fenced, isolated area to keep it away from people and other equipment.

a) Show that the resistor length, ℓ, is given by:

$$\ell = \sqrt{\frac{E_m R_D}{\rho C_p \Delta T}} \tag{8.76a}$$

In the above equation ρ is the electrical resistivity of the resistor material, which is often steel. Because the resistor adiabatically absorbs E_m, its temperature will obviously increase, and so will ρ; here, however, we may assume that ρ is constant. C_p is the resistor material's heat capacity, which is also assumed constant, an acceptable assumption here, particularly for T above 300 K. ΔT is the total increase in temperature of the resistor after adiabatic absorption of E_m.

b) Show that the resistor cross sectional area, $w\delta$, is given by:

$$w\delta = \sqrt{\frac{\rho E_m}{R_D C_p \Delta T}} \tag{8.76b}$$

Dependences of ℓ and $w\delta$ on these parameters are all reasonable.

c) Compute ℓ and $w\delta$ for the parameters of Hybrid III: $E_m \simeq 20\,\text{MJ}$; $R_D = 0.3\,\Omega$; and for steel, $\rho \simeq 10^{-6}\,\Omega\,\text{m}$ and $C_p \simeq 4\times10^6\,\text{J/m}^2\,\text{K}$; and $\Delta T \simeq 200\,\text{K}$.

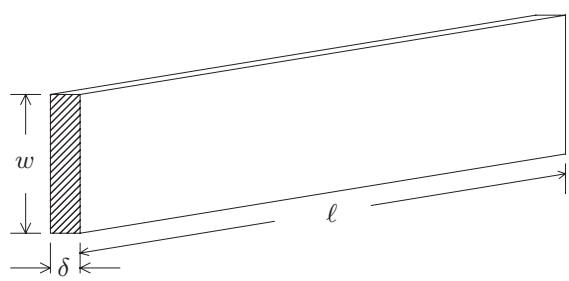

Fig. 8.22 Schematic drawing of a dump resistor in the form of a bar ℓ in length and $w\delta$ in cross section.

Solution to PROBLEM 8.5

a) The dump resistor's R_D is given by:

$$R_D = \frac{\rho\ell}{w\delta} \tag{S5.1a}$$

or

$$w\delta = \frac{\rho\ell}{R_D} \tag{S5.1b}$$

Adiabatic absorption of E_m raises the resistor's temperature by ΔT:

$$E_m = \ell w \delta C_p \Delta T \tag{S5.2a}$$

or

$$w\delta = \frac{E_m}{\ell C_p \Delta T} \tag{S5.2b}$$

Equating Eqs. $S5.1b$ and $S5.2b$, and solving for ℓ, we obtain:

$$\ell = \sqrt{\frac{E_m R_D}{\rho C_p \Delta T}} \tag{8.76a}$$

b) Inserting ℓ given by Eq. 8.76a into Eq. $S5.1b$, we have:

$$w\delta = \sqrt{\frac{\rho E_m}{R_D C_p \Delta T}} \tag{8.76b}$$

c) We compute ℓ and $w\delta$ for Hybrid III: $E_m \simeq 20\,\text{MJ}$; $R_D = 0.3\,\Omega$; $\rho \simeq 10^{-6}\,\Omega\,\text{m}$; $C_p \simeq 4\times10^6\,\text{J/m}^2\,\text{K}$; and $\Delta T \simeq 200\,\text{K}$.

$$\ell \simeq \sqrt{\frac{(2\times10^7\,\text{J})(0.3\,\Omega)}{(10^{-6}\,\Omega\,\text{m})(4\times10^6\,\text{J/m}^2\,\text{K})(200\,\text{K})}}$$

$$= 86.6\,\text{m}$$

$$w\delta \simeq \sqrt{\frac{(10^{-6}\,\Omega\,\text{m})(2\times10^7\,\text{J})}{(0.3\,\Omega)(4\times10^6\,\text{J/m}^2\,\text{K})(200\,\text{K})}}$$

$$\simeq 2.9\times10^{-4}\,\text{m}^2 \simeq 290\,\text{mm}^2$$

The dump resistor constructed for Hybrid III consisted of nearly 90 steel bars, each ∼1-m long, ∼5-cm wide, and 6-mm thick, electrically in series. Note that if ΔT had been limited to only 100 K, both ℓ and cross section $w\delta$ would have had to have been increased by ∼40%, i.e., $\ell \simeq 120\,\text{m}$ and $w\delta \simeq 410\,\text{mm}^2$.

DISCUSSION 8.2: "Slow" Discharge Modes for a Magnet

The power supplies most widely available in the laboratory setting are those that operate only in the $+V/+I$ quadrant. If such a supply is used to operate a superconducting magnet (of inductance L), it can take hours to discharge the magnet, unless of course it is discharged through the dump resistor.

Here, we discuss two simple techniques to achieve a "slow" discharge mode and set, though roughly, a discharge rate. The circuit diagram of each technique is shown in Fig. 8.23; in each circuit r_ℓ represents the total line resistance of the circuit, which is typically no greater than $\sim 1\,\mathrm{m}\Omega$.

When a slow discharge of magnet current, $I_m(t)$, is required in either technique, switch S is opened to activate either a low-resistance resistor r_d (Fig. 8.23a) or a set of series-connected diodes (Fig. 8.23b). Note that without one of these elements activated during the discharge mode, because $V_p \simeq 0$ for a $+V/+I$-quadrant supply, $V_m(t) = -r_\ell I_m(t)$, and $I_m(t)$ decays with a time constant of $\tau_m = L/r_\ell$. For a magnet of $L = 100\,\mathrm{H}$ and $r_\ell = 1\,\mathrm{m}\Omega$ of the circuit, for example, $\tau_m \simeq 10^5\,\mathrm{s}$; it will take at least a few days to discharge such a magnet.

A. Low-Resistance Resistor

When r_d is activated in the circuit, $V_m(t) = -(r_d + r_\ell) I_m(t)$: $I_m(t)$ decreases exponentially with $\tau_m = L/(r_\ell + r_d)$. Obviously, however, the rate of current decay, $dI_m(t)/dt$, is not constant; it decreases with $I_m(t)$:

$$\frac{dI_m(t)}{dt} = -\frac{I_m(t)}{\tau_m} \tag{8.77a}$$

For a magnet operating current of, for example, 250 A, r_d as high as $10\,\mathrm{m}\Omega$ may be used. Thus a magnet inductance of 100 H will result in $\tau_m \simeq 10^4\,\mathrm{s}$; the magnet will discharge in about half a day.

Design criteria for r_d is studied below in ***DISCUSSION 8.3***.

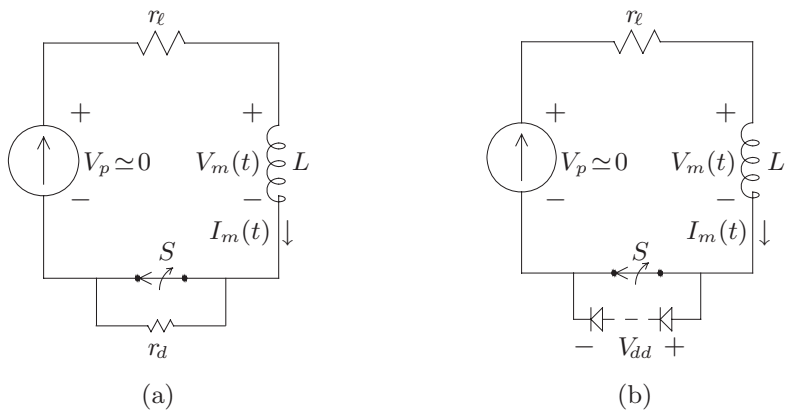

Fig. 8.23 Circuits for "slow" discharge modes: (a) low-resistance discharge resistor, r_d, activated by switch S; (b) a set of series-connected diodes activated. In each circuit r_ℓ represents the total line resistance and $V_p \simeq 0$.

DISCUSSION 8.2: "Slow" Discharge Modes for a Magnet (continuation)

B. Series of Diodes

Although an ideal diode operates with zero forward voltage, *real* diodes do not. Typically a diode generates a voltage in the range 0.1–0.5 V when carrying current. Unlike a resistor, this voltage is nearly independent of current above ∼1 A. Thus, a nearly constant rate of current decay may be maintained as the magnet current decays. With a total voltage across a set of series-connected diodes of V_{dd}, for $r_\ell I_m(t) \ll V_{dd}$, the current decay rate is given by:

$$\frac{dI_m(t)}{dt} = -\frac{V_{dd}}{L} \tag{8.77b}$$

For the same magnet of $L = 100\,\mathrm{H}$ used as an example above, with $V_{dd} = 2.5\,\mathrm{V}$ (from 5 to 10 diodes), the magnet current decays from 250 A to zero in 10,000 s, or ∼3 hours. Note that each diode here, air- or water-cooled, must be able to handle a power level from ∼25 W to ∼125 W.

DISCUSSION 8.3: Design of a Low-Resistance Resistor

The design procedure for a low-resistance resistor, r_d, is similar to the design of a dump resistor, studied in **PROBLEM 8.5**. One important difference is that this resistor must handle *power* rather than *energy*, because here $I_m(t)$ decays in a time scale of hours or at least minutes, definitely not seconds. For the same resistor geometry as with R_D, for $w \gg \delta$, there are two design equations for r_d:

$$r_d = \frac{\rho\ell}{w\delta} \tag{8.78a}$$

$$r_d I_m(0)^2 \simeq 2w\ell g_{cv} \tag{8.78b}$$

where $I_m(0)$ is the magnet current when the resistor is activated and g_{cv}, assumed constant here, is the natural convective heat transfer flux $[\mathrm{W/m^2}]$ on the resistor surface, generally (as applied here) of still air or, if the resistor is immersed in a bucket of water, of still water—the bucket must be large enough for the water to absorb the total dissipation energy without too much temperature rise.

Equation 8.78*b* expresses that the total Joule heating generated in the resistor, $r_d I_m(0)^2$, is balanced by the total convective heat emanating from the resistor's surface, given approximately by $2w\ell g_{cv}$ for $w \gg \delta$. Note also that $I_m(t)$, which actually is decaying slowly, is assumed constant and equal to $I_m(0)$ in Eq. 8.78*b*. Solving for ℓ from both equations, we obtain:

$$\ell \simeq r_d I_m(0)\sqrt{\frac{\delta}{2\rho g_{cv}}} \tag{8.79a}$$

$$w \simeq I_m(0)\sqrt{\frac{\rho}{2\delta g_{cv}}} \tag{8.79b}$$

Again, the dependences of ℓ and w on these parameters are plausible.

DISCUSSION 8.3: Design of a Low-Resistance Resistor (continuation)

Illustration Let us compute ℓ and w of: 1) an air-cooled resistor; and 2) a water-cooled resistor, for the following set of parameters: $r_d = 10\,\mathrm{m\Omega}$; $I_m(0) = 250\,\mathrm{A}$; $\rho = 10^{-6}\,\Omega\,\mathrm{m}$; and $\delta = 250\times10^{-6}\,\mathrm{m}$. Although g_{cv} depends on the temperature and orientation of the surface and cooling medium, take $g_{cv} \simeq 20\,\mathrm{W/m^2}$ for still air and $g_{cv} \simeq 20\,\mathrm{kW/m^2}$ for still water.

Air-Cooled Applying Eqs. 8.79*a* and 8.79*b*, we obtain:

$$\ell \simeq (0.01\,\Omega)(250\,\mathrm{A})\sqrt{\frac{(250\times10^{-6}\,\mathrm{m})}{2(10^{-6}\,\Omega\,\mathrm{m})(20\,\mathrm{W/m^2})}}$$

$$\simeq 6.3\,\mathrm{m}$$

$$w \simeq (250\,\mathrm{A})\sqrt{\frac{(10^{-6}\,\Omega\,\mathrm{m})}{2(250\times10^{-6}\,\mathrm{m})(20\,\mathrm{W/m^2})}}$$

$$= 2.5\,\mathrm{m}$$

Note that this 10-mΩ resistor must handle, initially, a total power of 625 W. A 10-mΩ air-cooled resistor satisfying the above two conditions may be constructed, for example, with 50 steel strips, each strip 250-μm thick, 6.3-m long and 5-cm wide, connected electrically in *parallel*.

Water-Cooled

$$\ell \simeq (0.01\,\Omega)(250\,\mathrm{A})\sqrt{\frac{(250\times10^{-6}\,\mathrm{m})}{2(10^{-6}\,\Omega\,\mathrm{m})(20\times10^{3}\,\mathrm{W/m^2})}}$$

$$\simeq 20\,\mathrm{cm}$$

$$w \simeq (250\,\mathrm{A})\sqrt{\frac{(10^{-6}\,\Omega\,\mathrm{m})}{2(250\times10^{-6}\,\mathrm{m})(20\times10^{3}\,\mathrm{W/m^2})}}$$

$$\simeq 8\,\mathrm{cm}$$

As may be seen from Eqs. 8.79*a* and 8.79*b*, both ℓ and w approach zero with increasing g_{cv}; however, the ratio ℓ/w is independent of g_{cv} (and r_d). Thus, if a combination of $I_m(0)$, g_{cv}, and r_d results, for example, in $\ell = 5\,\mathrm{cm}$ and $w = 2\,\mathrm{cm}$, dimensions perhaps too uncomfortably small, a "practical" water-cooled version of such a resistor may have *two* 250-μm thick steel strips, each 25-cm long and 5-cm wide, again, connected in parallel.

TRIVIA 8.3 List the items below in descending order of energy.

i) Caloric, burnt by man during an 8-h sleep;

ii) Electric, required to roast an 8-kg stuffed turkey in an oven;

iv) Geomechanical, released by a Richter 8 earthquake;

iii) Magnetic, stored in the Large Helical Device (LHD).

DISCUSSION 8.4: Overheating & Internal Voltage Criteria

Here we apply the overheating criterion (Eq. 8.30*a*) and internal voltage criterion (Eq. 8.40*b*) to derive the range of matrix current densities permissible for an adiabatic magnet such as a typical NMR magnet. Use copper (RRR = 50) as the matrix material.

Illustration Consider a solenoid coil of $a_1 = 0.15\,\text{m}$; $\alpha = 1.3$; $\beta = 3$; $E_m = 3\,\text{MJ}$; and $I_{op} = 300\,\text{A}$. From Fig. 3.14, we find $\mathcal{L}(\alpha = 1.3, \beta = 3) \simeq 0.54$.

Let us first apply the overheating criterion (Eq. 8.30*a*) for $f_r = 0.5$ and $T_f = 200\,\text{K}$. Also take $\gamma_{m/s} = 1$ for this copper composite superconductor. We may also use $\rho_m(T_f = 200\,\text{K}) = 1.11\times10^{-8}\,\Omega\,\text{m}$ and, from Fig. 8.2, $Z(T_f = 200\,\text{K}, T_i = 4.2\,\text{K}) = 10.5\times10^{16}\,\text{A}^2\,\text{s/m}^4$. Inserting these parameter values into Eq. 8.30*a*, we obtain the maximum limit of the matrix current density, $J^{sh}_{m_{op}}$, to limit T_f to 200 K:

$$J^{sh}_{m_{op}} = \left(\frac{1+\gamma_{m/s}}{\gamma_{m/s}}\right)\frac{f_r\pi(\alpha+1)\rho_m(T_f)Z(T_f,T_i)}{2}\sqrt{\frac{a_1}{2\mu_\circ\mathcal{L}(\alpha,\beta)E_m}} \tag{8.30a}$$

$$= \left(\frac{1+1}{1}\right)\frac{(0.5)\pi(1.3+1)(1.11\times10^{-8}\,\Omega\,\text{m})(10.5\times10^{16}\,\text{A}^2\,\text{s/m}^4)}{2}\times \sqrt{\frac{0.15\,\text{m}}{2(4\pi\times10^{-7}\,\text{H/m})(0.54)(3\times10^6\,\text{J})}}$$

$$\simeq 2(21.1\times10^8\,\text{J/m}^3)(0.19\,\text{A m/J}) \simeq 805\,\text{MA/m}^2 = 805\,\text{A/mm}^2$$

$J^{sh}_{m_{op}} \simeq 805\,\text{A/mm}^2$ is greater than most matrix current densities used even in "high-performance" magnets. What this implies is that because $J^{sh}_{m_{op}} \propto f_r$, at $J^{sh}_{m_{op}} = 300\,\text{A/mm}^2$, for example, $f_r \sim 0.2$ suffices to limit T_f to 200 K.

Let us now apply the internal voltage criterion (Eq. 8.40*b*) to solve $J^V_{m_{op}}$, the matrix current density meeting the voltage criterion, for the same magnet. Here let us take $V_{bk} = 10\,\text{kV}$.

$$J^V_{m_{op}} = \frac{2}{f_r(1-f_r)}\left[\frac{\sqrt{\mathcal{L}(\alpha,\beta)}}{\pi(\alpha+1)}\right]\left[\frac{V_{bk}I_{op}}{\rho_m(T_f)}\sqrt{\frac{2\mu_\circ}{a_1E_m}}\right] \tag{8.40b}$$

$$= \frac{2}{0.5(1-0.5)}\left[\frac{\sqrt{0.54}}{\pi(1.3+1)}\right]\left[\frac{(10^4\,\text{V})(300\,\text{A})}{(1.11\times10^{-8}\,\Omega\,\text{m})}\sqrt{\frac{2(4\pi\times10^{-7}\,\text{H/m})}{(0.15\,\text{m})(3\times10^6\,\text{J})}}\right]$$

$$= 8(0.102)(2.70\times10^{14}\,\text{A}^2/\text{m})(2.36\times10^{-6}\,\text{A}^{-1}\,\text{m}^{-1})$$

$$= 5.2\times10^8\,\text{A/m}^2 = 520\,\text{A/mm}^2$$

From these values of $J^{sh}_{m_{op}} = 805\,\text{A/mm}^2$ and $J^V_{m_{op}} = 520\,\text{A/mm}^2$, we may conclude that at least for this illustrative example, the internal voltage criterion is the one that limits the matrix current density for this magnet.

DISCUSSION 8.5: Protection of Bi2223 Tape Current Lead

Nowadays it is common to use HTS current leads between the terminals of a "dry" (cryogen-free) superconducting magnet at T_{cl} and the warm ends of the leads at T_{wm}, which is generally the 1st -stage of the cryocooler. Among several materials suitable for HTS, we consider here an HTS lead of Bi2223/Ag-Au tape, the same tape used in the *vapor-cooled* HTS current leads studied in **PROBLEMS 4.4**, **4.5**, and **4.6A**–**C**. As discussed there, Ag-Au instead of pure Ag must be used for current leads to reduce thermal conduction into the cold environment.

Consider a Bi2223/Ag-Au tape ℓ long and a total Ag-Au cross sectional area of a_m operating between the cold end ($z=0$) at temperature T_{cl} and the warm end ($z=\ell$) at temperature T_{wm} under adiabatic condition.

A. Peak-Temperature Spot Under Uniform Heating

We demonstrate first that if such a tape carrying transport current I_t becomes resistive over its *entire* length, melting or severe overheating is most likely at the axial (z) midpoint, $z \simeq \ell/2$. In the following thermal analysis, the matrix thermal conductivity, k_m, and electrical resistivity, ρ_m, are assumed temperature-independent. (Data of Ag-Au thermal conductivity and resistivity, shown in Figs. 4.23 and 4.24 on page 284, indicate this assumption is roughly valid.)

The power equation per unit conductor length under adiabatic condition may be given by:

$$a_m k_m \frac{d^2T}{dz^2} + \frac{\rho_m I_t^2}{a_m} = 0 \tag{8.80}$$

With $T(0)=T_{cl}$ and $T(\ell)=T_{wm}$, $T(\zeta)$, where $\zeta \equiv z/\ell$, is given by:

$$T(\zeta) = T_{cl} + (T_{wm} - T_{cl})\zeta + \frac{\rho_m \ell^2 I_t^2}{2a_m^2 k_m}(\zeta - \zeta^2) \tag{8.81}$$

The peak temperature, T_{pk}, occurs at axial location $\zeta(T_{pk})$ given by:

$$\zeta(T_{pk}) = \frac{1}{2} + \frac{a_m^2 k_m}{\rho_m I_t^2 \ell^2}(T_{wm} - T_{cl}) \tag{8.82a}$$

For $\zeta(T_{pk}) \simeq 0.5$, T_{pk} is given by:

$$T_{pk} \simeq \tfrac{1}{2}(T_{cl} + T_{wm}) + \frac{\rho_m I_t^2 \ell^2}{8a_m^2 k_m} \tag{8.82b}$$

We can show that for "typical" parameter values the second term of the right-hand side of Eq. 8.82*a* is negligible compared with 0.5: indeed T_{pk} in the tape occurs at the midpoint of the lead. Thus for $k_m = 2\,\mathrm{W/cm\,K}$ and $\rho_m = 1\times10^{-6}\,\Omega\,\mathrm{cm}$—these values corresponds roughly to those for Ag-5.3wt% (3at%)Au at 70 K (Figs. 4.23 and 4.24); $a_m = 8\times10^{-3}\,\mathrm{cm}^2$ (cross sectional area of 4-mm wide Bi2223/Ag-Au tape); $\ell = 15\,\mathrm{cm}$; $I_t = 50\,\mathrm{A}$; $T_{cl} = 10\,\mathrm{K}$; and $T_{pk} = 70\,\mathrm{K}$:

$$\frac{a_m^2 k_m}{\rho_m I_t^2 \ell^2}(T_{wm} - T_{cl}) = \frac{(8\times10^{-3}\,\mathrm{cm}^2)^2(2\,\mathrm{W/cm\,K})}{(1\times10^{-6}\,\Omega\,\mathrm{cm})(50\,\mathrm{A})^2(15\,\mathrm{cm})^2}(70\,\mathrm{K} - 10\,\mathrm{K})$$

$$\simeq 0.01$$

Thus the peak temperature point indeed occurs near the tape's axial midpoint.

DISCUSSION 8.5: Protection of Bi2223 Tape Current Lead (continuation)

From Eq. 8.82*b* we obtain:

$$T_{pk} \simeq \tfrac{1}{2}(T_{cl} + T_{wm}) + \frac{\rho_m I_t^2 \ell^2}{8 a_m^2 k_m}$$

$$= \tfrac{1}{2}(10\,\mathrm{K} + 70\,\mathrm{K}) + \frac{(1\times10^{-6}\,\Omega\,\mathrm{cm})(50\,\mathrm{A})^2(15\,\mathrm{cm})^2}{8(8\times10^{-3}\,\mathrm{cm}^2)^2(2\,\mathrm{W/cm\,K})} \simeq 590\,\mathrm{K}$$

B. Meltdown Time

An energy density of $\simeq 2900\,\mathrm{J/cm^3}$ is required to raise the temperature of silver from 70 K to 1223 K, its melting temperature. (For estimating the meltdown time for this tape, we assume the enthalpy of the silver-gold alloy to be that of silver.) With an average resistivity of this matrix between 70 K and 1200 K of $\sim 5\times 10^{-6}\,\Omega\,\mathrm{cm}$ and a constant matrix current density of $\sim 6000\,\mathrm{A/cm^2}$ ($= I_t/a_m$ with $I_t = 50\,\mathrm{A}$ and $a_m = 0.008\,\mathrm{cm^2}$), the matrix is heated at an average Joule heating of $\sim 200\,\mathrm{W/cm^3}$. Thus under an adiabatic condition in an evacuated environment of a cryocooled magnet where these leads are placed, it will take less than $\sim 15\,\mathrm{s}$ [$=(2900\,\mathrm{J/cm^3})/(200\,\mathrm{W/cm^3})$] to melt the tape; the tapes need to be continuously monitored and, as discussed below, protected.

C. Additional Remarks

As stated often in this book HTS is very stable, and an event such as that described above should not occur. However, although a short length of Bi2223/Ag-Au tape can readily, and quite inexpensively, be replaced, the consequence of a suddenly opened circuit can be highly dangerous and damaging to the system if the magnet to which the current leads are connected happens to have a large inductance—note that $V \propto L(dI/dt)$: the leads should *never* be open-circuited, unless the magnet terminals are shunted with a resistor robust enough to absorb the magnet energy and remain intact.

As already discussed in ***DISCUSSION 4.15*** and further studied in **PROBLEMS 4.6B** and **4.6C**, these tapes need to be "protected" with an additional strip of normal metal having a "low" thermal conductivity (to keep conduction heat input low) and "low" electrical resistivity.

Answer to TRIVIA 8.3 Quake (10^{18}, in J); LHD (10^9); turkey (10^8); sleep (10^6).

DISCUSSION 8.6: Active Protection of an MgB_2 Magnet

Here, we illustrate a "Detect-and-Activate-the-Heater" protection technique as applied to a 0.5-T/210-mm room-temperature bore magnet, wound with MgB_2 wire (0.84-mm bare diameter) and operated in persistent mode at 10 K. The magnet consists of a main coil (Coil M) and two correction coils (Coils C1 and C2). Key magnet parameters are summarized in Table 8.10. Figure 8.24, a schematic drawing of a 3-coil magnet, defines each solenoid's axial "left end" location, LE(z). For this magnet, Coil M, centered about $z = 0$, $\mathrm{LE_M}(z) = -b$, where b is half of its winding length ($2b$). For Coil C1, with its left end in the $-z$ region, $\mathrm{LE_{C1}}(z)$ is negative, while for Coil C2, with its left end in the $+z$ region, $\mathrm{LE_{C2}}(z)$ is positive.

Figure 8.25 shows a circuit with Coils M, C1, and C2 joined with superconducting splices and shunted with a persistent-current switch (PCS). The circuit contains a total of 4 superconducting splices. Note that in this arrangement, it is more convenient to have each coil contain an odd-number of layers.

Table 8.10: Parameters of a 3-Coil 0.5-T MgB_2 Magnet
— MgB_2 Wire Diameter (Bare): 0.84 mm —

Parameter		M	C1	C2
Operating temperature T_{op}	[K]	10		
Winding i.d./o.d. ($2a_1/2a_2$)	[mm]	260.0/ 268.6	280.0/ 285.3	
Winding length ($2b$)	[mm]	599.6	84.56	
LE(z)*	[mm]	−299.8	−299.8	215.24
Turns/layer; # Layers		624; 5	88; 3	
Total turns		3120	264	
Wire length	[m]	2591	235	
Operating current I_{op}	[A]	80.0		
Overall current density J_e @I_{op}	[A/mm^2]	96.8087	96.2504	
Center field $B_z(0,0)$ @I_{op}	[T]	0.479	0.021	
Center field $B_z(0,0)$@I_{op}	[T]	0.500		
Peak field $\lvert B_{pk}\rvert$ @I_{op}	[T]	0.6	0.5	
Self inductance	[H]	0.925	0.024	
Self inductance	[H]	1.219		
Total stored magnetic energy @I_{op}	[kJ]	3.9		

* Left End axial location. (see Fig. 8.24).

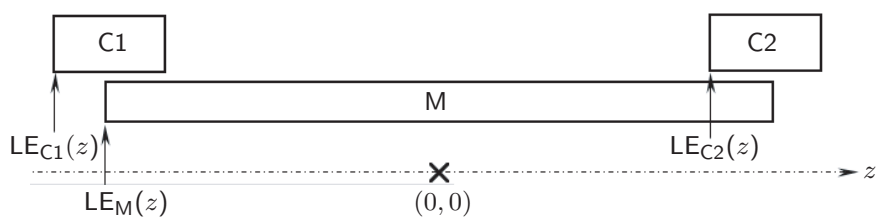

Fig. 8.24 Schematic drawing of a magnet comprised of three solenoids (C1, M, C2), defining each solenoid's "left end" axial location, LE(z). Note that for M, centered about $z = 0$, $\mathrm{LE_M}(z) = -b$, where b is half of its winding length ($2b$).

DISCUSSION 8.6: Active Protection of an MgB_2 Magnet (continuation)

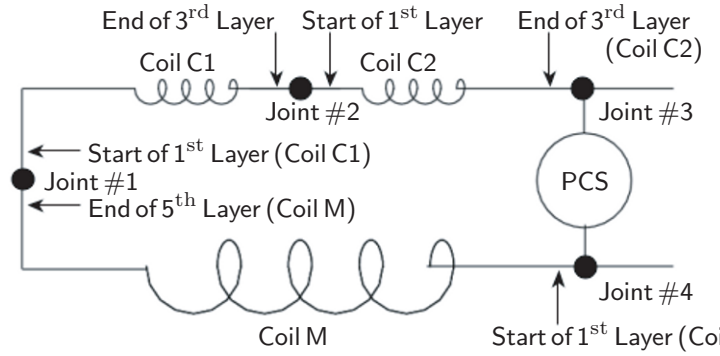

Fig. 8.25 Schematic drawing of a 3-coil arrangement, shunted by PCS for persistent-mode operation. The dots represent 4 superconducting MgB_2/MgB_2 splices.

A. Persistent-Mode Magnets—Passive Protection

A passive protection technique is generally used for persistent-mode superconducting magnets, e.g., MRI and NMR. Unlike the active protection technique, it generally does not rely on devices located outside the cryostat. Of the *persistent mode* NMR and MRI magnets operated to date, all LTS, virtually all of them rely on passive protection, primarily because in LTS windings high NZP velocities spread out the normal zone even if it was initiated at a hot spot, i.e., a very small volume. In a persistent-mode LTS magnet, the magnet is subdivided into many coils, shunted by resistors that facilitate energy transfer among coils as well as energy dissipation. However, the passive protection technique is not applicable to persistent-mode HTS magnets against a quench initiated at a hot spot.

B. Detect-and-Activate-the-Heater for a Persistent-Mode HTS Magnet

The "detect-and-dump" technique (**8.8.3**), used widely in large LTS magnets, protects the magnet by transferring most of the stored energy into a "dump" resistor connected across the magnet terminals. Because there is no switch that can be either superconducting when closed or truly open-circuited when open, the technique has yet to be applied to persistent-mode magnets. However, the "detect-and-activate-the-heater" technique, applied to LTS magnets [8.102–8.110], is applicable for persistent-mode magnets, the circuit of one example of which, applied to to an NMR magnet, is shown in Fig. 8.18.

In the detect-and-activate-the-heater technique (**8.8.4**), the portion forcibly driven normal, with a "protection heater," must be large enough to absorb the entire magnet energy and still remain at a temperature below 300 K. As illustrated below for this 3-coil magnet, it is necessary to drive *only* $\sim$*3%* of the entire winding to satisfy the <300-K requirement. Also as noted earlier, this protection heater may be planted in a "convenient" location in the winding, *irrespective* of the *size* or *location* of a hot spot. The important point here is to force a portion of the winding volume, *regardless of its location within the winding*, to absorb the entire magnetic energy and still remain well below 300 K to minimize stresses caused by differential thermal expansions of the materials within the winding.

DISCUSSION 8.6: Active Protection of an MgB_2 Magnet (continuation)

C. Minimum Winding Portion Required to be Driven Normal

As indicated in Table 8.10, a total of 3.9 kJ is stored by this 3-coil magnet at its operating current of 80 A. If we allow the forcibly-driven-resistive zone to reach a final temperature of 100 K, its enthalpy density (assuming the entire winding is thermally represented by copper) at 100 K is 94.3 J/cm^3. The total winding volume required to absorb 3.9 kJ is 41 cm^3 or a wire (0.84-mm diameter) length of 75 m. Because the entire magnet contains ~3000 m (Table 8.10), only ~3% of the entire winding is sufficient to absorb 3.9 kJ and still keep the maximum temperature to only 100 K, well below 300 K.

D. "Protection Heater"

We discuss key design issues for the "Protection Heater" for this 3-coil magnet: 1) location; 2) power requirement; 3) heater wire & placement; and 4) heater resistance & power supply.

Location As stated above, the location of a protection heater is not restricted: the designer can place it where it is easiest to install under *real* magnet assembly conditions. Most likely locations for this magnet are over the entire or a portion of either the 5th layer of Coil M or the 3rd layers of Coils C1 and C2. For this discussion, let us place the protection heater over Coils C1 and C2. A heater wire will be wound over the 3rd layers of Coils C1 and C2. Each 3rd layer has 88 turns (Table 8.10), containing 78-m long MgB_2 wire. The two 3rd layers thus have a total volume of 86 cm^3. An energy input of 3.9-kJ to the two 3rd layers translates to an energy density of 45 J/cm^3 (or 5 J/g): each 3rd layer will be heated to 75 K.

Power Requirement For this magnet operating at 10 K, the protection heater must heat each 3rd layer to the current-sharing temperature, T_{cs}, which actually varies along the axial direction. For this illustration, we choose $T_{cs} = 30$ K for the entire layer; a total heat input of 150 J is required—a copper enthalpy density at 30 K of 1.74 J/cm^3 with a volume of 86 cm^3. *After* the detection of a quench (see below), this energy will be imparted into the protection heater in ~0.2 s, then, by thermal diffusion, into the MgB_2 layer, driving it resistive in another ~0.1 s: the heated layer will be driven normal no later than ~0.3 s *after the detection* of a quench. The protection heater requires a power of 375 W (= 75 J/0.2 s).

Note that this power requirement may be reduced if the protection heater is placed in a high-field region of the magnet. Then T_{cs} can be 25 K (345 W, for the same hot-spot volume to be created) or even 20 K (130 W). The highest-field region is *beneath* the 1st layer of Coil M, before its 1st layer is wound and then the entire magnet assembly is heat treated.

Heater Wire & Placement To ensure intimate thermal contact between the protection heater and the MgB_2 wire in the 3rd layers of Coils C1 and C2, Cu90-Ni10 wire AWG#20 (0.81-mm diameter bare; ~0.9 mm diameter insulated) may be used, wrapped between turns of the layer, enabling the protection heater wire to form the 4th layer of a close-packed hexagonal arrangement. To improve thermal contact, the protection wire should be wet wound.

DISCUSSION 8.6: Active Protection of an MgB_2 Magnet (continuation)

Heater Resistance & Power Supply Each protection heater has a 10-K resistance of 25 Ω (10-K resistivity: 16.7 μΩ cm). A 10-A/100-V power supply can deliver a total of 800 W into two 25-Ω heaters, each 400 W. Each protection heater has an inductance (mostly due to mutual coupling to Coils M and C1 or C2) of ∼0.03 H: a required inductive voltage of ∼1 V to ramp up the heater current to 4 A in 0.1 s is negligible compared with a resistive voltage of 100 V. With a current density of ∼8 A/mm^2, the heater will not be overheated even if activated for >10 s.

E. Quench Detection: Heating Process & Required Detection Time

In the detect-and-activate-the-heater protection, the first critical step is the detection of the quench. We assume that a hot spot is adiabatically heated. We further assume that the matrix current remains constant at I_{op} (see below) or its density, $J_m(t) = J_{m_\circ} = I_{op}/A_m$. From Eq. 8.9*c* we may compute τ_{ah}, the time for the hot spot to be adiabatically heated from T_i to T_f:

$$\int_{T_i}^{T_f} \frac{C_m(T)}{\rho_m(T)}\, dT = \left(\frac{A_m}{A_{cd}}\right) J_{m_\circ}^2\, \tau_{ah} \tag{8.9c}$$

With $\rho_m = 0.017\,\mu\Omega\,\text{cm}$ (copper, $T_i = 10$ K), $A_m/A_{cd} = 0.19$, and $J_{m_\circ} = 762$ A/mm^2 (at $I_{op} = 80$ A), we compute $\tau_{ah} \simeq 1.5$ s for $T_f = 300$ K, the absolute limit. A quench must be detected in ∼0.5 s or less.

F. Hot Spot Size

The hot spot size may be estimated from the size of MPZ, R_{mz}, given by Eq. 6.33:

$$R_{mz} = \sqrt{\frac{3k_{wd}(T_c - T_{op})}{\rho_m J_m^2}} \tag{6.33}$$

In Eq. 6.33, R_{mz} is the radius of a *spherical* MPZ, in which its thermal conductivity, k_{wd}, is equal in the three orthogonal directions; $T_c = T_{cs}$, where T_{cs} is the current-sharing temperature, and $J_m = J_{m_\circ}$. For our application here, we assume $k_{wd} = k_m = 10$ W/cm K (copper, 10 K) and the thermal conduction is only along the wire axis—the MPZ is needle-shaped. With $T_{cs} \approx 30$ K for this MgB_2 wire at 80 A, $\rho_m = 0.017\,\mu\Omega\,\text{cm}$, and $J_{m_\circ} = 762$ A/mm^2, we obtain: $R_{mz} \simeq 2.5$ cm, i.e., the hot spot is 5-cm long along the wire. That is, any hot spot shorter than ∼5 cm will shrink, by conduction cooling along the wire axis, and return to superconducting. In the following analysis, let us assume that the hot spot remains 5-cm long as it is heated adiabatically during the next 1 s or so. (In reality, because NZP velocities of MgB_2 are comparable with those of LTS, as seen in Table 8.5, the actual length of an MgB_2 resistive zone can potentially be much greater than R_{mz}: the protection heater can thus be *considerably shorter* than that computed above.)

G. Growth of Hot-Spot Resistance and Resistive Voltage with Time

Until the protection heater is activated, at $t = 0.5$ s, we may assume the magnet current to remain at 80 A. Equation 8.9*c* may be used to compute $T(t)$, with τ_{ah} replaced by t. Table 8.11 gives time-dependent parameters of the hot-spot for the first 1.3 s, when its temperature reaches 265 K.

DISCUSSION 8.6: Active Protection of an MgB_2 Magnet (continuation)

Table 8.11: *Approximate* Parameter Values at Hot Spot During Quench

t [s]	T [K]	ρ_m [$\mu\Omega$ cm]	R_m [$\mu\Omega$]	V_r [mV]	dI_{op}/dt [mA/s]
0	30	0.017	81	6.5	−5.3
0.5	60	0.11	523	42	−34
1.0	150	0.72	3423	274	−225
1.3	265	1.55	7385	591	−485

H. Quench Detection Techniques

Voltage signals that may be used to activate the protection heater include: 1) voltages across Coils M, C1, and C2; 2) voltage across the persistent current switch (PCS), which is slightly inductive; and 3) voltage from a Rogowski coil, placed within the magnet chamber, that measures the magnet current (**PROBLEM 2.9**).

The voltages across Coil M, $V_M(t)$, Coil C1, $V_{C1}(t)$, and Coil C2, $V_{C2}(t)$, are:

$$V_M(t) = V_r(t) + (L_M + M_{MC1} + M_{MC2})\frac{dI_{op}(t)}{dt} \tag{8.83a}$$

$$V_{C1}(t) = (L_{C1} + M_{C1M} + M_{C1C2})\frac{dI_{op}}{dt} = V_{C2}(t) = -\tfrac{1}{2}V_M(t) \tag{8.83b}$$

where M_{MC1} and M_{MC2} are the mutual inductances between Coil M and, respectively, Coils C1 and C2, each 0.061 H; and $L_M = 0.925$ H (Table 8.10). Similarly, $L_{C1} = 0.024$ H (Table 8.10), $M_{C1M} = 0.061$ H, and $M_{C1C2} = 0.004$ H. Note that as long as the PCS remains superconducting:

$$V_M(t) + V_{C1}(t) + V_{C2}(t) = 0 \tag{8.83c}$$

At $t = 1.0$ s, for example, we have $V_r(t) = 274$ mV (Table 8.11). Inserting appropriate values into Eqs. 8.83*a* and 8.83*b*, we obtain: $V_M = 38.6$ mV and $V_{C1} = -20.0$ mV ($V_{C1} \simeq -\frac{1}{2}V_M$), each large enough to be used to trigger the protection heater.

Note that if more voltage taps are placed on Coil M, each across its smaller winding section, then one of these voltages may likely be dominated by $V_r(t)$, because for the same $V_r(t)$, e.g., 274 mV at $t = 1$ s, the negative inductive voltages over a smaller winding section would be smaller. Such a voltage at $t = 1$ s would be closer to 274 mV rather than 38.4 mV, as computed above across the entire Coil M.

One application of persistent-mode operation widely applied is MRI magnets, to date exclusively LTS-based but possibly HTS-based in the future. If the coil voltages are to trigger the protection heater, these voltages might include *very* large erroneous signals when the pulse gradient coil in such an MRI magnet is excited during MRI measurements. Although, averaged over one end to the other end of the gradient coil, its axial field is zero, still, "unbalanced" voltage signals may be large enough to be mistaken for a genuine quench voltage.

In this respect, it may be possible to make the voltages across the slightly inductive PCS and the Rogowski coil less susceptible to the gradient coil excitation. This can be accomplished by having each placed within the magnet enclosure where magnetic coupling with the gradient coil is minimal.

PROBLEM 8.6: Passive protection of an NMR magnet*

Using experimental results recorded for the NbTi coils of a 750-MHz (17.6 T) superconducting magnet developed at FBML as examples [8.101], we study details of voltage and current signals developed within a multi-coil insert of a persistent-mode NMR magnet. The full magnet system has 12 nested solenoidal coils, of which the 7 innermost coils are wound with Nb_3Sn conductors and the 5 outermost coils are wound with NbTi conductors. Each coil is impregnated with epoxy resin and incorporates the "floating-winding" technique [7.31, 7.32]. Figure 8.26 indicates the locations of the 12 coils.

As may be inferred from Fig. 8.26, Coils 10, 11, and 12 are so-called "correction" coils, whose primary function is to improve the field homogeneity at the magnet center; they form a variant of the notched solenoid studied in **PROBLEM 3.7**. Coil 9, wound on one coil form, has two sections, each shunted, and Coils 11 and 12 share one shunt resistor, as shown in Fig. 8.27.

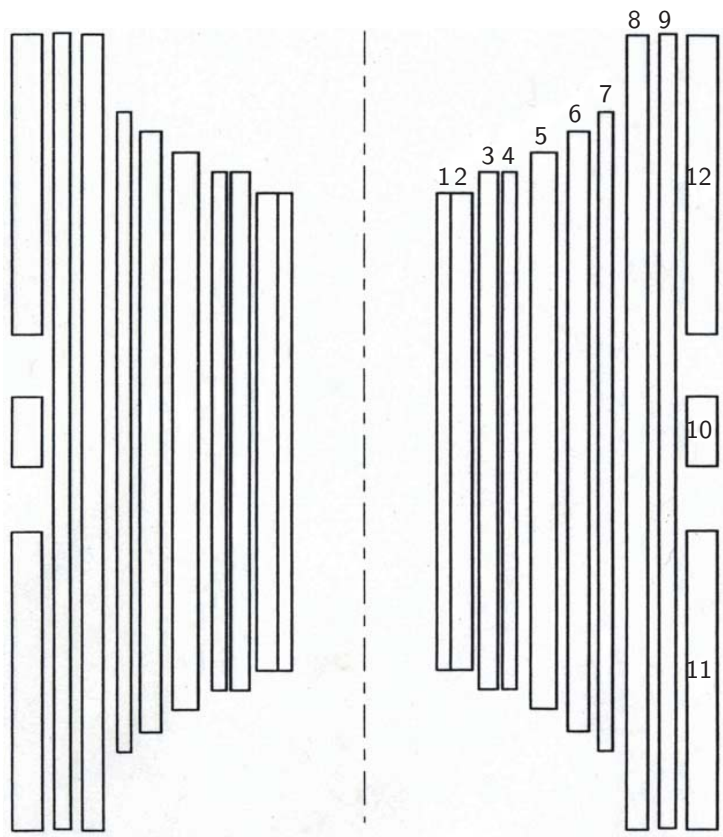

Fig. 8.26 Drawing showing the locations of 12 coils in a 750-MHz (17.6 T) magnet [8.101]. The horizontal scale in this sketch is 4.5 times the axial scale.

* Based on **Problem 8.11** in the 1st Edition (Plenum, 1994).

PROBLEM 8.6: Passive protection of an NMR magnet (continuation)

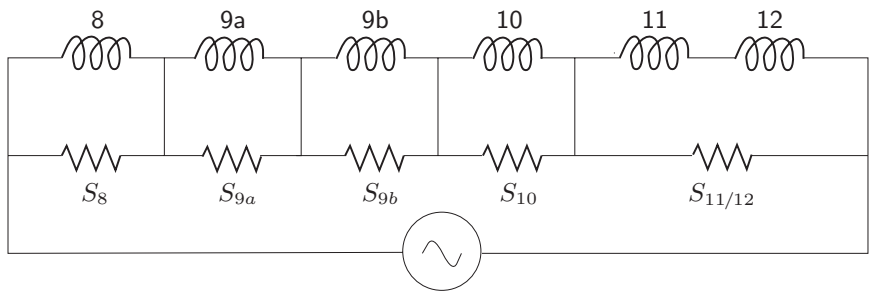

Fig. 8.27 Circuit for the NbTi coils.

Figure 8.27 includes neither a persistent switch nor diodes shunting the entire system because discussion here chiefly concerns premature quenching that occurs during system charge up when both the switch and the diodes are "open." Because of the presence of the power supply, the entire system is "shorted," as is the case when the system is in persistent mode.

The values of the inductance matrix and shunt resistors are given, respectively, in Tables 8.12 and 8.13. As is evident from Table 8.12, although ideally identical, Coils 11 and 12 actually have slightly different values of inductance.

Our rule of thumb in determining values of shunt resistors in such a multi-coil system is to first choose a total value of shunt resistance from voltage considerations. In this particular example, a value of $\sim 1.5\,\Omega$ was selected because at an operating current of 310 A, it would translate to a voltage level of ~ 500 V—a safe level. Each shunt resistor is then selected to be roughly proportional to each coil's total stored energy.

Table 8.12: Inductance Matrix [H] for the NbTi Coils

Coil	8	9a	9b	10	11	12
8	4.413	2.268	2.243	0.715	2.747	2.755
9a	2.268	1.344	1.343	0.427	1.645	1.649
9b	2.243	1.343	1.404	0.450	1.737	1.742
10	0.715	0.427	0.450	0.606	0.378	0.379
11	2.747	1.645	1.737	0.378	5.382	0.368
12	2.755	1.649	1.742	0.379	0.368	5.410

Table 8.13: Shunt Resistors [mΩ] for the NbTi Coils

S_8	S_{9a}	S_{9b}	S_{10}	$S_{11/12}$
288	156	165	58	868

PROBLEM 8.6: Passive protection of an NMR magnet (continuation)

Figure 8.28 shows a set of voltage traces recorded when the magnet quenched prematurely at 227 A. As evident from the traces, the quench started in Coil 9a; signals from AE sensors (not shown here) indicated the premature quench was caused by a mechanical event occurring in the magnet system. Because a resistive voltage first appeared in Coil 9a, it is most likely that the mechanical event took place in Coil 9a. Note that between $t = 1.6\,\text{s}$ and $t = 2.25\,\text{s}$, $V_{11/12}$, the sum of recorded voltages from Coils 11 and 12, is saturated.

Figure 8.29 shows a set of *computed* current traces through the coils based on the voltage traces shown in Fig. 8.28; Table 8.14 shows a set of dI/dt values at selected times for the current traces shown in Fig. 8.29.

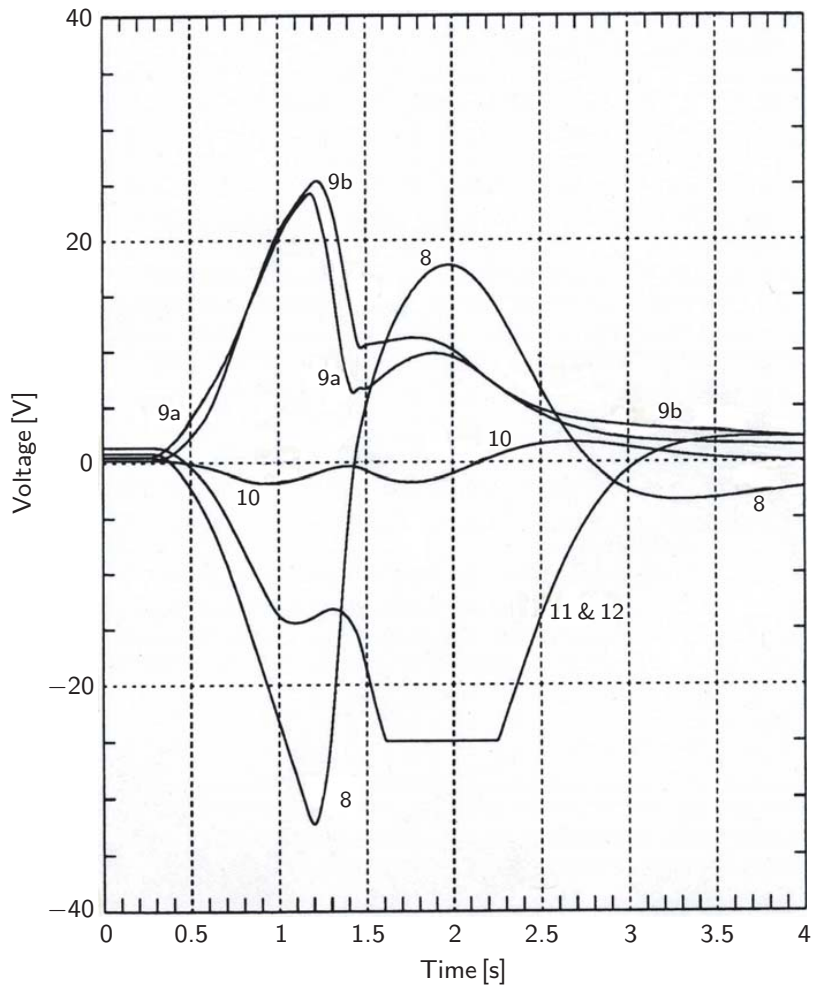

Fig. 8.28 Voltage traces recorded across Coils 8, 9a, 9b, 10, and 11/12 following a quench at 227 A [8.80].

PROBLEM 8.6: Passive protection of an NMR magnet (continuation)

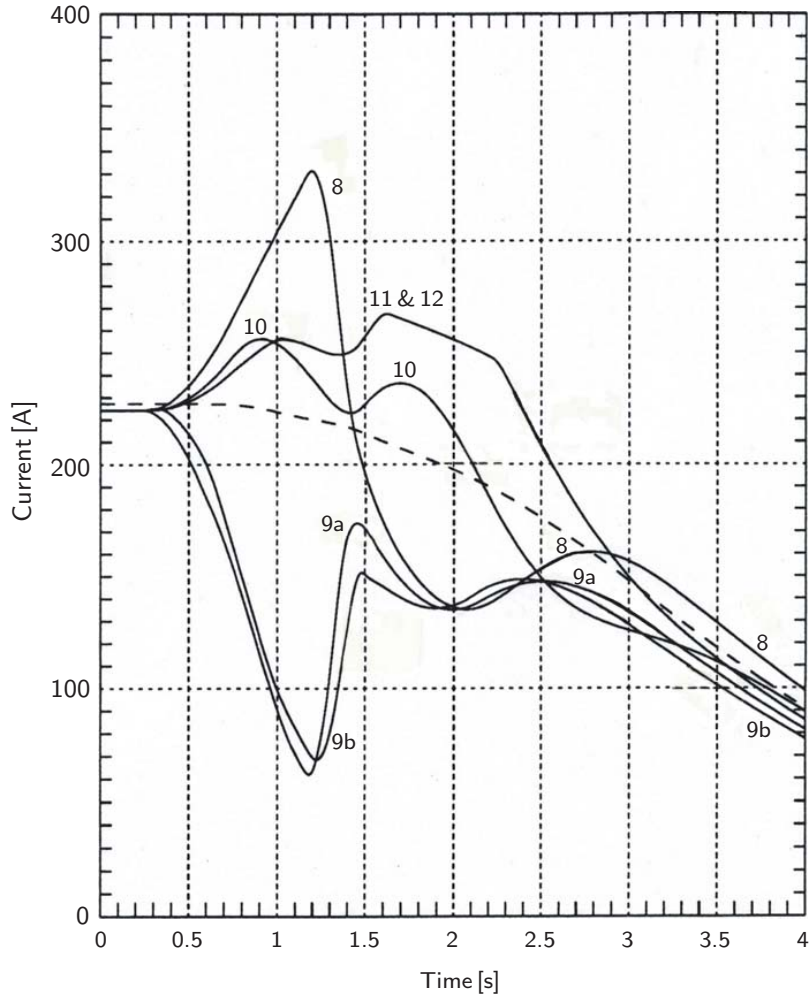

Fig. 8.29 Current traces through Coils 8, 9a, 9b, 10, and 11/12 corresponding to the voltage traces of Fig. 8.28. The dotted curve is the supply current, I_0.

Table 8.14: Values of dI/dt at Selected Times

	dI/dt [A/s]			
	$t = 0.5\,\text{s}$	$t = 1.0\,\text{s}$	$t = 1.5\,\text{s}$	$t = 4.0\,\text{s}$
Coil 8	84.5	147.2	−252.8	−56.1
Coil 9*a*	−154.1	−234.7	−62.1	−48.9
Coil 9*b*	−107.1	−198.1	−57.8	−42.8
Coil 10	41.3	−44.8	81.5	−47.4
Coils 11/12	33.6	19.3	113.1	−48.9

PROBLEM 8.6: Passive protection of an NMR magnet (continuation)

a) Show that the current in each coil may be determined from the coil's V trace according to the following equations:

$$I_8 = I_0 - \frac{V_8}{S_8} \tag{8.84a}$$

$$I_{9a} = I_0 - \frac{V_{9a}}{S_{9a}} \tag{8.84b}$$

$$I_{9b} = I_0 - \frac{V_{9b}}{S_{9b}} \tag{8.84c}$$

$$I_{10} = I_0 - \frac{V_{10}}{S_{10}} \tag{8.84d}$$

$$I_{11/12} = I_0 - \frac{V_{11/12}}{S_{11/12}} \tag{8.84e}$$

where I_0 is the power supply current.

b) Almost immediately after Coil 9a is driven normal, which is evident from its rising voltage trace (Fig. 8.28), Coil 9b follows, inducing excess currents in the rest of the coils (Fig. 8.29). Coil 10 is the next to go normal, followed by Coil 8, whose current starts decreasing at $t = 1.2$ s. Compute the sum of *inductive* voltages appearing across Coil 8 at $t = 0.5$ s and show that Coil 8 is still completely superconducting at that time.

c) Show that, although its voltage is still decreasing, Coil 8 already has a normal zone at $t = 1.0$ s, and estimate its resistance. Also discuss how we might determine the precise moment at which the normal zone appears in Coil 8.

d) Compute an *approximate* value of the net Joule heating [W] generated by the entire magnet (Coils 8–12) at $t = 4.0$ s. Pay attention to the word approximate.

e) At $t \sim 1$ s, when Coil 8 already has been driven normal, its peak field is ~ 6 T and the conductor's critical current (at 4.2 K) is ~ 900 A, well above the observed quench current of ~ 270 A (an average of Coil 8 currents at $t = 0.5$ s and $t = 1.0$ s, from Fig. 8.29). Offer plausible sources of the seemingly improbable quench initiated in Coil 8 at this low current.

f) Explain why Coils 11 and 12 are not shunted separately.

g) Make a general comment about the risk of not shunting the two coils (11 and 12) separately.

"For a successful technology, reality must take precedence over public relations, for nature cannot be fooled." —Richard P. Feynman

Solution to PROBLEM 8.6

a) From Fig. 8.27, it is clear that $I_8 = I_0 - I_{r8}$, where I_{r8} is the current flowing in shunt resistor 8: $I_{r8} = V_8/S_8$. Thus:

$$\begin{aligned} I_8 &= I_0 - I_{r8} \\ &= I_0 - \frac{V_8}{S_8} \end{aligned} \tag{8.84a}$$

Similarly, we have:

$$\begin{aligned} I_{9a} &= I_8 + I_{r8} - I_{r9a} = I_0 - \frac{V_8}{S_8} + \frac{V_8}{S_8} - \frac{V_{9a}}{S_{9a}} \\ &= I_0 - \frac{V_{9a}}{S_{9a}} \end{aligned} \tag{8.84b}$$

$$\begin{aligned} I_{9b} &= I_{9a} + \frac{V_{9a}}{S_{9a}} - \frac{V_{9b}}{S_{9b}} = I_0 - \frac{V_{9a}}{S_{9a}} + \frac{V_{9a}}{S_{9a}} - \frac{V_{9b}}{S_{9b}} \\ &= I_0 - \frac{V_{9b}}{S_{9b}} \end{aligned} \tag{8.84c}$$

$$\begin{aligned} I_{10} &= I_{9b} + \frac{V_{9b}}{S_{9b}} - \frac{V_{10}}{S_{10}} = I_0 - \frac{V_{9b}}{S_{9b}} + \frac{V_{9b}}{S_{9b}} - \frac{V_{10}}{S_{10}} \\ &= I_0 - \frac{V_{10}}{S_{10}} \end{aligned} \tag{8.84d}$$

$$\begin{aligned} I_{11/12} &= I_{10} + \frac{V_{10}}{S_{10}} - \frac{V_{11/12}}{S_{11/12}} = I_0 - \frac{V_{10}}{S_{10}} + \frac{V_{10}}{S_{10}} - \frac{V_{11/12}}{S_{11/12}} \\ &= I_0 - \frac{V_{11/12}}{S_{11/12}} \end{aligned} \tag{8.84e}$$

b) Voltage across Coil 8, V_8, is given by:

$$\begin{aligned} V_8 = V_r|_8 &+ L_8 \frac{dI_8}{dt} + M_{8,9a} \frac{dI_{9a}}{dt} + M_{8,9b} \frac{dI_{9b}}{dt} \\ &+ M_{8,10} \frac{dI_{10}}{dt} + M_{8,11} \frac{dI_{11}}{dt} + M_{8,12} \frac{dI_{12}}{dt} \end{aligned} \tag{S6.1}$$

where $V_r|_8$ is the resistive voltage across Coil 8 due to the presence of a normal zone. Inserting appropriate values at $t = 0.5$ s, taken from Tables 8.12 and 8.14, into the right-hand side of Eq. $S6.1$, we obtain:

$$\begin{aligned} V_8 \simeq V_r|_8 &+ (4.413\,\mathrm{H})(84.5\,\mathrm{A/s}) + (2.268\,\mathrm{H})(-154.1\,\mathrm{A/s}) \\ &+ (2.243\,\mathrm{H})(-107.1\,\mathrm{A/s}) + (0.715\,\mathrm{H})(41.3\,\mathrm{A/s}) \\ &+ (2.747\,\mathrm{H})(33.6\,\mathrm{A/s}) + (2.755\,\mathrm{H})(33.6\,\mathrm{A/s}) \end{aligned} \tag{S6.2a}$$

$$\begin{aligned} V_8 &= V_r|_8 + 372.9 - 349.5 - 240.2 + 29.4 + 92.4 + 92.6 \\ &= V_r|_8 - 2.5\,\mathrm{V} \end{aligned} \tag{S6.2b}$$

Solution to PROBLEM 8.6 (continuation)

From Fig. 8.28, we find $V_8 \simeq -2.3$ V at $t = 0.5$ s, which is nearly equal to the net inductive voltage given by Eq. $S6.2b$, making $V_r|_8 \simeq 0$ V at $t = 0.5$ s. Coil 8 thus is still superconducting at $t = 0.5$ s.

c) Again, inserting appropriate values into Eq. $S6.1$, we obtain V_8 at $t = 1.0$ s:

$$\begin{aligned} V_8 &= V_r|_8 + (4.413\,\mathrm{H})(147.2\,\mathrm{A/s}) + (2.268\,\mathrm{H})(-234.7\,\mathrm{A/s}) \\ &\quad + (2.243\,\mathrm{H})(-198.1\,\mathrm{A/s}) + (0.715\,\mathrm{H})(-44.8\,\mathrm{A/s}) \\ &\quad + (2.747\,\mathrm{H})(19.3\,\mathrm{A/s}) + (2.755\,\mathrm{H})(19.3\,\mathrm{A/s}) \qquad (S6.3a) \\ V_8 &= V_r|_8 + (649.6 - 532.3 - 444.3 - 32.0 + 53.0 + 53.2)\,[\mathrm{V}] \\ &= V_r|_8 - 252.9\,[\mathrm{V}] \qquad (S6.3b) \end{aligned}$$

According to the voltage trace of Fig. 8.28, $V_8 = -23$ V at $t = 1.0$ s, thus from Eq. $S6.3b$, we have $V_r|_8 \simeq 230$ V. From Fig. 8.29, we find $I_8 \simeq 306$ A, and thus $R_8 = 230\,\mathrm{V}/306\,\mathrm{A} = 0.75\,\Omega$.

We can determine the precise moment when a normal zone appears in Coil 8 by finding the time at which $V_r|_8$ just begins to become nonzero.

d) The Joule heating generated by the entire magnet, P_{mg}, is given by:

$$P_{mg} = \sum_{n=8}^{12} V_r|_n \times I_n \qquad (S6.4)$$

It is thus necessary to compute V_r for each coil as in **b)** or **c)**. However, at $t = 4.0$ s, we note that each coil has nearly the same values of: 1) voltage, $\tilde{V} \sim 0$ V (Fig. 8.28); 2) current, $\tilde{I} \sim 90$ A (Fig. 8.29); and 3) time rate of change of current, $d\tilde{I}/dt \sim -50$ A/s (Table 8.14). Thus, for this particular time Eq. $S6.4$ may be *approximated* by:

$$P_{mg} \simeq \left(\tilde{V} - \sum_{m,n=8}^{12} L_{m,n} \frac{d\tilde{I}}{dt} \right) \times \tilde{I} \qquad (S6.5)$$

Note that the term within the parentheses in Eq. $S6.5$ is equal to the approximate resistive voltage across the entire magnet. From Table 8.12, we obtain the sum of the inductances to be 60.25 H. With $d\tilde{I}/dt \simeq -50$ A/s and $\tilde{I} \simeq 90$ A, we have:

$$P_{mg} \simeq [0 - (60.25\,\mathrm{H})(-50\,\mathrm{A/s})](90\,\mathrm{A}) \simeq 270,000\,\mathrm{W} \qquad (S6.6)$$

Because $\tilde{V} \sim 0$, the inductive and resistive voltages are nearly balanced, and at this time the total resistive voltage has an amplitude of $\sim$3000 V ($\sim$270,000 W/90 A)—this is an example of an internal voltage generated within a quenching magnet, discussed in **8.3.3**. From this voltage, we estimate that the total magnet resistance has grown to $\sim 33\,\Omega$ ($\sim$3000 V/90 A).

e) According to our criterion, and incorporated in quench codes developed over the past ∼10 years at FBNML and successfully applied [8.45, 8.47, 8.55, 8.85], an induced quench in a target coil occurs when the target coil's transport current [in this case $I_8(t)$] reaches the critical current corresponding to temperature T_{op} (4.2 K) and maximum field within the coil. Based on this criterion, the observed premature quench should never have taken place at 270 A; it is much lower than 900 A, the estimated critical current of Coil 8's conductor at the time of the quench. Apparently, the criterion works well for premature quenches in the source coil occurring at relatively high currents, near designed operating currents, so that they are closer to the critical currents (at T_{op}) of the target coils.

It should be noted that the condition of constant conductor temperature at T_{op} is not valid, particularly in adiabatic windings subjected to time-varying magnetic field and current [8.79]. AC losses raise the local conductor temperature, reducing critical current in the target coil. Thus it is indeed possible to have a target coil quenching at a current close to the observed value of ∼270 A.

That coupling loss is an additional heating source in a quenching adiabatic winding is quite significant. Because filament twist pitch length (ℓ_p) is a key parameter in controlling coupling loss, it implies that ℓ_p is another critical design parameter relating to protection of these high-performance magnets; within a reasonable extent, ℓ_p should be specified to be intentionally long for protection purposes.

f) Both Coils 11 and 12 are situated off the magnet midplane. There is thus a net axial force acting on Coil 11 (located below the midplane) towards the midplane ($+z$-directed) and a net axial force acting on Coil 12 (located above the midplane) towards the midplane ($-z$-directed). As long as the currents through Coil 11 and Coil 12 are identical, there will be no net unbalancing axial force acting on the system. This force-balance condition can be preserved only if the two coils are connected in series with a common shunt resistor across them.

If each coil is shunted independently, the current induced in each coil will be different, potentially creating a massive net unbalanced force on the system. At $t = 1$ s, suppose, instead of both coils carrying a current of 250 A as is the case according to Fig. 8.29, Coil 11 carried 275 A and Coil 12 carried 225 A. Under this condition, the force pushing Coil 11 upward would be 581 kN and the force pushing Coil 12 down would be 525 kN, with a resulting net unbalanced upward axial force of 56 kN, or almost 6 tons!

g) Although not evident from these sets of voltage and current traces, particularly as the voltage trace for Coil 11/12 is saturated between $t = 1.3$ s and $t = 2$ s, the most critical danger in connecting Coils 11 and 12 in series and having a common shunt resistor is that in case of a quench in either Coil 11 or Coil 12, very high inductive voltages can be generated within the combined coil.

DISCUSSION 8.7: To Protect or Not to Protect an HTS Magnet

Whether to protect or not to protect an HTS magnet against *quench-induced damage* is a dilemma, because, under *normal operating conditions* an HTS magnet is unlikely to quench. One decision-making guide is economics: let us assign the costs of an *unprotected* HTS magnet, a quench detection/protection system, and replacing the damaged magnet with another unprotected magnet, respectively, as $\$_M$, $\$_{qp}$, and $\$_{rp}$. $\$_{rp}$ includes not only $\$_M$ but also, $\$_{ra}$, the costs associated with magnet replacement activities. Let us assign P_{dm} as the probability of having to replace the *quench-damaged* original unprotected magnet. Then the total costs of an HTS magnet armed with a quench detection/protection, $\$_{T/w}$, and of an unprotected HTS magnet but with $\$_{rp}$ to be added later, $\$_{T/wo}$, are given by:

$$\$_{T/w} = \$_M + \$_{qp} \tag{8.85a}$$

$$\$_{T/wo} = \$_M + P_{dm}(\$_M + \$_{ra}) \tag{8.85b}$$

In Eq. 8.85*a* it is assumed that a protected HTS magnet will never have to be replaced because of quench-induced damages. Thus to protect or not protect an HTS magnet depends on $\$_M$, $\$_{qp}$, $\$_{ra}$, and P_{dm}. If $\$_{qp}$ is large and P_{dm} is small enough such that $\$_{qp} > P_{dm}(\$_M + \$_{ra})$, then $\$_{T/w} > \$_{T/wo}$. Under this condition, economics dictates *not* to protect an HTS magnet against quench incidents.

REFERENCES

[8.1] P.F. Smith, "Protection of superconducting coils," *Rev. Sci. Instr.* **34**, 368 (1963).

[8.2] Z.J.J. Stekly, "Theoretical and experimental study of an unprotected superconducting coil going normal," *Adv. Cryogenic Eng.* **8**, 585 (1963).

[8.3] B.J. Maddock and G.B. James, "Protection and stabilization of large superconducting coils," *Rev. Sci. Instrum.* **34**, 368 (1963).

[8.4] D.L. Atherton, "Theoretical treatment of internal shunt protection for superconducting magnets," *J. Phys. E: Sci. Instr.* **4**, 653 (1971)

[8.5] M.A. Green, "Quench protection and design of large high current density superconducting magnets," *IEEE Trans. Magn.* **MAG-17**, 1793 (1981).

[8.6] D. Ciazynski, "Protection of high current density superconducting magnets," *IEEE Trans. Magn.* **MAG-19**, 700 (1983).

[8.7] M.A. Hilal and Y.M. Eyssa, "Self protection of high current density superconducting magnets," *IEEE Trans. Magn.* **25**, 1604 (1989).

[8.8] Lembit Salasoo, "Superconducting magnet quench protection analysis and design," *IEEE Trans. Magn.* **27**, 1908 (1991).

[8.9] Alexei V. Dudarev, Victor E. Keilin, Yurii D. Kuroedov, Alexei A. Konjukhov and Vytaly S. Vysotsky, "Quench protection of very large superconducting magnets," *IEEE Trans. Appl. Superconduc.* **5**, 226 (1995).

[8.10] L. Bottura, "Stability and protection of CICCs: an updated designer's view," *Cryogenics* **38**, 491 (1998).

[8.11] Joel H. Schultz, "Protection of superconducting magnets," *IEEE Trans. Appl. Superconduc.* **12**, 1390 (2002).

[8.12] J.W. Lue, R. C. Duckworth, M.J. Gouge, "Short-circuit over-current limitation of HTS tapes," *IEEE Trans. Appl. Superconduc.* **15** (2005).

[8.13] M. Okaji, K. Nara, H. Kato, K. Michishita, and Y. Kubo, "The thermal expansion of some advanced ceramics applicable as specimen holders of high T_c superconductors," *Cryogenics* **34**, 163 (1994).

[8.14] Cees Thieme and Garry Ferguson of American Superconductor Corp., (personal communication, 2004).

[8.15] J.P. Voccio, O.O. Ige, S.J. Young and C.C. Duchaine, "The effect of longitudinal compressive strain on critical current in HTS tapes," *IEEE Trans. Appl. Superconduc.* **11**, 3070 (2001).

[8.16] NIST website: www.ceramics.nist.gov/srd/summary/htsy123.htm.

[8.17] Volker Pasler, Günter Bönisch, Rainer Meyder, and Gernot Schmitz, "Deployment of MAGS, a comprehensive tool for magnet design and safety analysis, for quench and arc simulation of an ITER-FEAT coil," *IEEE Trans. Appl. Superconduc.* **12**, 1574 (2002).

[8.18] N.G. Anishchenko, R. Heller, Yu.A. Shishov, G.P. Tsvineva, and V.Ya.Vokov, "High voltage heavy current leads for liquid helium cryostats," *Cryogenics* **22**, 609 (1982).

[8.19] J. Gerhold, "Design criteria for high voltage leads for superconducting power systems," *Cryogenics* **24**, 73 (1984).

[8.20] B. Fallou, J. Galand, and B. Bouvier, "Dielectric breakdown of gaseous helium at very low temperatures," *Cryogenics* **10**, 142 (1970).

[8.21] J. Thoris, B. Leon, A. Dubois, and J.C. Bobo, "Dielectric breakdown of cold gaseous helium," *Cryogenics* **19**, 147 (1970).

[8.22] J. Gerhold, "Dielectric breakdown of cryogenic gases and liquids," *Cryogenics* **19**, 571 (1979).

[8.23] M.S. Naidu and V. Kamaraju, *High Voltage Engineering* 2nd Ed., (McGraw Hill, New York, 1995).

[8.24] T. Tominaka, N. Hara, and K. Kuroda, "Estimation of maximum voltage of superconducting magnet systems during a quench," *Cryogenics* **31**, 566 (1991).

[8.25] W.H. Cherry and J.I. Gittleman, "Thermal and electrodynamic aspects of the superconductive transition process," *Solid State Electronics* **1**, 287 (1960).

[8.26] C.N. Whetstone and C. Roos, "Thermal transitions in superconducting NbZr alloys," *J. Appl. Phys.* **36**, 783 (1965).

[8.27] V.V. Altov, M.G. Kremlev, V.V. Sytchev and V.B. Zenkevitch, "Calculation of propagation velocity of normal and superconducting regions in composite conductors," *Cryogenics* **13**, 420 (1973).

[8.28] D. Hagendorn and P. Dullenkopf, "The propagation of the resistive region in high current density coils," *Cryogenics* **14**, 264 (1974).

[8.29] L. Dresner, "Propagation of normal zones in composite superconductors," *Cryogenics* **16**, 675 (1976).

[8.30] K. Ishibashi, M. Wake, M. Kobayashi and A. Katase, "Propagation velocity of normal zones in a sc braid," *Cryogenics* **19**, 467 (1979).

[8.31] Osami Tsukamoto, "Propagation velocities of normal zones in a forced-flow cooled superconductor," *IEEE Trans. Magn.* **MAG-15**, 1158 (1979).

[8.32] B. Turck, "About the propagation velocity in superconducting composites," *Cryogenics* **20**, 146 (1980).

[8.33] A.Vll. Gurevich, R.G. Mints, "On the theory of normal zone propagation in superconductors," *IEEE Trans. Magn.* **MAG-17**, 220 (1981).

[8.34] P.H. Eberhard, G.H. Gibson, M.A. Green, E. Grossman, R.R. Ross, and J.D. Taylor, "The measurement and theoretical calculation of quench velocities within large fully epoxy impregnated superconducting coils," *IEEE Trans. Magn.* **MAG-17**, 1803 (1981).

[8.35] M. Kuchnir, J.A. Carson, R.W. Hanft, P.O. Mazur, A.D. McInturff and J.B. Strait, "Transverse quench propagation measurement," *IEEE Trans. Magn.* **MAG-23**, 503 (1987).

[8.36] H.H.J. ten Kate, H. Boschamn, L.J.M. van de Klundert, "Longitudinal propagation velocity of the normal zone in superconducting wires," *IEEE Trans. Magn.* **MAG-23**, 1557 (1987).

[8.37] K. Funaki, K. Ikeda, M. Takeo, K. Yamafuji, J. Chikaba and F. Irie, "Normal-zone propagation inside a layer and between layers in a superconducting coil," *IEEE Trans. Magn.* **MAG-23**, 1561 (1987).

[8.38] D.A. Gross, "Quench propagation analysis in large solenoidal magnets," *IEEE Trans. Magn.* **24**, 1190 (1988).

[8.39] A. Ishiyama and Y. Iwasa, "Quench propagation velocities in an epoxy-impregnated Nb_3Sn superconducting winding model," *IEEE Trans. Magn.* **24**, 1194 (1988).

[8.40] Y.Z. Lei, S. Han, "Quenching dynamic process and protection by shunt resistors of solenoid superconducting magnets with graded current density," *IEEE Trans. Magn.* **24**, 1197 (1988).

[8.41] Yan Luguang, Li Yiping and Liu Decheng, "Experimental investigation on normal zone propagation in a close-packed superconducting solenoid," *IEEE Trans. Magn.* **24**, 1201 (1988).

[8.42] D. Ciazynski, C. Curé, J.L. Duchateau, J. Parain, P. Riband, B. Turck, "Quench and safety tests on a toroidal field coil of Tore Supra," *IEEE Trans. Magn.* **24**, 1567 (1988).

[8.43] A.A. Konjukhov, V.A. Malginow, V.V. Matokhin, V.R. Karasik, "Quenching of multisection superconducting magnets with internal and external shunt resistors," *IEEE Trans. Magn.* **25**, 1538 (1989).

[8.44] Arnaud Devred, "General formulas for the adiabatic propagation velocity of the normal zone," *IEEE Trans. Magn.* **25**, 1698 (1989).

[8.45] C.H. Joshi and Y. Iwasa, "Prediction of current decay and terminal voltages in adiabatic superconducting magnets," *Cryogenics* **29**, 157 (1989).

[8.46] Yu.M. Lvovsky, "Thermal propagation of normal zone with increasing temperature level in helium-cooled and high temperature superconductors," *Cryogenics* **30**, 754 (1990).

[8.47] Z.P. Zhao and Y. Iwasa, "Normal-zone propagation in adiabatic superconducting magnets: I. Normal-zone propagation velocity in superconducting composites," *Cryogenics* **31**, 817 (1991).

[8.48] G. Lopez and G. Snitchler, "Quench propagation in the SSC dipole magnets" *IEEE Trans. Magn.* **27**, 1973 (1991).

[8.49] A. Ishiyama, Y. Sato, and M. Tsuda, "Normal-zone propagation velocity in superconducting wires having a CuNi matrix," *IEEE Trans. Magn.* **27**, 2076 (1991).

[8.50] M. Iwakuma, K. Funaki, M. Takeo and K. Yamafuji, "Quench protection of superconducting transformers," *IEEE Trans. Magn.* **27**, 2080 (1991).

[8.51] S. Fujimura and M. Morita, "Quench simulation of 4.7 tesla superconducting magnet for magnetic resonance spectroscopy," *IEEE Trans. Magn.* **27**, 2084 (1991).

[8.52] C. Haddock, R. Jayakumar, F. Meyer, G. Tool, J. Kuzminski, J. DiMarco, M. Lamm, T. Jeffery, D. Orris, P. Mazur, R. Bossert, J. Strait, "SSC dipole quench protection heater test results," *1991 Particle Accelerator Conf.*, 2215 (1991).

[8.53] E. Acerbi, G. Baccaglioni, M. Canali and L. Rossi, "Experimental study of the quench properties of epoxy impregnated coupled coils wound with NbTi and NbSn," *IEEE Trans. Magn.* **28**, 731 (1992).

[8.54] M.K. Chyu and C.E. Oberly, "Influence of operating temperature and contact thermal resistance on normal zone propagation in a metal-sheathed high-T_c superconductor tape," *Cryogenics* **32**, 519 (1992).

[8.55] R.H. Bellis and Y. Iwasa, "Quench propagation in high T_c superconductors," *Cryogenics* **34**, 129 (1994).

[8.56] G. Baccaglioni, M. Canali, L. Rossi and M. Sorbi, "Measurements of quench velocity in adiabatic NbTi and NbSn coils. Comparison between theory and experiments in small model coils and large magnets," *IEEE Trans. Magn.* **30**, 2677 (1994).

[8.57] Hunwook Lim and Yukikazu Iwasa, "Two-dimensional normal zone propagation in BSCCO-2223 pancake coils," *Cryogenics* **37**, 789 (1997).

[8.58] Nghia Van Vo, Hua Kun Liu and Shi Xue Dou, "Construction and normal zone propagation analysis of high T_c superconducting Bi(Pb)-2223/Ag class II coils and magnets," *IEEE Trans. Appl. Superconduc.* **7**, 893 (1997).

[8.59] S.B. Kim and A. Ishiyama, "Normal zone propagation properties in Bi-2223/Ag superconducting multifilament tapes," *Cryogenics* **38**, 823 (1998).

[8.60] S.S. Oh, Q.L. Wang, H.S. Ha, H.M. Jang, D.W. Ha and K.S. Ryu, "Quench characteristics of Bi-2223 coil at liquid helium temperature," *IEEE Trans. Appl. Superconduc.* **9**, 1081 (1999).

[8.61] V.S. Vysotsky, Yu. A. Ilyin, T. Kiss, M. Takeo, M. Lorenz, H. Hochmuth, J. Schneider, R. Woerdenweber, "Quench propagation in large area YBCO films," *IEEE Trans. Appl. Superconduc.* **9**, 1089 (1999).

[8.62] A.V. Dudarev, A.V. Gavrilin, H.H.J. ten Kate, D.E. Baynham, M.J.D. Courthold and C. Lesmond, "Quench propagation and protection analysis of the ATLAS toroids," *IEEE Trans. Appl. Superconduc.* **10**, 365 (2000).

[8.63] F.-P. Juster, J. Deregel, B. Hervieu, J.-M. Rey, "Stability and quench propagation velocities measurements on the 'racetrack' mock-up of ATLAS toroid coil," *IEEE Trans. Appl. Superconduc.* **10**, 677 (2000).

[8.64] J.W. Lue, M.J. Gouge, R.C. Duckworth, D.F. Lee, D.M. Kroeger, and J.M. Pfotenhauer, "Quench tests of a 20-cm long RaBiTS YBCO tape," *Adv. Cryogenic Engr.* **48**, 321 (2002).

[8.65] Naoyuki Amemiya, Noritaka Hoshi, Nobuya Banno, Takao Takeuchi, and Hitoshi Wada, "Quench propagation and stability of Nb_3Al superconductors made by rapid heating, quenching, and transformation process," *IEEE Trans. Appl. Superconduc.* **12**, 1001 (2002).

[8.66] R. Grabovickic, J.W. Lue, M.J. Gouge, J.A. Demko, R.C. Duckworth, "Measurements and numerical analysis of temperature dependence of stability and quench propagation of 9.5- and 20-cm long RaBiTS YBCO tapes," *IEEE Trans. Appl. Superconduc.* **13**, 1726 (2003).

[8.67] F. Trillaud, H. Palanki, U.P. Trociewitz, S.H. Thomson, H.W. Weiers, J. Schwartz, "Normal zone propagation experiments on HTS composite conductors," *Cryogenics* **43**, 271 (2003).

[8.68] François-Paul Juster, Alexey V. Dudarev, Philippe Fazilleau, and François Kircher,

"Conceptual and experimental results of the transverse normal zone propagation in the B0 ATLAS-barrel model coil," *IEEE Trans. Appl. Superconduc.* **14**, 1322 (2004).

[8.69] Atsushi Ishiyama, Masahiro Yanai, Toru Morisaki, Hiroshi Ueda, Yuh Shiohara, Teruo Izumi, Yasuhiro Iijima, and Takashi Saitoh, "Normal transition and propagation characteristics of YBCO tape," *IEEE Trans. Appl. Superconduc.* **15**, 1659 (2005).

[8.70] H. van Weeren, N.C. van den Eijinden, W.A.J. Wessel, P. Lezza, S.I. Schlachter, W. Goldacker, M. Dhallé, A. den Ouden, B. ten Haken, and H.H.J. ten Kate, "Adiabatic normal zone development in MgB_2 superconductors," *IEEE Trans. Appl. Superconduc.* **15**, 1667 (2005).

[8.71] E. Flock, G.K. Hoang, C. Kohler, P. Hiebel, and J.M. Kauffmann, "Measurement of velocities up to 1.1 km/s and test of a very fast quench inducing system," *IEEE Trans. Appl. Superconduc.* **15**, 1671 (2005).

[8.72] Shaolin Mao, Cesar A. Luongo, and David A. Kopriva, "Discontinuous Galerkin spectral element simulation of quench propagation in superconducting magnets," *IEEE Trans. Appl. Superconduc.* **15**, 1675 (2005).

[8.73] X. Wang, U.P. Trociewitz, J. Schwartz, "Near-adiabatic quench experiments on short $YBa_2Cu_3O_{7-\delta}$ coated conductors," *J. Appl. Phys.* **101**, 053904 (2007).

[8.74] Frederic Trillaud, Woo-Seok Kim, Yukikazu Iwasa, and John P. Voccio, "Quench behavior of a low stored energy magnet built with 2G HTS wire," *IEEE Trans. Appl. Superconduc.* **18**, 1329 (2008).

[8.75] Woo-Seok Kim, Frederic Trillaud, Yukikazu Iwasa, Xuan Peng, and Michael Tomsic, "Normal zone propagation in 2-dimensional YBCO winding pack models," *IEEE Trans. Appl. Superconduc.* **18**, 13337 (2008).

[8.76] C.A. Luongo, R.J. Lyod, F.K. Chen, and S.D. Peck, "Thermal-hydraulic simulation of helium expulsion from a cable-in-conduit conductor," *IEEE Trans. Magn.* **25**, 1589 (1989).

[8.77] L. Dresner, "Theory of thermal hydraulic quenchback in cable-in-conduit superconductors," *Cryogenics* **31**, 557 (1991).

[8.78] J.W. Lue, L. Dresner, S.W. Schwenterly, C.T. Wilson, and M.S. Lubell, "Investigating thermal hydraulic quenchback in a cable-in-conduit superconductor," *IEEE Trans. Appl. Superconduc.* **3**, 338 (1993).

[8.79] Mamoon I. Yunus, Yukikazu Iwasa, and John E.C. Williams, "AC-loss-induced quenching in multicoil adiabatic superconducting magnets," *Cryogenics* **35**, (1995).

[8.80] K. Takeuchi, Y.K. Kang, H. Hashizume, and Y. Iwasa, "Interfilament coupling loss for protection of superconducting multicoil magnets," *Cryogenics* **38**, 367 (1998).

[8.81] Yehia M. Eyssa, Ziad Melhem, "Effect of AC loss on quench propagation in impregnated magnets," *IEEE Trans. Appl. Superconduc.* **10**, 1380 (2000).

[8.82] V.S. Vysotsky, Yu.A. Ilyin, A.L. Rakhmanov, K. Funaki, M. Takeo, K. Shimohata, S. Nakamura, M. Yamada and K. Hasegawa, "Quench development and ultimate normal zone propagation 'velocity' in superconductors under fast current change," *IEEE Trans. Appl. Superconduc.* **11**, 2118 (2001).

[8.83] M.N. Wilson, "Computer simulation of the quenching of a superconducting magnet," (Rutherford High Energy Physics Laboratory Memo RHEL/M151, 1968).

[8.84] D. Eckert, F. Lange and A. Möbius, "A computer program simulating the quench of superconducting magnet systems," *IEEE Trans. Magn.* **MAG-17**, 1807 (1981).

[8.85] J.E.C. Williams, "Quenching in coupled adiabatic coils," *IEEE Trans. Magn.* **MAG-21**, 396 (1985).

[8.86] V. Kadambi and B. Dorri, "Current decay and temperatures during superconducting magnet coil quench," *Cryogenics* **26**, 157 (1986).

[8.87] K. Kuroda, S. Uchikawa, N. Hara, R. Saito, R. Takeda, K. Murai, T. Kobayashi, S. Suzuki, and T. Nakayama, "Quench simulation analysis of a superconducting coil," *Cryogenics* **29**, 814 (1989).

[8.88] O. Ozaki, Y. Fukumoto, R. Hirose, Y. Inoue, T. Kamikado, Y. Murakami, R. Ogawa and M. Yoshikawa, "Quench analysis of multisection superconducting magnet," *IEEE Trans. Appl. Superconduc.* **5**, 483 (1995).

[8.89] Yehia M. Eyssa and W. Denis Markiewicz, "Quench simulation and thermal diffusion in epoxy-impregnated magnet system," *IEEE Trans. Appl. Superconduc.* **5**, 487 (1995).

[8.90] Tomoyuki Murakami, Satoru Murase, Susumu Shimamoto, Satoshi Awaji, Kazuo Watanabe, "Two-dimensional quench simulation of composite CuNb/Nb_3Sn conductors," *Cryogenics* **40**, 393 (2000).

[8.91] V.S. Vysotsky, Yu. A. Ilyin, A.L. Rakhmanov and M. Takeo, "Quench development analysis in HTSC coils by use of the universal scaling theory," *IEEE Trans. Appl. Superconduc.* **11**, 1824 (2001).

[8.92] A. Korpela, T. Kalliohaka, J. Lehtonen and R. Mikkonen, "Protection of conduction cooled Nb_3Sn SMES coil," *IEEE Trans. Appl. Superconduc.* **11**, 2591 (2001).

[8.93] L. Imbasciati, P. Bauer, G. Ambrosio, V. Kashikin, M. Lamm, A.V. Zlobin, "Quench protection of high field Nb3Sn magnets for VLHC," *Proc. 2001 Particle Accelerator Conf.*, 3454 (2001).

[8.94] Yuri Lvovsky, "Conduction crisis and quench dynamics in cryocooler-cooled HTS magnets," *IEEE Trans. Appl. Superconduc.* **12**, 1565 (2002).

[8.95] Ryuji Yamada, Eric Marscin, Ang Lee, Masayoshi Wake, and Jean-Michel Rey, "2-D/3-D quench simulation using ANSYS for epoxy impregnated Nb_3Sn high field magnets," *IEEE Trans. Appl. Superconduc.* **13**, 159 (2003).

[8.96] Qiuliang Wang, Peide Weng, Moyan He, "Simulation of quench for the cable-in-conduit-conductor in HT-7U superconducting Tokamak magnets using porous medium model," *Cryogenics* **44**, 81 (2004).

[8.97] C. Berriaud, F.P. Juster, M. Arnaud, Ph. Benoit, F. Broggi, L. Deront, A. Dudarev, A. Foussat, M. Humeau, S. Junker, N. Kopeykin, R. Leboeuf, C. Mayri, G. Olesen, R. Gengo, S. Ravat, J-M. Rey, E. Sbrissa, V. Stepanov, H.H.J. ten Kate, P. Védrine, and G. Volpini, "Hot spot in ATLAS barrel toroid quenches," *IEEE Trans. Appl. Superconduc.* **18**, 1313 (2008).

[8.98] Taotao Huang, Elena Martínez, Chris Friend, and Yifeng Yang, "Quench characteristics of HTS conductors at low temperatures," *IEEE Trans. Appl. Superconduc.* **18**, 1317 (2008).

[8.99] Philippe J. Masson, Vincent R. Rouault, Guillaume Hoffman, and Cesar A. Luongo, "Development of quench propagation models for coated conductors," *IEEE Trans. Appl. Superconduc.* **18**, 1321 (2008).

[8.100] I. Terechkine and V. Veretennikov, "Normal zone propagation in superconducting focusing solenoids and related quench protection issues," *IEEE Trans. Appl. Superconduc.* **18**, 1325 (2008).

[8.101] A. Zhukovsky, Y. Iwasa, E.S. Bobrov, J. Ludlam, J.E.C. Williams, R. Hirose, Z. Ping Zhao, "750 MHz NMR Magnet Development," *IEEE Trans. Magn.* **28**, 644 (1992).

[8.102] R. Stiening, R. Flora, R. Lauckner, G. Tool, "A superconducting synchrotron

power supply and quench protection scheme," *IEEE Trans. Magn.* **MAG-15**, 670 (1979).

[8.103] D. Bonmann, K.-H. Meß, P. Schmüser, M. Schweiger, "Heater-induced quenches in a superconducting HERA test dipole," *IEEE Trans. Magn.* **MAG-15**, 670 (1979).

[8.104] A. Devred, M. Chapman, J. Cortella, A. Desportes, J. DiMarco, J. Kaugerts, R. Schermer, J.C. Tomkins, J. Turner, J.G. Cottingham, P. Dahl, G. Ganetis, M. Garber, A. Ghosh, C. Goodzeit, A. Greene, J. Herrera, S. Kahn, E. Kelly, G. Morgan, A. Prodell, E.P. Rohrer, W. Sampson, R. Shutt, P. Thompson, P. Wanderer, E. Willen, M. Bleadon, B.C. Brown, R. Hanft, M. Kuchnir, M. Lamm, P. Mantsch, D. Orris, J. Peoples, J. Strait, G. Tool, S. Caspi, W. Gilbert, C. Peters, J. Rechen, J. Royer, R. Scanlan, C. Taylor, and J. Zbasnik, "Investigation of heater-induced quenches in a full-length SSC R&D dipole," *Proc. Intn'l Conf. Magnet Tech. (MT11)*, (1990).

[8.105] H. Yoshimura, A. Ueda, M. Morita, S. Maeda, M. Nagao, K. Shimohata, Y. Matsuo, Y. Nagata, T. Yamada, M. Tanaka, "Heater-induced quenching in a model field winding for the 70MW class superconducting generator," *IEEE Trans. Magn.* **27**, 2088 (1991).

[8.106] E. Acerbi, M. Sorbi, G. Volpini, A. Daël, C. Lesmond, "The protection system of the superconducting coils in the Barrel toroid of ATLAS," *IEEE Trans. Appl. Superconduc.* **9**, 1101 (1999).

[8.107] Yehiha M. Eyssa, W. Denis Markiewicz, and Charles A. Swenson, "Quench heater simulation for protection of superconducting coils," *IEEE Trans. Appl. Superconduc.* **9**, 1117 (1999).

[8.108] V. Maroussov, S. Sanfilippo, A. Siemko, "Temperature profiles during quenches in LHC superconducting dipole magnets protected by quench heaters," *IEEE Trans. Appl. Superconduc.* **10**, 661 (2000).

[8.109] E.E. Burkhardt, A. Yamamoto, T. Nakamoto, T. Shintomi and K. Tsuchiya, "Quench protection heater studies for the 1-m model magnets for the LHC low-β quadrupoles," *IEEE Trans. Appl. Superconduc.* **10**, 681 (2000).

[8.110] Iain R. Dixon and W. Denis Markiewicz, "Protection heater performance of Nb_3Sn epoxy impregnated superconducting solenoids," *IEEE Trans. Appl. Superconduc.* **11**, 2583 (2001).

[8.111] W. Denis Markiewicz, "Protection of HTS coils in the limit of zero quench propagation velocity," *IEEE Trans. Appl. Superconduc.* **18**, 1333 (2008).

[8.112] J.M. Pfotenhauer, F. Kessler, and M.A. Hilal, "Voltage detection and magnet protection," *IEEE Trans. Appl. Superconduc.* **3**, 273 (1993).

[8.113] I.R. Dixon, W.D. Markiewicz, P. Murphy, T.A. Painter, and A. Powell, "Quench detection and protection of the wide bore 900 MHz NMR magnet at the National High Magnetic Field Laboratory," *IEEE Trans. Appl. Superconduc.* **14**, 1260 (2004).

[8.114] T. Ishigohka and Y. Iwasa, "Protection of large superconducting magnets: a normal-zone voltage detection method," *Proc. 10th Sympo. Fusion Eng.* (IEEE CH1916-6/83/0000-2050, 1983), 2050.

[8.115] Charles A. Swenson, Yehia M. Eyssa, and W. Denis Markiewicz, "Quench protection heater design for superconducting solenoids," *IEEE Trans. Magn.* **32**, 2659 (1996).

[8.116] Thomas Rummel, Osvin Gaupp, Georg Lochner, and Joerg Sapper, "Quench protection for the superconducting magnet system of Wendelstein 7-X," *IEEE Trans. Appl. Superconduc.* **12**, 1382 (2002).

Chapter 9
Solenoid *Examples*, HTS Magnets & Concluding Remarks

9.1 Introduction

This chapter consists of three segments. The first segment presents solenoid magnet ***Examples***, each accompanied by a study section, ***Questions/Answers*** (***Q/A***). The next segment discusses HTS, magnet applications and outlook. The chapter ends with brief concluding remarks.

The four solenoid magnet ***Examples*** described and studied here are selected not because of their especial importance nor uniqueness—no magnet system is unique or, perhaps to some, *every* magnet is unique. The selection stems chiefly from the author's familiarity with these magnets. In the ***Q/A*** section that follows each description, some of the design and operation issues, covered in the previous seven chapters, ***Chapters 2–8***, are studied and revisited.

Here, we emphasize once again our basic philosophy, first stated in ***Chapter 1***, that in any problem solving that requires numerical solution, the very first step is to get *ballpark* figures, computed on a *simple* model amenable to numerical solution. The ballpark figures quickly tell the magnet designer if the magnet is on the right track. This exercise is important with any magnet, simple or complex. An "innovative" magnet idea often begins with an individual. To assess whether the idea is *realistic* and worth pursuing further with colleagues or even forming a design team, the initiator must first compute *ballpark* figures of key design and operation parameters, those covered in ***Chapters 2–8***, e.g., from simple parameters like total ampere turns, overall operating current density, size and weight of the magnet, total length of conductor, to more intricate ones like stability and protection, forces, and cryogenic requirements. The key word here is *ballpark*: in the later stages of a magnet project, specialists in the design team, armed with sophisticated codes, will compute accurate parameter values. Leave the exact values to the specialists, but be prepared to verify that theirs indeed fall within the range of independently computed ballpark figures. The author hopes that after having studied ***Chapters 2–8***, the reader—a specialist in whatever area, electromagnetic fields, stresses, cryogenics, or even materials—will be capable of handling most of the questions included in the four magnet ***Examples*** presented below.

9.2 Solenoid Magnet *Examples*

The four solenoid magnet ***Examples*** described and studied are: 1) a hybrid magnet comprised of a large superconducting magnet with a resistive insert; 2) a magnet on a steel plate; 3) a flat HTS plate (disk) levitated by a magnetic field generated by solenoid coils below; and 4) a "solenoid" magnet comprising a stack of HTS annuli, each prepared from a bulk disk or coated conductor "plate."

"What good is a newborn baby?" —Ben Franklin

Y. Iwasa, *Case Studies in Superconducting Magnets: Design and Operational Issues*,
DOI: 10.1007/b112047_9,

EXAMPLE 9.2A: Series-Connected-Hybrid Magnet (SCH)

A high-field magnet, with a central axial field of 35–40 T, depending on bore size (32–50 mm), at the National High Magnetic Field Laboratory comprises principally a 5-coil high-homogeneity resistive (water-cooled) insert in the bore of a superconducting magnet. Because the superconducting magnet and 5-coil resistive insert are connected electrically in series and driven by the same DC power supply, the magnet is called a "Series-Connected-Hybrid" (SCH). Note that the SCH generates a central field greater than the highest field generated by any NHMFL resistive magnet (35 T) or superconducting magnet (21 T). Figure 9.1 shows a cross sectional drawing of the SCH magnet—with parameter values slightly different from the final values in the SCH magnet [9.1].

Although not included in Fig. 9.1, the SCH also contains a "thin" ($\alpha \simeq 1$) superconducting "shield" coil having a winding radius of about 1 m. The shield coil, of reverse polarity, reduces the fringe field of the SCH magnet. In the ***Q/A*** section, we shall compute the approximate ampere turns required for this superconducting shield coil. Also, we shall design an alternate shielding system comprised of a steel cylindrical shell.

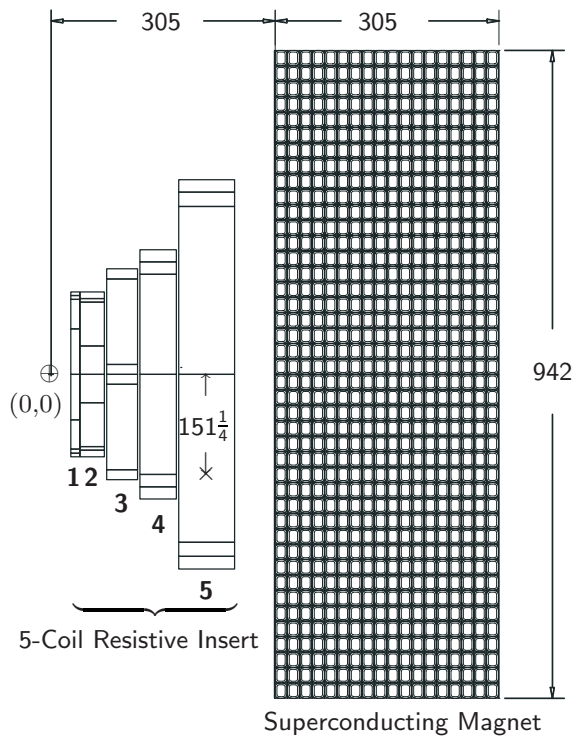

Fig. 9.1 Cross sectional view of one half of the SCH magnet at the NHMFL [9.1]—the superconducting "shield" coil (of radius ∼1 m) is not shown here. The winding dimensions, in mm, are approximate; × (in Coil 5) marks its magnetic center after a fault mode, discussed in the ***Q/A*** section.

EXAMPLE 9.2A: Series-Connected-Hybrid Magnet (SCH) (continuation)

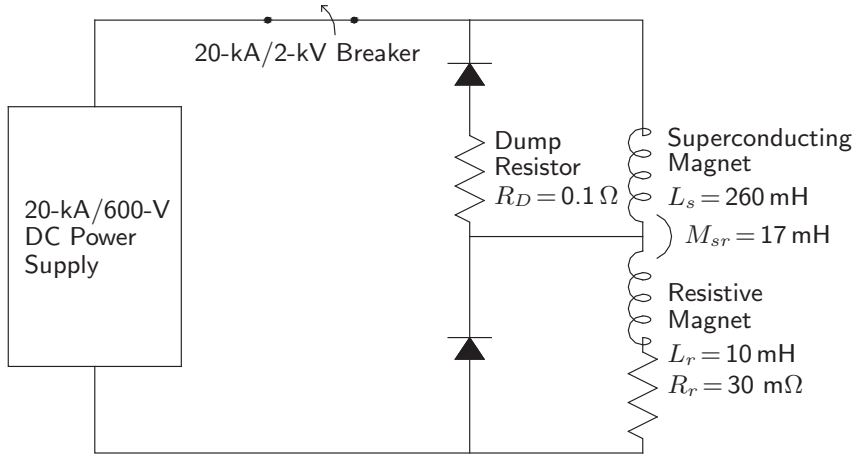

Fig. 9.2 Circuit diagram of the SCH magnet. [Courtesy: NHMFL, 2005]

Figure 9.2 shows a circuit diagram of the SCH, in which a superconducting magnet (of self inductance, $L_s = 260\,\text{mH}$) is connected in series with a resistive magnet (of $L_r = 10\,\text{mH}$, and resistance, $R_r = 30\,\text{m}\Omega$). The magnets are powered by a 20-kA/600-V supply. For protection, the superconducting magnet is shunted by a dump resistor, $R_D = 0.1\,\Omega$, with a diode connected in series; the resistive magnet is shunted by a diode. (Assume that both diodes are "ideal," i.e., zero forward resistance and infinite backward resistance.) As indicated in Fig. 9.2 the mutual inductance, M_{sr}, between the two magnets is 17 mH. In case of a malfunction of either magnet, the 20-kA/2-kV breaker is opened.

Table 9.1 lists key parameter values of the superconducting magnet and the CIC conductor used in the innermost layer of the magnet. Note that A_{sc}, $A_{\overline{m}}$, A_m, and A_{cl} are cross sectional areas in the CIC conductor, respectively, of Nb_3Sn; non-matrix metal; matrix metal (copper); and supercritical helium at 4.5 K.

Table 9.1: Parameters of
Superconducting Magnet & CIC Conductor

Parameters		*Value*
Superconducting Magnet		
Winding i.d. ($2a_1$)	[mm]	610.0
Winding o.d. ($2a_2$)	[mm]	1220.2
Winding height ($2b$)	[mm]	942.0
Turns/layer		42
Layers		18
Total turns (N)		756
CIC Conductor @ Innermost Layer		
$A_{sc}+A_{\overline{m}}$	[mm^2]	40.2
A_m	[mm^2]	57.4
A_{cl}	[mm^2]	76.0

Q/A 9.2A: SCH Superconducting Magnet

a) Overall Current Density What is the overall current density, λJ_{op}, of the superconducting magnet at its operating current, $I_{op}=20\,\text{kA}$?

• *The Answer to each question begins with a large, bold slanted letter, as* ***A****, below.*

Applying Eq. 3.108*a* with $N=756$ and $I=I_{op}=20\,\text{kA}$, we obtain:

$$\lambda J_{op} = \frac{NI}{2b(a_2-a_1)} \tag{3.108a}$$

$$= \frac{756(20\times10^3\,\text{A})}{(942.0\,\text{mm})(610.1\,\text{mm}-305.0\,\text{mm})} = 52.6\,\text{A/mm}^2$$

b) Central Field What is the field (magnetic induction) at the center, $B_z(0,0)$, generated by the superconducting magnet at $I_{op}=20\,\text{kA}$?

Similarly from Table 9.1, we have: $\alpha = (1220.2\,\text{mm})/(610.0\,\text{mm}) = 2.00$; $\beta = (942.0\,\text{mm})/(610.0\,\text{mm}) = 1.544$. Applying Eq. 3.110, we have:

$$B_z(0,0) = \frac{\mu_\circ NI}{2a_1(\alpha-1)}\ln\left(\frac{\alpha+\sqrt{\alpha^2+\beta^2}}{1+\sqrt{1+\beta^2}}\right) \tag{3.110}$$

Thus:

$$B_z(0,0) = \frac{(4\pi\times10^{-7}\,\text{H/m})(756)(20\times10^3\,\text{A})}{(0.610\,\text{m})(2.00-1)}\ln\left(\frac{2.00+\sqrt{(2.00)^2+(1.544)^2}}{1+\sqrt{1+(1.544)^2}}\right)$$

$$= 14.52\,\text{T}$$

c) Midplane Radial Field What is the radial component of the field at the midplane ($z=0$) at $r=a_2$, $B_r(z=0, r=2a_2)$, generated by the superconducting magnet? Assume the magnet winding to be an *ideal* solenoid.

The radial component of field along the *midplane* of an ideal solenoidal magnet or nested-coil magnet symmetric about its midplane is always zero: $B_r(0,a_2)=0$.

d) Inductance Using Eq. 3.81 and Fig. 3.14, compute an approximate value of the magnet's self inductance, L_s. As noted above the exact value is 260 mH.

Applying Eq. 3.81 and from Fig. 3.14, $\mathcal{L}(\alpha=2.00, \beta=1.544)\simeq 1.2$, we obtain:

$$L = \mu_\circ a_1 N^2 \mathcal{L}(\alpha,\beta) \tag{3.81}$$

$$L_s = (4\pi\times10^{-7}\,\text{H/m})(0.305\,\text{m})(756)^2(1.2) = 263\,\text{mH}$$

e) Stored Magnet Energy What is the total magnetic energy, E_{ms}, of the superconducting magnet at the operating current, I_{op}, of 20 kA?

Here we must include the effect of the mutual inductance. Thus:

$$E_{ms} = \tfrac{1}{2}(L_s + M_{sr})I_{op}^2$$

$$= \tfrac{1}{2}(260\,\text{mH}+17\,\text{mH})(20\,\text{kA})^2 = 55.4\,\text{MJ}$$

Q/A 9.2A: SCH Superconducting Magnet (continuation)

f) Diode Explain two functions of the diode connected in series with R_D across the superconducting magnet.

The diode, connected in the backward direction, performs two functions: 1) when the magnet is being energized, it prevents current from flowing through R_D; i.e., 100% of the supply current flows through the magnet; 2) when the switch is opened, it permits the current to be discharged through R_D.

g) Charging Voltage For a constant charging rate of 400 A/s, $dI_s/dt = dI_r/dt = dI_S/dt = 400$ A/s, where I_s is the current through the superconducting magnet, I_r is the current through the resistive magnet, and I_S is the power supply current, what is the required supply voltage, V_S, at $I_s = I_r = I_S = 10$ kA?

The supply voltage V_S is given by:

$$V_S = L_s\frac{dI_s}{dt} + M_{sr}\frac{dI_r}{dt} + M_{sr}\frac{dI_s}{dt} + L_r\frac{dI_r}{dt} + R_rI_r \qquad (g.1a)$$

$$= (L_s + 2M_{sr} + L_r)\frac{dI_S}{dt} + R_rI_S \qquad (g.1b)$$

Inserting appropriate values in Eq. $g.1b$, we have:

$$V_S = (260\,\text{mH} + 2\times 17\,\text{mH} + 10\,\text{mH})(400\,\text{A/s}) + (30\,\text{m}\Omega)(10\,\text{kA}) = 421.6\,\text{V}$$

h) Power What is the total instantaneous power, P_S, delivered to the magnets, superconducting and resistive, by the power supply when it is charging the magnets at a rate of $dI_S/dt = 400$ A/s when $I_S = 10$ kA?

As in **g)**, we have:

$$V_S = (L_s + 2M_{sr} + L_r)\frac{dI_S}{dt} + R_rI_S \qquad (g.1b)$$

$$= 421.6\,\text{V}$$

$P_S = V_SI_S$; thus: $P_S = (421.6\,\text{V})(10\,\text{kA}) = 4.216$ MW. Note that of the 4.216 MW, 1.216 MW $[= 4.216\,\text{MW} - (30\,\text{m}\Omega)\times(10\,\text{kA})^2]$ is "reactive," i.e., it is stored as magnetic energy in the two magnets, and as the current is reduced to zero through the supply, the magnetic energy is "returned" to the supply.

TRIVIA 9.1 List the items below in descending order of stress (tension or compression).

i) Maximum tension in the winding of a 35-T magnet;

ii) On the *Titanic*, at the bottom of the Atlantic;

iii) Sound of rock music;

iv) Synthesizing diamond.

Q/A 9.2A: SCH Superconducting Magnet (continuation)

i) 600-V Supply Voltage Show that at this rate of current increase, i.e., 400 A/s, the supply voltage maximum of 600 V is reached at $I_S \simeq 16$ kA.

The total inductive voltage required, V_{ind}, is given by:

$$V_{ind} = (L_s + 2M_{sr} + L_r)\frac{dI_S}{dt}$$

which, for $dI_S/dt = 400$ A/s, becomes:

$$V_{ind} = (260\,\text{mH} + 2\times 17\,\text{mH} + 10\,\text{mH})(400\,\text{A/s}) = 121.6\,\text{V}$$

We also have: $V_S = V_{ind} + R_r I_r$. Inserting $V_S = 600$ V and $R_r = 30\,\text{m}\Omega$, and solving for I_r, we find: $I_r = 15946.7$ A; $I_S \simeq 16$ kA.

j) 16 kA→20 kA Charging Time Show that beyond 16 kA (I_{16}), as the supply voltage is maintained at 600 V, it takes about one minute for the current to reach within ∼10 A of the operating current of 20 kA (I_{20}).

When the current reaches 16 kA, the supply runs out of voltage to maintain the charging rate of 400 A/s. Beyond $I_s(t) \geq I_{16} = 16$ kA, $I_s(t) = I_{20} + (I_{20} - I_{16})[1 - \exp(-t/\tau)]$, where $I_{20} = 20$ kA and τ, the effective circuit time constant, is ∼10 s, given by the total effective circuit inductance of 304 mH [= 260 mH + (2×17 mH)+ 10 mH] divided by 30 mΩ. In a minute, which is six time constants, the total current will be within 10 A ($\simeq 4000e^{-6}$) of 20 kA.

k) CIC—Helium Flow The CIC conductor has a helium cross sectional area of $A_{cl} = 76.0\,\text{mm}^2$ (Table 9.1). Supercritical helium of 3.5 atm and 4.5 K flows at a mass rate of $\dot{m}_{he} = 5$ g/s through the conduit. Show that the flow is turbulent with a Reynolds number, $\text{Re} \simeq 10^5$. Use the following parameter values—helium density: $\varrho_{he} = 0.132\,\text{g/cm}^3$; helium viscosity: $\nu_{he} = 35.9\times 10^{-6}\,\text{g/cm s}$; hydraulic diameter: $D_{he} = 1$ cm.

Fluid velocity, v_{he}, is given by: $\dot{m}_{he} = \varrho_{he} A_{cl} v_{he}$. Thus:

$$\begin{aligned} v_{he} &= \frac{\dot{m}_{he}}{\varrho_{he} A_{cl}} \\ &= \frac{(5\,\text{g/s})}{(0.132\,\text{g/cm}^3)(0.760\,\text{cm}^2)} \simeq 50\,\text{cm/s} \end{aligned}$$

Reynolds number Re is given by:

$$\begin{aligned} \text{Re} &= \frac{\varrho_{he} v_{he} D_{he}}{\nu_{he}} \\ &\simeq \frac{(0.132\,\text{g/cm}^3)(50\,\text{cm/s})(1\,\text{cm})}{(35.9\times 10^{-6}\,\text{g/cm s})} \simeq 1.8\times 10^5 \end{aligned}$$

Flow is turbulent when its Reynolds number exceeds ∼2300.

Q/A 9.2A: SCH Superconducting Magnet (continuation)

l) CIC—Cryostability At an operating current of $I_{op}=20\,\text{kA}$, is the CIC conductor cryostable? You may use the following parameter values: $A_m=57.4\,\text{mm}^2$; $f_d\mathcal{P}_D=30\,\text{mm}$; $T_c=10.3\,\text{K}$; $\rho_m=2\times10^{-8}\,\Omega\,\text{cm}$; helium mass flow rate, $\dot{m}_{he}=5\,\text{g/s}$.

From Eq. 6.30, we have:

$$I_{lim}=\sqrt{\frac{A_m f_p \mathcal{P}_D h_{he}(T_c-T_{op})}{\rho_m}} \tag{6.30}$$

Figure 6.3 (p. 359) shows liquid helium heat transfer coefficients. From this figure, we find that for $P=3.5\,\text{atm}$, $T_{op}=4.5\,\text{K}$, and $\Delta T=5.8\,\text{K}$, $h_q\simeq0.26\,\text{W/cm}^2\,\text{K}$ at $\text{Re}=10^5$. Noting that $h_{he}\propto\text{Re}^{0.8}$ (Eq. 6.29), $h_q\simeq0.42\,\text{W/cm}^2\,\text{K}$ at $\text{Re}=1.8\times10^5$. Thus:

$$I_{lim}=\sqrt{\frac{(57.4\times10^{-2}\,\text{cm}^2)(3\,\text{cm})(0.42\,\text{W/cm}^2\,\text{K})(5.8\,\text{K})}{(2\times10^{-8}\,\Omega\,\text{cm})}}\simeq14.4\,\text{kA}<20\,\text{kA}$$

That is, this superconducting magnet operates at ∼40% more than the "Stekly current" of 14.4 kA: this CIC conductor is *not* cryostable at 20 kA.

m) Current Dump Suppose that both magnets are at 20 kA, and the protection system detects a fault in either one of the magnets at $t=0$ and opens the 20-kA/2-kV breaker *without a delay*, i.e., at $t=0$. For a "quick" estimate of $I_s(t)$ and $I_r(t)$, solve for $I_s(t)$ and $I_r(t)$ *assuming* that $M_{sr}=0$, i.e., the two magnet circuits are *uncoupled*. Actually, the coupling is not quite negligible, i.e., $k_{sr}=M_{sr}/\sqrt{L_sL_r}=(0.017\,\text{H})/\sqrt{(0.260\,\text{H})(0.010\,\text{H})}=0.333$; nevertheless, the results with $M_{sr}=0$ are informative and give a "feel" for the time scale.

With $M_{sr}\neq0$ the circuit equation for each magnet is given by:

$$L_s\frac{dI_s(t)}{dt}+M_{sr}\frac{dI_r(t)}{dt}+R_DI_s(t)=0 \tag{$m.1a$}$$

$$M_{sr}\frac{dI_s(t)}{dt}+L_r\frac{dI_r(t)}{dt}+R_rI_r(t)=0 \tag{$m.1b$}$$

With $M_{sr}=0$ Eqs. $m.1a$ and $m.1b$ are then simplified to:

$$L_s\frac{dI_s(t)}{dt}+R_DI_s(t)=0 \tag{$m.2a$}$$

$$L_r\frac{dI_r(t)}{dt}+R_rI_r(t)=0 \tag{$m.2b$}$$

Equations $m.2a$ and $m.2b$ may be solved independently of each other:

$$I_s(t)=I_\circ e^{-tR_D/L_s} \tag{$m.3a$}$$

$$I_r(t)=I_\circ e^{-tR_r/L_r} \tag{$m.3b$}$$

where $I_\circ=20\,\text{kA}$, $L_s/R_D=2.6\,\text{s}\,(=260\,\text{mH}/0.1\,\Omega)$, and $L_r/R_r=0.33\,\text{s}\,(=10\,\text{mH}/30\,\text{m}\Omega)$. Equations $m.3a$ (solid circles) and $m.3b$ (open) are shown in Fig. 9.3.

Q/A 9.2A: SCH Superconducting Magnet (continuation)

m) Current Dump *Answer* (continuation)

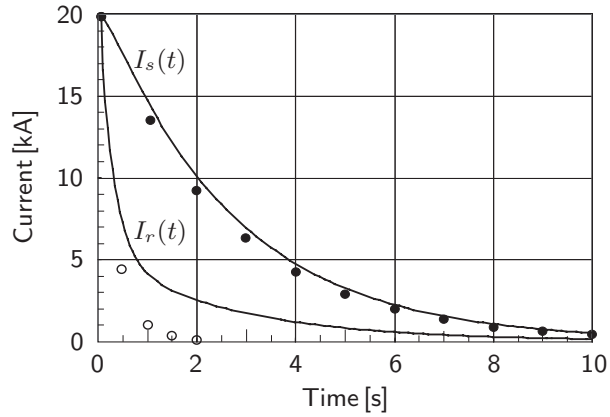

Fig. 9.3 $I_s(t)$ by Eq. $m.3a$ (solid circles) and $I_r(t)$ by Eq. $m.3b$ (open circles), both with $M_{sr}=0$. The curve nearby each gives the solution with $M_{sr}=0.017\,\mathrm{H}$.

n) Coupling Effect The magnets are of course inductively coupled—$M_{sr}\neq 0$. Explain why, for example, the solution for $I_s(t)$ with $M_{sr}=0.017\,\mathrm{H}$ shown in Fig. 9.3, traces above the solid circles of **m)** computed with $M_{sr}=0$.

We may express Eq. $m.1a$ as:

$$L_s\frac{dI_s(t)}{dt}=-R_D I_s(t)-M_{sr}\frac{dI_r(t)}{dt} \qquad (n.1)$$

Because $dI_r(t)/dt<0$, the term $-M_{sr}dI_r(t)/dt$ in Eq. $n.1$ is positive, making $|dI_s(t)/dt|$ with $M_{sr}\neq 0$ smaller than $|dI_s(t)/dt|$ with $M_{sr}=0$. That is, $I_s(t)$ decays more slowly with $M_{sr}\neq 0$ than with $M_{sr}=0$. Nevertheless, because k_{sr} is modest, the quick solution with $M_{sr}=0$ is not far off, at least for $I_s(t)$.

o) Effective Decay Time Constant As stated above in **n)**, when the inductive coupling of the two magnets is included, $I_s(t)$ and $I_r(t)$ decay more slowly than in the uncoupled system of **m)**. Assuming that the total magnetic energy stored in the superconducting magnet at 20 kA of $E_s=55.4\,\mathrm{MJ}$, as computed in **e)**, is entirely dissipated in the dump resistor (R_D) and that $I_s(t)$ in the coupled system is represented by a single "effective" time constant of τ_{eff}, compute τ_{eff}.

The magnetic energy of the superconducting magnet is dissipated all in R_D:

$$E_s=R_D\int_0^\infty I_s^2(t)\,dt \qquad (o.1a)$$

And because $I_s(t)=I_\circ e^{-t/\tau_{eff}}$, Eq. $o.1a$ becomes:

$$E_s=R_D\int_0^\infty I_\circ^2 e^{-2t/\tau_{eff}}\,dt=\frac{R_D I_\circ^2\tau_{eff}}{2} \qquad (o.1b)$$

Solving Eq. $o.1b$ for τ_{eff}, we have:

$$\tau_{eff}=\frac{2E_s}{R_D I_\circ^2}=\frac{2(55.4\times10^6\,\mathrm{J})}{(0.1\,\Omega)(2\times10^4\,\mathrm{A})^2}=2.77\,\mathrm{s}$$

Note that this is ∼6% greater than the 2.6 s computed for the *uncoupled* system.

Q/A 9.2A: SCH Superconducting Magnet (continuation)

p) Hysteresis Loss As the magnet is energized from 0 to B_m, hysteresis loss is generated within each superconducting strand. Make an estimate of e_{hy1}, the spatially-averaged hysteresis energy density of one Nb_3Sn filament of diameter $d_f = 42\,\mu$m in the strands within the innermost layer of the CIC conductor, as the magnet is *slowly* charged to 20 kA, at which $B_m = 14$ T. Start with Eq. 7.23*a* (Table 7.3B), valid for a *Bean slab* in the presence of transport current (Case 4*i*):

$$e_{hy} = \tfrac{1}{2}\mu_\circ H_p H_m (1+i)^2 \qquad [H_m \geq H_p(1-i)] \tag{7.23a}$$

Because we are dealing with a wire of diameter d_f, assumed to be of circular cross section, use $H_p = (8/3\pi)J_c(d_f/2)$, valid for wire in a perpendicular field (Eq. 5.29*b*). Next, because I_t starts at 0 and ends at 20 kA, which is well below I_c of nearly 40 kA, simplify Eq. 7.23*a* by making $(1+i)^2 \simeq 1$ in the equation. J_c defining H_p varies significantly between 0 and 14 T. That is, we must *integrate* Eq. 7.23*a* from $\mu_\circ H_m = B_m = 0$ to $B_m = 14$ T, the average field over the innermost layer at 20 kA:

$$e_{hy1} \simeq \frac{2d_f}{3\pi}\int_0^{B_m} J_c(B,T,\epsilon)dB \tag{$p.1$}$$

Here, $J_c(B,T,\epsilon)$, the critical current density of Nb_3Sn, includes dependences of J_c not only on B and T but also on ϵ, strain, because as the magnet is energized or discharged, strain acting on each composite Nb_3Sn strand changes. The dependence of T can also be important, because the strand temperature can rise unless the magnet is energized or discharged slowly enough for the composite to transfer heat to the coolant with negligible temperature rise. Generally the integration of Eq. $p.1$ is too complicated to be performed in a closed form.

However, we shall here perform a closed-form integration by: 1) changing the field at a rate *slow enough* to keep the composite at 4.5 K; and 2) neglecting the strain effects on J_c. For the composite Nb_3Sn strands in the magnet midplane and the innermost layer, we may use the average current density, $\tilde{J}_c(B, 4.5\,\text{K})$, given below:

$$\tilde{J}_c(B, 4.5\,\text{K}, \epsilon = 0) = \tilde{J}_c(0, 4.5\,\text{K})\frac{b_\circ}{b_\circ + B} \tag{$p.2$}$$

where $\tilde{J}_c(0, 4.5\,\text{K}) = 42 \times 10^9\ \text{A/m}^2$ and $b_\circ = 1$ T. Equation $p.2$ is a *rough* approximation of $J_c(B,T,\epsilon)$ for Nb_3Sn at 4.5 K and for $\epsilon = 0$.

Using Eq. $p.1$, we first perform the integral within Eq. $p.1$:

$$\int_0^{B_m} \tilde{J}_c(B, 4.5\,\text{K})\,dB = \tilde{J}_c(0, 4.5\,\text{K})b_\circ \int_0^{B_m} \frac{dB}{b_\circ + B} = \tilde{J}_c(0, 4.5\,\text{K})b_\circ \ln\left(\frac{b_\circ + B_m}{b_\circ}\right)$$

$$= (42\times 10^9\ \text{J/m}^2)(1\,\text{T})\ln 15 = 113.7\times 10^9\ \text{J/m}^4$$

Inserting this into Eq. $p.1$, we obtain:

$$e_{hy1} \simeq \frac{2(42\times 10^{-6}\,\text{m})}{3\pi}(113.7\times 10^9\ \text{J/m}^4) \simeq 1014\,\text{kJ/m}^3$$

Using GANDALF, Gavrilin obtains $e_{hy1} = 1039\,\text{kJ/m}^3$ for Eq. $p.1$; for the case $T = 4.5$ K and $\epsilon = 0$, as in our simple model above, he obtains $1122\,\text{kJ/m}^3$—greater than $1039\,\text{kJ/m}^3$ because $J_c(B, 4.5\,\text{K}, \epsilon = 0) > J_c(B, T > 4.5\,\text{K}, \epsilon > 0)$ [9.2].

Q/A 9.2A: SCH Superconducting Magnet (continuation)

q) Charging Rate vs. Helium Temperature Rise Hydraulically, each layer in this magnet is connected in parallel. Assuming that the *only* heat input to the coolant is the spatially-averaged hysteresis energy, compute the maximum *constant* current charging rate of the magnet, $(dI_s/dt)_{mx}$, from 0 to 20 kA, that limits the time-averaged temperature rise in the helium to $\Delta\tilde{T}_{he} \simeq 4.0\,\text{K}$ $(=\tilde{T}_{cs} - T_{op})$ in the innermost layer with a mass rate of $\dot{m}_{he} = 5\,\text{g/s}$. Here, $\tilde{T}_{cs}$ is the time-averaged current-sharing temperature, given by $T_{cs} = 10.3\,\text{K}$ at $I_{op} = 0$ and $T_{cs} = 6.7\,\text{K}$ at $I_{op} = 20\,\text{kA}$: $\tilde{T}_{cs} = 8.5\,\text{K}$. In this computation use $e_{hy} = 1014\,\text{kJ/m}^3$ computed above in **p)** under the condition of constant temperature.

Use the following property values for helium at 4.5 K and 3.5 atm: specific heat at constant pressure, $C_{he} = 4.28\,\text{J/g K}$; density, $\varrho_{he} = 0.132\,\text{g/cm}^3$, both assumed temperature- and pressure-independent, over the innermost layer. First show that the total hysteresis energy released in the innermost layer, E_{hy1}, is 3.5 kJ.

The total hysteresis energy, E_{hy1}, released in the innermost layer is given by:

$$E_{hy1} = e_{hy}(A_{sc} + A_{\overline{m}})\ell_1$$

where $A_{sc} + A_{\overline{m}} = 40.2\,\text{mm}^2$ and ℓ_1 is the total conductor length in the innermost layer. We have: $\ell_1 \simeq 2\pi(a_1 + w)(42)$, where a_1 is the winding inside radius, w is the conduit radial depth, and 42 is the number of turns per layer—all obtainable from Table 9.1. From Fig. 9.1 and Table 9.1, we know that the radial winding extent of the magnet, $a_2 - a_1$, is 305.1 mm, which contains 18 layers of the CIC conductor: $w = (305.1\,\text{mm})/18 \simeq 17\,\text{mm}$. Thus:

$$\ell_1 \simeq 2\pi(0.305\,\text{m} + 0.017\,\text{m})42 \simeq 85\,\text{m}$$

$$E_{hy1} = (1014 \times 10^3\,\text{J/m}^3)(40.2 \times 10^{-6}\,\text{m}^2)(85\,\text{m}) \simeq 3.5\,\text{kJ}$$

The time-averaged rate of change of helium enthalpy, dH_{he}/dt, from the inlet to the exit of the innermost layer at a flow rate of $\dot{m}_{he} = 5\,\text{g/s}$ is given by:

$$\begin{aligned}\frac{dH_{he}}{dt} &= C_{he}\dot{m}_{he}\Delta\tilde{T}_{he} \\ &= (4.28\,\text{J/g K})(5\,\text{g/s})(4.0\,\text{K}) \simeq 86\,\text{W}\end{aligned}$$

That is, the cooling power by helium in the innermost layer is 86 W for a time-averaged temperature rise of 4.0 K. This cooling power must be matched by the maximum dissipation rate, $P_{hy1_{mx}}$ given by:

$$P_{hy1_{mx}} = \frac{E_{hy1}}{\Delta t_{mn}} = 86\,\text{W} \qquad (q.1)$$

Solving Eq. $q.1$ for Δt_{mn}, we obtain:

$$\Delta t_{mn} = \frac{E_{hy1}}{P_{hy1_{mx}}} \simeq \frac{3.5\,\text{kJ}}{86\,\text{W}} \simeq 41\,\text{s}$$

Thus:

$$\left(\frac{dI_s}{dt}\right)_{mx} = \frac{\Delta I_s}{\Delta t_{mn}} \simeq \frac{20 \times 10^3\,\text{A}}{41\,\text{s}} \simeq 490\,\text{A/s}$$

A nominal charging rate of 400 A/s thus should keep the conductor below its current-sharing temperature, which varies from 10.3 K at $I_{op} = 0$ to 6.7 K at 20 kA.

Q/A 9.2A: SCH Superconducting Magnet (continuation)

r) Coupling Loss Using Eqs. 7.36 and 7.39*c* (Table 7.8), compute the coupling dissipation energy density, e_{cp}, for a strand of $D_{mf} = 0.6\,\text{mm}$ ($\simeq$ strand diameter) and $\ell_p = 10\,\text{mm}$, as the magnet is ramped from 0 to 20 kA ($B_m = 14\,\text{T}$) at a constant charging rate of 400 A/s or $\tau_m = 50\,\text{s}$ (for Triangular field excitation in Fig. 7.18). For this Nb_3Sn strand, $\tau_{cp} = 30\,\text{ms}$ [9.2].

With $\tau_m \gg \tau_{cp}$ the time-averaged e_{cp} for a triangular excitation is given by a combination of Eqs. 7.36 and 7.39*c*:

$$e_{cp} = 2\mu_\circ H_m^2 \left[1 + \tfrac{1}{4}\left(\frac{\pi D_{mf}}{\ell_p}\right)^2\right]\Gamma \tag{7.36}$$

$$\Gamma \simeq \frac{4\tau_{cp}}{\tau_m} \qquad (\tau_m \gg \tau_{cp}) \tag{7.39c}$$

$(\pi D_{mf}/\ell_p)^2 \ll 1$ and $H_m = B_m/\mu_\circ$ in Eq. 7.36; the charging time period covers only 1/2 of the complete triangular excitation (Fig. 7.18), thus a factor of 1/2 must also be introduced into Eq. 7.36. Thus, e_{cp} becomes:

$$\begin{aligned} e_{cp} &\simeq \tfrac{1}{2}\left(2\frac{B_m^2}{\mu_\circ}\right)\Gamma \\ &= \frac{4B_m^2\tau_{cp}}{\mu_\circ\tau_m} \end{aligned} \tag{r.1}$$

Inserting $B_m = 14\,\text{T}$, $\tau_{cp} = 30\,\text{ms}$, and $\tau_m = 50\,\text{s}$, we obtain:

$$e_{cp} = \frac{4(14\,\text{T})^2(30\times10^{-3}\,\text{s})}{(4\pi\times10^{-7}\,\text{T})(50\,\text{s})} \simeq 375\,\text{kJ/m}^3$$

Thus, the coupling dissipation is $\sim$1/3 as large as the hysteresis dissipation.

Answer to TRIVIA 9.1

Diamond (20,000, in atm); magnet (5,000); *Titanic* (400); rock (0.0004).

Q/A 9.2A: SCH Superconducting Magnet (continuation)

s) Hot-Spot Temperature Suppose that at $t = 0$, a quench is detected in the superconducting magnet and the breaker opened without a delay—opened at $t = 0$. Assume that the current in the superconducting magnet, $I_s(t)$, decays exponentially with an effective decay time constant, $\tau_{\mathit{eff}} = 2.77\,\mathrm{s}$, as computed in **o)**. Assuming also that the initial quench point—"hot spot"—is heated *adiabatically* by Joule heating, estimate the final temperature, T_f, reached at the hot spot. Also assume that only the CIC conductor—superconductor, non-matrix metal, and matrix (copper: RRR = 100)—absorbs the Joule heating and that the heat capacity of copper may be used to represent that of the entire conductor.

From Eq. 8.16*a* we have:

$$Z(T_f, T_i) = \left(\frac{A_m}{A_{cd}}\right) \int_0^\infty J_{m_\circ}^2 \, e^{-2t/\tau_{dg}} \, dt = \left(\frac{A_m}{A_{cd}}\right) J_{m_\circ}^2 \times \tfrac{1}{2}\tau_{dg} \qquad (8.16a)$$

With parameter values from Table 9.1, $A_m = 57.4\,\mathrm{mm}^2$; $A_{cd} = A_m + A_{sc} + A_{\overline{m}} = 97.6\,\mathrm{mm}^2$; and $J_{m_{op}} = I_{op}/A_m = (20,000\,\mathrm{A})/(57.4\times10^{-6}\,\mathrm{m}^2) = 3.48\times10^8\,\mathrm{A/m}^2$, inserted to Eq. 8.16*a* and $\tau_{dg} = \tau_{\mathit{eff}} = 2.77\,\mathrm{s}$ in Eq. *s*.1, and solving $Z_{cu}(T_f, T_i)$, $Z(T_f, T_i)$ for copper, we have:

$$\begin{aligned} Z_{cu}(T_f, T_i) &= \left(\frac{57.4\times10^{-6}\,\mathrm{m}^2}{97.6\times10^{-6}\,\mathrm{m}^2}\right)\left(3.48\times10^8\,\mathrm{A/m}^2\right)^2\left(\frac{2.77\,\mathrm{s}}{2}\right) \\ &\simeq 9.9\times10^{16}\,\mathrm{A}^2\,\mathrm{s/m}^4 \end{aligned}$$

From Fig. 8.2, we find that $Z_{cu}(T_f, T_i = 4.5\,\mathrm{K}) = 9.9\times10^{16}\,\mathrm{A}^2\,\mathrm{s/m}^4$ corresponds, for copper (RRR = 100), to $T_f \simeq 125\,\mathrm{K}$.

Trivia 9.2 Of the four contemporary mathematicians or physicists (born 1768–1776) below, who is credited with originating dimensional analysis.

i) Ampére; ii) Avogadro; iii) Biot; iv) Fourier.

Q/A 9.2A: SCH Superconducting Magnet (continuation)

t) Dump Initiation Delay A more realistic scenario includes a delay time, τ_{dl}, from the time the hot spot is created, $t = 0$, to the time the breaker is actually opened, initiating a dump. This is because it takes time for the hot spot voltage to rise to a detectable level and for the switch to open. Assuming that during this period, t_d, the current in the superconducting magnet remains at 20 kA, estimate the final hot spot temperature, T_f, for the same conditions and assumptions as **s)**, except here $\tau_{dl} = 0.5$ s.

Applying Eq. 8.66*b* with τ_{dg} in the equation substituted by τ_{eff}, Eq. 8.66*b* is modified and given by:

$$Z(T_f, T_i) = \left(\frac{A_m}{A_{cd}}\right)\left(\tau_{dl} + \tfrac{1}{2}\tau_{eff}\right)J^2_{m_{op}}$$
$$\simeq 13.5 \times 10^{16}\ \mathrm{A^2\,s/m^4}$$

From Fig. 8.2, we find that $Z_{cu}(T_f, T_i = 4.5\,\mathrm{K}) = 13.5 \times 10^{16}\ \mathrm{A^2\,s/m^4}$ corresponds, for copper (RRR = 100), to $T_f \simeq 225$ K, which is nearly the limit of acceptable hot spot temperature. Although, in reality, because of cooling by the coolant, T_f will likely be < 225 K, it is prudent to make sure that for this magnet the breaker switch is opened no later than 0.5 s after the initiation of a hot spot. This may imply that the hot spot must be detected within much less than 0.5 s of its initiation.

Figure 9.4 shows temperature (solid) and pressure (dashed) vs. time plots, computed by Gavrilin [9.2], who applied GANDALF for the case similar to that considered in **s)**, except in this analysis not only is the exact solution of $I_s(t)$ used but also effects of helium cooling and AC losses are included. Chiefly because of helium cooling, the hot spot temperature, T_f, reaches only ∼95 K instead of the 125 K computed in **s)** under adiabatic conditions and with $\tau_{dl} = 0$.. The analysis also shows that the peak helium pressure reached in the conduit is 23.5 atm.

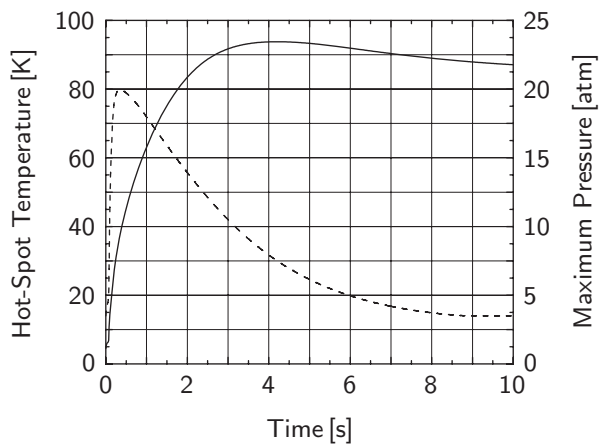

Fig. 9.4 Temperature (solid, the left y-axis) and pressure (dashed, the right y-axis) vs. time plots after a dump from 20 kA, computed by Gavrilin [9.2].

Q/A 9.2A: SCH Superconducting Magnet (continuation)

Table 9.2: Parameters of 5-Coil Resistive Insert [9.3]

Parameters	Coil 1	Coil 2	Coil 3	Coil 4	Coil 5
Winding i.d. ($2a_1$) [mm]	54.0	80.4	151.4	241.8	347.8
Winding o.d. ($2a_2$) [mm]	78.0	145.4	235.8	341.8	500.0
Winding height ($2b$) [mm]	239	238	317	353	605
Central field [T]	4.03	6.33	4.78	4.37	3.72

u) Fault-Mode Axial Forces One likely fault mode in the SCH magnet is a failure, at the nominal operating current of 20 kA, of the 5-coil resistive insert (Fig. 9.1), in which, under the worst scenario, an entire half of each coil is destroyed, and electrically shorted, with the remaining half still alive and generating field. With the top half of each coil shorted, the axial field center of each coil moves downward by $b/2$; in the case of Coil 5 (outermost) this is $151\frac{1}{4}$ mm, as indicated in Fig. 9.1. Table 9.2 lists key parameters of the 5-coil resistive insert [9.3].

When this happens the superconducting magnet will experience a downward axial force, which is matched by an upward force on the resistive magnet. Looking at Fig. 9.1, we may conclude that the largest force on the superconducting magnet will come from Coil 5, despite its central field being smallest, because: 1) Coil 5 is the largest; and 2) it is coupled most closely with the superconducting magnet. Following a step-by-step "simple" but "well-reasoned" procedure described below, compute ballpark forces on the superconducting magnet exerted by Coils 5 and 4. The aim here is to enable a non-specialist on the design team to obtain *ballpark* figures, realizing full well that the team's specialist will use a code to compute "accurate" values.

In **3.5** analytical methods are discussed to compute axial forces between combinations of "simple" solenoids, specifically, "ring" coils, thin-walled coils, and other cases. Of these combinations, the simplest is the force computation between two ring coils (Fig. 3.5), Coil A of diameter a_A, total turns N_A, and current I_A and Coil B of diameter a_B, total turns N_B, and current I_B.

Step-by-Step Procedure

The procedure consists of the following two steps.

Step 1 Model each coil as a ring coil that generates the same central field as the original coil. Compute the total number of turns, N, for the ring coil at 20 kA, the operating current of the SCH. Although the superconducting magnet and resistive coils both are more accurately modeled as "thin-walled" solenoids (Fig. 3.7) than as ring coils, the corresponding axial force expression is more complex than necessary for estimating these figures.

Step 2 Use Eq. 3.34 to compute the axial force between two ring coils: first between the superconducting ring coil (Coil A) and the resistive ring Coil 5 (Coil B); then between the superconducting ring coil (Coil A) and the resistive ring Coil 4 (Coil B).

Q/A 9.2A: SCH Superconducting Magnet (continuation)

u) Fault-Mode Axial Forces (continuation)

Review of Axial Force Between Two "Ring" Coils

For two "ring" coils, Coil A and Coil B, coaxially displaced from each other by a distance ρ, the axial force on Coil A due to Coil B, $F_{zA}(\rho)$, is given by:

$$F_{zA}(\rho) = \frac{\mu_\circ}{2}(N_A I_A)(N_B I_B)\frac{\rho\sqrt{(a_A + a_B)^2 + \rho^2}}{(a_A - a_B)^2 + \rho^2} \times \Big\{k^2 K(k) + (k^2 - 2)[K(k) - E(k)]\Big\} \tag{3.34}$$

$K(k)$ and $E(k)$ are the complete elliptic integrals, respectively, of the first and second kinds. The modulus, k, of the elliptic integrals for this system is given by:

$$k^2 = \frac{4a_A a_B}{(a_A + a_B)^2 + \rho^2} \tag{3.36}$$

We may compute N_A for the "superconducting ring" Coil A by using the field expression given by Eq. 3.111*a*:

$$B_z(0,0) = \frac{\mu_\circ NI}{2a_1} \tag{3.111a}$$

Here, $N = N_A$, $I = I_A$, and $a_1 = a_A$. An appropriate value of a_A for the superconducting coil is the mean winding radius given by its i.d. and o.d. (Table 9.1): $a_A \simeq 458\,\text{mm}$. Thus, with $B_z(0,0) = 14.52\,\text{T}$ and $I_A = 20\,\text{kA}$, we obtain:

$$N_A = \frac{2a_A B_z(0,0)}{\mu_\circ I_A} = \frac{2(0.458\,\text{m})(14.52\,\text{T})}{(4\pi\times10^{-7}\,\text{H/m})(2\times10^4\,\text{A})} = 529$$

Note that N_A is less than the magnet's real number of turns, 756, because to generate the same central field, a ring coil is much more efficient than the real magnet in which turns are distributed over a large winding cross section.

We must be a bit more careful modeling Coil 5 as "ring" coil 5 (Coil B): the central field of 3.72 T cannot be used, because it is the central field generated by Coil 5 before the fault. Now the axial length ($2b$) is halved, and thus we must first compute the central field generated by a Coil 5 of $\beta' = \beta/2$. For a "Bitter" magnet, the "field factor," $[F(\alpha,\beta)]_B$, is given by Eq. 3.115*b*:

$$[F(\alpha,\beta)]_B = \ln\left(\alpha\frac{\beta + \sqrt{1+\beta^2}}{\beta + \sqrt{\alpha^2+\beta^2}}\right) \tag{3.115b}$$

Because the rest of the coil parameters remain the same in the healthy half of the half-burned coil, the new central field, $[B'_z(0,0)]_B$ may be given in terms of the original central field $[B_z(0,0)]_B$ by:

$$\frac{[B'_z(0,0)]_B}{[B_z(0,0)]_B} = \frac{[F(\alpha,\beta']_B}{[F(\alpha,\beta)]_B} = \frac{\ln\left(\alpha\dfrac{\beta' + \sqrt{1+\beta'^2}}{\beta' + \sqrt{\alpha^2+\beta'^2}}\right)}{\ln\left(\alpha\dfrac{\beta + \sqrt{1+\beta^2}}{\beta + \sqrt{\alpha^2+\beta^2}}\right)} \tag{u.1}$$

Q/A 9.2A: SCH Superconducting Magnet (continuation)

u) Fault-Mode Axial Forces *Answer* (continuation)

Inserting into Eq. $u.1$, $[B_z(0,0)]_B = 3.72\,\text{T}$, $\alpha \simeq 1.44\,(=500.0\,\text{mm}/347.8\,\text{mm})$, $\beta \simeq 1.74\,(=605\,\text{mm}/347.8\,\text{mm})$, and $\beta' = \beta/2 \simeq 1.74/2 = 0.87$ for Coil 5, and solving for $[B'_z(0,0)]_B$, we obtain: $[B'_z(0,0)]_B = 2.66\,\text{T}$.

An appropriate value of a_B for Coil 5′ is the geometric mean, $a_B = \sqrt{a_1 a_2} = 208.5\,\text{mm}$ instead of the arithmetic mean, $(a_1+a_2)/2 = 212.0\,\text{mm}$, because the current density in Bitter coils is not uniform but varies as $\propto 1/r$ (Eq. 3.114). For simplicity, let us take $a_B = 174\,\text{mm}$. Thus, with $[B'_z(0,0)]_B = 2.66\,\text{T}$ and $I_B = 20\,\text{kA}$:

$$N_B = \frac{2(0.174\,\text{m})(2.66\,\text{T})}{(4\pi\times 10^{-7}\,\text{H/m})(2\times 10^4\,\text{A})} \simeq 37$$

With $a_A = 0.458\,\text{m}$, $a_B = 0.174\,\text{m}$, $a_A + a_B = 0.632\,\text{m}$ and $\rho = 0.151\,\text{m}$ (1/4 of Coil 5's original height), we first compute the modulus k:

$$\begin{aligned} k^2 &= \frac{4a_A a_B}{(a_A+a_B)^2+\rho^2} \qquad (3.36)\\ &= \frac{4(0.458\,\text{m})(0.174\,\text{m})}{(0.632\,\text{m})^2+(0.151\,\text{m})^2}\\ &\simeq 0.7550 \quad (k \simeq 0.8689) \end{aligned}$$

Inserting $K(0.8689) = 2.1655$, $E(0.8689) = 1.2079$, $a_A - a_B = 0.284\,\text{m}$, and the rest of other parameters into Eq. 3.34, we obtain the force on Coil A (superconducting magnet) by Coil B (half of Coil 5), $F_{zA}(\rho = 151\,\text{mm})$:

$$\begin{aligned} F_{zA}(151\,\text{mm}) &= \frac{(4\pi\times 10^{-7}\,\text{H/m})}{2}(529)(2\times 10^4\,\text{A})(37)(2\times 10^4\,\text{A})\\ &\quad\times\left[\frac{(0.151\,\text{m})\sqrt{(0.632\,\text{m})^2+(0.151\,\text{m})^2}}{(0.284\,\text{m})^2+(0.151\,\text{m})^2}\right.\\ &\qquad\left.\times\Big\{0.7550(2.1655)+(0.7550-2)(2.1655-1.2079)\Big\}\right]\\ &= (4.92\,\text{MN})\times\big[0.948\times 0.443)\big] = 2.06\,\text{MN} \end{aligned}$$

To compute the force on Coil A by a Coil B that is half of Coil 4, we have the following new parameters for Coil B: $\alpha = 1.41$; $\beta = 1.46$; $\beta' = 0.73$; $B'_z(0,0) = 2.96\,\text{T}$; $N_B \simeq 28$; $a_B = 0.121\,\text{m}$. With $\rho = 0.088\,\text{m}$; $a_A + a_B = 0.579\,\text{m}$; $a_A - a_B = 0.337\,\text{m}$; we have: $k^2 \simeq 0.6463$ $(k \simeq 0.8039)$, which gives $K(0.8039) \simeq 2.0030$ and $E(0.8039) \simeq 1.2728$. Inserting these values into Eq. 3.34, we obtain $F_{zA}(88\,\text{mm}) = 0.49\,\text{MN}$ on the superconducting magnet by the half-burnt Coil 4. This is less than a fourth of the force from Coil 5, suggesting that the contributions of Coils 1–3 may be neglected.

The total force (from Coils 1–5) computed with a code is 1.9 MN [9.3]. Our method, based on a simple analytical model requiring a "reasonable" computing period with a hand calculator, generates an answer (2.06 MN from Coil 5 only) that is well within the range expected of an estimated figure.

Q/A 9.2A: SCH Superconducting Magnet (continuation)

Magnetic Field Shielding

Because the larger a magnet, in size, field strength, or both, the further the reach of its fringe field, a "large" magnet is generally "shielded." Active shielding uses an electromagnet (shield coil); passive shielding, a ferromagnetic structure (steel shell). An active shield should be as far away from its main magnet as possible consistent with other design specifications, because it subtracts from the field; a passive shield usually adds to the field. High-field ($> 1\,\mathrm{T}$) MRI and most NMR magnets are now shielded, actively, passively, or by a combination of both.

As stated at the outset, the SCH magnet is housed in a cell among neighboring experimental cells. To minimize the field interferences on the experiments conducted in the neighboring cells, the SCH magnet system has a shield coil, as indicated on the right-hand side of the cross-sectional drawing of the SCH magnet shown in Fig. 9.5. The resistive magnet, which in comparison with the large-bore main superconducting magnet contributes little to the fringe field, is omitted from the drawing. The left-hand side of Fig. 9.5 shows a steel shell for passive shielding, an alternative way to shield the main superconducting magnet.

As shown in Fig. 9.5, the active shield coil, as first proposed for this SCH system [9.1], actually consists of two subcoils, one placed above and the other placed below the midplane; here each subcoil will be modeled as a ring coil. The steel shell is a cylinder that in the analysis here is modeled to completely surround the main magnet azimuthally. Important aspects of both elements are studied here.

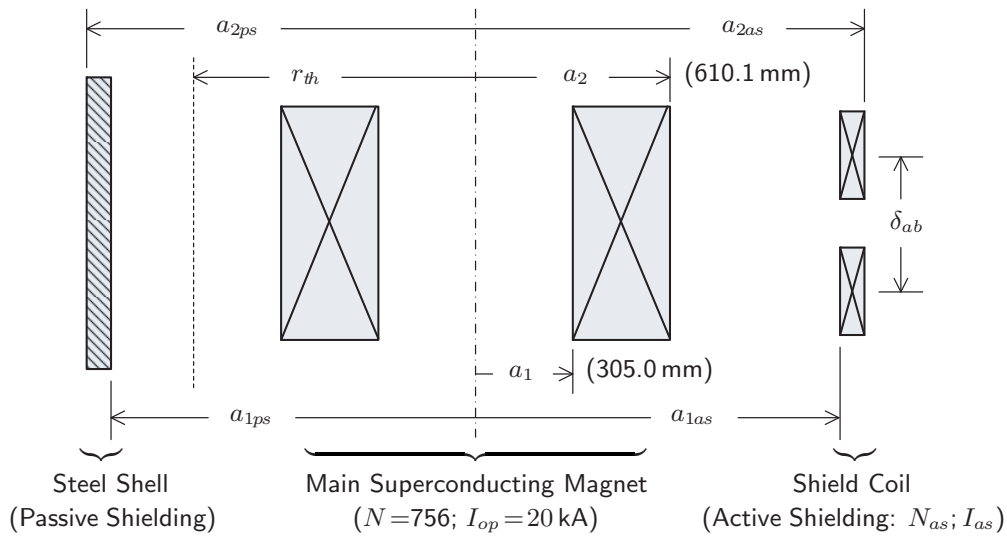

Fig. 9.5 Cross sectional view of the main superconducting magnet with either a shield coil (active shielding) or a steel shell (passive shielding). Note that the active shield coil consists of two subcoils, one above and the other below the midplane.

Q/A 9.2A: SCH Superconducting Magnet (continuation)

v) Active Shield Coil—Number of Turns Model the two-subcoil shield coil as a *single* shield coil. Then, transform both the main superconducting coil and this model shield coil to dipole moments. Now, estimate the total number of turns for this model shield coil to make its magnetic moment match that of the main magnet. The shield coil and the main magnet are connected in series but in *reverse polarity*, and operated at 20 kA.

The magnetic field *far* from the center of a solenoidal magnet, $\vec{H}_f$, may be modeled by a dipole moment (**PROBLEM 3.11**):

$$\vec{H}_f = H_0 \left(\frac{R_e}{r}\right)^3 (\cos\theta\,\vec{\imath}_r + \tfrac{1}{2}\sin\theta\,\vec{\imath}_\theta) \tag{3.163}$$

R_e is the dipole moment radius. For a solenoid of uniformly-distributed ampere-turns, NI, the product $H_0 R_e^3$ is given by Eq. 3.165:

$$H_0 R_e^3 = \tfrac{1}{6}(a_1^2 + a_2^2 + a_1 a_2)NI \tag{3.165}$$

where a_1 and a_2 are, respectively, the inside and outside winding radii of the magnet. Because of $\vec{H}_f \propto (R_e/r)^3$ (Eq. 3.163) and $H_0 R_e^3 \propto a_1^2$ (Eq. 3.165), we may indeed ignore the resistive insert here—$a_1 = 173.9$ mm for Coil 5 and $a_1 = 305.0$ mm for the superconducting magnet. Applying Eqs. 3.163 and 3.165 to the main superconducting magnet and shield coil (subscript *as*), we have:

$$a_1^2(1 + \alpha^2 + \alpha)NI_{op} = a_{1as}^2(1 + \alpha_{as}^2 + \alpha_{as})N_{as}I_{as} \tag{v.1}$$

where $\alpha_{as} = a_{2as}/a_{1as}$. Solving Eq. v.1 for N_{as}, with $I_{as} = I_{op}$, we obtain:

$$N_{as} = \left(\frac{a_1}{a_{1as}}\right)^2 \left(\frac{1+\alpha^2+\alpha}{1+\alpha_{as}^2+\alpha_{as}}\right) N \tag{v.2}$$

With $a_1 = 0.305$ m, $a_{1as} = 1.203$ m, $\alpha = 2.00$, $\alpha_{as} = 1.04$, and $N = 756$ inserted to Eq. v.2, N_{as} becomes:

$$N_{as} = \left(\frac{0.305\,\text{m}}{1.203\,\text{m}}\right)^2 \left(\frac{1+4+2}{1+1.08+1.04}\right)(756)$$

$$\simeq 109$$

The actual value is 78 for the shield coil [9.4], which actually consists of *two* subcoils, as shown in Fig. 9.5. The magnetic moment is undiminished by axial displacement of loops; only the field, not the magnetic moment, decreases if turns are spread out axially.

Q/A 9.2A: SCH Superconducting Magnet (continuation)

w) Field Subtraction from Central Field by Active Shield Coil As noted above, the active shield coil generates a field directed opposite from that of the superconducting magnet. Compute the axial field at the center, $B_z^{as}(0,0)$, of the active shield coil. Use the following parameters for the shield coil: $a_{1as}=1.203\,\text{m}$; $a_{2as}=1.250\,\text{m}$; $b_{as}=0.471\,\text{m}$ (in the actual system, the active shield coil consists of two shorter subcoils with a gap at the midplane [9.4]); $N_{as}=78$; and $I_{as}=20\,\text{kA}$.

Field computation is a straightforward application of Eq. 3.110:

$$B_z(0,0)=\frac{\mu_\circ NI}{2a_1(\alpha-1)}\ln\left(\frac{\alpha+\sqrt{\alpha^2+\beta^2}}{1+\sqrt{1+\beta^2}}\right) \tag{3.110}$$

With $N\to N_{as}=78$, $I\to I_{as}=20\,\text{kA}$, $\alpha\to\alpha_{as}=1.04$, $\beta\to\beta_{as}=0.392$, and $a_1\to a_{1as}=1.203$, $B_z^{as}(0,0)$ becomes:

$$B_z^{as}(0,0)=\frac{(4\pi\times10^{-7}\,\text{H/m})(78)(20\times10^3\,\text{A})}{(2.406\,\text{m})(1.04-1)}\ln\left(\frac{1.04+\sqrt{(1.04)^2+(0.392)^2}}{1+\sqrt{1+(0.392)^2}}\right)$$
$$\simeq 0.75\,\text{T}$$

Because without the active shield coil, the central field of the main superconducting magnet at 20 kA is 14.52 T, as computed in ***Q/A 9.1*: b)**, −0.75 T at the center by the active shield coil is slightly over 5%, which is not altogether inconsequential.

x1) Active Shield Coil—Interaction Force: 1 If the shield coil were a single coil as modeled, then there would be no net interaction force between it and the main magnet. In the original system, the shield coil is split into two subcoils. Still, there will be no net interaction force between the shield coil as a whole and the main magnet, but there is between each subcoil and the the main magnet. We shall here compute its *ballpark* magnitude by modeling both the main magnet and one of the subcoils as "ring coils." Take $\rho=0.277\,\text{m}$ (center-to-center displacement). Note that because δ_{ab} in Fig. 9.5 is equal to 2ρ, $\delta_{ab}=0.554\,\text{m}$.

The main magnet was already modeled as a "ring coil" in **t)** above: $N_A=529$; $a_A\simeq 458\,\text{mm}$. Similarly, we may model one of the subcoils as a "ring coil" generating a central field of 0.375 T (half of 0.75 T, though each is displaced vertically): $a_B=1.227\,\text{m}$ (average of a_{1as} and a_{2as}), and N_B is given by:

$$N_B\simeq\frac{(0.375\,\text{T})2a_B}{\mu_\circ I_B}=\frac{(0.375\,\text{T})2(1.227\,\text{m})}{(4\pi\times10^{-7}\,\text{H/m})(20\times10^3\,\text{A})}\simeq 37$$

It is not surprising that the "effective" number of turns of 37 is very close to the actual number of turns of 39, because each subcoil, with $\alpha=1.04$ and small β clearly indicates that it is essentially a ring coil ($\alpha=1$, $\beta=0$). First, we compute the modulus constant, k, given by Eq. 3.36 used in **t)** above.

$$k^2=\frac{4a_Aa_B}{(a_A+a_B)^2+\rho^2} \tag{3.36}$$
$$=\frac{4(0.458\,\text{m})(1.227\,\text{m})}{(0.458\,\text{m}+1.227\,\text{m})^2+(0.277\,\text{m})^2}\simeq 0.7709\quad(k\simeq 0.8780)$$

Q/A 9.2A: SCH Superconducting Magnet (continuation)

x1) Active Shield Coil—Interaction Forces: 1 *Answer* (continuation)

The interaction force between two "ring coils" is given by Eq. 3.34:

$$F_{z_A}(\rho) = \frac{\mu_\circ}{2}(N_A I_A)(N_B I_B)\frac{\rho\sqrt{(a_A+a_B)^2+\rho^2}}{(a_A-a_B)^2+\rho^2} \times\left\{k^2K(k)+(k^2-2)[K(k)-E(k)]\right\} \tag{3.34}$$

With $K(0.8780)=2.1957$, $E(0.8780)=1.1977$, $a_A+a_B=1.685\,\text{m}$, $a_A-a_B=-0.769\,\text{m}$, we obtain the force on Coil A (main magnet) by Coil B (the upper of the two subcoils), $F_{z_A}(\rho=0.277\,\text{m})$:

$$\begin{aligned} F_{z_A}(0.277\,\text{m}) &= \frac{(4\pi\times10^{-7}\,\text{H/m})}{2}(529)(2\times10^4\,\text{A})(37)(-2\times10^4\,\text{A}) \\ &\quad\times\left[\frac{(0.277\,\text{m})\sqrt{(1.685\,\text{m})^2+(0.277\,\text{m})^2}}{(-0.769\,\text{m})^2+(0.277\,\text{m})^2}\right. \\ &\qquad\left.\times\left\{0.7709(2.1957)+(0.7709-2)(2.1957-1.1977)\right\}\right] \\ &= -(4.91\,\text{MN})\times(0.7080\times0.4660) = -1.62\,\text{MN} \end{aligned}$$

The interaction force on the main magnet is negative (downward); the same force acts upward on the shield subcoil above the midplane; i.e., if the coil weren't restrained, it would fly away from the midplane. Of course combined with the second subcoil below, the *net* interaction force from the main magnet is zero.

x2) Active Shield Coil—Interaction Force: 2 Here we compute the *attractive* force between the two subcoils, modeling each as a "ring coil" of the same diameter (1.227 m), number of turns (37), and current (−20 kA), with $\rho=0.554\,\text{m}$, which in this case is equal to δ_{ab} of Fig. 9.5.

Because the rings have the same diameter (a), and though here the condition $\rho(=0.554\,\text{m}) \ll 2a(=2.454\,\text{m})$ is not strictly met, we use the much simpler version of Eq. 3.34 given by Eq. 3.39*d* valid for $\rho \ll 2a$, noting that here $N_B I_B = N_A I_A$:

$$\begin{aligned} F_{z_A}(\rho) &\simeq \mu_\circ(N_A I_A)(N_B I_B)\left(\frac{a}{\rho}\right) \qquad (3.39d) \\ &= \mu_\circ(N_A I_A)^2\left(\frac{a}{\rho}\right) \\ &= (4\pi\times10^{-7}\,\text{H/m})[(37)(-2\times10^4\,\text{A})]^2\left(\frac{1.227\,\text{m}}{0.554\,\text{m}}\right) \\ &\simeq 1.5\,\text{MN} \end{aligned}$$

This agrees quite well with 1.6 MN computed with a code [9.3].

Q/A 9.2A: SCH Superconducting Magnet (continuation)

y1) Passive Shield Shell: 1 An alternative to active shielding is passive shielding, achieved with ferromagnetic material, often steel (see **PROBLEM 2.3** and Table 2.5). The advantage of passive shielding over active shielding is generally the cost, but its cost advantage can diminish for "large" and "high-field" magnets. Another advantage, often overlooked, is its "reverse-shielding" capability, i.e., shielding the main magnet against the fringe fields of neighboring magnets. The biggest disadvantage of passive shielding is its massiveness.

Here, consider a steel cylinder of inside radius $a_1 \equiv a_{1as} = 1.203\,\text{m}$ and height $2b_s = 2a_{1as}$ (Fig. 9.5), equal to the active shield coil i.d. Assuming that the main superconducting magnet ($N = 756$; $I_{op} = 20\,\text{kA}$) may be modeled as a dipole moment and its $B_0R_e^3$ given by Eq. $v.1$ (ignoring the resistive insert), estimate the cylinder's outside radius, a_{2as}, that will make the cylinder's thickness sufficient to keep the magnetization of steel, $\mu_\circ M_s$, at 1.25 T, at which level the steel can still retain a high enough $(\mu/\mu_\circ)_{dif}$: $(\mu/\mu_\circ)_{dif} = 180$ (Table 2.5 for as-cast steel).

At $(\mu/\mu_\circ)_{dif} = 180$ we may treat the steel as *ideal* $(\mu/\mu_\circ)_{dif} = \infty$. Of all the flux lines of the main magnet emanating from the magnet bore, those at $r \geq a_{1as}$ enter the steel cylinder at the top and leave at the bottom, returning to the magnet bore. A bit complicated are the flux lines in the annular space between the magnet outer radius, $a_2 \simeq 0.610\,\text{m}$, and the steel cylinder's inner radius, $a_{1ps} = 1.203\,\text{m}$.

Here, each flux line follows a path of least "magnetic" resistance through steel rather than air. Thus, the flux line just outside $r = a_2$ may flow either vertically down in the air to the midplane over a distance of $b = 0.471\,\text{m}$ ($2b = 942.0\,\text{mm}$, Table 9.1) or else radially first in the air over a distance of $a_{1ps} - a_2 = 0.593\,\text{m}$ ($= 1.203\,\text{m} - 0.610\,\text{m}$) to the top of the steel cylinder and then vertically, "resistance-free," in the steel to the midplane; because $0.471\,\text{m} < 0.593\,\text{m}$, this particular flux line does not flow through the steel. Using this argument we may assign a threshold radius, r_{th}, beyond which flux lines detour to flow through the steel cylinder, roughly as $a_{1ps} - b = 0.732\,\text{m}$. That is, all the flux lines from $r_{th} = 0.732\,\text{m}$ to $r = \infty$ flow through the steel cylinder. Thus, the total flux from $r = r_{th}$ to ∞ at the midplane, $\Phi(r_{th}/\infty, z = 0)$ and that through the steel cylinder at the midplane, $\Phi_s(z = 0)$, are given, with $\alpha = a_2/a_1$, respectively by:

$$\Phi(r_{th}/\infty, z = 0) = \tfrac{1}{2}\left[\frac{\mu_\circ a_1^2(1+\alpha^2+\alpha)NI_{op}}{6}\right]\int_{r_{th}}^{\infty}\frac{2\pi r}{r^3}\,dr \qquad (y1.1a)$$

$$\Phi_z(z = 0) = \pi(a_{2ps}^2 - a_{1ps}^2)(\mu_\circ M_s) \qquad (y1.1b)$$

Because the two fluxes are equal, $\Phi(r_{th}/\infty, z = 0) = \Phi_z(z = 0)$, we have:

$$\frac{\mu_\circ a_1^2(1+\alpha^2+\alpha)NI_{op}}{6r_{th}} = (a_{2ps}^2 - a_{1ps}^2)(\mu_\circ M_s) \qquad (y1.2)$$

Solving Eq. $y1.2$ for a_{2ps}, we obtain:

$$a_{2ps} = \sqrt{a_{1ps}^2 + \frac{\mu_\circ a_1^2(1+\alpha^2+\alpha)NI_{op}}{6r_{th}(\mu_\circ M_s)}} \qquad (y1.3)$$

Q/A 9.2A: SCH Superconducting Magnet (continuation)

y1) Passive Shield Shell: 1 *Answer* (continuation)

Inserting appropriate parameter values in Eq. $y1.3$, we compute

$$a_{2ps} = \sqrt{(1.203\,\mathrm{m})^2 + \frac{(4\pi\times10^{-7}\,\mathrm{H/m})(0.305\,\mathrm{m})^2(7)(756)(20\times10^3\,\mathrm{A})}{6(0.732\,\mathrm{m})(1.25\,\mathrm{T})}}$$

$$= \sqrt{1.447\,\mathrm{m}^2 + 2.254\,\mathrm{m}^2} = 1.924\,\mathrm{m}$$

The steel cylinder thickness, $a_{2ps} - a_{1ps}$ thus becomes 72 cm. The total weight of this steel cylinder, 2.4-m high, is 133,000 kg or over 100 tonnes.

Because the field within the steel cylinder is chiefly axially (z)-directed and because the tangential field (here z-directed) must be continuous at the steel-air boundary, the magnetic field is given by $\sim\mu_\circ M_s/(\mu/\mu_\circ)_{dif}$, i.e., $1.25\,\mathrm{T}/180 = 0.0069\,\mathrm{T}$ or 69 gauss at $r = a_{1ps} = 1.203\,\mathrm{m}$ and $r = a_{2ps} = 1.924$ m; by $r \simeq 20\,\mathrm{m}$, the field falls to less than 1 gauss. From the law of flux continuity in the normal (axial) direction, the flux in the steel cylinder, 1.25 T and directed downward, becomes upward as it "returns" towards the magnet midplane, enhancing the central field of 14.52 T generated by the main superconducting magnet. In this respect this passive shielding is superior to active shielding.

y2) Passive Shield Shell: 2 Clearly, the further away from the main magnet the steel shell is placed, the thinner will be the shell thickness required, as indicated explicitly by Eq. $y1.3$. However, according to a basic principle of passive shielding, to cancel a given dipole moment the amount of steel is independent of the location of steel shielding, if the steel is magnetized to the same level. Here, consider Shell 2 of $a_{1ps} = 1.805\,\mathrm{m}$ (3.6-m high), 50% larger than Shell 1, and compute new a_{2ps} and check to see if the mass of Shell 2 is still 133,000 kg, computed above for Shell 1.

Using the same argument as above, we obtain a new threshold radius for flux lines: $r_{th} = a_{1ps} - b = 1.805\,\mathrm{m} - 0.471\,\mathrm{m} = 1.334\,\mathrm{m}$. Inserting appropriate parameter values in Eq. $w.3$, we compute

$$a_{2ps} = \sqrt{(1.805\,\mathrm{m})^2 + \frac{(4\pi\times10^{-7}\,\mathrm{H/m})(0.305\,\mathrm{m})^2(7)(756)(20\times10^3\,\mathrm{A})}{6(1.334\,\mathrm{m})(1.25\,\mathrm{T})}}$$

$$= \sqrt{3.258\,\mathrm{m}^2 + 1.237\,\mathrm{m}^2} = 2.120\,\mathrm{m}$$

The cylinder thickness, $a_{2ps} - a_{1ps}$, thus becomes 32 cm, less than half that of Shell 1, resulting in a total mass of 109,000 kg for Shell 2 cylinder (3.6-m high), somewhat less than that for Shell 1. This discrepancy implies that this simple analytic approach is valid only for a *ballpark* estimate of the mass of a steel shield.

Answer to TRIVIA 9.2 iv). The French mathematician Jean Baptise Joseph Fourier (1768–1830) made it clear, in his work on heat conduction, that a scientific equation must involve a consistent set of units.

EXAMPLE 9.2B: Superconducting Coil on Steel Plate

In this example of a solenoidal magnet system, we will apply the basic principle used to study field-shielding of a spherical volume by ferromagnetic material (**PROBLEM 2.3**) and the effect of steel yokes in an ideal dipole (**PROBLEM 3.8**) to study how the field generated by a superconducting coil is affected by a circular steel plate on which the coil is placed. We shall see that the steel plate enhances the field significantly above the plate and virtually eliminates the field below the plate. As in the cases of the field shielding and the dipole magnet, the steel here too is modeled by an "ideal" ferromagnetic material of $\mu/\mu_\circ = \infty$.

Figure 9.6 shows the cross sectional view of a superconducting coil placed on a circular steel plate of large diameter and thickness δ_{st}. The center of the z-r coordinates coincides with the coil's center. Here, the coil is drawn without its coil form. Table 9.3 presents parameters of the coil.

Figure 9.7 shows $B_z(z, r)$ plots at $z = 0$, 5, 7.5, 10, 12.5, 15, 17.5, and 20 mm generated by the coil at 25 A without the steel disk.

Table 9.3: Coil Parameters

Parameters	*Value*
Winding i.d. ($2a_1$) [mm]	40
Winding o.d. ($2a_2$) [mm]	70
Winding height ($2b$) [mm]	10
Total turns (N)	150

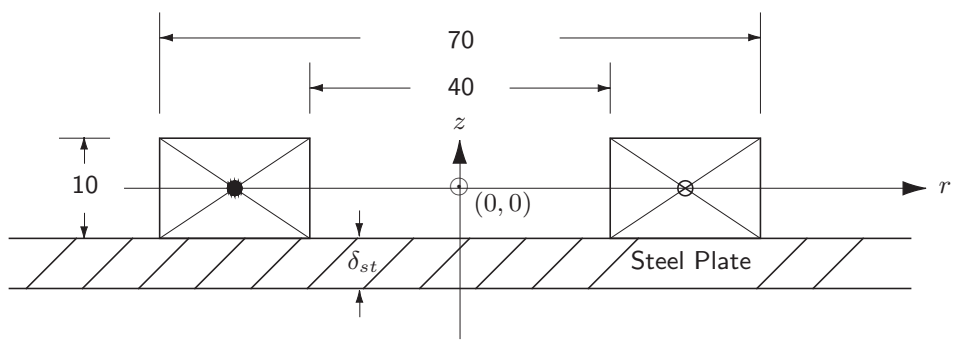

Fig. 9.6 Cross sectional view of a superconducting coil on a steel disk. Dimensions are in mm.

EXAMPLE 9.2B: Superconducting Coil on Steel Plate (continuation)

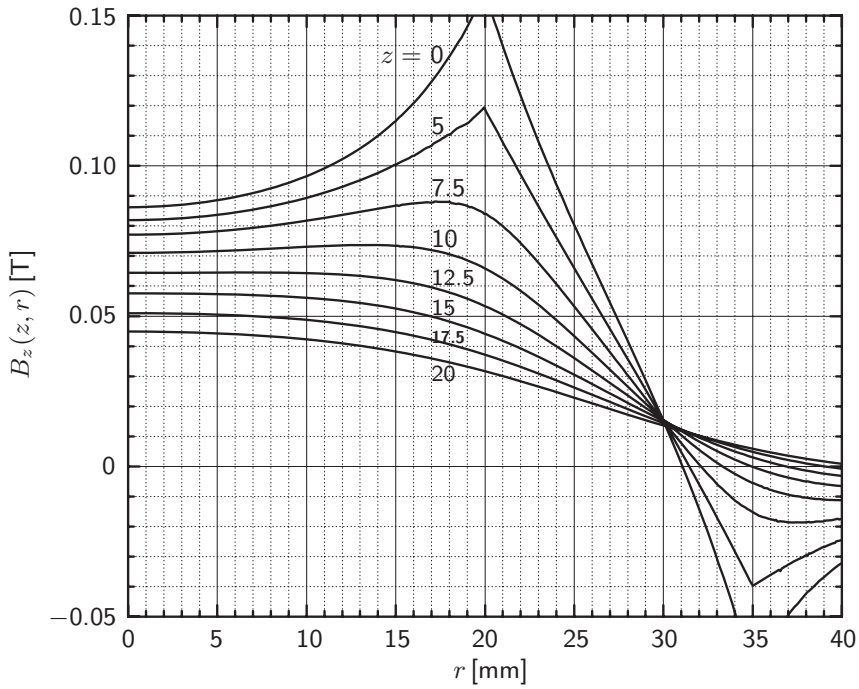

Fig. 9.7 $B_z(z,r)$ generated by the coil at $z=0$, 5, 7.5 10, 12.5, 15, 17.5, and 20 mm at 25 A without the steel plate. $B_z(0, 20\,\text{mm}) = 0.158$ T and $B_z(0, 35\,\text{mm}) = -0.068$ T.

Review of Inductance

As discussed in **3.7** the coil's self inductance, L, may be given from an equation relating Φ and I:

$$\Phi = LI \tag{3.78}$$

Φ is the total magnetic flux linkages at current I:

$$\Phi = 2\pi \sum_{j=1}^{N} \int_0^{R_j} r\, B_z(z_j, r)\, dr \tag{9.1}$$

where R_j is the radius of the j^{th} turn located at an axial distance $z = z_j$. Obviously this integration is quite tedious to carry out by hand, but this is unnecessary nowadays, with a variety of codes to compute inductances.

We shall here compute a "reasonably accurate" value of the inductance of the coil shown in Fig. 9.6 by combining Eq. 3.78 and a simplified version of Eq. 9.1. Thus:

$$L \simeq \frac{2N\pi}{I} \int_0^{a_2} B_z(z=0, r)\, r\, dr \tag{9.2}$$

In Eq. 9.2, the integrand of Eq. 9.1, $rB_z(z_j, r)$, is approximated by a simpler integrand involving only the field along the coil's *midplane* $B_z(0, r)$. Note that Eq. 9.2 gives the "upper limit" of L because not all N turns link the flux all the way to $r = a_2$; some in fact link the flux only up to a_1. Perhaps the midway point, $(a_1 + a_2)/2$, is a good compromise for the radial limit of the integration.

Q/A 9.2B: Superconducting Coil on Steel Plate

a) Coil Inductance Using Eq. 9.2 and the $B_z(0,r)$ plot of Fig. 9.7, estimate the coil's self inductance (with no steel disk). Use $B_z(0, r=20\,\text{mm}) = 0.158\,\text{T}$ and $B_z(0, r=35\,\text{mm}) = -0.068\,\text{T}$.

First, data for $B_z(0,r)$ and $B_z(0,r)\,r$ are tabulated in Table 9.4. Figure 9.8 shows the $B_z(0,r)r$ vs. r plot, from which $\int B_z(0,r)r\,dr$ and Φ may be computed:

$$\int_0^{a_2} B_z(0,r)r\,dr \simeq 38.0\,\text{T mm}^2 \quad \text{[shaded area in Fig. 9.8]}$$

$$= 3.80\times10^{-5}\,\text{T m}^2$$

$$\Phi = 2\pi(3.80\times10^{-5}\,\text{T m}^2) \simeq 23.9\times10^{-5}\,\text{T m}^2$$

Thus,

$$L = \frac{N\Phi}{I} \simeq \frac{150(23.9\times10^{-5}\,\text{T m}^2)}{(25\,\text{A})} \simeq 1.43\,\text{mH}$$

which is ∼10% above the actual value of 1.33 mH. Equation 9.2 overestimates L because $B_z(0,r)$ is greater than $B_z(z,r)$ averaged over the range $-5 \le z \le 5\,\text{mm}$. Note that because the $B_z(0,r)r$ integration is negative between $r \simeq 31\,\text{mm}$ and a_2 and it matches closely the positive integration between $(a_1+a_2)/2 = 27.5\,\text{mm}$ and 31 mm, the integration between 0 and a_2 turns out to be nearly equal to that between 0 and $(a_1+a_2)/2$, which as noted above is a more appropriate limit.

As discussed in **3.7.2**, for a solenoid of a_1, α, β, and number of turns N, its self inductance L may also be computed from:

$$L = \mu_o a_1 N^2 \mathcal{L}(\alpha,\beta) \tag{3.81}$$

where $\mathcal{L}(\alpha,\beta)$, shown in Fig. 3.14, depends only on α and β.

From Table 9.3 we have: $a_1 = 0.02\,\text{m}$; $\alpha = 70/40 = 1.75$; $\beta = 10/40 = 0.25$; and $N = 150$. Using the $\mathcal{L}(\alpha,\beta)$ plots of Fig. 3.14 and making linear interpolation between $\beta=0.2$ and $\beta=0.4$ lines at $\alpha=1.75$, we find $\mathcal{L}(1.75, 0.25) \simeq 2.35$. Thus:

$$L \simeq (4\pi\times10^{-7}\,\text{H/m})(0.02\,\text{m})(150)^2(2.35) = 1.33\,\text{mH}$$

which is indeed equal to the actual value.

Table 9.4: $B_r(0,r)$ & $B_z(0,r)r$

r [mm]	$B_z(0,r)$ [T]	$B_z(0,r)r$ [T mm]
0	0.0863	0
5	0.0886	0.443
10	0.0966	0.966
15	0.1150	1.725
20	0.1579	3.158
25	0.0735	1.838
30	0.0221	0.664
35	−0.0678	−2.373

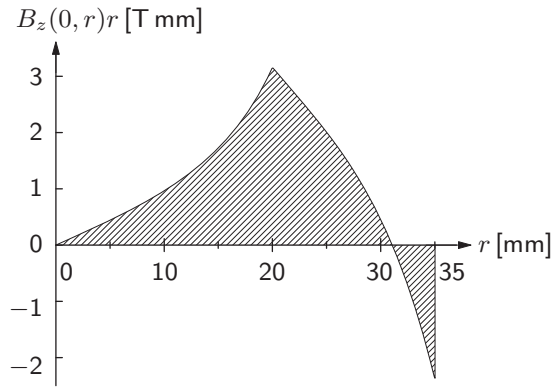

Fig. 9.8 $B_z(0,r)r$ vs. r plot.

Q/A 9.2B: Superconducting Coil on Steel Plate (continuation)

b) Steel Plate We shall now consider the steel plate. To simplify the problem, we first assume the plate to be of *infinite* permeability, i.e., $\mu/\mu_\circ = \infty$. Next, to simulate the plate's effect on the magnetic field above it, i.e., $z \geq -5\,\text{mm}$, we replace the plate with an image coil identical to the original coil directly beneath it, as illustrated in Fig. 9.9.

Explain how the image coil placed directly beneath the original coil simulates the effect of an ideal steel plate, by showing that the image coil satisfies the boundary conditions imposed at $(r, z = -5\,\text{mm})$ by this ideal steel plate.

The boundary condition for an ideal steel plate of $\mu/\mu_\circ = \infty$ is that the *tangential* (here radial) component of magnetic field at the plate surface must be zero, i.e., $B_r(z = -5\,\text{mm}, r) = 0$. That is, the field must enter or leave the plate in the direction normal to the disk surface. A coil identical to the original coil and right beneath it satisfies, through symmetry, this boundary condition at $z = -5\,\text{mm}$, the location of the upper face of the steel plate.

c) Field Enhancement by Steel Plate Using the model shown in Fig. 9.9, compute the coil's field at the center, $B_z(0,0)$, for the system shown in Fig. 9.6 when the coil is energized at 25 A.

W*ithout* the steel plate, the coil at 25 A, from Fig. 9.7, generates $[B_z(0,0)]_{\text{w/o}} \simeq 0.0863\,\text{T}$. *With* the steel plate, we must include the field contribution of the *image coil*, centered at $r = 0$ and $z = -10\,\text{mm}$.

$$\begin{aligned}[B_z(0,0)]_{\text{with}} &= [B_z(0,0) + B(z = 10\,\text{mm}, 0)]_{\text{w/o}} \\ &\simeq 0.0863 + 0.0711 \simeq 0.1574\,\text{T}\end{aligned}$$

The second term in the right-hand side is the contribution at $(z = 0,\, 0)$ of the image coil, whose center is at $(z = -10\,\text{mm}, 0)$. Note that the steel plate does not quite double the field in the upper region—it does so only at $z = -5\,\text{mm}$. It is as if the steel plate flipped the field in the lower region over to the upper region about the x-y plane at $z = -5\,\text{mm}$. Below an ideal steel plate, the field is zero.

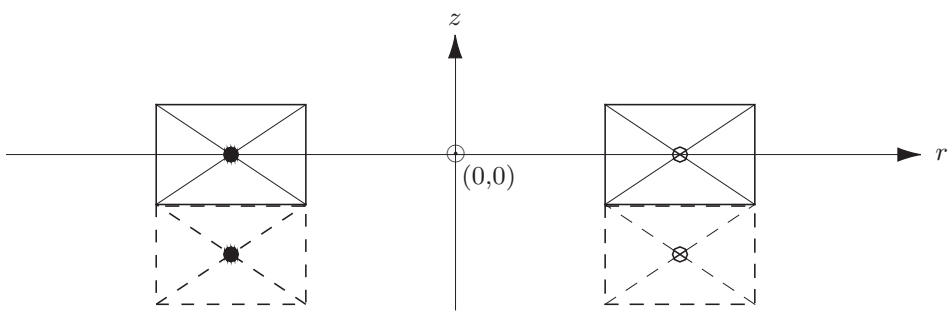

Fig. 9.9 Coil arrangement to model the effect of the steel plate. Dimensions are the same as in Fig. 9.6. An *image coil* identical to the original and directly beneath it replaces the steel plate, here idealized to be of of $\mu/\mu_\circ = \infty$.

Q/A 9.2B: Superconducting Coil on Steel Plate (continuation)

d) Plate Thickness Compute the minimum thickness of the steel plate required to keep the steel disk's magnetization induction ($\mu_\circ M_{st}$) below 1.25 T to ensure that our assumption of $\mu/\mu_\circ \gg 1$ for the steel is valid.

We proceed through the following steps: 1) Assume that the steel plate is of $\mu/\mu_\circ = \infty$; 2) Determine, from Fig. 9.7, $r = r_\pm$, the radial location at $z = -5$ mm at which the direction of *total* B_z (by the real and image coils) changes—B_z leaves the steel plate in the range $0 \le r \le r_\pm$ and enters it in the range $r \ge r_\pm$; 3) Determine the total flux leaving the steel plate in the range $0 \le r \le r_\pm$; and 4) Equate $\Phi_r(r = r_\pm)$ to the total flux flowing radially in the steel at $r = r_\pm$.

The total axial field at the ideal steel is *twice* $B_z(-5\,\text{mm}, r)$ of the real coil—twice because of the identical contribution by the image coil. Note that $B_z(-5\,\text{mm}, r) = B_z(5\,\text{mm}, r)$. Values of $2B_z(5\,\text{mm}, r)$ and $2B_z(5\,\text{mm}, r)r$ are given in Table 9.5. The $\int 2B_z r\, dr$ is obtained from the $2B_z(5\,\text{mm}, r)r$ plot shown in Fig. 9.10:

$$\int_0^{r_\pm} 2B_z(z = 5\,\text{mm}, r)r\, dr \simeq 7.22 \times 10^{-5}\,\text{T m}^2 \quad \text{(from Fig. 9.10)}$$

The total flux leaving the steel disk in the range $0 \le r \le r_\pm = 31.56$ mm (Fig. 9.10), $\Phi_{r_\pm}$, is thus:

$$\Phi_{r_\pm} = 2\pi(7.22 \times 10^{-5}\,\text{T m}^2) \simeq 45.4 \times 10^{-5}\,\text{T m}^2$$

This flux is flowing inward at $r = r_\pm$ and equal to the total flux flowing through the steel, Φ_{st}:

$$\Phi_{st} = 2\pi\, r_\pm \delta_{st}(\mu_\circ\, M_{st}) = \Phi_{r_\pm}$$

Solving the above equation for δ_{st}, we have:

$$\delta_{st} = \frac{\Phi_{r_\pm}}{2r_\pm(\mu_\circ\, M_{st})} = \frac{45.4 \times 10^{-5}\,\text{T m}^2}{2\pi(0.03156\,\text{m})(1.25\,\text{T})} \simeq 1.8\,\text{mm}$$

That is, a ∼2-mm thick steel plate should be ample for the job. From Table 2.5 we note that as-cast steel has $(\mu/\mu_\circ)_{dif} = 180$ at $\mu_\circ M = 1.25$ T.

Table 9.5:
$2B_z(5\,\text{mm}, r)$ and $2B_z(5\,\text{mm}, r)r$

r [mm]	$2B_z(5\,\text{mm}, r)$ [T]	$2B_z(5\,\text{mm}, r)r$ [T mm]
0	0.1640	0
5	0.1675	0.838
10	0.1788	1.788
15	0.2010	3.015
20	0.2377	4.754
25	0.1282	3.205
30	0.0344	1.032
31.56	0	0

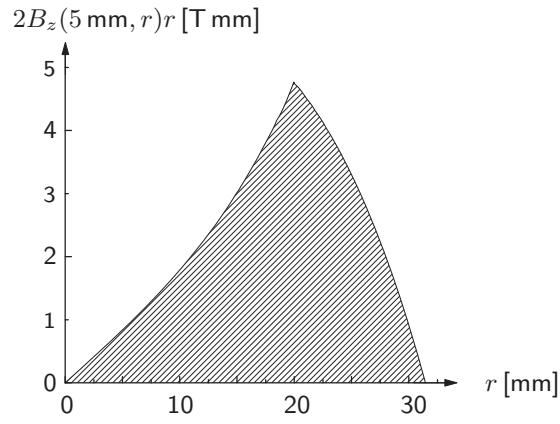

Fig. 9.10 $B_z(5\,\text{mm}, r)r$ vs. r plot.

Q/A 9.2B: Superconducting Coil on Steel Plate (continuation)

d) Plate Thickness *Answer* (continuation)

What should the plate's outer radius, r_{od}, be? Theoretically, it should be infinite, which of course is impractical. What we need to do is to integrate $rB_z(r, 5\,\text{mm})$ from $r_\pm$ to r_{od} such that the following condition is satisfied.

$$\int_{r_\pm}^{r_{od}} B_z(r, z=5\,\text{mm}) r\, dr > \sim (0.8) \int_0^{r_\pm} B_z(r, z=5\,\text{mm}) r\, dr$$

That is, the steel plate should extend to capture at least 80% of the flux leaving the plate from the inner region ($0 \le r \le r_\pm$). To satisfy the above condition, it turns out that r_{od} close to 60 mm is adequate.

EXAMPLE 9.2C: Levitation of a Flat HTS Plate

Figure 9.11 shows a cross sectional view of a system in which a flat HTS plate, δ_d-thick and radius R_d, is levitated z_ℓ above the center of two nested coils, Coils 1 and 2, energized "reversed" relative to each other. The two coils, each "formless," are placed on a steel plate. Note that the HTS plate, the coils, and the steel plate are axially coincident. Table 9.6 presents parameters of both coils.

Table 9.6: Coil Parameters

Parameters	Coil 1	Coil 2
Winding i.d. ($2a_1$) [mm]	40	20
Winding o.d. ($2a_2$) [mm]	70	30
Winding height ($2b$) [mm]	10	10
Total turns (N_s)	150	50

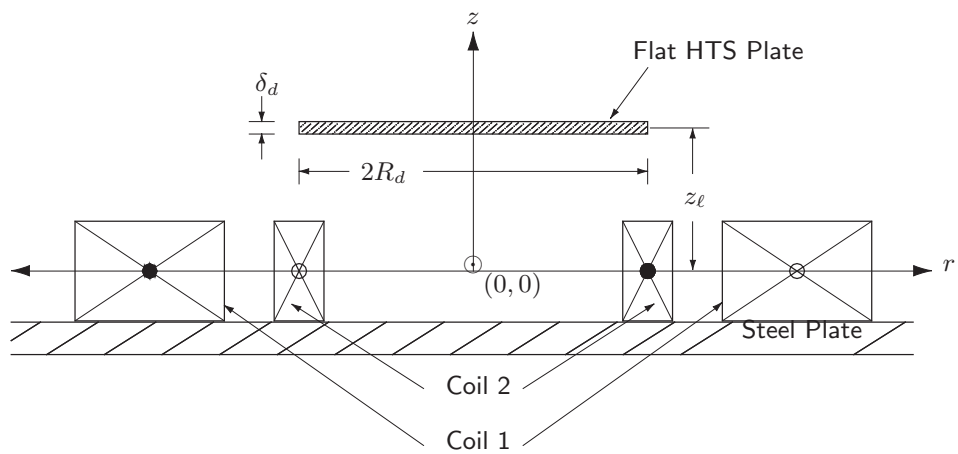

Fig. 9.11 Cross sectional view of a levitation system comprised of a flat HTS plate (of thickness δ_d and radius R_d) and two nested coils, Coils 1 and 2 energized *reversed* relative to each other. The two coils, each "formless," are placed on a steel plate. The drawing is only approximately in scale.

EXAMPLE 9.2C: Levitation of a Flat HTS Plate (continuation)

Figure 9.12 shows $B_z(z,r)$ vs. r plots at $z=0$, 5, 7.5, 10, 12.5, 15, 17.5, and 20 mm, with Coil 1 energized at 25 A *and* Coil 2 at -15 A; Fig. 9.13 shows $B_r(z,r)$ vs. z plots at $r=5$, 10, 12.5, 15, and 17.5 mm for the same currents as in Fig. 9.12. Note that the steel plate is *absent* in these plots.

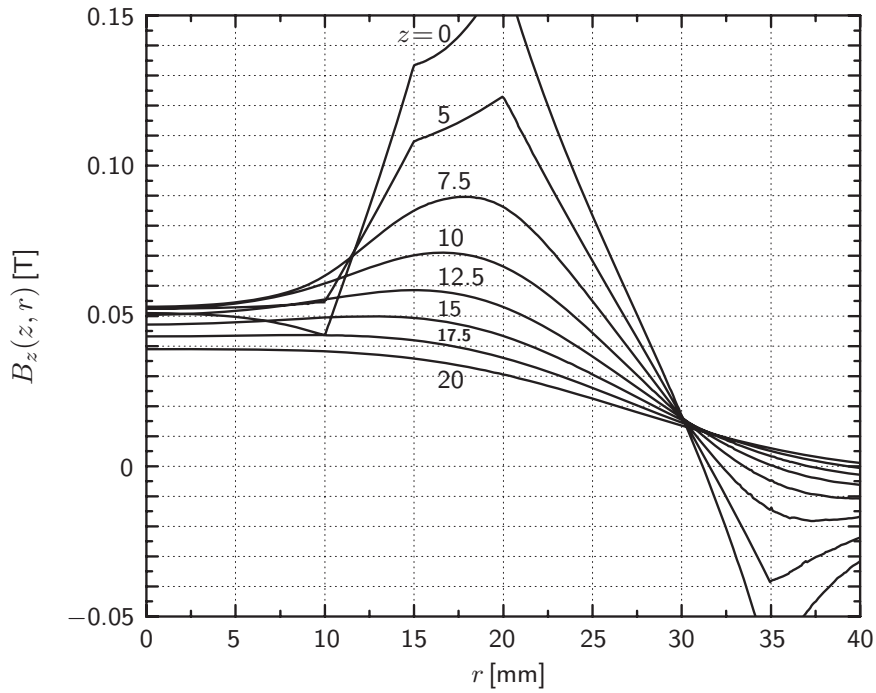

Fig. 9.12 $B_z(z,r)$ vs. r plots, at $z=0$, 5, 7.5, 10, 12.5, 15, 17.5, and 20 mm, with Coil 1 at 25 A and Coil 2 at -15 A *without* the steel plate.

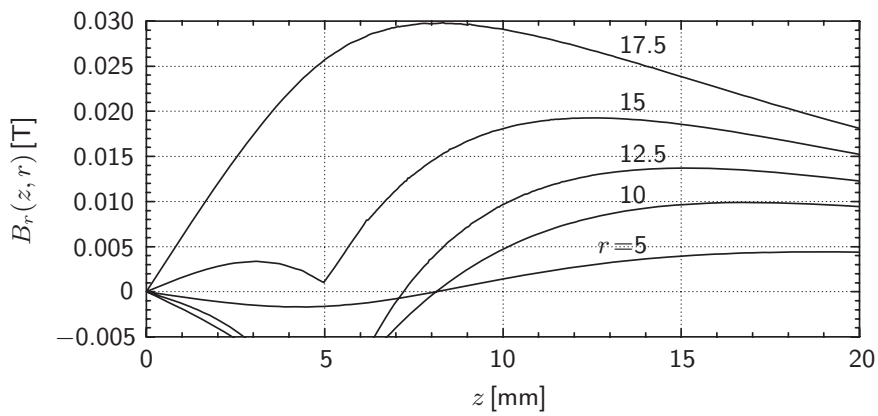

Fig. 9.13 $B_r(z,r)$ vs. z plots, at $r=5$, 10, 12.5, 15, and 17.5 mm, with Coil 1 at 25 A and Coil 2 at -15 A *without* the steel plate.

Q/A 9.2C: Levitation of a Flat HTS Plate

a) Levitation Force—Lift Assuming that the supercurrent induced in the flat HTS plate, I_s, is confined to the plate's rim, show first that the levitation force on the plate levitated axially z_ℓ above the center, $F_z(z_\ell)$, is given by:

$$F_z(z_\ell) = 2\pi R_d I_s B_r(z_\ell, R_d) \tag{9.3a}$$

where $B_r(z_\ell, R_d)$ is the radial field at (z_ℓ, R_d) generated by the two coils.

Next, modeling the plate as an infinitely long cylinder of the same radius exposed to a *uniform* axial field, $H_z(z_\ell, R_d) \ll J_c R_d$, the Bean's critical-state field, show the explicit dependence of $F_z(z_\ell, R_d,)$ on δ_d and $B_z(z_\ell, R_d,)$.

For the condition $H_z(z_\ell, R_d) \ll J_c R_d$, where J_c is the plate material's critical current density, the supercurrent, I_s, is confined to a thin surface layer of thickness δ_s. Assume that this surface current is uniform and confined to the rim. We may then equate the levitation force $F_z(z_\ell, R_d)$ to the Lorentz force on I_s at the rim $(r = R_d)$, which is the product of $2\pi R_d$, I_s, and $B_r(z_\ell, R_d)$:

$$F_z(z_\ell) = 2\pi R_d I_s B_r(z_\ell, R_d) \tag{9.3a}$$

According to the Bean's critical-state model, for $H_z(z_\ell, R_d) < H_p$, where $H_p = J_c R_d$ is the critical-state field, the supercurrent layer, δ_s, is given by:

$$\delta_s = \frac{H_z(z_\ell, R_d)}{J_c} = \frac{1}{J_c}\left[\frac{B_z(z_\ell, R_d)}{\mu_\circ}\right] \tag{a.1}$$

That is, the total supercurrent induced in the plate is given by:

$$I_s = \delta_d \delta_s J_c = \delta_d \left[\frac{B_z(z_\ell, R_d)}{\mu_\circ}\right] \tag{a.2}$$

Combining Eqs. 9.3a and a.2, we obtain:

$$F_z(z_\ell) = 2\pi R_d \delta_d \left[\frac{B_z(z_\ell, R_d) B_r(z_\ell, R_d)}{\mu_\circ}\right] \tag{9.3b}$$

Equation 9.3b states that $F_z(z_\ell) \propto B_z(z_\ell, R_d) B_r(z_\ell, R_d)$. That is, in this levitation system, the currents in the two coils may be varied to set a levitation height [9.5–9.8]. Also note that as long as the condition $\delta_s \ll R_d$ is satisfied, i.e., for "large" J_c, $F_z(z_\ell)$ is independent of J_c.

Our Picture of The Universe

—Passage from Stephen Hawking's *A Brief History of Time* [9.9].

A well-known scientist (some say it was Bertrand Russell) once gave a public lecture on astronomy. He described how the earth orbits around the sun and how the sun, in turn, orbits around the center of a vast collection of stars called our galaxy. At the end of the lecture, a little old lady at the back of the room got up and said: "What you have told us is rubbish. The world is really a flat plate supported on the back of a giant tortoise." The scientist gave a superior smile before replying, "What is the tortoise standing on?" "You're very clever, young man, very clever," said the old lady. "But it's turtles all the way down."

Q/A 9.2C: Levitation of a Flat HTS Plate (continuation)

b) YBCO Plate Using the $B_z(z,r)$ and $B_r(z,r)$ plots of Figs. 9.12 and 9.13, and Eq. 9.3*b*, compute $F_z(z_\ell)$ for a YBCO plate of $R_d = 15\,\text{mm}$ and $\delta_d = 5\,\text{mm}$ at a levitation height of $z_\ell = 10\,\text{mm}$, assuming that the steel plate is still *absent*. Also, compute the mass of this plate and show that at this height the levitation force can support the plate mass. YBCO density: $\varrho = 6.4\,\text{g/cm}^3$.

From Figs. 9.12 and 9.12, we obtain: $B_z(z = 10\,\text{mm}, r = 15\,\text{mm}) \simeq 0.070\,\text{T}$ and $B_r(z = 10\,\text{mm}, r = 15\,\text{mm}) \simeq 0.0181\,\text{T}$. Thus:

$$\begin{aligned} F_z(z_\ell) &= 2\pi R_d \delta_d \left[\frac{B_z(z_\ell, R_d) B_r(z_\ell, R_d)}{\mu_\circ}\right] \qquad (9.3b) \\ &\simeq \frac{2\pi(15\times10^{-3}\,\text{m})(5\times10^{-3}\,\text{m})(0.070\,\text{T})(0.0181\,\text{T})}{(4\pi\times10^{-7}\,\text{H/m})} \\ &\simeq 0.475\,\text{N} (\simeq 48.5\,\text{g}) \end{aligned}$$

The mass of the YBCO plate, m_p, is given by:

$$\begin{aligned} m_p &= \pi R_d^2 \delta_d \varrho \\ &= \pi(1.5\,\text{cm})^2(0.5\,\text{cm})(6.4\,\text{g/cm}^3) \simeq 23\,\text{g} \end{aligned}$$

Thus even in the *absence* of the steel plate, the levitation force on the plate at $z_\ell = 10\,\text{mm}$ is double the plate weight.

c) Induced Supercurrent Again, assuming the *absence* of the steel plate, compute the supercurrent layer, δ_s, for the same YBCO plate at $z_\ell = 10\,\text{mm}$ and show $\delta_s \ll R_d$. Use $J_c = 10^8\,\text{A/m}^2$. Also compute I_s.

Applying Eq. *a*.1 and noting $B_z(z_\ell, R_d) \simeq 0.070\,\text{T}$, we have:

$$\begin{aligned} \delta_s = \frac{H_z(z_\ell, R_d)}{J_c} &= \frac{1}{J_c}\left[\frac{B_z(z_\ell, R_d)}{\mu_\circ}\right] \qquad (a.1) \\ &\simeq \frac{(0.070\,\text{T})}{(10^8\,\text{A/m}^2)(4\pi\times10^{-7}\,\text{H/m})} \simeq 0.56\,\text{mm} \end{aligned}$$

The required condition of $\delta_s \ll R_d$ is indeed satisfied. Using the first two equations of Eq. *a*.2, we have:

$$\begin{aligned} I_s &= \delta_d \delta_s J_c \qquad (a.2) \\ &\simeq (5\times10^{-3}\,\text{m})(0.56\times10^{-3}\,\text{m})(10^8\,\text{A/m}^2) \simeq 280\,\text{A} \end{aligned}$$

This supercurrent of 280 A is induced in the YBCO plate when the plate is exposed to the axial field, $B_z(R_d, z_\ell)$, of 0.07 T.

Q/A 9.2C: Levitation of a Flat HTS Plate (continuation)

d) Suspension Stiffness Derive an expression for the suspension stiffness, k_z at $z = z_\ell$. Compute k_z for $R_d = 15\,\text{mm}$; $\delta_d = 5\,\text{mm}$; and $z_\ell = 10\,\text{mm}$.

The suspension stiffness at $z = z_\ell$ is given by:

$$k_z = -\frac{\partial F_z(z, R_d)}{\partial z}\bigg|_{z_\ell} \tag{$d.1$}$$

The minus sign indicates that $F_z(z, R_d)$ increases with *decreasing* z. Combining Eqs. 9.3*b* and *d*.1, we have:

$$k_z = -2\pi R_d \delta_d \left\{ \left[\frac{B_r(z_\ell, R_d)}{\mu_\circ} \right] \frac{\partial B_z(z, R_d)}{\partial z}\bigg|_{z_\ell} + \left[\frac{B_z(z_\ell, R_d)}{\mu_\circ} \right] \frac{\partial B_r(z, R_d)}{\partial z}\bigg|_{z_\ell} \right\} \tag{9.4}$$

Inserting appropriate parameter values in Eq. 9.4, we obtain:

$$\begin{aligned} k_z &\simeq -2\pi(15\times10^{-3}\,\text{m})(5\times10^{-3}\,\text{m}) \\ &\quad \times \left[\left(\frac{0.0181\,\text{T}}{4\pi\times10^{-7}\,\text{H/m}} \right)(-5.2\,\text{T/m}) + \left(\frac{0.070\,\text{T}}{4\pi\times10^{-7}\,\text{H/m}} \right)(1.1\,\text{T/m}) \right] \\ &= -2\pi(75\times10^{-6}\,\text{m}^2)\left(\frac{10^7}{4\pi}\,\text{m/H} \right)(-0.0943\,\text{T}^2/\text{m} + 0.0758\,\text{T}^2/\text{m}) \\ &\simeq 6.9\,\text{N/m} \end{aligned}$$

From Fig. 9.12 $k_z > 0$ at $R_d = 15\,\text{mm}$ and $z_\ell = 10\,\text{mm}$; we thus conclude that the plate is levitated stably against a small axial displacement, i.e., if the plate is pushed downward, the levitation force increases.

e) Resonant Frequency Compute the resonant frequency, ν_z, of the axial motion for this YBCO plate levitated at $z_\ell = 10\,\text{mm}$. Use $m_p = 23\,\text{g}$ computed in **b)** for the YBCO plate.

For a simple mass (m)-spring (k) system, the resonant frequency, ν, is given by:

$$\nu = \frac{1}{2\pi}\sqrt{\frac{k}{m}}$$

Thus:

$$\begin{aligned} \nu_z &\simeq \frac{1}{2\pi}\sqrt{\frac{(6.9\,\text{N/m})}{(23\times10^{-3}\,\text{kg})}} \\ &\simeq 3\,\text{Hz} \end{aligned}$$

When the plate is displaced vertically, it will oscillate with a frequency of 3 Hz.

Q/A 9.2C: Levitation of a Flat HTS Plate (continuation)

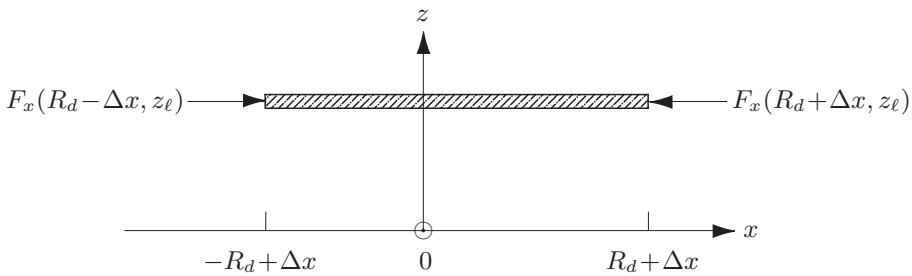

Fig. 9.14 Cross sectional view of a levitated HTS plate displaced in the lateral ($+x$) direction by Δx. The y-direction is into the paper.

f 1) Lateral Stability 1 Show that the HTS plate is stable at $z_\ell = 10\,\text{mm}$ against a small displacement in the lateral (in the r- or here x-axis) direction. Assume that the induced supercurrent in the plate is confined within a thin layer, δ_s, at the rim. Also, ignore the steel plate.

In the lateral (x-axis) direction, F_x is proportional to the cross product of I_s and B_z. Consider the HTS plate levitated axially aligned to the coils as shown in Fig. 9.11 (p. 572). $F_x(z_\ell, R_d)$ is $-x$-directed, because $I_s(z_\ell, R_d)$ is $-y$-directed and $B_z(x=0)$ is $+z$-directed: $F_x(z_\ell, R_d) \propto -I_s(z_\ell, R_d)B_z(z_\ell, R_d)\vec{\imath}_x$. $F_x(z_\ell, -R_d)$, on the other hand, is $+x$-directed, because $I_s(z_\ell, -R_d)$ is $+y$-directed, while $B_z(z_\ell, -R_d)$ remains $+z$-directed: $F_x(z_\ell, -R_d) \propto +I_s(z_\ell, R_d)B_z(z_\ell, R_d)\vec{\imath}_x$. Because $B_z(z_\ell, R_d) = B_z(z_\ell, -R_d)$ and $I_s(z_\ell, R_d) = -I_s(z_\ell, -R_d)$, we have:

$$\begin{aligned} F_x(z_\ell, R_d)+F_x(z_\ell, -R_d) &\propto -I_s(z_\ell, R_d)B_z(z_\ell, R_d)+I_s(z_\ell, -R_d)B_z(z_\ell, -R_d) \\ &= 0 \end{aligned}$$

That is, the net lateral force on the plate centered at $x=0$ is zero.

Now consider a slight lateral displacement of the plate in the $+x$ direction by Δx, as in Fig. 9.14. Here, we have:

$$\begin{aligned} F_x(z_\ell, R_d+\Delta x)+F_x(z_\ell, -R_d+\Delta x) \propto &-I_s(R_d+\Delta x)B_z(z_\ell, R_d+\Delta x) \\ &+I_s(-R_d+\Delta x)B_z(z_\ell, -R_d+\Delta x) \quad (f1.1) \end{aligned}$$

We may assume $I_s(z_\ell, R_d+\Delta x) \simeq I_s(z_\ell, R_d)$ and $I_s(z_\ell, -R_d+\Delta x) \simeq I_s(z_\ell, -R_d)$. Also because $I_s(z_\ell, R_d) = -I_s(z_\ell, -R_d)$ Eq. $f1.1$ may be simplified to:

$$\begin{aligned} F_x(z_\ell, R_d+\Delta x)+F_x(z_\ell, -R_d+\Delta x) \propto -I_s(R_d)\Big[&B_z(z_\ell, R_d+\Delta x) \\ &-B_z(z_\ell, -R_d+\Delta x)\Big] \quad (f1.2) \end{aligned}$$

From Fig. 9.12 we note that in the vicinity of $z = 10\,\text{mm}$ (z_ℓ) and $R_d = 15\,\text{mm}$, $B_z(z_\ell, R_d+\Delta x) > B_z(z_\ell, -R_d+\Delta x)$ for "small" Δx. Thus, the lateral force is restoring for a "small" lateral displacement. Note that the trace for $z = 10\,\text{mm}$ in Fig. 9.12 peaks at $r \simeq 16.5\,\text{mm}$; $\partial B_z/\partial r$ changes sign, and for a displacement of $\Delta x > 4\,\text{mm}$ the plate is no longer stable. The traces in Fig. 9.12 corresponding to $z \geq 12.5\,\text{mm}$ indicate that the plate is neutrally stable at $z_\ell \simeq 12.5\,\text{mm}$ and unstable for $z_\ell > 12.5\,\text{mm}$.

Q/A 9.2C: Levitation of a Flat HTS Plate (continuation)

f2) Lateral Stability 2 By demonstrating that the lateral spring constant, k_x, is positive at $r = R_d$, i.e., $k_x \equiv -\partial F_x(z_\ell, r)/\partial x > 0$, show that the plate is stable against a small radial displacement. Also determine the numerical values of k_x and ν_x, the natural frequency in the lateral direction, at $z = 10\,\text{mm}$ and $x = 15\,\text{mm}$.

To quantify the analysis in **f1)**, consider the differential force Δf_{x^+} on the rightmost element of current of length Δy: $\Delta f_{x^+} = I_s \Delta y B_z(R_d + \Delta x)$. Δf_{x^+} is balanced only incompletely by the force Δf_{x^-} on the corresponding leftmost element: $\Delta f_{x^-} = I_s \Delta y B_z(R_d - \Delta x)$. The net differential force $\Delta f_x = \Delta f_{x^+} + \Delta f_{x^-}$ is given by:

$$\Delta f_x(z, R_d) = 2 I_s \Delta y \frac{\partial B_z(z,r)}{\partial r}\bigg|_{R_d} \Delta x \qquad (f2.2)$$

The net force per unit current length is $\Delta f_x/\Delta y$. If this force were constant around the loop, the total differential force, ΔF_x, would be $2R_d \times \Delta f_x$. Actually, $\Delta f_x/\Delta y$ varies along the loop as $\sqrt{1-(r/R)^2}$; the average value is $\pi/4$ the peak value:

$$\Delta F_x(z, R_d) = \pi R_d I_s \frac{\partial B_z(z,r)}{\partial r}\bigg|_{R_d} \Delta x \qquad (f2.2)$$

k_x thus may be given by:

$$k_x(z, R_d) = \frac{\Delta F_x(z, R_d)}{\Delta x} = \pi R_d I_s \frac{\partial B_z(z,r)}{\partial r}\bigg|_{R_d}$$

Evaluating k_x for $R_d = 15\,\text{mm}$, $I_s = 280\,\text{A}$, and $\partial B_z(z_\ell, r)/\partial r = 1.08\,\text{T/m}$ at $z_\ell = 10\,\text{mm}$ and $R_d = 15\,\text{mm}$, we have: have:

$$k_x(z_\ell, R_d) = 2(15 \times 10^{-3}\,\text{m})(280\,\text{A})(1.08\,\text{T/m}) \simeq 14.2\,\text{N/m}$$

Compared with $k_z(z_\ell, R_d)$, the lateral stiffness, $k_x(z_\ell, R_d)$, is about double.

The natural frequency in the lateral direction, ν_x, is given by:

$$\nu_x = \frac{1}{2\pi}\sqrt{\frac{k_x}{m_p}} \qquad (f2.4)$$

$$\simeq \frac{1}{2\pi}\sqrt{\frac{14.2\,\text{N/m}}{(23 \times 10^{-3}\,\text{kg})}} \simeq 4\,\text{Hz}$$

These values are in the order of magnitude of measured values [9.5, 9.6]

TRIVIA 9.3 List the items below in descending order of number.

i) Air bubbles, in the winding of an epoxy-impregnated superconducting coil;

ii) Bubbles, in a freshly served glass of champagne;

iii) Helium-inflated toy balloons, just enough to lift a newborn baby;

iv) Stars, in our galaxy *The Milky Way*.

Q/A 9.2C: Levitation of a Flat HTS Plate (continuation)

g) Power Requirement Provided the power to liquify the nitrogen is ignored, it saves power to operate copper coils in a bath of liquid nitrogen boiling at atmospheric pressure. Compute the total electric power, $P_T = P_1 + P_2$, required by the two coils operating at 77.3 K, P_1 by Coil 1 at 25 A and P_2 by Coil 2 at 15 A. Assume that the "space factor" (λ) of each coil is 0.785. Use $\rho_{cd} = 2.5\,\mathrm{n\Omega\,m}$ as the resistivity of conductor (copper) at 77 K.

From Eq. 3.112, we have:

$$P = \rho_{cd} J^2 \lambda a_1^3 2\pi\beta(\alpha^2 - 1) \tag{3.112}$$

$$= \rho_{cd} \frac{(\lambda J)^2}{\lambda} a_1^3 2\pi\beta(\alpha^2 - 1)$$

With $\lambda J = NI/2b(a_2 - a_1) = NI/2a_1^2\beta(\alpha - 1)$, P becomes:

$$P = \frac{\pi\rho_{cd}(NI)^2(\alpha+1)}{2\lambda a_1 \beta(\alpha-1)} \tag{g.1}$$

For Coil 1 with $a_1 = 20\times10^{-3}$ m; $\alpha = 2a_2/2a_1 = (70\,\mathrm{mm})/(40\,\mathrm{mm}) = 1.75$ $\beta = 2b/2a_1 = (10\,\mathrm{mm})/(40\,\mathrm{mm}) = 0.25$, Eq. g.1 gives:

$$P_1 = \frac{\pi(2.5\times10^{-9}\,\Omega\,\mathrm{m})(150\times25\,\mathrm{A})^2(1.75+1)}{2(0.785)(20\times10^{-3}\,\mathrm{m})(0.25)(1.75-1)} \simeq 52\,\mathrm{W}$$

Similarly,

$$P_2 = \frac{\pi(2.5\times10^{-9}\,\Omega\,\mathrm{m})(50\times15\,\mathrm{A})^2(1.5+1)}{2(0.785)(10\times10^{-3}\,\mathrm{m})(0.5)(1.5-1)} \simeq 3\,\mathrm{W}$$

The total power dissipation by the two coils, $P_T = P_1 + P_2$, is thus about 55 W.

h) Liquid Nitrogen Boil-off Rate Compute an approximate boil-off rate, $\dot{Q}_\ell$ in [cm^3/h], of liquid nitrogen at a power dissipation of 55 W.

The liquid nitrogen boil-off rate, $\dot{Q}_\ell$, for power dissipation P is given by:

$$\dot{Q}_\ell = \frac{P}{h_L} \tag{h.1}$$

where h_L is the latent heat of vaporization of liquid nitrogen. With $h_L = 161\,\mathrm{J/cm^3}$ (Table 4.2), Eq. h.1 gives:

$$\dot{Q}_\ell = \frac{(55\,\mathrm{W})}{(161\,\mathrm{J/cm^3})} = 0.34\,\mathrm{cm^3/s} = 1224\,\mathrm{cm^3/h}$$

$$\sim 1\,\mathrm{liter/h}$$

For long operation of this system the cryostat holding the coils may require liquid nitrogen replenishment at a rate of ∼1 liter/h.

Q/A 9.2C: Levitation of a Flat HTS Plate (continuation)

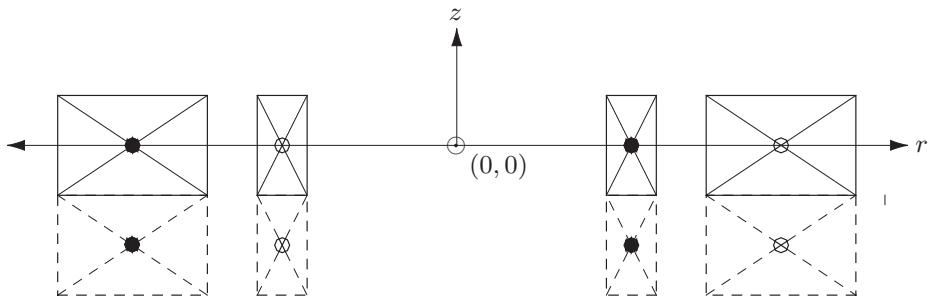

Fig. 9.15 Coil arrangement to model the presence of the steel plate in Fig. 9.11.

We shall now study the effects of the steel plate in Fig. 9.11. To simplify the problem, we first assume the plate to be of *infinite* permeability, i.e., $\mu/\mu_\circ = \infty$. Next, to take account of the plate's effect on the magnetic field above the plate, i.e., $z \geq -5\,\text{mm}$, we replace the steel plate with a two-coil unit identical to the original two-coil unit, placing it directly beneath the original unit, as illustrated in Fig. 9.15. (Note also here that each coil form is assumed to be "formless.")

i) With Steel Plate Now compute the levitation force $F_{z\text{steel}}(z_\ell)$ on the plate at $z_\ell = 10\,\text{mm}$ with an *ideal* steel plate ($\mu/\mu_\circ = \infty$). Also, discuss stability in the axial and radial directions.

Without the steel plate, we have, from Figs. 9.12 and 9.13, $[B_z(z_\ell, R_d)]_{\text{w/o}} \simeq 0.070\,\text{T}$ and $[B_r(z_\ell, R_d)]_{\text{w/o}} \simeq 0.019\,\text{T}$. With an *ideal* steel plate, the contribution of each of the *image* coils located at $z = -10\,\text{mm}$ must be included.

$$\begin{aligned}[B_z(z_\ell, R_d)]_{\text{with}} &= [B_z(z_\ell, R_d) + B_z(z_\ell + 10.0\,\text{mm}, R_d)]_{\text{w/o}} \\ &\simeq (0.070\,\text{T}) + (0.036\,\text{T}) = 0.106\,\text{T} \\ [B_r(z_\ell, R_d)]_{\text{with}} &= [B_r(z_\ell, R_d) + B_r(z_\ell + 10.0\,\text{mm}, R_d)]_{\text{w/o}} \\ &\simeq (0.018\,\text{T}) + (0.015\,\text{T}) = 0.033\,\text{T}\end{aligned}$$

Inserting these field values into Eq. 9.3*b*, we obtain:

$$\begin{aligned}F_z(z_\ell, R_d) &= 2\pi R_d \delta_d \left[\frac{B_z(z_\ell, R_d) B_r(z_\ell, R_d)}{\mu_\circ}\right] \qquad (9.3b) \\ &\simeq \frac{2\pi(15\times10^{-3}\,\text{m})(5\times10^{-3}\,\text{m})(0.106\,\text{T})(0.033\,\text{T})}{(4\pi\times10^{-7}\,\text{H/m})} \\ &\simeq 1.31\,\text{N} (\simeq 134\,\text{g})\end{aligned}$$

Thus, with an *ideal* steel plate, the system generates a levitation force that is six times the plate weight (0.23 N), i.e., the plate can support a load mass of more than 110 g. The system is stable in the axial direction ($k_z \simeq 6.9\,\text{N/m}$) as well as in the lateral direction ($k_x \simeq 9.1\,\text{N/m}$).

Example 9.2D: HTS "Annulus" Magnet

One magnet design option possible with HTS, but impossible with LTS, consists of a stack of many HTS bulk or plate annuli. Figure 9.16 shows schematic cross sectional views, each of $2a_1$ i.d. and $2a_2$ o.d. of: a) a bulk annulus of thickness δ_b; b) a thin-plate annulus of overall thickness δ_p and superconducting film thickness δ_f; and c) an "annulus magnet" of overall height $2b$ comprising a stack of bulk or plate annuli. Note that an annulus magnet contains neither splices nor terminals.

With YBCO and other rare-earth based HTS bulks [9.10–9.14], practical values for $2a_1$ and $2a_2$ are, respectively, 40–60 mm and 70–100 mm, making the development of a "small" NMR magnet based on these bulk annuli a realistic possibility [9.15]. Also, because coated YBCO conductor of width 40–100 mm is being developed [9.16, 9.17], it may become feasible in the very near future to punch out plate annuli from a wide strip of coated superconductor with a die.

Typically, the bulk annulus thickness, δ_b, is ∼10 mm, while the plate annulus thickness, δ_p, is ∼100 μm, with $\delta_f \simeq 1\,\mu$m. Thus an annulus magnet of $2b = 300$ mm, for example, will contain about 30 bulk annuli or ∼3000 plate annuli. Because each annulus is a loop, the energizing procedure of an annulus magnet is quite different from a wire-wound magnet—see **PROBLEM 1.2**.

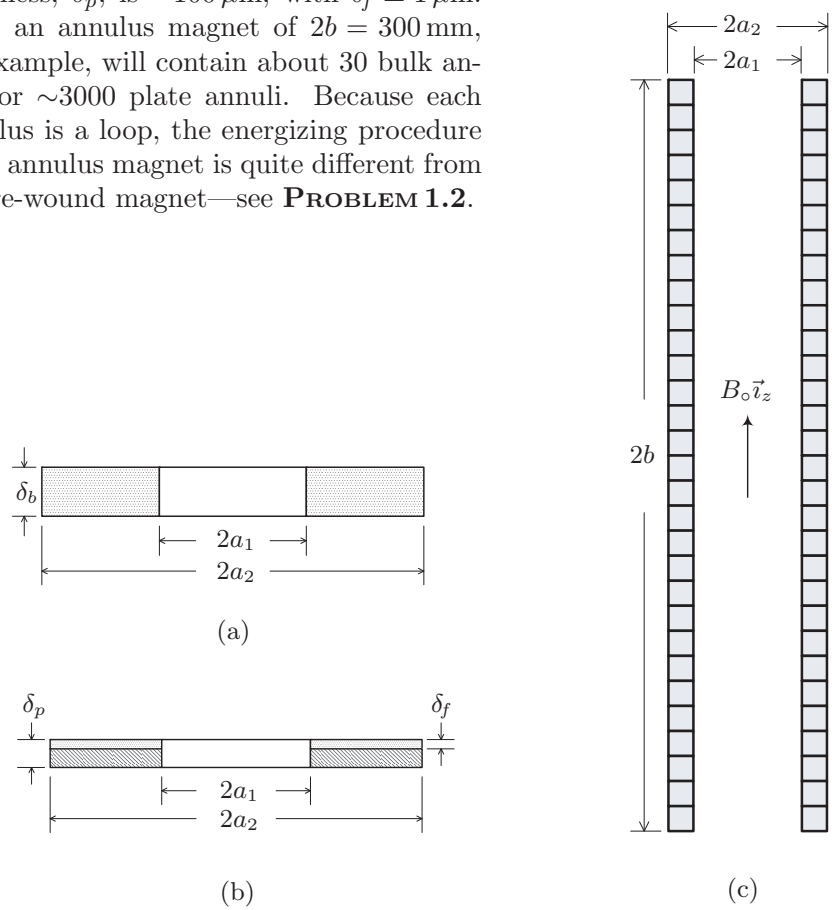

Fig. 9.16 Schematic cross sectional views, each of $2a_1$ i.d. and $2a_2$ o.d.: a) bulk annulus of thickness δ_b; b) thin-plate annulus of overall thickness δ_p and superconducting film thickness δ_f; and c) a magnet of overall height $2b$ assembled from a stack of bulk (or plate) annuli.

Q/A 9.2D: HTS "Annulus" Magnet

a) Overall (Engineering) Current Density Assuming that an annulus magnet is "long," i.e., $\beta \gg 1$, compute the overall current density, λJ (or J_e) required to generate an axial central field, $B_\circ$, of 11.74 T (corresponding to an NMR frequency of 500 MHz) for $2a_1 = 50$ mm, $2a_2 = 75$ mm, and $2b = 300$ mm.

With $\alpha = 1.5$ and $\beta = 6$, this "solenoidal" magnet may be considered "long;" i.e., the axial field at the magnet center, $B_\circ = B_z(0,0)$, may be given by Eq. 3.111*e*:

$$B_z(0,0) = \mu_\circ \lambda J a_1(\alpha - 1) \tag{3.111e}$$

Note that $B_z(0,0)$ is independent of the magnet length and directly proportional to the "winding" build. Solving Eq. 3.111*e* for λJ, we obtain:

$$\lambda J = \frac{B_z(0,0)}{\mu_\circ a_1(\alpha - 1)} = \frac{(11.74\,\mathrm{T})}{(4\pi \times 10^{-7}\,\mathrm{H/m})(0.025\,\mathrm{m})(1.5-1)} = 7.5 \times 10^8 \mathrm{A/m^2}$$

b) Current Density Requirement—Bulk vs. Plate Discuss the overall (engineering) current density found above for bulk annuli and plate annuli.

Although Fig. 9.16c shows the winding to be entirely occupied by bulk annuli or plate annuli, as discussed shortly, in a real annulus magnet a "thin" spacer is placed between adjacent annuli. These spacers not only strengthen the winding against magnetic forces but also, with different thickness depending on the axial location, are used to adjust the axial field distribution.

Bulk Because the spacer occupancy will be no greater than ∼10% of the entire winding volume, $\lambda J \simeq J_c$, where J_c is the bulk critical density. That is, in a bulk-annulus magnet the material critical current density should not be a limiting issue to generate a center field of 11.74 T (or even greater).

Plate Coated YBCO conductor, for example, is "loaded" with nonsuperconducting materials (e.g., buffer layer and substrate), whose total thickness in Fig. 9.16b is represented by $\delta_p - \delta_f$. Typically δ_p and δ_f are, as stated above, respectively, 75–100 μm and 1 μm. Thus, to achieve an overall current density of 10^8–10^9 A/m^2, YBCO film J_c must be at least 10^{10} A/m^2, a level achievable only at temperatures below 77 K.

c) Energizing Technique Discuss ways to energize a "large" and "high-field" annulus magnet.

Generally, it is not possible to change the flux enclosed by a superconducting loop unless at least part of the loop is in the normal state—the "flux gate" has to be open. Thus, it is impossible to energize even a superconducting loop (**PROBLEM 1.2**), let alone a full-fledged superconducting magnet, if the loop or the magnet remains superconducting.

As studied in ***DISCUSSION*** *7.4* (p. 455), a solution to energize a "conventional" persistent-mode magnet is the use of a persistent-current switch (PCS). Here, by conventional we mean a wire-wound magnet that can be energized with a power supply while the PCS maintains a small portion of the wire resistive.

Q/A 9.2D: HTS "Annulus" Magnet (continuation)

Another technique sometimes used is to place a "virgin" wire superconducting magnet (or a bulk disk), already in the superconducting state, in the bore of an external pulse-field magnet. The fast-varying magnetic field of the rising-and-falling pulse field heats up a part or most of the superconducting magnet, permitting flux penetration. By making sure that the superconducting magnet is well-cooled, it is possible to make the magnet return to the fully-superconducting state and "trap" a part of the pulse field, which will remain as a persistent-mode field. The disadvantages of this technique are: 1) it is difficult to accurately control the level of the resulting persistent-mode field, because it critically depends on heating/cooling conditions; and 2) for a large, high-field magnet, this pulse magnet itself becomes quite large and elaborate, with the usual complexities of a pulse magnet.

To energize a large and high-field annulus magnet, a DC and superconducting external field is the best choice. Figure 9.17 shows a schematic drawing of one of the early steps of a technique to energize an annulus magnet, which is here indicated as a stack of annuli (no spacers) with the center portion "notched" (see **PROBLEM 3.7**). The procedure for energizing an annulus magnet involves the following five steps.

1. Place the magnet/cryostat unit, still at room temperature, in the bore of an external DC superconducting magnet.
2. With the annulus magnet still in the normal state, expose the magnet to a field generated by the external magnet (Fig. 9.17). Field lines are schematically drawn in the figure.
3. Cool the annulus magnet to the fully superconducting state. Because these annuli are of Type II superconductors the field lines remain essentially unchanged as the annulus magnet is cooled through its transition temperature.

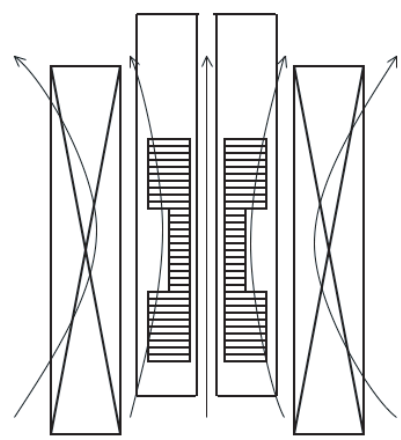

Fig. 9.17 Schematic drawing of an annulus magnet system after Step 2 of a technique to energize an annulus magnet. The magnet/cryostat unit, still at room temperature and placed in the bore of an external DC superconducting magnet, is exposed to a field generated by the external magnet.

Q/A 9.2D: HTS "Annulus" Magnet (continuation)

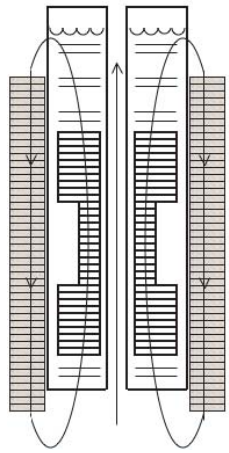

Fig. 9.18 Schematic drawing of an annulus magnet system after Step 5 of the energizing sequence. The annulus magnet, now cold and superconducting, is generating a persistent-mode field, which in turn is generated by the annuli, each with a supercurrent distribution induced when the external magnet was discharged to zero. A field-shielding assembly made of steel annuli surrounds the magnet/cryostat unit.

4. Discharge the external magnet, slowly, to zero, setting up a supercurrent distribution in each annulus, which in turn generates a persistent-mode field. This process is called "field-cooling."

5. Remove the magnet/cryostat unit from the external magnet and around it place a field-shielding assembly made of steel annuli. A schematic drawing of the whole assembly after Step 5 is shown in Fig. 9.18.

d) Field-Shielding It is desirable to minimize the fringe field outside a magnet. As shown in Fig. 9.18, an annulus magnet can be surrounded by a field-shielding assembly of steel annuli. Estimate the outside diameter, D_{so}, of steel annuli for the following parameters: steel annuli inside diameter, $D_{si} = 225\,\text{mm}$; $2a_1 = 50\,\text{mm}$; $2a_2 = 75\,\text{mm}$; $B_z(0,0) \equiv B_\circ = 11.74\,\text{T}$; $\mu_\circ M_s = 1.25\,\text{T}$.

Because virtually the entire axial flux of the bore flows through the steel assembly of D_{so} o.d. and D_{si} i.d., conservation of flux results in:

$$\frac{\pi}{3}(a_2^2 + a_2 a_1 + a_1^2)B_\circ \simeq \frac{\pi}{4}(D_{so}^2 - D_{si}^2)\mu_\circ M_s \qquad (d.1)$$

where $B_\circ$ is the central field. The left-hand side of Eq. $d.1$ represents the total flux in the magnet bore ($\pi B_\circ a_1^2$) plus that in the annular space between a_1 and a_2, where $B(r) = B_\circ(a_2 - r)/(a_2 - a_1)$, decreasing linearly from $B_\circ$ at a_1 to 0 at a_2; M_s is the magnetization of steel, low enough to make its effective $\mu \geq 100\mu_\circ$. With the parameter values inserted into Eq. $d.1$, we obtain: $D_{so} \simeq 296\,\text{mm}$.

Note that for this annulus magnet system with $D_{so} \simeq 296\,\text{mm}$, the steel annuli assembly occupies a considerable radial extent. Nevertheless, a radial extent of still only $\sim$0.15 m for a shielded magnet generating a center field of 11.74 T must be considered remarkably compact.

Q/A 9.2D: HTS "Annulus" Magnet (continuation)

e) Spacers Spacers between adjacent HTS annuli can satisfy key requirements of an annulus magnet. Describe these and propose an appropriate spacer material.

These requirements include: 1) mechanical reinforcement; 2) thermal stability; and 3) field homogeneity, for NMR magnets.

Mechanical At 11.7 T, for example, the maximum Lorentz-force induced tensile stress in each annulus, 50-mm i.d., 75-mm o.d, is ∼270 MPa, which is above the strength of YBCO bulk. High-strength spacers inserted between HTS annuli can be made to shoulder most of this load. An excellent candidate for the spacer is a high-strength sheet of Cu-Ag alloy [9.18], originally developed for high-field Bitter magnets. It has an ultimate strength close to 1,000 MPa, a Young's modulus ∼150 GPa, and nearly the same thermal conductivity as copper.

Thermal During the field-cooling process when the external electromagnet is discharged, AC losses, primarily hysteretic, will heat the bulk disks [9.19, 9.20]. Here, the field discharge rate can be reduced to limit the temperature rise. Still, it is desirable to use strong *and* thermally conductive spacers: the Cu/Ag alloy sheet deemed fit for mechanical strength above is also a good candidate to satisfy this thermal requirement.

Field Homogeneity It is possible to tailor the thickness of a spacer located at a specific axial location to achieve a desired spatial field homogeneity at the magnet center. Here, only the thickness matters.

f) Bulk vs. Plate Compare bulk annuli vs. plate annuli, citing pros and cons of these two options, including manufacturability.

Each option has strengths and weaknesses, as briefly discussed below.

Bulk As already remarked in **b)**, the overall current density of a bulk-based annulus magnet can be close to the material's J_c: this is the bulk's greatest strength. Thus, HTS bulk disks currently available may be assembled to build annulus magnets that can generate 12 T and greater. The weakest point perhaps is its thickness: 10 mm. It is likely that the distribution of the induced current in each annulus will not be uniform, making it difficult to achieve a desired field distribution. Another weak point is manufacturing of bulk annuli, because the center portion of each disk must be drilled out. This drilling process can be time-consuming and it might also damage superconducting properties of the annuli.

Plate The bulk's strong point is the plate's weak point and vice versa. Thus to build a high-field annulus magnet with plate annuli, the superconductor's J_c must be further enhanced, or the thickness of the superconducting film must be increased, or that of the nonsuperconducting materials must be reduced. The strongest point is the thinness ($\sim 1\,\mu$m) of the superconducting film. Compared with a bulk-based annulus magnet, it should be easier to tailor the spatial field homogeneity. Last but not least, it should be much easier, and thus less expensive, to mass produce annuli from thin plates than from bulk disks: simply "punch" out, with a die, thin annuli from a wide, e.g., 100 mm, coated superconductor strip, as cookies are punched out from a thin layer of dough moving on a conveyor.

Q/A 9.2D: HTS "Annulus" Magnet (continuation)

g) Stability Briefly discuss the thermal stability of an annulus magnet.

The operating temperature of an annulus magnet may range from 4.2 K (the magnet immersed in a bath of liquid helium) to as high as 77 K (liquid nitrogen). Because the energy density required to quench the annuli is well above the "energy margin," regardless of the annulus magnet's operating temperature, the magnet will be *very* stable against quenching induced by any disturbances likely to occur in this system. The only time the annuli may be overheated is during the field-cooling process [9.20]. To minimize overheating, the external field must be reduced at a slow enough rate.

h) Protection Briefly discuss protection of an annulus magnet.

The induced currents in the annuli are *not* series-connected. Each annulus may be considered a one-turn coil, inductively coupled to a significant degree only to its adjacent annuli. Thus, the likelihood of one annulus absorbing the *entire* stored magnetic energy of the magnet is negligible. Quenching may spread out *slowly* from one annulus to the adjacent annuli. In the worst case each annulus is heated by the magnetic energies stored by only itself and its most adjacent annuli.

i) Temporal Field Stability Briefly discuss the temporal field stability of an annulus magnet.

Even if the temperature is kept constant, when the current is induced initially in an HTS disk, it is expected to decay, caused chiefly by dissipation generated by motion of flux in the disk. This decay is no different from any Type II superconductor, LTS or HTS, wire or disk. However, after this initial period, which may last for a "long" period of time, the induced supercurrent will remain constant if the temperature and external field remain constant.

If the operating temperature, $T_{op}(t)$, of an annulus is to vary with time, the trapped field is expected to remain constant, provided the condition $T_{op}(t) < T_{fc}$ is maintained, where T_{fc} is the field-cooling temperature. Experimental results appear to confirm this field-independence when $T_{op}(t) < T_{fc}$ [9.21]; the results also show that this time-constancy of induced supercurrent appears to be firmer the further away (colder) T_{op} is from T_{fc}. This constancy of field under the condition of $T_{op}(t) < T_{fc}$ has recently been confirmed in flywheel energy storage systems based on bulk HTS disks [9.22]. To ensure a field constancy with time to the degree required, for example, by a high-resolution NMR magnet, T_{op} should be as far below T_{fc} as practical.

Answer to TRIVIA 9.3

Stars (10^{11}); champagne bubbles (10^{7}); helium balloons (10^{3}); air bubbles (0*).

* This is the goal, which we may nearly achieve by epoxy-impregnating the coil under vacuum.

9.3 HTS Magnets

9.3.1 Major Areas of Application—HTS (and LTS)

A technology is generally either enabling or replacing. If the technology is enabling, because of a feature or features that existing or (competing) technologies do not offer, it can compete with existing technologies by a criterion other than price, often the most common and crucial criterion in the marketplace. If replacing, the technology generally must compete with the existing technologies by price alone.

Listed in Table 9.7 on the next page are LTS and HTS applications, chiefly magnets, proven successful in the marketplace (*marketplace* in the table) or still in an R&D stage. The table also lists *selected* references, mostly of R&D papers and, with a few exceptions, exclusively those published either in *IEEE Transactions on Magnetics* or *Applied Superconductivity*, that report chiefly a *completed magnet* with *experimental results* and occasionally those focusing on specific design or operation issues, e.g., cryogenics, conductors, AC losses, protection, of a device. Rarely cited are those reporting results of only a design, modeling, or simulation study. For electric power applications, a few overview papers are included. Among *many* papers on a device or its upgraded versions from the *same* group, only a few papers are cited, generally one or two early papers and the latest ones, to reflect the team's activities. Each application is briefly discussed below.

Current Leads—Both LTS and HTS versions are commercial success; selected papers, both LTS and HTS, are cited in ***CHAPTER 4***.

Electric Power—With exceptions for fusion magnets, LTS magnets for electric power applications listed in the table have ended at the R&D stage. Obviously, as stated above, in term of sheer volume, electric power offers HTS the greatest opportunities, but at the same time poses difficult challenges.

- ***Generation & Storage: Fusion***; ***Generator***; ***SMES/Flywheel*** There are six on-going major superconducting fusion machines, all LTS-based, running (Tore Supra, Large Helical Device, KSTAR) or under development, listed in order of nearness to completion (EAST, Wendelstein 7-X, ITER). One small machine, LDX, uses an HTS magnet. As for Generator and SMES/Flywheel, HTS applications are in R&D stage.

- ***Distribution: Fault Current Limiter***; ***Transformer***; and ***Transmission*** All HTS applications are in R&D stage.

- ***End User: Motor***: HTS applications are in R&D stage.

MAGLEV—Although there are *many* applications of magnetic levitation, the papers cited are confined to MAGLEV applied to human transportation and electromagnetic launch (here, mostly analysis and design); HTS in R&D stage.

Magnetic Separation—LTS-based high-gradient magnetic separation (HGMS) is a marketplace success (*marketplace*), but in a limited way, really only for kaolin clay—HGMS for other materials, including water purification, is struggling [9.23]; HTS in R&D stage. As with other *marketplace* LTS systems listed in Table 9.7, no papers are cited for LTS systems; some HTS-based R&D papers are cited.

Table 9.7: Areas of Application for LTS and HTS—Chiefly Magnets

Application	Remarks [Selected references]
Current leads—*marketplace* (LTS; HTS, limited) {see CHAPTER 4}	
Electric Power—General Overview [9.24–9.29]	
• Generation & Storage:	
Fusion	LTS [9.30–9.56]; LTS/HTS [9.57, 9.58]
Generator	LTS* [9.59–9.62]; HTS [9.63–9.74]
SMES/Flywheel	LTS* [9.75–9.80]; HTS [9.81–9.111]
• Distribution:	
Fault Current Limiter	LTS* [9.112–9.115]; HTS [9.116–9.151]
Transformer	LTS* [9.152–9.156]; HTS [9.157–9.171]
Transmission	LTS* [9.172–9.179]; HTS [9.180–9.201]
• End User: Motor	LTS* [9.202–9.204]; HTS [9.205–9.233]
MAGLEV	LTS* [9.234–9.247]; HTS [9.248–9.258]
Magnetic Separation	LTS (*marketplace*); HTS [9.259–9.267]
Medical MRI	LTS (*marketplace*)
Research Magnets	
High Energy Physics	LTS* [9.268–9.336]; HTS [9.337–9.341]
High-Field DC Solenoids†	LTS (*marketplace*); LTS/HTS & HTS‡ [9.342–9.369]
NMR/MRI§	LTS (*marketplace*); LTS/HTS & HTS [9.370–9.385]
Silicon Wafer Processing	LTS (*marketplace*); HTS [9.386]

* Early (up to the mid 1980s, except for MAGLEV and High Energy Physics) papers listed for historical interest; others only analysis, concept, design, overview, plans, projection, or status.

† Hybrid magnet papers not listed (see CHAPTER 3 REFERENCES); selected *recent* papers on *cryogen-free* LTS magnets (above ∼10 T) listed.

‡ "Low-field" HTS coils included.

§ Selected papers on LTS magnets listed.

Medical MRI—HTS moving into R&D stage [9.28].

Research Magnets—Superconducting magnets dominate in research fields, because here performance often trumps price.

High Energy Physics *All* magnets—detectors, dipoles, quadrupoles —are LTS-based; HTS in early R&D stage.

High-Field DC Solenoids LTS/HTS (HTS as an insert to an LTS magnet), all HTS, and *cryogen-free LTS* (above ∼10 T) are in R&D stage.

NMR/MRI All marketplace magnets are LTS-based; high-field LTS/HTS (NMR) and HTS (MRI) in early R&D stage.

Silicon Wafer Processing LTS-based magnets are successful in the marketplace, though used only by wafer manufacturers; HTS is in R&D stage.

The successful superconducting applications listed above are, at least currently (2008), all LTS-based, despite operation at liquid helium temperatures. For the most prized applications—in terms of sheer volume—electric power, as noted above, LTS has been demonstrated to be not enabling: hope hinges on HTS.

9.3.2 Outlook on HTS Magnets

There are two groups of marketplace applications for HTS. The first belongs to those applications in which LTS has failed or which have never been explored by LTS. Here, the HTS's most distinctive enabling feature over LTS—the higher operating temperature—may enable it to succeed in these old or unexplored applications; a key to this success could, surprisingly, be less striking technical benefits such as a *less intrusive* cryogenic system, more likely achievable with operation at well above 4.2 K. For this group YBCO and BSCCO, with critical temperatures 93 K and >100 K, should have an edge over MgB_2 (39 K).

The second group is the one already conquered by LTS. For this group of applications, HTS is a *replacer* of, rather than an *enabler*, over LTS. Its success thus may not derive from its distinctive enabling feature but from the clearest criterion for any replacer: HTS must compete head-on against LTS on price. Here, it currently appears that MgB_2 is in a better position than BSCCO and YBCO.

The cost of running the cryogenic system surely decreases with operating temperature, but the overriding challenge to cryogenics, as remarked above, is to make it *less intrusive*, rather than to emphasize the improved efficiency of a higher operating temperature. Of course, as studied in ***DISCUSSION*** *7.5*, in applications where AC losses are present the cryogenic efficiency becomes a key or even decisive factor if a superconducting version can outperform its room-temperature counterpart. For a magnet of significance to the marketplace, equally important are also mechanical integrity, stability, protection, and conductor specification; on these issues, as we have studied, the impact of increased operating temperature, though complex and mixed, appears to favor HTS magnets.

9.4 Concluding Remarks

This 2nd Edition, like the 1st Edition, presents and discusses key design and operational issues for superconducting magnets, LTS and HTS, with, where appropriate, emphasis on issues that are more relevant to HTS magnets. The reader should have gained an enhanced understanding, and appreciation, that a higher operating temperature doesn't necessarily make the magnet designer's task easier. Finally, it is hoped that the 2nd Edition will be an essential companion to superconducting magnet designers, experienced specialists, as well as those just starting as professionals and as graduate students.

"Il resto nol dico, . . ." —*Figaro*

REFERENCES

[9.1] John R. Miller and Tom Painter (SCH presentations, April and August 2005).

[9.2] Andrey V. Gavrilin (SCH presentation, April 2005).

[9.3] Mark D. Bird (SCH presentation, August 2005).

[9.4] Iain Dixson (SCH presentation, August 2005).

[9.5] Yukikazu Iwasa and Haigun Lee, "'Electromaglev'—magnetic levitation of a superconducting disk with a DC field generated by electromagnets: Part 1 Theoretical and experimental results on operating modes, lift-to-weight ratio, and suspension stiffness," *Cryogenics* **37**, 807 (1997).

[9.6] Haigun Lee, Makoto Tsuda, and Yukikazu Iwasa, "'Electromaglev' 'active-maglev' —magnetic levitation of a superconducting disk with a DC field generated by electromagnets: Part 2 Theoretical and experimental results on lift-to-weight ratio and stiffness," *Cryogenics* **38**, 419 (1998).

[9.7] Makoto Tsuda, Haigun Lee, So Noguchi, and Yukikazu Iwasa, "'Electromaglev' ('active-maglev') — magnetic levitation of a superconducting disk with a DC field generated by electromagnets: Part 4 Theoretical and experimental results on supercurrent distributions in field-cooled YBCO disks," *Cryogenics* **39**, 893 (1999).

[9.8] Y. Iwasa, H. Lee, M. Tsuda, M. Murakami, T. Miyamoto, K. Sawa, K. Nishi, H. Fujimoto, and K. Nagashima, "Electromaglev—levitation data for single and multiple bulk YBCO disks," *IEEE Trans. Appl. Supercond.* **9**, 984 (1999).

[9.9] Stephen Hawking, *A Brief History of Time* (Bantam Books, New York, 1988).

[9.10] S. Jin, T.H. Tiefel, R.C. Sherwood, M.E. Davis, P.B. van Dover, G.W. Kammlott, R.A. Fastnacht, and H.D. Keith, "High critical currents in Y-Ba-Cu-O superconductors," *Appl. Phys. Lett.* **52**, 2074 (1988).

[9.11] K. Salama, V. Selvamanickam, L. Gao, and K. Sun, "High current density in bulk $YBa_2Cu_3O_x$ superconductor," *Appl. Phys. Lett.* **54**, 2352 (1989).

[9.12] S. Gotoh, M. Murakami, H. Fujimoto, and N. Koshizuka, "Magnetic properties of superconducting $YBa_2Cu_3O_x$ permanent magnets prepared by the melt process," *J. Appl. Phys.* **6**, 2404 (1992).

[9.13] N. Sakai, K. Ogasawara, K. Inoue, D. Ishihara, and M. Murakami, "Fabrication of melt-processed RE-Ba-Cu-O bulk superconductors with high densities," *IEEE Trans. Appl. Supercond.* **11**, 3509 (2001).

[9.14] Masaru Tomita and Masato Murakami, "High-temperature superconductor bulk magnets that can trap magnetic fields of over 17 tesla at 29 K," *Nature* **421**, 517 (2003).

[9.15] Yukikazu Iwasa, Seung-yong Hahn, Masaru Tomita, Haigun Lee, and Juan Bascuñán, "A 'persistent-mode' magnet comprised of YBCO annuli," *IEEE Trans. Appl. Superconduc.* **15**, 2352 (2005).

[9.16] M. Konishi, S. Hahakura, K. Ohmatsu, K. Hayashi, K. Yasuda, "HoBCO thin films for SN transition type fault current limiter," *Physica C* **412–414**, 1056 (2004).

[9.17] Marty Rupitch (personal communication, 2007).

[9.18] Y. Sakai, K. Inoue, T. Asano, and H. Maeda, "Development of a high strength, high conductivity copper-silver alloy for pulsed magnets," *IEEE Trans. Magn.* **28**, 888 (1992).

[9.19] H. Fujishiro and S. Kobayashi, "Thermal conductivity, thermal diffusivity and thermoelectric power in Sam-based bulk superconductors," *IEEE Trans. Appl. Supercond.* **12**, 1124 (2002).

[9.20] Hiroyuki Fujishiro, Tetsuo Oka, Kazuya Yokoyama, Masahiko Kaneyama, and Koshichi Noto, "Flux motion studies by means of temperature measurement in magnetizing processes for HTSC bulks," *IEEE Trans. Appl. Supercond.* **14**, 1054 (2004).

[9.21] K. Okuno, K. Sawa and Y. Iwasa, "Performance of the HTS bulk magnet in cryocooler system with cyclic temperature variation," *Physica C: Supercond.* **426–431**, 809 (2005).

[9.22] N. Koshizuka, "R&D of superconducting bearing technologies for flywheel energy storage systems," *Advances in Superconductivity XVIII* (Elsevier, 2006), 1103.

[9.23] Christopher Rey (private communication, 2007).

Papers Cited in Table 9.7: Electric Power

General Overview

[9.24] Mario Rabinowitz, "The Electric Power Research Institute's role in applying superconductivity to future utility systems," *IEEE Trans. Magn.* **MAG-11**, 105 (1975).

[9.25] Paul M. Grant "Superconductivity and electric power: promises, promises ... past, present and future," *IEEE Trans. Appl. Superconduc.* **7**, 112 (1997).

[9.26] William V. Hassenzahl, "Superconductivity, an enabling technology for 21st century power systems?," *IEEE Trans. Appl. Superconduc.* **11**, 1447 (2001).

[9.27] Donald U. Gubser, "Superconductivity: an emerging power-dense energy-efficient technology," *IEEE Trans. Appl. Superconduc.* **14**, 2037 (2004).

[9.28] Osami Tsukamoto, "Roads for HTS power applications to go into the real world: cost issues and technical issues," *Cryogenics* **45**, 3 (2005).

[9.29] Alex P. Malozemoff, "The new generation of superconductor equipment for the electric power grid," *IEEE Trans. Appl. Superconduc.* **16**, 54 (2006).

Fusion—Tore Supra

[9.30] B. Turck, "Six years of operating experience with Tore Supra, the largest Tokamak with superconducting coils," *IEEE Trans. Magn.* **32**, 2264 (1996).

[9.31] J.L. Duchateau and B. Turck, "Application of superfluid helium cooling techniques to the toroidal field systems of tokamaks," *IEEE Trans. Appl. Superconduc.* **9**, 157 (1999).

Fusion—Large Helical Device (LHD)

[9.32] T. Satow, N. Yanagi, S. Imagawa, H. Tamura, K. Takahata, T. Mito, H. Chikaraishi, S. Yamada, A. Nishimura, R. Maekawa, A. Iwamoto, N. Inoue, Y. Nakamura, K. Watanabe, H. Yamada, A. Komori, I. Ohtake, M. Iima, S. Satoh, O. Motojima, and LHD Group, "Completion and trial operation of the superconducting magnets for the Large Helical Device," *IEEE Trans. Appl. Superconduc.* **9**, 1008 (1999).

[9.33] S. Imagawa, N. Yanagi, H. Sekiguchi, T. Mito, and O. Motojima, "Performance of the helical coil for the Large Helical Device in six years' operation," *IEEE Trans. Appl. Superconduc.* **14**, 629 (2004).

[9.34] S. Imagawa, T. Obana, S. Hamaguchi, N. Yanagi, T. Mito, S. Moriuchi, H. Sekiguchi, K. Ooba, T. Okamura, A. Komori, and O. Motojima, "Results of the excitation test of the LHD helical coils cooled by subcooled helium," *IEEE Trans. Appl. Superconduc.* **18**, 455 (2008).

Fusion—EAST

[9.35] Peide Weng, Qiuliang Wang, Ping Yuan, Qiaogen Zhou, and Zian Zhu, "Recent development of magnet technology in China: Large devices for fusion and other applications," *IEEE Trans. Appl. Superconduc.* **16**, 731 (2006).

Papers Cited in Table 9.7: Fusion (continuation)

Fusion—KSTAR

[9.36] W. Chung, Y.B. Chang, J.H. Kim, J.S. Kim, K. Kim, M.K. Kim, S.B. Kim, Y.J. Kim, S.I. Lee, S.Y. Lee, Y.H. Lee, H. Park, K.R. Park, C. Winter, C.S. Yoon, and KSTAR Magnet Team, "The test facility for the KSTAR superconducting magnets at SAIT," *IEEE Trans. Appl. Superconduc.* **10**, 645 (2000).

[9.37] K. Park, W. Chung, S. Baek, B. Lim, S.J. Lee, H. Park, Y. Chu, S. Lee, K.P. Kim, J. Joo, K. Lee, D. Lee, S. Ahn, Y.K. Oh, K. Kim, J.S. Bak, and G.S. Lee, "Status of the KSTAR PF6 and PF7 coil development," *IEEE Trans. Appl. Superconduc.* **15**, 1375 (2005).

[9.38] S.H. Park, W. Chung, H.J. Lee, W.S. Han, K.M. Moon, W.W. Park, J.S. Kim, H. Yonekawa, Y. Chu, K.W. Cho, K.R. Park, W.C. Kim, Y.K. Oh, and J.S. Bak, "Stability of superconducting magnet for KSTAR," *IEEE Trans. Appl. Superconduc.* **18**, 447 (2008).

Fusion—Wendelstein 7-X (W7-X)

[9.39] T. Schild, D. Bouziat, Ph. Bredy, G. Dispau, A. Donati, Ph. Fazilleau, L. Genini, M. Jacquemet, B. Levesy, F. Molinié, J. Sapper, C. Walter, M. Wanner, and L. Wegener, "Overview of a new test facility for the W7X coils acceptance tests," *IEEE Trans. Appl. Superconduc.* **12**, 639 (2002).

[9.40] L. Wegener, W. Gardebrecht, R. Holzthum, N. Jaksic, F. Kerl, J. Sapper, and M. Wanner, "Status of the construction of the W7-X magnet system," *IEEE Trans. Appl. Superconduc.* **12**, 653 (2002).

[9.41] Juergen Baldzuhn, Hartmut Ehmler, Laurent Genini, Kerstan Hertel, Alf Hoelting, Carlo Sborchia, and Thierry Schild, "Cold tests of the superconducting coils for the Stellarator W7-X," *IEEE Trans. Appl. Superconduc.* **18**, 509 (2008).

Fusion—ITER

[9.42] C.D. Henning and J.R. Miller, "Magnet systems for the International Thermonuclear Experimental Reactor," *IEEE Trans. Magn.* **MAG-25**, 1469 (1989).

[9.43] D. Bruce Montgomery, Richard J. Thome, "US perspective on the ITER magnetics R and D program," *IEEE Trans. Appl. Superconduc.* **3**, 342 (1993).

[9.44] S. Shimamoto, K. Hamada, T. Kato, H. Nakajima, T. Isono, T. Hiyama, M. Oshikiri, K. Kawano, M. Sugimoto, N. Koizumi, K. Nunoya, S. Seki, H. Hanawa, H. Wakabayashi, K. Nishida, T. Honda, H. Matsui, Y. Uno, K. Takano, T. Ando, M. Nishi, Y. Takahashi, S. Sekiguchi, T. Ohuchi, F. Tajiri, J. Okayama, Y. Takaya, T. Kawasaki, K. Imahashi, K. Ohtsu, and H. Tsuji, "Construction of ITER common test facility for CS model coil," *IEEE Trans. Magn.* **32**, 3049 (1996).

[9.45] A. della Corte, M.V. Ricci, M. Spadoni, G. Bevilacqua, R.K. Maix, E. Salpietro, H. Krauth, M. Thoener, S. Conti, R. Garre, S. Rossi, A. Laurenti, P. Gagliardi, and N. Valle, "EU conductor development for ITER CS and TF Model Coils," *IEEE Trans. Appl. Superconduc.* **7**, 763 (1997).

[9.46] Arend Nijhuis, Niels H.W. Noordman, Oleg Shevchenko, Herman H.J. ten Kate, Neil Mitchell, "Electromagnetic and mechanical characterisation of ITER CS-MC conductors affected by transverse cyclic loading. III. Mechanical properties," *IEEE Trans. Appl. Superconduc.* **9**, 165 (1999).

[9.47] D. Ciazynski, P. Decool, M. Rubino, J.M. Verger, N. Valle, R. Maix, "Fabrication of the first European full-size joint sample for ITER," *IEEE Trans. Appl. Superconduc.* **9**, 648 (1999).

[9.48] D. Bessette, N. Mitchell, E. Zapretilina, and H. Takigami, "Conductors of the ITER

Papers Cited in Table 9.7: ITER (continuation)

magnets," *IEEE Trans. Appl. Superconduc.* **11**, 1550 (2001).

[9.49] A.M. Fuchs, B. Blau, P. Bruzzone, G. Vecsey, M. Vogel, "Facility status and results on ITER full-size conductor tests in SULTAN," *IEEE Trans. Appl. Superconduc.* **11**, 2022 (2001).

[9.50] T. Ando, T. Isono, T. Kato, N. Koizumi, K. Okuno, K. Matsui, N. Martovetsky, Y. Nunoya, M. Ricci, Y. Takahashi, and H. Tsuji, "Pulsed operation test results of the ITER-CS model coil and CS insert," *IEEE Trans. Appl. Superconduc.* **12**, 496 (2002).

[9.51] N. Cheverev, V. Glukhikh, O. Filatov, V. Belykov, V. Muratov, S. Egorov, I. Rodin, A. Malkov, M. Sukhanova, S. Gavrilov, V. Krylov, B. Mudugin, N. Bondarchouk, V. Yakubovsky, A. Cherdakov, M. Mikhailov, Yu. Konstantinov, Yu. Sokolov, G. Yakovleva, S. Peregudov, P. Chaika, V. Sytnikov, A. Rychagov, A. Taran, A. Shikov, V. Pantcyrny, A. Vorobieva, E. Dergunova, I. Abdukhanov, K. Mareev, and N. Grysnov, "ITER TF conductor insert coil manufacture," *IEEE Trans. Appl. Superconduc.* **11**, 548 (2002).

[9.52] R. Heller, D. Ciazynski, J.L. Duchateau, V. Marchese, L. Savoldi-Richard, and R. Zanino, "Evaluation of the current sharing temperature of the ITER Toroidal Field model coil," *IEEE Trans. Appl. Superconduc.* **13**, 1447 (2003).

[9.53] Kiyoshi Okuno, Hideo Nakajima, and Norikiyo Koizumi, "From CS and TF model coils to ITER: lessons learnt and further progress," *IEEE Trans. Appl. Superconduc.* **16**, 850 (2006).

[9.54] L. Chiesa, M. Takayasu, J.V. Minervini, C. Gung, P.C. Michael, V. Fishman, and P.H. Titus, "Experimental studies of transverse stress effects on the critical current of a Sub-Sized Nb_3Sn superconducting cable," *IEEE Trans. Appl. Superconduc.* **17**, 1386 (2007).

[9.55] P. Bruzzone, B. Stepanov, R. Wesche, E. Salpietro, A. Vostner, K. Okuno, T. Isono, Y. Takahashi, Hyoung Chan Kim, Keeman Kim, A.K. Shikov, and V.E. Sytnikov, "Results of a new generation of ITER TF conductor samples in SULTAN," *IEEE Trans. Appl. Superconduc.* **18**, 459 (2008).

[9.56] K. Seo, A. Nishimura, Y. Hishinuma, K. Nakamura, T. Takao, G. Nishijima, K. Watanabe, and K. Katagiri, "Mitigation of critical current degradation in mechanically loaded Nb_3Sn superconducting multi-strand cable," *IEEE Trans. Appl. Superconduc.* **18**, 491 (2008).

Fusion—LDX **[LTS/HTS]**

[9.57] Philip C. Michael, Alexander Zhukovsky, Bradford A. Smith, Joel H. Schultz, Alexi Radovinsky, Joseph V. Minervini, K. Peter Hwang, and Gregory J. Naumovich, "Fabrication and test of the LDX levitation coil," *IEEE Trans. Appl. Superconduc.* **13**, 1620 (2003).

[9.58] Philip C. Michael, Darren T. Garnier, Alexi Radovinsky, Igor Rodin, Vladimir Ivkin, Michael E. Mauel, Valery Korsunsky, Sergey Egorov, Alex Zhukovsky, and Jay Kesner, "Quench detection for the Levitated Dipole Experiment (LDX) charging coil," *IEEE Trans. Appl. Superconduc.* **17**, 2482 (2007).

Generator **[LTS]**

[9.59] J.L. Smith, Jr., J.L. Kirtley, Jr., P. Thullen, "Superconducting rotating machines," *IEEE Trans. Magn.* **MAG-11**, 128 (1975).

[9.60] C.E. Oberly, "Air Force application of lightweight superconducting machinery," *IEEE Trans. Magn.* **MAG-13**, 260 (1977).

***Papers Cited in Table 9.7: Generator* [LTS]** (continuation)

[9.61] J.L. Smith, Jr., G.L. Wilson, J.L. Kirtley, Jr., T.A. Keim, "Results from the MIT-EPRI 3-MVA superconducting alternator," *IEEE Trans. Magn.* **MAG-13**, 751 (1977).

[9.62] A.D. Appleton, J.S.H. Ross, J. Bumby, A.J. Mitcham, "Superconducting A.C. generators: Progress on the design of a 1300 MW, 3000 rev/min generator," *IEEE Trans. Magn.* **MAG-13**, 770 (1977).

***Generator* [HTS]**

[9.63] P. Tixador, Y. Brunet, P. Vedrine, Y. Laumond, J.L. Sabrie, "Electrical tests on a fully superconducting synchronous machine," *IEEE Trans. Magn.* **27**, 2256 (1991).

[9.64] T. Suryanarayana, J.L. Bhattacharya, K.S.N. Raju, K.A. Durga Prasad, "Development and performance testing of a 200 kVA damperless superconducting generator," *IEEE Trans. Energy Conversion* **12**, 330 (1997).

[9.65] Tanzo Nitta, Takao Okada, Yasuyuki Shirai, Takuya Kishida, Yoshihiro Ogawa, Hiroshi Hasegawa, Kouzou Takagi, and Hisakazu Matsumoto, "Experimental studies on power system stability of a superconducting generator with high response excitation," *IEEE Trans. Power Sys.* **12**, 906 (1997).

[9.66] K. Ueda, R. Shiobara, M. Takahashi, T. Ageta, "Measurement and analysis of 70 MW superconducting generator constants," *IEEE Trans. Appl. Superconduc.* **9**, 1193 (1999).

[9.67] Sung-Hoon Kim, Woo-Seok Kim, Song-yop Hahn and Gueesoo Cha, "Development and test of an HTS induction generator," *IEEE Trans. Magn.* **11**, 1968 (2001).

[9.68] M. Frank, J. Frauenhofer, P. van Hasselt, W. Nick, H.-W. Neumueller, and G. Nerowski, "Long-term operational experience with first Siemens 400 kW HTS machine in diverse configurations," *IEEE Trans. Appl. Superconduc.* **13**, 2120 (2003).

[9.69] Paul N. Barnes, Gregory L. Rhoads, Justin C. Tolliver, Michael D. Sumption, and Kevin W. Schmaeman, "Compact, lightweight, superconducting power generators," *IEEE Trans. Magn.* **41**, 268 (2005).

[9.70] Maitham K. Al-Mosawi, C. Beduz, and Y. Yang, "Construction of a 100 kVA high temperature superconducting synchronous generator," *IEEE Trans. Appl. Superconduc.* **15**, 2182 (2005).

[9.71] S.K. Baik, M.H. Sohn, E.Y. Lee, Y.K. Kwon, Y.S. Jo, T.S. Moon, H.J. Park, and Y.C. Kim, "Design considerations for 1 MW class HTS synchronous motor," *IEEE Trans. Appl. Superconduc.* **15**, 2202 (2005).

[9.72] L. Li, T. Zhang, W. Wang, J. Alexander, X. Huang, K. Sivasubramaniam, E.T. Laskaris, J.W. Bray, and J.M. Fogarty, "Quench test of HTS coils for generator application at GE," *IEEE Trans. Appl. Superconduc.* **17**, 1575 (2007).

[9.73] S.S. Kalsi, D. Madura, G. Snitchler, M. Ross, J. Voccio, and M. Ingram, "Discussion of test results of a superconductor synchronous condenser on a utility grid," *IEEE Trans. Appl. Superconduc.* **17**, 2026 (2007).

[9.74] Wolfgang Nick, Michael Frank, Gunar Klaus, Joachim Frauenhofer, and Heinz-Werner Neumüller, "Operational experience with the world's first 3600 rpm 4 MVA generator at Siemens," *IEEE Trans. Appl. Superconduc.* **17**, 2030 (2007).

***SMES/Flywheel* [LTS]**

[9.75] Roger W. Boom and Harold A. Peterson, "Superconductive energy storage for power systems," *IEEE Trans. Magn.* **MAG-8**, 751 (1972).

[9.76] J.D. Rogers, H.J. Boenig, J.C. Bronson, D.B. Colyer, W.V. Hassenzahl, R.D. Turn-

***Papers Cited in Table 9.7: SMES/Flywheel* [LTS]** (continuation)

er, and R.I. Schermer, "30-MJ superconducting magnetic energy storage (SMES) unit for stabilizing an electric transmission system," *IEEE Trans. Magn.* **MAG-15**, 820 (1979).

[9.77] T. Shintomi, M. Masuda, T. Ishikawa, S. Akita, T. Tanaka and H. Kaminosono, "Experimental study of power system stabilization by superconducting magnetic energy storage," *IEEE Trans. Magn.* **MAG-19**, 350 (1983).

[9.78] T. Onishi, H. Tateishi, K. Komuro, K. Koyama, M. Takeda, T. Ichihara, "Energy transfer experiments between 3 MJ and 4 MJ pulsed superconducting magnets," *IEEE Trans. Magn.* **MAG-21**, 1107 (1985).

[9.79] Shinichi Nomura, Koji Kasuya, Norihiro Tanaka, Kenji Tsuboi, Hiroaki Tsutsui, Shunji Tsuji-Iio, and Ryuichi Shimada, "Experimental results of a 7-T force-balanced helical coil for large-scale SMES," *IEEE Trans. Appl. Superconduc.* **18**, 701 (2008).

[9.80] A. Kawagoe, S. Tsukuda, F. Sumiyoshi, T. Mito, H. Chikaraishi, T. Baba, M. Yokoto, H. Ogawa, T. Hemmi, R. Abe, A. Nakamura, K. Okumura, A. Kuge, and M. Iwakuma, "AC losses in a conduction-cooled LTS pulse coil with stored energy of 1 MJ for UPS-SMES as protection from momentary voltage drops," *IEEE Trans. Appl. Superconduc.* **18**, 789 (2008).

***SMES/Flywheel* [HTS]**

[9.81] P. Stoye, G. Fuchs, W. Gawalek, P. Görnert, A. Gladun, "Static forces in a superconducting magnet bearing," *IEEE Trans. Magn.* **31**, 4220 (1995).

[9.82] P. Tixador, P. Hiebel, Y. Brunet, X. Chaud, P. Gautier-Picard, "Hybrid superconducting magnetic suspensions," *IEEE Trans. Magn.* **32**, 2578 (1996).

[9.83] S.S. Kalsi, D. Aized, B. Conner, G. Snitchler, J. Campbell, R.E. Schwall, J. Kellers, Th. Stephanblome, A. Tromm, P. Winn, "HTS SMES magnet design and test results," *IEEE Trans. Appl. Superconduc.* **7**, 971 (1997).

[9.84] S. Ohashi, S. Tamura, and K. Hirane, "Levitation characteristics of the HTSC-permanent magnet hybrid flywheel system," *IEEE Trans. Appl. Superconduc.* **9**, 988 (1999).

[9.85] Y. Miyagawa, H. Kameno, R. Takahata and H. Ueyama, "A 0.5 kWh flywheel energy storage system using a high-Tc superconducting magnetic bearing," *IEEE Trans. Appl. Superconduc.* **9**, 996 (1999).

[9.86] Shigeo Nagaya, Naoji Kashima, Masaharu Minami, Hiroshi Kawashima and Shigeru Unisuga, "Study on high temperature superconducting magnetic bearing for 10 kWh flywheel energy storage system," *IEEE Trans. Appl. Superconduc.* **11**, 1649 (2001).

[9.87] J.R. Fang, L.Z. Lin, L.G. Yan, and L.Y. Xiao, "A new flywheel energy storage system using hybrid superconducting magnetic bearings, *IEEE Trans. Appl. Superconduc.* **11**, 1657 (2001).

[9.88] Yevgeniy Postrekhin, Ki Bui Ma and Wei-Kan Chu, "Drag torque in high Tc superconducting magnetic bearings with multi-piece superconductors in low speed high load applications," *IEEE Trans. Appl. Superconduc.* **11**, 1661 (2001).

[9.89] Thomas M. Mulcahy, John R. Hull, Kenneth L. Uherka, Robert G. Abboud, John J. Juna, "Test results of 2-kWh flywheel using passive PM and HTS bearings," *IEEE Trans. Appl. Superconduc.* **11**, 1729 (2001).

[9.90] Amit Rastogi, David Ruiz Alonso, T.A. Coombs, and A.M. Campbell, "Axial and journal bearings for superconducting flywheel systems," *IEEE Trans. Appl. Super-*

Papers Cited in Table 9.7: SMES/Flywheel **[HTS]** (continuation)

conduc. **13**, 2267 (2003).

[9.91] Ryousuke Shiraishi, Kazuyuki Demachi, Mitsuru Uesaka, and Ryoichi Takahata, "Numerical and experimental analysis of the rotation speed degradation of superconducting magnetic bearings," *IEEE Trans. Appl. Superconduc.* **13**, 2279 (2003).

[9.92] Xiaohua Jiang, Xiaoguang Zhu, Zhiguang Cheng, Xiaopeng Ren, and Yeye He, "A 150 kVA/0.3 MJ SMES voltage sag compensation system," *IEEE Trans. Appl. Superconduc.* **15**, 574 (2005).

[9.93] C.J. Hawley and S.A. Gower, "Design and preliminary results of a prototype HTS SMES device," *IEEE Trans. Appl. Superconduc.* **15**, 1899 (2005).

[9.94] So Noguchi, Atsushi Ishiyama, S. Akita, H. Kasahara, Y. Tatsuta, and S. Kouso, "An optimal configuration design method for HTS-SMES coils," *IEEE Trans. Appl. Superconduc.* **15**, 1927 (2005).

[9.95] Ji Hoon Kim, Woo-Seok Kim, Song-Yop Hahn, Jae Moon Lee, Myung Hwan Rue, Bo Hyung Cho, Chang Hwan Im, and Hyun Kyo Jung, "Characteristic test of HTS pancake coil modules for small-sized SMES," *IEEE Trans. Appl. Superconduc.* **15**, 1919 (2005).

[9.96] Takumi Ichihara, Koji Matsunaga, Makoto Kita, Izumi Hirabayashi, Masayuki Isono, Makoto Hirose, Keiji Yoshii, Kazuaki Kurihara, Osamu Saito, Shinobu Saito, Masato Murakami, Hirohumi Takabayashi, Mitsutoshi Natsumeda, and Naoki Koshizuka, "Application of superconducting magnetic bearings to a 10 kWh-class flywheel energy storage system," *IEEE Trans. Appl. Superconduc.* **15**, 2245 (2005).

[9.97] Y.H. Han, J.R. Hull, S.C. Han, N.H. Jeong, T.H. Sung, and Kwangsoo No, "Design and characteristics of a superconductor bearing," *IEEE Trans. Appl. Superconduc.* **15**, 2249 (2005).

[9.98] T.A. Coombs, I. Samad, D. Ruiz-Alonso, and K. Tadinada, "Superconducting micro-bearings," *IEEE Trans. Appl. Superconduc.* **15**, 2312 (2005).

[9.99] Qiuliang Wang, Shouseng Song, Yuanzhong Lei, Yingming Dai, Bo Zhang, Chao Wang, Sangil Lee, and Keeman Kim, "Design and fabrication of a conduction-cooled high temperature superconducting magnet for 10 kJ superconducting magnetic energy storage system," *IEEE Trans. Appl. Superconduc.* **16**, 570 (2006).

[9.100] H.J. Kim, K.C. Seong, J.W. Cho, J.H. Bae, K.D. Sim, S. Kim, E.V. Lee, K. Ryu, and S.H. Kim, "3 MJ/750 kVA SMES system for improving power quality," *IEEE Trans. Appl. Superconduc.* **16**, 574 (2006).

[9.101] S. Nagaya, N. Hirano, H. Moriguchi, K. Shikimachi, H. Nakabayashi, S. Hanai, J. Inagaki, S. Ioka, and S. Kawashima, "Field test results of the 5 MVA SMES system for bridging instantaneous voltage dips," *IEEE Trans. Appl. Superconduc.* **16**, 632 (2006).

[9.102] T. Tosaka, K. Koyanagi, K. Ohsemochi, M. Takahashi, Y. Ishii, M. Ono, H. Ogata, K. Nakamoto, H. Takigami, S. Nomura, K. Kidoguchi, H. Onoda, N. Hirano, and S. Nagaya, "Excitation tests of prototype HTS coil with Bi2212 cables for development of high energy density SMES," *IEEE Trans. Appl. Superconduc.* **17**, 2010 (2007).

[9.103] M. Strasik, P.E. Johnson, A.C. Day, J. Mittleider, M.D. Higgins, J. Edwards, J.R. Schindler, K.E. McCrary, C.R. McIver, D. Carlson, J.F. Gonder, and J.R. Hull, "Design, fabrication, and test of a 5-kWh/100-kW flywheel energy storage utilizing a high-temperature superconducting bearing, *IEEE Trans. Appl. Superconduc.* **17**, 2133 (2007).

Papers Cited in Table 9.7: SMES/Flywheel **[HTS]** (continuation)

[9.104] Uta Floegel-Delor, Rolf Rothfeld, Dieter Wippich, Bernd Goebel, Thomas Riedel, and Frank N. Werfel, "Fabrication of HTS bearings with ton load performance," *IEEE Trans. Appl. Superconduc.* **17**, 2142 (2007).

[9.105] Keigo Murakami, Mochimitsu Komori, and Hisashi Mitsuda, "Flywheel energy storage system using SMB and PMB," *IEEE Trans. Appl. Superconduc.* **17**, 2146 (2007).

[9.106] Rubens de Andrade, Jr., Guilherme G. Sotelo, Antonio C. Ferreira, Luis G.B. Rolim, José da Silva Neto, Richard M. Stephan, Walter I. Suemitsu, and Roberto Nicolsky, "Flywheel energy storage system description and tests," *IEEE Trans. Appl. Superconduc.* **17**, 2154 (2007).

[9.107] Takeshi Shimizu, Masaki Sueyoshi, Ryo Kawana, Toshihiko Sugiura, and Masatsugu Yoshizawa, "Internal resonance of a rotating magnet supported by a high-T_c superconducting bearing," *IEEE Trans. Appl. Superconduc.* **17**, 2166 (2007).

[9.108] T. Suzuki, E. Ito, T. Sakai, S. Koga, M. Murakami, K. Nagashima, Y. Miyazaki, H. Seino, N. Sakai, I. Hirabayashi, K. Sawa, "Temperature dependency of levitation force and its relaxation in HTS," *IEEE Trans. Appl. Superconduc.* **17**, 3020 (2007).

[9.109] Qiuliang Wang, Yinming Dai, Souseng Song, Huaming Wen, Ye Bai, Luguang Yan, and Keeman Kim, "A 30 kJ Bi2223 high temperature superconducting magnet for SMES with solid-nitrogen protection," *IEEE Trans. Appl. Superconduc.* **18**, 754 (2008).

[9.110] Liye Xiao, Zikai Wang, Shaotao Dai, Jinye Zhang, Dong Zhang, Zhiyuan Gao, Naihao Song, Fengyuan Zhang, Xi Xu, and Liangzhen Lin, "Fabrication and test of a 1 MJ HTS magnet for SMES," *IEEE Trans. Appl. Superconduc.* **18**, 770 (2008).

[9.111] P. Tixador, M. Deleglise, A. Badel, K. Berger, B. Bellin, J.C. Vallier, A. Allais, and C.E. Bruzek, "First test of a 800 kJ HTS SMES," *IEEE Trans. Appl. Superconduc.* **18**, 774 (2008).

Fault Current Limiter **[LTS]**

[9.112] J.D. Rogers, H.J. Boenig, P. Chowdhuri, R.I. Schermer, J.J. Wollan, and D.M. Weldon, "Superconducting fault current limiter and inductor design," *IEEE Trans. Magn.* **MAG-19**, 1054 (1983).

[9.113] E. Thuries, V.D. Pham, Y. Laumond, T. Verhaege, A. Fevrier, M. Collet, M. Bekhaled, "Towards the superconducting fault current limiter," *IEEE Trans. Power Delivery* **6**, 801 (1991).

[9.114] T. Ishigohka and N. Sasaki, "Fundamental test of new DC superconducting fault current limiter," *IEEE Trans. Magn.* **27**, 2341 (1991).

[9.115] Tsutomu Hoshino and Itsuya Muta, "Load test on superconducting transformer and fault current limiting devices for electric power system," *IEEE Trans. Magn.* **30**, 2018 (1994).

Fault Current Limiter **[HTS]**

[9.116] D.W.A. Willen and J.R. Cave, "Short circuit test performance of inductive high T_c superconducting fault current limiters," *IEEE Trans. Appl. Superconduc.* **5**, 1047 (1995).

[9.117] W. Paul, Th. Baumann, J. Rhyner, F. Platter, "Tests of 100 kW High-T_c superconducting fault current limiter," *IEEE Trans. Appl. Superconduc.* **5**, 1059 (1995).

***Papers Cited in Table 9.7: Fault Current Limiter* [HTS]** (continuation)

[9.118] J. Acero, L. Garcia-Tabares, M. Bajko, J. Calero, X. Granados, X. Obradors, S. Pinol, "Current limiter based on melt processed YBCO bulk superconductors," *IEEE Trans. Appl. Superconduc.* **5**, 1071 (1995).

[9.119] H. Kado and M. Ichikawa, "Performance of a high-Tc superconducting fault current limiter 'Design of a 6.6 kV magnetic shielding type superconducting fault current limiter,' " *IEEE Trans. Appl. Superconduc.* **7**, 993 (1997).

[9.120] Minseok Joe and Tae Kuk Ko, "Novel design and operational characteristics of inductive high-Tc superconducting fault current limiter," *IEEE Trans. Appl. Superconduc.* **7**, 1005 (1997).

[9.121] J.X. Jin, S.X. Dou, H.K. Liu, C. Grantham, Z.J. Zeng, Z.Y. Liu, T.R. Blackburn, X.Y. Li, H.L. Liu, J.Y. Liu, "Electrical application of high Tc superconducting saturable magnetic core fault current limiter," *IEEE Trans. Appl. Superconduc.* **7**, 1009 (1997).

[9.122] D.J. Moule, P.D. Evans, T.C. Shields, S.A.L. Foulds, J.P.G. Price, J.S. Abell, "Study of fault current limiter using YBCO thick film material," *IEEE Trans. Appl. Superconduc.* **7**, 1025 (1997).

[9.123] Victor Meerovich, Vladimir Sokolovsky, Shaul Goren, Andrey B. Kozyrev, Vitaly N. Osadchy, and Eugene K. Hollmann, "Operation of hybrid current limiter based on high-Tc superconducting thin film," *IEEE Trans. Appl. Superconduc.* **7**, 3783 (1997).

[9.124] B. Gromoll, G. Ries, W. Schmidt, H.-P. Kraemer, B. Seebacher, B. Utz, R. Nies, H.-W. Neumueller, E. Baltzer, S. Fischer, B. Heismann, "Resistive fault current limiters with YBCO films 100 kVA functional model," *IEEE Trans. Appl. Superconduc.* **9**, 656 (1999).

[9.125] K. Tekletsadik, M.P. Saravolac, A. Rowley, "Development of a 7.5 MVA superconducting fault current limiter," *IEEE Trans. Appl. Superconduc.* **9**, 672 (1999).

[9.126] X. Granados, X. Obradors, T. Puig, E. Mendoza, V. Gomis, S. Piñol, L. García-Tabarés, J. Calero, "Hybrid superconducting fault current limiter based on bulk melt textured $YBa_2Cu_3O_7$ ceramic composites," *IEEE Trans. Appl. Superconduc.* **9**, 1308 (1999).

[9.127] E. Leung, B. Burley, N. Chitwood, H. Gurol, G. Miyata, D. Morris, L. Ngyuen, B. O'Hea, D. Paganini, S. Pidcoe, P. Haldar, M. Gardner, D. Peterson, H. Boenig, J. Cooley, Y. Coulter, W. Hults, C. Mielke, E. Roth, J. Smith, S. Ahmed, A. Rodriguez, A. Langhorn, M. Gruszczynski & J. Hoehn, "Design and development of a 15 kV, 20 kA HTS fault current limiter," *IEEE Trans. Appl. Superconduc.* **10**, 832 (2000).

[9.128] Masahiro Takasaki, Shinji Torii, Haruhito Taniguchi, Hiroshi Kubota, Yuki Kudo, Hisahiro Yoshino, Hidehiro Nagamura and Masatoyo Shibuya, "Performance verification of a practical fault current limiter using YBCO thin film," *IEEE Trans. Appl. Superconduc.* **11**, 2499 (2001).

[9.129] T. Janowski, H.D. Stryczewska, S. Kozak, B. Kondratowicz-Kucewicz, G. Wojtasiewicz, J. Kozak, P. Surdacki, and H. Malinowski, "Bi-2223 and Bi-2212 tubes for small fault current limiters," *IEEE Trans. Appl. Superconduc.* **14**, 851 (2004).

[9.130] Hans-Peter Kraemer, Wolfgang Schmidt, Bernd Utz, Bernd Wacker, Heinz-Werner Neumueller, Gerd Ahlf, and Rainer Hartig, "Test of a 1 kA superconducting fault current limiter for DC applications," *IEEE Trans. Appl. Superconduc.* **15**, 1986 (2005).

[9.131] Louis Antognazza, Michel Decroux, Mathieu Therasse, Markus Abplanalp, and

Papers Cited in Table 9.7: Fault Current Limiter **[HTS]** (continuation)

Øystein Fischer, "Test of YBCO thin films based fault current limiters with a newly designed meander," *IEEE Trans. Appl. Superconduc.* **15**, 1990 (2005).

[9.132] Min Cheol Ahn, Duck Kweon Bae, Seong Eun Yang, Dong Keun Park, Tae Kuk Ko, Chanjoo Lee, Bok-Yeol Seok, and Ho-Myung Chang, "Manufacture and test of small-scale superconducting fault current limiter by using the bifilar winding of coated conductor," *IEEE Trans. Appl. Superconduc.* **16**, 646 (2006).

[9.133] Kazuaki Arai, Hideki Tanaka, Masaya Inaba, Hirohito Arai, Takeshi Ishigohka, Mitsuho Furuse, and Masaichi Umeda, "Test of resonance-type superconducting fault current limiter," *IEEE Trans. Appl. Superconduc.* **16**, 650 (2006).

[9.134] T. Yazawa, Y. Ootani, M. Sakai, M. Otsuki, T. Kuriyama, M. Urata, Y. Tokunaga, and K. Inoue, "Design and test results of 66 kV high-Tc superconducting fault current limiter magnet," *IEEE Trans. Appl. Superconduc.* **16**, 683 (2006).

[9.135] Manuel R. Osorio, José A. Lorenzo, Paula Toimil, Gonzalo Ferro, José A. Veira, and Félix Vidal, "Inductive superconducting fault current limiters with Y123 thin-film washers versus Bi2223 bulk rings as secondaries," *IEEE Trans. Appl. Superconduc.* **16**, 1937 (2006).

[9.136] V. Rozenshtein, A. Friedman, Y. Wolfus, F. Kopansky, E. Perel, Y. Yeshurun, Z. Bar-Haim, Z. Ron, E. Harel, and N. Pundak, "Saturated cores FCL—A new approach," *IEEE Trans. Appl. Superconduc.* **17**, 1756 (2007).

[9.137] Ying Xin, Weizhi Gong, Xiaoye Niu, Zhengjian Cao, Jingyin Zhang, Bo Tian, Haixia Xi, Yang Wang, Hui Hong, Yong Zhang, Bo Hou, and Xicheng Yang, "Development of saturated iron core HTS fault current limiters," *IEEE Trans. Appl. Superconduc.* **17**, 1760 (2007).

[9.138] Rossella B. Dalessandro, Marco Bocchi, Valerio Rossi, and Luciano F. Martini, "Test results on 500 kVA-class MgB_2-based fault current limiter prototypes," *IEEE Trans. Appl. Superconduc.* **17**, 1776 (2007).

[9.139] S.I. Kopylov, N.N. Balashov, S.S. Ivanov, A.S. Veselovsky, V.S. Vysotsky, and V. D. Zhemerikin, "The effect of sectioning on superconducting fault current limiter operation," *IEEE Trans. Appl. Superconduc.* **17**, 1799 (2007).

[9.140] Keisuke Fushiki, Tanzo Nitta, Jumpei Baba, and Kozo Suzuki, "Design and basic test of SFCL of transformer type by use of Ag sheathed BSCCO wire," *IEEE Trans. Appl. Superconduc.* **17**, 1815 (2007).

[9.141] Hyo-Sang Choi and Sung-Hun Lim, "Operating performance of the flux-lock and the transformer type superconducting fault current limiter using the YBCO thin films," *IEEE Trans. Appl. Superconduc.* **17**, 1823 (2007).

[9.142] A. Gyore, S. Semperger, V. Tihanyi, I. Vajda, M.R. Gonal, K.P. Muthe, S.C. Kashyap, and D.K. Pandya, "Experimental analysis of different type HTS rings in fault current limiter," *IEEE Trans. Appl. Superconduc.* **17**, 1899 (2007).

[9.143] Carlos A. Baldan, Carlos Y. Shigue, Jerika S. Lamas, and Ernesto Ruppert Filho, "Test results of a superconducting fault current limiter using YBCO coated conductor," *IEEE Trans. Appl. Superconduc.* **17**, 1903 (2007).

[9.144] T. Hori, M. Endo, T. Koyama, I. Yamaguchi, K. Kaiho, M. Furuse, and S. Yanabu, "Study of kV class current limiting unit with YBCO thin films," *IEEE Trans. Appl. Superconduc.* **17**, 1986 (2007).

[9.145] Caihong Zhao, Zikai Wang, Dong Zhang, Jingye Zhang, Xiaoji Du, Wengyong Guo, Liye Xiao, and Liangzhen Lin, "Development and test of a superconducting fault current limiter-magnetic energy storage (SFCL-MES) system," *IEEE Trans. Appl. Superconduc.* **17**, 2014 (2007).

***Papers Cited in Table 9.7: Fault Current Limiter* [HTS]** (continuation)

[9.146] L.F. Li, L.H. Gong, X.D. Xu, J.Z. Lu, Z. Fang, and H.X. Zhang, "Field test and demonstrated operation of 10.5 kV/1.5 kA HTS fault current limiter," *IEEE Trans. Appl. Superconduc.* **17**, 2055 (2007).

[9.147] A. Usoskin, A. Rutt, B. Prause, R. Dietrich, and P. Tixador, "Coated conductor based FCL with controllable time response," *IEEE Trans. Appl. Superconduc.* **17**, 3475 (2007).

[9.148] Hyoungku Kang, Chanjoo Lee, Kwanwoo Nam, Yong Soo Yoon, Ho-Myung Chang, Tae Kuk Ko, and Bok-Yeol Seok, "Development of a 13.2 kV/630 A (8.3 MVA) high temperature superconducting fault current limiter," *IEEE Trans. Appl. Superconduc.* **18**, 624 (2008).

[9.149] Min Cheol Ahn, Dong Keun Park, Seong Eun Yang, and Tae Kuk Ko, "Impedance characteristics of non-inductive coil wound with two kinds of HTS wire in parallel," *IEEE Trans. Appl. Superconduc.* **18**, 640 (2008).

[9.150] Carlos A. Baldan, Carlos Y. Shigue, and Ernesto Ruppert Filho, "Fault current test of a bifilar Bi-2212 bulk coil," *IEEE Trans. Appl. Superconduc.* **18**, 664 (2008).

[9.151] Kei Koyanagi, Takashi Yazawa, Masahiko Takahashi, Michitaka Ono, and Masami Urata, "Design and test results of a fault current limiter coil wound with stacked YBCO tapes," *IEEE Trans. Appl. Superconduc.* **18**, 676 (2008).

***Transformer* [LTS]**

[9.152] H. Riemersma, P.W. Eckels, M.L. Barton, J.H. Murphy, D.C. Litz, J.F. Roach, "Application of superconducting technology to power transformers," *IEEE Trans. Power Apparatus and Systems* **PAS-100**, 3398 (1981).

[9.153] H.H.J. ten Kate, A.H.M. Holtslag, J. Knoben, H.A. Steffens and L.J.M. van de Klundert, "Status report of the three phase 25 kA, 1.5 kW thermally switched superconducting rectifier, transformer and switches," *IEEE Trans. Magn.* **MAG-19**, 1059 (1983).

[9.154] Y. Yamamoto, N. Mizukami, T. Ishigohka, K. Ohshima, "A feasibility study on a superconducting power transformer," *IEEE Trans. Magn.* **MAG-22**, 418 (1986).

[9.155] A. Fevrier, J.P. Tavergnier, Y. Laumond, M. Bekhaled, "Preliminary tests on a superconducting power transformer," *IEEE Trans. Magn.* **MAG-24**, 1059 (1988).

[9.156] E.M.W. Leung, R.E. Bailey, M.A. Hilal, "Hybrid pulsed power transformer (HPPT): magnet design and results of verification experiments," *IEEE Trans. Magn.* **MAG-24**, 1508 (1988).

***Transformer* [HTS]**

[9.157] K. Funaki, M. Iwakuma, M. Takeo, K. Yamafuji, J. Suchiro, M. Hara, M. Konno, Y. Kasagawa, I. Itoh, S. Nose, M. Ueyama, K. Hayashi, and K. Sato, "Preliminary tests of a 500 kVA-class oxide superconducting transformer cooled by subcooled nitrogen," *IEEE Trans. Appl. Superconduc.* **7**, 824 (1997).

[9.158] S.W. Schwenterly, B.W. McConnell, J.A. Demko, A. Fadnek, J. Hsu, F.A. List, M.S. Walker, D.W. Hazelton, F.S. Murray, J.A. Rice, C.M. Trautwein, X. Shi, R.A. Farrell, J. Bascuñan, R.E. Hintz, S.P. Mehta, N. Aversa, J.A. Ebert, B.A. Bednar, D.J. Neder, A.A. McIlheran, P.C. Michel, J.J. Nemec, E.F. Pleva, A.C. Swenton, W. Swets, R.C. Longsworth, R.C. Johnson, R.H. Jones, J.K. Nelson, R.C. Degeneff, and S.J. Salon, "Performance of a 1-MVA HTS demonstration transformer," *IEEE Trans. Appl. Superconduc.* **9**, 680 (1999).

[9.159] Maitham K. Al-Mosawi, Carlo Beduz, Yifeng Yang, Mike Webb and Andrew

***Papers Cited in Table 9.7: Transformer* [HTS]** (continuation)

Power, "The effect of flux diverters on AC losses of a 10 kVA high temperature superconducting demonstrator transformer," *IEEE Trans. Appl. Superconduc.* **11**, 2800 (2001).

[9.160] Ho-Myung Chang, Yeon Suk Choi, Steven W. Van Sciver, and Thomas L. Baldwin, "Cryogenic cooling temperature of HTS transformers for compactness and efficiency," *IEEE Trans. Appl. Superconduc.* **13**, 2298 (2003).

[9.161] Z. Jelinek, Z. Timoransky, F. Zizek, H. Piel, F. Chovanec, P. Mozola, L. Jansak, P. Kvitkovic, P. Usak, and M. Polak, "Test results of 14 kVA superconducting transformer with Bi-2223/Ag windings," *IEEE Trans. Appl. Superconduc.* **13**, 2310 (2003).

[9.162] P. Tixador, G. Donnier-Valentin, and E. Maher, "Design and construction of a 41 kVA Bi/Y transformer," *IEEE Trans. Appl. Superconduc.* **13**, 2331 (2003).

[9.163] Michael Meinert, Martino Leghissa, Reinhard Schlosser, and Heinz Schmidt, "System test of a 1-MVA-HTS-transformer connected to a converter-fed drive for rail vehicles," *IEEE Trans. Appl. Superconduc.* **13**, 2348 (2003).

[9.164] T. Bohno, A. Tomioka, M. Imaizumi, Y. Sanuki, T. Yamamoto, Y. Yasukawa, H. Ono, Y. Yagi and K. Iwadate, "Development of 66 kV/6.9 kV 2 MVA prototype HTS power transformer," *Physica C: Superconductivity* **426–431**, 1402 (2005).

[9.165] C.S. Weber, C.T. Reis, D.W. Hazelton, S.W. Schwenterly, M.J. Cole, J.A. Demko, E.F. Pleva, S. Mehta, T. Golner, and N. Aversa, "Design and operational testing of a 5/10-MVA HTS utility power transformer," *IEEE Trans. Appl. Superconduc.* **15**, 2210 (2005).

[9.166] Alessandro Formisano, Fabrizio Marignetti, Raffaele Martone, Giovanni Masullo, Antonio Matrone, Raffaele Quarantiello, and Maurizio Scarano, "Performance evaluation for a HTS transformer," *IEEE Trans. Appl. Superconduc.* **16**, 1501 (2006).

[9.167] H. Okubo, C. Kurupakorn, S. Ito, H. Kojima, N. Hayakawa, F. Endo, and M. Noe, "High-Tc superconducting fault current limiting transformer (HTc-SFCLT) with 2G coated conductors," *IEEE Trans. Appl. Superconduc.* **17**, 1768 (2007).

[9.168] I. Vajda, A. Gyore, S. Semperger, A.E. Baker, E.F.H. Chong, F.J. Mumford, V. Meerovich, and V. Sokolovsky, "Investigation of high temperature superconducting self-limiting transformer with YBCO cylinder," *IEEE Trans. Appl. Superconduc.* **17**, 1887 (2007).

[9.169] H. Kamijo, H. Hata, H. Fujimoto, A. Inoue, K. Nagashima, K. Ikeda, M. Iwakuma, K. Funaki, Y. Sanuki, A. Tomioka, H. Yamada, K. Uwamori, and S. Yoshida, "Investigation of high temperature superconducting self-limiting transformer with YBCO cylinder," *IEEE Trans. Appl. Superconduc.* **17**, 1927 (2007).

[9.170] S.W. Lee, Y.I. Hwang, H.W. Lim, W.S. Kim, K.D. Choi, and S. Hahn, "Characteristics of a continuous disk winding for large power HTS transformer," *IEEE Trans. Appl. Superconduc.* **17**, 1943 (2007).

[9.171] Yinshun Wang, Xiang Zhao, Junjie Han, Huidong Li, Ying Guan, Qing Bao, Liye Xiao, Liangzhen Lin, Xi Xu, Naihao Song, and Fengyuan Zhang, "Development of a 630 kVA three-phase HTS transformer with amorphous alloy cores," *IEEE Trans. Appl. Superconduc.* **17**, 2051 (2007).

***Transmission* [LTS]**

[9.172] R.L. Garwin and J. Matisoo, "Superconducting lines for the transmission of large amounts of electrical power over great distances," *Proc. IEEE* **55**, 538 (1967).

Papers Cited in Table 9.7: Transmission **[LTS]** (continuation)

[9.173] E. Bochenek, H. Franke, R. Wimmershoff, "Manufacture and initial technical tests of a high-power d.c. cable with superconductors," *IEEE Trans. Magn.* **MAG-11**, 366 (1975).

[9.174] E.B. Forsyth, "Progress at Brookhaven in the design of helium-cooled power transmission systems," *IEEE Trans. Magn.* **MAG-11**, 393 (1975).

[9.175] A.S. Clorfeine, B.C. Belanger, N.P. Laguna, "Recent progress in superconducting transmission," *IEEE Trans. Magn.* **MAG-12**, 915 (1976).

[9.176] I.M. Bortnik, V.L. Karapazuk, V.V. Lavrova, S.I. Lurie, Yu. V. Petrovsky, L.M. Fisher, "Investigations on the development of superconducting DC power transmission lines," *IEEE Trans. Magn.* **MAG-13**, 188 (1977).

[9.177] J.D. Thompson, M.P. Maley, L.R. Newkirk, F.A. Valencia, R.V. Carlson, G.H. Morgan, "Construction and properties of a 1-m long Nb_3Ge-based AC superconducting power transmission cable," *IEEE Trans. Magn.* **MAG-17**, 149 (1981).

[9.178] P. Klaudy, I. Gerhold, A. Beck, P. Rohner, E. Scheffler, and G. Ziemke, "First field trials of a superconducting power cable within the power grid of a public utility," *IEEE Trans. Magn.* **MAG-17**, 153 (1981).

[9.179] E.B. Forsyth and G.H. Morgan, "Full-power trials of the Brookhaven superconducting power transmission system," *IEEE Trans. Magn.* **MAG-19**, 652 (1983).

Transmission **[HTS]**

[9.180] J.W. Lue, M.S. Lubell, E.C. Jones, J.A. Demko, D.M. Kroeger, P.M. Martin, U. Sinha, and R.L. Hughey, "Test of two prototype high-temperature superconducting transmission cables," *IEEE Trans. Appl. Superconduc.* **7**, 302 (1997).

[9.181] M. Leghissa, J. Rieger, H.-W. Neumüller, J. Wiezoreck, F. Schmidt, W. Nick, P. van Hasselt, R. Schroth, "Development of HTS power transmission cables," *IEEE Trans. Appl. Superconduc.* **9**, 406 (1999).

[9.182] Y.B. Lin, L.Z. Lin, Z.Y. Gao, H.M. Wen, L. Xu, L. Shu, J. Li, L.Y. Xiao, L. Zhou, and G.S. Yuan, "Development of HTS transmission power cable," *IEEE Trans. Appl. Superconduc.* **11**, 2371 (2001).

[9.183] J.P. Stovall, J.A. Demko, P.W. Fisher, M.J. Gouge, J.W. Lue, U.K. Sinha, J.W. Armstrong, R.L. Hughey, D. Lindsay, and J.C. Tolbert, "Installation and operation of the Southwire 30-meter high-temperature superconducting power cable," *IEEE Trans. Appl. Superconduc.* **11**, 2467 (2001).

[9.184] D.W.A. Willen, F. Hansen, C.N. Rasmussen, M. Däumling, O.E. Schuppach, E. Hansen, J. Baerentzen, B. Svarrer-Hansen, Chresten Traeholt, S.K. Olsen, C. Ramussen, E. Veje, K.H. Jensen, J. Østergaard, S.D. Mikkelsen, J. Mortensen, M. Dam-Andersen, "Test results of full-scale HTS cable models and plans for a 36 kV, 2 kA_{rms} utility demonstration," *IEEE Trans. Appl. Superconduc.* **11**, 2473 (2001).

[9.185] Jeonwook Cho, Joon-Han Bae, Hae-Jong Kim, Ki-Deok Sim, Ki-Chul Seong, Hyun-Man Jang, and Dong-Wook Kim, "Development and testing of 30 m HTS power transmission cable," *IEEE Trans. Appl. Superconduc.* **15**, 1719 (2005).

[9.186] Shinichi Mukoyama, Noboru Ishii, Masashi Yagi, Satoru Tanaka, Satoru Maruyama, Osamu Sato, and Akio Kimura, "Manufacturing and installation of the world's longest HTS cable in the Super-ACE project," *IEEE Trans. Appl. Superconduc.* **15**, 1763 (2005).

[9.187] Ying Xin, Bo Hou, Yanfang Bi, Haixia Xi, Yong Zhang, Anlin Ren, Xicheng Yang, Zhenghe Han, Songtao Wu, and Huaikuang Ding, "Introduction of China's first live grid installed HTS power cable system," *IEEE Trans. Appl. Superconduc.* **15**,

***Papers Cited in Table 9.7: Transmission* [HTS]** (continuation)

1814 (2005).

[9.188] Takato Masuda, Hiroyasu Yumura, M. Watanabe, Hiroshi Takigawa, Y. Ashibe, Chizuru Suzawa, H. Ito, Masayuki Hirose, Kenichi Sato, Shigeki Isojima, C. Weber, Ron Lee, and Jon Moscovic, "Fabrication and installation results for Albany HTS cable," *IEEE Trans. Appl. Superconduc.* **17**, 1648 (2007).

[9.189] S. Mukoyama, M. Yagi, M. Ichikawa, S. Torii, T. Takahashi, H. Suzuki, and K. Yasuda, "Experimental results of a 500 m HTS power cable field test," *IEEE Trans. Appl. Superconduc.* **17**, 1680 (2007).

[9.190] Victor E. Sytnikov, Vitaly S. Vysotsky, Alexander V. Rychagov, Nelly V. Polyakova, Irlama P. Radchenko, Kirill A. Shutov, Eugeny A. Lobanov, and Sergei S. Fetisov, "The 5 m HTS power cable development and test," *IEEE Trans. Appl. Superconduc.* **17**, 1684 (2007).

[9.191] Lauri Rostila, Jorma R. Lehtonen, Mika J. Masti, Risto Mikkonen, Fedor Gömöry, Tibor Melíěk, Eugen Seiler, Jan Šouc, and Alexander I. Usoskin, "AC losses and current sharing in an YBCO cable," *IEEE Trans. Appl. Superconduc.* **17**, 1688 (2007).

[9.192] T. Hamajima, M. Tsuda, T. Yagai, S. Monma, H. Satoh, and K. Shimoyama, "Analysis of AC losses in a tri-axial superconducting cable," *IEEE Trans. Appl. Superconduc.* **17**, 1692 (2007).

[9.193] Daisuke Miyagi, Satoru Iwata, Norio Takahashi, and Shinji Torii, "3D FEM analysis of effect of current distribution on AC loss in shield layers of multi-layered HTS power cable," *IEEE Trans. Appl. Superconduc.* **17**, 1696 (2007).

[9.194] Satoshi Fukui, Takeshi Noguchi, Jun Ogawa, Mitsugi Yamaguchi, Takao Sato, Osami Tsukamoto, and Tomoaki Takao,"Numerical study on AC loss minimization of multi-layer tri-axial HTS cable for 3-phase AC power transmission," *IEEE Trans. Appl. Superconduc.* **17**, 1700 (2007).

[9.195] M.J. Gouge, J.A. Demko, R.C. Duckworth, D.T. Lindsay, C.M. Rey, M.L. Roden, and J.C. Tolbert, "Testing of an HTS power cable made from YBCO tapes," *IEEE Trans. Appl. Superconduc.* **17**, 1708 (2007).

[9.196] Naoyuki Amemiya, Zhenan Jiang, Masaki Nakahata, Masashi Yagi, Shinichi Mukoyama, Naoji Kashima, Shigeo Nagaya, and Yuh Shiohara, "AC loss reduction of superconducting power transmission cables composed of coated conductors," *IEEE Trans. Appl. Superconduc.* **17**, 1712 (2007).

[9.197] Makoto Hamabe, Atsushi Sasaki, Tosin S. Famakinwa, Akira Ninomiya, Yasuhide Ishiguro, and Satarou Yamaguchi, "Cryogenic system for DC superconducting power transmission line," *IEEE Trans. Appl. Superconduc.* **17**, 1722 (2007).

[9.198] H.J. Kim, D.S. Kwag, S.H. Kim, J.W. Cho, and K.C. Seong, "Electrical insulation design and experimental results of a high-temperature superconducting cable," *IEEE Trans. Appl. Superconduc.* **17**, 1743 (2007).

[9.199] J.F. Maguire, F. Schmidt, S. Bratt, T.E. Welsh, J. Yuan, A. Allais, and F. Hamber, "Development and demonstration of a HTS power cable to operate in the Long Island Power Authority transmission grid," *IEEE Trans. Appl. Superconduc.* **17**, 2034 (2007).

[9.200] C.S. Weber, R. Lee, S. Ringo, T. Masuda, H. Yumura, and J. Moscovic, "Testing and demonstration results of the 350 m long HTS cable system installed in Albany, NY," *IEEE Trans. Appl. Superconduc.* **17**, 2038 (2007).

[9.201] S.H. Sohn, J.H. Lim, S.W. Yim, O.B. Hyun, H.R. Kim, K. Yatsuka, S. Isojima, T.

Papers Cited in Table 9.7: Transmission **[HTS]** (continuation)

Masuda, M. Watanabe, H.S. Ryoo, H.S. Yang, D.L. Kim, S.D. Hwang, "The results of installation and preliminary test of 22.9 kV, 50 MVA, 100 m class HTS power cable system at KEPCO," *IEEE Trans. Appl. Superconduc.* **17**, 2043 (2007).

Motor **[LTS]**

[9.202] William J. Levedahl, "Superconductive naval propulsion systems," *Proc. 1972 Appl. Superconduc. Conf. (IEEE Publ. No. 72CH0682-5-TABSC)*, 26 (1972).

[9.203] Howard O. Stevens, Michael J. Superczynski, Timothy J. Doyle, John H. Harrison, Harry Messinger, "Superconductive machinery for naval ship propulsion," *IEEE Trans. Magn.* **MAG-13**, 269 (1977).

[9.204] R.A. Marshall, "3000 horsepower superconductive field acyclic motor," *IEEE Trans. Magn.* **MAG-19**, 876 (1983).

Motor **[HTS]**

[9.205] A. Takeoka, A. Ishikawa, M. Suzuki, K. Niki and Y. Kuwano, "Meissner motor using high-Tc ceramic superconductors," *IEEE Trans. Magn.* **25**, 2511 (1989).

[9.206] Alan D. Crapo and Jerry D. Lloyd, "Homopolar DC motor and trapped flux brushless DC motor using high temperature superconductor materials," *IEEE Trans. Magn.* **27**, 2244 (1991).

[9.207] C.H. Joshi, C.B. Prum, R.F. Schiferl, D.L. Driscoll, "Demonstration of two synchronous motors using high temperature superconducting field coils," *IEEE Trans. Appl. Superconduc.* **5**, 968 (1995).

[9.208] Michael J. Superczynski, Jr. and Donald J. Waltman, "Homopolar motor with high temperature superconductor field windings," *IEEE Trans. Appl. Superconduc.* **7**, 513 (1997).

[9.209] J.P. Voccio, B.B. Gamble, C.B. Prum, H.J. Picard, "125 HP HTS motor field winding development," *IEEE Trans. Appl. Superconduc.* **7**, 519 (1997).

[9.210] J.-T. Eriksson, R. Mikkonen, J. Paasi, R. Perälä and L. Söderlund, "A(n) HTS synchronous motor at different operating temperatures," *IEEE Trans. Appl. Superconduc.* **7**, 523 (1997).

[9.211] Drew W. Hazelton, Michael T. Gardner, Joseph A. Rice, Michael S. Walker, Chandra M. Trautwein, Pradeep Haldar, Donald U. Gubser, Michael Superczynski, Donald Waltman, "HTS coils for the Navy's superconducting homopolar motor/generator," *IEEE Trans. Appl. Superconduc.* **7**, 664 (1997).

[9.212] D. Aized, B.B. Gamble, A. Sidi-Yekhlef, J.P. Voccio, D.I. Driscoll, B.A. Shoykhet, B.X. Zhang, "Status of the 1000 HP HTS motor development," *IEEE Trans. Appl. Superconduc.* **9**, 1201 (1999).

[9.213] B. Oswald, M. Krone, M. Söll, T. Straßer, J. Oswald, K.-J. Best, W. Gawalek, L. Kovalev, "Superconducting reluctance motors with YBCO bulk material," *IEEE Trans. Appl. Superconduc.* **9**, 1201 (1999).

[9.214] P. Tixador, F. Simon, H. Daffix, M. Deleglise, "150-kW experimental superconducting permanent-magnet motor," *IEEE Trans. Appl. Superconduc.* **9**, 1205 (1999).

[9.215] John R. Hull, Suvankar SenGupta, and J.R. Gaines, "Trapped-flux internal-dipole superconducting motor/generator," *IEEE Trans. Appl. Superconduc.* **9**, 1229 (1999).

[9.216] Myungkon Song, YongSoo Yoon, WonKap Jang, Taekuk Ko, GyeWon Hong, In-Bae Jang, "The design, manufacture and characteristic experiment of a small-scaled high-Tc superconducting synchronous motor," *IEEE Trans. Appl. Super-*

Papers Cited in Table 9.7: Motor **[HTS]** (continuation)

conduc. **9**, 1241 (1999).

[9.217] L.K. Kovalev, K.V. Ilushin, S.M.-A. Koneev, K.L. Kovalev, V.T. Penkin, V.N. Poltavets, W. Gawalek, T. Habisreuther, B. Oswald, K.-J. Best, "Hysteresis and reluctance electric machines with bulk HTS rotor elements," *IEEE Trans. Appl. Superconduc.* **9**, 1261 (1999).

[9.218] Mochimitsu Komori, Kazunori Fukuda, and Akio Hirashima, "A prototype magnetically levitated stepping motor using high Tc bulk superconductors," *IEEE Trans. Appl. Superconduc.* **10**, 1626 (2000).

[9.219] Young-Sik Jo, Young-Kil Kwon, Myung-Hwan Sohn, Young-Kyoun Kim, Jung-Pyo Hong, "High temperature superconducting synchronous motor," *IEEE Trans. Appl. Superconduc.* **12**, 833 (2002).

[9.220] Woo-Seok Kim, Sang-Yong Jung, Ho-Yong Choi, Hyun-Kyo Jung, Ji Hoon Kim, and Song-Yop Hahn, "Development of a superconducting linear synchronous motor," *IEEE Trans. Appl. Superconduc.* **12**, 842 (2002).

[9.221] M. Frank, J. Frauenhofer, P. van Hasselt, W. Nick, H.-W. Neumueller, and G. Nerowski, "Long-term operational experience with first Siemens 400 kW HTS machine in diverse configurations," *IEEE Trans. Appl. Superconduc.* **13**, 2120 (2003).

[9.222] Hun-June Jung, Taketsune Nakamura, Itsuya Muta, and Tsutomu Hoshino, "Characteristics of axial-type HTS motor under different temperature conditions," *IEEE Trans. Appl. Superconduc.* **13**, 2201 (2003).

[9.223] Jungwook Sim, Myungjin Park, Hyoungwoo Lim, Gueesoo Cha, Junkeun Ji, and Jikwang Lee, "Test of an induction motor with HTS wire at end ring and bars," *IEEE Trans. Appl. Superconduc.* **13**, 2231 (2003).

[9.224] M.H. Sohn, S.K. Baik, Y.S. Jo, E.Y. Lee, W.S. Kwon, Y.K. Kwon, T.S. Moon, Y.C. Kim, C.H. Cho, and I. Muta, "Performance of high temperature superconducting field coils for a 100 HP motor," *IEEE Trans. Appl. Superconduc.* **14**, 912 (2004).

[9.225] S.D. Chu and S. Torii, "Torque-speed characteristics of superconducting synchronous reluctance motors with DyBCO bulk in the rotor," *IEEE Trans. Appl. Superconduc.* **15**, 2178 (2005).

[9.226] Hirohisa Matsuzaki, Yousuke Kimura, Eisuke Morita, Hideaki Ogata, Tetsuya Ida, Mitsuru Izumi, Hidehiko Sugimoto, Motohiro Miki, and Masahiro Kitano, "HTS bulk pole-field magnets motor with a multiple rotor cooled by liquid nitrogen," *IEEE Trans. Appl. Superconduc.* **17**, 1553 (2007).

[9.227] Stephen D. Umans, Boris A. Shoykhet, Joseph K. Zevchek, Christopher M. Rey, and Robert C. Duckworth, "Quench in high-temperature superconducting motor field coils: Experimental results at 30 K," *IEEE Trans. Appl. Superconduc.* **17**, 1561 (2007).

[9.228] M. Steurer, S. Woodruff, T. Baldwin, H. Boenig, F. Bogdan, T. Fikse, M. Sloderbeck, and G. Snitchler, "Hardware-in-the-loop investigation of rotor heating in a 5 MW HTS propulsion motor," *IEEE Trans. Appl. Superconduc.* **17**, 1595 (2007).

[9.229] Masataka Iwakuma, Akira Tomioka, Masayuki Konno, Yoshiji Hase, Toshihiro Satou, Yoshihiro Iijima, Takashi Saitoh, Yutaka Yamada, Teruo Izumi, and Yuh Shiohara, "Development of a 15 kW motor with a fixed YBCO superconducting field winding," *IEEE Trans. Appl. Superconduc.* **17**, 1607 (2007).

[9.230] Taesoo Song, Akira Ninomiya, and Takeshi Ishigohka, "Experimental study on induction motor with superconducting secondary conductors," *IEEE Trans. Appl. Superconduc.* **17**, 1611 (2007).

***Papers Cited in Table 9.7: Motor* [HTS]** (continuation)

[9.231] Taketsune Nakamura, Yoshio Ogama, and Hironori Miyake, "Performance of inverter fed HTS induction-synchronous motor operated in liquid nitrogen," *IEEE Trans. Appl. Superconduc.* **17**, 1615 (2007).

[9.232] J. López, J. Lloberas, R. Maynou, X. Granados, R. Bosch, X. Obradors, and R. Torres, "AC three-phase axial flux motor with magnetized superconductors," *IEEE Trans. Appl. Superconduc.* **17**, 1633 (2007).

[9.233] Hidehiko Sugimoto, Teppei Tsuda, Takaya Morishita, Yoshinori Hondou, Toshio Takeda, Hiroyuki Togawa, Tomoya Oota, Kazuya Ohmatsu, and Shigeru Yoshida, "Development of an axial flux type PM synchronous motor with the liquid nitrogen cooled HTS armature windings," *IEEE Trans. Appl. Superconduc.* **17**, 1637 (2007).

***Papers Cited in Table 9.7: MAGLEV* [LTS]**

[9.234] J.R. Powell and G.T. Danby, "Magnetic suspension for levitated tracked vehicles," *Cryogenics* **11**, 192 (1971).

[9.235] Tadatoshi Yamada, Masatami Iwamoto, and Toshio Ito, "Levitation performance of magnetically suspended high speed trains," *IEEE Trans. Magn.* **MAG-8**, 634 (1972).

[9.236] H.H. Kolm and R.D. Thorton, "Magneplane: guided electromagnetic flight," *IEEE Conf. Record, IEEE Cat. No. 72 CHO-682-5 TABSC*, 72 (1972).

[9.237] H. Coffey, J. Solinsky, J. Colton, and J. Woodbury, "Dynamic performance of the SRI Maglev vehicle," *IEEE Trans. Magn.* **MAG-10**, 451 (1974).

[9.238] H. Kimura, H. Ogata, S. Sato, R. Saito, and N. Tada, "Superconducting magnet with tube-type cryostat for magnetically suspended train," *IEEE Trans. Magn.* **MAG-10**, 619 (1974).

[9.239] H. Ichikawa and H. Ogiwara, "Design considerations of superconducting magnets as a Maglev pad," *IEEE Trans. Magn.* **MAG-10**, 1099 (1974).

[9.240] Y. Iwasa, W. Brown, and C. Wallace, "An operational 1/25-scale magneplane system with superconducting coils," *IEEE Trans. Magn.* **MAG-11**, 1490 (1975).

[9.241] David L. Atherton, Anthony R. Eastham, Boon-Teck Ooi, and O.P. Jain, "Forces and moments for electrodynamic levitation systems—large-scale test results and theory," *IEEE Trans. Magn.* **MAG-14**, 59 (1978).

[9.242] T. Ohtsuka and Y. Kyotani, "Superconducting maglev tests," *IEEE Trans. Magn.* **MAG-15**, 1416 (1979).

[9.243] C.G. Homan, C.E. Cummings, and C.M. Fowler, "Superconducting augmented rail gun (SARG)," *IEEE Trans. Magn.* **MAG-22**, 1527 (1986).

[9.244] Hiroshi Nakashima, "The superconducting magnet for the Maglev transport system," *IEEE Trans. Magn.* **30**, 1572 (1994).

[9.245] H. Nakao, T. Yamashita, Y. Sanada, S. Yamaji, S. Nakagaki, T. Shudo, M. Takahashi, A. Miura, M. Terai, M. Igarashi, T. Kurihara, K. Tomioka, M. Yamaguchi, "Development of a modified superconducting magnet for Maglev vehicles," *IEEE Trans. Appl. Superconduc.* **9**, 1000 (1999).

[9.246] Y. Yoshino, A. Iwabuchi, T. Suzuki, and H. Seino, "Property of mechanical heat generation inside the superconducting coil installed in MAGLEV inner vessel," *IEEE Trans. Appl. Superconduc.* **16**, 1803 (2006).

[9.247] Luguang Yan, "Development and application of the Maglev transportation system," *IEEE Trans. Appl. Superconduc.* **18**, 92 (2008).

***Papers Cited in Table 9.7: MAGLEV* [HTS]**

[9.248] C.E. Oberly, G. Kozlowski, C.E. Gooden, Roger X. Lenard, Asok K. Sarkar, I. Maartense, J.C. Ho, "Principles of application of high temperature superconductors to electromagnetic launch technology," *IEEE Trans. Magn.* **27**, 509 (1991).

[9.249] Kenneth G. Herd, E. Trifon Laskaris, and Paul S. Thompson, "A cryogen-free superconducting magnet for Maglev applications: design and test results," *IEEE Trans. Appl. Superconduc.* **5**, 961 (1995).

[9.250] A. Senba, H. Kitahara, H. Ohsaki and E. Masada, "Characteristics of an electromagnetic levitation system using a bulk superconductor," *IEEE Trans. Magn.* **32**, 5049 (1996).

[9.251] Mitsuyoshi Tsuchiya and Hiroyuki Ohsaki, "Characteristics of electromagnetic force of EMS-type maglev vehicle using bulk superconductors," *IEEE Trans. Magn.* **36**, 3683 (2000).

[9.252] Suyu Wang, Jiasu Wang, Xiaorong Wang, Zhongyou Ren, Youwen Zeng, Changyan Deng, He Jiang, Min Zhu, Guobin Lin, Zhipei Xu, Degui Zhu, and Honghai Song, "The man-loading high-temperature superconducting Maglev test vehicle," *IEEE Trans. Appl. Superconduc.* **13**, 2134 (2003).

[9.253] Tomoaki Takao, Akihiro Niiro, Soichiro Suzuki, Masahiro Hashimoto, Hiroki Kamijo, Junichiro Takeda, Toshihiro Kobayashi, and Hiroyuki Fujimoto, "Experimental and numerical analysis of lift force in magnetic levitation system," *IEEE Trans. Appl. Superconduc.* **15**, 2281 (2005).

[9.254] Ludwig Schultz, Oliver de Haas, Peter Verges, Christoph Beyer, Steffen Röhlig, Henning Olsen, Lars Kuhn, Dietmar Berger, Ulf Noteboom, and Ullrich Funk, "Superconductively levitated transport system—the SupraTrans project," *IEEE Trans. Appl. Superconduc.* **15**, 2301 (2005).

[9.255] W.J. Yang, Z. Wen, Y. Duan, X.D. Chen, M. Qiu, Y. Liu, L.Z. Lin, "Construction and performance of HTS Maglev launch assist test vehicle," *IEEE Trans. Appl. Superconduc.* **16**, 1124 (2006).

[9.256] Kenji Tasaki, Kotaro Marukawa, Satoshi Hanai, Taizo Tosaka, Toru Kuriyama, Tomohisa Yamashita, Yasuto Yanase, Mutsuhiko Yamaji, Hiroyuki Nakao, Motohiro Igarashi, Shigehisa Kusada, Kaoru Nemoto, Satoshi Hirano, Katsuyuki Kuwano, Takeshi Okutomi, and Motoaki Terai, "HTS magnet for Maglev applications (1)—coil characteristics," *IEEE Trans. Appl. Superconduc.* **16**, 1110 (2006).

[9.257] Jiasu Wang, Suyu Wang, Changyan Deng, Jun Zheng, Honghai Song, Qingyong He, Youwen Zeng, Zigang Deng, Jing Li, Guangtong Ma, Hua Jing, Yonggang Huang, Jianghua Zhang, Yiyu Lu, Lu Liu, Lulin Wang, Jian Zhang, Longcai Zhang, Minxian Liu, Yujie Qin, and Ya Zhang, "Laboratory-scale high temperature superconducting Maglev launch system," *IEEE Trans. Appl. Superconduc.* **17**, 2091 (2007).

[9.258] John R. Hull, James Fiske, Ken Ricci, and Michael Ricci, "Analysis of levitational systems for a superconducting launch ring," *IEEE Trans. Appl. Superconduc.* **17**, 2117 (2007).

***Papers Cited in Table 9.7: Magnetic Separation* [HTS]**

[9.259] M.A. Daugherty, J.Y. Coulter, W.L. Hults, D.E. Daney, D.D. Hill, D.E. McMurry, M.C. Martinez, L.G. Phillips, J.O. Willis, H.J. Boenig, F.C. Prenger, A.J. Rodenbush, and S. Young, "HTS high gradient magnetic separation system," *IEEE Trans. Appl. Superconduc.* **7**, 650 (1997).

[9.260] J. Iannicelli, J. Pechin, M. Ueyama, K. Ohkura, K. Hayashi, K. Sato, A. Lauder and C. Rey, "Magnetic separation of kaolin clay using a high temperature super-

Papers Cited in Table 9.7: Magnetic Separation **[HTS]** (continuation)

conducting magnet system," *IEEE Trans. Appl. Superconduc.* **7**, 1061 (1997).

[9.261] J.X. Jin, S.X. Dou, H.K. Liu, R. Neale, N. Attwood, G. Grigg, T. Reading, T. Beales, "A high gradient magnetic separator fabricated using Bi-2223/Ag HTS tapes," *IEEE Trans. Appl. Superconduc.* **9**, 394 (1999).

[9.262] H. Kumakura, T. Ohara, H. Kitaguchi, K. Togano, H. Wada, H. Mukai, K. Ohmatsu, H. Takei, and H. Okada, "Development of Bi-2223 magnetic separation system," *IEEE Trans. Appl. Superconduc.* **11**, 2519 (2001).

[9.263] N. Nishijima, N. Saho, K. Asano, H. Hayashi, K. Tsutsumi, and M. Murakami, "Magnetization method for long high-T_c bulk superconductors used for magnetic separation," *IEEE Trans. Appl. Superconduc.* **13**, 1580 (2003).

[9.264] C.M. Rey, W.C. Hoffman, Jr., and D.R. Steinhauser, "Test results of a HTS reciprocating magnetic separator," *IEEE Trans. Appl. Superconduc.* **13**, 1624 (2003).

[9.265] Shin-Ichi Takeda and Shigehiro Nishijima, "Development of magnetic separation of water-soluble materials using superconducting magnet," *IEEE Trans. Appl. Superconduc.* **17**, 2178 (2007).

[9.266] Qiuliang Wang, Yingming Dai, Xinning Hu, Shouseng Song, Yuanzhong Lei, Chuan He, and Luguang Yan, "Development of GM cryocooler-cooled Bi2223 high temperature superconducting magnetic separator," *IEEE Trans. Appl. Superconduc.* **17**, 2185 (2007).

[9.267] Dong-Woo Ha, Tae-Hyung Kim, Hong-Soo Ha, Sang-Soo Oh, Sung-Kuk Park, Sang-Kil Lee, and Yu-Mi Roh, "Treatment of coolant of hot rolling process by high gradient magnetic separation," *IEEE Trans. Appl. Superconduc.* **17**, 2189 (2007).

Papers Cited in Table 9.7: Research Magnets—HEP

High Energy Physics **[LTS]**

[9.268] Paul J. Reardon, "High energy physics and applied superconductivity," *IEEE Trans. Magn.* **MAG-13**, 704 (1977).

[9.269] Hiromi Hirabayashi, "Development of superconducting magnets for beam lines and accelerator at KEK," *IEEE Trans. Magn.* **MAG-17**, 728 (1981).

[9.270] H. Desportes, "Superconducting magnets for accelerators, beam lines and detectors," *IEEE Trans. Magn.* **MAG-17**, 1560 (1981).

[9.271] H. Brechna, E.J. Bleser, Y.P. Dmitrevskiy, H.E. Fisk, G. Horlitz, J. Goyer, H. Hirabayashi, J. Pérot, "Superconducting magnets for high energy accelerators," *IEEE Trans. Magn.* **MAG-17**, 2355 (1981).

[9.272] S. Wolff, "Superconducting HERA magnets," *IEEE Trans. Magn.* **24**, 719 (1988).

[9.273] R. Perin, "Progress on the superconducting magnets for the Large Hadron Collider *IEEE Trans. Magn.* **24**, 734 (1988).

[9.274] C. Taylor "SSC magnet technology," *IEEE Trans. Magn.* **24**, 820 (1988).

[9.275] P. Brindza, V. Bardos, A. Gavalya, J. O'Meara, W. Tuzel, "Superconducting magnets for CEBAF," *IEEE Trans. Magn.* **24**, 1264 (1988).

[9.276] R. Meinke, "Superconducting magnet system for HERA," *IEEE Trans. Magn.* **27**, 1728 (1991).

[9.277] F. Wittgenstein, "Detector magnets for high-energy physics," *IEEE Trans. Magn.* **28**, 104 (1992).

[9.278] N. Siegel for the LHC Magnet Team, "Status of the Large Hadron Collider and magnet program," *IEEE Trans. Appl. Superconduc.* **7**, 252 (1997).

Papers Cited in Table 9.7: Research Magnets—HEP (continuation)

[9.279] Martin N. Wilson, "Superconducting magnets for accelerators: a review," *IEEE Trans. Appl. Superconduc.* **7**, 727 (1997).

[9.280] David F. Sutter and Bruce P. Strauss, "Next generation high energy physics colliders: technical challenges and prospects," *IEEE Trans. Appl. Superconduc.* **10**, 33 (2000).

[9.281] Lucio Rossi, "The LHC main dipoles and quadrupoles toward series production," *IEEE Trans. Appl. Superconduc.* **13**, 1221 (2003).

[9.282] A. Devred, D.E. Baynham, L. Bottura, M. Chorowski, P. Fabbricatore, D. Leroy, A. den Oudem, J.M. Rifflet, L. Rossi, O. Vincent-Viry, and G. Volpini, "High field accelerator magnet R&D in Europe," *IEEE Trans. Appl. Superconduc.* **14**, 339 (2004).

[9.283] Akira Yamamoto, "Advances in superconducting magnets for particle physics," *IEEE Trans. Appl. Superconduc.* **14**, 477 (2004).

[9.284] D. Elwyn Baynham, "Evolution of detector magnets from CELLO to ATLAS and CMS and towards future developments," *IEEE Trans. Appl. Superconduc.* **16**, 493 (2006).

Detector Magnets

[9.285] P.H. Eberhard, M.A. Green, W.B. Michael, J.D. Taylor and W.A. Wenzel, "Tests on large diameter superconducting solenoids designed for colliding beam accelerators," *IEEE Trans. Magn.* **MAG-13**, 78 (1977).

[9.286] H. Desportes, J. Le Bars, and G. Mayayx, "Construction and test of the CELLO thin-walled solenoid," *Adv. Cryo. Engr.* **25**, 175 (1980).

[9.287] W.V. Hassenzahl, "Quenches in the superconducting magnet CELLO," *Adv. Cryo. Engr.* **25**, 185 (1980).

[9.288] Stefan Wipf, "Superconducting magnet system for a 750 GeV MUON spectrometer," *IEEE Trans. Magn.* **MAG-17**, 192 (1981).

[9.289] R.W. Fast, E.W. Bosworth, C.N. Brown, D.A. Finley, A.M. Glowacki, J.M. Jagger and S.P. Sobczynski, "14.4 m large aperture analysis magnet with aluminum coils," *IEEE Trans. Magn.* **MAG-17**, 1903 (1981).

[9.290] R. Bruzzese, S. Ceresara, G. Donati, S. Rossi, N. Sacchetti, M. Spadoni, "The aluminum stabilized Nb-Ti conductor for the ZEUS thin solenoid," *IEEE Trans. Magn.* **25**, 1827 (1989).

[9.291] A. Bonito Oliva, O. Dormicchi, M. Losasso, and Q. Lin, "Zeus thin solenoid: test results analysis," *IEEE Trans. Magn.* **27**, 1954 (1991).

[9.292] F. Kircher, P. Brédy, A. Calvo, B. Curé, D. Campi, A. Desirelli, P. Fabbricatore, S. Farinon, A. Hervé, I. Horvath, V. Klioukhine, B. Levesy, M. Losasso, J.P. Lottin, R. Musenich, Y. Pabot, A. Payn, C. Pes, C. Priano, F. Rondeaux, S. Sgobba, "Final design of the CMS solenoid cold mass," *IEEE Trans. Appl. Superconduc.* **10**, 407 (2000).

[9.293] A. Dael, B. Gastineau, J.E. Ducret, and V.S. Vysotsky, "Design study of the superconducting magnet for a large acceptance spectrometer," *IEEE Trans. Appl. Superconduc.* **12**, 353 (2002).

[9.294] S. Mizumaki, Y. Makida, T. Kobayashi, H. Yamaoka, Y. Kondo, M. Kawai, Y. Doi, T. Haruyama, S. Mine, H. Takano, A. Yamamoto, T. Kondo, and H. ten Kate, "Fabrication and mechanical performance of the ATLAS central solenoid," *IEEE Trans. Appl. Superconduc.* **12**, 416 (2002).

Papers Cited in Table 9.7: Detector Magnets (continuation)

[9.295] J.J. Rabbers, A. Dudarev, R. Pengo, C. Berriaud, and H.H.J. ten Kate, "Theoretical and experimental investigation of the ramp losses in conductor and coil casing of the ATLAS barrel toroid coils," *IEEE Trans. Appl. Superconduc.* **16**, 549 (2006).

[9.296] Jean-Michel Rey, Michel Arnaud, Christophe Berriaud, Romain Berthier, Sandrine Cazaux, Alexey Dudarev, Michel Humeau, René Leboeuf, Jean-Paul Gourdin, Christophe Mayri, Chhon Pes, Herman Ten Kate, and Pierre Védrine, "Cold mass integration of the ATLAS barrel toroid magnets at CERN," *IEEE Trans. Appl. Superconduc.* **16**, 553 (2006).

[9.297] C. Berriaud, A. Dudarev, J.J. Rabbers, F. Broggi, S. Junker, L. Deront, S. Ravat, E. Adli, G. Olesen, R. Pengo, P. Vedrine, C. Mayri, E. Sbrissa, M. Arnaud, F.P. Juster, J.-M. Rey, G. Volpini, A. Foussat, P. Benoit, R. Leboeuf, M. Humeau, V. Stepanov, A. Olyunin, I. Shugaev, N. Kopeykin, and H.H.J. ten Kate, "On-surface tests of the ATLAS Barrel Toroid Coils: Acceptance criteria and results," *IEEE Trans. Appl. Superconduc.* **16**, 557 (2006).

[9.298] Roger Ruber, Yasuhiro Makida, Masanori Kawai, Yoshinari Kondo, Yoshikuni Doi, Tomiyoshi Haruyama, Friedrich Haug, Herman ten Kate, Taka Kondo, Olivier Pirotte, Jos Metselaar, Shoichi Mizumaki, Gert Olesen, Edo Sbrissa, and Akira Yamamoto, "Ultimate performance of the ATLAS superconducting solenoid," *IEEE Trans. Appl. Superconduc.* **17**, 1201 (2007).

[9.299] François Kircher, Philippe Brédy, Philippe Fazilleau, François-Paul Juster, Bruno Levesy, Jean-Pierre Lottin, Jean-Yves Roussé, Domenico Campi, Benoît Curé, Andrea Gaddi, Alain Hervé, Giles Maire, Goran Perinić, Pasquale Fabbricatore, and Michela Greco, "Magnetic tests of the CMS superconducting magnet," *IEEE Trans. Appl. Superconduc.* **18**, 356 (2008).

[9.300] K. Barth, N. Delruelle, A. Dudarev, G. Passardi, R. Pengo, M. Pezzetti, O. Pirotte, H. Ten Kate, E. Baynham, and C. Mayri, "First cool-down and test at 4.5 K of the ATLAS superconducting barrel toroid assembled in the LHC experimental cavern," *IEEE Trans. Appl. Superconduc.* **18**, 383 (2008).

[9.301] Bernard Gastineau, André Donati, Jean-Eric Ducret, Dominique Eppelle, Philippe Fazilleau, Patrick Graffin, Bertrant Hervieu, Denis Loiseau, Jean-Pierre Lottin, Christophe Mayri, Chantal Meuris, Chhon Pes, Yannick Queinec, and Zhihong Sun, "Design status of the R3B-GLAD magnet: large acceptance superconducting dipole with active shielding, graded coils, large forces and indirect cooling by thermosiphon," *IEEE Trans. Appl. Superconduc.* **18**, 407 (2008).

Dipoles and Quadrupoles

[9.302] W.B. Sampson, "Superconducting magnets," *IEEE Trans. Magn.* **MAG-4**, 99 (1968).

[9.303] J. Bywater, M.H. Foss, L.E. Genens, L.G. Hyman, R.P. Smith, L.R. Turner, S.T. Wang, S.C. Snowdon, J.R. Purcell, "A six-tesla superconducting dipole magnet design and development program for POPAE," *IEEE Trans. Magn.* **MAG-13**, 82 (1977).

[9.304] F. Arendt, N. Fessler, P. Turowski, "Design and construction of superconducting quadrupole magnets at Karlsruhe," *IEEE Trans. Magn.* **MAG-13**, 290 (1977).

[9.305] A. Dael, F. Kircher, J. Perot, "Use of superconducting self-correcting harmonic coils for pulsed superconducting dipole or multipole magnets," *IEEE Trans. Magn.* **MAG-11**, 459 (1975).

[9.306] W.E. Cooper, H.E. Fisk, D.A. Gross, R.A. Lundy, E.E. Schmidt & F. Turkot, "Fermilab Tevatron quadrupoles," *IEEE Trans. Magn.* **MAG-19**, 1372 (1983).

Papers Cited in Table 9.7: Dipoles and Quadrupoles (continuation)

[9.307] P. Dahl, J. Cottingham, M. Garber, A. Ghosh, C. Goodzeit, A. Greene, J. Herrera, S. Kahn, E. Kelly, G. Morgan, A. Prodell, W. Sampson, W. Schneider, R. Shutt, P. Thompson, P. Wanderer, and E. Willen, "Performance of initial full-length RHIC dipoles," *IEEE Trans. Magn.* **MAG-24**, 723 (1988).

[9.308] K. Tsuchiya, K. Egawa, K. Endo, Y. Morita, N. Ohuchi, and K. Asano, "Performance of the eight superconducting quadrupole magnets for the TRISTAN low-beta insertions," *IEEE Trans. Magn.* **27**, 1940 (1991).

[9.309] J.L. Borne, D. Bouichou, D. Leroy, W. Thomi, "Manufacturing of high (10 tesla) twin aperture superconducting dipole magnet for LHC," *IEEE Trans. Magn.* **28**, 323 (1992).

[9.310] J.M. Baze, D. Cacaut, M. Chapman, J.P. Jacquemin, C. Lyraud, C. Michez, Y. Pabot, J. Perot, J.M. Rifflet, J.C. Toussaint, P. Vedrine, R. Perin, N. Siegel, T. Tortschanoff, "Design and fabrication of the prototype superconducting quadrupole for the CERN LHC project," *IEEE Trans. Magn.* **28**, 335 (1992).

[9.311] D. Leroy, J. Krzywinski, L. Oberli, R. Perin, F. Rodriguez-Mateos, A. Verweij, L. Walckiers, "Test results on 10 T LHC superconducting one metre long dipole models," *IEEE Trans. Magn.* **3**, 614 (1993).

[9.312] L. Coull, D. Hagedorn, V. Remondino, F. Rodriguez-Mateos, "LHC magnet quench protection system," *IEEE Trans. Magn.* **30**, 1742 (1994).

[9.313] E. Acerbi, M. Bona, D. Leroy, R. Perin, L. Rossi, "Development and fabrication of the first 10 m long superconducting dipole prototype for the LHC," *IEEE Trans. Magn.* **30**, 1793 (1994).

[9.314] P. Vedrine, J.M. Rifflet, J. Perot, B. Gallet, C. Lyraud, P. Giovannoni, F. Le Coz, N. Siegel, T. Tortschanoff, "Mechanical tests on the prototype LHC lattice quadrupole," *IEEE Trans. Magn.* **30**, 2475 (1994).

[9.315] Akira Yamamoto, Takakazu Shintomi, Nobuhiro Kimura, Yoshikuni Doi, Tomiyoshi Haruyama, Norio Higashi, Hiromi Hirabayashi, Hiroshi Kawamata, Seog-Whan Kim, Takamitsu M. Kobayashi, Yasuhiro Makida, Toru Ogitsu, Norihito Ohuchi, Ken-ichi Tanaka, Akio Terashima, Kiyosumi Tsuchiya, Hiroshi Yamaoka, Giorgio Brianti, Daniel Leroy, Romeo Perin, Shoichi Mizumaki, Shuichi Kato, Kenji Makishima, Tomohumi Orikasa, Tomoaki Maeto, Akira Tanaka, "Test results of a single aperture 10 tesla dipole model magnet for the Large Hadron Collider," *IEEE Trans. Magn.* **32**, 2116 (1996).

[9.316] S. Jongeleen, D. Leroy, A. Siemko and R. Wolf, "Quench localization and current redistribution after quench in superconducting dipole magnets wound with Rutherford-type cables," *IEEE Trans. Appl. Superconduc.* **7**, 179 (1997).

[9.317] Timothy Elliott, Andrew Jaisle, Damir Latypov, Peter McIntyre, Philip McJunkins, Weijun Shen, Rainer Soika, Rudolph M. Gaedke, "16 tesla Nb3Sn dipole development at Texas A&M University," *IEEE Trans. Appl. Superconduc.* **7**, 555 (1997).

[9.318] A.K. Ghosh, A. Prodell, W.B. Sampson, R.M. Scanlan, D. Leroy, and L.B. Oberli, "Minimum quench energy measurements on prototype LHC inner cables in normal helium at 4.4 K and in superfluid He at 1.9 K," *IEEE Trans. Appl. Superconduc.* **9**, 257 (1999).

[9.319] D.E. Baynham, D.A. Cragg, R.C. Coombs, P. Bauer, R. Wolf, "Transient stability of LHC strands," *IEEE Trans. Appl. Superconduc.* **9**, 1109 (1999).

[9.320] K. Artoos, T. Kurtyka, F. Savary, R. Valbuena, J. Vlogaert, "Measurement and analysis of axial end forces in a full-length prototype of LHC main dipole mag-

Papers Cited in Table 9.7: Dipoles and Quadrupoles (continuation)

nets," *IEEE Trans. Appl. Superconduc.* **10**, 69 (2000).

[9.321] Walter Scandale, Ezio Todesco and Paola Tropea, "Influence of mechanical tolerances on field quality in the LHC main dipoles," *IEEE Trans. Appl. Superconduc.* **10**, 73 (2000).

[9.322] R.M. Scanlan, D.R. Dietderich, and H.C. Higley, "Conductor development for high field dipole magnets," *IEEE Trans. Appl. Superconduc.* **10**, 288 (2000).

[9.323] S.A. Gourlay, P. Bish, S. Caspi, K. Chow, D.R. Dietderich, R. Gupta, R. Hannaford, W. Harnden, H. Higley, A. Lietzke, N. Liggins, A.D. McInturff, G.A. Millos, L. Morrison, R.M. Scanlan, "Design and fabrication of a 14 T, Nb3Sn superconducting racetrack dipole magnet," *IEEE Trans. Appl. Superconduc.* **10**, 294 (2000).

[9.324] V. Maroussov, S. Sanfilippo, A. Siemko, "Temperature profiles during quenches in LHC superconducting dipole magnets protected by quench heaters," *IEEE Trans. Appl. Superconduc.* **10**, 661 (2000).

[9.325] L. Bottura, P. Pugnat, A. Siemko, J. Vlogaert, and C. Wyss, "Performance of the LHC final design full scale superconducting dipole prototypes," *IEEE Trans. Appl. Superconduc.* **11**, 1554 (2001).

[9.326] Peter McIntyre, Raymond Blackburn, Nicholai Diaczenko, Tim Elliott, Rudolph Gaedke, Bill Henchel, Ed Hill, Mark Johnson, Hans Kautzky, and Akhdior Sattarov, "12 Tesla hybrid block-coil dipole for future hadron colliders," *IEEE Trans. Appl. Superconduc.* **11**, 2264 (2001).

[9.327] F. Simon, C. Gourdin, T. Schild, J. Deregel, A. Devred, B. Hervieu, M. Peyrot, J.M. Rifflet, T. Tortschanoff, T. Ogitsu, K. Tsuchiya, "Test results of the third LHC main quadrupole magnet prototype at CEA/Saclay," *IEEE Trans. Appl. Superconduc.* **12**, 266 (2002).

[9.328] T. Ogitsu, T. Nakamoto, N. Ohuchi, Y. Ajima, E. Burkhardt, N. Higashi, H. Hirano, M. Iida, N. Kimura, H. Ohhata, K. Tanaka, T. Shintomi, A. Terashima, K. Tsuchiya, A. Yamamoto, T. Orikasa, S. Murai, O. Oosaki, "Status of the LHC low-beta insertion quadrupole magnet development at KEK," *IEEE Trans. Appl. Superconduc.* **12**, 183 (2002).

[9.329] P. Fessia, C. Lanza, D. Perini, and T. Verbeeck, "First experience in the mass production of components for the LHC dipoles," *IEEE Trans. Appl. Superconduc.* **12**, 1256 (2002).

[9.330] Andrew V. Gavrilin, Mark D. Bird, Victor E. Keilin, and Alexey V. Dudarev, "New concepts in transverse field magnet design," *IEEE Trans. Appl. Superconduc.* **13**, 1213 (2003).

[9.331] Ryuji Yamada and Masayoshi Wake, "Quench problems of Nb_3Sn cosine theta high field dipole model magnets," *IEEE Trans. Appl. Superconduc.* **15**, 1140 (2005).

[9.332] M. Calvi, E. Floch, S. Kouzue, and A. Siemko, "Improved quench localization and quench propagation velocity measurements in the LHC superconducting dipole magnets," *IEEE Trans. Appl. Superconduc.* **15**, 1209 (2005).

[9.333] S. Feher, R.C. Bossert, G. Ambrosio, N. Andreev, E. Barzi, R. Carcagno, V.S. Kashikhin, V.V. Kashikhin, M.J. Lamm, F. Nobrega, I. Novitski, Y. Pischalnikov, C. Sylvester, M. Tartaglia, D. Turrioni, G. Whitson, R. Yamada, A.V. Zlobin, S. Caspi, D. Dietderich, P. Ferracin, R. Hannaford, A.R. Hafalia, and G. Sabbi, "Development and test of LARP technological quadrupole (TQC) magnet *IEEE Trans. Appl. Superconduc.* **17**, 1126 (2007).

[9.334] S. Caspi, D.R. Dietderich, P. Ferracin, N.R. Finney, M.J. Fuery, S.A. Gourlay, and A.R. Hafalia, "Design, fabrication, and test of a superconducting dipole magnet

Papers Cited in Table 9.7: Dipoles and Quadrupoles (continuation)

based on tilted solenoids," *IEEE Trans. Appl. Superconduc.* **17**, 2266 (2007).

[9.335] F. Nobrega, N. Andreev, G. Ambrosio, E. Barzi, R. Bossert, R. Carcagno, G. Chlachidze, S. Feher, V.S. Kashikhin, V.V. Kashikhin, M.J. Lamm, I. Novitski, D. Orris, Y. Pischalnikov, C. Sylvester, M. Tartaglia, D. Turrioni, R. Yamada, and A.V. Zlobin, "Nb_3Sn accelerator magnet technology scale up using cos-theta dipole coils," *IEEE Trans. Appl. Superconduc.* **18**, 273 (2008).

[9.336] Paul D. Brindza, Steven R. Lassiter, and Michael J. Fowler, "The cosine two theta quadrupole magnets for the Jefferson Lab super high momentum spectrometer," *IEEE Trans. Appl. Superconduc.* **18**, 415 (2008).

High Energy Physics **[HTS]**

[9.337] William B. Sampson, Arup K. Ghosh, John P. Cozzolino, Michael A. Harrison, and Peter J. Wanderer, "Persistent current effects in BSCCO common coil dipoles," *IEEE Trans. Appl. Superconduc.* **11**, 2156 (2001).

[9.338] A.I. Ageev, I.I. Akirnov, A.M. Andriishchin, I.V. Bogdanov, S.S. Kozub, K.P. Myznikov, D.N. Rakov, A.V. Rekudanov, P.A. Shcherbakov, P.I. Slabodchikov, A.A. Seletsky, A.K. Shikov, V.V. Sytnik, A.V. Tikhov, L.M. Tkachenko, and V.V. Zubko, "Test results of HTS dipole," *IEEE Trans. Appl. Superconduc.* **12**, 125 (2002).

[9.339] Hiromi Hirabayashi, Nobuhiro Kimura, Yasuhiro Makida, and Takakazu Shintomi, "Hydrogen cooled superferric magnets for accelerators and beam lines," *IEEE Trans. Appl. Superconduc.* **14**, 329 (2004).

[9.340] R. Gupta, M. Anerella, J. Cozzolino, J. Escallire, G. Ganetis, A. Ghosh, M. Harrison, A. Marone, J. Muratore, J. Schmalzle, W. Sampson, and P. Wanderer, "Status of high temperature superconductor magnet R&D at BNL," *IEEE Trans. Appl. Superconduc.* **14**, 1198 (2004).

[9.341] A. Godeke, D. Cheng, D.R. Dietderich, C.D. English, H. Felice, C.R. Hannaford, S.O. Prestemon, G. Sabbi, R.M. Scanlan, Y. Hikichi, J. Nishioka, and T. Hasegawa, "Development of wind-and-react Bi-2212 accelerator magnet technology," *IEEE Trans. Appl. Superconduc.* **18**, 516 (2008).

Table 9.7: Research Magnets—High-Field DC Solenoids

HTS & LTS/HTS (Includes ***Cryogen-Free Above ∼10 T LTS***)

[9.342] T. Kitamura, T. Hasegawa, H. Ogiwara, "Design and fabrication of Bi-based superconducting coil," *IEEE Trans. Appl. Superconduc.* **3**, 939 (1993).

[9.343] D. Aized, M.D. Manlief, C.H. Joshi, "Performance of high temperature superconducting coils in high background fields at different temperatures," *IEEE Trans. Magn.* **30**, 2010 (1994).

[9.344] Richard G. Jenkins, Harry Jones, Ming Yang, Michael J. Goringe, and Christopher R.M. Grovenor, "The construction and performance of BSCCO 2212 coils for use in liquid nitrogen at 64 K on an iron yoke in demonstrator devices," *IEEE Trans. Appl. Superconduc.* **5**, 503 (1995).

[9.345] Pradeep Haldar, James G. Hoehn, Jr., Y. Iwasa, L. Lim, M. Yunus, "Development of Bi-2223 HTS high field coils and magnets," *IEEE Trans. Appl. Superconduc.* **5**, 512 (1995).

[9.346] Drew W. Hazelton, Joseph A. Rice, Yusuf S. Hascicek, Huub W. Weijers and Steven W. Van Sciver, "Development and test of a BSCCO-2223 HTS high field insert magnet for NMR," *IEEE Trans. Appl. Superconduc.* **5**, 789 (1995).

Papers Cited in Table 9.7: High-Field Solenoids—HTS & LTS/HTS (continuation)

[9.347] J.F. Picard, M. Zouiti, C. Levillain, M. Wilson, D. Ryan, K. Marken, P.F. Hermann, E. Béghin, T. Verhaege, Y. Parasie, J. Bock, M. Baecker, J.A.A.J. Perenboom, J. Paasi, "Technologies for high field HTS magnets," *IEEE Trans. Appl. Superconduc.* **9**, 535 (1999).

[9.348] G. Snitchler, S.S. Kalsi, M. Manlief, R.E. Schwall, A. Sidi-Yekhief, S. Ige, R. Medeiros, T.L. Francavilla, D.U. Gubser, "High-field warm-bore HTS conduction cooled magnet," *IEEE Trans. Appl. Superconduc.* **9**, 553 (1999).

[9.349] Michiya Okada, Kazuhide Tanaka, Tsuyoshi Wakuda, Katsumi Ohata, Junichi Sato, Hiroaki Kumakura, Tsukasa Kiyoshi, Hitoshi Kitaguchi, Kazumasa Togano and Hitoshi Wada, "Fabrication of Bi-2212/Ag magnets for high magnetic field applications," *IEEE Trans. Appl. Superconduc.* **9**, 920 (1999).

[9.350] K. Ohmatsu, S. Hahakura, T. Kato, K. Fujino, K. Ohkura and K. Sato, "Recent progress of HTS magnet using Bi-2223 Ag-sheathed wire," *IEEE Trans. Appl. Superconduc.* **9**, 924 (1999).

[9.351] M. Newson, D.T. Ryan, M.N. Wilson and H. Jones, "High T_c insert coils for high field superconducting magnets-the Oxford programme," *IEEE Trans. Appl. Superconduc.* **10**, 468 (2000).

[9.352] Tsukasa Kiyoshi, Michio Kosuge, Michinari Yuyama, Hideo Nagai, Hitoshi Wada, Hitoshi Kitaguchi, Michiya Okada, Kazuhide Tanaka, Tsuyoshi Wakuda, Katsumi Ohata, and Junichi Sato, "Generation of 23.4 T using two Bi-2212 insert coils," *IEEE Trans. Appl. Superconduc.* **10**, 472 (2000).

[9.353] Sang-Soo Oh, Hong-Soo Ha, Hyun-Man Jang, Dong-Woo Ha, Rock-Kil Ko, Young-Kil Kwon, Kang-Sik Ryu, Haigun Lee, Benjamin Haid, and Yukikazu Iwasa, "Fabrication of Bi-2223 HTS magnet with a superconducting switch," *IEEE Trans. Appl. Superconduc.* **11**, 1808 (2001).

[9.354] So Noguchi, Makoto Yamashita, Hideo Yamashita, and Atsushi Ishiyama, "An optimal design method for superconducting magnets using HTS tape," *IEEE Trans. Appl. Superconduc.* **11**, 2308 (2001).

[9.355] H. Morita, M. Okada, K. Tanaka, J. Sato, H. Kitaguchi, H. Kumakura, K. Togano, K. Itoh, and H. Wada, "10 T conduction cooled Bi-2212/Ag HTS solenoid magnet system," *IEEE Trans. Appl. Superconduc.* **11**, 2523 (2001).

[9.356] Weijun Shen, Michael Coffey, Wayne McGhee, "Development of 9.5 T cryogen-free magnet," *IEEE Trans. Appl. Superconduc.* **11**, 2619 (2001).

[9.357] Tsukasa Kiyoshi, Shinji Matsumoto, Michio Kosuge, Michinari Yuyama, Hideo Nagai, Fumiaki Matsumoto, and Hitoshi Wada, "Superconducting inserts in high-field solenoids," *IEEE Trans. Appl. Superconduc.* **12**, 470 (2002).

[9.358] V. Cavaliere, M. Cioffi, A. Formisanao, and R. Martone, "Shape optimization of high Tc superconducting magnets," *IEEE Trans. Magn.* **38**, 1129 (2002).

[9.359] H.W. Weijers, Y.S. Hascicek, K. Marken, A. Mbaruku, M. Meinesz, H. Miao, S.H. Thompson, F. Trillaud, U.P. Trociewitz, and J. Schwartz, "Development of a 5 T HTS insert magnet as part of 25 T class magnets," *IEEE Trans. Appl. Superconduc.* **13**, 1396 (2003).

[9.360] Xiaohua Jiang, Xu Chu, Jie Yang, Nengqiang Jin, Zhiguang Cheng, Zhenmin Chen, Luhai Gou, and Xiaopeng Ren, "Development of a solenoidal HTS coil cooled by liquid or gas helium," *IEEE Trans. Appl. Superconduc.* **13**, 1871 (2003).

[9.361] Kazutomi Miyoshi, Masanao Mimura, Shin-ichiro Meguro, Takayo Hasegawa, Takashi Saitoh, Naoji Kashima, and Shigeo Nagaya, "Development of HTS coil

Papers Cited in Table 9.7: High-Field Solenoids—HTS & LTS/HTS (continuation)

with Bi-2223 transposed segment conductor," *IEEE Trans. Appl. Superconduc.* **14**, 766 (2004).

[9.362] F. Hornung, M. Kläser, T. Schneider, "Usage of Bi-HTS in high field magnets," *IEEE Trans. Appl. Superconduc.* **14**, 1102 (2004).

[9.363] R. Musenich, P. Fabbricatore, S. Farinon, C. Ferdeghini, G. Grasso, M. Greco, A. Malagoli, R. Marabotto, M. Modica, D. Nardelli, A.S. Siri, M. Tassisto, and A. Tumino, "Behavior of MgB2 react & wind coils above 10 K," *IEEE Trans. Appl. Superconduc.* **15**, 1452 (2005).

[9.364] M. Beckenbach, F. Hornung, M. Kläser, P. Leys, B. Lott, and Th. Schneider, "Manufacture and test of a 5 T Bi-2223 insert coil," *IEEE Trans. Appl. Superconduc.* **15**, 1484 (2005).

[9.365] Kenji Tasaki, Michitaka Ono, Toru Kuriyama, Makoto Kyoto, Satoshi Hanai, Hiroyuki Takigami, Hirohisa Takano, Kazuo Watanabe, Satoshi Awaji, Gen Nishijima, and Kazumasa Togano, "Development of a Bi2223 insert coil for a conduction-cooled 19 T superconducting magnet," *IEEE Trans. Appl. Superconduc.* **15**, 1512 (2005).

[9.366] R. Hirose, S. Hayashi, S. Fukumizu, Y. Muroo, H. Miyaka, Y. Okui, A. Ioki, T. Kamikado, O. Ozaki, Y. Nunoya, and K. Okuno, "Development of 15 T cryogen-free superconducting magnets," *IEEE Trans. Magn.* **16**, 953 (2006).

[9.367] L'ubomír Kopera, Pavol Kováč, and Tibor Meliěk, "Compact design of cryogen-free HTS magnet for laboratory use," *IEEE Trans. Magn.* **16**, 1415 (2006).

[9.368] Takashi Hase, Mamoru Hamada, Ryoichi Hirose, Yasuhide Nagahama, Koji Shikimachi, and Shigeo Nagaya, "Fabrication test of YBCO coil and multi-tape conductor," *IEEE Trans. Appl. Superconduc.* **17**, 2216 (2007).

[9.369] Justin Schwartz, Timothy Effio, Xiaotao Liu, Quang V. Le, Abdallah L. Mbaruku, Hans J. Schneider-Muntau, Tengming Shen, Honghai Song, Ulf P. Trociewitz, Xiaorong Wang, and Hubertus W. Weijers, "High field superconducting solenoids via high temperature superconductors," *IEEE Trans. Appl. Superconduc.* **18**, 70 (2008).

Papers Cited in Table 9.7: Research Magnets—NMR/MRI

NMR/MRI **[LTS]**

[9.370] J.E.C. Williams, L.J. Neuringer, E. Bobrov, R. Weggel, D.J. Ruben, and W.G. Harrison, "Magnet system of the 500 MHz NMR spectrometer at the Francis Bitter National Magnet Laboratory: I. Design and development of the magnet," *Rev. Sci. Instrum.* **52**, 649 (1981).

[9.371] E.S. Bobrov, R.D. Pillsbury, Jr., W.F.B. Punchard, R.E. Schwall, H.R. Segal, J.E.C. Williams, and L.J. Neuringer, "A 60 cm bore 2.0 tesla high homogeneity magnet for magnetic resonance imaging," *IEEE Trans. Magn.* **23**, 1303 (1987).

[9.372] W.D. Markiewicz, I.R. Dixon, C.A. Swenson, W.S. Marshall, T.A. Painter, S.T. Bole, T. Cosmus, M. Parizh, M. King, G. Ciancetta, "900 MHz wide bore NMR spectrometer magnet at NHMFL," *IEEE Trans. Appl. Superconduc.* **10**, 728 (2000).

[9.373] Tsukasa Kiyoshi, Shinji Matsumoto, Akio Sato, Masatoshi Yoshikawa, Satoshi Ito, Osamu Okazaki, Takayoshi Miyazaki, Takashi Miki, Takashi Hase, Mamoru Hamada, Takashi Noguchi, Shigeo Fukui, and Hitoshi Wada, "Operation of a 930-MHz high resolution NMR magnet at TML," *IEEE Trans. Appl. Superconduc.* **15**, 1330 (2005).

Papers Cited in Table 9.7: Research Magnets—NMR/MRI (LTS) (continuation)

[9.374] M. Tsuchiya, T. Wakuda, K. Maki, T. Shino, H. Tanaka, N. Saho, H. Tsukamoto, S. Kido, K. Takeuchi, M. Okada, and H. Kitaguchi, "Development of superconducting split magnets for NMR spectrometer," *IEEE Trans. Magn.* **18**, 840 (2008).

[9.375] Th. Schild, G. Aubert, C. Berriaud, Ph. Bredy, F.P. Juster, C. Meuris, F. Nunio, L. Quettier, J.M. Rey, and P. Vedrine, "The Iseult/Inumac whole body 11.7 T MRI magnet design," *IEEE Trans. Magn.* **18**, 904 (2008).

NMR **[LTS/HTS]**

[9.376] Tsukasa Kiyoshi, Shinji Matsumoto, Michio Kosuge, Michinari Yuyama, Hideo Nagai, Fumiaki Matsumoto, and Hitoshi Wada, "Superconducting inserts in high-field solenoids," *IEEE Trans. Appl. Superconduc.* **12**, 470 (2002).

[9.377] Haigun Lee, Juan Bascuñán, and Yukikazu Iwasa, "A high-temperature superconducting (HTS) insert comprised of double pancakes for an NMR magnet," *IEEE Trans. Appl. Superconduc.* **13**, 1546 (2003).

[9.378] W. Denis Markiewicz, John R. Miller, Justin Schwartz, Ulf P. Trociewitz, and Huub Weijers, "Perspective on a superconducting 30 T/1.3 GHz NMR spectrometer magnet," *IEEE Trans. Appl. Superconduc.* **16**, 1523 (2006).

[9.379] Juan Bascuñán, Wooseok Kim, Seungyong Hahn, Emanuel S. Bobrov, Haigun Lee, and Yukikazu Iwasa, "An LTS/HTS NMR magnet operated in the range 600–700 MHz," *IEEE Trans. Appl. Superconduc.* **17**, 1446 (2007).

[9.380] T. Kiyoshi, A. Otsuka, S. Choi, S. Matsumoto, K. Zaitsu, T. Hase, M. Hamada, M. Hosono, M. Takahashi, T. Yamazaki, and H. Maeda, "NMR upgrading project towards 1.05 GHz," *IEEE Trans. Appl. Superconduc.* **18**, 860 (2008).

MRI **[HTS]**

[9.381] Minfeng Xu, Michele Ogle, Xianrui Huang, Kathleen Amm, Evangelos T. Laskaris, "Iterative EM design of an MRI magnet using HTS materials," *IEEE Trans. Appl. Superconduc.* **17**, 2192 (2007).

[9.382] M. Modica, S. Angius, L. Bertora, D. Damiani, M. Marabotto, D. Nardelli, M. Perrella, M. Razeti, and M. Tassisto, "Design, construction and tests of MgB2 coils for the development of a cryogen free magnet," *IEEE Trans. Appl. Superconduc.* **17**, 2196 (2007).

[9.383] Roberto Penco and Giovanni Grasso, "Recent development of MgB_2-based large scale applications," *IEEE Trans. Appl. Superconduc.* **17**, 2291 (2007).

[9.384] Marco Razeti, Silvano Anguis, Leonardo Bertora, Daniele Damiani, Roberto Marabotto, Marco Modica, Davide Nardelli, Mauro Perrela, and Matteo Tassisto, "Construction and operation of cryogen free MgB_2 magnets for open MRI system," *IEEE Trans. Appl. Superconduc.* **18**, 882 (2008).

[9.385] Weijun Yao, Juan Bascuñán, Woo-Seok Kim, Seungyong Hahn, Haigun Lee, and Yukikazu Iwasa, "A solid nitrogen cooled MgB_2 'demonstration' coil for MRI applications," *IEEE Trans. Appl. Superconduc.* **18**, 912 (2008).

Papers Cited in Table 9.7: Silicon Wafer Processing **[HTS]**

[9.386] M. Ono, K. Tasaki, Y. Ohotani, T. Kuriyama, Y. Sumiyoshi, S. Nomura, M. Kyoto, T. Shimonosono, S. Hanai, M. Shoujyu, N. Ayai, T. Kaneko, S. Kobayashi, K. Hayashi, H. Takei, K. Sato, T. Mizuishi, M. Kimura, and T. Masui, "Testing of a cryocooler-cooled HTS magnet with silver-sheathed Bi2223 tapes for silicon single-crystal growth applications," *IEEE Trans. Appl. Superconduc.* **12**, 984 (2002).

Appendix 1A

Physical Constants and Conversion Factors

Table A1.1: Selected Physical Constants*

Speed of light	c	3.00×10^{8} m/s
Permeability of free space	$\mu_\circ$	$4\pi\times10^{-7}$ H/m
Permittivity of free space	$\epsilon_\circ$	8.85×10^{-12} F/m
Avogadro's number	N_A	6.023×10^{23} particle/mole
Electronic charge	e	1.60×10^{-19} C
Electron rest mass	$m_\circ$	9.11×10^{-31} kg
Proton rest mass	$M_{p_\circ}$	1.67×10^{-27} kg
Planck's constant	h	6.63×10^{-34} J s
Boltzmann's constant	k_B	1.38×10^{-23} J/K
Gas constant	R	8.32×10^{3} J/kg-mole K
Molal gas volume	V_R	22.4 m^3/kg-mole
Stefan-Boltzmann constant	σ_{SB}	5.67×10^{-8} W/m^2 K^4
Acceleration of gravity	g	9.81 m/s^2
Wiedemann-Franz number	Λ	2.45×10^{-8} W Ω/K^2

* Except for the permeability of free space, values are approximate.

Table A1.2: Selected Conversion Factors

"Common" Non-SI Units*	SI Units*
Electromagnetic	
1 gauss	10^{-4} T
1 oersted	$250/\pi$ A/m
1 emu/cm^3	1000 A/m
Pressure	
1 mmHg (1 torr)	*133* Pa
1 atm (760 torr)	*101* kPa
1 bar (*750* torr)	0.1 MPa
1 psi (*52* torr)	*6.9* kPa
Viscosity	
1 poise	0.1 Pa s (0.1 kg/m s)
Energy & Power	
1 eV	*1.6* $\times 10^{-19}$ J
1 cal	*4.18* J
1 BTU	*1055* J
1 hp (horsepower)	*746* W
Temperature	
0°C	*273* K
1 eV	*11600* K
Mass	
1 lb	*0.45* kg
1 metric ton	1000 kg
Dimension	
1 in	25.4 mm
1 French league	*4* km
1 liter (1000 cm^3)	0.001 m^3
1 ft^3 (*28.3* liter)	*0.0283* m^3

* Values in italics are approximate.

Appendix 1B

Uniform-Current-Density Solenoidal Coil Field Error Coefficients

As discussed in **3.4**, the product $F(\alpha,\beta)E_n(\alpha,\beta)$ is given by Eq. 3.15*b*:

$$F(\alpha,\beta)E_n(\alpha,\beta) = \frac{1}{M_n\,\beta^{n-1}}\left[\frac{f_n(\alpha=1,\beta)}{(1+\beta^2)^{n-0.5}} - \frac{\alpha^3 f_n(\alpha,\beta)}{(\alpha^2+\beta^2)^{n-0.5}}\right] \qquad (3.15b)$$

$f_{n+1}(\alpha,\beta)$ may be derived from the following recurrence formula:

$$f_{n+1}(\alpha,\beta) = \frac{1}{(n+1)M_n}\frac{\partial}{\partial\beta}\left[\frac{f_n(\alpha,\beta)}{(\alpha^2+\beta^2)^{(n-0.5)}}\right]$$

Values of M_n and expressions of $f_n(\alpha,\beta)$ for n from 2 to 20 are given below:*

$n=2$: $M_2=2$; $f_2(\alpha,\beta)=1$

$n=3$: $M_3=6$; $f_3(\alpha,\beta)=\alpha^2+4\beta^2$

$n=4$: $M_4=24$; $f_4(\alpha,\beta)=2\alpha^4+7\alpha^2\beta^2+20\beta^4$

$n=5$: $M_5=40$; $f_5(\alpha,\beta)=2\alpha^6+9\alpha^4\beta^2+12\alpha^2\beta^4+40\beta^6$

$n=6$: $M_6=240$; $f_6(\alpha,\beta)=8\alpha^8+44\alpha^6\beta^2+99\alpha^4\beta^4+28\alpha^2\beta^6+280\beta^8$

$n=7$: $M_7=336$; $f_7(\alpha,\beta)=8\alpha^{10}+52\alpha^8\beta^2+143\alpha^6\beta^4+232\alpha^4\beta^6-112\alpha^2\beta^8+448\beta^{10}$

$n=8$: $M_8=896$; $f_8(\alpha,\beta)=16\alpha^{12}+120\alpha^{10}\beta^2+390\alpha^8\beta^4+715\alpha^6\beta^6+1080\alpha^4\beta^8$
$-1008\alpha^2\beta^{10}+1344\beta^{12}$

$n=9$: $M_9=1152$; $f_9(\alpha,\beta)=16\alpha^{14}+136\alpha^{12}\beta^2+510\alpha^{10}\beta^4+1105\alpha^8\beta^6+1480\alpha^6\beta^8$
$+2592\alpha^4\beta^{10}-2688\alpha^2\beta^{12}+1920\beta^{14}$

$n=10$: $M_{10}=11520$; $f_{10}(\alpha,\beta)=128\alpha^{16}+1216\alpha^{14}\beta^2+5168\alpha^{12}\beta^4+12920\alpha^{10}\beta^6$
$+20995\alpha^8\beta^8+19976\alpha^6\beta^{10}+49632\alpha^4\beta^{12}-46464\alpha^2\beta^{14}+21120\beta^{16}$

$n=11$: $M_{11}=14080$; $f_{11}(\alpha,\beta)=128\alpha^{18}+1344\alpha^{16}\beta^2+6384\alpha^{14}\beta^4+18088\alpha^{12}\beta^6$
$+33915\alpha^{10}\beta^8+44436\alpha^8\beta^{10}+23408\alpha^6\beta^{12}+114048\alpha^4\beta^{14}-88704\alpha^2\beta^{16}+28160\beta^{18}$

$n=12$: $M_{12}=33792$; $f_{12}(\alpha,\beta)=256\alpha^{20}+2944\alpha^{18}\beta^2+15456\alpha^{16}\beta^4+48944\alpha^{14}\beta^6$
$+104006\alpha^{12}\beta^8+156009\alpha^{10}\beta^{10}+177268\alpha^8\beta^{12}-2288\alpha^6\beta^{14}+494208\alpha^4\beta^{16}$
$-311168\alpha^2\beta^{18}+73216\beta^{20}$

The author thanks Robert Weggel for supplying these expressions of $f_n(\alpha,\beta)$.

$n=13$: $M_{13}=39936$; $f_{13}(\alpha,\beta)=256\alpha^{22}+3200\alpha^{20}\beta^2+18400\alpha^{18}\beta^4+64400\alpha^{16}\beta^6$
$+152950\alpha^{14}\beta^8+260015\alpha^{12}\beta^{10}+324268\alpha^{10}\beta^{12}+355160\alpha^8\beta^{14}-228800\alpha^6\beta^{16}$
$+1006720\alpha^4\beta^{18}-512512\alpha^2\beta^{20}+93184\beta^{22}$

$n=14$: $M_{14}=186368$; $f_{14}(\alpha,\beta)=1024\alpha^{24}+13824\alpha^{22}\beta^2+86400\alpha^{20}\beta^4+331200\alpha^{18}\beta^6$
$+869400\alpha^{16}\beta^8+1651860\alpha^{14}\beta^{10}+2340135\alpha^{12}\beta^{12}+2465460\alpha^{10}\beta^{14}$
$+3027960\alpha^8\beta^{16}-3615040\alpha^6\beta^{18}+7742592\alpha^4\beta^{20}-3214848\alpha^2\beta^{22}+465920\beta^{24}$

$n=15$: $M_{15}=215040$; $f_{15}(\alpha,\beta)=1024\alpha^{26}+14848\alpha^{24}\beta^2+100224\alpha^{22}\beta^4+417600\alpha^{20}\beta^6$
$+1200600\alpha^{18}\beta^8+2521260\alpha^{16}\beta^{10}+3991995\alpha^{14}\beta^{12}+4850640\alpha^{12}\beta^{14}$
$+4232160\alpha^{10}\beta^{16}+6980480\alpha^8\beta^{18}-10286848\alpha^6\beta^{20}+14137344\alpha^4\beta^{22}$
$-4845568\alpha^2\beta^{24}+573440\beta^{26}$

$n=16$: $M_{16}=491520$; $f_{16}(\alpha,\beta)=2048\alpha^{28}+31744\alpha^{26}\beta^2+230144\alpha^{24}\beta^4+1035648\alpha^{22}\beta^6$
$+3236400\alpha^{20}\beta^8+7443720\alpha^{18}\beta^{10}+13026510\alpha^{16}\beta^{12}+17678835\alpha^{14}\beta^{14}$
$+18886320\alpha^{12}\beta^{16}+12335200\alpha^{10}\beta^{18}+33747584\alpha^8\beta^{20}-49956608\alpha^6\beta^{22}$
$+49334272\alpha^4\beta^{24}-14135296\alpha^2\beta^{26}+1392640\beta^{28}$

$n=17$: $M_{17}=557056$; $f_{17}(\alpha,\beta)=2048\alpha^{30}+33792\alpha^{28}\beta^2+261888\alpha^{26}\beta^4+1265792\alpha^{24}\beta^6$
$+4272048\alpha^{22}\beta^8+10680120\alpha^{20}\beta^{10}+20470230\alpha^{18}\beta^{12}+30705345\alpha^{16}\beta^{14}$
$+36455760\alpha^{14}\beta^{16}+35305600\alpha^{12}\beta^{18}+11776512\alpha^{10}\beta^{20}+81808896\alpha^8\beta^{22}$
$-109531136\alpha^6\beta^{24}+82722816\alpha^4\beta^{26}-20054016\alpha^2\beta^{28}+1671168\beta^{30}$

$n=18$: $M_{18}=10027008$; $f_{18}(\alpha,\beta)=32768\alpha^{32}+573440\alpha^{30}\beta^2+4730880\alpha^{28}\beta^4$
$+24442880\alpha^{26}\beta^6+88605440\alpha^{24}\beta^8+239234688\alpha^{22}\beta^{10}+498405600\alpha^{20}\beta^{12}$
$+818809200\alpha^{18}\beta^{14}+1074687075\alpha^{16}\beta^{16}+1132428880\alpha^{14}\beta^{18}+1047367552\alpha^{12}\beta^{20}$
$-149334528\alpha^{10}\beta^{22}+3085089280\alpha^8\beta^{24}-3565506560\alpha^6\beta^{26}+2143272960\alpha^4\beta^{28}$
$-444530688\alpha^2\beta^{30}+31752192\beta^{32}$

$n=19$: $M_{19}=11206656$; $f_{19}(\alpha,\beta)=32768\alpha^{34}+606208\alpha^{32}\beta^2+5304320\alpha^{30}\beta^4$
$+29173760\alpha^{28}\beta^6+113048320\alpha^{26}\beta^8+327840128\alpha^{24}\beta^{10}+737640288\alpha^{22}\beta^{12}$
$+1317214800\alpha^{20}\beta^{14}+1893496275\alpha^{18}\beta^{16}+2209194460\alpha^{16}\beta^{18}$
$+2080028192\alpha^{14}\beta^{20}+2015437312\alpha^{12}\beta^{22}-1533862400\alpha^{10}\beta^{24}+6968944640\alpha^8\beta^{26}$
$-6839951360\alpha^6\beta^{28}+3365732352\alpha^4\beta^{30}-603291648\alpha^2\beta^{32}+37355520\beta^{34}$

$n=20$: $M_{20}=24903680$; $f_{20}(\alpha,\beta)=65536\alpha^{36}+1277952\alpha^{34}\beta^2+11821056\alpha^{32}\beta^4$
$+68956160\alpha^{30}\beta^6+284444160\alpha^{28}\beta^8+881776896\alpha^{26}\beta^{10}+2130960832\alpha^{24}\beta^{12}$
$+4109710176\alpha^{22}\beta^{14}+6421422150\alpha^{20}\beta^{16}+8205150525\alpha^{18}\beta^{18}$
$+8620015404\alpha^{16}\beta^{20}+7193248608\alpha^{14}\beta^{22}+8412511744\alpha^{12}\beta^{24}$
$-11477921280\alpha^{10}\beta^{26}+30055434240\alpha^8\beta^{28}-25007497216\alpha^6\beta^{30}$
$+10287710208\alpha^4\beta^{32}-1608155136\alpha^2\beta^{34}+87162880\beta^{36}$

Appendix II

Thermodynamic Properties of Cryogens

Most thermodynamic property values given here (and generally given only up to three significant figures) are for "ballpark" computation and "first-cut" design. For hydrogen (H_2), properties of "normal" hydrogen (n-H_2) are listed. As for enthalpy, it is its *difference* between two temperatures or at a phase transition that matters; i.e., an enthalpy is not always set to 0 at 0 K as is the case with the specific heat from which the enthalpy vs. temperature data are computed. Therefore, enthalpy values given here may numerically differ from those given in other sources, but the *difference* agrees reasonably well.

Symbols: T_b, T_{ct}, T_m, T_s, and $T_\triangle$, respectively, boiling, critical, melting, saturation, and triple temperatures [K]; P_s: saturation pressure [torr/***atm***]; ϱ: density [kg/m^3]; h: enthalpy:[kJ/kg]; h_L: heat of fusion (at T_m or $T_\triangle$) or vaporization (at T_b) [kJ/kg]; h_ℓ: volumetric heat of vaporization [J/cm^3]; k: thermal conductivity [W/m K]; ν: viscosity [Pa s (pascal second)]; Pr: Prandtl number.

Property Data Sources

Because most property data presented in the above tables are compiled from many sources, the sources are grouped together and presented below. Recognize that some property values—all based on measurement—do *not agree* exactly.

Randall F. Barron, *Cryogenic Systems* 2nd Ed., (Clarendon Press, Oxford, 1985).

GASPAK (V.D. Arp and R.D. McCarty of Cryodata Inc.).

V.A. Grigoriev, Yu.M. Pavlov, and E.V. Ametistov, *Boiling of Cryogenic Liquids* (in Russian; Energia, Moscow, 1977).

R.T. Jacobsen, S.G. Penoncello, and E.W. Lemmon, *Thermodynamic Properties of Cryogenic Fluid* (Plenum, New York, 1997).

E.W. Lemmon, M.O. McLinden, and D.G. Friend, *Thermal Properties of Fluid Systems* (NIST Chemistry WebBook; http://webbook.nist.gov).

R.D. McCarty, *Thermophysical Properties of Helium-4 from 2 to 1500 K with Pressures to 1000 Atmospheres* (NBS Technical Note 631, 1972).

Robert D. McCarty, *The Thermodynamic Properties of Helium II from 0 K to the Lambda Transitions* (NBS Technical Note 1029, 1980).

NIST Reference Fluid Thermodynamic and Transport Properties Database (REFPROP): Version 8.0. Website: http://www.nist.gov/srd/nist23.htm

V.A. Rabinovich, A.A. Vasserman, V.I. Nedostup, L.S. Veksler, *Thermophysical Properties of Neon, Argon, Krypton, and Xenon* (Hemisphere Pub. Corp., New York, 1988).

Russell B. Scott, *Cryogenic Engineering* (1963 Edition reprinted in 1988 by Met-Chem Research, Boulder, CO).

Property Data Sources continue on next page.

Table A2.1: Selected Properties of Cryogens at 1 atm

Property		He	n-H_2	Ne	N_2	Ar	O_2
Boiling temperature, T_b	[K]	4.22	20.39	27.10	77.36	87.28	90.18
Heat of vaporization, h_L	[kJ/kg]	20.7	443	85.9	199	162	213
h_ℓ	[J/cm^3]	2.6	31.3	104	161	226	243
Density(T_b, liquid)	[kg/m^3]	125	70.8	1206	807	1394	1141
Density(T_b, vapor)	[kg/m^3]	16.9	1.33	9.37	4.60	5.77	4.47
Density @273 K (0°C)*	[kg/m^3]	0.179	0.090	0.900	1.251	1.784	1.429
@293 K (20°C)	[kg/m^3]	0.166	0.083	0.834	1.158	1.652	1.324
Density(T_b, liquid)/density(273 K)		700	787	1340	645	781	798
Density(T_b, liquid)/density(293 K)		753	853	1446	697	844	862

* Standard conditions.

Property Data Sources (continuation from p. 621)

T.A. Scott, "Solid and liquid nitrogen," *Physics Reports* **27C**, 89 (1976).

P.C. Souers, *Hydrogen Properties for Fusion Energy* (University of California Press, Berkeley, 1986).

R.B. Stewart, *ASHRAE Thermodynamic Properties of Refrigerants* (American Society of Heating, Refrigerating and Air Conditioning Engineers, New York, 1969).

Thomas R. Strobridge, *Thermodynamic Properties of Nitrogen* (National Bureau of Standards, Technical Note 129, 1962).

V.V. Sychev, A.A. Vasserman, A.D. Kozlov, G.A. Spiridnonov, and V.A. Tsymarny, *Thermodynamic Property of Helium, Neon, Argon, Krypton and Xenon*—A Series of Property Tables, National Standard Reference Data Service of the USSR.

E. Yu. Tonkov, *High Pressure Phase Transformations, Volume 2* (Gordon and Breach, 1992).

Steven W. Van Sciver, *Helium Cryogenics* (Plenum Press, New York, 1986).

Table A2.2: Density and Enthalpy Data of Solid Cryogens at 1 bar*/1 atm

	Neon (1 bar)		Nitrogen (1 atm)		Argon (1 bar)	
T [K]	ϱ [kg/m^3]	h [kJ/kg]	ϱ [kg/m^3]	h [kJ/kg]	ϱ [kg/m^3]	h [kJ/kg]
4	1507	0.02	1032	0.008	1771	0.01
5	1507	0.09	1032	0.021	1771	0.015
6	1506	0.10	1032	0.044	1771	0.024
8	1505	0.31	1032	0.15	1771	0.08
10	1503	0.75	1031	0.38	1771	0.20
12	1499	1.43	1031	0.80	1771	0.42
15	1490	2.76	1029	1.85	1769	0.96
20	1466	6.78	1027	4.74	1765	2.20
22	1452	8.84	1025	6.29	1763	2.80
24.56	1429 1240†	12.0 24.2†	1022	8.51	1760	3.90
30	—	—	1016	14.5	1752	6.12
35.61‡	—	—	1002 994	22.7 30.8	1742	8.90
40	—	—	989	37.1	1731	11.3
45	—	—	981	44.3	1725	14.2
50	—	—	970	52.1	1715	17.3
60	—	—	949	68.9	1691	23.9
63.16	—	—	946 877†	74.3 100.0†	1683	25.5
70	—	—	—	—	1664	31.1
80	—	—	—	—	1633	39.1
83.81	—	—	—	—	1619	42.3 71.6†

* 1 bar = 750 torr = 0.987 atm.

† *Liquid* phase.

‡ Solid-to-solid phase transition; nitrogen expands and absorbs an energy density of 8.17×10^3 [kJ/kg].

Table A2.3a: Helium at Saturation

T [K]	p* [torr/***atm***]	ρ† [kg/m^3]		h† [kJ/kg]	
1.50	3.53	145	*0.15*	0.26	*22.61*
1.55	4.47	145	*0.19*	0.32	*22.85*
1.60	5.59	145	*0.23*	0.39	*23.09*
1.65	6.90	145	*0.27*	0.48	*23.33*
1.70	8.45	145	*0.33*	0.58	*23.56*
1.75	10.2	145	*0.38*	0.70	*23.79*
1.80	12.3	145	*0.45*	0.84	*24.02*
1.85	14.6	145	*0.52*	1.00	*24.25*
1.90	17.2	145	*0.60*	1.18	*24.47*
1.95	20.2	145	*0.69*	1.38	*24.69*
2.00	23.4	146	*0.78*	1.63	*24.91*
2.05	27.0	146	*0.89*	1.92	*25.13*
2.10	31.0	146	*0.99*	2.23	*25.33*
T_λ: 2.18	38.0	146	*1.18*	—	*25.41*
2.20	39.9	146	*1.24*	3.28	*25.51*
2.30	50.4	146	*1.50*	3.57	*25.91*
2.40	62.5	145	*1.81*	3.82	*26.30*
2.50	76.6	145	*2.14*	4.05	*26.68*
2.60	92.6	144	*2.52*	4.27	*27.04*
2.80	133	142	*3.40*	4.73	*27.71*
3.00	182	141	*4.46*	5.23	*28.33*
3.25	257	139	*6.08*	5.93	*28.99*
3.50	352	136	*8.09*	6.72	*29.52*
3.75	470	133	*10.5*	7.62	*29.91*
4.00	615	129	*13.6*	8.65	*30.12*
4.22	760/***1.00***	125	*16.9*	9.71	*30.13*
4.30	***1.07***	124	*18.2*	10.1	*30.1*
4.40	***1.17***	121	*20.2*	10.7	*30.0*
4.50	***1.28***	119	*22.1*	11.3	*29.8*
4.75	***1.58***	112	*28.7*	13.0	*29.0*
5.00	***1.93***	101	*39.3*	15.4	*27.3*
T_{ct}: 5.20	***2.24***	69.6		21.4	

* In torr below 760 torr (1 atm) and in ***atm*** above 760 torr.

† Italics are for the vapor phase.

Table A2.3b: Density and Enthalpy Data of Helium at 1, 6, and 10 atm

	1 atm		6 atm		10 atm	
T [K]	ϱ [kg/m^3]	h [kJ/kg]	ϱ [kg/m^3]	h [kJ/kg]	ϱ [kg/m^3]	h [kJ/kg]
2.5	147	4.58	156	7.56	161	9.93
3.0	143	5.64	153	8.45	159	10.7
3.5	138	6.96	150	9.55	157	11.7
4.0	130	8.70	146	10.9	153	13.0
4.224	125 16.9	9.71 30.13	145	11.6	151	13.6
4.5	14.5	32.5	140	12.5	148	14.4
5.0	11.9	36.2	133	14.6	144	16.2
5.5	10.3	39.5	124	17.2	138	18.2
6	9.15	42.5	112	20.3	131	20.5
7	7.53	48.4	78.5	30.0	115	26.0
8	6.44	54.0	54.1	40.5	94.5	33.4
9	5.64	59.5	42.2	48.9	75.5	42.1
10	5.02	64.9	35.1	56.1	62.4	50.3
12	4.13	75.7	27.0	69.0	46.9	64.3
14	3.52	86.3	22.2	81.0	37.9	77.1
16	3.07	96.9	18.9	92.6	32.0	89.4
18	2.72	107	16.5	104	27.8	101
20	2.44	118	14.7	115	24.6	113
25	1.95	144	11.5	142	19.3	141
30	1.62	170	9.65	169	16.0	168
35	1.39	196	8.26	196	13.6	195
40	1.22	222	7.22	222	11.9	222
45	1.08	248	6.42	249	10.6	249
50	0.973	274	5.78	275	9.54	275
55	0.885	300	5.25	301	8.68	301
60	0.811	326	4.82	327	7.96	328
65	0.749	352	4.45	353	7.36	354
70	0.696	378	4.13	379	6.84	380
75	0.649	404	3.86	405	6.39	406
80	0.609	430	3.62	431	5.99	432
90	0.541	482	3.22	484	5.34	484
100	0.487	534	2.90	536	4.81	537
125	0.390	664	2.33	666	3.86	667
150	0.325	794	1.94	796	3.22	797
175	0.279	924	1.66	925	2.76	927
200	0.244	1054	1.46	1055	2.42	1057
225	0.217	1183	1.30	1185	2.15	1186
250	0.195	1313	1.17	1315	1.94	1316
275	0.177	1443	1.06	1445	1.76	1446
300	0.163	1573	0.973	1575	1.62	1576

Table A2.4a: Nitrogen at Saturation

T [K]	p* [torr]/[***atm***]	ρ† [kg/m^3]		h† [kJ/kg]	
T_m: 63.16	93.48	868	*0.67*	0	*216.1*
64	109	865	*0.77*	1.74	*216.9*
65	131	861	*0.92*	3.80	*217.9*
66	154	857	*1.07*	5.86	*218.8*
67	182	853	*1.24*	7.7	*219.7*
68	213	849	*1.43*	10.0	*220.7*
69	249	844	*1.65*	12.1	*221.6*
70	288	840	*1.89*	14.1	*222.5*
71	334	836	*2.16*	16.2	*223.4*
72	384	831	*2.46*	18.3	*224.2*
73	440	827	*2.78*	20.4	*225.1*
74	502	823	*3.14*	22.4	*226.0*
75	570	818	*3.53*	24.5	*226.8*
76	645	814	*3.96*	26.6	*227.6*
T_b: 77.364	760/***1.00***	807	*4.60*	29.4	*228.7*
78	***1.08***	804	*4.93*	30.7	*229.1*
79	***1.21***	800	*5.48*	32.8	*229.9*
80	***1.35***	795	*6.07*	34.8	*230.6*
82	***1.67***	786	*7.40*	39.0	*232*
84	***2.05***	776	*8.94*	43.1	*233*
86	***2.48***	766	*10.7*	47.3	*235*
88	***2.98***	756	*12.7*	51.5	*236*
90	***3.55***	746	*15.0*	55.7	*237*
92	***4.20***	735	*17.6*	59.9	*237*
94	***4.93***	724	*20.6*	64.3	*238*
96	***5.75***	713	*23.9*	68.7	*239*
98	***6.66***	702	*27.7*	73.1	*239*
100	***7.68***	690	*31.9*	77.7	*239*
102	***8.80***	677	*36.7*	82.4	*239*
104	***10.03***	664	*42.0*	87.2	*239*
106	***11.4***	651	*48.0*	92.2	*239*
108	***12.9***	637	*54.8*	97.2	*238*
110	***14.5***	622	*62.6*	102	*237*
112	***16.2***	606	*71.4*	108	*236*
114	***18.1***	589	*81.5*	113	*234*
116	***20.2***	570	*93.4*	119	*232*
118	***22.4***	549	*107*	125	*230*
120	***24.8***	525	*124*	132	*226*
T_{ct}: 126.3	***33.6***	254		194	

* In torr below 760 torr (1 atm) and in ***atm*** above 760 torr.

† Italics are for the vapor phase.

Table A2.4b: Density and Enthalpy Data of Nitrogen at 1, 15, and 20 atm

	1 atm		15 atm		20 atm	
T [K]	ϱ [kg/m^3]	h [kJ/kg]	ϱ [kg/m^3]	h [kJ/kg]	ϱ [kg/m^3]	h [kJ/kg]
64	865	1.82	867	2.97	897	3.39
65	861	3.87	863	5.02	864	5.43
66	857	5.93	859	7.06	860	7.47
67	853	7.99	855	9.12	856	9.52
68	849	10.1	851	11.2	852	11.6
69	844	12.1	847	13.2	848	13.6
70	840	14.2	843	15.3	844	15.7
71	836	16.3	839	17.3	839	17.7
72	832	18.3	834	19.4	835	19.8
73	827	20.4	830	21.4	831	21.8
74	823	22.5	826	23.5	827	23.9
75	818	24.5	821	25.5	822	25.9
76	814	26.6	817	27.6	818	28.0
77	809	28.6	812	29.6	813	30.0
77.364	807 4.60	29.4 228.7	811	30.4	812	30.7
79	4.50	230	803	33.7	804	34.1
80	4.44	232	799	35.8	800	36.1
85	4.15	237	775	46.0	776	46.3
90	3.90	242	750	56.2	752	56.5
95	3.68	248	723	66.8	725	67.0
100	3.48	253	694	77.8	697	77.9
105	3.31	258	661	89.6	665	89.5
108	3.21	262	639	97.1	644	96.8
110.60	3.13	264	617 6.51	104.0 237.0	623	104
112	3.09	266	6.29	240	611	107
114	3.04	268	6.01	243	592	113
115.823	2.99	270	5.79	246	571 9.22	118.6 232.6
118	2.93	272	5.56	250	8.59	238
120	2.88	274	5.37	253	8.13	242
125	2.76	280	4.97	260	7.28	252
130	2.65	285	4.65	267	6.67	260
135	2.55	290	4.37	274	6.19	268
140	2.46	295	4.14	281	5.81	275
150	2.29	306	3.76	293	5.20	288
200	1.71	358	2.64	351	3.56	349
250	1.37	410	2.07	406	2.77	404
275	1.24	436	1.87	433	2.50	431
300	1.14	462	1.71	459	2.28	458

Table A2.5: Hydrogen, Neon, and Argon at Saturation

T [K]	p* [torr]/[***atm***]	ρ† [kg/m^3]		h† [kJ/kg]	
Normal Hydrogen					
$T_\triangle$: 13.95	57.6	76.9	*0.14*	213	*662*
T_m : 14.0	59.2	76.9	*0.14*	213	*662*
15	100.7	76.0	*0.22*	221	*672*
16	161.5	75.1	*0.34*	228	*680*
17	246	74.2	*0.49*	236	*688*
18	361	73.2	*0.69*	244	*696*
19	510	72.2	*0.94*	253	*702*
20.28	760/***1.00***	70.8	*1.34*	265	*710*
21	***1.23***	70.0	*1.62*	272	*714*
22	***1.61***	68.7	*2.07*	283	*718*
23	***2.07***	67.4	*2.61*	395	*722*
T_{ct} : 32.94	***13.0***	32.2		555	
Neon					
24.55‡	325	1248	*4.41*	28.2	*117.0*
25	383	1241	*5.12*	29.0	*117.4*
26	539	1224	*7.00*	30.9	*118.1*
T_b : 27.10	760/***1.00***	1207	*9.58*	33.0	*118.8*
28	***1.30***	1189	*12.2*	34.8	*119.3*
29	***1.71***	1170	*15.7*	36.8	*119.8*
30	***2.21***	1151	*20.0*	38.8	*120.1*
31	***2.80***	1131	*25.0*	40.9	*120.4*
32	***3.51***	1111	*30.9*	43.1	*120.6*
T_{ct} : 44.40	***26.2***	483		92.5	
Argon					
83.78§	515	1415	*4.05*	71.9	*235.1*
85	593	1407	*4.60*	73.2	*235.6*
86	662	1401	*5.08*	74.2	*235.9*
T_b : 87.28	760/***1.00***	1394	*5.77*	75.6	*236.4*
88	***1.08***	1388	*6.18*	76.4	*236.7*
89	***1.19***	1382	*6.80*	77.5	*237.0*
90	***1.32***	1376	*7.45*	78.6	*237.4*
95	***2.11***	1344	*11.5*	84.2	*238.9*
T_{ct} : 150.86	***48.3***	536		189.9	

* In torr below 760 torr (1 atm) and in ***atm*** above 760 torr.

† Italics are for the vapor phase.

‡ $T_\triangle = 24.556$ K; $T_m = 24.56$ K.

§ $T_m = 83.8$ K; $T_\triangle = 83.806$ K.

Table A2.6: Density and Enthalpy Data of Neon at 1, 10, and 20 atm

	1 atm		10 atm		20 atm	
T [K]	ϱ [kg/m^3]	h [kJ/kg]	ϱ [kg/m^3]	h [kJ/kg]	ϱ [kg/m^3]	h [kJ/kg]
27.10	1207 9.58	0 85.8	1213	0.43	1218	0.97
28	9.22	86.9	1197	2.12	1203	2.63
29	8.85	88.1	1179	4.02	1185	4.50
30	8.52	89.2	1160	5.97	1167	6.42
32	7.94	91.5	1119	10.06	1128	10.4
33	7.68	92.5	1097	12.21	1108	12.5
34	7.43	93.6	1074	14.43	1086	14.7
36	6.99	95.8	1023	19.13	1038	19.2
37.62	6.67	97.5	974.5 88.2	23.31 86.80	994.6	23.1
40	6.25	100	77.0	91.3	916.9	29.7
42.34	5.89	103	69.5	95.0	787.3 212.9	39.1 78.6
44	5.66	104	65.2	97.4	172.1	85.5
46	5.41	106	61.0	100	148.9	90.7
48	5.18	109	57.4	103	134.0	94.8
50	4.96	111	54.3	105	123.1	98.3
55	4.50	116	48.0	111	104.1	106
60	4.12	121	43.2	117	91.5	113
65	3.80	126	39.4	123	82.1	119
70	3.52	131	36.2	129	74.7	125
75	3.29	137	33.6	134	68.7	131
80	3.08	142	31.3	140	63.7	137
85	2.90	147	29.3	145	59.4	143
90	2.74	152	27.6	150	55.7	148
95	2.59	157	26.1	156	52.5	154
100	2.46	163	24.7	161	49.7	159
110	2.24	173	22.4	172	44.9	170
120	2.05	183	20.5	182	40.9	181
130	1.89	193	18.9	193	37.7	192
140	1.76	204	17.5	203	34.9	202
150	1.64	214	16.3	214	32.5	213
160	1.54	224	15.3	224	30.5	223
180	1.37	245	13.6	245	27.1	244
200	1.23	266	12.2	266	24.3	265
220	1.12	286	11.1	286	22.1	286
240	1.02	307	10.2	307	20.3	307
260	0.945	328	9.4	328	18.7	328
280	0.878	348	8.7	348	17.4	349
300	0.819	369	8.2	369	16.2	369

Table A2.7: Selected Thermodynamic Properties of Cryogen *Gases* at 1 atm

T [K]	5	10	20	30	50	75	100	150	200	250	300
Density, ϱ [kg/m^3] {Liquid: He (125); n-H_2 (70.8); Ne (1206); N_2 (807); Ar (1394)}*											
He	16.9†	5.02	2.44	1.62	0.97	0.65	0.49	0.32	0.24	0.20	0.16
n-H_2	**88.5**‡	**88.2**	1.33†	0.85	0.49	0.33	0.25	0.16	0.12	0.10	0.08
Ne	**1520**	**1517**	**1484**	9.37†	4.97	3.30	2.47	1.64	1.23	0.98	0.82
N_2	**1031**	**1031**	**1027**	**1016**§	**970**	4.60†	3.48	2.29	1.71	1.37	1.14
Ar	**1771**	**1771**	**1765**	**1752**	**1715**	5.77†	4.98	3.25	2.44	1.95	1.62
Thermal Conductivity, k [mW/m K] {He (19.6); n-H_2 (119); Ne (113); N_2 (140); Ar (123)}											
He	10.6†	15.6	25.3	31.9	46.8	60.7	73.6	96.9	118	137	155
n-H_2	**400**	**800**	15.8†	22.9	36.2	51.6	68.0	98.5	128	155	177
Ne	**3500**	**950**	**370**	9.86†	14.1	18.2	22.2	29.8	36.9	43.3	49.2
N_2	**4350**	**1450**	**500**	**280**§	**690**	7.23†	9.33	13.7	18.0	22.1	25.8
Ar	**3250**	**3575**	**1410**	**900**	**500**	5.48†	6.41	9.58	12.5	15.2	17.7
Viscosity, ν [10^{-6}Pa s] {He (3.56); n-H_2 (13.2); Ne (130); N_2 (158); Ar (252)}											
He	1.24†	2.15	3.37	4.37	6.09	7.88	9.47	12.4	15.0	17.4	19.9
n-H_2	—	—	1.11†	1.61	2.49	3.41	4.21	5.60	6.81	7.93	8.96
Ne	—	—	—	4.77†	8.18	11.4	14.4	19.3	23.8	27.9	31.7
N_2	—	—	—	—	—	5.41†	6.98	10.1	13.0	15.6	17.9
Ar	—	—	—	—	—	7.43†	8.39	12.2	15.9	19.5	22.7
Prandl Number, Pr											
He	0.90†	0.72	0.68	0.68	0.67	0.66	0.67	0.68	0.67	0.68	0.69
n-H_2	—	—	0.77†	0.75	0.72	0.71	0.70	0.72	0.72	0.72	0.73
Ne	—	—	—	0.56†	0.62	0.65	0.67	0.67	0.66	0.66	0.66
N_2	—	—	—	—	—	0.81†	0.80	0.77	0.75	0.73	0.72
Ar	—	—	—	—	—	0.74†	0.71	0.67	0.67	0.67	0.67

* Values for liquid at saturation temperature, T_s, given between braces, { }.

† At saturation temperature, T_s, at *1 atm,* e.g., $T_s = 4.22$ K (He), 87.28 K (Ar).

‡ Bold: solid state.

§ Solid-solid phase transition at 35.61 K: $c_p = 1.63$ [kJ/kg K] at 35.6^- K and $c_p = 1.30$ [kJ/kg K] at 35.6^+ K; heat of transition: 8.17 kJ/kg. See C_p [J/cm^3 K] vs. T plots (Fig. 4.2 on p. 223).

Appendix III

Physical Properties of Materials

In using property data presented in this Appendix, we should be well aware that although most data are given to at least three significant figures, implying these particular data are quite accurate, they do not necessarily accurately represent the property value of the specific material for which we seek information. Among property data presented here, those that are subject to considerable degrees of variation from one material batch to another include: thermal conductivity data (Fig. A3.1); mechanical property data (Table A3.1); thermal expansion data (Table A3.2), particularly of non-metals.

Property Data Sources

A.F. Clark, "Low temperature thermal expansion of some metallic alloys," *Cryogenics* **8**, 282 (1968).

C.C. Clickner, J.W. Ekin, N. Cheggour, C.L.H. Thieme, Y. Qiao, Y.-Y. Xie, A. Goyal, "Mechanical properties of pure Ni and Ni-alloy substrate materials for Y-Ba-Cu-O coated superconductors," *Cryogenics* **46**, 432 (2006).

Robert J. Corruccini and John J. Gniewek, *Specific Heats and Enthalpies of Technical Solids at Low Temperatures* (NBS Monograph 21, 1960).

Cryogenic Materials Data Handbook Volumes 1 and 2 (Martin Marietta Corp. Air Force Materials Laboratory, 1970).

C.C. Koch and D.S. Easton, "A review of mechanical behavior and stress effects in hard superconductors," *Cryogenics* **17**, 391 (1977).

Materials Engineering Materials Selector 1987 (Penton Publishing, Cleveland, OH).

J.H. McTaggart and G.A. Slack, "Thermal conductivity data of General Electric No. 7031 varnish," *Cryogenics* **9**, 384 (1969).

T. Nishio, Y. Itoh, F. Ogasawara, M. Suganuma, Y. Yamada, U. Mizutani, "Superconducting and mechanical properties of YBCO-Ag composite superconductors," *J. Materials Science* **24**, 3228 (1989).

Russell B. Scott, *Cryogenic Engineering* (1963 Edition reprinted in 1988 by Met-Chem Research, Boulder, CO).

N.J. Simon, E.S. Drexler, and R.P. Reed, *Properties of Copper and Copper Alloys at Cryogenic Temperatures* (NIST Monograph 177, 1992).

N.J. Simon and R.P. Reed, *Structural Materials for Superconducting Magnets* (Preliminary Draft, 1982).

David R. Smith and F.R. Fickett, "Low-temperature properties of silver," *J. Res. Natl. Inst. Stand. Technol.* **100**, 119 (1995).

Y.S. Touloukian, R.W. Powell, C.Y. Ho, and P.G. Klemens, *Thermophysical Properties of Matter, Volume 2*, (IFI/Plenum, New York-Washington, 1970).

Y.S. Touloukian and R.K. Kirby, *Thermophysical Properties of Matter, Volume 12* (IFI/Plenum, New York-Washington, 1975).

A3.1a Thermal Conductivity vs. Temperature Plots: Mainly Conductive Materials

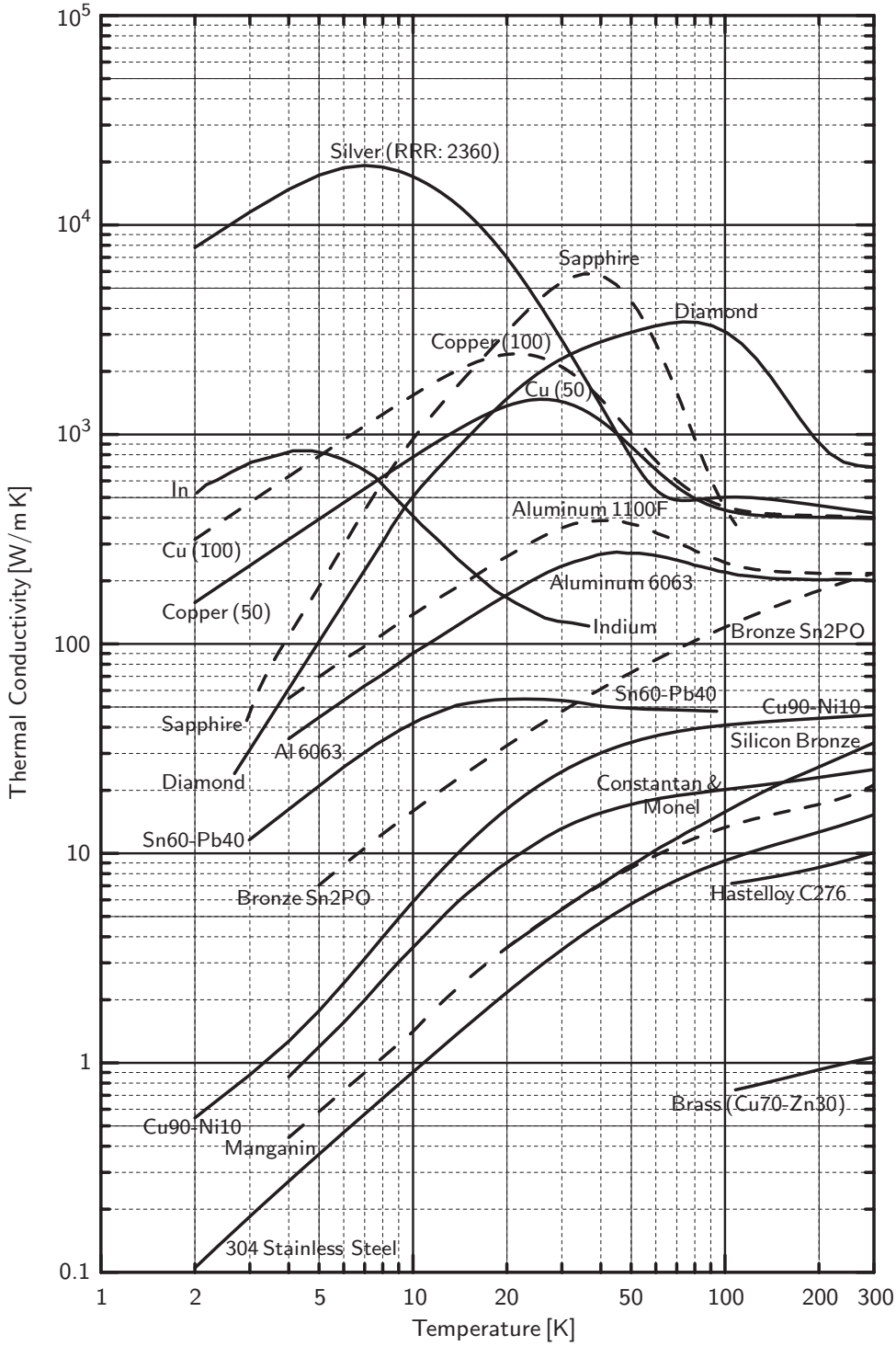

Fig. A3.1a Thermal conductivity vs. temperature plots of mainly conductive materials. (For clarity, selected plots are in dashed lines.)

A3.1b Thermal Conductivity vs. Temperature Plots: Nonconductive Materials

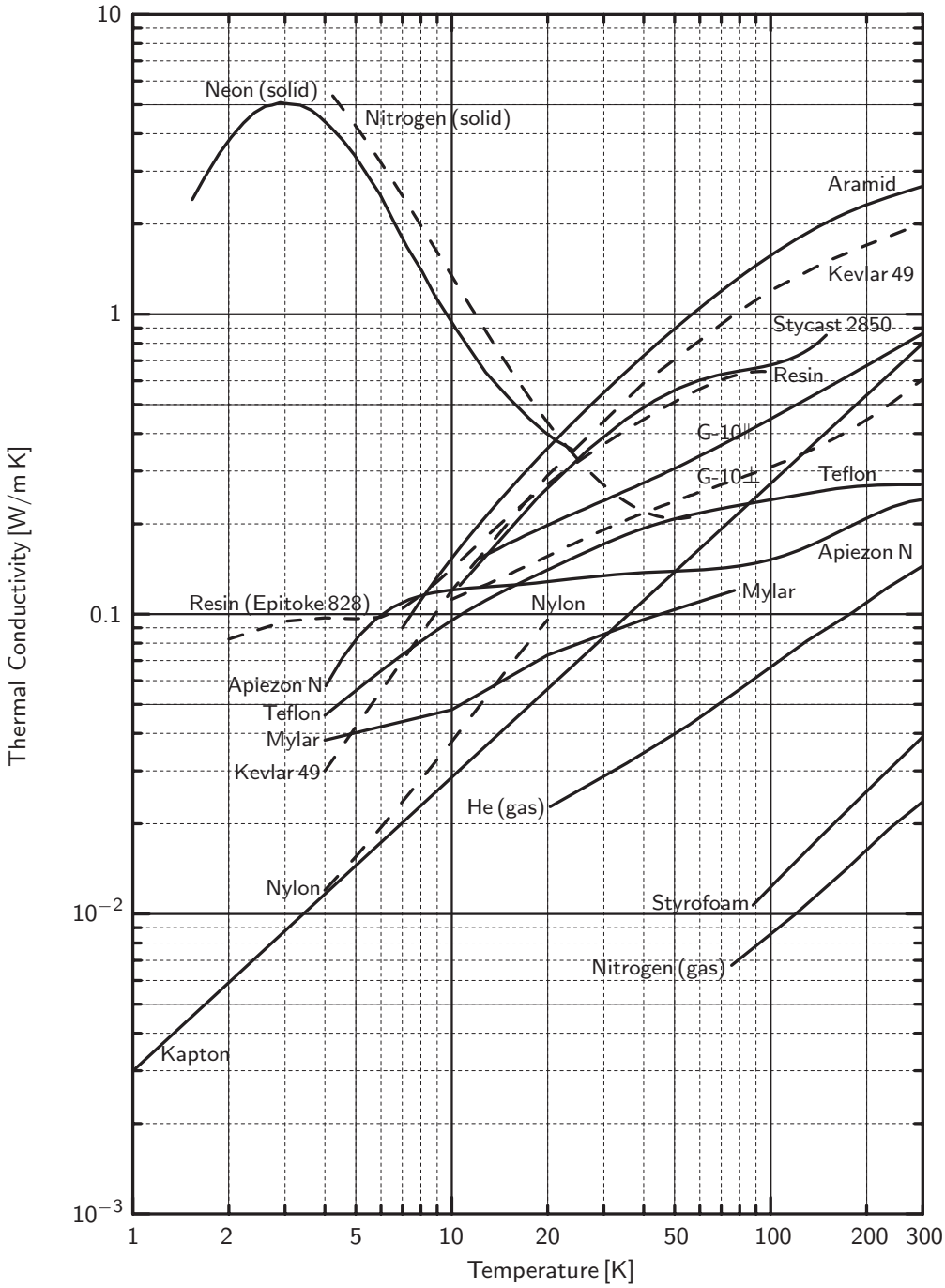

Fig. A3.1b Thermal conductivity vs. temperature plots for nonconductive materials; G-10∥ in the direction parallel to warp fibers and G-10⊥ in the direction normal to cloth. (For clarity, selected plots are in dashed lines.)

A3.2a Heat Capacity vs. Temperature Plots: Aluminum, Copper, Silver, and Stainless Steel

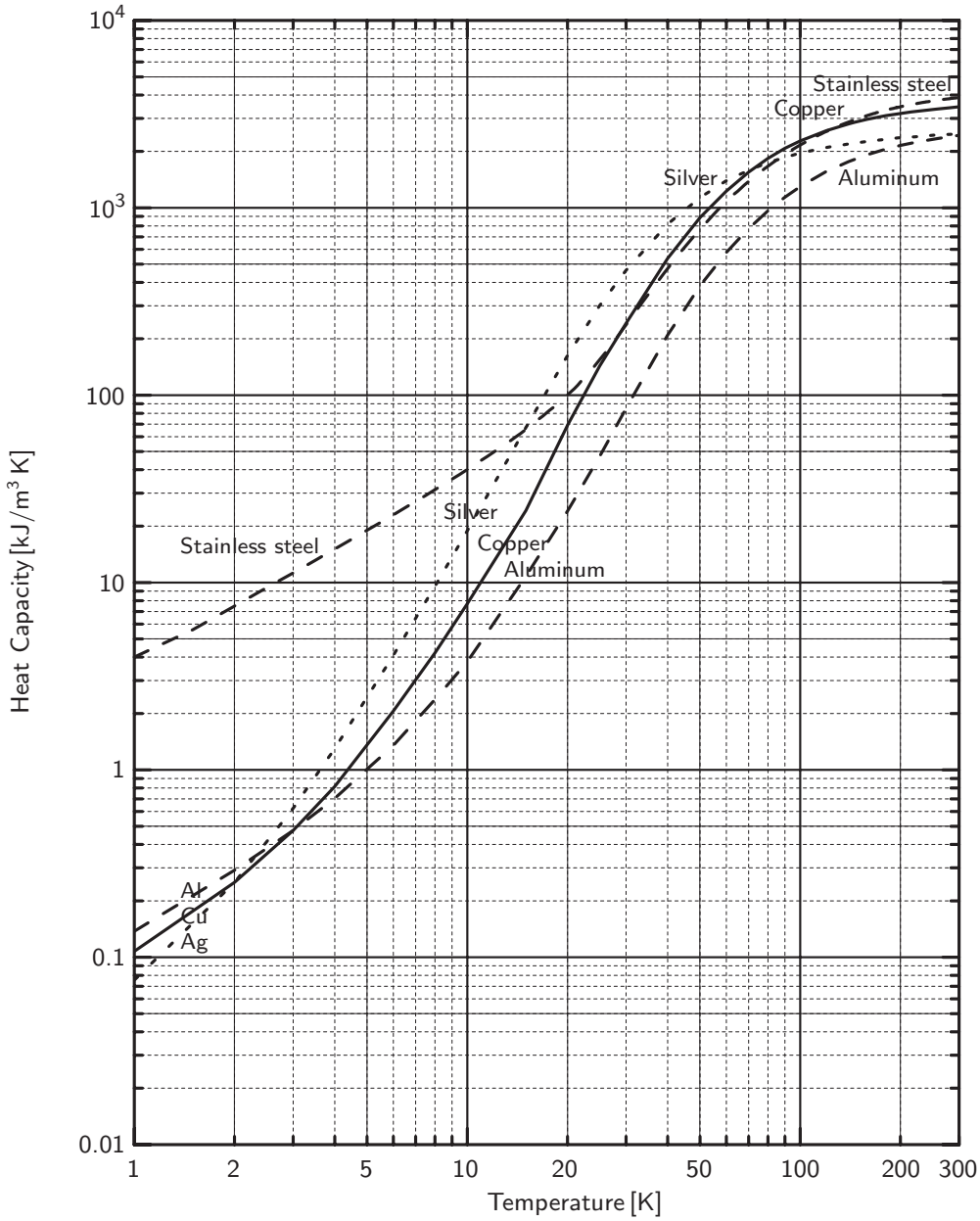

Fig. A3.2a Heat capacity vs. temperature plots for aluminum, copper, silver, and stainless steel. Converted from specific heat [J/kg K] data with constant densities: Aluminum (2700 kg/m^3); Copper (8960 kg/m^3); Silver (10490 kg/m^3); Stainless steel (7900 kg/m^3).

A3.2b Enthalpy vs. Temperature Plots: Aluminum, Copper, Silver, Stainless Steel; Solid Neon, Solid Nitrogen

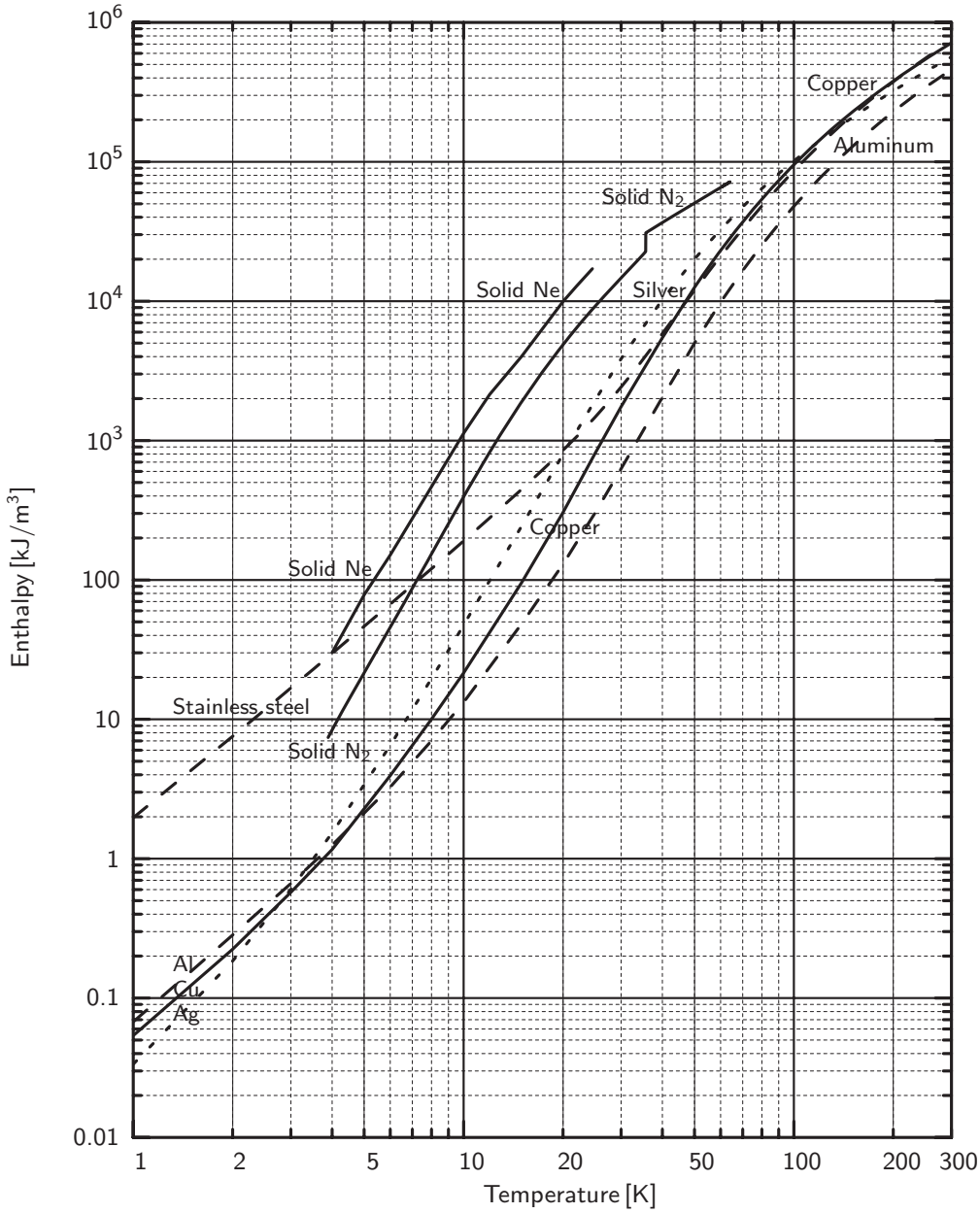

Fig. A3.2b Enthalpy vs. temperature plots for aluminum, copper, silver, stainless steel. Converted from specific heat [J/kg K] data with constant densities: Aluminum (2700 kg/m^3); Copper (8960 kg/m^3); Silver (10490 kg/m^3); Stainless steel (7900 kg/m^3). For densities of solid neon and nitrogen, at 1 bar, see Table A2.2.

Table A3.1: Heat Capacity Data for Selected Materials

	Density @"Room Temperature" [kg/m^3]					
	Copper	Nickel	Tungsten	"Epoxy"	Kapton	Teflon
	8960	8908	19250	1150	1140	2200
	Heat Capacity [kJ/m^3 K]					
T [K]	Copper	Nickel	Tungsten	"Epoxy"	Kapton	Teflon
2	0.251	2.16	0.304	0.116	0.164	0.2*
4	0.816	4.48	0.757	0.869	1.34	3*
6	2.06	7.30	1.51	3.70	4.43	10*
8	4.21	10.6	2.71	9.25	10.1	22*
10	7.71	14.4	4.50	17.5	18.9	39.6
15	24.2	27.6	14.0	48.7	54.5	106
20	69.0	51.7	34.7	92.1	105	167
25	143	90.0	81.0	143	164	224
30	242	149	151	195	226	275
40	538	339	354	271	349	363
50	887	608	639	383	465	444
60	1.23×10^3	918	930	490	571	524
70	1.55×10^3	1.24×10^3	1.16×10^3	588	670	603
80	1.84×10^3	1.54×10^3	1.38×10^3	679	762	686
90	2.08×10^3	1.82×10^3	1.56×10^3	761	850	770
100	2.28×10^3	2.07×10^3	1.71×10^3	836	933	849
120	2.58×10^3	2.48×10^3	1.94×10^3	969	1.09×10^3	1.01×10^3
140	2.80×10^3	2.80×10^3	2.12×10^3	1.09×10^3	1.24×10^3	1.16×10^3
160	2.97×10^3	3.05×10^3	2.25×10^3	1.19×10^3	1.38×10^3	1.32×10^3
180	3.10×10^3	3.25×10^3	2.35×10^3	1.29×10^3	1.52×10^3	1.49×10^3
200	3.19×10^3	3.41×10^3	2.41×10^3	1.40×10^3	1.66×10^3	1.63×10^3
220	3.26×10^3	3.54×10^3	2.46×10^3	1.51×10^3	1.79×10^3	1.76×10^3
240	3.32×10^3	3.65×10^3	2.50×10^3	1.63×10^3	1.92×10^3	1.89×10^3
260	3.37×10^3	3.76×10^3	2.54×10^3	1.77×10^3	2.04×10^3	2.01×10^3
280	3.41×10^3	3.86×10^3	2.58×10^3	1.93×10^3†	2.14×10^3	2.22×10^3
300	3.46×10^3	3.96×10^3	2.62×10^3	2.10×10^3†	2.28×10^3	2.24×10^3

* Interpolated.

† Extrapolated.

Table A3.2: Enthalpy Data for Selected Materials

	Density @"Room Temperature" [kg/m^3]					
	Copper	Nickel	Tungsten	"Epoxy"	Kapton	Teflon
	8960	8908	19250	1150	1140	2200
	Enthalpy [kJ/m^3]					
T [K]	Copper	Nickel	Tungsten	"Epoxy"	Kapton	Teflon
2	0.224	2.15	0.29	0.087	0.102	
4	1.165	8.73	1.32	0.857	1.37	
6	3.94	20.3	3.50	5.02	6.79	
8	10.0	38.1	7.62	17.5	20.9	
10	21.5	63.2	14.7	43.9	49.3	103
15	95.9	165	57.2	204	225	462
20	305	365	178	551	620	1.14×10^3
25	806	704	456	1.14×10^3	1.29×10^3	2.13×10^3
30	1.75×10^3	1.29×10^3	1.03×10^3	1.99×10^3	2.13×10^3	3.39×10^3
40	5.47×10^3	3.68×10^3	3.48×10^3	4.29×10^3	5.14×10^3	6.58×10^3
50	1.25×10^4	8.35×10^3	8.39×10^3	7.56×10^3	9.22×10^3	1.06×10^4
60	2.31×10^4	1.59×10^4	1.62×10^4	1.19×10^4	1.44×10^4	1.54×10^4
70	3.70×10^4	2.67×10^4	2.68×10^4	1.73×10^4	2.06×10^4	2.11×10^4
80	5.39×10^4	4.06×10^4	3.95×10^4	2.37×10^4	2.78×10^4	2.75×10^4
90	7.37×10^4	5.75×10^4	5.41×10^4	3.09×10^4	3.59×10^4	3.48×10^4
100	9.50×10^4	7.69×10^4	7.05×10^4	3.89×10^4	4.48×10^4	4.29×10^4
120	1.44×10^5	1.23×10^5	1.07×10^5	5.70×10^4	6.50×10^4	6.14×10^4
140	1.98×10^5	1.75×10^5	1.48×10^5	7.75×10^4	8.83×10^4	8.29×10^4
160	2.55×10^5	2.34×10^5	1.92×10^5	1.00×10^5	1.15×10^5	1.08×10^5
180	3.16×10^5	2.97×10^5	2.37×10^5	1.25×10^5	1.44×10^5	1.36×10^5
200	3.80×10^5	3.64×10^5	2.85×10^5	1.52×10^5	1.75×10^5	1.67×10^5
220	4.44×10^5	4.33×10^5	3.35×10^5	1.81×10^5	2.10×10^5	2.01×10^5
240	5.10×10^5	5.05×10^5	3.85×10^5	2.13×10^5	2.47×10^5	2.37×10^5
260	5.77×10^5	5.79×10^5	4.35×10^5	2.47×10^5	2.87×10^5	2.76×10^5
280	6.45×10^5	6.56×10^5	4.87×10^5	2.84×10^5*	3.09×10^5*	3.18×10^5
300	7.13×10^5	7.34×10^5	5.39×10^5	3.24×10^5*	3.53×10^5*	3.64×10^5

* Extrapolated.

Table A3.3: Mechanical Properties of Selected Materials

Material	σ_U [MPa]		σ_Y [MPa]		E [GPa]	
T [K]	295	77	295	77	295	77
Aluminum 6061 (T6)	315	415	280	380	70	77
Copper (annealed)	160	310	70	90	70	100
Copper (1/4 hard)	250	350	240	275	130	150
Copper (1/2 hard)	300		280		130	
Nickel	345→2000		51	58	60	70
Silver	190	295	40–60	45–70	82	90
Stainless steel 304	550→ 1030	1450→ 1860	200→ 620	260→ 1400	190→ 190	200→ 200
Stainless steel 316LN	1290	1790	1100	1400	185	195
Epoxy	40	100	—	—	27	28
G-10 (warp/normal)	280/240	—	—	—	18/14	—
Mylar	145	215	—	—	7	13
Teflon	14	105	—	—	0.4	5

Table A3.4: Mean Linear Thermal Expansion Data of Selected Materials
$[L(T) - L(293\,\mathrm{K})]/L(293\,\mathrm{K})$ [%]

Material	T [K]				
	20	80	140	200	973†
Aluminum	−0.415*	−0.391	−0.312	−0.201	—
Brass (70Cu-30Zn)	−0.369	−0.337	−0.260	−0.163	+1.30
Bronze	−0.330	−0.304	−0.237	−0.150	+1.33
Copper	−0.324	−0.300	−0.234	−0.148	+1.3
Nickel	−0.224	−0.211	−0.171	−0.111	—
Silver	−0.409	−0.360	−0.270	−0.171	+1.50
Stainless steel 304	−0.306	−0.281	−0.222	−1.40	+1.32
Epoxy	−1.15	−1.02	−0.899	−0.550	—
G-10 (warp)	−0.241	−0.211	−0.165	−0.108	—
G-10 (normal)	−0.706	−0.638	−0.517	−0.346	—
Phenolic (normal)	−0.730	−0.643	−0.513	−0.341	—
Teflon (TFE)	−2.11	−1.93	−1.66	−1.24	—
Nb_3Sn	−0.171	−0.141	−0.102	−0.067	+0.55
Cu/NbTi wire	−0.265	−0.245	−0.190	−0.117	—
Solder (50Sn-50Pb)	—	−0.510	−0.365	−0.229	—

* An aluminum bar 1-m long at 293 K *shrinks* by 4.15 mm when cooled to 20 K.

† A common Nb_3Sn reaction temperature.

‡ crosswise.

Appendix IV

Electrical Properties of Normal Metals

Property Data Sources

A.F. Clark, G.E. Childs, and G.H. Wallace, "Electrical resistivity of some engineering alloys at low temperatures," *Cryogenics* **10**, 295 (1970).

F.R. Fickett, "Aluminum 1. A review of resistive mechanisms in aluminum," *Cryogenics* **11**, 349 (1971).

F.R. Fickett, "Oxygen-free copper at 4 K: resistance and magnetoresistance," *IEEE Trans. Magn.* **MAG-19**, 228 (1983).

A.M. Hatch, R.C. Beals, and A.J. Sofia, *Bench-scale experiments on superconducting material joints* (Final Report, Avco Everett Research Laboratory, November 1976; unpublished).

Y. Iwasa, E.J. McNiff, R.H. Bellis, and K. Sato, "Magnetoresistivity of silver over the range 4.2–159 K," *Cryogenics* **33**, 836 (1993).

G.T. Meaden, *Electrical Resistance of Metals* (Plenum Press, New York 1965).

Materials at low temperatures, Eds. Richard P. Reed and Alan F. Clark (American Society For Metals, 1983).

Jean-Marie Noterdaeme, *Demountable resistive joint design for high current superconductors* (Master of Science Thesis, Department of Nuclear Engineering, Massachusetts Institute of Technology, 1978).

M.T. Taylor, A. Woolcock, and A.C. Barber, "Strengthening superconducting composite conductors for large magnet construction," *Cryogenics* **8**, 317 (1968).

Guy Kendall White, *Experimental Techniques in Low-Temperature Physics* (Clarendon Press, Oxford, 1959).

J.L. Zar, "Electrical switch contact resistance at 4.2°K," *Adv. Cryo. Engr.* **13**, 95 (1968).

A4.1 Normalized Electrical Resistivity vs. Temperature Plots: Conductive Metals and Stainless Steel

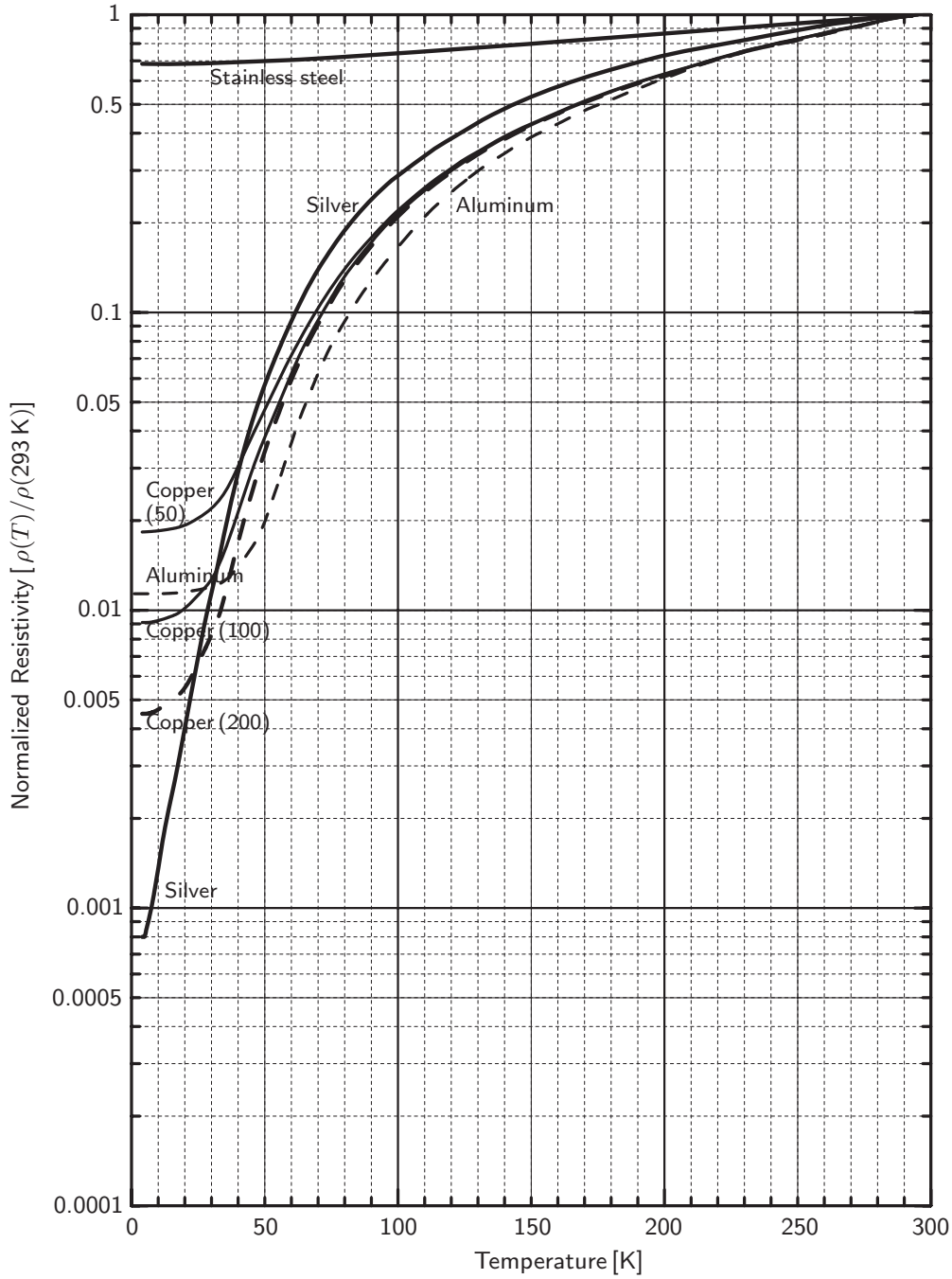

Fig. A4.1 Normalized zero-field $\rho(T)$ plots for conductive metals and stainless steel: aluminum (99.99%, $\rho \leq$26.44 nΩ m); copper (RRR= 50, $\rho \leq$17.14 nΩ m); copper (100, $\rho \leq$17.03 nΩ m); copper (200, $\rho \leq$16.93 nΩ m); silver (99.99%, $\rho \leq$16.00 nΩ m). Stainless steel (304L $\rho \leq$725 nΩ m) represents a "typical" alloy. For each metal, $\rho(T)$ is normalized to its zero-field resistivity at 293 K.

A4.2 RRR vs. Magnetic Field Plots: Aluminum; Copper; Silver

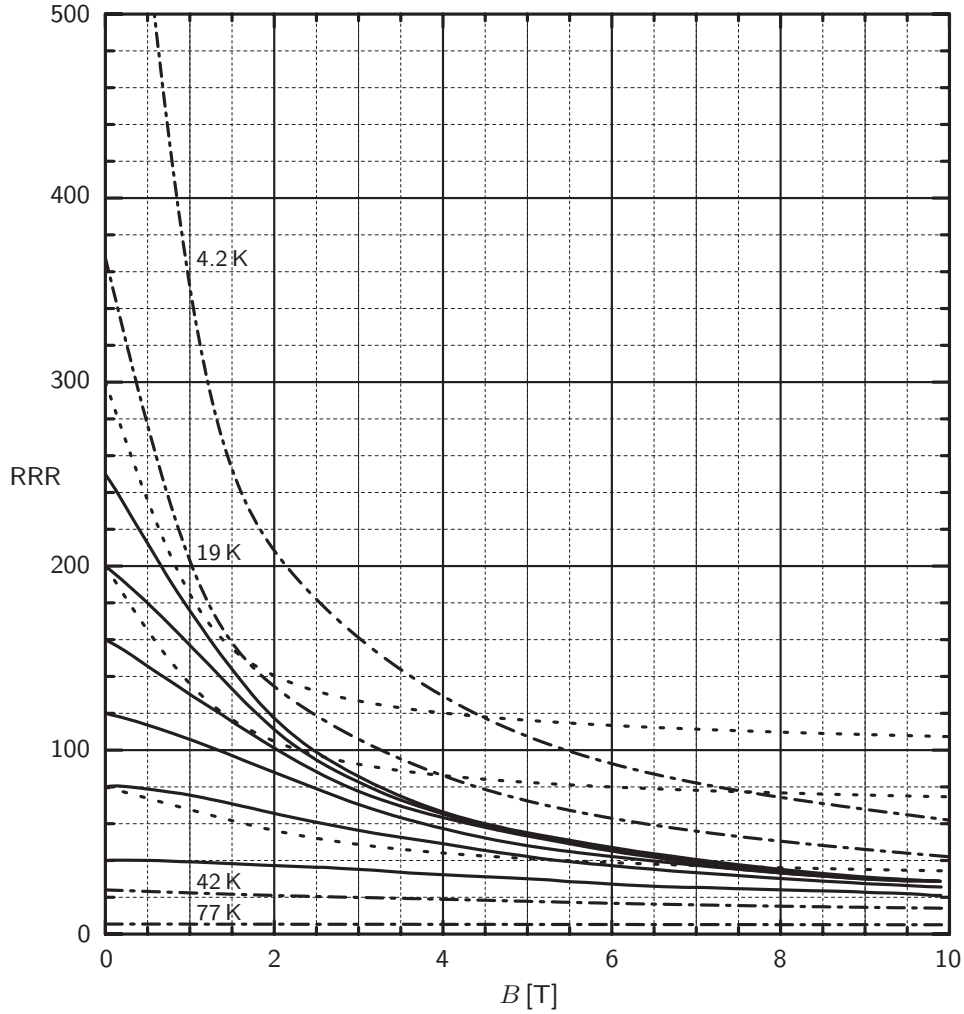

Fig. A4.2 RRR vs. magnetic field plots: copper (solid) and aluminum (dotted), both at 4.2 K, and silver (dash-dotted, with temperatures indicated—RRR = 735 at 0 T). At 77 K, field-dependence of RRR for copper is similar to that of silver.

Table A4.1: 4.2-K Contact Resistance vs. Contact Pressure Data*

Copper Surface Treatment	Contact Resistance [pΩ m^2]				
Contact Pressure [MPa]	7	30	100	200	400
Bare, "freshly cleaned"	100	25	5	0.2	—
Oxidized	—	—	—	3	1
Silver plated	1–10	0.4–3	0.2–0.8	0.04–0.06	—
Silver plated (10-μm thick)	1	0.9	—	—	—
Gold plated (1.3-μm thick)	14	6	—	—	—

* Based on >100 MPa data of Noterdaeme and 7- and 30-MPa data of Zar.

Table A4.2: Electrical Resistivity vs. Temperature Data of Selected Metals
$\rho(T) = \rho(76\,\mathrm{K}) + \varsigma(T - 76\,\mathrm{K})$ for $T \geq 76\,\mathrm{K}$ (Eq. A2.1)
$\rho\,[\mathrm{n\Omega\,m}]$; $T\,[\mathrm{K}]$; $\varsigma\,[\mathrm{n\Omega\,m/K}]$

Metal	Resistivity [nΩ m]						
T [K]	4	20	40	76	273	295*	ς
Aluminum 1100	0.82	0.84	1.14	3.10	26.7	29.3	0.120
Aluminum 6061	13.8	13.9	14.1	16.6	39.4	41.9	0.116
Hastelloy C [a]	1230	1230	1236	1240	1268	1271	0.142
Copper OFHC	0.16	0.17	0.28	2.00	15.6	17.1	0.069
Brass (Cartridge) [b]	42	42	43	47	67	69	0.102
(Naval) [c]	33	33	35	39	63	66	0.122
(Red) [d]	27	27	28	30	47	49	0.086
Bronze (Aluminum) [e]	139	138	140	140	162	164	0.112
(Commercial) [f]	21	21	22	24	39	41	0.076
(Ni-Al) [g]	157	157	158	160	184	187	0.122
(Phosphor) [h]	86	86	88	89	105	107	0.081
90Cu-10Ni	167	167	168	169	184	186	0.076
70Cu-30Ni	364	365	366	367	384	386	0.086
Stainless steel 304L	496	494	503	514	704	725	0.964
310	685	688	694	724	873	890	0.756
316	539	538	546	566	750	771	0.934

* Based on Eq. A2.1 given at the top of this table.

[a]: 58Ni-16Mo-15Cr-5Fe-3W; [b]: 70Cu-30Zn; [c]: 59Cu-40Zn; [d]: 84Cu-15Zn

[e]: 91Cu-7Al; [f]: really brass, 89Cu-10Zn; [g]: 81Cu-10Al-5Ni; [h]: 94Cu-5Sn-0.2P

Table A4.3: Electrical Resistivity of Selected Heater Metals*

Heater Metal	ρ [nΩ m]		
	$\leq 20\,\mathrm{K}$	76 K	295 K
Evanohm (75Ni-20Cr-2.5Al-2.5Cu)	1326	1328	1337
Chromel A (80Ni-20Cr)	1020	1027	1055
Constantan (60Cu-40Ni)	460	466	490
Cupron (55Cu-45Ni)	431	458	476
Manganin (86Cu-12Mn-2Ni)	425	444	475
Tophet A (80Ni-20Cr)	1087	1090	1120
NbTi	600†	—	—

* Data for brass, bronze, and stainless steel are given in Table A4.2.

† In the normal state.

Appendix V

Properties of Superconductors

Properties of superconductors in this Appendix, like properties of materials in ***Appendix III***, are *representative* and intended for use chiefly in the early stages of magnet design. Unlike a design of a conventional electric motor, for example, in which the designer can choose the copper wire from a wire catalogue, except for a few cases involving staple items such as mass-produced, NbTi-based "standard" MRI magnets, the design process of a superconducting magnet must *still* often include design of superconductors by the magnet engineer, specifically tailored for the magnet. That is, currently in nearly all superconducting magnets, superconductor manufacturers are involved from the early design stage. This practice, it is hoped, will (and should) end in time as more magnets are mass-produced, leading to a wide availability of a variety of "standard" magnet-grade superconductors.

Property Data Sources & Selected References

Selected References list only those papers that include data relevant to *magnet design*; no purely *materials-related* papers on superconductors are included.

$J_c(B)$ Data of LTS and HTS

Peter J. Lee (http://magnet.fsu.edu/∼lee/plot/plot.htm)—mostly only 4.2-K data.

$J_c(B,T)$ Data of NbTi and Nb_3Sn

C.R. Spencer, P.A. Sanger and M. Young, "The temperature and magnetic field dependence of superconducting critical current densities of multifilamentary Nb_3Sn and NbTi composite wires," *IEEE Trans. Magn.* **MAG-15**, 76 (1979).

K.F. Hwang and D.C. Larbalestier, "Generalized critical current density of commercial Nb46.5, Nb50 and Nb53 w/o Ti multifilamentary superconductors," *IEEE Trans. Magn.* **MAG-15**, 400 (1979).

M.S. Lubell, "Empirical scaling formulas for critical current and critical field for commercial NbTi," *IEEE Trans. Magn.* **MAG-19**, 754 (1983).

Michael A. Green, "Calculating J_c, B, T surface for niobium titanium using a reduced-state model," *IEEE Trans. Magn.* **25**, 2119 (1989).

L. Bottura, "A practical fit for the critical surface of NbTi," *IEEE Trans. Appl. Superconduc.* **10**, 1054 (2000).

Arno Godeke, *Performance Boundaries in Nb_3Sn Superconductors* (Ph.D. thesis, University of Twente, Enschede, The Netherlands, 2005); also in J.P. Lee website, ibid.

Nikolai Schwerg and Christine Vollinger, "Development of a current fit function for NbTi to be used for calculation of persistent current induced field errors in the LHC main dipoles," *IEEE Trans. Appl. Superconduc.* **16**, 1828 (2006).

Takashi Hase (Kobe Steel; personal communication).

Property Data Sources & Selected References continue on p. 647.

A5.1 Current Densities of NbTi, Nb_3Sn, MgB_2, YBCO, Bi2223

Current densities of NbTi, Nb_3Sn, MgB_2 (wires) and YBCO and Bi2223 (tapes), are summarized in Table A5.1; the table does not include Bi2212 data—see Lee's website for 4.2-K data. (In the table, J_c and J_e are rounded off to the nearest 0 or 5 A/mm^2 and those interpolated or extrapolated are in italics.) At the present time (2008), $J_e(B,T)$ performances of MgB_2 and YBCO are improving at rates greater than those of NbTi, Nb_3Sn, Bi2223, (and Bi2212). The best sources for the latest data of these superconductors are the conductor manufacturers' websites.

Note that the *overall* current density, J_{ov} or λJ_{op}, in any magnet wound with NbTi, Nb_3Sn, MgB_2, YBCO, Bi2223, (or Bi2212) will be less than J_c (or J_e) given in Table A5.1. To satisfy other design requirements, e.g., electrical, mechanical, protection, stability, each superconductor must contain other non-superconducting materials, making $J_{ov} < J_c$ (or J_e). In fact, even in the *ultimate limit* of improvement, i.e., $J_c = \infty$, J_{ov} will remain well below 1000 A/mm^2.

A5.2 Scaling Laws for NbTi and Nb_3Sn

Scaling laws, developed for NbTi and Nb_3Sn over the years, are presented here.

NbTi

Critical Field vs. Temperature, $b_{c2}(t)$ The reduced critical upper field, $b_{c2}(t) \equiv B_{c2}(T)/B_{c2}(T=0)$, where $t \equiv T/T_c(B=0)$, is given by

$$b_{c2}(t) = 1 - t^{1.7} \qquad (A5.1)$$

$B_{c2}(T=0)$ and $T_c(B=0)$, for five values of Ti content, are $B_{c2} = [14.5, 14.2, 14.4, 14.4, 14.25\,\mathrm{T}]$ and $T_c(B=0) = [9.2, 8.5, 8.9, 9.2, 9.35\,\mathrm{K}]$. Lubell's choices are: 14.5 T and 9.2 K—the first combination.

Critical Current Density, $J_c(b,\ t)$ The critical current density as functions of reduced field, $b \equiv B/B_{c2}(T)$ and t, $J_c(b,t)$ [A/m^2] is given by:

$$J_c(b,t) = \frac{C_\circ}{B} b^\alpha (1-b)^\beta (1-t^n)^\gamma \qquad (A5.2)$$

where B [T] is the magnetic field the NbTi superconductor is exposed to. Constants $C_\circ$ [T], α, β, and γ depend on Ti content. Each constant has *correspondingly* five values: $C_\circ$ (23.8, 28.6, 28.5, 37.7, and 28.4 T); α (0.57, 0.76, 0.64, 0.89, 0.80); β (0.90, 0.85, 0.75, 1.10, 0.89); and γ (1.90, 1.76, 2.30, 2.09, and 1.87).

Nb_3Sn

Critical Current Density, $J_c(b,\ t,\epsilon)$ The critical current density as a function of reduced field, $b \equiv B/B_{c2}(T)$, t, and strain ϵ, $J_c(b,t,\epsilon)$ [A/m^2], is given by:

$$J_c(b,t,\epsilon) = \frac{C}{B} s(\epsilon)(1-t^{1.52})(1-t^2) b^p (1-b)^q \qquad (A5.3)$$

where C [T], p, and q are parameters. $s(\epsilon)$ is a very complicated function of ϵ that contains several parameters. The important point here is that J_c, as with that for NbTi, decreases with magnetic field as $1/B$ and its temperature dependence is steeper than that for NbTi.

Table A5.1: J_c or J_e Data: NbTi, Nb_3Sn, MgB_2 (Wires); YBCO, Bi2223 (Tapes)
—YBCO & Bi2223 $\|/\perp$:* Field Parallel/Perpendicular to Tape's Broad Surface—

J_c (NbTi, MgB_2), Non-Copper J_c (Nb_3Sn), or J_e (YBCO & Bi2223) [A/mm^2]									
T [K]	B [T]→	3	5	8	12	15	20	25	30
1.8	NbTi	>5000	>4000	>3000	900	NA†	NA	NA	NA
	Nb_3Sn[a)]	>2000	>2000	>2000	>2000	>2000	*800*	155	NA
4.2	NbTi	>3000	2500	1000	NA	NA	NA	NA	NA
	Nb_3Sn[a)]	>2000	>2000	>2000	>2000	1700	475	—‡	NA
	Nb_3Sn[b)]	>2000	>2000	*1400*	840	475	130	—	NA
	Nb_3Sn[c)]	3350	2100	1250	660	*375*	*100*	—	NA
	MgB_2	1930	900	165	—	NA	NA	NA	NA
	YBCO $\|$	1350	1270	1155	980	905	*810*	NA	NA
	$\perp$	425	310	230	175	*155*	NA	NA	NA
	Bi2223 $\|$	*900*	900	900	800	700	590	490	400
	$\perp$	*560*	530	500	485	*465*	*455*	*440*	*435*
10	Nb_3Sn[c)]	1400	850	375	70	*10*	—	—	—
	MgB_2	1595	610	75	—	NA	NA	NA	NA
	Bi2223 $\|$	*725*	*725*	*725*	630	*560*	*450*	*350*	*300*
	$\perp$	505	455	390	350	*325*	*285*	*265*	*245*
15	MgB_2	1160	280	20	NA	NA	NA	NA	NA
20	MgB_2	585	80	—	NA	NA	NA	NA	NA
	YBCO$\perp$	130	90	*65*	—	NA	NA	NA	NA
	Bi2223 $\|$	*730*	650	575	*510*	*460*	*370*	*280*	*200*
	$\perp$	385	325	260	200	170	*130*	*100*	*75*
30	Bi2223 $\|$	640	540	480	*365*	*300*	*200*	*150*	*100*
	$\perp$	230	150	80	45	—	—	—	—
35	YBCO$\perp$	80	55	*35*	—	NA	NA	NA	NA
T [K]	B [T]→	*s.f.*§	0.1	0.3	0.5	0.8	1	3	5
50	Bi2223 $\|$	*760*	*760*	*590*	525	455	420	250	165
	$\perp$	*760*	485	305	215	140	105	—	—
65	YBCO $\|$	205	195	180	160	145	*100*	NA	NA
	$\perp$	205	115	80	55	45	*20*	NA	NA
66	Bi2223 $\|$	*405*	*405*	295	250	200	185	75	25
	$\perp$	*405*	225	105	50	—	—	—	—
70	Bi2223 $\|$	*330*	*330*	240	175	160	135	40	—
	$\perp$	*330*	175	70	25	—	—	—	—
77	YBCO $\|$	100	95	85	75	60	55	NA	NA
	$\perp$	100	80	45	30	15	—	—	—
	Bi2223 $\|$	220	220	150	120	90	75	—	—
	$\perp$	220	100	30	—	—	—	—	—

* $J_e\|\,(B,T)/J_e(77\,\mathrm{K}, s.f.)$ and $J_e\perp(B,T)/J_e(77\,\mathrm{K}, s.f.)$ ratios for YBCO and Bi2223 may be assumed constant for different values of $J_e(77\,\mathrm{K}, s.f.) = J_e\|\,(77\,\mathrm{K}, s.f.) = J_e\perp(77\,\mathrm{K}, s.f.)$.

† Data not available

‡ J_c or J_e too low for magnet applications.

§ Self field: ∼0.1 T for parallel field; ∼0.01 T for perpendicular field.

a) Internal tin; b) ITER; c) ITER barrel.

A5.3 Mechanical and Thermal Properties

A superconductor, LTS or HTS, never is used by itself. To meet stability, protection, and mechanical requirements, a magnet winding *and* a conductor itself *always* contain other, non-superconducting, materials. Indeed, for a magnet, the most important requirement of a superconductor is a critical current performance ample enough for the magnet's operating current, temperature, and magnetic field ranges. Although in most magnet designs precise mechanical and thermal data of superconductors, if available, are useful, this is usually not the case. The same is true for the magnet winding consisting of different materials. For a composite conductor or winding, a "mixture rule" is widely used to include the properties of constituent materials. Table A5.2 presents *approximate* (italics) mechanical—density (ϱ), Young's modulus (E), yield strength (σ_Y)—and thermal—conductivity (k) and heat capacity (C_p)—data of the five magnet-grade superconductors, and those of, for mechanical, stainless steel (S.S.) and, for thermal, copper. These properties are discussed briefly below.

Young's Modulus and Yield Strength In "low-field" and "small" magnets, chiefly of NbTi, copper matrix (σ_Y, >250 MPa below ∼100 K), added to the NbTi to meet stability and protection requirements, is often sufficient, with a contribution from the NbTi. To minimize bending strains in those more strain sensitive than NbTi, e.g., Nb_3Sn and YBCO, the superconductors are sometimes placed at or near their neutral axes. Note also that among these superconductors, NbTi is the most tolerant of tensile strains; even at 1% it retains 95% of zero-strain J_c. Strain-to-failure, here defined as a strain beyond which strain-induced degradation of J_c is not reversible, varies among these superconductors, ranging 0.2–0.45%. Each composite superconductor has a nonlinear stress-strain curve indicative of its respective constituents and is amenable to mixture-rule estimates.

Thermal Conductivity As discussed in ***CHAPTER 5***, the thermal conductivities of these superconductors are at least two orders of magnitude smaller than that of copper over the entire temperature range of interest: the superconductor contributes negligibly to thermal conduction. Also, fine superconductor dimensions (1–100 μm) in composite conductors benefit thermal conduction to substrates. Here too, the mixture rule may be sufficient for most analyses.

Table A5.2: Selected Mechanical and Thermal Property Data
—Comparison with Stainless Steel (S.S) & Cu (RRR = 50)—

Mechanical Property	NbTi	Nb_3Sn	MgB_2	YBCO	Bi2223	S.S.
ϱ @ 295 K [kg/m^3]	6550	8950	2600	6380	4350	*7900*
E @ <100 K [GPa]	55–65	<100				*200*
σ_Y @ < 100 K [MPa]	*	< 50				*250*
Thermal Property	NbTi	Nb_3Sn	MgB_2	YBCO	Bi2223	Cu
k @ 10 K [W/m K]	∼1					*5000*
@ 100 K [W/m K]	< 10					*30000*
C_p @ 30 K [kJ/m^3 K]	*380*	*280*	*4*	*120*	NA	*240*
@ 90 K [kJ/m^3 K]	*2000*	*1400*	NA	*670*	*700*	*2100*

* Ultimate tensile strength: 1.04 GPa at 76 K and 1.28 GPa at 4.2 K.

A5.3 Mechanical and Thermal Properties (continuation)

Heat Capacity As a simplification step in protection analyses of ***CHAPTER 8*** to compute the final temperature of a "hot-spot," we equate, on a *volumetric basis*, the temperature-dependent heat capacity of a superconductor with that of copper. From Table A5.2, we may conclude that this simplification is roughly valid, though less so with MgB_2, YBCO, and Bi2223. At least for YBCO tape, however, this discrepancy is really moot, because YBCO occupies so small a fraction ($\sim$1%) of the total tape cross section.

Property Data Sources & Selected References (continuation, from p. 643)

$J_c(B,T)$ and $J_c(B,T)$ Data of MgB_2, YBCO, Bi2223, (and Bi2212)

The latest $J_c(B,T)$ and $J_e(B,T)$ data are best obtained from the HTS manufacturers. Selected sources of MgB_2, YBCO, Bi2223, (and Bi2212) *conductors* are listed below.

MgB_2: Columbus Superconductors; Hyper Tech Research.

YBCO: American Superconductor Corp. (AMSC); European High Temperature Superconductors (EHTS); SuperPower.

Bi2223: AMSC (while current stock lasts); EHTS; Innova Superconductor Technology (InnoST); Sumitomo Electric.

Bi2212: Nexans; Oxford Superconducting Technology.

Potential sources in R&D stage for MgB_2, YBCO, or Bi2223 include: MgB_2—Hitachi; Western Superconducting Technologies (WST); YBCO—Fujikura; InnoST; Nexans; Seo-Nam; Sumitomo Electric (HoBCO with holmium replacing yttrium); WST.

Sources of Data in Table A5.1 (Personal Communication)

MgB_2: David Doll and Matthew A. Rindfleisch (Hyper Tech Research).

Also, M.D. Sumption, M. Bhatia, M. Rindfleisch, M. Tomsic and E.W. Collings, "Transport properties of multifilamentary, *in situ* route, Cu-stabilized MgB_2 strands: one metre segments and the $J_c(B,T)$ dependence of short samples," *Superconductor Science and Technology* **19**, 155 (2006).

YBCO: John P. Voccio (AMSC).

Also, D. Turrioni, E. Barzi, M. Lamm, V. Lombardo, C. Thieme, and A.V. Zlobin, "Angular measurements of HTS critical current for high field solenoids," *Adv. Cryogenic Engr. Mat.* **54**, 451 (2008).

Bi2223: Shin-ichi Kobayashi (Sumitomo Electric).

Strain Effects on J_c of NbTi and Nb_3Sn

J.W. Ekin, "Strain scaling law for flux pinning in practical superconductors. Part 1: Basic relationship and application to Nb_3Sn conductors," *Cryogenics* **20**, 611 (1980).

J.W. Ekin, "Relationships between critical current and stress in NbTi," *IEEE Trans. Magn.* **MAG-23**, 1634 (1987).

W. Denis Markiewicz, "Elastic stiffness model for the critical temperature T_c of Nb_3Sn including strain dependence," *Cryogenics* **44**, 895 (2004).

David M J Taylor and Damian P Hampshire, "The scaling law for the strain dependence of the critical current density in Nb_3Sn superconducting wires," *Supercond. Sci. Technol.* **18**, S241 (2005).

Strain Effects on J_c of NbTi and Nb_3Sn (continuation)

W. Denis Markiewicz, "Invariant temperature and field strain functions for Nb_3Sn composite superconductors," *Cryogenics* **46**, 846 (2006).

Najib Cheggour, Jack W. Ekin, and Loren F. Goodrich, "Critical-current measurements on an ITER Nb_3Sn strand: effect of axial tensile strain," *IEEE Trans. Appl. Superconduc.* **17**, 1366 (2007).

Mechanical and Thermal Properties—LTS and HTS

Curt Schmidt, "Simple method to measure the thermal conductivity of technical superconductors, e.g., NbTi," *Rev. Sci. Instrum.* **54**, 454 (1979).

T. Nishio, Y. Itoh, F. Ogasawara, M. Suganuma, Y. Yamada, and U. Mizutani, "Superconducting and mechanical properties of YBCO-Ag composite superconductors," *J. Mat. Science* **24**, 3228 (1989).

Ctirad Uher, "Review: Thermal conductivity of high-T_c superconductors," *J. Superconduc.* **3**, 337 (1990).

H. Ledbetter, "Elastic constants of polycrystalline $Y_1Ba_2Cu_3O_x$," *J. Mat. Sci. Res.* **7**, 11 (1992).

S. Ochiai, K. Hayashi, and K. Osamura, "Strength and critical density of Bi(Pb)-Sr-Ca-Cu-O and Y-Ba-Cu-O in silver-sheathed superconducting tapes," *Cryogenics* **32**, 799 (1992).

W. Schnelle, O. Hoffels, E. Braun, H. Broicher, and D. Wohlleben, "Specific heat and thermal expansion anomalies of high temperature superconductors," *Physics and Materials Science of High Temperature Superconductors – II* (Kluwer Publishers, Dordrecht, The Netherlands, 1992), 151.

John Yau and Nick Savvides, "Strain tolerance of multifilament Bi-Pb-Sr-Ca-Cu-O/silver composite superconducting tapes," *Appl. Phys. Lett.* **65**, 1454 (1994).

Neil McN. Alford, Tim W. Button, Stuart J. Penn and Paul A. Smith, "$YBa_2Cu_3O_x$ low loss current leads," *IEEE Trans. Superconduc.* **5**, 809 (1995).

Y. Yoshino, A. Iwabuchi, K. Katagiri, K. Noto, N. Sakai, and M. Murakami, "An evaluation of mechanical properties of YBaCuO and (Sm,Gd)BaCuO bulk superconductors using Vickers hardness test at cryogenic temperatures," *IEEE Trans. Superconduc.* **12**, 1755 (2002).

K.P. Weiss, M. Schwarz, A. Lampe, R. Heller, W.H. Fietz, A. Nyilas, S.I. Schlachter, and W. Goldacker, "Electromechanical and thermal properties of Bi2223 tapes," *IEEE Trans. Superconduc.* **17**, 3079 (2007).

Arman Nyilas, Kozo Osamura, and Michinaka Sugano, "Mechanical and physical properties of Bi-2223 and Nb_3Sn superconducting materials between 300 K and 7 K," *Supercond. Sci. Technolo.* **16**, 1036 (2003).

G. Nishijima, S. Awaji, K. Watanabe, K. Hiroi, K. Katagiri, T. Kurusu, S. Hanai, and H. Takano, "Mechanical and superconducting properties of Bi-2223 tape for 19 T cryogen-free superconducting magnet," *IEEE Trans. Appl. Superconduc.* **14**, 1210 (2004).

Koji Shikimachi, Naoji Kashima, Shigeo Nagaya, Takemi Muroga, Seiki Miyata, Tomonori Watanabe, Yutaka Yamada, Teruo Izumi, and Yuh Shiohara, "Mechanical properties of YBaCuO formed on Ni-based alloy substrates with IBAD buffer layers," *IEEE Trans. Appl. Superconduc.* **15**, 3548 (2005).

Najib Cheggour, Jack W. Ekin, and Cees L.H. Thieme, "Magnetic-field dependence of the reversible axial-strain effect in Y-Ba-Cu-O coated conductors," *IEEE Trans. Appl. Superconduc.* **15**, 3577 (2005).

Appendix VI

*Glossary**

A-15: The cubic crystalline structure of most intermetallic compound LTS, e.g., Nb_3Al, Nb_3Sn, V_3Ga. Also known as the beta-tungsten (β-W) structure.

AC loss: Energy (power) dissipation in a conductor caused by a time-varying magnetic field, transport current, or both; includes HYSTERESIS LOSS, COUPLING LOSS, SELF-FIELD LOSS, EDDY-CURRENT LOSS.

Active shielding: A technique to reduce a FRINGING FIELD with magnets of reverse polarity; used in some MRI ($> 1.5\,T$) and NMR ($> 9\,T$) superconducting magnets.

Adiabatic demagnetization: A cooling technique that makes use of the magnetic field and temperature dependences of entropy of a paramagnetic material to achieve a temperature of millikelvins and below.

Adiabatic magnet: A magnet with its interior winding not exposed to liquid CRYOGEN; its primary cooling source, e.g., liquid CRYOGEN, is outside the winding.

AE (***A****coustic* ***E****mission*)***:*** Acoustic signals emitted by a sudden mechanical event in a structure, e.g., a magnet, being loaded (charged) or unloaded (discharged); can detect a conductor motion or epoxy fracture event and determine its site. See KAISER EFFECT.

Anisotropy: Property of exhibiting different values in different directions, e.g., magnetic field orientation effect on superconductor CRITICAL CURRENT DENSITIY.

ATLAS (***A T****oroidal* ***LHC A****pparatu****S***)***:*** A large (overall: 25-m diameter and 46-m long) particle detector superconducting magnet system for LHC, consisting of an inner Solenoid and an axially-long Barrel Toroid, which is flanked by End-Cap Toroids.

BCS theory: A microscopic theory of superconductivity by J. **B**ardeen, L.N. **C**ooper, and J.R. **S**chrieffer of the University of Illinois, published in 1957; explains electromagnetic and thermodynamic properties of LTS.

Bean slab: A one-dimensional model of a bulk TYPE II SUPERCONDUCTOR introduced in 1962 by C.P. Bean of the General Electric Research Laboratory to formulate a phenomenological theory of magnetization.

Bi2212: One variant of BSCCO; processable into wire of round or other cross section.

Bi2223: Another variant of BSCCO; processable only into tape.

Breakdown voltage: The voltage at which an insulator fails. An important parameter for magnet operation at DISCHARGE VOLTAGEs above $\sim 1\,kV$.

Bronze process: For making MULTIFILAMENTARY CONDUCTORs of A-15 superconductors, e.g., Nb_3Sn, V_3Ga; independently developed in 1970 for Nb_3Sn by A.R. Kaufman at the Whittaker Corp., U.S.A. and E.W. Howelett at the Atomic Energy Research Establishment in England, and for V_3Ga by K. Tachikawa at the National Research Institute for Metals (now the National Institute for Materials Science), Tsukuba, Japan.

BSCCO: A bismuth-based HTS; $(BiPb)_2Sr_2Ca_{n-1}Cu_nO_{2n+4}$; $n = 2$ results in BSCCO (Bi2212) having T_c of $\sim 85\,K$, $n = 3$ in BSCCO (Bi2223) with T_c of $\sim 110\,K$. H. Maeda of the National Research Institute for Metals is credited with the discovery in 1989.

Bubble chamber: A chamber filled with superheated liquid cryogen (often hydrogen), in a magnet, usually superconducting, to study high-energy particle interactions.

---

* Includes terms discussed and mentioned only briefly or not at all in the main text but which are of general interest in superconducting magnet technology and its applications. Also many oft-cited acronyms in the superconducting magnet community are briefly described.

Carnot cycle: A reversible thermodynamic cycle, composed of two adiabatic and two isothermal processes, in which a working fluid operates between two thermal reservoirs to produce work or refrigeration most efficiently. The French physicist and military engineer N.L.S. Carnot (1796–1832) published the theory in 1824: *"Reflexions sur la Puissance Motrice du Feu"* (*"Reflections on the Motive Power of Fire"*). See STIRLING CYCLE.

CEA (***C****ommissariat à l'****E****nergie* ***A****tomique*)***:*** A French government research organization with centers throughout France; its superconducting magnet and cryogenics activities are at Saclay (∼30 km southwest of Paris) and Cadarache (∼40 km north of Aix-en-Provence).

CERN (***C****onseil* ***E****uropéen pour la* ***R****echerche* ***N****ucléaire*)***:*** Located outside Geneva on the Swiss/French border, an international center for high-energy physics research. See LHC.

CIC (***C****able-****I****n-****C****onduit*) ***conductor:*** A cable of transposed MULTIFILAMENTARY CONDUCTORS (usually NbTi or Nb_3Sn) encased in a high-strength conduit, through which cooling fluid, generally SUPERCRITICAL HELIUM, is forced.

CMS (***C****ompact* ***M****uon* ***S****olenoid*)***:*** A superconducting detector magnet (together with ATLAS and two others) for LHC; with overall dimensions of 15-m diameter, 21.5-m long and a mass of over 1.25×10^6 kg, it generates a center field of 4 T.

Coercive force: The magnetic field required to demagnetize a magnetized material.

Coherence length: The distance over which the superconducting-normal transition takes place; introduced by A.B. Pippard (Cambridge University) in the early 1950s.

Composite superconductor: A conductor with one or more strands or tapes of superconductor in a matrix of normal metal; may be a MULTIFILAMENTARY CONDUCTOR.

Cooper pair: The paired electrons responsible for superconductivity (BCS THEORY).

Copper-to-superconductor ratio: The volumetric ratio of copper to superconductor in a COMPOSITE SUPERCONDUCTOR (like NbTi), or the ratio of copper to *non-copper* in a composite superconductor (like Nb_3Sn) which includes other metals.

Coupling loss: AC LOSS generated by field-induced currents between filaments and/or strands in a MULTIFILAMENTARY SUPERCONDUCTOR or CIC CONDUCTOR.

Coupling time constant: The predominant decay time constant of field-induced currents in a MULTIFILAMENTARY SUPERCONDUCTOR or CIC CONDUCTOR.

Critical current, I_c***:*** The maximum current a conductor can carry and still remain superconducting at a given temperature and magnetic field.

Critical current density, J_c***:*** One of the three material-specific parameters that defines the critical surface for superconductivity. In a TYPE II SUPERCONDUCTOR, J_c is sensitive to metallurgical processing.

Critical field, H_c***:*** One of the three material-specific parameters that defines superconductivity; insensitive to metallurgical processing. In a TYPE II SUPERCONDUCTOR, there are two critical fields: LOWER (H_{c1}) and UPPER (H_{c2}).

Critical state model: For magnetic behavior of a BEAN SLAB; in the critical state, every part of the slab operates at its CRITICAL CURRENT DENSITY.

Critical temperature, T_c***:*** The temperature that defines the transition from the superconducting to the normal state; distinguishes HTS from LTS.

Cryocirculator: A CRYOCOOLER equipped with two helium circulators that provide high-pressure streams of helium gas, typically one at 80 K and the other at 20 K.

Cryocooled magnet: A magnet cooled by a CRYOCOOLER or CRYOGENERATOR.

Cryocooler: A low-temperature refrigerator consisting generally of two stages, the 1st and 2nd, each stage providing cooling, respectively, typically in the range 50–70 K and 4.2–20 K; indispensable for a "DRY" (CRYOGEN-FREE) magnet, LTS or HTS.

Cryogen: A liquid that boils at a CRYOGENIC TEMPERATURE; e.g., helium (4.22 K at 1 atm), hydrogen (20.39 K), neon (27.10 K), nitrogen (77.36 K), argon (87.28 K).

Cryogen-free magnet: A magnet not immersed in a bath of a liquid CRYOGEN. See CRYOCOOLED MAGNET and DRY MAGNET.

Cryogenic temperature: A temperature below ∼150–200 K.

Cryopump: A pump utilizing low temperature to create and maintain a high vacuum.

Cryostable magnet: A magnet satisfying the STEKLY or "equal-area" criterion.

Cryostat: An enclosing container, made usually of metal, or for some AC applications, of insulating material, to maintain a cryogenic environment. See DEWAR and STYROFOAM.

Current sharing temperature: The temperature at which the transport current (I_t) in the conductor equals the superconductor CRITICAL CURRENT: $I_t = I_c(T_{cs})$.

Cyclotron magnet: A magnet used to produce energetic protons or electrons.

DAPAS (***D****evelopment of* ***A****dvanced* ***P****ower System by* ***A****pplied* ***S****uperconductivity*)***:*** Initiated in 2001 by Korean government, a 10-year R&D project on YBCO tape and applications of HTS to electric power (cable, fault-current limiter, motor, transformer).

DESY (***D****eutsches* ***E****lektronen* ***SY****nchrotron*)***:*** A German government-run high-energy physics research center, with principal facilities in Hamburg. See HERA.

Dewar: A vacuum vessel for holding a CRYOGEN. Named for its developer James Dewar.

Dilution refrigerator: A millikelvin-range refrigerator that makes use of the difference in entropies of He^3 and He^4; typically provides a refrigeration of 100 μW at 50 mK.

Dipole magnet: A magnet that generates a uniform field transverse to its axis over most of its bore; deflects charged particles in particle accelerators and MHD systems.

Discharge voltage: The maximum voltage appearing across the terminals of a superconducting magnet during a DUMP. Also called dump voltage.

Double pancake (coil): See PANCAKE COIL.

Driven-mode: Normal operating mode for a superconducting magnet, energized with a power source. For a magnet to maintain a "constant" field in driven mode, it requires a highly stable current source. See PERSISTENT-MODE.

Dry magnet: 1) A magnet wound without epoxy or other filler material; 2) a magnet not relying on liquid CRYOGEN for cooling.

Dump: A forced discharge of the current in a superconducting magnet in an emergency. A dump often involves opening a switch connecting the power source and the magnet and discharging most of the stored magnetic energy through a DUMP RESISTOR.

Dump resistor: A resistor through which the current in the superconducting magnet is forced to flow during a DUMP; generally placed outside the magnet CRYOSTAT.

EAST (***E****xperimental* ***A****dvanced* ***S****uperconducting* ***T****okamak*)***:*** An R&D superconducting TOKAMAK at the Institute of Plasma Physics in Hefei, China.

Eddy-current loss: A loss generated by eddy currents induced in conductive metal by a time-varying magnetic field.

Energy margin: The maximum input pulse energy (or energy density) a small winding region can tolerate and still remain superconducting; a stability parameter.

Engineering Current Density (J_e): CRITICAL CURRENT of a superconductor divided by the total cross section of the conductor.

Epoxy-impregnated magnet: An ADIABATIC MAGNET bonded with epoxy to minimize conductor motion incidents that trigger PREMATURE QUENCHes in LTS magnets.

Fault mode: A failure of a superconducting magnet system; magnet parameters generally specified on anticipated fault modes that result in the most extreme conditions.

FEA (***F****inite* ***E****lement* ***A****nalysis*)***:*** A computer-based numerical analysis technique for solving, for example, complex stress distributions in a magnet system.

Flux jumping: A thermal instability in a superconductor in which flux motion induces heat generation, which cascades to cause additional magnetic flux motion.

Flux pinning: A mechanism that inhibits fluxoid motion. The flux pinning force is thought to be supplied by the crystal structure; can be increased by material impurities and inhomogeneities caused by cold working and heat treatment to produce large J_c.

Formvar: Trade name for polyvinylformal, a venerable (century old) insulator material applicable to superconductors, despite the CRYOGENIC TEMPERATURE.

Fringing field: The magnetic field, usually a nuisance, outside a magnet system.

G-10: A laminated, thermosetting composite of epoxy and glass fabric, used in magnets and CRYOSTATs as a high-strength material where metals are unsuitable.

Gas (or vapor)-cooled lead: A current lead connecting the magnet inside the CRYOSTAT to the power source outside; the cold vapor of the boiling helium is funneled through the lead, reducing the heat load (by conduction and Joule heating) to the magnet.

GLAG theory: A phenomenological theory developed in the 1950s by V. **G**inzburg, L. **L**andau, A. **A**brikosov, and L. **G**orkov that explains the magnetic behavior of a TYPE II SUPERCONDUCTOR; describes the relationship between COHERENCE LENGTH and PENETRATION DEPTH, as well as the MIXED STATE and UPPER CRITICAL FIELD.

G-M (***G****ifford-****M****cMahon*) ***cycle:*** A variant of the STIRLING CYCLE suitable for CRYOCOOLERs; developed by W. Gifford and H. McMahon in the early 1960s.

Gradient coil: A coil that generates an axial H-field that varies linearly with position.

Hall probe: A sensor for measuring magnetic field. Based on the principle of the Hall effect: its output voltage, for a given supply current, is proportional to field strength.

He I: Another name for the non-superfluid liquid of ordinary helium (He^4).

He II: Another name for SUPERFLUID HELIUM.

He^3: A helium isotope with atomic weight 3; boils at 3.19 K at 1 atm. Naturally, $\sim 1/10^6$ as abundant as He^4. See DILUTION REFRIGERATOR.

He^4: A natural isotope of helium with atomic weight 4; boils at 4.22 K at 1 atm.

HERA (***H****adron* ***E****lektron* ***R****ing* ***A****nlage*)***:*** A particle accelerator (1992-2007) at DESY.

High-performance magnet: A magnet having a high OVERALL CURRENT DENSITY, usually an ADIABATIC MAGNET; most magnets are now high-performance.

Hot spot: The small region in the winding that attains the highest temperature after a QUENCH; generally it is at a quench initiation point.

Hot-spot temperature: The highest temperature reached at the HOT SPOT immediately after a QUENCH; hot-spot temperatures below 200 K are considered safe.

HT-7U: An R&D superconducting TOKAMAK, now called EAST.

HTS (***H****igh-****T****$_c$* ***S****uperconductor*)***:*** A class of TYPE II SUPERCONDUCTORs with T_c above $\sim$25 K, considered the limit for LTS. All HTS discovered to date, except MgB_2, are PEROVSKITE oxides, the first of which, $La_{1.85}Ba_{0.15}CuO_4$ ($T_c = 35$ K), was discovered in 1986 by K.A. Müller and J.G. Bednorz of the IBM Zürich Research Laboratory.

Hybrid (magnet): A magnet comprised of both WATER-COOLED and superconducting magnets to enhance the total magnetic field.

Hybrid shielding: A MAGNETIC SHIELDING technique which combines both ACTIVE SHIELDING and PASSIVE SHIELDING; used in some MRI and NMR magnets.

Hysteresis loss: An energy loss due to the hysteretic effect of a material property, e.g., magnetization of a TYPE II SUPERCONDUCTOR or ferromagnetic material.

Index number: The exponent n in the voltage (electric field) vs. current (current density) relationship for a superconductor; typically, n is between 10 and 100.

Induction heating: Heating generated in conductive metal by a time-varying magnetic field—called induction heating when desired and EDDY-CURRENT LOSS when it is not.

Internal diffusion process: A modified BRONZE PROCESS for Nb_3Sn developed in 1974 by Y. Hashimoto of the Mitsubishi Electric Corp.

Irreversible field: A magnetic field above which a superconductor carries insufficient transport current to be useful for magnet operation.

Iseult: A French-German project at CEA Saclay to construct a 11.74-T (500-MHz)/900-mm bore MRI superconducting magnet for cerebral imaging—all NbTi, operated at 1.8 K with a magnetic energy of ∼330 MJ; in Germany, INUMAC (Isolde, initially).

ITER (***I****nternational* ***T****hermonuclear* ***E****xperimental* ***R****eactor*)***:*** A multi-nation project to construct a break-even TOKAMAK, in the CEA Cadarache facilities, France.

"Jelly-roll" process: A process for making NbTi, Nb_3Sn, and other LTS, in which "foiled" conductor ingredients are rolled to form the basic ingot. Developed in 1976 by W.K. McDonald of Teledyne Wah Chang; also used to manufacture some HTS.

Josephson effect: A quantum effect characterized by the tunnelling of superelectrons through the insulator of a JOSEPHSON JUNCTION, and observable as current flow without a driving potential; based on the theoretical work (1964) of B. Josephson.

Josephson junction: A device with two superconducting plates separated by an oxide layer. Josephson junctions are used in SQUID and other micro-scale electronic devices.

J-T (***J****oule-****T****homson*) ***valve:*** A needle valve across which the working fluid expands adiabatically and isenthalpically; the expansion process is irreversible.

Kaiser effect: A mechanical behavior observed in a structure under cyclic loading in which events, e.g., conductor motion and epoxy fracture in a superconducting magnet, appear only when the loading exceeds the maximum level achieved in the previous cycle. Discovered by J. Kaiser in the early 1950s. See AE (ACOUSTIC EMISSION).

Kapitza resistance: The thermal boundary resistance which occurs at the interface when heat flows from a solid to liquid helium; discovered by P. Kapitza in 1941.

Kapton: Trade name for a polyimide film; useful as an insulating material.

Kevlar: Trade name for a strong and lightweight para-aramid synthetic fiber. Of three varieties of Kevlar, 29, 49, and 149, 49 is used in most cryogenic applications.

Kohler plot: A plot that combines the effects of magnetic field and temperature on the electrical resistivity of a conductive metal at CRYOGENIC TEMPERATUREs.

KSTAR (***K****orean* ***S****uperconducting* ***T****ok****A****mak* ***R****eactor*)***:*** A superconducting TOKAMAK for fusion science and technology R&D, at the Korea Basic Science Institute in Taejon.

Lambda point: The temperature below which ordinary liquid helium (He^4) becomes SUPERFLUID HELIUM; it is 2.172 K at a pressure of 38 torr (0.050 atm).

Laser cooling: A technique that uses photons, an "atom laser," to remove heat from atoms to cool them to a very low temperature—nanokelvins and picokelvins.

Layer winding: A technique to fabricate a solenoidal coil by winding conductor helically around a mandrel, one layer at a time.

LHC (***L****arge* ***H****adron* ***C****ollider*)**:** The largest particle accelerator and collider built to date, situated in CERN with a main ring (nearly circular) of 8.5-km diameter. See ATLAS and CMS; SSC and TEVATRON.

LHD (***L****arge* ***H****elical* ***D****evice*)**:** A superconducting STELLARATOR in operation at the National Institute for Fusion Science, Toki-shi, Japan. See WENDELSTEIN 7-X (W7-X).

Lorentz force: The most important force in a magnet, arising from the interaction of magnetic field and current; named for the Dutch physicist H. Lorentz (1853–1928).

Lower critical field, H_{c_1}**:** The magnetic field at which a superconductor's magnetic behavior departs from perfect diamagnetism.

LTS (***L****ow-****T****$_c$* ***S****uperconductor*)**:** Mostly metallic superconductors with $T_c < 25\,\mathrm{K}$, the first LTS (mercury) discovered in 1911 by H. Kamerlingh Onnes. During the 1950s, B.T. Matthias and others at the Bell Telephone Laboratories discovered many that are useful for magnets, e.g., Nb_3Sn; J.K. Hulm and R.D. Blaugher at the Westinghouse Research Laboratories are credited with basic studies (1961) of alloys of NbTi.

Maglev (***Mag****netic* ***lev****itation*)**:** Levitation by a magnetic force, attractive or repulsive. A German-made "attractive" (with permanent magnets) Maglev, of 500-km/h top speed (nominal: 430 km/h) and 30-km length, between the Pudong International Airport and Shanghai downtown, has been in operation since 2004. A 500-km/h 370-km long "repulsive" (with superconducting magnets) Maglev line between Tokyo and Nagoya is scheduled for operation in 2025; called "Linear" in Japan because the vehicle propulsion is based on the principle of a linear motor.

Magnet-grade superconductor: A superconductor meeting rigorous specifications of a magnet *and* available commercially. See NbTi, Nb_3Sn, Bi2212, Bi2223, MgB_2, YBCO.

Magnetic confinement: A technique in fusion reactors to confine and stabilize a hot plasma with magnetic field. See TOKAMAK and STELLARATOR.

Magnetic drag force: A drag force that arises from EDDY-CURRENT LOSS.

Magnetic pressure: A pressure equal to the magnetic energy density.

Magnetic refrigeration: Refrigeration based on ADIABATIC DEMAGNETIZATION.

Magnetic shielding: Shielding of persons or field-sensitive equipment from a FRINGING FIELD. See ACTIVE SHIELDING and PASSIVE SHIELDING.

Meissner effect: The phenomenon of complete expulsion of magnetic flux from the interior of a superconductor. Perfect diamagnetism is the most defining property of a superconductor; discovered in 1933 by W. Meissner and R. Ochsenfeld.

"Melt" process: Short for the melt-powder-melt-growth (MPMG) process that yields uniform high-quality YBCO; developed in 1991 by M. Murakami of the International Superconductivity Technology Center (ISTEC), Tokyo.

MgB_2 (Magnesium diboride): Currently the only nonoxide-HTS, a metalloid, discovered in 2001 by a team led by J. Akimitsu of the Aoyama University, Tokyo, with $T_c = 39\,\mathrm{K}$; produced as MULTIFILAMENTARY CONDUCTOR (wire and tape).

MHD (***M****agneto****H****ydro****D****ynamic*)**:** The study of the motion of an electrically conducting fluid in a magnetic field.

Mixed state: The presence of normal-state "islands" in a superconducting sea in a TYPE II SUPERCONDUCTOR over most of its magnetic field range. See GLAG THEORY.

MPZ (***M****inimum* ***P****ropagating* ***Z****one*)**:** The largest volume within a magnet winding that can support Joule heating without growing.

MRI (***M****agnetic* ***R****esonance* ***I****maging*)**:** Magnetic fields to create, through NMR, visual images of the brain and other body parts for diagnostic purposes. See ISEULT.

Multifilamentary conductor: A COMPOSITE SUPERCONDUCTOR consisting of many superconducting filaments (each typically $< 100\,\mu$m diameter), imbedded in a matrix of normal metal, with TRANSPOSITION or twisting to minimize AC LOSSes.

Mylar: Trade name for a polyester sheet (25–150 μm thickness); used as electrical or thermal insulator. More brittle than KAPTON at CRYOGENIC TEMPERATUREs.

Nb_3Sn: An intermetallic compound of niobium and tin. It and NbTi are the only LTS-based MAGNET-GRADE SUPERCONDUCTORs.

NbTi: Alloys of niobium and titanium, typically ∼50wt.%Ti; the most widely used MAGNET-GRADE SUPERCONDUCTOR (LTS or HTS).

NMR (***N****uclear* ***M****agnetic* ***R****esonance*)***:*** A quantum effect characterized by the absorption and reradiation of radio waves by nuclei in a magnetic field. NMR spectroscopy is used to study, for example, the molecular structures of organic compounds, especially proteins. Higher fields improve resolution and signal-to-noise ratio. The resonant frequency of protons (^{1}H), proportional to field, is 42.576 MHz at 1 T and 1 GHz at 23.49 T.

Nomex: Trade name for aramid; used as an insulating sheet between conductors.

NZP (***N****ormal* ***Z****one* ***P****ropagation*) ***velocity:*** The velocity of the normal-superconducting boundary; NZP velocities are much greater in LTS than in HTS.

OFHC (***O****xygen-****F****ree-****H****igh-****C****onductivity*) ***copper:*** A high-purity copper used widely in normal-metal conductors, particularly for low-temperature applications.

Ohmic heating magnet: A PULSE MAGNET that heats and stabilizes the plasma.

Overall current density: Total ampere-turns divided by the winding cross section.

Pancake coil: A "pancake-like" flat coil in which the conductor spirals outward from the center, each turn in the same plane. A DOUBLE-PANCAKE (COIL) is wound with a conductor that spirals in from the outside of one pancake and then spirals back out in the other; the helical transition turn at the inside diameter is continuous.

Paper magnet: A magnet that ends in design stage; useful for parametric study.

Passive shielding: MAGNETIC SHIELDING that generally uses ferromagnetic materials such as steel; in a cryogenic environment, HTS cylinders may be used.

PCS (***P****ersistent-****C****urrent* ***S****witch*)***:*** Shunting the terminals of a PERSISTENT-MODE superconducting magnet, it is either *closed* (superconducting) or *open* (resistive).

Penetration depth: The depth within which a surface supercurrent flows to exclude a magnetic field from the interior of a TYPE I SUPERCONDUCTOR. The concept was introduced by the brothers F. London and H. London in the 1930s.

Permanent magnet: A magnet made of magnetized ferromagnetic material with a high COERCIVE FORCE; it can provide magnetic fields up to ∼2 T over a small volume.

Perovskite: The cubic structure of most HTS, ferroelectric, ferro- and antiferri-magnetic materials. Named for the Russian minister Count L.A. von Perovski (1792–1856).

Persistent-mode: A mode for an energized superconducting magnet, decoupled from its power source and shunted by a PCS, to maintain a "constant" field. See DRIVEN-MODE.

Phenolic: A thermosetting resin, usually reinforced with laminae of linen, cotton, or even paper; weaker but easier to machine than G-10.

Piezoelectric effect: The coupling of mechanical and electric effects in which a strain in some crystals, e.g., quartz, induces an electric potential and vice versa; an AE sensor utilizes this effect. Discovered in 1880 by P. Curie (1859–1906).

Poloidal magnet: A PULSE MAGNET that generates a field in the axial (vertical) direction for plasma stabilization in a MAGNETIC CONFINEMENT-based fusion machine.

***ppm** (**p**arts **p**er **m**illion):* A dimensionless number to express a trace quantity of a substance or a deviation from a norm, e.g., a small change in field strength.

Prandtl number: A dimensionless coefficient equal to the ratio of kinematic viscosity to thermal diffusivity, a measure of the relative diffusion rates of momentum and heat in convective heat transfer. Named for L. Prandtl (1875–1953).

Premature quench: A QUENCH of a superconducting magnet below the designed operating current; still "occasionally" occurs in *some* LTS-based ADIABATIC MAGNETs.

Pulse magnet: A magnet that generates a field over a short duration, ranging from microseconds to a fraction of a second.

Quadrupole magnet: A magnet that generates a linear gradient field transverse to its axis over the central region of its bore; focuses particles in particle accelerators.

Quench: The superconducting-to-normal transition; specifically, the rapid irreversible process in which a magnet or a part of a magnet is driven fully normal.

***R3B-GLAD** (**R**eactions with **R**elativistic **R**adioactive **B**eams of Exotic Nuclei-**G**SI **L**arge **A**cceptance **D**ipole):* A CEA Saclay designed superconducting magnet system (six RACETRACK MAGNETs), to be installed at GSI (**G**esellschaft für **S**chwer**i**onenforschung, Darmstadt, Germany), to study the structure of exotic nuclei or the reaction mechanisms.

Racetrack magnet: A magnet resembling a racetrack, wound in a plane, each turn having two parallel sides, joined by a semi-circle at each end.

React-and-wind: A coil-winding technique used for a superconductor, e.g., Nb_3Sn and HTS, that has already been reacted; applicable only when winding-induced strains in the superconductor can be kept below the superconductor's strain tolerance limit.

Regenerator: A component in STIRLING and G-M CYCLEs, storing and releasing heat during isochoric processes; for operation below ∼10 K, rare-earth materials proven useful.

Reynolds number: The dimensionless ratio of inertial forces to viscous forces; characterizes the viscous flow of fluids. Named for O. Reynolds (1842–1912).

***RHIC** (**R**elativistic **H**eavy **I**on **C**ollider):* A superconducting particle accelerator and collider in operation since 2000 at the Brookhaven National Laboratory, Long Island, NY.

***RRR** (**R**esidual **R**esistivity **R**atio):* The ratio of a metal's electrical resistivity at 273 K to that below ∼10 K (often 4.2 K); indicative of the metal's purity.

Rutherford cable: A flat two-layer cable suitable for low AC LOSS applications, developed in the 1970s at the Rutherford Appleton Laboratory, England. Laid at an angle to the conductor axis, MULTIFILAMENTARY CONDUCTOR strands in each layer alternate on two sides of the cable, with a TWIST PITCH LENGTH defined by the tilt angle and the cable width; some have a high-strength strip between the strand layers for reinforcement.

Saddle magnet: A magnet with windings that resemble a saddle; saddles may be configured to produce the fields of a dipole (2); a quadrupole (4), a sextuple (6), ...

Saturation magnetization: The maximum magnetization of a ferromagnetic material.

Search coil: A coil for measuring a magnetic field; requires a very stable integrator to convert the search coil output voltage to a voltage proportional to the field strength.

Self-field loss: A hysteresis AC LOSS in a superconductor due to the magnetic field generated by a transport current.

***SFCL** (**S**uperconducting **F**ault **C**urrent **L**imiter):* A superconducting version of an FCL, a device to limit the current surge during a fault in a utility power line.

Shim coils: A set of "corrective" coils, superconducting or copper (operated at room-temperature) or both, added to the main field to make the resultant field meet spatial field requirements. Sometimes ferromagnetic materials are used to achieve the same goal.

Skin depth: The distance from a metal surface at which the amplitude of a sinusoidally time-varying magnetic field, due to the SKIN EFFECT, is 0.37 ($= 1/e$) the surface field.

Skin effect: A phenomenon of an induced surface current in a metal shielding most of the interior of the metal from a time-varying magnetic field. See SKIN DEPTH.

SMES (***S****uperconducting* ***M****agnetic* ***E****nergy* ***S****torage*)***:*** The magnetic storage of electrical energy in a superconducting magnet for power conditioning by an electric utility.

SOR (***S****ynchrotron* ***O****rbital* ***R****adiation*)***:*** A device to produce x-rays by means of accelerating electrons in a magnetic field, generated usually by superconducting magnets.

SQUID (***S****uperconducting* ***QU****antum* ***I****nterference* ***D****evice*)***:*** A device using the JOSEPHSON EFFECT to measure the smallest possible change in magnetic flux.

SSC (***S****uperconducting* ***S****uper* ***C****ollider*)***:*** Terminated in 1993, would have been the largest (larger than LHC) particle accelerator and collider for high-energy physics research.

Stekly criterion: A design criterion for a CRYOSTABLE MAGNET, in which the cooling flux matches the conductor's full normal-state Joule heating flux.

Stellarator: A toroidal plasma fusion MAGNETIC CONFINEMENT machine, invented by Lyman Spitzer (1914-1997) of the Princeton University; the first Stellarator built in 1951 at the Princeton Plasma Physics Laboratory. See LHD and WENDELSTEIN 7-X (W7-X).

Stirling cycle: A cycle incorporating a REGENERATOR. Invented, in the late 1810s, by a Scottish minister, R. Stirling (1790–1878); has the same efficiency as CARNOT CYCLE.

Storage dewar: An insulated container of liquid CRYOGEN. See CRYOSTAT and DEWAR.

Stycast: Trade name for an epoxy resin. Stycast 2850 is used in cryogenic experiments as a sealant and as a thermally conductive (among organic materials) adhesive.

Styrofoam: Trade name for polysterene foam; usable for a liquid-nitrogen CRYOSTAT.

Subcooled superfluid helium: SUPERFLUID HELIUM above its equilibrium pressure.

Submicron conductor: A MULTIFILAMENTARY CONDUCTOR having filaments of diameter $0.1 \sim 0.5\,\mu$m to reduce HYSTERESIS LOSS in 60-Hz applications.

SULTAN (Superconducting Test Facility, in German)***:*** An 11-T split-pair solenoid with a 100-mm midplane gap for testing high-current superconducting cables in a field perpendicular to their axis, at PSI (Paul Scherrer Institute) in Villigen, Switzerland.

Superconducting generator/motor: A generator/motor with a superconducting rotor.

Superconducting power transmission: Transmission of electrical power, AC or DC, using superconducting cables.

Supercritical helium: Helium above the critical point (2.26 atm and 5.20 K).

Superfluid helium: A liquid helium state with extraordinary properties that exists below 2.172 K, the LAMBDA POINT. See He II, SUBCOOLED SUPERFLUID HELIUM.

Superinsulation: Aluminized MYLAR sheets used in the vacuum space, primarily in the 80–300 K range, of a CRYOSTAT to reduce radiation heat input.

Teflon: Trade name for polytetrafluoroethylene. Valued, both in bulk and as a coating, for its low friction coefficient and retention of toughness at CRYOGENIC TEMPERATUREs.

Tevatron: The first superconducting particle accelerator, operated since the 1980s at the Fermi National Laboratory, Batavia, IL; its size and performance surpassed by LHC.

Tokamak (*Toroidal Chamber in Magnetic Coils,* in English)***:*** A toroidal-shaped thermonuclear fusion machine that incorporates MAGNETIC CONFINEMENT to contain a hot plasma; conceived in the 1950s by L.A. Artsimovich and A.D. Sakharov of the Kurchatov Institute of Atomic Energy, Moscow. See EAST, ITER, KSTAR, TORE SUPRA.

Tore Supra: A TOKAMAK with superconducting magnets in a bath of SUBCOOLED SUPERFLUID HELIUM; in operation since 1988 at the CEA Cadarache.

Toroidal magnet: A magnet that generates a field in the toroidal (azimuthal) direction to confine a hot plasma; the superconducting version is DC.

Training: Behavior of a HIGH-PERFORMANCE MAGNET whose successive PREMATURE QUENCHes gradually approach the design operating current.

Transfer line: A double-walled vacuum insulated line for transferring liquid helium from a STORAGE DEWAR to a CRYOSTAT.

Transposition: In a transposed cable, every strand occupies every radial location in the cable's overall diameter over its repeat length.

Triple point: The equilibrium state for solid, liquid, and vapor phases. Triple points of hydrogen (13.8033 K), neon (24.5561 K), oxygen (54.3584 K), argon (83.8058 K), mercury (234.3156 K), and water (273.16 K) are fixed points in the International Temperature Scale of 1990 (ITS-90). Helium does not have a triple point.

Twist pitch length: The linear distance over which 1) a filament of a twisted MULTIFILAMENTARY CONDUCTOR makes one complete spiral, or 2) a strand of transposed cable completes its repeat pattern. See TRANSPOSITION.

Type I superconductor: A superconductor that exhibits the MEISSNER EFFECT up to its critical field; called a "soft superconductor" because of its low mechanical strength.

Type II superconductor: A superconductor exhibiting the MIXED STATE; also called a "hard superconductor;" an alloy of lead-bismuth was the first Type II superconductor, discovered in 1930 by W. J. de Haas and J. Voogd of the Leiden University.

Upper critical field, H_{c_2}***:*** The magnetic field at which a TYPE II SUPERCONDUCTOR loses its superconductivity completely.

Vapor-cooled lead: See GAS (OR VAPOR)-COOLED LEAD.

von Mises stress: A measure of stress particularly appropriate for ductile materials. A material with principal stresses, σ_1, σ_2, and σ_3, will begin to yield when its von Mises stress, given by $\sqrt{[(\sigma_1-\sigma_2)^2+(\sigma_2-\sigma_3)^2+(\sigma_3-\sigma_1)^2]/2}$, exceeds the YIELD STRESS.

Water-cooled magnet: A magnet, usually made of copper or copper alloys, cooled by water, generally forced through the winding or through tubes in a cooling plate.

Wendelstein 7-X (W7-X): An R&D superconducting STELLARATOR, to be installed in Greifswald, Germany, for the Max Planck Institute for Plasma Physics; named for the Wendelstein peak, south of Munich, bordering Austria. See LHD.

Wind-and-react: A coil preparation technique consisting of two stages: winding of a coil with an "unreacted" superconductor, followed by heat treatment of the wound coil; used for a conductor such as Nb_3Sn when winding-induced strains likely would degrade the superconductor. The process is more difficult than the REACT-AND-WIND process, primarily because the high reaction temperature precludes the use of many materials, e.g., organic insulators, in the winding before the heat treatment.

YBCO: An yttrium-based HTS ($YBa_2Cu_3O_{7-\delta}$) with $T_c = 93$ K, discovered in 1987 by groups, at the University of Alabama and the University of Houston, led by P.W. Chu. Initially fabricated only in bulk; now also available as coated conductor (tape).

Yield stress: The stress at which a material begins to deform plastically, deviating from the material's initial elastic, i.e., linear, stress-strain behavior. See VON MISES STRESS.

Young's modulus: The material's stiffness, equal to the ratio of stress to strain in its *elastic* stress-strain range. Known by various terms, including modulus of elasticity.

Appendix VII
Quotation Sources and Character Identification

Jonathan Livingston (Preface, p. vii)
A seagull in Richard Bach's *Jonathan Livingston Seagull, A Story* (Avon Books, 1970); devotes his life perfecting, and teaching others, flying skills.

An old proverb (Preface, p. viii)
This and its variations are in many cultures. A Japanese version: "When we talk about next year, Demon roars."

Michael Faraday (p. 24)
P.E. Andrew, *Michael Faraday* (Wheaton & Co., 1937).

Victor F. Weisskopf (p. 36)
American J. Phys. **45**, 422 (1977).

Donald Rumsfeld (p. 70)
at a Department of Defense news briefing (February, 2002).

Bob Dylan (p. 70)
from the album *The Freewheelin' Bob Dylan* (released in 1963).

Mathias J. Leupold (p. 135)
Personal communication (1991).

Lady Bracknell (p. 147)
A guardian in Oscar Wilde's trivial comedy for serious people *The Importance of Being Earnest* (Avon Books, 1965).

Obi Wan Kenobi (p. 179)
A Jedi master, mentor to Luke Skywalker, and later an outlaw in the Tatooine mountains in George Lucas's *Star Wars* (A Del Rey Book, 1976).

Owen Warland (p. 224)
A youthful watchmaker in Nathaniel Hawthorne's allegorical tale *The Artist of the Beautiful* (A Fawcett Premier Book, 1966).

Henry D. Thoreau (p. 250)
Walden (A Signet Classic, 1960).

Heike Kamerlingh Onnes (p. 320)
K. Mendelssohn, *The Quest for Absolute Zero, The Meaning of Low Temperature Physics* (World University Library, 1966). In the original Dutch: *"Door meten tot weten."*

Immanuel Kant, Jean-Paul Sartre, Frank Sinatra (p. 328)
A 5-word epitome of each man's philosophy.

Bertrand Russell (p. 361)
Great Essays in Science, edited by Martin Gardner (A Washington Square Press Book, 1957).

Captain Nemo (p. 382)
The captain of the *Nautilus* in Jules Verne's science fiction *20,000 Leagues Under the Sea* (Translated from the French by Anthony Bonner, A Bantam Pathfinder Edition, 1962).

Arthur C. Clarke (p. 382)
Profiles of the Future, An Inquiry into the Limits of the Possible (Popular Library, 1977).

Robert Jordan (p. 387)
A Montanan mercenary in the Spanish Civil War in Ernest Hemingway's *For Whom the Bell Tolls* (Penguin Books, 1966).

O'Hara (p. 414)
Played by Peter Lorre, a member of the sophisticated beachcombers headed by Billy Dannreuther (Humphrey Bogart) in John Huston's whimsical thriller *Beat the Devil* (Santana-Romulus Production; released by United Artists, 1954).

Ada (p. 414)
Adelaida Durmanov Veen, the cousin of the protagonist in Vladimir Nabokov's poetic, antiworld novel *Ada or Ardor: A Family Chronicle* (A Fawcett Crest Book, 1969).

Ned Land (p. 453)
A Canadian harpooner on board the *Abraham Lincoln* and later a crew member of the *Nautilus* in *20,000 Leagues Under the Sea, ibid.*

Holly Golightly (p. 457)
A rural Texan turned New York's amoral playgirl in Truman Capote's *Breakfast at Tiffany's* (A Signet Book, 1959).

Medea (p. 496)
In Greek legend, an enchantress, daughter of King Æetes of Colchis, wife of Jason, whom she helped in obtaining the Golden Fleece; a heroine in many poems (e.g., Pindar, Ovid), plays (Euripides, Seneca, Glover), and operas (Mayr, Cherubini). The quotation is from Euripides' tragedy *Medea* (Translation by Philip Vellacott, Penguin Book, 1963).

Ambrose Bierce (p. 506)
The Devil's Dictionary (Dover Publications, 1958).

Richard P. Feynman (p. 534)
Rogers Commission Report on the Space Shuttle Challenger *Accident* (1986).

C. Auguste Dupin (p. 537)
An eccentric genius in Edgar Allan Poe's *The Murders in the Rue Morgue* (An Airmont Classic, 1962).

Ben Franklin (p. 545)
Reputed response to the question "what good is it?" on Montgolfier's hot air balloon experiment. *American Heritage Magazine* **25** (1973).

Figaro (p. 589)
An original and witty liar, a valet in W.A. Mozart's comic opera *Le Nozze di Figaro* (Libretto by Lorenzo da Ponte). A rough translation: "The rest I need not say, . . ."

INDEX

A page number is in **bold** when the subject is defined, described, or discussed; it is in *italics* for data (plots, tables) or figures. Also *italicized* is a parenthesized note on an entry. Generally only those entries (and names) in the ***GLOSSARY*** pertinent to the subjects in the main text are indexed. Although the *Passages* are subject to indexing, their footnotes, *Quotations*, or ***TRIVIA*** are not.

The following rules apply to a word that appears *often*: 1) if *common generic* of this textbook, e.g., *magnet(s)*, it is omitted as a primary entry but combined with other primary entries, e.g., *adiabatic*; and 2) if, like *Bean*, it has many topics, its page numbers are omitted, nearly or entirely, but its subtopics, e.g., *slab*, are entered, indented, beneath it with their page numbers; the rules also apply to subtopics, e.g., *AC losses*, and sub-subtopics, if any, e.g., *hysteresis*.

Generally for materials, e.g., *copper*, only page numbers listing their property values, e.g., *enthalpy*, are entered; the rule conversely applies to property entries: thus, e.g., *solid cryogens (SAr, SN_2, SNe)* under *enthalpy*.

Selected symbols defining, with one exception, dimensionless parameters all unique to this textbook.

"Time always plays an asymmetric game: looking into the future, a decade or a generation seems so long that almost anything is achievable, yet looking back to the past, even a generation seems only yesterday."